WILEY

PULSED LASER DEPOSITION OF THIN FILMS

Applications-Led Growth of Functional Materials

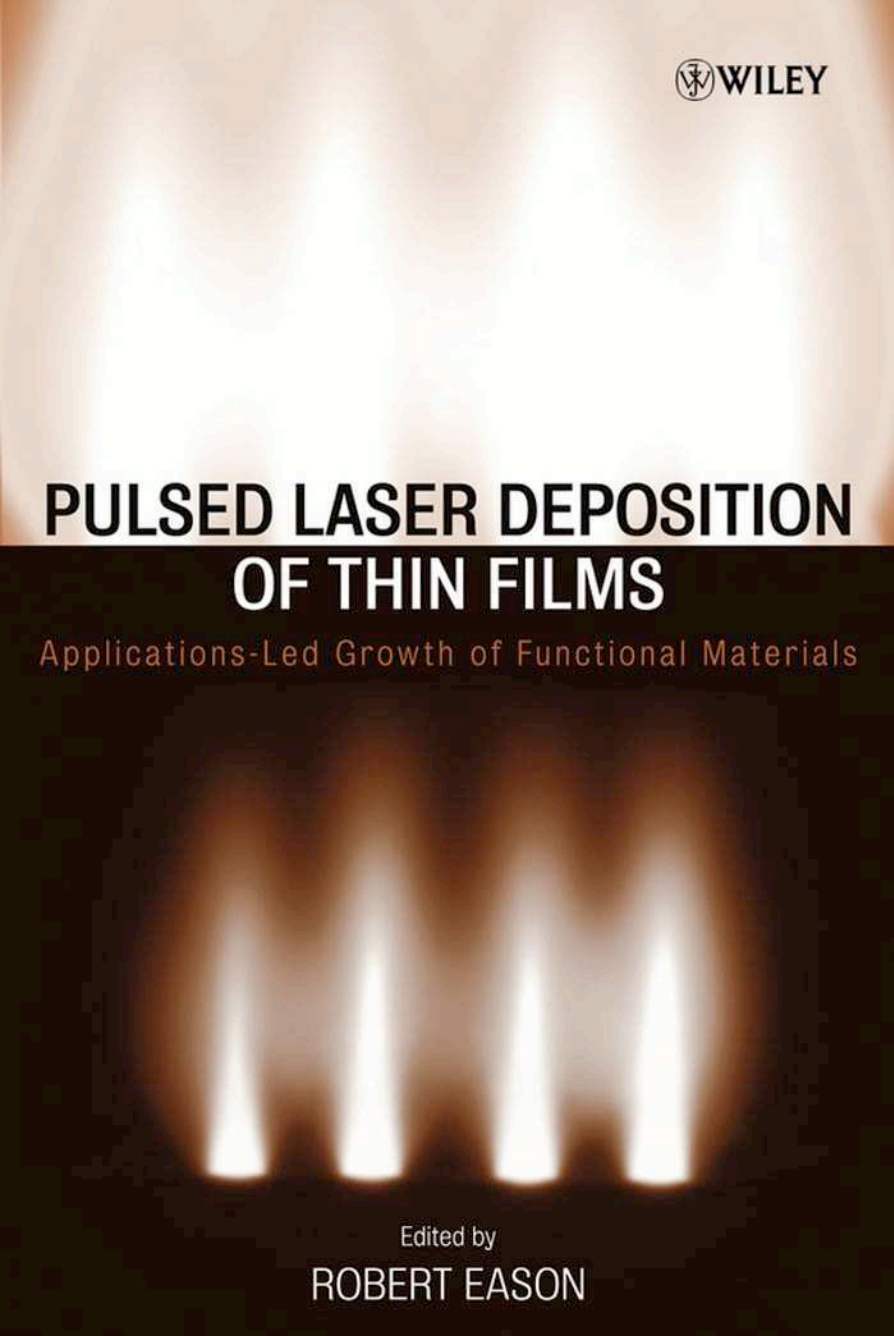

Edited by

ROBERT EASON

PULSED LASER DEPOSITION OF THIN FILMS

THE WILEY BICENTENNIAL–KNOWLEDGE FOR GENERATIONS

Each generation has its unique needs and aspirations. When Charles Wiley first opened his small printing shop in lower Manhattan in 1807, it was a generation of boundless potential searching for an identity. And we were there, helping to define a new American literary tradition. Over half a century later, in the midst of the Second Industrial Revolution, it was a generation focused on building the future. Once again, we were there, supplying the critical scientific, technical, and engineering knowledge that helped frame the world. Throughout the 20th Century, and into the new millennium, nations began to reach out beyond their own borders and a new international community was born. Wiley was there, expanding its operations around the world to enable a global exchange of ideas, opinions, and know-how.

For 200 years, Wiley has been an integral part of each generation's journey, enabling the flow of information and understanding necessary to meet their needs and fulfill their aspirations. Today, bold new technologies are changing the way we live and learn. Wiley will be there, providing you the must-have knowledge you need to imagine new worlds, new possibilities, and new opportunities.

Generations come and go, but you can always count on Wiley to provide you the knowledge you need, when and where you need it!

William J. Pesce

WILLIAM J. PESCE
PRESIDENT AND CHIEF EXECUTIVE OFFICER

Peter Booth Wiley

PETER BOOTH WILEY
CHAIRMAN OF THE BOARD

PULSED LASER DEPOSITION OF THIN FILMS

APPLICATIONS-LED GROWTH OF FUNCTIONAL MATERIALS

Edited by

Robert Eason
Optoelectronics Research Centre
University of Southampton, UK

WILEY-INTERSCIENCE
A JOHN WILEY & SONS, INC., PUBLICATION

Published by John Wiley & Sons, Inc., Hoboken, New Jersey
Published simultaneously in Canada

Library of Congress Cataloging-in-Publication Data:

Pulsed laser deposition of thin films:applications-led growth of functional materials/
edited by Robert Eason.
p. cm.
"A Wiley-Interscience publication."
Includes bibliographical references and index.
ISBN-13: 978-0-471-44709-2
ISBN-10: 0-471-44709-9
1. Thin films. 2. Laser beams–Industrial applications. I. Eason, Robert, 1953-

TA418.9T45P85 2006
621.3815′2–dc22 2006044264

Printed in the United States of America

10 9 8 7 6 5 4 3 2 1

Dedication

I would like to dedicate this book to my mother, Mrs. Helena Eason, and to my daughters, Katie Alice, Emily Beth, and Jessica Rosanna. I do not know if they are devotees of PLD and all its varied possibilities, but if not, then there is always time to change track, I believe.

I would further like to thank all the authors for their patience and resilience in the face of adversity, and the editorial time dilation phenomenon that has somehow extended the due date for publication. Mea culpa to all.

Finally, many thanks to Doug Chrisey who was an editor on PLD1 and with whom I have had many discussions concerning PLD2. Although in the end he does not appear as a co-editor, in the early stages he was a guiding light in steering this book to completion. Doug, many thanks.

CONTENTS

PREFACE

In the last 15–20 years, pulsed laser deposition (PLD) has emerged as one of the most popular and intrinsically simple techniques for depositing a wide range of the most exciting materials being explored for next-generation applications. Such sustained popularity is due to the inherent versatility, flexibility, and speed of a process that can be applied to essentially *any* material, from simple metals, through binary compounds, to multicomponent high-quality single crystals. Starting in late 1986 with the discovery of high-temperature superconductors (HTS), the technique of pulsed laser deposition was ''reinvented'' from its early demonstration following the invention of high-power pulsed laser sources in the 1960s. HTS materials are perovskites and as such presented unique challenges for thin-film deposition; they were multicomponent, they were oxides, and their final properties were highly dependent on oriented and/or epitaxial film growth.

In retrospect, it is clear that it was the excitement and perhaps unrealistic potential of the HTS materials in numerous applications that fueled this rediscovery of PLD. Today the technique is being applied to the widest possible range of material growth from single atomic layers to quasi-bulk crystalline materials with thicknesses exceeding 100 μm. In this context, therefore, PLD must be viewed as a unique process technology for material growth of both thin and thick films, capable of the rapid production of device–quality functional materials.

In 1994, *Pulsed Laser Deposition of Thin Films* was successfully published by Wiley and has become the handbook of PLD for the past decade. It was clear, however, that a second volume was necessary as PLD has moved on considerably during this period. A new text that reflected this dramatic change of emphasis and direction was also needed. PLD as a technique is now used by numerous researchers from very different experimental backgrounds and has found ready application in industrial, academic, and government laboratories. This new volume summarizes the *state-of-the-art progress* in the PLD technique, the new materials that have been grown, and the application areas to which they are being applied.

The intention is that this volume serves as a benchmark upon which all subsequent work would be measured. For new researchers entering the field, it will serve as a springboard to promote their awareness into topical new activities. Perhaps more importantly, however, this text will be the final one to deal exclusively with research and development applications; any subsequent texts must inevitably address the fully commercial uses of PLD. This text, therefore, will be used as the bridge for the transition of PLD from the laboratory to full commercial fabrication, which hopefully will be the subject of the third text in this PLD trilogy to be published in a further 10 years time.

This volume has been arranged in the following manner:

Section 1 provides a single-chapter introduction to the technique of PLD of complex materials and is directed specifically toward applications. It has been a deliberate editorial policy in this text neither to include nor duplicate the same level of theoretical description of the physics behind laser-produced plasmas that appeared in the first volume, and that is otherwise covered in many other specialist texts. Apart from the physics associated with ultrafast PLD using picosecond and femtosecond laser sources that appears in Section 2, Chapter 5, the text has been devoted to applications, materials, and devices.

Section 2 discusses the use of PLD in nonstandard or unconventional format and covers resonant infrared laser induced PLD (Chapter 2) and matrix-assisted growth techniques (MAPLE) for deposition of polymers or other fragile species (Chapter 3). The technique of reflection high-energy

electon diffraction (RHEED) is the subject of Chapter 4 and discusses the use of in-situ diagnosis of the growth of epitaxial thin films. This technique is then subsequently applied to examine growth kinetics in Chapter 8. The use of ultrashort (picosecond and femtosecond) laser pulses for PLD is discussed in Chapter 5, and this chapter alone contains a detailed analysis of laser–plasma interaction in this ultrashort pulse time frame. Multiple targets to eliminate or reduce the problem of particulates is covered in Chapter 6, and the results of this technique for supersmooth film growth is shown. The combinatorial approach to PLD growth is discussed in Chapter 7, illustrating the potential advantages for rapid high-throughput material optimization. The final chapter in this section, Chapter 9, covers industrial scale-up of an area that must be addressed if PLD is ever to escape from the laboratory into the fully commercial arena.

Section 3 addresses the detailed growth and characterization of a range of materials that have been selected to be both topical and representative of those functional device-quality materials that are the goal of current PLD growth and research. The ordering of chapters in this section does not follow any particular sequence: topics covered span elemental materials such as carbon, and its diamond-like thin-film phase (Chapter 15), pure metals and alloys (Chapter 16), binary compounds such as ZnO and GaN (Chapters 12 and 13), to the more complicated and experimentally demanding multicomponent materials such as powders for drug encapsulation (Chapter 10), thin conducting oxide films (Chapter 11), and high-temperature superconductors (Chapter 14).

The intention in this section was to provide example systems where PLD has a definite edge over other deposition techniques, and the reader is encouraged to view the content in this section within this intentionally broad remit. The aim was to show the unique capability of PLD for a diverse range of materials and discipline-specific application areas.

Section 4 presents a differently slanted selection of application areas, but this time focuses on broader ''themed'' material classes and devices. The section opens with waveguide materials (Chapter 17) and addresses single-crystalline optical waveguide growth of films with thicknesses that can exceed 100 μm. Chapter 18 concerns biomaterials for application in biocompatible, bioactive thin layers for bone and dental surgery and implantology. Chapters 19, 20, and 21 discuss recent developments and applications in the very broad categories of thermoelectrics, piezoelectrics, and ferroelectrics and emphasis is placed in all these chapters on the precision required, and achieved, through PLD growth where device-quality material is paramount. The section concludes with chapters on solid-state materials for electrochemical applications (Chapter 22) and tribological coatings (Chapter 23) for wear-resistant and friction-reducing coatings.

Section 5 presents two chapters that fall in the area of new concepts. Chapter 24 discusses the highly topical area of laser ablative synthesis of single-wall carbon nanotubes, and the final chapter concerns quasicrystals, materials that exhibit quasi-periodic order exhibiting 5- or 10-fold rotational symmetry.

It is hoped that this second volume, PLD2, produces as much excitement within the materials community as PLD1 did a decade ago. The number of researchers in the field must have expanded 10-fold during the past 10 years, and at this rate of growth, PLD3, to be expected sometime around 2015, must surely be set to beat all sales records. I hope the readers enjoy the book and find it a useful manual, tutorial handbook, and reference bible.

ROB EASON

July 2006

CONTRIBUTORS

Stephen J. Barrington, Optoelectronics Research Centre, University of Southampton, Southampton, SO17 1BJ, United Kingdom

Dave H. A. Blank, MESA+ Institute for Nanotechnology, Faculty of Science and Technology, University of Twente, P.O. Box 217, 7500 AE Enschede, The Netherlands

Daniel-Dennis McAlevy Bubb, Department of Physics, Rutgers University—Camden, Camden, New Jersey 08102 and Naval Research Laboratory, Code 6365, Washington, D.C. 20375

Chonglin Chen, Department of Physics and Astronomy, University of Texas at San Antonio, 6900 N. Loop 1604 W, San Antonio, Texas 78249

Floriana Craciun, Instituto dei Sistemi Complessi, Consiglio Nazionale delle Ricerche, Via del Fosso del Cavaliere 100, I-00133 Rome, Italy

Valentin Craciun, Major Analytical Instrumentation Center, Materials Science and Engineering, University of Florida, Gainesville, Florida 32611

Anne Dauscher, Laboratoire de Physique des Matériaux (UMR 7556), Ecole Nationale Supérieure des Mines de Nancy, Parc de Saurupt, F-54042 Nancy, France

Margaret I. Davis, Nanotherapeutics, Inc., Alachua, Florida 32615 and National Institute on Alcohol Abuse and Alcoholism, Rockville, Maryland 20852

Maria Dinescu, National Institute for Lasers, Plasma and Radiation Physics, Institute of Atomic Physics, P.O. Box MG-16, 76900 Bucharest, Romania

Robert W. Eason, Optoelectronics Research Centre, University of Southampton, Southampton, SO17 1BJ, United Kingdom

Barbel Eppler, Nanotherapeutics, Inc., Alachua, Florida 32615

James M. Fitz-Gerald, University of Virginia, Charlottesville, Virginia 22904

Eugene G. Gamaly, Centre for Ultra-High Bandwidth Devices for Optical Systems and Australian Photonics Cooperative Research Centre, Laser Physics Centre, Research Schoool of Physical Science and Engineering, Australian National University, Canberra, ACT 0200, Australia

André Gorbunoff, University of Applied Sciences—Dresden, Friedrich-List-Platz 1, D-01069 Dresden, Germany

Jim Greer, PVD Products, 231 Andover Street, Wilmington, Massachusetts 01887

Christos Grivas, Optoelectronics Research Centre, University of Southampton, Southampton, SO17 1BJ, United Kingdom

Richard F. Haglund, Jr., Department of Physics and Astronomy and W. M. Keck Foundation Free-Electron Laser Center, Vanderbilt University, Nashville, Tennessee 37235

Jim S. Horwitz, Materials Sciences and Engineering Division, Office of Basic Energy Sciences, U.S. Department of Energy, 1000 Independence Avenue, SW, Washington, D.C. 20585-1290

Miroslav Jelínek, Institute of Physics ASCR, Prague, Czech Republic

John G. Jones, Air Force Research Laboratory, Materials and Manufacturing Directorate, 2941 P St., Bldg. 654, Wright-Patterson Air Force Base, Ohio 45433-7750

Oliver Jost, University of Technology Dresen, Dresden, Germany

Heungsoo Kim, Naval Research Laboratory, Code 6364, 4555 Overlook Ave., SW, Washington, D.C. 20375

Hans-Ulrich Krebs, Institut für Materialphysik, University of Göttingen, Friedrich-Hund-Platz 1, 37077 Göttingen, Germany

Bertrand Lenoir, Laboratoire de Physique des Matériaux (UMR 7556), Ecole Nationale Supérieure des Mines de Nancy, Parc de Saurupt, F-54042 Nancy, France

Thomas Lippert, Paul Scherrer Institut, General Energy Research Department, 5232 Villigen PSI, Switzerland

Barry Luther-Davies, Centre for Ultra-High Bandwidth Devices for Optical Systems and Australian Photonics Cooperative Research Centre, Laser Physics Centre, Research Schoool of Physical Science and Engineering, Australian National University, Canberra, ACT 0200, Australia

James G. Lunney, Physics Department, Trinity College, Dublin 2, Ireland

Timothy C. May-Smith, Optoelectronics Research Centre, University of Southampton, Southampton, SO17 1BJ, United Kingdom

Andrew L. Mercado, University of Virginia, Charlottesville, Virginia 22904

Ion N. Mihailescu, National Institute for Lasers, Plasma and Radiation Physics. Lasers Department, Bucharest, Romania

Eric Millon, Laboratoire Spectrométrie de Masse et de Chimie Laser, Université de Metz, 1 Bd Arago, Technopôle 2000, 57078 Metz Cedex 3, France

Macarena J. Montenegro, Paul Scherrer Institut, General Energy Research Department, 5232 Villigen PSI, Switzerland

David P. Norton, University of Florida, Department of Materials Science and Engineering, Gainesville, Florida 32611

Roger J. Narayan, Joint Department of Biomedical Engineering, University of North Carolina at Chapel Hill, 152 MacNider Hall, Campus Box 7575, Chapel Hill, North Carolina 27599-7575

Valentin Nelea, National Institute for Lasers, Plasma and Radiation Physics. Lasers Department, Bucharest, Romania

Donagh O'Mahony, Physics Department, Trinity College, Dublin 2, Ireland

Jacques Perrière, Groupe de Physique des Solides, Universités Paris VI et VII, Tour 23, 2, Place Jussieu, 75251 Paris Cedex 05, France

Alberto Piqué, Naval Research Laboratory, Materials Science and Technology Division, Code 6364, Washington, D.C. 20375

Guus Rijnders, MESA+ Institute for Nanotechnology, Faculty of Science and Technology, University of Twente, P. O. Box 217, 7500 AE Enschede, The Netherlands

Andrei V. Rode, Centre for Ultra-High Bandwidth Devices for Optical Systems and Australian Photonics Cooperative Research Centre, Laser Physics Centre, Research School of Physical Science and Engineering, Australian National University, Canberra, ACT 0200, Australia

Bernd Schey, AxynTeC Thin Film Technology GmbH, Augsburg, Germany

David P. Shepherd, Optoelectronics Research Centre, University of Southampton, Southampton, SO17 1BJ, United Kingdom

Ichiro Takeuchi, Department of Materials Science and Engineering and Center for Superconductivity Research, University of Maryland, College Park, Maryland 20742

James D. Talton, Nanotherapeutics, Inc., Alachua, Florida 32615

Andrey A. Voevodin, Air Force Research Laboratory, Materials and Manufacturing Directorate, 2941 P St., Bldg. 654, Wright-Patterson Air Force Base, Ohio 45433-7750

Philip R. Willmott, Swiss Light Source, Paul Scherrer Institut, CH-5232 Villigen, Switzerland

Jeffrey S. Zabinski, Air Force Research Laboratory, Materials and Manufacturing Directorate, 2941 P St., Bldg. 654, Wright-Patterson Air Force Base, Ohio 45433-7750

SECTION 1

CHAPTER 1

Pulsed Laser Deposition of Complex Materials: Progress Towards Applications

DAVID P. NORTON

University of Florida, Department of Materials Science and Engineering, Gainesville, Florida

1.1 INTRODUCTION

In experimental science, it is a rare thing for a newly discovered (or rediscovered) synthesis technique to immediately deliver both enhanced performance and simplicity in use in a field of accelerating interest. Nevertheless, such was the case with the rediscovery of pulsed laser deposition (PLD) in the late 1980s. The use of a pulsed laser as a directed energy source for evaporative film growth has been explored since the discovery of lasers [Hass and Ramsey, 1969; Smith and Turner, 1965]. Initial activities were limited in scope and involved both continuous-wave (cw) and pulsed lasers. The first experiments in pulsed laser deposition were carried out in the 1960s; limited efforts continued into the 1970s and 1980s. Then, in the late 1980s, pulsed laser deposition was popularized as a fast and reproducible oxide film growth technique through its success in growing in situ epitaxial high-temperature superconducting films [Inam et al., 1988]. The challenges for in situ growth of high-temperature superconducting oxide thin films were obvious. The compounds required multiple cations with diverse evaporative properties that had to be delivered in the correct stoichiometry in order to realize a superconducting film. Simultaneously, the material was an oxide, requiring an oxidizing ambient during growth. Pulsed laser deposition had several characteristics that made it remarkably competitive in the complex oxide thin-film research arena as compared to other film growth techniques. These principle attractive features were stoichiometric transfer, excited oxidizing species, and simplicity in initial setup and in the investigation of arbitratry oxide compounds. One could rapidly investigate thin-film deposition of nearly any oxide compound regardless of the complexity of the crystal chemistry. Significant development of pulsed laser deposition has continued and over the past 15 years, PLD has evolved from an academic curiousity into a broadly applicable technique for thin-film deposition research [Saenger, 1993; Kaczmarek, 1997; Willmott and Huber, 2000; Dubowski, 1988; Dieleman et al., 1992]. Today, PLD is used in the deposition of insulators, semiconductors, metals, polymers, and even biological materials. Few material synthesis techniques have enjoyed such rapid and widespread penetration into research and application venues.

Pulsed Laser Deposition of Thin Films: Applications-Led Growth of Functional Materials
Edited by Robert Eason

1.2 WHAT IS PLD?

The applicability and acceptance of pulsed laser deposition in thin-film research rests largely in its simplicity in implementation. Pulsed laser deposition is a physical vapor deposition process, carried out in a vacuum system, that shares some process characteristics common with molecular beam epitaxy and some with sputter deposition. In PLD, shown schematically in Figure 1.1, a pulsed laser is focused onto a target of the material to be deposited. For sufficiently high laser energy density, each laser pulse vaporizes or ablates a small amount of the material creating a plasma plume. The ablated material is ejected from the target in a highly forward-directed plume. The ablation plume provides the material flux for film growth. For multicomponent inorganics, PLD has proven remarkably effective at yielding epitaxial films. In this case, ablation conditions are chosen such that the ablation plume consists primarily of atomic, diatomic, and other low-mass species. This is typically achieved by selecting an ultraviolet (UV) laser wavelength and nanosecond pulse width that is strongly absorbed by a small volume of the target material. Laser absorption by the ejected material creates a plasma. For the deposition of macromolecular organic materials, conditions can be chosen whereby absorption is over a larger volume with little laser absorption in the plume. This permits a large fraction of the molecular material to be ablated intact. For polymeric materials, transfer of intact polymer chains has been demonstrated. For even ''softer'' materials in which the direct absorption by the laser would be destructive to molecular functionality, the formation of composite ablation targets consisting of the soft component embedded in an optically absorbing matrix has been investigated (see, e.g., Chapter 3).

Several features make PLD particularly attractive for complex material film growth. These include stoichiometric transfer of material from the target, generation of energetic species, hyperthermal reaction between the ablated cations and the background gas in the ablation plasma, and compatibility with background pressures ranging from ultrahigh vacuum (UHV) to 1 Torr. Multication films can be deposited with PLD using single, stoichiometric targets of the material of interest, or with multiple targets for each element. With PLD, the thickness distribution from a

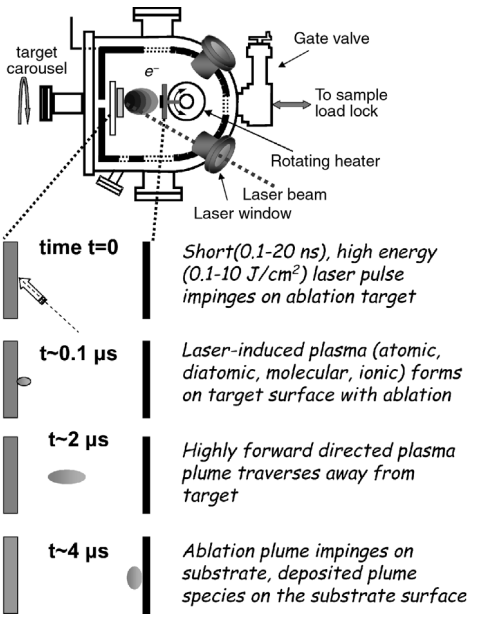

Figure 1.1 Schematic of the PLD process.

stationary plume is quite nonuniform due to the highly forward-directed nature of the ablation plume. To first order, the distribution of material deposited from the ablation plume is symmetric with respect to the target surface normal and can be described in terms of a $\cos^n(\theta)$ distribution, where n can vary from $\sim$4–30. However, raster scanning of the ablation beam over the target and/or rotating the substrate can produce uniform film coverage over large areas, and this topic is covered in Chapter 9.

One of the most important and enabling characteristics in PLD is the ability to realize stoichiometric transfer of ablated material from multication targets for many materials. This arises from the nonequilibrium nature of the ablation process itself due to absorption of high laser energy density by a small volume of material. For low laser fluence and/or low absorption at the laser wavelength, the laser pulse would simply heat the target, with ejected flux due to thermal evaporation of target species. In this case, the evaporative flux from a multicomponent target would be determined by the vapor pressures of the constituents. As the laser fluence is increased, an ablation threshold is reached where laser energy absorption is higher than that needed for evaporation. The ablation threshold is dependent on the absorption coefficient of the material and is thus wavelength dependent. At still higher fluences, absorption by the ablated species occurs, resulting in the formation of a plasma at the target surface. With appropriate choice of ablation wavelength and absorbing target material, high-energy densities are absorbed by a small volume of material, resulting in vaporization that is not dependent on the vapor pressures of the constituent cations.

In pulsed-laser deposition, a background gas is often introduced that serves two purposes. First, the formation of multication thin-film materials often requires a reactive species (e.g., molecular oxygen for oxides) as a component of the flux. The amount of reactant gas required for phase formation will depend on the thermodynamic stability of the desired phase. Interaction of ablated species with the background gas often produces molecular species in the ablation plume. These species facilitate multication phase formation. In addition to actively participating in the chemistry of film growth, the background gas can also be used to reduce the kinetic energies of the ablated species. Time-resolved spectroscopy studies of ablation plume expansion have shown that kinetic energies on the order of several hundred electron volts can be observed [Chen et al., 1996]. A background gas can moderate the plume energies to much less than 1 eV. The vapor formed by laser ablation compresses the surrounding background gas resulting in the formation of a shock wave. Interaction with the ambient gas slows the ablation plume expansion.

For the deposition of multication materials, target selection can have significant impact on film growth properties, including particulate density, epitaxy, phase formation, and deposition rate. As a minimum requirement, ablation requires a target material possessing a high optical absorption coefficient at the selected laser wavelength. In general, the phase of the target does not need to be the same as that of the desired film. Only the cation stoichiometry need be identical to that of the films, assuming stoichiometric transfer and negligible evaporation from the film surface. For ceramic targets, one prefers target materials that are highly dense, as this will reduce particulate formation during the ablation process. As an alternative to polycrystalline ceramics, the use of single crystals as ablation targets has been investigated and shown to be effective in further reduction of droplet densities [Li et al., 1998]. The exception to this is wide bandgap insulators, such as Al_2O_3, where insufficient optical absorption makes single crystals unattractive as ablation targets. For soft materials, including biological materials, the target might be the material of interest or the material embedded in a matrix of an optically absorbing substance that does not deposit but yields an efficient ablation process.

An alternative to ceramic or single-crystal targets is reactive PLD where the targets consist of the constituent cations, while the anion is supplied by the background gas. In general, the ablation process is less efficient for metal cations due to higher reflectivity and thermal conductivity. In addition, films deposited via ablation of metal targets can exhibit high particulate densities due to the ejection of molten droplets: for some systems, this problem can be addressed by using liquid metal targets. For some specific multication systems, metal targets have useful advantages. For the growth of multication films in which cation purity is an important issue, metals are often available with the

highest purity. In addition, for insulators that possess particularly wide optical bandgaps, such as MgO, the ablation efficiency from ceramic or single-crystal targets is low for commercially available pulsed laser wavelengths.

One also needs to consider the laser wavelength used for ablation. Efficient ablation of the target material requires the nonequilibrium excitation of the ablated volume to temperatures well above that required for evaporation. This generally requires the laser pulse to be short in duration, high in energy density, and highly absorbed by the target material. For ceramic targets, this is most easily achieved via the use of short wavelength lasers operating in the ultraviolet. High-energy ultraviolet laser pulses can be readily provided via excimer lasers or frequency-tripled or quadrupled Nd : YAG solid-state lasers. In some cases, a more efficient source is an infrared laser whose energy corresponds to a vibrational mode of the ablation target material [Bubb et al., 2002].

In laser ablation, each ablation pulse will typically provide material sufficient for the deposition of only a submonolayer of the desired phase. The amount of film growth per laser pulse will depend on multiple factors, including target–substrate separation, background gas pressure and laser spot size, and laser energy density. Under typical conditions, the deposition rate per laser pulse can range from 0.001 to 1 Å per pulse. As such, PLD enables laser shot-to-shot control of the deposition process that is ideal for multilayer and interface formation where submonolayer control is needed. This degree of control can be seen from the in situ surface studies using reflection high-energy electron diffraction (RHEED), as discussed in detail in Chapter 8 [Bozovic and Eckstein, 1995; Foxon, 1991]. RHEED provides a means of determining the crystallinity and smoothness of a surface, and oscillations in the intensity of diffraction spots during film growth correlate to the atomic layer-by-layer growth of the material. Figure 1.2 shows the specular intensity of RHEED data for an epitaxial oxide film being deposited by PLD [Rijnders et al., 2000]. Two types of time-

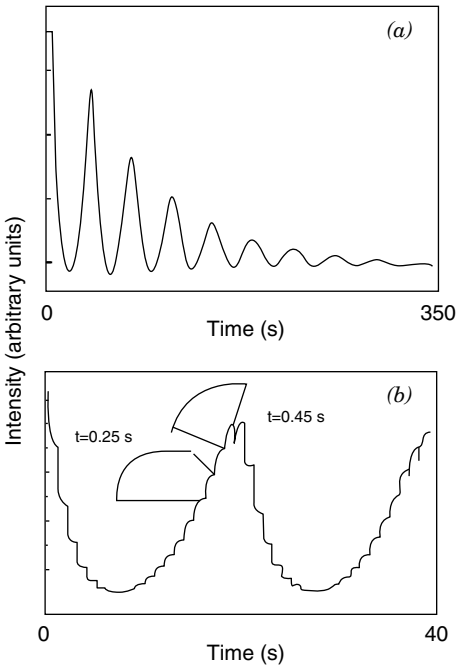

Figure 1.2 The specular RHEED intensity during PLD at 1 Hz ($T = 750°C$, $pO_2 = 3$ Pa). The insets give enlarged intensity after one laser pulse at 0.9 and 0.95 unit-cell layer coverage θ. Also shown is (a) intensity variations of the specular reflection during PLD at 1 Hz and (b) interval deposition using the laser repetition rate of 10 Hz ($T = 800°C$, $pO_2 = 10$ Pa) [Rijnders et al., 2000].

dependent structure can be observed in the RHEED intensity plot. First, the oscillations observed in the intensity in Figure 1.2a represent the deposition of single unit cells of the oxide film. Specular RHEED intensity is dependent on the spatial coherence of the surface atoms. As layer-by-layer growth cycles through submonolayer coverage of the surface, RHEED intensity decreases, while for completed layers, the intensity is high. The oscillations seen in Figure 1.2a indicate that unit cell by unit cell growth on an atomically flat surface is occurring. The superimposed time-dependent substructure in the RHEED intensity seen in Figure 1.2b corresponds to surface redistribution of ablation plume species that have condensed on the surface from an individual ablation pulse. The time dependence of this structure yields insight into the nucleation and growth of the film at the submonolayer level for the arrival of each ablation plume.

For multicomponent film growth, most of the limitations identified early in the development of PLD have been allieviated. A key development for the utilization of pulsed laser deposition for applications in industry has been the realization of schemes by which large area substrates can be effectively coated. The dynamics of the laser ablation process result in a highly focused plume of material ejected from the target. While this leads to a deposition efficiency on the order of 70%, it also results in a significant variation in deposition rate over distances on the order of a few centimeters. For uniform film thickness over large areas, manipulation of the plume–substrate positioning is required. Several approaches have been implemented to overcome this limitation, the most straightforward being to combine substrate rotation with rastering of the ablation beam over a large ablation target. This will, to first order, provide a means for covering large area substrates. However, one must take into account the decrease in plume energies and change in plume stoichiometry as one moves to the edge of the plume region.

In pulsed laser deposition, the kinetic energies of ions and neutral species in the ablation plume can range from a few tenths to as high as several hundred electron volts. These energies are sufficient to modify the stress state of films through defect formation as has been documented for ion-beam-assisted approaches. The most common consequence of allowing deposition from an unabated energetic plume is the introduction of compressive stress. The origin of compressive stress due to energetic bombardment is associated with subsurface damage from the impinging energetic species, as schematically illustrated in Figure 1.3, leading to interstitial defects [Norton et al., 1999]. In this

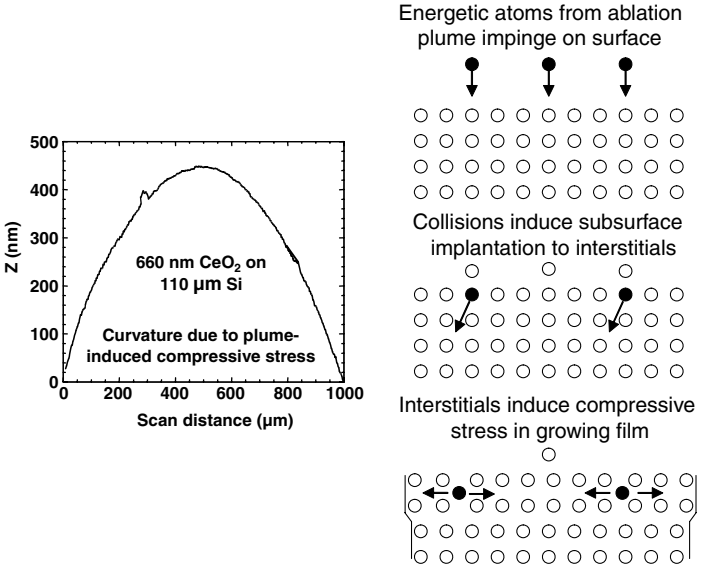

Figure 1.3 Schematic of plume-induced stress in PLD-deposited films.

case, the energetic depositing atoms displace underlying atoms in the film, resulting in atoms displaced to interstitial sites. Stress on the order of gigapascals has been observed. For thin substrates, this compressive stress can be sufficient to induce bowing of the structure as indicated in Figure 1.3 for CeO_2 on a thin Si wafer. The kinetic energy necessary for the onset of recoil implantation of surface atoms into the film interior through bombardment is material dependent but is often observed for ion bombarding energies of a few electron volts or greater [Muller, 1989]. For oxides, the energetic bombarding cations can also preferentially sputter oxygen atoms from the surface, resulting in films that are oxygen deficient. The kinetic energy of ablated species is largely dependent on laser energy and gas-phase collisions. Fortunately, the use of a background gas to thermalize the plume is usually effective in eliminating this problem.

Another potential issue with PLD is the ejection of micron-size particles in the ablation process. This is often observed when the penetration depth of the laser pulse into the target material is large. If these particles are deposited onto the substrate, they present obvious problems in the formation of multilayer device structures. The use of highly dense ablation targets and ablation wavelengths that are strongly absorbed by the target tends to reduce or eliminate particle formation. Mechanical techniques have been developed to reduce particle density in the event that target density and/or laser wavelength optimization fails to eliminate particulates. These include velocity filters [Pechen et al., 1995], off-axis laser deposition [Holzapfel et al., 1992], and line-of-sight shadow masks [Trajanovic et al., 1997]. Cross-beam techniques have also been considered as described in Chapter 6.

In addition to particles ejected from the ablation targets, one can also observe nanoparticles that form in the gas phase when the background pressure is sufficiently high for heterogeneous particle nucleation. These particles can become embedded in a depositing film. Figure 1.4 shows a cross-section transmission electron microscopy image of a CeO_2 film with the initial growth occurring at high pressure while the remaining film was grown at low pressure. CeO_2 nanoparticles are clearly evident in the epitaxial CeO_2 thin-film matrix [Norton et al., 1998]. In particular, the nanoparticles, with diameters ranging from 10 to 40 nm, are seen in the layer formed by ablating a CeO_2 target in a hydrogen–argon background gas at a pressure of 200 mTorr. In contrast, the upper part of the CeO_2 film is devoid of nanoparticles and was deposited in a background pressure of 10^{-5} Torr where gas-phase collisions are minimal. While the formation of nanoparticles is generally undesirable for thin-film growth, this heterogeneous gas-phase nucleation has been intentionally exploited in the synthesis and study of nanomaterials, including oxides and semiconductors.

While stoichiometric transfer of target composition is readily achieved for nearly every material, this does not ensure stoichiometric film growth at elevated temperature if any of the cation species possess high vapor pressures. Specific cations for which the sticking coefficient is an issue include K, Li, Na, Tl, Mg, Pb, Cd, and Zn. We consider as an example $ZnGa_2O_4$ [Lee et al., 1999], which is a wide bandgap semiconducting spinel that is of interest as a phosphor material. Films deposited using a stoichiometric single $ZnGa_2O_4$ target will show significant Zn deficiency for elevated deposition temperatures due to the higher vapor pressure of Zn relative to that of Ga. Figure 1.5 shows the

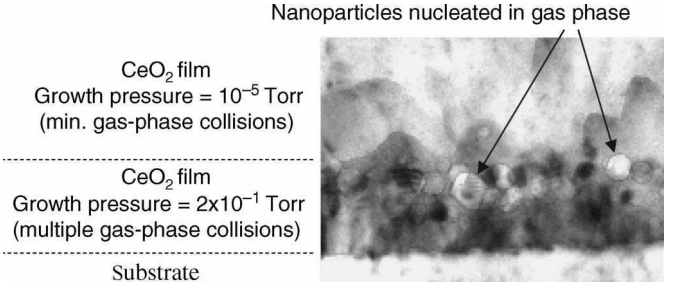

Figure 1.4 Cross-section TEM image of a CeO_2 film grown at high and low pressure, with CeO_2 nanoparticles forming at the high background pressure.

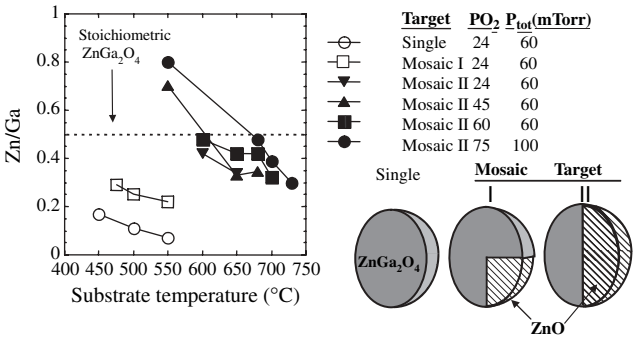

Figure 1.5 Plot of the Zn/Ga ratio for $ZnGa_2O_4$ films deposited using mosaic ablation targets.

Zn/Ga ratio for films deposited at several different background pressures. Note that stoichiometric $ZnGa_2O_4$ corresponds to a Zn/Ga ratio of 0.5. Using a stoichiometric target, a Zn/Ga ratio as low as 0.12 is observed for films deposited at 500°C. The optimal growth temperature, on the order of 600–700°C, yields even greater deficiency in Zn content. One means of compensating for the loss of the volatile species in the films is to use a mosaic target consisting of the desired material and an additional region rich in the volatile component. Figure 1.5 compares the results for $ZnGa_2O_4$ films deposited with a single $ZnGa_2O_4$ target versus mosaic $ZnGa_2O_4$/ZnO targets. Stoichiometric $ZnGa_2O_4$ films required a target mosaic of 50% $ZnGa_2O_4$, 50% ZnO. The additional ZnO flux provides a means of overcoming the disparity in cation vapor pressure. Note that the stoichiometry also depended on oxygen partial pressure, which likely reflects the difference in vapor pressure for Zn as compared to ZnO.

1.3 WHERE IS PULSED LASER DEPOSITION BEING APPLIED?

Given the attractive characteristics of pulsed laser deposition in the synthesis of multicomponent thin-film materials, a number of applications are being actively pursued using this technique. In some cases, the application focuses on the synthesis of a thin-film material or structure. In other cases, the research has targeted the development of specific devices. It is interesting to consider specific structures, devices, and applications for which PLD has been successfully applied. Many of these topics are discussed in more detail in later chapters in Parts 3 and 4.

1.3.1 Complex Oxide Film Growth

In the growth of crystalline oxides, PLD has proven to be most effective. The growth of complex oxides requires the delivery of a growth flux with the correct stoichiometry in an oxidizing ambient that is favorable for the desired phase formation. The utility of pulsed laser deposition in reproducing target stoichiometry has been demonstrated for a number of multication oxides. Early success in realizing stoichiometric $YBa_2Cu_3O_7$ clearly delineated this advantage for pulsed laser deposition. In recent years, even more complex crystal structures have been successfully grown using this approach. Consider, for example, the growth of the Y-type magnetoplumbite $Ba_2Co_2Fe_{12}O_{22}$ compound. This material is a ferromagnetic oxide of potential interest in thin-film magnetic device applications [Sudakar et al., 2003]. The epitaxial growth of $Ba_2Co_2Fe_{12}O_{22}$ is challenging as it possesses a remarkably complex crystal structure as illustrated in Figure 1.6a. The unit cell possesses a huge lattice parameter of 43.5 Å. Despite the complexity of the crystal structure, the epitaxial growth of $Ba_2Co_2Fe_{12}O_{22}$ has been realized via pulsed laser deposition [Ohkubo et al., 2003]. Figure 1.6b and 1.6c show the X-ray diffraction data for an epitaxial film, along with the

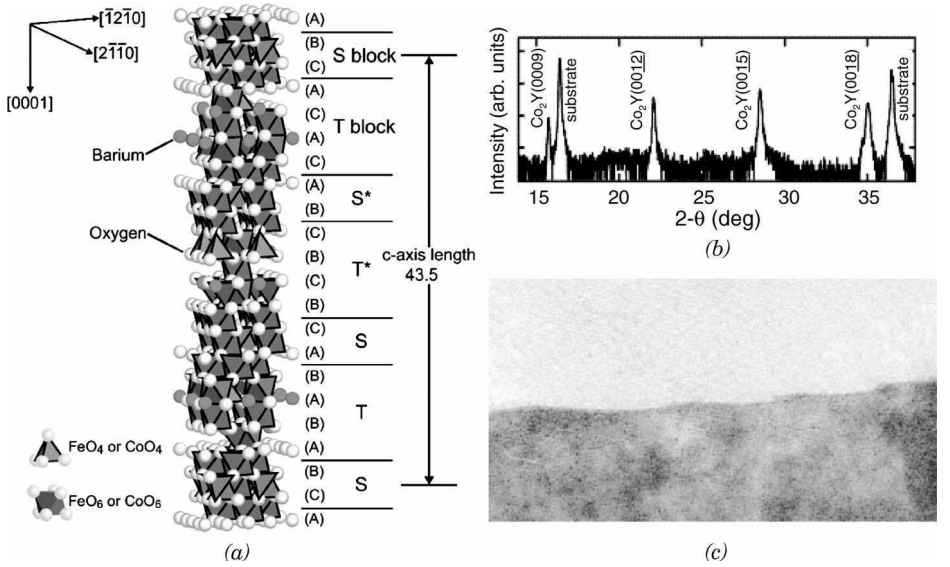

Figure 1.6 Crystal structure, X-ray diffraction data, and TEM image of a $Ba_2Co_2Fe_{12}O_{22}$ film grown by PLD [Ohkubo et al., 2003].

cross-sectional transmission electron microscopy (TEM) image. It should be noted that this result was obtained using a combinatorial synthesis approach in which multiple process parameters (composition, temperature) are explored in parallel through the use of combinatorial arrays or compositional spread techniques. Pulsed laser deposition has proven to be easily adaptable to combinatorial techniques for thin-film research. The ability to grow epitaxial, multication complex inorganic thin films has been, and continues to be, one of the enabling strengths of PLD.

1.3.2 Epitaxial Interface and Superlattice Formation

Developments in oxide PLD film growth have provided remarkable opportunities in the synthesis of epitaxial heterostructures and superlattices [Yilmaz et al., 1991; Fernandez et al., 1998; Chang et al., 1999; Smolenskii et al., 1984; Xu et al., 2000]. Superlattices of oxides, such as the (001) $KNbO_3/KTaO_3$ perovskite structure shown in Figure 1.7, have been realized for a number of material systems, with individual layers as thin as a single unit cell [Christen et al., 1996, 1998; Specht et al., 1998]. Excellent film flatness and crystallinity are evidenced in these films, and the interfaces can be

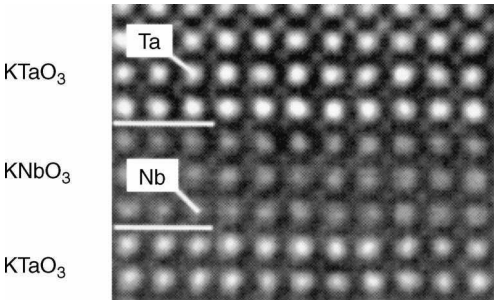

Figure 1.7 Cross-section *Z*-contrast STEM image of a $KTaO_3/KNbO_3$ superlattice structure grown by pulsed laser deposition.

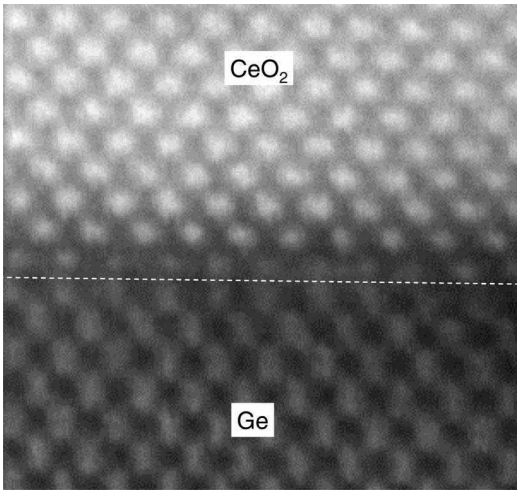

Figure 1.8 Cross-section *Z*-contract STEM image of a CeO_2/Ge epitaxial interface fabricated using PLD.

compositionally sharp on an atomic scale as seen in Figure 1.7. In the formation of atomically abrupt interfaces and superlattice structures, PLD is competitive with other film growth techniques, including molecular orbital chemical vapor deposition (MOCVD) and molecular beam epitaxy (MBE). The formation of epitaxial oxide superlattices has been used to investigate the effects of reduced dimensionality on a number of phenomena. Superconductivity in single unit cell $YBa_2Cu_3O_7$ layers was first demonstrated using PLD. Low dimensionality behavior has been investigated for ferroelectric and magnetic oxides.

Pulsed laser deposition also yields the opportunity to create atomically abrupt interfaces between materials that are chemically dissimilar, including epitaxial metal–oxide and semiconductor–oxide structures. A key factor in the formation of atomically abrupt interfaces between oxide films and nonoxide surfaces is to identify conditions where undesirable interfacial reactions are minimal yet compatible with oxide epitaxy. Laser ablation film growth is particularly well suited for nucleation in a reactive environment since it is compatible with a large range of background pressures. For example, a hydrogen-assisted nucleation approach has been used to grow atomically abrupt, epitaxial CeO_2/Ge interfaces [Norton et al., 2000]. During the initial nucleation of CeO_2 on Ge, the hydrogen partial pressure and substrate temperature are chosen such that the native oxide, GeO_2, is thermodynamically unstable, and under these conditions, the epitaxial growth of an oxide can be achieved on the Ge surface without interference from native oxides. The deposited oxide material must itself be thermodynamically stable under the conditions used during nucleation, and epitaxy will be determined by the chemistry and structure of the two materials. For CeO_2 nucleated on (001) Ge in hydrogen gas using pulsed laser deposition, the film can be epitaxial with an interface that is atomically abrupt as is evident in the cross-section Z-contrast scanning transmission electron microscopy image shown in Figure 1.8. A similar approach has been used to form epitaxial interfaces between various oxides and metals (e.g., Ni and Ni alloys), as well as compound semiconductors, including InP. The latter is of interest as it provides a means of integrating electronic oxides with photonic and microwave electronics.

1.3.3 Superconducting Electronic Devices

Given the remarkable success of PLD in the epitaxial growth of high-temperature superconducting (HTS) thin films, it is not surprising that numerous device applications have been explored. Potential electronics applications involving PLD-grown HTS films include high-frequency electronics for

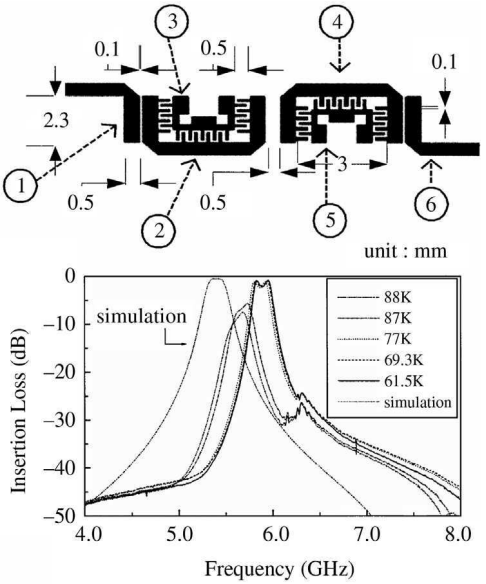

Figure 1.9 Design and characteristics of a hairpin-type HTS microstrip bandpass filter fabricated using PLD [Jung and Kang, 2003].

radio frequency (RF)/microwave communications and superconducting quantum interference devices (SQUIDs) for the detection of minute magnetic fields. For wireless communication, RF filters based on high-temperature superconducting thin films promise to deliver excellent performance in reducing interference from out-of-band signals. The enabling characteristic is the low loss in the microwave frequency range for epitaxial oxide superconducting films, which PLD is extremely effective at producing. Multipole filters have been demonstrated for operation in the gigahertz range [Jhon et al., 2003; Jung and Kang, 2003]. Figure 1.9 shows the design and characteristics of a hairpin-type HTS microstrip bandpass filter designed to operate in the gigahertz frequency range. In this case, the superconductor was $YBa_2Cu_3O_7$ deposited by pulsed laser deposition. The characteristics of the bandpass films are shown at various temperatures, and the performance of HTS bandpass filters compares very favorably to that of a copper filter, which is the conventional technology for this application.

For the detection of small magnetic fields in imaging, SQUID structures grown by PLD have been explored. A number of device configurations have been demonstrated, including artificial barrier and grain boundary superconducting/normal metal/superconducting (SNS) junctions. These devices have been implemented into fully functional SQUID-based systems. Figure 1.10 shows a schematic of a multichannel scanning SQUID microscope that utilizes PLD-grown $YBa_2Cu_3O_7$ devices [Matthews et al., 2003]. Scanning SQUID microscopy utilizes the output of SQUIDs as a sample is scanned under the SQUID array. The device maps out small gradients in magnetic fields. The instrument shown utilizes a multichannel scanning SQUID head. The SQUID array is attached to a 77 K cold-finger that is physically isolated from the sample ambient. This permits interrogation of samples that are operating at or above room temperature. With the ability to detect small magnetic fields, scanning SQUID microscopy has proven useful for a number of applications. For example, the nondestructive imaging of buried interconnects in integrated circuits is possible due to magnetic fields induced by currents in the interconnects. HTS SQUIDS have also been explored for geomagnetic imaging [Itozaki, 2001] and biomagnetism studies [Kobayashi and Uchikawa, 2003]. The former is useful in mapping subterrestial structure associated with fossil fuel deposits. The latter can be used to map neural activity in the brain.

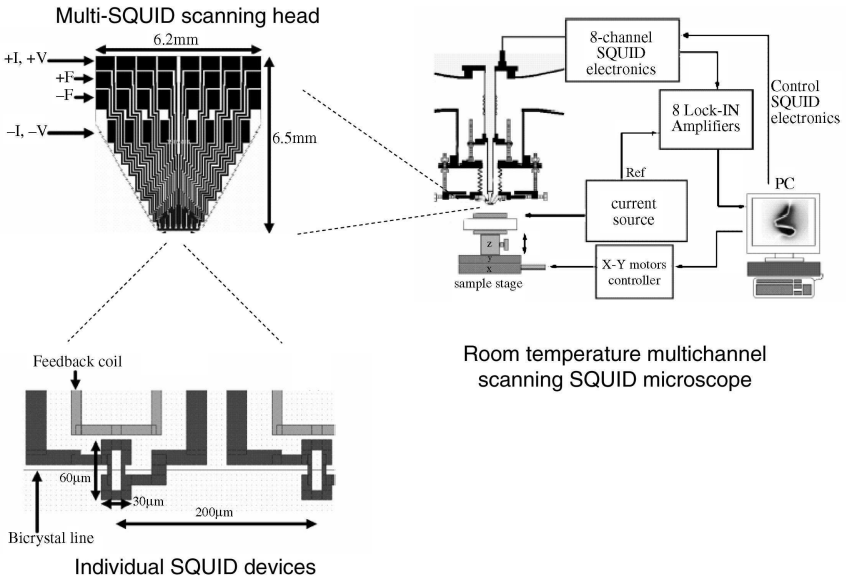

Figure 1.10 Multichannel scanning SQUID microscope using PLD-deposited HTS thin films [Matthews et al., 2003].

1.3.3.1 Fabrication of Superconducting Wires

Another area where pulsed laser deposition has played a significant role in HTS applications is in high-temperature superconducting coated conductors. The formation of epitaxial $YBa_2Cu_3O_7$ films on biaxially textured tapes is the leading candidate for producing a viable high-temperature superconducting technology. The formation of biaxially textured HTS material is a necessary condition for high critical current density in HTS compounds. The formation of biaxially textured HTS-coated conductors involve two distinct aspects, both of which can involve pulsed laser deposition. First, one must achieve a substrate tape that possesses sufficient in-plane and out-of-plane crystallographic texture in a top-most oxide layer that is compatible with epitaxial $YBa_2Cu_3O_7$ film growth. Second, an epitaxial $YBa_2Cu_3O_7$ film must be grown on the tape surface. In the rolling-assisted biaxially textured substrates (RABiTS) process, illustrated in Figure 1.11, substrate tapes of

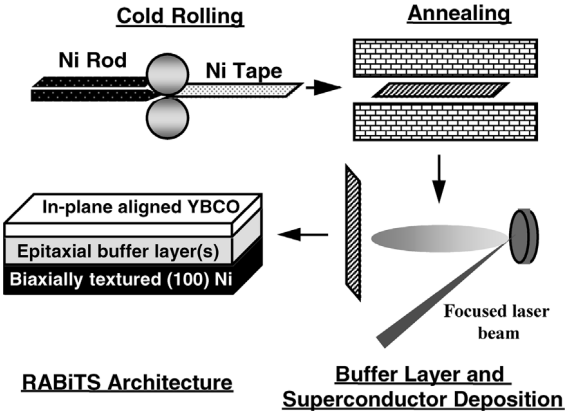

Figure 1.11 Schematic of the RABiTS process for HTS-coated conductor fabrication.

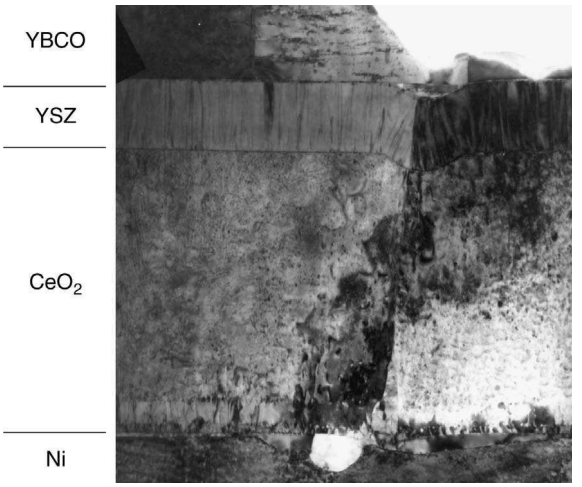

Figure 1.12 Cross-section TEM image of an epitaxial RABiTS structure fabricated using PLD.

pure nickel or nickel alloys are formed by progressive rolling deformation followed by annealing [Norton et al., 1996]. The resulting metal tapes have a relatively sharp biaxial, ''cube'' texture, with ⟨100⟩ face-centered cubic (fcc) crystalline axes directed along both the rolling direction and perpendicular to the tape plane. The epitaxial growth of appropriate oxide buffer layers is necessary in order to provide a chemically compatible biaxially textured template for subsequent epitaxial growth of the active HTS material. The formation of the epitaxial buffer and HTS layers has been achieved using pulsed laser deposition. Figure 1.12 shows the cross-sectional TEM image of the multilayer RABiTS structure. Note that this approach is among the most challenging applications involving epitaxial film growth as the integrity of the epitaxial structure must be maintained throughout the length of the conductor, which could be on the order of kilometers. In another approach, known as ion-beam-assisted deposition (IBAD), an energetic ion beam, typically consisting of Ar ions, is directed along a certain crystallographic direction simultaneously with the deposition of the desired film [Iijima et al., 1992]. The impinging ions induce an in-plane texture in the growing film due to creation of anisotropic damage that is dependent on the local crystallographic orientation of the corresponding grain. The depositing flux for film growth during ion bombardment can be provided via pulsed laser deposition. The net result is a buffer layer that is crystallographically textured both in-plane and out-of-plane. Using this approach, coated conductor tapes that are several meters in length have been realized in which the superconducting film is deposited by means of pulsed laser deposition [Watanabe et al., 2003]. A third approach that has been employed to achieve in-plane texture with suitable buffer layers involves deposition at an inclined angle. This technique, known as inclined substrate deposition (ISD), is dependent on the anisotropic shadowing of certain grain orientations during film deposition. It can be accomplished using a pulsed laser ablation plume as the inclined deposition flux source [Ohmatsu et al., 2003]. Using pulsed laser deposition with reel-to-reel capability, biaxially textured ISD tapes up to 50 m in length have been realized.

1.4 EXPLORING NOVEL OXIDE DEVICES CONCEPTS

With the ability to deposit a wide array of complex oxides as films, PLD has proven particularly useful in exploring novel concepts for device functionality using electronic oxides. In silicon microelectronics, continued reduction in device dimensions for metal–oxide–semiconductor field-

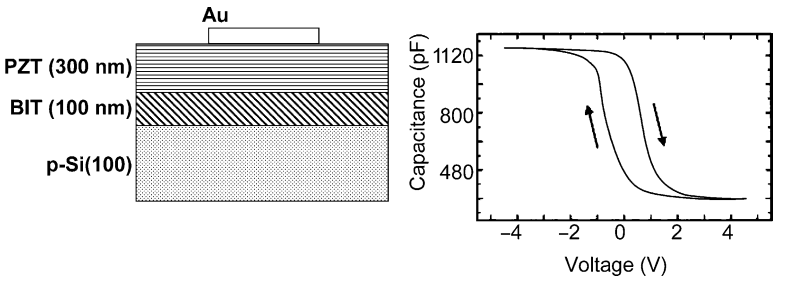

Figure 1.13 Capacitance versus bias voltage characteristics of Au/PZT/BIT/*p*-Si diode between −4.5 and 4.5 V bias voltage at a bias frequency of 100 kHz. The thickness of PZT and BIT were 300 and 100 nm, respectively [Yu et al., 2001].

effect transistor (MOSFET) devices requires an increase in gate capacitance beyond that accessible through a continued reduction in the SiO_2 gate dielectric thickness. This can be accomplished only though the use of gate dielectrics that possess a dielectric constant that is higher than that for SiO_2. PLD has been used in examining various gate oxide materials, including epitaxial, polycrystalline, and amorphous dielectrics as potential alternatives to SiO_2 in Si MOSFET development [Lee et al., 2003]. With the ability to deposit almost any oxide compound, PLD has been particularly useful in assessing material-specific issues related to interface reactions and interface stability. PLD has also been used in exploring various concepts related to memory devices based on ferroelectrics. For ferroelectric memory devices, such as the Au/Pb($Zr_{0.52}Ti_{0.48}$)O_3/$Bi_4Ti_3O_{12}$/*p*-Si diode shown in Figure 1.13 [Yu et al., 2001], memory is accomplished via the polarization hysteresis associated with domain switching in ferroelectric films as observed in the figure showing the *C–V* curve for the fabricated diode. Research activities have included both polycrystalline and epitaxial ferroelectric structures using PLD for ferroelectric film growth [Migita et al., 2002].

Pulsed laser deposition has also played a key role in exploring more radical oxide device concepts, including various electric field-effect devices based on semiconducting oxide materials. For example, trivalent cation-doped $SrTiO_3$ undergoes a metal–insulator transition at low carrier concentration and exhibits high mobility values at low temperature. The field-gated modulation of cation-doped Mott insulators, such as doped $SrTiO_3$, for field-effect transistor (FET) functionality is being explored, including the formation of ferroelectric field-effect epitaxial heterostructures [Marre et al., 2003]. Using pulsed laser deposition, patterned field-effect devices have been grown, consisting of lanthanum-doped $SrTiO_3$ as the channel and Pb(Zr,Ti)O_3 as the ferroelectric gate. Modulation of the semiconducting channel conductance with electric field has been demonstrated.

1.4.1 Tunable Microwave Electronics

For many paraelectric/ferroelectric oxides, the dielectric constant exhibits a shift to a lower value when a large electric field is imposed on the material. If these materials are incorporated as high-frequency circuit elements, the high-frequency response of the circuit becomes tunable with the applications of a voltage across this paraelectric/ferroelectric element. Dielectric thin films that exhibit an electric-field-tunable permittivity are attractive for advanced wireless communication components, including matching networks, time delay devices, phase-shifting antenna arrays, and voltage-controlled oscillators. High-performance microwave filters stand to benefit from the capability to electrically tune their frequency of operation using dielectrics with a tunable permittivity and low dielectric loss [Moeckly et al., 2003; Subramanyam et al., 2003]. This function has been demonstrated with voltage-tunable dielectric materials, such as $SrTiO_3$, deposited by PLD. Loss tangents on the order of 0.001 at 65 K have been realized for PLD-grown $SrTiO_3$, while maintaining acceptable tunability. Tunable filters with normal metal or high-temperature superconductor electrodes have been extensively studied, using, for example, conductor–ferroelectric–dielectric

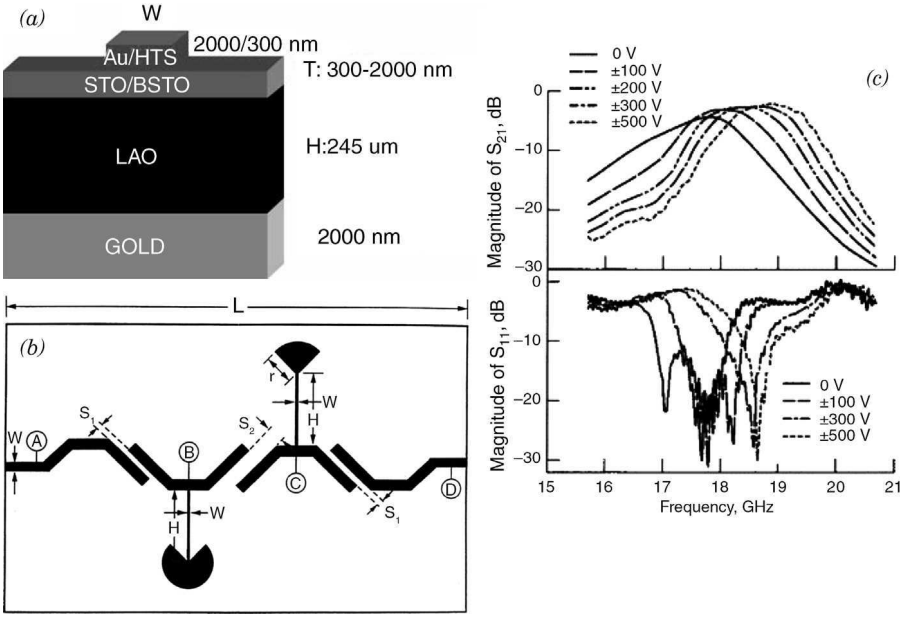

Figure 1.14 Figure showing (a) a $SrTiO_3$ tunable microstrip structure and (b) optimized filter with the following dimensions: $W = 80\,\mu m$, $L = 6.8\,mm$, $S_1 = 100\,\mu m$, $S_2 = 300\,\mu m$, $w = 12.5\,\mu m$, $H = 1.33\,mm$, and $r = 200\,\mu m$. Also shown in (c) is the swept frequency response of a tunable filter at 77 K for bipolar bias voltages between 0 and ± 500 V [Subramanyam et al., 2003].

microstrip configurations. Tunability is achieved through the nonlinear direct current (dc) electric field dependence of the relative dielectric constant of the ferroelectric/paraelectric thin film. For example, Figure 1.14 shows the multilayer device design, structure, and performance for a two-pole ferroelectric tunable filter using a $YBa_2Cu_3O_7/SrTiO_3/YBa_2Cu_3O_7$ two-layered microstrip. This particular structure, grown by PLD, yields an insertion loss of 1.5 dB, and large frequency tunability ($\sim$2.3 GHz) at 24 K, with a peak electric field of 80 kV cm^{-1} for electrical tuning. Tunable dielectrics and high-temperature superconductors have been integrated into lumped-element $YBa_2Cu_3O_7$ microwave resonators and filters in order to tune their center frequencies. Figure 1.15 shows a

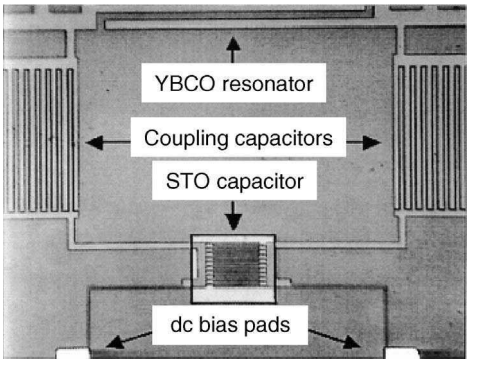

Figure 1.15 Photograph of a monolithic tunable resonator fabricated with PLD that utilizes superconducting YBCO and tunable $SrTiO_3$ [Moeckly et al., 2003].

photograph of a monolithic tunable resonator fabricated with PLD that utilizes superconducting $YBa_2Cu_3O_7$ and tunable $SrTiO_3$ [Moeckly et al., 2003; Subramanyam et al., 2003]. Coplanar waveguide-type phase shifters controlled by an external dc bias field have been fabricated on PLD-grown (Ba,Sr)TiO_3 films (Kim et al., 2002). These results demonstrate the possible application of ferroelectric tunable devices in high-power tunable wireless telecommunication.

1.4.2 Wide Bandgap Electronics

In the development of wide bandgap oxide electronics, pulsed laser deposition has been a major contributor. While pulsed laser deposition does not yield device-quality material in elemental or most III–V semiconductors, the properties of PLD-grown oxide semiconductors are generally equivalent to that realized with other thin-film growth techniques and suitable for devices. Among the thin-film semiconductor materials, by far the most extensively investigated is ZnO, which is a direct bandgap semiconductor with $E_g = 3.2\,\text{eV}$ (see also Chapter 12). Substituting Mg on the Zn site in epitaxial films can increase the bandgap to approximately 4.0 eV while still maintaining the wurtzite structure. The latter represents a metastable compound that is stabilized via epitaxial film growth. Epitaxial wurtzite $Zn_{1-x}Mg_xO$ thin films have been realized using PLD with x as large as 0.35 [Ohtomo et al., 1998]. As a wide-bandgap semiconductor, transparency to visible light provides opportunities to develop transparent electronics, UV optoelectronics, and integrated sensors, all from the same material system.

(Zn,Mg)O thin films grown by PLD are being explored for a number of device applications. For example, the fabrication of ultraviolet photodetectors has been achieved using $Mg_xZn_{1-x}O$ thin films on Si(100) for $Mg_xZn_{1-x}O$ with the Zn/Mg ratio varying from the Zn-rich wurtzite to the Mg-rich cubic. Figure 1.16 shows the optical transmittance for (Zn,Mg)O films grown by PLD over the entire solid solution. Also shown is the optical response for a PLD-grown photodetector array designed for ultraviolet detection [Yang et al., 2003; Takeuchi et al., 2003]. Photodetectors fabricated with $Mg_{0.68}Zn_{0.32}O/SrTiO_3/Si$ structures show peak photoresponse at 225 nm, which is in the deep UV region.

For the realization of transparent electronics, the formation of novel wide-bandgap oxide junction devices has also been explored using PLD. Transparent trilayered oxide films of ZnO/NiO/indium tin oxide have been fabricated for transparent *pn* junction formation. ZnO is the *n*-type

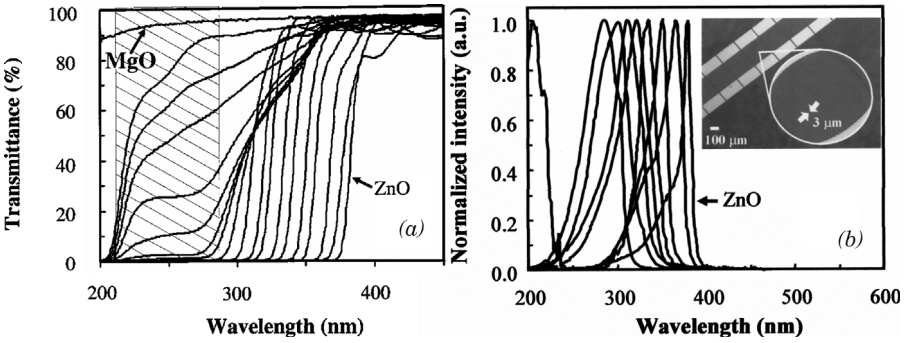

Figure 1.16 UV–VS photon transmission spectra (a) of the composition spread $Mg_xZn_{1-x}O$ thin film grown by PLD for UV photodetectors. The shaded area is the phase-separated region. The two arrows mark the approximate optical absorption edges due to the wurtzite and cubic phase of $Mg_xZn_{1-x}O$. Also shown (b) is the normalized spectral response of an array of UV photodetectors based on a composition spread of $Mg_xZn_{1-x}O$. The active area of each device was $250 \times 220\,\mu\text{m}^2$. Composition variation within each detector is less than 2.4 mol %. The inset shows an enlarged picture of interdigited electrodes used as detectors. Each finger width and the finger separation is 3 μm. The electrodes were fabricated from a 200-nm-thick gold layer using the standard photolithography [Takeuchi et al., 2003].

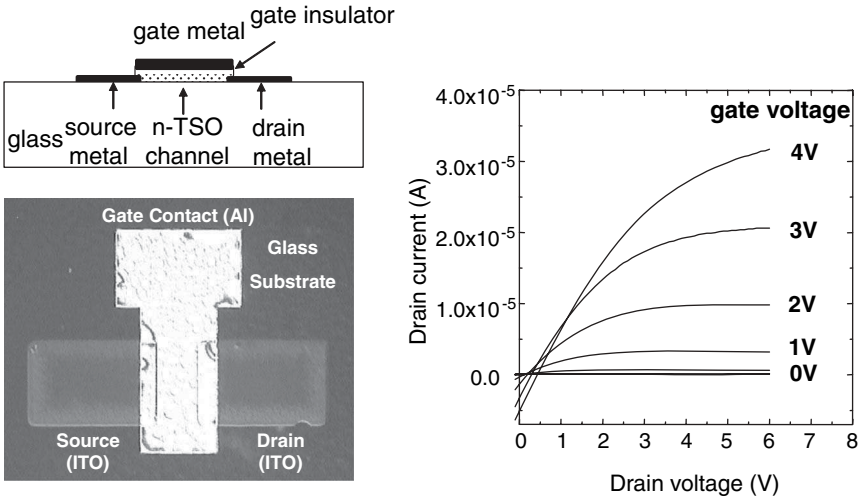

Figure 1.17 ZnO thin-film transistor fabricated using PLD.

material while NiO is a *p*-type wide-bandgap semiconducting oxide. The PLD-grown films, patterned to yield *p*-NiO/*n*-ZnO diodes, exhibit rectifying *pn* junction I–V characteristics [Ohta et al., 2003]. PLD has been used to develop transparent diodes based on other semiconductor oxides. Transparent homojunctions have been fabricated by pulsed laser deposition of *p*- and *n*-type $CuInO_2$ delafossite-type oxide films [Yanagi et al., 2001]. These *p–n* homojunctions exhibit rectifying characteristics with a turn-on voltage of $\sim$1.8 V.

In addition to two-terminal diodes, three-terminal oxide FET structures have also been realized using pulsed laser deposition [Nishii et al., 2003]. Figure 1.17 shows a ZnO thin-film transistor (TFT) that uses a HfO_x and a ZnO channel. Such devices are potentially attractive for replacing amorphous silicon (a-Si) TFTs in active matrix liquid-crystal displays as the wide bandgap yields a transistor that is transparent and unaffected electrically by the display emission. Field-effect mobility on the order of 2–7 $cm^2\,V^{-1}\,s^{-1}$ has been realized for devices grown by PLD at 400°C or less, making the process compatible with glass or perhaps even plastic substrate material.

In ZnO-based heterostructures, one of the more interesting possibilities is to access the large direct bandgap and develop a viable UV photonics technology. Using PLD, a UV light-emitting diode has been demonstrated in a *p–n* heterojunction composed of transparent conductive oxides, namely *p*-$SrCu_2O_2$ and *n*-ZnO [Ohta et al., 2002]. Multilayered Ni/$SrCu_2O_2$/ZnO/ITO epitaxial structures were grown on YSZ (111). The *p–n* junction was fabricated by conventional photolithography, followed by reactive ion etching. The resultant device exhibited rectifying I–V characteristics with a turn-on voltage of 3 V. Band edge electroluminescence centered at 382 nm was observed for an applied forward bias voltage larger than 3 V, as seen in Figure 1.18. The peak position for the electroluminescence correlated closely to the photoluminescence peak seen in the same structure.

Another electronic device that has been explored using PLD-grown (Zn,Mg)O thin-film heterostructures is a resonant tunneling diode (RTD). Double-barrier resonant tunneling diodes are attractive for ultrahigh frequency mixing, microwave-millimeter wave oscillation circuits, and multivalued logic. For the (Zn,Mg)O system, the higher energy gap in $Zn_xMg_{1-x}O$ combined with the lower energy gap of the ZnO can provide a barrier/quantum well heterostructure suitable for an RTD. To this end, semiconducting ZnO quantum well heterostructures, such as that shown schematically in Figure 1.19, have been fabricated via PLD [Iliadis et al., 2002]. ZnO quantum wells placed between $Zn_{0.8}Mg_{0.2}O$ barriers exhibit resonant tunneling as evidenced by a negative differential resistance.

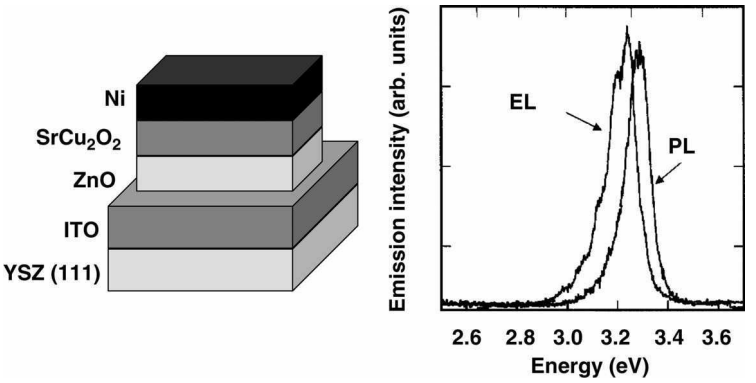

Figure 1.18 Schematic and characteristics of a $SrCu_2O_2$/ZnO light-emitting *pn* junction [Ohta et al., 2002].

Within the wide-bandgap area, PLD has also proven somewhat useful in developing nitride-based structures as well. The most common means of growing nitride semicondutors is MOCVD, which requires relatively high temperatures for film growth. The energetics of PLD results in epitaxial nitride film growth at substantially lower temperatures, although electronic properties equivalent to that realized via MOCVD or MBE have yet to be demonstrated. However, for certain specific properties, PLD-grown nitrides have proven interesting. One example is with AlN. One of the challenges with AlN is in achieving high carrier densities due to the large bandgap of 6.2 eV. Using PLD, low-resistivity aluminum nitride films have been realized via simultaneous carbon and oxygen doping during pulsed laser deposition [Kai et al., 2003]. Carrier concentrations on the order of 10^{18} cm^{-3} have been achieved. AlN is also potentially useful in surface acoustic-wave (SAW) device applications as it is piezoelectric, radiation-hard, has a wide direct bandgap, and exhibits a high SAW phase velocity (6000 m/s). For harsh environment applications of SAW devices, its excellent dielectric properties, thermal conductivity, thermal stability, and chemical inertness make AlN attractive. The thermal expansion coefficient of AlN is similar to that of silicon, which enables integration of AlN in thin-film form with silicon-based integrated circuit (IC) technology. Therefore, fabrication of good-quality AlN thin films on silicon and related devices is particularly attractive.

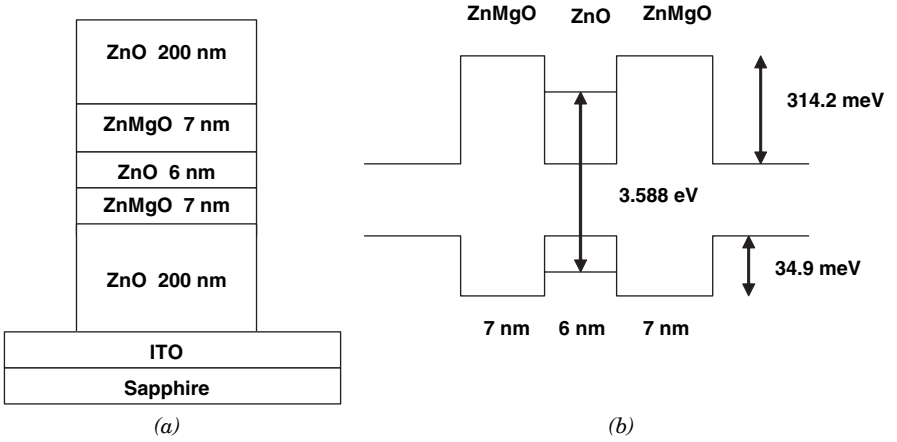

Figure 1.19 Schematic of a PLD-grown (Zn,Mg)O-based thin-film resonant tunneling diode [Iliadis et al., 2002].

Using PLD, surface acoustic-wave device resonance at 345 MHz has been realized for 1.5-μm-thick AlN films grown on (111) Si [Liu et al., 2003].

1.5 THIN-FILM OPTICS

Another area where PLD has proven useful is in the development of active and passive thin-film optical components. Thin-film optics requires films that demonstrate a desirable linear and/or nonlinear optical response and that have low losses, requiring minimal defects and low surface roughness. The exploitation of PLD in thin-film optics research has included crystalline, polycrystalline, and amorphous thin-film materials. For example, in the area of amorphous waveguides, PLD has been used for the deposition of sulfide glasses (e.g., As_2S_3). Chalcogenide glasses, such as As_2S_3, are low-phonon-energy materials transparent from the visible to the midinfrared. For arsenic trisulfide, the nonlinear refractive index and nonlinear figure of merit make it an attractive material for ultrafast all-optical switching. In As_2S_3, films with the proper stoichiometry and local chemical bonding, configurations undergo an index change associated with a photodarkening phenomenon. This effect can be used to fabricate diffractive as well as waveguide structures. Using PLD, atomically smooth 5-μm-thick As_2S_3 chalcogenide glass thin films have been deposited for low-loss waveguide applications [Zakery et al., 2003]. As_2S_3 films that were deposited by PLD have been shown to be photosensitive at wavelengths close to the band edge ($\sim$520 nm) [Rode et al., 2002]. Waveguide losses as low as 0.2 dB/cm at 1550 nm have been achieved in PLD films with laser-written waveguides [Zakery, 2002]. PLD has also been used to investigate rare-earth or transition-metal doped host materials for solid-state thin-film lasers and optical amplifers.

Ultraviolet to visible solid-state lasers are of interest for high-density optical data storage, displays, and infrared sensors, while amplifiers are needed for optical communication networks. One approach to realizing short-wavelength solid-state lasers is through frequency up-conversion. Within this approach, the intrinsic energy level matching of certain rare-earth ions yields light emission with higher energy photons than that of an incident pump beam. This is a multiphoton process that does not require coherence between the exciting photons. Most activities in frequency up-conversion have focused on bulk materials, but there is significant incentive to realize this process in a thin-film structure. Using PLD, wavelength up-conversion has been realized in $Zn_{0.3}Al_{0.25}Pb_{0.3}Li_{0.098}Yb_{0.1}Tm_{0.022}F_{2.354}$ amorphous fluoride films [Guanshi et al., 2003]. Ultraviolet and blue up-conversion emission was observed under infrared excitation at 978 nm, and the ultraviolet emissions were significantly enhanced in the film as compared to the target material.

The fabrication of electrooptical thin-film devices via PLD is also of significant interest. In this area, ferroelectric oxides dominate. For example, with a large electrooptical coefficient and high optical transparency, $BaTiO_3$ is an attractive candidate for thin-film electrooptical devices, and waveguide phase modulators have been realized from $BaTiO_3$ grown by PLD. For electrooptics, the crystallographic orientation of the film is important in achieving optimum device function. Using PLD, epitaxial films of $BaTiO_3$ with either the *c* axis or *a* axis oriented vertical to the substrate surface can be realized for waveguide synthesis. For any thin-film waveguide structure, the roughness of the interfaces will largely determine the optical losses for materials with good crystallinity. Film roughness on the order of 1 nm root mean square (rms) can be achieved with PLD, which is sufficient for waveguides with low scattering losses. Figure 1.20 shows a schematic of a Mach–Zehnder waveguide modulator fabricated using PLD for film growth [Petraru et al., 2002]. The propagation loss of the PLD-grown planar waveguide was measured to be 2–3 dB/cm at 633 nm. Using electrodes deposited besides the waveguides, electrooptic modulation has been demonstrated at 633 and 1550 nm wavelengths. Theoretical modeling of the Mach–Zehnder modulators for both crystalline orientations of the $BaTiO_3$ films yields the Pockels coefficients $r_{51} = 80\,\text{pm/V}$ for the *c*-axis film and an effective Pockels coefficient $r_{\text{eff}} = 734\,\text{pm/V}$ for the *a*-axis films at 633 nm wavelength, which compare favorably with bulk values.

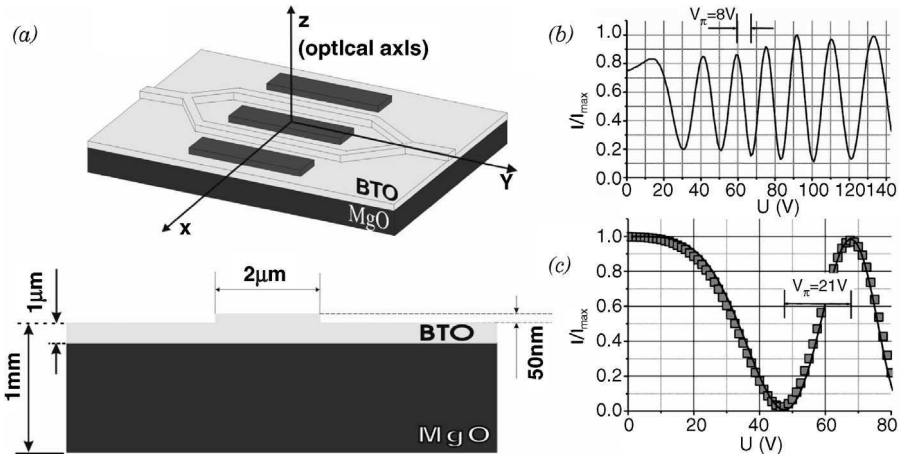

Figure 1.20 Mach–Zehnder waveguide modulator fabricated using $BaTiO_3$ grown by PLD [Petraru et al., 2002].

1.6 OXIDE SENSOR DEVICES

Applications employing metal oxide materials include a variety of sensor devices, most notably structures for chemical detectors, based on semiconducting oxides, and infrared detectors, based on oxides with strongly temperature-dependent resistivity and pulsed laser deposition has been used to fabricate a number of device structures for optical and gas sensor applications. For infrared (IR) detection, some of the most dramatic changes in resistivity with temperature occur in oxides that undergo metal–insulator transitions, such as vanadium oxide, and bolometers based on vanadium oxide have been examined for uncooled infrared detection. Figure 1.21 shows a microbolometer element, without air-gap thermal isolation, that was fabricated using pulsed laser-deposited vanadium oxide as the IR sensing layer [Kumar et al., 2003]. The high-temperature coefficient of resistance for vanadium oxide makes it an attractive material for uncooled microbolometers. The performance of the uncooled microbolometer was measured in the spectral region 8–15 μm, yielding a responsivity of 12 V/W.

In the area of solid-state gas sensing, metal oxide semiconductors have been leading candidates for several years. These sensor devices have the potential for use in multiarray configurations, including the development of a so-called electronic nose. In conventional devices, the gas-sensitive oxide is typically in the form of a thick microcrystalline film. When gases adsorb onto the surface of these metal oxides, a change in conductance is observed that is proportional to the gas concentration

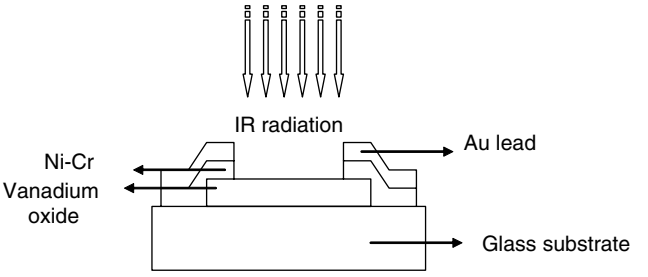

Figure 1.21 Microbolometer element, without air-gap thermal isolation, was fabricated using pulsed laser deposited vanadium oxide as the IR sensing layer [Kumar et al., 2003].

of interest. Metal-oxide-based semiconductor sensors respond well to an array of gases but suffer from limited sensitivity. In recent years, nanocrystalline metal oxide powders have been employed to improve the gas-sensing properties of these sensors. The use of nanocrystalline films as opposed to microcrystalline powders has significant advantage due to an increased surface area for a given mass of detector material. Ideally, the radius of the particles will be on the order of the thickness of the depletion layer in the semiconductor that is created when the gas molecules are adsorbed onto the surface of the nanoparticles. Traditionally, wet chemistry methods, such as sol–gel techniques, have been used to deposit the metal oxide nanocrystalline films. However, chemical methods can lead to modification of the semiconducting oxide surface and subsequent changes in gas-sensing properties. Pulsed laser ablation offers the advantage of producing nanocrystalline powders without chemical treatment. For example, using PLD, tin-oxide-based sensors have been fabricated for detecting NO_2 [Starke et al., 2002]. Among the oxides of nitrogen involved in air pollution, NO_2 is the most important in terms of health risk and potential environmental damage. It is produced together with NO by the oxidation of nitrogenous compounds in fuel combustion. NO_2 is toxic in concentrations above 20 ppm and is thought to cause asthma at significantly lower levels. The monitoring of NO_2 is typically carried out using bulky analytical equipment. However, the implementation of small mobile stations employing semiconductor gas sensors has several significant advantages over other

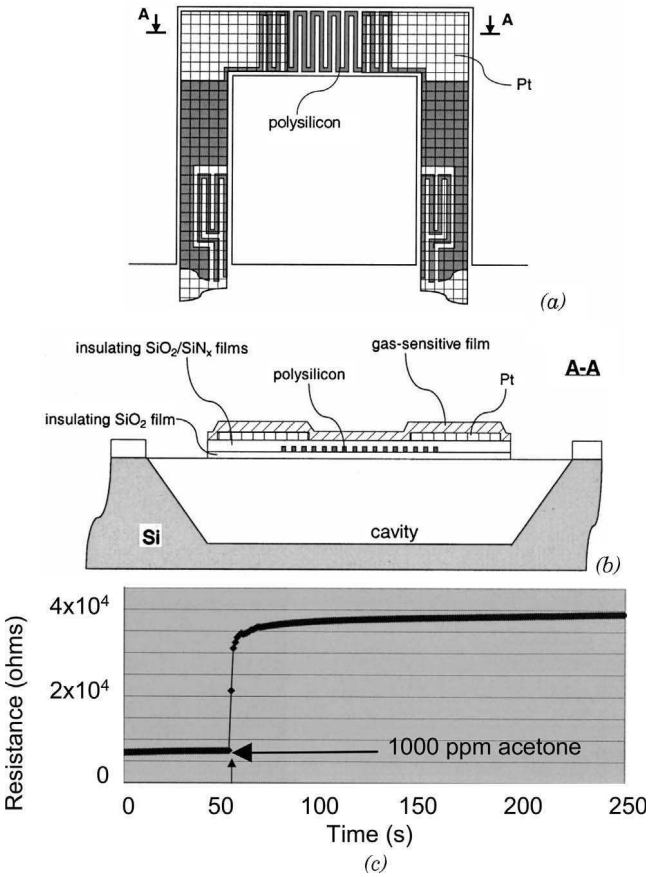

Figure 1.22 Schematic of a sensor device in which thin films of gas-sensitive materials based on the $SrFeO_{2.5+x}$ nonstoichiometric perovskite family were deposited onto the diaphragms by room temperature pulsed laser deposition [Grudin et al., 2002].

technologies, including low price and small dimensions. Gas sensors produced using laser-ablated nanocrystalline metal oxides have been tested for use as NO_2 detectors with particular emphasis on cross sensitivity to NO [Starke et al., 2002]. Very high sensitivities to low NO_2 levels together with fast response times have been observed for both SnO_2 and In_2O_3 nanomaterials deposited using PLD.

For many metal oxides, the sensitivity increases significantly if the material is heated. PLD-grown metal oxide thin-film devices have been fabricated with integrated microheaters for gas sensing at elevated temperatures. Suspended microstructures consisting of a thin oxide/nitride diaphragm with embedded polysilicon heaters have been fabricated using a standard complementary metal–oxide–semiconductor process and simple postprocessing. Figure 1.22 shows a schematic of such a device in which thin films of gas-sensitive materials based on the $SrFeO_{2.5+x}$ nonstoichiometric perovskite family were deposited onto the diaphragms by room temperature PLD [Grudin et al., 2002]. The utility of PLD in this application is in the ability to deposit the material on the membrane at room temperature, and successful chemical sensor functionality was demonstrated. When the heated membrane was exposed to volatile organic compounds such as acetone and methanol, a reversible 10- to 100-fold increase in sensor film resistance was observed, with response times as low as 1 s.

1.7 PROTECTIVE COATINGS AND BARRIERS

Extensive effort has been invested in the development of barrier layers and protective coatings using PLD. This work includes the deposition of borides, nitrides, and carbides. Research in the fabrication of superhard boride coatings using PLD has included binary (e.g., BN) and ternary (e.g., $AlMgB_{14}$) compounds [Marotta et al., 2003; Tian et al., 2003]. Nanoindentation tests show that the hardness of $AlMgB_{14}$ films prepared by pulsed laser deposition can be on the order of 45–50 GPa [Tian et al., 2003]. Extremely low friction coefficients of 0.04–0.05, due to a self-lubricating effect, are observed in nanoscratch tests. Tungsten nitride (WN_x) is of interest as a barrier to diffusion of metals, such as copper. WN_x films have been grown on silicon and glass slide substrates by laser ablating a tungsten target in a molecular nitrogen ambient [Soto et al., 2003]. The gas-phase reaction of tungsten and nitrogen produces WN_x films; the nitrogen is integrated in the tungsten matrix changing gradually the electronic configuration, chemical states, and film properties. The films are low resistivity and dense, making them attractive for diffusion barrier applications. In recent years, carbon nitride (CN_x) has also received considerable attention both for fundamental studies and applications. The primary interest in this material is in realizing the superhard C_3N_4 phase that is predicted but has proven difficult to produce. In an effort to realize C_3N_4 films, laser ablation of carbon-containing targets, including graphite, in various nitrogen-containing atmospheres has been pursued [Szorenyi et al., 2003].

Pulsed laser deposited diamond-like carbon (DLC) films have received significant attention for protective coatings due to the high hardness, scratch resistance, smooth surface morphology, chemical inertness, high thermal conductivity, and large bandgap of DLC materials, and this topic is discussed in more detail in Chapter 15. These properties make DLC films attractive for wear resistance in hip joints, disk drive coatings, and displays. A conventional means of achieving DLC is through plasma-enhanced CVD, but a drawback of this technique is the residual hydrogen that is included in the film composition, which limits the film properties. Pulsed laser deposition can be used to achieve a large sp^3/sp^2 bonding fraction without the presence of hydrogen during deposition. Using PLD, sp^3/sp^2 ratios higher than 0.8 have been reported [Haverkamp et al., 2003]. The plasma properties of the plume largely determines the quality of the thin films deposited on the substrate. One challenge is in obtaining diamond-like carbon films of thickness exceeding 1 μm, as the internal compressive stress that leads to delamination needs to be minimized. Stable DLC films with thickness greater than 1 μm have been produced, however, by appropriate steps of thermal annealing following pulsed laser deposition [Mosaner et al., 2003].

1.7.1 Biocompatible Coatings

In addition to coatings for tribology applications (see Chapter 23), PLD fabrication of biocompatible coatings has been actively pursued, and this is further discussed in Chapter 18. For example, hydroxylapatite and calcium orthophosphate are used as biocompatible coatings on dental and orthopedic implants. The chemical nature of these two compounds is similar to that of bone. As an alternative to the commercial plasma spray coating technique, pulsed laser deposition has been applied for the production of these biocompatible coatings [Arias et al., 2002, 2003]. One limitation with hydroxylapatite and calcium orthophosphate thin films is their poor mechanical characteristics, including hardness, tensile and cohesive strength, and adhesion to metallic surfaces is also an issue [Nelea et al., 2002]. Recently, film growth using UV-assisted PLD was examined, and the resulting films were found to be crystalline and exhibit good mechanical characteristics with values of hardness and Young's modulus of 6–7 and 150–170 GPa, respectively. UV irradiation during deposition enhanced gas reactivity and atom mobility during film growth, increasing the tensile strength of the film.

In pharmacutical drug development, PLD has been explored for particle coatings suitable for controlled drug delivery. Controlled pulmonary drug release systems require a biodegradable polymer on the drug particle surfaces, and controlling this coating thickness is critical to practical application. Nanofunctionalized drug particles, in particular budesonide, have been synthesized using pulsed laser deposition on particles as illustrated in Figure 1.23 [Singh et al., 2002]. In vitro studies indicate that the dry half-life release for the budesonide is enhanced from 1.2 to over 60 min by a nanoscale coating deposited by PLD on the drug particle.

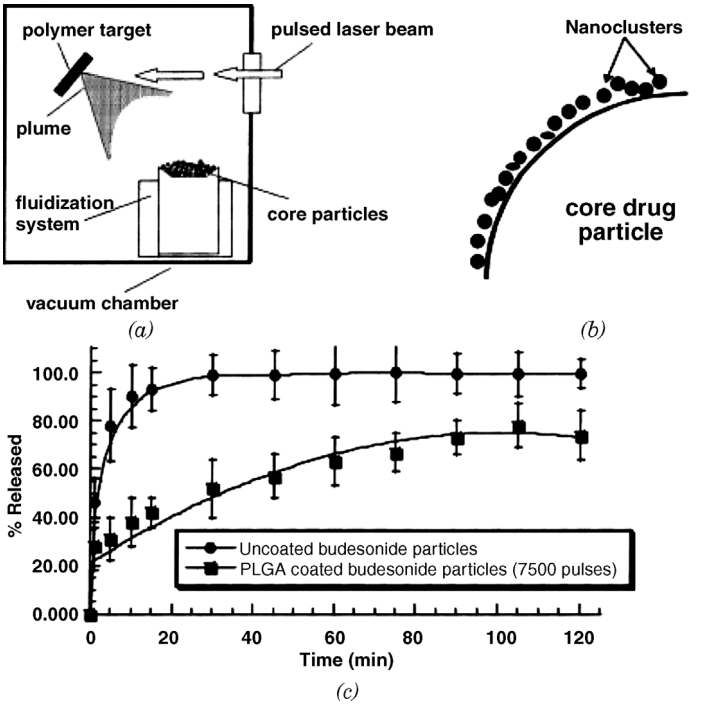

Figure 1.23 (a) Schematic diagram of the pulsed laser deposition system for drug particle coating. Shown in (b) is a schematic diagram of a nanofunctionalized particle (not to scale). Also shown (c) are the in vitro dissolution profiles of coated and uncoated budesonide particles [Singh et al., 2002].

1.8 NANOMATERIAL SYNTHESIS

In recent years, significant attention has been given to the synthesis of nanomaterials including nanocrystals, nanowires, and nanocomposites, and PLD has proven useful across all of these areas. There is considerable interest, for example, in nanoscale semiconductor materials for photonic applications [Orii et al., 2003]. The reduction in particle size in semiconductors yields quantum confinement effects that can facilitate optical transitions in otherwise indirect bandgap materials, including Si. Using pulsed laser ablation of silicon in high-purity He background gas, silicon nanoparticles can be synthesized, and these nanoparticles exhibit narrow-band visible light emission. Tunable, narrow-band light-emitting Si nanoparticles produced by pulsed laser ablation may be applicable for a range of optoelectronic devices.

Considerable interest has also developed recently in the synthesis and exploitation of semiconductor nanowires. Specific applications include nanotransistors, nanosensors, and fundamental studies of quantized electronic systems. Numerous techniques have proven useful in the synthesis of homogeneous wires, but few have yielded nanowires with composition modulation either radially or along the length of the wire. Heterostructured one-dimensional semiconductor nanostructures are interesting systems, potentially useful in light-emitting devices and thermoelectrics [Wu et al., 2002]. Recently, a film growth process that is a hybrid of pulsed laser ablation and chemical vapor deposition was used to synthesize semiconductor nanowires with periodic longitudinal heterostructures. Using this process, shown schematically in Figure 1.24, single-crystal nanowires with Si/SiGe superlattice structure along the length of the wire have been obtained. A cross-sectional transmission electron microscopy image of a compositionally modulated nanowire is shown in Figure 1.25. The nanowire grows in a block-by-block fashion with a compositional profile modulation along the wire axis. Heterojunction and superlattice synthesis using this approach could prove enabling as applications of semiconductor nanowires are explored.

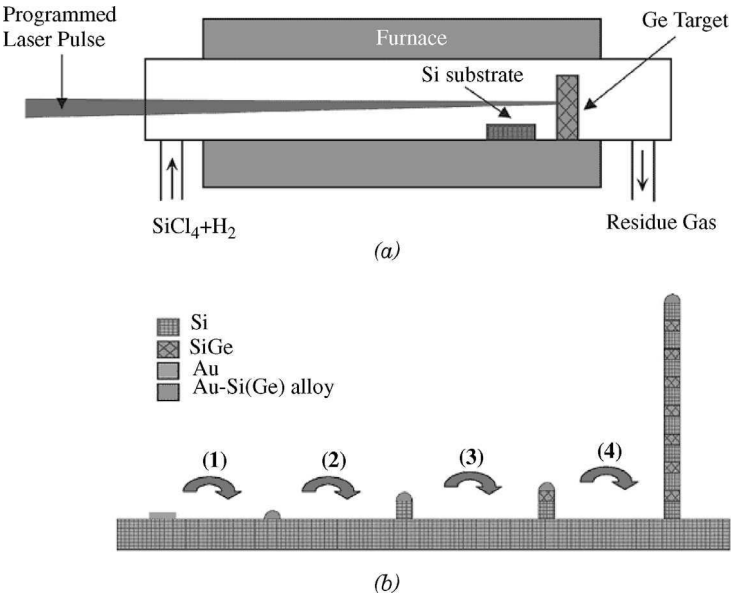

Figure 1.24 Film growth process that is a hybrid of pulsed laser ablation and chemical vapor deposition was used to synthesize semiconductor nanowires with periodic longitudinal heterostructures [Wu et al., 2002].

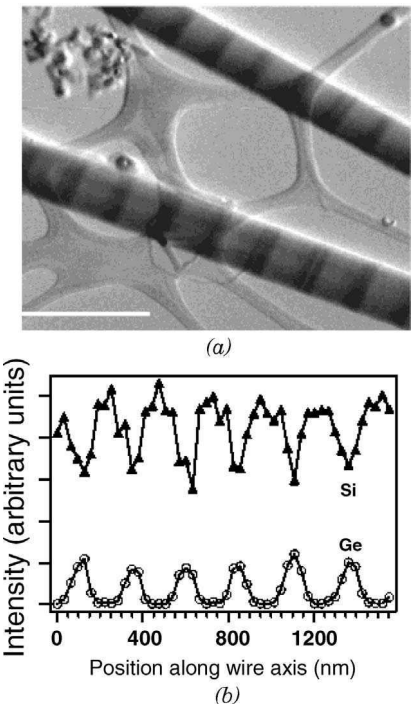

Figure 1.25 Cross-sectional transmission electron microscopy image of a single-crystal compositionally modulated nanowire with a Si/SiGe superlattice structure along the length of the wire [Wu et al., 2002].

1.9 POLYMER AND ORGANIC THIN FILMS

Much of the work involving PLD has focused on the synthesis of inorganics, particularly oxides. However, in recent years, the use of PLD has been extended to the deposition of "soft" materials, including polymers, organics, and even biological materials. For example, it has been shown that adherent, compact, and pinhole-free films of poly(tetrafluoroethylene) (PTFE or Teflon) can be deposited as a protective coating on metal surfaces using PLD [Blanchet et al., 1993]. Polytetrafluoroethylene coatings are useful for improved tribology and in providing a chemical barrier against corrosion. Applications of Teflon coatings on arbitrary metal pieces include the prevention of allergic reactions that are induced by certain metals when brought into contact with human skin. Examples where Teflon coatings are being explored include metal implants and tooth fillings, and even body jewelry. Unlike inorganics where the complete decomposition of the target molecule by plume formation is desirable, ablation plumes formed during effective PTFE deposition using PLD consists of intact polymer molecules. Studies indicate that the particles consist of four types of morphology, ranging from small particles (50 nm in diameter) to particle size greater than 10 μm. Other thin organic films that have been obtained by pulsed laser deposition include poly(methyl methacrylate) (PMMA) polymer [Cristescu et al., 2003], metal acetylacetonates InAcAc, NiAcAc, and metallophthalocyanines PcNi, PcCo and PcFe [Frycek et al., 2003].

One limitation with the deposition of polymeric or organic films using PLD is the light-induced decomposition of the molecules that often occurs upon ablation. To enhance the efficiency and minimize decomposition for pulsed laser deposition of polymer and organic films, ablation from targets doped with small amounts of photosensitizer has been explored. With this technique, ablation proceeds by excitation not of the target materials but of the doped sensitizer. By utilizing relatively

efficient photosensitized thermal reactions, ablation can be induced at longer laser wavelength and lower fluence, thus avoiding the photochemical decomposition that is typically observed in the UV ablation of polymeric materials. For example, using this approach, the deposition of PTFE using a graphite-doped PTFE target was achieved employing a near-infrared (1064 nm) Nd : YAG laser.

1.9.1 Biological Thin-Film Materials

The deposition of proteins, deoxyribonucleic acid (DNA), and other biopolymer thin films is of significant interest for application and fundamental studies. The development of novel biomedical devices often requires the ability to deposit selected biomaterials onto a given surface. Devices where this capability is applicable include microfluidic biosensors and biochips, biocompatable coatings for medical implants, and gene recognition microarrays. An effective deposition technique for biological material must conserve the stoichiometry, molecular arrangement, and specific orientation in order to maintain functionality. Recently, it has been demonstrated that the effective deposition of biomaterials may be possible using pulsed laser deposition. For example, using PLD, the deposition of simple proteins, such as silk fibroin, which is expected to have functional applications in medicine and bioelectronics, has been reported [Tsuboi et al., 2001]. As seen in Figure 1.26, the protein possesses a simple primary structure where the secondary structures are β-sheet crystals and amorphous random coils. Normal laser deposition at 351 nm using neat fibroin targets resulted in thin films of fibroin with a random coiled structure as deduced from infrared spectroscopy. Ablation was triggered by two-photon excitation of the peptide chains that destroys the β-sheet structure. By using anthracene as a photosensitive dopant in the ablation target, destruction of the β-sheet structure was avoided, resulting in thin fibroin films having both random coil and β-sheet structures. Thin films of bovine serum albumin (BSA) protein have also been

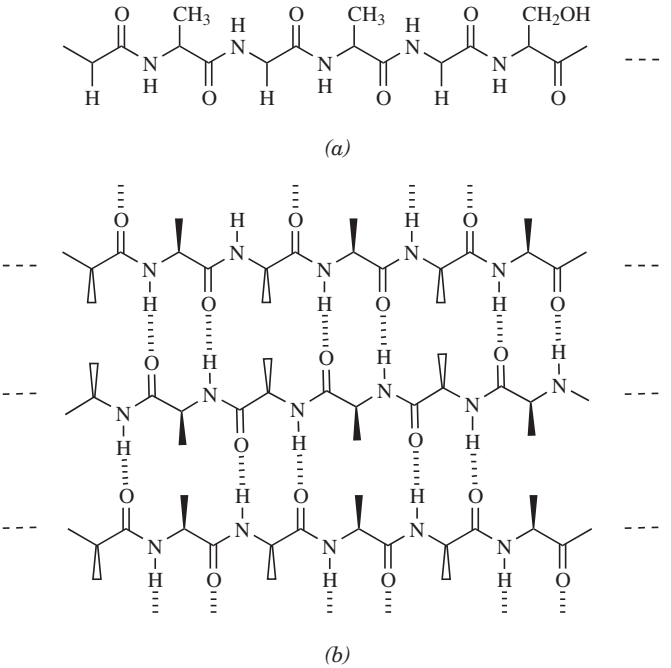

Figure 1.26 (a) Main component in the primary structure of silk fibroin. The sequence of amino acids in this protein can be roughly described as Gly–Ala–Gly–Ala–Gly–Ser, with some tyrosine, valine, tryptophan, etc. content. (b) Schematic illustration of antiparallel β-sheet structure [Tsuboi et al., 2001].

prepared by pulsed laser deposition [Hernandez-Perez et al., 2003]. Using a KrF excimer laser beam focused on a target made of pressed powder, 1 μm films with low roughness could be obtained on silica substrates at room temperature. The Fourier transform infrared spectra of the films, recorded in attenuated total reflection configuration, was nearly identical to those of the starting powders. Fluences higher than $0.6\,J\,cm^{-2}$ are necessary for the conservation of the protein molecules as indicated by IR spectroscopy. Atomic force microscopy images show the protein to be deposited as particles of about 100 nm diameter without clear ordering.

The use of a photosensitizer in the deposition of thin films using target ablation can involve transfer of material either in vacuum or in an atmospheric pressure ambient. The two related techniques have been described as matrix-assisted pulsed laser evaporation (MAPLE) or MAPLE direct write (MDW). MAPLE involves laser ablation in a vacuum and is applicable for biocompatible coatings that are compatible with a low-pressure environment [Pique et al., 1999]. MDW is a localized deposition technique suitable for material deposition of proteins and/or tissue [Wu et al., 2003]. The MAPLE direct write process has been shown to be applicable in forming microarrays from active proteins and living cells. Both techniques are discussed in much more detail in Chapter 3.

1.10 SUMMARY

From its humble beginnings as a curious means for ''laser jocks'' to deposit thin films to the current utilization in the fabrication of inorganic and organic devices, PLD has emerged as a mainstream film growth technique in the research laboratory. The continued development and exploitation of this technique holds numerous opportunities and challenges. Its strengths in oxide thin-film research will continue to be exploited as investigations into the multifunctional character of oxides proceed in the coming years. The possibility of decoupling the laser ablation process from the deposited material of interest via the use of matrix-assisted absorption is clearly advantageous for developing thin films of soft macrostructures. One aspect that has been only marginally explored but holds significant promise is the possibility of tuning the ablation laser wavelength to specific optical absorption channels that yield tailored plume chemistry and alternative film properties. Perhaps most challenging will be the penetration of pulsed laser deposition into large-scale device production in the near future. Despite the challenges of capital cost, deposition throughput, and industrial acceptance, the advantages of pulsed laser deposition will undoubtedly yield application in production as development continues into the twenty-first century.

REFERENCES

Arias, J. L., Mayor, M. B., Pou, J., Leon, B., and Perez-Amor, M. (2002), *Vacuum* **67**, 653–657.

Arias, J. L., Mayor, M. B., Pou, J., Leon, B., and Perez-Amor, M. (2003), *Appl. Surf. Sci.* **208/209**, 57–60.

Blanchet, G. B., Fincher, C. R., Jr., Jackson, C. L., Shah, S. I., and Gardner, K. H. (1993), *Science* **262**, 719–721.

Bozovic, I., and Eckstein, J. N. (1995), *MRS Bull.* **20**, 32–38.

Bubb, D. M., Papantonakis, M. R., Horwitz, J. S., Haglund, R. F. Jr., Toftmann, B., McGill, R. A., and Chrisey, D. B. (2002), *Chem. Phys. Lett.* **352**, 135–139.

Chang, W., Horwitz, J. S., Kim, W.-J., Pond, J. M., Kirchoefer, S. W., Gilmore, C. M., Qadri, S. B., and Chrisey, D. B. (1999), *MRS Symp. Proc.* **541**, 693–698.

Chen, K. R., Leboeuf, J. N., Wood, R. F., Geohegan, D. B., Donato, J. M., Liu, C. L., and Puretzky, A. A. (1996), *J. Vac. Sci. Technol. A* **14**, 1111–1114.

Christen, H.-M., Boatner, L. A., Budai, J. D., Chisholm, M. F., Gea, L. A., Marrero, P. J., and Norton, D. P. (1996), *Appl. Phys. Lett.* **68**, 1488–1490.

Christen, H.-M., Specht, E. D., Norton, D. P., Chisholm, M. F., and Boatner, L. A. (1998), *Appl. Phys. Lett.* **72**, 2535–2537.

Cristescu, R., Socol, G., Mihailescu, I. N., Popescu, M., Sava, F., Ion, E., Morosanu, C. O., and Stamatin, I. (2003), *Appl. Surf. Sci.* **208/209**, 645–650.

Dieleman, J., van de Riet, E., and Kools, J. C. S. (1992), *Jpn. J. Appl. Phys. Pt. 1* **31**, 1964–1971.

Dubowski, J. J. (1988), *Chemtronics*, **3**, 66–76.

Fernandez, F. E., Pumarol, M., Marrero, P., Rodriguez, E., and Mourad, H. A. (1998), *Mater. Res. Soc. Symp. Proc*. **493**, 365–370.

Foxon, C. T. (1991), *Appl. Surf. Sci*. **50**, 28–33.

Frycek, R., Myslik, V., Vrnata, M., Vyslouzil, F., and Kocourek, M. J. T. (2003), *Diffusion and Defect Data Part B* **90/91**, 541–546.

Grudin, O., Marinescu, R., Landsberger, L. M., Kahrizi, M., Frolov, G., Cheeke, J. D. N., Chehab, S., Post, M., Tunney, J., et al. (2002), *J. Vac. Sci. Technol. A* **20**, 1100–1104.

Guanshi, Q., Weiping, Q., Changfeng, W., Shihua, H., Jisen, Z., Shaozhe, L., Zhao, D., and Huangqing, L. (2003), *J. Appl. Phys.* **93**, 4328–4330.

Hass, G., and Ramsey, J. B. (1969), *Appl. Opt.* **8**, 1115–1118.

Haverkamp, J., Mayo, R. M., Bourham, M. A., Narayan, J., Jin, C., and Duscher, G. (2003), *J. Appl. Phys.* **93**, 3627–3634.

Hernandez-Perez, M. A., Garapon, C., Champeaux, C., Shahgaldian, P., Coleman, A., and Mugnier, J. (2003), *Appl. Surf. Sci.* **208/209**, 658–662.

Holzapfel, B., Roas, B., Schultz, L., Bauer, P., and Saemann-Ischenko, G. (1992), *Appl. Phys. Lett*. **61**, 3178–3180.

Iijima, Y., Tanabe, N., Kohno, O., and Ikeno, Y. (1992), *Appl. Phys. Lett.* **60**, 769–771.

Iliadis, A. A., Krishnamoorthy, S., Wei Y., Choopun, S., Vispute, R. D., and Venkatesan, T. (2002), *Proc. SPIE* **4650**, 67–74.

Inam, A., Hedge, M. S., Wu, X. D., Venkatesan, T., England, P., Miceli, P. F., Chase, E. W., Chang, C. C., Tarascon, J. M., and Wachtman, J. B. (1988), *Appl. Phys. Lett*. **53**, 908–910.

Itozaki, H. (2001), *Phys. C* **357/360** (Pt. 1), 7–10.

Jhon, H.-S., Chang, H. J., Kyoung, B. H., Seong, S. M., Jong, G. Y., and Jia, Q. X., and Sang, Y. L. (2003), *IEEE Trans. Appl. Superconduct.* **13**, 294–296.

Jun, Y., Hua, W., Xiaomin, D., Wenli, Z., Yunbo, W., Yuankai, Z., and Jianhong, Z. (2001), *Solid-State Electron.*, **45**, 411–415.

Jung, K. R., and Kang, J. H. (2003), *IEEE Trans. Appl. Superconduct.* **13**, 291–293.

Kaczmarek, S. (1997), *Proc. SPIE* **3187**, 129–134.

Kai, Y., Yoshimura, M., Mori, Y., and Sasaki, T. (2003), *Jpn. J. Appl. Phys. Pt. 2 (Lett.)* **42**, L229–L231.

Kim, W. J., Kim, E.-K., Moon, S. E., Han, S. K., Lee, S. J., and Kang, K. Y. (2002), *Mater. Res. Soc. Symp. Proc.* **720**, 191–196.

Kobayashi, K., and Uchikawa, Y. (2003), *IEEE Trans. Magn.* **39**, 3378–3380.

Kumar, R. T., Karunagaran, B., Mangalaraj, D., Narayandass, S. K., Manoravi, P., Joseph, M., Gopal, V., Madaria, R. K., and Singh, J. P. (2003), *Int. J. Infrared Millimeter Waves* **24**, 327–334.

Lee, Y. E., Norton, D. P., and Budai, J. D. (1999), *Appl. Phys. Lett*. **74**, 3155–3157.

Lee, P. F., Dai, J. Y., Wong, K. H., Chan, H. L. W., and Choy, C. L. (2003), *J. Appl. Phys.* **93**, 3665–3667.

Li, Y., Yao, X., and Tanabe, K. (1998), *Phys. C* **304**, 239.

Liu, J.-M., Chong, N., Chan, H. L. W., Wong, K. H., and Choy, C. L. (2003), *Appl. Phys. A* **76**, 93–96.

Marotta, V., Orlando, S., Parisi, G. P., and Santagata, A. (2003), *Appl. Surf. Sci.* **208/209**, 575–581.

Marre, D., Tumino, A., Bellingeri, E., Pallecchi, I., Pellegrino, L., and Siri, A. S. (2003), *J. Phys. D (Appl. Phys.)* **36**, 896–900.

Matthews, J., Lee, S. Y., Wellstood, F. C., Gilbertson, A. F., Moore, G. E., and Chatraphorn, S. (2003), *IEEE Trans. Appl. Superconduct.* **13**, 219–222.

Migita, S., Sakamaki, K., Si, B. X., Ota, H., Tarui, Y., and Sakai, S. (2002), *Trans. Inst. Electron. Inform. Commun. Eng. C* **J85-C**, 14–22.

Moeckly, B. H., Peng, L. S.-J., and Fischer, G. M. (2003), *IEEE Trans. Appl. Superconduct.* **13**, 712–715.

Mosaner, P., Bonelli, M., and Miotello, A. (2003), *Appl. Surf. Sci.* **208/209**, 561–565.

Muller, K.-H. (1989), in *Handbook of Ion Beam Processing Technology*, J. J. Cuomo, S. M. Rossnagel, and H. R. Kaufman (Eds.), Noyes Publications, Westwood, NJ, 241–278.

Nelea, V., Pelletier, H., Iliescu, M., Werckmann, J., Craciun, V., Mihailescu, I. N., Ristoscu, C., and Ghica, C. (2002), *J. Mater. Sci.: Mater. Med.* **13**, 1167–1173.

Nishii, J., Hossain, F. M., Takagi, S., Aita, T., Saikusa, K., Ohmaki, Y., Ohkubo, I., Kishimoto, S., Ohtomo, A., et al. (2003), *Jpn. J. Appl. Phys. Pt. 2 (Lett.)* **42**, L347–L349.

Norton, D. P., Goyal, A., Budai, J. D., Christen, D. K., Kroeger, D. M., Specht, E. D., He, Q., Saffian, B., Paranthaman, M., Klabunde, C. E., Lee, D. F., Sales, B. C., and List, F. A. (1996), *Science* **274**, 755–757.

Norton, D. P., Park, C., Prouteau, C., Christen, D. K., Chisholm, M. F., Budai, J. D., Pennycook, S. J., Goyal, A., Sun, E. Y., Lee, D. F., Kroeger, D. M., Specht, E., Paranthaman, M., and Browning, N. D. (1998), *Mater. Sci. Eng. B (Solid-State Mater. Adv. Technol.)* **56**, 86–94.

Norton, D. P., Park, C., Budai, J. D., Pennycook, S. J., and Prouteau, C. (1999), *Appl. Phys. Lett.* **74**, 2134–2136.

Norton, D. P., Budai, J. D., and Chisholm, M. F. (2000), *Appl. Phys. Lett.* **76**, 1677–1679.

Ohkubo, I., Matsumoto, Y., Ueno, K., Chikyow, T., Kawasaki, M., and Koinuma, H. (2003), *J. Crystal Growth* **247**, 105–109.

Ohmatsu, K., Muranaka, K., Taneda, T., Fujino, K., Takei, H., Hobara, N., Honjo, S., and Takahashi, Y. (2003), *IEEE Trans. Appl. Superconduct.* **13**, 2462–2465.

Ohta, H., Orita, M., Hirano, M., and Hosono, H. (2002), *Key Eng. Mater.* **214/215**, 75–80.

Ohta, H., Hirano, M., Nakahara, K., Maruta, H., Tanabe, T., Kamiya, M., Kamiya, T., and Hosono, H. (2003), *Appl. Phys. Lett.* **83**, 1029–1031.

Ohtomo, A., Kawasaki, M., Sakurai, Y., Ohkubo, I., Shiroki, R., Yoshida, Y., Yasuda, T., Segawa, Y., and Koinuma, H. (1998), *Mater. Sci. Eng.* **B56**, 263–266.

Orii, T., Hirasawa, M., and Seto, T. (2003), *Appl. Phys. Lett.* **83**, 3395–3397.

Pechen, E. V., Varlashkin, A. V., Krasnosvobodtsev, S. I., Brunner, B., and Renk, K. F. (1995), *Appl. Phys. Lett.* **66**, 2292–2294.

Petraru, A., Schubert, J., Schmid, M., and Buchal, Ch. (2002), *Appl. Phys. Lett.* **81**, 1375–1377.

Pique, A., McGill, R. A., Chrisey, D. B., Leonhardt, D., Mslna, T. E., Spargo, B. J., Callahan, J. H., Vachet, R. W., Chung, R., and Bucaro, M. A. (1999), *Thin Solid Films* **355/356**, 536–541.

Rijnders, G., Koster, G., Leca, V., Blank, D. H. A., and Rogalla, H. (2000), *Appl. Surf. Sci.* **168**, 223–226.

Rode, A. V., Zakery, A., Samoc, M., Charters, R. B., Gamaly, E. G., and Luther-Davies, B. (2002), *Appl. Surf. Sci.* **197/198**, 481–485.

Saenger, K. L. (1993), *Proc. Adv. Mater.* **3**, 1–24.

Singh, R. K., Kim, W.-S., Ollinger, M., Craciun, V., Coowantwong, I., Hochhaus, G., and Koshizaki, N. (2002), *Appl. Surf. Sci.* **197/198**, 610–614.

Smith, H. M., and Turner, A. F. (1965), *Appl. Optics* **4**, 147.

Smolenskii, G. A., Bokov, V. A., Isupov, V. A., Krainik, N. N., Pasynkov, R. E., and Sokolov, A. I. (1984), *Ferroelectrics and Related Materials*, Gordon and Breach, London, 607–659.

Soto, G., de la Cruz, W., Castillon, F. F., Diaz, J. A., Machorro, R., and Farias, M. H. (2003), *Appl. Surf. Sci.* **214**, 58–67.

Specht, E. D., Christen, H.-M., Norton, D. P., and Boatner, L. A. (1998), *Phys. Rev. Lett.* **80**, 4317–4320.

Starke, T. K. H., Coles, G. S. V., and Ferkel, H. (2002), *Sensors and Actuators B (Chem.)* **B85**, 239–245.

Subramanyam, G., Van Keuls, F. W., Miranda, F. A., Romanofsky, R. R., and Warner, J. D. (2003), *Mater. Chem. Phys.* **79**, 147–150.

Sudakar, C., Subbanna, G. N., and Kutty, T. R. N. (2003), *J. Appl. Phys.* **94**, 6030–6033.

Szorenyi, T., and Fogarassy, E. (2003), *J. Appl. Phys.* **94**, 2097–2101.

Takeuchi, I., Yang, W., Chang, K.-S., Aronova, M. A., Venkatesan, T., Vispute, R. D., and Bendersky, L. A. (2003), *J. Appl. Phys.* **94**, 7336–7340.

Tian, Y., Bastawros, A. F., Lo, C. C. H., Constant, A. P., Russell, A. M., and Cook, B. A. (2003), *Appl. Phys. Lett.* **83**, 2781–2783.

Trajanovic, Z., Choopun, S., Sharma, R. P., and Venkatesan, T. (1997), *Appl. Phys. Lett.* **70**, 3461–3463.

Tsuboi, Y., Goto, M., and Itaya, A. (2001), *J. Appl. Phys.* **89**, 7917–7923.

Watanabe, T., Shiohara, Y., and Izumi, T. (2003), *IEEE Trans. Appl. Superconduct.* **3**, 2445–2451.

Willmott, P. R., and Huber, J. R. (2000), *Rev. Modern Phys.* **72**, 315–328.

Wu, Y., Fan, R., and Yang, P. (2002), *Nano Lett.* **2**, 83–86.

Wu, P. K., Ringeisen, B. R., Krizman, D. B., Frondoza, C. G., Brooks, M., Bubb, D. M., Auyeung, R. C. Y., Pique, A., Spargo, B., et al. (2003), *Rev. Sci. Instrum.* **74**, 2546–2557.

Xu, B., Cross, B. L. E., and Bernstein, J. J. (2000), *Thin Solid Films* **377/378**, 712–718.

Yanagi, H., Ueda, K., Ohta, H., Orita, M., Hirano, M., and Hosono, H. (2001), *Solid State Commun.* **121**, 15–17.

Yang, W., Hullavarad, S. S., Nagaraj, B., Takeuchi, I., Sharma, R. P., Venkatesan, T., Vispute, R. D., and Shen, H. (2003), *Appl. Phys. Lett.* **82**, 3424–3426.

Yilmaz, S., Venkatesan, T., and Gerhard-Multhaupt, R. (1991), *Appl. Phys. Lett.* **58**, 2479–2481.

Yu, J., Wang, H., Dong, X. M., Zhou, W. L., Wang, Y. B., Zheng, Y. K., Zhao, J. H. (2001), *Solid-State Electronics* **45**(3), 411–415.

Zakery, A. (2002), *J. Phys. D (Appl. Phys.)* **35**, 2909–2913.

Zakery, A., Ruan, Y., Rode, A. V., Samoc, M., and Luther-Davies, B. (2003), *J. Opt. Soc. Am. B (Opt. Phys.)* **20**, 1844–1852.

SECTION 2

CHAPTER 2

Resonant Infrared Pulsed Laser Ablation and Deposition of Thin Polymer Films

DANIEL-DENNIS McALEVY BUBB

Department of Physics, Rutgers University—Camden, Camden, New Jersey and
Naval Research Laboratory, Code 6365, Washington, D.C.

RICHARD F. HAGLUND, JR.

Department of Physics and Astronomy and W. M. Keck Foundation Free-Electron Laser Center, Vanderbilt University, Nashville, Tennessee

Pulsed laser deposition (PLD) of thin films is now used in materials research laboratories round the world for prototyping thin films of many inorganic materials and even in some device fabrication protocols. This development has been made possible by the increasing versatility and reliability of the ultraviolet (UV) excimer laser as it evolved particularly after the 1980s. However, progress in UV-PLD of organic molecules and polymers has been inconsistent, largely because UV-PLD has two characteristics that are intrinsically incompatible with organic and polymeric materials: the high photon energy of KrF and ArF lasers (5.0 and 6.4 eV, respectively) produces photochemical reactions in the ablated material that are almost always undesirable; and the energetic species in the ablation plume can sputter or damage any material that has already been deposited.

These two facts highlight an important difference between laser ablation for machining—achieved very effectively by both nanosecond excimer lasers and femtosecond near-infrared Ti:sapphire lasers—and laser ablation for thin-film deposition. In the case of deposition, it is absolutely essential that the polymers transferred to the gas phase from the ablation target are physically and chemically intact, so that the desired polymer properties appear in the deposited film.

In this chapter, we review recent developments in resonant infrared (RIR) pulsed laser ablation, a process that by virtue of the low photon energy overcomes the inherent disadvantages of UV-PLD in the case of organic or polymeric materials. RIR-PLD has been shown during the past 5 years to work with many different families of polymers and, thanks to recent developments in lasers, has significant promise for integration into commercial thin-film processing technologies. We begin with an overview of some variants of PLD and then introduce several analytical techniques that can be used to assess the success of PLD of organics and polymers. Following a review of results on several different families of polymers that have been deposited by RIR-PLD, we conclude with discussions of the mechanism of RIR-PLD as it is presently

Pulsed Laser Deposition of Thin Films: Applications-Led Growth of Functional Materials
Edited by Robert Eason

understood. A brief synopsis of laser types that may be developed to make RIR-PLD as reliable as current UV-PLD concludes the chapter.

2.1 TECHNOLOGICAL SIGNIFICANCE OF ORGANIC THIN-FILM DEPOSITION

Thin films of organic molecules and polymers play critical roles in myriad electronic, photonic, mechanical, medical, sensor, and thermal control technologies, with an attendant importance therefore attached to methods of deposition. To name just a few obvious examples: Antistiction coatings are crucial to the reliable operation of micromechanical systems ranging from the accelerometers at the heart of automobile air-bag technology to the magnetic disk drives found in computers and portable music players. Multilayer organic and polymer films provide the requisite light-emitting and carrier transport functions for organic and polymer light-emitting devices and flexible displays. Organic thin-film transistors are being developed for everything from computer and television displays to active-label technologies for supermarket checkout lanes. It is thus no exaggeration to say that deposition of organic and polymeric thin films is a critical component of one of the broadest and largest markets in the world.

In the current state of the art, a wide variety of deposition techniques can be found in industry, many of them still not optimized either for performance, reliability, or environmentally benign process technology. For example, in the organic light-emitting diode (OLED) manufacturing process, it is not uncommon to employ a mixture of vacuum- and liquid-phase deposition techniques since small organic light-emitting molecules (e.g., Alq3) can be deposited in vacuum, while some of the polymer carrier-transport materials must be deposited in the liquid phase. The need to go outside the normal vacuum processing loop found elsewhere in the semiconductor industry makes for added time, complexity, and cost in the manufacturing process and also reduces product yield and device reliability. Small organic molecules can be deposited by thermal evaporation in ultrahigh vacuum (organic molecular beam epitaxy, or OMBE), but polymers are destroyed by thermal evaporation, thus reducing the palette of materials available to the process and device design communities. Moreover, OMBE is a slow process, not compatible with making inexpensive organic thin films at the level needed for RFID (radio-frequency identification) applications in the retail industry. Poly(tetrafluoroethylene) (PTFE) would be a very desirable antistiction coating, but it cannot be deposited in liquid phase because PTFE is insoluble. Many other examples exist that further illustrate this point.

Hence there is a strong technological motivation to find a reliable vapor deposition process that would have the following characteristics: It would be solvent free, vacuum compatible, conformal, and produce defect-free thin films with extremely precise thickness control at high deposition rates. It should be compatible with standard fabrication line technologies as currently exist in semiconductor fabrication facilities. Finally, the process should have cost and reliability characteristics similar to those of contemporary vacuum deposition techniques (e.g., sputter deposition) with which the industry is already familiar.

In addition, however, the topic of infrared laser ablation and deposition of polymers is interesting as a surface science problem, involving as it does two interesting questions:

1. How, if at all, is it possible to break the relatively weak intermolecular bonds that hold, for example, a glassy polymer together without breaking the stronger intramolecular bonds that give the polymer its unique chemical and physical properties?
2. What are the salient differences that arise when those intermolecular bonds are subjected to intense *vibrational*, rather than *electronic*, excitation?

As will become apparent, both questions take us into largely uncharted waters at the edge of previously well-explored territory.

2.2 LASER-BASED METHODS FOR DEPOSITION OF POLYMER THIN FILMS: AN OVERVIEW

In this section, we review briefly several different implementations of PLD as have been applied to the problem of organic or polymer deposition. The last of these introduces the new concept of resonant infrared laser ablation and deposition.

2.2.1 Pulsed Laser Deposition with UV Lasers

Soon after the development of PLD and the subsequent demonstration that it was capable of synthesizing thin films of multicomponent materials [Cheung and Sankur, 1988, and also see Chapter 1], researchers began to wonder if the same strategy could be employed to deposit thin polymer and polymeric films [Chrisey and Hubler, 1994]. Early attempts to do so utilized ultraviolet, usually excimer, lasers, which hereafter shall be referred to as UV-PLD. These efforts built upon laser ablation studies performed by Srinivasan et al. in the 1980s [Srinivasan and Braren, 1989]. Nylon, polycarbonate, and poly(methylmethacrylate) were several of the polymers that were deposited in thin-film form by so-called pulsed laser evaporation [Hansen and Robitaille, 1988]. Poly(tetrafluoroethylene) and other fluoropolymers were deposited using the fourth harmonic (266 nm) of a Nd : YAG laser, and it was found that the morphology could be controlled through changing the substrate temperature [Blanchet, 1993]. Further studies showed that the evaporation process could be viewed as a kind of flash pyrolysis in which the polymer target was converted to a vapor that consists of monomer and small oligomeric fragments. Both unzipping and nonunzipping polymers alike behaved similarly upon pulsed laser excitation; a large quantity of monomer was present in the ablation plume despite the fact that for condensation polymers, monomer is not usually present in the mass spectrum during thermal pyrolysis [Blanchet, 1996]. In this sense, the laser can be viewed as the agent that opens a route to nonequilibrium reaction pathways, which can in turn be exploited to deposit thin films or investigate novel reactions. When a substrate is placed in the path of the ablation plume, the monomer–oligomeric fragments recombine and are deposited as a polymeric thin film, with the repolymerization reaction possibly catalyzed by the presence of radicals. Smooth films of fluoropolymers that faithfully reproduce the chemical structure and composition of the starting material were deposited by this method.

In retrospect, it seems that the picture of laser ablation as a thermal route to fast unzipping should be updated to include the possibility of direct scission of pendant groups by photochemical reactions, and the intensity in a focused UV laser beam during an ablation experiment is certainly sufficient to accomplish this. Experiments with a poly(ethylene-vinyl acetate)–carbon nanocomposite and a 193-nm ArF laser showed that there was preferential loss of vinyl acetate groups during laser ablation and thin-film deposition, and that both photothermal and photochemical mechanisms could be present to account for this loss [Bubb et al., 2001c]. Therefore, the use of UV lasers in polymer PLD experiments presents certain challenges that may not be overcome if the goal is to deposit a polymer film with the same chemical structure as the starting material.

2.2.2 Matrix-Assisted Pulsed Laser Evaporation

An alternative approach to PLD for the deposition of polymer and other organic films was developed at the Naval Research Laboratory in the late 1990s and is known as matrix-assisted pulsed laser evaporation (MAPLE) [Piqué et al., 1999; Chrisey et al., 2003]. In this approach, a polymer or other organic to be deposited is dissolved in an appropriate solvent, and the solution is decanted into a metal target die where it is frozen. The frozen target is then placed into a vacuum chamber and the experiment proceeds as with PLD. MAPLE has been used to deposit a variety of materials such as chemoselective polymers [Piqué et al., 1999], proteins [Ringeisen et al., 2001], and other organic materials. In Figure 2.1, a schematic of the MAPLE process is shown.

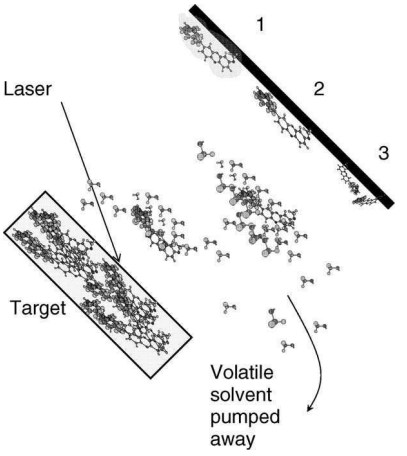

Figure 2.1 Schematic of MAPLE process. Events 1, 2, and 3 are discussed in the text.

Three of the many possible outcomes are shown. In the first (1), a "chunk" of the target is ejected so that frozen solvent lands on the substrate. Subsequently, it will melt and cause structuring in the film. This has been observed during MAPLE of biodegradable polymers [Mercado et al., 2004] and results in unfavorable film deposition conditions. The second outcome in Figure 2.1 is the preferred outcome. Here, an isolated polymer chain is ejected into the gas phase and lands on the substrate while remaining intact throughout the process. Currently, it is not known whether this outcome actually occurs. In the final case (3), the polymer chain is cut either through direct photochemical interactions with the laser or through interactions with reactive species produced by the laser. This outcome has been observed during MAPLE of poly(ethylene glycol) (PEG) using a laser wavelength of 193 nm and $CHCl_3$ as a matrix [Bubb et al., 2002a]. Cl* radicals were produced by the laser and attacked the polymer either in the plume or in the film and resulted in chemical modification of the polymer film. Furthermore, these reactive species may result in the polymerization of the solvent molecules such that they result in a film themselves [Bubb et al., 2004]. So, it is clear that the choice of matrix is of essential concern in MAPLE experiments. The choice of laser wavelength is also important—UV lasers have sufficient photon energy to cause photochemical reactions of many types. In contrast, performing MAPLE at infrared wavelengths seems to minimize some of these unfavorable results [Toftmann et al., 2004; Bubb et al., 2004].

2.2.3 Photosensitized Ablation and Deposition

Photosensitized ablation and deposition is a technique that is closely related to MAPLE. In this technique a target material that is very weakly absorbing at the chosen wavelength is "doped" with a strong absorber such as anthracene. This permits the use of laser wavelengths such as 351 and 355 nm that induce less electronic excitation than UV lasers operating near 300 nm and below. The strongly absorbing dye causes the laser energy to be absorbed in a small enough volume to cause sufficient heating for material to be ejected, but since the target material is nearly transparent to the laser destructive excitations are minimized. Polystyrene has been deposited in this fashion using anthracene as a sensitizer and a 351-nm laser as the excitation source [Tsuboi and Itaya, 1999]. It is impossible to deposit polystyrene (or any other phenyl-ring containing polymer for that matter) using a laser wavelength below 248 nm because the phenyl rings strongly absorb the radiation and electron delocalization results in bond breaking. The use of laser wavelengths above 248 nm was unsuccessful in depositing a film because the laser energy was not absorbed strongly enough to cause material ejection from the target. In addition to polystyrene, silk fibroin has also been deposited by this technique [Tsuboi et al., 2002a] along with several other polymers [Tsuboi et al., 2002b].

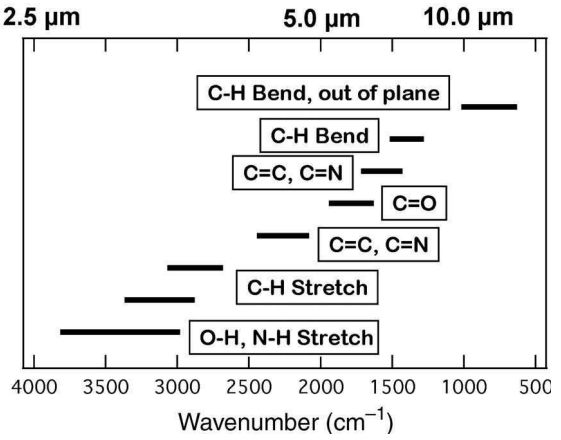

Figure 2.2 Ranges of vibrational frequencies for specific vibrational modes in organic and polymeric materials. Only carbon, nitrogen, and oxygen bonds are shown; in the case of fluorinated organics or polymers, the bands will lie slightly to the red side of nearby modes [e.g., C–F vs. C–N bonds in poly(tetrafluoroethylene)].

2.2.4 Resonant Infrared Pulsed Laser Deposition

Resonant infrared pulsed laser deposition (RIR-PLD) is based on the concept that excitation of a weak vibrational resonance in an organic or polymeric substrate can induce localized vibrational excitation that leads to the breaking of the relatively weak intermolecular bonds. This requires the use of either a fixed-frequency laser that happens to be in resonance with a vibrational mode of the polymer to be deposited or a laser that can be tuned to such a mode. Many of the relevant vibrational modes lie in the ''molecular fingerprint'' region of the IR spectrum (2–10 μm), as shown in Figure 2.2, and we accordingly focus further attention on this wavelength range.

Because the light source for almost all of the IR PLD experiments carried out to date was the W. M. Keck Foundation Free-Electron Laser (FEL) at Vanderbilt University [Edwards et al., 1996], we present here a brief description of the FEL. An FEL comprises three essential elements: a high-brightness electron source and accelerator that brings the electron beam to relativistic velocities, an undulator or wiggler in which the electrons undergo a periodic acceleration induced by spatially alternating magnetic fields, and an optical cavity that feeds back a portion of the photons generated into the accelerated electron beam. The concept is illustrated schematically in Figure 2.3. Optical gain is produced by a purely classical electromagnetic field effect produced through the interaction of the cavity photons with the electron beam. The relationship between the output wavelength, wiggler period, beam energy E_{Beam}, and magnetic field B is given to lowest order by the following expression:

$$\lambda_{\text{FEL}} = \frac{\lambda_{\text{Wiggler}}}{2\gamma^2}[1 + \kappa^2(B)] \equiv \frac{E_{\text{Beam}}}{m_0 c^2} \tag{2.1}$$

where κ is a quantity of order unity that depends on the on-axis magnetic field, and γ is the ratio of electron beam kinetic energy to the electron rest mass m_0c^2.

Unlike a conventional laser, in which the laser medium and mode of excitation largely determine the output wavelength and temporal pulse structure, the FEL makes is possible to choose these factors by the choice of beam energy, magnetic field, wiggler period, and temporal structure imposed on the electron beam. The Vanderbilt FEL, based on an S-band klystron to drive a 3-m RF accelerator, has a temporal pulse structure consisting of a 3- to 6-μs macropulse at a repetition rate of

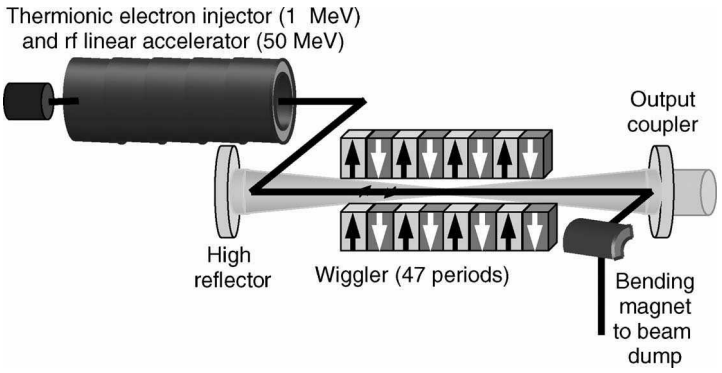

Figure 2.3 Schematic of the free-electron laser, showing the electron gun and accelerator; the wiggler or undulator in which the electron beam is driven into periodic spatial oscillations by a magnetic field in which the orientation of the field alternates; and an optical cavity that feeds back the requisite portion of the beam to create the FEL gain.

30 Hz (or submultiples thereof); the macropulse in turn consists of a train of ~1-ps pulses separated by 350 ps (the frequency of the klystron is 2.865 GHz). The energy in each macropulse is of order 33–100 mJ, depending on wavelength providing a typical average power of 1–3 W at 30 Hz. The wiggler period and magnetic field are such as to provide a continuous laser tuning range from 2 to 10 μm, thus effectively covering the molecular fingerprint region.

The FEL can be tuned throughout its range with a bandwidth less than 2%, macropulse energies between 33 and 100 mJ, and pulse durations of 5–6 μs. For RIR-PLD experiments, the laser beam is scanned over the polymer or organic target in the standard fashion. Macropulse fluences producing reasonable ablation and deposition conditions are found to range between 0.1 and 5 J/cm^2, corresponding to an average intensity of up to 1 MW/cm^2 over the macropulse and transient intensities approaching 1 GW/cm^2 for each micropulse. This produces an unusual temporal sequence similar to that proposed by Gamaly et al. and illustrated in Figure 2.4; the interpulse spacing of micropulses is sufficiently short, and the micropulse energies sufficiently small, that there is only a small rise in target temperature followed by a relaxation period in which much of the incident energy dissipates before the next micropulse arrives. This leads to a substantially smaller temperature rise than would

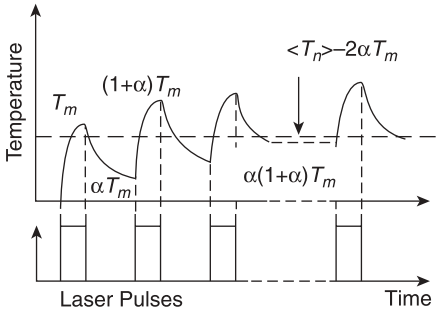

Figure 2.4 Schematic illustration of the temperature rise in a target irradiated by the high repetition rate sequence of micropulses in the free-electron laser. The small amount of energy deposited by each FEL micropulse largely dissipates before the next micropulse arrives, leading to an overall much smaller temperature rise than would be expected from the deposition of the entire FEL macropulse energy all at once.

occur were the target to absorb the energy of the full macropulse all at once. The effects of this curious excitation and relaxation sequence are discussed in more detail in Section 2.4.

2.2.5 Summary of Techniques

Several techniques for polymer thin-film deposition have been discussed such as UV-PLD, MAPLE, and photosensitized ablation and deposition. Each of these presents some advantages but none is wholly without disadvantages. For UV-PLD, the intense interaction between a focused UV laser and an organic material can result in photomodification of the target material and also the deposited film. In the best case scenario, the target is reduced to its constituent monomer by intense laser heating; and for the deposition of a polymer film, reactive species must be present to catalyze the necessary reaction. If polymerization is incomplete or pendant functional groups are lost to direct scission photoreactions, the chemical structure of the thin film will be different from the starting material. Practitioners of MAPLE seek to limit the direct interaction between the laser and the polymer to be deposited by using a matrix. However, if the laser wavelength–matrix combination is not chosen properly, photochemical interactions can produce results just as unfavorable to those with UV-PLD. Finally, photosensitized ablation is useful for those situations where target material is transparent to the laser wavelength, but an appropriate sensitizer causes sufficient volumetric energy density to eject material from the target. However, it is not clear that an appropriate sensitizer will be found or that the sensitizer will not itself become part of the film. Photochemical reactions are also possible in this wavelength regime as well. Therefore, we have explored resonant infrared pulsed laser ablation and deposition (RIR-PLD) of polymer films as an alternative to these techniques for the deposition of thin polymer films.

2.3 DEPOSITION, ABLATION, AND CHARACTERIZATION OF SELECTED POLYMERS

Over the course of the past 5 years, we have demonstrated successful infrared laser ablation of a variety of polymer species. In these cases, ''successful'' has been defined by a number of different characterizations of the deposited material that appear to show that the polymers are effectively transferred from ablation target to gas-phase plume to thin deposited films with their local and long-range structures essentially intact. In the following section, we describe the characterization tools we have used for this purpose and discuss their application to specific polymers of interest.

2.3.1 Characterization of Deposited Material

Obviously, the critical step in evaluating material processing techniques is characterization of the result, which in our case, is a thin film deposited upon a substrate. In the studies described in this text, the goal has always been to identify those characterization techniques that give the greatest amount of information for the least investment of effort. There are numerous possible characterization techniques for organic materials. The list in Table 2.1 is not exhaustive; it will simply serve to illustrate our approach to this difficult problem by highlighting several important characterization techniques.

2.3.1.1 Fourier Transform Infrared Spectroscopy

Fourier transform infrared (FTIR) spectroscopy [Smith, 1999] is extremely useful for organic materials with functional groups that absorb light in the mid-infrared (2.5–25 μm or 4000–400 cm^{-1}). In the experiments described here, FTIR is used as a process evaluator; the starting material and deposited film are compared in order to look for changes in the chemical structure of the film relative to the starting material. However, the infrared absorbance spectrum is indicative of the properties of

TABLE 2.1 Characterization Methods Applicable to Pulsed Laser Deposited Polymer Thin Films

Technique	Information	Limitation	Strength	Comments
Fourier transform infrared (FTIR) spectroscopy	Chemical structure (integrity) of repeat unit	No information on number of repeat units and hence, molecular weight	Is not material intensive, if damaged will help to deduce the mechanism; can be used as a quick diagnostic	
Nuclear resonance magnetic (NMR) spectroscopy	Chemical structure (integrity) of repeat unit	Endgroup analysis *may* permit qualitative molecular weight determination; but information is largely about repeat unit; must create proton exchange environment	Similar to FTIR; gives information about bonding and proton environment (or carbon atom, fluorine atom, etc.)	
Size exclusion chromatography (SEC, GPC)	Average molecular weight and higher order moments	Requires dissolution in appropriate mobile phase and calibration of columns—not an absolute value (relative to standards)	Litmus test for segmentation; can be coupled with other techniques, i.e. light scattering viscometry	
Matrix-assisted laser desorption and ionization mass spectrometry (MALDI-MS)	Weight- and number-average molecular weight, relative concentrations	Need protocol (possibly separate) for each polymer	Extremely versatile, can be used to analyze mixtures, extremely sensitive (sub-amol)	Electrospray ionization is similar and similarly applicable
Quasi-elastic light scattering	Average molecular weight	Can require filtering of small volume samples, easy to contaminate with dust, etc; insoluble fractions not analyzed	Can be coupled with column chromato-graph techniques to separately analyze fractions—very powerful and versatile	
Electron and optical microscopy	Morphology	Does not tell much about physicochemical properties	Aside from usual morphological considerations can be used to determine if residual material remains after washing of coated wafer—can indicate cross-linking	

the basic repeat unit (monomer) and contains very little information about the number of repeat units. Small changes in the midinfrared absorbance due to either new or missing bands typically reflect significant rearrangement of the polymer. This presents an entirely new challenge in characterization. Since the basic chemical structure of the polymer thin film is altered, mass spectroscopic techniques such as size exclusion chromatography (SEC), electrospray ionization (ESI), or matrix-assisted laser desorption and ionization (MALDI) mass spectrometry (MS) are unlikely to provide quantitative information on the molecular weight distributions for reasons that will be discussed in forthcoming sections. Comparisons of infrared absorbance spectra are most meaningful when the midinfrared spectra are nearly identical, as the assignment of the mass peaks will depend on the chemical structure of the molecule. A related useful technique is nuclear magnetic resonance (NMR) spectroscopy.

2.3.1.2 Size Exclusion Chromatography

In column chromatographic mass spectroscopic techniques such as SEC, the retention time of molecules dissolved in carrier solvent is inversely proportional to the logarithm of the molecular weight. The quantities measured by SEC are the number-average molar mass M_n and the weight-average molar mass M_w, which are defined, respectively, as

$$M_n = \sum_j N_j M_j \Big/ \sum_k N_k \qquad M_w = \sum_j N_j M_j^2 \Big/ \sum_k N_k M_k \tag{2.2}$$

where N_j is the number of polymers of molecular mass M_j. Thus, we identify M_n and M_w as the first and second moments of the polymer mass distribution.

The limitations of SEC are encountered when the polymer film is chemically altered in some other way other than simple segmentation, that is, shortening of the chains. This is related to the difficulty mentioned above with FTIR. If the deposited material has a different affinity for the column, then spurious quantitative results will be obtained. Generally speaking, if the infrared spectrum of the deposited film is visibly changed with respect to the native material, we consider SEC only a provider of qualitative results. Other difficulties one can encounter in using SEC to characterize films is that there is a very small sample volume under test, and it is extremely easy to contaminate with dust or even wash-off from a filter. Finally, if there is any cross-linking or creation of insoluble material during the film deposition process, the films mass spectrum cannot be analyzed by this method.

2.3.1.3 Matrix-Assisted Laser Desorption and Ionization Mass Spectrometry (MALDI-MS)

Soft ionization mass spectroscopy techniques such as MALDI and ESI are extremely useful for organic materials [Herbert and Johnstone, 2003]. In both techniques, the mass spectrum is obtained through the generation of ions that attach to the organic and ''softly'' ionize it. In MALDI a laser is focused on a composite target of matrix (ion producer) and guest (analyte) in vacuum. The laser vaporizes the material and fragments the matrix but not the polymer, and somehow the organic material becomes ionized. The plume of emitted material is introduced into a mass spectrometer where it can be identified. ESI is similar; in this technique an organic material is co-dissolved with a solvent–salt mixture and placed in a capillary tube. An electric potential is applied between the capillary tube and the entrance window of a mass spectrometer, which causes the introduction of a charged organic in the mass spectrometer, which is then identified by conventional means. A potential weakness of these techniques is that it is necessary for the material to become ionized for detection to occur. If the material is chemically altered, it is possible that some fractions will ionize differently than expected and that the observed mass spectrum may become skewed. In this case, infrared absorbance measurements will guide us in determining whether we suspect there may be such fractions. Otherwise, MALDI, for example, is an extraordinarily versatile technique, possessing zeptomole sensitivity.

2.3.1.4 Optical, Electron, and Atomic Force Microscopy

For the most part, the first concern in depositing polymer thin films is in preserving the chemical structure of the polymer. For applications, the critical property is often morphology. Physical vapor deposition techniques are very versatile; however, serious drawbacks include the production and deposition of particulates that can mar the uniformity of deposited films. Various forms of microscopy are useful to assess the deposited film morphology. The most useful is scanning electron microscopy (SEM), because of its large horizontal and vertical dynamic range. Since many polymers are insulators, it is necessary to go to low voltages to avoid sample charging; hence the most useful SEM tools are those with cold-cathode field emission electron guns that can still achieve high resolution at voltages as low as 1 keV. In addition, atomic force microscopy (AFM) is a very versatile tool for the characterization of polymer films and is capapble, for example, of characterization of multiplayer films [Lobo et al., 1999].

2.3.2 Choice of Polymers for Early Studies

Given that characterization of the deposited films is an essential part of the process evaluation, polymers that can have their physicochemical properties specified precisely were chosen for early RIR-PLD studies. Two such polymers that can be characterized with high confidence are polyethylene glycol (PEG) and polystyrene (PS). Both are available in average molecular weights from less than 1000 Da to greater than 1,000,000 Da. Polystyrene is used to calibrate infrared spectrometers and both polymers are used to calibrate chromatographic columns. In practical terms, this means that if SEC is used to characterize the deposited films, then an *absolute* number- and weight-average molecular weight can be determined. Both of these polymers (PEG, PS) are also used as calibrants for soft ionization mass spectroscopic techniques such as MALDI-MS and ESI. Other polymers that might be of technological interest but that do not have appropriate mass standards will have to have their molecular weight specified relative to one of these standards.

2.3.3 Polyethylene Glycol

2.3.3.1 Comparing UV-PLD and RIR-PLD

Initial studies focused on comparisons of RIR-PLD with UV-PLD in order to demonstrate the importance of resonant vibrational excitation, and PEG was the polymer chosen for these studies. Characterization was accomplished through FTIR, SEC, MALDI, and ESI. The chemical structure of PEG is shown in Figure 2.5 along with the wavelengths of the major stretching modes (−CO, −CH, −OH). Directly comparing UV-PLD and RIR-PLD of PEG we found that when the laser was tuned to a vibrational resonance (i.e., 2.90 μm for the OH stretch) it was possible to deposit thin films that accurately match the IR spectra of the starting material [Bubb et al., 2001a]. In contrast, PEG

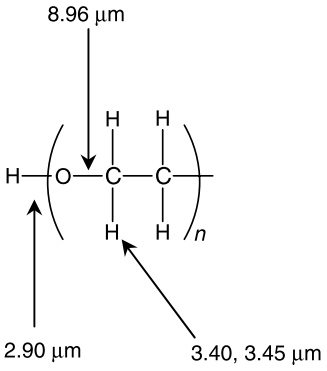

Figure 2.5 Chemical structure of PEG and wavelengths of selected vibrational modes.

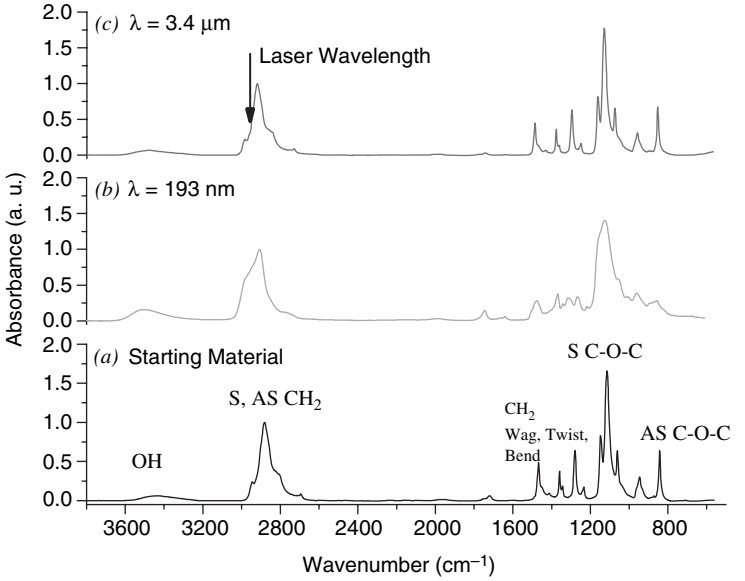

Figure 2.6 Infrared absorbance spectrum of UV- and RIR-PLD films compared with starting material.

thin films that are deposited using an ArF UV laser (λ = 193 nm) do not have the same physical and chemical properties as the starting material. The midinfrared absorbance spectra of a UV-PLD film, a RIR-PLD film, and the starting material are displayed for comparison in Figure 2.6. Examining the spectra of the UV-PLD films, it is found that the changes in positions of the bands are sufficient to warrant description of the UV-deposited material as ''PEG-like.'' In stark contrast, the RIR-PLD film appears to have a nearly identical infrared absorbance spectrum to that of the starting material.

Next, molecular weight distributions of the deposited films are compared with the native polymer. Given that the UV-PLD deposited film has been severely chemically altered, its mass spectrum is presented only for qualitative purposes. Figure 2.7 displays the ESI mass spectra of the starting material and UV- and RIR-PLD films. It is important to note that the concentrations of the solutions that are injected into the ESI time-of-flight mass spectrometer are the same in all cases. Although apparently random and noisy, there are real peaks in the UV-PLD deposited film's spectrum. Due to the alteration of the UV-PLD film's chemical structure, we once again refer to it as ''PEG-like,'' as there is no correlation between the peaks in its spectrum and the native material. The agreement between the RIR-PLD film's mass spectrum and the starting material is evident. Most encouraging in all of these results is that similar results are obtained using a fixed frequency Er:YAG (2.94 μm) laser operating either at a free-running pulse width of about 300 μs or Q switched with a pulse of 150 ns [Haglund et al., 2003]. This suggests that the execution of RIR-PLD is not limited to an exotic light source such as the FEL, and tabletop laser-based deposition chambers are capable of making contributions in this area as well.

2.3.3.2 Mode-Specific Behavior in RIR-PLD of PEG

Further studies with PEG have demonstrated the importance of resonant excitation and shown that there is more to RIR-PLD than simply performing PLD at a wavelength that does not cause electronic excitation [Bubb et al., 2002a]. What may be most interesting about RIR-PLD, from a scientific standpoint, is the apparent mode-specific behavior with respect to the deposition rate and molecular weight distributions of the deposited films. In experiments with PEG, films were deposited using off-resonant light, and the infrared absorbance spectrum showed that substantial chemical and structural modification had occurred. In Figure 2.8, we display the mid-infrared

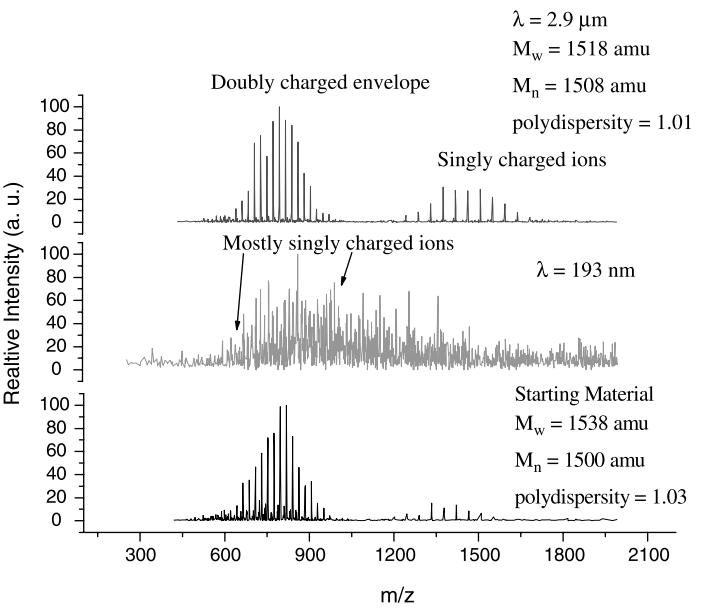

Figure 2.7 Electrospray ionization mass spectra of laser-deposited PEG films.

absorbance of a film deposited using both nonresonant (4.17 μm) and resonant (3.4 μm) light. Both the infrared absorbance and mass spectra show similar results: the films deposited with off-resonance irradiation are chemically altered with respect to the native polymer and its resonant counterpart.

Finally, the molecular weight distributions of the films depend upon the particular bond being excited. A comparison of excitation of −OH (2.90 μm) and −CH (3.45 μm) stretching modes showed that the films deposited by excitation of the terminal −OH showed no alteration even up to extremely high fluences while the −CH deposited films were segmented. The deposition rate was also seen to strongly depend upon the particular mode being excited. In Figure 2.9 we show the

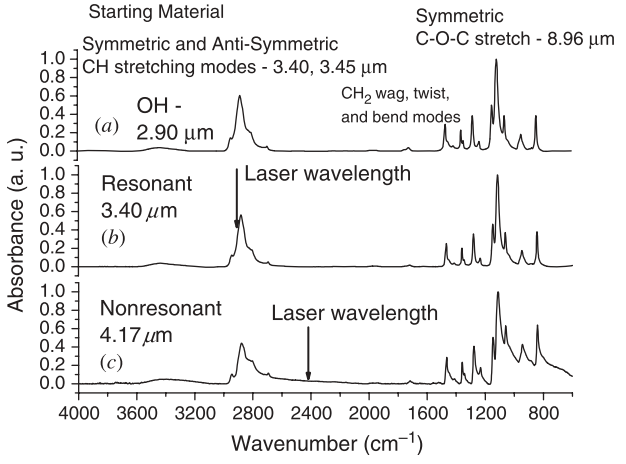

Figure 2.8 Infrared spectra for (*a*) starting material, (*b*) film deposited at 3.40 μm (on resonance), and (*c*) off resonance at 4.17 μm.

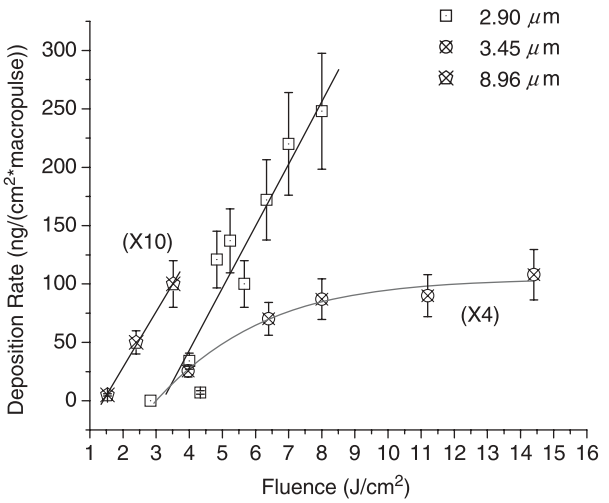

Figure 2.9 Deposition rate for three different vibrational modes during RIR-PLD of PEG.

deposition rate as a function of fluence for three modes [Bubb et al., 2002b]. The bond (—OH) with the smallest oscillator strength gives the highest deposition rate while the one with the largest (—CO) apparently has the smallest deposition rate. One interpretation of these results is that exciting the bond most responsible for the interchain interactions leads to the most efficient desorption while doing the least damage to the polymer. Further studies will attempt to sort out the respective roles of the intermolecular interactions and entanglement; however, this is expected to be a formidable challenge.

2.3.4 Polystyrene

2.3.4.1 Large Molecular Weight Polystyrene

Polystyrene is a ''model'' polymer much as PEG. It is also a mass spectroscopic standard, thus facilitating identification of laser-processed material. In experiments with ~ 300 kDa polystyrene, it was found that it was not possible to deposit material without fragmentation. Presumably, above 100 kDa, entanglement of polymer chains is going to dominate intermolecular interactions. It was observed that the molecular weight distribution of films was reduced by a factor of 10–15; however, the infrared absorbance spectrum is unchanged [Bubb et al., 2002c].

In complete contrast to RIR-PLD experiments with polyethylene glycol, it was not possible to deposit a polystyrene film using off-resonant radiation in the fluence range investigated in these studies. Instead, it was observed that irradiation with 2.90 μm light produced defects in the material that charred the target but did not result in any deposition at all. Presumably the much larger penetration depth of the nonresonant light does not allow the energy per volume to exceed the ablation threshold.

2.3.4.2 Small Molecular Weight Polystyrene: Mode-Specific Effects

Resonant infrared ablation and deposition experiments were performed, however, with lower molecular weight polystyrene ($\sim$10,800 kDa) and a number of interesting results were observed [Bubb et al., 2006]. The ablation yield, which was defined as mass deposited per unit substrate area per laser shot, was found to depend on the wavelength of excitation. Figure 2.10 shows a portion of the infrared spectrum of polystyrene along with the location of these vibrational bands on the molecule. Note that the width of the 3.43-μm vibrational band (saturated CH stretch) is approximately 3 times that of the 3.31-μm band (unsaturated CH stretch), leading us to conclude the lifetime

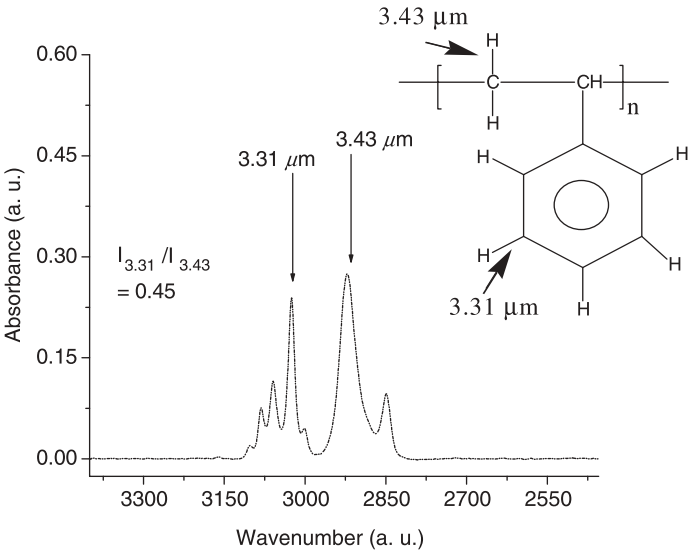

Figure 2.10 Infrared spectrum and chemical structure of polystyrene.

of the unsaturated CH must be three times greater than its saturated counterpart. This likely has implications for the mechanism of ablation as will be discussed in Section 2.4 of this chapter.

In Figure 2.11, we display the ablation yield as a function of the number of laser pulses for these two wavelengths, and it is approximately 1.5 times greater for the 3.31-μm vibrational band in comparison with the 3.43-μm vibrational band. This occurs despite the fact that the absorption coefficients are nearly the same at these two wavelengths; for an ablation process governed purely by thermodynamics, one would then expect the deposition rates to be nearly the same. As will be discussed in Section 2.4, the differences in the yield are expected to be related to the lifetime.

The molecular weight distributions of the deposited films are similar in both cases ($\sim$7000 g/mol). However, the film deposited with 3.31 μm radiation has an average molecular

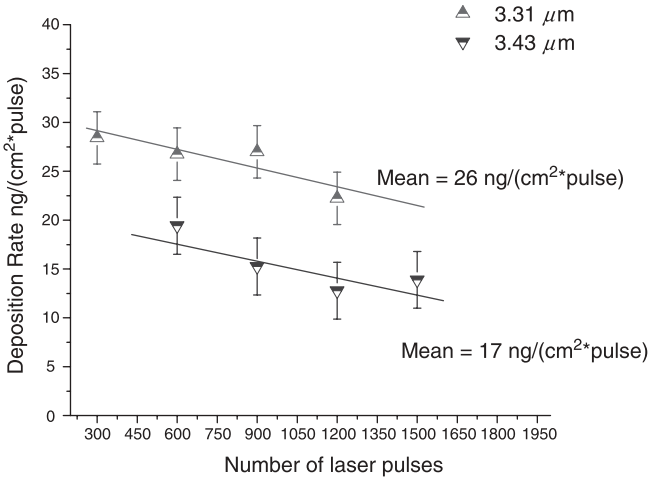

Figure 2.11 Ablation yield of polystyrene for two wavelengths.

weight of about 400–500 g/mol greater than the film deposited using a wavelength of 3.43 μm—a small but real difference.

2.3.5 Deposition of Application-Oriented Polymers by RIR-PLD

2.3.5.1 Biodegradable Polymers: PLGA

As a physical vapor deposition technique, PLD can be used to coat nonplanar substrates. One potential high-impact application area is coating substrates of various types with biocompatible surfaces. PLD has also been demonstrated as a particle-coating tool [Fitz-Gerald et al., 1999] that can produce uniform coatings on collections of agitated particles in a fluidized-bed reactor in vacuum (see also Chapter 10). In fact, UV-PLD can be used to coat drug particles with micron-sized particles that are obtained from laser ablation of poly(DL-lactide-*co*-glycolide) (PLGA) targets. For example, it has been reported that optimum drug delivery for the lungs is facilitated by a thin porous time-release coating of PLGA on 1- to 5-μm drug particles [Hardy and Chadwick, 2000]. The chemical structure of PLGA is shown in Figure 2.12.

A copolymer of poly(lactic acid) (PLA) and poly(D-,L- glycolide) (PGA), PLGA is broken down into PLA and PGA by hydrolysis. PLGA can be used to controllably release therapeutic levels of drugs by creating a thin permeable barrier on drug particles that degrades over time. PLA is hydrolyzed to lactic acid, which is metabolized through the Krebs cycle and then excreted as carbon dioxide and water. PGA is converted to glycolic acid monomer by hydrolysis and esterases. The glycolic acid monomers are either excreted directly in urine or may form glycine, which is converted into serine and subsequently to pyruvic acid, which also enters the Krebs cycle [Athanasiou et al., 1998]. Evidently then, for PLGA to form an effective time-release coating, it must not be chemically altered since other products cannot be guaranteed to have a metabolic pathway in the Krebs cycle.

Researchers have used PLD to create time-release coatings on drug particles [Talton et al., 2000]. In this work, small (micron-size) drug particles are coated with PLGA. However, conventional UV-PLD was used in this process. As discussed earlier in the chapter, intense UV radiation generates a number of strong photochemical reactions that can include σ–σ^* transitions that can cause direct dissociation and rupture of bonds, and in this fashion entire pendant groups may be lost. Additionally, π–π^* transitions are excited as well, and the consequent delocalization of electrons can lead to reversals of bond order and other photochemical rearrangement. In general, polymers contain strongly UV-absorbing moieties (in this case C=O) and will certainly undergo photolysis. The question then becomes: Is the deposited material photochemically altered material or are oligomeric fragments deposited with a substantial part of the polymer destroyed and volatilized? Since the excitation process is both electronic and thermal, the relaxation channels can be expected to be similarly complex. The form of the deposited film will depend intimately on the reaction pathways that are made available through the energy randomization. Typically, it has been difficult to diagnose mechanisms of polymer ablation through gas-phase mass spectrometry and spectral emission measurements except in those rare cases where a product points definitively in the direction of a particular mechanism. An additional complication arises from the fact that the postdeposition analysis tools, that is, gel permeation chromatography (GPC) and FTIR, change from a simple comparison to analysis of an unknown. For these reasons, biodegradable coatings require a

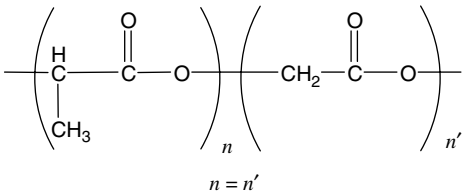

Figure 2.12 Chemical structure of PLGA.

TABLE 2.2 Summary of Results for RIR-PLD of PLGA

Sample	M_w (g/mol)	M_n (g/mol)	Polydispersity
Native polymer	8495	6950	1.222
Excited with 3.40 μm	3125	1027	3.05
Excited with 2.90 μm	3470	1322	2.63

method of processing that does not raise concerns about potential toxicity that may arise if the chemical structure of PLGA is altered, since the by-products may not break down into biodegradable components.

To test the applicability of RIR-PLD in the area of biocompatible coatings, PLGA (50 : 50) was deposited by exciting the −CH, and −OH stretch, respectively [Bubb et al., 2002d]. The output of the Vanderbilt free-electron laser was focused onto a solid target of the polymer and the films were deposited using 2.90 μm (resonant with O−H stretch) and 3.40 μm (C−H) light at macropulse fluences of 7.8 and 6.7 J/cm^2, respectively. It was found that the deposition rate was 100–200 nm per minute, which is extremely high. Given that the process conditions were not optimized, this suggests that industrial-scale processing may be achievable by these means, as concern about the use of a low-throughput serial process has always been a limiting factor in the application of PLD to industrial settings.

While the infrared absorbance spectrum of the PLGA films is nearly identical to that of the native polymer, the average molecular weight of the films is found to be approximately 40% of the starting material. The results for GPC measurements on native material and RIR-PLD thin films are summarized in Table 2.2 and displayed in Figure 2.13. Although there is some segmen tation of the chains, these results show that coatings of PLGA could be reasonably expected to be broken down and metabolized in the Krebs cycle and as such are suitable for time-release applications.

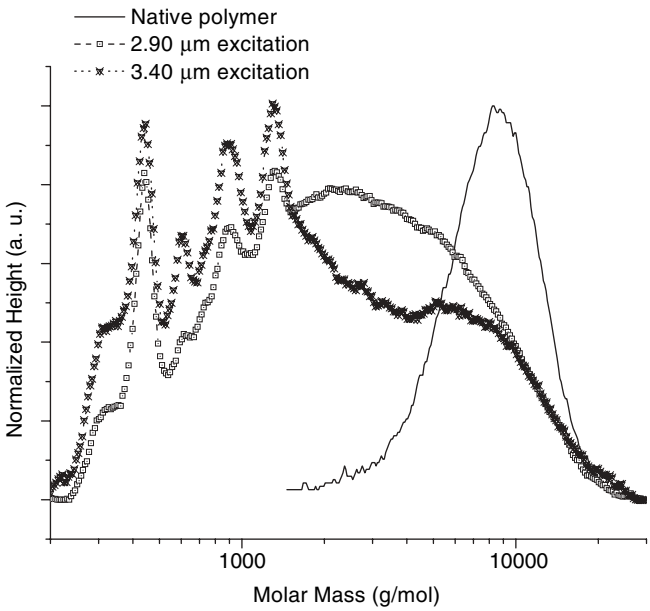

Figure 2.13 GPC results for RIR-PLD of PLGA.

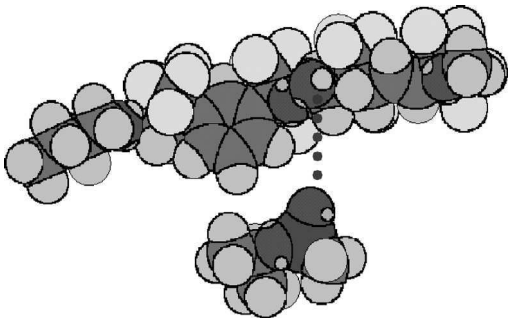

Figure 2.14 Schematic of GB-SARIN interacting with one repeat unit of FPOL via hydrogen bonding interaction.

2.3.5.2 Chemoselective Oligomers and Polymers: FPOL and SXFA

Functionalized polymers that are designed for chemical sensing applications can resemble viscous liquids rather than solids. Several of these polymers have been deposited by RIR-PLD without loss of functionality and with no apparent reduction in molecular weight. These results are significant because the polymers that have been deposited in this manner have fragile secondary structure that could be easily lost during physical vapor deposition, thus rendering them unsuitable for their intended application.

A common chemical sensing architecture consists of a functionalized polymer film deposited on an active substrate. Through sorption processes, the polymer film interacts with the target analyte and swells, thus providing the basis for a sensing mechanism. Perhaps the most common type of sensor architecture depends on surface acoustic wave oscillators coated with a functionalized polymer [McGill et al., 1998]. Figure 2.14 displays a pictorial representation of one repeat unit of fluoropolyol interacting with GB–Sarin, a deadly nerve agent.

Crucial to the success of this particular approach are the following items. First, the polymer must be designed properly, that is, it should swell in response to the target analyte and not to contaminants such as water and common organic vapors. Obviously a processing technique that compromises the functionality of the native polymer will produce less effective sensors. Second, to ensure proportional response across the entire sensor, the film should be of uniform thickness over the active area of the sensor.

Resonant infrared PLD has been used to deposit both fluoropolyol (FPOL), a sorbent, chemoselective oligimer [Orear et al., 1971] and fluoroalcohol poly(siloxane) (SXFA), a functionalized polymer. The chemical structure of these two polymers is shown in Figure 2.15.

The SXFA films were successfully grown by exciting the polymer at wavelengths 2.90 (−OH) and 3.37 μm (−CH). The infrared absorbance spectra, displayed in Figure 2.16, show the IR absorption of the bulk starting material compared to that of the films deposited at both wavelengths. The "before-and-after" spectra were normalized in each case to the amplitude of the large peak near 9.3 μm, to facilitate comparison of relative band intensities. In both cases, the near

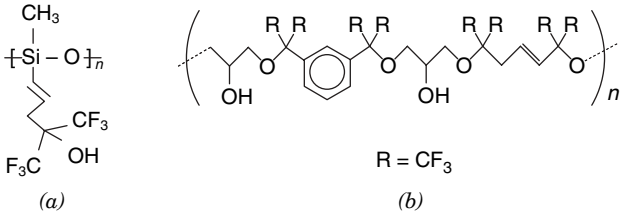

Figure 2.15 Chemical structure of (a) SXFA and (b) FPOL.

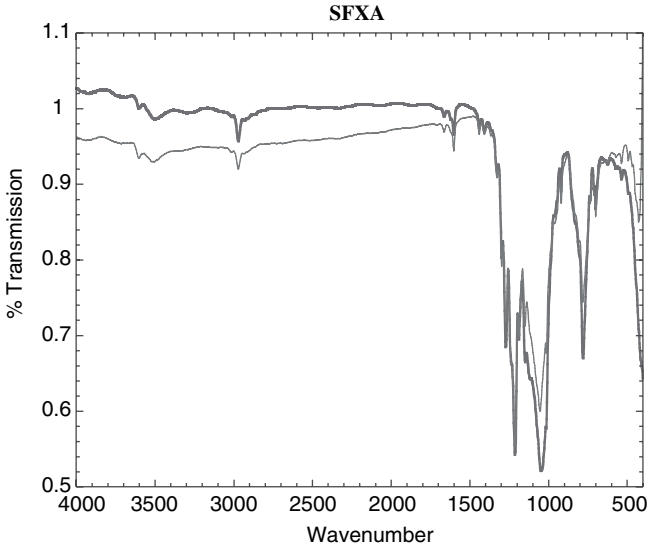

Figure 2.16 Infrared transmission spectra of SXFA films.

indistinguishability of the FTIR spectra of the films from that of the bulk starting materials confirms that the local chemical structure and properties of the SXFA are preserved.

Resonant infrared PLD has also been used to deposit fluoropolyol via excitation of the −OH stretch [Bubb et al., 2001b]. Here we observe similar results to those with SXFA. SEC results, displayed in Figure 2.17, show that there is no apparent reduction in the molecular weight distribution

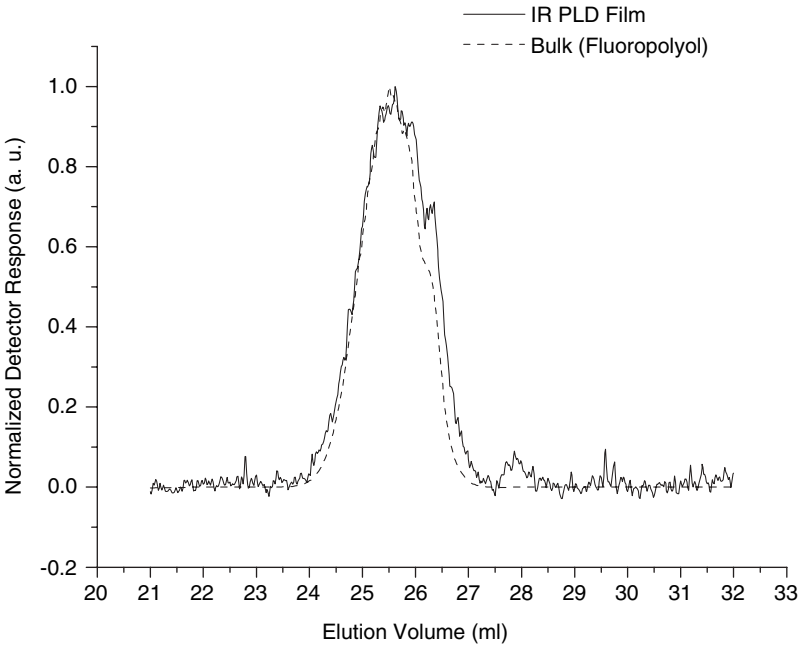

Figure 2.17 Size exclusion chromatography of fluoropolyol thin film compared with starting material.

of the films with respect to the starting material. These results show that RIR-PLD is capable of transferring fragile functionalized polymers without disturbing either the chemical structure or the molecular weight distribution. The most exciting aspect of these results is that the fragile secondary structure appears to be preserved.

2.3.5.3 Technologically Important Polymers: PTFE

From an application standpoint poly(tetraflouroethylene) is a material with an array of desirable mechanical, optical, thermal, chemical, and tribological properties that have led to its widespread use in a variety of thin-film technologies and has long been of interest to practitioners of PLD. Some early studies in PLD of polymers focused on polymers such as PTFE due to their relatively high unzipping rate. In these works, laser ablation of polymers is viewed as a type of flash pyrolysis where the long polymer chains are reduced to monomers and short oligomeric fragments. The presence of radicals catalyzes repolymerization on a substrate. The film properties were found to be greatly improved if the substrate was heated above the glass temperature of the polymer.

There are many ways in which to deposit PTFE films, among which are vacuum evaporation, sputtering, ion-beam-assisted deposition [He et al., 1998], plasma polymerization, ultraviolet pulsed laser deposition [Li et al., 1998; Blanchet, 1993], and even synchrotron radiation [Katoh and Zhang, 1999].

Films of PTFE deposited by RIR-PLD have shown impressive properties. Both a commercial PTFE rod (Teflon) and pressed pellets from PTFE powder (Goodfellow) were used as targets. The pressed pellet was sintered at 275°C for several days before use. The free-electron laser was tuned to either the C–F bond at 8.26 μm or a weak mode at 4.2 μm that is identified as a combination band in the literature [Papantonakis and Haglund, 2004]. The deposition rate (Fig. 2.18) is impressively high for both modes at 20–25 Å/s for a fluence of 2 J/cm^2 at 8.26 μm. This corresponds to a 0.5-μm-thick film in less than 5 min, which is very similar to that obtained with PLGA.

The PTFE films deposited in this way were found to have good crystalline properties, even when deposited at room temperature. In fact, the films seem to have superior X-ray diffraction (XRD) spectra, shown in Figure 2.19, compared to films deposited by UV-PLD on metal surfaces and annealed at 500°C [Huber et al., 2001]. Finally, the morphological properties are highlighted in Figure 2.20. The film is relatively free of particulates and the feature size is about 100 nm. These properties compare extremely favorably with other reports in the literature.

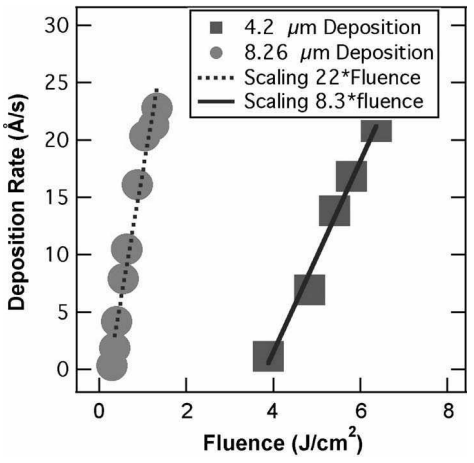

Figure 2.18 Deposition rate dependence for RIR-PLD of PTFE.

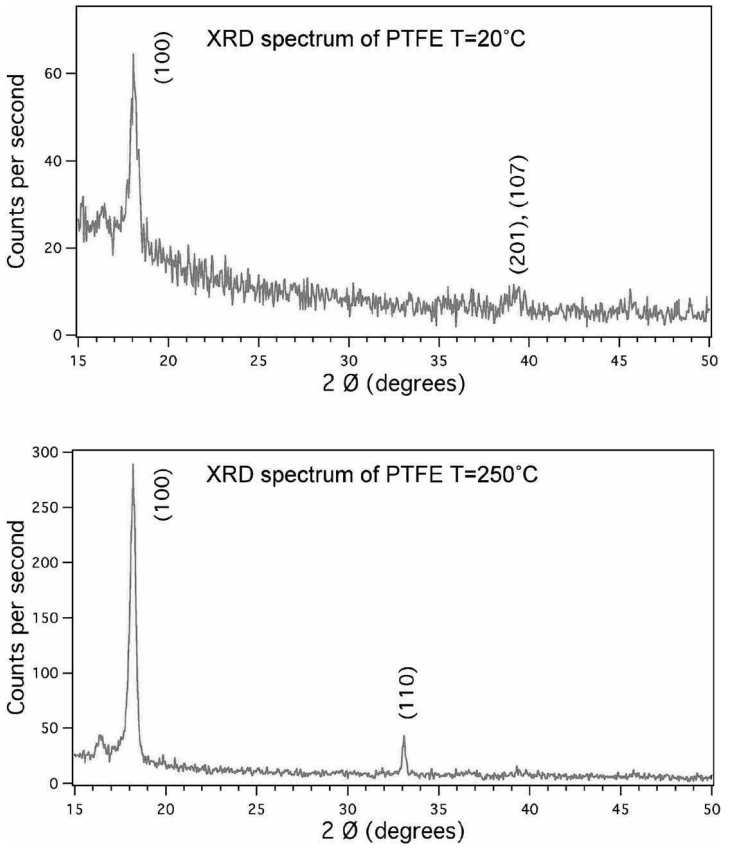

Figure 2.19 Crystallinity of PTFE films deposited at (a) room temperature and (b) 250°C.

2.3.5.4 Thermosetting Polymers: Polyimide

All of the polymers described in previous sections are thermoplastic polymers, meaning that they undergo melting above a well-defined temperature. There is, however, another large family of polymers, the so-called thermosets, in which the polymer is initially part of a precursor or prepolymer solution that polymerizes and cross-links only upon the application of heating above the glass transition of the polymer. Following the curing process, the cross-linked polymer usually has enhanced properties compared to the prepolymer, such as increased toughness, strength, or insulating capacity. Since polyimides (PIs) were introduced by DuPont in the early 1960s, polyimide films have been used as wire insulation, substrates for printed circuit boards, solar cell panels, and have replaced the polycarbonates as gas-filled laser target windows.

It has recently been demonstrated that it is possible to transfer the prepolymer for polyimide without initiating cross-linking. Polyimides are synthesized by a two-step process. First, pyromellitic dianhydride (PMDA) and 4,4′oxidianiline (ODA) are dissolved in the polar solvent *N*-methyl pyrrolidinone (NMP) to form the prepolymer solution poly(amic acid), PAA. Our precursor solution of 15 wt % PAA in NMP was obtained from Sigma Aldrich. The choice of solvent can affect the degree of cross-linking and the chain length in the polymer. NMP promotes longer chains prior to the cross-linking step by increasing melt flow. The second step requires a thermal cure, typically with temperatures above 150°C, to induce cyclodehydration. Generally the PAA is cured well in excess of

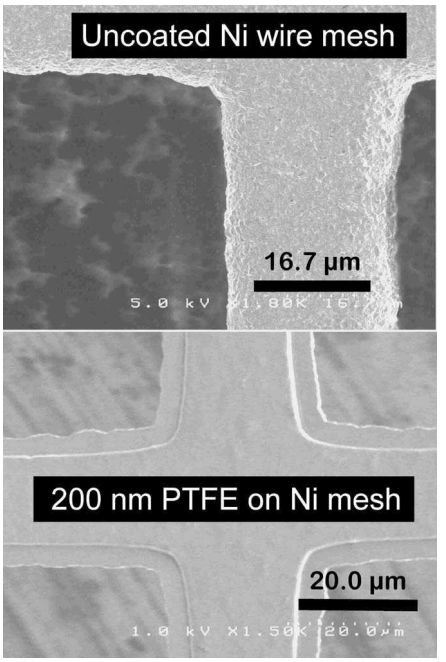

Figure 2.20 (Top) Scanning electron micrograph of a 25 μm Ni wire mesh section, prior to coating. (Bottom) Scanning electron micrograph of the Ni wire mesh coated with a 200 nm-thick film of poly(tetrafluoroethylene) using the free-electron laser at a wavelength of 8.26 μm. The apparent recession of the PTFE film from the edge of the Ni mesh is reproducible but thus far unexplained.

150°C (around 250°C) to ensure complete conversion to polyimide. The water-removal step requires that the film be thin and uniform to prevent water vapor from becoming trapped.

Liquid PAA was frozen with liquid nitrogen and ablated at a wavelength of 3.45 μm to resonate with a strong absorption band in the NMP; the NMP thus acts as a matrix to assist in the ejection of intact PAA molecules. The precursor PAA material was deposited at fluences above 0.5 J/cm^2 in both air and vacuum. When the deposited material was wiped with the solvent NMP immediately after deposition, the material was easily removed, demonstrating that neither curing nor cross-linking occurred in PAA during the laser transfer. After heating to 150°C on a laboratory hotplate for 30 min, on the other hand, the deposited film could not be removed with an NMP wipe. At the cure temperature used our PAA was probably not fully imidized but still sufficiently converted to resist dissolving in NMP. Additionally the as-transferred PAA did not exhibit the characteristic color change that normally accompanies the imidization process. Figure 2.21 shows a typical ablation plume obtained by laser flash shadowgraphy at 10 μs following FEL excitation.

The results of this experiment are interesting in two ways: First, they indicate that this important class of polymers can also be produced by RIR-PLD, opening a number of interesting technological possibilities. Second, measurements made of the shock wave produced during the ablation of the prepolymer solution show that the velocity of the shock wave is subsonic over a wide range of PAA concentrations (Fig. 2.22), lending additional weight to the qualitative sense that RIR-PLD is inherently ''gentler'' than the UV-PLD process, proceeding not only with much less electronic excitation in most cases but also at lower velocities. This picture is consistent, incidentally, with similar experiments on resonant IR laser ablation of inorganic materials.

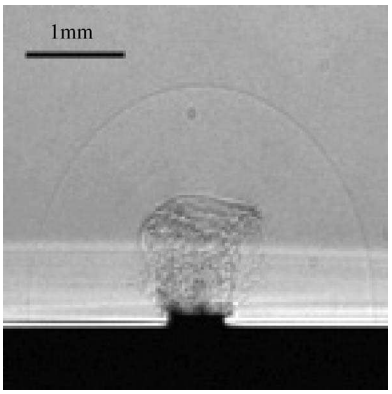

Figure 2.21 Shadowgraph of the ablation plume produced by resonant excitation of the poly(amic acid) precursor for polyimide. The concentration of the poly(amic acid) in the solvent NMP is 15%; the wavelength used for the FEL-induced ablation is 3.45 μm.

2.4 MECHANISM OF RESONANT INFRARED LASER ABLATION

Relatively little is known about the mechanisms of materials modification, ablation, and thin-film growth initiated by high spatio-temporal densities of *vibrational* excitation. Nevertheless, important clues can be gleaned from some recent experiments. Since most of the successful RIR-PLD experiments to date used the Vanderbilt free-electron laser, we focus on this laser irradiation protocol. Some experimental checks have been carried out using a mechanically *Q*-switched Er : YAG laser (2.94 μm), but much evidence suggests that the mechanism in this case is purely thermal. Related work has been performed on laser ablation of biological tissues [Vogel and Venugopalan, 2003].

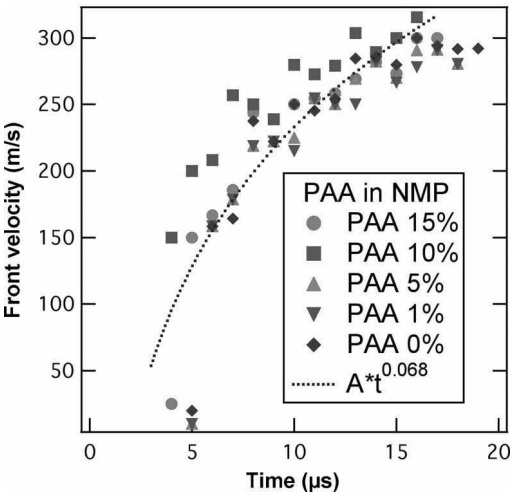

Figure 2.22 Shock-front velocity for poly(amic acid) in NMP ablated in air as a function of concentration, showing that the front velocity is driven primarily by the excitation of the NMP matrix. Note that the velocity rises rapidly following excitation and saturates at a subsonic velocity.

In resonant IR excitation of targeted vibrational modes, the IR photons transfer their energy to specific molecular degrees of freedom. These anharmonic vibrations couple relatively slowly to the harmonic vibrations that constitute the phonon bath. Typical relaxation times for such anharmonic excitations are in the 1- to 10-ps range, so that nuclear motion and bond breaking can begin, if the density of excitation is sufficiently high, before the energy leaks out of the excited mode on a time scale of picoseconds [Dlott and Fayer, 1989]. At the intensities characteristic of the FEL micropulses, it is appropriate to couch the discussion of mechanisms in terms of absorbed intensity I rather than fluence. The ablation yield or deposition rate must scale with energy per unit volume (E/V) but can include an intensity-dependent absorption term as follows:

$$\text{Yield} \propto (E/V) \cong F_L \alpha(\omega, I) \cong I_0 \tau_L [\alpha_0(\omega) + \beta I] \tag{2.3}$$

where F is the laser fluence, α is the absorption coefficient, and ω and I are the laser frequency and intensity, respectively. Because the FEL micropulse duration is short compared to the relaxation time of the initial anharmonic vibrational excitation, we are justified in considering the 1-ps FEL micropulses as ''ultrafast'' in the same sense as this terminology is usually applied to femtosecond laser processing by electronic excitation.

The apparently efficient surface vaporization process observed in RIR-PLD is not typical of thermal evaporation. Consider the evidence from RIR-PLD experiments.

1. Velocity distributions and shock-wave measurements seem to suggest a relatively low-velocity, subsonic plume expansion.
2. The experiments with poly(amic acid) show that the temperature of the material does not reach as high as 150°C since otherwise the PAA would cross-link and imidize.
3. Temperature rise calculations show that at the fluences characteristics of RIR-PLD, the temperature only rises by tens of degrees.

In some cases, such as PTFE, it is plausible that ablation is initiated by multiphoton absorption by near-surface PTFE molecules, leading to the rupture of the weak intermolecular van der Waals bonds in the target. Indeed, for conditions typical of the FEL in recent experiments, the two-, three-, and four-photon excitation probabilities range from 1 to 20%. These probabilities are probably enhanced by the bandwidth (ca. $16\,\text{cm}^{-1}$) of the FEL micropulses, which is large enough to overcome the inherent anharmonicity that might otherwise inhibit vibrational ladder climbing. Evidence for nonlinear absorption is found in dramatically reduced optical penetration depths in IR ablation of $NaNO_3$, $CaCO_3$, and amorphous SiO_2 [Haglund et al., 2003].

Therefore, in conceptualizing the process mechanistically we have to account for how the polymers might be ejected intact into the gas phase. There are at least two distinct processes at work. In thermal equilibrium, due to the long macropulse, the temperature is raised by some tens of degrees. Since the viscosity satisfies the Vogel–Fulcher law:

$$\frac{\eta}{\eta_0} = \exp\left(\frac{B}{T - T_0}\right) \tag{2.4}$$

with $B \sim 700\,^\circ\text{C}$ and $T_0 \sim 50\,^\circ\text{C}$, the temperature rise of about $100\,^\circ\text{C}$ during the macropulse means that the viscosity decreases by a significant amount. At the same time, the polymers are swelling due to the rise in temperature in the focal volume; polymers near the surface of the melt zone can be ejected into the gas phase as weak intermolecular hydrogen bonds are broken by the laser-induced vibrational excitation. Presumably vaporization could be accompanied by uncoiling associated with the competition between entropic configuration energy and the energy gained by the polymer when it assumed its free volume in the polymer melt [Jones, 2002]. If there is a stress wave, with propagation times on the order of nanoseconds in the drop-cast target, this could abet the ejection of surface molecules, as indeed shadowgraphs of the ablation plume seem to indicate.

2.5 LASERS FOR INFRARED LASER ABLATION AND DEPOSITION

The recent studies by Luther-Davies and collaborators on laser processing of materials using ultrashort pulses at high pulse repetition frequency (PRF) represent a watershed in thinking about laser materials processing [Gamaly et al., 1999]. Their approach is based on the idea that laser ablation thin-film deposition is best accomplished by a vaporization mechanism that employs relatively modest pulse energies to ablate a small amount of material, relatively high intensity to enhance cross section, and high PRF to optimize throughput. The first of these criteria ensures that collateral damage, particulate emission, and undue thermal loading are minimized. The second of these follows from the fact that reaction *rates* are fundamentally proportional to intensities and cross sections, rather than to fluence; in addition, at high intensities, nonlinear effects may produce additional yield of desirable products. High PRF serves both to maximize throughput and to produce a nearly continuous vapor stream during deposition.

Up to now there have been few systematic tests of this novel materials-processing paradigm. Mode-locked Nd : YAG lasers have $\sim$100-ps pulses during which the material reaches thermal equilibrium and cannot deliver really high intensities, although good-quality films of amorphous carbon have been made in this way [Rode et al., 1999]. Moreover, given their fixed frequencies, it is not possible to optimize the spatio-temporal density of electronic excitation in the ablation target.

Tunable, picosecond free-electron lasers, on the other hand, provide an ideal testing ground for these concepts. With micropulse durations in the 0.5- to 2-ps range, these lasers deliver energy in a time scale comparable to or shorter than vibrational relaxation times. Because these lasers produce as much as tens of microjoules in these picosecond pulses, they achieve intensities in the 10^{10}- to 10^{11}-W/cm^2 range, sufficient to initiate multiphoton processes if desired and to sustain high reaction rates. With micropulse repetition frequencies in the 50-MHz to 3-GHz range, and macropulse repetition rates ranging from 30 Hz to continuous, they can deliver extremely high average powers (Neil et al., 2000). Finally, because FELs can be tuned to select the desired mode of material absorption, the density of vibrational excitation can be controlled.

The first successful experiments on RIR-PLD were carried out using a free-electron laser; given its broad tunability, high average power and high micropulse peak power, the results produced were consistent in many respects with the models proposed by Gamaly et al. [1999] as well as with the concept of ablation by spatially and temporally dense vibrational excitation. However, over the long run, the FEL in its present incarnations is viable principally as a research tool. The capital cost of the Vanderbilt FEL, for example, was on the order of $3 million and has annual maintenance and operating costs on the order of $1 million. This is a level of complexity and expenditure that is simply not consistent with the requirements of a commercial processing facility, despite the enviable reliability record of most of the free-electron lasers currently operating. Fortunately, there are alternatives, which we briefly discuss in this section.

It is quite possible that fixed frequency lasers can in some cases reproduce the results of the FEL in resonant IR-PLD. This is illustrated in Figure 2.23, in which the FTIR spectra for poly(ethylene glycol), PEG1450, and the fluorinated polysiloxane SXFA are compared for RIR-PLD carried out under otherwise identical conditions with the Vanderbilt FEL and a Q-switched Er : YAG laser. Despite the very different peak intensities at which these two experiments were carried out, the FTIR spectra are nearly identical, showing that the local electronic structure of the polymers is largely preserved. While no other tests have been applied, this experiment at least suggests that nanosecond fixed-frequency lasers may be a viable alternative to the tunable free-electron laser for some processes.

One of the most interesting alternatives to the free-electron laser is an all-solid-state system built recently at the Australian National University. The oscillator is a Nd : VO_4 laser with a very long cavity made from a multipass optical cell that gives an effective resonator length on the order of 100 m; this reduces the frequency of mode locking to the low-megahertz range, while still making it possible to have a pulse duration less than 50 ps. This places such a solid-state laser system in the parameter space appropriate to the low-fluence, high-intensity, high-pulse-repetition frequency

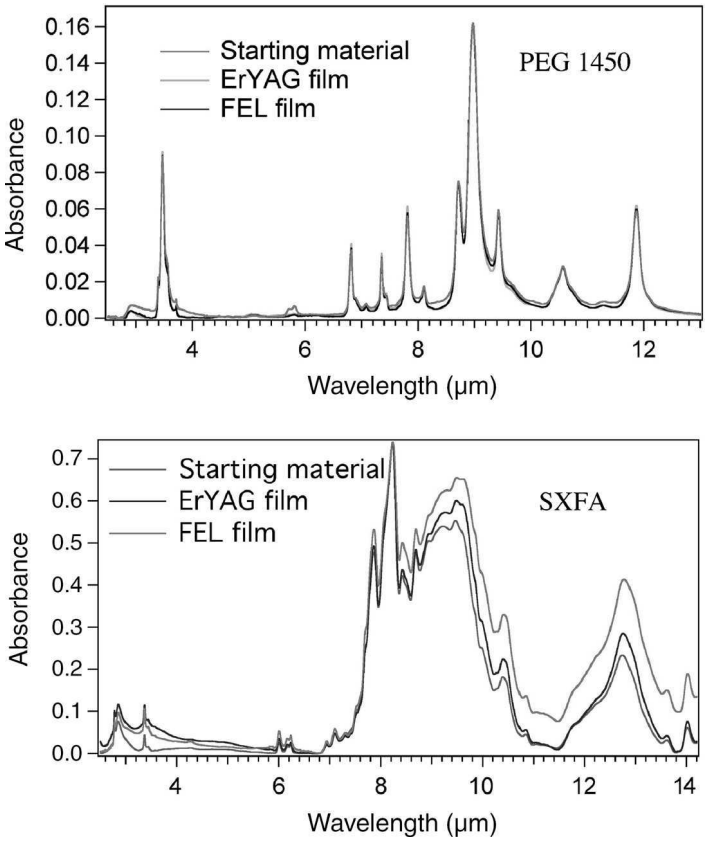

Figure 2.23 Comparison of the Fourier transform infrared spectra of films deposited by the free-electron laser and a *Q*-switched Er : YAG laser at a wavlength of 2.94 μm. Upper spectrum, poly(ethylene glycol) (PEG 1450); lower spectrum, the fluorinated siloxane polymer SXFA.

laser-processing regime. By using periodically poled $LiNbO_3$ crystals to mix white light with the fundamental 1.064-μm laser beam, this system can also produce midinfrared light with wavelengths out to 4 μm while producing average powers as high as 3.5 W at 3.5 μm. The laser has in fact run for 18-h days for over a year with high reliability, making it a credible candidate for an ''industrial-strength'' tunable IR laser. What is critical here is that the system, apart from the multipass long-cavity oscillator, can be constructed entirely from commercial components. The cost—on the order of $350,000–450,000—is not unreasonable for such a system.

2.6 CONCLUSIONS

As demonstrated in these examples, resonant infrared pulsed laser deposition offers a new route to conformal, solvent-free thin-film processing of organic molecules and polymers. RIR-PLD is new in two ways: (1) It has proven to be successful where UV-PLD has failed; and (2) it is based on an entirely different physical process, that is, weakly resonant vibrational, rather than electronic, excitation as the fundamental ablation mechanism. Deposition rates are high, and the polymers successfully deposited thus far by RIR-PLD span a large range of different applications, including sensors, antistiction coatings, coatings of biomedical interest, electronic and optical polymers, and

thermosetting polymers. This suggests that RIR-PLD can indeed be the basis for industrial-scale processing tools, provided that an appropriate laser can be found to substitute for the tunable free-electron laser used as a discovery tool in the recent history of RIR-PLD experiments. At present, the effects of temporal pulse duration on the successful deposition of polymers and other organic materials, including biomaterials, is largely unknown. It has been shown, for example, that large proteins and nucleic acids can be deposited successfully by the picosecond pulse train of the FEL, but not at the same laser wavelength using a nanosecond laser. This issue, therefore, remains as an important scientific question to be further investigated. Meanwhile, however, there is a large and interesting field to be explored, particularly the application of RIR-PLD to the fabrication of passive multilayer thin-film structures and active devices based on organics and polymers, such as organic light-emitting diodes and polymer light-emitting diodes.

Acknowledgments

Research at Rutgers University–Camden is supported by the National Science Foundation (Grant DMI-0323621) and a Cottrell College Award from the Research Corporation. Research in RIR-PLD at Vanderbilt University is supported by contracts with the Naval Research Laboratory (N00173-05-P-0059 and N00173-05-P-0922) and the W. M. Keck Foundation Free-Electron Laser Center grant administered by the Air Force Office of Scientific Research (Contract F49620-01-1-0429) for the Medical Free-Electron Laser program of the Department of Defense.

REFERENCES

Athanasiou, K. A., Agrawal, C. M., Barber, F. A., and Burkhart, S. S. (1998), *Arthroscopy—J. Arthroscopic Related Surg.* **14**, 726–737.

Blanchet, G. B. (1993), *Appl. Phys. Lett.* **62**, 479–481.

Blanchet, G. B. (1996), *J. Appl. Phys.* **80**, 4082–4089.

Bubb, D. M., Horwitz, J. S., Callahan, J. H., McGill, R. A., Houser, E. J., Chrisey, D. B., Papantonakis, M. R., Haglund, R. F., Galicia, M. C., and Vertes, A. (2001a), *J. Vac. Sci. Technol. A* **19**, 2698–2702.

Bubb, D. M., Horwitz, J. S., McGill, R. A., Chrisey, D. B., Papantonakis, M. R., Haglund, R. F., and Toftmann, B. (2001b), *Appl. Phys. Lett.* **79**, 2847–2849.

Bubb, D. M., McGill, R. A., Horwitz, J. S., Houser, E. J., Stroud, R. M., Wu, P., Ringeisen, B. R., Pique, A., and Chrisey, D. B. (2001c), *J. Appl. Phys.* **89**, 5739–5746.

Bubb, D. M., Wu, P. K., Horwitz, J. S., Callahan, J. H., Galicia, M., Vertes, A., McGill, R. A., Houser, E. J., Ringeisen, B. R., and Chrisey, D. B. (2002a) *J. Appl. Phys.* **91**, 2055–2058.

Bubb, D. M., Papantonakis, M. R., Toftmann, B., Horwitz, J. S., McGill, R. A., Chrisey, D. B., and Haglund, R. F. (2002b), *J. Appl. Phys.* **91**, 9809–9814.

Bubb, D. M., Papantonakis, M. R., Horwitz, J. S., Haglund, R. F., Toftmann, B., McGill, R. A., and Chrisey, D. B. (2002c), *Chem. Phys. Lett.* **352**, 135–139.

Bubb, D. M., Toftmann, B., Haglund, R. F., Horwitz, J. S., Papantonakis, M. R., McGill, R. A., Wu, P. W., and Chrisey, D. B. (2002d), *Appl. Phys. A Mater. Sci. Process.* **74**, 123–125.

Bubb, D. M., O'Malley, S. M., Antonacci, C., Simonson, D., and McGill, R. A. (2004), *J. Appl. Phys.* **95**, 2175–2177.

Bubb, D. M., Johnson, S. L., Belmont, R. J., Schriver, K. E., R. F., Haglund, J., Antonacci, C., and Yeung, L. S. (2006), *Appl. Phys. A*, **83**, 147–151.

Cheung, J. T., and Sankur, H. (1988), *CRC Crit. Rev. Solid State Mater. Sci.* **15**, 63–109.

Chrisey, D. B., and Hubler, G. K. (Eds.) (1994), *Pulsed Laser Deposition of Thin Films*, Wiley-Interscience, New York.

Chrisey, D. B., Piqué, A., McGill, R. A., Horwitz, J. S., Ringeisen, B. R., Bubb, D. M., and Wu, P. K. (2003), *Chem. Rev.* **103**, 553–576.

Dlott, D. D., and Fayer, M. D. (1989), *J. Opt. Soc. Am. B Opt. Phys.* **6**, 977–994.

Edwards, G. S., Evertson, D., Gabella, W., Grant, R., King, T. L., Kozub, J., Mendenhall, M., Shen, J., Shores, R., Storms, S., and Traeger, R. H. (1996), *IEEE J. Sel. Top. Quant. Electron.* **2**, 810–817.

Fitz-Gerald, J. M., Singh, R. K., Gao, H., Wright, D., Ollinger, M., Marcinka, J. W., and Pennycook, S. J. (1999), *J. Mater. Res.* **14**, 3281–3291.

Gamaly, E. G., Rode, A. V., and Luther-Davies, B. (1999), *J. Appl. Phys.* **85**, 4213–4221.

Haglund, R. F., Bubb, D. M., Ermer, D. R., Hubler, G. K., Houser, E. J., Horwitz, J. S., Ivanov, B., Papantonakis, M. R., Ringeisen, B. R., and Schriver, K. E. (2003), *Proc. SPIE* **5063**, 13–23.

Hansen, S. G., and Robitaille, T. E. (1988), *Appl. Phys. Lett.* **52**, 81–83.

Hardy, J. G., and Chadwick, T. S. (2000), *Clin. Pharmacokinet.* **39**, 1–4.

He, J. L., Li, W. Z., Wang, L. D., Wang, J., and Li, H. D. (1998) *Nucl. Instrum. Methods Phys. Res. Sect. B* **135**, 512–516.

Herbert, C. G., and Johnstone, R. A. W. (2003), *Mass Spectrometry Basics*, CRC Press, Boca Raton, FL.

Huber, N., Heitz, J., Bauerle, D., Schwodiauer, R., Bauer, S., Niino, H., and Yabe, A. (2001), *Appl. Phys. A Mater. Sci. Process.* **72**, 581–585.

Jones, R. A. L. (2002), *Soft Condensed Matter*, Oxford, New York.

Katoh, T., and Zhang, Y. (1999), *Appl. Surf. Sci.* **139**, 165–168.

Li, S. T., Arenholz, E., Heitz, J., and Bauerle, D. (1998), *Appl. Surf. Sci.* **125**, 17–22.

Lobo, F. M., Pereira-da-Silva, M. A., Raposo, M., Faria, R. M., Jr, O. N. O., and Pereira-da-Silva, M. A. (1999), *Nanotechnology* **10**, 389–393.

McGill, R. A., Chung, R., Chrisey, D. B., Dorsey, P. C., Matthews, P., Piqué, A., Mlsna, T. E., and Stepnowski, J. L. (1998), *IEEE Trans. Ultrasonics Ferroelectrics Freq. Control* **45**, 1370–1380.

Mercado, A. L., Allmond, C. E., Hoekstra, J. G., and Fitz-Gerald, J. M. (2004), *Appl. Phys. A* **81**, 591–599.

Neil, G. R., Bohn, C. L., Benson, S. V., Biallas, G., Douglas, D., Dylla, H. F., Evans, R., Fugitt, J., Grippo, A., Gubeli, J., Hill, R., Jordan, K., Krafft, G. A., Li, R., Merminga, L., Piot, P., Preble, J., Shinn, M., Siggins, T., Walker, R., and Yunn, B. (2000), *Phys. Rev. Lett.* **84**, 5238–5238.

Orear, J. G., Griffith, J. R., and Reines, S. A. (1971), *J. Paint Technol.* **43**, 113–119.

Papantonakis, M. R., and Haglund, R. F. (2004), *Appl. Phys. A Mater. Sci. Process.* **79**, 1687–1694.

Piqué, A., McGill, R. A., Chrisey, D. B., Leonhardt, D., Mlsna, T. E., Spargo, B. J., Callahan, J. H., Vachet, R. W., and Bucaro, M. A. (1999), *Thin Solid Films* **356**, 536–541.

Ringeisen, B. R., Callahan, J., Wu, P. K., Piqué, A., Spargo, B., McGill, R. A., Bucaro, M., Kim, H., Bubb, D. M., and Chrisey, D. B. (2001), *Langmuir* **17**, 3472–3479.

Rode, A. V., Luther-Davies, B., and Gamaly, E. G. (1999), *J. Appl. Phys.* **85**, 4222–4230.

Smith, B. (1999), *Infrared Spectral Interpretation*, CRC Press, New York.

Srinivasan, R., and Braren, B. (1989), *Chem. Rev.* **89**, 1303–1316.

Talton, J., Fitz-Gerald, J., Singh, R., and Hochlaus, G. (2000) In *Proceedings of Respiratory Drug Delivery VII*, Vol. 1, R. N. Dalby, P. R. Byron, S. J. Farr, and J. Peart (Eds.), Serentec Press, Raleigh, North Carolina, pp. 67–74.

Toftmann, B., Papantonakis, M. R., Auyeung, R. C. Y., Kim, W., O'Malley, S. M., Bubb, D. M., Horwitz, J. S., Schou, J., Johansen, P. M., and Haglund, R. F. (2004), *Thin Solid Films* **453/454**, 177–181.

Tsuboi, Y., Adachi, H., Yamada, K., Miyasaka, H., and Itaya, A. (2002a), *Jpn. J. Appl. Phys. Pt. 1* **41**, 4772–4779.

Tsuboi, Y., Adachi, H., Yamamoto, E., and Itaya, A. (2002b), *Jpn. J. Appl. Phys. Pt. 1* **41**, 885–890.

Tsuboi, Y., and Itaya, A. (1999), *Appl. Phys. Lett.* **74**, 3896–3898.

Vogel, A., and Venugopalan, V. (2003), *Chem. Rev.* **103**, 577–644.

CHAPTER 3

Deposition of Polymers and Biomaterials Using the Matrix-Assisted Pulsed Laser Evaporation (MAPLE) Process

ALBERTO PIQUÉ

Naval Research Laboratory, Materials Science and Technology Division, Code 6364, Washington, D.C.

3.1 INTRODUCTION

Polymeric and biomaterial thin films are poised to play a pivotal role in the development of next-generation electronic devices, passivation coatings, and chemical and biological sensors. It is anticipated that these applications will require tighter tolerances on the structural, morphological, and chemical composition of the thin films used in their fabrication. Depending on the particular application, it might, for example, be desirable to deposit films containing single or multilayer structures of different organic or polymeric materials, homogeneous composite materials, or materials with graded compositions. In many situations, it might also be necessary to discretely deposit the layers, achieve conformal coverage, and provide high-quality films, especially with regard to surface coverage uniformity and thickness control.

For electronic and optical device applications, the materials of choice cover a wide range from organic and polymeric materials to organic dye molecules. Some examples where these materials might be employed include the fabrication of organic thin-film transistors, organic light-emitting displays, flexible optical waveguides, nonlinear and optical limiting devices, and other optoelectronic components. Thin films of polymeric, inorganic, and organic materials also play an important role in high-performance dielectrics, optical data storage, passivation and encapsulation coatings for electronic devices, ionically conductive membranes for batteries and fuel cells, organic electroluminescent materials for optical communications and displays, and novel inorganic/polymeric structures with light-emitting or semiconducting properties for imaging, sensing, or organic thin-film transistor devices.

Polymer and organic coatings have a wide range of pharmaceutical, bioengineering, and sensing applications. In fact, thin films of polymers and biomaterials are the basis of the chemoselective or biospecific layers that make possible the operation of most types of chemical and biochemical sensor systems, and gene and protein recognition microarrays. In the biomedical field, thin films of numerous types of biomaterials are essential in diverse areas such as tissue engineering, spatial patterning of cells, time-release drug delivery systems, antiinflammatory coatings for medical implants and implantable devices, and novel biocompatible adhesives for wound closure, eye repair, and nerve reconstruction.

Pulsed Laser Deposition of Thin Films: Applications-Led Growth of Functional Materials
Edited by Robert Eason

3.2 LIMITATIONS OF PLD FOR THE GROWTH OF ORGANIC THIN FILMS

Attempts to deposit thin films of organic and polymeric materials by pulsed laser deposition (PLD) date back to the first report by Smith and Turner [1965] who demonstrated the growth of thin films of fuchsine (an organic dye) and Ni-dimethyl glyoxime (a pigment used in paints and cosmetics). Despite this early report, little additional work was performed in PLD of organics and polymers for the next 20 years until Hansen and Robitaille demonstrated the use of pulsed ultraviolet (UV) lasers for depositing films of several polymers such as polyethylene, polycarbonate, polyimide, and poly(methylmethacrylate), or PMMA [Hansen, 1988a, 1988b]. Their results showed an improvement of the laser ablation behavior and film morphology with decreasing laser wavelengths. Hansen and Robitaille further observed indications that the film quality is enhanced by working at laser energies near the ablation threshold of the polymers. However, they also noted a decrease in the molecular weight of all the films that they prepared. Since then, there has been a large number of reports on the use of PLD for growing thin films of many types of polymeric and organic materials. A recent literature survey of the results published in this area can be found in the review by Chrisey et al. [2003].

Despite the extensive list reported in the literature of polymer and biomaterials deposited by PLD, fundamentally the use of PLD for the deposition of organic and polymeric materials has provided, at best, mixed results. Despite the large number of variables explored in deposition parameter space by numerous research groups, the quality of the films produced by PLD has only been adequate for a very small number of systems. By using a pulsed UV laser to ablate the various organic and polymeric targets, it is not surprising that the resulting films will tend to show some degree of irreversible decomposition or damage. In fact, the question from early studies of polymer laser ablation has been whether the ablative decomposition takes place primarily through photochemical or photothermal pathways. Upon absorption of the UV pulse, the organic molecules are excited into high-energy electronic states that might result in direct bond dissociation, that is, photochemical, or instead decay through lattice vibrations with considerable heating of the surrounding molecules, that is, photothermal effects. Given the fact that in most organic materials the chemical bonds have energies well below the UV photon energies, some degree of photochemistry is expected to occur during the PLD process. However, the decomposition pathways are mainly determined by the chemical structure of the organic molecule itself. As a result, the products of the interaction between the UV photons and the organic or polymeric molecule tend to be extremely difficult to predict and thus control.

Only for a small group of addition polymers such as poly(tetrafluoroethylene) (PTFE) and PMMA, the absorbed UV radiation causes the simple photothermal depolymerization of the starting material into its monomer building blocks, resulting in the reversible unzipping of the polymer chains [Blanchet, 1993a]. Blanchet's work showed that under the appropriate conditions it is possible to deposit high-quality PTFE and poly(vinyfluoride) (PVF) thin films by PLD [Blanchet et al., 1993; Blanchet and Fincher, 1994]. More often than not, however, the interaction of the UV photons with the polymeric or organic molecules causes the loss or decomposition of functional groups, or in the case of condensation polymers the resulting photochemistry is responsible for the substantial modification of the starting material. Such modifications might be acceptable for some applications, but in general, the use of UV lasers for depositing thin films of polymeric and biomaterials require more subtle approaches than those offered by PLD alone.

3.3 FUNDAMENTALS OF THE MAPLE PROCESS

As described in the previous section, laser processing of polymer and biomaterial thin films using traditional PLD is not a viable option for depositing organic coatings that faithfully replicate the properties and functionality of the starting materials. One approach that has shown great promise is known as matrix-assisted pulsed laser evaporation, or MAPLE. The MAPLE process was developed

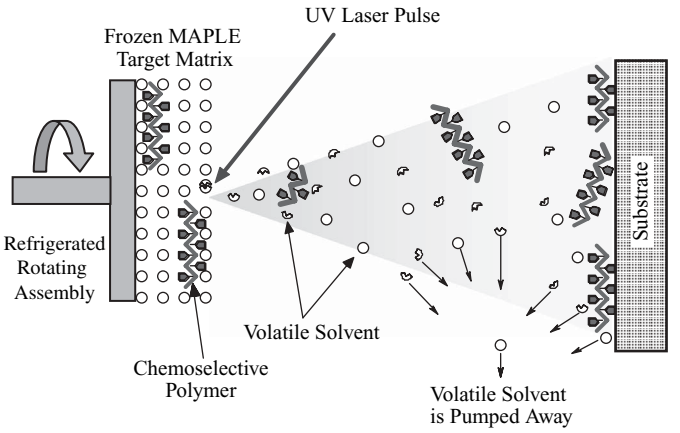

Figure 3.1 Schematic diagram showing the basic elements of the MAPLE process.

in the late 1990s at the U.S. Naval Research Laboratory to provide a gentler pulsed laser evaporation process for functionalyzed polymers [McGill and Chrisey, 2000]. The MAPLE technique has been used successfully for depositing thin and uniform layers of chemoselective polymers, as well as organic compounds such as simple carbohydrates and their polymers [Piqué et al., 1998a, 1998b, 1999]. MAPLE is a variation of conventional PLD. It provides, however, a less damaging approach for transferring many different organic and polymeric compounds that include small and large molecular weight species, from the condensed phase into the vapor phase. In MAPLE, a frozen matrix consisting of a solution of a polymeric compound dissolved in a relatively volatile solvent is used as the laser target. The solvent and solution concentration are selected so that the material of interest can dissolve to form a dilute, particulate-free solution and also so that the majority of the laser energy is initially absorbed by the solvent molecules and not by the solute molecules. A simple schematic illustrating the MAPLE process is shown in Figure 3.1. As in conventional PLD, both solute and solvent molecules leave the target from the region illuminated by the laser pulse along a direction normal to the MAPLE target surface.

In MAPLE, the target usually contains < 5 wt % of solute material, that is, polymer or biomaterial to be deposited. Thus, each polymer or biomaterial molecule is surrounded or shielded by a large amount of solvent or matrix. This configuration reduces both thermal and photonic damage to the polymer or biomaterial in solution during their laser-induced volatilization. Instead, the matrix molecules absorb the laser radiation and rapidly leave the surface. Ideally, the solute molecules are entrained in the plume of matrix molecules leaving the frozen target due to collisions between the matrix and the embedded polymer or biomaterial molecules. Molecular dynamics simulations of the laser ablation of large molecules embedded into a low-molecular-weight matrix show in fact that as a result of the laser excitation, clusters containing polymer molecules surrounded by matrix molecules are ejected together with the matrix material [Itina et al., 2001]. By careful optimization of the MAPLE deposition conditions, this process can occur without any significant polymer or biomaterial decomposition. The MAPLE process depletes the target of solvent and polymer in the same concentration as the starting matrix.

A typical MAPLE deposition system consists of a conventional PLD chamber with a modified substrate holder that might contain a thickness monitor such as a quartz microbalance or a surface acoustic wave (SAW) resonator as shown in the schematic in Figure 3.2. The purpose of either of these is to monitor the deposition rate in real time, which might vary independent of laser parameters due to nonuniformities inherent in the frozen matrix target. The substrates are typically at room temperature during the MAPLE deposition process, but they can be heated slightly to anneal the

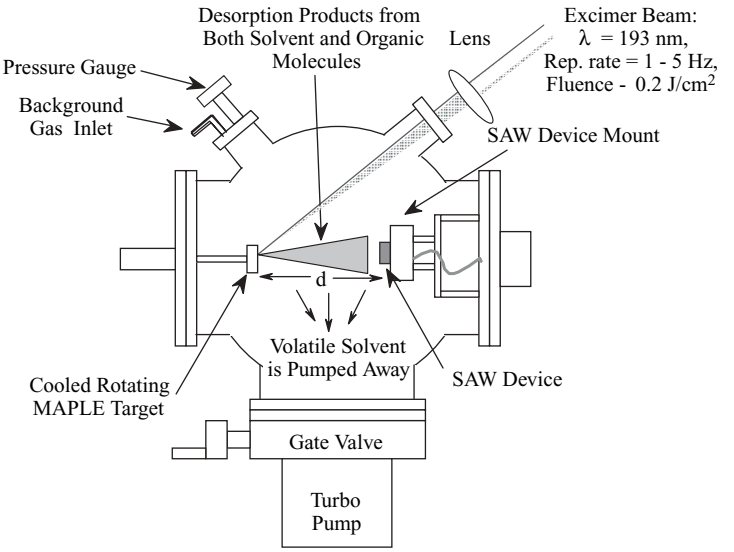

Figure 3.2 Schematic diagram illustrating the components of a MAPLE deposition system.

growing film. Typically, an excimer laser is used (KrF at 248 nm or ArF at 193 nm) with 10- to 30-ns pulse width, at repetition rates between 1 and 20 Hz, focused to a 1- to 10-mm^2 spot size on the target, although other types of lasers with wavelengths ranging from the visible to the infrared (IR) can be employed as well. The laser fluence at the target is typically set between 0.01 and 0.5 J/cm^2, depending on the solute material and solvent used. The depositions can be carried out at pressures ranging from vacuum to a few hundred millitorr and in the presence of inert or reactive background gases, in the same manner as conventional PLD. The matrix solution is prepared by dissolving the organic or polymeric material to be deposited in a solvent such as water, various types of alcohols such as acetone, toluene, and so forth. To make a target, a few milliliters of the solution are flash frozen in a target die by submerging it in liquid nitrogen (LN_2). Once frozen, the MAPLE target is mounted on a cryogenically cooled rotating target holder with the open die end facing the laser as shown in the photograph in Figure 3.3. Once the chamber is evacuated, the target can be cooled to any temperature between 270 and 100 K depending on the design of the refrigerated rotating target holder. In short, the MAPLE processing parameters are: composition of the target matrix, target and substrate temperature, target-to-substrate distance, type of background gas and pressure, laser wavelength, laser fluence, and laser repetition rate.

When a substrate is positioned directly in the path of the plume, a coating starts to form from the evaporated solute molecules, while the volatile solvent molecules, which have very low sticking coefficients, are evacuated by the pump in the deposition chamber. The MAPLE technique is analogous to the analytical technique of matrix-assisted laser desorption/ionization–mass spectrometry (MALDI-MS) [Vertes et al., 1993]. MALDI-MS is a soft ionization technique that allows the desorption and ionization of large molecular species ($\approx$ 10–1000 kDa), and this process has been developed specifically for studying large organic molecules and polymeric materials to accurately determine their molecular weight distributions. In MAPLE the target is generally refrigerated in order to freeze the matrix solution, while in MALDI the matrix is usually solid at room temperature, and this adds a further level of complexity to the setup required for performing MAPLE depositions. However, the cooling of the targets for MAPLE can be accomplished relatively easily with the use of LN_2 cooling stages as described in the previous paragraph and shown in the photograph in Figure 3.3.

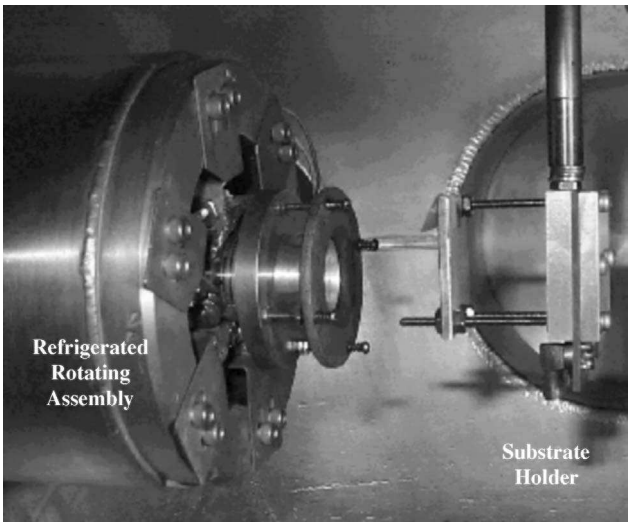

Figure 3.3 Photograph of the interior of a MAPLE chamber. The refrigerated target holder is on the left, the brass block on the right holds the substrates to be coated.

The main difference between the MAPLE and MALDI techniques lies in the treatment of the evaporated species and in the selection of the matrix. In the MAPLE process the polymer or organic molecule is not deliberately ionized and is collected on a substrate to form a coating rather than being directed into a mass spectrometer. This aspect can be observed during the MAPLE process, for which, when conducted at low laser fluences, there is no visible emission from the plume of desorbed material generated as the laser strikes the frozen matrix target. Figure 3.4a shows a photograph of a MAPLE target at the moment when the laser hits its surface. There is no visible emission noticeable and only for some solvents can a weak luminescence be observed where the laser pulse hits the target. However, only those regions on the target where the laser strikes are eroded during deposition, while the rest of the target surface remains intact, as can be observed in the photograph in Figure 3.4b. Additional evidence that the release of the solvent and solute molecules to the vapor phase is due to the laser interaction with the target and not from evaporation from the vacuum-exposed surface of the frozen matrix can be obtained from the response of the film thickness monitor inside the MAPLE chamber. Figure 3.5 shows the response of a SAW resonator used as a thickness monitor during a typical MAPLE deposition run. As the plot shows, the frequency of the SAW resonator changes only when the laser is on. Note also the two different slopes of the SAW response corresponding to two laser fluences, indicating that the deposition rate changes as a function of laser energy during the MAPLE process. It is worth pointing out that once the laser beam begins hitting the MAPLE target, the vacuum pressure inside the chamber increases noticeable, most likely due to the vaporization of the matrix, and that at low laser repetition rates, that is, 1 Hz, oscillations in pressure in sync with the laser pulses can be observed.

One advantage of the MAPLE process is that it can easily be combined with noncontact shadow masks to limit the deposition to only those required areas on a substrate. This is important for fragile substrates and is much less time-consuming than subsequent removal by patterning and etching. Furthermore, many polymer and organic coatings will not survive the solvents used to wash off the resists making them incompatible with standard lithographic processes. In such cases, MAPLE deposition of the polymer or organic through a shadow mask might be the only way to deposit discrete thin-film structures of these materials. The MAPLE process has been used successfully to deposit polymer films through masks with features in the micron range as shown by

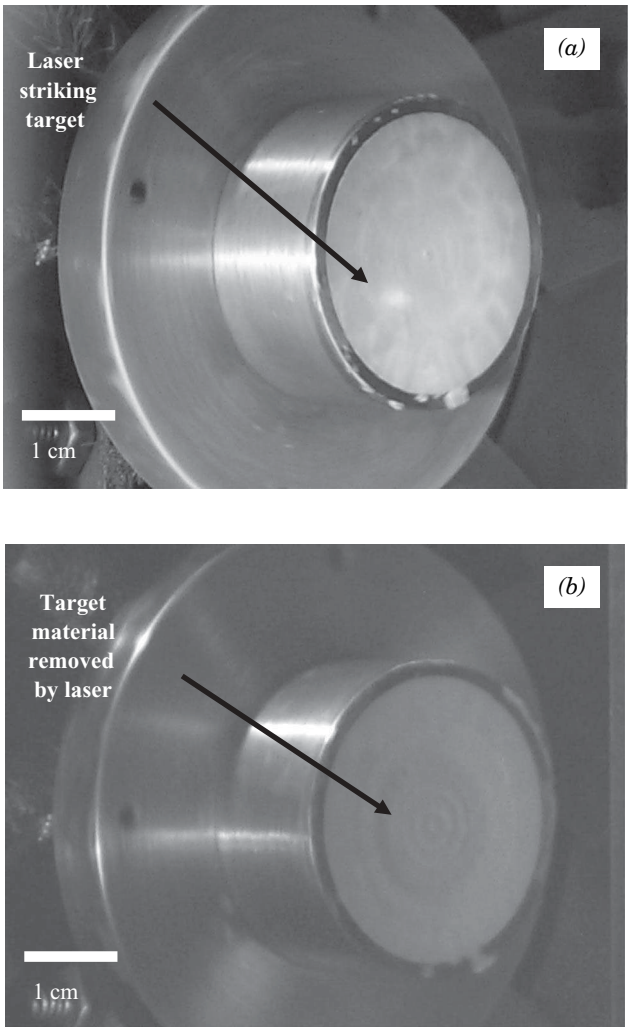

Figure 3.4 Photographs of MAPLE targets, (a) during deposition, showing the laser striking the target, and (b) after deposition, showing the eroded area on the target corresponding to the region where the laser hit.

the optical micrograph in Figure 3.6. This capability is very important for the manufacture of sensor arrays and electronic devices.

3.3.1 Growth of Polymer Thin Films

The initial MAPLE studies were performed on polymer solutions with a specific goal of depositing thin, homogeneous films of chemoselective polymers onto sensing platforms such as SAW devices [McGill et al., 1998a]. The constraints for thin-film deposition onto these devices were not being met by traditional spray coating techniques, which left large areas of inhomogeneous films due to solvent drying effects.

This problem, typical of spray coating and other polymer deposition techniques such as ink jet, spin coating, and dip coating, is due to the use of a solution to dispense the polymer on the surface.

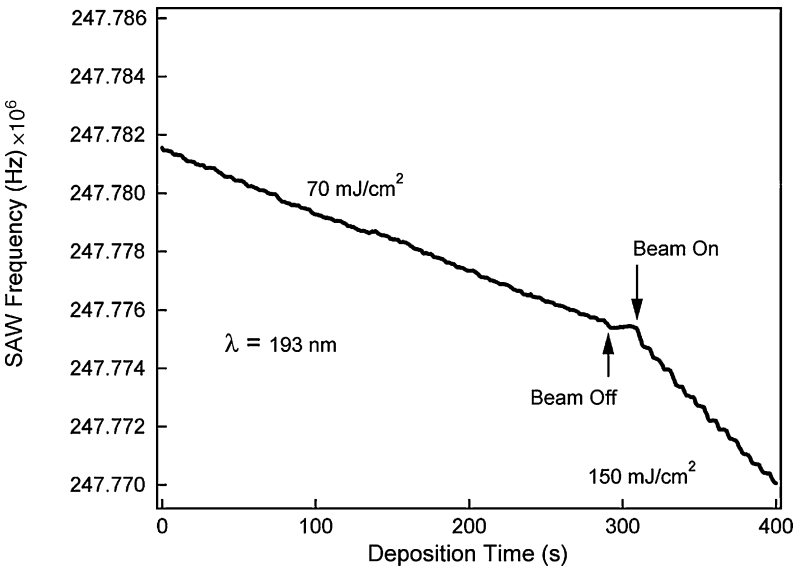

Figure 3.5 Plot showing the frequency shift from a SAW resonator as a function of time during MAPLE deposition. Note that the frequency shifts only when the laser is hitting the frozen target (beam on) and that the frequency shift is proportional to the film deposition rate, which increases with laser fluence.

The resulting uneven and unpredictable wetting, distribution, and evaporation of the solvent molecules are responsible for the nonuniform polymer coatings. MAPLE can deposit the same polymer chemoselective agents without solvent effects because the process is pseudo-dry, eliminating the solvent during deposition by performing the experiments under vacuum.

The early experiments using the MAPLE technique focused on depositing a hydrogen bond acid-functionalized polysiloxane molecule known as SXFA [fluoroalcohol poly(siloxane)] [McGill et al., 1994]. The MAPLE-deposited films showed higher sensitivities and faster response times to chemical threats than their spray-coated counterparts [Piqué et al., 1999; McGill et al., 1998a, 1998b). Figure 3.7 shows micrographs of two SAW devices, one coated by spraying and the other by MAPLE. It is obvious from these images that a uniform film can be obtained with the MAPLE process. Fourier transform infrared (FTIR) spectroscopy analysis of the MAPLE-deposited SXFA films showed that their spectra was essentially identical to that of bulk SXFA samples, with very similar absorbance ratios for the key absorption bands.

To achieve the desired sensor signal kinetics, it was required that the SXFA films were of the order of 10–50 nm thick and highly uniform across the whole area. Measuring the thickness of these extremely soft polymer films using profilometry techniques proves to be very difficult since the stylus can easily scratch the films. Noncontact techniques such as ellipsometry can be used as long as the index of refraction (n) of the polymer is well characterized. If n is not known, atomic force microscopy (AFM) techniques can be used to measure the thickness of MAPLE-deposited films on very flat substrates such as silicon. Figure 3.8 shows an AFM image taken across a step on an SXFA film MAPLE deposited on (100) Si.

More recently, the growth of electrically conductive polymers and light-emitting polymer thin films using MAPLE has been studied. Polypyrrole is an electrically conductive polymer that exhibits good optical transmission across the visible range and is chemically stable under ambient conditions. Given these properties, it is ideally suited for use as a transparent electrode for flexible display applications. Using the MAPLE technique with a frozen deionized water matrix target, polypyrrole thin films have been deposited on glass substrates with electrical conductivities and optical transmissions similar to those of their bulk counterparts [Piqué, 2002]. Thin films of

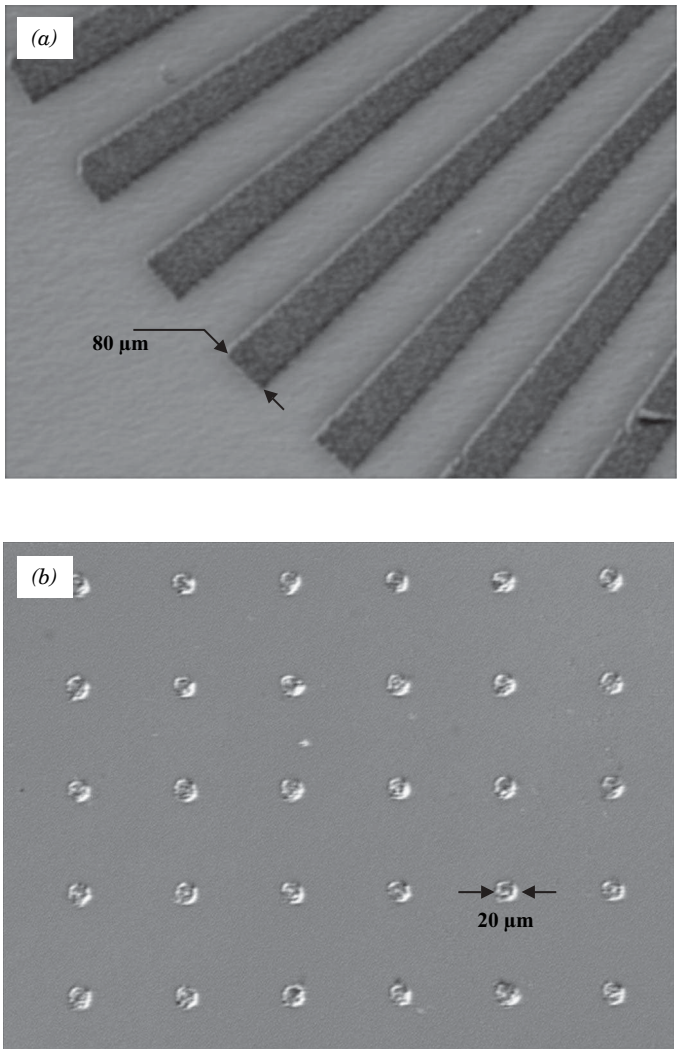

Figure 3.6 Optical micrographs showing two distinct patterns, (a) and (b), generated after MAPLE depositing an additive polymers through a shadow mask.

electroluminescent and photoluminescent polymers have also been prepared using the MAPLE technique. The electroluminescent polymer poly[2-methoxy-5-(2′-ethylhex-yloxy)-1,4-phenylene vinylene] (MEH-PPV) has been processed via MAPLE into thin-film form using toluene and tetrahydrofuran solvent matrices [Toftmann, 2004]. The authors evaluated the effect of theses two solvents and also two different UV wavelengths (193 and 248 nm) on the quality of their films and found that for any of these two matrices, the 193-nm MAPLE films resulted in chemically modified materials as indicated by FTIR analysis. This modification was attributed to photodecomposition of the matrix molecules, resulting in excited species, which could react with the electroluminescent polymer. This effect will be further discussed later in the chapter.

Thin films of another visible light-emitting polymer, $[Ru(bpyPMMA_2)_3](PF_6)_2$, have also been prepared by MAPLE using a dimethoxyethane matrix. The resulting films display photoluminescence emission at 610 nm (orange) when exited with UV light as in their bulk counterparts

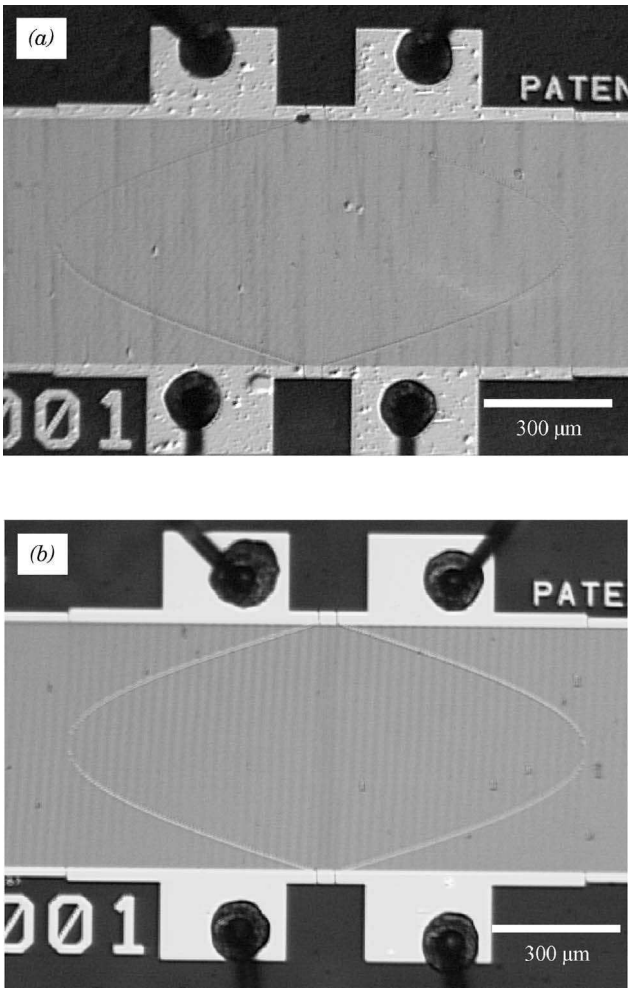

Figure 3.7 Optical micrographs showing the surface of SAW devices coated with a chemoselective polymer (SXFA) by (a) spray coating and (b) MAPLE.

[Fitz-Gerald et al., 2005]. However, the authors report that the gel permeation chromatography analysis of the MAPLE-deposited $[Ru(bpyPMMA_2)_3](PF_6)_2$ films revealed several key differences from the native material consistent with both polymer coupling reactions and some polymeric ligand dissociation from the ruthenium chromophore.

The MAPLE process has also been used to deposit thin films of various electrooptic polymers such as *N*-(4-nitrophenyl)-(L)-prolinol (NPP) and tris-(8-hydroxyquinoline) aluminum (Alq3) [Piqué, 2002]. The NPP films showed optical absorption coefficients very similar to those of drop-cast NPP films, indicating that there was no apparent decomposition of the NPP molecules after being deposited by MAPLE. In the case of the Alq3 films, the MAPLE-deposited samples exhibited optical absorption spectra different from those of bulk Alq3, indicative of some degree of decomposition that might have occurred during the MAPLE process. Since chloroform was used as the matrix/solvent for the MAPLE of the Alq3 films, it is most likely that the decomposition was caused by the generation of Cl free radicals originating from photochemically decomposed chloroform solvent molecules.

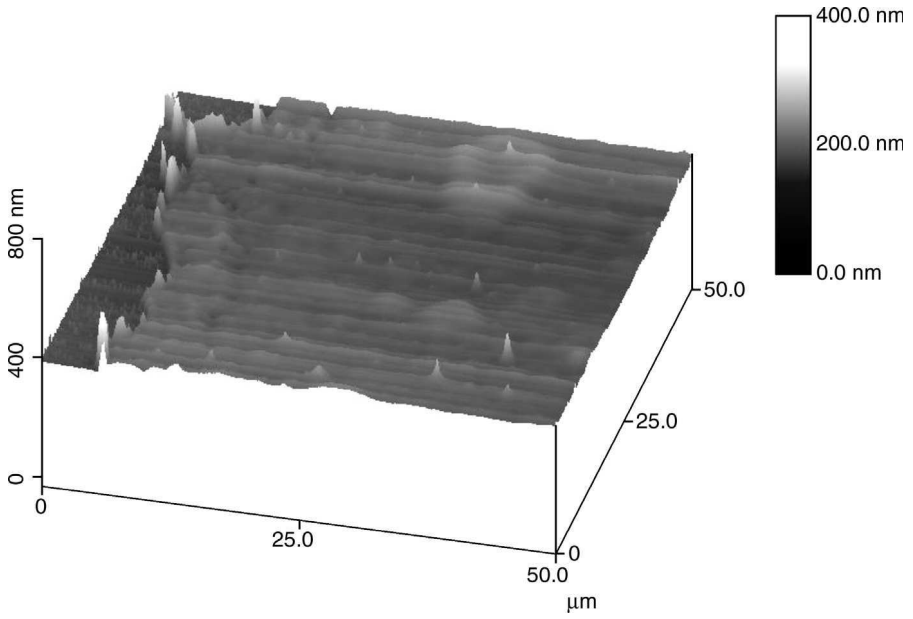

Figure 3.8 AFM image showing the edge of a 100-nm-thick chemoselective polymer (SXFA) film deposited on a silicon substrate by MAPLE.

The interaction between reactive species generated by the laser pulses and the solute molecules has been studied in particular for the growth of polyethylene glycol (PEG) thin films [Bubb et al., 2002]. PEG was chosen for these experiments because of its use as a molecular weight standard for MALDI, and thus its molecular weight distribution is well characterized. By comparing the FTIR spectra of MAPLE-deposited PEG films from two different matrices, water and chloroform, Bubb et al. [2002], discovered the presence of nonnative C–Cl absorption bands when chloroform was used as the matrix. Furthermore, mass spectra analysis showed that the PEG films made with chloroform matrices had lower average molecular weights, confirming decomposition of the starting material. None of these effects were observed for the MAPLE-deposited PEG films with water matrices. The results of this work are very relevant since they demonstrated that the type of matrix or solvent used for MAPLE can greatly affect the chemical structure and molecular weight distribution for a deposited polymer or organic film.

Finally, the MAPLE technique has also been used to deposit single-wall-nanotube (SWN)–polymer composite films. Such composites are very relevant for electronic and also biomedical applications since their mechanical, chemical, and electrical properties can be varied by controlling the type of polymer and/or the SWN loading used to make the composite. Using MAPLE, thin films of various SWN–polymer composites have been demonstrated [Wu et al., 2000]. For this work various ratios of SWN were mixed with either polystyrene (PS) or PEG in an organic solvent solution and cryogenically frozen in order to produce the MAPLE target. Scanning electron microscopy (SEM) analysis of the MAPLE-deposited films of SWN–PS or SWN–PEG composites showed that the SWN had been transferred without signs of breakage and were uniformly embedded within each of the two polymers. Figure 3.9 shows an SEM image from one such film where the presence of individual SWN fibers embedded in the polymer matrix can be seen clearly.

3.3.2 Growth of Biomaterial Thin Films

Biomaterials encompass a large class of materials that range from simple polymers such as poly(lactic acid) (PLA) and poly(glycolic acid) (PGA) for tissue engineering to enzymes, proteins,

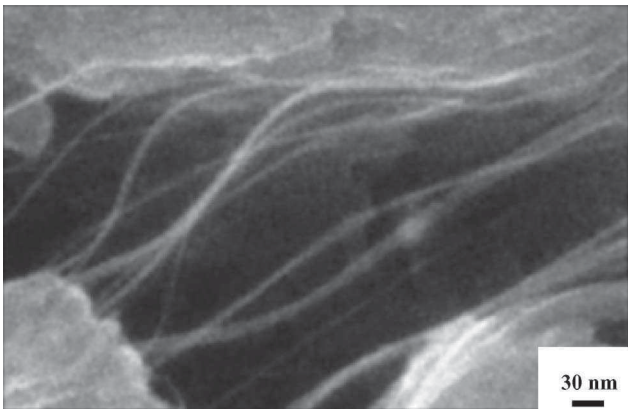

Figure 3.9 SEM micrograph of a MAPLE-deposited composite made with a polymer matrix, poly(ethylene glycol), and carbon nanotubes. The individual carbon nanotubes can be clearly seen along a fracture made in the film prior to this image being taken.

antibodies, and nucleic acids. They have found key applications in the chemical and food industries, agriculture, textiles, pharmaceuticals, and medical areas. These materials fundamentally differ from passive materials such as metals and dielectrics due to their inherent activity, that is, they have specific biochemical functions. Therefore, any processing of these materials must preserve these functions if it is to be successful. For example, a hormonal protein binds to a receptor on a cell whose function it will alter. If this protein is denatured and loses its structure, it will no longer be able to bind to the cell at the specific site, that is, it has lost its functionality. Denaturing can be the result of many factors, including processing conditions. Furthermore, the mass and size of the biomaterial molecules are also important considerations in preserving their functionality. Simply put, the processing of biomaterials in thin-film form requires preserving their molecular function and size, which are more stringent requirements than the retention of composition for passive materials.

The MAPLE technique has been used with great success for the deposition of thin films of organic molecules exhibiting a wide range of molecular weights (MW). Thin films of various carbohydrate molecules such as glucose (MW: 180.2 amu), sucrose (MW: 342.3 amu), and dextran (average MW: 148,000 amu) have been deposited from frozen targets made from aqueous solutions of each sugar [Piqué et al., 1998b, 1999]. FTIR analysis of the MAPLE films indicated that their chemical structure was identical to that of the bulk material, while electrospray mass spectrometry showed that both the glucose and sucrose films made by MAPLE had the same average weights as those of the native sugars. The FTIR and electrospray mass spectra corresponding to sucrose from both bulk and a MAPLE-deposited film can be seen in Figure 3.10. In the case of the MAPLE films of dextran, the electrospray mass spectrometry showed that their average molecular weight was about half of the bulk material, which might be an indication of a limit on the size of molecules that can be deposited intact by MAPLE. Critescu et al. [2004a] have also reported on the growth of a type of polysaccharide known as pullulan using MAPLE.

The effect of the background gas on the growth of the carbohydrate films has also been studied. FTIR spectra of the films deposited by MAPLE in a background pressure of Ar saturated with water vapor, instead of dry Ar gas, showed an increase in the absorption bands characteristic of the O–H stretch [Piqué et al., 1999]. The data suggests that the MAPLE technique might be useful for depositing thin films of organic hydrated compounds such as hydrogels. Thin films of hydrogel materials, that is, dextran, can be used in applications such as biosensors and biofilms. In such cases, a highly hydrated surface or water retaining surface is required to support higher order macromolecular structures or allow diffusion of molecules such as analytes or nutrients for detection and metabolism, respectively.

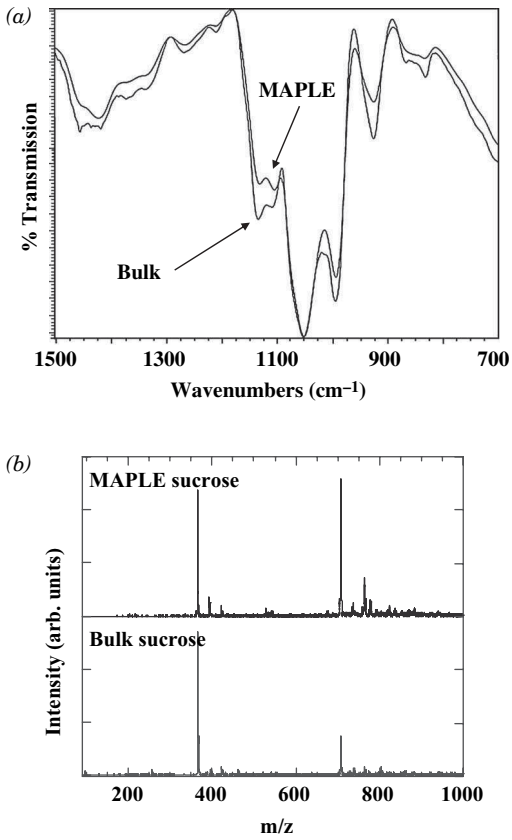

Figure 3.10 (a) FTIR spectra showing the carbohydrate fingerprint region from bulk sucrose and a sucrose film deposited by MAPLE. (b) Electrospray mass spectra of sucrose from bulk and a MAPLE film samples.

Thin films of several biocompatible polymers such as polyethylene glycol (PEG) [Bubb et al., 2001; Wu et al., 2001], the copolymer of PGA and PLA, that is, poly(D,L-lactide-*co*-glycolide) (PLGA) [Wu et al., 2003; Mercado et al., 2003, 2005], and collagen [Critescu et al., 2004b] have been prepared by MAPLE. The numerous biomedical applications of these materials demand the preservation of their chemical structure during the deposition process. For example, PEG films made by PLD have been shown to undergo irreversible modification due to photochemical decomposition of the starting molecule [Bubb et al., 2001]. On the other hand, films by MAPLE of PEG in a water matrix show little or no difference from the bulk as indicated by various characterization techniques such as FTIR, MALDI–time of flight (MALDI-TOF), and electrospray ionization (ESI) [Bubb et al., 2001]. Recent studies using frozen solutions of PEG in water have shown that it is possible to deposit PEG films via MAPLE at much higher laser fluences (2.5–7 J/cm^2) than previously reported [Rodrigo, 2004]. In a separate work from this group, pulses from a third-harmonic (355 nm) Nd : YAG laser were used to deposit very rough PEG films covered with aggregates having diameters of 5–10 μm [Toftmann et al., 2005]. At such high fluences, visible emission from the plume of ionized and excited species was clearly observed [Rodrigo et al., 2005], which makes it highly unlikely for the PEG molecules to survive the deposition process without enduring any changes to their functionality and molecular weight.

The MAPLE process has also been successfully used in the growth of active protein thin films. Such films might play an important role in the development of next-generation microfluidic

biosensors and biochips, coating drug particles with functional films for controlled time-release dosage, microneedle coatings for various therapeutic applications [DNA (deoxyribonucleic acid) vaccines, gene therapy], coatings to prevent device failure due to biofouling, and biocompatible coatings for medical implants. Using the MAPLE technique, thin and uniform films of horseradish peroxidase (HRP) and insulin have been deposited on a variety of substrates such as Si, NaCl, and gold- and platinum-coated Si [Ringeisen et al., 2001]. MALDI-TOF and liquid chromatography/electrospray ionization mass spectrometry studies on MAPLE-deposited insulin films demonstrated near-intact transfer of this protein with little or no photoinititaed decomposition. Infrared spectra of the HRP films showed that the chemical and physical structure of the protein was maintained post-MAPLE transfer. A solvent-phase activity test performed on HRP films also indicated that the majority of the transferred protein retains its chemical and physical structure as well as its biological activity. These results represent the first demonstration that pure films of intact and active biomolecules can be deposited using a vapor deposition technique. Additional studies have been performed on MAPLE-deposited thin films of other biomaterials such as biotinylated bovine serum albumin (BSA) and phospholipid polymers, all of which demonstrated maintained function and chemical structure [Wu et al., 2003]. Other reports of the growth of thin films of proteins by MAPLE include the work by Stamatin et al. [2005], who reported the growth of thin films of fibrinogen blood proteins using a physiological serum for the matrix, and the work by Patz et al. [2005] who reported the use of MAPLE to deposit mussel-adhesive protein analog copolymer thin films with a uniform distribution of ripplelike structures that affect the film's wetting behavior.

Simple glucose biosensor elements have been produced from MAPLE-deposited films of glucose oxidase (GOD) on gold electrodes. Traditionally, the GOD coatings are deposited onto the metal electrodes using ink jet techniques and then encapsulated with a polyurethane layer. The ink jet generated layers have a very nonuniform thickness and their full coverage of the electrode surface is hard to control. The response of these sensors suffer from variations between sets of electrodes due to the nonuniformity of the GOD films, as shown in the optical micrograph in Figure 3.11a. Using MAPLE to deposit through a shadow mask, it is possible to only coat the metal electrodes for a glucose sensor with very uniform 200-nm-thick GOD films as shown in Figure 3.11b. The capability with MAPLE to deposit films through a shadow mask has also been used to demonstrate the ability to generate a simple array of two distinct adjacent materials (HRP and a fluorescent-tagged dextran) on the same substrate [Ringeisen et al., 2001]. The above examples demonstrate that the MAPLE process can be used to deposit the active materials required for the fabrication of protein, antibody, or DNA bioarrays required for the development of the next generation of biosensors and lab-on-a-chip systems.

3.4 CURRENT STATUS OF MAPLE: CHALLENGES AND OPPORTUNITIES

Despite the great success achieved with the MAPLE technique for the deposition of polymers and biomaterials, this process is not without certain important drawbacks. First, the typical deposition rates that can be achieved with MAPLE are about an order of magnitude lower than those for conventional PLD. Given that most of the organic compounds to be deposited have a very large UV absorption cross section, it is necessary for the matrix solution to contain low concentrations (< 2 wt %) of the polymer or biomaterial solute molecules in order to minimize their interaction with the UV photons. Finally, the solvent molecules might be subject to photochemical reactions during their interaction with the laser pulse, which in some cases can result in the generation of highly reactive radicals that can alter the chemical structure and functionality of the solute polymer or biomaterial being deposited. As mentioned earlier in this chapter, this effect was first reported by Bubb et al. in their study of MAPLE-deposited PEG films as a function of the type of solvent used for the matrix. They discovered that matrices containing chloroform as the solvent resulted in the formation of reactive radicals such as Cl*, which can adversely affect the PEG films

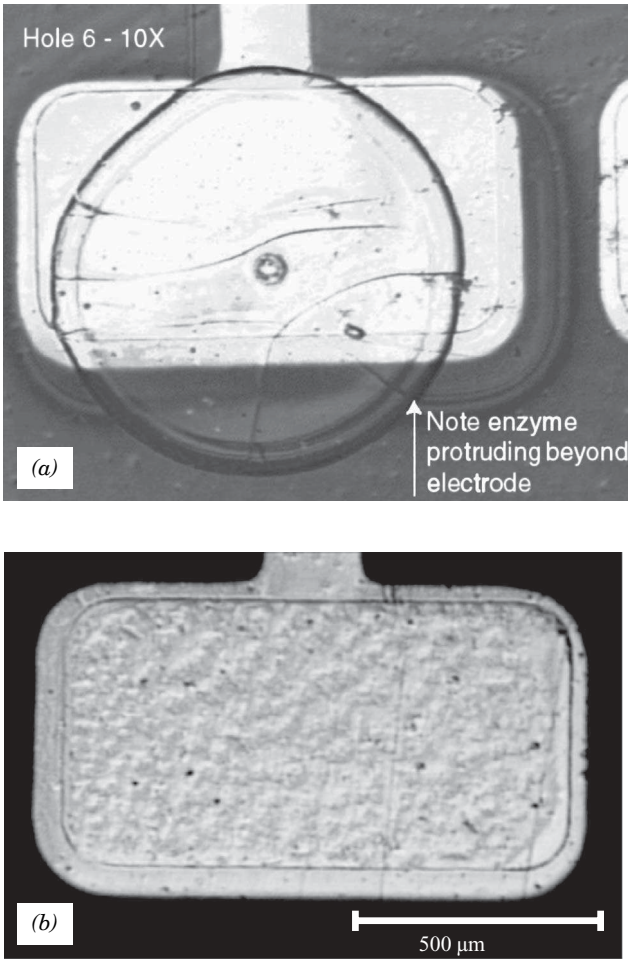

Figure 3.11 Optical micrographs comparing single metal electrodes for a glucose sensor coated with a glucose oxidase film deposited by (a) ink jet and (b) MAPLE.

deposited by MAPLE [Bubb et al., 2002]. This effect can probably explain most of the published results reporting the change or modification of the native material after being deposited via MAPLE. So far, the use of water as a matrix for MAPLE has been very successful; however, many polymers and certain biomaterials are not at all soluble in water, and thus the search continues for new organic solvents for making MAPLE matrices that do not generate reactive species upon their interaction with a UV laser pulse.

It is worth mentioning a new variant of MAPLE, which uses an IR laser rather than a UV laser to vaporize a solvent–solute matrix. This process named resonant IR-MAPLE, or RIR-MAPLE, has been used with great success to deposit thin films of an electroluminescent polymer, MEH-PPV [Toftmann et al., 2004], a sorbent chemoselective oligomer, fluoropolyol [Bubb et al., 2004], and a conductive polymer, polyaniline [Bubb et al., 2005]. For the MEH-PPV depositions by RIR-MAPLE, chloroform was used as the solvent for the matrix, while the emission from the free-electron laser (FEL) at the W.M. Keck Foundation Free-Electron Laser Center at Vanderbilt University, tuned to a wavelength of 8.2 μm, was used as the light source. This laser wavelength was selected since it was expected to couple strongly to an absorbance band at 8.2 μm in $CHCl_3$.

The resulting MEH-PPV films had very smooth surfaces and showed identical FTIR spectra to that of the bulk material [Totmann et al., 2004]. For the fluoropolyol and polyaniline films, an Er : YAG laser emitting at 2.94 μm was used and *t*-butanol or methanol served as solvents for the matrix [Bubb et al., 2004, 2005]. Again, the RIR-MAPLE resulted in films virtually identical to the starting materials. Furthermore, RIR-MAPLE can be carried out at much higher laser fluences (3–5 J/cm^2) and also larger matrix concentrations (15–20 wt %), thus resulting in deposition rates that are over an order of magnitude higher than with traditional UV-MAPLE. The main obstacle that limits the implementation of the IR-MAPLE technique by other groups is the lack of appropriate IR sources. Ideally, if free-electron laser sources were readily available, it would be possible for other researchers to experiment with RIR-MAPLE by tuning the laser wavelength to other matrix-resonant absorption bands, which would only interact with the matrix solvent and leave the polymer material undisturbed. In reality, very few labs can boast these kind of facilities. Instead, some types of pulsed IR lasers such as the Er : YAG might offer a more practical option as laser sources for RIR-MAPLE, although further work is required to determine the viability of using 2.93-μm laser pulses for evaporating matrices made from other solvents besides various types of alcohols.

Another aspect that must be taken into consideration when using MAPLE is the resulting film surface morphology. Under certain conditions, that is, low laser fluence, low laser repetition rate, low solute concentration in the matrix, and/or lower temperature of the target matrix, it is possible to produce very smooth and uniform coatings with MAPLE. More often than not, however, the surface morphology of the films tends to be rough and in some cases large droplets are present as well. The film roughness not only depends on processing conditions but also on the type of polymer or organic being deposited and in the case of many biomaterials might not be modifiable due to the characteristic intrinsic arrangements of the molecular chains. For some applications, such as in biosensors, higher surface areas resulting from the rough film morphology might be desirable since they increase the area for analyte binding. The rough protein films that can be generated by MAPLE can potentially increase the detection capability of a biosensor by increasing the active protein area exposed to a particular analyte.

In most cases, however, the surface of MAPLE-deposited films shows a high density of micrometer-sized droplets as can be seen in the optical micrograph from Figure 3.12 showing a

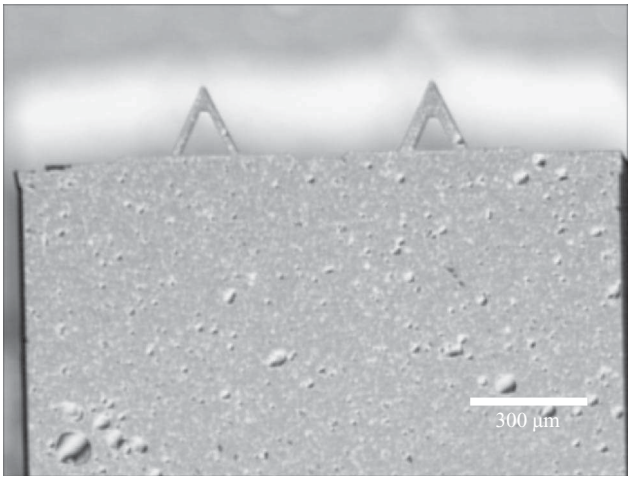

Figure 3.12 Optical micrograph image showing an AFM cantilever substrate coated by MAPLE showing a high density of droplets generated during deposition.

Si substrate with an AFM cantilever tip coated with a chemoselective polymer. Several authors have reported these kinds of surfaces for MAPLE films grown at high deposition rates [Toftmann et al., 2005; Sellinger et al., 2005]. Molecular-level dynamic simulations of the initial stages of the ejection of species from the frozen matrix target during MAPLE reveal the ejection of solute molecules in the form of a solvent–solute cluster. It is likely that these clusters are responsible for the formation of the droplets observed in the MAPLE films. These simulations also indicate that the ejection of single solute molecules does not occur during MAPLE (Leveugle et al., 2005). The authors conclude that the deposition of smooth and uniform thin films using the MAPLE technique may be difficult to achieve given the existence of these clusters traveling from the target to the substrate. Although significant simplifications were made for the purpose of these models, such as neglecting any heat diffusion effects and ignoring the absorption of laser radiation by the solute molecules, the results of these simulations are worth considering given the numerous reports of films deposited with MAPLE covered with a high density of droplets.

One approach being explored to mitigate the formation of droplets in the films deposited using the MAPLE technique is to place the substrate parallel to the deposition axis rather than normal to it. This method developed at the U.S. Naval Research Laboratory is called off-axis MAPLE. Figure 3.13 shows a simple schematic illustrating the setup for off-axis MAPLE. Preliminary tests using this configuration to deposit chemoselective polymers on AFM cantilevers for a highly sensitive chemical sensor system have shown great promise in almost eliminating the presence of droplets in the films. Interestingly, the deposition rate in the off-axis configuration is only reduced by a factor of $\frac{1}{2}$ to $\frac{1}{3}$ of the normal MAPLE deposition rate. Figure 3.14 shows an AFM image taken near the edge of a chemoselective polymer film deposited on a Si substrate using off-axis MAPLE. The enhanced surface smoothness and uniformity can be better appreciated by comparing this AFM image to that of the traditional MAPLE-deposited film shown in Figure 3.8.

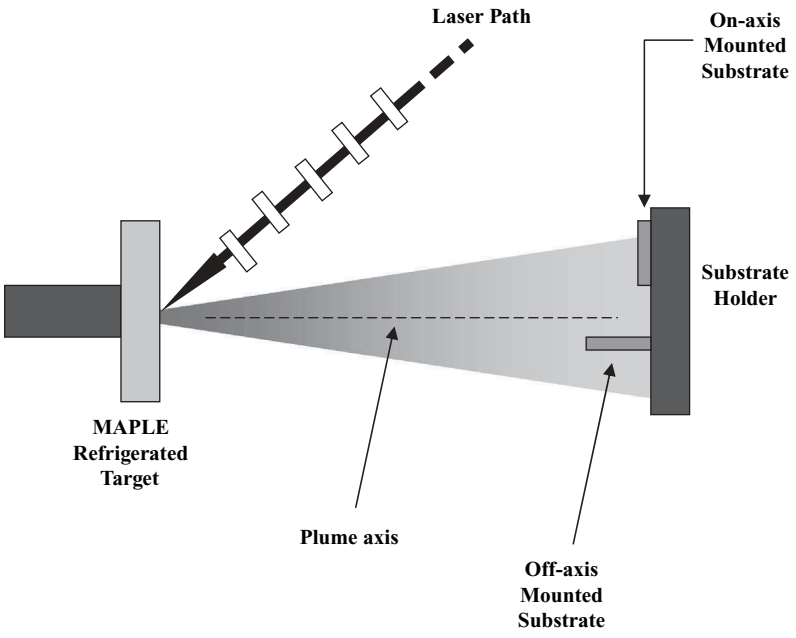

Figure 3.13 Schematic diagram showing the arrangement of the target and substrate for off-axis MAPLE.

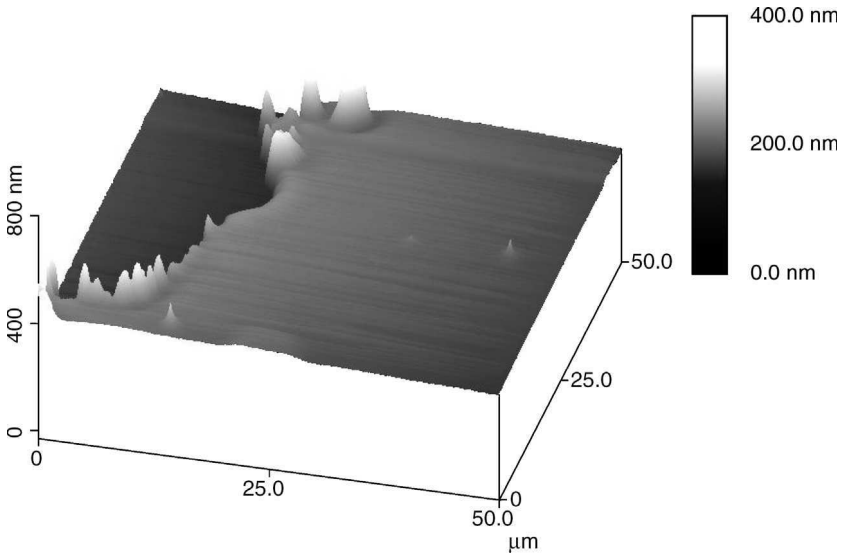

Figure 3.14 AFM image showing the edge of a 100-nm-thick chemoselective polymer (SXFA) film deposited on a silicon substrate by off-axis MAPLE.

3.5 FUTURE OF MAPLE

Table 3.1 provides a list of the different polymer and organic materials that have been successfully deposited to date using the MAPLE technique. In addition to demonstrating the capability for depositing various organic materials using MAPLE, several of the studies cited in the previous sections have investigated the MAPLE process under different conditions such as type of matrix solvent, polymer or biomaterial solute concentration, laser energy, and laser wavelength. In general, the results demonstrate that the material properties such as chemical structure and functionality depend strongly upon the laser wavelength, matrix, and energy used in the experiment. These studies highlight the potential limitations with UV-MAPLE experiments and have spurred studies of the MAPLE process using less energetic wavelengths such as IR.

The effect of the laser pulsewidth on the film chemical structure and morphology is a parameter that has not yet been explored. So far, all the work to date has been conducted with nanosecond pulses, except for the tests performed at Vanderbilt University using its FEL at 8.2 μm with bursts of picosecond pulses. Given the success obtained by performing PLD with femtosecond laser pulses, performing MAPLE depositions with ultrashort laser pulses might be an obvious direction to explore. However, the resulting nonthermal ablation characteristic of femtosecond PLD might not be conducive to the generation of smooth and droplet-free MAPLE films given the propensity of cluster generation during the laser interaction with the frozen MAPLE target. In fact in the previous section, the results of molecular-level dynamics simulations described the formation and release of large clusters of solute/solvent during MAPLE assuming the use of picosecond laser pulsewidths [Leveugle et al., 2005]. Perhaps the use of longer laser pulses (> 100 ns), with wavelengths strongly absorbed by the solvent in the matrix, might be more appropriate for the growth of thin films. Longer laser pulses would result in the light–matrix interaction to be closely photothermal in nature, thus allowing the gentle vaporization of the solute due to the exchange of thermal energy with the surrounding solvent matrix molecules. Another parameter that has not been properly explored in the work performed with MAPLE to date is the effect of substrate temperature on film growth. Few studies have been conducted to determine if the morphology of MAPLE-deposited films can be

TABLE 3.1 List of Polymeric, Organic, and Biological Materials Deposited by MAPLE

Material	Solvent Matrix	Laser Wavelength (nm)	References
Fluoroalcoholpolysiloxane (SXFA)	Ter-butyl alcohol	248	Piqué [1999]
Glucose	H_2O	193	Piqué [1998]
Sucrose	H_2O	193	Piqué [1998]
Dextran	H_2O	193	Piqué [1998]
Pullulan	Dimethyl sulfoxide	248	Critescu [2003]
Poly(ethylene glycol) (PEG)	H_2O	193	Bubb [2002]
Poly(ethylene glycol) (PEG)	H_2O	355(Nd : YAG)	Rodrigo [2004], Toftmann [2005]
Poly(ethylene glycol) (PEG)	Isopropanol, acetone, toluene	355 (Nd : YAG)	Rodrigo [2005]
Polypyrrole	$CHCl_3$	193	Piqué [2002]
N-(4-nitrophenyl)-(L)-prolinol (NPP)	$CHCl_3$	193	Piqué [2002]
Tris-(8-hydroxyquinoline) aluminum (Alq3)	$CHCl_3$	193	Piqué [2002]
Poly[2-methoxy-5-(2'-ethylhex-yloxy)-1,4-phenylene vinylene] (MEH-PPV)	Toluene or tetrahydrofuran	193, 248	Toftmann [2004]
Poly[2-methoxy-5-(2'-ethylhex-yloxy)-1,4-phenylene vinylene] (MEH-PPV)	$CHCl_3$	8.2 μm (RIR-MAPLE)	Toftmann [2004]
Fluoropolyol	Ter-butyl alcohol	193, 248	Bubb [2004]
$[Ru(bpyPMMA_2)_3](PF_6)_2$	Dimethoxyethane	248	Fitz-Gerald [2005]
Poly(DL-lactide-*co*-glycolide) (PLGA)	$CHCl_3$	248	Mercado [2003]
Poly(DL-lactide-*co*-glycolide) (PLGA)	Ethyl acetate	193	Wu [2003]
Carbon nanotubes/polysteryne Carbon nanotubes/PEG	Toluene	248	Wu [200]
Collagen	H_sO	248	Critescu [2004]
Insulin	Phosphate buffer solution	193	Ringeisen [2001]
Horseradish peroxidase (HRP)	Phosphate buffer solution	193	Ringeisen [2001]
Biotinylated bovine serum albumin (BSA)	Glycerol/phosphate buffer solution	193	Wu [2003]
Fibrinogen blood proteins	Physiological serum	193	Stamatin [2005]
Mussel-adhesive proteins	H_sO	193	Patz [2005]
Fluoropolyol	Ter-butyl alcohol, or methanol	2.94 μm (RIR-MAPLE)	Bubb [2004]
Polyanaline	Methanol	2.94 μm (RIR-MAPLE)	Bubb [2005]

improved by varying the substrate temperature during or after deposition. It might be possible to reduce or even eliminate the characteristic droplets or clusters present on films of many polymers and certain biomaterials with low glass transition temperatures, by slightly heating the substrate. These two parameters—laser pulsewidth and substrate temperature—are just two examples of several deposition parameters whose effect on the quality of the films grown by MAPLE should to be studied in the future.

The use of the MAPLE technique has so far been limited to depositing films on small area substrates without a true multilayer capability. This is mainly due to the fact that most MAPLE

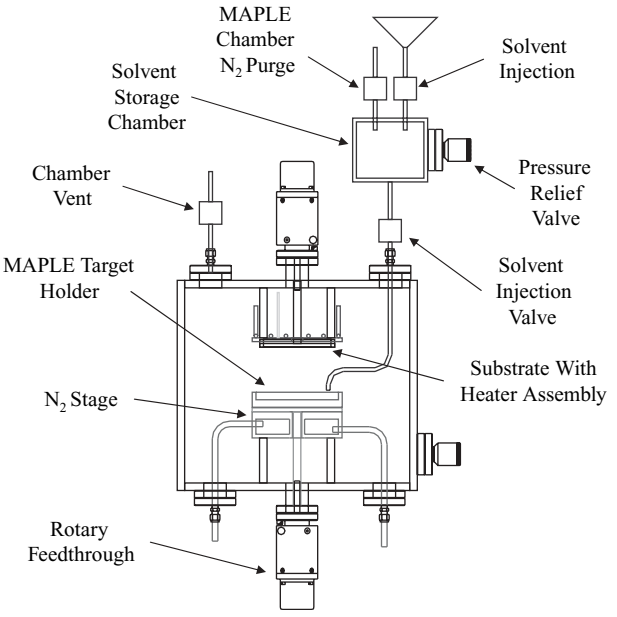

Figure 3.15 Schematic of a large-area, high-throughput, multitarget MAPLE system. (Drawing courtesy of PVD Products, Inc.)

systems currently available have been built by retrofitting existing PLD systems with a refrigerated stage capable of accommodating only one target. If instead a MAPLE system were to be designed from the start to accommodate refrigerated targets and large area substrates, many of these issues would disappear. Toward this end, various designs have been proposed for MAPLE scale-up purposes. Figure 3.15 for example shows a schematic for a MAPLE system that allows the solvent–polymer mix to be injected into a dry vacuum chamber and frozen in situ [Greer, 2003]. This reduces the amount of water vapor that can be trapped in the volume or surface of the target material. The chamber has a large door with a pair of differentially pumped O-rings. Pumping between the O-rings with the chamber at atmosphere isolates the interior of the chamber from the outside. Dry nitrogen is bled into the system through the nitrogen vent for about 1 h. The chamber pressure is relieved by an overpressure relief valve. This process displaces water vapor, oxygen, and the other constituents of air. The solvent storage chamber is also purged in the same manner. The solvent–polymer mix is then injected into the solvent chamber from where it is then injected into the main chamber and into the cup of the MAPLE target holder using a tube. LN_2 is then injected into the stage to cool down the solvent–polymer mix. A thermocouple (not shown in the figure) can be used to monitor the temperature. The MAPLE target holder must be designed to have excellent thermal contact with the LN_2 cooling stage and yet be able to rotate freely. An external rotary feedthrough is then used to rotate the MAPLE target. During deposition the laser beam can be rastered across the MAPLE target surface to utilize as much of the target material as possible.

Clearly the need for such systems most likely will be driven by specific applications where the attributes of the MAPLE process offer unique advantages. For instance, using MAPLE, multilayers of distinct organic or polymeric materials can be deposited in situ, enabling protective overcoats or membranes of organic materials to be easily formed. Furthermore, layers of organic materials with graded composition could be formed by alternating the ratio of material removed from different targets. Finally, co-depositions could also be performed by using multicomponent targets with proteins or DNA combined with polymers or other functional materials to aid in stability, adhesion onto nontraditional surfaces, or molecular activity.

Current studies at the U.S. Naval Research Laboratory are focused on applying MAPLE to biomolecules that are used in biosensors with the goal of fabricating a functioning chip-scale device. There are plans to explore the extent to which MAPLE can be used to transfer different biomolecules such as DNA or antibodies perhaps investigating how different wavelengths such as IR change the film qualities. The current studies also highlight the need for further investigations to determine the best methods to adhere MAPLE-deposited biomolecules to different surfaces without perturbing their activity. Recent efforts directed toward the creation of polymer–protein composites to increase adhesion have been successful, but patterning such composite materials has produced agglomerate-rich films. To mitigate this effect, methods are being explored to modify the substrate surface to increase material adhesion as well as to chemically immobilize deposited molecules in situ. MAPLE also holds potential to deposit not only biomolecules but also a matrix that serves to maintain the activity of the sensitive material or help adhere it to the substrate. Overall, MAPLE shows promise as a novel and versatile technique to deposit and pattern thin, active biomolecular films of varying thickness and surface morphologies.

3.6 SUMMARY

This chapter has provided highlights of several attributes of the MAPLE technique for depositing organic, polymeric, and biomaterial thin films. MAPLE is capable of forming thin films over a wide range of thicknesses from 10 nm to over 1 μm and with accurate thickness control (<0.1 nm/laser shot). Many current technologies using surface-assembled monolayers are only capable of depositing monolayers, while other thick-film deposition techniques, such as ink jet printing, are unable to control thickness and film uniformity. MAPLE's thickness control and accurate material placement, therefore, may be particularly useful for the development of next-generation coatings for sensor applications as in the case of thick-film amperometric biosensors where accurate thickness control and uniform film coverage are crucial to signal output. The surface morphology of the films can also be controlled by MAPLE, enabling this technique to tune the roughness of films to meet specific device requirements. Furthermore, by combining MAPLE with other laser-based techniques such as PLD, it might be possible to grow structures consisting of metal electrodes, active biological molecules, and a polymer or biomaterial coating to immobilize and protect the underlying materials. Multiple materials can also be patterned adjacently on the same substrate, enabling microarrays to be fabricated with feature size and spacing as small as 20 μm. MAPLE is unique because it is able to combine these attributes into one processing tool to fabricate structures unattainable by other technologies.

It is worth concluding this chapter with the observation that the use of the MAPLE technique has expanded steadily since it was first reported back in 1998. As the number of publications on the study and applications of the MAPLE process grows, new variants of the technique and further understanding of its mechanism are sure to develop. As discussed throughout this chapter, MAPLE is not a foolproof process and many issues remain. However, its ability to extend the inherent advantages of PLD by which a thin film of a material of interest can be generated, namely simplicity and speed, to the world of polymeric and biomaterials should not be ignored.

REFERENCES

Blanchet, G. B. (1993a), *Appl. Phys. Lett*. **62**, 479.

Blanchet, G. B., and C. R. Fincher (1994), *J. Adv. Mater.* **6**, 881.

Blanchet, G. B., C. R. Fincher, C. L. Jackson, S. I. Shah, and K. H. Gardner (1993), *Science* **262**, 719.

Bubb, D. M., B. R. Ringeisen, J. H. Callahan, M. Galicia, A. Vertes, J. S. Horwitz, R. A. McGill, E. J. Houser, P. K. Wu, A. Piqué, and D. B. Chrisey (2001), *Appl. Phys. A*, **73**, 121.

Bubb, D. M., P. K. Wu, J. S. Horwitz, J. H. Callahan, M. Galicia, A. Vertes, R. A. McGill, E. J. Houser, B. R. Ringeisen, and D. B. Chrisey (2002), *J. Appl. Phys*. **91**, 2055.

Bubb, D. M., S. M. O'Malley, C. Antonacci, D. Simonson, and R. A. McGill (2004), *J. Appl. Phys*. **95**, 2175.

Bubb, D. M., S. M. O'Malley, C. Antonacci, R. Belmont, R. A. McGill, and C. Crimi (2005), *Appl. Phys. A*, **81**, 119.

Chrisey, D. B., A. Piqué, R. A. McGill, J. S. Horwitz, B. R. Ringeisen, D. M. Bubb, and P. K. Wu (2003), *Chem. Rev.* **103**, 553.

Critescu, R., I. Stamatin, D. E. Mihaiescu, C. Ghica, M. Albulescu, I. N. Mihailescu, and D. B. Chrisey (2004a), *Thin Solid Films* **453/454**, 262.

Critescu, R., D. E. Mihaiescu, G. Socol, I. Stamatin, I. N. Mihailescu, and D. B. Chrisey (2004b), *Appl. Phys. A* **79**, 1023.

Fitz-Gerald, J. M., G. Jennings, R. Johnson, and C. L. Frazer (2005), *Appl. Phys. A*, **80**, 1109.

Greer, J. (2003), PVD Products, Wilmington, MA, private communication, November.

Hansen, S. G., and T. E. Robitaille (1988a), *Appl. Phys. Lett*. **52**, 81.

Hansen, S. G., and T. E. Robitaille (1988b), *J. Appl. Phys*. **64**, 2122.

Itina, T. E., L. V. Zhigilei, and B. J. Garrison (2001), *Nucl. Instrum. Methods Phys. Res. B* **180**, 238.

Leveugle, L., L. V. Zhigilei, A. T. Sellinger, and J. M. Fitz-Gerald (2005), paper presented at the Eighth International Conference on Laser Ablation, Banff, Canada, September.

McGill, R. A., and D. B. Chrisey (2000), U.S. Patent 6,025,036, February 15.

McGill, R. A., M. H. Abraham, and J. Grate (1994), *CHEMTEC* **24**, 27.

McGill, R. A., D. B. Chrisey, A. Piqué, and T. E. Mlsna (1998a), *SPIE Proc*. **3274**, 255.

McGill, R. A., R. Chung, D. B. Chrisey, P. C. Dorsey, P. Matthews, A. Piqué, T. E. Mlsna, and J. I. Stepnowski (1998b), *IEEE Trans. Ultrason. Ferr.* **45**, 1370.

Mercado, A. L., J. M. Fitz-Gerald, R. Johnson, and J. D. Talton (2003), *Mater. Res. Soc. Symp. Proc*. **780**, Y4.4.1.

Mercado, A. L., C. E. Allmond, F. G. Hoekstra, and J. M. Fitz-Gerald (2005), *Appl. Phys. A* **81**, 591.

Patz, T., R. Critescu, R. Narayan, N. Menegazzo, B. Mizaikoff, P. B. Messersmith, I. Stamatin, I. N. Mihailescu, and D. B. Chrisey (2005), *Appl. Surf. Sci*. **248**, 416.

Piqué, A., R. A. McGill, D. B. Chrisey, J. H. Callahan, and T. E. Mlsna (1998a), *Mater. Res. Soc. Symp. Proc*. **526**, 375.

Piqué, A., D. B. Chrisey, B. J. Spargo, M. A. Bucaro, R. W. Vachet, J. H. Callahan, R. A. McGill, D. Leonhardt, and T. E. Mlsna (1998b), *Mater. Res. Soc. Symp. Proc*. **526**, 421.

Piqué, A., R. A. McGill, D. B. Chrisey, D. Leonhardt, T. E. Mslna, B. J. Spargo, J. H. Callahan, R. W. Vachet, R. Chung, and M. A. Bucaro (1999), *Thin Solid Films* **355/356**, 536.

Piqué, A., P. K. Wu, B. R. Ringeisen, D. M. Bubb, J. S. Melinger, R. A. McGill, and D. B. Chrisey (2002), *Appl. Surf. Sci*. **186**, 408.

Ringeisen, B. R., J. Callahan, P. K. Wu, A. Piqué, B. Spargo, R. A. McGill, M. Bucaro, H. Kim, D. M. Bubb, and D. B. Chrisey (2001), *Langmuir* **17**, 3472.

Rodrigo, K., B. Toftmann, J. Schou, and R. Pedrys (2004), *Chem. Phys. Lett*. **399**, 368.

Rodrigo, K., B. Toftmann, J. Schou, and R. Pedrys (2005), *J. Low Temp. Phys*. **139**, 683.

Sellinger, A. T., E. Leveugle, K. Gogick, G. Peman, L. V. Zhigilei, and J. M. Fitz-Gerald, (2005), paper presented at the Eighth International Conference on Laser Ablation, Banff, Canada, September.

Smith, H. M., and A. F. Turner (1965), *Appl. Opt*. **4**, 147.

Stamatin, L., R. Critescu, G. Socol, A. Moldovan, D. Mihaiescu, I. Stamatin, I. N. Mihailescu, and D. B. Chrisey (2005), *Appl. Surf. Sci*. **248**, 422.

Toftmann, B., M. R. Papantonakis, R. C. Y. Auyeung, W. Kim, S. M. O'Malley, D. M. Bubb, J. S. Horwitz, J. Schou, P. M. Johansen, and R. F. Haglund (2004), *Thin Solid Films* **453/454**, 177.

Toftmann, B., K. B. Rodrigo, J. Schou, and R. Pedrys (2005), *Appl. Surf. Sci*. **247**, 211.

Vertes, A., R. Gijbels, and F. Adams (Eds.) (1993), *Laser Ionization Mass Analysis*, Wiley, New York.

Wu, P. K., J. Fitz-Gerald, A. Piqué, D. B. Chrisey, and R. A. McGill (2000), *Mater. Res. Soc. Symp. Proc*. **617**, J2.3.1.

Wu, P. K., B. R. Ringeisen, J. Callahan, M. Brooks, D. M. Bubb, H. D. Wu, A. Piqué, B. Spargo, R. A. McGill, and D. B. Chrisey (2001), *Thin Solid Films* **398/399**, 607.

Wu, P. K., B. R. Ringeisen, D. B. Krizman, C. G. Frondoza, M. Brooks, D. M. Bubb, R. C. Y. Auyeung, A. Piqué, B. Spargo, R. A. McGill, and D. B. Chrisey (2003), *Rev. Sci. Instrum.* **74**, 2546.

CHAPTER 4

In Situ Diagnostics by High-Pressure RHEED During PLD

GUUS RIJNDERS AND DAVE H. A. BLANK

MESA+ Institute for Nanotechnology, University of Twente, The Netherlands

4.1 INTRODUCTION

Many surface processes during deposition and growth determine thin-film properties such as crystallinity and surface morphology and are therefore the subject of much attention. Reflection high-energy electron diffraction (RHEED) is most often used to study the mechanisms and film surface processes during growth.

The pulsed laser deposition (PLD) technique is probably the most versatile method for the fabrication of oxide thin films because of its unique features: a high pulse deposition rate and the controllable kinetic energy of the deposited particles. With the introduction of high-pressure RHEED [Rijnders et al., 1997], growth rate control on an atomic level as well as in situ growth studies at the typical oxygen deposition pressures used during PLD of complex oxides has become possible. In this chapter, a PLD system equipped with high-pressure RHEED will be described, including its unique features.

4.2 BASIC PRINCIPLES

In PLD a pulsed highly energetic laser[1] is focused on a target resulting in ablation of material. At the early stage of the laser pulse a dense layer of vapor is formed in front of the target. Energy absorption during the remainder of the laser pulse causes both the pressure and temperature of this vapor to increase, resulting in partial ionization. This layer expands from the target surface due to the high pressure and forms the so-called plasma plume. During this expansion, internal thermal and ionization energies are converted into the kinetic energy (several hundred electron volts) of the ablated particles. Attenuation of the kinetic energy due to multiple collisions occurs during expansion into the low-pressure background gas. Typically, a background pressure of 1–50 Pa is used for deposition of complex oxides, and at these pressures, thermalization occurs at a penetration length comparable to the target-to-substrate distance. Several models, such as the ''drag force'' and

[1]Usually an excimer laser or frequency up-converted Nd : YAG laser is used. Both produce intense laser pulses in the UV range at repetition rates that may approach several hundred hertz.

Pulsed Laser Deposition of Thin Films: Applications-Led Growth of Functional Materials
Edited by Robert Eason

the ''shock wave'' model [Geohegan, 1992a, 1992b], have been proposed that describe this attenuation in low and high background pressure, respectively. Using an adiabatic thermalization model [Strikovski and Miller, 1998], a characteristic length scale is determined that defines the ''plasma range'', and plasma particles thermalize at distances larger than this characteristic length.

Ambient gas parameters, that is, mass and pressure, determine the interaction with the ablated particles and, subsequently, the kinetic energy of the particles arriving at the substrate. As a consequence, this kinetic energy can be varied from high initial energy in vacuum to low energies resulting from thermalization at sufficiently large ambient pressure. This wide range is a unique feature of PLD and can be used to modify thin-film growth. Here, the diffusivity [Dam and Stäuble-Pümpin, 1998; Blank et al., 1999] and both the absorption and desorption probability [Tyunina et al., 1998] of the energetic particles at the film surface are the controllable parameters.[2]

Another unique feature of PLD is the high deposition rate. In PLD of oxides, for instance, the high-temperature superconductor $YBa_2Cu_3O_7$ (RE123), typical deposition rates range from 10^{-2} to 10^{-1} nm/pulse with deposition pulse duration[3] on the order of several microseconds to $\sim 500\,\mu s$ [Okada et al., 1997; Cheing and Horwitz, 1992]. As a result, the deposition rate can be as high as 10^2–10^5 nm/s [Geohegan and Puretzky, 1995; Chern at al., 1992]. This value is orders of magnitude higher than achievable with other physical vapor deposition (PVD) techniques such as sputter deposition and molecular beam epitaxy (MBE), which have typical deposition rates of 10^{-2}–10^{-1} nm/s. The short duration of the intense deposition pulse has implications for the nucleation and growth processes. This is illustrated by comparing the pulse duration with the mean diffusion time t_D of deposited atoms, which is given by

$$t_D = v^{-1} \exp\left(\frac{E_A}{k_B T}\right) \tag{4.1}$$

where v is the attempt frequency for atomistic processes, E_A is the activation energy for diffusion, and k_B is the Boltzmann constant. Here, the mean diffusion time t_D is of interest because it sets the time scale for the atomistic processes, including collision and nucleation. For complex oxides E_A ranges from a few tenths of an electron volt to more than 2 eV, and typical growth temperatures range from 800 to more then 1100 K. Using Eq. (4.1) the mean diffusion time can be estimated. For a wide range of deposition conditions t_D exceeds the deposition pulse duration. As a consequence, the deposition can be regarded as instantaneous for every pulse. In PLD, this instantaneous deposition is followed by a relative long time interval, where no deposition takes place. During this time interval, which is determined by the pulse repetition rate, the adatoms rearrange on the surface by migration and subsequent incorporation through nucleation and growth. This rearrangement can be considered as an anneal process. Because of the instantaneous deposition, the two basic processes, that is, random deposition and growth through rearrangement are separated in time, which is again unique for PLD.[4]

Parameters that control the instantaneous deposition rate are the laser energy density at the target, pulse energy, distance between target and substrate, and the ambient gas properties, that is, pressure and mass. The average growth rate is determined by the pulse repetition rate and can be varied independently from the instantaneous deposition rate.

The extremely high deposition rate leads to a very high degree of supersaturation $\Delta\mu$ [Markov, 1995]:

$$\Delta\mu = k_B T \ln\frac{R}{R_0} \tag{4.2}$$

[2]Bombardment with highly energetic particles on the film surface during growth may lead to a defective crystal structure for the film and should be avoided.

[3]Note the deposition pulse duration differs from the laser pulse duration.

[4]In most deposition techniques the deposition flux is continuous. As a result, deposition and surface relaxation occurs simultaneously.

where k_B is the Boltzmann constant, R is the actual deposition rate, and R_0 is its equilibrium value at temperature T. The high degree of supersaturation $\Delta\mu$ causes two-dimensional (2D) nucleation of a high density of extremely small[5] clusters. Because of the instantaneous deposition under typical PLD conditions, the nucleation takes place after the deposition pulse and can be considered as postnucleation [Fuenzalida, 1998, 2000]. Subcritical clusters are unstable in the time interval between the deposition pulses and dissociate into mobile atoms. These nucleate into new clusters or cause stable clusters to grow. The latter process is similar to Oswald ripening where larger islands grow at the expense of small islands or clusters. The separated random deposition and subsequent growth is, furthermore, advantageous for the study of growth kinetics.

4.3 HIGH-PRESSURE RHEED

Reflection high-energy electron diffraction (RHEED) has become an important tool in surface science because of its high surface sensitivity. It utilizes diffraction of electrons by surface atoms and provides information of the periodic arrangement of the surface atoms. Because of the compatibility with (ultra) high-vacuum deposition techniques, it is often used for the investigation of the surface morphology during thin-film growth. It requires minimal hardware and is thus a relatively low-cost analysis technique.

4.3.1 Geometry and Basic Principles of RHEED

A schematic drawing of a typical RHEED geometry is sketched in Figure 4.1. The incident electron beam (e-beam) strikes the sample surface at a grazing angle θ_i. The electrons are monoenergetic with a typical energy of $E \sim 10$–50 keV. The corresponding amplitude of the wavevector $\mathbf{k_0}$ for these high-energy electrons can be estimated using

$$E = \sqrt{\frac{\hbar^2 |\mathbf{k_0}|^2}{m^*}} \tag{4.3}$$

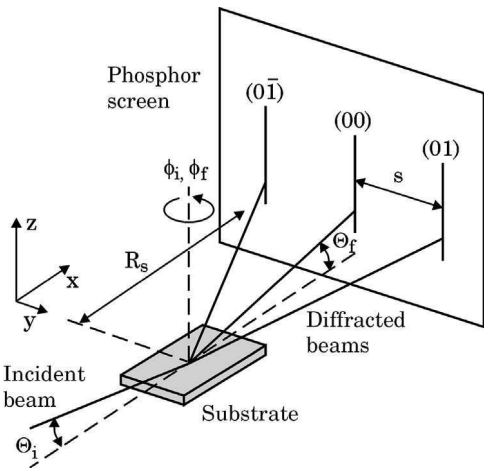

Figure 4.1 Schematic view of the RHEED geometry. $\Theta_I(\Theta_F)$ and $\phi_I(\phi_F)$ are the incident and azimuthal angles of the incident (diffracted) beam. R_S is the distance between substrate and phosphor screen and S the distance between the diffraction spots or streaks.

[5]For PLD, the clusters can be as small as one atom to a few molecular blocks of the complex oxides.

where m^* is the effective mass of the electron. Without relativistic correction (which should be only a few percent for the energies of interest), the electron wavelength λ can be estimated by

$$\lambda(\text{Å}) = \sqrt{\frac{150}{E}} \tag{4.4}$$

with E given in electron volts. At the typical energies used in RHEED, the electron wavelength λ is ~ 0.05–0.1 Å, which is an order of magnitude smaller than the thickness of an atomic layer.

The angle of incidence is typically set to a few degrees (0.1°–5°). At these grazing angles the penetration depth is as small as a few atomic layers, which makes RHEED an extremely surface sensitive diffraction technique so the electrons are easily scattered by surface steps and terraces. The coherence length [Lagally et al., 1989], which is the maximum distance between reflected electrons that are able to interfere, is determined by the beam convergence and the energy spread of the electrons, and is typically of the order of several hundreds nanometers.

The electron gun (e-gun) and phosphor screen (which acts as the detector) are located far from the sample to avoid any interference with the deposition process. In this geometry, electrons are scattered from the crystal surface, resulting in a characteristic diffraction pattern on the phosphor screen. This pattern is instantaneously displayed and can be used to define the crystallographic surface structure of, for instance, a growing thin film.

Kinematic[6] scattering theory is used to describe weakly interacting diffraction techniques, such as X-ray or neutron diffraction. RHEED, however, involves strong interaction [Kawamura, 1989] of the electrons with the periodic potential of the crystal surface and can, therefore, not be described quantitatively by the kinematic approach. Nevertheless, the kinematic approach is used for both physical understanding and qualitative description of RHEED.

Reflection high-energy electron diffraction spots are produced when the momentum of the incident beam and that of the diffracted beam differ by a reciprocal lattice vector $\mathbf{G}$:

$$\mathbf{k_S} - \mathbf{k_0} = \mathbf{G} \tag{4.5}$$

where $\mathbf{k_S}$ and $\mathbf{k_0}$ are the wavevectors of the diffracted and incident beams. A useful geometrical representation of the conditions for diffraction in elastic scattering, that is, $|\mathbf{k_S}| = |\mathbf{k_0}|$, is provided by the Ewald sphere construction, depicted in Figure 4.2. Here, the reciprocal lattice of a 2D surface is a

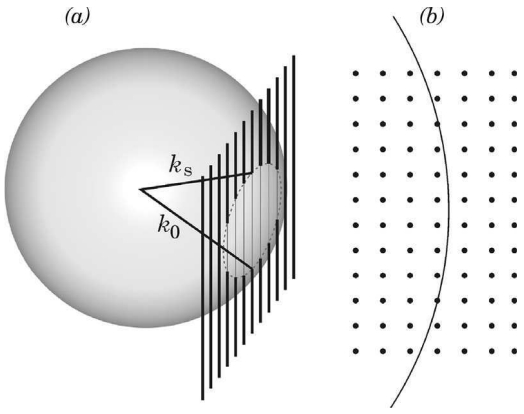

Figure 4.2 Ewald sphere construction in (a) three dimensions and (b) a section of the horizontal $z = 0$ plane.

[6]Only single elastic scattering is assumed.

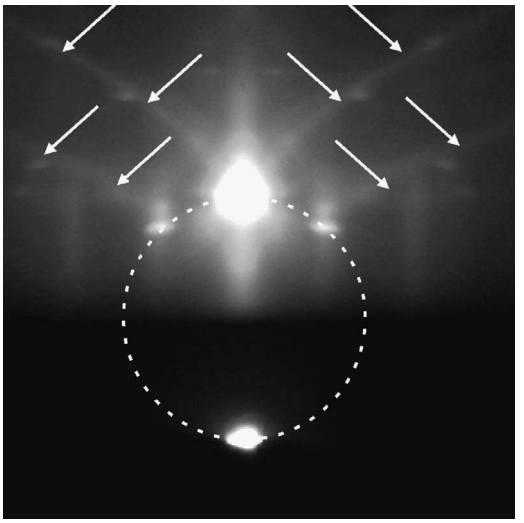

Figure 4.3 Typical RHEED pattern as recorded from a perfect $SrTiO_3$ surface.

lattice of infinitely thin rods, perpendicular to the surface. The tip of the incident wavevector is attached to a reciprocal lattice rod. The Ewald sphere is defined by the sphere around the origin of $\mathbf{k_0}$ with radius $|\mathbf{k_0}|$ (equals $2\pi/\lambda$ for elastic scattering). The condition for diffraction is satisfied for all $\mathbf{k_s}$ connecting the origin of $\mathbf{k_0}$ and a reciprocal lattice rod. For perfect[7] surfaces, this results in diffraction spots lying on concentric circles, called Laue circles. Figure 4.3 shows a diffraction pattern of a perfect $SrTiO_3$ surface [Koster et al., 1998]. It exhibits sharp diffraction spots lying on the zeroth-order Laue circle, that is, intersections of the $(0\,k)$ rods with the Ewald sphere. Due to the substrate size and RHEED geometry, that is, e-beam diameter and grazing angle, part of the e-beam is not blocked by the substrate and is visible in the diffraction pattern. The specular reflected beam is the diffraction spot ''lying'' on the same rod as the incident beam. It is, therefore, never forbidden, unlike other spots.

Due to the high electron energy used in RHEED, the Ewald sphere is very large compared to the reciprocal lattice spacing of oxide crystals. As a result, only a few reciprocal lattice rods are intersected at the small grazing incidence angle. Essentially, a one-dimensional map of the reciprocal space is obtained; see Figure 4.2b. Other areas of the reciprocal space are mapped by rotation of the sample about the incident angle or, alternatively, the azimuthal angle ϕ_i.

4.3.1.1 Kikuchi Lines

As mentioned previously, RHEED is a strong interaction diffraction technique and dynamical scattering has to be taken into account. As a result nonlinear effects such as multiple scattering occur leading to anomalies in the RHEED intensity. One of these anomalies is a phenomenon often observed in RHEED, the Kikuchi lines. They originate from diffraction of diffuse scattered electrons and appear as curved lines on the phosphor screen, indicated by arrows in Figure 4.3. The intensity of a diffraction spot or streak is affected at intersections with Kikuchi lines, since diffusive scattered electrons contribute to the diffracted intensity. Intensity measurements during growth near such intersections should be avoided.

Kikuchi lines move rigidly fixed to the crystal and are, therefore, often used to determine the crystal orientation and for alignment of the e-beam. The occurrence of clear and sharp Kikuchi lines is an indication of a flat and crystalline surface.

[7]Here, perfect refers to a clean and atomically flat, single-domain crystalline surface.

4.3.2 Utility of RHEED: Surface Properties

4.3.2.1 Determination of Lattice Parameter

From the spot positions in a RHEED pattern of a perfect low index plane, one can determine the in-plane lattice constants. Using polar coordinates, the rectilinear projections of the scattering wavevector $\mathbf{k_S}$ can be written as

$$k_{s_x} = |\mathbf{k_0}|(\cos\,\theta_f\,\cos\,\phi_f - \cos\,\theta_i\,\cos\,\phi_i) \tag{4.6a}$$

$$k_{s_y} = |\mathbf{k_0}|(\cos\,\theta_f\,\sin\,\phi_f - \cos\,\theta_i\,\sin\,\phi_i) \tag{4.6b}$$

$$k_{s_z} = |\mathbf{k_0}|(\sin\,\theta_f + \sin\,\theta_i) \approx |\mathbf{k_0}|(\theta_f - \theta_i) \quad \text{(for small angles)} \tag{4.6c}$$

with k_{s_x} and k_{s_y} in the low index plane, k_{s_z} perpendicular to the low index plane, θ_i and ϕ_i the incident and azimuthal angles of the incoming beam, and θ_f and ϕ_f the incident and azimuthal angles of the final (diffracted) beam; see Figure 4.1. For the incident beam directed along a low index direction ($\phi_i = 0$), the lattice parameters d_x (parallel to the incident beam) and d_y (perpendicular to the incident beam) can be derived from the angles of Bragg reflections using Eq. (4.6) by

$$\frac{n}{d_x} = \frac{1}{\lambda}(\cos\,\theta_f - \cos\,\theta_i) \tag{4.7a}$$

where $\phi_f = 0$, that is, for intersections of the Ewald sphere with (h0) rods, and

$$\frac{n}{d_y} = \frac{1}{\lambda}(\cos\,\theta_f\,\sin\,\phi_f) \tag{4.7b}$$

where n is the order of the reflection. The angles can be determined directly by dividing the relative on-screen distances by the sample-to-screen distance R_S, assuming only small angles.

4.3.2.2 Determination of Vicinal Angle

RHEED can be used to measure the average terrace width on vicinal surfaces. A vicinal surface is created by a slight miscut of the substrate surface along an orientation close to a high symmetry one. It is made up of low index terraces, for example, (001) or (101), separated by unit cell steps in the case of perovskite substrates. The terrace width is determined by the miscut angle (in the remainder of the text referred to as the vicinal angle β), defined as the angle between the actual surface plane and the high symmetry plane. Here, the diffracted intensity is the product of the diffraction due to the in-plane lattice constant on the terraces times the diffraction due to the additional periodicity of the step-terrace structure; see Figure 4.4 for the Ewald construction. At the out-of-phase condition, the diffracted intensity is most sensitive for the step-terrace structure on the surface and splitting of the RHEED spot is observed. From the splitting angle $\Delta\theta_f$ the vicinal angle β can be estimated using [Pukite et al., 1989]:

$$\Delta\theta_f = \left(\frac{2\pi}{kd}\right)\frac{\beta\,\cos\,\phi_{p,i}}{\beta\,\cos\,\phi_{p,i} + \langle\theta_f\rangle} \tag{4.8}$$

where $\beta\,\cos\,\phi_{p,i}$ is the projected vicinal angle along the incident beam direction and $\langle\theta_f\rangle \sim \theta_i$ is the average diffraction angle. Figures 4.4c and 4.4d show diffraction patterns[8] of a vicinal[9] $SrTiO_3$

[8]Here, the incident beam is directed perpendicular to the step ledges. In the parallel direction no splitting is observed due to the one-dimensional mapping of the reciprocal space in RHEED.

[9]The step-terrace surface can still be considered as perfect, consisting of atomically flat and crystalline terraces and unit cell height step ledges.

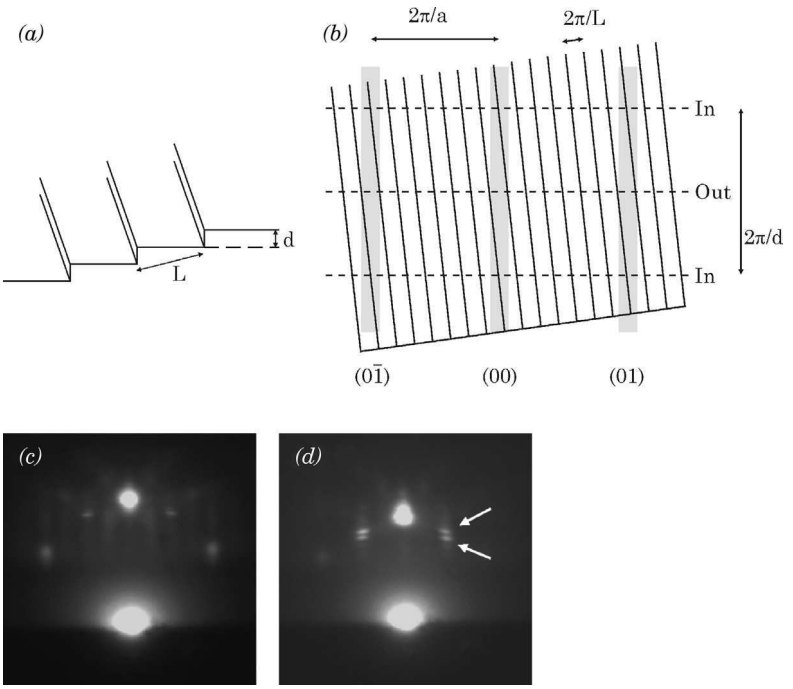

Figure 4.4 (a) Real space and (b) reciprocal space of a vicinal surface with a the in-plane lattice parameter, d the step height, and L the terrace width. RHEED patterns as recorded from a vicinal $SrTiO_3$ surface with incident beam perpendicular to the step ledges: (c) in-phase condition and (d) out-of-phase condition.

surface at both in-phase and out-of-phase conditions, respectively. Here, a value of $\sim 0.25^\circ$ is determined for the vicinal angle β.

4.3.2.3 Nonperfect Surfaces

As shown, intersection of the Ewald sphere with the reciprocal lattice rods of a perfect crystalline surface produces sharp diffraction spots lying on Laue circles. Deviations from such perfect surfaces, like additional roughness and crystal defects, cause broadening of spots or a change in the position of the spots. Figure 4.5 shows RHEED patterns taken from such nonperfect surfaces. In Figure 4.5a, besides spots lying on the zeroth Laue circle, two additional spots are observed marked by the arrows. Here, the RHEED pattern is the sum of diffraction from two different domains of an $SrTiO_3$ substrate surface. Rotation around the azimuthal axis revealed that the two domains have different in-plane orientation; see Figure 4.5b. The RHEED pattern can be described by adding the reciprocal lattices from both domains in the Ewald sphere construction.

A roughened surface, for instance, a surface consisting of a random distribution of terraces and steps, is accompanied by broadening of the lattice rods. As a result, streaks occur due to intersections with the Ewald sphere. As an example a RHEED pattern is shown in Figure 4.5c taken after deposition of a 4-unit-cell thick Y123 layer.

Penetration of the e-beam through protrusions, for instance, small three-dimensional (3D) islands or small asperities, results in transmission spots. The reciprocal lattice rods are replaced by the bulk reciprocal lattice and, consequently, streaks are replaced with spots. A RHEED pattern of such rough surface is given in Figure 4.5d, after nonoptimized deposition of several unit cell layers of Y123 on $SrTiO_3$.

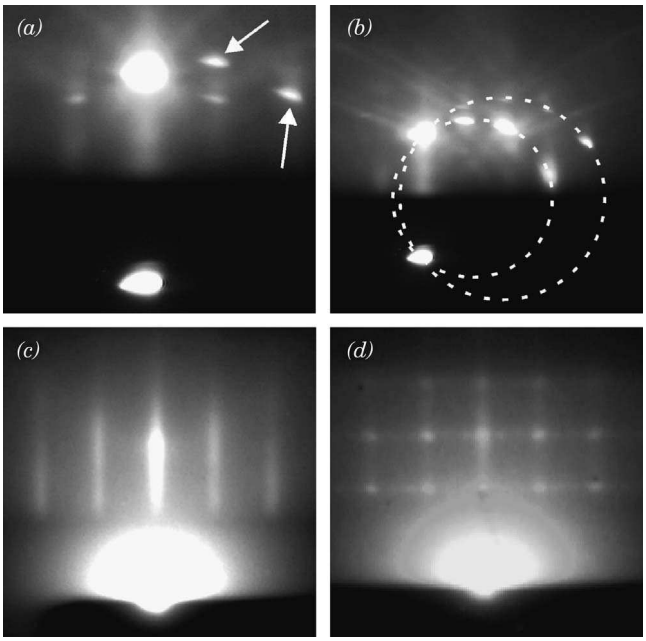

Figure 4.5 RHEED patterns recorded from nonperfect crystalline surfaces: $SrTiO_3$ surface with two domain structure, (a) azimuthal angle $\phi_i = 0$ and (b) off-azimuthal angle, (c) 4 unit cell thick Y123 layer, and (d) several unit cell layers of Y123 deposited using nonoptimized conditions.

4.3.3 Utility of RHEED: Monitoring Thin-Film Growth

In the early days of RHEED, the surface sensitivity was exploited mainly for the study of cleaved crystals and surface reconstruction. Nowadays, the main applications are thin-film growth monitoring and the study of growth kinetics. The existence of intensity oscillations [Neave et al., 1983] corresponding to the 2D growth of atomic or molecular layers is probably the most important reason to use RHEED. Here, the surface is periodically roughened and smoothened during the 2D nucleation and growth, resulting in a periodically varying density of surface steps. Electrons are easily scattered out of the specular beam by the step edges since the layer thickness is much larger than the wavelength of the electrons. As a result, periodic intensity variations are expected during 2D growth, which can be used to determine the growth rate.

4.3.3.1 Electron Scattering

The pressure in a RHEED setup has to be sufficiently low to avoid electron scattering by the ambient gas. Attenuation of the e-beam intensity is to be expected at high ambient pressure due to elastic and inelastic electron scattering [García et al., 2001]. Furthermore, a low pressure is required near the filament of the e-gun. With the introduction of the differentially pumped e-gun[10], the maximum operating pressure was raised to $\sim$1 Pa [Karl and Stritzker, 1992]. To increase the operating pressure in RHEED to the high deposition pressures used in PLD of oxides, both of these requirements have to be fulfilled: A low pressure in the e-gun should be maintained and the attenuation of the e-beam intensity has to be minimized. The latter can be expressed as

[10]Usually a heated tungsten filament is used as the electron source. To avoid breakage or a short lifetime, the pressure needs to be well below 10^{-4} Pa. Here, the pressure in the e-gun is still well below 10^{-4} Pa.

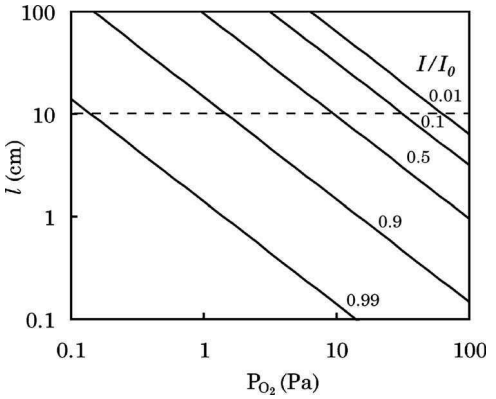

Figure 4.6 Attenuation I/I_0 of a 10-keV electron beam as a function of the oxygen pressure P_{O_2} and penetration length 1. The dashed line represents the traveling distance in the high-pressure RHEED setup.

[García et al., 1997]

$$\frac{I}{I_0} = \exp\left(-\frac{l}{L_E}\right) \tag{4.9a}$$

where L_E is the mean free path of the electrons, l is the distance of the traveling path of the electrons, and I_0 is the intensity of the beam for $l \ll L_E$, that is, at sufficiently low pressure. The mean free path L_E is defined as

$$L_E = \frac{1}{\sigma_T n} \tag{4.9b}$$

where σ_T is the total cross section (both elastic and inelastic) for scattering and n is the molecular density given by

$$n = \frac{P}{k_B T} \tag{4.9c}$$

with P is the pressure, k_B is the Boltzmann constant, and T is the temperature.

At the high electron energies used in RHEED the total cross-section σ_T decreases with increasing electron energy. Unfortunately, no experimental data for electron scattering by O_2 at the high electron energies (>10 keV) used in RHEED have been reported. By extrapolating experimental data, however [García et al., 2001], a value for $\sigma_T \sim 3 \times 10^{-21}$ m^2 at 10 keV is determined. Using this value, the attenuation I/I_0 can be estimated. Figure 4.6 shows the distance l for a 10-keV e-beam, calculated using Eq. (4.9) as a function of the oxygen pressure for several values of I/I_0. From this figure it becomes clear that the traveling distance has to be reduced to minimize electron scattering losses at the high oxygen pressures used in PLD.

4.4 HIGH-PRESSURE RHEED SETUP

To satisfy the two requirements, that is, low pressure in the e-gun and short traveling distance at high pressure, a two-stage, differentially pumped RHEED system has been developed. A schematic view of this high-pressure RHEED system is depicted in Figure 4.7. The e-gun (EK-2035-R, STAIB

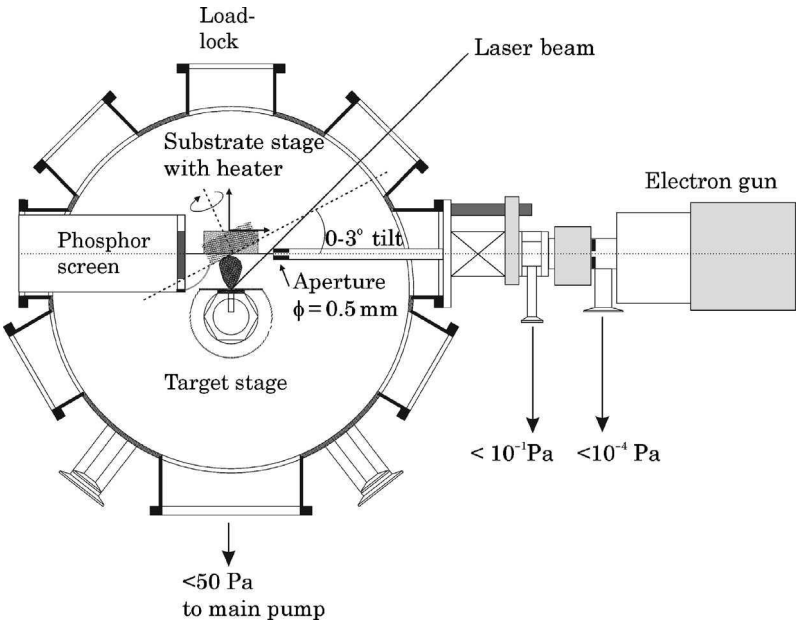

Figure 4.7 Schematic view of the deposition chamber, including the electron source assembly. The system is fully computer controlled including selection of the targets allowing for automated multilayer deposition.

Instrumente) has a minimum beam size of $\sim$250 μm [full width at half maximum (FWHM)], even at the working distance of 500 mm. It is mounted on a flange connected to a stainless steel extension tube with an inner diameter of 8 mm. A differential pumping unit is used to maintain a vacuum of better than 10^{-4} Pa in the e-gun. An aperture (diameter 0.5 mm) separates the tube from the deposition chamber. The pressure in the tube, which depends on the pump speed and the size of the aperture, is kept below 10^{-1} Pa. Using this two-stage pumping system, the pressure in the deposition chamber can be increased up to 100 Pa maintaining the low pressure in the electron source. The e-beam, which passes through the apertures inside the differential pumping unit and the tube, enters the deposition chamber near the substrate at a distance of 50 mm. The *XY* deflection capability of the electron source is used to direct the e-beam through the aperture at the end of the tube.

The fluorescent phosphor screen (diameter 50 mm) is mounted on a flange located near the substrate. The distance between the screen and substrate is 50 mm, and the screen is shielded from the laser plasma to minimize deposition. The electron source, including the extension tube, is mounted on a *XYZ* stage allowing adjustment of the distance between substrate and end of the tube.

Using the extension tube, the traveling distance in the high-pressure regime is reduced to 100 mm. Intensity losses due to electron scattering inside the extension tube are negligible since the pressure is kept well below 10^{-1} Pa. In the high-pressure regime, however, a significant decrease in the intensity ($I/I_0 \sim 0.01$) is expected at oxygen pressure $P_{O_2} \sim 100$ Pa. However, compensation of the scattering losses is possible by adjusting the filament current, and hence total e-beam current.

At large working distance, the e-beam is deflected over several millimeters by small magnetic fields, comparable to the earth's magnetic field. Therefore, special care has been taken to shield the e-beam from magnetic fields using μ-metal. Furthermore, the substrate can be rotated in order to adjust the angle of incidence and azimuthal angle of the e-beam on the substrate. The diffraction pattern is monitored using a Peltier-cooled charge-coupled device (CCD) camera and acquisition software (K-Space Associates). The software allows for time-resolved spot intensity measurement. The minimum acquisition time for each data point is 33 ms.

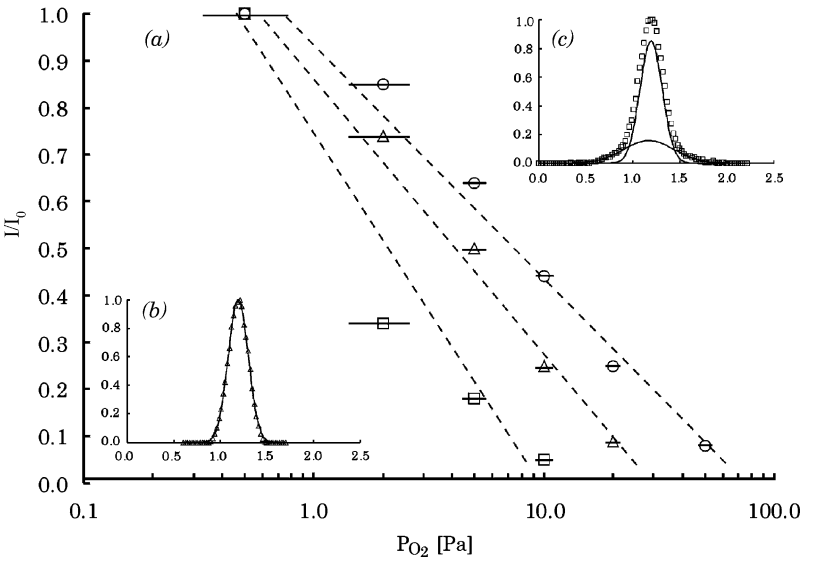

Figure 4.8 (a) Attenuation I/I_0 versus oxygen pressure of the e-beam peak intensity at electron energy of 10 (□), 20 (Δ), and 30 (O) keV, respectively. The insets show the e-beam shapes (20 keV) at (b) 10^{-1} Pa and an attenuated e-beam at (c) 50 Pa; Δ and □ are measurement points, the solid lines Gaussian fits.

At an oxygen pressure of 50 Pa, the specularly reflected spot is still clearly visible. Consequently, growth monitoring is feasible by measurement of the intensity variations of the specularly reflected beam.

The attenuation[11] of the e-beam intensity was measured in high P_{O_2} for different values of the electron energies; see Figure 4.8. From the slopes, a value of 1.6×10^{-21}, 1.3×10^{-21}, and 1.1×10^{-21} m^2 was determined for the total cross section for scattering using Eq. (4.9) for electron energies of 10, 20, and 30 keV, respectively. As expected, a smaller σ_t is observed at higher electron energy of 30 keV. Increase of the electron energy is, therefore, beneficial for the application of RHEED at high deposition pressure. The insets in Figure 4.8 show the typical e-beam shapes for a nonattenuated e-beam at $P_{O_2} = 10^{-1}$ Pa (b) and an attenuated e-beam at $P_{O_2} = 50$ Pa (c). At low pressure the shape could be fitted by a single Gaussian curve with FWHM ~ 215 mm. At higher pressure, not only broadening of the e-beam is observed, FWHM ~ 240 mm, but also the occurrence of a diffuse background. Electrons are scattered in the forward direction [García et al., 2001] leading to a divergent e-beam[12]. The increase of the diffuse intensity of the primary e-beam at the high pressure in Figure 4.9 is a clear signature of this effect.

In the experiments described in this chapter and Chapter 8, a KrF excimer laser (Lambda Physic Compex 105, wavelength $\lambda = 248$ nm) with maximum pulse repetition rate of 50 Hz was used. The maximum pulse energy was 650 mJ with pulse duration ~ 25 ns. A mask was used to select the most homogeneous part of the laser beam, resulting in a spatial energy variation of $\sim 5\%$. The mask is projected at an inclination of 45° on the target by means of a focusing lens (focal length ~ 450 mm). The energy density on the target is controlled by adjustment of both mask size and demagnification.

[11]Here, we measured the peak intensity from the spot of the primary e-beam on the phosphor screen using the *K*-space acquisition equipment. Although nonlinearities are expected, relative measurements only are adequate for this purpose. Here, I_0 is the peak intensity of the e-beam at $P_{O_2} < 10^{-2}$ Pa. No attenuation is observed at this pressure.

[12]The coherence length in RHEED is determined by the spread in both electron energy and beam convergence/divergence. As a result, a smaller coherence length is expected at higher ambient pressure.

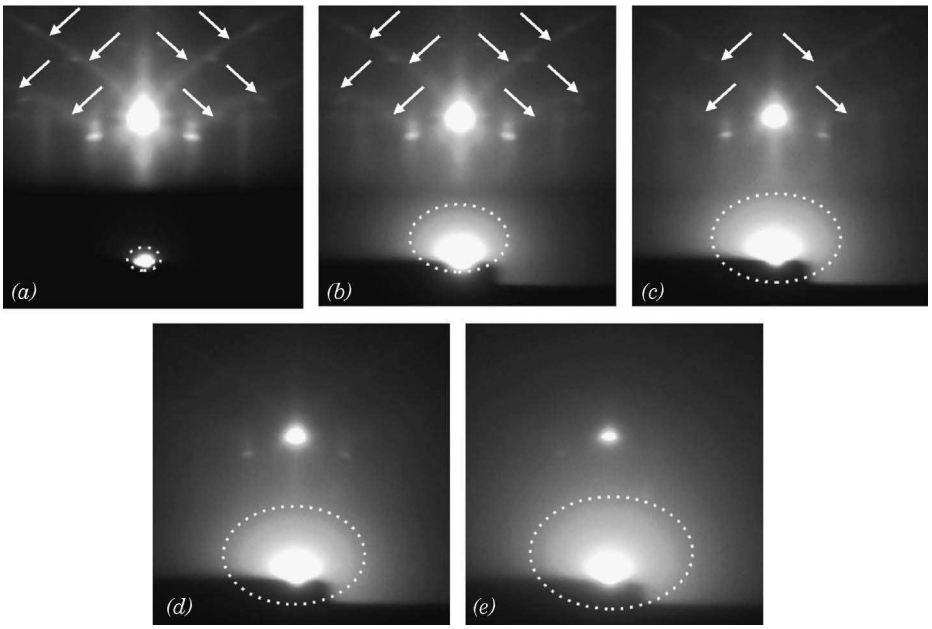

Figure 4.9 RHEED patterns from a perfect $SrTiO_3$ surface recorded at different oxygen pressure: (a) 10^{-5} Pa, (b) 10^{-1} Pa, (c) 7 Pa, (d) 15 Pa, and (e) 50 (Pa). The arrows indicate the Kikuchi lines; the additional intensity due to the diffuse forward scattered incident electrons is indicated by the dotted lines.

The multitarget holder and substrate holder including heater are mounted on a computer-controlled *XYZ* rotation stage and can be inserted via a load-lock system without breaking the vacuum (base pressure $\sim 10^{-5}$ Pa). The controlled temperature of the heater (resistively heated using thermo-coax wires) is measured using a K-type thermocouple.

Oxygen gas (purity >4.5) as well as inert gasses (He, Ne, Ar, purity >4.0) can be used as deposition gas. The deposition pressure (10^{-1}–10^{2} Pa) is controlled by the effective pump speed and the total gas mass flow (Brooks Instruments, 0–40 mL/min at 10^5 Pa). The effective pump speed is adjusted through a variable restriction between the deposition chamber and turbo-molecular drag pump.

4.5 CONCLUSIONS

Pulsed laser deposition differs from other PVD techniques because of two unique features, that is, the wide range in the kinetic energy of the ablated particles arriving at the substrate and the high deposition rate during the pulse. Both features can be exploited to manipulate the growth characteristics. A change in the kinetic energy of the impinging particles results in a change of the effective diffusion coefficient, whereas the high supersaturation during the deposition pulse is used to impose layer-by-layer like growth. The short deposition pulses, typically for PLD, cause a separation of the deposition and growth in time: Almost no nucleation and growth takes place during the deposition pulse. Determination of the kinetic growth parameters from RHEED intensity variations in between the deposition pulses is, therefore, less complicated.

Considered an ultra-high-vacuum analysis tool in many textbooks, RHEED has been utilized in low-pressure thin-film growth techniques such as MBE. The development of high-pressure RHEED enabled growth monitoring and growth characterization at the high pressures used in PLD. Growth

control in PLD on an atomic level is, therefore, feasible; making PLD an advanced research technique.

First growth studies with high-pressure RHEED showed the influence of the substrate morphology on the (initial) growth of complex oxides by PLD. Since the evolution of the film surface morphology is one of the key processes in thin-film growth, atomically flat and crystalline substrate surfaces are essential for the controlled growth of atomically flat thin films.

REFERENCES

Blank, D. H. A., G. J. H. M. Rijnders, G. Koster, and H. Rogalla (1999), *Appl. Surf. Sci.* **139**, 17–23.

Cheung, J., and J. Horwitz (1992), *MRS Bull*. **17**, 30–36.

Chern, M. Y., A. Gupta, and B. W. Hussey (1992), *Appl. Phys. Lett.* **60**, 3045–3047.

Dam, B., and B. Stäuble-Pümpin (1998), *J. Mater Sci.: Mater El.* **9**, 217–226.

Fuenzalida, V. M. (1998), *J. Crystal Growth* **183**, 497–503.

Fuenzalida, V. M. (2000), *J. Crystal Growth* **213**, 157–160.

García, G., M. Roteta, and F. Manero (1997), *Chem. Phys. Lett*. **264**, 589–595.

García, G., F. Blanco, and A. Williart (2001), *Chem. Phys. Lett*. **335**, 227–233.

Geohegan, D. B (1992a), *Thin Solid Films* **220**, 138–145.

Geohegan, D. B. (1992b), in *Laser Ablation of Electronic Materials: Basic Mechanisms and Applications*, E. Fogarassy and S. Lazare (Eds.), North Holland, Amsterdam, p. 73.

Geohegan, D. B., and A. A. Puretzky (1995), *Appl. Phys. Lett.* **67**, 197–199.

Karl, H., and B. Stritzker (1992), *Phys. Rev. Lett.* **69**, 2939–2942.

Kawamura, T. (1989), in *Reflection High Energy Electron Diffraction and Reflection Electron Imaging of Surfaces*, P. K. Larsen and P. J. Dobson (Eds.), Plenum, London, pp. 501–522.

Koster, G., B. L. Kropman, G. J. H. M. Rijnders, D. H. A. Blank, and H. Rogalla (1998), *Appl. Phys. Lett.* **73**, 2920–2922.

Lagally, M. G., D. E. Savage, and M. C. Tringides (1989), in *Reflection High Energy Electron Diffraction and Reflection Electron Imaging of Surfaces*, P. K. Larsen and P. J. Dobson (Eds.), Plenum, London, pp. 139–174.

Markov, V. A. (1995), *Crystal Growth for Beginners*, World Scientific, London, pp. 81–86.

Neave, J. H., B. A. Joyce, P. J. Dobson, and N. Norton (1983), *Appl. Phys. A* **31**, 1–6.

Okada, T., Y. Nakata, M. Maeda, and W. K. A. Kumuduni (1997), *J. Appl. Phys*. **82**, 3543–3547.

Pukite, P. R., P. I. Cohen, and S Batra (1989), in *Reflection High Energy Electron Diffraction and Reflection Electron Imaging of Surfaces*, P. K. Larsen and P. J. Dobson (Eds.), Plenum, London, pp. 427–447.

Rijnders, A. J. H. M., G. Koster, D. H. A. Blank, and H. Rogalla (1997), *Appl. Phys. Lett*. **70**, 1888–1890.

Strikovski, M., and J. H. Miller (1998), *Appl. Phys. Lett*. **73**, 1733–1735.

Tyunina, M., J. Levoska, and S. Leppävuori (1998), *J. Appl. Phys*. **83**, 5489–5496.

CHAPTER 5

Ultrafast Laser Ablation and Film Deposition

EUGENE G. GAMALY, ANDREI V. RODE, and BARRY LUTHER-DAVIES

Research School of Physical Science and Engineering, Australian National University, Canberra, Australia

5.1 INTRODUCTION

This chapter provides an overview of the fundamental theoretical and experimental aspects of ablation of solids using short $<10^{-11}$-s pulses from high-repetition-rate (1–100 MHz) lasers. The goal of this study is the production of a fully atomized continuous flow of ablated material. We demonstrate that use of atomized flow in the deposition process results in films with superb quality. The optimal laser conditions have been established for both the single-pulse ablation mode, and for high-repetition-rate ablation. We observe that the short dwell time in the high-repetition-rate laser–target interaction leads to coupling between successive laser pulses and thereby incubation of the heating and evaporation processes. This results in a reduction of the laser ablation threshold. Practical recipes are provided that lead to efficient ablation and control the phase state of the vapor as a self-consistent function of laser parameters, namely, the pulse duration, the energy per pulse, and the wavelength, all adjusted to the target parameters. We demonstrate implementation of these recipes for deposition of high-quality micron-thick optical films for optical waveguide applications.

Pulsed laser deposition (PLD) when applied in its conventional form using low-repetition-rate lasers emitting nanosecond-range pulses [Chrisey and Hubler, 1994; Miller and Haglund, 1998] generally leads to poor quality films contaminated by particles. It has been shown that this is a direct consequence of the use of the particular pulse parameters [Gamaly et al., 1999; Rode et al., 1999] that lead to a large volume of material being evaporated by each pulse. For example, the plume produced in this regime expands as a supersaturated vapor and therefore condensation occurs during the early stage of the expansion resulting in the formation of droplets from the vapor phase, which are then deposited onto the substrate.

A solution to such droplet formation has been found with a deeper insight into the physics of the laser ablation process. It has been shown that the formation of droplets can be eliminated by changing the mode of operation of the laser. Similar average laser powers are employed, but the energy is delivered in shorter pulses (10 ps and shorter, rather than 10 ns), at energies around 6 orders of magnitude lower (microjoules rather than joules) but at much higher repetition rates ($\approx$10 MHz rather than $\approx$10 Hz). We have called this mode of operation *ultrafast pulsed laser deposition* (UFPLD). Each single short low-energy high-intensity pulse evaporates relatively few ($\sim 10^{11}$–10^{12}) atoms per pulse [Rode et al., 1999; Perry et al., 1999], thereby inhibiting the condensation of droplets

Pulsed Laser Deposition of Thin Films: Applications-Led Growth of Functional Materials
Edited by Robert Eason

during the fast nonequilibrium expansion. To compensate for the reduced ablated mass per pulse, high pulse repetition rates are then used to achieve a high average deposition rate. The high repetition rate maintains the average atomic flow in a plume at a high level of 10^{19}–10^{20} atoms/s. Furthermore controlling the laser intensity distribution within the focal spot offers a way to create a fully atomized plume.

The ultrafast laser ablation method has already been applied to produce atomically smooth, diamond-like carbon films [Perry et al., 1999; Rode et al., 1999] with total elimination of macroscopic particles from the film surface. Recently As_2S_3 chalcogenide optical films [Rode et al., 2002] have been produced with similar surface quality and high homogeneity. A simple method to produce a flat ''top-hat'' intensity distribution over the focal spot has been proposed and implemented for the deposition of high surface quality silicon films using femtosecond pulses from a Ti : sapphire laser [Gamaly et al., 2004]. However, many parameters must be controlled that affect the quality of the films produced by UFPLD, including the laser intensity distribution on the target surface, the scanning speed of the laser focal spot over the target, the energy level of the prepulse (in Ti : sapphire lasers) and postpulse (in excimer lasers), the pressure of the reactive gas in the experimental chamber, and so forth.

In spite of the lack of complete understanding of a number of features of femtosecond laser ablation such as the angular variation of the stoichiometry [Millon et al., 2003] and isotopic content in the plume [Pronko et al., 1999], or the influence of energetic ions on the defect formation and crystallinity in the deposited films, femtosecond lasers have been successfully applied for deposition of high-quality thin films of a number of materials. This includes deposition of amorphous diamond-like carbon films [Banks, 1999], nitride [Zhang et al., 2000; Ristoscu et al., 2003], and oxide optical films [Pronko and Pan, 2001; Okoshi et al., 2000; Millon et al., 2002]. Direct laser printing of microstructures with femtosecond lasers, so-called laser-induced forward transfer (LIFT) was successfully demonstrated in the direct development of computer-generated holograms and other diffractive optical microstructures [Mailis et al., 1999; Zergioti et al., 1999, 2003]. It was shown that ultrashort laser pulses produce a better etching and printing quality, thus improving the established method of excimer laser microetching.

In this chapter we consider nonthermal mechanisms of ablation with subpicosecond pulses and define the optimal conditions for creating a fully atomized vapor flow for deposition of high-quality optical films specifically with UFPLD. There are a variety of processes involved in laser-induced changes of the target morphology, such as target amorphization, breakdown of target integrity—damage (appearance of cracks, peeling of flakes from the surface), melting, ablation, and plasma formation. All these processes have different thresholds and lead to a succession of target transformations with increasing laser intensity. The optimum combination of laser parameters (pulse duration, energy per pulse, wavelength, intensity distribution) tuned to the target parameters such as binding energy, density, and thermal diffusivity can be found to produce an atomized flow of ablated vapors from any material. The temperature, density, the atomic content, and the degree of ionization in the vapor phase, all depend on the incident laser parameters and therefore can also be controlled. The control over the state of the expanding laser-produced plume can be achieved through the proper choice of pulse duration, wavelength, and energy along with a proper spatial and temporal distribution of the laser intensity during the pulse and across the focal spot while keeping the absorbed laser energy above some specific threshold.

A general assumption of most theoretical models of PLD is that the successive pulses ablate the target independently. Conventionally, the laser beam is continuously scanned over the target surface in order to prevent crater formation and maintain the same interaction mode for successive pulses. However, the beam scanning velocity (1–10 m/s) using conventional oscillating mirror scanners is not high enough to physically separate the pulses from a megahertz repetition rate pulse train, and up to several thousand pulses can hit the surface at the same place. It has been found that in ablation of solids by megahertz repetition rate lasers, therefore, coupling between pulses leads to a change in the interaction mode and a reduction of the ablation threshold in comparison to the single-pulse mode.

This chapter is organized as follows. In Section 5.2 we describe the laser–matter interaction and ablation physics, and present experimental data on deposition of different materials using ultrafast ablation and using a beam shaping technique. Section 5.3 relates to the ablation of various solids by high-repetition-rate lasers, while Section 5.4 presents results on deposition of films. In Section 5.5 we discuss the existing high-repetition-rate lasers currently available for ultrafast laser deposition. Finally, we summarize the recent status of the ablation and thin-film deposition studies and present our vision for future prospects for the method.

5.2 ABLATION BY SHORT INDEPENDENT LASER PULSES AND DEPOSITION OF FILMS

Applications of material ablation by powerful lasers often require precise control over the properties of the ablated plume. In this section we discuss briefly the basics of the laser–matter interaction and laser ablation physics, and show that such precise control can be achieved by linking the laser parameters to the specific properties of the material to be ablated.

5.2.1 Short-Pulse Laser–Matter Interaction

To remove (to ablate) an atom from a solid surface by a laser pulse, the energy delivered to a single atom should exceed the binding energy of that atom. The energy absorbed in the target material per unit surface area depends on the laser fluence F_0, which is the time integral of the laser intensity $I_0(t)$ over the pulse duration t_p. Therefore, the ablation rate is a function of fluence. A typical ablation threshold is of the order of 0.1–1 J/cm^2, depending on the target material and the laser wavelength. For example, laser ablation with 100-fs pulse requires an intensity in a range above 10^{13} W/cm^2 [Du et al., 1994; Stuart et al., 1995; Perry et al., 1999; Bonse et al., 2002; Momma et al., 1997], while 10-ns pulses ablate the same material at much lower intensities: $\sim 10^8$–10^9 W/cm^2 [Gamaly et al., 1999].

One can distinguish between various kinds of ablation on the basis of the following arguments. First, we recall that the fundamental interaction of light with matter involves the following physical processes. The incident laser radiation first penetrates the target and induces oscillations of the optical electrons. These electrons gain energy from the oscillating field through the disruption of the oscillating phase due to random collisions with atoms. The electron oscillation energy thereby converts to electron excitations. Following this, the electrons transfer energy to the lattice (ions) by means of electron–phonon (electron–ion) collisions over a period characterized by the temperature equilibration time, t_{e-L}, and by means of electron heat conduction with a characteristic time, t_{th}.

The short-pulse interaction takes place when the laser pulse duration, t_p, is shorter than both these relaxation times, $t_p < \{t_{e-L}, t_{\text{th}}\}$ and generally requires the pulse duration to be less than a picosecond. It has been shown [Du et al., 1994; Stuart et al., 1995; Perry et al., 1999] that for most materials ablated using such ultra-short-duration pulses, the average intensity used for ablation is above 10^{13} W/cm^2, and this exceeds the ionization threshold. Therefore, the target material is ionized early in the laser pulse creating a high-density plasma. Free electrons absorb the laser energy in the resulting plasma via either inverse Bremsstrahlung or resonance absorption. The ions remain cold during the short pulse because $t_p < \{t_{e-L}, t_{\text{th}}\}$, and at very high intensities even long after the pulse, there is not enough time to transfer energy from electrons to ions. However, the electrons and ions can interact through an electrostatic field that can appear due to charge separation. This field becomes significant if the energy absorbed by the electrons exceeds a characteristic energy of ~ 10 eV (the Fermi energy in metals). Energetic electrons can then escape from the target and pull ions from the solid via the electrostatic field resulting from charge separation. This nonequilibrium process is known as electrostatic ablation [Gamaly et al., 2002].

Conversely, the long-pulse interaction appears when the pulse duration is longer than both relaxation times, $t_p > \{t_{e-L}, t_{\text{th}}\}$. The electrons and the lattice are then in thermal equilibrium during

the pulse, and therefore the laser–matter interaction and ablation proceeds under equilibrium conditions. Ablation in this regime is close to conventional equilibrium evaporation and is referred to as thermal ablation. Here we primarily concentrate on the short-pulse interaction regime associated with picosecond and subpicosecond laser pulses, although reference is also made to the thermal regime particularly as it relates to accumulative effects appearing when high repetition pulse trains are employed. We also differentiate laser ablation from the equilibrium process of laser evaporation, where the atoms removed from the surface are only those at the high-energy tail of the Maxwellian distribution.

5.2.1.1 Skin Effect

The pulse duration in the short-pulse laser–matter interaction regime is shorter than all characteristic relaxation times, and therefore it is shorter than the expansion time. Thus, a femtosecond laser pulse interacts with a solid target whose density remains almost constant during the laser pulse. The major process during the laser–target interaction is heating of electrons by the electromagnetic field of the laser. However, the electron number density n_e, the electron–ion collision frequency v_{ei}, the absorption coefficient A, and the skin-depth l_s are all generally functions of both laser intensity and time. It has been shown [Gamaly et al., 2002] that the above quantities, while changing rapidly during the very early part of the pulse, become approximately constant for most of the remaining period up to the end of the pulse. Thus, the skin effect approximation can be used to describe the interaction of a subpicosecond pulse with matter.

As a result, the relation $E(x) = E(0)\exp[-x/l_s]$ can be used to describe the variation of the laser electric field $E(x)$ as a function of the penetration depth x into a solid target. The characteristic field penetration length, or skin depth l_s, is conventionally expressed through the imaginary part of the refractive index k and the laser frequency ω as $l_s = c/\omega k$ [Landau et al., 1984; Raizer, 1977]. The dielectric function ε in the Drude form describes well conditions in both the solid state and ionized state that is generated during the laser pulse before ablation:

$$\varepsilon = 1 - \frac{\omega_{pe}^2}{\omega\,(\omega + i\nu_{ei})} = \varepsilon' + i\varepsilon'' \qquad \varepsilon^{1/2} = n + ik \tag{5.1}$$

where $\omega_{pe} = (4\pi e^2 n_e/m_e)^{1/2}$ is the electron plasma frequency, m_e is the electron mass, and v_{ei} is an effective collision frequency of electrons with the lattice (ions).

5.2.1.2 Transient Ionization in the Laser Field

For low laser intensities most dielectrics are transparent for incident wavelengths down to the ultraviolet range. Low absorption implies that large real and small imaginary parts characterize the complex dielectric function at low laser intensity. An increase in the laser intensity, and as a result an increase in the energy available for electron excitation, leads to ionization of the target in a skin layer by single-photon ionization, multiphoton ionization, and ionization by electron impact (avalanche ionization). The imaginary part, and hence the absorption, thus increases due to ionization. The degree of ionization increases with increasing laser intensity and with decreasing laser wavelength.

It has been shown [Perry et al., 1999; Gamaly et al., 2002; Pronko et al., 1998] that the relative role of impact ionization and multiphoton ionization depends dramatically on the relation between the electron quiver energy in the laser field and the ionization potential. Electron impact ionization is the main ionization mechanism in the long (nanosecond) pulse regime. Multiphoton ionization dominates the laser interaction at intensities above 10^{13}–$10^{14}\,\mathrm{W/cm^2}$, which are characteristic of the short-pulse regime, depending on the laser wavelength and the ionization potential of the material. For a 100-fs pulse at 800 nm this corresponds to a laser fluence of $\sim 10\,\mathrm{J/cm^2}$. The ionization time can be shorter than the pulse duration, in which case the ionization threshold depends on the laser intensity and decreases with an increase in the photon energy.

It is usual to suggest that the ionization (or optical breakdown) threshold is achieved when the electron number density reaches the critical density corresponding to the incident laser wavelength [Raizer, 1977; Kruer, 1987]. The ionization threshold for the majority of materials lies at intensities between 10^{13} and $10^{14}\,\mathrm{W/cm^2}$ (at a laser wavelength $\lambda \sim 1\,\mu\mathrm{m}$) with a strong nonlinear dependence on intensity. For example, for a silica target at an intensity of $2 \times 10^{13}\mathrm{W/cm^2}$, avalanche ionization dominates, and the first ionization energy is not reached by the end of a 100-fs pulse at 1064 nm. At $10^{14}\,\mathrm{W/cm^2}$ multiphoton ionization dominates and the full first ionization is completed in the first 20 fs of the laser pulse. When the ionization is completed, plasma is formed in the skin layer. This plasma has a free-electron density comparable to the ion (solid) density of about $10^{23}\,\mathrm{cm^{-3}}$. Hence, for the derivation of scaling relations the electron number density (and thus the electron plasma frequency) is considered to be constant and equal to the atomic number density.

5.2.1.3 Electron-to-Ion Energy Transfer Time

To achieve conditions for ablation, the average electron energy should increase from the initial value at room temperature up to the Fermi energy E_F, that is, up to several electron volts. The energy of an atom (ion) to be ablated should exceed the binding atomic energy, E_b, which equals the energy of evaporation per atom. The electron–electron equilibration time is of the order of magnitude of the reciprocal electron plasma frequency, that is, $\sim \omega_{\mathrm{pe}}^{-1} \sim 10^{-2}$ fs and hence is much shorter than any pulse duration. Therefore the electron energy distribution during the heating process is close to equilibrium and follows the evolution of the laser intensity in time, adiabatically adjusting to any intensity changes.

The electron–ion collision frequency increases with temperature from the low-temperature limit in the initial state where the lattice temperature dominates the electron–phonon interaction [Il'insky and Keldysh, 1994]. In the opposite high-temperature limit the effective frequency of electron–ion Coulomb collisions decreases with the electron temperature, and the electron temperature T_e dominates the electron–ion interaction [Kruer, 1987]. Thus, the effective collision frequency has a maximum at a temperature approaching the Fermi energy. Following the references [Perry et al., 1999; Eidmann et al., 2000; Gamaly et al., 2002], it seems reasonable to assume that $\nu_{\mathrm{ei}} \approx \omega_{\mathrm{pe}}$ in the energy range around the Fermi energy for further estimates of the ablation threshold. One can use the following interpolation for the frequency of the momentum transfer in electron–ion collisions for a nonideal plasma in the temperature range $T_e \geq E_b$:

$$\nu_{\mathrm{ei}} \approx \nu \left(\frac{T_e}{E_b}\right)^{-3/2} \qquad \nu \approx \omega_{\mathrm{pe}} \tag{5.2}$$

It is convenient to scale temperature with the binding energy E_b. Thus, under the ablation conditions for which $T_e \geq E_b$ the inequality holds $\nu_{\mathrm{ei}} \sim \omega_{\mathrm{pe}} \gg \omega$. Therefore the electron mean free path is much smaller than the skin depth. That is, the conditions for the normal skin effect to be valid are justified, and one can use the exponential spatial dependence for the field. The electron–ion energy transfer time in dense plasmas can be expressed through the collision frequency as

$$\tau_{\mathrm{ei}} \approx \frac{M}{m_e}\omega_{\mathrm{pe}}^{-1} \tag{5.3}$$

Taking Cu as an example ($M_{\mathrm{cu}} = 63.54$ au, $n_e = 0.845 \times 10^{23}\,\mathrm{cm^{-3}}$, $\omega_{\mathrm{pe}} = 1.64 \times 10^{16}\,\mathrm{s^{-1}}$), we estimate the ion heating time as $\tau_{\mathrm{ei}} = 7 \times 10^{-12}$ s, which is in agreement with the values suggested in the literature [Malvezzi et al., 1986; Luther-Davies et al., 1992; Perry et al., 1999; Eidmann et al., 2000]. A similar estimate for silica yields 6.4×10^{-12} s. These estimates demonstrate that the ions remain cold during a subpicosecond laser pulse for both metals and dielectrics. For this reason one can apply a steplike plasma density profile for the laser absorption calculations as we will consider explicitly in the next section.

Now, let us estimate the electron heat conduction time. The electron thermal diffusion coefficient, D, is expressed through the effective collision frequency as follows [Lifshitz and Pitaevskii, 1981]:

$$D = l_e \frac{v_e}{3} \approx \frac{v_e^2}{3\omega_{\text{pe}}} \tag{5.4}$$

here l_e and v_e are the electron mean free path and velocity, respectively. The electron heat conduction time t_{heat}, which is the time for the electron temperature smoothing across the skin depth l_s, now becomes

$$t_{\text{heat}} \approx l_s^2/D \tag{5.5}$$

For copper ($l_s = 67.4\,\text{nm}$ at $780\,\text{nm}$, $D \sim 1\,\text{cm}^2/\text{s}$) the electron heat conduction time becomes $t_{\text{heat}} \sim 45\,\text{ps}$. Thus, all the absorbed energy is confined in the electron component during the laser–matter interaction time with subpicosecond and picosecond pulses, and the energy losses are negligible.

5.2.1.4 Absorption Mechanisms

At intensities above $10^{14}\,\text{W/cm}^2$ the ionization time for a dielectric is just a few femtoseconds, typically much shorter than the pulse duration of $\sim 100\,\text{fs}$. The electrons produced by ionization in dielectrics then dominate the absorption in the same way as the free carriers in metals, and the characteristics of the laser–matter interaction become independent of the initial state of the target. As a result, inverse Bremsstrahlung and resonance absorption (for p-polarized light at oblique incidence) become the major absorption mechanisms for both metals and dielectrics.

We have shown in the previous section that near the ablation threshold the following conditions hold: $\nu_{\text{ei}} \sim \omega_{\text{pe}} > \omega$. The link between dielectric function and refractive index can be simplified in accordance with relations [Landau et al., 1984]:

$$\begin{gathered}
\varepsilon' \approx \frac{\omega^2}{\omega_{\text{pe}}^2} \qquad \varepsilon'' \approx \frac{\omega_{\text{pe}}}{\omega}\left(1 + \frac{\omega^2}{\omega_{\text{pe}}^2}\right)^{-1} \\
n = \left(\frac{\sqrt{\varepsilon'^2 + \varepsilon''^2}}{2} + \frac{\varepsilon'}{2}\right)^{1/2} \qquad k = \left(\frac{\sqrt{\varepsilon'^2 + \varepsilon''^2}}{2} - \frac{\varepsilon'}{2}\right)^{1/2} = \frac{\varepsilon''}{2n}
\end{gathered} \tag{5.6}$$

The absorption coefficient then immediately follows from the Fresnel formulas:

$$A = 1 - R \approx \frac{4n}{(n+1)^2 + n^2} \tag{5.7}$$

and the skin depth (absorption depth) becomes

$$l_s = \frac{c}{\omega k} \approx \left(\frac{2c^2}{\omega\omega_{\text{pe}}}\right)^{1/2}\left(1 + \frac{\omega^2}{\omega_{\text{pe}}^2}\right)^{1/2} \tag{5.8}$$

The ratio of the absorption coefficient to the skin depth (a weak function of material properties [Rozmus and Tikhonchuk, 1990; Luther-Davies et al., 1992]) that enters into calculations of the electron temperature below becomes

$$\frac{A}{l_s} \approx \frac{2\omega}{c}\left(1 + \frac{1}{n} + \frac{1}{2n^2}\right)^{-1} \tag{5.9}$$

The function in brackets depends weakly on the material and laser parameters. For example, for copper ablation at 780 nm ($\omega = 2.415 \times 10^{15}\,\mathrm{s}^{-1}$; $\omega_{\mathrm{pe}} = 1.64 \times 10^{16}\,\mathrm{s}^{-1}$) it has the value 0.585, while for gold ablation at 1064 nm ($\omega = 1.77 \times 10^{15}\,\mathrm{s}^{-1}$; $\omega_{\mathrm{pe}} = 1.876 \times 10^{16}\,\mathrm{s}^{-1}$) the value is 0.65. Thus, we assume in further estimates that

$$\frac{A}{l_s} \approx \frac{2\omega}{c} = \frac{4\pi}{\lambda}$$

5.2.1.5 Electron Temperature in the Skin Layer

The energy conservation law for conditions of $t_{\mathrm{heat}}, \tau_{\mathrm{ei}} > t_p$ takes the simple form of an equation for the change in the electron energy (or temperature T_e) due to absorption in a skin layer [Gamaly and Tikhonchuk, 1988; Rozmus and Tikhonchuk, 1990, 1992; Luther-Davies et al., 1992]:

$$c_e(T_e) n_e \frac{\partial T_e}{\partial t} = -\frac{\partial Q}{\partial x} \qquad Q = AI_0 \exp\left\{-\frac{2x}{l_s}\right\} \tag{5.10}$$

where Q is the absorbed energy flux in the skin layer, $A = I/I_0$ is the absorption coefficient, $I_0 = cE^2/4\pi$ is the incident laser intensity, and n_e and c_e are the number density and the specific heat of the conducting electrons. The integration of Eq. (5.10) yields

$$T_e = \frac{4}{3}\frac{AI_0\, t}{l_s n_e} \exp\left\{-\frac{2x}{l_s}\right\} \qquad T_e \approx E_F \tag{5.11}$$

The relationship expressed in Eq. (5.11) represents an appropriate scaling law for the electron temperature in the skin layer. The energy conservation law in one dimension yields

$$\int_0^\infty \frac{3}{2} n_e T_e(x)\, dx = AF \equiv F_a = I_0 t_p \tag{5.12}$$

where F_a denotes the absorbed laser fluence (energy density per unit area). The experimental data correlate well with the prediction of Eq. (5.11). For example, the estimate of the skin depth in a copper target irradiated by a Ti : sapphire laser ($\lambda = 780\,\mathrm{nm}$, $\omega = 2.415 \times 10^{15}\,\mathrm{s}^{-1}$; $(\nu_{\mathrm{ei}}) \approx \omega_{\mathrm{pe}} = 1.64 \times 10^{16}\,\mathrm{s}^{-1}$, $n_e = 0.845 \times 10^{23}\,\mathrm{cm}^{-3}$) gives $l_s = 69\,\mathrm{nm}$. The maximum electron temperature at the surface of the copper target under a fluence $AI_0 t_p = 1\,\mathrm{J/cm}^2$ reaches $T_e = 7.5\,\mathrm{eV}$, which is close to the Fermi energy for copper.

5.2.2 Ablation Mechanisms

An atom (ion) can be removed from a solid (ablated) if its total energy exceeds the binding energy (i.e., the energy of vaporization per particle), $E_{\mathrm{total}} > E_b$. The kinetic energy of a free particle should be $E_{\mathrm{kin}} = (E_{\mathrm{total}} - E_b) > 0$ allowing the atom (ion) to leave the solid. This is a general case of nonequilibrium ablation by ultrashort laser pulses. Two nonequilibrium ablation mechanisms occur depending on the relation between pulse duration and relaxation times and on the absorbed energy—electrostatic ablation and nonequilibrium ablation at $T \geq E_b$.

Ablation can also proceed under equilibrium conditions at $T < E_b$ when the energy distribution is Maxwellian. This is the case of conventional thermal evaporation when only a few particles with energy $\geq E_b$ from the high-energy tail of the equilibrium distribution can be removed from a solid. In either case the removal of atoms requires the atom (ion) to acquire energy equal to the binding energy. We consider all these cases below.

5.2.2.1 Electrostatic Ablation

The electrons in the skin layer can gain energy exceeding the threshold energy required to leave a solid target during the pulse. All energy losses due to electron–ion Coulomb collisions and heat conduction are negligible for an ultrashort pulse that complies with the conditions $t_{\text{heat}}, \tau_{\text{ei}} > t_p$. As a result energetic electrons can escape the solid and create a strong electric field due to charge separation from the parent ions. The magnitude of this field depends directly on the electron kinetic energy $E_e \sim (T_e - E_{\text{esc}})$($E_{\text{esc}}$ is the work function) and on the gradient of the electron density along the normal to the target surface, assuming one-dimensional expansion. The force of the electric field applied to the cold ions is associated with the gradient of the electron pressure. The field due to charge separation, or the gradient of electron pressure, pulls ions out of the solid target if the electron energy is larger than the binding energy E_b of ions in the lattice. The maximum energy of ions dragged from the target reaches $E_i(t) \approx ZE_e(t) \approx Z(T_e - E_{\text{esc}} - E_b)$.

It has been shown in Gamaly et al., [2002] that when the laser fluence exceeds the ablation threshold the time necessary for an ion to acquire such energy is comparable and even shorter than the pulse duration. For example, for copper at $F = 1\,\text{J/cm}^2$ this time is less than 40 fs. This electrostatic acceleration of ions is well known from studies of plasma expansion and has been termed ''electrostatic ablation'' [Gamaly et al., 2002] in applications of ablation of solids by ultrashort pulses. Under nonequilibrium conditions close to and above the ablation threshold, electrostatic ablation is the only ablation mechanism occurring during the laser pulse because there is no time for equilibration of the electron and ion temperatures, the ions remain cold and conventional thermal ablation is negligible.

Two processes are responsible for terminating electrostatic ablation: a space charge that builds up in the plasma plume and two-dimensional effects associated with plume expansion. The characteristic time for the electrostatic ablation is comparable to subpicosecond pulse duration and usually lasts ~ 100 fs.

5.2.2.2 Nonthermal Ablation ($T > E_b$)

To establish an equilibrium energy distribution for the ions (atoms) several processes should be completed. First, the absorbed energy should be transferred from the electrons to the ions. Second, ion–ion collisions should establish an equilibrium distribution and this requires the occurrence of *many* collisions. Third, the ion ablation rate should be lower than the thermal velocity of the ions. One can see that at some value of the absorbed intensity, I_a, the ablation velocity exceeds the sound velocity, $v_{\text{abl}} > v_s = (T/M_a)^{1/2}$, which is responsible for establishing the equilibrium distribution by means of atom–atom (or ion–ion) collisions. Thus, the rate at which the solid is transformed into vapor is higher than the equilibration rate. Hence the equilibrium has no time to be established, and therefore evaporation (ablation) proceeds in a nonequilibrium fashion.

5.2.2.3 Thermal Ablation (Evaporation) ($T < E_b$)

After the pulse ends when conditions in a target and in the vapor are close to those in equilibrium, the ablation characteristics can be estimated by results taken from conventional thermodynamics. Thermal evaporation takes place when the saturated vapor is in thermodynamic equilibrium with a solid, and the evaporation process is stationary. The ablation rate (the number of ablated atoms per square centimeter per second) in these conditions can be estimated on the basis of thermodynamics as the equilibrium evaporation rate of a solid into vacuum [Landau and Lifshitz, 1980]:

$$(n_a v_a)_{\text{equilibrium}} \propto n_{\text{vap}} \left(\frac{2T}{M}\right)^{1/2} \exp\left(-\frac{E_b}{T}\right) \tag{5.13}$$

where n_{vap} is the density of the saturated vapors close to the solid–vapor interface. Thus, only particles with energy $> E_b$ from the high-energy tail in the Maxwellian distribution [Landau et al., 1984] can leave the solid. However, caution should be exercised when applying thermodynamic

relations to laser ablation with short pulses because conditions in the expanding plume are usually far from equilibrium.

5.2.3 Ablation Thresholds

The definition of ablation threshold has an obvious physical limit: At least one atom should be removed from the target surface to mark the beginning of the ablation process. The ablation threshold under conditions when the focal spot diameter is much larger than the absorption depth is thus defined as removal of one atomic monolayer.

5.2.3.1 Ablation Threshold for Metals ($t_{heat}, \tau_{ei} > t_p$)

The minimum energy that an electron needs to escape from a solid equals the work function. To drag an ion out of the target, the electron must have an additional energy equal to or larger than the ion binding energy. Hence, the ablation threshold for metals can be defined by the following condition: The electron energy in the surface layer $d \ll l_s$ by the end of the laser pulse must reach a value equal to the sum of the atomic binding energy and the work function. Using Eq. (5.11) for the electron temperature, we obtain the condition to reach the ablation threshold as

$$E_e = E_b + E_{\text{esc}} = \frac{4}{3}\frac{AI_0 t_p}{l_s n_e} \tag{5.14}$$

The threshold laser fluence for ablation of metals is then defined as the following:

$$F_{\text{th}}^m \equiv I_0 t_p = \frac{3}{4}(E_b + E_{\text{esc}})\frac{l_s n_e}{A} \tag{5.15}$$

We assume that the number density of the conducting electrons is unchanged during the laser–matter interaction process. After inserting $A/l_s = 4\pi/\lambda$ into Eq. (5.15) the approximate formula for the ablation threshold takes the following form:

$$F_{\text{th}}^m \equiv I_0 t_p \approx \frac{3}{8}(E_b + E_{\text{esc}})\frac{cn_e}{\omega} \equiv \frac{3}{8}(E_b + E_{\text{esc}})\frac{\lambda n_e}{2\pi} \tag{5.16}$$

Equation (5.16) predicts that the threshold fluence is proportional to the laser wavelength: $F_{\text{th}} \sim \lambda$. We demonstrate later that this relationship agrees well with the experimental data.

5.2.3.2 Ablation Threshold for Dielectrics ($t_{heat}, \tau_{ei} > t_p$)

Although the ablation mechanism for ionized dielectrics is similar to that for metals, there are distinct differences however. First, additional energy is needed to create the free carriers, that is, to transfer the electrons from the valence band to the continuum. Therefore, energy equal to the ionization potential, J_i, should be delivered to each valence electron. Second, the number density of free electrons depends on the laser intensity and time during the interaction process. However, if the intensity during the pulse exceeds the ionization threshold, then the first ionization stage is completed well before the end of the pulse, and the number density of free electrons saturates at a level $n_e \sim n_a$, where n_a is the number density of atoms in the target. Under such conditions the threshold fluence for ablation of dielectrics, taking into account the above corrections, is defined as follows:

$$F_{\text{th}}^d = \frac{3}{4}(E_b + J_i)\frac{l_s n_e}{A} \tag{5.17}$$

Therefore, as a general rule, the ablation threshold for a dielectric in the ultrashort laser–matter interaction regime must be higher than that for metals, assuming that all the atoms in the interaction

zone are at least singly ionized. Because the absorption in the ionized dielectric also occurs in a skin layer, one can use the relation $l_s/A \approx \lambda/4\pi$ to obtain rough estimates and scaling relations.

Another feature of the ablation thresholds defined above for the case $t_{\text{heat}}, \tau_{\text{ei}} > t_p$ is that they do not depend explicitly on the pulse duration and intensity. However, we have presented just a first-order approximation. Certain dependencies, though weak, are hidden in the absorption coefficient and in the number density of free electrons.

An intermediate regime occurs for conditions $\tau_{\text{ei}}, t_{\text{heat}} < t_p$ for laser pulse durations $t_p > 0.5\,\text{ps}$ and at the intensities less than $10^{11}\,\text{W/cm}^2$, where heat conduction should now be taken into account. The thickness of target layer heated during a pulse longer than a picosecond becomes $l_s/2 + l_{\text{heat}}$. Here $l_{\text{heat}} = (Dt_p)^{1/2}$ is the heat diffusion depth, D is the heat diffusion coefficient defined by Eq. (5.4). The ablation threshold for this case can be obtained with the help of Eq. (5.15), by replacing $l_s/2\, with\, l_s/2 + l_{\text{heat}}$:

$$F_{\text{th}}^m \approx \frac{3}{2}(E_b + E_{\text{esc}})\frac{n_e}{A}\left(\frac{l_s}{2} + l_{\text{heat}}\right) \tag{5.18}$$

The well-known $t_p^{1/2}$ time dependence for the long-pulse threshold fluence [Afanasiev and Krokhin, 1971; Anisimov et al., 1971] immediately follows from this equation in the limit $l_s/ \ll l_{\text{heat}}$:

$$F_{\text{th}} \approx \frac{(Dt_p)^{1/2}E_b n_a}{A} \tag{5.19}$$

Thus, formulas for the ablation thresholds for ultrashort and long laser pulses are naturally linked as a continuous function of the pulse duration.

5.2.3.3 Comparison to the Experimental Data

Below we compare the above formulas to the experimental data. Where it is available, we present the full span of pulse durations from the femtosecond to nanosecond range for ablation of metals and dielectrics.

Metals We apply Eq. (5.15) for calculation of the ablation threshold for copper and gold targets ablated by 780-nm laser radiation. The copper parameters are: density $8.96\,\text{g/cm}^3$, binding energy (heat of evaporation per atom) $E_b = 3.125\,\text{eV/atom}$, $E_{\text{esc}} = 4.65\,\text{eV/atom}$, and $n_a = 0.845\times10^{23}$ cm^{-3}. The calculated threshold $F_{\text{th}} \sim 0.51\,\text{J/cm}^2$ (for $A \cong 1$) is in agreement with the experimental figure 0.5–0.6 J/cm^2 given in Gamaly and Tikhonchuk [1988], though the absorption coefficient was not specified. For long-pulse ablation taking into account the thermal diffusivity of copper of $1.14\,\text{cm}^2/\text{s}$ it was predicted $F_{\text{th}}[\text{J/cm}^2] = 0.045 \times (t_p[\text{ps}])^{1/2}$ [Gamaly et al., 2002].

For a gold target ($E_b = 3.37\,\text{eV/atom}$, $E_{\text{esc}} = 5.1\,\text{eV}$, $n_e = 5.9 \times 10^{22}\,\text{cm}^{-3}$) ablated by a laser wavelength of 1053 nm, the ablation threshold from Eq. (5.15) is $F_{\text{th}} = 0.5\,\text{J/cm}^2$. That figure should be compared to the experimental value of $0.45 \pm 0.1\,\text{J/cm}^2$ [Stuart et al., 1996]. For long-pulse ablation assuming the constant absorption coefficient of $A = 0.74$, one finds for gold $F_{\text{th}}[\text{J/cm}^2] = 0.049 \times (t_p[\text{ps}])^{1/2}$ [Gamaly et al., 2002]. We should note here that for the long pulses we take $1.3\,\text{cm}^2/\text{s}$ for the value of thermal diffusivity, which corresponds to equilibrium conditions with an ion-dominated heat capacity. The experimental points from Stuart et al. [1996] and the calculated curve are presented in Figure 5.1.

Fused Silica An estimate for the ablation threshold for silica from Eq. (5.17) taking $n_e \cong 7\times 10^{22}\,\text{cm}^{-3}$, $(E_b + J_i) \cong (3.7 + 13.6)\,\text{eV}$ [Sosman, 1965] using a laser at $\lambda = 1053\,\text{nm}(\omega = 1.79\times 10^{15}\,\text{s}^{-1}$; and $l_s/A \sim 1.6 \times 10^{-5}\,\text{cm}$) gives $F_{\text{th}} = 2.35\,\text{J/cm}^2$, which is in qualitative agreement with the experimental figures $\sim 2 \pm 0.5\,\text{J/cm}^2$ [Perry et al., 1999]. Equation (5.17) also predicts the correct wavelength dependence of the threshold: $F_{\text{th}} = 1.84\,\text{J/cm}^2$ for $\lambda = 825\,\text{nm}$ and $F_{\text{th}} = 1.17$ J/cm^2 for $\lambda = 526\,\text{nm}$ (cf. Fig. 5.2). The experimental threshold fluences for subpicosecond laser

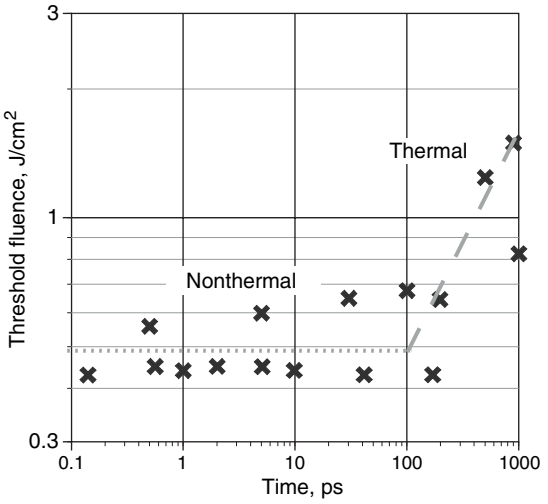

Figure 5.1 Threshold laser fluence for ablation of gold targets versus laser pulse duration [Gamaly et al., 2002]. The experimental points are from Stuart et al. [1996].

pulses [Perry et al., 1999] are: $2-2.5\,\mathrm{J/cm^2}(\lambda = 1053\,\mathrm{nm})$, $\sim 2\,\mathrm{J/cm^2}(\lambda = 825\,\mathrm{nm})$, and $1.2-1.5\,\mathrm{J/cm^2}(\lambda = 526\,\mathrm{nm})$.

Using the following parameters for fused silica at a wavelength of $825\,\mathrm{nm}(D = 0.0087\,\mathrm{cm^2/s}$, $E_b = 3.7\,\mathrm{eV/atom}$, $n_a = 0.7 \times 10^{23}\,\mathrm{cm^{-3}}$, and $A \sim 3 \times 10^{-3})$, one obtains a good agreement with the experimental data shown in Perry et al. [1999] for laser pulse durations from 10 ps to 1 ns. For the long-pulse regime the following relation holds: $F_{\mathrm{th}}[\mathrm{J/cm^2}] = 1.29 \times (t_p[\mathrm{ps}])^{1/2}$ (see Fig. 5.3). The ablation threshold of $4.9\,\mathrm{J/cm^2}$ for fused silica for laser parameters $t_p = 5\,\mathrm{fs}$, $\lambda = 780$ nm, intensity $\sim 10^{15}\,\mathrm{W/cm^2}$ has been reported in Lenzner et al. [1999]. This value is almost three times higher

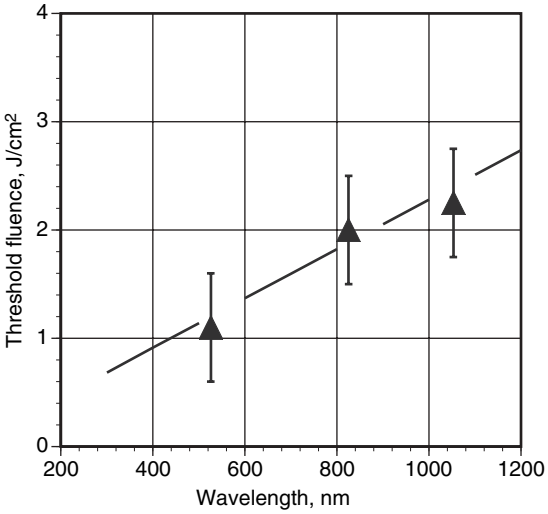

Figure 5.2 Threshold fluence for laser ablation of fused silica target as a function of the laser wavelength for subpicosecond laser pulses [Gamaly et al.,[2002].

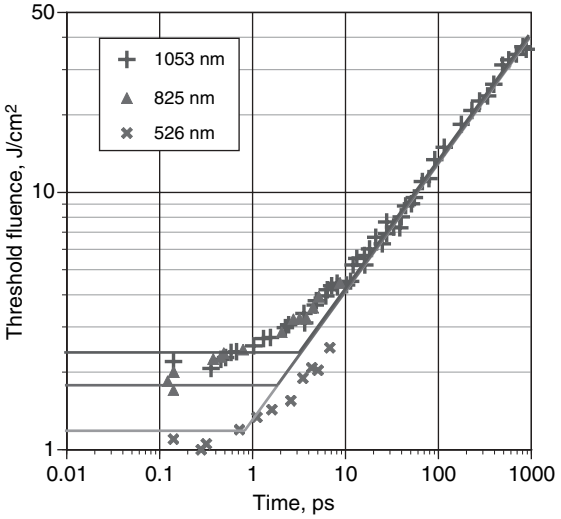

Figure 5.3 Threshold laser fluence for ablation of a fused silica target versus laser pulse duration [Gamaly et al., 2002].

than that of Perry et al. [1999] and Stuart et al. [1996] and from the prediction of Eq. (5.17). However, the absorption coefficient as well as the prepulse to main pulse contrast ratio was not specified in Lenzner et al. [1999].

In Sokolowski-Tinten et al. [1998] a crater of depth 120 nm was drilled into BK7 glass by a 100-fs 620-nm laser pulse at an intensity of $1.5 \times 10^{14}\,\mathrm{W/cm^2}$. Assuming that the number density, the binding and ionization energies in the BK7 glass target are similar to fused silica, we can estimate the ablation depth and on this basis predict the threshold value of $1.0\,\mathrm{J/cm^2}$. This is in reasonable agreement with the measured value in Stuart et al. [1996]: $F_{\mathrm{th}} = 1.4\,\mathrm{J/cm^2}$, while Eq. (5.17) predicts $F_{\mathrm{th}} = 1.34\,\mathrm{J/cm^2}$.

We note that the most reliable experimental data for the ablation threshold are those obtained by extrapolation of the experimental dependence of the ablated depth versus the laser fluence to the "zero" depth value. As one can see from the above comparisons, the experimental data on the ablation threshold determined in this way are in excellent agreement with the formulas presented above. It should be particularly emphasized that there are no fitting parameters in the calculations presented here.

5.2.4 Ablation Rate, Mass, and Depth

The energy deposited in the skin layer is transported inside the bulk of a target in the form of heat or a shock wave depending on the relationship between laser and material parameters. The ablation wave closely follows the heat (or shock) front. It is appropriate to present the ablation front as a discontinuity where the conservation laws for mass, momentum, and energy are fulfilled in a close analogy with the similar conditions at the shock wave front [Afanasiev and Krokhin, 1971]. All parameters at the ablation front are directly related to the laser parameters via conservation laws. These relations allow maximum values to be obtained for the ablation rate, ablated mass and depth compatible with conservation laws as functions of laser and material parameters. For example, the maximum ablation velocity (and ablation rate) follows from the energy flux conservation [Afanasiev and Krokhin, 1971]:

$$v_{\mathrm{abl}} \le \frac{I_a}{nE_b} \qquad (nv)_{\mathrm{abl}} \le \frac{I_a}{E_b} \tag{5.20}$$

Here I_a is the absorbed laser intensity, n is the atomic number density in a target. The ablation depth per pulse then immediately follows from the ablation rate:

$$l_{\text{abl}} \leq \frac{I_a t_p}{n E_b} = \frac{F_a}{n E_b} \tag{5.21}$$

The ablated mass per pulse can be obtained from

$$m_{\text{abl}} = S_{\text{foc}} l_{\text{abl}} M n = \frac{A E_{\text{las}} M}{3 E_b} \tag{5.22}$$

Here S_{foc} and $E_{\text{las}} = F_a \times S_{\text{foc}}$ are, respectively, the focal spot area and laser energy per pulse; M is atomic mass of the target material. The only conclusion on the ablation time, t_{abl}, that follows from the conservation laws is that it should be longer than the pulse duration $t_{\text{abl}} > t_p$. It was implicitly assumed above that the whole absorbed energy is entirely spent on ablation. Taking into account the energy expended on ionization, as kinetic and thermal energy reduces the ablation rate, ablated mass, depth, and velocity while the ablation time increases. These corrections can be found for the different transient ablation regimes listed above. However, all the above formulas allow for direct comparison with experimental data as we demonstrate below. They are also helpful in interpretation and planning of the experiments.

The mass ablated during the thermal stage $m_{\text{abl}}^{\text{th}} = M S_{\text{foc}} \int_{t_0}^{\infty} (n_i v_i)_{\text{eq}} dt$ can be calculated by Eq. (5.13) taking the time dependence of the temperature after the end of the pulse. One can see that this mass is much less than that ablated during the nonthermal stage due to the presence of the small exponential factor.

5.2.5 Atomization of Laser Plume: Spatial Pulse Shaping

In applications of laser ablation for the deposition of thin films it is necessary to control the composition of the laser-produced plume. It is well known that laser plumes containing macroscopic particles and liquid droplets result in a poor-quality deposited film. This is a major obstacle for many potentially attractive industrial applications of PLD. In this section we present a simple way to control the composition of the plume and to achieve the fully atomized gas phase by a single subpicosecond laser pulse.

There are two major reasons for the plume to have a more complex composition. The first relates to the spatial intensity variations across the laser focal spot. There are a variety of processes that transform the state of a target exposed to a pulse of intense laser radiation, and the onset of all these processes depends on the incident laser intensity. The processes that appear progressively as the laser intensity increases are structural phase transitions, destruction of the target integrity (appearance of cracks, flaking of the surface), melting, ablation, and finally ionization. The spatial intensity distribution across the focal spot usually has a Gaussian-like form. Therefore a plume produced by a laser with such intensity variations can contain material in different phase states: gas, melt, and so forth.

Another source of the liquid droplets in the plume is condensation of vapor during the expansion. As a result, a plume arriving at the substrate consists of a mixture of gas and liquid phases. Therefore, to ensure that deposition at a substrate occurs from a homogeneous gas plume one needs two conditions to be fulfilled: (1) the local fluence at every point across the focal area should exceed the ablation threshold, and (2) the conditions that maintain the expanding plume in the gas phase should be satisfied. Below we formulate both conditions and demonstrate their implementation in an experiment.

5.2.5.1 Local Energy Thresholds for the Phase Transitions

First, we take into account the spatial distribution of the absorbed energy over the target surface. Equation (5.11) becomes

$$E_e(r,x,t) = \frac{2F(r,t)}{n_e l_s}\exp\left\{-\frac{2x}{l_s}\right\} \tag{5.23}$$

where $F(r,t) = \phi(r)\int_0^t A(t')I(t')dt'$. The r coordinate corresponds to the distance from the center of a circular focal spot on the target surface, while the x coordinate is normal to the surface; $\phi(r)$ is a dimensionless function (e.g., Gaussian-like) describing the axially symmetric spatial distribution. The absorbed energy in a monoatomic surface layer with thickness $d_a = n_a^{-1/3} \ll l_s$ at the end of the laser pulse becomes

$$E_e(r,x,t) \approx \frac{2F(r,t_p)}{n_e l_s} \tag{5.24}$$

We define a local threshold, which depends on position within the focal spot, for any laser-induced transformation of the material using the condition that the absorbed energy defined by Eq. (5.24) equals the energy, $\varepsilon_{\text{transf}}$, required for the particular phase transformation [Gamaly et al., 2002]:

$$E_{\text{transf}} = E_e \cong \frac{2F(r,t_p)}{n_e l_s} \tag{5.25}$$

It is obvious that the threshold energy density (fluence), $F_{\text{thr}} = AI_{\text{thr}} \times t_p \sim E_{\text{transf}}$, scales with the characteristic energy required for the particular type of phase transition. For example, the ratio of ablation threshold to the melting threshold equals the ratio of the heat of vaporization H_{vap} to the heat of melting H_{melt}. This ratio varies for most materials within a range $\sim$5–30. For example, for a silicon target used in the experiments below $H_{\text{vap}} = 10.6$ kJ/g; $H_{\text{melt}} = 1.66$ kJ/g [Weast and Astle, 1981], and $H_{\text{vap}}/H_{\text{melt}} = 6.4$.

One can see that to control the phase state of the plume, energy in excess of the phase transition threshold should be deposited. This condition emphasizes that the threshold energy should be significantly higher than that required to just break the interatomic bonds. Sufficient kinetic energy should be additionally delivered to an unbound atom to remove it from the solid and maintain it in the desired vapor state. The production of a droplet-free deposition process imposes the additional condition that the gas state of the vapor should be effectively collisionless.

5.2.5.2 Criterion for Total Atomization of Ablated Plume

The energy threshold for total atomization of the ablated plume can be calculated on the basis of thermodynamic arguments similar to those used to derive the criterion for complete vaporization of material by strong shock waves [Zel'dovich and Raizer, 2002]. The deposited laser energy is used to break the interatomic bonds and also provides the kinetic energy to the expanding plume. The magnitude of the kinetic energy sufficient to keep the expanding plume in a gaseous state containing noninteracting atoms determines the absorbed energy threshold for target atomization. Let us consider briefly the required level of laser fluence, F_{atom}, for total atomization of the target material with subpicosecond laser pulses.

The equation of state of the ablated material in conditions close to that for the solid–vapor phase transition can be presented as a sum of the elastic pressure (related exclusively to the interatomic interaction) and the thermal pressure:

$$\begin{aligned} E &= E_c(V) + c_s TN \\ P &= P_{\text{th}} + P_c = c_s \frac{NT}{V}\Gamma(V) + P_c \end{aligned} \tag{5.26}$$

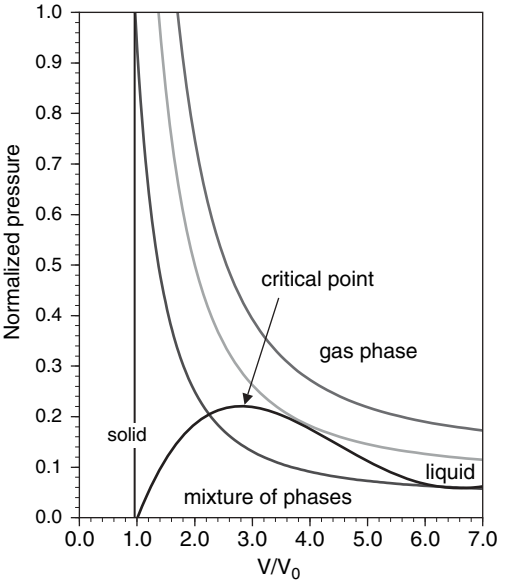

Figure 5.4 *P-V* diagram of vapor states in the plume at various levels of absorbed laser energy and thus at different initial normalized pressures. The total atomization (gas phase) is achieved when the *P-V* curve is above the critical point and above the curve of phase equilibrium (the Clapeyron–Clausius equation) between the mixture of phases and the gas phase (dashed curve).

The elastic (''cold'') pressure, $P_c = -dE_c/dV$ (and the corresponding energy, E_c), is temperature independent. The Gruneisen coefficient, $\Gamma(V) > 0$, changes from ~ 2 for the solid state to $\frac{2}{3}$ for the ideal gas during the evaporation process. By definition, the integral over the cold pressure from initial volume to infinity equals the binding energy:

$$-\int_{V_0}^{\infty} P_c(v)\, dV = E_b \tag{5.27}$$

The important practical issue of target ablation and further expansion of vapor relates to the definition of the phase state of the ablated matter in the different areas of phase space in *P,n* or *T,n* planes. The material is swiftly elevated to high temperature under the action of a short powerful laser pulse while the initial density remains unchanged. The phase states of the expanding ablated material lie along curves for adiabatic expansion (entropy is conserved during expansion), as shown in Figure 5.4. If the initial temperature of expansion is lower than a specific value defined below, the expansion curves cross the phase equilibrium curve that separates the states of a single phase from the states with a mixture of phases. The states above the first adiabatic curve touching the critical point represent the atomic state of a homogeneous phase at $V > V_0 (n < n_0)$.

The pressure at the equilibrium solid–vapor interface grows with the temperature increase until the critical point. The boiling curve in *PT* plane ends in a critical point, at P_{cr} and T_{cr}. The critical point is the maximum of the phase equilibrium curve in *PV* and *TV* planes. The difference between the solid, the melt, and the vapor ceases to exist in a critical state, that is, the density of all phases has the same value, V_{cr}. Although the critical values are poorly known for many materials, it has been established, however, that T_{cr} constitutes a small fraction of the binding energy, usually $T_{\text{cr}} \sim (0.1\text{–}0.2)E_b$ [Zel'dovich and Raizer, 2002].

The adiabatic curve, which separates the single-phase area from the mixture of phases, and the phase equilibrium curve have only one common point, that is, the critical point. One can find the initial temperature for a material at initial density that begins to expand along this adiabatic curve by applying the above condition with the help of (5.26):

$$P_{\rm cr} = c_s n_{\rm cr} T_{\rm cr} \Gamma(n_{\rm cr}) + P_c(n_{\rm cr}) \tag{5.28}$$

The critical and initial parameters are linked through the equation of adiabatic expansion:

$$\frac{T_{\rm cr}}{T_0} = \left(\frac{n_{\rm cr}}{n_0}\right)^{\Gamma(n_{\rm cr})} \tag{5.29}$$

We remember here that the density-dependent Gruneisen coefficient, Γ, plays the same role as the adiabatic constant, $\Gamma \sim \gamma - 1$. Note that at the critical point, vapor is described as an ideal gas, $\Gamma(n_{\rm cr}) \sim \frac{2}{3}$. Now the initial temperature, T_0, of a laser-excited solid that should pass through the critical point during adiabatic expansion is easily expressed through the critical parameters from Eqs. (5.27)–(5.29):

$$T_0 = \frac{3}{2}\frac{P_{\rm cr} + |P_c(n_{\rm cr})|}{c_s n_{\rm cr}} \left(\frac{n_0}{n_{\rm cr}}\right)^{2/3} \tag{5.30}$$

The critical parameters, at least in principle, can be related to the binding energy and initial density [Zel'dovich and Raizer, 2002; Landau and Lifshitz, 1980]. For example, using known experimental data for aluminium [More et al., 1988] and interpolation for the "cold" pressure one obtains: $P_{\rm cr} = 1.84\,{\rm kbar} \cong 5.55 \times 10^{-3}\, E_b n_0$; $n_0/n_{\rm cr} \sim 26$ and $|P_c(n_{\rm cr})| \approx 0.015\, E_b n_0$. Thus, the adiabatic expansion curve for aluminium touching the phase equilibrium curve at the critical point must start at $T_0 \sim 4.9 \times E_b$ (where T_0 is the maximum temperature at the end of the laser pulse), in agreement with the qualitative estimates from Gamaly et al., [2004]. The practical conclusion from this result is that the aluminium skin layer heated homogeneously to $T_0 \geq 5E_b$ at its initial density then expands adiabatically in a homogeneous state of atomic vapor. Accordingly, all states of expansion starting at lower temperature shall cross the phase equilibrium curve inevitably entering into states containing a mixture of phases. A similar qualitative conclusion for atomization of the ablated plume can be made for all solids because the binding energy for most solids lies in the range of 2–5 eV.

Thus, energy approximately 3–5 times larger than the binding energy should be deposited into a solid, $E_{\rm th} \sim 3E_b$, to transform the target into a fully atomized gas. We should note here that the exact value of the above numerical coefficient depends strongly on the equation of state in a range $V_0 < V < V_{\rm crit}$ for a particular material. Therefore, the laser energy density necessary to transform the ablated material into the atomized vapor should comply with the following condition: $F_{\rm atom} > 4F_{\rm thr}$.

The qualitative dependence of normalized pressure, $P/(E_b/V_0)$ on normalized volume (V/V_0) during the adiabatic expansion starting at the same initial density $n = V_0^{-1}$ and with the different initial normalized pressure (3, 2, 1). The dashed curve corresponds to the states of phase equilibrium (Clapeiron–Clausius curve). This curve separates the states representing the mixture of phases (at $P < P_{\rm crit}$) from the states of a homogeneous phase or atomized vapors (at $P > P_{\rm crit}$). We should stress that this function is poorly known for most materials. One clearly sees from Figure 5.4 that the expansion from the initial state with energy $E > 5E_b$ keeps the expanding vapor in a gas state while at a lower initial energy a mixture of states is unavoidable.

5.2.5.3 Surface Damage and Evaporation

If the total deposited laser energy is close to the binding energy, $E_{\rm total} \sim E_b$, then the heated target experiences only a small density decrease from the normal solid density. The pressure in the material

in this case is comparable to the bulk modulus. Therefore, the final state of the target affected by the laser at this energy level might be considered as ''damaged'', resulting in the formation of cracks, flakes, delamination of the surface, and so forth, depending on the presence of defects and impurities in the initial state of the target. If the deposited energy is in a range $E_b < E_{\text{total}} < (3\text{–}5)E_b$, then the final state of the expanding vapor may fall within a region of the *P-V* plane where the mixture of phases is energetically favorable (Fig. 5.4). This leads to condensation of vapor into liquid droplets. We should keep in mind that the thresholds above were introduced locally, that is, different regions of the beam can create different phase states depending on the local beam intensity. One should also note that the energy estimates are rather conservative (overestimated) because they are based on the assumption of thermodynamic equilibrium. In reality, and especially for short pulses, the expansion time is shorter than the equilibration time. Therefore, the expansion of vapor proceeds in the kinetic regime, and thus condensation processes are decelerated.

5.2.5.4 Optimum Pulse Profile for Atomization of the Plume

Temporal Shape of Short Pulses The chirped pulse amplification (CPA) technique [Maine et al., 1988] commonly used for the generation of energetic subpicosecond pulses often produces a prepulse containing a significant amount of energy. It is well known that to achieve the short-pulse interaction mode a high-contrast ratio is required between the energy of the short pulse and the prepulse. A detailed discussion of the methods for providing a high contrast ratio can be found in Luther-Davies et al. [1992] and Wharton et al.[2001]. We note that efficient methods to suppress the prepulse include gain narrowing, the use of a saturable absorber and frequency conversion.

There is an additional source of such a prepulse, namely amplified spontaneous emission (ASE) from the laser amplifiers. The intensity contrast ratio of the main pulse/ASE is generally about 10^6, while the duration of the ASE pulse can be of 0.2–2 ns [Luther-Davies et al., 1992; Wharton et al., 2001]. For example, if the prepulse associated with the ASE is of nanosecond length, $t \sim 1$ ns, and $A \sim 1$, then the intensity in the ASE prepulse of 10^8 W/cm^2 can damage the target surface before the main pulse arrives. Recently, ASE effects on femtosecond laser–matter interactions have been revisited, and it was once more confirmed that the ASE could significantly affect the interactions of a main short pulse with the target [Wharton et al., 2001]. To eliminate ASE the laser design must include successive stages of amplification interspersed with spatial filters [Luther-Davies et al., 1992].

Spatial Shaping: ''Top-Hat'' Spatial Distribution To demonstrate the importance of the spatial distribution of the laser intensity, we apply the above reasoning to the problem of obtaining efficient atomization of an expanding plume produced by ablation of a material. First, we assume that the temporal pulse shape is Gaussian and the pulse is free of ASE, prepulses and postpulses. In most practical cases the laser intensity across the focal spot is assumed to have a Gaussian distribution with axial symmetry (beam axis is at $r = 0$):

$$\phi(r) = \exp\left\{-\ln 2 \frac{r^2}{r_f^2}\right\}$$

The focal spot radius, r_f, is defined by the condition $\phi(r_f) = I/2$. The part of the total energy confined in a circle of radius r is given as follows:

$$\left\{\int_0^r \phi(r')\pi dr'^2\right\}\left(\frac{\pi r_f^2}{\ln 2}\right)^{-1} = 1 - \exp\left\{-\frac{r^2}{r_f^2}\ln 2\right\} \tag{5.31}$$

On the basis of the results of the previous sections one can estimate the phase state of the ablated plume for any peak absorbed laser fluence. Choosing, for example, a laser fluence, $AI_m t_p$,

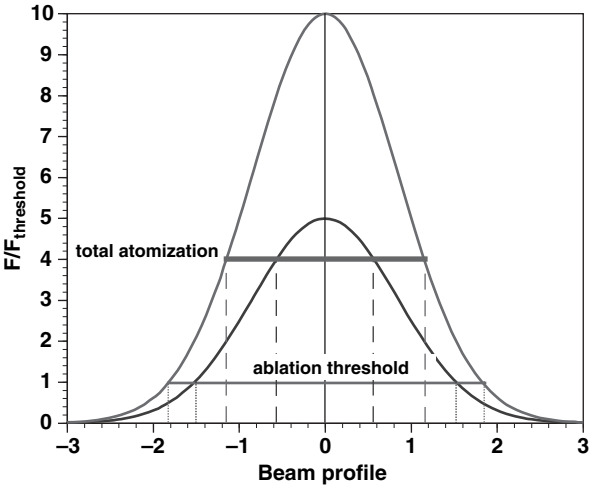

Figure 5.5 Gaussian beam profile in the focal spot with the maximum fluence of $5F_{\text{thr}}$ and $10F_{\text{thr}}$. The beam radius is measured in the units of FWHM radius. The increase of maximum fluence in the beam from $5F_{\text{thr}}$ to $10F_{\text{thr}}$ improves the energy utilized for total atomization from 20 to 60% and reduces the ''mixture of phases'' energy part from 60 to 30%. Accordingly, the target area producing total atomization (gas) phase in the plume is increased four times.

5 times larger than the ablation threshold (Fig. 5.5), one can easily calculate that only 20% of the pulse energy goes into ''full atomization'' of the target material, and this occurs in the beam area where $F > 4F_{\text{thr}}(0 < r < 0.57r_f)$. The ''mixture of phases'' is produced where $F_{\text{thr}} < F < 4F_{\text{thr}}$, and this region contains $\sim 60\%$ of the beam energy $(0.57r_f < r < 1.52r_f)$. The part of the beam where the ''surface damage'' is most probable at $F < F_{\text{thr}}(r > 1.52r_f)$ consumes $\sim 20\%$ of the total absorbed laser energy. Therefore, the target area producing a mixture of phases in the plume is about sixfold larger than that where total atomization occurs. Thus this plume is highly likely to contain particulates or droplets and lead to the deposition of a contaminated film.

The ratio of the beam area producing a mixture of phases to that producing the fully atomized vapor can be obviously reduced by increasing the peak fluence. For example, the part of absorbed energy used up for full atomization of vapor increases by three times, from 20 to 60%, if the peak absorbed fluence is increased from $5F_{\text{thr}}$ to $10F_{\text{thr}}$ (Fig. 5.5). Nevertheless incomplete atomization still results.

Clearly, it is very difficult to obtain complete atomization using a Gaussian beam, and it is obvious that it would be preferable to use a ''top-hat'' intensity distribution where the absorbed fluence everywhere exceeds about four times the ablation threshold. A simple way to move toward the top-hat profile is to truncate the low-energy wings in the spatial distribution with an aperture and employ a relay-imaging focusing scheme to image the top-hat beam onto the target. Below we describe the experimental procedure and experiments where this idea has been implemented in femtosecond laser ablation of silicon [Gamaly et al., 2004].

5.2.5.5 Experiments: Ablation and Deposition of Silicon Films by Spatially Shaped Pulses

Three series of deposition experiments were conducted using a 150-fs laser: (a) with the target located at the focal spot at the maximum intensity; (b) with the target located at the image plane of the 2.2-mm-diameter aperture; and (c) at the same target position but with the aperture removed. Optical micrographs of the resulting films are shown in Figure 5.6.

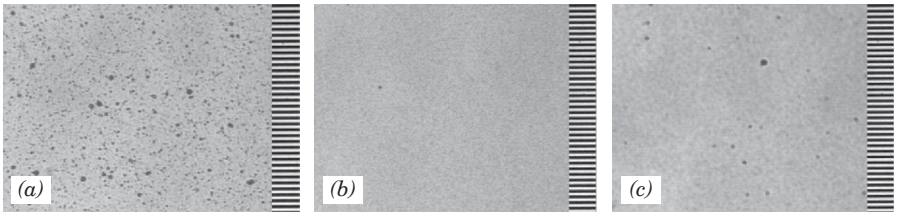

Figure 5.6 Optical microscope images of Si film surfaces deposited under different focusing conditions of the same laser beam: (a) Target is in the focal spot; the density of droplets is $> 1000\,\mathrm{cm}^{-2}$; (b) target is in the image plane of a 2.2-mm iris with $\times 20$ demagnification; the density of droplets is reduced to $\sim 10\,\mathrm{cm}^{-2}$; and (c) target is in the same image plane as in (b), the iris is open; the droplets density increases to $\sim 100\,\mathrm{cm}^{-2}$. A 10-μm scale is shown on the left border of each image.

The analysis of these optical images revealed that the density of 1–10 μm droplets on the substrate surface was above $1000\,\mathrm{cm}^{-2}$ when the target was positioned in the focal plane where the absorbed laser fluence was $A_F = 65\,\mathrm{J/cm^2} \times 0.64 = 41.6\,\mathrm{J/cm^2} (I_{\mathrm{abs}} = 2.8 \times 10^{14}\,\mathrm{W/cm^2})$. By placing the target in the image plane of the aperture, the maximum fluence of the truncated beam was reduced to $A_F = 1.6\,\mathrm{J/cm^2} \times 0.64 = 1\,\mathrm{J/cm^2} (I_{\mathrm{abs}} = 6.8 \times 10^{12}\,\mathrm{W/cm^2})$. This eliminated droplets almost totally from the deposited Si film: The density of droplets was reduced below $10\,\mathrm{cm}^{-2}$. To test the influence of the low-intensity wings in the spatial pulse profile on droplet formation, another deposition was performed with the target in the same position but with the aperture removed. The density of droplets then increased to above $100\,\mathrm{cm}^{-2}$. This expriment provided a clear demonstration that the low-intensity wings in the spatial distribution are responsible for the formation of droplets on the deposited film surface.

Positioning the target in the image of the aperture may also eliminate the problem of droplet formation from any prepulse. The effect of the prepulse could be estimated in the following way. The measured 1-ns prepulse containing 12.7 μJ results at most in $5.4 \times 10^7\,\mathrm{W/cm^2}$ absorbed laser intensity in the target before the arrival of the main pulse. The depth of the heat wave propagation, l_{heat} can be estimated as $l_{\mathrm{heat}} = \sqrt{-at_{p-p}}$; here a is thermal diffusivity ($a_{\mathrm{Si}} = 0.85\,\mathrm{cm^2\,s^{-1}}$ [Weast and Astle, 1981]) and t_{pp} is the prepulse duration, thus $l_{\mathrm{heat}} = 0.29\,\mu\mathrm{m}$. This leads to a maximum absorbed energy in the heated volume below the target surface of $1.26 \times 10^3\,\mathrm{J/g}$. This value is below the heat of melting of $1.66 \times 10^3\,\mathrm{J/g}$ for Si [Weast and Astle, 1981], thus the prepulse could not melt the target in the focal spot before the arrival of the main subpicosecond pulse. However, the energy of the prepulse would still be high enough to cause some material transformation such as, for example, the formation of cracks, which may be the reason for the presence of a small number of micron-size particles on the deposited film seen in the right image in Figure 5.6.

5.3 CUMULATIVE ABLATION OF SOLIDS BY HIGH-REPETITION-RATE SHORT-PULSE LASERS

The interaction of pulse trains from megahertz repetition rate lasers with matter appears to be significantly different from single-pulse interaction due to accumulation of the effects of successive pulses. The number of pulses on the target surface at high repetition rate may reach thousands per spot because the scanning speed of the laser over the target surface is normally too slow to physically separate successive pulses (the time between the successive pulses for megahertz lasers is of the order of hundreds of nanoseconds). This results in density accumulation from the remnants of previous pulses in the vicinity of a solid surface.

The coupling between the successive pulses, when single-pulse energy is insufficient to produce ablation, gradually transforms the laser–matter interaction into a regime where much stronger laser–target coupling occurs that results in the ablation threshold being exceeded. Therefore, although the

first m pulses hitting the same target spot (from the total number of N pulses per spot) may transform the target surface but lead to no substantial ablation, the remaining N-m pulses do produce ablation. Thus, the ablation length averaged by the large number of pulses corresponds to an energy per pulse lower than that for the single-pulse threshold.

The mechanisms for the coupling of successive pulses in ablation of metals and transparent dielectrics with low heat conduction (such as silica and glasses) are different. We explain cumulative ablation of metals by the gradual plume density and temperature increase in the vicinity of the target surface due to slow thermal ablation between successive pulses. This buildup of temperature and density leads to a change in the laser–matter interaction mode from absorption in the skin layer to absorption on a plasma density gradient.

The time between pulses is too short for complete cooling of an irradiated spot on a transparent dielectric to occur between successive pulses. Thus, in this case, the laser irradiates a spot already heated by the previous pulses and the surface temperature gradually rises until it exceeds the temperature required for evaporation. Thus, the energy accumulation within the target is the major effect in cumulative ablation of poorly absorbing dielectrics. As a result, high-repetition-rate pulse trains allow precise control over the temperature at the sample surface via the ''dwell'' time, allowing ablation to occur under conditions when the single-pulse fluence is insufficient to ablate the material.

The cumulative effect in high-repetition-rate laser interaction with matter has been observed during ablation of carbon by a laser with 76-MHz repetition rate [Rode et al. 1999]. The effects of high-repetition-rate ablation that include smoothing of the spatial intensity distribution and cumulative heating, have both been observed in ablation and deposition of chalcogenide glasses [Rode et al., 2002]. Cumulative heating in the bulk of transparent glass was also reported in Schaffer et al. [2003].

In this section we will consider briefly experiments on ablation of aluminum, copper, steel, lead, and silicon targets with a 4.1-MHz pulse rate 10-ps mode-locked laser in air and in vacuum at conditions above and below the single-pulse threshold.

5.3.1 Dwell Time and Number of Pulses per Focal Spot

Many laser pulses arrive at the same spot on the target surface at repetition rate of 1–100 MHz. From the known oscillation mode of the scanning mirrors one can easily estimate the maximum, $t_{\max}$, and minimum, $t_{\min}$, near the turning points where the laser beam ''dwells'' over a focal spot of a diameter, d_f, for a given scanning frequency, ω_s, repetition rate R_{rep}, and scanning area of size a. The laser beam spends the maximum time near the beam's turning points because the scanning velocity passes through zero while changing direction and because the beam crosses the same spot twice. For simple harmonic oscillations the maximum dwell time is expressed as follows ($\omega_s t_{\max} \ll 1$):

$$t_{\max} = \frac{4}{\omega_s}\left(\frac{d_f}{a}\right)^{1/2} \tag{5.32}$$

Similarly, the minimum dwell time near the center of a scanning area becomes

$$t_{\min} = \frac{d_f}{a\omega_s} \tag{5.33}$$

For the conditions in our experiments ($\omega_s \sim 60\,\text{Hz}, a \sim 15\,\text{mm},\ d_f = 25\text{–}125\,\mu\text{m},\ R_{\text{rep}} = 4.1\,\text{MHz}$) the number of laser pulses per spot varies from 115 in the middle of the scanning area for the maximum fluence with a small spot, to $\sim 2.5 \times 10^4$ for the lowest fluence with the largest spot. In deposition experiments with a 76-MHz repetition rate laser ($d_f = 25\,\mu\text{m}$; $a \sim 50\,\text{mm}$; $\omega_s \sim 100\,\text{Hz}$) the number of pulses per spot lies in a range from 38 to 7×10^4 [Rode et al., 1999]. Therefore during ablation by high (megahertz) repetition rate lasers using $\sim 100\,\text{Hz}$ scanners, numerous pulses interact with the same spot making the interaction regime drastically different from a single-pulse interaction mode.

5.3.2 Smoothing of the Evaporation Conditions on the Surface

There is an appealing effect connected with both the high-repetition pulse rate and the beam scanning speed. A single laser pulse focused at a target surface produces a Gaussian intensity distribution across the focal spot. If the maximum intensity of a single pulse only slightly exceeds the ablation threshold, then the plume produced by such a pulse contains a mixture of phases: liquid droplets, flakes, and the like. The spatial intensity distribution must be modified to control the phase state of the ablated vapors as demonstrated earlier.

The use of a high repetition rate is, however, a natural way to improve the evaporation conditions at the surface, and thus to produce a plume of homogeneous phase. Indeed, the scanning speed is much lower than the repetition rate in experiments presented here. The laser beam moves less than 0.1 μm between two successive pulses. As a result, the spatial intensity distribution over the target surface 'integrates' over time, and the evaporation conditions become almost homogeneous. All the imperfections of a single beam are smoothed with the successive pulses heating the same surface spot several times. As the result, it may be unnecessary to control the intensity distribution as required for single-pulse irradiation.

5.3.3 Ablation in Air and in Vacuum

The results on ablation of metals and silicon targets under the experimental conditions above and below the single-pulse threshold are presented in this section. Al, Cu, steel (Fe), Pb, and Si samples were exposed to 25–26 W of second-harmonic (532 nm) radiation from a mode-locked Nd : YVO_4 laser with energy per pulse on the target surface $E_p = 6.5\,\mu J$, pulse duration $t_p = 13$ ps, and repetition rate 4.1 MHz [Kolev et al., 2003; Luther-Davies et al., 2004]. The energy per pulse and pulse duration were fixed while the focal area was varied from $S_{f,\min} = 5 \times 10^{-6}\,cm^2$ [$d_f = 25\,\mu m$ FWHM (full width at half maximum)] to $S_{f,\max} = 1.2 \times 10^{-4}\,cm^2$ ($d_f = 124\,\mu m$). This corresponds to a range of fluences from 1.3 to $5.4 \times 10^{-2}\,J/cm^2$, and intensities from $1.0 \times 10^{11}\,W/cm^2$ to $4.2 \times 10^{9}\,W/cm^2$. Ablation was performed in both air and vacuum.

The amount of material ablated during a 60-s exposure was measured by weighing the sample with the accuracy of $\pm 10^{-4}$ *g* before and after ablation. The ablated mass per single pulse, m_{av}, was determined as the mass averaged over the 2.46×10^8 pulses. For further analysis it is convenient to introduce the ablation depth per single pulse as follows:

$$l_{abl} = \frac{m_{av}}{S_f \rho} \tag{5.34}$$

here ρ is the target density and S_f is the focal spot area. The ablation threshold was determined from the experimental data using the condition that the thickness of the ablated layer at the threshold fluence should be equal to the thickness of one atomic layer. The measured ablation depths in air and in vacuum for various materials as a function of the incident laser fluence are presented in Figures 5.7 and 5.8. An unexpected conclusion follows from the measured data: the ablation thresholds for all the solids studied were found to be noticeably lower than those for single-pulse experiments [Gamaly et al., 2002]. The ablation experiments were also performed in vacuum to clarify the role of air on the accumulation effect. It is instructive to discuss the results for metals and silicon separately because the physical reasons for the accumulation of temperature and increase of the laser–target coupling are different for these materials.

Metals The ablation threshold in vacuum is larger for all metals than that in air. Both curves for ablation depth versus fluence, in air and in vacuum, merge at a fluence in excess of the single-pulse-ablation threshold. Hence, we conclude that air increases the accumulation effect, most probably due to enhanced thermal ablation as discussed above. Indeed, the temperature at the end of a single pulse at a fluence value corresponding to the measured multipulse threshold varies from 0.24 eV for lead to

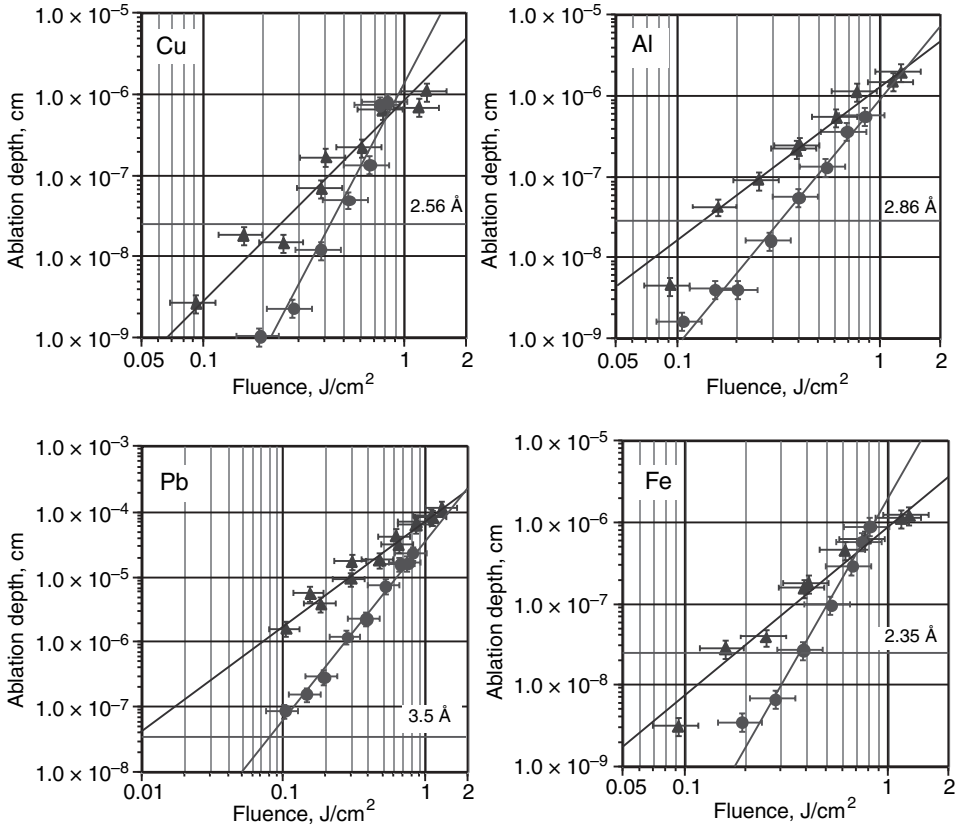

Figure 5.7 Ablation depth as a function of fluence in experiments with Cu, Al, Pb, and Fe, in air (triangles) and in vacuum (circles). Ablation threshold is determined here, tentatively, as the fluence required for the removal of a single atomic layer (atomic layer thicknesses are also shown in the graphs).

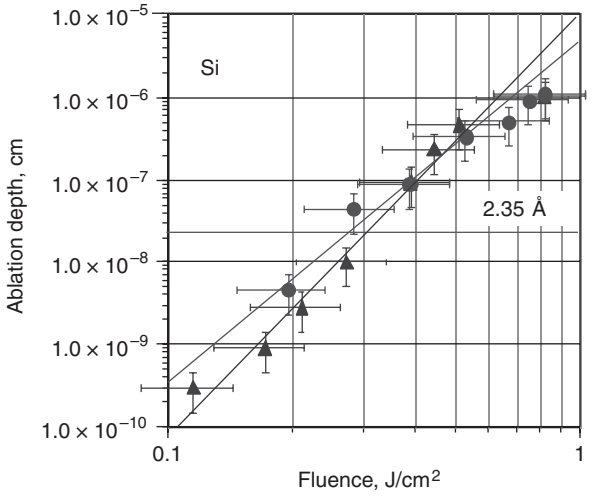

Figure 5.8 Ablation depth as a function of fluence in experiments with Si, in air (triangles) and in vacuum (circles).

1.59 eV for steel, in excess of the boiling temperature for these materials but less than the binding energy, which is in a range of 1.795 eV (lead) to 3.695 eV (iron). Thus, thermal evaporation starting after the first pulse under conditions where plume expansion is suppressed (keeping vapor density and temperature higher than that for the saturated state) allows the ablation threshold for a single pulse to be reached after several pulses.

Silicon The difference between the ablation threshold in air and in vacuum is small for silicon. Therefore, the effect of suppressed plume expansion on the energy accumulation is insignificant. Hence it is clear that compared to the metals, the low heat conduction losses dominate the accumulation effect. Indeed, the cooling time for silicon is 2.5×10^{-5} s equal to the time for ~ 100 successive pulses to arrive. The first pulse heats the sample to only several hundred kelvins. Thus, successive pulses build up the temperature eventually creating the density gradient in the plume by thermal evaporation, until the vapor is ionized, which leads to the change in the interaction mode to that with a plasma. The temperature at the solid–plasma interface in the laser–plasma interaction increases to the level exceeding the binding energy of 4.1 eV after approximately 100 pulses. Efficient ablation then continues during the subsequent several hundred pulses after the laser–plasma interaction regime has been established because the scan rate used allowed several thousand pulses to hit the same spot in these experiments.

It follows from the experimental results and analysis presented above that high-quality thin films of different materials including low absorbing dielectrics (absorption depth $\sim \mu$m) such as silicon in the infrared (IR), silica, chalcogenide glasses, and sapphire can be deposited by using very high repetition rate lasers (1–100 MHz) by an appropriate self-consistent choice of laser wavelength, repetition rate, and energy per pulse. The self-consistent combination of laser and material parameters determines the optimum conditions for ablation and deposition. Control over the phase state of a plume, the elimination of droplets, and high ablation rate can all be simultaneously achieved and has already been demonstrated using silicon and chalcogenide glasses [Rode et al., 2002; Gamaly et al., 2004].

5.4 EXPERIMENTAL RESULTS: DEPOSITION OF THIN FILMS BY SHORT-PULSE MHz REPETITION RATE LASERS

In this section we present the experimental results on ablation and deposition of different materials performed with megahertz repetition rate lasers. There are two sets of experiments. The first set relates to ablation of carbon by a 76-MHz repetition rate laser under conditions when the single-pulse energy was above the ablation threshold. The second set comprises ablation of metals, silicon, and chalcogenide glasses by a megahertz repetition rate laser for conditions when the energy of a single pulse is insufficient to produce ablation. We demonstrate that ablation occurs due to the energy accumulation from the successive pulses hitting the same spot on the sample. This new ablation mode allows ablation of any material including transparent semiconductors at a very high ablation rate. The features of this new ablation mode and future direction are discussed.

5.4.1 Deposition of Amorphous Carbon Films

The 76-MHz, 60-ps, 300-nJ pulses from a mode-locked Nd : YAG laser ($\lambda = 1.064$ μm) were used in these experiments [Rode et al., 1999]. The intensity on the target surface was 2.8×10^9 W/cm^2, which corresponds to a fluence of 1.44 J/cm^2, which is above the ablation threshold.

The number of particles visible with an optical microscope on the carbon film deposited using this laser was less than one particle per square millimeter. Scanning electron micrograph (SEM) images revealed that the deposited film had a very fine surface texture with nanoscale irregularities. Atomic force microscopy (AFM) surface microroughness measurements revealed a saturation-like behavior of the root-mean-square (rms) roughness almost at the atomic level

(<1 nm). Raman spectroscopy of the deposited films indicated that the films consisted of a mixture of sp^3 and sp^2 bonded amorphous carbon. The thickness of the amorphous carbon film deposited simultaneously on two 4-inch silicon wafers varied by only $\pm 5\%$ over an area of $\sim 250\,\text{cm}^2$. The deposition rate was ~ 2–6 Å/s at a distance of ~ 150 mm from the target, which is 10–30 times higher than that achieved with conventional high-energy low-repetition-rate nanosecond lasers.

5.4.2 Deposition of Chalcogenide Glass Films

The films of chalcogenide glasses with atomically smooth surface were produced by ablating solid glass targets in vacuum using a 7-W frequency-doubled mode-locked Nd : YAG laser (532 nm, repetition rate 76 MHz; 50 nJ/pulse; 60 ps; intensity on the target $I = 2.65 \times 10^8\ \text{W/cm}^2$) [Rode et al., 2002].

A well-known advantage of the pulsed laser deposition technique is that it can result in accurate transfer of the stoichiometry of a multicomponent target to a film deposited on a substrate. This is particularly important in materials containing weakly bonded volatile components such as sulfur, where thermal evaporation often results in marked changes in stoichiometry. High optical quality As_2S_3 chalcogenide glass films have been deposited using the high-repetition-rate laser [Rode et al., 2002]. The surface of the deposited films was at the atomic level with rms roughness of the order of 0.42 nm. The resulting films were highly photosensitive and could be used without thermal annealing for waveguide fabrication using the photo-darkening process [Rode et al., 2002].

We now discuss and analyze the experimental data to demonstrate the effects of cumulative heating in multipulse laser ablation. At low intensity the absorption depth in the chalcogenide glass is large ($\sim 2\,\mu$m at 532 nm). Therefore, the average temperature increase after one pulse in the heated layer is about ~ 150 K. By the time the next pulse arrives at the same spot after a time interval $\Delta t = 13$ ns, little has happened inside the target. The heat propagates a negligible distance of $(Dt)^{1/2} = 4.5 \times 10^{-6}$ cm before the next pulse arrives. Cooling starts only when the heat conduction distance becomes comparable to the focal spot radius $\sim r_{\text{foc}} = 10^{-3}$ cm. Thus, around 5×10^4 pulses can arrive at the same spot before significant cooling occurs. However, the interaction regime begins to change well before this cooling can occur, and therefore the energy absorbed from the subsequent pulses simply accumulates in the focal region.

In the presence of negligible heat losses, the second pulse heats the target to the melting temperature of the glass. After several pulses (~ 4–6) the temperature rises above the boiling point of ~ 1000 K. Thus, the slow process of thermal ablation begins after the sixth to seventh pulse. The temperature continues to rise reaching 1 eV/atom after 100 pulses, and correspondingly the vapor velocity gradually increases up to $\sim 1.5 \times 10^5$ cm/s. Hence the vapor expands a distance of $\sim 20\,\mu$m (approximately equal to the focal spot diameter) in the time between pulses. If we suppose that there is a linear density profile in this expanding plume, $[n = n_0(1 - x/x_0)]$, and that the absorption length scales in inverse proportion to the density $l_a \sim n^{-1}$, then one can estimate the optical thickness of the plume (the absorption depth) as follows:

$$\int_0^{x_0} \frac{dx}{l} = \frac{1}{n_0 l_0} \int_0^{x_0} n(x)dx = \frac{x_0}{2l_0} \tag{5.35}$$

The absorption in the plume becomes significant when the plume size is comparable with the absorption length at the initial density. One can assume one-dimensional (1D) expansion (the expansion length is approximately equal to the focal spot diameter), and the average vapor density is ~ 0.1 of solid-state density. Even after 100 pulses heat conduction losses remain negligible since the heat wave has only propagated a distance of 0.45 μm assuming the initial value for heat conduction still applies. However, at $T \sim 1$ ev (~ 0.1 of the ionization potential) ionization will become significant ($\sim 10\%$) and, therefore, electron heat conduction starts to dominate over thermal

conduction. For example, when the whole material has become singly ionized, the electron thermal diffusion becomes $\sim 1\,\mathrm{cm}^2/\mathrm{s}$—as large as that for metals. Due to ionization the absorption mode also changes, and absorption occurs near the critical density (due to plasma formation) significantly increasing the temperature in that zone. Therefore, the negative effect of the increasing electron heat conduction is overwhelmingly compensated by the changed interaction mode. The estimate for the electron temperature at the critical density ($n_c = 0.1 n_0$) from energy conservation gives

$$T_e \approx M_{\mathrm{av}} \left(\frac{I_{\mathrm{abs}}}{\rho_{\mathrm{crit}}} \right)^{2/3} \tag{5.36}$$

Thus, for $I = 2.65 \times 10^8\,\mathrm{W/cm}^2$; $\rho_{\mathrm{crit}} = 0.32\,\mathrm{g/cm}^3$; $M_{\mathrm{av}} = 49$, a single pulse increases the electron temperature by 2.1 eV—a value comparable to the binding energy. The ion velocity reaches $2 \times 10^5\,\mathrm{cm/s}$, therefore, the plume expands 26 μm between the pulses—a distance that is still comparable with the focal spot diameter. Thus, the isentropic expansion maintains its 1D character and the density decreases ~ 10 times in the time between the pulses, while the temperature decreases $(10)^{2/3} = 4.6$ times to ~ 0.4 eV. Taking the minimum temperature between pulses as $0.2 T_{\mathrm{single}}$, one obtains the maximum temperature after N pulses as $T_n \sim 1.25 T_{\mathrm{single}} \sim 2.6\,eV$, slightly exceeding the As_2S_3 binding energy of 2.2 eV. From the figures above, saturation at the maximum temperature occurs after the third pulse since $T_3 = 1.25 \times T_{\mathrm{single}}$. Electron heat conduction then transfers the absorbed energy from the critical surface to the solid–vapor interface.

5.5 SHORT-PULSE HIGH-REPETITION-RATE LASER SYSTEMS

Ultrafast lasers, which generate optical pulses in the picosecond and femtosecond range, have progressed over the last decade from complicated and specialized laboratory systems to compact and reliable instruments. The use of diode lasers, which replaced inefficient flashlamps for optical pumping, and fast semiconductor saturable absorber mirrors (SESAMs) has dramatically improved short-pulse lasers. New applications and new fundamental research areas have opened up due to the availability of extremely high temporal resolutions in the femtosecond range, extreme optical intensities up to $10^{20}\,\mathrm{W/cm}^2$, and high repetition rates greater than 100 GHz [Keller, 2003].

Let us consider the main laser parameters required for ultrafast laser deposition. The transition to the ultrafast regime of ablation occurs when the laser pulse duration is shorter than thermal diffusion time for dissipating the absorbed laser energy from the skin layer, that is, approximately in the 0.1- to 10-ps range. The average laser power determines the number of atomic bonds broken in the material to be ablated. The current low-repetition-rate excimer lasers commonly used for laser deposition experiments have pulse energy up to 1 J at pulse rates of up to 50 Hz, that is, with average power of ~ 50 W. Higher rates, up to 2 kHz, are available but at much lower single-pulse energy. Consequently, the average power of an ultrafast high-repetition-rate laser should be in excess of 50 W to compete in deposition rate with conventional laser deposition systems. However deposition with megahertz repetition rate lasers has, as discussed in the previous sections, the advantages of (i) forming of a continuous flow of ablated atoms; (ii) of changing the interaction mode, which can lead to a reduction of the ablation threshold in comparison to that required for single pulses, and (iii) smoothing the effective intensity distribution allowing the creation of a single homogeneous phase in the ablated plume.

Ultraviolet (UV) laser radiation is, in general, much better absorbed by most materials, so short wavelengths are preferable in many applications with picosecond lasers. The absorption problem can also be overcome by absorbing the laser wavelength via a particular absorption resonance in the material, that is, if a tuneable laser is available. However, if the laser intensity is high enough to achieve sufficient ionization of the laser plume during the laser pulse, the laser–plasma absorption

permits laser ablation of any material at the same wavelength, such as in the case with femtosecond laser ablation of transparent dielectrics. With subpicosecond pulses the level of required intensity is, in general, above 10^{13} W/cm^2.

Succinctly, the ultrafast laser in the deposition system should have the following parameters: average power 50 W and higher; pulse duration 10 ps and shorter; single-pulse energy should be sufficient to provide the laser fluence on the target surface three to four times the threshold of the particular material to be ablated; repetition rates in the few megahertz range, and the wavelength should preferably be in the UV spectral range (if the level of intensity below the optical breakdown threshold), or continuously tuned to a precise absorption wavelength of the target material. We should note here that each particular target material would require individual tuning of the laser parameters to achieve optimal evaporation conditions for total atomization in the laser plume.

There is a major technical obstacle that still exists between the megahertz-repetition-rate laser deposition technology and its widespread commercialization, which is that there is no commercially available laser system that matches the above parameters for ultrafast laser deposition technology. Furthermore, despite the excellent results already demonstrated and the significant progress in overcoming many fundamental and technical obstacles, the process of industrial application is still constrained by economic barriers that face almost any new high-technology process.

In this section, we briefly consider two different ultrafast high average power laser systems so far developed for ultrafast laser deposition application. One is a table-top SESAM mode-locked diode-pumped solid-state laser, and another one is a single-pass free-electron laser (FEL) based on an electron beam accelerator [Neil et al., 2000]. Both laser systems generate picosecond and subpicosecond pulses with megahertz pulse rates, and both lasers can be tuned to a precise wavelength. In solid-state lasers this could be achieved using optical parametric oscillators (OPO), while in FEL, wavelength tunability is an intrinsic property. The major difference, however, is in the output power: The average power of table-top solid-state lasers is in the range of tens of watts, while a 50-m-long FEL based on the electron accelerator has an average power level up to 10 kW. Both laser systems have already demonstrated record high deposition rates and excellent quality of the deposited films. The wavelength tunability of the FEL in the IR was successfully applied to the deposition of polymers resulting in films with little chemical modification and without change in molecular weight distribution. With solid-state lasers the output of OPOs is approaching the peak power level required for ultrafast laser deposition experiments although such systems have not yet been applied to this problem.

5.5.1 Table-top 50-W Solid-State Ultrafast Laser System

Picosecond and femtosecond lasers have been developed with ever-increasing average power in recent years. High average power can be achieved directly from a laser oscillator with a diode-pumped thin disk and SESAM for passive mode-locking [Innerhofer et al., 2003; Aus der Au et al., 2000; Brunner et al., 2002], or with the use of an additional amplifier stage [Kolev et al., 2003]. With the first scheme, a 60-W average power Yb disk laser producing 810-fs pulses at the wavelength 1030 nm at 34.3 MHz repetition rate was reported recently [Innerhofer et al., 2003], which is a record for the subpicosecond range. The pulse energy reached 1.75 μJ and 1.9 MW peak power. The thermal lensing effects in the dispersive mirrors and a significant additional nonlinear phase shift contributed by the mirrors are currently the limiting factors for any further power increase. A significant further improvement of the laser increasing the output power and reducing the additional nonlinearity from the mirrors may be achieved by multipasses through the disk, which allows one to reduce the intracavity average power and peak intensity.

The second scheme using amplification was used to design a laser system especially for ultrafast laser deposition experiments, and this will be treated in more detail [Luther-Davies et al., 2004;

Kolev et al., 2003]. A crystal of $Nd:YVO_4$ (1% Nd) was pumped by a fiber-coupled laser diode module of nominal power 18 W and a center wavelength 805 nm. The laser-oscillator was a mode-locked diode-pumped solid-state laser with an exceptionally long optical resonator (up to 100 m), and provided 12-ps pulses. Standard mode-locked solid-state lasers usually produce pulses at repetition rates around 50–100 MHz, determined entirely by the length of their optical cavity. Reducing the repetition rate to several megahertz while maintaining the same average power results in an increase of the pulse energy and peak power, respectively. Lowering the repetition rate of mode-locked lasers through increase of the optical cavity requires careful attention to the resonator design to maintain high optical stability.

Providing a variable cavity length up to 100 m with a table-top laser is a complex problem. For cavity extension of our laser-oscillator, a novel design Herriott-type multipass cell (MPC) [Herriott et al., 1964] was developed, allowing laser operation at four different repetition rates: 1.5, 2.6, 4.1, and 28 Hz. In each of the three modes of operation, the laser was continuous wave (cw) mode-locked with an InGaAs quantum well semiconductor saturable absorber mirror(s) (SESAMs) [Keller et al., 1992] grown by metal–organic chemical vapor deposition (MOCVD) at the Australian National University [Lederer et al., 2001]. The ability to switch between different repetition rates provides a way of tuning the pulse peak power to the optimal value for the ablation, which depends on the heat conduction, latent heat of evaporation, and density of the particular target material. Taking into account various constraints, an optimized design was developed for the MPC that fitted comfortably on a 3-m-long optical table while minimizing the number of reflections and, hence, cavity loss. This was a 9/18-pass cell, consisting of two spherical concave mirrors precisely separated by a calculated distance. At the lowest repetition rate of 1.5 MHz there were up to 72 reflections from the MPC mirrors per cavity round trip.

The oscillator beam was amplified by passing several times through a diode-pumped slab-shaped $Nd:YVO_4$ crystal, which was end-pumped and had two polished surfaces. The pumping unit consisted of a 4-bar diode laser stack emitting radiation at 808 nm with an output power of 160 W, a planar waveguide integrator, and an imaging optic. A significant advantage of this amplifier setup is that the beam quality is only decreased slightly after passing the amplifier. The beam quality was investigated via a measurement of the M^2 value. In the stable direction an M^2 value of 1.15 was measured, while in the unstable direction the M^2 was found to be 1.4. The average output power achieved from the amplifier was ~ 48 W. Having high peak power pulses of relatively long picosecond-range duration (as compared with femtosecond lasers) makes the next stage of the system (frequency conversion) highly efficient. This efficient conversion ($>80\%$) into second harmonic and further down into the UV range through external frequency doubling, tripling, and quadrupling helps increase the laser energy absorption in the target material and improves the overall efficiency of the laser ablation process.

We tested the ablation efficiency with the new laser by measuring the ablated mass of aluminum, copper, steel, led, and silicon samples [Luther-Davies et al., 2004]. Experiments on ablation of metals demonstrated a significant increase in evaporation rate to the level of 10^{-4}–10^{-2} g/s, depending on the target material, which, to our knowledge, is a record high for laser ablation with any existing table-top laser system.

The laser will allow very efficient nonlinear frequency conversion to the tunable visible–IR wavelengths. Shortening the pulse duration below 10 ps could be done via soliton mode-locking [Kärtner et al., 1996; Jung et al., 1995] using a Gires–Tournois interferometer for dispersion and strongly nonlinear glass for self-phase modulation management. Further power scaling to 100 W plus average power is possible with a further amplification stage, which will expand the use of the laser for many different applications.

5.5.2 Free-Electron Laser

A free-electron laser is a monochromatic powerful laser source of picosecond and subpicosecond pulses with megahertz-range repetition rate. The average FEL power achieved recently in the

Thomas Jefferson National Accelerator Facility in the United States was up to 10 kW in the IR [Neil et al., 2000], and with a potential of achieving up to 1 kW in UV range [Yu et al., 2003]. It provides an opportunity to study the combined effects of subpicosecond pulses, above 1 kW average power, wavelength tunability (currently in IR), and variable repetition rates in the megahertz range. The laser can be run in both the macropulsed mode at repetition rate up to 10 kHz with macropulses in the microsecond to millisecond ranges, where each macropulse contains picosecond or subpicosecond micropulses at fixed repetition rates of 18.7, 37.4, or 74.8 MHz, as well as in cw mode with a continuous train of micropulses at the same fixed repetition rates. The highest deposition rate of 200 Å/s was recently reported for Nd film deposition [Shinn, 2000]. However, the major drawback of the FEL its total immobility and an extremely high cost.

The free-electron laser was recently used for deposition of Ni–Fe permaloy magnetic films, which are sensitive to deposition conditions. The films were deposited with various repetition rates, and it was found that the best films were produced with the cw mode and at higher repetition rates [Reilly et al., 2003]. The deposited films had smooth surface quality with 4.4-nm rms roughness, and showed a strong [111] $FeNi_3$ peak in the X-ray diffraction spectra. High film quality has a striking effect on magnetization. The films demonstrated very low coercivity of 2 G, while the low-repetition-rate deposited films were highly coercive (115 G) due to a combination of crystallized Fe phase, less crystalline orientation, and rougher surface. The experiments with magnetic films confirmed the earlier observation with ultrafast deposition of diamond-like carbon films [Gamaly et al., 1999; Rode et al., 1999] that better film quality, as measured by crystalline structure, film smoothness, and magnetic properties, is achieved by having lower energy per pulse but higher repetition rates.

The major strength of the FEL for PLD application is its wavelength tunability. The availability of this broadly tuneable infrared high average power FEL is particularly attractive for deposition of polymers [Bubb et al., 2001a, 2001b]. With conventional UV lasers the absorption of photons leads directly to the excitation of electronic states. The excited polymer undergoes rapid pyrolysis and depolymerization followed by repolymerization at the substrate. If repolymerization is incomplete, this can lead to both reduction in molecular weight and change in chemical structure. In contrast, the excitation wavelength of the FEL could be chosen to be resonant with the vibrational wavelength of the target polymer so that the laser energy is controllably channeled into the vibrational excitation in the electronic ground state. As a result, the molecular weight distribution of the target material and the deposited films have very similar profiles indicating that the material transferred without any significant change in the molecular weight. The FEL has been demonstrated to be successful in depositing films of sorbent chemoselective polymers without any apparent changes in physical or chemical properties [Bubb et al., 2001b] and with significant increase in the deposition rates. The photochemical instability of this polymer precludes the use of UV laser deposition.

The results on ultrafast deposition with FEL have demonstrated the ability to produce high-quality films with very high deposition rates and offer the opportunity to extend pulsed laser deposition to complex polymer materials for a number of new biomedical applications such as drug delivery, tissue engineering, spatial pattering of cells, and antifouling coatings.

5.6 CONCLUDING REMARKS

Thin-film production by any method for applications in photonics, optics, electronics, and nanotechnology should possess several important properties: the stochiometry (atomic content) of the initial material should be preserved; the films should be homogeneous, defect and contamination free; the surface finish should approach that of an atomic monolayer; and last but not least, the ablation–deposition rate should match the requirements for industrial applications. It follows from this review that laser ablation by powerful short-pulse multimegahertz repetition rate lasers meets all the above conditions and offers the best solution for ideal ablation and deposition of any solid

material. In summary, we present the main results and a practical guide for the deposition of thin films.

All materials are transformed into the plasma state under the action of a single intense ($>10^{13}$ W/cm^2), subpicosecond laser pulse very early in that pulse [Gamaly et al., 2002]. The resulting laser–plasma interaction ensures strong absorption and heating of the material to a temperature above the ablation threshold. Typically the mass of a material ablated by a single short (~ 100 fs) pulse is equivalent to about 1 μm^3 of solid. Nonequilibrium expansion after the pulse along with the small amount of material ablated inhibits condensation of the plume into droplets. Therefore such a plume used for thin-film deposition can produce a droplet-free surface. The energy deposition in space and time on the surface depends on the laser intensity distribution during the pulse and across the focal spot. To ensure the phase transformation of the ablated material to the same state (atomized vapor) the intensity distribution over the focal spot should be top-hat-like for a single pulse [Gamaly et al., 2004]. Thus, the practical recipe for choosing single laser pulse parameters for ablation or machining of any material including semiconductors and transparent dielectrics is as follows. The laser pulse duration should be short, prepulse and postpulse free, have a top-hat-like spatial intensity distribution across the focal spot, a laser wavelength in the UV range (optimized for the particular material), and a fluence in a range 1–10 J/cm^2 depending on the nature of the sample used. The absorbed laser fluence has to be 3–5 times higher than the ablation threshold to keep the expanding plume in an atomic state. Using such a pulse one can deposit films of atomic surface quality of such different materials as carbon and chalcogenide glass as has been demonstrated experimentally [Rode et al., 1999, 2002].

To compensate the small amount of material ablated per short pulse, high-repetition-rate lasers should be used. Indeed, the use of short-pulse, few-megahertz repetition rate lasers produces the highest ablation and deposition rate of any known methods. Studies of multi-megahertz laser–matter interaction and ablation uncovered several phenomena that bring applications of the laser ablation–deposition process closer. First, the megahertz laser–matter interaction involves accumulation processes due to coupling between successive pulses that changes the interaction mode and thereby reduce the ablation threshold. As a result, high-repetition-rate lasers can ablate a material at fluences below the single-pulse limit. The most striking example presented is ablation and deposition of chalcogenide glass when the single-pulse threshold is around 10 times higher than that required for ablation using a 76-MHz pulse train [Rode et al., 2002]. Another effect of megahertz-rate ablation relates to the smoothing of the evaporation conditions over the focal spot on the target surface because the successive pulses heating the target are shifted by only a small fraction of a micron. Therefore, the spatial pulse shaping, which is required for a single pulse to control the phase state of the plume, is unnecessary in the megahertz-rate ablation regime as demonstrated during deposition of chalcogenide glass films with high optical quality [Rode et al., 2002].

Finally, one can say that ablation by powerful short-pulse multi-megahertz repetition rate lasers appears to be the ultimate solution for the ablation, deposition, and micromachining problems of any material. However a commercial supplier of short-pulse, megahertz repetition-rate lasers with flexible parameters is now needed to make the ultrafast pulsed laser ablation technique ready for a broad range of industrial applications. Fortunately, solid-state laser technology has now reached the point where commercial systems could become available.

REFERENCES

Afanasiev, Yu. V., and Krokhin, O. N. (1971), in *Physics of High Energy Density*, P. Calderola and H. Knoepfel, (Eds.), Academic, New York.

Anisimov, S. I., Imas, Y. A., Romanov, G. S., and Khodyko, Yu. V. (1971), Consultant Bureau, Springfield.

Aus der Au, J., Spühler, G. J., Südmeyer, T., Paschotta, R., Hövel, R., Moser, M., Erhard, S., Karszewski, M., Giesen, A., and Keller, U. (2000), *Opt. Lett.* **25**, 859–861.

Banks, P. S., Dinh, L., Stuart B. S., Feit, M. D., Komashko, A. M., Rubenchik, A. M., Perry, M. D., and McLean, W. (1999), *Appl. Phys. A* **69**, S347–S353.

Bonse, J., Baudach, S., Kruger, J., Kautek, W., and Lenzner, M. (2002), *Appl. Phys. A* **74**, 19–25.

Brunner, F., Südmeyer, T., Innerhofer, E., Morier-Genoud, F., Paschotta, R., Kisel, V. E., Shcherbitsky, V. G., Kuleshov, N. V., Gao, J., Contag, K., Giesen, A., Keller, U. (2002), *Opt. Lett.* **27**, 1162–1164.

Bubb, D. M., Horwitz, J. S., Callahan, J. H., McGill, R. A., Houser, E. J., Chrisey D. B., Papantonakis, M. R., Haglund, Jr., R. F., Galicia, M. C., and Vertes, A. (2001a), *J. Vac. Sci. Technol. A* **19**, 2698–2702.

Bubb, D. M., Horwitz, J. S., McGill, R. A., Chrisey, D. B., Papantonakis, M. R., Haglund, Jr., R. F., and Toftmann, B. (2001b), *Appl. Phys. Lett.* **79**, 2847–2849.

Chrisey, D. B., and G. K. Hubler (Eds.) (1994), *Pulsed Laser Deposition of Thin Films*, Wiley, New York.

Du, D., Liu, X., Korn, G., Squier, J., and Mourou G. (1994), *Appl. Phys. Lett.* **64**, 3071–3073.

Eidmann, K., Meyer-ter-Vehn, J., Schlegel, T., and Huller, S. (2000), *Phys. Rev. E* **62**, 1202–1214.

Gamaly, E. G., and V. T. Tikhonchuk (1988), *JETP Lett.* **48**, 453–456.

Gamaly, E. G., Rode, A. V., and Luther-Davies, B. (1999), *J. Appl. Phys.* **85**, 4213–4221.

Gamaly, E. G., Rode, A. V., Tikhonchuk, V. T., and Luther-Davies, B. (2002), *Phys. Plasmas* **9**, 949–957.

Gamaly, E. G., Rode, A. V., Uteza, O., Kolev, V. Z., Luther-Davies, B., Bauer, T., Koch, J., Korte, F., and Chichkov, B. N. (2004), *J. Appl. Phys.* **95**, 2250–2257.

Herriott, D., Kogelnik, H., and Kompfner, R. (1964), *Appl. Opt.* **3**, 523–530.

Il'insky, Yu. A., and Keldysh, L.V. (1994), *Electromagnetic Response of Material Media*, Plenum, New York.

Innerhofer, E., Südmeyer, T., Brunner, F., Häring, R., Aschwanden, A., Paschotta, R., Hönninger, C., Kumkar, M., and Keller, U. (2003), *Opt. Lett.* **28**, 367–369.

Jung, D., Kärtner, F. X., Brovelli, L. R., Kamp, M., and Keller, U. (1995), *Opt. Lett.* **20**, 1892–1894.

Kärtner, F. X., Jung, I. D., and Keller, U. (1996), *IEEE J. Sel. Top. Quant. Electron* **2**, 540–556.

Keller, U. (2003), *Nature* **424**, 831–838.

Keller, U., Miller, D. A. B., Boyd, G. D., Chiu, T. H., Ferguson, J. F., and Asom, M. T. (1992), *Opt. Lett.* **17**, 505–507.

Kolev, V. Z., Lederer, M. J., Luther-Davies, B., and Rode, A. V. (2003), *Opt. Lett.* **28**, 1275–1277.

Kruer, W. L. (1988), *The Physics of Laser Plasma Interaction*, Addison-Wesley, Redwood City, CA.

Landau, L. D., and Lifshitz, E. M. (1980), *Statistical Physics*, Pergamon Oxford.

Landau, L. D., Lifshitz, E. M., and Pitaevskii, L. P. (1984), *Electrodynamics of Continuous Media*, Pergamon, Oxford.

Lederer, M. J., Kolev, V. Z., Luther-Davies, B., Tan, H. H., and Jagadish C. (2001), *J. Phys. D Appl. Phys.* **34**, 2455–2460.

Lenzner, M., Kruger, J., Kautek, W., and Krausz, F. (1999), *Appl. Phys. A* **69**, 465–466.

Lifshitz, E. M., and Pitaevskii, L. P. (1981), *Physical Kinetics*, Pergamon, Oxford.

Luther-Davies, B., Gamaly, E. G., Wang, Y., Rode, A. V., and Tikhonchuk, V. T. (1992), *Sov. J. Quant. Electron.* **22**, 289–325.

Luther-Davies, B., Kolev, V. Z., Lederer, M. J., Madsen, N. R., Rode, A. V., Giesekus, J., Du, K.-M., and Duering, M. (2004), *Appl. Phys. A*, in press.

Mailis, S., Zergioti, I., Koundourakis, G., Ikiades, A., Patentalaki, A., Papakonstantinou, P., Vainos, N. A., and Fotakis, C. (1999), *Appl. Opt.* **38**, 2301–2308.

Maine, P., Strickland, D., Bado, P., Pessot, M., and Mourou, G. (1988), *IEEE Quant. Electron* **24**, 398–403.

Malvezzi, M., Bloembergen, N., and Huang C. Y. (1986), *Phys. Rev. Lett.* **57**, 146–149.

Miller, J. C., and Haglund, R. F., Jr. (Eds.) (1998), *Laser Ablation and Desorption*, Academic, San Diego.

Millon, E., Albert, O., Loulergue, J. C., Etchepare, J., Hullin, D., Seiler, W., and Perriere, J. (2002), *J. Appl. Phys.* **88**, 6937–6939.

Millon, E., Perriere, J., Defourneau, R. M., Defourneau, D., Albert, O., and Etchepare, J. (2003), *Appl. Phys. A* **77**, 73–80.

Momma, C., Nolte, S., Chichkov, B. N., Alvensleben, F. V., and Tunnermann, A. (1997), *Appl. Surf. Sci.* **109/110**, 15–19.

More, R. M., Warren, K. H., Young, D. A., and Zimmerman, G. B. (1988), *Phys. Fluids* **31**, 3059–3078.

Neil, G. R., Bohn, C. L., Benson, S. V., Biallas, G., Douglas, D., Dylla, H. F., Evans, R., Fugitt, J., Grippo, A., Gubeli, J., Hill, R., Jordan, K., Li, R., Merminga, L., Piot, P., Preble, J., Shinn, M., Siggins, T., Walker, R., and Yunn, B. (2000), *Phys. Rev. Lett.* **84**, 662–665.

Okoshi, M., Higashikawa, K., and Hanabisa, M. (2000), *Appl. Surf. Sci.* **154/155**, 424–427.

Perry, M. D., Stuart, B. C., Banks, P. S., Feit, M. D., Yanovsky, V., and Rubenchik, A. M. (1999), *J. Appl. Phys.* **85**, 6803–6810.

Pronko, P. P., and Pan, X. Q. (2001), *Laser Focus World* **37**(4), 103–105.

Pronko, P. P., VanRompay, P. A., Horvath, C., Loesel, F., Juhasz, T., Liu, X., and Mourou, G. (1998), *Phys. Rev. B* **58**, 2387–2390.

Pronko, P. P., VanRompay, P. A., Zhang, Z., and Nees, J. A. (1999), *Phys. Rev. Lett.* **83**, 2596–2598.

Raizer, Yu. P. (1977), *Laser-Induced Discharge Phenomena*, Consultant Bureau, New York.

Reilly, A., Allmond, C., Watson, S., Gammon, J., and Kim, J. G. (2003), *J. Appl. Phys.* **93**, 3098–3101.

Ristoscu, C., Mihailescu, I. N., Velegrakis, M., Massaouti, M., Klini, A., and Fotakis C. (2003), *J. Appl. Phys.* **93**, 2244–2250.

Rode, A. V., Luther-Davies, B., and Gamaly, E. G. (1999), *J. Appl. Phys.* **85**, 4222–4230.

Rode, A. V., Zakery, A., Samoc, M., Gamaly, E. G., and Luther-Davies, B. (2002), *Appl. Surf. Sci.* **197/198**, 481–485.

Rozmus, W., and Tikhonchuk, V. T. (1990), *Phys. Rev. A* **42**, 7401–7412.

Rozmus, W., and Tikhonchuk, V. T. (1992), *Phys. Rev. A* **46**, 7810–7814.

Schaffer, C. B., Garcia, J. F., and Mazur E. (2003), *Appl. Phys. A* **76**, 351.

Shinn, M. D. (2000), *Proc. SPIE* **4065**, 434–445.

Sokolowski-Tinten, K., Bialkowski, J., Cavalieri, A., Boing, M., Schuler, H., and von der Linde, D. (1998), *Proc. SPIE* **3343**, 47–57.

Sosman, R. B. (1965), *The Phases of Silica*, Rutgers University Press, New Bruswick, NJ.

Stuart, B. C., Feit, M. D., Rubenchik, A. M., Shore, B. W., and Perry, M. D. (1995), *Phys. Rev. Lett.* **74**, 2248–2251.

Stuart, B. C., Feit, M. D., Herman, S., Rubenchik, A. M., Shore, B. W., and Perry, M. D. (1996), *J. Opt. Soc. Am. B* **13**, 459–468.

Weast, R. C., and Astle, M. J. (Eds.) (1981), *CRC Handbook of Chemistry and Physics, 60th ed. CRC Press, Boca Raton, FL.*

Wharton, K. B., Boley, C. D., Komashko, A. M., Rubenchik, A. M., Zweiback, J., Crane, J., Hays, G., Cowan, T. E., and Ditmire, T. (2001), *Phys. Rev. E* **64**, 025401, 1–4.

Yu, L. H., DiMauro, L., Doyuran, A., Graves, W. S., Johnson, E. D., Heese, R., Krinsky, S., Loos, H., Murphy, J. B., Rakowsky, G., Rose, J., Shaftan, T., Sheehy, B., Skaritka, J., Wang, X. J., and Wu, Z. (2003), *Phys. Rev. Lett.* **91**, 074801.

Zel'dovich, Ya. B., and Raizer, Yu. P. (2002), *Physics of Shock Waves and High-Temperature Hydrodynamic Phenomena*, Dover Publications, Mineola, NY.

Zergioti, I., Mailis, S., Vainos, N. A., Ikiades, A., Grigoropoulos, C. P., and Fotakis, C. (1999), *Appl. Surf. Sci.* **138/139**, 82–86.

Zergioti, I., Papazoglou, D. G., Karaiskou, A., Fotakis, C., Gamaly, E., and Rode, A. (2003), *Appl. Surf. Sci.*, **208/209**, 177–180.

Zhang, Z., VanRompay, P. A., Nees, J. A., Clarke, R., Pan, X., and Pronko, P. P. (2000), *Appl. Surf. Sci.* **154/155**, 165–171.

CHAPTER 6

Cross-Beam PLD: Metastable Film Structures from Intersecting Plumes

ANDRÉ GORBUNOFF
University of Applied Sciences–Dresden, Dresden, Germany

6.1 INTRODUCTION

In the present chapter the properties of metastable film structures synthesized via high-vacuum cross-beam pulsed laser deposition (CBPLD) are considered. In the high-vacuum regime the atoms of the background gas influence neither the propagation of the plume of the ablated species from the target to the substrate nor the film properties. CBPLD is a particular high-vacuum PLD variant where the transport of molten droplets to the substrate is reliably prevented through filtering out in the intersecting ablation plumes. The absence of these macroinclusions in the films allows the implementation of a large number of surface averaging methods to characterize the structure and properties of the films produced.

The following topics will be discussed in this chapter:

1. Consideration of PLD as a highly nonequilibrium hyperthermal particle beam deposition technique with a specific shallow implantation (''subplantation'') film growth mode
2. The metastable phase formation in PLD as an inherent PLD feature
3. Principles of operation and spatio-energetical characteristics of CBPLD
4. Properties of transition layers between adjacent layer materials in CBPLD
5. Characterization of metastable phases that develop in thin films of binary alloys of two representative materials systems co-deposited in CBPLD

It will be concluded that the properties of the ablation plume in CBPLD are comparable to those in conventional (or direct) PLD. Consequently the results obtained for CBPLD can be extended for PLD in general. Only high-vacuum PLD will be implied in this chapter.

6.1.1 Energetic Particles in PLD

As with the other processes that include phase transitions, all vapor deposition techniques have an essentially nonequilibrium nature. The resulting film properties are therefore generally highly dependent on the deposition conditions. There are only a few factors that significantly determine the nucleation and growth kinetics, microstructure evolution, and properties of films grown by physical

Pulsed Laser Deposition of Thin Films: Applications-Led Growth of Functional Materials
Edited by Robert Eason

vapor deposition: the type and energy of condensing species, the deposition rate, the substrate temperature and the substrate material. Whereas the nature of the substrate and temperature are more or less independent variables, those connected with the species arriving on the substrate are strongly dependent on the deposition technique chosen.

6.1.1.1 Interaction of Energetic Particles with Solids

The most significant energetic particle–solid interactions that control the properties of thin films deposited from particles within the energy range relevant for thin-film deposition are summarized in Figure 6.1. By particles we imply any kind of atomic species (neutral atoms, ions, small clusters) that arrive at the substrate. The thermal particles cover the energy range below 1 eV, whereas the accelerated ions usually have energies exceeding 1 keV. The energy range in between these two is frequently referred to as ''hyperthermal'' and may be considered most typical for PLD.

Surface Precleaning Typical desorption energies of physisorbed impurities are less than 1 eV and of chemisorbed ones on the order of 1–10 eV. The sublimation energy of clean metal surfaces lies also in the latter range. Bombardment with particles of these energies may lead to the removal of surface contaminants and atoms near the surface considerably improving the film adhesion to the substrate.

Layer-by-Layer Film Growth The collapse of unstable clusters starting from the ion energy of 0.1 eV and the displacement of surface atoms by ballistic collisions at 10 eV enhance the mobility of adatoms and can turn the films from the island growth to the layer-by-layer growth mode. The disruption of the column growth makes layers more homogeneous and prevents in addition the absorption of gases and water in voids between the columns.

Sputtering The particle energy threshold for ejection of target atoms is less than 30 eV for most materials. Resputtering of loosely bound species contributes to the collapse of voids and the formation of a denser crystalline or amorphous microstructure of the films. In addition, the

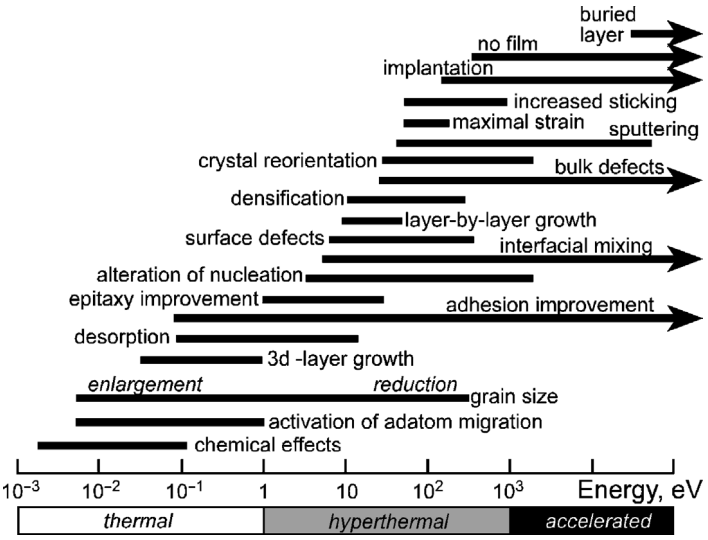

Figure 6.1 Energy ranges for particle–solid interactions that most significantly influence the thin film properties.

backscattered material randomizes the deposition direction and hence fills in the shadowed ''valleys'' that develop in the absence of the ion bombardment. Near the threshold, however, the atom ejection is very sensitive to the microstructure of the target and especially to the properties of its surface layer. The preferential sputtering of surface species may lead to changes in the film composition.

Structural Defects Defect formation on the surface and in the bulk affects most significantly the microstructure of growing films.

Short-lived surface point defects (vacancies) have a formation threshold of $\approx$20 eV. They mostly intensify the nucleation rate, which in turn determines the grain size of the thin-film material [Guseva, 1986]. These defects can even promote the growth of homoepitaxial superlattices on disordered layers on the surface of oriented substrates [Gaponov et al., 1981]. Similar effects are observed during the ion-beam-assisted deposition where the growing film is additionally bombarded by high-energy noble gas atoms [Greene, 1994; Esch et al., 1995; Kalff et al., 1997]. However, the opposite effects of the nuclei dissociation and intensification of island formation through the ion-enhanced surface diffusion is also possible [Smidt, 1990]. To avoid this effect, Wulfhekel et al. [1996] have suggested gentle bombardment of the growing surface with low-energy ($\approx$1 keV) ions *before* the deposition of a film monolayer. Using this pulsed ion-beam-assisted deposition, they have forced the layer-by-layer growth of Ni on Cu at room temperature via thermal deposition.

Permanent lattice defects (Frenkel pairs) arise at collision energies above $\geq$40 eV. Having a low activation energy for diffusion of about 0.1 eV, interstitials can easily reach dislocations or grain boundaries where they can form small clusters. They introduce an extra volume in the grain boundaries. Since the film is bound to the substrate, this extra volume can produce a high compressive stress and enlargement of the lattice parameter in the growth direction [Krebs, 1997]. Ion bombardment of more refractory materials can beneficially affect their hardness and yield stress.

A practical significance of the ion-induced defect formation phenomena is that the microstructure of ion-bombarded films is practically independent of the substrate temperature.

Implantation Typical displacement energies of atoms in metals are of the order of 20 eV. With increasing ion energy ε above the displacement energy threshold, they penetrate increasing deeply into the substrate. At $\varepsilon > 30$ eV (the so-called critical energy of subplantation [Uhlmann et al., 1997]), the maximum of the projectile distribution moves beneath the free surface of the substrate. The penetration of incoming film particles beneath the surface of the substrate reduces their mobility and contributes to the reduction of the grain size and porosity through the permanent grain renucleation. The most marked decrease in the crystallite size occurs at ion energies $\lesssim$100 eV. Films produced at energies above 150 eV are usually free of voids and no longer show columnar grain morphology. Further increase of the ion energy can lead to another increase of the grain size [Smidt, 1990].

The high initial nucleation density and mixing implantation of incident particles increase their probability of sticking and can greatly improve the adhesion of the film to the substrate.

Subplantation Film Growth Mode The range of the projectile particles with an energy of 1 keV in solids does not exceed a couple of monolayers (Fig. 6.2). This shallow subsurface implantation (''subplantation'') of incoming hyperthermal particles gives rise to a unique *subplantation film growth mode*. The subplantational model of film growth from hyperthermal ion beams was first suggested by Lifshitz et al. [1990, 1993], and it cannot be reduced to any of three ''classical'' growth models (Stranski–Krastanow, Frank–Van der Merwe, and Volmer–Weber). Instead of being deposited onto the substrate surface, the hyperthermal particles exhibit shallow implantation into the upper monolayers of the surface material. Since the volume diffusion coefficient is many orders of magnitude smaller than that of surface diffusion (4–5 orders of magnitude lower even at the melting temperature), no significant redistribution of the implanted and replaced atoms, as compared to the atoms on the surface, can take place at room temperature. The result is the configurational freezing

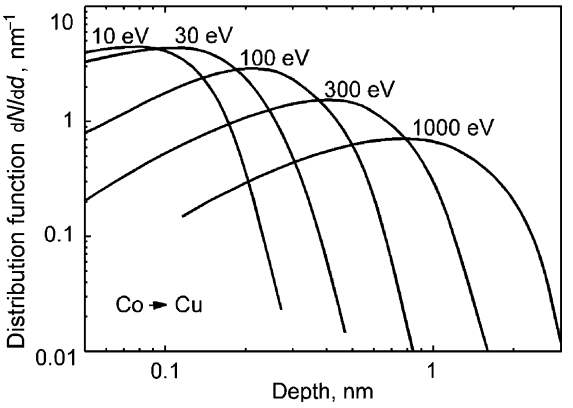

Figure 6.2 Monte Carlo ballistic simulations (the TRIM code [SRIM, 2003]) of the distribution function dN/dd of projectile Co ions as a function of the depth d beneath a Cu target surface at different hyperthermal projectile energies.

of incorporated structural defects, an extended solubility of finite miscible materials and corresponding internal stresses. The film grows therefore beneath the free surface in some frozen-in metastable state. Although this film growth mode is now generally acknowledged to be the peculiar mode of film growth from hyperthermal particle beams [Nastasi et al., 2000], the subplantational growth model has been mainly applied so far for the description of the growth of diamond-like carbon coatings (see, e.g., Jäger and Belov [2003] and also Chapter 15). It will be demonstrated in the following sections that subplantation is the main growth mode for the wide range of materials deposited by PLD.

6.1.1.2 PLD as a Hyperthermal Ion Beam Technique

As seen from Figure 6.1, the most diverse energetic particle-induced phenomena take place in the hyperthermal energy interval. However, in comparison to thermal particles and accelerated ions, which are routinely implemented in film deposition and implantation technology, hyperthermal energy particles are instrumentally difficult to produce and to handle, and have therefore a great development potential. As will be demonstrated in Section 6.2.2, the laser ablation plasma in vacuum represents perhaps the most efficient source of energetic particles in the hyperthermal energy region. Therefore, besides all its known disadvantages, PLD is a promising hyperthermal ion beam deposition technique. Through the subplantation growth mode, PLD is especially advantageous for the fabrication of single- and multilayer film structures with unusual physical properties.

With regard to the influence of the above phenomena on the film structure and properties, it is reasonable to group the energetic particles in PLD into the characteristic energy intervals listed in Table 6.1.

6.1.2 Origin of Metastable Film Structures in PLD

In nanostructured materials a large fraction of atoms reside in or adjacent to defects, which leads to significant changes in the resultant properties of the solid. From the thermodynamical viewpoint, these nanostructured materials possess an excess Gibbs free energy, or, in other words, they are in a metastable state. Most frequently the excess free energy can be attained by energizing the system followed by rapidly reducing the mobility of atoms (quenching) to effect the configurational freezing. The energizing can be attained, for example, by melting, evaporation, sputtering, dissolution, irradiation, implantation, mechanical deformation, or creation of interfaces. The diffusive motion of atoms within bulk phases, along grain boundaries, and across the free surface can

TABLE 6.1 Characteristic Energy Intervals of Energetic Particles in PLD with Reference to Their Effects on Film Structure and Properties

Energy Range (eV)	Ion-Induced Effects
1–10	Surface cleaning, 3D film growth.
10–40	Surface defects, cluster disintegration, void collapse, enhanced adatom mobility, layer-by-layer film growth. Thresholds of bulk defect formation and sputtering. Chemical effects have a considerable influence on the final distribution of the film and substrate materials.
40–100	Permanent lattice damage, grain size reduction, amorphization. Impact effects are sensitive to the surface and bulk crystalline structure. The penetration depth of incoming particles is still influenced by the chemical properties of film–substrate materials.
>100	Intensive sputtering, collisional cascades, ballistic implantation and mixing, and ''subplantational'' film growth mode. The ratio of surface-to-bulk defects is well below unity. The influence of the chemical affinity and crystallinity of the film–substrate materials on the outcome of the energetic particle collision weakens.

roughly be considered as frozen below a reduced temperature T/T_m of ≈ 0.4, ≈ 0.1, and ≈ 0.2, respectively [Cahn and Greer, 1996]. Since the melting point of most metals, T_m, is $> 1000^\circ$C, their bulk atomic configuration cannot undergo significant changes at room temperature, and they can be considered as configurationally frozen and kinetically metastable.

The kind of metastability (morphological, compositional, or structural) that can be realized under given experimental conditions is dependent on the particular material system under consideration. For example, systems with a large negative heat of mixing and high mobility of one of the constituents (e.g., Fe–Al) tend to extended solid solubility and amorphization [Chopra, 1969; Giessen, 1982]. The formation of extended solid solutions and amorphous phases has also been observed in several systems with a positive heat of mixing, such as Fe–Cr or Cu–Co [Gente et al., 1993].

The thermalization rate of the deposited material in PLD is extremely high and lies between $\langle \varepsilon \rangle / \tau = 10^{11}$–$10^{18}$ K/s, where $\langle \varepsilon \rangle \sim 100$ eV is the mean ion energy and τ is the relaxation time. The upper limit corresponds to the thermalization of the ion cascades with $\tau \leq 10^{-11}$ s and the lower limit is determined by the duration of the deposition pulse in PLD, $\tau \sim 10^{-5}$ s, which is determined by the arrival time spread of the ablation species at the substrate. Under such extremely nonequilibrium formation conditions, the kinetic factors (diffusion rates) rather than thermodynamic ones (potential barrier heights) play a major role in formation of the physical structure of the growing films. Along with the low mobility of subplanted adatoms, it makes the formation of metastable phases in PLD highly probable. The selected examples below support this inference.

Bykovski et al. [1988] have compared the structure of Co films deposited by PLD and by thermal evaporation. The PLD films were highly dispersed nanocrystalline with a dominating face-centered cubic (fcc) microstructure, whereas the thermally deposited films had the stable low-temperature hexagonal close-packed (hcp) crystalline microstructure of cobalt.

Krebs and Bremert [1993] reported on the formation of amorphous phases in $Fe_{50}M_{50}$ (M = Zr, Nb, Ti, Hf), $Cu_{50}Zr_{50}$, and $Pd_{80}Si_{20}$ alloys deposited by PLD. Instead of the decomposition in the immiscible materials systems such as Fe–Nb, Fe–Ag, and Fe–Cu, a continuous series of polycrystalline supersaturated solid solutions were formed.

A homogeneous nonequilibrium crystalline alloy with a supersaturation of >44 at % Ag in the PLD-co-deposited Ag–Ni system was reported by van Ingen et al. [1994]. It is remarkable that this material system possesses such a high driving force for decomposition that the constituents are insoluble in both the solid and the liquid equilibrium states.

Blyakhman et al. [1995] reported on the formation of supersaturated paramagnetic phases in nanometer-period Fe–C and Fe–Cr multilayers. Upon high-temperature annealing these metastable solutions decompose with a formation of a ferromagnetic phase.

A pronounced enlargement of the lattice parameter in the growth direction in PLD elementary, multilayer, and alloy films has been observed by Luo and Krebs [1995] and Störmer and Krebs [1995]. This enlargement has been attributed to high internal stresses due to the interface mixing of the neighboring materials in multilayers. Below a critical bilayer thickness of about 4 nm the Fe/Nb multilayers were completely amorphous. The authors argue that in the materials systems such as Fe–Nb, with a negative heat of mixing, the formation of the equilibrium crystalline intermetallic compounds is suppressed due to the high quenching rates. The observed amorphous phase formation in the demixing Fe–Ag system is believed to be more energetically favored as a nanocrystalline solid with an increased interfacial energy.

A noncubic ''interface phase'' in laser-deposited Fe–Al multilayers has been detected by Geilman et al. [1997], and it will be demonstrated in Section 6.3.2.2 that this is an amorphous Fe–Al alloy.

It is important to note here that it is the laser ablation process that produces the atomization of the target material in PLD. It has an explosive-like character and is accompanied by the formation of particulates (droplets, debris, powder particles), which are transferred by the ablation plume to the substrate and incorporated in the growing film. This problem is often considered as a major drawback of conventional or direct PLD (DPLD) where the substrate is immediately exposed to the laser-induced plasma. Since the amount of material in the droplets can be even higher than in the film itself, the interpretation of the results of the film characterization by surface-averaging methods may be misleading. For example, the X-ray diffraction spectrum of the crystal structure of PLD Fe–Al films in Figure 6.3 deposited without any droplet removal technique shows sharp peaks of the crystalline phases of two metals. On the basis of this observation one can make the conclusion that the alloy is decomposed into two independent Al- and Fe-rich phases. However, these crystalline peaks disappear completely after application of the macroparticle separation technique revealing the true amorphous microstructure of the alloy.

A concise review of the major mechanisms of particulate formation and the most important measures for their prevention can be found elsewhere [see, e.g., Gorbunoff, 2002]. In the following section, one of the most effective droplet separation techniques, the gas-dynamic droplet filtering in colliding laser plumes, will be considered in more detail.

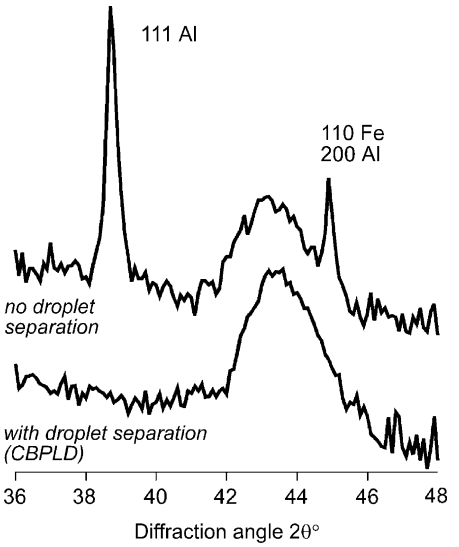

Figure 6.3 XRD (Cu–K_α) spectrum of the similar Fe–Al multilayers deposited with and without droplet separation [Levin et al., 2001].

6.2 TECHNIQUE OF CROSS-BEAM PLD

6.2.1 Basic Idea and Instrumentation

The idea of gas-dynamic droplet separation in colliding laser plumes was initially proposed by Gaponov et al. [1982]. In this technique two colliding laser ablation plumes interact with each other, and the gaseous species are redirected toward a substrate placed outside the directional patterns of either ablation plume. The heavy macroparticles, which were at that time believed to be due to condensation, are not deflected from their original trajectories and cannot therefore reach the substrate. Experience has shown, however, that the macroparticles are ejected from the laser-ablated surface of the target, which is why the technique cannot work well in this initially proposed scheme.

The technique was applied a decade later for the deposition of high-temperature superconducting ceramics in a background oxygen atmosphere of 20–100 Pa by Pechen et al. [1992] and Strikovsky et al. [1993]. In addition to the scheme of Gaponov et al. [1982] both groups introduced a special diaphragm that shadowed the substrate from the direct exposure of the primary ablation plumes. Despite a definite reduction of the round-shaped droplets splashed from the targets, Strikovsky et al. [1993] have observed a large number of faceted crystallites embedded in the film, whose surface density was dependent on the separation of the substrate from the interaction zone. It was suggested that these were particles that had been either condensed in the supercooled vapor near the substrate or nucleated on the substrate itself. Lambert et al. [1999] have used the same technique to deposit cryolite films but also found about 5000 microinclusions/cm^2 per 1 nm of film thickness.

The present form of this crossed-beam technique has now been named cross-beam PLD (CBPLD) [Gorbunov et al., 1996]. It allows a radical reduction of any form of macroparticle contamination in the PLD films and will be discussed in detail below.

The principle of thin-film deposition by CBPLD is apparent from Figure 6.4a. It can be considered as a twinned PLD where two cylindrical targets are brought so close to each other that the emerging ablation plumes can interact. The essential part of the system is a diaphragm, which is

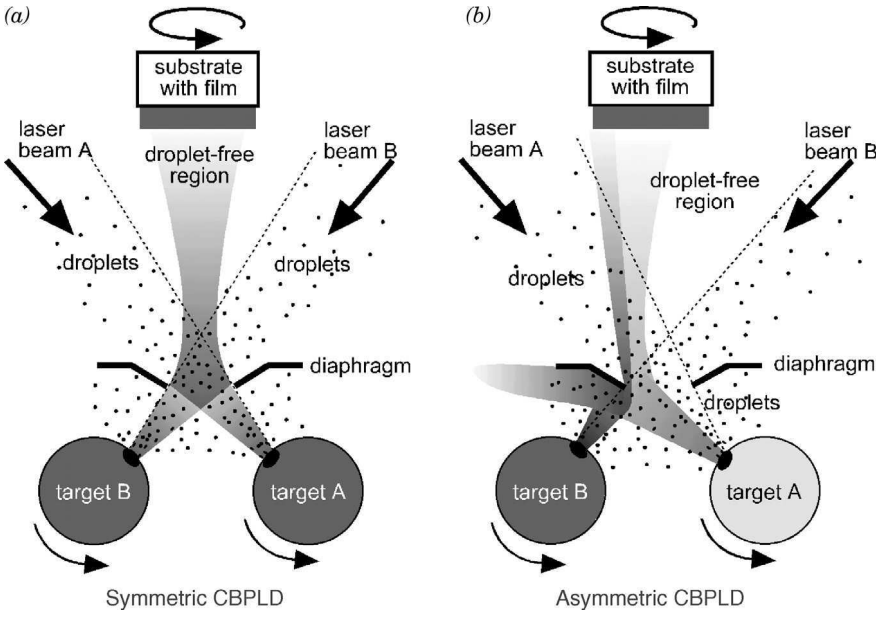

Figure 6.4 Principle of operation of (a) symmetric and (b) asymmetric cross-beam PLD [Gorbunov et al., 1996; Tselev et al., 2001].

designed and positioned in such a way that it screens the substrate from the direct line-of-sight of each ablation plume. Without laser synchronization, both plasma plumes do not interact and propagate fully independently. No deposition of either film or macroparticles can therefore occur. If both lasers are triggered simultaneously, the plasma plumes intersect each other about the axis of symmetry of the system. If the local plasma density in this intersection region is high enough (this point will be considered in Section 6.2.2) and the horizontal momentum components of both colliding laser plumes compensate each other, the resultant plasma flow can effectively be deflected toward the substrate.

Heavy macroparticles ejected from the targets or condensed at the early stages of the plasma evolution will not be deflected since their velocity is much smaller than that of the plasma. They enter the intersection region later than the core of the plasma cloud, when the local plasma density and their own concentration are too low to induce collisions and provide sufficient momentum transfer in the direction of the substrate.

The condition for the horizontal momentum compensation is fulfilled automatically in the case of the same target materials if the laser ablation conditions are equal for both targets. This mode of operation is realized in the symmetric CBPLD presented in Figure 6.4a. However, the target materials do not necessarily have to be identical. An interesting option of CBPLD consists of the possibility of ablating two different materials, which can be mixed directly in the colliding laser plumes and subsequently deposited onto the substrate. This asymmetric mode of CBPLD operation for co-deposition of different materials with continuously variable ratios is depicted schematically in Figure 6.4b. An additional ''balancing'' of the plasma fluxes through the adjustment of the respective laser fluences on each target is required here, to obtain the correct direction and composition of the resulting plasma plume.

The shape of the diaphragm appears to play a decisive role for the deposition of inclusion-free films. An analysis of the geometry of the plume interaction with the diaphragm revealed that irregular macroinclusions in the films deposited by Pechen et al. [1992], Strikovsky et al. [1993], and Lambert et al. [1999] are flakes of the film that are initially deposited onto the diaphragm and subsequently peeled off under heavy plasma impacts. With an improperly chosen diaphragm shape, these flakes are transported with the plasma flow toward the substrate. To avoid this effect, Gorbunov et al. [1996] have proposed to use a V-shaped diaphragm formed in such a way that the plasma striking its edge is deflected away from the diaphragm opening. This simple solution resulted in a reduction of at least a factor of 1000 in the surface density and the areal extent of macroinclusions in such CBPLD films. The extreme difference between the surface appearance of the Fe–Al multilayers of the same composition deposited by DPLD and CBPLD is demonstrated in Figure 6.5. Large

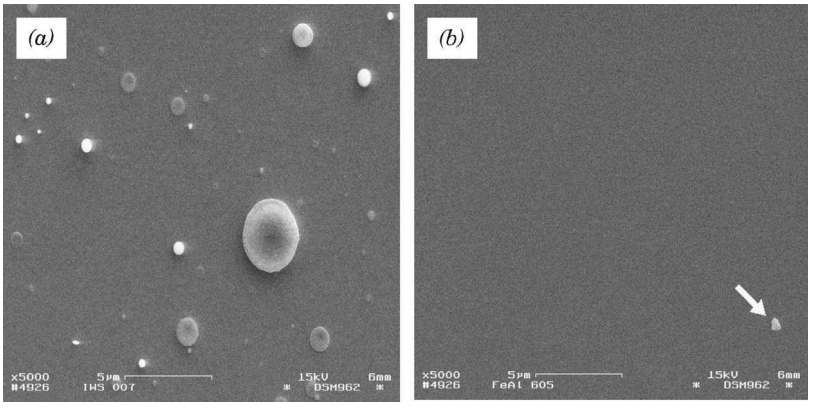

Figure 6.5 Comparison of the appearance of similar Fe–Al multilayers deposited by (a) direct PLD and (b) CBPLD. The arrow in (b) points to a dust particle on the film surface that has been used for focusing.

droplets of < 1–25 μm in size emitted from the target cover the surface of the DPLD film (Fig. 6.5a); by comparison, they are completely absent in the CBPLD films (Fig. 6.5b).

The following CBPLD arrangement has been used in most experiments described below. The laser ablation of the targets was performed by two Q-switched solid-state lasers supplying 15-ns pulses of up to 1 J energy with a pulse repetition rate of 15 Hz at the wavelength $\lambda = 1.08$ μm. The laser beams were focused on the surface of cylindrical targets at a peak laser intensity of 1–2 GW/cm^2 (corresponding to a laser fluence of 7.5–15 J/cm^2). This intensity belongs to the regime where the film deposition rate is practically independent on the laser fluence [Gaponov, 1985], thus stabilizing the deposition rate against slight pulse-to-pulse variations of the laser energy. The target mount allows a sequential deposition from two pairs of spirally rotating targets. The purity of targets was 99.95 at % or better. All the films considered in this chapter were deposited at room temperature on oxidized silicon wafers with an oxide layer thickness of 500 nm.

The deposition is performed in a high-vacuum chamber with a base pressure of 10^{-6} Pa, and the film thickness is controlled by a quartz monitor. Electrostatic ion collectors (Langmuir probes in the ion current saturation mode) biased to -15 V were used for alignment of the system and monitoring the deposition process.

The structure and composition of the films was studied by high-resolution transmission electron microscopy (TEM), energy-dispersive X-ray spectroscopy, electron energy loss spectroscopy, selected area electron diffraction (ED), X-ray reflectometry and diffraction (XRD), Rutherford backscattering, and extended X-ray absorption fine structure spectroscopy (EXAFS). The films for the TEM characterization were deposited on a freshly cleaved face of a NaCl monocrystal. The nanoindentation tests were performed by using an electrostatic transducer attached to an atomic force microscope. The electrical resistivity of the films was measured by a standard four-point probe method with 1-mm separated gold-plated probes in a linear arrangement. The current through the sample during measurements did not exceed 1.5 mA. The potential drop was measured by a high-ohmic digital voltmeter. Magnetization measurements have been carried out in the in-plane geometry by a superconducting magnetometer. Lift-mode magnetic force microscopy (MFM) served for the local qualitative magnetic characterization of the films.

6.2.2 Spatio-energetical Characteristics of the Plume in CBPLD

The plasma deflection toward the substrate in CBPLD is a result of particle collisions in the intersection region, which inevitably brings about a transformation of the plasma characteristics. Of practical importance for PLD are energies, the ionization ratio of the plasma species, the efficiency of the target material usage, as well as new spatial distribution in the redirected plasma jet. These characteristics were studied by Gorbunov et al. [1996] and Tselev et al. [1999a, 1999b, 2001], and the main results of these studies are summarized below.

6.2.2.1 Particle Energies in CBPLD

The dynamics of the colliding ablation plasma plumes can be visualized using the Langmiur probe technique. The arrangement of the probes and the probe signals in three different experimental situations is presented in Figure 6.6. At early instants signals 1 and 2 from probe A for both DPLD and CBPLD coincide. This means that the most energetic particles at the leading edge of each individual laser plume cross one another almost without interaction. When the plasma density in the intersection region increases sufficiently that the particles can undergo collisions, they can start being deflected toward the substrate. This time will be referred to in the following as *the first deflection instant.* For iron this corresponds to an ion energy $\varepsilon_i = 730$ eV. At this instant signal 2 drops sharply in comparison to signal 1. After the densest part of the plasma passes the intersection region, the plasma density starts to decrease, the intersection region becomes more transparent for the particles of each primary plasma plume, and low-energy ions can again reach probe A. This time will be referred to as *the second deflection instant.* As a result, in the CBPLD geometry, the primary plasma jets propagating along the target normal lose their ''middle-energy'' part, which is deflected toward the substrate.

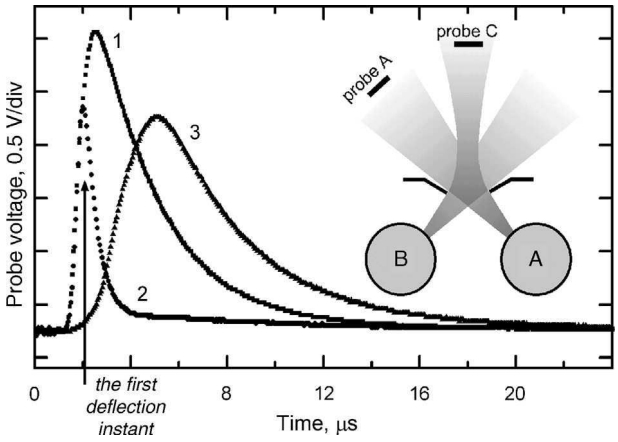

Figure 6.6 Probe arrangement and signals for an iron target [Tselev et al., 1999a, 1999b, 2001]. (1) Probe A, laser A (geometry of direct PLD); (2) probe A, lasers A+B; (3) probe C, lasers A+B (CBPLD geometry).

As was discussed in Section 6.1.1, the energy of particles impinging on the surface of the substrate during film deposition plays a determining role in the structural and physical properties of the growing films. That is why the energy composition of the plasma plume, which contains both neutral atoms and ions, is one of the most important characteristics of any deposition technique.

The highest energy of plasma ions $\varepsilon_{i\max}$ has been determined from the very beginning of the Langmuir probe signal. The mean ionic energies $\langle\varepsilon_i\rangle$ can be derived from the corresponding ion energy distribution functions, which can be extracted under the appropriate assumptions [Tselev et al., 1999a, 1999b] from the probe signals. Ion energies in both DPLD and CBPLD are compared in Table 6.2.

The whole energetic composition of the plasma plume can be found by taking into account the neutral components of the plasma. Since these plasma neutrals are not registered by the ion probe, Tselev et al. [1999a, 1999b] have simply assumed that their mean kinetic energy comprises 10% of that of ions, which is in reasonable agreement with the experimental data of Akhsakhalyan et al. [1982]. One can then obtain the mean kinetic energy $\langle\varepsilon\rangle$ of the whole atomic particle content of the plasma stream:

$$\begin{cases} \langle\varepsilon\rangle \approx (0.9\beta + 0.1)\langle\varepsilon_i\rangle & \beta \leq 1 \\ \langle\varepsilon\rangle = \langle\varepsilon_i\rangle & \beta > 1 \end{cases} \tag{6.1}$$

The ionization ratio of the plasma, β, can be found by comparing the total elementary charge per unit area registered by the probe with the atom number per unit area of the film grown in one deposition pulse. In doing so, however, one should take into account that the number of atomic species forming the film can differ considerably from the number of the species arriving at the substrate due to factors such as incorporation of droplets and resputtering. For example, Jordan et al. [1995] have observed that the ion dose (measured by a Faraday cup) was higher than the deposited mass (measured by a quartz thickness monitor) by a factor of 2. Franghiadakis et al. [1998] have compared the amount of the deposited material integrated over the whole angular distribution range with the total amount of material ablated from the target, and they have estimated the sticking coefficient of Si in excimer PLD to be only 0.25.

The contribution from droplets in CBPLD can be ignored. To account for the resputtering, one can assume that only energetic ions contribute substantially to the sputtering of the film material. The effective sputtering yield $\langle Y\rangle$ can then be determined for each material by averaging the

TABLE 6.2 Maximum $\varepsilon_{i\,\max}$ and Mean $\langle\varepsilon_i\rangle$ Kinetic Energies of Plasma Ions Effective Sputtering Yield $\langle Y\rangle$, Plasma Ionization Ratio β, Mean Kinetic Energies of Plasma Particles $\langle\varepsilon\rangle$ in DPLD (D) and CBPLD (CB)

Target (Z)	Al (13)		Ti (22)		Fe (26)		Co(27)		Pt (78)	
PLD Kind	D	CB	D	CB	D	CB	D	CB	D	CB
$\varepsilon_{i\,\max}$, eV	1374	724	1724	850	2011	972	2296	773	1940	1998
$\langle\varepsilon_i\rangle$, eV	247	121	263	121	274	84	319	85.8	247	112
$\langle Y\rangle$, ion^{-1}	0.68	0.38	0.55	0.26	0.8	0.24	0.82	0.22	0.77	0.28
β	0.76	1.26	0.6	1.02	0.47	0.79	0.52	0.9	0.56	0.7
$\langle\varepsilon\rangle$, eV	195	121	169	121	143	68	182	78	150	82

Source: From Tselev et al. (1999b).

sputtering yield $Y(\varepsilon_i)$ for a given ion energy ε_i throughout the whole ion energy distribution by using the approximate relationship derived by Zalm [1984]:

$$Y(\varepsilon_i) \approx \frac{1.9}{\Omega}\sqrt{Z}(\sqrt{\varepsilon_i} - 0.09\sqrt{\Omega}) \tag{6.2}$$

where Ω is the sublimation energy in electron volt/atom and Z is the atomic number. The effective sputtering yield $\langle Y\rangle$, the ionization ratio β corrected for resputtering, and the mean energy of the whole atomic plasma species $\langle\varepsilon\rangle$ are presented in Table 6.2. It is seen that the resulting $\langle\varepsilon\rangle$(CBPLD) lies between 0.5 and 0.75 of $\langle\varepsilon\rangle$(DPLD). This energy reduction correlates well with the energy loss factor in inelastic scattering of two atoms, which can be estimated as $\cos^2\varphi = 0.62$ with $\varphi = 38°$ being the half-angle between the laser beams.

Grouping of particles into their characteristic energy intervals according to the scheme proposed in Table 6.1 is presented in Figure 6.7. It is seen that despite the different distributions

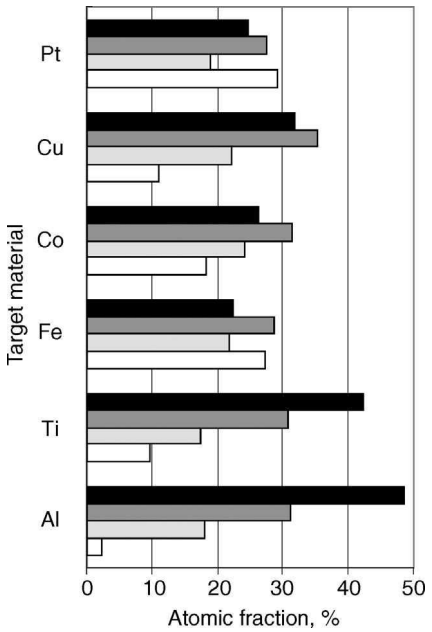

Figure 6.7 Distributions of the particles in CBPLD ablation plumes of selected metals into energy groups: (white) 1–10 eV; (light gray) 10–40 eV; (dark gray) 40–100 eV; (black) >100 eV.

of the particles over their specified energy groups, more than one half of all the particles can penetrate deeper than one surface monolayer into the substrate, giving rise to the subplantation growth mode of the PLD films.

As can be seen from Table 6.2, the ionization ratio of the ablation plume β in CBPLD is roughly twice as large as β (DPLD) and can exceed 100%. This has been confirmed by spectroscopic investigations by Tselev et al. [2001]. They have also compared the cross sections of possible ionization reactions and found that a collision between two excited atoms resulting in deexcitation of one and subsequent ionization of the other one, $A^{ex} + A^{ex} \rightarrow A^{+} + A + e$, should be the most probable mechanism of the additional plume ionization in CBPLD.

6.2.2.2 Efficiency of Plume Interaction in CBPLD

The amount of redirected material determines the efficiency of the material usage in CBPLD. It is reasonable to assume that the leading edge of the plasma plume is composed mainly of energetic ions. The plasma number density n^* in the interaction zone at the first deflection instant can be determined from the ion current density $j^*(t)$ measured by probe A:

$$n^* = \frac{tj^*(t)}{eL}\left(\frac{L}{l}\right)^3 \tag{6.3}$$

where the $(L/l)^3$ scales the measured number density near the probe to that in the intersection region, L and l being the distances of the probe A and the intersection zone from the target surface, respectively.

The calculated critical value for most of the metals investigated was $n^* \approx 1.4 \times 10^{15}\,\mathrm{cm}^{-3}$ [Tselev et al., 2001]. The corresponding mean free path, λ^*, of a probe ion traveling through the plasma plume was $\approx 6\,\mathrm{mm}$, accounting only for the particles of one plume and assuming that ions interact gas dynamically at the energies corresponding to the first deflection instant. As one would expect, the value found for λ^* is comparable with the thickness of the interaction zone in the direction of plume propagation. That is why n^* and λ^* are more or less the same for all materials studied. In other words, in order to be deflected, the plume particles have to experience at least one large-angle scattering within the intersection zone.

At the second deflection instant, the decreasing plasma density n reaches n^* again, the colliding beams penetrate each other without interaction and with no deflection of the ablated material toward the substrate. The CBPLD deposition pulse is thus over. The interaction of the plasma plumes at these later stages of the plume development is dominated by the neutral plasma species. To estimate the flux of neutrals in the interaction zone, Tselev et al. [2001] have used the data of Akhsakhalyan et al. [1982] who have studied the neutral part of the ablation plasma of Cr under similar experimental conditions. From the condition that the plasma particle density $n = n^*$ one can deduce that the second deflection instant corresponds to an energy for neutrals of roughly 6 eV.

Figure 6.8 presents the whole energy spectrum $dN/d\varepsilon$ of plasma particles in DPLD obtained by combining the energy spectrum of neutrals from Akhsakhalyan et al. [1982] with those measured in the probe experiments in Figure 6.6. Particles with energies in the range between 6 eV (the second deflection instant) and 730 eV (the first deflection instant) are effectively redirected toward the substrate in CBPLD. The number of these particles compared to the full number of gaseous ablation species yields the theoretical effectiveness of the material deflection process in CBPLD. For the metals considered in Table 6.2 it appears to be $> 99\%$, that is, practically all the plasma particles are effectively deflected toward the substrate. The condensation and scattering of the plasma species on the diaphragm reduces this effectiveness to an overall value of about 50% [Tselev et al., 1999a].

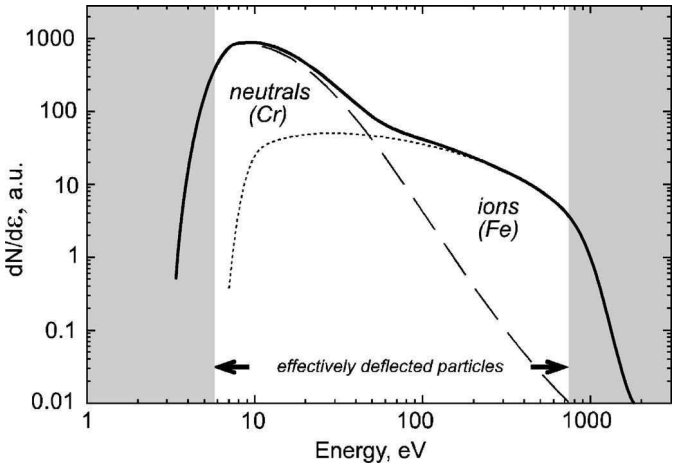

Figure 6.8 Combined energy spectrum of ablation particles in a DPLD plasma plume: (dashed line) Cr neutrals [Akhsakhalyan et al., 1982], (dotted line) Fe ions [Tselev et al., 1999a, 1999b], (solid line) the overall spectrum. The particles that exhibit no significant interaction in the intersection zone of CBPLD have energies in the shaded areas.

6.2.2.3 Spatial Distribution of Ablation Plume in CBPLD

Figure 6.9 presents a typical distribution of the film thickness across the substrate for symmetric CBPLD. It has an elliptical shape with the major axis along the larger side of the diaphragm aperture. The majority of the deposited material is concentrated in this central maximum, and the primary maxima of the individual plasma plumes are effectively suppressed.

The distribution of the deposited material on the substrate is connected with the angular distribution of the resulting plasma plume. For a point source of material the width of the film

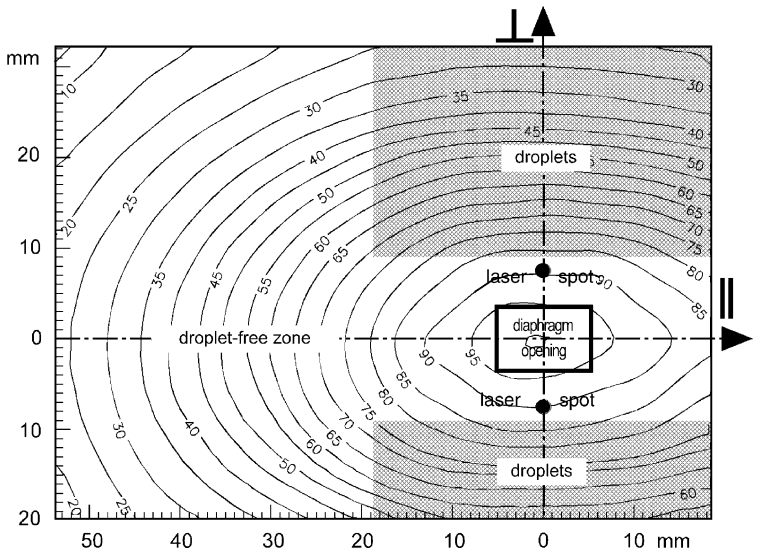

Figure 6.9 Normalized spatial distribution of a nickel film deposited on a glass plate positioned at 34.5 mm from the diaphragm [Gorbunov et al., 1996]. The unshaded area is protected against droplets.

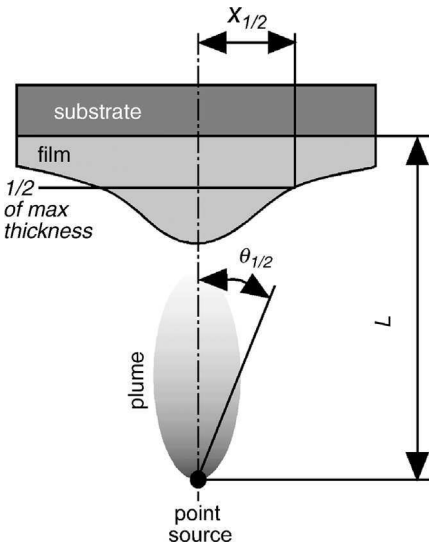

Figure 6.10 Definition of the dimensionless film width $\Delta = x_{1/2}/L$ and the angle of plasma divergence $\theta_{1/2}$.

thickness distribution can be characterized by a dimensionless film width $\Delta = x_{1/2}/L$, where $x_{1/2}$ is the coordinate of the point where the thickness of the film decreases to one half of its maximum, and L is the separation of the substrate from the point source. This geometry is further explained in Figure 6.10. The plasma divergence angle $\theta_{1/2}$ is the half-angle between the symmetric directions in the ablation plume where the material flux is half the value at its maximum. Since the intersection region is not negligibly small, this angle cannot be determined so straightforwardly as can be done in the case of DPLD [Akhsakhalyan et al., 1988; Gorbunov and Konov, 1989].

To visualize the trajectories of the plasma outflow, Tselev et al. [1999b] have used a reticle projection technique. It turned out that the position of the virtual plasma point source, s_{pl}, and $2\theta_{1/2}$ computed from Δ according to the procedure described by Gorbunov and Konov [1989] depend on the direction of the plasma expansion. For the parallel direction (in Fig. 6.9) the virtual source lies 6.1 mm below the diaphragm and the plasma has the largest divergence angle $2\theta_{1/2} = 56^\circ (\Delta_\parallel = 0.42)$. For the perpendicular direction the virtual source lies 8.5 mm above the diaphragm and $2\theta_{1/2} = 38^\circ (\Delta_\perp = 0.31)$ (these are typical values for metals. Carbon deposits have $\Delta_\parallel = 0.73$ and $\Delta_\perp = 0.36$). In all cases the values determined for $2\theta_{1/2}$ and Δ are comparable to those typical for the DPLD process [Akhsakhalyan et al., 1988; Gorbunov and Konov, 1989].

In the deposition experiments, the substrate was positioned off-axis in the plasma plume and was rotated in such a way that it undergoes many revolutions during the deposition of a single layer of material. This allows for further improvement in the uniformity of the film distribution on the substrate to better than 2% across the surface of a substrate 20 mm long. Typical deposition rates for metals lie in the range 1–4 pm/pulse at a diaphragm–substrate distance of 60 mm.

6.3 NANOSCALE MULTILAYER DEPOSITION

The functionality of many modern thin-film and multilayer-based devices depends on the flatness and sharpness of the transition layers between neighboring materials. As follows from Section 6.2.2, PLD is characterized by an extended range of the kinetic energies of the plasma particles and combines therefore many of the features of low particle energy deposition, ion-beam-assisted

deposition, and ion implantation. This unique combination results in excellent values of surface and interface roughness of PLD films and multilayers when compared to other conventional deposition techniques.

On the one hand, the ion-induced collapse of unstable clusters on the surface of the growing film and voids beneath the surface as well as sputtering of loosely bounded adatoms ''polish out'' the protruding spikes and roughness. On the other hand, the growth of the outer surface roughness via surface diffusion and coalescence of adatoms in islands is suppressed due to a greatly reduced bulk diffusion in the subplantational growth mode. Consequently, the roughness of PLD multilayer films depends neither on thickness of individual layers nor on the overall thickness of the whole layer stack as is typical for conventional deposition techniques. On the contrary, in low-energy particle deposition techniques the film grows ''on the surface'' of the substrate and surface diffusion plays an essential role in the redistribution of the film material. Due to the virtual absence of droplets in CBPLD films they are highly suitable for roughness determination.

6.3.1 Morphological and Compositional Roughness in PLD

Prokert et al. [2001] have characterized the interface roughness of CBPLD Co–Cu multilayers with a nanometer period by X-ray diffraction. To increase the material contrast they used the anomalous X-ray diffraction of synchrotron radiation tuned close to the K-absorption edges of the Co (7709 eV) and Cu (8975 eV) atoms. The diffuse X-ray scattering revealed an extraordinary high lateral roughness correlation length of many micrometers. This value approximately represents the mean distance between the bulges in the interfaces between two materials and is far larger than that of any other known deposition techniques [cf. de Bernabé et al., 1998]. Most probably it reflects the intrinsic waviness of the substrate and is not inherent to the deposition method itself.

Another interesting finding of Prokert et al. [2001] is the suppression of the correlated layer-to-layer roughness with increasing values of the individual layer thickness. This is in direct contrast to what is usually observed in thermal or sputtering deposition methods where the roughness increases throughout the layer stack and is highly correlated with a lateral correlation length of the order of the film thickness [Fullerton et al., 1993]. A progressive reduction of the interface root-mean-square (rms) roughness to 0.3–0.5 nm with the increasing number of individual layers in nanometer-period multilayers as a result of ion bombardment during the deposition was also observed by Schlatmann et al. [1994] and Przybylski [1998].

Low-angle specular X-ray reflectometry of CBPLD multilayers [Prokert et al., 2001; Levin et al., 2001] reveals, however, effective rms roughness values for the interfaces in the range of 0.1–1.5 nm, which is comparable or even higher than that typical for the widely used technique of magnetron sputtering. This apparent ''roughness'' arises from the ballistic intermixing between the film and underlying material with the formation of a compositionally graded transition layer between the film and the substrate. This so-called compositional roughness (as opposed to the morphological roughness, which originates from physical nonplanarity of the interfaces) seems to be unavoidable in PLD and will be discussed in the next section.

6.3.2 Determination of the Compositional Profile

6.3.2.1 Ballistic Monte Carlo Simulations

Figure 6.11 presents simulations of the influence of the laser source on the transition layer (TL) formation during the PLD of Al on Fe. The simulations have been performed by a dynamic Monte Carlo code TRIDYN 4.0 [Möller and Eckstein, 1984]. The whole energy spectrum of the plasma particles was divided into four intervals according to the grouping scheme of Table 6.1 with the mean energy representative for each interval. Further details of the simulations can be found elsewhere [Gorbunoff, 2002].

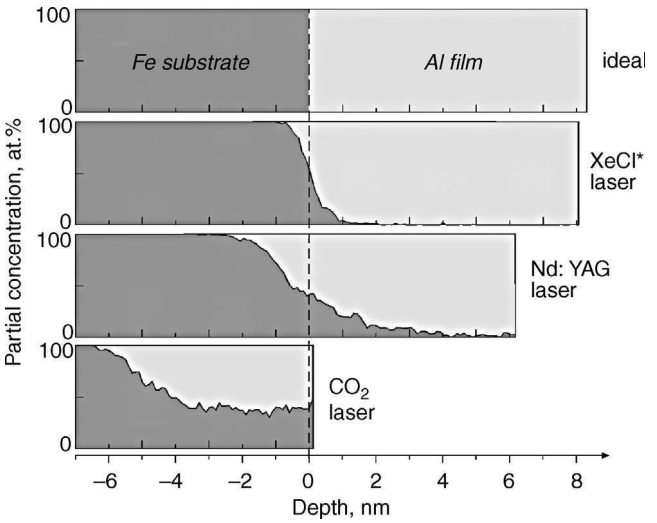

Figure 6.11 TRIDYN simulations of the Al film deposition (light gray) on an Fe substrate (gray) by PLD with different laser plasma sources. The beam is incident from the right. A dose of incoming Al particles of $5 \times 10^{16}\,\mathrm{cm}^{-2}$ is the same in all cases. The depth scale is related to the initial substrate surface position.

As can be seen from Figure 6.11, the excimer laser plasma source ($\lambda = 0.308\,\mu\mathrm{m}$) with the lowest particles energies ($\langle\varepsilon\rangle \approx 10\,\mathrm{eV}$) provides the deposition conditions that are closest to the ideal ones without intermixing and sputtering. With the Nd laser–plasma sources ($\lambda = 1.06\,\mu\mathrm{m}$, $\langle\varepsilon\rangle \approx 200\,\mathrm{eV}$), more pronounced compositionally graded TLs are formed several nanometers thick. The implantation and the sputtering in the case of the CO_2 laser–plasma source ($\lambda = 10.6\,\mu\mathrm{m}$, $\langle\varepsilon\rangle \approx 1000\,\mathrm{eV}$) are so high that the incoming ablation particles etch the substrate material. The sputtering yield of Al appears to be somewhat lower than of Fe, and the Al atoms substitute the iron atoms in the subsurface layer. However, the net sputtering yield is so high that the position of the free surface of the whole sample remains practically unchanged after the given particle dose.

The formation of compositionally graded TLs between successive layers should also influence the structure of the PLD-synthesized nanometer-period multilayers. Figure 6.12 presents the TRIDYN-simulated steady-state modulation amplitude (MA) of Fe–Al multilayers formed under the conditions of CBPLD. One sees that MA of 90 at % is reached first in 13-nm-period multilayers, whereas 2-nm-period multilayers with MA < 10 at % can be considered as compositionally homogeneous.

The Monte Carlo simulations are generally based on a number of simplifying assumptions that greatly facilitate the consideration of atomic collisions and cascades in solids: universal interatomic interaction potentials, the binary collision approximation, a jelly structure, and the linear cascade regime. Although these assumptions yield satisfactory results at particle energies $\varepsilon \approx 150\,\mathrm{eV}$ [Lifshitz et al., 1993], they are strictly valid at ε values exceeding 1 keV. For this reason they can be used only for rough estimations of the TL thickness. Especially in the low-energy region experimental verification of the simulation results is highly desirable.

6.3.2.2 Phenomenological Model

A good materials contrast of the constituents facilitates cross-sectional TEM studies of transition regions between the individual elements in Fe–Al multilayers. The atomically resolved TEM images of the transition region between the individual materials in Fe-on-Al and Al-on-Fe bilayers manufactured by CBPLD are shown in Figure 6.13. The comparison of both samples clearly

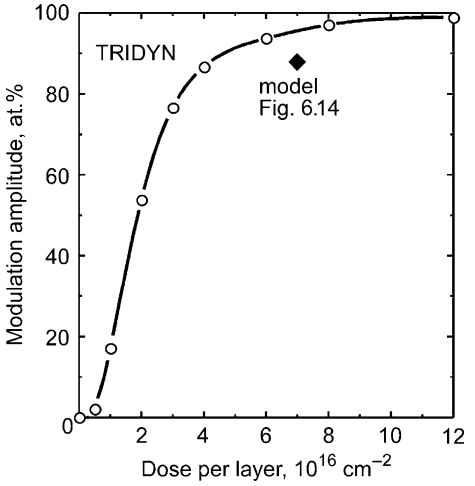

Figure 6.12 Modulation amplitude of Fe–Al multilayers far from the free surface and the substrate simulated by TRIDYN (open circles). Individual layers are assumed to be deposited under typical conditions of CBPLD with the same dose per layer. The diamond represents the modulation amplitude derived from the model profile in Figure 6.14.

demonstrates that the sequence of the deposition also considerably influences the resulting structure of PLD multilayers. In the Fe-on-Al bilayers (Fig. 6.13a), the transition between the crystalline phases appears to be abrupt and rough. On the contrary, the transition between both metals in the Al-on-Fe (Fig. 6.13b) is smoother, and the crystalline phases of individual materials are separated by an amorphous buffer layer having a thickness d_{buffer} of 3–4 nm. Analytical TEM investigations of Geisler et al. [1999] showed that this amorphous buffer layer has a composition $C_{\text{Al}} = 77 \pm 10$ at %, that is, it represents only a part of the whole TL. The whole thickness of the composition profile in both TLs appeared to be 6 nm for Al-on-Fe and 8 nm for Fe-on-Al and is displayed in Figure 6.13.

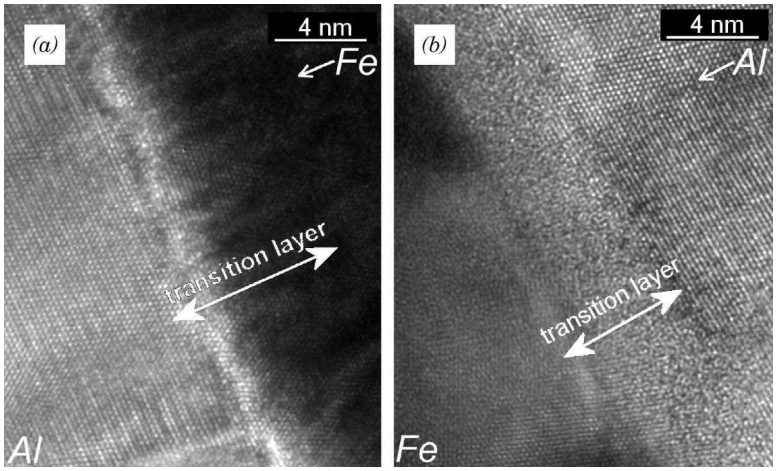

Figure 6.13 High-resolution TEM images of the transition regions between individual materials in (a) Fe-on-Al and (b) Al-on-Fe bilayers manufactured by CBPLD. Arrows in the upper right corners show the direction of deposition. The double-headed arrows indicate the position and the whole thickness of transition layers.

By a rational combination of the above simulated and experimental data Tselev et al. [2002] have developed a phenomenological approach to reconstruct the compositional profile in the TLs. The following assumptions were made:

1. The volume of the ''film'' atoms implanted beneath the ''film–substrate'' boundary should be equal to the volume of the ''substrate'' atoms displaced above it.
2. The implantation depth and sputtering are mainly determined by the particles with the highest kinetic energy, for which the binary collision approximation is valid. Consequently, the maximum range, the deepest portions of the concentration profile, and the position of the ''film–substrate'' boundary can be adopted from the TRIDYN simulations.
3. The compositional range of the amorphous phase in PLD co-deposited Fe–Al alloys lies between 75 and 87 at % Al (as will be proved in Section 6.4.1.1) and is only controlled by the properties of the materials system itself and the energy of incoming particles. Therefore the amorphous buffer layer can serve as a marker for the run of the concentration profile in the given concentration range: $d_{\text{buffer}}(\text{Al-on-Fe}) \approx 4\,\text{nm} \gg d_{\text{buffer}}(\text{Fe-on-Al})$.
4. The shapes of both Al-on-Fe and Fe-on-Al are similar. This assumption is based on the fact that the penetration depth in the hyperthermal energy range of PLD is controlled mainly by the particle momentum [Gilmore and Sprague, 1996; Sprague and Gilmore, 1996]. Though Fe ions in CBPLD are less energetic than Al ions (see Table 6.2), the momenta of both species are similar.

The above conditions determine rather unambiguously the shape of a model compositional profile. It appears to be more asymmetric and extended than is predicted by the TRIDYN simulations. This specific asymmetric shape for the model profile with a steep fall in the middle concentration range and a long roll-off in the portions close to the free surface results in a characteristic saw-tooth shape of the steady-state concentration profile in multilayers as presented in Figure 6.14. As a result, the thickness of alternating phases in TLs deposited from a hyperthermal particle source appears to be dependent on the deposition sequence. In Fe–Al multilayers it is the case for the amorphous phase shown schematically in the upper part of Figure 6.14. Consequently, one can conclude that the asymmetry of the composition profile of transition layers between individual materials is an inherent peculiarity of PLD where the subplantational material supply is accompanied by a low diffusivity of the embedded atoms in the substrate matrix.

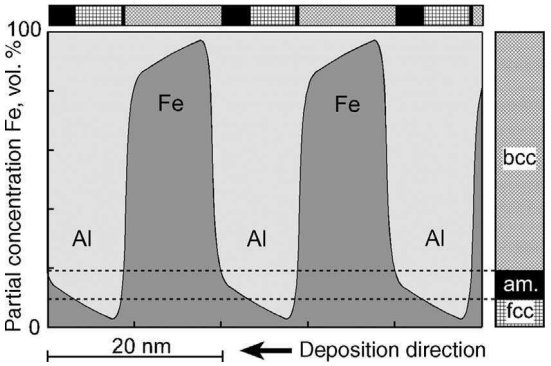

Figure 6.14 Concentration profile in a 20-nm period Fe–Al multilayer constructed from the model transition layers (TLs) proposed by Tselev et al. [2002]. The asymmetry of TLs results in the alternation of the amorphous buffer layer thickness (black) between the bcc (cross-hatched) and fcc (right-hatched) phases in the multilayer cross section shown schematically as a bar in the upper part of the figure.

6.4 ABNORMAL PHASE FORMATION IN CO-DEPOSITED ALLOYS

Following the discussion in Section 6.1.2, there exist reasons to expect PLD films to form in some material-specific frozen-in nonequilibrium metastable state, which may especially apply in the case of alloys. By co-deposition, their enforced mixture can occur even if the starting materials are not miscible according to the equilibrium phase diagram. However, the metastable phase formation in PLD film growth has not attracted much attention so far. In this section the metastable phase formation in two binary materials systems, Fe–Al and Fe–Cr co-deposited via the asymmetric CBPLD, will be studied. Asymmetric CBPLD additionally provides a possibility to continuously vary the resulting film composition within a certain range.

As has been demonstrated above, the kind of metastability that arises in PLD films should be very material specific. Both Fe–Al and Fe–Cr materials systems have a miscibility gap in the equilibrium bulk-phase diagram, but they strongly differ in their energies of mixing, atomic masses and sizes, and chemical affinity.

6.4.1 Amorphous Fe–Al Alloys

6.4.1.1 Materials System Fe–Al

Fe–Al is a system with a negative heat of mixing of -0.81 eV/atom and a pronounced atomic size difference of 14%. It has a complicated equilibrium phase diagram with a wide solubility range (up to 46 at % Al) in the Fe-rich part of the equilibrium phase diagram, negligible solubility (up to 0.03 at % Fe) in the Al-rich one, and a number of intermetallic compounds with complex lattice structures in a compositional range of 65–80 at % Al. However, the formation of intermetallic compounds with a complicated crystalline structure in systems with a large negative heat of mixing and an atomic size difference $>10\%$ is often suppressed due to configurational freezing. Instead, they tend to form crystalline or amorphous extended single-phase solid solutions [Cahn and Greer, 1996].

No crystalline phases form in CBPLD–Fe/Al multilayers with a nominal thickness of individual layers below 6 nm [Geisler et al., 1999; Gorbunov et al., 1999; Noetzel et al., 1999]. The same amorphization effect was observed in single-layer Fe–Al alloys co-deposited from individual Al and Fe targets in asymmetrical CBPLD [Gorbunov et al., 1999]. The plane view TEM micrographs and selected area diffraction patterns revealed a nanocrystalline body-centered cubic (bcc) phase at $C_{Al} = 0$–67 at %, an amorphous phase between 75 and 87 at % Al, and a nanocrystalline fcc phase at higher Al concentrations (Fig. 6.15). The same phase sequence was found in sputtered [Shiga et al., 1985] and ball-milled [Dong et al., 1991; Sheng et al., 1997;

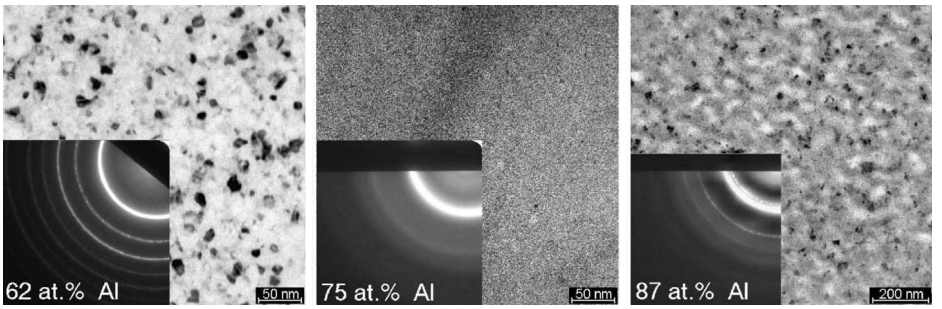

Figure 6.15 TEM and ED pictures of 20-nm-thick Fe–Al alloys of specified compositions [Gorbunov et al., 1999].

Eelman et al., 1998] alloys, and ion-beam mixed multilayers [Hohmuth et al., 1989; Alexandre et al., 1993; Baumvol, 1993]. In thermodynamic equilibrium this compositional range corresponds to the formation of complex intermetallic phases. However, no intermetallic phases were found in the as-deposited samples. It seems that the mobility of subplanted atoms during the deposition process is not high enough to overcome the kinetic barrier for the formation of the above complex intermetallic structures.

6.4.1.2 Mechanism of Amorphization

No thickness limitation for the formation of amorphous co-deposited Fe–Al alloys has been found. It can be concluded therefore that the interfacial stabilization is not the reason for the observed amorphization effect. At the same time, it cannot be a consequence of a solid-state reaction (SSR). First, in contrast to, for example, the Fe–Nb system, the free energy of the amorphous Fe–Al phase is higher than the free energies of the simple (bcc and fcc) crystalline structures for all Fe–Al compositions [Huang et al., 1997]. A decomposition of the amorphous Fe–Al phase with the formation of the intermetallic phase FeAl at interfaces of multilayers already starts at a temperature as low as 150°C [Hohmuth et al., 1989; Akdeniz and Mekhrabov, 1998; Levin et al., 2000]. It is thus thermodynamically unfavorable that the amorphous structure would form in this system as a result of SSR. Second, for any SSR to occur, chemically driven long-range diffusion is necessary. Kelly et al. [1996] have found that the onset temperature of vacancy diffusion in these multilayers is sufficiently higher than the room temperature value at which all the deposition experiments were carried out. This means that long-range processes such as diffusion or chemical reactions in the Fe–Al system are frozen and no SSR can occur at room temperature. Finally, the concept of SSR cannot explain the apparent thickness difference between the amorphous (disordered) buffer layers in the cases of Fe-on-Al and Al-on-Fe depositions in Figure 6.13.

A practical conclusion, which can be drawn from these arguments, is that the amorphous phase in both co-deposited Fe–Al alloys and nanometer-period multilayers is formed during the thermalization of the energetic atoms in the ion-induced collision cascades on a time-scale $\sim 10^{-11}$ s.

Sheng et al. [1997] have interpreted the amorphization of mechanically alloyed $Fe_{100-x}Al_x$ at values of $x \geq 70$ in the context of the elastic instability caused by enormous supersaturation of the constituents. The theory of elastic instability was introduced by Koike [1993] who concluded that the destabilization of the crystalline phase and its collapse into the amorphous state takes place when the lattice strain due to incorporated defects softens the elastic constant to a critical value of 40–50% of its defect-free value. Following these studies, Gorbunov et al. [1999] have compared the microhardness of single Fe and Al films, and their CBPLD alloys and multilayers. Assuming the microhardness scales as the square of the indentation depth, one can derive from the indentation curves in Figure 6.16 that increasing C_{Al} from 60 to 77 at % is accompanied by a reduction of the microhardness to the values comparable with those of Sheng et al. [1997]. Therefore, it is reasonable to conclude that it is possibly the elastic instability that is responsible for the transformation of the strained bcc nanocrystalline solid into the amorphous state when the Al concentration becomes higher than 67 at %.

Further consideration of Figure 6.16 shows that co-deposited Fe–Al alloys remain much harder than their multilayer counterparts. The reason is that besides the rigid bcc structure, the increased difficulty in creating and moving of dislocations in nanocrystalline metals additionally enhances the mechanical strength (the Hall–Petch effect). Amorphous solids have no underlying periodic lattice and no plane slipping. They can be deformed only through the movement of atomic groups, which requires increased shear stress as compared to their crystalline counterparts. This makes amorphous Fe–Al alloys attractive for a variety of technological applications, for which a high specific strength (strength-to-density ratio) and a good corrosion resistance are important features [Reuther, 1998].

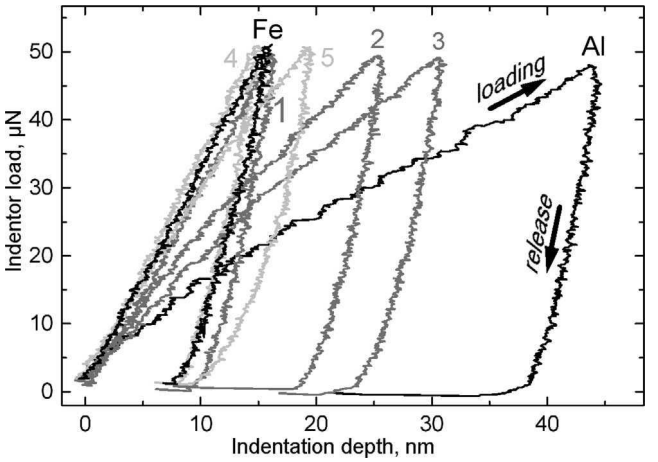

Figure 6.16 Nanoindentation tests of different Fe–Al film structures: single Fe and Al films (black lines), 25-nm period multilayers with mean compositions $Fe_{76}Al_{24}$ (1), $Fe_{40}Al_{60}$ (2), $Fe_{28}Al_{72}$ (3), and co-deposited $Fe_{40}Al_{60}$ (4) and $Fe_{23}Al_{77}$ (5) alloys. [Gorbunov et al., 1999]. The thickness of all samples was above 100 nm.

6.4.2 Paramagnetic Fe–Cr Alloys

6.4.2.1 Materials System Fe–Cr

Different electronic configuration results in different ferromagnetic ordering of these isostructural elements. Iron is ferromagnetic with a Curie temperature, T_C, of 770°C. Chromium is spin-density wave antiferromagnetic. Its Neél temperature is 38°C and decreases very rapidly with increasing Fe concentration in Cr-rich Fe–Cr alloys. The Fe–Cr materials system has potential in giant magnetoresistance applications.

Both Fe and Cr crystallize at room temperature in the bcc crystal structure, while the difference in their lattice constants is only 1%. Their heat of mixing is slightly positive, $+0.25$ eV/atom at $T = 1100$°C. However, according to the stable phase diagram, they tend to decompose into Fe- and Cr-rich bcc solid solutions below 830°C. Long annealing of nearly equiatomic alloys somewhat below this temperature results in the formation of a paramagnetic tetragonal σ phase. Both the decomposition of the system into two bcc phases and the σ-phase formation can be easily suppressed by nonequilibrium processing of the alloy, so that a continuous series of disordered bcc solutions can be formed over the whole composition range.

A number of metastable phases have been observed in thin Fe–Cr films: a paramagnetic distorted σ-like phase in magnetron sputtered $Fe_{55}Cr_{45}$ films [Kortright et al., 2000], a χ phase in $Fe_{82.5}Cr_{17.5}$ [Simmonds et al., 1996], and an icosahedral phase [Khmelevskaya et al., 1998]. Kimoto and Nishida [1967] and Yukawa et al. [1970] have found a primitive cubic δ phase (Al5 or Cr_3Si type) in nanometer-sized particles of Cr and $Fe_{100-x}Cr_x$ alloys ($x < 40$ at % Cr) prepared by evaporation in a low-pressure Ar atmosphere. Doherty et al. [1977] have also reported on the formation of the δ phase in pure Cr films deposited in high vacuum.

Structural investigations of CBPLD co-deposited $Fe_{100-x}Cr_x$ alloy films revealed pronounced structural transformations as the Cr content x of the films increases. These transformational sequences are summarized in Figure 6.17 and illustrated in Figures 6.18 and 6.19.

Low-chromium-content alloys consist of a bcc α phase with a lattice parameter close to that of pure Fe and a grain size of 20–40 nm (Fig. 6.18a). Higher Cr content gives rise to a tetragonal distortion of the initial lattice, which is observable from the shoulder of the (110) peak of the XRD

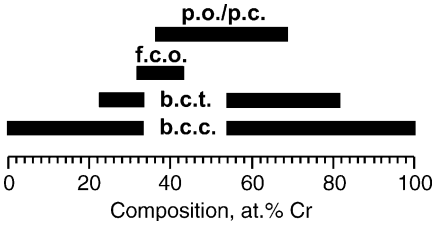

Figure 6.17 Existence regions of the metastable phases in Fe–Cr alloy films prepared by co-deposition in CBPLD at room temperature [Gorbunov et al., 2005].

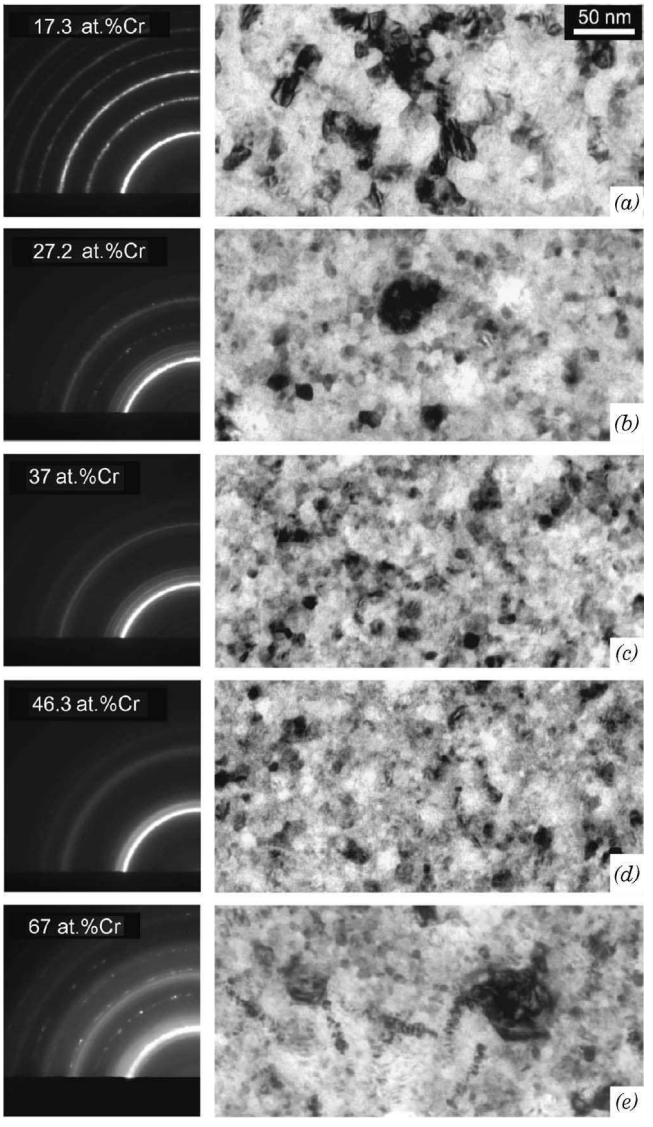

Figure 6.18 ED and TEM images of CBPLD Fe–Cr alloys with specified compositions [Gorbunov et al., 2002].

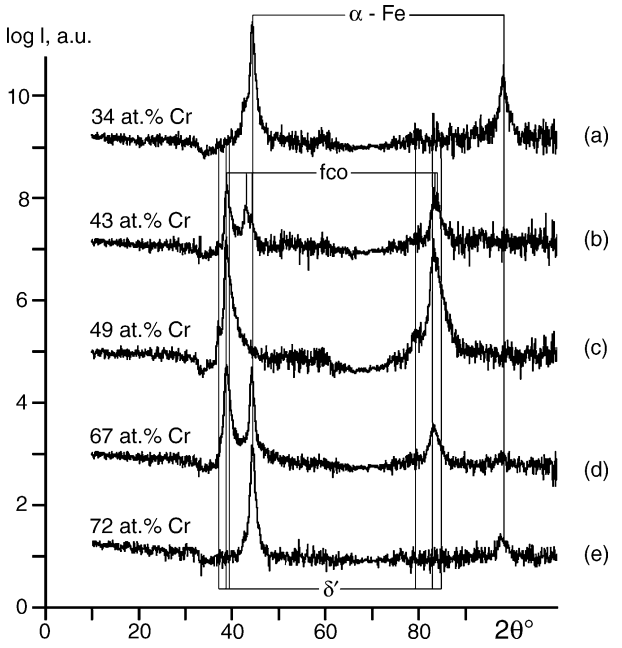

Figure 6.19 XRD patterns of Fe–Cr films (θ–2θ scans) with specified compositions [Gorbunov et al., 2002; Levin et al., 2002a]. The positions of the α-Fe, face-centered orthorhombic (fco), and δ'-phase peaks are also indicated. The XRD contribution of the substrate has been subtracted.

pattern in Figure 6.19a. Simultaneously, another phase starts to form that gives rises to the formation of new reflections near the (110) in the ED pattern in Figure 6.18b.

As x increases further, the bcc (200) reflection in Figure 6.18c disappears and a completely new XRD pattern forms (Fig. 6.19b). Levin et al. [2002a] have attributed it to a new face-centered orthorhombic (fco) phase with lattice parameters of 0.378, 0.4085, and 0.4201 nm. The grain size of this phase becomes smaller.

At nearly equiatomic composition the grains become as small as 3–7 nm and produce only diffuse haloes in the ED pattern in Figure 6.18d. However, careful XRD investigations of Levin et al. [2002a] revealed that this phase has an orthorhombically distorted primitive lattice of Cr_3Si type with lattice parameters of 0.457, 0.464, and 0.483 nm (Fig. 6.19c). Gorbunov et al. [2002] have proposed the naming of this new phase as a δ' phase in view of its close relationship to the cubic primitive δ–Cr phase ($a = 0.4588$ nm) in chromium nanoparticles reported by Kimoto and Nishida (1967).

The recovery of stable bcc phase formation is evident in X-ray diffraction patterns of high-Cr alloys (Fig. 6.19d). It is accompanied by the appearance of large bcc crystallites embedded in the fine nanocrystalline matrix. These bcc crystallites produce sharp-point bcc reflections on the background of diffuse haloes of the δ'-phase matrix in the ED pattern (Fig. 6.18e). Only the bcc and the tetragonally distorted bcc Cr phase can be observed at $x \geq 72$ at % Cr (Fig. 6.19e).

6.4.2.2 Ordering Effect

The EXAFS investigations of the δ' phase by Gorbunov et al. [2002] revealed pronounced differences in the next-neighbor arrangement of resonantly absorbing Fe and Cr atoms. Figure 6.20 compares EXAFS spectra of two samples with $x = 24.5$ and 62 at % Cr. In the low-Cr bcc α phase (Fig. 6.20a), the patterns for both metals coincide. This means that atoms of both kinds have statistically the same arrangement of near neighbors, a natural expectation for disordered alloys. This is not the case for the δ' phase (Fig. 6.20b). The strong peak at about 2.2 Å for Fe is

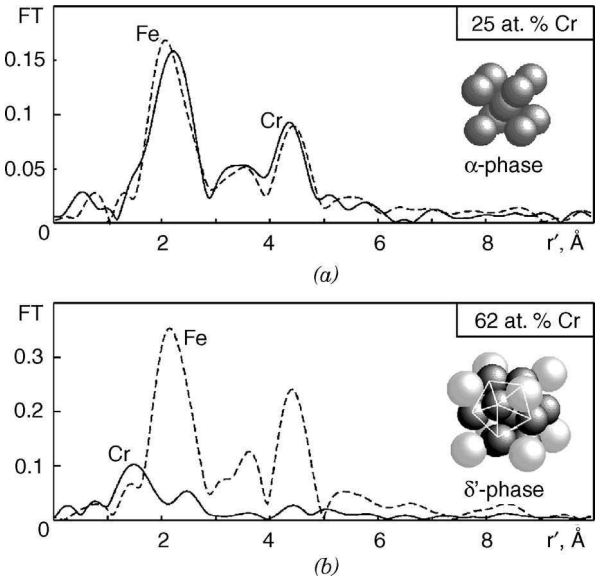

Figure 6.20 Cr–K (full line) and Fe–K (broken line) Fourier transforms of the EXAFS functions of specified alloys [Gorbunov et al., 2002]. The balls in sketch (a) represent the statistically equiprobable positions of Fe and Cr atoms in disordered bcc alloys. The most probable positions of Fe (light balls) and Cr (dark balls) atoms in the elementary cell of the δ' phase are illustrated in sketch (b). Note the icosahedral coordination of Cr atoms.

an indication of a well-defined, single nearest-neighbor coordination shell around Fe atoms, while on the contrary, a pronounced damping of the peak for the case of Cr is apparent. These observations suggest that both atomic kinds in the alloy occupy specific lattice positions or, in other words, that the alloy is at least partly *ordered*. Iron atoms preferably occupy ''body center'' and ''corner'' sites of the elementary cell with single coordination shells at a distance of about 0.26 nm around them. Chromium atoms tend to take up twinned positions at faces of the elementary cell (black balls in Fig. 6.20b), having therefore three neighbor shells at about 0.23, 0.26, and 0.28 nm with 2, 4, and 8 atoms, respectively. It is interesting to note that the icosahedrally coordinated chromium atoms in the Cr_3Si-type crystal structure indicated in Figure 6.20b can cause fivefold symmetry effects observed by Khmelevskaya et al. [1998] in ion-bombarded Fe–Cr alloys.

The formation of the ordered phases in the as-deposited Fe–Cr alloys can also be qualitatively supported by the measurements of the electrical resistivity ρ of the alloys since it is quite sensitive to the structural imperfections. In full accordance with the Nordheim rule, the enrichment with the solute results in the rising of ρ at both sides of the composition scale. However, as one can deduce from Figure 6.21, a pronounced minimum of ρ is observed at nearly equiatomic composition, where the primitive orthorhombic (po) δ'-phase alloys form. Such behavior of ρ is typical for ordered intermetallic compounds with less electron scattering on the disordered impurity atoms.

In general, it must be mentioned that the formation of ordered phases with complex crystalline structure by energetic deposition is a rather infrequently observed phenomenon; it is likely to have been reported by Gorbunov et al. [2002] for the first time under the conditions of PLD.

6.4.2.3 Magnetic Transformations

Ferromagnetic ordering is a material property that is very sensitive to the separation between neighboring atoms and thus is closely connected with crystallographic properties of the alloys.

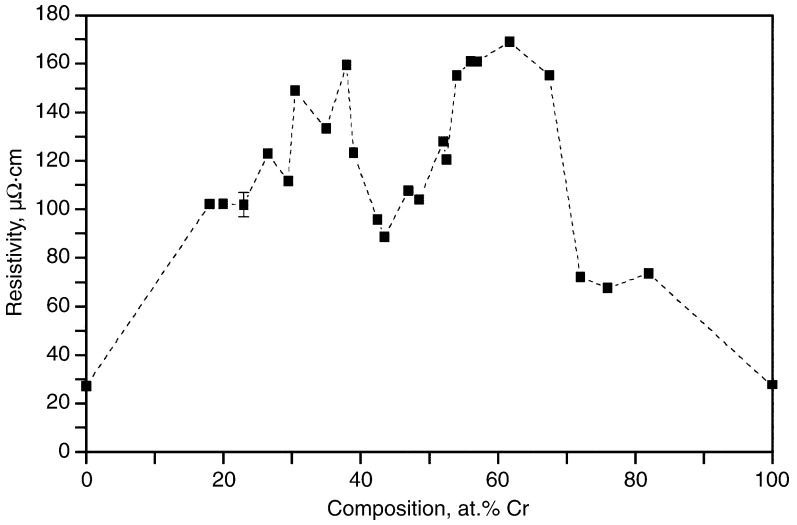

Figure 6.21 Electrical resistivity ρ of the as-deposited alloys (solid squares) as a function of the Cr content x. The line is only a guide for the eye [Gorbunov et al., 2005].

According to literature data [Wijn, 1986], the mass magnetization (the magnetic moment per unit mass) σ for the undercooled bcc Fe–Cr solid solutions decreases practically linearly with the Cr concentration x, until the alloy becomes paramagnetic at room temperature at x above 67 at %. The experimental values of σ of the deposited alloys in comparison with the literature data are displayed in Figure 6.22. It is seen that low-Cr-content alloys demonstrate the same $\sigma(x)$ trend as the bulk bcc

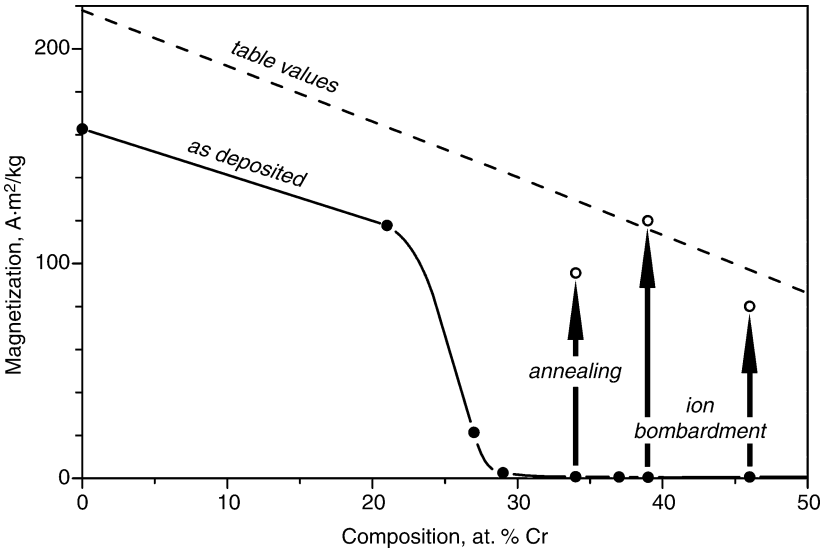

Figure 6.22 Dependence of the magnetization σ of as-deposited Fe–Cr alloys (solid circles) on the film composition x, measured in a field of 1 kOe. The open circles demonstrate the effect of ion bombardment with 40-keV Cr ions at doses 5×10^{15} Cr cm^{-2} ($x = 39$ at % Cr) and 2×10^{16} Cr cm^{-2} ($x = 47$ at % Cr) and thermal annealing at 425°C ($x = 34$ at % Cr) for 50 h under high-vacuum conditions [Gorbunov et al., 2005]. The magnetization behavior of bulk metastable bbc Fe–Cr solid solutions from Wijn [1986] is given by the dashed line.

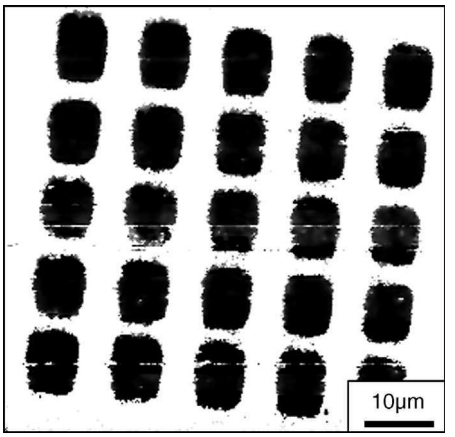

Figure 6.23 Lift-mode MFM phase image of a $Fe_{63}Cr_{37}$ alloy locally implanted with 5×10^{15} Cr ions cm^{-2} at an ion energy of 60 keV (black areas) [Gorbunov et al., 2005]. The MFM tip–sample separation was 113 nm.

Fe–Cr alloys. The reduced magnetization is reasonable to attribute to the enlarged unit cell parameter of the alloys [Gorbunov et al., 2005].

As x exceeds 20 at % Cr, the magnetization rapidly decreses to zero and the alloy becomes completely paramagnetic at $x = 27$ at % Cr. According to Figure 6.17, this concentration region corresponds to the formation of the tetragonally distorted body-centered phase and is characterized by an enlarged lattice spacing [Gorbunov et al., 2005]. Subsequent postprocessing results in the formation of the bcc α-Fe-like phase, reduction of the unit cell parameter, and the restoration of the ferromagnetic order in the alloys studied. To achieve this it was sufficient to heat the alloys to a temperature above 400°C [Levin et al., 2002b] or to implant them with 40-keV Cr ions to a dose of the order of 10^{16} Cr cm^{-2} [Wieser et al., 2002; Gorbunov et al., 2005]. As seen in Figure 6.22, their magnetization practically reaches the table values for the metastable bcc Fe–Cr alloys independently on the starting phase.

Metastable film materials represent promising media for one-step fabrication of nanostructures through local postprocessing [Gorbunoff, 2002]. The advantage of the ion-beam-induced phase transformations is that they take place with no gross alteration of the sample surface morphology. Gorbunov et al. [2005] have used the ion-induced phase and magnetic transformations in metastable Fe–Cr alloys for direct writing of ferromagnetically arranged areas in a nonmagnetic matrix of the same material by using a tightly focused ion beam. They have implanted an array of $5 \times 5\ \mu m^2$ areas of a $Fe_{63}Cr_{37}$ film alloy with 60 keV Cr ions to a dose 5×10^{15} Cr ions cm^{-2}, which, according to Wieser et al. [2002] should render them ferromagnetic. In fact, they possessed a clear contrast to the surrounding nonprocessed areas in the frequency, phase, and amplitude MFM images, indicating a strong magnetic interaction with the MFM tip (Fig. 6.23). In the topographic mode the ion-beam-processed areas appeared as depressions only 2 nm deep. Since an ion beam can be focused down to a few nanometers, this technique can also be implemented for direct ion beam writing of surface magnetic structures on the nanometer scale.

6.5 CONCLUSIONS

1. A unique set of film growth conditions distinguishes high-vacuum PLD from other thin film physical deposition techniques. The pulsed, intrinsically highly nonequilibrium nature of PLD with a broad energy distribution and high quenching rates of condensing hyperthermal

particles combines the features of physical vapor deposition, ion beam sputtering, and implantation techniques. It gives rise to the subplantational film growth mode with shallow subsurface implantation and low diffusivity of the embedded atoms in the underlying material.

2. Cross-beam PLD can be considered as a useful extension of the direct PLD technique. In this system an intersection zone of two ablation plumes from dual simultaneously irradiated targets forms a filter for droplets and high-energy plasma particles. It allows an effective solution of the problem of droplet transfer onto the film, which is considered to be one of the major drawbacks of PLD. The absence of droplets in CBPLD facilitates characterization of the structure, phase composition, and properties of the deposited films and multilayers by surface-averaging techniques. The spatio-energetic characteristics of the ablation plume in CBPLD appear to be comparable with those typical for conventional PLD.
3. Due to the subplantation growth mode in PLD with greatly reduced bulk diffusion, the subsequent arrival of condensing particles does not contribute to the development of the outer surface roughness. As a consequence, the surface and interface roughness of the PLD films depends neither on the thickness of the individual layers nor on the overall thickness of the whole multilayer stack. Contrary to conventional deposition techniques, the roughness is highly noncorrelated and tends to decrease with increasing film thickness. The lateral roughness correlation length far exceeds that of any other known deposition technique.
4. The specific asymmetric shape of the concentration profile in the transition layer between two adjacent materials is an inherent peculiarity of PLD. It has a steep fall in the deepest portions of the film material and a longer roll-off in those portions closer to the free surface. In PLD of multilayers, this shape of the concentration profile makes the thickness of alternating phases dependent on the deposition sequence.
5. The effects of subplantation, rapid quenching, configurational freezing, and resputtering of incoming energetic particles in PLD reduce the influence of the heat of mixing and solid-state diffusion on the phase composition of the deposited layered materials. The formation of highly randomized, very fine grained nanocrystalline, or quasi-amorphous, very smooth uniform films in a material-specific metastable state is a natural consequence of this unique set of film growth conditions. The metastable phase formation has to be considered as a rule rather than an exception in PLD.
6. The use of dual targets of different materials in CBPLD makes it possible to mix them directly in the colliding laser plumes. It contributes additionally to the nonequilibrium nature of PLD and can drive certain binary systems toward the extended solid solubility of materials, the formation of abnormal metastable nanocrystalline or amorphous structures, and even the formation of new ordered intermetallic phases.
7. The metastable alloys synthesized by CBPLD demonstrate a promising combination of physical properties. Amorphous Fe–Al thin-film alloys can find application as corrosion protection coatings. Irreversible phase transformations induced in metastable intermetallic Fe–Cr phases by local heat treatment or ion bombardment have the potential to be used for a single-step fabrication of stable magnetic nanostructures.

Acknowledgments

The author wishes to thank A. D. Akhsakhalyan, A. Yu. Belov, L. Bischoff, K. Brand, D. Eckert, H. Geisler, A. Levin, A. Mensch, M. Mertig, D. C. Meyer, J. Noetzel, P. Paufler, W. Pompe, F. Prokert, H. Reuther, A. E. Tselev, B. Wolf, and E. Wieser for their valuable contribution in performing experiments and discussing results at different stages of the work. Different parts of the work were supported by the German Federal Ministry for Education and Research (BMBF), the Max-Planck-Society (MPG), and the German Research Foundation (DFG).

REFERENCES

Akdeniz, M. V., and A. O. Mekhrabov (1998), *Acta Mater.* **46**, 1185–1192.

Akhsakhalyan, A. D., Yu. A. Bityurin, S. V. Gaponov, A. A. Gudkov, and V. I. Luchin (1982), *Sov. Phys. Tech. Phys*. **27**, 969–973.

Akhsakhalyan, A. D., S. V. Gaponov, V. I. Luchin, and A. P. Chirimanov (1988), *Sov. Phys. Tech. Phys*. **33**, 1146–1151.

Alexandre, J. L., M. A. Z. Vasconcellos, R. Hübler, S. R. Teixeira, and I. J. R. Baumvol (1993), *Nucl. Instrum. Meth.* **B80/81**, 436–441.

Baumvol, I. J. R. (1993), *Nucl. Instrum. Meth.* **B74**, 98–104.

Blyakhman, Yu., N. I. Polushkin, A. D. Akhsakhalyan, S. A. Gusev, N. N. Salashchenko, and V. G. Semenov (1995), *Phys. Rev. B* **52**, 10303–10314.

Bykovski, Yu. A., L. I. Litinskaya, C. M. Sil'nov, and E. A. Sotnichenko (1988), *Fizika i Khimiya Obrabotki Materialov*, No.4, 44–49 (in Russian).

Cahn, R. W., and A. L. Greer (1996), in *Physical Metallurgy*, R. W. Cahn and P. Haasen (Eds.), Elsevier Science BV, Amsterdam, pp. 1724–1830.

Chopra, K. L. (1969), *Thin Film Phenomena*, McGraw-Hill, New York, pp. 199–214.

de Bernabé, A., M. J. Capitán, H. E. Fischer, and C. Prieto (1998), *J. Appl. Phys.* **84**, 1881–1888.

Doherty, C. J., J. M. Poate, and J. H. Voorhoeve (1977), *J. Appl. Phys.* **48**, 2050–2054.

Dong, Y. D., W. H. Wang, L. Liu, K. Q. Xiao, S. H. Tong, and Y. Z. He (1991), *Mater. Sci. Eng.* **A134**, 867–871.

Eelman, D. A., J. R. Dahn, G. R. MacKay, and R. A. Dunlap (1998), *J. Alloy. Compd.* **266**, 234–240.

Esch, S., M. Bott, T. Michely, and G. Comsa (1995), *Appl. Phys. Lett*. **67**, 3209–3211.

Franghiadakis, Y., C. Fotakis, and P. Tzanetakis (1998), *J. Appl. Phys.* **84**, 1090–1094.

Fullerton, E. E., J. Pearson, C. H. Sowers, S. D. Bader, X. Z. Wu, and S. K. Sinha (1993), *Phys. Rev.* **B48**, 17432–17444.

Gaponov, S. V. (1985), in *Laser-Assisted Modification and Synthesis of Materials*, S. Metev (Ed.), Sofia University, Sofia, pp. 216–229.

Gaponov, S. V., B. M. Luskin, and N. N. Salaschenko (1981), *Solid State Commun.* **39**, 301–302.

Gaponov, S. V., A. A. Gudkov, and A. A. Fraerman (1982), *Sov. Phys. Tech. Phys.* **27**, 1130–1133.

Geilman, T., J. Chevallier, M. Fanciulli, G. Weyer, V. Nevolin, and A. Zenkevitch (1997), *Appl. Surf. Sci.* **109/110**, 570–574.

Geisler, H., A. Mensch, A. Gorbunov, A. Tselev, J. Noetzel, K. Brand, and H. Worch (1999), *Z. Metallkd.* **90**, 691–698.

Gente, C., M. Oering, and R. Bormann (1993), *Phys. Rev. B* **48**, 13244–13252.

Giessen, B. C. (1982), in *Proceedings of the Fourth International Conference on Rapidly Quenched Metals*, T. Masumoto and K. Suzuki (Eds.), Japan Inst. Met., Sendai, p. 213.

Gilmore, C. M., and J. A. Sprague (1996), *Surf. Coat. Technol.* **83**, 146–150.

Gorbunoff, A. (2002), *Laser-Assisted Fabrication of Thin Film Nanostructures*, VDI-Verlag, Düsseldorf.

Gorbunov, A. A., and V. I. Konov (1989), *Sov. Phys. Tech. Phys*. **34**, 1271–1275.

Gorbunov, A. A., W. Pompe, A. Sewing, S. V. Gaponov, A. D. Akhsakhalyan, I. G. Zabrodin, I. A. Kas'kov, E. B. Klyenkov, A. P. Morozov, N. N. Salaschenko, R. Dietsch, H. Mai, and S. Völlmar (1996), *Appl. Surf. Sci.* **96–98**, 649–655.

Gorbunov, A. A., A. E. Tselev, D. Elefant, H. Geisler, G. Henninger, A. Mensch, D. C. Meyer, B. Wolf, P. Paufler, W. Pompe, C. M. Schneider, and H. Worch (1999), *Appl. Phys.* **A69** (Suppl.), S463–S466.

Gorbunov, A., A. A. Levin, A. Mensch, D. C. Meyer, A. Tselev, P. Paufler, W. Pompe, and D. Eckert (2002), *Appl. Surf. Sci.* **197/198**, 392–397.

Gorbunov, A., A. A. Levin, D. C. Meyer, L. Bischoff, D. Eckert, B. Köhler, M. Mertig, T. Weissbach, E. Wieser, and W. Pompe (2005), *Cryst. Res. Technol*. **40**, 106–113.

Greene, J. E. (1994), in *Handbook of Deposition Technologies for Films and Coatings*, R. F. Bunshah (Ed.), Noyes Publications, Park Ridge, NJ, pp. 681–738.

Guseva, M. B (1986), *Izv. AN SSSR Fiz.* **50**, 459–464.

Hohmuth, K., V. Heera, and B. Rauschenbach (1989), *Nucl. Instrum. Methods* **B39**, 136–143.

Huang, B., K. N. Ishihara, and P. H. Shingu (1997), *Mater. Sci. Eng.* **A231**, 72–79.

Jäger, H. U., and A. Yu. Belov (2003), *Phys. Rev. B.* **68**, 024201.

Jordan, R., D. Cole, J. G. Lunney, K. Mackay, and D. Givord (1995), *Appl. Surf. Sci.* **86**, 24–28.

Kalff, M., M. Greeman, M. Morgenstern, T. Michely, and G. Comsa (1997), *Appl. Phys. Lett.* **70**, 182–184.

Kelly, R., A. Miotello, É. Knystautas, and S. Lo Russo (1996), *Surf. Coat. Tech.* **83**, 156–161.

Khmelevskaya, V. S., V. G. Kraposhin, and V. G. Malynkin (1998), *Int. J. Non-Equilib. Pr.* **10**, 323–331.

Kimoto, K., and I. Nishida (1967), *J. Phys. Soc. Jpn.* **22**, 744–756.

Koike, J. (1993), *Phys. Rev. B* **47**, 7700–7704.

Kortright, J. B., S.-K. Kim, and H. Ohldag (2000), *Phys. Rev. B* **61**, 64–67.

Krebs, H.-U. (1997), *Int. J. Non-Equilib. Pr.* **10**, 3–24.

Krebs, H.-U., and O. Bremert (1993), *Appl. Phys. Lett.* **62**, 2341–2343.

Lambert, L., F. Grangeon, and M. Autric (1999), *Appl. Surf. Sci.* **138/139**, 574–580.

Levin, A. A., D. C. Meyer, and P. Paufler (2000), *J. Alloys Comp.* **297**, 59–67.

Levin, A. A., D. C. Meyer, A. Gorbunov, A. Tselev, P. Gawlitza, H. Mai, W. Pompe, and P. Paufler (2001), *Thin Solid Films* **391**, 47–56.

Levin, A. A., D. C. Meyer, A. Tselev, A. Gorbunov, W. Pompe, and P. Paufler (2002a), *J. Alloys Comp.* **334**, 159–166.

Levin, A. A., D. C. Meyer, A. Gorbunov, A. Tselev, W. Pompe, and P. Paufler (2002b), *J. Alloys Comp.* **347**, 171–177.

Lifshitz, Y., S. R. Kasi, and J. W. Rabalais (1990), *Phys. Rev. B* **41**, 10468–10479.

Lifshitz, Y., C. D. Roux, K. Boyd, W. Eckstein, and J. W. Rabalais (1993), *Nucl. Instrum. Methods* **B83**, 351–356.

Luo, Y., and H.-U. Krebs (1995), *J. Appl. Phys.* **77**, 1482–1487.

Möller, W., and W. Eckstein (1984), *Nucl. Instrum. Methods* **B2**, 814–818.

Nastasi, M., W. Möller, and W. Ensinger (2000), in *Handbook of Plasma Immersion Ion Implantation and Deposition*, A. Anders (Ed.), Wiley, New York, pp. 179, 189.

Noetzel, J., K. Brand, H. Geisler, A. Gorbunov, A. Tselev, E. Wieser, and W. Möller (1999), *Appl. Phys.* **A68**, 497–504.

Pechen, E. V., S. I. Krasnosvobodtsev, G. Kessler, A. Richter, M. Panzner, O. Grossman, and A. Teresiak (1992), *Phys. Status. Solidi A* **131**, 179–189.

Prokert, F., J. Noetzel, N. Schell, E. Wieser, W. Matz, and A. Gorbunov (2001), *Thin Solid Films* **394**, 164–173.

Przybylski, M. (1998), *Hyperfine Interact.* **113**, 135–163.

Reuther, H. (1998), *Hyperfine Interact.* **111**, 135–140.

Schlatmann, R., C. Lu, J. Verhoeven, E. J. Puik, and M. J.van der Weil (1994), *Appl. Surf. Sci.* **78**, 147–157.

Sheng, H. W., Y. H. Zhao, Z. Q. Hu, and K. Lu (1997), *Phys. Rev. B* **56**, 2302–2305.

Shiga, M., T. Kikawa, K. Sumiyama, and Y. Nakamura (1985), *J. Magn. Soc. Jpn.* **9**, 187–190 (in Japanese).

Simmonds, M. C., R. C. Newman, S. Fijitomo, and J. S. Collington (1996), *Thin Solid Films* **279**, 4–6.

Smidt, F. A. (1990), *Int. Mater. Rev.* **35**, 61–128.

Sprague, J. A., and C. M. Gilmore (1996), *Thin Solid Films* **272**, 244–254.

SRIM Version 2003.20 (2003), www.srim.org.

Störmer, M., and H.-U. Krebs (1995), *J. Appl. Phys.* **78**, 7080–7078.

Strikovsky, M. D., E. B. Klyuenkov, S. V. Gaponov, J. Schubert, and C. A. Copetti (1993), *Appl. Phys. Lett.* **63**, 1146–1148.

Tselev, A., A. Gorbunov, and W. Pompe (1999a), *Appl. Surf. Sci.* **138/139**, 12–16.

Tselev, A., A. Gorbunov, and W. Pompe (1999b), *Appl. Phys.* **A69**, 353–358.

Tselev, A., A. Gorbunov, and W. Pompe (2001), *Rev. Sci. Instrum.* **72**, 2665–2672.

Tselev, A., A. Gorbunov, W. Pompe, and K. Brand (2002), *J. Vac. Sci. Technol.* **A20**, 1557–1765.

Uhlmann, S., Th. Frauenheim, and Y. Lifshitz (1997), *Phys. Rev. Lett.* **81**, 641–644.

van Ingen, B. R. P., R. H. J. Fastenau, and E. J. Mittemeijer (1994), *Phys. Rev. Lett.* **72**, 3116–3119.

Wieser, E., H. Reuther, F. Prokert, A. Gorbunov, A. Tselev, W. Pompe, A. A. Levin, D. C. Meyer, and P. Paufler (2002), *J. Appl. Phys.* **92**, 572–577.

Wijn, H. P. J. (Ed.) (1986), *Landolt-Börnstein*, NS III **19a**, Springer, Berlin.

Wulfhekel, W., I. Beckmann, N. N. Lipkin, G. Rosenfeld, B. Poelsema, and G. Comsa (1996), *Appl. Phys. Lett.* **69**, 3492–3494.

Yukawa, N., M. Hida, T. Imura, and M. Kawamura (1970), *Inst. Met. J.* **34**, 348–355 (in Japanese).

Zalm, P. C. (1984), *J. Vac. Sci. Techol.* **B2**, 151–152.

CHAPTER 7

Combinatorial Pulsed Laser Deposition

ICHIRO TAKEUCHI

Department of Materials Science and Engineering and Center for Superconductivity Research, University of Maryland, College Park, Maryland

7.1 INTRODUCTION

The combinatorial approach to materials is an emerging paradigm of research methodology that aims to drastically increase the efficiency at which new compounds are discovered and improved. In a single experiment, up to thousands of different compositions can be synthesized and screened for desired physical properties [Koinuma and Takeuchi, 2004]. Within the last 20 years, combinatorial chemistry and high-throughput screening for new drugs and biomolecules have already revolutionized the pharmaceutical and DNA (deoxyribonucleic acid) sequencing industries [Lebl, 1999].

The shear amount of existing literature and cumulative knowledge in all of materials science, which consists of a myriad of subdisciplines (classified mostly by different classes of materials), seems enormous. Yet, the total number of known complex functional materials is actually miniscule compared to the vast phase space of all possible multicomponent compounds that can be formed by combining different elements from the periodic table. At the end of the 1980s, J. C. Phillips estimated that approximately 24,000 inorganic phases were known. Among them, 16,000 are binary and pseudobinary compounds, and only 8000 are ternary and pseudoternary compounds [Phillips, 1989]. If we choose about 60 elements from the periodic table to form ternary compounds, there are $\sim$34,000 possible ternary systems, and a large fraction of these are yet to be explored. In addition, within each ternary system, different stoichiometries can naturally give rise to a variety of different structures and properties. The most comprehensive way to study a ternary system is to map its compositional phase diagram. To map the structure–composition–physical property relationship of ternary systems with the conventional method of making and testing one composition at a time with small compositional increments requires a very large number of experiments.

It is our view that to systematically explore the inexhaustibly large phase space of unknown complex systems, the conventional sequential trial-and-error method has to be replaced with more time-efficient and cost-effective methods. The combinatorial approach is an attempt at tackling this challenge by *simultaneously* performing a large number of experiments.

Pulsed Laser Deposition of Thin Films: Applications-Led Growth of Functional Materials
Edited by Robert Eason

7.2 COMBINATORIAL APPROACH TO MATERIALS

The combinatorial approach to functional and electronic materials is best implemented in the form of thin-film combinatorial libraries. On a substrate as small as 1 cm^2, thousands of different compositions can be integrated, synthesized, and screened for the desired physical properties. The feasibility and utility of this concept has been demonstrated in the discoveries of a number of new materials with much improved physical properties [Xiang et al., 1995, Briceño et al., 1995; Danielson et al., 1998; Takeuchi et al., 2003a].

Figure 7.1 is a schematic depicting the experimental steps of the combinatorial approach to materials. In this particular scheme, the library is synthesized using the thin-film precursor technique (discussed below), but the overall picture is representative of combinatorial thin-film techniques in general. In the first step, fabrication of a thin-film library with a large number of compositionally varying sites is achieved by carrying out a series of thin-film depositions in conjunction with precisely positioned shadow masks that allow spatially selective deposition. Here, using a series of masks, different combinations of amorphous precursor multilayers are deposited at unique sites on the library chip. Following the deposition, the chip is thermally processed to diffuse the precursors and to form the desired phases. Finally, various parallel measurements and/or scanning probe techniques are used to rapidly characterize the specific physical properties of interest and screen the library. This last step is often the biggest bottleneck in the overall combinatorial experimentation process. The scope of the materials systems and properties that can be addressed is often dictated by the availability and capabilities of high-throughput characterization techniques.

This chapter will review the utility of pulsed laser deposition (PLD) techniques in fabrication of combinatorial samples (thin-film libraries and composition spreads). While it is well known that PLD can be used for deposition of different types of materials systems, combinatorial PLD performed to date has largely focused on metal oxide materials, and, thus, the discussions and examples covered in this chapter will be restricted to metal oxide systems only.

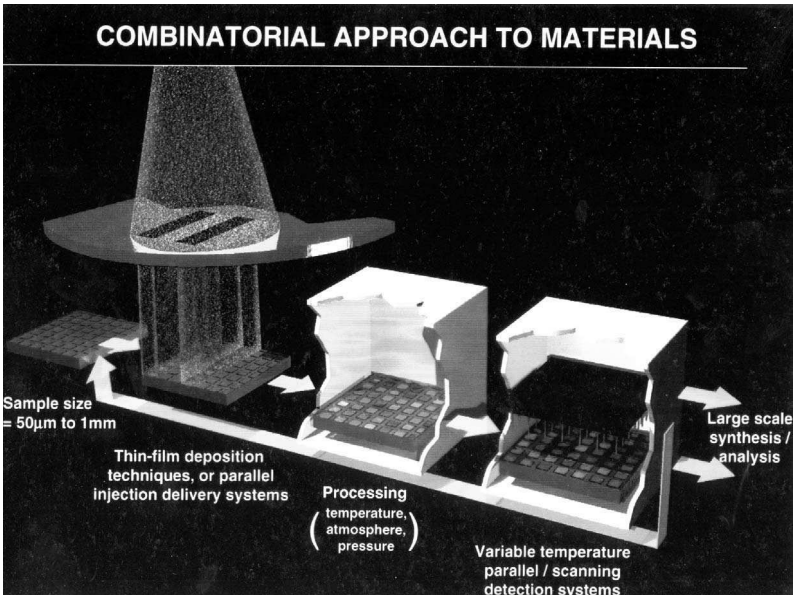

Figure 7.1 Schematic showing experimental steps of a combinatorial experiment. Following a cycle of steps, the experiment can be repeated with appropriate feedback. The precursors can also be delivered using an ink-jet technique.

7.3 PULSED LASER DEPOSITION FOR FABRICATION OF COMBINATORIAL LIBRARIES

There are a number of thin-film deposition techniques that can be used for fabrication of combinatorial samples. Essentially, any physical vapor deposition technique can be used for achieving the spatially selective deposition facilitated by implementation of shadow masks as shown in the first step in Figure 7.1. In some instances, application of chemical vapor deposition techniques to combinatorial synthesis have also been demonstrated [Xia et al., 2004; Choo et al., 2005].

Pulsed laser deposition has several key advantages over other techniques for use in library fabrication. Laser ablation of materials from bulk targets is a highly nonequilibrium process that allows stoichiometric transfer and delivery of controlled target composition to the substrate. This aspect is particularly crucial for metal oxides where materials systems of interest often consist of multiple components with different vapor pressures.

Depositions can be performed in high vacuum or in low pressure of reactive gases. A single film can be made in a relatively short period of time with a quick turn-around. By monitoring the number of laser pulses, one can control the deposition of materials at an atomic layer level, and by incorporating a layer-by-layer deposition technique, one can design and explore novel materials systems that do not exist in bulk form. One requirement of the deposition technique in performing fabrication of combinatorial libraries is that it needs to facilitate deposition of a number of different materials in a single deposition sequence. In PLD, target materials do not need to be biased, and a multiple-target carousel allows sequential deposition of different materials in a single run. In general, PLD systems are relatively inexpensive, and they can be set up quickly and easily with minimum maintenance requirements.

7.4 SYNTHESIS TECHNIQUE USING THIN-FILM PRECURSORS

The very first demonstration of the combinatorial approach to materials was performed using libraries fabricated by the thin-film precursor technique [Xiang et al., 1995]. The goal here is to survey as diverse a compositional variation as possible in individual experiments using mathematically designed masking strategies. A series of high-precision shadow masks are used to define the layout of multilayers of amorphous precursors for all the sites. Elemental metals, simple metal oxides, flourides, and carbonates are often used as precursors. For instance, to make $(Ba,Sr)TiO_3$, a multilayer consisting of amorphous layers of BaF_2, SrF_2, and TiO_2 are used, as shown in Figure 7.2. The substrate is usually held at or near room temperature (up to 100–200°C) during the deposition of precursor layers. Postannealing and heat treatment are used for diffusion of amorphous precursors and phase formation.

There are different combinatorial mask configurations to effectively create and investigate large compositional phase spaces. Figure 7.3 illustrates the quaternary combinatorial masking scheme [Wang et al., 1998]. This scheme involves n different masks, which successively subdivide the substrate into a series of self-similar patterns of quadrants. The rth ($1 \leq r \leq n$) mask contains 4^{r-1} openings where each opening exposes one quarter of the area exposed in the preceding mask. Within

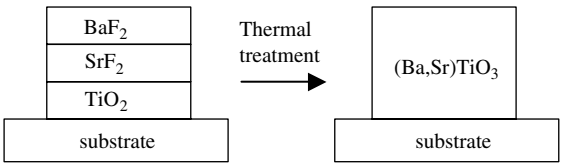

Figure 7.2 Scheme of phase formation in the precursor technique. An amorphous precursor multilayer deposited at room temperature is converted to a crystalline compound.

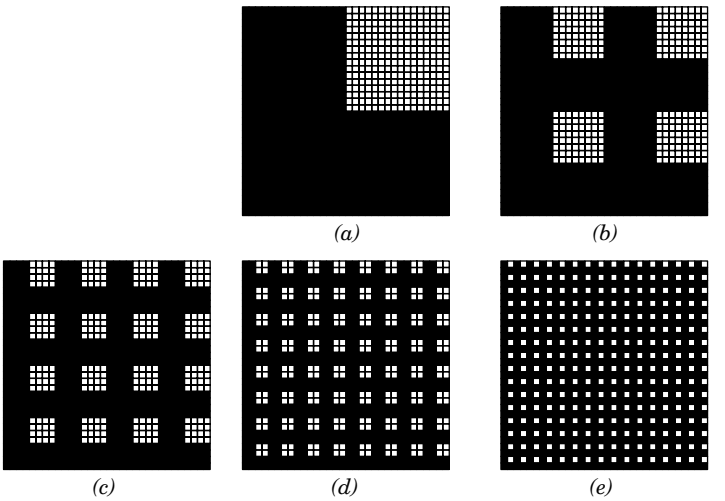

Figure 7.3 Set of physical shadow masks used in the quaternary masking strategy. Each mask is used in up to 4 depositions.

each opening, there are an array of 4^{n-r} gridded sample sites. Each mask is used in up to four sequential depositions, where for each deposition the mask is rotated by 90°. This process results in up to 4^n different combinations of precursors created after $4 \times n$ precursor depositions. This can be effectively applied to survey a large number of different compositions, each consisting of up to n-elemental components, and each component is selected from a group of up to four precursors. In many ways, the use of the precursor technique, and a masking strategy such as this, brings out the most in the combinatorial approach since the number of compositionally varying samples is determined in a mathematically combinatorial way.

Implementation of masking schemes is accomplished using either physical shadow masking or photolithographic lift-off steps. Because of its high spatial resolution and alignment accuracy, the lift-off method is particularly suitable for generating chips containing a high density of sites. The trade-off is that after each deposition, a lift-off step and spinning and patterning of the next layer of photoresist needs to be performed. Figure 7.4 is a photograph (taken in daylight) of a 1024-member library chip designed to search for new luminescent materials. This library was laid out mostly using PLD together with lift-off of each layer using 5 quaternary masks on a 1-inch × 1-inch substrate. The photograph was taken following the deposition prior to annealing [Wang et al., 1998]. Individual sites on the library all appear different due to the varied thicknesses and different optical indexes of precursor multilayer films. The color variation and its distribution in the library reflect the diversity one can achieve using this technique. This particular experiment yielded a number of leads in new luminescent materials and has led to the discovery of an efficient blue-emitting photoluminescent composite material, $Gd_3Ga_5O_{12}/SiO_2$ [Wang et al.,1998].

Although it may appear straightforward, phase formation by annealing amorphous mutilayers of precursors is far from conventional for making stoichiometric compounds, as initially it was not clear that this synthesis approach would generate meaningful crystalline compounds. As an example, in annealing a multilayer, nucleation could occur at each interface between precursors resulting in formation of multiple binary phases instead of the desired multielement single phase. In fact, many failed attempts at converting the precursors into crystalline compounds were made before an effective multistep annealing process was found [Xiang et al., 1995]. This approach was inspired by the work of Johnson and colleagues at the University of Oregon on metal precursor interdiffusion [Fister and Johnson, 1994]. It takes advantage of competition between interdiffusion and nucleation

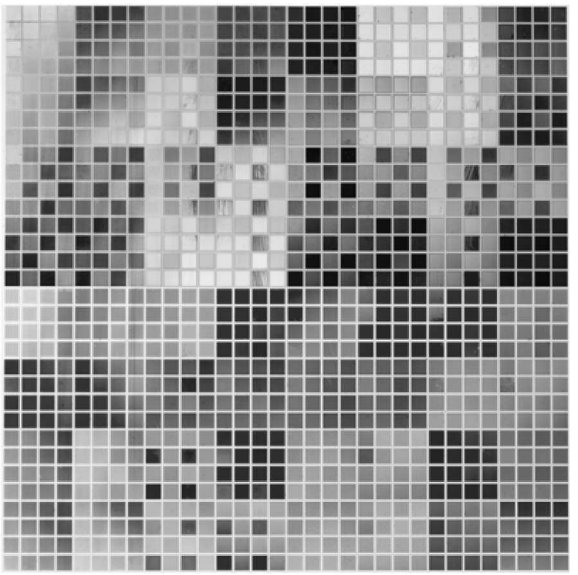

Figure 7.4 Photograph of a luminescent materials library (1 inch × 1 inch). The library was laid out using the quaternary masking technique implemented using photolithography [Wang et al., 1998].

at the interfaces of precursor layers. For every bilayer combination, there exists a critical thickness determined by the kinetics, below which interdiffusion at the interface is dominant over nucleation. Therefore, it is possible to interdiffuse the precursor layers to form an intermediate amorphous state close in stoichiometry to the desired crystalline phase before the nucleation of thermodynamically stable phases starts. We found that most metal alloys or oxide compounds can be formed from multilayers of metal and/or metal oxide precursors through controlled thermal treatments. Prior to synthesizing a full library, a few sampling experiments are performed for a representative composition in order to arrive at appropriate processing conditions for the entire library. It is crucial that one does not place ''too much variation'' on a given library where ideal processing conditions among different selected compositions may be vastly different.

We have found that multistep annealing of amorphous precursor multilayers yields not only predominantly single-phase materials, but can also produce *epitaxial* thin films on lattice-matched substrates [Chang et al., 1998]. This is mostly indicated by X-ray diffraction of resulting films displaying peaks from the desired single phase. In particular, we have extensively studied the microstructural properties of $BaTiO_3$ films on $LaAlO_3$ substrates fabricated from BaF_2/TiO_2 bilayers. We found that the ϕ scan of the (101) planes of the films display a clear fourfold symmetry indicating that the films are in-plane aligned with the substrate. To further examine the microstructural details of these, we have also performed high-resolution transmission electron microscopy (TEM) and found that the films do indeed consist mostly of large epitaxial grains that had nucleated at the film–substrate interface [Takeuchi et al., 2001; Bendersky, 2002].

It is known that properties such as dielectric and mechanical losses can be dramatically influenced by addition of small amounts of elemental or compound dopants. To study the effects of different dopants on the dielectric properties of $(Ba_{1-x}Sr_x)TiO_3$, a library consisting of four different stoichiometries of $(Ba_{1-x}Sr_x)TiO_3$ thin films ($x = 1.0$, 0.8, 0.7, and 0.5) as hosts was generated. The hosts were doped with different combinations of up to three out of nine different metallic elements with each dopant added in excess of 1 mol % with respect to the $(Ba_{1-x}Sr_x)TiO_3$ host [Chang et al., 1998]. The quaternary combinatorial masking scheme was used to generate $4^4 = 256$ different dopant combinations in 16 steps. To fabricate the library, TiO_2 (870 Å) was deposited first to

generate an array of 256 samples, each $650 \times 650\,\mu m^2$, on a (100) LaO substrate. This was then followed by deposition of BaF_2, SrF_2, and different dopants in the following sequence: B_1: Fe_2O_3 (7 Å); B_2: W(5 Å); B_3: CaF_2(12 Å); C_1: Cr(4 Å); C_2: Mn_3O_4(7 Å); C_3: CeO_2(12 Å); D_1: MgO(7 Å); D_2: Y_2O_3(10 Å); D_3: La_2O_3(12 Å); A_1: BaF_2(1640 Å); A_2: SrF_2 (270 Å) + BaF_2(1320 Å); A_3: SrF_2(410 Å) + BaF_2(940 Å); A_4: SrF_2(680 Å) + BaF_2(830 Å), where A, B, C, and D denote the quaternary masks used in the deposition steps, the subscript i indicates an $(i-1) \times 90^\circ$ clockwise rotation of the mask relative to the orientation of the mask shown in Figure 7.3, and the numbers in parentheses indicate the film thickness. The dopant layers were sandwiched between TiO_2 and the fluoride materials to prevent evaporation during subsequent annealing steps. The library was then heated at 400°C in flowing oxygen for 24 h to initiate mixing of the precursors (TiO_2, BaF_2, and SrF_2) as well as diffusion of the dopants. This was followed by a further annealing in flowing oxygen at 900°C for 1.5 h.

A scanning microwave microscope was used for nondestructive quantitative dielectric characterization of the thin-film library at 1 GHz. We have found that all the films doped with W consistently give dielectric loss significantly lower than other films [Chang, 1998; Takeuchi, 1998]. Following this work, a careful study of high-quality in situ grown films of W-doped $(Ba_{1-x}Sr_x)TiO_3$ by J. Horwitz at Naval Research Laboratory has yielded a record low microwave loss, tan δ of 0.005 at room temperature [Chang et al., 1999]. This represents a significant improvement in the material for tunable microwave device applications.

7.5 HIGH-THROUGHPUT THIN-FILM DEPOSITION

In incorporating the combinatorial strategy into PLD, our philosophy was to maintain and enhance the versatility and the relative simplicity of PLD. To this end, we have developed at the University of Maryland a compact 8-inch-diameter combinatorial thin-film deposition flange where all the necessary components for creating combinatorial libraries and composition spreads of different designs are integrated in a single vacuum flange [Chang et al., 2004], a photograph of which is shown in Figure 7.5. Essentially, it is a 1.5-inch-diameter substrate–mounting heater plate (which can go up

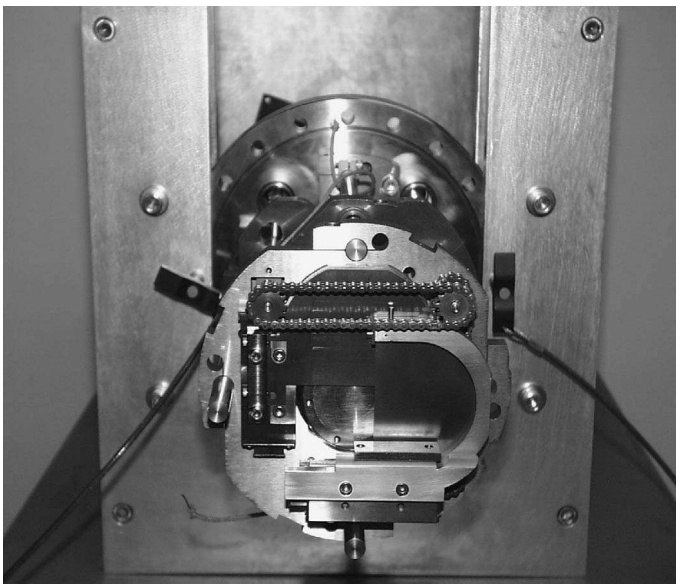

Figure 7.5 Photograph of a combinatorial thin-film deposition flange on a stand. It can be mounted in any appropriate physical vapor deposition chamber to perform combinatorial library synthesis.

to $\sim 800^{\circ}$C) integrated with a two-dimensional shuttering system. The shutters allow spatially selective shadow deposition of different layouts anywhere on mounted substrates up to 1 inch ^{2}. The main advantage of the flange is that it is not a permanent fixture to any one system, and it can be placed on any deposition system as long as the flange size is compatible. We have used one combinatorial flange on several different PLD chambers each dedicated to a specific materials system to demonstrate its portable nature. The current version of the flange is approximately 19 inches in height and weighs approximately 25 lb. The heart of the flange is entirely modular, and it can, in principle, be placed on flanges of any sizes 6 inches and up. Although it was originally developed for PLD, it is also applicable to other physical vapor deposition systems such as sputtering and evaporation processes where shadow deposition is readily achievable. We have recently successfully implemented one to an electron beam deposition system, where it is used to make libraries of metallic alloy systems [Ohguchi et al., 2005].

The flange contains motors and feedthroughs for driving the automated shutter system. The motors drive the shafts that rotate the chains to which the shutters/masks are connected. The overlapping $x - y$ shutters are made of ~ 300-μm-thick stainless steel sheets. The heater plate located immediately behind the shutters is rotatable in an automated manner with an indexed angle, and the spacing between the heater plate and the shutter plates is adjustable. The substrate surface can be brought as close as 100 μm away from the shutter for room temperature deposition, or as far away as 5 cm (for postdeposition annealing at elevated temperatures.) For in situ growth of films at elevated temperatures, the distance between the substrate surface and the shutter is typically 300–500 μm, which is required for minimizing the heat transfer from the heater to the shutter system and then onto other parts of the mechanical assembly.

Apertures of any shapes can be cut into the shutter plates depending on the required layout design of a particular combinatorial experiment. For instance, it can be a simple square opening used for fabricating composition spreads (described below) or a set of window patterns with the quaternary masking configuration discussed above. The shutter plates and the heater plates are replaceable, and they are exchanged from experiment to experiment to minimize cross contamination through resputtering of materials deposited on them. We have found that the two overlapping shutters, which move in two orthogonal directions, combined with a rotatable heater allow us to accommodate virtually any type of library/spread layout designs. The shutters can move with variable speeds from 0.18 to 1.2 mm/s. The shutter-driving motors, the target carousel, which fits up to 6 target materials, and the laser are all synchronized by a computer and controlled via Labview compiled software.

Using the aperture patterns for the two shutters, as shown in Figure 7.5, one can make a discrete library where thin-film samples of different compositions are deposited on separated individual sites of square areas. Figure 7.6 is a photograph of a gas sensor library made in this manner [Aronova et al., 2003]. The utility of combinatorial libraries for gas sensor applications is twofold: One is to search and optimize the compositions for high sensitivity and selectivity of gases, and the other is to make use of the natural array geometry of the libraries for an electronic nose, where an array of sensors is multiplexed for gas identification by pattern recognition. Prior to the deposition of 16 sites on the library, a two-terminal Au electrode pattern was created by a lift-off process on a sapphire substrate. Then 500-Å-thick sensor films of different compositions were deposited on selected areas (2 mm$\times$2 mm) at fixed positions on the Au electrode pattern. The array consisted of 16 compositions where SnO_2 was the host material and ZnO, WO_3, In_2O_3, Pt, and Pd were the dopants. The films were deposited at 550°C in oxygen partial pressure of 2×10^{-3} Torr. These dopants were selected based on previous reports on single-composition gas sensor studies.

One major drawback of PLD is the limited area of uniformly deposited film thickness on substrates because of the finite size of the plasma plume. Under a typical deposition condition of 100 mTorr of O_2, this area is at most ~ 1 cm^2. Because the gas sensor library chip was 1 inch^2, deposition was performed in four steps where a quarter of the substrate was exposed for deposition at a time. This was facilitated by 90° rotations of the substrate between steps. To create thin films of selected chemical compositions, we deposited materials in a layer-by-layer process where SnO_2 and other layers were deposited in an alternating manner. Each layer of SnO_2 and its dopant material was

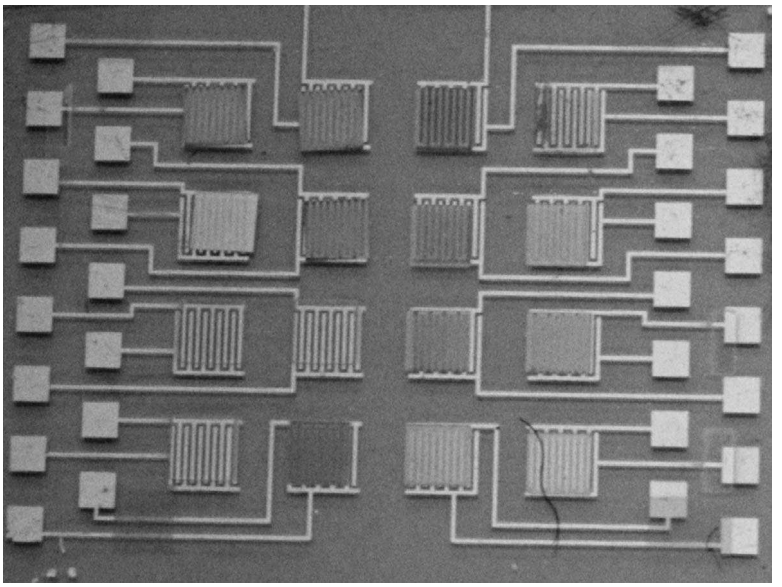

Figure 7.6 Photograph of an electronic nose: a combinatorial library of semiconductor based gas sensors (1 inch × 1 inch) [Aronova et al., 2003].

less than 4 Å thick so that dopants are intimately mixed at a subnanometer level. For deposition of the 16 sensors, the total deposition time of one library was ~ 3.5 h, most of which was spent on moving and aligning the automated shutters. Testing of the chips was successfully performed in a gas flow chamber where all sensors were electrically connected to the outside electronics to monitor its resistance change. We were able to demonstrate the detection of different gas species by pattern recognition. In this manner, the entire library is used as one electronic nose device [Aronova et al., 2003].

7.6 COMBINATORIAL LASER MOLECULAR BEAM EPITAXY

In view of the fact that every crystalline material is composed of molecular layers stacked periodically and that modern electronic devices have nanoscale layer structures [Koinuma, 1998], it is desirable to develop a scheme for parallel fabrication of layered structures so that one can quickly find the best combinations in layered lattices and optimum fabrication conditions. Koinuma and co-workers implemented the methods of combinatorial laser molecular-beam epitaxy (CLMBE) [Koinuma, 2002; Koinuma et al., 1999] to create artificial oxide lattices and heterojunctions, with each layer composition, thickness, and sequence controlled at the atomic scale. Molecular layers are deposited from several kinds of solid sources through a series of physical shadow masks placed on a heated substrate, and the deposited materials are crystallized in as-grown states. Key features of a CLMBE system include a set of physical masks for spatially selective film deposition, a scanning reflection high-energy electron diffraction (RHEED) system for *in situ* diagnostics of film growth mode at various sites on a substrate, and a fiber-guided Nd : YAG laser for substrate heating, as shown in Figure 7.7a. By monitoring the growth mode with RHEED and by synchronizing the target exchange with mask movements, synthesis of a number of atomic-layer-controlled materials can be coordinated on a single substrate.

The effectiveness of combinatorial lattice integration using the CLMBE system was demonstrated in the concurrent fabrication of a set of $SrTiO_3/BaTiO_3$ superlattices with equimolar ratios and different periodicities at an oxygen pressure of 1.0×10^{-6} Torr and a substrate

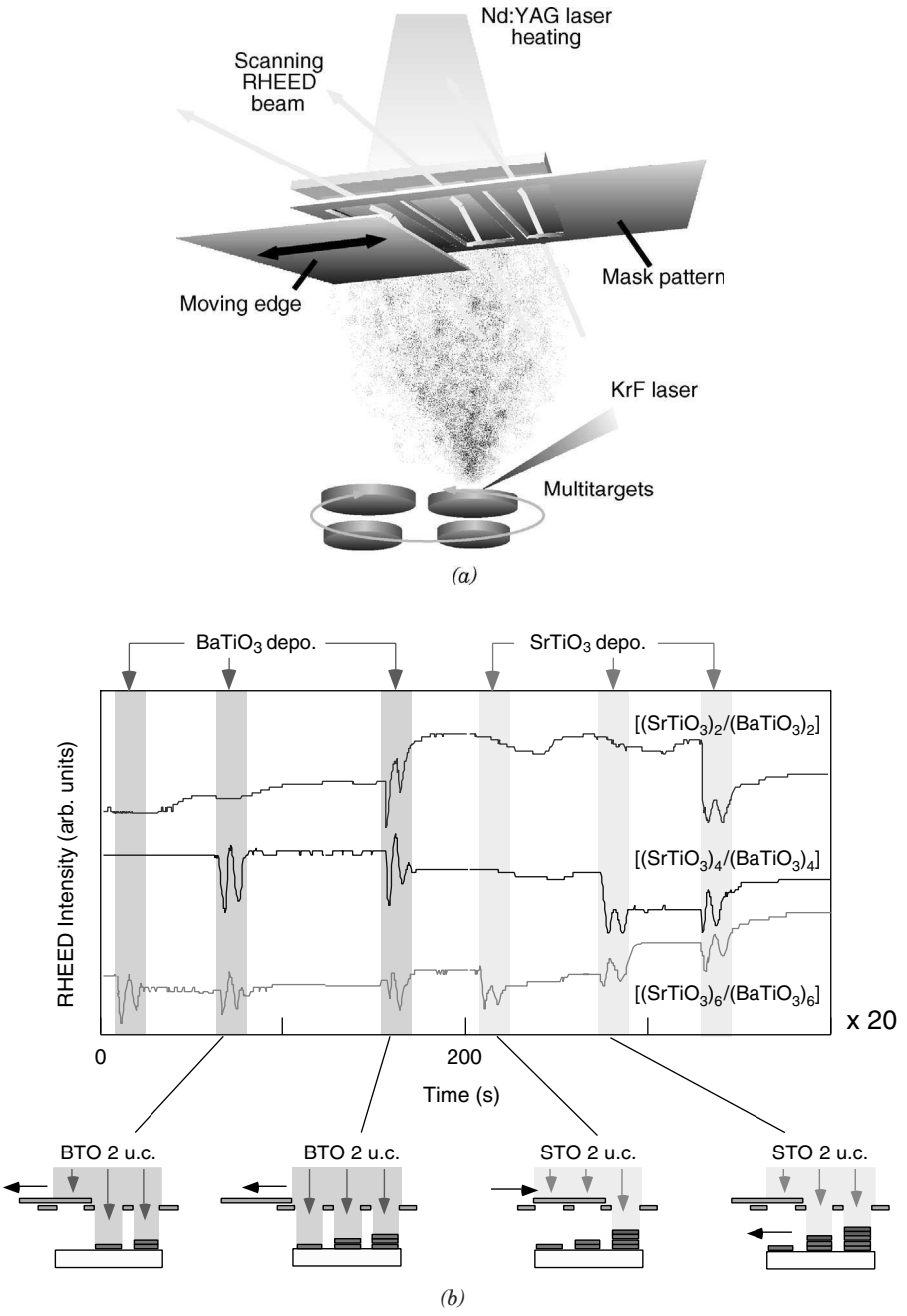

Figure 7.7 Fabrication of an atomically controlled materials library. (a) Schematic setup for parallel growth of epitaxial superlattices. (b) Simultaneously obtained reflection high-energy electron diffraction (RHEED) intensities versus time for three $SrTiO_3/BaTiO_3$ superlattices fabricated. The deposition sequence is shown below the graph.

temperature of 700°C [Ohnishi et al., 2001]. The use of chemically etched $SrTiO_3(001)$ substrates with atomically flat surfaces enabled observation of clear RHEED intensity oscillations, each of which corresponded to the growth of a unit cell layer (0.4 nm) of each oxide. Synchronization of the RHEED beam sweeping across the substrate surface with a pair of coils and image acquisition were combined with motion of the physical masks to simultaneously control the growth of as many as 10 strips of thin films in parallel on a single substrate. RHEED traces for the growth of three different periodicities are shown in Figure 7.7b. Incorporating 90° substrate rotation can enable fabrication of as large as a 10×10 matrix of superlattices.

The Nd : YAG laser, which heats substrates up to 1400°C in 1 atm of O_2, can also be used to create a temperature gradient on a substrate [Koida et al., 2002a]. Fine tuning the optimum deposition temperature is a typical experiment in any thin-film research, and this capability allows one to explore temperature as a combinatorial parameter. Thus, it is now possible to simultaneously optimize temperature and composition in a single experiment. This technique has been successfully implemented in optimizing different materials [Minami et al., 2002; Tsukazaki et al., 2002; Koida, 2002b].

A good example of serendipitous discovery brought about by the combinatorial approach is the unexpected finding of optically transparent magnetism in TiO_2 anatase films doped with Co from a library made with CLMBE [Matsumoto et al., 2001a]. Ferromagnetic semiconductors formed by doping magnetic impurities into host semiconductors are key materials for spintronics, where the correlation between the spin and the charge of electrons gives rise to spin-dependent functionalities such as giant magnetoresistance and spin field-effect transistors. All known magnetic semiconductors until now had been based on nonoxides such as GaAs and ZnSe, and their highest Curie temperature was ~ 100 K. There was a theoretical prediction that ZnO would become ferromagnetic when doped with certain $3d$ transistion elements, but to date no sign of ferromagnetism has been observed in such systems.

Titanium dioxide (TiO_2) is commonly used for photocatalysis for water cleavage and is well known for its unique properties including high refractive index, excellent optical transmittance in the visible and infrared regions, and high dielectric constant. Libraries of $3d$ transistion-metal-doped TiO_2 were originally fabricated by CLMBE in a search for photocatalysts. When their magnetic properties were checked with a scanning superconducting quantum interference device (SQUID) microscope, Co-doped TiO_2 was found, surprisingly, to exhibit ferromagnetism at room temperature while maintaining its transparency and single phase up to the composition of 8% Co. To systematically study the changes in film properties as a function of doping level, a library containing nine $Ti_{1-x}Co_xO_2$ films with different x values was fabricated. TEM of the films has indicated no sign of segregation of impurity phases in the compositional range of $x < 0.08$.

Figure 7.8 shows a series of images taken with the SQUID microscope at 3 K for anatase TiO_2 films with different Co contents ($x = 0.06$) on a combinatorial chip. In all of the Co-doped films, magnetic-domain structures of around 20 μm are observed. With increasing Co content in the film, the magnitude of the magnetic field is systematically enhanced as a result of increased spontaneous magnetization. This observation established the presence of long-range order in the Co-doped TiO_2 anatase phase. Further magnetic characterization indicated that the films are ferromagnetic even at room temperature. The spontaneous magnetic moment per Co atom was deduced to be 0.32 μ_B from M-H curves. From a temperature-dependent magnetization measurement, T_c was estimated to be higher than 400 K, significantly higher than that of known nonoxide ferromagnetic semiconductors. At present, the exact nature of the magnetic long-range order in Codoped TiO_2 is not understood. Recently, Co-doped TiO_2 rutile films were also found to exhibit robust ferromagnetism at room temperature [Matsumoto et al., 2001b]. The films were also found to display excellent optical transmission with a bandgap of 400 nm (3.1 eV). Transparent ferromagnets have the potential for serving the integration of electronic circuits and magnetic storage with the user interface in a single flat-panel display.

This finding has opened up a new field of oxide-based dilute magnetic semiconductors where researchers around the world are now investigating a variety of oxide materials with similar magnetic properties [MRS, 2003].

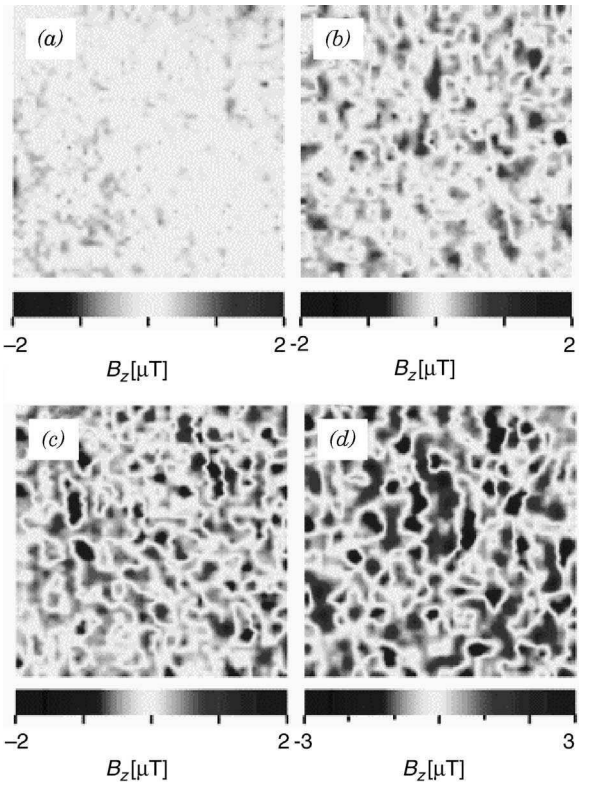

Figure 7.8 Series of scanning superconducting quantum interference device (SQUID) microscope images (200 μm × 200 μm) taken at 3 K for anatase TiO_2 thin films with different Co concentration ($Ti_{1-x}Co_xO_2$) on a combinatorial chip. B_z stands for magnetic field in the perpendicular direction. (a) $x = 0$, (b) $x = 0.02$, (c) $x = 0.03$, and (d) $x = 0.06$. Magnetic domain structures are observed suggesting the presence of long-range magnetic ordering [Matsumoto, 2001a].

7.7 COMPOSITION SPREADS AND COMBINATORIAL MATERIALS SCIENCE

In addition to serving the discovery/optimization needs of materials in key technology areas, the combinatorial approach can be used to address fundamental solid-state physics and chemistry questions as well. Composition spread experiments are highly effective in rapidly mapping compositional phase diagrams and systematically investigating physical properties that vary across compositional ranges [Chang et al., 1999; Yoo et al., 2000; Takeuchi et al., 2003b]. They can be used to map out the details of known materials systems or probe previously unexplored materials phase space. This represents a novel and rapid way to construct composition–structure–property relationships. Co-sputtering had been used as the main technique for creating thin-film composition spreads [Hanak, 2003; van Dover, 1998]. Recently, the advent of combinatorial PLD has led to a new technique, which allows synthesis of in situ epitaxially grown composition spreads.

In this technique, typically, two ceramic targets (whose compositions serve as the two end compositions of the spread) are ablated in an alternating manner. A linear compositional gradient across the spread can be created by performing a series of shadow depositions through a rectangular opening in a shutter, which moves back and forth over the substrate during the deposition. The motion of the shutter is synchronized with the firing of the laser in such a way so that for each deposition, a thickness gradient ''wedge'' is created on a chip. To ensure alloylike intermixing of

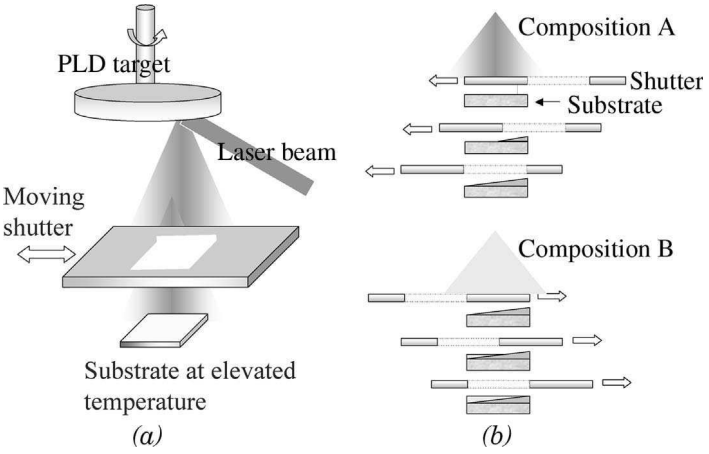

Figure 7.9 Fabrication scheme of a linear epitaxial composition spread. (a) Laser ablation is performed while the shutter with an edge moves across the substrate creating a thickness wedge. (b) Layers of alternating wedges are deposited for compositions A and B. Each layer at the thick end is less than a unit cell. This process is repeated for as many cycles as necessary.

two compositions at the atomic level at any position on the spread, less than a unit cell is deposited for each pair of depositions (for the two targets), and up to hundreds of pairs of gradient deposition are carried out for making relatively thick samples. This process is shown schematically in Figure 7.9. The resulting spread has a composition varying continuously from one component at one end to another at the other end. The samples are typically less than 1 cm long in the spread direction.

This technique has the advantage that it provides specifically designed layouts of compositional spread, unlike in co-sputtering where composition distribution is dictated by the very nature of the co-sputtering process from multiple targets. By ablating three targets in a repeating cycle, one can also use this method to construct ternary phase diagram chips on an equilateral triangular-shaped sample area [Hasegawa et al., 2004; Takahashi et al., 2004]. This synthesis was first demonstrated for composition spreads of the manganite $La_{1-x}Sr_xMnO_3$ system where the composition was varied continuously from $LaMnO_3$ at one end to $SrMnO_3$ at the other [Fukumura et al., 2000]. In this study, a variety of characterization techniques was used to obtain mapping of structure–composition–magnetic properties, and a magnetic phase diagram across the spread chip was obtained.

$Ba_{1-x}Sr_xTiO_3$ composition spreads were made using $BaTiO_3$ and $SrTiO_3$ targets on $LaAlO_3$ substrates, and a multimode scanning microwave microscope was used for their dielectric characterization at microwave frequencies [Chang et al., 2001]. Measurements were taken on the spread at different positions as the microscope tip was scanned over the spread, so that data was collected as a function of composition. Figure 7.10 shows the composition-spread profile of the dielectric constant at three different frequencies measured simultaneously at room temperature. The profile shows a continuous change with the expected compositional dependence: The peak in the profile is located near $Ba_{0.65}Sr_{0.35}TiO_3$, which has its Curie temperature near room temperature. On either side of this composition, the dielectric constant is lower.

From Figure 7.10, it is evident that the dielectric constant tends to decrease as the measurement frequency is increased for compositions with high Ba/Sr ratio. This frequency dispersion is minimal or close to zero near the $SrTiO_3$ end of the spread. It increases with increasing Ba content, reaches the highest values for x at around 0.2–0.4, and decreases again as x approaches zero. The observed dispersion here directly points to the presence of strong dielectric relaxation, and it is closely tied to the onset of ferroelectricity. It is largest for compositions experiencing the ferroelectric transitions. Above and below the transition temperature, the dispersion is reduced.

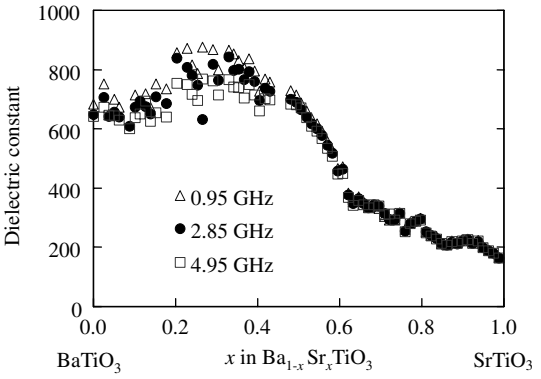

Figure 7.10 Dielectric constant versus composition on an epitaxially fabricated $Ba_{1-x}Sr_xTiO_3$ spread measured using a multimode microwave microscope at 0.95, 2.85, and 4.95 GHz simultaneously at room temperature.

This behavior is entirely consistent with the behavior of the soft mode near the paraelectric-ferroelectric transition, where the mode undergoes significant softening [Lines and Glass, 1977]. The dielectric frequency dispersion is maximum near the compositions undergoing transition, and above and below the transition range, it is markedly lower [Booth et al., 2005]. Thus, a single temperature measurement of the composition spread here allows an indirect probe of the temperature-dependent behavior of the entire (Ba,Sr)TiO_3 system.

In another example, composition spreads of the wide bandgap semiconductor system, $Mg_xZn_{1-x}O$ were fabricated *in situ* from ZnO and MgO targets on (0001)-oriented sapphire [Takeuchi et al., 2003c]. Unlike the other examples, the two end compositions have totally disparate crystal structures (hexagonal for ZnO and cubic for MgO). Studies of solubility limits and phase separation of structurally disparate compounds are common themes in materials science, and they pose particularly interesting questions in thin-film samples where nonequilibrium deposition processes and structural coherency with a compatible substrate can lead to formation of metastable phases. This epitaxial composition spread has allowed us to completely map the phase evolution and separation processes in the $Mg_xZn_{1-x}O$ thin-film system.

A scanning X-ray microdiffractometer was used to study the structural evolution across the spread. Figure 7.11 shows 2θ versus composition versus X-ray intensity from 30° to 50° for ZnO to $Mg_{0.81}Zn_{0.19}O$. The diffraction measurement was taken with the ω-scan mode, and at each 2θ, intensities are integrated in χ in the range of $\approx \pm 7.5°$. The relative change in the intensities of the peaks tracks the evolution of the phase changes as the composition is continuously varied. Starting from the pure ZnO end, the intensity of the (0002) peak from the hexagonal (Zn,Mg)O phase is seen to linearly decrease as x is increased. This is due to the continuous change in the structure factor of this phase as a function of composition. At around $x = 0.45$, the peak from the (111)-oriented cubic (Mg,Zn)O starts to develop, and its intensity saturates at $x = 0.6$. In addition, there is another peak at $2\theta \approx 42.6°$, which displays a transient behavior. Its 2θ value indicates that it is a (200) peak from the (100)-oriented cubic (Mg,Zn)O.

The phase-separated region is identified by the coexistence of X-ray peaks from the cubic and hexagonal phases. Compared to data from bulk $Mg_xZn_{1-x}O$, we find that the solubility of Mg in the deposited ZnO-based hexagonal phase is significantly extended (from 2 to 37 mol %), while it is about the same for mixing Zn into the deposited MgO-based cubic phase ($\sim$40 mol %). In Figure 7.12, we plot the normalized peak intensities versus composition. It is evident that in the phase-separated region, cubic (Mg,Zn)O is represented by both (100) and (111) orientations, and the (100)-oriented phase is associated with the presence of the hexagonal (Zn,Mg)O. Thus, just by studying the structural phase evolution in the spread, one can begin to gain insight into the physics of the phase separation process.

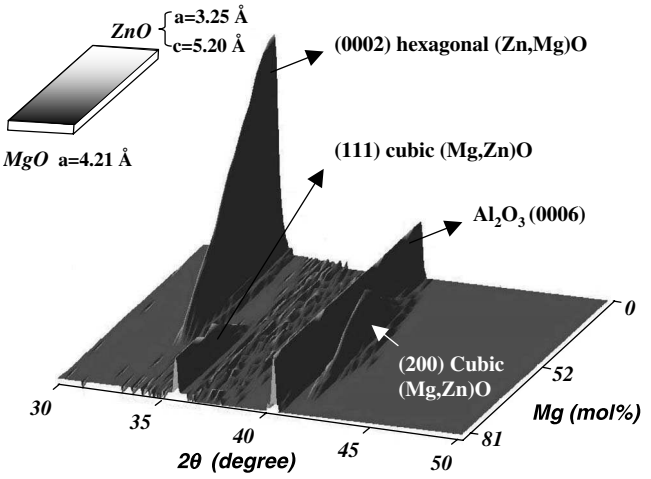

Figure 7.11 X-ray diffraction of a $Mg_xZn_{1-x}O$ composition spread taken with a 300-μm-diameter spot X-ray beam: 2θ versus composition with intensity integrated in χ in the range of $\pm 7.5^\circ$ with respect to the substrate normal is shown. The composition range shown is $x = 0 - 0.81$. The total thickness at each position on a spread was typically 200 nm. The sample was approximately 6 mm long in the spread direction. The left inset is a schematic of the spread chip and the lattice constants of the end compositions.

A TEM investigation of the spread in the phase-separated region revealed that the (100)-oriented cubic phase is growing pseudoepitaxially on the (0001)-oriented hexagonal (Zn,Mg)O with the following relationship:

$$(0001)_{\text{sapphire}}//(0001)_{\text{hex (Zn,Mg)O}}//(100)_{\text{cubic (Mg,Zn)O}}$$
$$(01\bar{1}0)_{\text{sapphire}}//(2\bar{1}\bar{1}0)_{\text{hex (Zn,Mg)O}}//(0\bar{1}1)_{\text{cubic (Mg,Zn)O}}$$

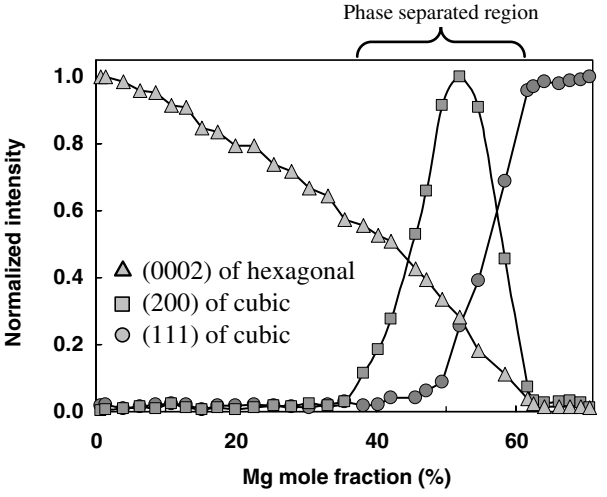

Figure 7.12 Normalized X-ray intensity as a function of composition. The triangles, squares, and circles are from hexagonal (0002), cubic (200), and cubic (111) peaks, respectively. The decrease in the intensity of (0002) is primarily due to the continuous change in the structure factor of the phase.

To the best of our knowledge, such an epitaxial relationship between a *c*-axis-oriented hexagonal crystal and a (100)-oriented cubic phase has never been reported before.

The bandgap at different spots on the spread was extracted from ultraviolet transmission measurements. In the low-Mg fraction region where the film remains hexagonal, the gap changes linearly from 3.27 to 4.28 eV. There is no well-defined bandgap between 4.3 and 5.4 eV, due to the phase separation. In the cubic single-phase end of the phase diagram, the bandgap increases nonlinearly with increasing Mg fraction from 5.4 to 7.8 eV.

The continuously changing bandgap across the spread was used as a basis for compact broadband photodetector arrays with a range of detection wavelengths separately active at different locations on the spread film. An array of Au-interdigitated electrodes was deposited to fabricate metal–insulator–metal structures as photodetectors; 25 detectors were fabricated along the length of one spread, and the composition-spread photodetector has successfully been demonstrated in the wavelength range of 290–380 nm using the ZnO to $Mg_{0.4}Zn_{0.6}O$ region of the spread [Takeuchi et al., 2003c].

The use of entire composition spreads as simultaneously active integrated devices opens up possibilities for a variety of other monolithic ''functionally broadband'' device components such as arrays of vertical cavity surface-emitting lasers with a continuously changing emission wavelength and arrays of actuators with a continuously changing piezoelectric response.

7.8 CONCLUSION

This chapter has presented a review of the development and the utility of combinatorial PLD. PLD provides a versatile and effective thin-film fabrication technique ideal for synthesis for a variety of combinatorial samples. Thin-film libraries have been used to discover various new compounds. Composition spreads have been demonstrated as a powerful tool for quickly mapping the composition–structure–property relationship in different materials systems. Examples were also presented where entire libraries/spreads are used as integrated individual devices.

Acknowledgments

The author is grateful to many colleagues for extensive collaboration and many insightful discussions over the years. I would particularly like to acknowledge the following colleagues for key contributions in the work described here: X.-D. Xiang, H. Chang, Y. Yoo, C. Gao, P. G. Schultz, K.-S. Chang, M. A. Aronova, W. Yang, R. D. Vispute, L. A. Bendersky, and H. Koinuma.

REFERENCES

Aronova, M. A., Chang, K. S., Takeuchi, I., Jabs, H., Westerheim, D., Gonzalez-Martin, A., Kim, J., and Lewis, B. (2003), *Appl. Phys. Lett*. **83**, 1255–1257.

Bendersky, L. A., Lu, C. J., Scott, J. H., Chang, K., and Takeuchi, I. (2002) *J. Mater. Res*. **17**, 2499–2506.

Booth, J. C., Ono, R. H., Takeuchi, I., and Chang, K.-S. (2005), *Appl. Phys. Lett*. **87**, 082908.

Briceño, G., Chang, H., Sun, X., Schultz, P. G., and Xiang, X.-D. (1995), *Science* **270**, 273–275.

Chang, H., Gao, C., Takeuchi, I., Yoo, Y., Wang, J., Schultz, P. G., Xiang, X.-D., Sharma, R. P., Downes, M., and Venkatesan, T. (1998), *Appl. Phys. Lett*. **72**, 2185–2187.

Chang, H., Takeuchi, I., and Xiang, X.-D. (1999), *Appl. Phys. Lett*. **74**, 1165–1167.

Chang, K.-S., Aronova, M. A., Famodu, O., Takeuchi, I., Lofland, S. E., Hattrick-Simpers, J., and Chang, H. (2001), *Appl. Phys. Lett.*. **79**, 4411–4413.

Chang, K.-S., Aronova, M. A., and Takeuchi, I. (2004), *Appl. Sur. Sci*. **223**, 224–228.

Chang, W., Horowitz, J. S., Kim, W.-J., Pond. J. M., Kirchoefer, S. W., and Chrisey, D. B. (1999), in *Ferroelectric Thin Films*, Vol. VII, Materials Research Society Symposium Proceedings 541, R. E. Jones, R. W. Schwartz, S. R. Summerfelt, and I. K. Yoo (Eds.), Materials Research Society, Warrendale, PA, p. 699.

Choo, J. O., Adomaitis, R. A., Henn-Lecordier, L., Cai, Y., and Rubloff, G. W. (2005), *Rev. Sci. Instrum*. **76**, 062217-1–062217-10.

Danielson, E., Devenney, M., Giaquinta, D. M., Golden, J. H., Haushalter, R. C., McFarland, E. W., Poojary, D. M., Reaves, C. M., Weinberg, W. H., and Wu, X.-D. (1998), *Science* **279**, 837–839.

Fister, L., and Johnson, D. C. (1994), *J. Am. Chem. Soc*. **116**, 629–633.

Fukumura, T., Ohtani, M., Kawasaki, M., Okimoto, Y., Kageyama, T., Koida, T., Hasegawa, T., Tokura, Y., and Koinuma, H. (2000), *Appl. Phys. Lett*. **77**, 3426–3428.

Hanak, J. J. (2003), in *Combinatorial Materials Synthesis*, X.-D. Xiang and I. Takeuchi (Eds.), Marcel Dekker, New York.

Hasegawa, K., Ahmet, P., Okazaki, N., Hasegawa, T., Fujimoto, K., Watanabe, M., Chikyow, T., and Koinuma, H. (2004), *Appl. Surf. Sci*. **223**, 229–232.

Koida, T., Komiyama, D., Koinuma, H., Ohtani, M., Lippmaa, M., and Kawasaki, M., (2002a), *Appl. Phys. Lett*. **80**, 565–567.

Koida, T., Wakisaka, T., Itaka, K., Matsumoto, Y., and Koinuma, H. (2002b), *Appl. Phys. Lett*. **81**, 4995–4997.

Koinuma, H. (1998), *Solid State Ionics* **108**, 1–7.

Koinuma, H. (2002), *Appl. Surf. Sci*. **189**, 179–187.

Koinuma, H., and Takeuchi, I. (2004), *Nature Mater.* **3**, 429–438.

Koinuma, H., Koida, T., Ohnishi, T., Komiyama, D., Lippmaa, M., and Kawasaki, M. (1999), *Appl. Phys*. **A69**, S29.

Lebl, M. (1999), *J. Comb. Chem*. **1**, 3–24.

Lines, M. E., and Glass, A. M. (1977), *Principles and Applications of Ferroelectrics and Related Materials*, Oxford University Press, New York.

Matsumoto, Y., Murakami, M., Shono, T., Hasegawa, T., Fukumura, T., Kawasaki, M., Ahmet, P., Chikyow, T., Koshihara, S-Y., and Koinuma, H. (2001a), *Science* **291**, 854–856.

Matsumoto, Y., Takahashi, R., Murakami, M., Koida, T., Fan, X.-J., Hasegawa, T., Fukumura, T., Kawasaki, M., Koshihara, S., and Koinuma, H. (2001b), *Jpn. J. Appl. Phys*. **40**, L1204–L1206.

Minami, H., Itaka, K., Ahmet, P., Komiyama, D., Chikyow, T., Lippmaa, M., and Koinuma, H. (2002), *Jpn. J. Appl. Phys*. **41**, L149–L151.

MRS Bulletin **28** (2003), October 2003, special issue on spintronics.

Ohguchi, H., Takeuchi, I., Josell, D., and Bendersky, L. A. (2005), to be published.

Ohnishi, T., Komiyama, D., Koida, T., Ohashi, S., Stauter, C., Koinuma, H., Ohtomo, A., Lippmaa, M., Nakagawa, N., Kawasaki, M., Kikuchi, T., and Omote, K. (2001), *Appl. Phys. Lett*. **79**, 536–538.

Phillips, J. C. (1989), *Physics of High T_c Superconductors*, Academic, New York.

Takahashi, R., Kubota, H., Murakami, M., Yamamoto, Y., Matsumoto, Y., and Koinuma, H. (2004), *J. Comb. Chem*. **6**, 50–53.

Takeuchi, I., Chang, H., Gao, C., Schultz, P. G., Xiang, X.-D., Sharma, R. P., Downes, M., and Venkatesan, T. (1998), *Appl. Phys. Lett*. **73**, 2185–2187.

Takeuchi, I., Chang, K., Sharma, R. P., Bendersky, L. A., Chang, H., Xiang, X.-D., Stach, E. A., and Song, C.-Y. (2001), *J. Appl Phys*. **90**, 2474–2478.

Takeuchi, I., van Dover, R. B., and Koinuma, H. (2003a), *MRS Bull*., **27**, 301–308.

Takeuchi, I., Famodu, O. O., Read, J. C. Aronova, M. A., Chang, K.-S., Craciunescu, C., Lofland, S. E., Wuttig, M., Wellstood, F. C., Knauss, L., and Orozco, A. (2003b), *Nature Mater.* **2**, 180–184.

Takeuchi, I., Yang, W., Chang, K.-S., Aronova, M. A., Venkatesan, T., Vispute, R. D., and Bendersky, L. A. (2003c), *J. Appl. Phys*. **94**, 7336–7340.

Tsukazaki, A., Saito, H., Tamura, K., Ohtani, M., Koinuma, H., Sumiya, M., Fuke, S., Fukumura, T., and Kawasaki, M. (2002), *Appl. Phys. Lett*. **81**, 235–237.

van Dover, R. B., Schneemeyer, L. F., and Fleming, R. M. (1998), *Nature* **392**, 162–164.

Wang, J., Yoo, Y., Gao, C., Takeuchi, I., Sun, X.-D., Chang, H., Xiang, X.-D., and Schultz, P. G. (1998), *Science* **279**, 1712–1714.

Xia, B., Smith, R. C., Moersch, T. L., and Gladfelter, W. L. (2004), *Appl. Surf. Sci*. **223**, 14–19.

Xiang, X.-D., Sun, X.-D., Briceno, G., Lou, Y., Wang, K.-A., Chang, H., Wallace-Freedman, W. G., Chen, S.-W., and Schultz, P. G. (1995), *Science* **268**, 1738–1740.

Yoo, Y. K., Duewer, F. W., Yang, H., Yi, D., Li, J.-W., and Xiang, X.-D. (2000), *Nature* **406**, 704–706.

CHAPTER 8

Growth Kinetics During Pulsed Laser Deposition

GUUS RIJNDERS and DAVE H. A. BLANK

MESA+ Institute for Nanotechnology, University of Twente, The Netherlands

8.1 INTRODUCTION

The application of thin films in electronic devices, relying on multilayer technology, requires (atomically) smooth film surfaces and interfaces. Understanding of the different mechanisms affecting the growth mode is, therefore, necessary to control the surface morphology during thin-film growth.

Two independent processes, that is, nucleation and growth of islands, play an important role during vapor-phase epitaxial growth on an atomically flat surface. Here, nucleation causes the formation of surface steps and subsequent growth causes the lateral movement of these steps. Both processes are determined by kinetics since they take place far from thermodynamic equilibrium. These kinetic processes affect the final surface morphology and are, therefore, extensively studied.

The applicability of high-pressure reflection high-energy electron diffraction (RHEED) to extract the kinetic parameters, determining the growth of complex oxides in pulsed laser deposition (PLD), will be demonstrated. The deposition and growth are separated in time in PLD, and this enables us to measure the kinetic parameters for different growth conditions by monitoring the decay of the adatom density between the deposition pulses. In this chapter the homoepitaxial growth of $SrTiO_3$ is used as a model system to demonstrate the influence of growth kinetics during PLD.

8.2 GROWTH MODES AT THERMODYNAMIC EQUILIBRIUM

The thermodynamic approach to crystal growth is used to describe crystal growth close to equilibrium, that is, for a thermodynamically stable system. Local fluctuations from equilibrium lead to nucleation, which gives rise to a phase transition from, for instance, the gas to the solid phase. A supersaturated [Markov et al., 1991] gas phase is a prerequisite for the formation of these nuclei, whereas the formation probability is determined by the activation energy. Nuclei will be formed until a critical density is reached. From this point onwards the nuclei will grow and crystallization is in progress.

This thermodynamic approach has been used to determine growth modes of thin films close to equilibrium [Bauer, 1958], that is, only at small or moderate supersaturation. In this approach the

Pulsed Laser Deposition of Thin Films: Applications-Led Growth of Functional Materials
Edited by Robert Eason

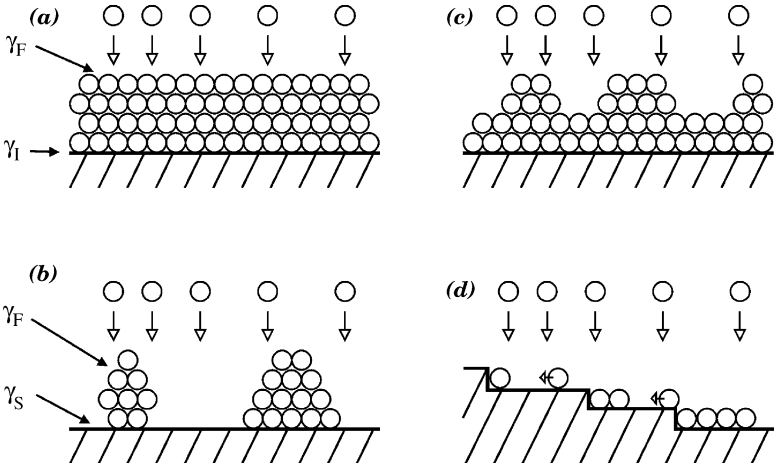

Figure 8.1 Film growth modes—layer-by-layer: (a) Frank-Van der Merwe, island; (b) Volmer–Weber (c), Stranski–Krastanov, (d) and step flow.

balance between the free energies of film surface (γ_F), substrate surface (γ_S), and the interface between film and substrate (γ_I) is used to determine the film morphology. Three different growth modes, schematically depicted in Figure 4.1, can be distinguished. In the case of layer-by-layer growth (Fig. 8.1a; Frank-van der Merwe growth mode), the total surface energy, that is, $\gamma_F + \gamma_I$, of the wetted substrate is lower than the surface energy of the bare substrate γ_S. Strong bonding between film and substrate reduces γ_I such that $\gamma_F + \gamma_I < \gamma_S$.

On the other hand, when there is no bonding between film and substrate, three-dimensional (3D) islands are formed. The film does not wet the substrate because this would lead to an increase of the total surface energy. This growth mode is referred to as the Volmer–Weber growth mode; see Figure 8.1b. In heteroepitaxial growth, the so-called Stranski–Krastanov growth mode can occur; see Figure 8.1c. Here, the growth mode changes from layer by layer to island growth. During heteroepitaxial growth, the lattice mismatch between substrate and film gives rise to biaxial strain, resulting in an elastic energy that grows with increasing layer thickness. Misfit dislocations at or near the substrate–film interface will be formed if the layer thickness exceeds a critical thickness h_c. At this thickness it is thermodynamically favorable to introduce dislocations because the elastic energy, relieved by the dislocations, becomes comparable to the increase in the interfacial energy. In other words, misfit dislocations are necessarily introduced to relieve the mismatch strain[1] and, therefore, equilibrium defects.

8.3 GROWTH KINETICS

In many vapor-phase deposition techniques, for example, PLD, the growing film is usually not in thermodynamic equilibrium and kinetic effects have to be considered. Because of the limited surface diffusion, the deposited material cannot rearrange itself to minimize the surface energy. The high supersaturation of the vapor leads to a large nucleation rate, and kinetic effects will lead to the occurrence of different growth modes.

[1]To relieve the misfit strain, the Burgers vector of the dislocation should have a component parallel to the substrate surface. Two extreme cases of misfit dislocations are edge dislocations (Burgers vector is directed perpendicular to the dislocation) and screw dislocations (Burgers vector is directed parallel to the dislocation). Usually, dislocations have a mixed character.

8.3.1 Homoepitaxial Growth Modes

In homoepitaxial growth the deposited material is identical to the substrate material and the crystalline structure of the substrate is extended into the growing film, and complicating effects such as lattice parameter misfit and thermal expansion coefficients do not play a role. Consequently, only two-dimensional (2D) growth modes are expected, depending on the behavior of the deposited species [Rosenfeld et al., 1997]. This behavior is determined by a number of kinetic parameters, among which are the surface diffusion coefficient (D_S) of the adatoms, the sticking probability of an adatom arriving at the edge of a terrace, and the additional energy barrier (E_S) for adatoms to descend the edge to a lower terrace. Of these mentioned kinetic parameters, the diffusion coefficient is probably the most important one as it determines the average distance an atom can travel on a flat surface before being trapped. This distance is the surface diffusion length l_D and can be defined by

$$l_D = \sqrt{D_S \tau} \tag{8.1}$$

where τ is the residence time before reevaporation. The surface diffusion coefficient D_S is generally expressed as

$$D_S = \nu a^2 \exp\left(-\frac{E_A}{k_B T}\right) \tag{8.2}$$

where E_A is the activation energy for diffusion, ν the attempt frequency, and a the characteristic jump distance. From Eq. (8.2) it is clear that the deposition temperature is important because it controls the diffusivity of the adatoms. To understand the possible 2D growth modes on both singular and vicinal substrates, two diffusion processes have to be considered. First, the diffusion of atoms on a terrace (intralayer mass transport) and second the diffusion of an atom to a lower[2] terrace (interlayer mass transport). Both processes are determined by the kinetic parameters.

A fast intralayer mass transport will lead to step flow growth on a vicinal surface; see Figure 8.1d. In this case l_D is sufficiently larger than the average terrace width l_T. The mobility of adatoms is high enough to enable atoms to reach the edges of the substrate steps. Here, steps act as a sink for the deposited atoms diffusing toward the steps and nucleation on the terraces is prevented. As a result, the steps will propagate leading to step flow growth. A growing vicinal surface will be stable if both the terraces keep the same width and the step ledges remain straight. If this is not the case, step meandering or step bunching can occur and, subsequently, the distribution in l_T broadens.

If the intralayer mass transport is not fast enough, nucleation on the terraces occurs. Initially, nuclei will be formed until a saturation density is reached. After the saturation, the probability for atoms to attach to an existing nucleus exceeds the probability to form a new nucleus and islands will start to grow. The interlayer mass transport will have a large effect on the growth mode in this case. Two extreme growth modes can be distinguished, that is, ideal layer-by-layer growth and ideal multilayer growth.[3] To obtain a layer-by-layer growth mode, a steady interlayer mass transport must be present; atoms deposited on top of a growing island must, first, reach the island edge and, second, diffuse to the lower layer. In the ideal case, layer-by-layer growth is obtained if nucleation starts after completion of a layer. When there is no or very limited interlayer mass transport, nucleation will occur on top of islands before these islands have coalesced. This so-called second-layer nucleation[4]

[2]Because of the higher coordination number for atoms at a step, diffusion of atoms to a higher terrace is usually neglected.

[3]Here, ideal refers to multilayer growth with no interlayer mass transport.

[4]The probability for second-layer nucleation is related to a critical island size R_C. It is the mean island radius at a critical time during submonolayer growth where stable clusters nucleate on top of the islands. If R_C is small compared to the mean distance between islands in the first layer, islands will nucleate a second layer and multilayer growth will occur. An important parameter, which influences R_C, is the energy barrier for atoms to descend across the step edge to a lower terrace. An additional energy step edge barrier E_S has to be overcome if this energy barrier is large compared to E_A. Large values of E_S will lead to accumulation of adatoms on top of islands, leading to an increased second-layer nucleation rate and, therefore, to a smaller value of R_C.

will lead to multilayer growth. The growth mode in real systems far from equilibrium will lie between the two extreme growth modes.

8.3.2 Homoepitaxial Growth Study of $SrTiO_3$

The specular RHEED intensity, monitored during homoepitaxial growth of $SrTiO_3$ at the deposition temperature of 850, 750, and 650°C is depicted in Figures 8.2a, 8.2b, and 8.2c, respectively. The oxygen deposition pressure was set to 3 Pa, and under these conditions,[5] 2D nucleation and growth is observed, indicated by the clear intensity oscillations. The oscillation periods correspond to the deposition time of one unit cell layer. At the highest temperature, full recovery is obtained at completion of every unit cell layer. Here, the growth mode can be described as ideal unit cell layer by layer.

The angle of incidence of the electron beam (e-beam) was set to $\sim 1^\circ$, resulting in a diffraction condition corresponding to the in-phase condition. Reflections from unit cell layers at different levels add constructively, and a constant maximum intensity is predicted by the kinematic theory[6] for this condition. RHEED intensity variations are nevertheless observed at the in-phase diffraction condition, caused by diffuse scattering at surface step edges. Electrons are easily scattered out of the specular beam by the step edges since the unit cell layer thickness is much larger than the wavelength of the electrons. The specular RHEED intensity is, therefore, a measure of the surface step density. During 2D nucleation and growth, oscillation of the step density is caused by the periodic formation, that is, nucleation, and coalescence of growing islands. Note that a minimum specular RHEED intensity will be observed at the maximum step density.

Assuming instantaneous nucleation[7] and subsequent 2D growth of equally spaced islands by step propagation, the step density S can be determined by the widely used step density model [Stoyanov, 1988; Stoyanov and Michailov, 1988]. Without second layer nucleation, S is given by

$$S = 2\sqrt{\pi N_S}(1-\theta)\sqrt{-\ln(1-\theta)} \tag{8.3}$$

where N_S is the number of nuclei per unit area. Both the diffusivity of the deposited material and deposition rate determine the quantity N_S and, therefore, the amplitude of the step density oscillation. The shape of the RHEED intensity, measured at the in-phase diffraction condition during homoepitaxial growth of $SrTiO_3$, supports the applicability of the step density model oscillations. A maximum step density $S_{\mathrm{MAX}} = \sqrt{2\pi N_S/e}$ is reached at a surface coverage $\theta \sim 0.39$.[8] This corresponds to the observed RHEED intensity minimum at $\theta \sim 0.4$ in Figure 8.2.

8.3.2.1 Determination of Kinetic Growth Parameters on Singular Surfaces

The RHEED intensities in Figure 8.2 are clearly modulated by the laser pulse, giving rise to the typical RHEED intensity relaxations [Karl and Stritzker, 1992; Achutharaman et al., 1994]. Following the model described above, that is, instantaneous nucleation just at the start of every monolayer, this relaxation behavior is attributed to particles (metal atoms or metal–oxide molecules) diffusing toward the step edges of the islands. Incorporation of these particles at the step edges causes the islands to grow resulting in a change in the step density. The evolution of the step density after every pulse is, therefore, a direct result from the decay of the density of the diffusing particles, which depends on the diffusivity and the average travel distance; see Eq. (8.1). This distance is determined by the nucleation density N_S and the average island size, the latter depending on the coverage, giving rise to the coverage-dependent characteristic relaxation times; see Figure 8.2b.

[5]The distance between target and substrate was set to 58 mm, the laser energy density on target to 1.3 J/cm^2, and the spot size to 1.4 mm^2.

[6]Reflections from unit cell layers at different levels add destructively at the out-of-phase condition.

[7]Instantaneous nucleation can be expected during PLD because of the high pulse deposition rate and, subsequently, a high supersaturation within the deposition pulse; see Chapter 4.

[8]At constant rate of nucleation and step propagation a maximum in the step density is expected at coverage $\theta = 0.5$.

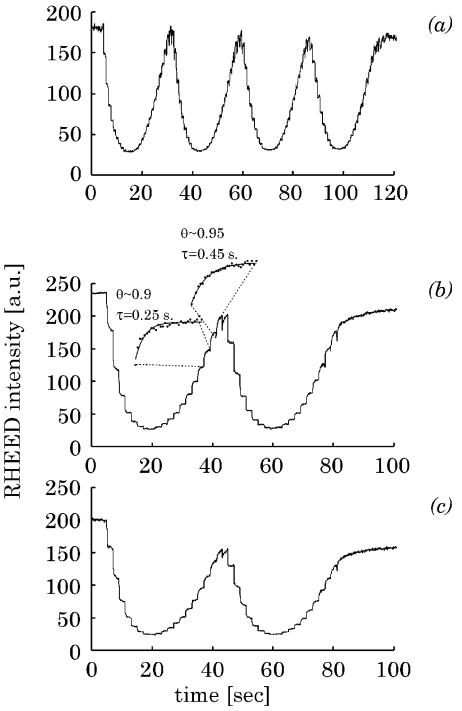

Figure 8.2 Specular RHEED intensity oscillations during homoepitaxial growth of $SrTiO_3$ at (a) 3 Pa, 850°C, (b) 750°C, and (c) 650°C. The insets in (b) show the enlarged intensities after a laser pulse at different coverage.

This dependence is illustrated by the following proposed model. The density of diffusing particles[9] on top of a circular, 2D island can be found by solving the time-dependent diffusion equation [Koster, 1999] given by

$$\frac{\partial^2 n_S}{\partial r^2} + \frac{1}{r}\frac{\partial n_S}{\partial r} = \frac{1}{D_S}\frac{\partial n_S}{\partial s} \tag{8.4a}$$

with the initial condition $n_S(r, 0) = n_0$, the density of instantaneously deposited particles due to one laser pulse. The boundary conditions are given by

$$n_s(r = r_0) = n_{se} \tag{8.4b}$$

and

$$\left(\frac{\partial n_S}{\partial r}\right)_{r=0} = 0 \tag{8.4c}$$

where n_{se} is the equilibrium density at the island edge; $n_{se} \sim 0$ assuming the edge is acting as a perfect sink.[10] The solution of Eqs. (8.4) is of the form

$$n_S(r, t) = n_0 \sum_{m=1}^{\infty} A_m(r; r_0) \exp\left(-\frac{t}{\tau_m}\right) \tag{8.5}$$

[9]Here, no nucleation on top of islands is assumed.
[10]For this to be true the step edge must be nonreflecting. This is valid if the additional step edge energy barrier $E_S \sim 0$.

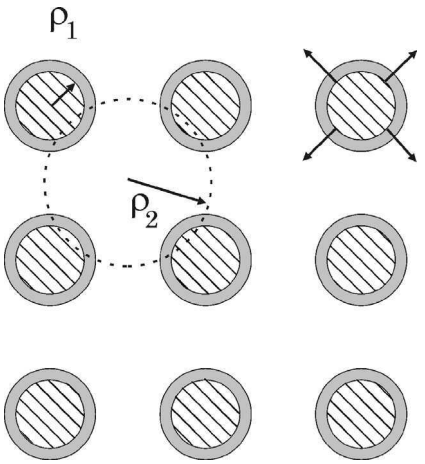

Figure 8.3 Schematic view of the coverage θ, given by the (hatched) area of the 2D islands. The density is determined by the nucleation density N_S. ρ_1 represents the radius of the islands at given coverage θ, whereas ρ_2 represents the radius of the area between the growing islands, given by $1 - \theta$. The gray area represents the change in coverage due to one deposition pulse.

where τ_m is given by

$$\tau_m = \frac{r_0^2}{D_S(\mu_m^{(0)})^2} \tag{8.6}$$

where A_m are prefactors depending only weakly on r and r_0. Equation (8.5) converges rapidly and, for long enough time, only the first term needs to be considered ($\mu_m^{(0)}$ are the roots of Bessel functions, $\mu_1^{(0)} = 2.40$). Without nucleation on top of the 2D island, an exponential decrease in the density of diffusing particles is expected after the deposition pulse. This exponential decrease depends on the size of the growing islands, which depends on the coverage via:

$$\pi r \rho_2^2(t) = \frac{\theta(t)}{N_S} \tag{8.7}$$

where $\pi\rho_2^2(t)$ is the area of the islands; see Figure 8.3. Substituting Eq. (8.7) into Eq. (8.6) gives the exponential decay time of diffusing particles on top of a 2D island as a function of the coverage θ:

$$\tau_2 = \frac{\theta}{D_S(\mu_1^{(0)})^2 \pi N_S} \tag{8.8}$$

The index 2 indicates diffusing particles at the 2^e level, that is, on top of the islands. The same approach can be followed for diffusing particles deposited between the islands. Here, the maximum travel distance of a diffusing particle is also determined by the coverage-dependent size of the islands (see Fig. 8.3). The area between the islands can be approximated by

$$\pi\rho_1^2(t) = \frac{1 - \theta(t)}{N_S} \tag{8.9}$$

Substituting Eq. (8.9) into Eq. (8.6) gives the exponential decay time (now indexed 1) of diffusing particles between 2D islands as a function of the coverage θ:

$$\tau_1 = \frac{1-\theta}{D_S(\mu_1^{(0)})^2 \pi N_S} \tag{8.10}$$

From the equations above it follows that, with increasing coverage, the decay time in the density of diffusing particles on top of a growing island is increasing. On the other hand, the decay time in the density of diffusing particles between islands is decreasing with increasing coverage.

The change in the coverage $\Delta\theta(t)$ after a deposition pulse can be approximated by

$$\Delta\theta_n(t) = \frac{\theta_{n-1}}{n_P}\left[1 - \exp\left(-\frac{t}{\tau_2}\right)\right] + \frac{1-\theta_{n-1}}{n_P}\left[1 - \exp\left(-\frac{t}{\tau_1}\right)\right] \tag{8.11}$$

where θ_{n-1} is the coverage before applying the pulse and n_P the number of pulses needed for completion of one monolayer, that is, $\theta = 1$. Here, $1/n_P$ represents the density of deposited particles. Multiplication of this density by θ_{n-1} and $1 - \theta_{n-1}$ gives the total number of particles, expressed in θ, deposited on top and in between the islands, respectively.

Figure 8.4a shows $\theta(t)$ for $N_S = 2 \times 10^{11}/\text{cm}^2$, $T = 850°\text{C}$, $E_A = 2.2\,\text{eV}$, and $n_P = 20$, calculated using the model described above.[11] Using Eq. (8.3) the evolution of the step density $S(t)$ can be calculated; see Figure 8.4b. Assuming a direct coupling between $S(t)$ and the diffuse scattering of electrons, the reflected RHEED intensity is approximated by

$$I(t) \propto 1 - \frac{S(t)}{S_{\max}} \tag{8.12}$$

which is shown in Figure 8.4c for the parameters given above. The simple model describes the observed RHEED intensity variations in Figure 8.2 qualitatively, as shown by the coverage-dependent characteristic relaxation time after every pulse. However, the observed RHEED intensity shows a pronounced decrease just after each pulse is applied. This effect is especially visible in Figure 8.2b at coverage close to unity. This difference can be explained by the contribution of the diffusing particles. Not only surface steps but also the diffusing particles themselves act as diffuse scatterers for electrons [Van der Wagt, 1994]. The decay in the particle density n_s on top and between the islands is described by Eq. (8.5) using the time constants given by Eqs. (8.8) and (8.10), respectively. Assuming a direct coupling of the averaged particle density and the diffusive scattered intensity, an exponential increase of the intensity is expected, given by

$$I \sim I_0\left[1 - \exp\left(-\frac{t}{\tau}\right)\right] \tag{8.13}$$

where I_0 is determined by the particle density just after the deposition pulse and τ is given by Eqs. (8.8) and (8.10) for particles deposited on top and in between the island. Here, only the first term of Eq. (8.5), that is, $m = 1$, is used.

The evolution of the step density and the density of diffusing particles determine the relaxation behavior of the RHEED intensity. The time dependence of both is expected to be comparable since the two contributions are coupled. At coverage close to unity ($\theta = 0.7 - 1$), most of the deposited material is deposited on top of the growing islands and only one time constant has to be considered.

[11]The parameters are chosen such that the density of diffusing particles is approximately zero before the next pulse is applied.

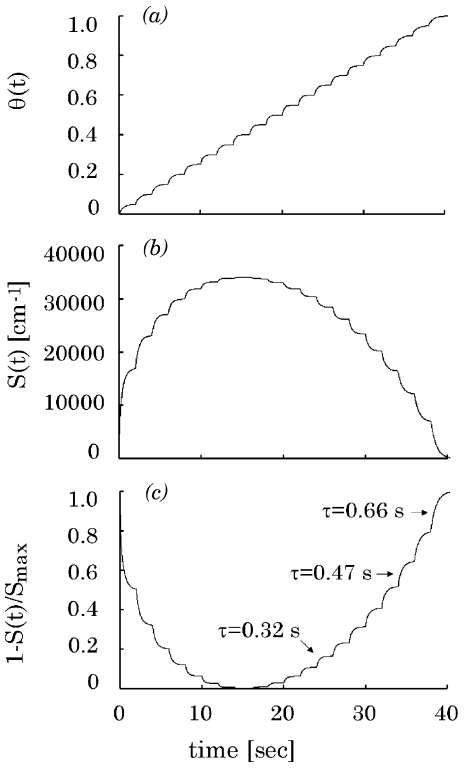

Figure 8.4 Calculated coverage $\theta(t)$ during (a) monolayer growth, (b) the corresponding surface step density $S(t)$, and (c) corresponding RHEED intensity, given by $1 - S(t)/S_{\max}$. Here, the nucleation density N_S is $2 \times 10^{11}/\text{cm}^2$, the temperature is 850°C, the energy barrier of diffusion E_A is 2.2 eV, and the number of pulses for one monolayer n_p is 20.

At these values of the coverage, the characteristic relaxation times can be used to estimate the activation energy for diffusion E_A. Figures 8.5a and 8.5b show the characteristic relaxation time versus temperature for different values of the coverage during the homoepitaxial growth of $SrTiO_3$ at a deposition pressure of 20 and 3 Pa, respectively. A value for E_A of 2.2 ± 0.2 eV is derived for a

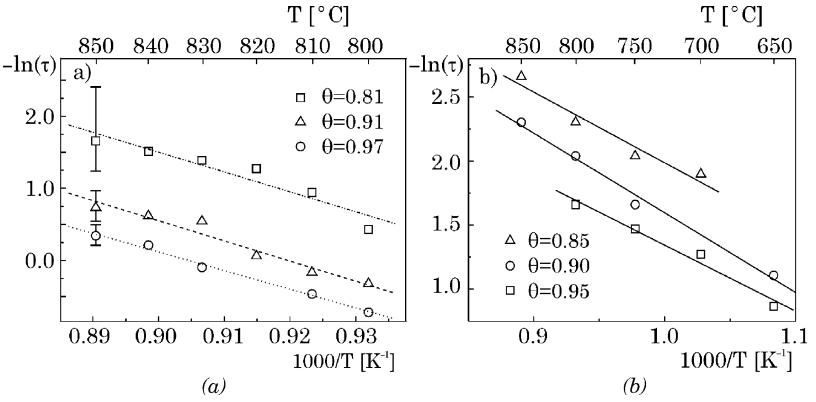

Figure 8.5 Arrhenius plot for the relaxation times obtained from a fit with Eq. (8.13) for different coverage and temperature at oxygen deposition pressures of (a) 20 Pa and (b) 3 Pa.

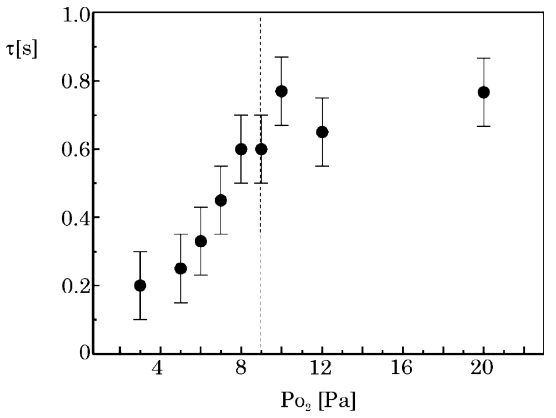

Figure 8.6 Relaxation time versus oxygen deposition pressure for $\theta \sim 0.95$ and substrate temperature of 850°C.

deposition pressure of 20 Pa, and 0.48 ± 0.05 eV for a deposition pressure of 3 Pa. The difference is attributed to the kinetic energy of the particles arriving at the substrate.

At the pressure of 20 Pa the visible plasma range was smaller than the target-to-substrate distance and the particles are expected to be thermalized [Strikovski and Miller, 1998]. At the lower pressure of 3 Pa the kinetic energy of the particles is expected to be larger leading to a reduced effective energy barrier for diffusion.

In Figure 8.6, the relaxation times are plotted versus the oxygen deposition pressure at a constant temperature of 850°C. At deposition pressures below 9 Pa, an increase in the relaxation time is observed for increasing deposition pressure and, consequently, a smaller kinetic energy of the arriving particles. However, above 9 Pa, the relaxation time is almost independent of the deposition pressure. At these higher pressures, the arriving particles are expected to be thermalized.

Reliable determination of the activation energy for diffusion E_A from the temperature-dependent characteristic relaxation times is only possible assuming the average travel distance for diffusing particles to be approximately constant in the temperature range of interest. That is, only small variations in the step density S are allowed and, as a consequence, only small variations of the coverage θ and the nucleation density N_S are allowed; see eqs. (8.8) and (8.10). The first requirement is easily obtained by depositing a sufficiently small amount of material in one pulse. The latter, however, is affected by the supersaturation $\Delta\mu$ and diffusivity D_S of the material. Both depend on the substrate temperature; with increasing temperature $\Delta\mu$ and D_S are decreasing. Consequently, the nucleation density N_S is not expected to be constant over a wide temperature range. A higher nucleation density N_S at lower temperature decreases the average travel length of the deposited material and the corresponding relaxation times will decrease; see Eqs. (8.8) and (8.10).

In conclusion, varying the temperature not only changes the diffusivity D_S but also N_S. As a result, the slope in the Arrhenius plots decrease and, subsequently, a smaller value for E_A is determined.

To overcome the temperature-dependent nucleation density and corresponding change in the average travel distance, step flow growth can be employed. No nucleation takes place during this growth mode, resulting in a steady average travel distance. Extraction of the energy barrier for diffusion during step flow growth is, therefore, more reliable, as will be discussed in the following section.

8.3.2.2 Determination of Kinetic Growth Parameters on Vicinal Surfaces

The transition from 2D to step flow growth on a vicinal substrate is often used to determine the adatom diffusion length. Either the substrate temperature, determining the surface diffusion length

l_D, or the vicinal angle, determining the terrace width l_T, is changed. A transition occurs when the diffusion length of adatoms becomes comparable to the terrace width, that is, $l_D \approx l_T$. It has been proposed [Neave et al., 1985] to use RHEED to determine this transition as a function of the growth conditions. This technique has been used by several groups [Shitara et al., 1992a, 1992b; Zandvliet et al., 1991] to estimate the surface migration parameters. The RHEED intensity is expected to be constant during step flow growth, whereas RHEED intensity oscillations occur during 2D nucleation and growth.

However, nucleation, being a stochastic process, can take place on a terrace smaller than the diffusion length. Furthermore, the absence of RHEED intensity oscillations is not always a clear signature of pure step flow growth. Even when a steady RHEED intensity is observed, nucleation on the terraces may occur. Such a "mixed" growth mode causes a constant step density and, therefore, a constant RHEED intensity. This growth behavior is observed during growth of $SrRuO_3$ on vicinal TiO_2 terminated $SrTiO_3$; see Choi et al., [2001].

During step flow growth, the step ledges of the vicinal substrates act as a sink for diffusing particles and nucleation on the terraces is prevented, resulting in a steady step density, determined by the vicinal angle of the substrate. The coverage-dependent average island size in 2D nucleation and growth is replaced by the constant average terrace width of the vicinal substrate. Measurements of RHEED characteristic relaxation times during step flow growth at different temperature can, therefore, be used to determine the energy barrier for diffusion more reliably.

The relaxation time is inversely proportional to the diffusivity:

$$\tau \sim \frac{C}{D_S} \tag{8.14}$$

where C is a constant, determined by the vicinal angle of the substrate.

Figures 8.7a and 8.7b show the RHEED intensity variations during homoepitaxial step flow growth of $SrTiO_3$ at different oxygen deposition pressures and temperatures, using a substrate with

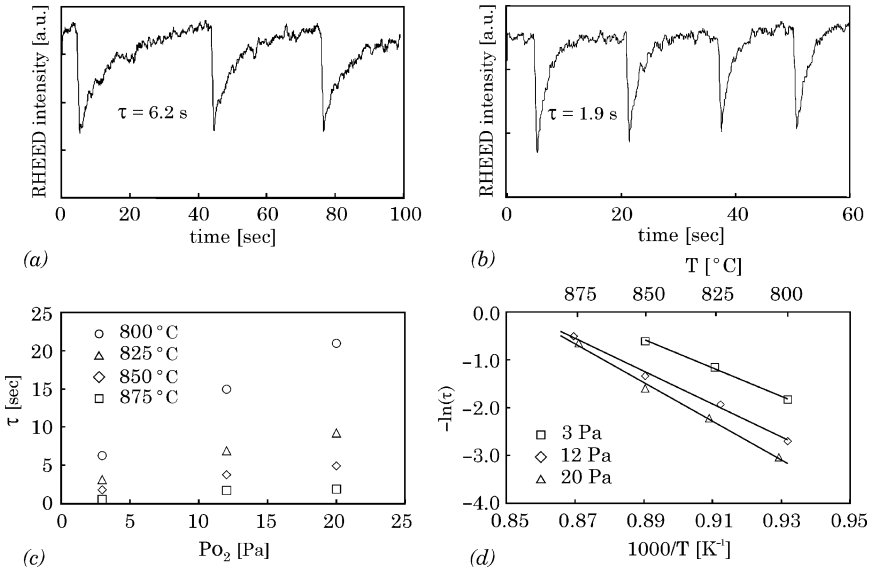

Figure 8.7 Specular RHEED intensity variations during homoepitaxial step flow growth of $SrTiO_3$ at oxygen deposition pressure of (a) 3 Pa and 800°C and (b) at 20 Pa and 875°C. Relaxation times obtained from a fit with Eq. (8.13) for (c) different temperature and oxygen deposition pressure and (d) the same values in the Arrhenius form.

vicinal angle of $\sim 2^\circ$, corresponding to an average terrace width of ~ 10 nm. Full intensity recovery is observed in these cases, indicating step flow growth. The characteristic relaxation time, obtained by a fit using Eq. (8.13), versus oxygen deposition pressure for different temperatures is given in Figure 8.7c. A clear dependence of the relaxation times on the oxygen deposition pressure is observed. The sharp transition observed during 2D growth is, however, not observed at step flow conditions. In Figure 8.7d, the data is presented in an Arrhenius plot. From the slopes a value for the energy barrier of diffusion E_A of 2.6 ± 0.3, 3.0 ± 0.3, and 3.5 ± 0.3 eV have been derived for oxygen deposition pressures of 3, 12, and 20 Pa, respectively. As expected, these values are larger than the values derived during 2D growth. A lower value for E_A is nevertheless found at the lowest oxygen deposition pressure, which can be attributed to the kinetic energy of the particles arriving at the substrates.

The activation energy E_A for the diffusing particles is expected to be smaller than the estimated values [Lippmaa et al., 2000]. Due to the high supersaturation in the deposition pulse, nucleation of a high density of 2D clusters does occur. These clusters are, however, unstable after the deposition pulse and dissociate into the mobile particles. The absolute values of E_A are, therefore, related to the dissociation of the clusters as well as the diffusion of the particles.

8.4 PULSED LASER INTERVAL DEPOSITION

The possibility to control the growth during PLD using high-pressure RHEED allows for atomic engineering of oxide materials and growth of heterostructures with atomically smooth interfaces. Layer-by-layer growth[12] is a prerequisite: Nucleation of each next layer may only occur after the previous layer is completed. Occasionally, the deposition conditions such as the substrate temperature and oxygen pressure can be optimized for true 2D layer-by-layer growth, for example, homoepitaxy on $SrTiO_3$ (001); see Figure 8.2a. The relatively high temperature in combination with a low oxygen pressure enhances the diffusivity of the adatoms on the surface. As a result, the probability of nucleation on top of a 2D island is minimized, that is, the adatoms can migrate to the step edges of the 2D islands and nucleation only takes place on fully completed unit cell layers.

The probability of second-layer nucleation, however, increases at lower substrate temperature and/or higher deposition pressure, leading to multilevel growth. This is indicated by the damping of RHEED intensity oscillations. See, for example, Figure 8.8a, where $SrTiO_3$ is depositing at a temperature of 800°C and oxygen pressure of 10 Pa with a continuous pulse repetition rate of 1 Hz.

In general, roughening of the surface is observed during deposition of different kinds of materials, that is, metals, semiconductors, and insulators. Assuming only 2D nucleation, determined by the supersaturation, limited interlayer mass transport results in nucleation on top of 2D islands before completion of a unit cell layer. One can still speak of a 2D growth mode. However, nucleation and incorporation of adatoms at step edges is proceeding on an increasing number of unit cell levels, which is seen by damping of the RHEED intensity oscillations.

Several groups [Markov et al., 1991; Rosenfeld et al., 1993, 1995] have investigated the possibility of growth manipulation by enhancement of the interlayer mass transport. Manipulation by periodical ion bombardment or varying the growth parameters during growth, such as temperature and growth rate, was used to increase the number of nucleation sites and thus to decrease the average island size. This will enhance the transport of material from an island to a lower level. Usually, for epitaxy of complex oxide materials, the regime of temperatures and pressures is limited by the stability of the desired phases, for example, $Y_1Ba_2Cu_3O_7$ can only be grown in a specific temperature and pressure regime [Hammond and Bormann, 1989]. At low temperatures,

[12]To obtain atomically smooth film surfaces, a 2D growth mode is essential. It can either be layer-by-layer growth or step flow growth. However, in the case of step flow growth, rate control with RHEED is not possible.

a-axis oriented films are formed whereas at high temperatures the material decomposes. Periodically ion bombardment would change the stoichiometry of the deposited material and cannot be used for the growth manipulation. A different approach is the use of surfactants; see, for instance Vrijmoeth et al., [1994]. However, a suitable candidate for complex oxides has to our knowledge not yet been found. Improvement of the interlayer mass transport by applying temperature variations or periodic ion bombardment during growth of complex oxides is, therefore, almost not feasible. Manipulation of the growth rate, that is, both the instantaneous and average growth rate, can be used to impose layer-by-layer growth. Here, the unique features of PLD are employed. In PLD, a high density of small 2D nuclei is formed due to the high supersaturation just after the deposition pulse. Subsequently, larger islands are formed through recrystallization in between deposition pulses, exhibited by the typical relaxation of the RHEED intensity of the specular spot during PLD. As a result, the probability of second layer nucleation on the growing islands increases. Hence, to decrease this probability, coarsening should be avoided. This can be achieved by maintaining the high supersaturation for a longer time by decreasing the time between the deposition pulses. The latter is easily obtained at high repetition rates.[13] For that reason we have introduced a growth method [Koster et al., 1999] based on a periodic sequence: fast deposition of the amount of material needed to complete one unit cell layer in a short [Koster et al., 1998a][14] interval followed by a long interval in which no deposition takes place and the deposit can reorganize by recrystallization. This makes it possible to grow in a unit cell layer-by-layer fashion in a growth regime (temperature, pressure) where otherwise island formation would dominate the growth.

Figure 8.8b shows the RHEED intensity during 10 cycles of $SrTiO_3$ deposition[15] (at 10 Hz) and subsequently a period of no deposition, using the same oxygen pressure and substrate temperature as in Figure 8.7a, following the new approach. In this case the number of pulses needed per unit cell layer was estimated to be about 27 pulses. Formation of a multilayer growth front is suppressed, indicated by the small decay of the intensity after each unit cell layer; in Figure 8.8c the intensities at each maximum of both methods are compared.

The small decrease of the maximum intensity is ascribed to the fact that only an integer number of pulses can be given to complete one unit cell layer, resulting in small deviations between the deposited and the required amount of material. A higher number of pulses decreases this deviation and is, therefore, favorable. The deposition time for one unit cell layer, however, should be smaller or comparable to the characteristic relaxation time. This is visualized in Figure 8.8d. Here, the intensity change during deposition of one unit cell layer at 10 Hz is shown. The shape of the intensity curve at 10 Hz strongly resembles the parabola when calculating the intensity change of a two-level growth front with random distributed island and island sizes using Eq. (8.3).

From the shape of the curve it can be seen that the time needed to deposit one unit cell layer is still too long. This is because the deposition time interval of 2.7 s is longer than the characteristic relaxation time (~ 0.5 s). However, a significant suppression of the formation of a multilevel system has already been achieved. This suppression is clearly noticed by comparison of the surface morphologies after deposition using ''standard'' PLD and the new approach; see Figures 8.8e and 8.8f, respectively. At least four levels are observed on the terraces in Figure 8.8e, compared to only two levels in Figure 8.8f.

Using the method presented above [Rijnders et al., 2000; Blank et al., 2000], it is possible to impose a single-level 2D growth mode or layer-by-layer growth mode with PLD despite unfavorable deposition conditions for $SrTiO_3$ with respect to mobility. The value of this method is demonstrated in the epitaxial growth and the infinite layer structure $SrCuO_2/BaCuO_2$ [Koster, 1999; Koster et al., 2001], for which the choice of temperature and pressure is more critical, proving the importance of this growth method.

[13]Nowadays, intense ultraviolet (UV) lasers are commercially available with pulse repetition rates up to several hundred hertz.
[14]The deposition interval should be on the order of the characteristic relaxation times (typically 0.5 s).
[15]An $SrTiO_3$ substrate with a small vicinal angle ($< 0.2^\circ$) was selected for this study to exclude step flow like growth behavior.

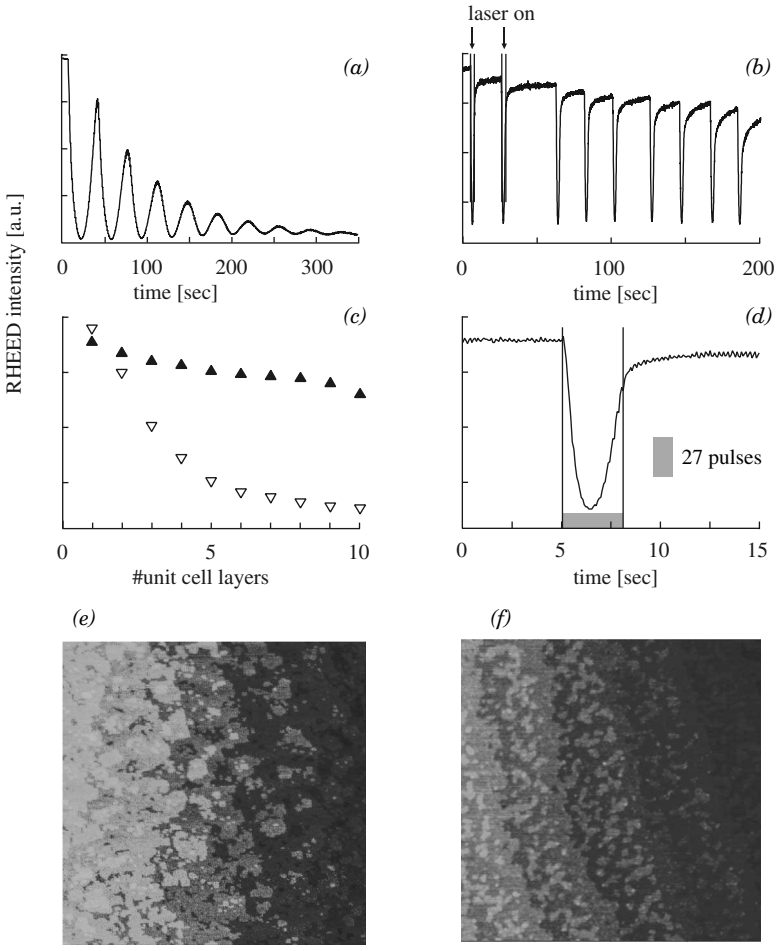

Figure 8.8 Specular RHEED intensity recorded during homoepitaxial growth of $SrTiO_3$ at 10 Pa and 800°C using (a) "standard" PLD and (b) interval PLD. Intensity maxima using (c) "standard" PLD, ▽, and interval PLD, ▲. (d) Intensity variation during one deposition interval. The surface morphologies of ∼30-nm-thick $SrTiO_3$ films are depicted in the atomic force microscopy (AFM) micrographs ($1 \times 1\,\mu m^2$): (e) "standard" PLD and (f) interval PLD.

8.5 CONCLUSIONS

The growth of complex oxides occurs far from thermal equilibrium and, therefore, is dominated by kinetic processes. High-pressure RHEED is used to extract the energy barrier for diffusion E_A and showed a dependence of E_A on the oxygen deposition pressure attributed to the kinetic energy of the deposited particles. Reliable determination of E_A is feasible under step flow growth conditions. Here, a steady step density causes a constant average travel distance for the diffusing particles. It is shown that this constant distance is essential for the reliable determination of E_A.

It is shown that a single-level 2D growth mode or layer-by-layer growth mode for $SrTiO_3$ can be imposed with PLD despite unfavorable deposition conditions with respect to mobility. Depositing every unit cell layer at a very high deposition rate followed by a relaxation interval, the typical high supersaturation in PLD is extended keeping the average island size as small as possible. Therefore,

the interlayer mass transport is strongly enhanced and the formation of a multilevel growth front does not occur. This technique, which we call pulsed laser *interval* deposition, is unique for PLD as no other technique has the possibility to combine very high deposition rates with intervals of no deposition in a fast periodic sequence.

REFERENCES

Achutharaman, V. S., N. Chandresekhar, O. T. Valls, and A. M. Goldman (1994), *Phys. Rev. B* **50**, 8122–8125.

Bauer, E. (1958), *Z. Kristallogr.* **110**, 372.

Blank, D. H. A., G. Koster, G. A. J. H. M. Rijnders, E. van Setten, P. Slycke, and H. Rogalla (2000), *J. Crystal Growth* **211**, 98–105.

Choi, J.-H., C.-B. Eom, G. Rijnders, H. Rogalla, and D. H. A. Blank (2001), *Appl. Phys. Lett.* **79** 1447–1449.

Hammond, R. H., and R. Bormann (1989), *Phys. C* **162–164**, 703.

Karl, H., and B. Stritzker (1992), *Phys. Rev. Lett.* **69**, 2939–2942.

Koster, G. (1999), "Artificially Layered Oxides by Pulsed Laser Deposition," Ph.D. Thesis, University of Twente, The Netherlands.

Koster, G., A. J. H. M. Rijnders, D. H. A. Blank, and H. Rogalla (1998), *Mater. Res. Soc. Symp. Proc.* **526**, 33–37.

Koster, G., G. J. H. M. Rijnders, D. H. A. Blank, and H. Rogalla (1999), *Appl. Phys. Lett.* **74**, 3729–3731.

Koster, G., K. Verbist, G. Rijnders, H. Rogalla, G. van Tendeloo, and D. H. A. Blank (2001), *Phys. C* **353**, 167–183.

Lippmaa, M., N. Nakagawa, M. Kawasaki, S. Ohashi, and H. Koinuma (2000), *Appl. Phys. Lett*. **76**, 2439–2441.

Markov, V. A., O. P. Pchelyakov, L. V. Sokolov, S. I. Stenin, and S. Stoyanov (1991), *Surf. Sci*. **250**, 229–234.

Neave, J. H., P. J. Dobson, B. A. Joyce, and J. Zhang (1985), *Appl. Phys. Lett.* **47**, 100–102.

Rijnders, G., G. Koster, V. Leca, D. H. A. Blank, and H. Rogalla (2000), *Appl. Surf. Sci.* **168**, 223–226.

Rosenfeld, G., R. Servaty, C. Teichert, B. Poelsema, and G. Comsa (1993), *Phys. Rev. Lett.* **71**, 895–898.

Rosenfeld, G., B. Poelsema, and G. Comsa (1995), *J. Crystal Growth* **151**, 230.

Rosenfeld, G., B. Poelsema, and G. Comsa (1997), in *Growth and Properties of Ultrathin Epitaxial Layers,* D. A. King and D. P. Woodruff (Eds.), Elsevier Science, Amsterdam, Chapter 3.

Shitara, T., D. D. Vvedensky, M. R. Wilby, J. Zhang, J. H. Neave, and B. A. Joyce (1992a), *Phys. Rev. B* **46**, 6825–6833.

Shitara, T., J. Zhang, J. H. Neave, and B. A. Joyce (1992b), *J. Appl. Phys.* **71**, 4299–4304.

Stoyanov, S. (1988), *Surf. Sci.* **199**, 226–242.

Stoyanov, S., and M. Michailov (1988), *Surf. Sci.* **202**, 109–124.

Strikovski, M., and J. H. Miller (1998), *Appl. Phys. Lett*. **73**, 1733–1735.

Van der Wagt, J. P. A. (1994), "Reflection High-Energy Electron Diffraction during Molecular-Beam Epitaxy," Ph.D. Thesis, Stanford University.

Vrijmoeth, J., H. A. van der Vegt, J. A. Meyer, E.Vlieg, and R. J. Behm (1994), *Phys. Rev. Lett.* **72**, 3843

Zandvliet, H. J. W., H. B. Elswijk, D. Dijkkamp, E. J. van Loenen, and J. Dieleman (1991), *J. Appl. Phys.* **70**, 2614–2617.

CHAPTER 9

Large-Area Commercial Pulsed Laser Deposition

JIM GREER

PVD Products, Wilmington, Massachusetts

9.1 INTRODUCTION

It has been over a decade since the publication of *Pulsed Laser Deposition of Thin Films* edited by Chrisey and Hubler [1994]. At that time, the state of the art for large-area film growth by pulsed laser deposition (PLD) was effectively limited to substrates of 5 inches in diameter. During the late 1980s and early 1990s PLD was considered a somewhat novel and experimental deposition process for providing a means to fabricate thin films of complex oxide materials. Since then, its popularity has grown significantly and the process is now accepted as a standard physical vapor deposition (PVD) technique. Since 1992, however, it has been demonstrated that the PLD process is scalable to substrates at least 8 inches in diameter [Greer and Tabat, 1995a]. While it is expected that PLD can be scaled up to even larger diameter circular substrates, there are no pressing applications requiring such equipment at the present time.

One relatively recent application, however, that puts large demands on PLD process equipment is that of coated conductors. In this case, PLD can be used to deposit both oxide buffer layers and high-temperature superconductor (HTS) films onto long metal tapes about 1 cm wide. Requirements for coated-conductor applications have pushed the technology of commercial PLD hard over the past few years. As an example, present research tools using PLD for coated conductors have produced continuous high-quality YBCO films, at least 1.5 μm thick on 200 m of metal tape. The area defined by this tape is equivalent to a 64-inch (1.62-m) diameter substrate, and such a large effective substrate size puts serious demands on all of the deposition equipment, including the excimer laser itself, target, optical components, as well as the substrate heater.

Since about 1990 several companies have been established specifically to meet the demand for PLD research and manufacturing equipment, and over the past 10 years there has been a strong focus on PLD equipment development. Commercial equipment is readily available for both R&D and prototype production applications, and while some scientists and researchers are still building their own equipment, many now choose to purchase commercially, ensuring the advantages of obtaining fully functional and proven systems in a relatively short timescale.

Current systems offer a wide variety of capabilities and options, making them very attractive to scientists who want to focus more on materials science or device fabrication then equipment

Pulsed Laser Deposition of Thin Films: Applications-Led Growth of Functional Materials
Edited by Robert Eason

development. These commercial systems are, of course, more expensive than a home-built system. Present offerings for commercially available PLD equipment include systems that handle substrates from 10 to 150 mm in diameter, and systems for combinatorial synthesis of materials by PLD are also available. Pricing for systems (not including the price of the laser) can range from about $65,000 for a very basic model to over $750,000 depending on substrate size, and other system capabilities and diagnostics. These tools can be fully ultra high vacuum (UHV) compatible, include load-locks for substrates as well as targets, and include a variety of other features. While systems capable of handling substrates as large as 8 inches in diameter have been advertised, none have been sold to date to this author's knowledge. Commercial systems have also been developed and sold for coating long metal tapes.

This chapter will review the progress made in scaling PLD up to 8-inch-diameter substrates as well as look at the development and issues relating to the commercialization of PLD equipment for both standard substrates as well as coated conductors.

9.2 ADVANCES IN LARGE-AREA PLD FILMS

Since 1992 the scale-up to larger diameter substrate sizes has been led primarily by the method of laser beam rastering over large-diameter targets [Greer and Tabat, 1995a, 1995b]. Figure 9.1 shows a schematic of such a system. In this case, a mirror held in a kinematic mirror mount rasters the incident laser across a large-diameter rotating ablation target, using a programmable linear actuator. The substrate is located just offset from the target and is, of course, rotated as well. The raster pattern utilized will depend on many parameters including the laser beam size, shape, and orientation, target-to-substrate distance, background gas pressure, and substrate temperature. Usually, the target diameter is larger than that of the substrate and the raster scan rate is usually fairly slow compared to that of either substrate or target rotation speeds.

Figure 9.2 shows normalized film thickness data obtained by the laser rastering technique for two silicon substrates 150 mm (6 inches) and 200 mm (8 inches) in diameter. The material deposited was yttria (Y_2O_3) on substrates held at room temperature and the film thickness was measured using an ellipsometer. The maximum variation in film thickness (defined as the difference between the minimum and maximum values obtained across the substrate divided by the average film thickness) for the 780-nm-thick Y_2O_3 film deposited on the 150-mm-diameter substrate was found to be 7.1% (or $\pm 3.6\%$).

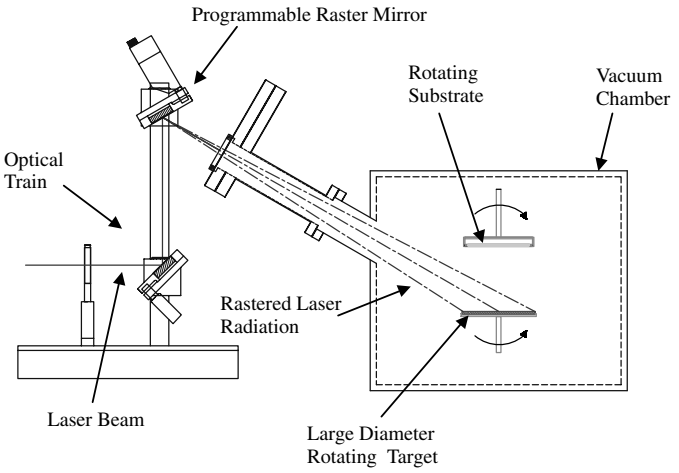

Figure 9.1 Schematic of a large-area PLD system utilizing laser rastering over large-diameter targets.

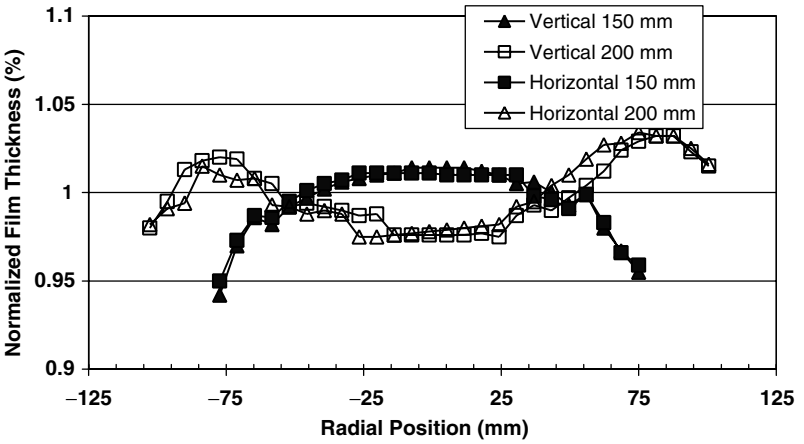

Figure 9.2 Normalized film thickness data obtained from two Y_2O_3 films deposited onto: (a) 150-mm-diameter silicon substrate and (b) a 200-mm-diameter silicon substrate. The thickness was measured in two mutually perpendicular directions (horizontal and vertical) across each substrate.

Neglecting the four points located at a radial position of $\pm$74.5 mm (affected by shadowing of the substrate holder), the maximum variation in film thickness was found to be $\pm$2.3%. The maximum variation in film thickness measured from a 570-nm-thick film deposited over a 200-mm-diameter substrate was found to be 6.7% ($\pm$3.4%). These films were deposited using a laser fluence of 3.0 J/cm^2 at 100 Hz, (total power on target was 30 W) in an Ar background pressure of 7.5 mTorr. The average film growth rates for Y_2O_3 was 0.4 and 0.3 μm/h, or 1.1 and 0.83 Å/s, for the 150- and 200-mm-diameter substrates, respectively. Y_2O_3 is a refractory material with a relatively low ablation rate as well as low sputter rate.

The deposition rates displayed here are very competitive with those achievable using radio-frequency (RF) magnetron sputtering for this material. For a material such as YBCO, deposition rates three times higher could be expected under identical conditions, however, YBCO usually is grown at higher background pressures, thus somewhat reducing the overall deposition rate due to backscattering of the ablated material. Figure 9.3 shows the normalized film thickness achievable using a commercially available PLD system [Boughaba et al., 1999]. In this case the material deposited was $\sim$100 nm of Ta_2O_5 in an oxygen background pressure of 30 mTorr. The film thickness variation for each wafer is shown as a function of three substrate temperatures: (a) 250°C, (b) 400°C, and (c) 650°C with the average deviation ranging from $\pm$0.4 to $\pm$1.5%. There is a slight change in the film thickness and thickness profile as the temperature is increased due to the change in gas density in front of the substrate. This change in gas density reduces the number of collisions the vapor will make on its way to the substrate, thus increasing film thickness. The slight reduction in gas density due to the hotter substrate accounts for the drop in film thickness from 106 nm for the film grown at 650°C down to 97 nm for the film grown at 250°C.

Besides uniformity of film thickness, the uniformity of composition of the deposited films is also of paramount importance, especially for the multicomponent oxides that are routinely grown via PLD. Figure 9.4 shows the chemical composition obtained from a 2-μm-thick YBCO film deposited onto a 150-mm silicon substrate at room temperature with a background pressure of 2 mTorr of oxygen using the laser rastering technique. The composition was obtained using energy dispersive X-ray (EDX) analysis with a calibration standard evaluated via Rutherford backscattering spectroscopy (RBS). The composition was measured across the wafer in two mutually perpendicular directions at a total of 50 locations. The atomic variation in composition was found to be $\pm$1.4, $\pm$1.2, and $\pm$0.8 atomic percent for Y, Ba, and Cu, respectively. These fluctuations were on the same

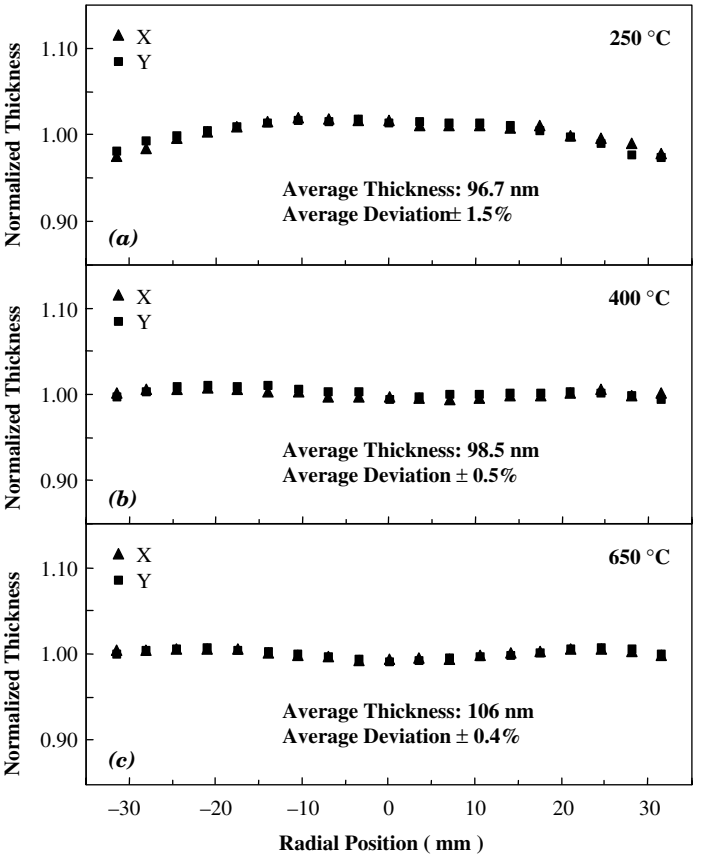

Figure 9.3 Normalized film thickness obtained from three Ta_2O_5 films deposited onto 3-inch silicon substrates at (a) 250°C, (b) 400°C, and (c) 650°C; *X* and *Y* refer to orthogonal measurement directions.

order of magnitude as the standard errors of the EDX system used, that is, ± 1.48, ± 0.17, and ± 0.36 atomic percent, for Y, Ba, and Cu, respectively. A larger YBCO film was not grown for the demonstration of compositional uniformity due to the lack of availability of a larger YBCO target at the time these experiments were being conducted.

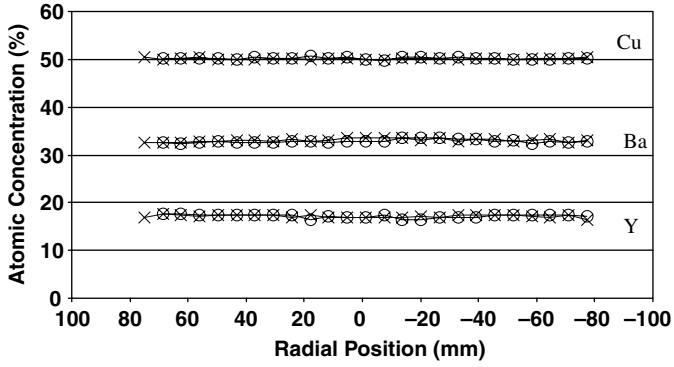

Figure 9.4 Film composition uniformity of a thick YBCO film deposited onto a 150-mm diameter silicon substrate.

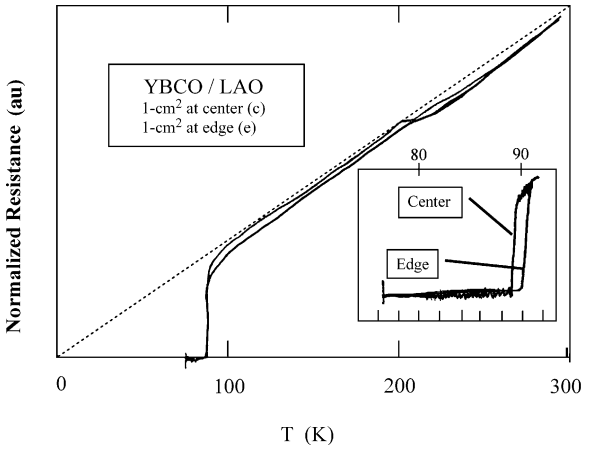

Figure 9.5 T_c vs. temperature for two 1-cm samples grown in a commercial large-area PLD system: (a) sample located at the center of the rotating substrate holder and (b) sample located at a distance of 35 mm from the center of the rotating substrate holder.

It is well known that obtaining high-quality YBCO thin films requires a careful balance of substrate temperature, chamber pressure, laser fluence, and the like. Thus, the ability to grow large-area and uniform YBCO films via PLD requires that these parameters be kept constant over the entire substrate area. Figure 9.5 displays the critical temperature, T_c, data obtained from two 1-cm^2 YCBO films on $LaAl_2O_3$ substrates grown in a large-area PLD system. One sample was positioned at the center of the substrate holder, while the center of specimen B was located 35 mm out from the center of rotation. The films were grown using a substrate temperature of 750°C and an oxygen pressure of 175 mTorr with a target-to-substrate distance of 150 mm. The T_c values of these two films were found to be 89.5 and 89.9 K for the film located at center and edge, respectively. Rocking curves of the (006) peak obtained via XRD of these two films produced full width at half maximum (FWHM) values of 0.35° and 0.32° for the center and edge sample, respectively, indicating the films have a strong preferential orientation in the (001) direction.

As another example, YBCO was deposited onto sapphire with a CeO_2 buffer layer in a commercially available 5-inch PLD system. The CeO_2 buffer layer was deposited at 690°C in 175 mTorr of O_2. The YBCO was deposited at 700°C in 175 mTorr of O_2. The YBCO film thickness was ~250 nm. A map of the critical current, J_c, characteristics of this film was measured using a noncontact technique and are displayed in Figure 9.6 [Develos-Bagarinao et al., 2003], showing a variation of less than 10% over the substrate surface.

9.3 ISSUES WITH SCALE-UP FOR PLD

As one scales up the PLD process there are a variety of issues that need to be addressed to obtain reproducible, high-quality films or long lengths of coated conductors. These issues include laser power and beam stability, proper design of the optical components, robust substrate heaters, large target size and motion, and deposition rate monitoring.

Excimer lasers are clearly the economical choice for large-area commercial scale-up of the PLD process, as they can provide reliable average powers ranging from 6 W up to 300 W at 248 nm (KrF) or 308 nm (XeCl). As substrate size increases, higher laser power becomes more important to achieve useful average film growth rates. In the author's opinion, lasers with higher repetition rates and slightly lower pulse energy are preferable to lasers with higher energy per pulse and lower repetition rates for obtaining films with useful deposition rates. Thus, a laser that provides 200 pulses

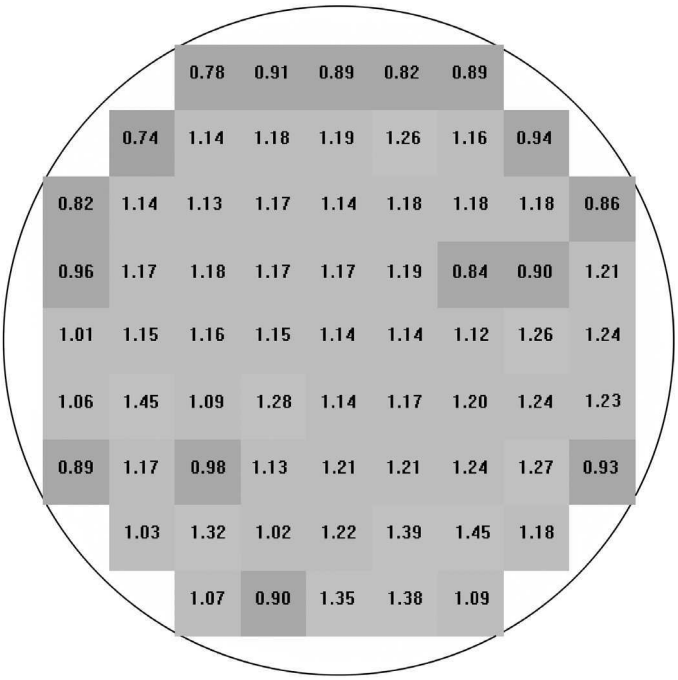

Figure 9.6 Map of J_c obtained from a YBCO film grown on a CeO_2/sapphire 2-inch-diameter substrate. YBCO film was 250 nm thick.

per second (pps) and 400 mJ/pulse (80 W) is more useful than a laser that produces 150 pps with 600 mJ of energy (90 W). For substrates 50 mm in diameter a smaller average power of 6 W is acceptable for most materials if thick films are not required or refractory materials are not of significant interest. As the substrate size grows, however, higher power becomes more important. For systems with 125-mm-diameter substrates, lasers with at least 30 W are needed to achieve acceptable film growth rates. Currently, for coated-conductor research many systems are using large industrial lasers providing up to 300 W (1 J per pulse, 300 Hz, at 308 nm) on the target. Dealing with such high-power density becomes a problem for ceramic targets, for example. Localized heating of the ceramic can cause nonuniform thermal expansion leading to target cracking. Also, local heating of the surface of the target can cause melting. Thus, the target surface must move at a fairly high velocity to minimize these thermal effects. If refractory materials are to be deposited or high fluence can yield unique film properties that cannot be obtained with lower fluence, then lasers with higher energy ($\sim$1 J/pulse) should be considered. However, lasers with energy outputs of 250 to 600 mJ/pulse are more than adequate for most materials.

One important issue that needs to be properly addressed for large-area PLD using large-diameter targets with laser beam scanning is maintaining constant fluence at the target surface. As the laser beam is rastered across a large diameter target the distance from the focusing lens to the target changes, altering the laser spot size, and thus fluence, and for targets above 100 mm in diameter, this effect becomes significant. To solve this problem, modern optical beam delivery systems (trains) utilize active beam compensation with large-diameter targets as shown in Figure 9.7. Here the focusing lens is mounted on a linear stage driven by a programmable actuator whose motion is slaved to that of the raster mirror. As the laser beam is walked across the target the focus lens position moves to keep the path length from the lens to target constant. Using this method one can keep the laser fluence variations to a similar level of the intrinsic pulse-to-pulse stability (typically $\pm$1% at 248 nm) of the excimer laser itself.

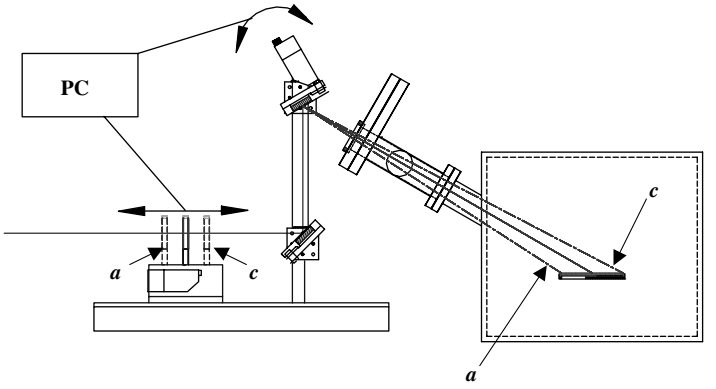

Figure 9.7 Schematic of an active fluence compensation scheme for a large-area PLD system using large-diameter targets. The position of the focusing lens is slaved to the raster mirror, keeping the laser beam path constant. For example, when the focusing lens is located at position *a*, the raster mirror ensures that the laser is focused at position *a* on the target, and likewise for positions *c*.

9.3.1 Intelligent Windows

Another issue that quickly arises with large-area, thick-film low-pressure deposition processing, and systems that use load-locks, is coating on the laser beam entrance window [Greer et al., 1997]. Even though the ablation plume is forward directed, a fraction of the plume material condenses on the laser entrance window with each laser pulse. Over multiple pulses this film will build up and start to absorb a significant fraction of the incident laser energy. Depending on the material properties and the chamber pressure, as much as 40% (or more) of the incident energy can be absorbed. This reduction in fluence will significantly reduce the film deposition rate per pulse and may also alter some of the films' relevant properties. In some cases, the condensed material will be ablated off the laser optic, but in this case it may also remove some of the optical material (fused silica) and permanently damage the optic, further degrading the deposition process. Thus, in most systems the laser window needs to be removed periodically after some few depositions and properly cleaned. The effect of window coating is reduced when running at higher background pressures and as the angle of incidence (AOI) of the laser beam is increased away from the target normal. Thus, if designing a system, an AOI of 60° for the laser beam will make more sense than an AOI of 45° to minimize window coating problems.

Figure 9.8 shows a photograph of a product called the Intelligent Window (IW) that has been designed to eliminate window coating in a practical way. The window consists of a pair of vacuum flanges housing a large-diameter ultraviolet (UV) transparent fused silica disk. The disk sits in between an antireflective (AR) coated optic that lets the laser beam enter the deposition chamber and a molybdenum aperture on the downstream side. The fused silica disk intercepts ablated material that travels back toward the AR-coated optic. As only the area defined by the aperture becomes coated, once the exposed section of the disk is coated sufficiently to reduce the laser energy by some predetermined amount (typically by about 10%), the window can be rotated to expose a new section of the disk to the laser and backscattered material. The usable area of the disk is typically 20–60 times that of the area of the laser beam significantly increasing the lifetime of the window before cleaning is required. Once completely coated, the disk can be removed and a replacement disk installed. The disks are easily cleaned using the optical polishing paste for the excimer laser optics. For coated-conductor applications the diameter of the disk and flanges are increased significantly to provide the maximum lifetime possible for the optical beam path.

Another useful feature of the IW is the ability to measure the energy that has traversed through the entire optical train. Using a linear actuator a beam splitter can be inserted into the beam path and

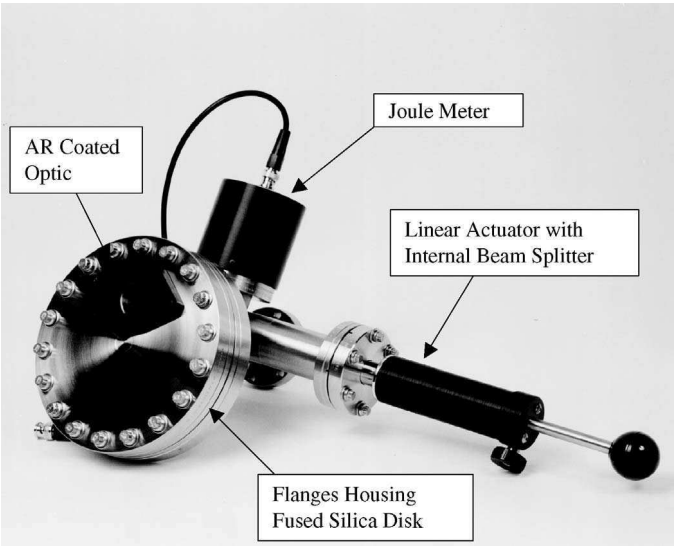

Figure 9.8 Photograph of an Intelligent Window used to keep the laser beam path clean for an extended period of time and provide in situ fluence measurements. (Photograph Courtesy of PVD Products, Inc.)

reflect the beam back out of the chamber to a UV detector. Thus, the energy that has passed through the entire optical train (laser, lens, mirrors, window, etc.) can be monitored and adjusted prior to or even during deposition. Starting a deposition using the IW to set the fluence on the target is a much more accurate and reproducible technique than simply monitoring the energy output of the excimer laser. Utilizing the in situ energy monitor of the Intelligent Window allows problems with the laser or optical components to be found early on, well before the fluence drops significantly and film properties start to degrade. The features of the IW, that is, disk rotation and energy measurement, can also be fully automated if desired.

9.3.2 Substrate Heaters

Substrate heaters are one of the most important components of any PLD system and are routinely used, for example, for perovskite oxide films that require growth temperatures above 700°C in an oxygen environment. There are three basic types of heating schemes that have been used in PLD systems, namely resistive-type heaters, infrared (IR) lamp heaters, and laser heaters. Each of these systems has advantages and disadvantages, and the choice mainly rests on the particular application and budget of the end user.

Basic low-cost resistive heaters usually utilize an Inconel sheath heating element brazed to an Inconel block. These heaters are robust and reliable and can readily heat samples to temperatures of 950°C. However, when using these types of heaters, the samples must be bonded to the heater block with either a silver or platinum paste to achieve good thermal conductivity between the block and substrate. This technique is very popular for small 1- or 2-cm^2 size samples but is problematic as the sample size gets progressively larger. When bonding substrates of 50 or 75 mm (or larger) diameter with silver paste, it becomes very difficult to achieve a uniform bond thickness and thus uniform substrate temperature. Differential thermal expansion between the substrate and Inconel block also becomes an issue as the substrate size increases. Removing samples that have been bonded to heater blocks also becomes difficult after the paste has been fired; the paste is difficult to remove from the reverse side of the substrate, and this in turn makes postprocessing of the samples difficult. For these type of heaters a thermocouple bonded to the heater block will

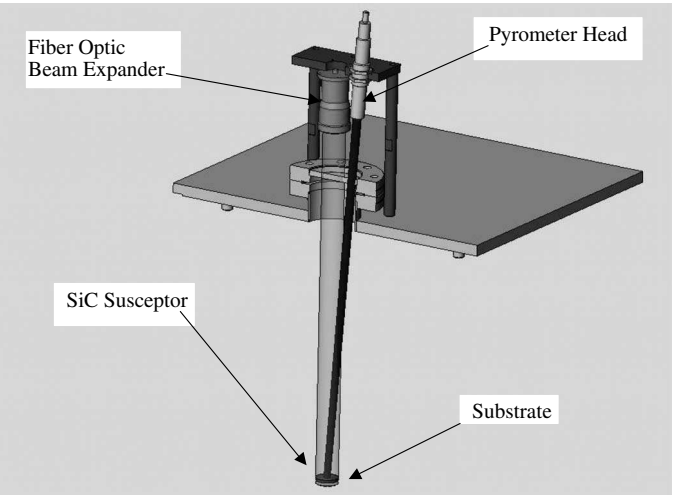

Figure 9.9 Schematic of laser heater assembly showing the fiber-optic beam expander and pyrometer head. The substrate sits about 1 mm below the SiC susceptor.

provide a fairly accurate measurement of the substrate temperature as long as the substrate is bonded to the block. These heaters can also be used for lower substrate temperatures if a bonding agent is not used.

Alternatives to Inconel resistive heaters are direct radiative heating using a laser, IR heat lamps, or boroelectric heaters, which are fine if oxygen is not present in the system, but if used with oxygen should not be raised above about 750°C otherwise damage will occur. Laser heaters have been used to heat small samples, typically ~2 cm in diameter to temperatures in excess of 1000°C. In this case, an Nd : YAG or infrared laser (CO_2 or diode laser bars and stacks) is focused onto a susceptor (or directly onto the substrate if nontransparent at the laser wavelength) from outside the chamber. The substrate is positioned in close proximity to the susceptor and radiatively heated. Figure 9.9 shows a schematic of the laser heater principle. Figure 9.10 shows a photograph of a Haynes susceptor slug being heated via an Nd : YAG laser with 150-W output. In this case the laser beam was 1.2 cm in diameter and heated the bottom surface a thick 2.5 cm diameter slug up to 850°C (the top surface of the slug having a temperature of 1200°C). Using an optical pyrometer on the slug or substrate, this system can be run in a closed-loop mode to obtain excellent temperature stability. Laser heating is fine for small sample sizes but is not practical for substrates above about 2.5 cm in diameter. Laser beam heating of small samples provides a minimum of out-gassing (useful for UHV systems), very high substrate temperatures, fast ramp times, and the ability to run in most process gases over a wide variety of pressures. Currently IR diode laser bars and stacks are available with output powers between 25 and 250 W, and these lasers are sufficient for heating samples up to 2.5 cm diameter to temperatures required for most perovskite oxides.

Heaters based on IR lamps can be used very effectively in PLD systems to heat samples without the use of silver paste. Figure 9.11 shows the inside of a deposition chamber that houses a blackbody IR lamp heater assembly. Lamps are operated with peak blackbody emission in the visible, at ~1200 K or higher, which also generates considerable IR power. The lamps are surrounded by a water-cooled housing to minimize the heat load on other internal components and the chamber walls. A bank of lamps sits directly above the substrate spinner assembly, and a second set of lamps sits above a water-cooled plate located directly above the target surface and well below the substrate surface. Either Au reflective coatings or reflecting shields separate the lamps from the

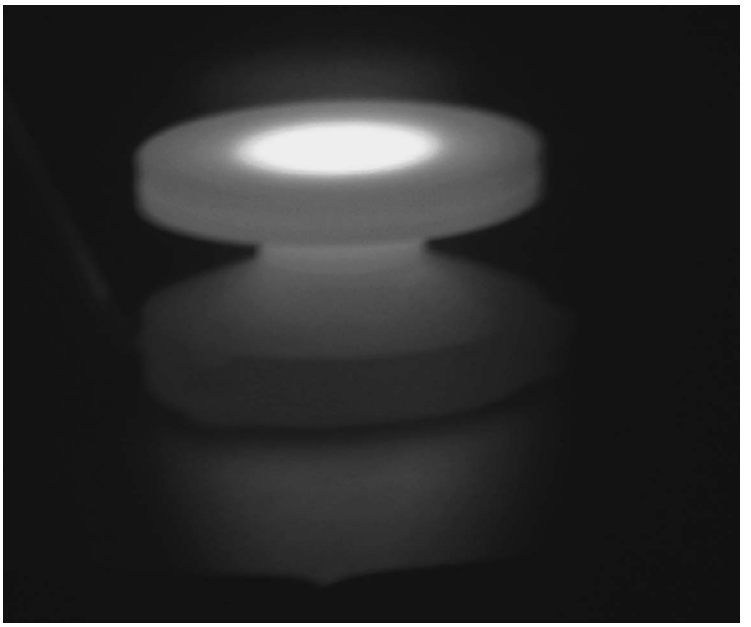

Figure 9.10 Photograph of a 25-mm-diameter Haynes alloy slug. The bottom surface is heated to over 850°C by 150 W of laser radiation. (Photograph courtesy of PVD Products, Inc.)

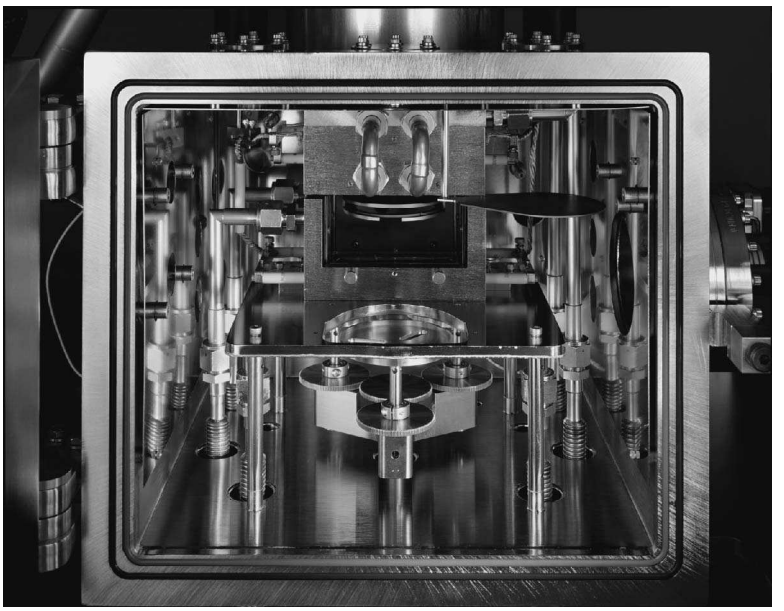

Figure 9.11 Photograph of the inside of a PLD-3000 system showing the water-cooled blackbody substrate heater housing and high-temperature oxygen-resistant substrate spinner assembly. (Photograph courtesy of PVD Products, Inc.)

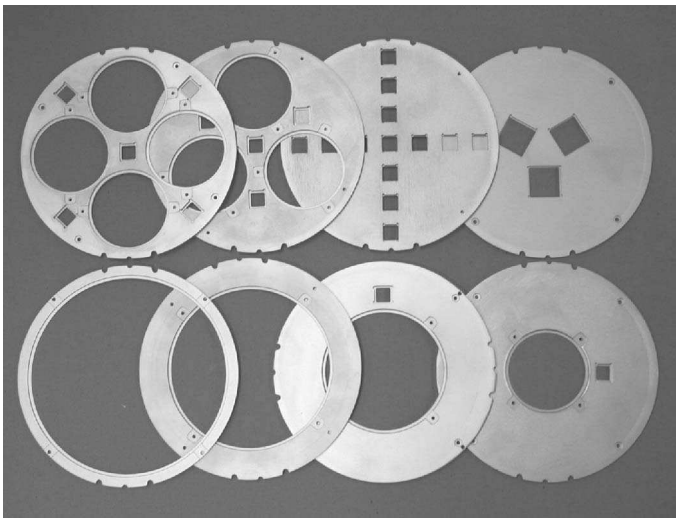

Figure 9.12 Photograph of a set of Inconel substrate holders from a 5-inch PLD system. As seen, a wide range of substrates can be handled by a large-area system. (Photograph courtesy of PVD Products.)

water-cooled surfaces to minimize heat losses. Substrates are placed in Inconel rings machined so they are held only at the edges. Figure 9.12 shows a photo of a range of substrate holders for a 5-inch PLD system. As seen, a wide variety of substrate arrangements can be accommodated in a large system. Figure 19.13 shows how the substrates sit in machined pockets of the Inconel rings. In this case no clamping of the substrate is required (or desired) to obtain uniform temperatures. The substrate rings are then inserted into a substrate spinner assembly that is then raised via a Z-stage mounted on top of the chamber to obtain the proper target-to-substrate distance. Thermocouples sit

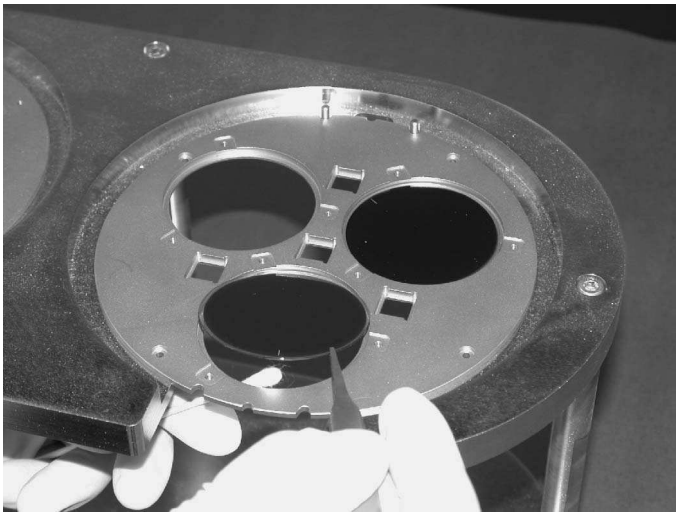

Figure 9.13 Photograph of two 2-inch-diameter YBCO-coated LaAlO3 substrates sitting in an Inconel ring from a 5-inch PLD system. The substrates are held only at the edges in this type of system providing uniform for both heating and ease of substrate handling.

above the substrate spinner assembly and are used to provide the input for a closed-loop temperature control unit. The thermocouple temperature can be significantly different (more than 100°C at about 850°C) than that of the substrate. The best measurement of substrate temperature is thus achieved via a pyrometer. This works fine for substrates such as silicon but is more complicated for transparent substrates such as sapphire or $LaAlO_3$. With multiple lamps and reflecting surfaces surrounding the substrate, the substrate will reach a high steady-state temperature. Uniformity is excellent with these heaters, typically better than ±3°C over a 5-inch-diameter Si substrate. The advantages of a blackbody-style heater are very high substrate temperatures and uniformity can be achieved, and the reverse sides of the substrate remain clean for postdeposition processing. The drawbacks of this type of heater design are initial high cost, and the fact that such a heater must be put through a careful calibration in order to know the actual substrate temperature for transparent substrates.

It should be pointed out that substrate temperature is one of the key parameters in most PLD growth processes. If the substrate is rotating, it becomes difficult to connect a thermocouple to monitor the temperature. Thus, pyrometers for temperature measurement are the only logical choice. Measuring substrate temperature of materials such as silicon is fairly straightforward at temperatures above about 600°C using most pyrometers. Measuring the substrate temperature for sapphire or $LaAlO_3$, however, which are both transparent in the IR, at wavelengths where pyrometers typically make their measurements becomes much more difficult. Usually the pyrometer will read the temperature of any structure behind the transparent substrate. Thus, using careful calibration from a floating thermocouple is the only logical choice at the present time. The development of a pyrometer that can measure temperatures of IR transparent substrates would be most useful for the PLD process. Some new pyrometers are currently being developed for specific applications, but a low-cost pyrometer that can work with all materials of interest over a wide temperature range has yet to be realized.

9.3.3 Heaters for Coated Conductors

Heaters for coated conductors are inherently different than those for standard circular substrates due to the geometrical differences of the substrates, and thus several issues need to be addressed. First, as the tape is pulled through the heater and its ''deposition zone,'' the front surface of the tape becomes coated with YBCO (or buffer film) and its emissivity will increase. This has the effect of reducing the tape temperature as it traverses through the deposition zone. Figure 9.14 is a schematic of a tape heater consisting of a bank of 16 IR lamps housed within a water-cooled assembly. The tape is moving from left to right as indicated in the figure. The lamps are divided into eight zones (Z1 to Z8) with each zone individually controlled by a thermocouple (TC) assembly and power supply. Below the heater is a graph of the tape temperature distribution throughout the heater box with the vertical dashed lines indicating the deposition zone. The curve labeled (a) is the desired tape temperature during the deposition process (750°C). However, due to the increase in emissivity during deposition, the tape temperature will drop as indicated by line (b). By increasing the power in zones Z3 through Z6, the temperature profile without deposition can be increased as indicated by line (c). Thus, as the tape passes through the deposition zone, the actual temperature will approach the desired curve as indicated by (a). The effect of emissivity can be significant, dropping the temperature more than 100°C over distances of 50–100 mm depending on tape speed and deposition rate. Using such multizone compensation has been very successful at achieving excellent film properties. As an example, Los Alamos National Labs have reported achieving an $I_c = 370$ A in a 50-cm length of tape, $I_c = 425$ A in a 7-cm length of tape; and, when slicing this tape to a width of 6 mm, they were able to achieve an $I_c = 530$ A/cm width [Gibbons, 2005]. Current I_c is the maximum current that can be passed through the tape before it goes normal. A photograph of the multizone heater used in this work is shown in Figure 9.15.

A more recent approach to growing coated conductors at high speed is called multiplume, multiroll PLD. In this case, the tape is wound on sets of large-diameter rollers and runs through the

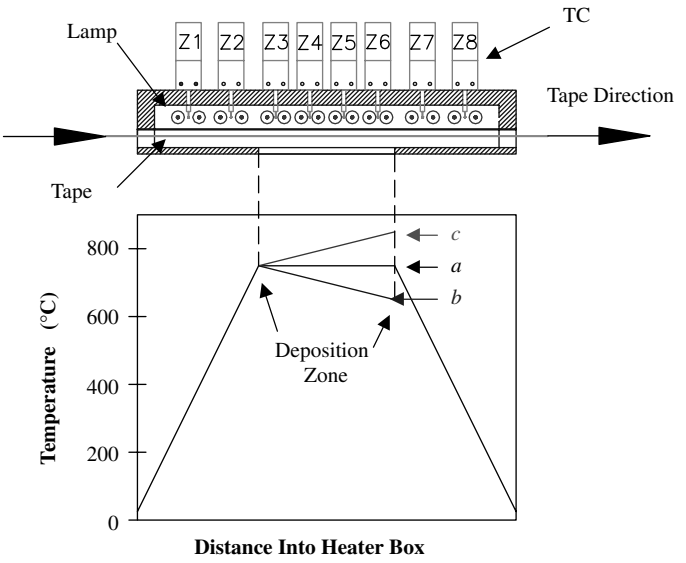

Figure 9.14 Schematic showing a cross section of an eight-zone heater assembly with a metal tape being pulled to the right. The lower graph shows *a* the desired tape temperature within the heater during deposition of YBCO; *b* the actual tape temperature if no compensation is used for emissivity changes of the tape during deposition of YBCO; and *c* the temperature profile setting for the heater to achive the desired temperature (*a*) during deposition of YBCO.

deposition zone multiple times. For this type of arrangement contact heaters have been utilized as shown in Figure 9.16. In this instance a large Inconel block is heated from above via lamps. The rollers are each on individual bearings so the tape tension is kept fairly constant for each lane of tape. The tape is kept in contact with the surface of the Inconel that has a large machined radius on its

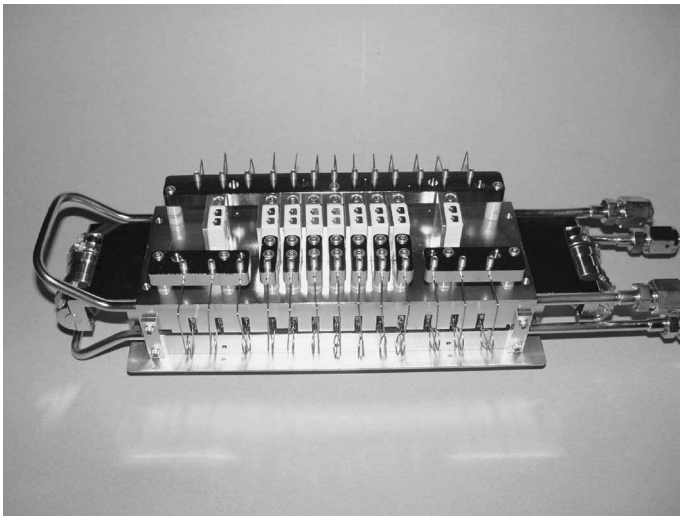

Figure 9.15 Photograph of a 9-zone tape heater. Deposition zone is located on the bottom of the heater and thus not seen in this photograph. (Photograph courtesy of PVD Products.)

Figure 9.16 Photograph of a multilane tape heater. Four lanes of tape can be seen in intimate contact with the Inconel block. Banks of lamps located above the Inconel assembly are used to heat the block. One set of guide rollers can be seen on the left side of the heater block. Also seen is the port where the laser beam enters the chamber pointing down at the large target pedestal. Seen at the back of this port is the aperture that defines the laser beam entrance area of the Intelligent Window. (Photograph courtesy of PVD Products.)

bottom surface. These types of heaters are readily able to heat coated-conductor tapes to temperatures in excess of 850°C. One of the down sides of this type of heater is that the spaces between the tapes tend to build up a lot of material during the long deposition process. Thus, cleaning between each run (typically 100–200 m) is required. Figure 9.17 shows a photo of the multilane, multiplume heater showing the four individual plumes emanating from a slot in the water-cooled plate that sits above the target assembly. The multiple plumes are created by rastering the mirror in synch with the laser beam. This spreads out the laser energy on the target as well as provides for a larger deposition area.

Figure 9.17 Photograph of a multiplume system. Seen clearly are four plumes coming through the large cutout in the water-cooled plate that sits directly above the large target surface.

9.3.4 Target Size and Manipulation

When designing a PLD system, choosing the proper target size to use is very important. For small substrates, such as 1 inch in diameter or smaller, small 1-inch-diameter targets are a good choice. However, as substrate size increases, the size of the target needs to increase to be able to achieve uniform films and reproducible results from run to run, or even during a single run. Attempts to deposit high-quality films on a large substrate using a target with a diameter smaller than that of the substrate is counterproductive for the reasons outlined below.

As the rotating target is ablated during deposition, two types of morphological changes take place to the target, as shown in Figure 9.18. The first morphological change is the gross deformation of the target surface. When using small rotating targets, the surface will quickly become trenched, which in turn alters the laser beam spot size and thus, fluence, and the plume angle will also start to tilt due to presence of the trench. As the plume angle tilts, the center of the plume is no longer directed at the center of the substrate, causing a wide variety of problems including nonlinear film deposition rates as a function of time. Systems utilizing small targets usually require target resurfacing after each run to minimize these types of effects, and this requires physical removal of the target from the chamber, leading to a large waste of material and the additional potential for target contamination. In some cases, target resurfacing may alter the target stoichiometry requiring a subsequent burn-in step.

One technique that has been used to minimize the trenching effect is target rastering under a fixed-position laser beam. Target rastering is usually possible with properly designed target carousels. Swinging the target through a large arc underneath the laser beam and adjusting the velocity as a function of target position can provide the proper rastering pattern. Target rastering will allow the user to utilize more of the target surface and reduce the overall rate of target trenching. Rastering is difficult with small 1-inch-diameter targets but is useful for larger targets if laser beam rastering is not used. When designing a system, care should be taken not to raster directly through the center of the target as this will quickly produce a deep trench at the center of the target that grossly distorts the plume shape.

The second type of morphological change that occurs to a target surface is seen on a microscopic scale. As the laser beam etches the target, small cones are formed that tend to point back toward the incident laser beam. Cones form as a consequence of repeated melting, cooling, and recrystalization

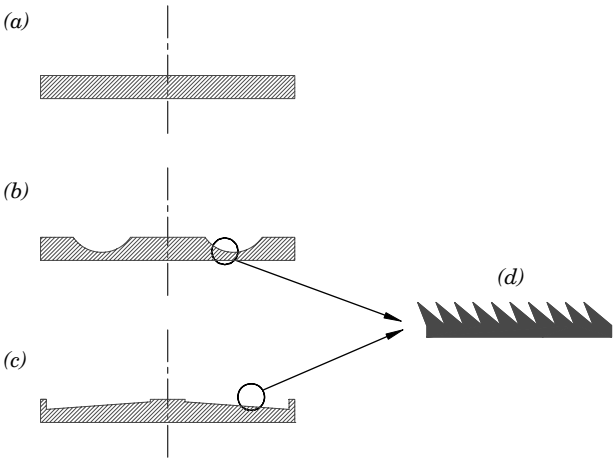

Figure 9.18 Schematic of (a) a new target surface; (b) used small-diameter target showing gross morphological change due to fixed position laser beam; (c) used large-diameter target showing gross morphological change with laser or mechanical rastering; and (d) microscopic morphology changes due to the laser beam. The cones will point back in the direction of the incident laser beam.

of material on the target surface and reach a size of a few microns in length. As the cones form, they spread the laser beam energy out over a larger area, thus reducing the effective laser fluence and hence deposition rate. Thus, used targets have a lower deposition rate and higher particle generation rate than that of a fresh target surface. However, once the cones are formed, the deposition rate should remain constant, barring any other gross morphological changes. The second effect of cone formation is that the plume angle is slightly tilted back toward the incident laser beam. This angular change can also change deposition rates over time, but on a much slower scale than the gross morphological changes discussed above. By rastering the laser beam completely across the target surface (either by using a raster mirror or target manipulation), cone formation can be reduced to some degree but not completely eliminated. Rastering over the entire surface also helps reduce the small particulates that are usually incorporated in laser-deposited films.

As substrate size is increased to above 2 inches, substrate rotation and large targets utilizing laser rastering are required to achieve uniform film properties. Utilizing targets that are only marginally larger than that of the substrate with laser rastering can yield highly uniform films while at the same time making excellent use of the target surface. Some vendors of commercially available large-area systems do not recommend target resurfacing of large-area targets. Once the target surface has reached a steady state of cone formation, the deposition process becomes predictable. Large-area systems utilize targets that are between 100 and 200 mm in diameter depending on substrate size and application.

Target heating from large-area substrate heaters can be a problem for large diameter targets. Most commercial PLD systems protect the targets with a large water-cooled plate that sits directly above the target surface. A slot in the plate is provided to allow the laser beam to ablate the active target and the plume to expand out toward the substrates. The substrate radiation will usually heat the center of the target more then the target edges, which leads to nonuniform thermal expansion of the target and ultimately cracking of the large-diameter targets. However, cracked targets are routinely used in large-area PLD systems with no noticeable effect on film properties.

9.3.5 Target Manipulation for Coated Conductors

One application that pushes target technology very hard is that of coated conductors. Numerous groups worldwide are currently growing high-quality buffer layers and YBCO thin films on flexible metal tapes that are 1 cm wide and 200 m long and about 100 μm thick. Typically the buffer layers are fairly thin at less than 200 nm. However, the YBCO films required are typically 1 to 2 μm thick. Comparing this to the deposition of a 500-nm film of YBCO over a 125-mm-diameter substrate for microwave applications is rather instructive. A 125-mm-diameter substrate is equivalent to an effective area of about 122 cm^2. The area of the 200-m-long metal tape is 2×10^4 cm^2 and the film is four times as thick. Thus, for a 2 μm film deposited on the metal tape, about 650 times as much material must be removed from the target assuming the same target utilization rate. Thus, for coated-conductor applications, this comparison should serve to confirm that large target size is of paramount importance to obtain uniform film thickness along the entire length of the tape. Also, if trying to achieve a reasonable deposition rate, high powers, typically 150–250 W are used, and thus fast target motion is needed to minimize local heating and cracking of the target material under such intense laser radiation.

To deal with the long-term effects of target erosion in reel-to-reel systems, a new type of target manipulator has been developed such that over a period of time the laser beam is incident on any one spot of the target from a full 360°. Such motion greatly eliminates cone formation and keeps the plume normal to the target surface. This later fact is very important for tape applications where the tape is only 1 cm wide. In this case any slight angular tilt in the plume can produce a large drop in the deposition rate along the length of the tape, as shown in Figures 9.19a and 9.19b.

For coated conductors a stationary beam is sufficient as uniformity is achieved by pulling the tape through the plume. Thus, to achieve long life from the target surface, the target motion must be

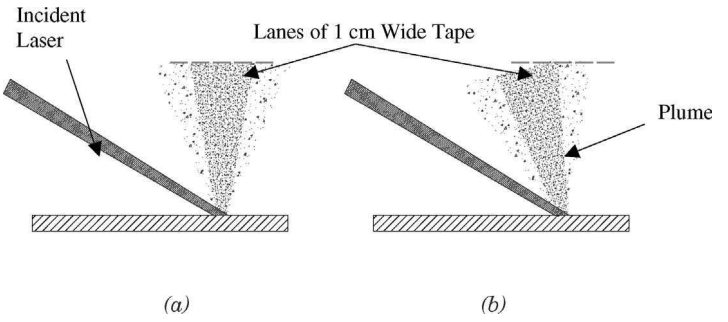

Figure 9.19 (a) Plume coming off normal from a new target surface with a row of five lanes of tape. (b) Plume coming off a used target tilted back toward the laser beam significantly changing the averaged deposition rate on the tape.

controlled in a different manner. Figure 9.20a shows a large-diameter target for which the laser beam is fixed in position and the target is moved in a programmed *X-Y* raster pattern producing the crosshatched ablation pattern on the target surface. The target is not rotated during this *X-Y* motion. When the target reaches the end of its *X-Y* motion, the target is rotated by a fixed angle Θ as shown in Figure 9.20b. The rotation angle Θ should not be an exact divisor of 360°, and in the case shown an angle of 26.5° was used. Repeating the *X-Y*-Θ motion many times ensures that every point on the target surface will be exposed to the laser beam from a full 360° after sufficient rotations as seen in Figure 9.20c. Such a motion sequence then eliminates any preferential orientation of laser-induced cones, keeping the laser beam normal to the target surface for extended periods. Figure 9.21 shows a photo of a two-position *X-Y*-Θ target manipulator (each target in this case is 8 inches in diameter). The unit uses both vacuum stepper motors and external motors to drive a fully vacuum compatible *X-Y* stage. Vacuum stepper motors are also used for target indexing and rotation. Scroll rates are typically about 100 mm/s. This high speed helps minimize the local heating on the target surface due to high laser power.

Figures 9.22a and 9.22b show photographs of both sides of a 6-inch YBCO target surface. Figure 9.22a is a photograph of the top surface obtained from a target using standard laser beam rastering over the whole target surface during standard substrate rotation for 6 h of laser ablation at 248 nm, 200 Hz, and 300 mJ. The texture of the surface is evidently caused by the cones that are pointing back toward the direction of the incident laser beam. By contrast, Figure 9.22b shows the bottom target surface obtained from the same target after it was exposed under identical conditions

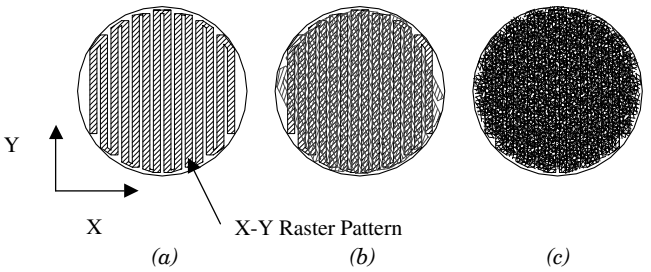

Figure 9.20 (a) Large-diameter target showing the pattern produced in the target surface by moving the target under a fixed position laser beam with the proper *X-Y* scan. (b) Same target surface after the target has been rotated through 26.5° and undergone a second *X-Y* raster scan. (c) The same target surface after 7 such *X-Y*-Θ raster scans.

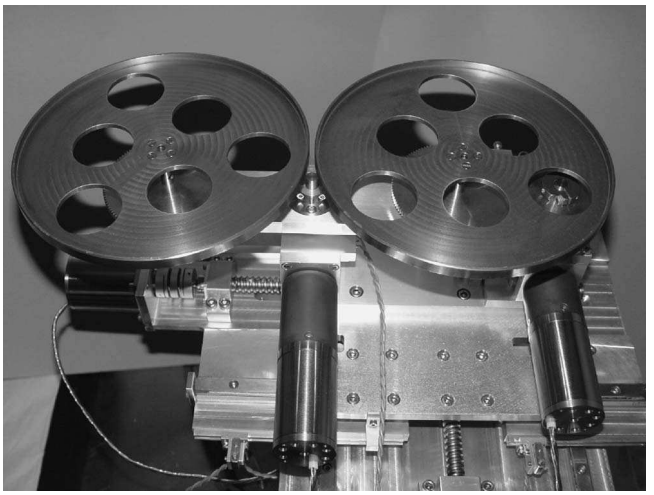

Figure 9.21 Photograph of an *X*-*Y*-Θ target manipulator. In this case there are two 8-inch-diameter targets. Seen are several of the vacuum stepper motors used to drive the various degrees of freedom.

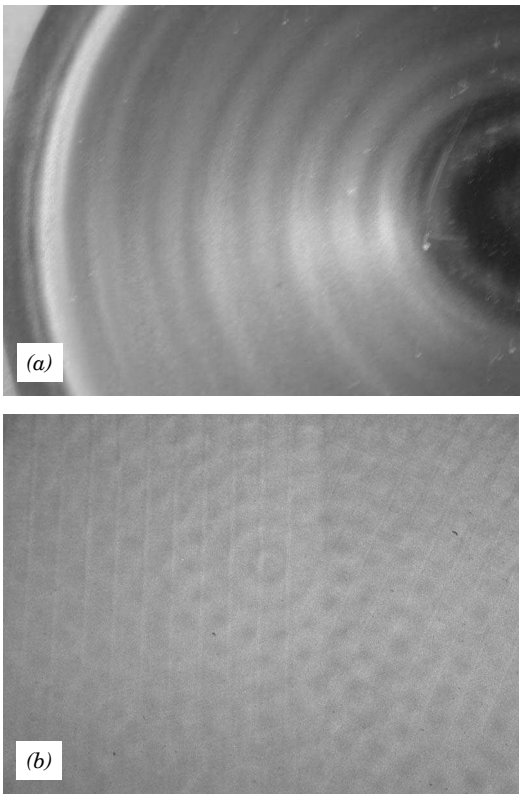

Figure 9.22 Photographs of two YBCO target surfaces. (a) Large-diameter target surface modified by standard laser beam rastering. Note the texture in the target surface pointing back toward the laser beam. (b) Large-diameter target surface modified by laser beam exposure from a full 360° at target each location. In this case there is minimum cone formation and little target texturing evident.

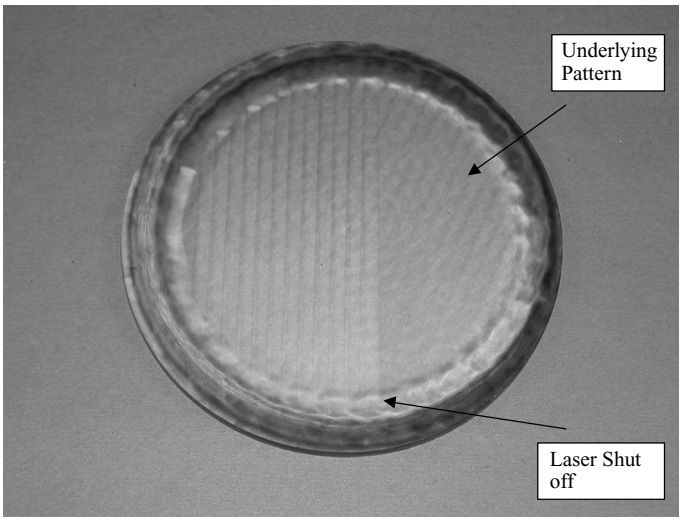

Figure 9.23 Photograph of a 6-inch YBCO target after multiple X-Y-Θ scans under an excimer laser beam. The laser was shut off in the middle of the scan as indicated. The underlying pattern produced by the previous scan is visible.

to the laser beam using the new type of X-Y-Θ target manipulator. Here the texture is very different, and no discernable cone formation or preferential direction is seen. Figure 9.23 shows a photo of the whole target surface. The last raster pattern is evident showing the X-Y motion. The laser ablation was stopped somewhere in the middle of the X-Y scan and the end of the pattern can clearly be seen.

9.3.6 Deposition Rate Monitors

Standard PVD techniques such as evaporation and sputtering have relied on a quartz crystal microbalance (QCM) to monitor and control the film deposition rate. Unfortunately, a QCM does not work well for large-area PLD processing [Greer et al., 1997] for a variety of reasons. First, most PLD processing occurs at high substrate temperatures. The radiation from the substrate is usually enough to drive the quartz crystal temperature far from its stable operating point, yielding undesirable noise and nonlinear effects. Second, the forward direction of the ablation plume creates very unrealistic tooling factors for the QCM as only a very small fraction of the plume will arrive at the QCM head. If laser beam rastering is used, then the tooling factor becomes a dynamic function of laser position. While QCMs have been used successfully to monitor film deposition rates on small substrates at low growth rates, when growing large-area films using high laser repetition rates and therefore fairly high average film growth rates, the heat of formation of the film condensing on the crystal and induced intrinsic film stress produced also causes problems. A rate monitor based on the principle of atomic absorption has been developed for the PLD process but also found to have a variety of problems. Ellipsometry may be used for deposition rate monitoring, but only for a certain class of materials. Reflection high-energy electron diffraction (RHEED) is a tool that has also been used to monitor film growth rates but is not practical for a large-area system when deposition pressures are high. At present, deposition rate monitoring remains one outstanding issue for the PLD process. Typically, large-area films of a given thickness are grown based on the total power incident on the target, time, and experience with a particular target and material. Using an in situ fluence monitor, such as that available with the Intelligent Window,

allows the user to monitor the energy about to hit the target, helping obtain a more accurate film thickness.

9.4 COMMERCIAL SYSTEMS

A wide variety of commercial equipment is available today from vendors worldwide, and the design and performance of various systems can vary widely. Figure 9.24 shows a photo of a low-cost commercially available PLD system used for small-area (2-inch diameter and smaller) substrates. This system is turbo-pumped, handles multiple targets, and has been designed for R&D in a university environment. It includes a laptop computer that controls the substrate heater, mass flow controllers (MFC) flow rate, target rotation speed, and target raster pattern and selects the active target (from a bank of three or six) and controls the excimer laser.

A more sophisticated PLD system is shown in Figure 9.25 and is capable of depositing uniform films onto substrates 5 inches in diameter or multiple smaller substrates. It includes a three-position target manipulator with 6-inch-diameter targets along with a blackbody-style substrate heater. This heater, based on a bank of IR heat lamps, can easily heat silicon substrates to 950°C and sapphire or $LaAlO_3$ substrates to 850°C. The system is also run via a computer that controls the chamber pressure using a closed-loop control system, substrate temperature, MFC flow rates, substrate rotation speed, target rotation speed and target selection, laser beam raster pattern, laser parameters, and data logging. Both of these systems are based on a rectangular box style chamber that has a front-mounted hinged door. This allows the user to easily exchange targets or substrates through the front door without having to remove any flanges or hardware. These systems also are designed so that the targets are held in their pedestals and the substrates are held in the substrate rings by gravity.

Figure 9.24 Photograph of a low-cost small-area commercially available PLD system. (Photograph courtesy of PVD Products, Inc.)

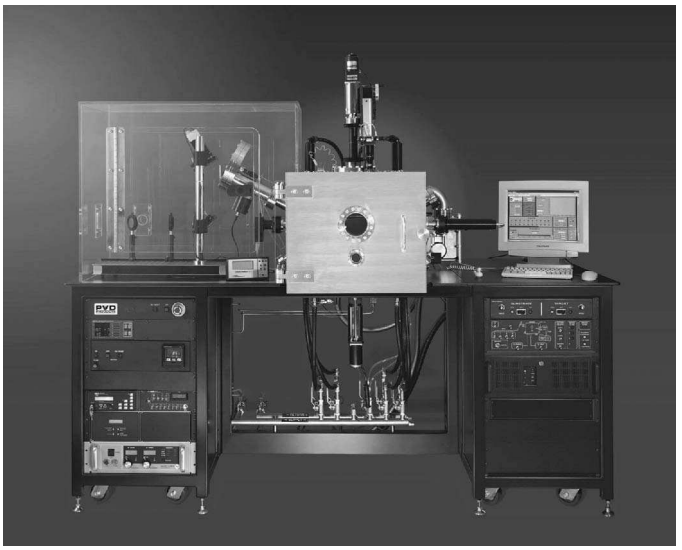

Figure 9.25 Photograph of a commercially available large-area PLD system that can be used for either R&D or production. (Photograph courtesy of PVD Products, Inc.)

Figure 9.26 shows a photograph of a coated-conductor PLD deposition tool. The system is composed of three separate chambers, two reel chambers, and one main deposition chamber. The reels are designed to handle over 500 m of tape, and tape speeds can vary from 0.1 to 20 m/h. Using clutches the torque on the reels, and thus the tension on the tape, can be chosen and maintained. The system is turbo-pumped and includes closed-loop pressure control via a capacitance manometer and stepper motor controlled gate valve. To heat the tape to deposition temperatures of 850°C the system

Figure 9.26 Photograph of a commercially available reel-to-reel coated-conductor PLD system. (Photograph courtesy of PVD Products, Inc.)

includes a multizone heater based on a bank of multiple IR lamps. The entire heater assembly is mounted on a large Z-stage that allows the user to adjust the target-to-substrate distance from about 40 to 100 mm. The system was designed with three 6-inch-diameter targets and a X-Y-Θ target manipulator that allows each point on the target to be exposed to the laser beam from a full 360°.

Recently, an upgraded version of this system that uses multiple lanes of tape on a contact style heater and synchronized laser rastering to form multiplumes has yielded 212 m of tape with a critical current of 245 A. The figure of merit, FOM, defined by the length of tape and critical current in this case is 52,000. This is the highest FOM for any coated conductor reported to date by any deposition technique.

9.5 COMMERCIAL COMPONENTS

Many laboratories build their own deposition systems to meet their own specific needs or budgets, and in many cases, purchasing specific components designed for PLD for a custom system may be useful. Components can include complete optical trains and Intelligent Windows, target manipulators with load locks, and various types of substrate heaters. As an example, Figure 9.27 shows a multitarget manipulator holding eight 1-inch-diameter targets. This unit includes a water-cooled plate located in front of the targets and a removable aperture for the laser beam and plume to expand. It is housed in a load-lock chamber and mounted to a long stroke Z-stage along with a motorized dual-axis magnetically coupled rotary feedthrough providing computer control of target rotation, target rastering, and target indexing. Each of these items usually can be designed to meet customer requirements, especially if discussions with the vendors take place before the deposition chamber has been fully defined. Another example of commercial components (the multizone heater) has already been shown in Figure 9.15, a multizone heater used for a coated-conductor application. Such a heater has yielded short lengths (7 cm) of coated conductors with I_c values greater then 500 A/cm-width.

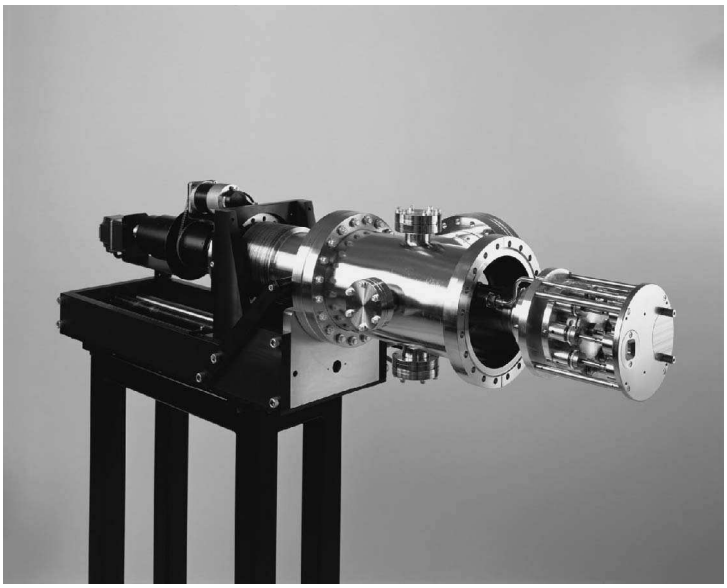

Figure 9.27 Photograph of a load-locked 8-position PLD target manipulator. (Photograph courtesy of PVD Products, Inc.)

9.6 CONCLUSIONS

Pulsed laser deposition technology has been steadily maturing over the past decade. Laser deposition has emerged as an important PVD technique for the fabrication of complex thin-film materials and is now found in several hundred research labs around the world. It has been demonstrated that the PLD process can be used to deposit films onto substrates as large as 200 mm in diameter with very good film uniformity of both film thickness and composition at deposition rates similar to that of magnetron sputtering. Given the recent results obtained with coated-conductor systems, it is apparent that PLD would be able to coat even larger diameter substrates if the need arises.

New products and equipment for both R&D and production are now being commercialized at a steady pace. Applications are emerging that require high throughput for standard wafers and long lengths of coated conductors. These applications are driving vendors to develop even newer deposition tools with many unique features, and many vendors are now providing PLD equipment for both small and large substrates, as well as coated conductors and individual components. It is expected that PLD will continue to mature and become an *industrial* process like sputtering and evaporation over the next 10 years. The development of a good deposition rate monitor is still one area that needs to be properly addressed for the PLD process, however. This rate monitor must be compatible with high substrate temperature, rotating substrates, a wide variety of materials, high background gas pressures, and the pulsed arrival rate of material at the substrate surface. Finally, a technique to accurately measure substrate temperatures of IR transparent rotating substrates would also be very useful not only for the PLD process but for many other PVD techniques as well.

REFERENCES

Boughaba, S., Islam, M. U, Sproule, G. I., and Graham, M. J. (1999) *Mater. Res. Soc. Proc.* **567**, 527–533.

Chrisey, D. B., and Hubler, G. K. (1994), *Pulsed Laser Deposition of Thin Films*, Wiley, New York.

Develos-Bagarinao, K., Yamasaki, H., Nakagawa, Y., Obara, H., and Yamada, H. (2003), *Phys. C* **392–396**, 1229–1235.

Gibbons, B. (2005), private communication, August.

Greer, J. A., and Tabat, M. D. (1995a), *J. Vac. Sci. Technol. A* **13**(3), 1175–1181.

Greer, J. A., and Tabat, M. D. (1995b), *Mat. Res. Soc. Symp. Proc.* **338**, 151–161.

Greer, J. A., Tabat, M. D., and Lu, C. (1997), *Nucl. Instrum. Methods Phys. Res. B* **121**, 357–362.

SECTION 3

CHAPTER 10

Coating Powders for Drug Delivery Systems Using Pulsed Laser Deposition

JAMES D. TALTON and BARBEL EPPLER

Nanotherapeutics, Inc., Alachua, Florida

MARGARET I. DAVIS

Nanotherapeutics, Inc., Alachua, Florida and National Institute on Alcohol Abuse and Alcoholism, Rockville, Maryland

ANDREW L. MERCADO and JAMES M. FITZ-GERALD

University of Virginia, Charlottesville, Virginia

10.1 INTRODUCTION

Pharmaceutical formulations that provide for delivery of a drug over an extended period of time have revolutionized the pharmaceutical industry. Whether the delivery is sustained, modified, controlled, extended, or delayed, the concept is generally the same—provide in a single dose what previously required multiple doses. The desire is to provide an effective concentration of the drug for an appropriate length of time.

There are several advantages to such formulations. For example, having a lower concentration of the drug in the body for a longer period of time lowers the incidence of toxicity for drugs with a narrow therapeutic window and often improves the overall effect. Also, patient compliance is improved when the dosing regimen is decreased; a patient is far more likely to take a single daily dose than to take two, three, or even four doses daily. This is true for drugs delivered orally as well as injected, inhaled, or delivered by transdermal or transmucosal diffusion.

Traditionally, sustained release has been achieved by placing a coating material over the drug particles or granules, and thus, tablets, capsules, caplets, pills, and other formulations with coated granules have been provided. Depending on the desired drug release properties, a drug core may be coated with a single layer of coating, or alternating coatings may be provided, or the drug may actually be interdispersed within the coating material.

Oral and other sustained release dosage forms have largely been based on wet or dry granulation methods. These systems utilize spray coating or mechanical mixing of a core drug particle and/or excipient granule with a polymer, for example, a cellulose, polyacrylate, or degradable polyester to control the rate of release of the active drug substance. In addition, traditional matrix systems may contain a gel-forming excipient, for example, polyvinyl alcohol (PVA), polyethylene oxide

Pulsed Laser Deposition of Thin Films: Applications-Led Growth of Functional Materials
Edited by Robert Eason

(or polyethylene glycol, PEG), celluloses, and the like, that form a gel layer after delivery that releases the drug over time by diffusion of the drug through the matrix. A limitation of these systems is that multistage scale-up from the laboratory to commercial-scale production of formulations can be lengthy and difficult, often requiring specialized equipment and expensive solvents. Additionally, known systems produce formulations that have a relatively high concentration of polymer, thick coatings, and tend not to be reproducibly manufactured with identical release profiles.

An improved method for preparing coated drug particles that does not suffer these limitations was developed in the late 1990s involving pulsed laser deposition (PLD). Utilizing PLD of polymers as a source of coating material, directing the plume over a fluidized bed of drug particles produces thin, continuous coatings for sustained-release or other delivery applications. This chapter will describe the types of coatings that can be applied to pharmaceutical powders, characterization of the coatings and powders produced, and examples of these drug delivery systems in vitro and in vivo.

10.2 BACKGROUND

Microencapsulation of drugs powders in the pharmaceutical industry, mainly for improving the flow properties before pressing into tablets, has been used for several decades. Microencapsulated particles for controlled or sustained-release systems, which slow the release of a drug into the biological solution surrounding a particle, are becoming more popular as the industry adopts more ''once-a-day'' dosages. This technique can also provide additional patent protection from generic manufacturers. Wet or dry physical mixing, performed in large ribbon or V-shaped mixers and spray-coating in fluid-beds, are used where a small amount of drug and a blend of inactive materials (excipients) are incorporated into spherical granules ($>100\,\mu m$ diameter). Newer drug delivery systems, based on controlling the particle size to enhance the desired properties, such as inhaled powders, which must be 1–5 μm in diameter to be inhaled efficiently, are already available in several commercial products. Although granulation technologies are efficient for preparing drug formulations for simple processes such as tableting, interest in microencapsulating drugs into micron (microparticles) or submicron (nanoparticle) size particles is growing.

Currently there are several different ways of microencapsulating drugs into microparticles/nanoparticles to form a barrier or film between the particle and its environment, mainly through emulsion and spray-drying techniques. One of the earliest methods of microencapsulation, known as ''prilling,'' using ammonium nitrate explosive was described in a German patent in 1918. Prilling of the molten nitrate was simply done with slowly rotating disks or buckets (with holes) or by means of relatively simple showerheads at the top of tall ''prilling towers'' 30–70 m high. This early version of spray-drying, which leads to drying and solidification as the droplet falls down the tower, is aided by a counter-current airstream upward. Special metal powders, sodium hydroxide, stearic acid, fats, and certain wax powders are still produced this way. Wax pellets that carry a 50/50 payload of proteolytic enzymes for detergent use was one of the earliest described microencapsulated product formed by prilling. The particle size distribution, however, is as fine as only the 200–500 μm range.

The most widely used physical technique, the spray-drying process, typically uses a two-nozzle spray assembly, allowing air from an annular port to atomize the liquid stream to form fine particles, carrying the microencapsulated product in a dispersed state. Small droplets (typically 1–200 μm) with high surface areas are dried by an upward airflow in the drying chamber, which flash-evaporates the solvent or aqueous media, and the dried particles are collected in a second chamber. Other physical techniques include the spinning disk and coextrusion processes. The spinning disk method, similar to the spray-drying process, uses an emulsion or suspension containing the main ingredient, prepared with a solution or melt of the coating material. Typical extrusion systems involve concentric nozzles, which pump a core material through an inner nozzle while the shell formulation is pumped through the annulus, allowing true ''core–shell'' morphologies of particles typically 100 μm to 6 mm in size. Complex coacervation, phase separation, gelation, and use of supercritical

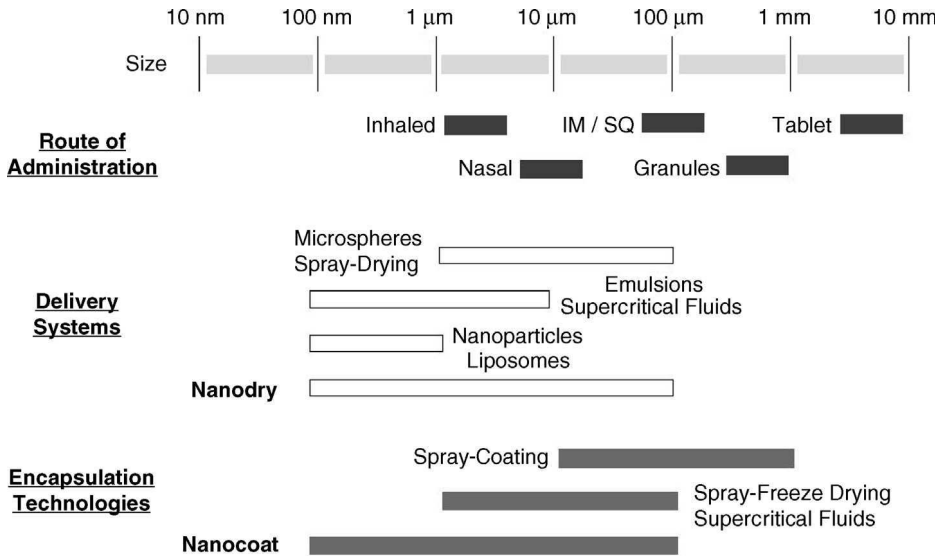

Figure 10.1 Diagram of relevant pharmaceutical particle sizes and different preparation technologies.

fluids are chemical microencapsulation techniques that develop highly stable microcapsules as small as 0.5 µm, which is smaller than some bacteria.

Each microencapsulation technique described above utilizes liquid solvents to apply a coating to the surface of a core particle or form a drug particle embedded in a matrix of an excipient. While spray-coating techniques for encapsulating larger particles ($>100\,\mu m$) have been available for decades, many inhaled and injectable systems require smaller microencapsulated particles ($<100\,\mu m$) that cannot be processed using these systems (see Fig. 10.1).

10.2.1 Wet Powder Coating Techniques

Wet particle coating techniques primarily involve spray-coating a material, such as a polymer or cellulose, onto a core particle to increase the particle size (granulation), sustain release, taste mask, or improve the shelf life. Top or bottom (Wurster) spray-coating systems, characterized by the location of the spray nozzle, spray an atomized flow of coating solution, suspension, or other coating vehicle onto particles suspended in a fluidizing airstream. The atomized coating material collides with the particles as they are carried away from the nozzle, and heated fluidizing air is used to evaporate the coating material solvent shortly after colliding with the particles. The coating material is left on the particles as a developing film or coating, and the process continues until each particle is coated to the desired film thickness. These systems have excellent industrial applicability with batch sizes up to hundreds of kilograms but utilize large amounts of solvent and coating material to produce continuous coatings. Spray-coating systems also have limited applicability to micron-sized particles due to the fact that the spray nozzles typically produce droplets from 10 to greater than 100 µm in size, which may be larger than the particle they are meant to coat. Other systems utilizing emulsion or solvent evaporation systems have limited industrial scalability and have large solvent requirements even for small batches.

10.2.2 Dry Powder Coating Techniques

Dry particle coating techniques, which attach coating materials onto the surface of larger core particles by mechanical or thermal means, offer a promising alternative approach to liquid-based

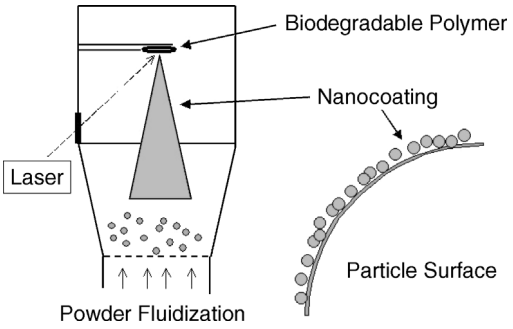

Figure 10.2 Simplified diagram of Nanocoat process for microencapsulating powder formulations.

coating systems. Several dry coating methods have been developed, primarily based on high shear mixing of dry preformed core and coating particles. The strong mechanical forces and the accompanying heat generated can cause layering and even embedding of the guest particles onto the surface of the host particles. Because the core particle incorporating a drug may reach high temperatures, some heat-sensitive pharmaceutical ingredients may not be appropriate. Another technique, magnetically assisted impaction coating (MAIC), utilizes impaction of agitated magnetic beads to coat soft particles without substantial heat generation. However, some evidence of iron contamination has been observed due to the magnetic beads [Singh et al., 1997].

Utilizing similar fluid-bed systems as spray-coating systems, the Nanocoat encapsulation technique generates a spray of nanoscale particles (Fig. 10.2), enabling the coating of a wider range of particle size ($< 1\ \mu m$ to $> 100\ \mu m$). Generation of nanometer-size particles using laser deposition has been shown for a variety of organic and inorganic materials, which can be used successfully to form thin films on particles. Interestingly, because of the insulating and transition temperature properties of polymers, slow release coatings can be produced on core particles at room temperature and atmospheric pressure.

10.2.3 Deposition of Polymer Thin Films

Thin films of several organic materials have been processed via nonvacuum routes, such as spin casting, electrochemical deposition, dip coating, solvent evaporation, and aerosol coating, as well as plasma and thermal evaporation [Skrobis et al., 1990; Bopp et al., 1997; Wu and Wallace, 1998; Sakurai et al., 2002; Young et al., 2000]. As an example, recent applications of polymers conjugated to optical and optoelectronic devices require the formation of thin polymer films of high quality (retained functionality, thickness, morphology, etc.) [Skotheim et al., 1996]. Although spin casting has been widely used, this technique is limited to polymers dissolved in certain solvents. Moreover, the volume dilution of the optically active main chains in the derivative forms modified for solubility results in reduced linear and nonlinear optical responses as compared with their parent polymers [Heeger et al., 1988; Lee and Mittler-Neher, 1992]. In most cases plasma polymerization, a specific type of plasma-enhanced chemical vapor deposition, has been used. Therefore, organic thin films obtained in this way were also named as plasma polymer films. Along with the rapidly developing field of plasma polymerization [Bell, 1980; Shi, 1996], several other vacuum methods of thin polymer film preparation have been used: (1) electron beam irradiation [Favia and d'Agostino, 1998; Inagaki and Makino, 1997], (2) ultraviolet (UV) light vapor irradiation [Sowa et al., 2000; Hishmeh et al., 1996], (3) thermally assisted vacuum evaporation [D'Almeida et al., 2001], and sputtering [Biederman, 2000]. However, these techniques can only be used in special cases where polymers with a low molecular weight evaporate as polymer units and condense on the substrate without chemically reacting. When heated to their evaporation temperature, most polymers are fragmented,

and these gaseous fragments ''condense'' on the substrate without creating a proper polymer network. Furthermore, the use of high energies and temperatures in plasma processing and UV curing of fragile polymers is prohibitive [Gengenbach and Griesser, 1998; Cui et al., 2001; Kiesow and Heilmann, 1999]. In addition, there are some less conventional methods that are a direct carryover from inorganic processing, namely PLD and matrix-assisted pulsed laser evaporation (MAPLE), as described in detail in Chapter 3.

In brief, MAPLE was developed at the Naval Research Laboratory (Washington, D.C.) in the late 1990s, mainly for the deposition of thinner polymer films achievable by PLD for chemical sensor applications, such as detection of nerve and mustard gases (McGill and Chrisey, 1999). Although it is somewhat less conventional in terms of thin-film deposition processes, MAPLE is similar to PLD except that the polymer target is dissolved in a solvent and frozen [Dyer and Karnakis, 1994; Blanchet, 1996; Blanchet and Fincher, 1993; Bubb et al., 2002a; Li et al., 1996]. Conventional PLD is largely an inorganic thin-film deposition technique used for the deposition of complex, multicomponent materials (ceramics, superconductors, metals, etc.) [Singh and Biunno, 1988; Cheung and Sankur, 1988; Fitz-Gerald et al., 1999a; Chrisey and Horwitz, 1991; Geohegan and Puretzky, 1999; Lowndes and Geohegan, 1996], as discussed in depth in subsequent chapters. PLD typically utilizes the output of a pulsed UV laser focused onto a solid target that undergoes rapid ablation, creating nearly atomic (partially ionized) species that are deposited upon a nearby (~ 5 cm distance) substrate. In MAPLE processing, the ''target'' consists of a polymer dissolved in an absorbing solvent with a high vapor pressure. The purpose of the volatile solvent in the target is to aid desorption by optically absorbing a majority of the laser energy and subsequently vaporizing when the laser energy is converted to thermal energy [Zhigilei et al., 2003; Dreisewerd, 2003]. Solvents that are sufficiently volatile and do not form a film once evaporated by the laser are ideal.

10.3 LASER-ASSISTED METHODS OF COATING PARTICLES

With specific classes of organic-based materials, laser ablation provides an excellent means for producing a directed flow of submicron particles in the form of heated polymer agglomerates, which are distinctly different than liquid spray methods currently used in industry for microencapsulation. Process conditions include: (1) control of the target or substrate positioning, (2) control of the target or substrate temperature, (3) exposure of the target or substrate to particular gases compared to room air, (4) exposure of the target or substrate to an additional energy source (such as an ion beam or UV light), and/or (5) postprocessing of the coated substrate, such as high-temperature curing or further chemical modification, to produce the desired results.

Laser deposition has been widely used to grow thin films of a wide variety of organic materials over the last 20 years, but few have utilized laser deposition to coat powders. Originally called the atomic flux coating process (AFCP) by Fitz-Gerald et al., the first application of using PLD to coat powders was demonstrated in the literature (Fitz-Gerald et al., 1998, 1999b; Gao et al., 1998). Except for the powder fluidization system, the AFCP technique resembled a standard laser deposition system. Efficient fluidization of the powder was found to be critical, since the difficulty of separating particles under 100 μm because of electrostatic properties is known. Fluidization of the core particles was also achieved by vibrational or pneumatic techniques to expose the entire surface of the core particles to the plume [Fitz-Gerald et al., 1999a].

Thin-film deposition of high-molecular-weight polymers was demonstrated at lower laser energies (< 1 J/cm^2) than those used to ablate metal and inorganic thin films. PLD has been used to deposit films of polydimethylsiloxane (PDMS), poly(methyl methacrylate) (PMMA), and poly(ethylene glycol) (PEG) at low pressures (100 mTorr). These conditions were visibly successful in producing optically clear polymer coatings at low laser energies.

Two related biodegradable polymers, poly(lactic acid) (PLA) and poly(lactic-*co*-glycolic acid) (PLGA), applied to micron-size budesonide powders displayed sustained release properties in vitro and improved pulmonary residence times in vivo in rats (Talton, 1999). PLA, a homopolymer of

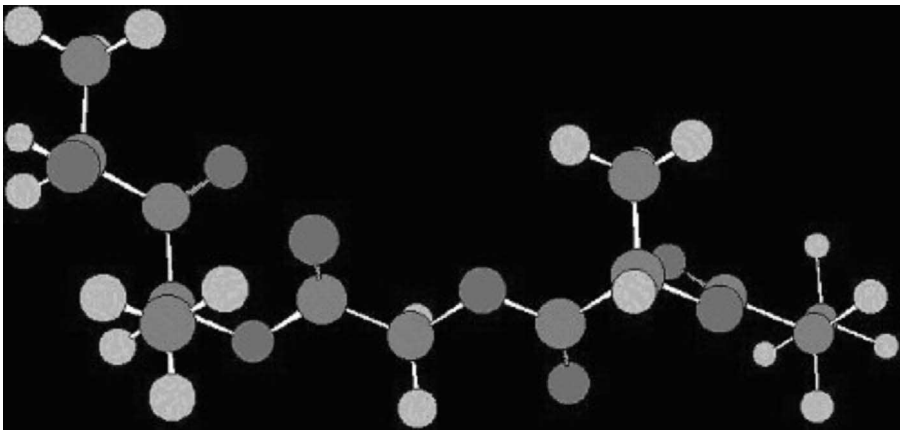

Figure 10.3 Three-dimensional diagram of the PLGA monomer structure.

lactic acid (LA), and PLGA, a copolymer composed of LA and glycolic acid (GA) monomers, are approved by the Food and Drug Administration (FDA) as excipients (nonactive ingredient) in several injectable controlled-release systems. A three-dimensional drawing of PLGA is shown in Figure 10.3. Similar to biodegradable microspheres, polymers with higher degrees of crystallinity lead to slower release (PLA) than more amorphous copolymers (PLGA) (Atala and Mooney, 1997). PLA and PLGA are easily ablated with PLD over a range of pressures at low energies (200–600 mJ/cm^2), making them ideal polymers for microencapsulation of drug powders.

The laser deposition method for coating particles is particularly suited for those types of powders in which a thin coating is desirable, that is, drugs/pharmaceuticals, cosmetics, and the like. Drug delivery systems, such as injectable suspensions or inhaled powders, involving microencapsulated particles in a biodegradable or biocompatible polymer, may be produced under nonaqueous, nonsolvent manufacturing conditions using PLD. The coating may impart a number of characteristics to the particulate material, including altering its surface properties, its dispersion properties, or its rate of diffusion and/or release of the active drug.

10.3.1 Experimental Configurations

The deposition systems for conventional PLD and MAPLE are shown in Figure 10.4. For PLD of PLGA (or other polymers), a solid disk of PLGA is typically heat pressed at 140°C in a Carver press at 10,000 psi. For the MAPLE, a 1 wt % polymer/chloroform ($CHCl_3$) solution of PLGA is vortex mixed and frozen in liquid nitrogen to form a solid target. The frozen target was then inserted onto a liquid nitrogen cold stage (temperature $\sim$110 K) due to the fact that chloroform has a melting temperature of -63°C.

For comparison of both methods, the chamber was pumped down to a base pressure of 10^{-6} Torr and then backfilled to 100 mTorr with argon. During MAPLE processing, since the volatiles must be pumped out of the system during deposition, a continuous flow of Ar is maintained. For comparison purposes, films were deposited onto silicon and sodium chloride substrates at room temperature using a pulsed excimer laser ($\lambda = 248$ nm) operating at 5 Hz with a 25-ns pulsewidth. Energy regimes of 0.1 to 1.0 J/cm^2 and 0.2 to 1.0 J/cm^2 were investigated for MAPLE and PLD, respectively.

Coating of powders with the laser deposition technique comprises two equally important components, the powder fluidization system and the laser deposition system. Powder fluidization whereby particles are suspended by shaking a vessel or in a rapidly moving stream of gas to induce flowing motion ensures that each particle is coated uniformly on the surface. The initial AFCP setup involved a typical PLD vacuum chamber with a target rotator oriented downward at approximately a

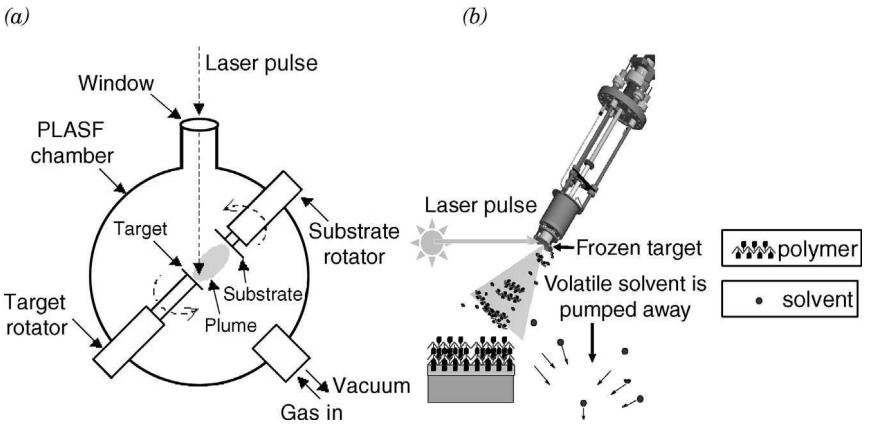

Figure 10.4 Experimental setup for thin films by (a) conventional PLD and (b) MAPLE.

45° angle and a powder cup on a shaker system. The laser enters the chamber through a quartz window and ablates coating material from the polymer target producing a conical-shaped plume. The core particles are mechanically fluidized during the batch run. By controlling the batch run time, amount and size of the particles being coated, the fluidization, the laser wavelength, pulse frequency, and background gas and gas pressure during deposition, the resulting coating thickness and morphology on the core particle can be varied.

10.3.2 Polymeric Coating Materials

Both natural and synthetic polymers have been used to encapsulate drugs. Polysaccharides, such as different types of celluloses, starches, alginates, and chitosan, have been used extensively for over 50 years. More recently, research has been devoted to the development of synthetic biocompatible or biodegradable polymer systems, such as ethylene-vinyl acetate (EVA), polylactic acid (PLA), and poly(acrylic acid) (PAA). Polymers used for microencapsulation in drug delivery systems should have the following characteristics:

1. They should be nontoxic.
2. Degradation products, if any, should be nontoxic and should be readily removed from the body.
3. The polymer and the method of preparation should not affect the drug.

Microencapsulating drug particles provides control over the drug release kinetics by changing different properties of the ''microcapsule,'' that is, the size of the core particle and the polymer type, wettability, and thickness. The disadvantage of microencapsulating drug particles in the pharmaceutical industry is mainly the additional manufacturing steps that must be added. Most methods (not PLD) utilize organic solvents that can affect the drug or denature proteins and also be harmful in vivo if any residual solvent remains behind in the microcapsules. Sterilization of microcapsules, via γ irradiation, for example, also poses a problem, as this has been shown to cause degradation of the polymer, changing the release kinetics.

10.3.3 Particle Fluidization

Fluidization of the core particles, which are generally larger than the size of the coating particles, can be produced within a chamber that has a large enough volume to permit particle movement.

Powder fluidization chambers are typically stainless steel or glass cylinders that taper toward the top to allow free movement of the top layer of particles. Fluidization using vibration or a gas requires a screen or filter above the fluid bed, with a mesh slightly smaller than the average size of the particles. Gas fluidization produces a sufficient lift to raise the center of the powder bed upward in the coating chamber, falling out of the gas stream around the edge of the chamber and being recirculated. The coating process then continues until the desired coating thickness is achieved.

Except for the powder fluidization system, Nanocoat resembles a standard PLD system. In most cases the chamber will be separate from the laser. However, if one uses compact lasers such as solid-state or excimer lasers operating from 248 to 1056 nm, the laser can be attached to the side of the chamber. The specific conditions that affect the deposition of coatings include control of the (i) laser fluence, (ii) laser spot size, (iii) gas composition and flow rate, (iv) laser repetition rate, and (v) total number of pulses and wavelength of the laser light itself. By controlling each of these parameters, which are very material specific, the integrity, microstructure, topology, architecture, thickness, and adhesion of the coatings on the drug particles can be varied.

10.4 MICROENCAPSULATED PHARMACEUTICAL FORMULATIONS

Microencapsulating pharmaceutical powders using PLD have applications in inhalation through the respiratory tract, as well as, nasally, orally, parenterally, or transdermally. Formulations that would benefit from coating include drugs used in controlled or targeted release formulation, taste-masking, or particulate surface modification prior to tableting or capsule filling, for example, a pulmonary dry-powder formulation of a glucocorticoid asthma drug microencapsulated with a thin-film polymer coating of a biodegradable polymer. Comparing PLD to other microencapsulation methods is difficult since no other solventless process has demonstrated similar high encapsulation efficiency, similar or improved flow properties, and thickness that does not reduce the inhaled fraction.

10.4.1 Characterization of Deposited Polymers

10.4.1.1 Scanning Electron Microscopy

Scanning electron microscopy (SEM) was performed to characterize the thickness and morphological characteristics of the deposited materials. SEM micrographs of MAPLE and PLD-deposited films, as a function of fluence, are shown in Figures 10.5 and 10.6, respectively. Films deposited via MAPLE, regardless of laser energy, had varied amounts of surface features and matrix trace patterns on the surface. At fluences $>0.2\,J/cm^2$, the particulate population (25–500 nm) becomes more pronounced, and apparent matrix effects are minimized with film thickness ranging from 30 to 150 nm. The PLD-deposited films showed a significant range of features in comparison to the MAPLE-deposited films. At energies $>0.2\,J/cm^2$ significant film roughness and deposition were observed with thicknesses ranging from 50 to 2.2 μm.

10.4.1.2 Fourier Transform Infrared (FTIR) Spectroscopy Analysis

Distinct functional groups in the PLGA polymer preferentially absorb tunable infrared (IR) light, specifically when the frequency of the IR light is equal to the vibrational frequency of distinct functional groups inside the polymer backbone, the IR light is absorbed by the polymer and changes the dipole moment, or the molecular vibration, of the atom. These molecular vibrations are equivalent to the stretching or bending of atomic bonds in the PLGA functional groups. The optically absorbing functional groups, or chromophores, in the PLGA polymer and the particular molecular vibrations of these functional groups observed in the FTIR spectra were

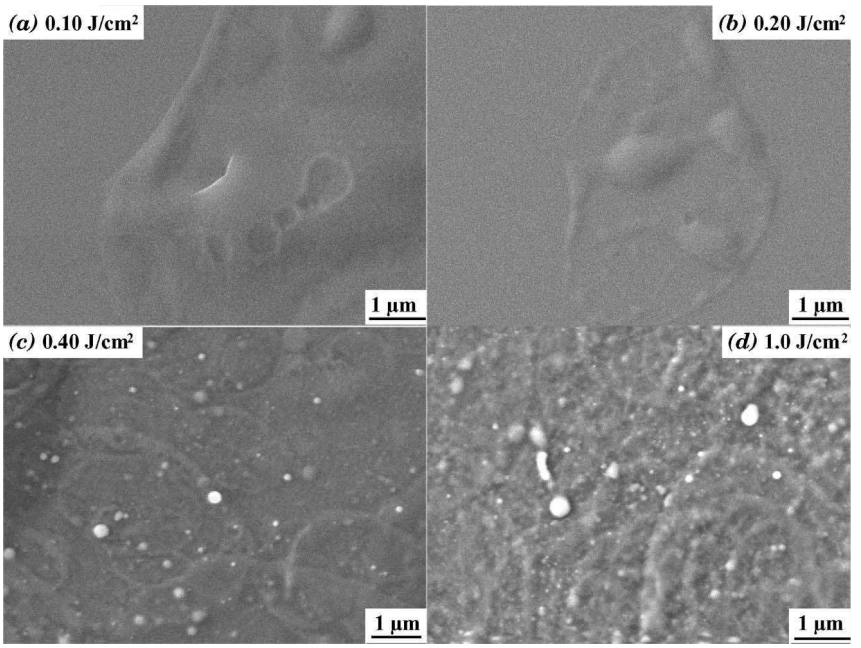

Figure 10.5 Scanning electron microscope images of MAPLE deposited thin films of PLGA. The SEM micrographs show trends of particulate formation, showing morphology effects in terms of matrix patterns, particle roughness, and droplet formation as a function of laser fluence.

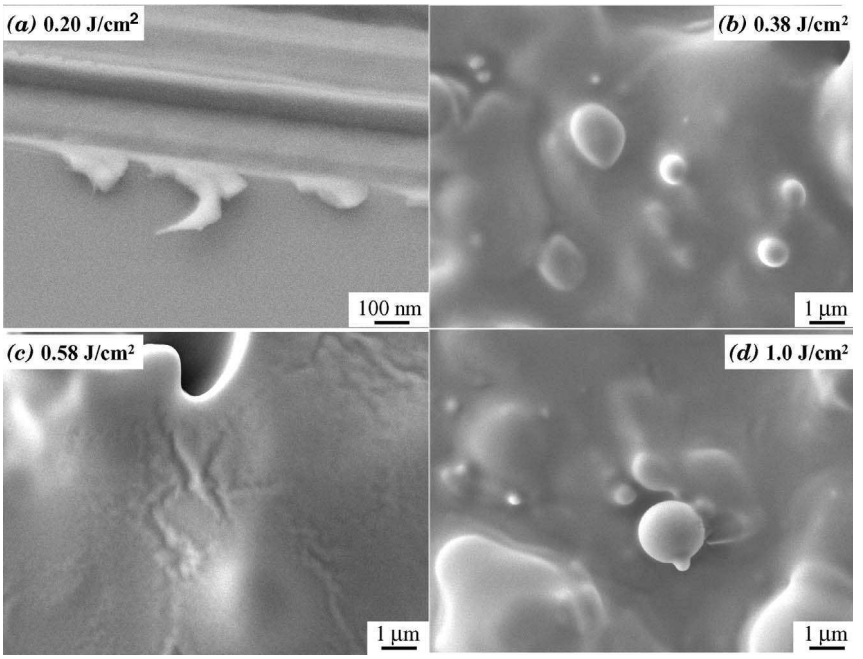

Figure 10.6 Scanning electron microscope images of PLD-deposited thin films of PLGA. The images show increased surface roughness and undulations for energy densities above 0.2 J/cm^2. The films are absent of solvent surface patterning and show large areas of low roughness.

TABLE 10.1 FTIR Molecular Vibrations and Distinct Functional Groups

Functional Group	Corresponding Peak
OH end group	3509.9 cm^{-1}
C—H Stretch of CH_3	3010 and 2955 cm^{-1}
C—H Stretch of CH_2	2885 cm^{-1}
C=O Stretch	1762.6 cm^{-1}
C—O Stretch	1186–1089.6 cm^{-1}
C—H Bends	1450–850 cm^{-1}

the O—H end groups, the C—H stretches, C=O stretch, C—H bends, and the C—O stretch [Li et al., 2001]. These optically absorbing functional groups in PLGA and corresponding FTIR spectrum peaks are shown in Table 10.1. The peak at 3509.9 cm^{-1} corresponds to the vibrational excitation of the OH end group in the PLGA native. The peaks at 3010 and 2955 cm^{-1} coincide with the C—H stretches of the CH_3 groups. The peak at 2885 cm^{-1} was indicative of the C—H stretch of CH_2 while the peak at 1762.6 cm^{-1} corresponded to the carbonyl, or C=O, vibrational excitation. Peaks at 1450–800 cm^{-1} are deemed to be the traditional ''fingerprint'' region for this material, which is an important baseline identifier for each compound and is very distinct for each. Figure 10.7 shows the native PLGA spectra, while Figure 10.8 shows spectra from both the MAPLE (Fig. 10.7a) and PLD (Fig. 10.7b) deposited materials. The results from the FTIR spectra show that the deposited films resemble the native polymer to a finite degree. Overall, characteristic peaks at 1700 cm^{-1} and fingerprint regions at 1450 cm^{-1} appeared similar. However, there is an additional peak at 760 cm^{-1} not visible in the native PLGA profile that could be identified as a C—Cl stretch for MAPLE-processed films only (Bubb et al., 2002a).

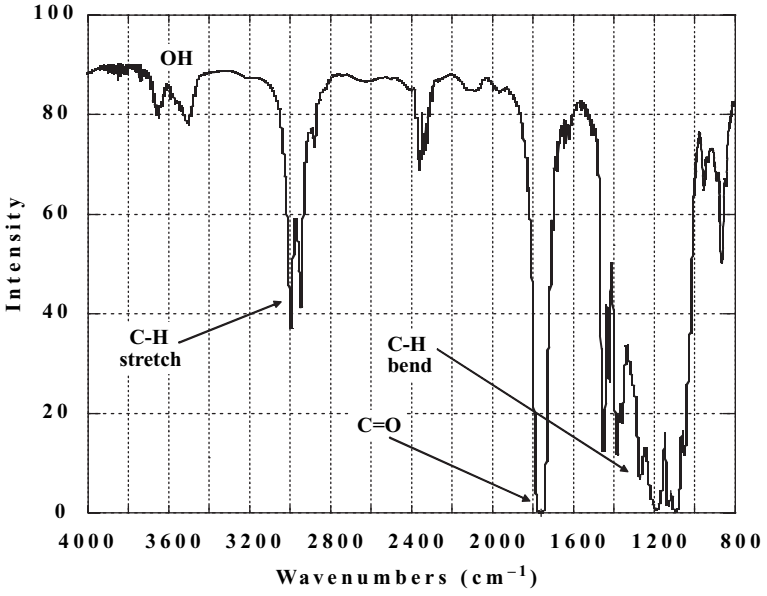

Figure 10.7 FTIR spectra for native PLGA showing characteristic features at 3600, 3000, 1800, and 1200 cm^{-1}, respectively.

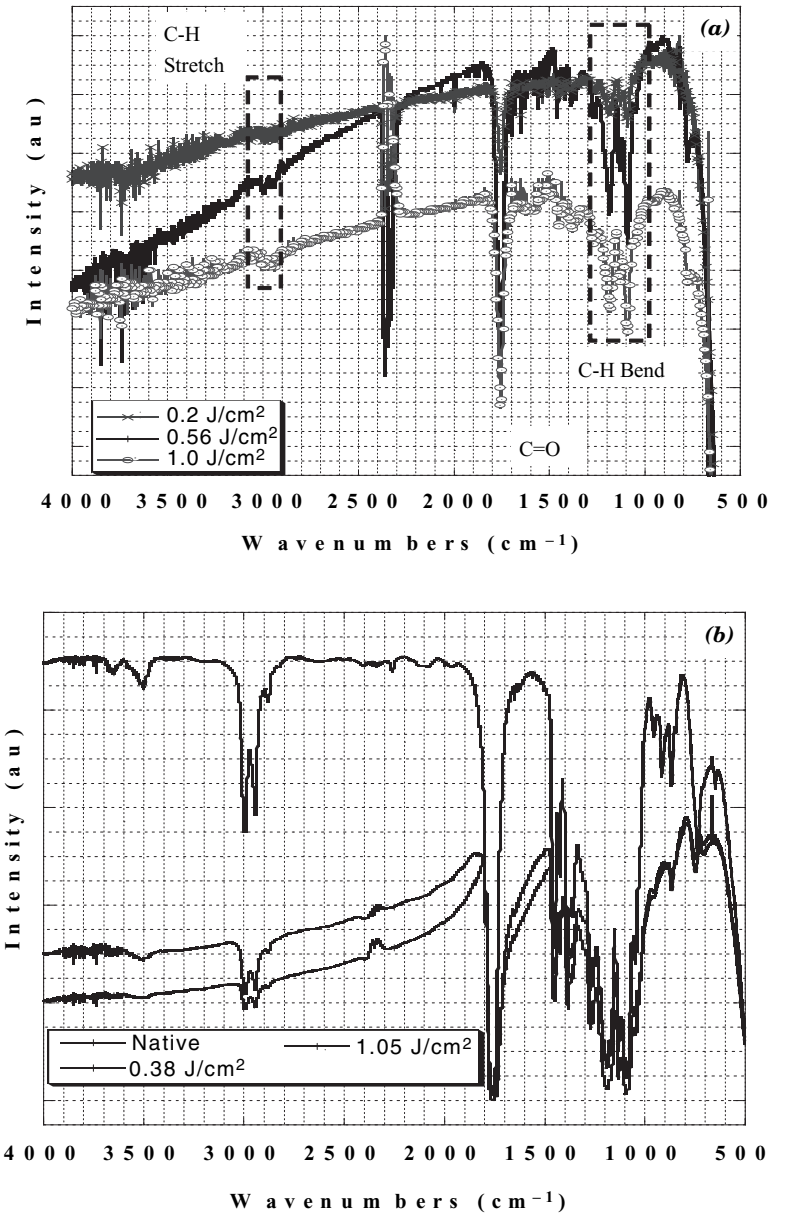

Figure 10.8 FTIR spectra for (a) MAPLE and (b) PLD-deposited PLGA. While strong correlations of the fingerprint regions at 1200 cm^{-1} and the C–H stretch between the native and deposited films exist, there is no clear evidence to suggest laser induced degradation has occurred.

10.4.1.3 Nuclear Magnetic Resonance (NMR) Analysis

The functional groups in the PLGA molecule were compared using proton NMR, and their resulting signals are shown in Table 10.2. The peak at approximately 7.260 ppm corresponded to the deuterated chloroform peak. Deuterated chloroform was used to dissolve the PLGA films and measured using ^{1}H NMR. The multiplet at 5.2 ppm coincided with the resonance in the CH

TABLE 10.2 Peaks in the NMR Spectra Corresponding to the Measurement of Proton Resonance of Distinct Functional Groups of PLGA

Functional Group	Corresponding Peak
Lactic acid CH	Multiplet at 5.2 ppm
Glycolic acid CH_2	Multiplet at 4.8 ppm
Methyl groups of the D- and L-Lactic acid repeat units	Overlapping doublets at 1.55 ppm
Methyl group attached to the hydroxyl endgroup	1.25 ppm

species in the lactic acid while the multiplet at 4.8 ppm corresponded to the resonance of the CH_2 species in the glycolic acid (Hrkach and Langer, 1996). These peaks were complex multiplets because of the different D-lactide, L-lactide, and glycolic acid monomers that make up PLGA. The overlapping doublets at 1.55 ppm were attributed to the chiral methyl groups in the lactic acid monomer units for both D- and L-stereographic configurations. Finally, the peak at approximately 1.25 ppm was associated with the methyl groups attached to the hydroxyl end group of the polymer.

Standard solutions were prepared by dissolving the deposited films in deuterated chloroform, $CDCl_3$. The NMR spectra of the native PLGA is shown in Figure 10.9. Figure 10.10 shows the comparative NMR spectra from the MAPLE (Fig. 10.10a) and PLD (Fig. 10.10b) deposited materials. Specifically, the multiplets associated with the lactide and glycolide groups were similar for both native PLGA and MAPLE-processed PLGA films. However, this NMR compilation showed a broadening in the chiral methyl group peak at 1.55 and 1.25 ppm. The broadening in the chiral methyl group peak was indicative of smaller molecular weight oligomers as compared to the native PLGA polymers due to an increasing interference of various processing of chiral methyl group peaks for smaller molecular weight oligomers [Skrobis et al., 1990]. At higher energies, a trend in decomposition of the deposited PLGA to lower molecular weight species, which are chemically identical, may be observed with differing mobilities, stemming from the breaking of lactic acid and glycolic acid chains [Skrobis et al., 1990].

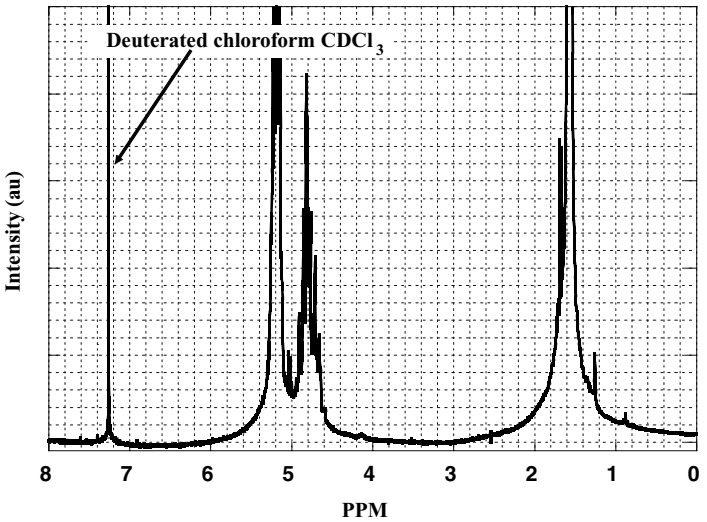

Figure 10.9 Nuclear magnetic resonance spectra from native PLGA showing the methyl groups at 1.25 and 1.55 ppm and the glycolic and lactic acid groups at 4.8 and 5.2 ppm, respectively.

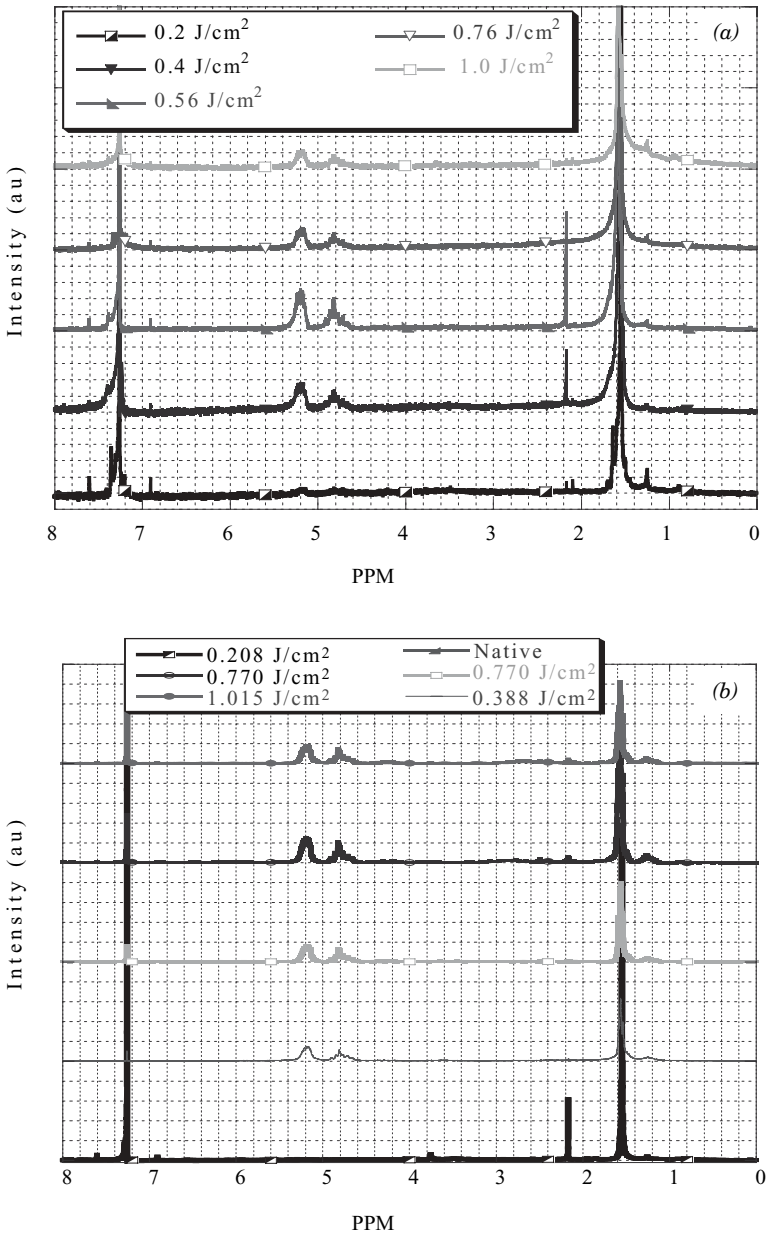

Figure 10.10 Nuclear magnetic resonance spectra of PLGA deposited by (a) MAPLE and (b) PLD at fluences ranging from 0.2 to 1.0 J/cm^2.

10.4.1.4 Gel Permeation Chromatography (GPC) Analysis

Gel permeation chromatography analysis of native PLGA in $CHCl_3$ (flow rate = 1 mL/min) is shown in Figure 10.11. Molecular weight estimates using the refractive index with linear polystyrene (PS) standards indicates an average molecular weight, M_w, of $\sim$100 kDa for the native polymer. GPC analysis of the PLD and MAPLE-deposited materials shown in Figure 10.11 reveal significant variations from the starting native material. Estimates using linear standard PS calibration standards

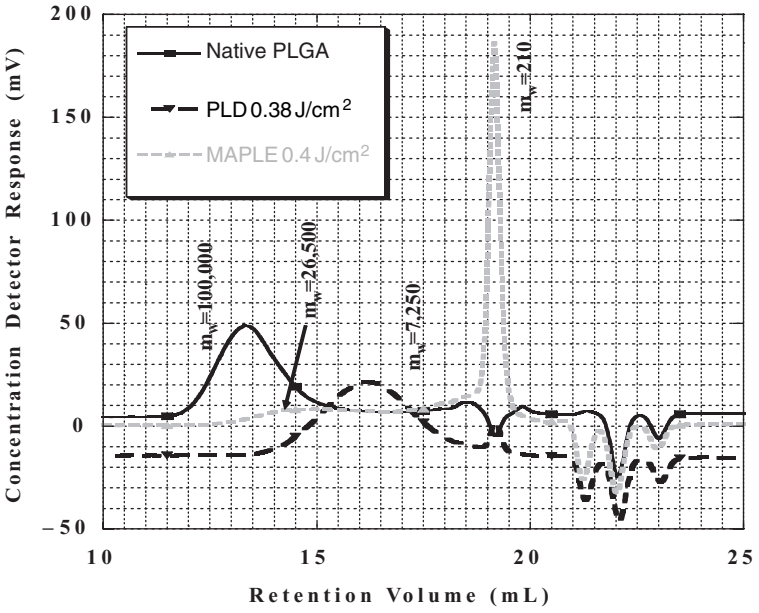

Figure 10.11 GPC overlay spectra of MAPLE and PLD-deposited thin films.

suggest a M_w of $\sim$25 kDa for MAPLE, with a significant shift of the oligomer peak at higher elution volumes to a M_w of $\sim$200 Da (monomer). However, MAPLE-deposited materials had significant overlap of the shoulder with the main peak, precluding accurate molecular weight determination of the higher molecular weight component formed in the deposition process. Materials deposited by PLD (at 0.38 J/cm^2) show contrary behavior with the oligomer peak remaining at a higher $M_w \sim 7$ kDa and a monomer peak occurring at higher elution volumes with a M_w of $\sim$200 Da as shown in Figure 10.11.

10.4.2 Microencapsulated Inhaled Therapies

One of the first examples of using PLD to microencapsulate powders was performed with budesonide, an inhaled glucocorticoid currently used in asthma therapy. Several glucocorticoids are currently available in treating various pulmonary diseases, including asthma, sarcoidosis, and other conditions associated with alveolitis. Although systemic glucocorticoid therapy is effective in such conditions, prolonged administration carries the risk of toxicity and side effects. In attempts at reducing systemic side effects, several clinically efficacious glucocorticoids, including budesonide, have been employed for delivery as aerosols or dry powders.

In a recent study, it was shown that the most beneficial pulmonary effects were achieved with the slowest dissolving of three different glucocorticoid powders administered intratracheally in rats [Talton et al., 1999]. In contrast, lung targeting (ratio of local to systemic effects) was not observed with the fastest dissolving glucocorticoid, budesonide, administered intratracheally, presumably because of the fast dissolution and absorption of the lipophilic steroid [Derendorf et al., 1995]. Although there are other pharmacokinetic factors that vary in this class of drugs, it was proposed that pulmonary targeting of budesonide may be improved if the release rate could be reduced through the PLD microencapsulation process.

In addition, to demonstrate the ability of improving the systemic bioavailability by changing the surface properties of the particle, inhaled formulations of promethazine, an injectable motion sickness drug, was investigated. Since nausea and gastrointestinal motility may reduce the already low oral bioavailability of promethazine (22–25%) and delivery through the lungs is relatively fast with effects possible within minutes, an alternative route of administration to oral

delivery would be advantageous when motion sickness is present. Promethazine micronized powders, coated to provide an increase in bioavailability, could be inhaled and bioavailable immediately through the lungs.

Preliminary experiments with different polymers, PLGA, poly(ethylene glycol) (PEG), and chitosan (CHI), were coated onto inert particles to measure the cell uptake, and onto micronized budesonide (BUD) and promethazine (PMZ) to measure improvement in the local and systemic disposition.

10.4.2.1 Cell Uptake

Macrophage phagocytosis assays using different coatings on inert particles revealed preferential uptake of PLGA-coated over PEG-coated microspheres. J774-A1 macrophages incubated for 30 min with 1 mg/mL of coated particles showed a threefold higher uptake of PLGA-coated spherical powders when compared to PEG-coated powders (Figs. 10.12a–f). The increased uptake of

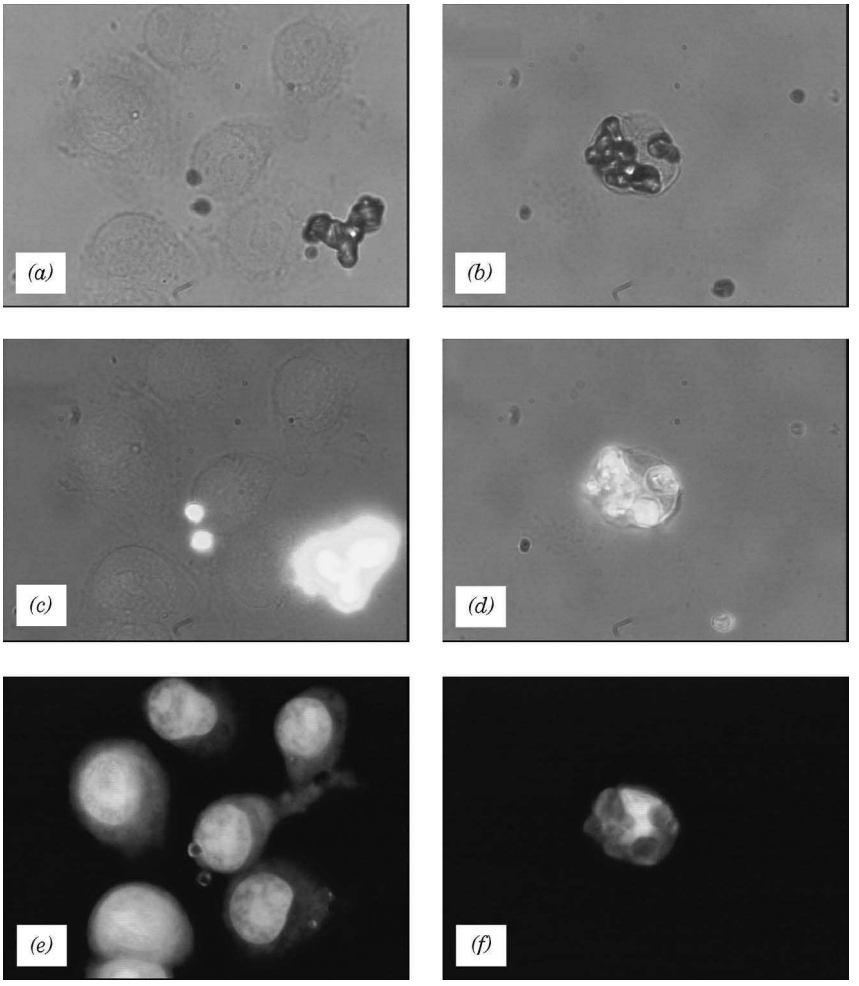

Figure 10.12 Images of J774-A1 macrophages incubated for 30 min with PEG (a, c, e) or PLGA (b, d, f) coated fluorescent spheres. Cells imaged by conventional light microscopy are depicted in (a) and (b). Images collected using both low-level conventional illumination and epi-fluorescence (excitation 465–495 nm, emission 515–555 nm) are shown in (c) and (d). Cells stained with propidium iodide (a nucleic acid intercalating agent) and imaged by epi-fluorescence (excitation 528–552 nm, emission 578–632 nm) are shown in (e) and (f). Images were collected at 1500× magnification.

PLGA-coated particles (3.1 particles/cell), compared to uncoated silica particles (2.0 particles/cell), is likely due to their electronegative ζ potential. Coatings with PEG, which is neutrally charged, showed reduced uptake (1.1 particle/cell, Figs. 10.12 a, c, and e). The preferential uptake of PLGA-coated particles by phagocytic cells may result from chemoattraction of these cells to an acidic environment [Lutsiak et al., 2002; Newman et al., 2002; Lacasse et al., 1998].

Cellular uptake and binding assays provide relevant information regarding interactions with lung components in the surfactant layer and potential interactions of coated particles with phagocytic and nonphagocytic cells. PLGA-coated BUD25 has previously been shown to have a substantially higher bioavailability, as well as efficacy profile in rats, compared to uncoated BUD potentially due to increased macrophage uptake. PEG-coated particles displayed low binding to cells, as well as decreased plasma protein and dextran adsorption [Lacasse et al., 1998]. PEG, because of its neutral charge, has previously been used with injectable liposomes to impart "stealth" properties with reduced phagocytosis [Fu et al., 2002]. Interestingly, reduced binding was also observed using the Nanocoat coating process, but with less than 1% additional excipient load.

10.4.2.2 Controlled-Release Behavior

The controlled-release behavior of coated budesonide was measured in vitro by monitoring the difference in dissolution in phosphate-buffered saline. Inhalation-grade budesonide dry powders in the 1 to 5-μm range were coated with PLGA using both PLD and MAPLE. The dissolution behavior was tested in phosphate-buffered saline (50 mM, pH 7.4) using a USP (United States Pharmacopeil Convention) dissolution bath and sodium dodecyl sulfate (SDS) (0.5%) as a surfactant. Figure 10.13 shows the dissolution profiles of two PLGA-coated budesonide preparations (10 and 25 min PLD coating times) in comparison to uncoated budesonide (BUD). Dissolution of coated powders was biexponential with an initial burst of free drug (30–40%) and a half-life of release $(t_{50\%})$ of the sustained fraction of the coated particles of 29 min for preparation 1 (10-min coating time, BUD10) and 60 min for a preparation 2 (25-min coating time, BUD25). The dissolution half-life of BUD was significantly faster than coated BUD25 and BUD10. In addition, investigations with PLA-coated triamcinolone acetonide, with a half-life of release $(t_{50\%})$ of 16.7 h compared to 0.6 h for uncoated powders, showed that slower-degrading polymers could be used for potentially once-a-day delivery regimens in the lung (see Fig. 10.14b).

The dissolution behavior of the PLGA-coated powders using MAPLE were identical to the uncoated powders (data not shown). One reason for the poor release characteristics of the MAPLE-

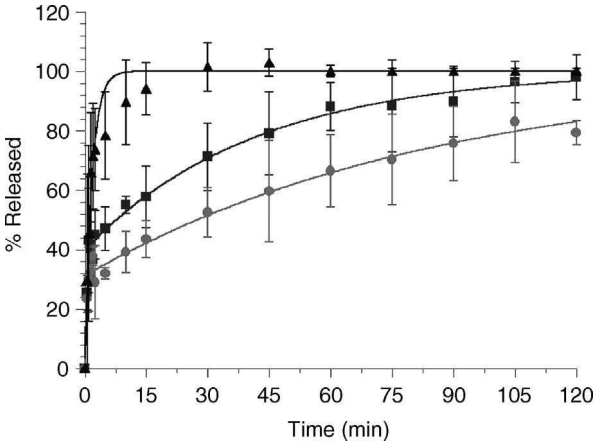

Figure 10.13 Effect of polymer and coating time on dissolution behavior. Uncoated budesonide vs. PLGA-coated budesonide in pH 7.4 PBS (50 mM, 0.5% SDS) at 37°C $(n = 3)$. Profiles are shown for BUD (▲), and PLGA-coated powders for 10 min (BUD10) (■) and 25 min (BUD25) (●).

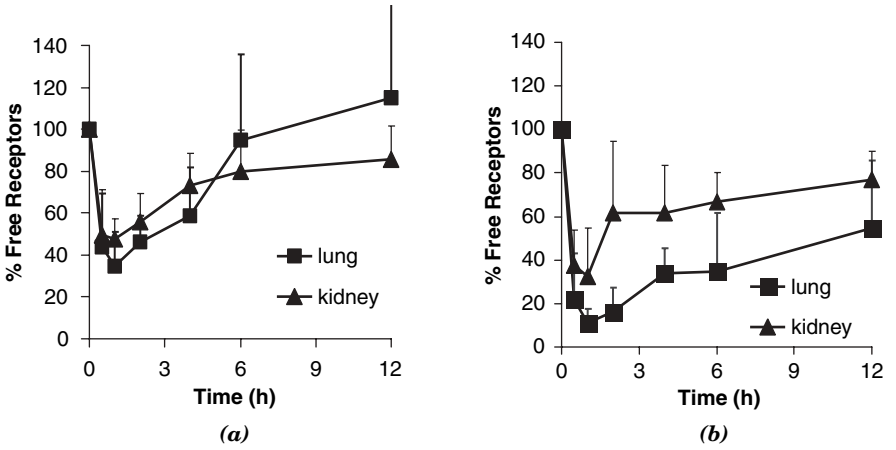

Figure 10.14 Receptor occupancy profiles for (a) BUD administered into the lungs compared to (b) PLGA-coated BUD25 administered into the lungs (100 μg/kg dose).

coated powders may be due to the low percentage (1%) of polymer in the starting target, which results in thin films on flat substrates (low surface area), which will be further reduced on particles due to the high surface area. While preliminary results did not demonstrate sustained release, further research using MAPLE may permit increased coating thicknesses or the use of thin coatings (1–20 nm) to modify the surface charge, wettability, or flow properties of the bulk powders.

Pulmonary targeting was assessed in an animal model that uses the differential receptor occupancy in the lung and systemic organs as a surrogate marker of pulmonary selectivity. Figure 10.14a shows the lack of significant pulmonary targeting when uncoated BUD was tested. In contrast, the use of the PLGA-coated BUD25 formulation significantly increased the difference between kidney and lung receptor occupancies (Fig. 10.14b), indicating substantial pulmonary selectivity.

The receptor-binding profiles for BUD25 showed an improvement in pulmonary targeting over BUD-free powders in the lung versus liver and lung versus kidney. In addition, the pulmonary mean effect time (MET), or the time an effective drug concentration is present in a tissue, of BUD25 increased almost 2 h to 5.5 h compared to 3.6 h for BUD [Derendorf et al., 1995]. Thus, improvement in pulmonary targeting by changing the dissolution rate of budesonide suggests that the increase in pulmonary targeting of BUD25 powders is obtained by controlling the release rate of budesonide into the lung.

10.4.2.3 Improved Bioavailability

Coatings with PLA, PEG, and two other natural excipients, hydroxy-propyl-methyl-cellulose (HPMC) and chitosan (CHI), showed similar release profiles to uncoated milled promethazine (PMZ-m), most likely due to the high water solubility of PMZ in addition to agglomeration upon fluidization. Although dissolution results of PLA, PEG600, HPMC, and CHI-coated PMZ compared to uncoated powders appeared relatively similar, sustained release was not a desired property for an inhaled delivery system of this drug since this may reduce to time-of-onset of antinausea effect.

Initial in vivo pharmacokinetics of PMZ were tested with uncoated and coated formulations delivered intratracheally and intravenously. The 1-h bioavailability of CHI-coated PMZ was increased (33%) compared to uncoated PMZ-m powder (25%), while PLA and PEG600-coated PMZ showed reduced absorption in the first several hours near the limits of detection (Fig. 10.15). In addition, the 5-h bioavailability of CHI-coated PMZ further was significantly higher (70%) compared to uncoated milled powder (40%). Although preliminary, this data agrees well with

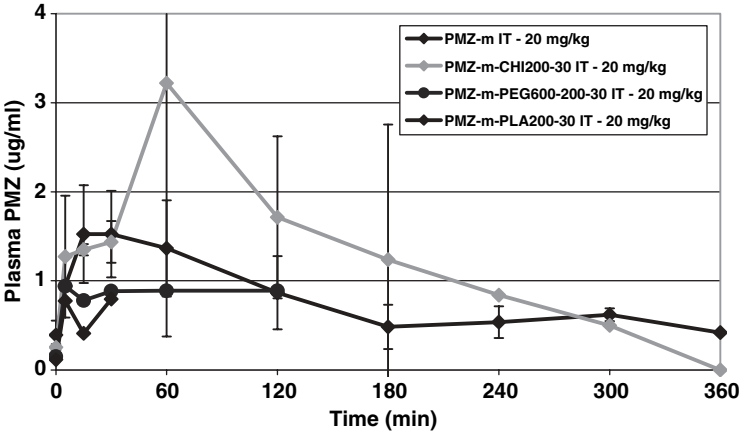

Figure 10.15 A 6-h pharmacokinetic profile of IT administration of uncoated PMZ (◆), PMZ-*m*-CHI200-30 (◆), PMZ-*m*-PEG600-200-30 (●), and PMZ-*m*-PLA200-30 (◆).

published reports of increases in the mucosal absorption of many drugs using chitosan, but not with the extremely small quantities ($<1\%$) delivered using the Nanocoat process.

10.5 MANUFACTURING AND SCALEUP

The Nanocoat microencapsulation process begins with a precursor powder and ends with a final product that is a microencapsulated powder or granule. For each 1- to 40-kg batch, the powder is dry and sufficient batches are scheduled in-line with particle production, milling, or spray-drying. Again, equipment is thoroughly cleaned and validated prior to its reuse for manufacturing different bulk substances.

Manufacturing of a Nanocoat microencapsulated powder may begin from a lyophilized, granulated, spray-dried, or milled powder and may include other ingredients. A typical spray-coater fluidized-bed system with modifications is used for coating powders. An initial drying/deagglomeration step may be used before or during coating using proprietary conditions. The coating chamber is equipped with a blower or fluidization gas input, a jacket for heating and cooling, hookups for charging raw materials and for discharging the microencapsulated powder, control systems for temperature and pressure, a nitrogen supply for padding and purging the reactor, and a sealed port on the side for taking samples and adding bulk and other solid materials. In additional steps the powder may be added to or recirculated during coating, as well as spray-coated with additional materials as a final step for granulation. A flow diagram of a typical coating chamber for microencapsulation and final manufacturing and packaging step for a final dosage form is shown in Figure 10.16.

After coating, microencapsulated powders may then be granulated, wet or dry mixed, or packaged directly into a final dosage form. Typical formulating operations are to convert the microencapsulated powder into a final, usable form, such as a powder blister for inhalation or a tablet for oral administration. Preferably, for enteric-coated capsules, microencapsulated powders would be physically mixed with excipients, dispersing agents, stabilizers, and other materials in a vertical blender and then moved to a hopper for a capsule filler. Final steps, such as applying an enteric coating, would be applied using standard pharmaceutical equipment.

Batch production records are used and describe each manufacturing step in detail. At various stages in the formulation and packaging process, quality control checks are utilized. All raw materials are checked prior to use in a process, and the final dosage forms require a myriad of tests to assure therapeutic benefit. For example, the content uniformity, color, homogeneity, dissolution,

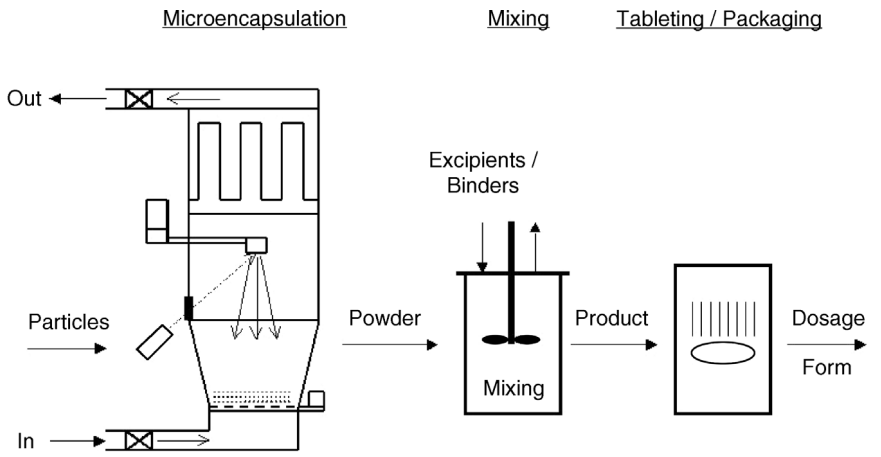

Figure 10.16 Flow diagram for the Nanocoat process.

stability, identity, and potency of the product must be determined and meet stated ranges. Representative samples are collected at the end of the formulation stage and submitted to the chemical and/or microbiological laboratories for final assaying. Representative samples are also collected during packaging operations. The quality control unit of the pharmaceutical manufacturing company has the responsibility and authority to approve or reject all raw materials, in-process materials, packaging materials including containers, closures, and labeling materials, as well as the final product.

10.6 SUMMARY

The suitability of the Nanocoat encapsulation method, more specifically the use of rapid thermal evaporation from a pulsed excimer laser for applying nanometer thick coatings of biodegradable polymers onto dry powders, has been demonstrated. The method has only been previously applied to the synthesis of engineered, nanofunctionalized particulate materials with unique optical, cathodoluminescent, and electrical properties. In general, it has been shown that material can be deposited as nanometric coatings (10–1000 nm) on core particles ranging from submicron to millimeters in size. When the method is applied to coatings of particles in the micron or submicron range, the coating material is generally less than 1% by mass, and coating times are under one hour without the need for drying solvents.

Early studies have demonstrated that it is possible to use PLD for coating of inhaled dry powders in the range of 1–5 μm with PLGA and PLA. The coating material retains its chemical integrity, although a significant reduction in the average molecular weight is observed for both PLD and MAPLE conditions. The generation of low-molecular-weight degradation species did not result in cytotoxicity when measured in vitro in cell culture or detectable toxicity in vivo [Coowanitwong, 2003], most likely due to the extremely low concentration of coating material of the final product.

The most appealing advantage of this technology is the possibility of applying ultrathin coatings onto dry powders without the necessity of wet chemistry. While the presented work concentrated on PLGA and PLA, additional unpublished studies have indicated the general suitability of this method to deposit a number of biomedically relevant materials. The exact assessment of the applied coating thickness is, so far, hampered by the lack of suitable analytical techniques. There is, however, evidence for the nanometer thickness of the coatings on particles. Individual droplets of PLGA deposited onto silica wafers and smooth silica particles 100 nm or less have been observed using SEM. In addition, SEMs of particles did not show any size difference between coated and uncoated

budesonide. In addition, HPLC analysis of dissolved coated and uncoated budesonide was unable to show a difference in the budesonide content between the two preparations (data not shown). Using the information of these experiments it seems safe to say that the polymer content is smaller than 1% of the net weight of the preparations, while still producing marked sustained-release profiles.

Limited cell culture work performed in macrophage cell lines so far indicated no sign of toxicity of the material, which would be expected considering the low polymer-to-drug ratio. Laser energy could potentially induce chemical reactions and the toxicity by laser-induced degradation products cannot necessarily be excluded. The lack of cell toxicity over that seen with uncoated material, even at extremely high concentrations ($>100\,\mu g/mL$) employed in these assays, in conjunction with preliminary NMR and size exclusion chromatography work, seems to suggest that possible breakdown products of PLGA particles with lower molecular weights are similar in chemical nature and nontoxic.

Most importantly, the modulation in surface properties translated into a significant increase in pulmonary targeting, quite in agreement with the prior findings on reduced dissolution rate of the investigated particles. Compared to other technologies for sustained pulmonary targeting, this technique has the advantage of reduced polymer load, high flexibility in usable polymers, and direct applicability for dry powder technologies. The method has the potential for a wide variety of pharmaceutical applications, ranging from coatings to improved agglomeration and flowability, stability, cell uptake and interactions, as well as controlling the release rate of the drug. The technique seems to be suitable not only for pulmonary delivery but also a variety of other local or systemic forms of administration.

Acknowledgments

Partial financial support for this work was provided by the National Science Foundation through grant No. DMII-042263 and NASA contract No. NAS9-00121.

REFERENCES

Atala, A., and Mooney, D. J. (1997), in *Synthetic Biodegradeable Polymer Scaffolds*, J. P. Vacanti and R. Langer (Eds.), Birkhauser, Boston, MA.

Bell, A. T. (1980), *Top. Curr. Chem*. **94**, 43.

Biederman, H. (2000), *J. Vac. Sci. Technol. A*. **18**(4), 1642–1648.

Blanchet, G. B. (1996), *Chemtech* **26**, 31–35.

Blanchet, G. B., and Fincher, J. C. R. (1993), *Science* **262**, 719–721.

Bopp, M. A., Tarrach, G., Lieb, M. A., and Meixner, A. J. (1997), *J. Vac. Sci. Technol. A* **15**(3), 1423–1426.

Bubb, D. M., Wu, P. K., Horwitz, J. S., Callahan, J. H., Galicia, M., Vertes, A., McGill, R. A., Houser, E. J., Ringeisen, B. R., and Chrisey, D. B. (2002a), *J. Appl. Phys. A* **91**(4), 2055–2059.

Bubb, D. M., Toftmann, B., Haglund, Jr., R. F., Horwitz, J. S., Papantonakis, M. R., McGill, R. A., Wu, P. K., and Chrisey, D. B. (2002b), *Appl. Phys. A: Mat. Sci. Proc*. **74**(1), 123–125.

Cheung, J. T., and Sankur, H. (1988), *CRC Crit. Rev. Solid State Mater. Sci.* **15**(1), 63–109.

Chrisey, D. B., and Horwitz, J. S. (1991), *Thin Solid Films* **206**, 111–115.

Coowanitwong, I. (1983), "Characterization of Sustained-Release Formulation of Inhaled Rifampin for Tuberculosis Therapy/by Intira Coowanitwong," Ph.D. Thesis, University of Florida College of Pharmacy.

Cui, X., Hetke, J., Wiler, J. A., Anderson, D. J., and Martin, D. C. (2001), *Sensors and Actuators A* **93**, 8–18.

D'Almeida, K., Bernede, J. C., Ragot, F., Godoy, A., Diaz, F. R., and Lefrant, S. (2001), *J. Appl. Polym. Sci.* **82**(8), 2042–2055.

Derendorf, H., Hochhaus, G., Rohatagi, S., Mollmann, H., Barth, J., Sourgens, H., and Erdmann M. (1995), *J. Clin. Pharmacol.* **35**(3), 302-305.

Dreisewerd, K. (2003), *Chem. Rev.* **103**, 395–425.

Dyer, P. E., and Karnakis, D. M. (1994), *Appl. Phys. Lett*., **64**(11), 1344–1346.

Favia, P., and d'Agostino, R. (1998), *Surf. Coat. Technol*.**98**, 1102.

Fitz-Gerald, J. M., and Singh, R. K. (1998), *Mater. Res. Soc. Proc.* **501**, 363–368.

Fitz-Gerald, J. M., Trottier, T. A., Holloway, P. H., and Singh, R. K. (1998), *Appl. Phys. Lett*. **72**(15), 1838–1839.

Fitz-Gerald, J. M., Rack, P. D., Trottier, T. A., Ollinger, M., Pennycook, S. J., Gao, H., and Singh, R. K. (1999a), *J. Appl. Phys*. **86**(3), 1759–1761.

Fitz-Gerald, J. M., Singh, R. K., Gao, H., Wright, D., Ollinger, M., Marcinka, J. W., and Pennycook, S. (1999b), *J. Mater. Res*., **14**, 3281.

Fu, J., Fiegel, J., Krauland, E., and Hanes, J. (2002), *Biomaterials* **23**(22), 4425–4433.

Gao, H., Yan, Y., Fitz Gerald, J. M., Kumar, D., Singh, R. K., and Pennycook, S. J. (1998), *Microsc. Microanal.*, **4**, 756.

Gengenbach, T. R., and Griesser, H. J. (1998)., *J. Polym. Sci.* **36**, 985–1000.

Geohegan, D. B., and Puretzky, A. A. (1999), *Appl. Phys. Lett*. **67**(2), 197–199.

Heeger, A. J., Kivelson, S., Schrieffer, J. R., and Su, W. P. (1988), *Rev. Mod. Phys.* **60**, 781–850.

Hishmeh, G. H., Barr, T. I., Skylarov, A., and Hardcastle, S. (1996), *J. Vac. Sci. Technol. A*. **14**(3), 1330–1338.

Hrkach, J. S., and Langer, R. (1996), *Biomaterials* **18**(1), 27–30.

Inagaki, N., and Makino, M. (1997), *J. Appl. Polymer Sci.* **64**(6), 1031–1039.

Kiesow, A., and Heilmann, A. (1999), *Thin Solid Films* **344**, 338–341.

Lacasse, F. X., Filion, M. C., Phillips, N. C., Escher, E., McMullen, J. N., and Hildgen, P. (1998), *Pharm. Res.* **15**(2), 312–317.

Lee, T. M., and Mittler-Neher, S. (1992), *Opt. Mater.* **1**, 65.

Li, Z. F., Yang, Z. Y., and Xiao R.F (1996), *J. Appl. Phys*. **80**(9), 5398–5403.

Li, Y. P., Zhang, X. Y., Gu, Z. H., Zhou, Z. H., Yuan, W. F., Zhou, J. J., Zhu, J. H., and Gao, X. J. (2001), *J. Controlled Release* **71**, 203–211.

Lowndes, D. H., and Geohegan, D. B. (1996), *Science* **273**, 898–903.

Lutsiak, M. E., Robinson, D. R., Coester, C., Kwon, G. S., and Samuel, J. (2002), *J. Pharm. Res.* **19**(10), 1480–1487.

McGill, R. A., and Chrisey, D. B. (1999), *MAPLE Patent, Navy Case* No. 78,117.

Newman, K. D., Elamanchili, P., Kwon, G. S., and Samuel, J. (2002), *J. Biomed. Mater. Res*. **60**(3), 480–486.

Sakurai, S., Furukawa, C., Okutsu, A., Miyoshi, A., and Nomura, S. (2002), *Polymer* **43**(11), 3359–3364.

Shi, F. F. (1996), *Surf. Coat. Technol*. **82**, 1.

Singh, R. K., and Biunno, N. (1988), *Appl. Phys. Lett*. **53**(11), 1013–1015.

Singh, R. K., Ata, A., Fitz-Gerald, J. M., Rabinovich, Y., and Hendrickson, W. (1997), *KONA, J. Powder Sci. Technol.*, **15**, 121–131.

Skotheim, T. A., Elsenbaumer, R. L., and Reynolds, J. R. (Eds.) (1996), *Handbook of Conducting Polymers*, 2nd ed., Marcel Dekker, New York.

Skrobis, K., Denton, D. D., and Skrobis, A. (1990), *Polym. Eng. Sci.* **30**(3), 193–196.

Sowa, M. J., Pohray, V., and Cecchi, J. L. (2000), *J. Vac. Sci. Technol. A*. **18**(5), 2122–2129.

Talton, J. D. (1999), "Pulmonary Targeting of Inhaled Glucocorticoid Dry Powders," Ph.D. Thesis, University of Florida College of Pharmacy.

Talton, J. D., Fitz-Gerald, J. M., Singh, R., and Hochhaus, G. (1999), "Pulmonary Targeting of Poly(lactic-co-glycolic acid) Coated Budesonide Dry Powders vs. Uncoated Powders Using an Ex Vivo Receptor Binding Assay in Rats," Poster, National AAPS Conference, pp. 67–74.

Wu, W. L., and Wallace, W. E. (1998), *J. Vac. Sci. Technol. B* **16**(4), 1958–1963.

Young, T. H., Huang, Y. H., and Chen, L. Y. (2000), *J. Membr. Sci.* **164**(1), 111–120.

Zhigilei, L., Leveugle, E., Garrison, B. J., Yingling, Y. G., and Zeifman, M. (2003), *Chem. Rev.* **103**, 321–348.

CHAPTER 11

Transparent Conducting Oxide Films

HEUNGSOO KIM

Naval Research Laboratory, Code 6364, Washington, D.C.

11.1 INTRODUCTION

Transparent conducting oxide (TCO) films have been used extensively in the optoelectronics industry because they exhibit high electrical conductivity, high optical transmittance in the visible region, and high reflectance in the infrared (IR) region. Since the first report of TCO growth by Bädeker [1907], who prepared cadmium oxide (CdO) thin films grown by the thermal oxidation of sputtered cadmium, TCO films have been widely utilized as an essential part of many optoelectronic devices: transparent electrodes in flat-panel displays and solar cells; transparent heating elements for automobile and aircraft windows; and transparent heat reflecting window material for buildings, lamps, solar collectors, gas sensors, and antireflection coatings.

A large number of TCO materials have been investigated over the years such as In_2O_3, SnO_2, ZnO, and CdO as well as their doped oxides. Although most research on TCO materials has been focused on the above oxides, there have been some efforts on making multicomponent oxides to improve the electrical conductivity and optical transparency of the films, such as Ga_2O_3–In_2O_3, In_2O_3–ZnO, In_2O_3–SnO_2, ZnO–SnO_2, In_2O_3–$MgIn_2O_4$, $MgIn_2O_4$–$Zn_2In_2O_5$, $ZnSnO_3$–$ZnIn_2O_5$, and $ZnIn_2O_5$–$GaInO_3$ [Minami, 1999]. All of the TCO materials mentioned above are *n*-type semiconductors. However, there have been some efforts on developing *p*-type TCO films, such as $CuAlO_2$ [Yanagi et al., 2000], $CuGaO_2$ [Kawazoe et al., 1997], $SrCu_2O_2$ [Kudo et al., 1998], and N-doped ZnO [Joseph et al., 1999; Guo et al., 2001]. Of all the TCO films, the most widely used TCO for optoelectronic device application is indium tin oxide (ITO). Other TCOs are available for specific applications, and, for example, SnO_2 films are in practical use for architectural glass applications. Impurity-doped ZnO films have also attracted much attention as the transparent electrode in many device applications because they are nontoxic and inexpensive and have comparable electrical and optical properties to ITO.

There are several comprehensive reviews on the deposition of TCO films. Holland [1958] reviewed the early work up to 1955. Vossen [1977] and Haacke [1977] reported comprehensive reviews to the mid-1970s. Manifacier [1982], Jarzebski [1982], and Chopra et al. [1983] covered the work in this area up to the early 1980s. Hamberg and Granqvist [1986] reported detailed experimental work on indium tin oxide films. Hartnagel et al. [1995] presented comprehensive reviews on the growth techniques, properties, and applications of TCOs. More recently, some of the critical issues related to new TCO materials, such as processing and criteria for applications

Pulsed Laser Deposition of Thin Films: Applications-Led Growth of Functional Materials
Edited by Robert Eason

and theoretical models, have been addressed in MRS Bulletin [2000]. Even though the above reviewers reported various growth techniques for TCO films, the pulsed laser deposition (PLD) technique for the deposition of TCO materials has not been reviewed in detail by the above reviewers. The objective of this chapter is to review the unique properties of TCO films, to examine structural, electrical, and optical properties of TCO films grown by PLD on various substrates (glass, plastic, single crystal), and to demonstrate some of the applications of TCO films grown by PLD.

11.2 UNIQUE PROPERTIES OF TCO FILMS

11.2.1 Electrical Properties

Electrical resistivity (ρ) of TCO films depends on the carrier concentration (N) and carrier mobility (μ) as follows: $\rho = 1/(Ne\mu)$, where e is the electron charge. Since e is a constant, to achieve lower resistivity of the films, the carrier concentration (N) and carrier mobility (μ) should be simultaneously maximized, and the maximum carrier concentration can be achieved by oxygen vacancies and doping.

If an oxygen vacancy is created in a perfect crystal, two electrons are created in the crystal and contribute to the electrical conduction as ionized donors. However, the creation of too many oxygen vacancies forms suboxides: for example, in a SnO_2 film, if too many oxygen vacancies are created, SnO will be formed. In addition to the oxygen vacancies, doping also changes the electrical conduction of TCOs. If host cations are substituted by elements with a valence higher than that of the host, the extra electrons can become conduction electrons. To preserve the charge neutrality, substitution of a higher valence element for a host cation creates extra electrons. For example, if Sn is substitutionally incorporated in In_2O_3, an extra electron is created in the lattice. Effective substitutional doping can be achieved by selecting a dopant of the same size as or smaller than the host ion being replaced and by assuming that no compounds of the dopant oxide are formed. It is also possible to improve the electrical conduction by anionic doping. If anion (i.e., oxygen) sites are substituted with lower valence anions such as chlorine or fluorine, this also creates conduction electrons.

The majority of research designed to decrease the resistivity of the TCO material has focused on increasing the free carrier concentration in the thin-film material through the use of dopants and oxygen vacancies. However, increasing the carrier density via doping or oxygen vacancies is self-limiting because at some point the increased number of free carriers decreases the mobility of the film due to carrier–carrier scattering. Hence, there is a trade-off between the carrier density and the carrier mobility for achieving low resistivity. In general, for a completely degenerate material, the relationship between the carrier density and carrier mobility can be expressed by $\mu \propto n^{-2/3}$ [Johnson and Lark-Horovitz, 1947].

11.2.2 Optical Properties

The TCO films act as a selective transmitting layer. They are only transparent in the visible and near-infrared range between wavelengths of about 0.4 and 1.6 μm. For very short wavelengths ($\lambda < 0.4\,\mu m$) absorption is observed due to the fundamental energy gap, and for long wavelengths ($\lambda > 1.6\,\mu m$) high reflection occurs due to the plasma absorption edge. Both the fundamental bandgap and plasma absorption depend on the carrier density and the effective mass, which can be controlled by deposition conditions such as doping level, substrate deposition temperature, oxygen deposition pressure, and film thickness. In general, both edges shift toward lower wavelengths (higher energies) with increasing carrier density of the TCO film [Kim et al., 1999b].

The transmittance and reflectance data can be used to calculate absorption coefficients of the films at different wavelengths. The absorption coefficient, α, is given by the relation [Chopra et al., 1983]

$$\alpha = \frac{1}{t} \ln \left[\frac{(1-R)^2}{T} \right] \tag{11.1}$$

where t is the film thickness. The absorption coefficient data can be used to determine the bandgap, E_g, using the relation [Tauc et al., 1966]

$$\alpha h\nu \approx (h\nu - E_g)^{1/2} \tag{11.2}$$

where $h\nu$ is the photon energy.

11.3 ADVANTAGES OF PLD FOR TCO FILMS

As the sophistication of devices based on TCO materials increases, improved electrical and optical properties of the TCO films are required. Hence, many thin-film deposition techniques have been utilized to improve the electrical and optical properties of these films, and the deposition parameters play an important role in controlling these. These techniques include vacuum evaporation, sputtering, chemical vapor deposition, and spray pyrolysis [Hartnagel et al., 1995]. However, these techniques require either a high substrate temperature during deposition (300–500°C) or a postdeposition anneal of the films at high temperature (400–700°C). These high-temperature treatments generally damage surfaces of both the substrate and the film. There have been some efforts to produce high-quality films at low substrate temperature using sputtering and electron beam evaporation, which often result in amorphous films with poor electrical properties.

Pulsed laser deposition has been utilized to grow high-performance TCO films, and PLD provides several advantages compared to other techniques. The composition of the films grown by PLD is quite close to that of the target, even for a multicomponent target. PLD films crystallize at lower substrate temperatures relative to other physical vapor deposition (PVD) techniques due to the high kinetic energies (>1 eV) of the ejected atoms and ionized species in the laser-produced plasma [Chrisey and Hubler, 1994]. Due to the low crystallization temperature, PLD can be used to grow TCO films especially on plastic substrates, which is essential for fabrication of flexible flat-panel displays. Adurodija et al. [2000] reported that crystalline, low resistivity, and highly transparent films have been prepared from In_2O_3 and ITO targets at a low substrate deposition temperature (T_s) of 100°C using PLD coupled with in situ pulsed laser irradiation. The films deposited at room temperature yielded a low resistivity of $\sim 2 \times 10^{-4}$ Ω-cm even though they were amorphous. The lowest resistivity of 9.4×10^{-5} Ω-cm was achieved at 300°C [Adurodija et al., 2000].

Another advantage of PLD for the growth of TCO films is an extremely smooth film surface compared to films grown by other physical vapor deposition techniques. Suzuki et al. [2001] reported the production of ITO films with low resistivity and flat surface morphology using a magnetic field applied perpendicular to the plume produced by PLD. Magnetic fields act on charged particles in laser-produced plumes and affect the ionization of species such as atoms and molecules, thereby increasing plasma density [Tachiki and Kobayashi, 1999]. Suzuki et al. [2001] showed that the ITO films (30 nm thick) grown at 300°C showed the lowest resistivity of 7.2×10^{-5} Ω-cm and a visible transmittance of more than 90% as well as having very smooth film surfaces with an average surface roughness of 6.1 Å. Kim et al. [1999a] also showed that the root mean square (rms) surface roughness of 4.5 Å was achieved for ITO films grown by PLD (KrF, 248 nm) on glass at 300°C, which is one order of magnitude smaller than that (40 Å) of commercial ITO deposited by sputtering (see Fig. 11.1).

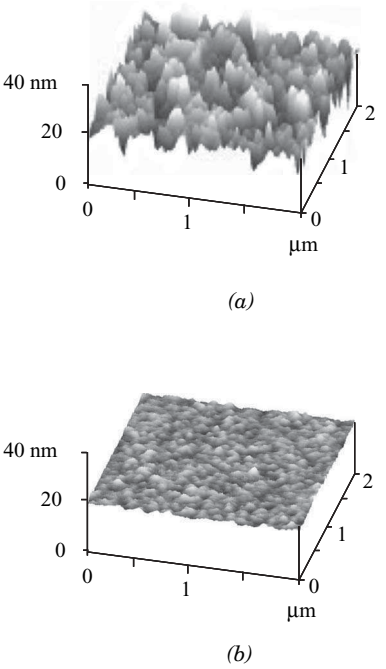

Figure 11.1 AFM images (2 μm × μm) of the ITO films grown on glass substrates by (a) sputtering (supplied by Planar America) and (b) PLD (KrF: 248 nm). Note that the scale in the z direction (20 nm/div.) is greatly expanded with respect to the scales in the x and y directions (1.0 μm/div.) and, therefore, in fact, the crystallites are flat and broad in the lateral direction [Kim et al., 1999a].

11.4 OPTIMUM PLD CONDITIONS FOR TCO FILMS

The substrate temperature and oxygen background gas pressure are typical deposition conditions that can be easily controlled during deposition to obtain ITO films with high electrical conductivity and optical transparency. Other PLD parameters that are under experimental control are film thickness, laser fluence, and target-to-substrate distance.

11.4.1 Substrate Deposition Temperature

Substrate deposition temperature is an important PLD parameter. The conductivity of the ITO films increases as the substrate deposition temperature is increased from room temperature to $\sim 300^{\circ}$C [Kim et al., 1999b, 1999c]. The increase in conductivity with an increase in the substrate deposition temperature can be explained by the fact that the grain size increases significantly with increasing growth temperature, thus reducing the grain boundary scattering and increasing the conductivity. It is also observed that the optical transmittance (T) in the visible range (400–700 nm) increases slightly with increasing the substrate temperature from room temperature to $\sim 300^{\circ}$C, and this again is related to the increase in grain size of the films with increasing substrate temperature. The magnitude of the change in electrical and optical properties of ITO films with varying substrate deposition temperature may also depend on the other deposition conditions such as target composition, oxygen partial pressure, fluence, and target-to-substrate distance.

The substrate deposition temperature also affects other properties of the film such as the direct bandgap and the plasma wavelength. The direct bandgap of the ITO films increases from 3.89 to 4.21 eV as the substrate deposition temperature increases from room temperature to 300°C [Kim

et al., 1999b]. This shift of the bandgap can be explained by the Burstein–Moss effect [Burstein, 1954; Moss, 1964] in which the absorption edge shifts toward higher energy with an increase of carrier concentration. The plasma wavelength (or cut-off wavelength, λ_p), which is defined as Transmittance = Reflectance, where the dielectric-like transmission equals the metallic-like IR reflectance, is observed to initially decrease with increasing substrate deposition temperature up to 100°C and then slightly increase up to 300°C [Kim et al., 1999b].

11.4.2 Oxygen Deposition Pressure

The oxygen deposition pressure also affects the electrical and optical properties of the TCO films. The conductivity of the ITO films deposited at room temperature is very sensitive to oxygen pressure [Zheng and Kwok, 1993; Kim et al., 1999c]. High-conductivity ITO films are obtained only between 5 and 15 mTorr of oxygen. However, the conductivity of the ITO films deposited at 300°C is less dependent on the oxygen pressure. The increase in the conductivity with a decrease in oxygen pressure from 50 to 10 mTorr can be explained by the number of oxygen vacancies in the ITO films. Decreasing the oxygen pressure increases the number of oxygen vacancies in the film and thus increases the carrier concentration and the film conductivity. However, this increase in carrier concentration also leads to a decrease in the optical transmittance due to an increase in free carrier absorption. Figure 11.2 shows this inverse relationship between the conductivity and transmittance of the ITO films. The optical transmittance in the visible range increases with an increase of oxygen pressure from 10 to 50 mTorr for the ITO films grown at both 25 and 300°C. This is related to the improvement of the film crystallinity with increasing oxygen pressure since the width of the (222) X-ray diffraction (XRD) peak decreased while the intensity of the (222) peak increased with increasing oxygen pressure. For higher temperature growth the optimal oxygen pressure slightly shifts to lower pressure. However, the optimum oxygen deposition pressure for low-resistivity ITO films shifts from 10 to 40 mTorr as the target-to-substrate distance increases from 4.3 to 5.8 cm.

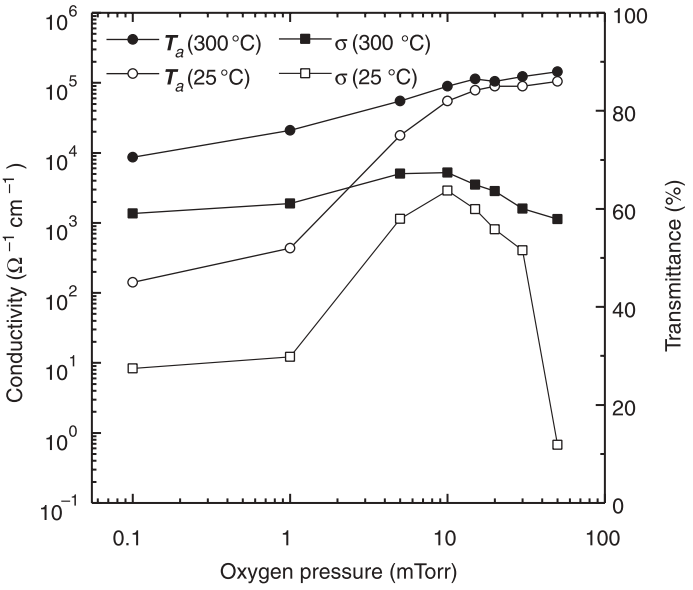

Figure 11.2 Variation of electrical conductivity (σ) and average optical transmittance (T_a) as a function of oxygen pressure for the ITO films grown by PLD at 25 and 300°C. Film thickness was about 200 nm for all films. All transmittance values were determined as an average in the visible range from 400 to 700 nm. ■ (σ, 300°C); □ (σ, 25°C); ● (T_a, 300°C); ○ (T_a, 25°C) [Kim et al., 1999c].

Wu et al. [1999] reported that the optimum films grown at room temperature are significantly oxygen rich; the ratio of $O/(In + Sn)$ is ~ 1.62 compared to that (~ 1.5) of the films grown at high temperature.

The sensitivity to variation of the oxygen partial pressure at room temperature can be explained by the nature of PLD [Zheng and Kwok, 1993]. They have observed from an optical time-of-flight study that laser-generated atoms and ions travel toward the substrate with a time duration of $\sim 10\,\mu s$ and peak velocities of $\sim 10^6$ cm/s. At too low oxygen pressures, the density of various species is not uniform on the surface of the substrate because of the different velocity for each species. This situation creates defect centers in the film, which increases the film resistivity. However, if the oxygen pressure is too high, the velocities of various species in the laser-generated plume will be slowed down due to the collisions with the oxygen molecules, and then the surface activation of the species will not be possible. Therefore, at the optimal oxygen pressure, the uniform velocity distribution of various species can be achieved, leading to a reduction in the density of defect centers in the film, which decreases the film resistivity.

The oxygen pressure also affects the direct bandgap and the plasma wavelength of ITO films. The direct bandgap of the ITO films decreases from 4.14 to 3.63 eV as the oxygen pressure increases from 1 to 50 mTorr. This decrease in the direct bandgap with an increase in oxygen pressure is due to a decrease in carrier concentration. This is also explained by the Burstein–Moss shift [Burstein, 1954; Moss, 1964], which is related to the carrier concentration of the film. The plasma wavelength of the ITO films increases from 1380 to 3100 nm with increasing oxygen pressure from 1 to 50 mTorr [Kim et al., 1999c].

11.4.3 Film Thickness

Film thickness is also an important factor to control the properties of ITO films, and film thickness is directly proportional to the number of laser shots. For thinner films (< 100 nm thick), the effect of surface scattering on the charge carriers becomes more important than the grain boundary scattering (Holmelund et al., 2002; Kim et al., 2000a). The resistivity of the ITO films initially decreases with an increase in the film thickness up to 220 nm and remains almost constant with further increases in the film thickness up to 870 nm [Kim et al., 2000a]. It has been reported that the carrier density increases with an increase in the film thickness up to 220 nm and then remains almost constant with further increases in the film thickness up to 870 nm, and the Hall mobility increases with increasing film thickness. XRD measurements indicate that the thicker films are more crystalline and have larger grains than thinner films; the 220-nm-thick film has an average grain size of 20 nm and the 870-nm-thick film has an average grain size of 26 nm. Thus, the initial decrease in resistivity is due to an increase in both carrier density and carrier mobility of the films. For thicker films (> 300 nm), the resistivity remains constant because both carrier density and carrier mobility become independent of film thickness [Kim et al., 2000a].

11.4.4 Other Laser Conditions

The laser wavelength also affects the properties of TCO films since the light absorption in the target is much stronger at shorter wavelengths. In general, excimer lasers, such as ArF (193 nm) [Zheng and Kwok, 1993], KrF (248 nm) [Kim et al., 1999b], and XeCl (308 nm) [Hiramatsu et al., 1998], have been utilized to produce the majority of TCO films grown by PLD. However, solid-state lasers, such as frequency-tripled Nd : YAG (355 nm) can also be used for the growth of TCO films [Holmelund et al., 2002]. Even though the absorption of the laser light at the wavelength of 355 nm is much smaller than that from excimer lasers, reasonable resistivity values ($2-3 \times 10^{-4}$ Ω-cm) are achieved for the ITO films grown by the solid-state laser (355 nm), which are comparable to those ($1-2 \times 10^{-4}$ Ω-cm) for the ITO films grown by excimer lasers.

Deposition rate can be controlled by many parameters such as laser fluence, oxygen partial pressure, and target-to-substrate distance. The deposition rate increases with increasing fluence,

TABLE 11.1 PLD Conditions of ITO Thin Films

Target	5 wt % SnO_2 + 95 wt % In_2O_3
Ratio of Sn/In (film)	0.048 ± 0.005
Substrate	Glass, quartz
Laser repetition frequency (Hz)	10
Laser fluence (J/cm^2)	1–2
Target-to-substrate distance (mm)	48
Oxygen partial pressure (mTorr)	10 (1.3 Pa)
Substrate temperature (°C)	250
Electrical resistivity (Ω cm)	$\sim 2 \times 10^{-4}$
Carrier density (cm^{-3})	1.2×10^{21}
Hall mobility (cm^2 V^{-1} s^{-1})	28

From Kim et al. [1999b].

decreasing oxygen partial pressure, and decreasing the target-to-substrate distance, and is linearly proportional to the laser fluence. The effect of the laser fluence on the ablation depth of an ITO target in vacuum at 248 nm has been analyzed by Coutal et al. [1996]; the threshold laser energy for ablation was 0.3 J/cm^2, and the deposition rate linearly increases with increasing laser fluence up to 1 J/cm^2, followed by a slight increase up to 2 J/cm^2. The laser fluence also affects the properties of ITO films. Low-resistivity films can be obtained at high fluence because the ejected species created at high fluence are much more energetic and can traverse the background gas to the substrate for crystalline film growth. Typical deposition conditions for ITO films are summarized in Table 11.1.

11.5 LASER-DEPOSITED TCO FILMS

High-quality thin films of many TCOs have been deposited by PLD. A large portion of the research has focused on ITO thin films for many optoelectronic or electrooptic device applications. Other TCO films grown by PLD include Al-, Ga-, Zr-, and Sn-doped ZnO [Kim et al., 2002b, 2003], Zr-doped In_2O_3 [Kim et al., 2001a], Zr-doped SnO_2 [Qadri et al., 2000], Sb-doped SnO_2 [Kim and Piqué, 2004], $Zn_xIn_yO_z$ [Phillips et al., 1995], $GaInO_3$ [Phillips et al., 1994], and In_2O_3–Sc_2O_3 [Qadri et al., 2002]. Recently, PLD has been also used to grow *p*-type TCO films for *p-n* heterojunction device applications.

11.5.1 ITO Films

11.5.1.1 ITO Films on Glass Substrates

Indium tin oxide thin films retain the crystal structure of bulk-undoped In_2O_3. In_2O_3 has the cubic bixbyte structure (also called c-type rare-earth oxide structure) and belongs to the space group [cI80 (Mn_2O_3), Ia3 (206); JCPDS (Joint Committee on Powder Diffraction Standards) Card No.: 06-0416]. The unit cell of In_2O_3 with a lattice constant of 10.118 Å contains 80 atoms (JCPDS Card No.: 06-0416). However, the lattice parameters of ITO films are nominally larger than the 10.118 Å value for In_2O_3 powder. This increase in lattice constants of the ITO films can be explained by the substitutional incorporation of Sn^{2+} ions into In^{3+} sites and/or the incorporation of Sn ions in the interstitial positions. Since the radius of Sn^{2+} ions (0.93 Å) is larger than that of In^{3+} (0.79 Å), the substitution of Sn^{2+} for In^{3+} may result in a lattice expansion [Wu et al., 1994]. This increase in lattice constant may be also related to oxygen deficiency and strain effects due to thermal expansion coefficient mismatch between the film ($7.2 \times 10^{-6}/^{\circ}C$) and glass substrate ($4.6 \times 10^{-6}/^{\circ}C$). The increase in lattice parameter is found to depend on the deposition conditions, the lattice parameter

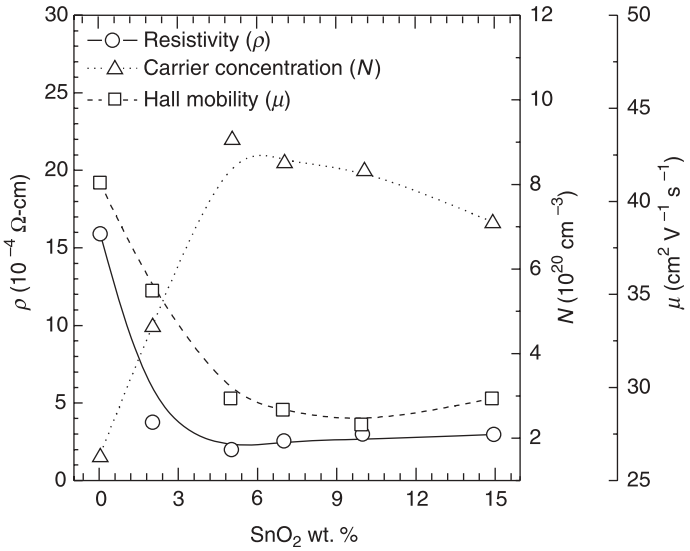

Figure 11.3 Dependence of resistivity, carrier concentration, and Hall mobility on SnO_2 content for the deposited ITO films. The substrate deposition temperature was kept at 250°C and the oxygen pressure was 10 mTorr during deposition [Kim et al., 1999b].

increasing with increasing substrate deposition temperature and decreasing with increasing oxygen deposition pressure. Moreover, tin doping changes the grain size of the films. The width of the (222) peak is slightly larger as a result of tin doping, indicating that the grain size of the films became smaller. The calculated grain size of the undoped (0 wt %) and tin-doped (10 wt %) films was ~ 30 nm and ~ 20 nm, respectively [Kim et al., 1999b].

The electrical properties of ITO films strongly depend on the doping concentration in the film. The results in Figure 11.3 show that 5 wt % of SnO_2 is the optimal doping level in the target for obtaining high-conductivity ITO films [Kim et al., 1999b]. For the case of undoped In_2O_3 films, the carrier density and resistivity were 1.5×10^{20} cm^{-3} and 1.6×10^{-3} Ω-cm, respectively. The resistivity of the ITO films was observed to initially decrease with increasing SnO_2 content up to 5 wt %. It was also observed that the carrier density increased with increasing SnO_2 content up to 5 wt%. This initial increase in carrier density resulted in a decrease in the resistivity as a result of the donor electrons from the Sn dopant [Manifacier, 1982]. However, the resistivity of the films, after reaching a minimum (at 5 wt % of SnO_2), gradually increased with a further increase in the SnO_2 content up to 15 wt %. This is due to an increase in the concentration of the electron traps as a result of excess Sn doping. Above the critical Sn content (corresponding to about 5 wt % of SnO_2), excess Sn atoms may occupy interstitial positions and some Sn atoms may also form defects such as Sn_2O, Sn_2O_4, and SnO, which act as carrier traps rather than electron donors [Hartnagel et al., 1995]. The decrease in carrier density and increase in resistivity beyond 5 wt % of SnO_2 is due to increased disorder of the crystal lattice, which causes phonon scattering and ionized impurity scattering and results in a decrease in mobility [Mizuhashi, 1980]. Manifacier [1982] also suggested that for the ITO films with higher doping levels, the increase in resistivity is due to an increase in disorder, which decreases the mobility and free carrier density. It is further seen from Figure 11.3 that Hall mobility decreases with increasing SnO_2. The decrease in mobility with increase in Sn dopant level was caused by ionized impurity scattering. The optimum SnO_2 content in the ITO target (for minimum resistivity film) was 5 wt %. X-ray photoelectron spectroscopy (XPS) measurements indicated that the Sn/In ratio (~ 0.048) of ITO films is similar to that (~ 0.050) of the target [Kim et al, 1999b].

11.5.1.2 ITO Films on Flexible Plastic Substrates

Although ITO films deposited on rigid glass substrates have been widely used as transparent conducting electrodes, in many optoelectronic and electrooptic devices, glass substrates are unsuitable for certain applications such as electronic maps, smart cards, and portable computers where flexibility, weight, and/or safety issues are important. Glass is very brittle, cannot be easily deformed, and is too heavy, especially for large-area displays. These disadvantages can be overcome using flexible substrates, which are robust, light-weight, and cost effective, and for these reasons, flexible plastic substrates have been used for TCO film growth. Optically transparent plastics with high glass transition temperatures are desired for many optoelectronic devices. In addition, they need to withstand the growth conditions of metal oxides while maintaining their mechanical and optical properties. Polyethylene terephthalate (PET) has been widely used as a substrate material for the growth of transparent conducting oxide thin films, and a resistivity of 1000 μΩ-cm was reported by Minami et al. [1995] for ITO films grown by direct current (DC) magnetron sputtering on PET followed by annealing at 150°C for 100 h. Ma et al. [1997] obtained a resistivity of 700 μΩ-cm for ITO films deposited on PET at a substrate temperature of 180°C using reactive evaporation. Kulkarni et al. [1998] reported a resistivity of 1250–2500 μΩ-cm for ITO films coated on PET using radio frequency (RF) sputtering.

Since the films grown by PLD can be crystallized at low temperature, TCO films grown by PLD on plastic substrates yield much lower resistivities compared to the films grown by other techniques at low temperatures. Kim et al. [2001b] have reported a study of the electrical, optical, and structural properties of ITO films deposited by PLD on flexible PET substrates as a function of substrate temperature and oxygen deposition pressure. They have deposited ITO films on PET substrates at low temperatures (25–120°C) using a KrF excimer laser (Lambda Physics LPX 305, 248 nm, and pulse duration of 30 ns). Figure 11.4 shows a plot of the ITO electrical resistivity as a function of oxygen partial pressure (P_{O_2}) during deposition for films grown on PET substrates held at two different temperatures, T_s (25 and 100°C). It is clear that the ITO resistivity is very sensitive to the oxygen partial pressure. This oxygen pressure dependence behavior is very similar to ITO films grown on glass substrates. Low values of film resistivity can be obtained only over a small range of oxygen pressures between 40 and 45 mTorr. Resistivity values of 7×10^{-4} Ω-cm and 4.1×10^{-4} Ω-cm were reproducibly obtained for ITO films deposited at 25 and 100°C, respectively. It was also reported that ITO films grown by PLD ($T_s = 125$°C and $P_{O_2} = 40$ mTorr) on PET substrates are partially crystalline as determined by XRD [Kim et al., 2001b].

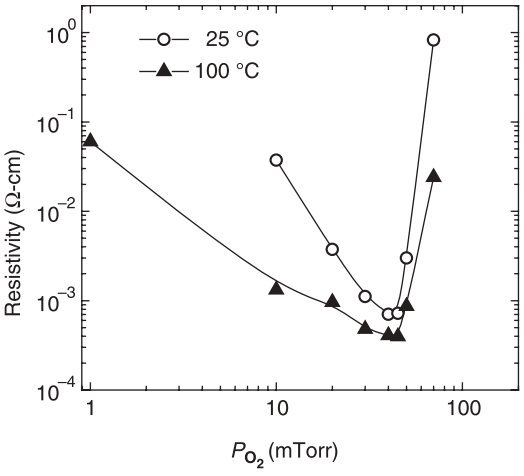

Figure 11.4 Resistivity versus oxygen partial pressure during deposition for films deposited on PET substrates held at two different temperatures (25 and 100°C). The film thickness is about ~200 nm. [Kim et al., 2001b].

11.5.1.3 Highly Oriented ITO Films

To reduce the resistivity of ITO films by improving carrier mobility, PLD has been used to grow highly oriented ITO thin films on single-crystal substrates such as yttria-stabilized zirconia (YSZ) and MgO. It is worthwhile to compare the crystal quality of heteroepitaxial films deposited on single-crystal substrates with that of randomly oriented polycrystalline films deposited on amorphous glass substrates because this comparison can be used to clarify the conduction mechanism of ITO films. It is important that a proper lattice and thermal match exists between the film and the substrate as this is essential for such a heteroepitaxial growth. Tarsa et al. [1993] reported a resistivity of 5×10^{-4} Ω-cm for oriented In_2O_3 films grown on both YSZ and MgO by PLD. Ohta et al. [2000a] reported that highly conductive ITO films with resistivity of less than 1×10^{-4} Ω-cm could be grown heteroepitaxially on single-crystal YSZ (100) substrates using the PLD technique.

Since the lattice mismatch between YSZ and ITO is less than 1%, the heteroepitaxial growth of ITO films can be easily obtained on a single-crystal YSZ substrate. Figure 11.5 shows X-ray diffraction patterns for ITO films grown on (a) glass and (b) single-crystal YSZ substrates under the same deposition conditions ($T_s = 300°C$ and $P_{O_2} = 10$ mTorr) [Kim et al., 2002c]. All of the peaks can be assigned to a cubic phase of In_2O_3 (JCPDS Card No. 06-0416) without other phases, such as SnO_2. For the ITO film grown on glass, an integrated intensity ratio of the (400) peak to the (222) peak is 0.34, which is close to the value of 0.30 for the randomly oriented polycrystalline material indexed in the JCPDS database for In_2O_3. Therefore, the X-ray data indicate that the ITO film deposited on glass is polycrystalline. However, as shown in Figure 11.5b, the ITO film on a YSZ substrate shows only intense (h00) planes parallel to the (100) YSZ plane. This preferential orientation of the ITO film arises from the excellent lattice match between ITO and YSZ ($a_{o\text{ITO}} = 10.18$ to 10.24 Å and $a_{o\text{YSZ}} = 5.189$ Å) (JCPDS Card No. 30-1468). The crystal quality of ITO/YSZ film was confirmed by a ω scan (out-of-plane rocking curve) for the ITO(400) peak. As shown in Figure 11.5c, the full-width at half-maximum (FWHM) of 0.32° is observed in the ω scan of the ITO(400) peak. This narrow peak is due to the small lattice mismatch, and consequently indicates strong preferential alignment between the film and the substrate [(h00)ITO//(h00)YSZ]. The grain sizes, calculated from the diffraction patterns in Figure 11.5, were 22 and 45 nm for ITO/glass and ITO/YSZ, respectively.

Electrical properties of highly oriented ITO films can be compared to those of the film grown on glass. Table 11.2 shows the resistivity, Hall mobility, and carrier density of the ITO films grown on a single-crystal YSZ substrate and a glass substrate [Kim et al., 2002c]. Both films were deposited at 300°C and in a mixed gas atmosphere (12 mTorr of Ar and 6 mTorr of O_2). The electrical resistivity of the ITO films on YSZ was observed to be $\sim 1.6 \times 10^{-4}$ Ω-cm, which is slightly lower than that ($\sim 2.1 \times 10^{-4}$ Ω-cm) of ITO films grown by PLD on glass. This slightly reduced resistivity for the ITO on YSZ was due to the higher observed mobility ($34\ cm^2\ V^{-1}\ s^{-1}$) compared to that of ITO film on glass ($28\ cm^2\ V^{-1}\ s^{-1}$). The low resistivity of the ITO/YSZ is a consequence of the high carrier mobility, which may be due to a decrease in grain boundary scattering resulting from the oriented crystal nature of the deposited ITO films. However, the

TABLE 11.2 Resistivity and Hall Mobility of ITO Films Deposited on a Single-Crystal YSZ and a Glass Substrate by PLD[a]

Film/Substrate	Thickness Å	Resistivity (Ω cm)	Carrier Concentration (cm^{-3})	Hall Mobility ($cm^2\ V^{-1}\ s^{-1}$)
ITO/YSZ	3000	1.6×10^{-4}	1.15×10^{21}	34
ITO/glass	3000	2.1×10^{-4}	1.06×10^{21}	28

[a]Both films were produced under the same deposition conditions; 300°C and in a mixed gas atmosphere (12 mTorr of Ar and 6 mTorr of O_2).

From Kim et al. [2002c].

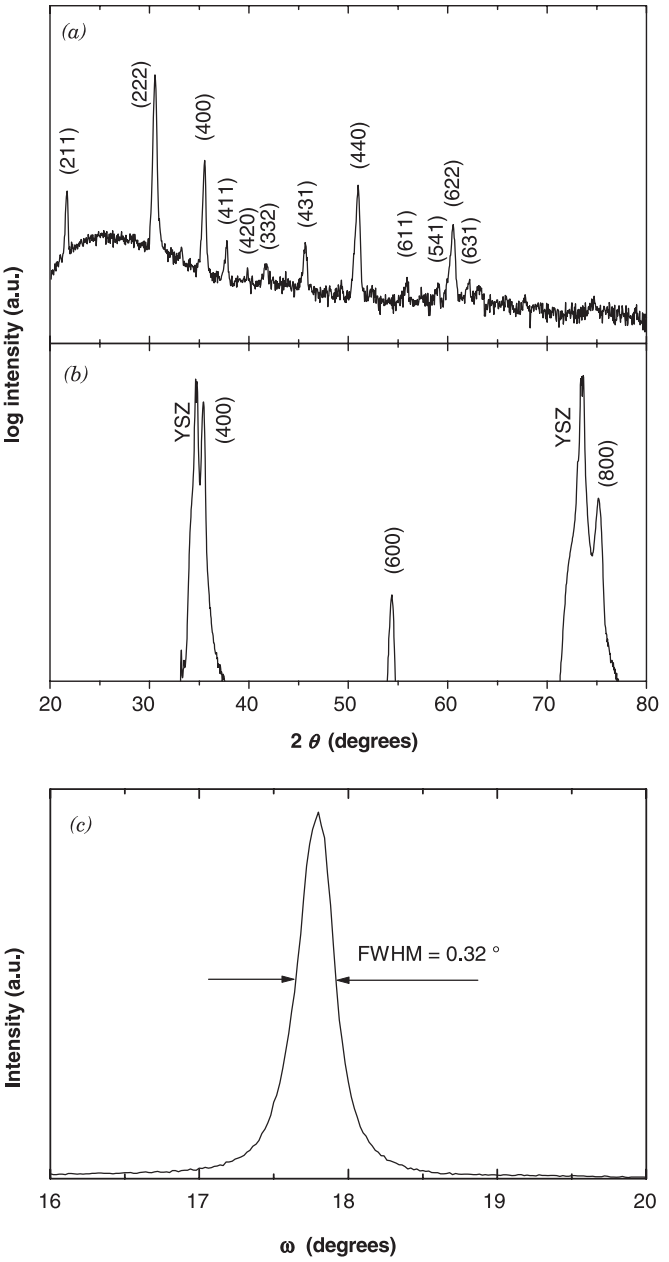

Figure 11.5 X-ray diffraction (θ-2θ) patterns for ITO thin films deposited on (a) glass and (b) single-crystal YSZ substrates; (c) ω-scan (out-of-plane rocking curve) of the (400)ITO peak shown in (b). The film thickness is about 200 nm for both films [Kim et al., 2002c].

resistivity of the ITO film on YSZ is almost the same as the best result ($1-2\times10^{-4}$ Ω-cm) observed from the ITO films on glass. This indicates that the electrical properties of the ITO films deposited by PLD do not depend significantly on the film crystallinity and the substrate material. These results are similar to the reports on In_2O_3 films deposited on YSZ by PLD [Tarsa et al.,

1993] and on ITO films grown by sputtering on YSZ [Taga et al., 1996]. However, there have been reports that the heteroepitaxial ITO films grown by PLD on YSZ at very high temperature (600–900°C) show very low resistivity ($<1.0 \times 10^{-4}$ Ω-cm) [Ohta et al., 2000a, 2002].

11.5.2 Undoped and Doped ZnO Films

Most of the research on PLD TCO films has been focused on ITO films. Recently, doped zinc oxide thin films have been widely studied for their use as transparent conducting electrode materials (see also Chapter 12). Unlike the more commonly used ITO, ZnO is a nontoxic and inexpensive material. It is chemically (and thermally) stable under hydrogen plasma processes that are commonly used for the production of solar cells [Hartnagel et al., 1995]. ZnO is a II–VI *n*-type semiconductor with a bandgap of about 3.3 eV at room temperature and a hexagonal wurtzite structure [Lide, 1991]. Pure zinc oxide films are highly transparent in the visible range (400–700 nm) and have low electrical conductivity. However, nonstoichiometric or impurity (Group III elements) doped zinc oxide films have high electrical conductivities as well as high optical transparencies. Nonstoichiometric zinc oxide films have unstable electrical properties because the sheet resistance of ZnO films increases under either oxygen chemisorption and desorption [Gopel and Lampe, 1980] or heat treatment in vacuum or in inert gas at 400°C [Minami et al., 1984]. Unlike the nonstoichiometric ZnO films, impurity-doped ZnO films show stable electrical and optical properties. Among the zinc oxide films doped with Group III elements such as barium, aluminum, gallium, and indium, aluminum-doped zinc oxide (AZO) films show the lowest electrical resistivity [Minami et al., 1985; Hiramatsu et al., 1998]. AZO films have low resistivity of $1-4\times10^{-4}$ Ω-cm [Kim et al., 2000b; Minami et al., 1985; Hu and Gordon, 1992; Hiramatsu et al., 1998], which is similar to that of ITO films [Kim et al., 1999b].

Electrical properties of Al-doped ZnO films strongly depend on the Al doping concentration. Figure 11.6 shows the typical variation of electrical resistivity (ρ), carrier density (N), and Hall mobility (μ) as a function of the Al content in the targets [Kim et al., 2000b]. The resistivity of the AZO films is found to initially decrease with increasing Al content up to 0.8 wt %. This decrease in

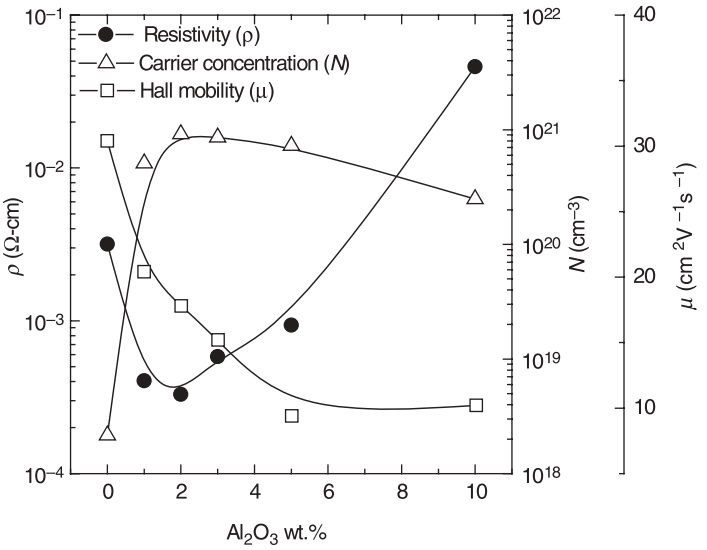

Figure 11.6 Dependence of electrical resistivity (ρ), carrier concentration (N), and Hall mobility (μ) on the Al content in the targets used to deposit the AZO films ($\sim$100 nm) by PLD. All films were deposited at 200°C in 0.67 Pa (= 5mTorr) of oxygen [Kim et al., 2000b].

resistivity is due to an increase in free carrier concentrations as a result of the donor electrons from the Al dopant. This initial increase in carrier density in the AZO films was due to the substitutional incorporation of Al^{3+} ions at Zn^{2+} cation sites or incorporation of Al ions in interstitial positions. However, the resistivity of the AZO films, after reaching a minimum (at 0.8 wt % of Al), gradually increases with a further increase in the Al content up to 4 wt %. When the Al content in the target is greater than 0.8 wt %, excess Al doping forms nonconducting Al_2O_3 clusters in the films causing crystal disorder, which act as carrier traps rather than electron donors [Hu and Gordon, 1992; Aktaruzzaman et al., 1991]. The excess Al doping decreases the carrier concentration in the film and consequently increases the resistivity. It is further seen from Figure 11.6 that the Hall mobility of the AZO films decreases with increasing Al content. This decrease in mobility is also associated with the observed decrease in grain size of the AZO films. At the optimized conditions for minimum resistivity and maximum transparency (200°C and 5 mTorr of oxygen), the electrical resistivity of the AZO films ($\sim$300 nm thick) was 3.7×10^{-4} Ω-cm and the average optical transmittance in the visible range was 91%. The optical properties of AZO films, such as bandgap, refractive index, and plasma wavelength, are strongly dependent on the Al-doping concentration, that is, carrier concentration [Kim et al., 2000b]. The absorption edge shifts toward shorter wavelength (higher energy) with increasing carrier concentration. Thus, the largest bandgap is observed for the film with highest carrier concentration (0.8 wt % of Al content). It is found that the refractive index and the plasma wavelength of AZO films are inversely related to the carrier concentration. Therefore, the optical properties can be easily controlled by changing the carrier density through Al doping.

Epitaxial thin films of AZO have been deposited on single-crystal sapphire (0001) substrates by PLD. Figure 11.7 shows XRD $\theta/2\theta$ scans for AZO films grown on single-crystal sapphire substrates [Kim et al., 2002a]. Films were grown at $T_s = 400$°C and $P_{O_2} = 40$ mTorr. It can be seen from Figure 11.7a that the AZO film grown on sapphire shows a textured structure with a strong preferential alignment between the films and the substrate [AZO(000*l*)// sapphire(000*l*)]. The crystal quality of AZO/sapphire film was confirmed by a ω scan (out-of-plane rocking curve), which was measured for the (0002) AZO peak. As shown in Figure 11.7b, the FWHM of 1.29° is observed in the ω scan of the (0002) AZO peak. The FWHM values decrease from 3.38° to 0.32° as the growth temperature increases from 250 to 680°C. The XRD in-plane ϕ scan for the $(10\bar{1}4)$ plane of the AZO film is shown in Figure 11.7c. In-plane measurements indicate that the films are epitaxial with the AZO $(10\bar{1}0)$ plane aligned with the sapphire $(11\bar{2}0)$ plane, suggesting that the unit cell of the AZO films is rotated by 30° with respect to that of the sapphire substrate.

For the films grown under optimum conditions ($T_s = 250$°C and $P_{O_2} = 7$ mTorr), the lowest resistivity values of AZO/glass and AZO/sapphire were 4.0×10^{-4} Ω-cm and 2.2×10^{-4} Ω-cm, respectively. The low resistivity in the case of AZO/sapphire is due to the improved crystal quality of the films, which leads to a decrease in grain boundary scattering and an increase in the carrier mobility, which results in a lower film resistivity [Kim et al., 2002a].

11.5.3 Other *n*-Type TCO Films

There have been many reports on other *n*-type TCO films grown by PLD. These include Zr- and Ga-doped ZnO [Kim et al., 2003; Hiramatsu et al., 1998], Sn-doped ZnO [Qadri et al., 2000], Zr-doped In_2O_3 [Kim et al., 2001a], Sb-doped SnO_2 [Kim and Piqué, 2004], ZrO_2–SnO_2 [Qadri et al., 2000], $Zn_xIn_yO_z$ [Phillips et al., 1995], $GaInO_3$ [Phillips et al., 1994], and In_2O_3–Sc_2O_3 [Qadri and Kim, 2002]. Table 11.3 outlines some of the *n*-type TCO films grown by PLD.

11.5.4 *p*-Type TCO Films

Pulsed laser deposition has been also used to deposit *p*-type TCO films, such as $CuAlO_2$, $CuGaO_2$, and $SrCu_2O_2$ [Kawazoe et al., 1997; Kudo et al., 1998; Yanagi et al., 2000]. With these *p*-type TCO films, *p-n* junctions exclusively from TCO materials can be fabricated, which enables one to develop

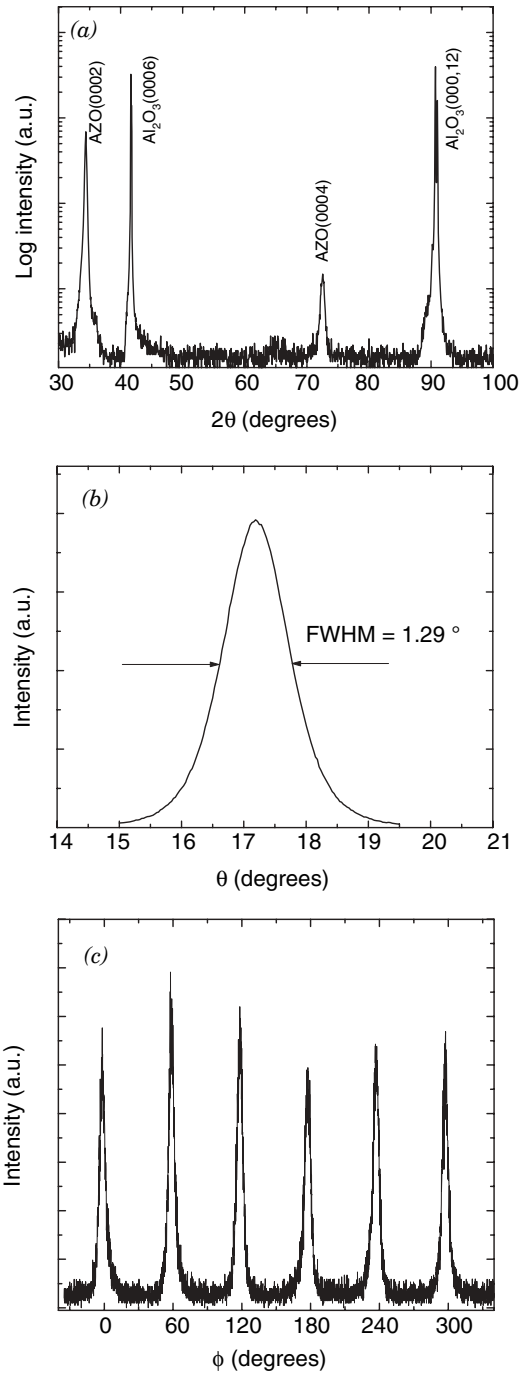

Figure 11.7 X-ray diffraction (θ-2θ) pattern for AZO thin film deposited on single-crystal sapphire (0001) substrates. (b) ω-scan (out-of-plane rocking curve) of the (0002) AZO peak shown in (a). (c) XRD in-plane ϕ scan belonging to the $(10\bar{1}4)$ plane of the AZO film (~ 200 nm). The detector was fixed at $2\theta = 81.368^{\circ}$. The film thickness is about 200 nm for both films [Kim et al., 2002a].

TABLE 11.3 Selected Electrical Properties of *n*-Type TCO Films Grown by PLD

Material	Resistivity ($10^{-4}\,\Omega\,cm$)	Carrier Concentration ($10^{20}\,cm^{-3}$)	Hall Mobility ($cm^2\,V^{-1}\,S^{-1}$)	References
In_2O_3:Sn (ITO)	1.9	11.4	29	Kim et al. [1999a]
	1.2	12	40	Adurodija et al. [2002]
	1.0	15	50	Ohta et al. [2002]
$GaInO_3$	25	4	10	Phillips et al. [1994]
$Zn_xIn_yO_z$:Sn	4	3.4	46	Phillips et al. [1995]
In_2O_3:Zr	2.5	10	25	Kim et al. [2001a]
In_2O_3–Sc_2O_3	16–100			Qadri and Kim [2002]
ZnO	90	0.23		Hiramatsu et al. [1998]
ZnO:Al	1.4	~10.1	~40	Hiramatsu et al. [1998]
ZnO:Ga	2.7	~20.1	~15	Hiramatsu et al. [1998]
ZnO:Zr	5.6			Kim et al. [2003]
SnO_2:Sb	11	1.8	4	Kim and Piqué [2004]

transparent thin-film transistors and ultraviolet light-emitting diodes (LEDs) [Prins et al., 1996]. Both $CuAlO_2$ (CAO) and $CuGaO_2$ (CGO) films have a crystal structure of delafossite, AMO_2, where A is a monovalent cation (Cu, Ag, etc.) and M is a trivalent ion (Al, Ga, In, etc.). The layers of A and MO_2 are alternately stacked along the *c*-axis. The optical bandgap for CAO and CGO was calculated to be ~3.5 and ~3.6 eV, respectively. Electrical conductivity for CAO and CGO was 0.95 and 0.63 S/cm, respectively. Unlike CAO and CGO, $SrCu_2O_2$ (SCO) has an O–Cu–O dumbbell-shaped structure similar to Cu_2O [Kawazoe et al., 2000]. The optical bandgap and the conductivity of SCO were 3.3 eV and 4.83×10^{-2} S/cm. The main advantage of the SCO is the low deposition temperature (~300°C) compared to CAO and CGO. N-type conductivity has been also realized in $AgInO_2$ (AIO) with the delafossite structure. The AIO films grown by PLD on Al_2O_3 substrates showed a very high carrier density of $3.3 \times 10^{20}\,cm^{-3}$ and conductivity of 73 S/cm [Ibuki et al., 2000].

Recently, a new *p*-type TCO has been realized in a thin film of N-doped ZnO deposited by PLD combined with a plasma gas source [Joseph et al., 1999; Guo et al., 2001; Matsui et al., 2004]. Guo et al. have deposited *p*-type N-doped ZnO films on fused silica and glass by PLD using a pure Zn metal target in N_2O plasma, and they reported that the *p*-type ZnO films show a resistivity of 2–5 Ω-cm, carrier density of $3–6\times10^{18}\,cm^{-3}$, and Hall mobility of $0.1–0.4\,cm^2\,V^{-1}\,s^{-1}$ as well as an optical transmission of 90% in the visible spectral range. The electrical and optical properties of the N-doped ZnO films grown by PLD are sufficient to make transparent *p-n* homojunctions for some practical applications, such as ultraviolet (UV) and blue LEDs. Some selected PLD conditions and properties of *p*-type TCO films are summarized in Table 11.4.

11.6 APPLICATIONS OF TCO FILMS

Although TCO films have found a variety of applications, there have been only few intended applications for PLD TCO films. These applications and some other potential use of PLD films are discussed below.

11.6.1 Display Devices

There is a growing need for TCO materials in the field of flat-panel displays including liquid crystal displays (LCD) and organic light-emitting diodes (OLED) [Gustafsson et al., 1992; Kido et al., 1996; Rajagopal and Khan, 1998; He and Kanicki, 2000]. These applications use TCO films as their

TABLE 11.4 PLD Conditions of $CuAlO_2$, $CuGaO_2$, $SrCu_2O_2$, and N-Doped ZnO Films and Their Electrical Properties

	$CuAlO_2$[a]	$CuGaO_2$[b]	$SrCu_2O_2$[c]	N-doped ZnO[d]
Substrate	Al_2O_3 (0001)	Al_2O_3 (0001)	SiO_2 glass	Fused silica, glass
Laser wavelength/laser repetition frequency (Hz)	248 nm/20	248 nm/20	248 nm/1–2	193 nm/1–5
Laser fluence (J/cm^2)	5	6	2.5	1
Target-to-substrate distance (mm)	25	25	40	N/A
Background gas pressure (Torr)	(O_2 flow) 9.75×10^{-3} (1.3 Pa)	(O_2 flow) 67.5×10^{-3} (9 Pa)	(O_2 flow) 5.25×10^{-6} (7×10^{-4} Pa)	(N_2O flow) 1.35×10^{-4} (1.8×10^{-2} Pa)
Substrate temperature (°C)	600	700	300	450
Postannealing (hours × temperature) (h × °C)	3 × 690	N/A	2 × 300	N/A
Electrical conductivity ($S\,cm^{-1}$)	0.34	6.3×10^{-2}	4.8×10^{-2}	0.2–0.5
Carrier density (cm^{-3})	2.7×10^{19}	1.7×10^{18}	6.1×10^{17}	$3–6 \times 10^{18}$
Hall mobility ($cm^2\,V^{-1}\,s^{-1}$)	0.13	0.23	0.46	0.1–0.4

[a]From Yanagi et al. [2000].
[b]From Kawazoe et al. [2000].
[c]From Kudo et al. [1998].
[d]From Guo et al. [2001].

transparent electrode, and frequently it is required to pattern the TCO layer. A commonly used TCO for these applications is ITO because it has low resistivity and can be easily patterned with dilute etchants (e.g., 5% H_2SO_4 or 5% HCl in H_2O or a mixture of dilute HCl and HNO_3). However, in the case of SnO_2 coatings, wet chemical etching is more difficult and requires electrolytic action because of its high chemical stability. For some cases, where wet etching cannot produce homogeneous patterns, dry etching techniques, such as plasma etching and laser etching, have been used for the required patterning of TCO films. Although plasma etching is the commonly used technique, laser etching has been considered as an alternative to plasma etching. An excimer laser ($\lambda = 248$ nm) has been used to pattern ITO and SnO_2 films; 20–50 μm linewidth patterns have been demonstrated in both ITO and SnO_2 films. Recently, high-speed laser patterning of ITO thin films has been demonstrated using a diode-pumped *Q*-switched Nd : YLF laser [Yavas and Takai, 1998]. High process speeds of 1 m/s could be achieved. The use of lasers for electrode patterning has significant potential because laser etching of any TCO material is possible with various laser wavelengths.

Recently, the TCO films grown by PLD have been successfully used as an anode material for OLED devices [Kim et al., 1999a, 1999b, 1999c, 2000a, 2000b, 2001a, 2001b, 2002b, 2002c]. Since the organic thin films employed in the OLEDs are directly deposited on the TCO anode, the surface properties of the TCO films may affect the characteristics of the devices. In general, PLD films are extremely smooth so that the OLED device based on a PLD TCO anode can improve the device efficiency. Furthermore, a high work function of the TCO layer is essential to improve the efficiency of hole injection from the TCO layer to the hole transport organic layer in the OLED device. ITO is the commonly used anode material so far because it has a relatively high work function (~ 4.8 eV) and low sheet resistance (10–20 Ω/square) with a film thickness of 100–200 nm. The thickness of ITO films in OLEDs is also expected to affect the device performance [Kim et al., 2000a]. The optimum thickness of the ITO anode to achieve a maximum efficiency of OLED devices was observed to be about 60–100 nm. The device with the optimum thickness of ITO anode showed an external quantum efficiency of about 0.85% at 100 A/m^2.

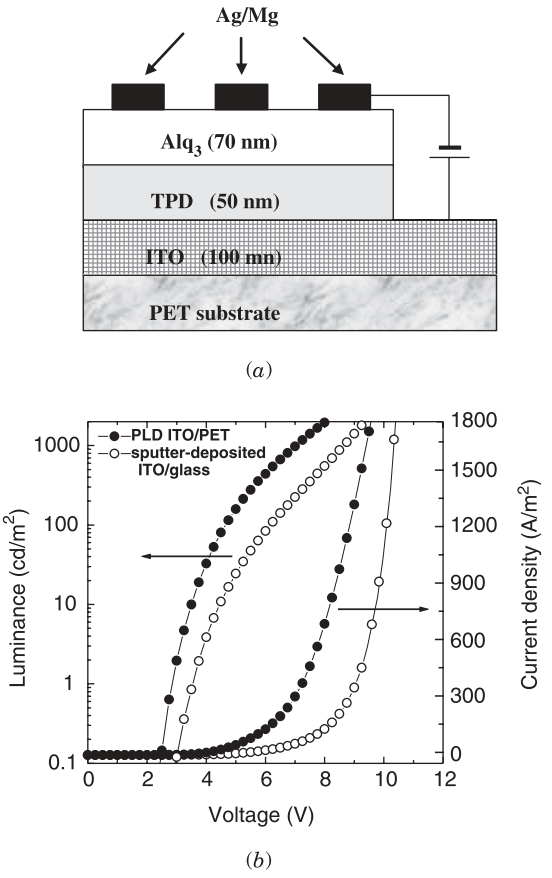

Figure 11.8 (a) Schematic structure of an OLED device with an ITO anode deposited on PET by PLD. (b) Current density (J), applied voltage (V), and luminance (L) characteristics for the OLED device based on PLD ITO/PET (70 Ω/sq.) and sputter-deposited (commercial) ITO/glass (20 Ω/sq.). The thickness of both ITO films is ∼100 nm [Kim et al., 2001b].

The use of PLD-grown ITO films on flexible PET as transparent anode electrodes for OLEDs has been also demonstrated with improved luminous power efficiency [Kim et al., 2001b]. Figure 11.8 shows a schematic structure of an OLED device and a comparison of the characteristics of current density (J), voltage (V), and luminance (L) output for OLEDs made using both PLD-grown ITO on PET and commercial sputter-deposited ITO (supplied by Applied Films, USA) on glass. A luminous power efficiency of 1.6 lm/W measured at 100 A/m^2 for the device fabricated on ITO/PET is slightly higher than that ($\sim$1.5 lm/W) measured for a control device made on the commercial ITO/glass under the same conditions.

Although ITO has been so far the most commonly used anode material in OLED devices, it is not always an ideal anode contact for OLEDs because of the high energy barrier for hole injection at its interface with the hole transport layer (HTL) and diffusion of indium into the organic layers [Gautier et al., 1996; Kim et al., 1998]. One approach for improving the performance of OLEDs is to develop new anode materials with high work functions. Many efforts have focused on improving the hole injection efficiency at the ITO anode–organic interface in OLED devices; they include treating the ITO surface with an oxygen plasma or UV ozone [Wu et al., 1997; Kim et al., 1998], introducing self-assembled monolayers or conducting polymers between the ITO and the HTL [Steuber et al.,

1999; Bharathan and Yang, 1998; Ho et al., 1998], and utilizing highly oriented ITO [Kim et al., 2002c]. Few studies have focused on developing new anode materials as alternatives to ITO for OLED devices [Andersson et al., 1998; Zhou et al., 1999; Kim et al., 2000b, 2001a; Cui et al., 2001]. The Zr-doped In_2O_3 (ZIO) films grown by PLD have been successfully used as a transparent anode contact in OLED devices with the external quantum efficiency of 0.9% at a current density of 100 A/m^2, which is slightly higher than the device based on the sputter-deposited ITO anode [Kim et al., 2001a]. The Al-doped ZnO (AZO) films grown by PLD at 200°C have also been used as an anode contact to fabricate OLEDs [Kim et al., 2000b]. Unfortunately, the external quantum efficiency measured from these devices was about 0.3% at a current density of 100 A/m^2. This low efficiency is due to the low work function ($\sim$4.0 eV) of the AZO in comparison to that of commercially sputter-deposited ITO ($\sim$4.8 eV). The Zr-doped ZnO (ZZO) films grown by PLD have been successfully used as an anode material for OLED devices. The OLED device fabricated on ZZO anodes exhibit external electroluminescence (EL) quantum efficiencies comparable to the control device fabricated on commercial ITO [Kim et al., 2003]. Maximum light output of $\sim$18700 cd/m^2 was achieved at 16 V for the device based on the PLD ZZO anode.

11.6.2 Photovoltaic Devices

Pulsed laser deposition (PLD) has also been used to develop TCO-based solar cells. TCO materials provide some advantages in solar cell applications, as they can be used either as active *n*-type semiconductors in heterojunction solar cells or transparent electrodes. TCO films allow transmission of solar radiation directly to the active region without loosing much intensity so that TCO-based solar cells can produce high sensitivity in the high photon energy region of the solar spectrum. TCO films can also provide antireflection coatings for the active region as well as a low resistance contact to the junction. In addition, the fabrication cost is very low because of a lower junction formation temperature.

InP is a very attractive semiconductor used for photovoltaic solar cells. The most commonly used technique for ITO/InP solar cells is sputtering [Keavney and Spitzer, 1988], while a spray pyrolysis has been used for fabrication of ITO/Si cells [Ashok et al., 1980]. In comparison with sputtering, PLD provides some advantages for heterojunction solar cell applications. High-quality ITO films can be grown at low temperature by PLD due to high energies of the ejected species in the plume. This low-temperature process is very important in fabrication of ITO/InP cells because the InP is extremely sensitive to thermal treatments. The use of PLD for ITO/*p*-InP photovoltaic devices has been demonstrated by Jia et al. [1995]. A schematic diagram of the structure is shown in Figure 11.9. Au : Zn and Au were sequentially evaporated on the backside of the InP for the ohmic contact. The Au pad was the ohmic contact of ITO. The typical open-circuit voltage (V_{oc}) of the cells was 660 and 610 mV, and short-circuit current density (J_{sc}) was 23.5 and 23 mA/cm^2, for the cells fabricated at room temperature and 310°C, respectively. The open-circuit voltage was improved to some extent by using a low deposition temperature during ITO deposition, and this improvement was believed to

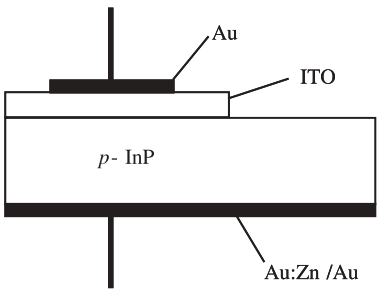

Figure 11.9 Diagram of the ITO/*p*-InP photovoltaic device used for I–V measurements either in the dark or under illumination [Jia et al., 1995].

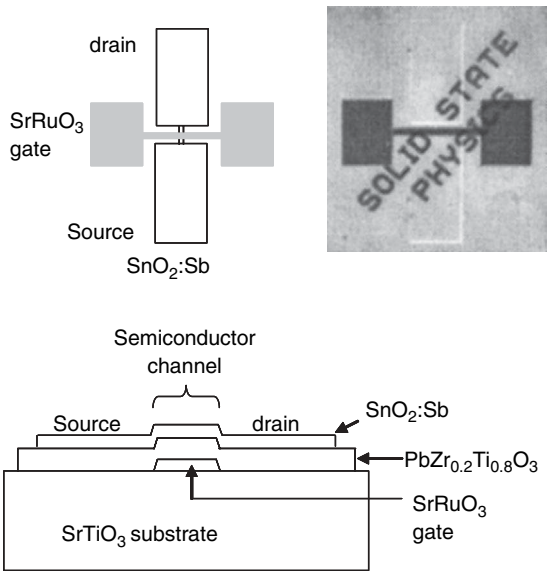

Figure 11.10 Picture and schematic diagram of the transistor (top view and cross-sectional view). In the picture, the text "solid-state physics" was read through the device. The picture size is 1.4 mm × 1.8 mm [Prins et al., 1996].

be from the better surface properties of the InP. The dark current–voltage measurement indicated higher leakage current for the devices fabricated at 310°C. Due to the low junction formation temperature in TCO-based heterojunction solar cells, PLD TCO films can be used to improve the photovoltaic parameters such as open-circuit voltage, short-circuit current, and conversion efficiency.

Heteroepitaxial growth of ITO films has been established by PLD on Si substrates with a CeO_2 ultrathin buffer layer for solar cell applications [Tashiro et al., 2002]. Both ITO and CeO_2 buffer layers were grown on Si substrates at room temperature and showed heterostructure of ITO(111)/CeO_2(111)/Si(111) with the epitaxial relationship of $[\bar{1}10]_{ITO}//[\bar{1}10]_{CeO2}//[1\bar{1}0]_{Si}$. The heterojunction of [ITO: 100 nm thick/CeO_2: 3 nm thick/*p*-Si(111)] showed solar cell characteristics with the V_{oc} of 210 mV, J_{sc} of 29 mA/cm^2, and energy conversion efficiency of $\sim 4\%$. The room temperature epitaxial growth technique makes TCO films useful for developing the next generation of organic photovoltaic devices.

11.6.3 Transparent Thin-Film Field-Effect Transistor (FET)

Field-effect transistors with TCO materials have been receiving much attention because the wide bandgap TCO provides interesting opportunities for optical applications, such as on-screen electronic devices in displays, cameras, and projectors. PLD has been used to fabricate a ferroelectric transparent field-effect transistor on a $SrTiO_3$ (100) substrate, which consists of a high-mobility Sb-doped SnO_2 semiconductor layer (110 nm), $PbZr_{0.2}Ti_{0.8}O_3$ ferroelectric insulator (160 nm), and $SrRuO_3$ (140 nm) as a gate electrode [Prins et al., 1996]. A schematic diagram and picture of the transistor are shown in Figure 11.10. With this transistor structure, using gate voltage pulses of 100 μs duration and a pulse height of ± 3 V, a change of a factor of 2 in the remnant conductance is achieved.

Pulsed laser deposition has been used for epitaxial growth of Ni/$SrCu_2O_2$/ZnO/ITO multilayered film on extremely flat YSZ (111) surfaces for UV LEDs using hetero *p-n* junctions composed of TCOs. A relatively sharp electroluminescence band, centered at 382 nm can be generated at a

forward bias greater than 3 V. The photovoltage could be also obtained when the device was irradiated with UV light [Ohta, et al., 2000b].

11.7 CONCLUSION AND FUTURE DIRECTIONS

Several issues must be addressed before PLD TCO can be used commercially for device applications, such as OLEDs, LCDs, and photovoltaics. One of the issues is to produce large-area TCO films with uniform thickness, and the second is to reduce the particulate density, especially, for display applications. Among many TCO materials, ITO is the preferred TCO material for display applications. An alternative TCO to ITO must be developed because the indium is expensive and its worldwide supply is limited. Doped ZnO will be a good candidate as an alternative to ITO since the doped ZnO films have comparable electrical and optical properties with ITO and ZnO is a cheap, abundant, and nontoxic material.

The PLD technique has the ability to easily produce high-quality TCO films with low resistivity at very low temperatures compared to other deposition techniques. For high resolution device applications, PLD is the optimum choice for growth of TCO films with low resistivity and high transmittance. Specifically, transparent heterojunction devices with *n*-type and *p*-type TCO films as active semiconductor materials will attract much attention in many optical applications. A recently realized *p*-type ZnO film would be an important TCO material because it can be used to fabricate transparent *p-n* homojunctions, which will have many potential applications in the optoelectronics industry.

For some specific applications, the choice of a suitable TCO material is strongly dependent on the structural, electrical, and optical properties of TCO materials. Since PLD can easily control the film composition and properties, it is a very useful technique to investigate the structure–property relationship of TCO films and their devices.

Acknowledgments

The author wishes to thank all those who have contributed to this research at Naval Research Laboratory. This work was supported by the Office of Naval Research (ONR).

REFERENCES

Adurodija, F. O., H. Izumi, T. Ishihara, H. Yoshoka, and M. Motoyama (2000), *J. Mater. Sci. Lett.* **19**, 1719.

Adurodija, F. O., H. Izumi, T. Ishihara, H. Yoshoka, M. Motoyama, and K. Murai (2002), *Vacuum* **67**, 209.

Andersson, A., N. Johansson, P. Bröms, N. Yu, D. Lupo, and W. R. Salaneck (1998), *Adv. Mater.* **10**, 859.

Aktaruzzaman, A. F., G. L. Sharma, and L. K. Malhotra (1991), *Thin Solid Films* **198**, 67.

Ashok, S., P. P. Sharma, and S. J. Fonash (1980), *IEEE Trans. Electron Dev.* **27**, 725.

Bädeker, K. (1907), *Ann. Phys. (Leipzig)* **22,** 749.

Bharathan, J. M., and Y. Yang (1998), *J. Appl. Phys.* **84**, 3207.

Burstein, E. (1954), *Phys. Rev.* **93**, 632.

Chopra, K. L., S. Major, and D. K. Pandya (1983), *Thin Solid Films* **102**, 1.

Chrisey, D. B., and G. K. Hubler (1994), *Pulsed Laser Deposition of Thin Films*, Wiley, New York.

Coutal, C., A. Azema, and J. C. Roustan (1996), *Thin Solid Films* **288**, 248.

Cui, J., A. Wang, N. L. Edleman, J. Ni, P. Lee, N. R. Armstrong, and T. J. Marks (2001), *Adv. Mater.* **13**, 1476.

Gautier, E., A. Lorin, J. M. Nunzi, A. Schalchli, J. J. Benattar, and D. Vital (1996), *Appl. Phys. Lett.* **69**, 1071.

Gopel, W., and U. Lampe (1980), *Phys. Rev. B.* **22**, 6447.

Guo, X.-L., H. Tobata, and T. Kawai (2001), *J. Crystal Growth* **223**, 135.

Gustafsson, G., Y. Cao, G. M. Treacy, F. Klavetter, N. Colaneri, and A. J. Heeger (1992), *Nature* **357**, 477.

Haacke, G. (1977), *Annu. Rev. Mater. Sci.* **7**, 73.

Hamberg, I., and C. G. Granqvist, *J. Appl. Phys.* **60**, (1986), R123.

Hartnagel, H. L., A. L. Dawar, A. K. Jain, and C. Jagadish (1995), *Semiconducting Transparent Thin Films*, vol. 1, Institute of Physics, Philadelphia.

He, Y., and J. Kanicki (2000), *Appl. Phys. Lett.* **76**, 661.

Hiramatsu, M., K. Imaeda, N. Horio, and M. Nawata (1998), *J. Vac. Sci. Technol.* **A16**, 669.

Ho, P. K. H., M. Granstrom, R. H. Friend, and N. C. Grenham (1998), *Adv. Mater.* **10**, 769.

Holland, L. (1958), *Vacuum Deposition of Thin Films*, Wiley, New York, p. 492.

Holmelund, E., B. Thestrup, J. Schou, N. B. Larsen, M. M. Nielsen, E. Johnson, and S. Tougaard (2002), *Appl. Phys.* **A74**, 147.

Hu, J., and R. G. Gordon (1992), *J. Appl. Phys.* **71**, 880.

Ibuki, S., H. Yanagi, K. Ueda, H. Kawazoe, and H. Hosono (2000), *J. Appl. Phys.* **88**, 3607.

Jarzebski, Z. M. (1982), *Phys. Status Solidi* **A71**, 13.

Jia, Q. X., J. P. Zheng, H. S. Kwok, and W. A. Anderson (1995), *Thin Solid Films* **258**, 260.

Johnson, V. A., and K. Lark-Horovitz (1947), *Phys. Rev.* **71**, 374.

Joseph, M., H. Tabata, and T. Kawai (1999), *Jpn. J. Appl. Phys.* **38**, L1205.

Kawazoe, H., M. Yasukawa, H. Hyodo, M. Kurita, H. Yanagi, and H. Hosono, (1997), *Nature* **389**, 939.

Kawazoe, H., H. Yanagi, K. Ueda, and H. Hosono (2000), *MRS Bull.* **25**, 28.

Keavney, C. J., and M. B. Spitzer (1988), *Appl. Phys. Lett.* **52**, 1439.

Kido, J., K. Hongawa, K. Pkuyama, and K. Nagai (1996), *Appl. Phys. Lett.* **68**, 217.

Kim, H., and A. Piqué (2004), *Appl. Phys. Lett.* **84**, 218.

Kim, J. S., M. Granström, R. H. Friend, N. Johansson, W. R. Salaneck, R. Daik, W. J. Feast, and F. Cacialli (1998), *J. Appl. Phys.* **84**, 6859.

Kim, H., A. Piqué, J. S. Horwitz, H. Mattoussi, H. Murata, Z. H. Kafafi, and D. B. Chrisey (1999a), *Appl. Phys. Lett.* **74**, 3444.

Kim, H., C. M. Gilmore, A. Piqué, J. S. Horwitz, H. Mattoussi, H. Murata, Z. H. Kafafi, and D. B. Chrisey (1999b), *J. Appl. Phys.* 86, 6451.

Kim, H., J. S. Horwitz, A. Piqué, C. M. Gilmore, and D. B. Chrisey (1999c), *Appl. Phys.* **A69**, S447.

Kim, H., J. S. Horwitz, G. P. Kushto, A. Piqué, Z. H. Kafafi, C. M. Gilmore, and D. B. Chrisey (2000a), *J. Appl. Phys.* **88**, 6021.

Kim, H., A. Piqué, J. S. Horwitz, H. Murata, Z. H. Kafafi C. M. Gilmore, and D. B. Chrisey (2000b), *Thin Solid Films* **377/378**, 798.

Kim, H., J. S. Horwitz, G. P. Kushto, S. B. Qadri, Z. H. Kafafi, and D. B. Chrisey (2001a), *Appl. Phys. Lett.* **78**, 1050.

Kim, H., J. S. Horwitz, G. P. Kushto, Z. H. Kafafi, and D. B. Chrisey (2001b), *Appl. Phys. Lett.* **79**, 284.

Kim, H., J. S. Horwitz, S. B. Qadri, and D. B. Chrisey (2002a), *Thin Solid Films* **420/421**, 107.

Kim, H., J. S. Horwitz, W. H. Kim, A. J. Makinen, Z. H. Kafafi, and D. B. Chrisey (2002b), *Thin Solid Films* **420/421**, 539.

Kim, H., J. S. Horwitz, W. H. Kim, Z. H. Kafafi, and D. B. Chrisey (2002c), *J. Appl. Phys.* **91**, 5371.

Kim, H., J. S. Horwitz, W. H. Kim, S. B. Qadri, and Z. H. Kafafi (2003), *Appl. Phys. Lett.* **83**, 3809.

Kudo, A., H. Yanagi, H. Hosono, and H. Kawazoe (1998), *Appl. Phys. Lett.* **73**, 220.

Kulkarni, A. K., T. Lim, M. Khan, and K. H. Schulz (1998), *J. Vac. Sci. Technol.* **A16**, 1636.

Lide, D. R. (1991), *Handbook of Chemistry and Physics*, 71st ed., CRC, Boca Raton, FL.

Ma, J., S. Li, J. Zhao, and H. Ma (1997), *Thin Solid Films* **307**, 200.

Manifacier, J. C. (1982), *Thin Solid Films* **90**, 297.

Matsui, H., H. Saeki, T. Hawai, and H. Tabata (2004), *J. Appl. Phys.* **95**, 5882.

Minami, T. (1999), *J. Vac. Sci. Technol.* **A17**, 1765.

Minami, T., H. Nanto, and S. Takata (1984), *Jpn. J. Appl. Phys.* **23**, L280.

Minami, T., H. Sato, H. Nanto, and S. Takata (1985), *Jpn. J. Appl. Phys.* **24**, L781.

Minami, T., H. Sonohara, T. Kakumu, and S. Takata (1995), *Thin Solid Films* **270**, 37.

Mizuhashi, M. (1980), *Thin Solid Films* **70**, 91.

Moss, T. S. (1964), *Proc. Phys. Soc. London Sect. B* **67**, 775.

MRS Bulletin **25** (2000), 15–65.

Ohta, H., M. Orita, M. Hirano, H. Tanji, H. Kawazoe, and H. Hosono (2000a), *Appl. Phys. Lett.* **76**, 2740.

Ohta, H., K. Kawamura, M. Orita, N. Sarukura, M. Hirano, and H. Hosono, (2000b), *MRS Symp.* **623**, 283.

Ohta, H., M. Orita, M. Hirano, and H. Hosono (2002), *J. Appl. Phys.* **91**, 3547.

Phillips, J. M., J. Kwo, G. A. Thomas, S. A. Carter, et al. (1994), *Appl. Phys. Lett.* **65**, 115.

Phillips, J. M., R. J. Cava, G. A. Thomas, S. A. Carter, et al. (1995), *Appl. Phys. Lett.* **67**, 2246.

Prins, M. W., K.-O. Grosse-Holz, G. Muller, J. F. M. Cillessen, J. B. Giesbers, R. P. Weening, and R. M. Wolf (1996), *Appl. Phys. Lett.* **68**, 3650.

Qadri, S. B., and H. Kim (2002), *J. Appl. Phys.* **92**, 227.

Qadri, S. B., H. Kim, H. R. Khan, et al. (2000), *Thin Solid Films*, **377/378**, 803.

Rajagopal, A., and A. Khan (1998), *J. Appl. Phys.* **84**, 355.

Steuber, F., J. Staudigel, M. Stössel, J. Simmerer, and A. Winnacker (1999), *Appl. Phys. Lett.* **74**, 3558.

Suzuki, A., T. Mastsushita, T. Aoki, Y. Yoneyama, and M. Okuda (2001), *Jpn. J. Appl. Phys.* **40**, L401.

Tachiki, M., and T. Kobayashi (1999), *Jpn. J. Appl. Phys.* **38**, 3642.

Taga, N., H. Odaka, Y. Shigesato, I. Yasui, and T. E. Haynes (1996), *J. Appl. Phys.* **80**, 978.

Tauc, J., R. Grigorovici, and A. Vancu (1966), *Phys. Status Solidi* **15**, 627.

Tarsa, E. J, J. H. English, and J. S. Speck (1993), *Appl. Phys. Lett.* **62**, 2332.

Tashiro, J., A. Sasaki, S. Akiba, S. Satoh, T. Watanabe, H. Funakubo, and M. Yoshimoto (2002), *Thin Solid Films* **415**, 272.

Vossen, J. L. (1977), *Phys. Thin Films* **9**, 1.

Wu, W. -F., B. -S. Chiou, and S. -T. Hsieh (1994), *Semicon. Sci. Technol.* **9**, 1242.

Wu, C. C., C. I. Wu, J. C. Strum, and A. Kahn (1997), *Appl. Phys. Lett.* **70**, 1348.

Wu, Y., C. H. Maree, R. F. Haglund, Jr., J. D. Hamilton, M. A. Paliza, and R. A. Weller (1999), *J. Appl. Phys.* **86**, 991.

Yanagi, H., H. Kawazoe, A. Kudo, M. Yasukawa, and H. Hosono (2002), *J. Electroceram.* **4**, 407.

Yavas, O., and M. Takai (1998), *Appl. Phys. Lett.* **73**, 2558.

Zheng, J. P., and H. S. Kwok (1993), *Appl. Phys. Lett.* **63**, 1.

Zhou, X., J. He, L. Liao, M. Lu, Z. Xiong, X. Ding, X. Hou, F. Tao, C. Zhou, and S. Lee (1999), *Appl. Phys. Lett.* **74**, 609.

CHAPTER 12

ZnO and ZnO-Related Compounds

JACQUES PERRIÈRE

Groupe de Physique des Solides, Universités Paris VI et VII, Paris, France

ERIC MILLON

Laboratoire Spectrométrie de Masse et de Chimie Laser, Université de Metz, Metz, France

VALENTIN CRACIUN

Major Analytical Instrumentation Center, Materials Science and Engineering, University of Florida, Gainesville, Florida

12.1 INTRODUCTION

ZnO is a II–VI semiconductor possessing a large number of interesting properties that have been the focus of intense research for many years. Due to recent and exciting developments in several key areas, pure or doped ZnO films appear to be a highly promising new and advanced functional material. Clear evidence of this is the fact that more than 1500 papers have been published on ZnO thin-film growth and properties in the last 5 years.

ZnO is a material that is very stable at high temperature ($T_{\text{melt}} = 1975^{\circ}\text{C}$ while above 1200°C it dissociates and sublimes) and can withstand the high-temperature annealing processes involved in the manufacturing of microelectronic circuits. It is also much more resistant to radiation damage than other common semiconductor materials, being well adapted for electronic applications in high-irradiation environments, such as space-based applications.

ZnO is also well-known as a piezoelectric material that has been used in surface acoustic wave (SAW) devices for delay lines, filters and resonators in wireless communications, and signal processing. However, one of the most exciting applications of ZnO films is certainly related to its optical properties. Since the bandgap energy of ZnO is 3.37 eV at room temperature, it is transparent in both the visible and near ultraviolet–visible wavelength region. The exciton binding energy is quite high (60 meV), and it luminesces in the ultraviolet (UV) region (around 380 nm) making ZnO a possible future contender for UV and blue-light-emitting devices. This large excton binding energy permits excitonic recombination above room temperature, and, as a result, optically pumped lasing has been observed in epitaxial or polycrystalline ZnO thin films [Bagnall et al., 1997; Ohtomo et al., 1998a]. In addition, due to its wide and direct bandgap and its large photoresponse, ZnO is also very suitable for UV photodetector applications.

ZnO doped with various atoms can lead to new or enhanced functional properties with interesting potential applications. As an electronic conductor, ZnO may be used as transparent and conducting

Pulsed Laser Deposition of Thin Films: Applications-Led Growth of Functional Materials
Edited by Robert Eason

electrodes for flat-panel displays and solar cells. For example, doping with Group III elements (Al, Ga, In) or Si and H decreases its resistivity to below $10^{-4}\,\Omega\,\mathrm{cm}$, while keeping the high optical transparency of the intrinsic host ZnO material. Wide bandgap semiconductors are known as interesting host matrices for rare-earth (RE) atoms leading to their high luminescence efficiency at room temperature. Thus, Nd, Sm, Eu, and Er-doped ZnO thin films have been studied for potential applications in optics and optoelectronics such as visible or infrared emitting devices, planar optical waveguide amplifiers, while Li doping introduces ferroelectric properties in ZnO. In the new and exciting field of dilute magnetic semiconductors, ZnO films have been doped with transition-metal atoms (Mn, Co, Ni, etc.) that introduce local magnetic moments into the lattice, to obtain room temperature ferromagnetic semiconductors that could be used as spin injectors in spintronics.

Last, but not least, the low toxicity of ZnO compared with other wide bandgap semiconductors has to be emphasized. ZnO is used in pharmacy as a fungicide and ingredient in many medicines and ointments. Thus the use of Zn and oxygen rather than more harmful elements reduces the toxicological risks in the manufacturing of future devices. Moreover, ZnO is abundant and relatively inexpensive.

This large number of applications of ZnO are mainly based on thin films or multilayer structures involving the functional properties of the bulk material. Thin films of ZnO and ZnO-related compounds have been grown by a wide variety of chemical as well as physical methods: metalorganic chemical vapor deposition (CVD), electrophoretic deposition, atmospheric pressure vapor-phase epitaxy, spray pyrolysis, sol–gel, electron beam evaporation, direct current (DC) or radio frequency (RF) sputtering, ion-beam-assisted deposition, plasma (electron cyclotron resonance or RF)-assisted molecular beam epitaxy, and pulsed laser deposition (PLD). This last growth method has attracted particularly widespread interest due to its intrinsic specificities as already presented in Chapter 1. One specific advantage of the PLD technique for ZnO is the growth under a wide range of oxygen-reactive gas pressures (from vacuum up to near atmospheric pressure) leading first to a precise control of the oxygen incorporation in the films, tuning the electrical conduction over many orders of magnitude, from highly conductive to highly insulating, and second, to the possible formation of metastable phases with new properties.

As a result, ZnO thin-film growth by PLD with or without any dopants or alloyed atoms has been intensively studied, and the physical functional properties of the films have been extensively investigated as a function of the growth conditions such as laser wavelength, pulse duration, repetition rate, fluence, substrate temperature, oxygen pressure, target–substrate distance, and nature of the substrate. The epitaxial growth of ZnO and ZnO-related compounds on various single crystalline substrates has been reported [Vispute et al., 1997; Narayan et al., 1998], as well as the formation of multilayers and superlattices [Ohtomo et al., 1999a, 1999b; Sun et al., 2000].

In this chapter, we will first review the general features of ZnO thin films grown by PLD in order to specify the optimum range of the parameters for the growth of dense, stoichiometric, and crystalline ZnO layers. The most recent interesting applications of such films are also presented. In a second section, the specific problems of epitaxial growth are reported and discussed. The correlations between the structural defects in the epitaxial films and their physical properties are analyzed, and the most important applications of ZnO epitaxial films are described. The formation of nanocrystalline films is then considered. There have been two different ways to obtain such films: PLD under ''high-pressure'' atmospheres and the use of ultrashort laser pulses (femtoseconds) are presented as well as the very specific applications that can be envisaged for such nanocrystalline films. Finally, we discuss some future research themes related to the PLD of ZnO films.

12.2 ZnO THIN-FILM GROWTH BY PLD: GENERAL FEATURES

12.2.1 Historical Background

Thin ZnO films have been deposited on a wide variety of substrates (amorphous to single crystals), by PLD employing nanosecond or femtosecond lasers. The pulse duration plays an

important role in the crystalline state of the PLD-grown ZnO films, and this will be presented and discussed in Section 12.4. Here we will focus on the influence of the main experimental growth conditions.

The first studies regarding laser ''sputtering'' of ZnO were performed using a tunable dye laser [Nakayama et al., 1982; Nakayama, 1983]. Although the authors were not interested in growing thin films, several important findings were reported that are still valid: (i) nonlinear dependence of ablation yield on the laser fluence, (ii) laser ablation is a threshold process, (iii) the value of the threshold depends on the laser wavelength, and (iv) non-Maxwellian velocity distribution of ejected particles. Based on these characteristics, it was assumed that laser ablation is a nonthermal process, related to the dense electron–hole plasma [Nakayama, 1983]. After many detailed studies, it is now believed that laser ablation with nanosecond (ns) pulses is essentially a thermal process, although a complex and not yet fully understood one.

The first report about PLD of ZnO films used a pulsed CO_2 laser to ''evaporate'' a ZnO target [Sankur and Cheung, 1983]. Regardless of the nature of the substrate, smooth and transparent ZnO films were highly textured with the (0002) planes parallel to the substrate. The electrical conductivity depended on the oxygen pressure used: Films deposited at low oxygen pressure were conductive while those deposited under an oxygen glow discharge at about 10^{-2} mbar, as well as annealed films, were found to be highly insulating. The deposited films also exhibited piezoelectric properties with an insertion loss at 240 MHz of 65 dB when measured in an interdigitated transducer.

The next major step in the development of the PLD of ZnO was the use of nanosecond-pulsed lasers, Nd : YAG and excimer, that offer many advantages with respect to pulsed CO_2 lasers. The quality of the deposited films was improved, more so for the films deposited using the KrF laser (248 nm). Very detailed studies regarding the optimization of nanosecond-pulsed laser ablation of ZnO [Ianno et al., 1992] showed that the optimum laser fluence is around 2–3 J/cm^2, while the oxygen pressure for conducting and highly textured and dense films should be around $2–3 \times 10^{-3}$ mbar, depending on the target–substrate distance used. Using these conditions, as shown in Figure 12.1, ZnO films that exhibited a full-width at half-maximum (FWHM) of the rocking curve around 2° were deposited at 350°C [Craciun et al., 1994]. These films also exhibited a dense columnar structure and a relatively smooth surface morphology.

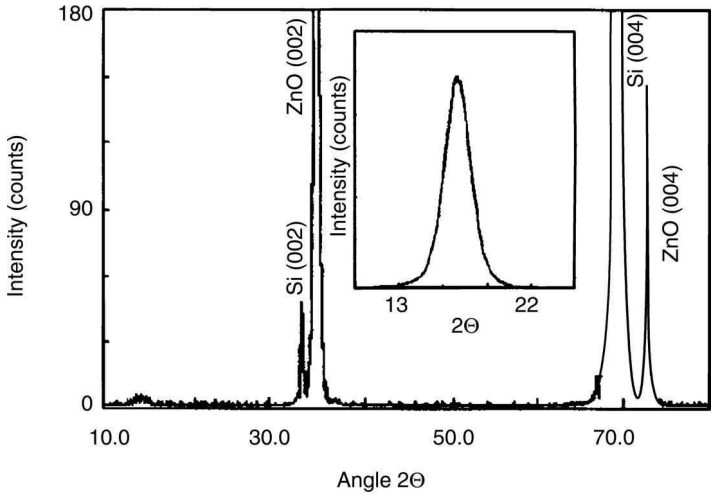

Figure 12.1 XRD pattern of a ZnO film grown by PLD (KrF laser 248 nm, fluence 2.1 J/cm^2) on a Si substrate at 350°C under an oxygen pressure of 2.5×10^{-3} mbar. From Craciun et al. [1994], used with permission from the American Institute of Physics.

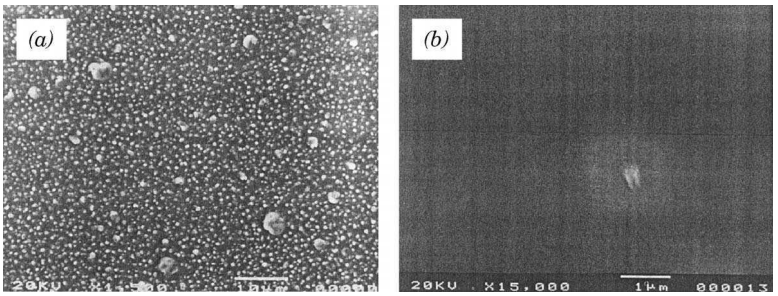

Figure 12.2 SEM images of ZnO films grown by PLD at (a) 1064 nm and (b) 248 nm wavelengths. From Ianno et al. [1992] used with permission from Elsevier.

12.2.2 Surface Morphology and Texture

It has been found experimentally that ZnO deposited by 248- or 266-nm lasers exhibited a far superior morphology than films deposited with 532- or 1064-nm lasers, regardless of the experimental conditions. As a matter of fact, scanning electron microscopy (SEM) of ZnO films deposited with 1064 nm (Fig. 12.2a) presents a high density of particles, while the films deposited with 248-nm laser radiation are essentially featureless (Fig. 12.2b) [Ianno et al., 1992]. It has been suggested that a laser wavelength that is absorbed in a larger volume, such as 532 or 1064 nm, where the optical absorption coefficient of the ZnO target is lower than $10^4\ \text{cm}^{-1}$, results in volume heating and the formation of a rather deep liquid pool that lasts for hundreds of nanoseconds. Under these conditions it is possible to experience subsurface volume boiling that will result in the ejection of a large quantity of micrometer-sized droplets [Craciun and Craciun, 1999]. In the case of 248- or 266-nm laser irradiation, because the optical absorption coefficient is much higher, above $5 \times 10^5\ \text{cm}^{-1}$, the liquid pool that forms is very thin, and the heterogeneously or homogeneously nucleated bubbles cannot reach the critical dimension and afterwards explode and splash the substrate with droplets. Clear indication of volume boiling was found by SEM investigations of the target surface after laser irradiation with different wavelengths [Craciun et al., 1995]. It is worth mentioning that similar target morphologies exhibiting cavities created by subsurface volume boiling have been found for a large number of oxide and semiconductor targets whenever the laser wavelength used for ablation was poorly absorbed.

A further proof of the key role of the optical absorption coefficient in the subsurface volume boiling effect as a source for droplets emission was evidenced by inducing changes in the optical properties of the target at the laser wavelength used for ablation and monitoring the droplets density [Guillot-Noel et al., 1996]. Owing to the energy bandgap of ZnO (3.3 eV), the optimum laser wavelength must therefore be lower than 380 nm. Nowadays, by using such lasers the formation of smooth, dense, optically transparent, electrically conductive, and crystalline hexagonal ZnO thin films by PLD is widely reported.

ZnO thin films deposited by PLD at room temperature are found to be amorphous or poorly crystalline, their X-ray diffraction diagrams only showing broad peaks that may be attributed to some glasslike structure or very small crystallites. With increasing substrate temperatures (higher than 200°C), rather well-defined peaks are observed in the diffraction patterns. The patterns generally exhibit only the (0002) and (0004) lines indicating a textured growth: the ZnO films tend to be *c*-axis oriented with their hexagonal basal plane parallel to the substrate, regardless of the nature of the substrate. Indeed, on amorphous substrates or crystalline substrates having hexagonal symmetry, the ZnO films generally grow with (000l) texture.

The texture in thin-film growth is classically explained by a minimization of the surface free energy: γ_f, γ_s, γ_i, and γ_e being the free surface energy for the film–air, substrate–air, film–substrate interfaces, and the epitaxial energy gain, respectively, the surface free energy increases due to

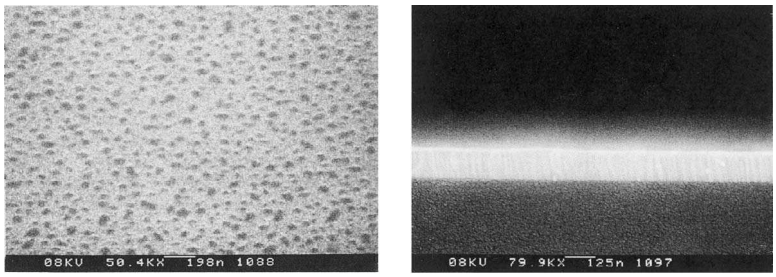

Figure 12.3 SEM images of a ZnO film grown by PLD (KrF laser 248 nm, fluence 2.1 J/cm^2) on a Si substrate at 350°C under an oxygen pressure of 2.5×10^{-3} mbar: (a) top view of the surface and (b) cross section. From Craciun et al. [1994], used with permission from the American Institute of Physics.

the presence of the film as given by $G = (\gamma_f - \gamma_s) + \gamma_i - \gamma_e$. The film will thus grow in the orientation leading to a minimum value of G. In the case of an epitaxial thin-film growth, the γ_e term can become predominant and impose a specific texture on the film. We have observed such a situation for the growth of hexagonal ZnO films on some cubic substrates, otherwise the γ_f is predominant and imposes a specific texture corresponding to the lower surface free energy. It is thus tempting to conclude that the (000l) plane of the ZnO has a lower surface free energy. However, this does not take into account the fact that ZnO is a polar crystal (alternate stacking of Zn and O planes) with a net dipole moment on the (000l) basal plane. This causes the surface free energy to diverge, while the other prismatic planes have a lower surface free energy [Tasker, 1979]. Therefore to minimize the surface free energy, in the first step of the growth, ZnO islands with the (000l) texture will nucleate [to minimize the (000l) plane area] [Goria et al., 1999], and the high growth rate along this *c*-axis will lead to columnar growth that is classically observed in ZnO thin films (see Fig. 12.3). Thin ZnO films therefore exhibit a rather smooth morphology. However, if the thickness is increased, then submicron structures having a pyramidal shape with a hexagonal base start to appear [Vasco et al., 2001].

With increasing temperature (from 300 to 750°C), the height of the diffraction peaks increases, while the FWHM of the peaks decreases, indicating an improvement of the quality of crystalline growth. This low temperature for crystalline thin-film formation is one of the advantages of the PLD technique, which can be related to the kinetic energy of the species (in the 10- to 100-eV range), which are emitted by the target at each laser pulse. This high kinetic energy enhances the surface mobility of these species and enables the growth of crystalline films. The expansion of the plume created for each laser pulse irradiation of a ZnO target has been studied by spatially and temporally resolved optical spectroscopy [Claeyssens et al., 2002]. Such analytical methods allow the determination of the nature and energy of the various species present in the plasma. The plume produced by pulsed laser ablation of a ZnO target at 193 nm in vacuum is characterized according to optical emission spectra with species assignable to electronically excited Zn^{+*} cations and Zn^* and O^* neutrals together with an accompanying subset of fast electrons [Claeyssens et al., 2002].

12.2.3 Control of the Stoichiometry

The stoichiometry of ZnO films is an important parameter that plays a major role on their physical properties. This point is important since the conductivity of ZnO thin films is, among other parameters, a function of the oxygen vacancy concentration. In fact, oxygen vacancies create defect states in the bandgap energy of ZnO that induce the green deep-level emission in photoluminescence. These defect states are responsible for an absorption in the visible region and for optical

losses in waveguide configurations. Therefore, for electrical and optical applications, oxygen deficiency in PLD-grown ZnO films has to be avoided.

The origin of a Zn-to-O ratio greater than unity in the ZnO films must be related to the optimized growth conditions by PLD. On one hand, vacuum or very low oxygen pressures often used in PLD correspond to growth conditions involving an unbalanced incorporation of zinc and oxygen atoms in the films. On the other hand, ZnO being able to sublime when heated above 1200°C, Zn atoms could recondense on the film surface after repeated laser irradiation while the oxygen is lost by vacuum pumping. Indeed nonstoichiometric film growth is assumed to be the norm when PLD is carried out under conditions leading to the formation of a sufficiently dense plasma to cause material redeposition on the target [Claeyssens et al., 2002].

The various published papers reporting on the influence of oxygen pressure on the crystalline state of ZnO films present some differences from the growth conditions considered to be optimum. The reason behind this relates to the fact that the oxygen pressure P and target-to-substrate distance d are not independent parameters, and the following relationship has been experimentally determined: $P \times d^{\gamma} = \text{constant}$, γ being a positive exponent depending upon the materials [Kwok et al., 1997].

The growth process of ZnO thin films generally includes a cooling down step under high oxygen pressure (about 100 mbar), to incorporate oxygen in the films after the high-temperature deposition [Pons Y Moll, 2003]. Such a procedure has been found efficient, according to the fact that UV–visible absorption spectroscopy of such films shows a high transmittance followed by a quite sharp absorption edge at 3.3 eV, the bandgap energy value of ZnO single-crystal material.

Another approach has been proposed to facilitate the incorporation of oxygen atoms in the films. It has been known from the investigations of HTC (high temperature superconducting) thin-film deposition that the use of a more reactive oxygen atmosphere such as N_2O or ozone has a beneficial effect on the quality of the deposited film. To obtain ozone and atomic oxygen inside the deposition chamber, a low-pressure Hg lamp that emits 185 nm radiation, which can photodissociate molecular oxygen, has been used in some experiments. Since UV photon bombardment of the substrate during deposition has shown to increase the crystallinity of the deposited film, the lamps were positioned to face the substrate [Craciun et al., 1999, 2000]. It has been suggested that adatoms that absorb UV photons can have a higher surface mobility and therefore can travel larger distances until they find lower energy lattice positions or are desorbed. Although the enhanced mobility could explain the improved crystallinity measured from films deposited under otherwise identical conditions, it has yet to be proved directly. The enhanced desorption was confirmed by a relatively lower growth rate during UV-assisted PLD than conventional PLD. The application of this UV-assisted PLD technique resulted in the growth of epitaxial ZnO layers on sapphire substrates that exhibited similar quality to the ZnO layers deposited at substrate temperatures at least 200°C higher [Craciun et al., 1999, 2000].

The use of a rather high oxygen pressure, of the order of 10^{-3}–10^{-2} mbar, during deposition might cause an additional problem. Although the ZnO contains some oxygen vacancies and the films are conductive, there are some oxygen atoms that are trapped inside the grown oxide layer. These oxygen atoms give rise to a shoulder toward higher binding energy in the O_{1s} X-ray photoelectron spectroscopy (XPS) spectrum [Craciun et al., 2000] that has also been observed in RF-sputtered films grown at similar oxygen pressures [Puchert et al., 1996; Chen et al., 2000c]. Several studies attributed this shoulder to OH or H_2O species absorbed in the film [Meng et al.,1994; Lu et al., 2000]. However, it has been shown that the area of this shoulder depends on the oxygen pressure used during ablation, and it was usually smaller for films deposited using UV-PLD because the oxygen pressure is lower than that used during conventional PLD. Moreover, films deposited at very low pressures or metallic films oxidized in situ did not exhibit this peak, thus ruling out the explanation that this shoulder is due to hydroxides formed during atmospheric exposure. These results seem to indicate that PLD of oxides deposited at relatively high oxygen pressures might contain loosely bound oxygen or physisorbed oxygen species. Further investigations to clarify this aspect are under way.

12.2.4 Recent Applications and Developments

Due to its wide bandgap, ZnO is a material transparent both in the visible and near UV–visible regions, and is electrically conductive (*n*-type). It has been used therefore for transparent conducting electrodes in place of expensive Sn-doped In_2O_3, for flat-panel displays and solar cells [Hu and Gordon, 1992]. Doping with various elements (Al, Ga, In) is a well-known route to increase the electrical conductivity [Suzuki et al., 1996; Hiramatsu et al., 1998]. As a result, Al-doped zinc oxide (AZO) thin films have been used as an anode contact for organic light-emitting diodes (OLED) [Kim et al., 2000], and see Chapter 11. Figure 12.4 shows the characteristics of an OLED with an AZO anode. The device structure used in this work is shown in the inset of Figure 12.4a. The external quantum efficiency was about 0.3% at a current density of 100 A/cm^2, and this low efficiency is due to the low work function of AZO. However, the low work function of AZO makes it an attractive candidate for use as the cathode in OLEDs [Kim et al., 2000].

In another work, ZnO has been used as an active channel layer in a transparent thin-film transistor (TFT) that can operate in the presence of visible light [Masuda et al., 2003]. In this device, a double gate insulator consisting of SiO_2 and SiN_x was effective in suppressing leakage current and enabling

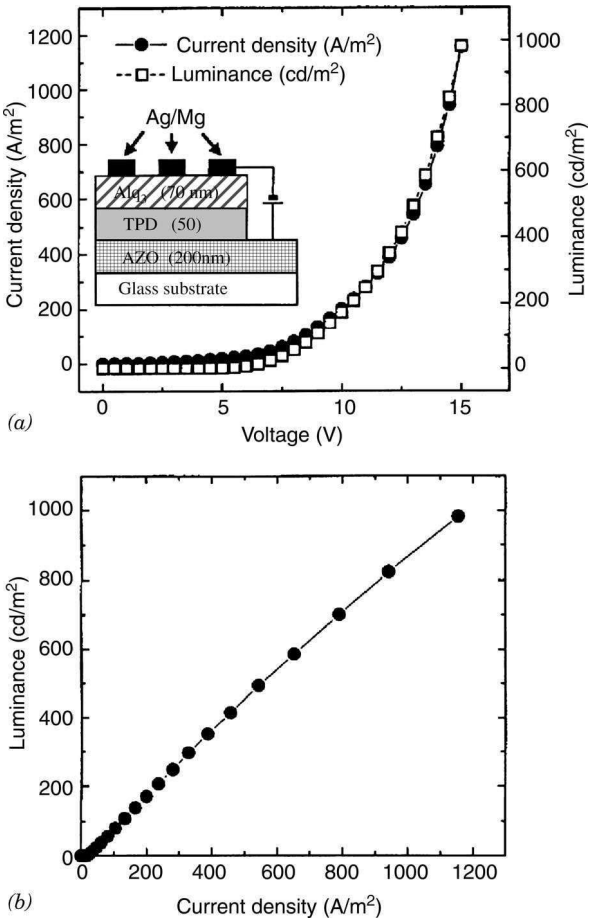

Figure 12.4 (a) Current density–voltage–luminance (J-V-L) and (b) luminance–current density (L-J) characteristics of a heterostructure device schematically represented in the inset of (a). From Kim et al. [2000], used with permission from the American Institute of Physics.

the ZnO-TFT to operate successfully. The I_{on}/I_{off} ratio was more than 10^5 for transistors fabricated on Si wafers, while the optical transmittance of transistors fabricated on glass substrate was more than 80%.

An interesting point relates to (000l)-oriented ZnO films grown by PLD on amorphous substrates. Such textured films on fused silica substrates were used as alignment layers for the growth of *c*-axis-oriented GaN films [Xiao et al., 1996]. Moreover, these semiconducting ZnO buffer layers can also be used as transparent electrodes for GaN in the fabrication of photonic devices. ZnO luminescent films have been prepared on indium-tin-oxide-(ITO)-coated glass substrates deposited by PLD at room temperature [Wei et al., 2001]. A postdeposition annealing treatment was necessary to observe luminescent characteristics. Similarly, ZnO films have been grown by PLD on GaAs [Ryu et al., 2000a, 2000b]. Despite the fact that these textured ZnO films do not exhibit exceptional crystalline quality, very strong emission features associated with exciton transitions were observed, making ZnO films on GaAs a plausible system for short-wavelength visible or UV light-emitting diodes (LEDs).

A great deal of work has been carried out on the photoluminescence properties at 1.54 μm of Er-doped low-bandgap semiconductors. However, the low efficiency of luminescence at room temperature precludes any real applications. This thermal quenching was found to decrease with increasing bandgap energy of the semiconducting material. ZnO appeared thus as an interesting material to limit this thermal quenching. The optical properties of Er-doped ZnO have therefore been investigated [Komuro et al., 1999, 2000a, 2000b] in view of lightwave communication devices such as LEDs, laser diodes, or optical amplifiers. The results seem to be strongly dependent upon the precise growth process [Komuro et al., 2000a, 2000b; Pons Y Moll, 2003].

For numerous applications, it is necessary to grow both *p*- and *n*-type ZnO films: *n*-type ZnO films are easily obtained through various doping of elements such as Al, Ga or In, but the formation of *p*-type ZnO presents some difficulties. Synthesis of *p*-type ZnO film by arsenic doping has been reported on (00l) GaAs substrates [Ryu et al., 2000c]. During deposition at a sufficiently high temperature (450°C), arsenic atoms from the GaAs substrate can diffuse into the growing ZnO layer. This leads to As concentrations in ZnO in the 10^{17}–10^{21} atoms/cm^3 range, depending on the conditions. Being a good acceptor, *p*-type films are obtained with an acceptor peak located at 3.2 eV with a 100-meV binding energy. However, the problems related to the solubility of As in ZnO and possible secondary phase formation have also to be considered [Pearton et al., 2003].

As nitrogen is an acceptor in ZnSe, it has also been considered to be a good acceptor candidate for ZnO. Nitrogen incorporation can be improved by the use of atomic nitrogen created in a nitrogen plasma [Basillais et al., 2000], but nitrogen plasma-assisted PLD of ZnO films does not lead to the formation of *p*-type ZnO films despite nitrogen incorporation [Pearton et al., 2003]. Following theoretical considerations, it has been proposed that co-doping of donor and acceptor dopants can promote the formation of *p*-type ZnO [Yamamoto and Yoshida, 1999]. PLD of a Ga-doped ZnO target in the presence of nitrogen atoms coming from an electron cyclotron resonance plasma source has been used therefore to check this point [Joseph et al., 1999, 2000]. A poor reproducibility in the results was obtained, but *p*-type films with a hole concentration of 4×10^{19} cm^{-3} and a room temperature resistivity of 2 Ω cm have been formed with this process. Further studies were then carried out to precisely determine the optimal conditions on the ratio of Ga and N concentrations for the formation of *p*-type ZnO films [Sumya et al., 2003; Tsukazaki et al., 2002], but no clear conclusions can be drawn since the results depend upon processing conditions and are very difficult to reproduce [Pearton et al., 2003]. The formation of reliable *p*-type ZnO films by the co-doping method is still an open problem.

12.3 ZnO EPITAXIAL THIN FILMS

Many applications of ZnO thin films only require polycrystalline material without a serious need for films free from structural defects. However, when considering future applications dealing with

optical devices such as lasers or LEDs, high-quality epitaxial thin films have to be obtained. In fact, ultraviolet laser emission has been observed above room temperature in epitaxial ZnO thin films [Ohtomo et al., 1998a; Bagnall et al., 1997], leading to a large number of publications devoted to the formation of ZnO epitaxial layers.

12.3.1 ZnO Epitaxial Growth on Sapphire

A large volume of the work on the study of the growth of epitaxial ZnO thin films by PLD, used *c*-cut Al_2O_3 single crystals as substrates. Despite the large lattice mismatch in their basal hexagonal planes (the in-plane parameters are 0.3249 and 0.4758 nm, respectively, for ZnO and Al_2O_3), rather good crystalline quality ZnO thin films have been obtained by PLD and reported by various groups [Vispute et al., 1997; Narayan et al., 1998; Craciun et al., 1999], with FWHM rocking curves lower than 0.05°. Complementary information on the presence of structural defects in the films can be obtained by Rutherford backscattering (RBS) measurements in channeling geometry (Fig. 12.5), via the ratio of channeling to random yield, that is, the χ_{min} value. The χ_{min} values as low as 2% have been measured in the surface region of ZnO films, close to the value for ZnO single crystals, indicating a low level of structural defects in such films at least in the surface region [Craciun et al., 1999]. In fact the increase in backscattering yield toward lower energies in the RBS spectrum shown in Figure 12.5 indicates an increasing concentration of defects toward the interface with the substrate, a phenomenon that is classically observed in epitaxial thin films in the case of a large lattice mismatch between film and substrate.

The in-plane orientation of the ZnO films on *c*-cut sapphire can be determined by asymmetrical X-ray diffraction, and a typical pole figure of the $(10\bar{1}1)$ ZnO plane is shown in Figure 12.6. The presence of six poles for the $(10\bar{1}1)$ ZnO demonstrates a sixfold symmetry with a rotation of 30° of the ZnO axes with respect to the sapphire axes [Narayan et al., 1998; Craciun et al., 2000]. The epitaxial relationship that can be deduced from this pole figure is the following: ZnO (0001) $[10\bar{1}0]$ // Al_2O_3 (000l) $[11\bar{2}0]$, and this has also been reported for the growth of ZnO films on sapphire by other deposition methods [Goria et al., 1999; Chen et al., 1998; Kang et al., 1998].

Such an epitaxial relationship is related to the fact that the direct stacking of ZnO hexagons on Al_2O_3 hexagons would lead to a very large lattice mismatch (higher than 30%), which precludes the

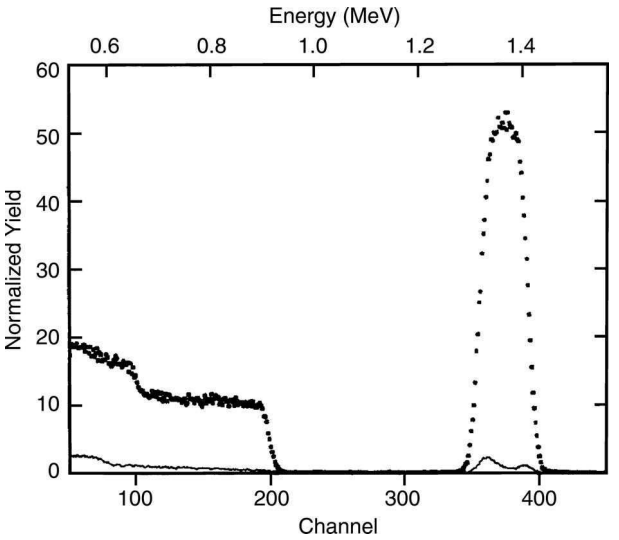

Figure 12.5 RBS spectra in random (black line) and channeling (dots) geometries for a ZnO film epitaxially grown on a *c*-cut sapphire substrate. From Craciun et al. [1999], used with permission from Springer-Verlag.

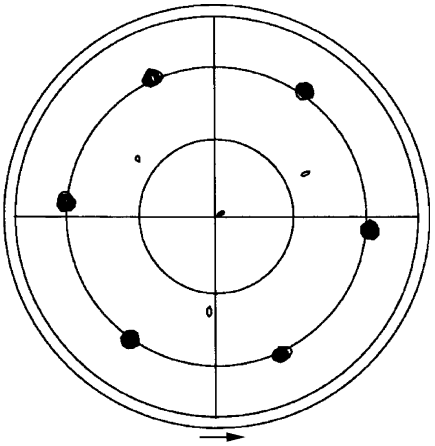

Figure 12.6 $(10\bar{1}1)$ ZnO pole figure recorded for a ZnO film epitaxially grown on a *c*-cut sapphire substrate. From Craciun et al. [1999], used with permission from Springer-Verlag.

existence of such an epitaxial orientation. A better situation is obtained by a 30° rotation of the ZnO hexagons with respect to the sapphire unit cell as schematically illustrated in Figure 12.7, in which the $[2\bar{1}\,\bar{1}0]$ orientation of ZnO aligns with the $[1\bar{1}00]$ direction of Al_2O_3.

With this 30° rotation the lattice mismatch (18%) between film and substrate in this direction, can be drastically reduced by considering the "domain matching epitaxy" [Narayan et al., 1998] in which *p* ZnO unit cells match with *m* Al_2O_3 unit cells. In that case, by the coincidence of 6ZnO distances with $7Al_2O_3$ distances, the lattice match decreases toward 1.38%, leading therefore to a low level of residual strain in the ZnO film. This situation means that the Zn atoms of the first ZnO plane are bound with the oxygen atoms of the last plane of the sapphire substrate. It is presumed in this case that the surface plane of the Al_2O_3 substrate is an oxygen plane, which is generally observed for ionic oxides [Sun et al., 1994].

It is worth noting that heteroepitaxial thin films with a large lattice mismatch with the substrate commonly exhibit a high concentration of structural defects near the interface, which lead to

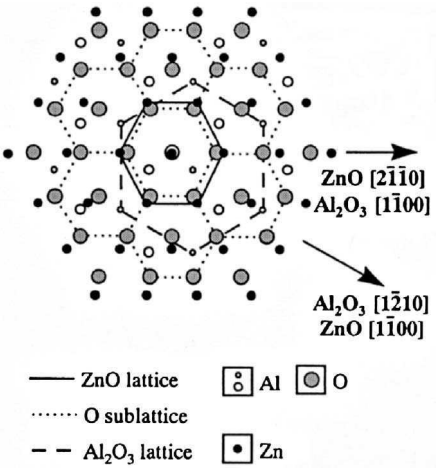

Figure 12.7 Schematic diagram showing the epitaxial relationship of ZnO (000l) grown on Al_2O_3 (000l). From Chen et al. [1998], used with permission from the American Institute of Physics.

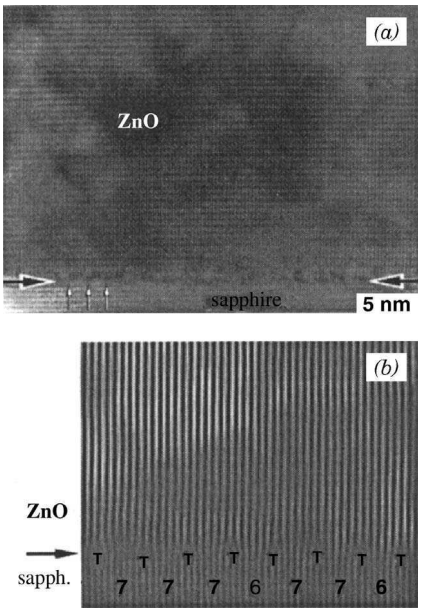

Figure 12.8 (a) High-resolution TEM cross-sectional image of the ZnO film near the film–substrate interface. The terminating planes corresponding to the misfit dislocations are indicated by small white arrows. (b) Fourier-filtered image using opposite $\{10\bar{1}0\}_{ZnO}//\{11\bar{2}0\}_{sapphire}$ reflexes showing the match of the corresponding planes. Misfit dislocations at the interface are indicated. From Narayan et al. [1998], used with permission from the American Institute of Physics.

dechanneling effects observed in Figure 12.5. Most of these defects are dislocations and planar defects (stacking faults). High-resolution transmission electron microscopy has been used [Narayan et al., 1998] to investigate the nature of the ZnO–sapphire interface and the defects that are present. The TEM micrograph presented in Figure 12.8a, clearly shows that this interface is atomically sharp, without any interdiffusion layer between film and substrate. The dislocations are present at this interface when every seventh $(2\bar{1}\,\bar{1}0)$ plane of sapphire terminates at this interface [Narayan et al., 1998]. The domain lattice epitaxy governing this epitaxial growth is shown in Figure 12.8b, where there is a missing plane in the film after every six to seven substrate planes.

The electrical and optical properties of ZnO provide a very sensitive indicator of the material quality [Ashkenov et al., 2003; Bae et al., 2000; Washington et al., 1998; Zeng et al., 2002]. The relatively low carrier mobility of the ZnO films is due to grain boundary scattering, the presence of a high concentration of grain boundaries being related to the incoherent growth associated with the large lattice mismatch. Moreover, structural defects, doping, impurity, and strain in the films broaden or shift the exciton resonance and increase the broadband deep-level emission, which is observed in photoluminescence experiments [Shim et al., 2002; Ong et al., 2002]. A typical photoluminescence spectrum recorded for a ZnO epitaxial film is shown in Figure 12.9, with the exciton contribution at 370 nm and the broad luminescence centered around 600 nm [Sun and Kwok, 1999]. Numerous papers have therefore reported that the physical properties of ZnO thin films grown by PLD were found to show a strong correlation with their crystalline state (mosaicity, grain size, and residual stresses) [Jin et al., 2001a; Bae et al., 2000, 2001]. As a matter of fact, the defects evidenced at the film–substrate interface (see Fig. 12.8) have large consequences on the ZnO optical properties [Sun and Kwok, 1999]. By using cathodoluminescence, it is possible to study the ZnO in-depth luminescence, and it has been found that the deep-level emission intensity increases with depth, that is, toward the film–substrate interface, due to the poor interfacial crystal quality [Ong et al., 2001]. Moreover, a strong dependence has been observed between the intensity ratios of this defect

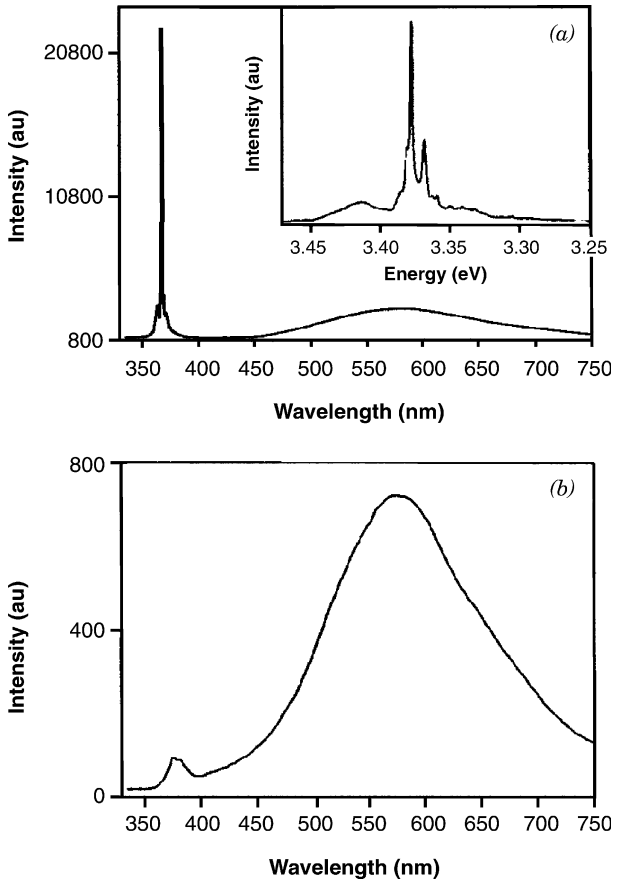

Figure 12.9 (a) Photoluminescence spectrum of a ZnO film grown on *c*-cut sapphire measured at 10 K. The inset depicts the energy spectrum of the band-edge luminescence. (b) Photoluminescence spectrum measured at room temperature. From Sun and Kwok [1999], used with permission from the American Institute of Physics.

emission to the excitonic emission and the structural imperfection of the epitaxial ZnO layers [Ong et al., 2002].

To improve the physical properties of epitaxial ZnO films, various techniques have been explored. For example, the effects of a postdeposition anneal in oxygen at an elevated temperature (800°C) were studied, and it was found that such oxygen annealing improved the resistivity, luminescence properties, and excitonic features. These improvements were likely due to the reduction of excess zinc, removal of point defects, and better crystallinity [Muth et al., 1999]. Moreover, other results showing that the oxygen pressure during PLD mainly controls the growth mode, degree of epitaxy, and defect density [Jin et al., 2000a, 2000b; Bae et al., 2001], led to the definition of a two-step process in which a low oxygen pressure (10^{-4}–10^{-3} mbar) is used in the initial stages of growth to control the epitaxy of the film, while a higher pressure (about 10^{-2} mbar) is then used to obtain smooth films with high optical quality, high electron mobility, and low background carrier concentration [Choopun et al., 1999].

To improve the crystalline quality of ZnO thin films on *c*-cut sapphire substrates, another method is based on the use of buffer layers between film and substrate. Based on an approach already verified for the growth of GaN epitaxial layers, the insertion of a low-temperature (about 500°C) deposited ZnO layer has been used to optimize the film quality [Nakamura et al., 2002; Kaidashev et al., 2003].

The ZnO films subsequently grown on such low-temperature buffer layers were found to be of higher crystalline quality (a decrease of the FWHM rocking curve by more than 50%), with the surface morphology and flatness being also improved. Photoluminescence spectra showed the intensity of the deep-level green emission at 2.3 eV to be negligible compared to the excitonic emission. Moreover, this excitonic emission presented a very narrow photoluminescence linewidth of 1.7 meV at low temperature [Kaidashev et al., 2003]. These results are believed to be due to the fact that the low-temperature buffer layer relaxes the strain due to the lattice mismatch [Nakamura et al., 2002].

The use of a GaN buffer layer on sapphire to grow epitaxial ZnO thin films by PLD has been also explored [Vispute et al., 1998]. RBS, ion channelling, and high-resolution TEM revealed that high-quality epitaxial ZnO films have been grown by PLD on epitaxial GaN layers on sapphire (0001) substrates. These ZnO on GaN heterostructures, which showed good luminescence properties, demonstrate the feasibility of integrating ZnO/GaN optoelectronic devices [Vispute et al., 1998]. In the same way, the use of a thin MgO buffer layer on Al_2O_3 substrates improves the surface morphology of the ZnO films grown on such structures, leading to an atomically flat surface and better crystallinity of the epitaxial ZnO layers [Chen et al., 2000a].

It is worth noting that the epitaxial growth of a film on a substrate with a large lattice mismatch generally leads to the nucleation of isolated islands with a further lateral expansion and coalescence of these islands during growth, that is, a columnar growth is observed as in the case of ZnO on sapphire. However, if a regular step array is present on the substrate surface, these steps will act as traps for the deposited species and will promote a rapid lateral growth suppressing the island nucleation and as a result the columnar growth would be avoided. Such a process has been observed during the ZnO film growth on $MgAlO_4$ (111)-oriented substrates, presenting regular terraces (450 nm width and 0.47 nm height), obtained by specific chemical pretreatment of the substrate [Chen et al., 2000b]. Despite the 8% lattice mismatch, X-ray diffraction, photoluminescence, and electrical measurements indicate that high-quality ZnO epitaxial layers were obtained in this way by plasma-assisted molecular beam epitaxy [Chen et al., 2000b].

12.3.2 ZnO Epitaxial Growth on Other Substrates

To overcome all the structural defects induced in ZnO films by the lattice mismatch to sapphire, other substrates have been considered for growth of epitaxial ZnO thin films. Hexagonal $ScMgAlO_4$ (0001) with a lattice constant of $a = 3.246$ Å leading to a lattice mismatch as low as 0.09% has therefore been employed for the PLD growth of ZnO. The crystalline quality of such films grown on $ScMgAlO_4$ shows a drastic improvement with respect to sapphire substrates [Ohtomo et al., 1999b; Makino et al., 2000a]. The films present the following epitaxial relationship ZnO(000l)[$11\bar{2}0$]// $ScMgAlO_4$(0001)[$11\bar{2}0$], that is, a perfect hexagon-on-hexagon growth. The FWHM of rocking curves as low as 0.01° were routinely obtained, while the in-plane orientation fluctuations were limited ($<0.02°$). Such films presented a high surface smoothness with improved electrical properties [Ohtomo et al., 1999a]: Indeed, room temperature Hall measurements indicate a high electron mobility (100 cm^2/Vs) and a low n-type residual carrier concentration (10^{15} cm^{-3}).

ZnO films epitaxially grown on $ScMgAlO_4$ also present improved optical properties, as indicated by photoluminescence measurements [Makino et al., 2002; Koida et al., 2003]. An intense bound exciton emission at 3.36 eV was observed in such films, while the green deep-level emission was negligible. In addition, the linewidth of emission line due to excitons was claimed [Makino et al., 2002] to achieve the smallest recorded value of less than 0.8 meV, that is, a value six times lower than that of the best ZnO films grown on c-cut sapphire substrates. Therefore, the use of lattice-matched $ScMgAlO_4$ substrates greatly improved not only the crystalline quality but also their optical properties. As a result, such an improvement could lead to a reduction in the pumping threshold for laser action, induced by the narrowed width of exciton states [Makino et al., 2002].

ZnO epitaxial films were also grown on $LiNbO_3$ (0001) substrates by PLD. The smaller lattice misfit (8.5%) between the [$10\bar{1}0$] ZnO direction and $LiNbO_3$ along the [$11\bar{2}0$] direction, as compared with that for the case of sapphire substrates favored the epitaxial growth of ZnO films [Yin et al., 2000].

Although an overall characterization of the optical properties of the ZnO films was not reported, the transmittance spectra of these ZnO films showed a sharp absorption edge at 375.6 nm. The heteroepitaxial growth by PLD of ZnO films on yttria-stabilized zirconia (YSZ) single crystals has also been considered [Ohta et al., 1999]. The (111)-oriented YSZ substrates were used and at a 800°C substrate temperature, epitaxial ZnO films presenting an atomically flat surface were obtained with the following in-plane orientation: ZnO [11$\bar{2}$0]//YSZ [110], related to a specific domain matching epitaxy. The influence of film thickness was evidenced through a correlated increase of crystalline grain size and Hall mobility in the epitaxial ZnO layers [Ohta et al., 1999]. The epitaxial growth of ZnO thin films was also studied on various single-crystals substrates such as (La,Sr)TiO_3 [Sugiura et al., 2002], InP [Ramamoorthy et al., 2001], and NaCl [Henley et al., 2002].

Silicon has been also tested as a substrate for ZnO epitaxial growth. In that case, AlN and GaN thin films were used [Tiwari et al., 2002a] as buffer layers to promote the epitaxial growth of ZnO thin films on (111)-oriented Si single crystals. Such ZnO films grown on AlN or GaN layers were found to be epitaxial with preferred in-plane orientation, while those directly grown on Si (111) only showed a textured structure. These films possessed noticeable tensile strain that led to major effects on the physical properties of the ZnO grown material [Tiwari et al., 2002a].

12.3.3 Epitaxial Growth of ZnO-Related Compounds

Among the doped or alloyed ZnO compounds, the most interesting case seems to be $Mg_xZn_{1-x}O$ according to the very specific structural and physical properties [Ohtomo et al., 1998b; Sharma et al.,1999; Teng et al., 2000a], which can be obtained as a function of the Mg concentration: By changing the Mg concentration from $x = 0$ to $x = 1$, the bandgap of this compound can be tuned from 3.3 to 7.8 eV. Precise analyses reveal the evolution of $Mg_xZn_{1-x}O$ bandgap energy and crystal structure with the composition, and this is schematically summarized in Figure 12.10 [Yang et al., 2003]. For an Mg composition lower than 37%, $Mg_xZn_{1-x}O$ presents the classical hexagonal wurtzite structure (h-MgZnO), and the bandgap varies from 3.3 to 4.28 eV in this composition range. A pure cubic phase (c-MgZnO) is observed for Mg concentration higher than 62%, and the bandgap energy varies from 5.4 to 7.8 eV in this region. For an Mg composition lying between 37 and 62%, a mixing of the hexagonal and cubic phases is obtained, while the bandgap varies between the range of 4.3 to 5.4 eV.

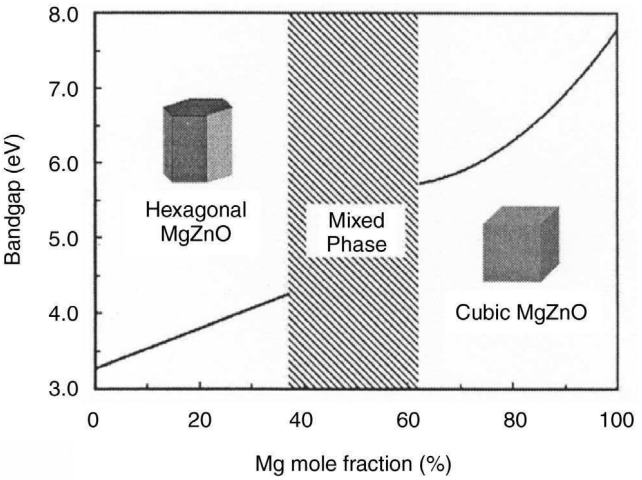

Figure 12.10 Bandgap energy as a function of Mg content in $Mg_xZn_{1-x}O$ films. The films have the wurtzite and cubic crystal structure for Mg composition $<37\%$ and $>62\%$, respectively. From Yang et al. [2003], used with permission from the American Institute of Physics.

The epitaxial growth of $Mg_xZn_{1-x}O$ in these two phases was studied by PLD on different substrates. $Mg_{0.34}Zn_{0.66}O$ thin films with the hexagonal wurtzite structure were thus grown on *c*-cut sapphire substrates [Ohtomo et al., 1998b; Yang et al., 2001], under experimental conditions similar to the growth of ZnO on this substrate. Highly oriented *c*-axis films were obtained with narrow rocking curves (FWHM = 0.14°), and RBS ion channeling studies show a χ_{min} value of 5%, characteristic of a rather good crystalline quality. The Φ scan measurements confirm the epitaxial growth of the h-MgZnO films on sapphire substrates with the 30° rotation of the film axis with respect to the substrate axis, which is also observed for the case of ZnO wurtzite growth on *c*-cut sapphire.

The growth of c-MgZnO films was also reported [Yang et al., 2003]. In this case, Si (100) single-crystal substrates were used, and to overcome the large lattice mismatch between film and substrate, a $SrTiO_3$ buffer layer was grown on Si before the c-MgZnO film formation. This buffer layer was epitaxially grown on the Si substrate and leads to the formation of c-MgZnO films showing sharp diffraction peaks, with a moderate mosaicity (FWHM = 0.23°). RBS in channeling geometry allowed the determination of the optimal conditions for high crystalline quality: A χ_{min} value of 4% for Zn in the near surface region was obtained for substrate temperatures in the 400–500°C range. Higher temperatures lead to an increase in the χ_{min} values, surface roughness, and mosaicity of the films. The epitaxial relationships between the buffer layer and Si substrate and between the c-MgZnO film and buffer layer were studied by Φ scan measurements. The c-MgZnO and $SrTiO_3$ films follow a cube-on-cube alignment, with a 45° rotation of the unit cell with respect to the in-plane Si axes [Yang et al., 2003].

12.3.4 Main Applications of Epitaxial ZnO Films

12.3.4.1 Buffer Layers

Due to their emerging applications in optoelectronics, GaN thin films have been grown on a variety of substrates. Among them, sapphire appears as the most interesting as it can be obtained in large-area wafers at a low cost. However, its poor structural and thermal match to GaN leads to nitride films grown on Al_2O_3 containing a high density of defects, which affect the resultant electrical properties of the GaN films. As the lattice mismatch between GaN and ZnO is quite small (2.2% in their basal plane), ZnO has been considered as a promising substrate material for GaN growth. However, the cost of ZnO substrates is very high and large-area ZnO single-crystal substrates are not presently commercially available. An alternate approach is to use high-quality ZnO buffer layers on other substrates, for example, *c*-cut sapphire [Ueda et al., 1998; Sun et al., 1998; Dinescu et al., 1998; Wang et al., 2002b]. Epitaxial GaN thin films were thus grown by PLD on *c*-cut sapphire substrates with a thin ZnO buffer layer. For an optimized temperature of 600°C, the GaN films show the following in-plane epitaxial relationship: GaN $[10\bar{1}0]$//ZnO $[10\bar{1}0]$//Al_2O_3 $[11\bar{2}0]$, while the surface morphology of the GaN films was greatly improved in comparison to the direct growth on sapphire substrates without a ZnO buffer layer [Sun et al., 1998].

ZnO thin films epitaxially grown by PLD on sapphire substrates have also been used as buffer layers for the further growth of AlN thin films [Vispute et al., 1997]. These epitaxial nitride films showed FWHM rocking curves lower by 50% than that of AlN films directly grown on sapphire. In the future, it can be expected that this approach could be used for the epitaxial growth of other wide bandgap nitride materials, like InN or III–V alloy nitride compounds.

12.3.4.2 Light Emission

As stated above, due to its specific properties, ZnO is a very promising material for use in the manufacture of blue/green/white light-emitting diodes. In addition to a high crystalline quality for the ZnO layers, the realization of such devices requires the control of the *p* doping of this material. However, due to the difficulty of fabricating *p*-type ZnO, no UV emission based on a *p-n* junction has yet been obtained. Another approach has been followed to realize a UV LED operating at room temperature using a *p-n* heterojunction composed of transparent conductive oxides: *p*-type $SrCu_2O_2$

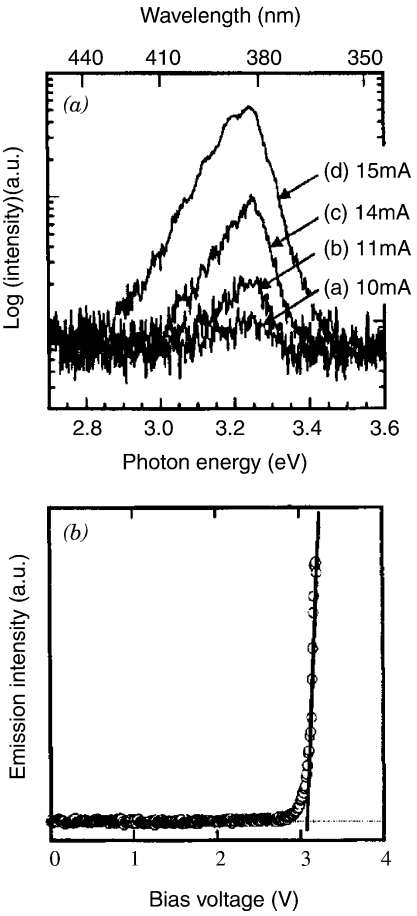

Figure 12.11 (a) UV emission spectra of the p-$SrCu_2O_2$/n-ZnO p-n junction LED for several currents. (b) LED emission intensity as a function of bias voltage, the turn-on voltage is about 3 V. From Ohta et al. [2000], used with permission from the American Institute of Physics.

and n-type ZnO [Ohta et al., 2000; Hosono et al., 2002]. This LED structure was formed on YSZ (111)-oriented single crystal, and an indium tin oxide (ITO) film was first epitaxially grown on this substrate, followed by n-type ZnO and p-type $SrCu_2O_2$ films successive depositions. All these layers were grown by PLD and X-ray diffraction analysis showed that high crystalline quality films were epitaxially grown in each case with specific in-plane orientations. Finally a nickel metal layer used as a p-electrode was deposited on top of the multilayered film.

Figure 12.11 shows the emission spectrum observed through the transparent ITO electrode for various injection currents. The relatively sharp emission band centered at 382 nm could be due to the transition associated with an electron–hole plasma in ZnO [Ohta et al., 2000]. This UV emission was observed at room temperature for forward-bias voltages greater than 3 V, and the efficiency was estimated at a low value of 10^{-3} %. This low value was believed to be improved by avoiding the spatial inhomogeneities at the ZnO–$SrCu_2O_2$ interface, which were observed by transmission electron microscopy [Ohta et al., 2000].

Due to the large exciton binding energy (59 meV), room temperature lasing in ZnO epitaxial films on sapphire with a low threshold has been observed. An interesting improvement in this field

has been obtained by the use of superlattices based on alternate layers of ZnO and $Mg_xZn_{1-x}O$. Such superlattices were grown by PLD on well-adapted $ScMgAlO_4$ single crystals, and they were found to possess a very high crystalline quality and atomically flat surfaces and interfaces [Ohtomo et al., 1999b, 2000]. Improved optical properties were demonstrated via efficient UV-stimulated emission up to 377 K due to the combined effects of excitons and quantum confinement in the $ZnO/Mg_xZn_{1-x}O$ multiquantum wells [Chia et al., 2003]. In fact the exciton binding energies of these multiquantum wells were larger than that of epitaxial ZnO films, and increased with a decrease of the well widths, reaching 86 meV for a 1.75-nm-thick width [Sun et al., 2000].

Such enhancement is thus very favorable for the preservation of excitons at higher temperatures. Moreover, by varying the Mg composition of the Mg_xZnO_{1-x} layers, a tunable emission energy in the 3.2- to 3.4-eV range was possible. The measured threshold for stimulated emission was 11 kW/cm^2 [Ohtomo et al., 2000], far better than the best value (24 kW/cm^2) observed in epitaxial ZnO layers.

12.3.4.3 Light Detection

Due to their wide and direct bandgap and large photoresponse, ZnO films are very interesting for UV photodetector applications. However, photodiodes based on polycrystalline material exhibited slow operating speed and low quantum efficiency due to a large number of recombination centers. An improvement is the use of epitaxial films, and a further great improvement in this field is the use of epitaxial films of a ZnO-related compound. As a matter of fact, UV photodetectors based on a metal–semiconductor–metal structure have been realized with the $Mg_xZn_{1-x}O$ compound [Yang et al., 2001, 2003]. In the case of the cubic high Mg composition phase, c-MgZnO films were epitaxially grown on Si substrates with a $SrTiO_3$ buffer layer, and the interdigitated finger patterns, 250 μm long, 5 μm wide, with 5 μm spacing were patterned from a gold film [Yang et al., 2003]. This device shows a peak spectral response at 225 nm corresponding to the bandgap of the c-MgZnO film (5.51 eV). The UV–visible rejection ratio was found to be more than one order of magnitude for the device. By varying the Mg concentration, it could be possible to detect over a wide range of the UV spectrum with a cut-off wavelength from 157 to 230 nm [Yang et al., 2003]. Moreover, the possibility of growing such cubic MgZnO films on substrates like Si or GaAs demonstrates its promising interest for integration in microelectronics or optoelectronics.

Photodetectors for a different wavelength domain have been based on the hexagonal low Mg concentration phase of the $Mg_xZn_{1-x}O$ compound [Yang et al., 2001]. In fact, metal–semiconductor–metal photodetectors have been realized, based on $Mg_{0.34}Zn_{0.66}O$ thin films epitaxially grown on *c*-cut sapphire substrates. In that case, the peak response of the detector was centred at 308 nm, in good agreement with the energy bandgap of the film. The visible rejection ratio exceeded four orders of magnitude, indicating a high degree of visible blindness [Yang et al., 2001]. An 8-ns rise time, and 1.4-μs fall time were also reported for these photodetectors based on the hexagonal MgZnO compound.

12.3.4.4 Spintronics

There is currently much interest in a new type of electronics: spin electronics or spintronics, for which the spin of charge carriers provides novel functionalities for devices such as spin-based light-emitting diodes, resonant tunneling diodes, and field-effect transistors. All these potential devices, which combine spin and charge, need the injection of spins into semiconductor heterostructures. In principle, this may be done by the use of ferromagnetic metals, but due to the decrease in conductivity at the metal–semiconductor interface, the spin injection efficiency is too low for such metals to be used in applications. Another approach is the use of so-called diluted magnetic semiconductors (DMS) as spin injectors, like Mn-doped ZnSe which could be used at very low temperatures (liquid He), this material presenting a low Curie temperature (i.e., transition to the ferromagnetic state). However, if spintronics is to become practical, one needs spin injectors that can function at and above room temperature, that is, ferromagnetic materials.

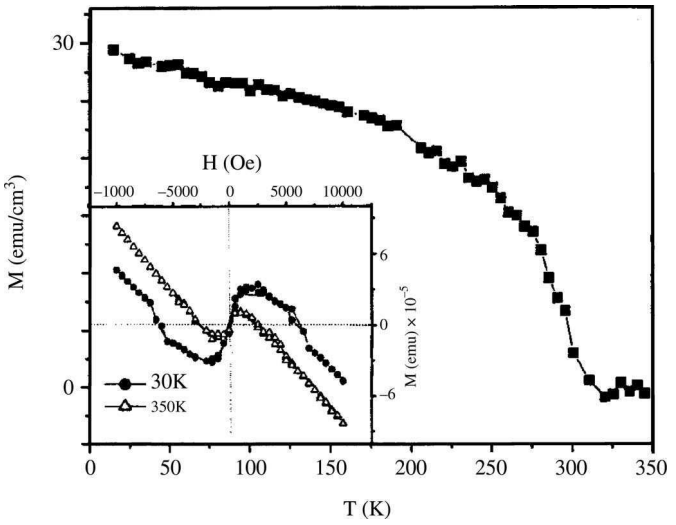

Figure 12.12 $M(T)$ of a Co-doped (5%) ZnO film recorded under 2000 G. The inset depicts the M(H) at 30 and 350 K; the 350-K signal is due to the background component of the substrate. From Prellier et al. [2003], used with permission from the American Institute of Physics.

Some doped wide bandgap semiconductors (GaN, ZnO) have been predicted [Dietl et al., 2000] to be ferromagnetic at $T > 300$ K. As a result, Mn, Ni, V, and Cr-doped ZnO films were grown by PLD [Tiwari et al., 2002b; Wakano et al., 2001; Saeki et al., 2001], and high-quality epitaxial films were generally produced on sapphire substrates [Fukumura et al., 1999; Pearton et al., 2003]. In the particular case of Mn doping, the dopant concentration (0.35) is much higher than the equilibrium value (0.13), a result that can be related to a specificity of the PLD process, that is, the growth occurs out of equilibrium, leading to the formation of a metastable phase. However, in contradiction with theoretical predictions, no signature of ferromagnetic ordering could be detected in these Mn-doped ZnO films even down to liquid He temperature. DC magnetization data from SQUID measurements showed a paramagnetic behavior for all the films whatever the Mn concentration. Therefore $Zn_{1-x}Mn_xO$ films cannot be used as spin injectors, and the case of Co-doped ZnO has been envisaged following some theoretical simulations [Dietl et al., 2000; Pearton et al., 2003].

Pulsed laser deposition has also been used to grow $Co_xZn_{1-x}O$ films on *c*-cut sapphire substrates, however, despite a high crystalline quality of the films, ferromagnetic features with a Curie temperature higher than room temperature were observed in only some of the Co-doped ZnO films with poor reproducibility [Ueda et al., 2001; Jin et al., 2001b]. Moreover the origin of the ferromagnetism in the films was not clearly established and could be related to the presence of Co clusters in the films [Kim et al., 2003a; Tabata et al., 2001b]. Recently, Co-doped ZnO films were grown by reactive PLD of Zn and Co metallic targets under ambient oxygen [Prellier et al., 2003]. The $M(T)$ curve presented in Figure 12.12 shows ferromagnetism in the films with a Curie temperature around 300 K. Moreover, the increase in the lattice parameter as the Co content increases permits the exclusion of the hypothesis of the existence of Co clusters [Prellier et al., 2003] in such films. The growth of these ferromagnetic films by PLD opens therefore the route for the fabrication of spin-based electronics.

12.4 ZnO NANOCRYSTALLINE FILMS

The synthesis and study of nanocomposite (nanoparticles in a matrix) and nanocrystalline films based on particles with a mean size in the range of 1–20 nm has become a major interdisciplinary

area of research over the past 10 years. In the case of semiconductor nanocrystalline materials, a change of the electronic properties via the quantum confinement effect occurs as the size of the nanocrystal decreases. In addition, surface effects play a major role in the properties of the nanostructures due to the fact that the ratio of surface atoms to internal atoms increases with decreasing nanoparticle size.

These points have given rise to studies on the formation of ZnO nanocrystals by various chemical methods (mainly sol–gel process) and of nanocrystalline thin films produced by PVD-CVD techniques. Laser ablation has been, of course, used to grow polycrystalline or epitaxial films displaying grain sizes in the submicrometer (a few hundred nanometers) or nanometer (5–30 nm) ranges. Actually, two distinct ways can be used to form nanocrystalline thin films. First, the so-called high-pressure PLD that consists of performing laser ablation under oxygen pressures a little bit higher (up to 1.33 mbar) than that which is classically employed in reactive PLD (less than 0.5 mbar). Second, for several years, lasers emitting pulses in the femtosecond (fs) temporal range have been available leading to extensive studies on both the fundamental aspects of laser–matter interactions and thin-film growth by PLD with such ultrashort laser sources. Indeed, ZnO was one of the first oxide compounds whose growth by femtosecond PLD was studied, the first papers having been published in 2000 [Okoshi et al., 2000; Millon et al., 2000].

12.4.1 Nanosecond PLD under High Oxygen Pressure

As reported in Section 12.2, high crystalline quality ZnO films may be grown under a rather wide range of oxygen pressures. However, the pressure used in PLD for ZnO films and more generally speaking for oxides cannot be arbitrarily increased due to the occurrence of new phenomena leading to strong modifications in the surface morphology of the deposited layers. Indeed films grown under pressures higher than several millibars resemble the random stacking of particles, produced by gas-phase collisions between the ablated species and the background gas. However, experiments performed in such pressure range (1–10 mbar) have been judiciously used to synthesize semiconductor (GaAs) nanocrystals by using laser ablation in a nitrogen flowing gas [Perrière et al., 2001]. At very high pressures (higher than 100 mbar) the particles tend to aggregate in snowflake structures [Lowndes et al., 1999], which cannot find application in the field of high-quality thin films, but rather in chemistry (catalysts, sensors) as porous materials with a high surface reactivity.

It is therefore possible to grow ZnO films composed of nanometer-sized crystallites. The average out-of-plane grain size estimated through the FWHM of the (0002) diffraction peak ranges from 5 to 20 nm as the oxygen pressure is increased from 10^{-5} to 1.33 mbar [Dinh et al., 1999; Mitra et al., 2001; Mitra and Thareja, 2001]. Nevertheless, the precise control of the crystal size in three dimensions strongly depends upon the experimental growth conditions (target-to-substrate distance, substrate temperature, laser wavelength). The in-plane grain size can be estimated by atomic force microscopy (AFM) measurements and is found to vary from 20 to 200 nm, lower oxygen pressures inducing smaller grain size. In addition, the surface roughness [root mean square (rms) value] is increased abruptly when the oxygen pressure is higher than 0.33 mbar. At around 1.33 mbar, the film becomes powdery with noticeable clustering of grains [Mitra et al., 2001]. Figure 12.13 depicts a typical example of ZnO grain morphology observed in nanocrystalline films grown under two different oxygen pressures. The corresponding out-of-plane grain size estimated from the Scherrer equation (XRD analysis) is around 16 and 10 nm, respectively.

Another parameter that has to be taken into account for further properties and applications in the field of spontaneous or stimulated emission is the thickness of the ZnO film related to the grain size. It has been reported that ZnO films epitaxially grown on sapphire substrate at room temperature by laser molecular beam epitaxy (MBE) displayed hexagonally shaped nanocrystals with an average size of 257 and 45 nm for film thickness of 200 and 55 nm, respectively [Ohtomo et al., 1998a], and stimulated emission was observed with very low pumping intensity when the crystal size is adjusted to be optimum (about 50 nm). Finally, the control of oxygen pressure is needed for obtaining the correct stoichiometry (Zn : O ratio close to 1). This is of prime importance for photo- or

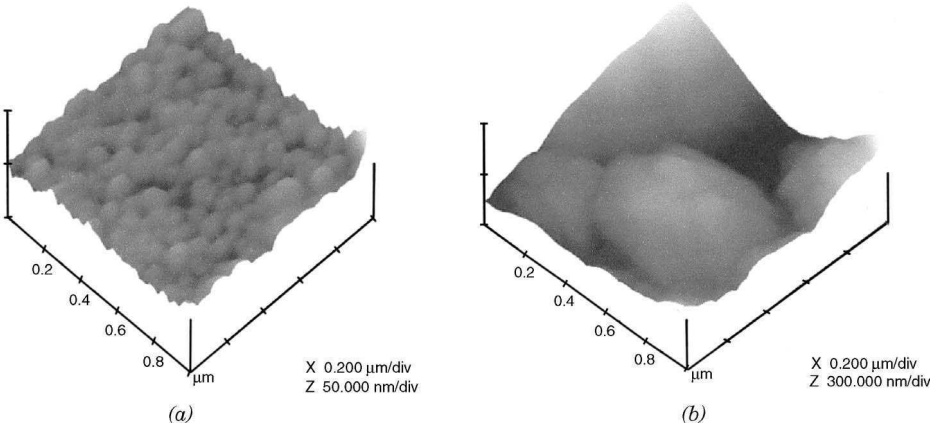

Figure 12.13 AFM images of ZnO films deposited at (a) 0.066 mbar and (b) 1.2 mbar. From Mitra et al. [2001] used with permission from Elsevier.

cathodoluminescent properties that require stoichiometric ZnO films [Jin et al., 2000a, 2000b; Im et al., 2000]. As a result, Figure 12.14 shows the effect of oxygen pressure on the photoluminescence spectra for ZnO films. The broad and intense peak centred at 395 nm corresponds to the deep blue level due to interband transition [Mitra and Thareja 2001].

As a summary, PLD under high oxygen pressures allows the growth of epitaxial thin films characterized by the stacking of crystallites of a few nanometer size in the main axis growth

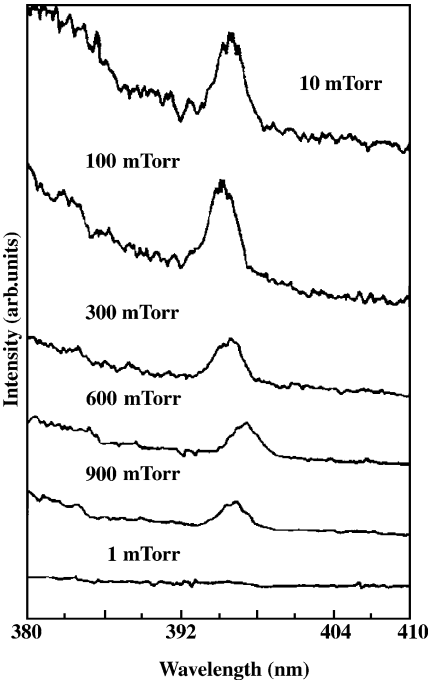

Figure 12.14 Photoluminescence spectra of ZnO films grown on glass substrate at room temperature under various oxygen pressures (excitation source: 355 nm, 5 ns Nd:YAG laser). From Mitra and Thareja [2001], used with permission from the American Institute of Physics.

direction while the in-plane size is at least approximately tens of nanometers. It appears that the precise control of the grain size and the structural defects in the crystallites are very sensitive to the experimental growth conditions. The reproducible formation of ZnO films both displaying high structural quality and crystallites with regular shape and homogeneous size in the nanometer range requires additional studies in the future.

12.4.2 Femtosecond PLD

The first aim of the use of femtosecond pulses for growing thin films was to avoid the formation of micrometer size droplets induced by thermal effects in the target, which generally occur during laser ablation in the nanosecond regime. As nonthermal melting appears on a subpicosecond time scale, it was therefore expected that ablation with ultrashort laser pulses would be the consequence of a multiphoton ionization process with minimal thermal diffusion effects when the laser intensity was not far above the ablation threshold. This new source should solve or at least reduce the limitations of PLD films due to droplet formation. Nowadays, this subject is still a matter of discussion and no precise answer can be given about the possible formation of droplets or clusters at the film surface. Nevertheless, the use of femtosecond lasers for the growth of thin films leads to interesting and novel results as determined by the structural and morphological properties of the deposited films. Since 2000, several compounds such as BN, AlN, DLC, AlCuFe quasicrystals, SnO_2, $BaTiO_3$, and ZnO have therefore been studied for thin-film formation by femtosecond PLD.

Ti : sapphire lasers emitting around 100–150 fs pulses at 780–800 nm or colliding pulse mode (CPM) locked dye lasers (620 nm, 100 fs) are generally used for PLD experiments. The laser energy and the focused spot size on the target are smaller than those employed in nanosecond PLD and the power density is higher than 10^{12} W/cm^2. One of the major differences observed in femtosecond PLD compared with nanosecond is the range of oxygen pressures available for growing femtosecond PLD films. Due to a strong clustering effect that is still not completely understood, the upper oxygen pressure is around 10^{-2} mbar in femtosecond PLD. Experiments performed at higher pressures lead to nonadhesive and snowflake deposits indicating that an efficient coalescence process in the plume occurs in the femtosecond regime even at relatively low pressures. This explains why all the ZnO films (and other oxides) are grown under vacuum (less than 10^{-5} mbar). Crystalline ZnO films with good optical transparency can be grown on quartz substrates [Okoshi et al., 2000]. Smooth, dense, stoichiometric and (00l)-textured ZnO films are produced on sapphire substrates, and display the same epitaxial relationships to those observed for nanosecond ZnO PLD films [Millon et al., 2000]. The surface of the femtosecond films is free of droplets or particles, but the crystalline quality is lower than that of films grown in the nanosecond regime [Perrière et al., 2002]. Table 12.1 summarizes the structural properties of both nanosecond and femtosecond PLD ZnO films.

The rocking curve measurements performed to evaluate the mosaic spread of the crystallites indicate rather large values (higher than 1°), meaning that the film mosaicity is not as good as that obtained for nanosecond PLD films. Moreover, it is worth noting that such angular distributions of the *c*-axis orientations are observed for ZnO films grown either on crystalline (sapphire, silicon) or amorphous (SiO_2) substrates. This fact is one of the major differences to films grown in the nanosecond regime for which the use of single-crystal substrates leads to a decrease of the FWHM of

TABLE 12.1 Structural Properties of ZnO Films Grown by Femtosecond or Nanosecond PLD

	Rocking Curve FWHM (deg)	RBS χ_{min} (%)	FWHM ϕ Scan (deg)	Stresses (MPA)	Crystallite Size (nm)
Femtosecond films	1.3–2	60–80	1.39	−330	10–15
Nanosecond films	0.3	2	0.65	−550	50

From Perrière et al. [2002].

the rocking curves. In addition, the high χ_{min} values (60–80%) measured in RBS experiments in channeling geometry indicate the presence of a large amount of defects in the crystallites. Though the ZnO films grown by femtosecond PLD are also epitaxial on *c*-cut sapphire substrates, broader in-plane angular distributions (about 1.4°—see Table 12.1) are measured for such films. The crystallite sizes are rather different too, as the average out-of-plane grain size of ZnO films grown by femtosecond PLD is smaller, highlighting the fact that the femtosecond films are formed by the stacking of nanocrystallites (10–15 nm thick, 100–200 nm large) along the *c*-axis, while nanosecond films are the result of a columnar growth.

The last point to be addressed concerns the residual stresses of the films [Perrière et al., 2002]. The thermal stresses due to the difference in the thermal expansion coefficients of the substrate and ZnO films are expected to be the same in the nanosecond and femtosecond PLD processes. On the contrary, the intrinsic component of the residual stresses, which are related to phenomena occurring during the growth, can be different in the two cases. The lower absolute values of residual stresses measured by XRD experiments (negative values correspond to compressive stresses) for femtosecond films (Table 12.1) can only be explained by the dynamical aspect of the deposition process. In fact, it has been observed by charge-coupled device (CCD) imaging and time-resolved spectroscopy [Albert et al., 2003] that ions with a high kinetic energy are emitted by the target during femtosecond laser ablation. In the case of ZnO, Zn ions were oberved with a kinetic energy close to 1 KeV [Perrière et al., 2002], while the highest energy measured in nanosecond PLD does not exceed a few hundred electron volts. The bombardment of the growing ZnO films by such energetic species during femtosecond PLD is believed to produce a large structural disorder (atomic sputtering and defect creation) allowing changes in microstructure and stress relaxation during the growth [Perrière et al., 2002].

12.4.3 Applications of Nanocrystalline ZnO Films

Optical application and more specifically laser emission require materials with a high crystalline quality such as bulk single crystals or heteroepitaxial films grown on lattice-matched substrates displaying large domains in a near-single-crystal state. Due to its direct bandgap of 3.26 eV at room temperature, and its large exciton binding energy (60 meV), ZnO is a good candidate for UV laser emission. The increasing search in the field of integrated photonic circuits gives rise to studies involving ZnO thin films as microlasers. Two routes have been investigated for UV lasing with ZnO films. The first one is based on the use of ZnO nanocrystalline thin films epitaxially grown on sapphire substrates [Ohtomo et al., 1998a]. Such high crystalline quality films are expected to achieve high-efficiency stimulated emission under optical pumping due to the recombination of excitons at room temperature ($kT = 25$ meV). The excitonic emission is related to the confinement of excitons in hexagonally shaped nanocrystals with a small size (50 nm). Laser action therefore occurs in the cavities formed by two cleaved facets [Bagnall et al., 1997]. The stimulated emission at 3.2 eV recorded for epitaxial ZnO films grown on sapphire increases with increasing pumping intensity and is the result of an exciton–exciton collision process that occurs even at room temperature [Ohtomo et al., 1998a]. When the crystal size is adjusted around 50 nm, excitons are confined in these nanocrystals and stimulated emission is observed with a pumping threshold intensity of 24 kW/cm^2 (pumped by a frequency-tripled Nd : YAG laser at 355 nm, 10 Hz, 15 ps).

An alternative source of coherent light emission consists of lasing occurring in disordered and random media. Such effects have been demonstrated in zinc oxide powder and polycrystalline ZnO films [Cao et al., 1999] and are due to strong optical scattering within the micrometer size cavities. Despite the fact that scattering induces optical losses, it helps laser emission by forming closed-loop paths (Fig. 12.15) [Cao et al., 1998].

These closed-loop paths could serve as ring cavities for light and would be due to the emitted light that might return to the scattering center from which it was previously scattered [Cao et al., 1999]. In fact the refractive index of the grain boundary is lower than that of the grain itself due to the lack of excitonic resonance [Ong et al., 2000]. This refractive index difference between the grain and

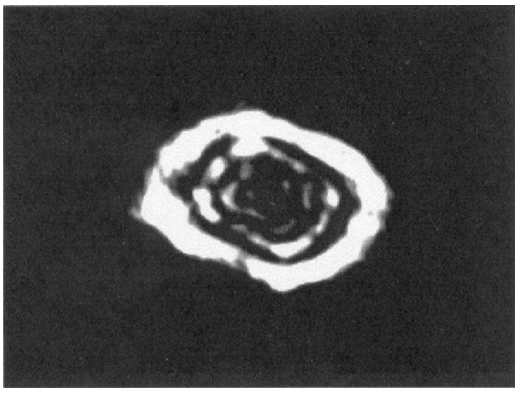

Figure 12.15 Two-dimensional amplified image of the excitation area above the lasing threshold of a polycrystalline ZnO film grown on an amorphous silica substrate. The excitation spot from a 355-nm, 15-ps laser is around 35 μm and is located in the middle of the picture. From Cao et al. [1998], used with permission from the American Institute of Physics.

grain boundary would be the origin of the formation of laser cavities by the strong optical scattering in a highly disordered crystalline structure.

Laser emission can be observed in all directions and the pump intensity required to reach the lasing threshold depends on the excitation area. The size and shape of such two-dimensional laser resonators are determined by both the structural (grain boundary, crystallite size, film thickness) and optical properties (scattering cross section, optical losses) of the ZnO films. As highlighted for nanocrystalline ZnO films epitaxially grown on sapphire, the laser emission increases with film thickness and depends upon laser power pumping [Mitra et al., 2001; Cao et al., 2000]. Figure 12.16 shows the laser emission for a 1.5-μm-thick ZnO film grown on a glass substrate at room temperature. According to AFM and XRD data, the corresponding nanocrystallite size is around 50 and 10 nm for the in-plane and out-of-plane directions, respectively.

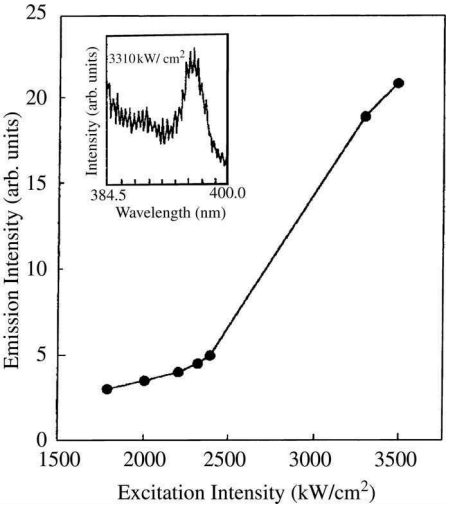

Figure 12.16 Laser emission from a polycrystalline ZnO film grown on a glass substrate, as a function of the laser pumping intensity (excitation source: 355 nm, 5 ns Nd:YAG laser); the inset shows the laser emission spectrum. From Mitra et al. [2001] used with permission from Elsevier.

Finally, some interesting results obtained for nanocrystalline undoped or Er-doped ZnO films must be mentioned despite the fact that such layers have also been grown by other techniques such as sol–gel, sputtering, and plasma enhanced chemical vapor deposition (PECVD). Er-doped nanocrystalline ZnO layers obtained by chemical methods have been used as amplifying planar waveguide structures at 1.54 μm [Mais et al., 1999]. According to the rather good crystalline quality of ZnO thin films grown by PLD, it could therefore be expected to improve the optical response of such systems.

Moreover, recently second-harmonic generation in nanocrystalline oxide thin films has been reported [Shi et al., 2000], while the second-order susceptibilities observed in very thin (50 nm) epitaxial ZnO films are enhanced and can be larger than that of single-crystal ZnO [Wang et al., 2002a]. It would be therefore interesting to check the second-harmonic generation in nanocrystalline ZnO films. More generally the nonlinear optical properties of nanocrystalline ZnO films could be promising according to the measurements reported on the third-order optical nonlinearity ($\chi^{(3)}$) in ZnO microcrystallite thin films [Zhang et al., 1999; Makino et al., 2000b] and the enhancement of the $\chi^{(3)}$ in semiconducting nanocrystallites [Lettieri and Maddalena, 2002], via quantum confinement effects.

12.5 CONCLUSIONS AND FUTURE PERSPECTIVES

In this chapter, we have reviewed the main work devoted to the PLD growth of ZnO thin films during the last decade. The large volume of original results and promising applications reported in the literature for these ZnO films is a guarantee that this research theme will remain a hot topic in the coming years. From the present state of the art that has been reported here, one can foresee several important directions for future investigations.

For the epitaxial growth of ZnO films, sapphire will remain the substrate of choice due to its relatively low price, high quality, and large size availability. It is therefore necessary to find the most adequate buffer layer on such a substrate to reduce or even avoid the residual strain in ZnO epilayers resulting from the large lattice mismatch. The first step to achieve this reduction will be to establish the origin of the stresses in the films, that is, thermal, intrinsic, or extrinsic stresses, since this has not been done yet and it could definitely help in the search for the ideal buffer layer. Up to now *c*-cut sapphire substrates have usually been used for ZnO epitaxial growth, but other crystalline orientations of Al_2O_3 have to be considered in the future, according to some specificities of ZnO. For example, epitaxial ZnO films grown on *R*-cut sapphire substrates were found to possess a strong optical anisotropy at near bandgap photon energies, which has been used to realize an optically addressed ultraviolet light modulator [Wraback et al., 1999].

It is worth emphasizing that in the field of epitaxial growth, the pulsed laser deposition technique offers ideal conditions to realize the synthesis and kinetic stabilization of metastable phases in thin films. The bombardment of the growing film during PLD with energetic species ($>$100 eV) coming from the target at each laser pulse leads to a high surface diffusion of adatoms, enabling the growth of high-quality crystalline films at low or moderate substrate temperatures, whereas the bulk atomic diffusion is low, and therefore precludes any phase transformation in the deposited films. This suggests that if a metastable phase could be epitaxially grown by PLD on a well-suited substrate, it might therefore be ''stabilized.'' This epitaxial stabilization by PLD could be used, for example, to obtain cubic ZnO in thin-film form. Indeed, the thermodynamic stable phase of ZnO is the hexagonal wurtzite structure, but a metastable zincblende structure has been theoretically predicted and even reported using a ZnS buffer layer on a GaAs substrate [Ashrafi et al., 2000] or a multilayer structure ($Pt/Ti/SiO_2/Si$) [Kim et al., 2003b]. The formation of this cubic ZnO structure by PLD using well-matched substrates is therefore a future challenge worth exploring due to the specific properties that could be induced by the cubiclike structure.

To enhance some of its physical properties or induce new functional properties in devices, ZnO films have been doped with various elements. This process will be further developed in the near future. Two issues should be carefully examined, however: the respective valence of Zn and dopants

and the difference in their ionic radii. The first step will be to find out the localization of the dopants in the ZnO lattice. Some of them clearly substitute perfectly to Zn atom sites in the lattice, but due to their large size or for charge equilibrium, others could segregate at grain boundaries, introduce defects in the structure, or lead to the formation of new phases. These deleterious effects could be a limitation for the incorporation of new elements in ZnO thin films. Studies on the localization of the dopants and their effects on the lattice structure could help in the understanding of the change in ZnO properties associated with given dopants.

Two examples of this approach should be mentioned: first, the increase in exciton binding energy in multiquantum well structures would lead to studies on superlattices (ZnO/ZnO-related compounds), in order to increase this exciton binding energy up to values allowing the fabrication of UV emission devices working at high temperatures. In addition, the possibility of changing the emission wavelength by the nature of the dopant could certainly be investigated in the future. On the other hand, the formation of reliable *p*-type ZnO thin films is also an important challenge for the coming years, and doping or co-doping of ZnO with well-chosen elements will certainly be a key issue in the future.

Another interesting application area that is certain to develop further is the low-temperature growth of ZnO films. There are already many high-tech areas such as displays, solar cells, and sensors where the use of plastic substrates will not withstand temperatures in excess of 100–200°C. The technique has already made several inroads in these areas, but further developments such as UV or ion-assisted PLD could bring many interesting results.

Due to the potential applications of nanocrystalline ZnO thin films (UV lasers, second-harmonic generation), the main future objectives of PLD research dealing with the formation of such films should be the control of the size and the structural defects (nature and concentration) of the nanocrystallites, their mosaicity and possible epitaxial relationships on well-suited substrates. To reach these objectives, a clear understanding of the growth mechanisms of such films is necessary. This means that the phenomena taking place during the gas-phase condensation in the high-pressure nanosecond laser ablation process have to be elucidated, while the effects of the high-energy species bombardment during the femtosecond pulsed laser deposition have to be analyzed and theoretically described.

Finally, let us mention that the explosive development of studies dealing with nanosciences and nanotechnologies will have, of course, noticeable consequences in the field of laser ablation of ZnO. Indeed, laser ablation appears to be a well-suited technique for the formation of nanocomposite films, that is, nanocrystals in a host matrix [Teng et al., 2000b] or for the synthesis of nanocrystals [Perrière et al., 2001; Nichols et al., 2001], which can be embedded afterwards in various matrices (polymers or oxides). Studies of the properties of ZnO (and ZnO-related compounds) nanocrystals and ZnO-based nanocomposites could thus be based in the future on films and nanostructures synthesized by the laser ablation method.

REFERENCES

Albert, O., Roger, S., Glinec, Y., Loulergue, J. C., Etchepare, J., Boulmer-Leborgne, C., Perrière, J., and Millon, E. (2003), *Appl. Phys.* **A76**, 319.

Ashkenov, N., Mbenkum, B. N., Bundesmann, C., Riede, V., Lorenz, M., Spemann, D., Kaidashev, E. M., Kasic, A., Schubert, M., Grundmann, M., Wagner, G., Neumann, H., Darakchieva, V., Arwin, H., and Monemar, B. (2003), *J. Appl. Phys.* **93**, 126.

Ashrafi, A. B. M., Ueta, A., Avramescu, A., Kumano, H., Suemune, I., Ok, Y. W., and Seong T. Y. (2000), *Appl. Phys. Lett.* **76**, 550.

Bae, S. H., Lee, S. Y., Jin, B. J., and Im, S. (2000), *Appl. Surf. Sci.* **154/155**, 458.

Bae, S. H., Lee, S. Y., Jin, B. J., and Im, S. (2001), *Appl. Surf. Sci.* **169/170**, 525.

Bagnall, D. M., Chen, Y. F., Zhu, Z., Yao, T., Koyoma, S., Shen, M. Y., and Goto, T. (1997), *Appl. Phys. Lett.* **70**, 2230.

Basillais, A., Laidani, N., Boulmer-Leborgne, C., Mathias, J., Laurent, A., and Perrière, J. (2000), *Appl. Phys. A* **71**, 619.

Cao, H., Zhao, Y. G., Hong, H. C, Ho, S. T., Dai, J. Y., Wu, J. Y., and Chang, R. P. H. (1998), *Appl. Phys. Lett.* **73**, 3656.

Cao, H., Zhao, Y. G., Ho, S. T., Seelig, E. W., Wang, Q. H., and Chang, R. P. H. (1999), *Phys. Rev. Lett.* **82**, 2278.

Cao, H., Xu, J. Y., Seelig, E. W., and Chang, R. P. H. (2000), *Appl. Phys. Lett.* **76**, 2997.

Chen, Y., Bagnall, D. M., Koh, H. J., Park, K. T., Hiraga, K., Zhu, Z., and Yao, T. (1998), *J. Appl. Phys.* **84**, 3912.

Chen, Y., Ko, H. J., Hong, S. K., and Yao, T. (2000a), *Appl. Phys. Lett.* **76**, 559.

Chen, Y., Hong, S. K., Ko, H. J., Nakajima, M., and Yao, T. (2000b), *Appl. Phys. Lett.* **76**, 245.

Chen, M., Wang, X., Yu, Y. H., Pei, Z. L., Bai, X. D., Sun, C., Huang, R. F., and Wen, L. S. (2000c), *Appl. Surf. Sci.* **158**, 134.

Chia, C. H., Makino, T., Tamura, K., Segawa, Y., Kawasaki, M., Ohtomo, A., and Koinuma, H. (2003), *Appl. Phys. Lett.* **82**, 1848.

Choopun, S., Vispute, R. D., Noch, W., Balsamo, A., Sharma, R. P., Venkatesan, T., Lliadis, A., and Lock, D. C. (1999), *Appl. Phys. Lett.* **75**, 3947.

Claeyssens, F., Cheesman, A., Henley, S. J., and Ashfold, M. N. R. (2002), *J. Appl. Phys.* **92**, 6886.

Craciun, V., and Craciun, D. (1999), *Appl. Surf. Sci.* **138/139**, 218.

Craciun, V., Elders, J., Gardeniers, J. G. E., and Boyd, I. W. (1994), *Appl. Phys. Lett.* **65**, 2963.

Craciun, V., Amirhaghi, S., Craciun, D., Elders, J., Gardeniers, J. G. E., and Boyd, I. W. (1995), *Appl. Surf. Sci.* **86**, 99.

Craciun, V., Perrière, J., Bassim, N., Singh, R. K., Craciun, D., and Spear, J. (1999), *Appl. Phys. A* **69**, 5533.

Craciun, V., Singh, R. K., Perrière, J., Spear, J., and Craciun, D. (2000), *J. Electrochem. Soc.* **147**, 1077.

Dietl, T., Ohno, H., Matsukara, F., Cibert, J., and Ferrand, D. (2000), *Science* **287**, 1019.

Dinescu, M., Verardi, P., Boulmer-Leborgne, C., Gerardi, C., Mirenghi, L., and Sandu, V. (1998), *Appl. Surf. Sci.* **127–129**, 559.

Dinh, L. M., Schildbach, M. A., Balooch, M., and McLean II, W. M. (1999), *J. Appl. Phys.* **86**, 1149.

Fukumura, T., Jin, Z., Ohtomo, A., Koinuma, H., and Kawasaki, M. (1999), *Appl. Phys. Lett.* **75**, 2366.

Goria, C. R., Emanetoglu, N. W., Liang, S., Mayo, W. E., Lu, Y., Wraback, M., and Shen, H. (1999), *J. Appl. Phys.* **85**, 2595.

Guillot-Noel, O., Gomez-San Roman, R., Perrière, J., Hermann, J., Boulmer-Leborgne, C., and Barboux, P. (1996), *J. Appl. Phys.* **80**, 1803.

Henley, S. J., Ashfold, M. N. R., and Cherns, D. (2002), *Thin Solid Films* **422**, 69.

Hiramatsu, M., Imaeda, K., Horio, N., and Nawata, M. (1998), *J. Vac. Sci. Technol.* **A16**, 669.

Hosono, H., Ohta, H., Hayashi, K., Orita, M., and Hirano, M. (2002), *J. Crystal Growth* **237–239**, 496.

Hu, J., and Gordon, R. G. (1992), *J. Appl. Phys.* **71**, 880.

Ianno, N. J., McConville, L., Shaikh, N., Pittal, S., and Snyder, P. G. (1992), *Thin Solid Films* **220**, 92.

Im, S., Jin, B. J., and Yi, S. (2000), *J. Appl. Phys.* **87**, 4558.

Jin, B. J., Bae, S. H., Lee, S. Y., and Im, S. (2000a), *Mater. Sci. Eng.* **B71**, 301.

Jin, B. J., Im, S., and Lee, S. Y. (2000b), *Thin Solid Films* **366**, 107.

Jin, B. J., Woo, H. S., Im, S., Bae, S. H., and Lee, S. Y. (2001a), *Appl. Surf. Sci.* **169/170**, 521.

Jin, Z., Fukumora, T., Kawasaki, M., Ando, K., Saito, H., Sekigushi, T., Yoo, Y. Z., Murakami, M., Matsumoto, Y., Hasegawa, T., and Koinuma, H. (2001b), *Appl. Phys. Lett.* **79**, 3824.

Joseph, M., Tabata, H., and Kawai, T. (1999), *Jpn. J. Appl. Phys.* **38**, L1205.

Joseph, M., Tabata, H., Saeki, H., Ueda, K., and Kawai, T. (2000), *Physica B* **302/303**, 140.

Kaidashev, E. M., Lorenz, M., Von Weackstern, H., Rahn, A., Semmelhack, H. C., Han, K. H, Benndorf, G., Bundesmann, C., Hochmuth, H., and Grundmann, M. (2003), *Appl. Phys. Lett.* **82**, 3901.

Kang, H. B., Nakamura, K., Lim, S. H., and Shindo, D. (1998), *Jpn. J. Appl. Phys.* **37**, 781 (1998).

Kim, H., Gilmore, C. M., Horwitz, J. S., Pique, A., Murata, H., Kushto, G. P., Schlaf, R., Kafafi, Z. H., and Chrisey, D. B. (2000), *Appl. Phys. Lett.* **76**, 259.

Kim, J. H., Kim, H., Kim, D., Ihm, Y. E., and Choo, W. K. (2003a), *Physica B* **327**, 304.

Kim, S. K., Jeong, S. Y., and Cho, C. R. (2003b), *Appl. Phys. Lett.* **82**, 562.

Koida, T., Chichibu, S. G., Uedano, A., Tsukazaki, A., Kawasaki, M., Sota, T., Segawa, Y., and Koinuma, H. (2003), *Appl. Phys. Lett.* **82**, 532.

Komuro, S., Katsumata, T., Morikawa, T., Zhao, X., Isshiki, H., and Aoyagi, Y. (1999), *Appl. Phys. Lett.* **74**, 377.

Komuro, S., Katsumata, T., Morikawa, T., Zhao, X., Isshiki, H., and Aoyagi, Y. (2000a), *J. Appl. Phys.* **88**, 7129.

Komuro, S., Katsumata, T., Morikawa, T., Zhao, X., Isshiki, H., and Aoyagi, Y. (2000b), *Appl. Phys. Lett.* **76**, 3935.

Kwok, H. S., Kim, H. S., Kim, D. H., Shen, W. P., Sun, X. W., and Xiao, R. F. (1997), *Appl. Surf. Sci.* **109/110**, 595.

Lettieri, S., and Maddalena, P. (2002), *J. Appl. Phys.* **91**, 5564.

Lowndes, D. H., Rouleau, C. M., Thundat, T. G., Duscher, G., Kenik, E. A., and Pennycook, S. J. (1999), *J. Mater. Res.* **14**, 359.

Lu, Y. F., Ni, H. Q., Mai, Z. H., and Ren, Z. M. (2000), *J. Appl. Phys.* **88**, 498.

Mais, N., Reithmaier, J. P., Forchel, A., Kohls, M., Spanhel, L., and Müller, G. (1999), *Appl. Phys. Lett.* **75**, 2005.

Makino, T., Chia, C. H., Tuan, N. T., Segawa, Y., Kawasaki, M., Ohtomo, A., Tamura, K., and Koinuma, H. (2000a), *Appl. Phys. Lett.* **76**, 3549.

Makino, T., Tuan, N. T., Segawa, Y., Chia, C. H., Ohtomo, A., Kawasaki, M., and Koinuma, H. (2000b), *J. Lumin.* **87/89**, 210.

Makino, T., Tamura, K., Chia, C. H., Segawa, Y., Kawasaki, M., Ohtomo, A., and Koinuma, H. (2002), *J. Appl. Phys.* **92**, 7157.

Masuda, S., Kitamura, K., Okumora, Y., Miyatake, S., Tabata, H., and Kawai, T. (2003), *J. Appl. Phys.* **93**, 1624.

Meng, L. J., Moreira, de Sa C. P., and Santos, M. P. (1994), *Appl. Surf. Sci.* **78**, 57.

Millon, E., Albert, O., Loulergue, J. C., Etchepare, J., Hulin, D., Seiler, W., and Perrière, J. (2000), *J. Appl. Phys.* **88**, 6937.

Mitra, A., and Thareja, R. K. (2001), *J. Appl. Phys.* **89**, 2025.

Mitra, A., Thareja, R. K., Ganesan, V., Gupta, A., Sahoo, P. K., and Kulkarni, V. N. (2001), *Appl. Surf. Sci.* **174**, 232.

Muth, J. F., Kolbas, R. M., Sharma, A. K., Oktyabrsky, S., and Narayan, J. (1999), *J. Appl. Phys.* **85**, 7884.

Nakamura, T., Yamada, Y., Kusumori, T., Minoura, H., and Muto, H. (2002), *Thin Solid Films* **411**, 60.

Nakayama, T. (1983), *Surf. Sci.* **133**, 101.

Nakayama, T., Itoh, N., Kawai, T., Hashimoto, K., and Sakata, T. (1982), *Rad. Effects Lett.* **67**, 129.

Narayan, J., Dovidenko, K., Sharma, A. K., and Oktyabrsky, S. (1998), *J. Appl. Phys.* **84**, 2597.

Nichols, W. T., Keto, J. W., Henneke, D. E., Brock, J. R., Malyavanatham, G., Becker, M. F., and Glicksman, H. D. (2001), *Appl. Phys. Lett.* **78**, 1128.

Ohta, H., Tanji, H., Orita, M., Hosono, H., and Kawazoe, H. (1999), *Epitaxial Growth Principles and Applications*, MRS Symposium, Warrendale, PA, p. 309.

Ohta, H., Kawamura, K., Orita, M., Hirano, M., Sarakura, N., and Osono, H. (2000), *Appl. Phys. Lett.* **77**, 475.

Ohtomo, A., Kawasaki, M., Sakurai, Y., Yoshida, Y., Koinuma, H., Yu, P., Tang, Z. K., Wong, G. K. L., and Segawa, Y. (1998a), *Mater. Sci. Eng. B* **54**, 24.

Ohtomo, A., Kawasaki, M., Koida, T., Masubuchi, K., Koinuma, H., Sakurai, Y., Yoshida, Y., Yasuda, T., and Segawa, Y. (1998b), *Appl. Phys. Lett.* **72**, 2466.

Ohtomo, A., Tamura, K., Saikusa, K., Takahashi, T., Makino, T., Segawa, Y., Koinuma, H., and Kawasaki, M. (1999a), *Appl. Phys. Lett.* **75**, 2635.

Ohtomo, A., Kawasaki, M., Ohkubo, I., Koinuma, H., Yasuda, T., and Segawa, Y. (1999b), *Appl. Phys. Lett.* **75**, 980.

Ohtomo, A., Tamura, K., Kawasaki, M., Makino, T., Segawa, Y., Tang, Z. K., Wong, G. K. L., Matsumoto, Y., and Koinuma, H. (2000), *Appl. Phys. Lett.* **77**, 2204.

Okoshi, M., Higashikawa, K., and Hanabusa, M. (2000), *Appl. Surf. Sci.* **154/155**, 424.

Ong, H. C., Dai, J. Y., Hung, K. C., Chan, Y. C., Chang, R. P. H., and Ho, S. T. (2000), *Appl. Phys. Lett.* **77**, 1484.

Ong, H. C., Li, A. S. K., and Du, G. T. (2001), *Appl. Phys. Lett.* **78**, 2667.

Ong, H. C., Zhu, A. X. E., and Du, G. T. (2002), *Appl. Phys. Lett.* **80**, 941.

Pearton, S. J., Abernathy, C. B., Overberg, M. E., Thaler, G. T., Norton, D. P., Theodoropoulou, N., Hebard, A. F., Park, Y. D., Ren, F., Kim, J., and Boatner, L. A. (2003), *J. Appl. Phys.* **93**, 1.

Perrière, J., Millon, E., Chamarro, M., Morcrette, M., and Andreazza, C. (2001), *Appl. Phys. Lett.* **78**, 2949.

Perrière, J., Millon, E., Seiler, W., Boulmer-Leborgne, C., Craciun, V., Albert, O., Loulergue, J. C., and Etchepare, J. (2002), *J. Appl. Phys.* **91**, 690.

Pons, Y., and Moll, O. (2003), Ph.D. Thesis, Universités Paris, Paris, France, October.

Prellier, W., Fouchet, A., Mercey, B., Simon, Ch., and Raveau, B. (2003), *Appl. Phys. Lett.* **82**, 3490.

Puchert, M. H., Timbrell, P. Y., and Lamb, R. N. (1996), *J. Vac. Sci. Technol.* **A14**, 2220.

Ramamoorthy, K., Sanjeeviraja, C., Jayachandran, M., Sankaranarayanan, K., and Bhattacharya, P. (2001), *J. Crystal Growth* **226**, 281.

Ryu, Y. R., Zhu, S., Look, D. C., Wrobel, J. M., Jeong, H. M., and White, H. W. (2000a), *J. Crystal Growth* **216**, 326.

Ryu, Y. R., Zhu, S., Budai, J. D., Chandrasekhar, H. R., Micelli, P. F., and White, H. W. (2000b), *J. Appl. Phys.* **88**, 201.

Ryu, Y. R., Zhu, S., Look, D. C., Wrobel, J. M., Jeong, H. M., and White, H. W. (2000c), *J. Crystal Growth* **216**, 330.

Saeki, H., Tabata, H., and Kawai, T. (2001), *Solid State Commun.* **120**, 439.

Sankur, H., and Cheung, J. T. (1983), *J. Vac. Sci. Technol.* **A1**, 1806.

Sharma, A. K., Muth, J. F., Teng, C. W., Jin, C., Kvit, A., Kolbas, R. M., and Holland, O. W. (1999), *Appl. Phys. Lett.* **75**, 3327.

Shi, W., Chen, Z., Zhao, T., Lu, H., Zhou, Y., and Yang, G. (2000), *J. Am Opt. Soc.* **B17**, 235.

Shim, E. U., Kang, H. S., Kang, J. S., Kim, J. H., and Lee, S. Y. (2002), *Appl. Surf. Sci.* **186**, 474.

Sugiura, M., Nakashima, Y., Nakasaka, T., and Kobayashi, T. (2002), *Appl. Surf. Sci.* **197/198**, 472.

Sumya, M., Fuke, S., Tsukazaki, A., Tamura, K., Ohtomo, A., Kawasaki, M., and Koinuma, H. (2003), *J. Appl. Phys.* **93**, 2562.

Sun, X. W., and Kwok, H. S. (1999), *J. Appl. Phys.* **86**, 408.

Sun, C. J., Kung, P., Saxler, A., Ohsato, H., Haritos, K., and Razeghi, M. (1994), *J. Appl. Phys.* **75**, 3964.

Sun, X. W., Xiao, R. F., and Kwok, H. S. (1998), *J. Appl. Phys.* **84**, 5776.

Sun, H. D., Makino, T., Tuan, N. T., Segawa, Y., Tang, Z. K., Wong, G. K. L., Kawasaki, M., Ohtomo, A., Tamura, K., and Koinuma, H. (2000), *Appl. Phys. Lett.* **77**, 4250.

Suzuki, A., Matsushita, T., Wada, N., Sakamoto, Y., and Okuda, N. (1996), *Jpn. J. Appl. Phys.* **35**, L56.

Tabata, H., Saeki, M., Guo, S. L., Choi, J. H, and Kawai, T. (2001), *Physica B* **308–310**, 993.

Tasker, P .W. (1979), *J. Phys. C: Solid State Phys.* **12**, 4977.

Teng, C. W., Muth, J. F., Özgür, Ü., Bergmann, M. J., Everitt, H. O., Sharma, A. K., Jin, C., and Narayan, J. (2000a), *Appl. Phys. Lett.* **76**, 979.

Teng, C. W., Muth, J. F., Kolbas, R. M., Hassan, K. M., Sharma, A. K., Kvit, A., and Narayan, J. (2000b), *Appl. Phys. Lett.* **76**, 43.

Tiwari, A., Park, M., Jin, C., Wang, H., Kumar, D., and Narayan, J. (2002a), *J. Mater. Res.* **17**, 2480.

Tiwari, A., Jin, C., Kvit, A., Kumar, D., Muth, J. F., and Narayan, J. (2002b), *Solid State Commun.* **121**, 371.

Tsukazaki, A., Saito, H., Tamura, K., Ohtani, M., Koinuma, H., Sumya, M., Fuke, S., Fukumura, T., and Kawasaki, M. (2002), *Appl. Phys. Lett.* **81**, 235.

Ueda, T., Huang, T. F., Spruytte, S., Lee, H., Yuri, M., Itoh, K., Baba, T., and Harris, J. S. (1998), *J. Crystal Growth* **187**, 340.

Ueda, K., Tabata, H., and Kawai, T. (2001), *Appl. Phys. Lett.* **79**, 988.

Vasco, E., Rubio-Zuazo, J., Vasquez, L., Prieto, C., and Zaldo, C. (2001), *J. Vac. Sci. Technol.* **B19**, 224.

Vispute, R. D., Talyansky, V., Trajanovic, Z., Choopun, S., Downes, M., Sharma, R. P., Venkatesan, T., Woods, M. C., Lareau, R. T., Jones K. A., and Lliadis, A. A. (1997), *Appl. Phys. Lett.* **70**, 2735.

Vispute, R. D., Talyansky, V., Choopun, S., Sharma, R. P., Venkatesan, T., He, M., Tang, X., Halpern, J. B., Spencer, M. G., Li, Y. X., Salamanca-Riba, L. G., Lliadis, A. A., and Jones, K. A. (1998), *Appl. Phys. Lett.* **73**, 348.

Wakano, T., Fujimora, N., Morinaga, Y., Abe, N., Ashida, A., and Ito, T. (2001), *Physica E* **10**, 260.

Wang, G., Kiehne, G. T., Wong, G. K. L., Ketterson, J. B., Liu, X., and Chang, R. P. H. (2002a), *Appl. Phys. Lett.* **80**, 401.

Wang, R. P., Muto, H., Yamada, Y., and Kusumori, T. (2002b), *Thin Solid Films* **411**, 69.

Washington, P. L., Ong, H. C., Dai, J. Y., and Chang, R. P. H. (1998), *Appl. Phys. Lett.* **72**, 3261.

Wei, J., Zhang, B., Yao, N., Wang, X., Ma, H., and Wang, S. (2001), *J. Vac. Sci. Technol.* **B19**, 1082.

Wraback, M., Shen, H., Liang, S., Gorla, C. R., and Lu, Y. (1999), *Appl. Phys. Lett.* **74**, 507.

Xiao, R. F., Liao, H. B., Cue, N., Sun, X. W., and Kwok, H. S. (1996), *J. Appl. Phys.* **80**, 4226.

Yamamoto, T., and Yoshida, H. K. (1999), *Jpn. J. Appl. Phys.* **38**, L166.

Yang, W., Vispute, R. D., Choopun, S., Sharma, R. P., Venkatesan, T., and Shen, H. (2001), *Appl. Phys. Lett.* **78**, 2787.

Yang, W., Hullavarad, S. S., Nagaraj, B., Takeushi, I., Sharma, R. P., Venkatesan, T., Vispute, R. D., and Shen, H. (2003), *Appl. Phys. Lett.* **82**, 3424.

Yin, J., Liu, Z. G., Liu, H., Wang, X. S., Zhu, T., and Liu, J. M. (2000), *J. Crystal Growth* **220**, 281.

Zeng, J. N., Low, J. K., Ren, Z. M., Liew, T., and Lu, Y. F. (2002), *Appl. Surf. Sci.* **197/198**, 362.

Zhang, W., Wang, H., Wong, K. S., Tang, Z. K., Wong, G. K. L., and Ravinder, J. (1999), *Appl. Phys. Lett.* **75**, 3321.

CHAPTER 13

Group III Nitride Growth

DONAGH O'MAHONY and JAMES G. LUNNEY
Physics Department, Trinity College, Dublin, Ireland

13.1 INTRODUCTION

AlN, GaN, and InN have long been considered as promising materials for high power electronics and lighting applications. Nevertheless, difficulties associated with Group III nitride thin-film growth led to a lengthy dormant period through most of the 1970s and 1980s for nitride research and subsequently saw other materials, particularly the II–VI chalcogenides and SiC, come to the fore as potential candidates for such device applications. Only AlN was of any significant interest during this period, primarily as an electronically insulating thermal conductor [Slack and McNelly, 1976]. Eventually, it was the somewhat unexpected development of Group III nitride[1] based LEDs and laser diodes (LDs) in the early 1990s [Nakamura et al., 1993] that triggered the "blue" lighting revolution of the last decade. For a review of some of the major developments in Group III nitride growth, see, for example, Pankove and Moustakas [1998].

Today, most commercially available Group III nitride multilayer device structures are grown by metal-organic chemical vapor deposition (MOCVD) or molecular beam epitaxy (MBE). These well-established vapor deposition techniques have proved most practical for commercially realizing device fabrication, but there are several reasons why it is of interest to explore pulsed laser deposition (PLD) growth of nitrides [Lowndes, 1998]. These include a comparatively high degree of stoichiometric material transfer from target film, flexible doping options for complex compositions, and the capability for producing thin layers with sharp interfaces as may be required in lattice-matching buffer layers, heterostructures, or quantum-well active layers, all of which are particularly important for optoelectronic device fabrication. PLD of these nitrides may also indirectly provide some useful information for the rapidly expanding Group III nitride laser machining industry, which has recently emerged as an effective alternative to chemical or plasma etching techniques [Kim et al., 2001; Fujii et al., 2004].

This chapter is presented as an overview of Group III nitride growth using PLD for those new to the topic and aims to highlight aspects of the growth technique that require particular care and attention. The chapter outline is broadly grouped as follows: relevant material properties, characteristics of the deposition environment, and finally a selective overview of the properties of PLD-grown nitrides and their potential for device fabrication.

[1]Although the term *Group III nitrides* is used throughout the text, here the discussion is limited to AlN, GaN, and InN.

Pulsed Laser Deposition of Thin Films: Applications-Led Growth of Functional Materials
Edited by Robert Eason

13.2 PROPERTIES OF GROUP III NITRIDES AND GROUP III METALS

13.2.1 Group III Nitrides

Group III nitrides are very stable compounds and can only be wet-etched with highly aggressive agents such as hot NaOH or H_2SO_4 [Strite and Morkoc, 1992], but plasma (and more recently laser) etching is the preferred technique in device fabrication. The nitrides are classified as adamantine (diamond-like) compounds as their atoms have tetrahedral coordination, which leads to excellent hardness and high thermal conductivities ($>1\,W\,cm^{-1}\,K^{-1}$) for device-grade crystals [Slack, 1973]. The nitride bond is comparatively strong with bond energies of 2.88, 2.24, and 1.93 eV per bond for AlN, GaN, and InN, respectively, compared to 1.63 eV per bond in GaAs [Harrison, 1989; Bhattacharya et al., 2002]. Group III nitrides crystallize in the wurtzite (hexagonal) structure at typical film growth temperatures ($<1000°C$) and nitriding pressures (up to 10^5 Pa), however, the cubic zinc-blende phase can be obtained under carefully controlled deposition conditions on cubic substrates [Okumura et al., 1997]. Bandgap energies for the nitrides correspond to photon wavelengths in the ultraviolet (UV) for AlN, blue for GaN and red for InN (see Table 13.1), and since UV excimer lasers commonly employed in PLD are well above the bandgap of InN and GaN, strong absorption at the target surface is to be expected. For AlN, the ArF ($h\nu = 6.4$ eV) excimer laser should be an efficient ablation or machining tool. Unintentionally doped nitride films and powders have a high *n*-concentration leading to yellow luminescence, though there is still considerable debate whether this is due to impurities (e.g., oxygen), strain-induced defects at the film–substrate surface, or on-site vacancies (see, e.g., Pankove and Moustakas [1998]). Many properties of polycrystalline nitride powder pellets used as laser ablation targets in PLD differ considerably from the properties of single crystals [Kitanin et al., 1998]. It has been highlighted by several authors that nitride powders have significant levels of impurities, especially oxygen but also silicon [Slack and McNelly, 1976; Unland et al., 2003], and depending on the method of preparation, pressed powder pellets are also likely to have a lower density and significant void fraction compared with bulk crystals (see Section 13.2.4). These factors reduce both the mechanical strength and thermal conductivity of the material [Slack, 1973; Krukowski et al., 1998]. Furthermore, defect and grain boundary-related sub-band-edge absorption levels tends to broaden the optical absorption range of the powders compared to single crystals [Cazzanelli et al., 1998].

13.2.2 Thermal Decomposition of Group III Nitrides

While the lack of reliable thermodynamic data for Group III nitrides, particularly GaN and InN has been highlighted recently [Ranade et al., 2000; Onderka et al., 2002; Unland et al., 2003], Group III nitrides are clearly characterized by high melting temperatures (>2000 K) and require very high nitrogen pressures (>kilobars) [Porowski and Grzegory, 1997] near

TABLE 13.1 Some Relevant Properties of AlN, GaN, and InN[a]

	AlN	GaN	InN	Units
Density	3.23–3.28	6.15[b]	6.81 ± 0.05	$g\,cm^{-3}$
Bandgap[c]	6.2–6.3	3.4–3.5	1.9	eV
Melting point	>3500	~2800	~2200	K
Thermal conductivity	2.85	1.30	1.76[d]	$W\,cm^{-1}\,K^{-1}$
	0.7[e]	0.3[e]	0.45[e]	

[a]Single-crystal values are taken from Edgar [1994], except for [b][Chin et al., 1994], [c][Strite and Morkoc, 1992], [d][Krukowski et al., 1998]. [e]Polycrystalline ceramic thermal conductivities were estimated using the result of Krukowski et al. [1998].

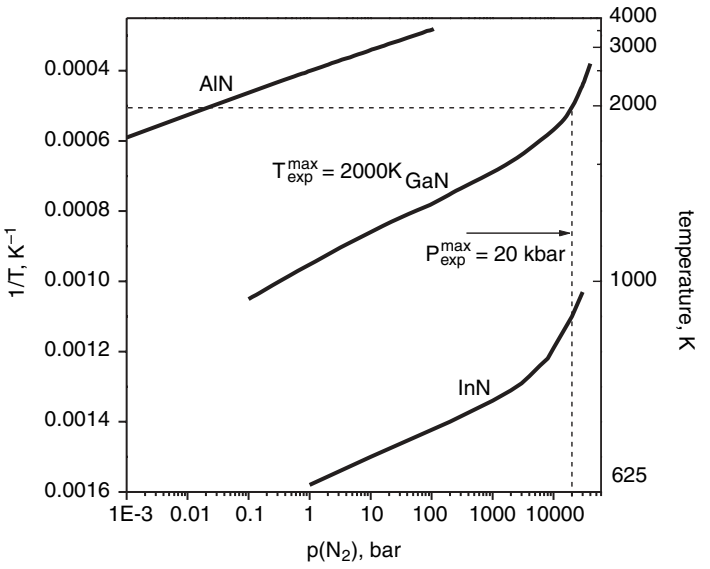

Figure 13.1 Temperature variation of the equilibrium N_2 vapor pressure over AlN, GaN, and InN [Porowski and Grzegory, 1997]. The dotted lines indicate the maximum temperature and pressures used in the measurements. Reprinted with permission from Elsevier and the authors (© 1997).

their melting temperatures to prevent decomposition (Fig. 13.1). This renders industry standard crystallization techniques such as Czochralski method impractical for bulk crystal growth [Karpinski et al., 1984]. There has been considerable debate regarding the vapor composition over heated nitrides, but the most recent experimental evidence suggests that diatomic nitride molecules are absent from the vapor [Onderka et al., 2002; Bogdanov et al., 2003; Unland et al., 2003]. Rather, the nitride decomposes yielding Group III liquid and/or vapor (X) and molecular nitrogen:

$$XN_{(\text{Solid})} \leftrightarrow X_{(\text{liquid,gas})} + \tfrac{1}{2}N_{2(\text{gas})} \tag{13.1}$$

Newman [1997] has used Munir and Searcy's [1965] total vapor pressure data to determine the decomposition flux of GaN as a function of temperature (Fig.13.2). The calculated flux correlates well with previously reported deposition data for MBE-grown GaN and may also serve as a guide for PLD users. Typically in PLD, the growth rate is ~ 0.1 Å per laser shot, which for GaN (density $= 6.15$ g cm^{-3}) corresponds to a deposition flux of $\sim 10^{14}$ cm^{-2} s^{-1} at 10 Hz shot repetition rate (note dashed line in Fig. 13.2b). Thus, it might be expected that above 800°C, decomposition will compete with deposition and indeed this seems to be the case in PLD of GaN [Cole and Lunney, 1997; Vispute et al., 1999]. Note that for growth in aggressive environments such as NH_3, the Gibbs free energy of the nitride-forming reaction is lowered and decomposition is less problematic [Newman, 1997]. The considerable discrepancy between the N_2 vapor pressure required to prevent decomposition (Fig. 13.1) and the total vapor pressure over the nitrides (e.g., Fig. 13.2; see also the discussion in Unland et al. [2003]) has been attributed to strong surface bonding that, fortunately from a film growth point of view, kinetically limits the decomposition reaction rate [Averyanova et al., 1997]. However, the Group III metal can act as a catalyst [Schoonmaker et al., 1965] for the decomposition reaction, thus the effective rate may be conversely enhanced.

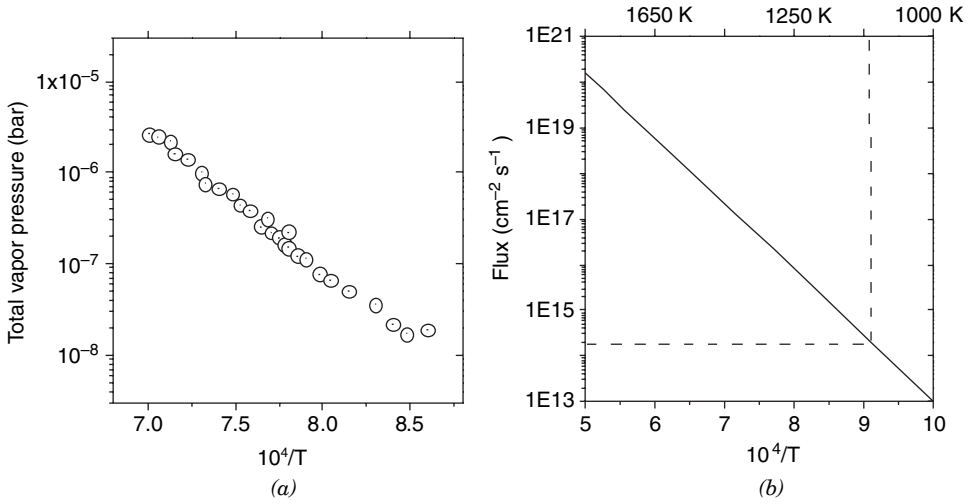

Figure 13.2 (a) Total vapor pressure (left) over a heated GaN pressed powder pellet, using the data tabulated in Munir and Searcy [1965]. (b) Corresponding evaporation flux as calculated using the Hertz–Langmuir–Knudsen equation (see also Newman [1997]). The dashed line indicates a decomposition flux of 10^{14} cm^{-2} s^{-1} at 850°C (1125 K).

13.2.3 Group III Elements: Al, Ga, and In

Group III metals, in particular gallium and indium, are characterized by low melting temperatures but high boiling temperatures and correspondingly have some of the longest liquid ranges among the elements (see Table 13.2). The rigid and directional bonds in the orthorhombic gallium crystal lead to a rather inefficient packing structure and, unlike most metals, results in an increase in density on melting [Wittenberg and DeWitt, 1972]. As in the case of the nitrides, there are several factors that should be taken into account when using Group III metal targets in PLD or modeling laser ablation of these metals. Gallium is classed as a semimetal, and is characterized by comparatively low electrical and thermal conductivity [Jiemin and Lamvik, 1998], in particular when compared with aluminum. Group III metals tend to oxidize quite easily; an exposure of (10–100) Langmuir (1 Langmuir $= 10^{-4}$ Pa s $\sim 10^{-6}$ mbar s) air is sufficient to form an oxide layer of a few nanometer thickness [Regan et al., 1997; Do and McIntyre, 1999]. It is also worth noting that these metals, when liquid, exhibit normal incidence reflectivity in excess of 90% at visible and near-visible laser wavelengths (1–5 eV) [Kofman et al., 1979; Krishnan and Nordine, 1993]. The reflectivity of Al in the solid state is also of this magnitude [Shiles et al., 1980], whereas for Ga and In [Bor and Bartholomew, 1967] the values are somewhat lower and vary considerably depending on

TABLE 13.2 Properties of Al, Ga, and In[a]

	Aluminum	Gallium	Indium	Units
Crystal structure	Cubic	Orthorhombic	Tetragonal	
Density[b]	2.7 (2.4)	5.91 (6.1)	7.3(7.0)	g cm^{-3}
Melting point[b]	933	303	429	K
Boiling point[b]	2792	2500	2301	K
Heat of vaporization	294[b]	264[c]	241[c]	kJ mol^{-1}
Thermal conductivity	2.37[b]	0.436 (0.278)[d]	0.816[b]	W cm^{-1} K^{-1}

[a]Values in parentheses are for the liquid phase (taken from[b] [Lide, 1998], [c][Geiger et al., 1987], and [d][Jiemin and Lamvik, 1998]).

the polarization of the incident light with Ga exhibiting considerable optical anisotropy [Kofman et al., 1977].

13.2.4 Target Preparation

Group III metal targets are commercially available to 99.999999% purity, but pressed pellets prepared from nitride powders (typically 99.99% purity) have, until recently, been the preferred choice of target. To the best of our knowledge, hot-pressed or sintered GaN or InN targets are not commercially available at present. Preparation of ceramic targets for laser ablation involves grinding and pressing of the powders followed by calcination to remove volatile impurities such as Group III oxides [Slack and McNelly, 1976]. This is followed by sintering of the pressed pellets, often repeatedly [German, 1996], to obtain a high density and mechanically robust target [Hampshire, 1986]. A sintering temperature of approximately 0.5–0.7 T_{melt} is generally recommended to promote densification and to facilitate atomic diffusion throughout the target, but temperatures of this magnitude (>2000 K) and the correspondingly enormous N_2 pressures required to prevent decomposition (Fig. 13.1) are beyond the capability of most sintering facilities. As such GaN and InN targets used in PLD are likely to be highly porous and brittle [Cole and Lunney, 1997; O'Mahony et al., 2003b]. AlN can withstand significantly higher temperatures without decomposing at 1 bar N_2, and high-density AlN ceramics have even been prepared at temperatures as high as 1800°C (1 h) in a N_2 flow at atmospheric pressure [Cappelli et al., 2002].

Metal targets require comparatively little preparation aside from a predeposition ablation run to remove any native oxide layer on the target surface. Target melting must be accounted for when using gallium or indium; thus, the PLD apparatus may need to be reconfigured to prevent spillage of the molten metal (see, e.g., Xiao et al. [1996]). Up to 10% Al is soluble in Ga at room temperature [Jayaganthan and Hajra, 1996], making it an unsuitable target holding material for PLD of GaN. Liquid targets tend to have considerable surface curvature, making the laser spot size and laser fluence difficult to determine accurately. While heating the target will reduce the viscosity [Spells, 1936] and subsequently the surface tension somewhat ($\sim$mN m^{-1} K^{-1} [Kolevzon, 1999]), but the problem of a curved target surface is perhaps best tackled by use of a shallow large-diameter target holder [Watanabe et al., 1996]. Liquid gallium also has a tendency to supercool easily [Borisov et al., 1999] and its viscosity rises sharply below the melting temperature, thus any subsequent rapid solidification will tend to freeze-in any surface structure [Kofman et al., 1977] and may crack glass target holders.

13.3 LASER ABLATION OF GROUP III NITRIDES AND GROUP III METALS

13.3.1 General Characteristics of the Ablation Process in PLD

Pusled laser deposition involves intense heating and material ablation, by evaporation or otherwise, of the irradiated target surface; the degree of heating and depth of the heated layer being primarily determined by the condition of the target surface and the characteristic optical and thermal diffusion lengths of the ''bulk'' target material. For pulses of nanosecond duration, the ablated material exists as a thin layer of partially ionized vapor at the end of the laser pulse, and the subsequent expansion of this vapor plume is primarily driven by pressure gradients strongly peaked in a forward direction. When the plume has propagated more than a few millimeters from the target surface, the major part of the initial thermal energy in the vapor is converted to the directed kinetic energy of the atoms and ions, which are considerably more massive than the electrons [Anisimov et al., 1996; Hansen et al., 1999]. In the presence of a sufficiently dense background gas, coupling of this kinetic energy to the gas becomes significant and its effects can be clearly identified at a few centimeters from the target by time-of-flight techniques. From a PLD point of view, relevant growth parameters that affect the ablation mechanism and subsequently the film quality can be generally categorized as follows: choice of (i) laser type, that is, pulse duration, wavelength, and fluence, (ii) background gas type and

pressure, and (iii) substrate type and temperature. This section deals with the first two parameters, that is, laser and background gas characteristics, and how the choice of these parameters affects the ablation mechanism and ultimately how it may influence film quality in PLD.

13.3.2 Characteristics of the Ablation Process in Vacuum

13.3.2.1 Nitride Target Ablation in Vacuum

Before considering some of the effects related to laser wavelength, pulse duration, and fluence, it is important to note that decomposition or ''metallization,'' that is, preferential evaporation of nitrogen, from the irradiated region of the target surface is invariably associated with nanosecond ablation of Group III nitrides [Ichige et al., 1988]. This effect has been widely reported in the ablation of single-crystal nitrides [Kelly et al., 1996; Wong et al., 1998; Tavernier and Clarke, 2001; Safadi et al., 2005] and has been adapted to ''write'' conducting Al circuitry in AlN ceramics [Morita et al., 1989; Hirayama et al., 2001]. For GaN, decomposition has even been identified in the desorption regime ($\sim$10 mJ cm^{-2}) [Namiki et al., 1991], and mass spectrometry revealed that the N_2/Ga ratio may be as high as $\sim$10 [Ichige et al., 1988].

While it clearly appears that a decomposition process is taking place in nanosecond ablation of nitrides, the underlying ablation mechanisms are still unclear. Desorption studies have identified a bond-breaking electronic mechanism that dimerizes both Group III and V species before being ejected from the surface [Namiki et al., 1991], but how relevant this is to highly decomposed ceramic target surfaces with high concentrations of defects and grain boundaries is debatable. Considering that the optical absorption coefficients of the nitrides, especially GaN and AlN, vary strongly across the commonly used excimer wavelengths, a clear influence of laser type on the ablation mechanism might be expected, particularly for single-shot experiments. On the other hand, if, after several pulses, the depth of the metal-rich layer is much greater than the optical penetration depth (which is clearly the case when using microsecond pulses [Hirayama et al., 2001]), then the ablation mechanism is likely to mimic that of a Group III metal. Making comparisons between ablation studies using ceramic targets is unreasonable considering the presumably wide variation in target quality (especially, GaN and InN, which are difficult to sinter). More conclusive agreement is apparent from studies using single-crystal nitrides. For example, several groups have reported an ablation threshold for GaN single-crystal films, with values of 0.3 J cm^{-2} [Wong et al., 1998; Akane et al., 2000; Chu et al., 2001] and 0.42 J cm^{-2} observed for 248 nm [Kelly et al., 1996] (20 ns) and 355 nm (5 ns) laser pulses, respectively. The corresponding ablation depth per pulse just above the threshold was 35 nm at $\lambda = 248$ nm and 70 nm at $\lambda = 355$ nm, which correlates well with the value of 55 nm measured by Zhang et al. [1998] and optical absorption depth for GaN in this spectral range [Muth et al., 1997]. For high-resolution laser machining of GaN, shorter laser wavelengths are generally preferred, indicating that thermal damage can be limited accordingly. It also suggests a process dominated by strong above band-edge absorption and direct photoionization of the irradiated region [Zhang et al., 1998; Akane et al., 2000]. When using a fluence of a few J cm^{-2}, the ablation plume is considerably ionized (Fig. 13.3) and the dominant ions are Group III species [McKiernan and Mosnier, 2002; Ristoscu et al., 2003]. Direct photoionization of the target material may be significant as in the case of wide bandgap oxide dielectrics [Dickinson et al., 1994; Gilgenbach et al., 1994]. It is also clear that for ablation in vacuum at moderate fluence (1–10 J cm^{-2}), the mean energy of metal ions in the plume can be of the order of 5–10 eV (see Fig. 13.3b).

The ablation threshold for ceramic targets is likely to be less than that of single crystals [Gunster et al., 2001; O'Mahony, 2004] because of their inferior mechanical strength and high defect density, but in any case the fluence used in PLD of GaN is typically 2–5 J cm^{-2} to obtain sufficient yields for deposition.

While the ablation of ceramic AlN has been of considerable interest for some time now, only recently has the ablation of single-crystal AlN been reported. Safadi et al. [2005] have observed an incubatory effect in the ablation of single-crystal AlN using 248-nm (25-ns) pulses, where several laser pulses were required for the ablation rate at near threshold fluence to stabilize. There may be

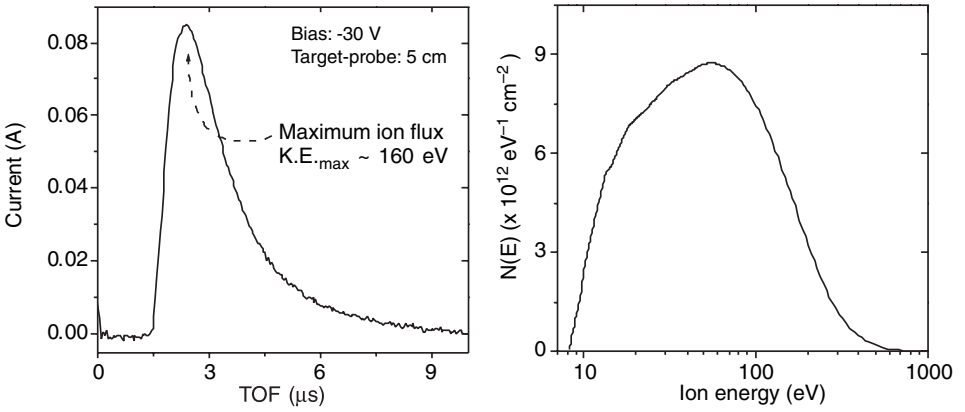

Figure 13.3 Ion characteristics for GaN ablation at 2.5 J cm^{-2} (248 nm, 27 ns) in high vacuum measured using a negatively biased (−30 V) flat Langmuir ion probe with a projected ion collecting area of 0.06 cm^2: (a) Ion time-of-flight (TOF) signal at 5 cm from the target (left) and (b) the corresponding ion energy distribution, assuming only singly charged Ga^+ ions are collected by the probe. Adapted from O'Mahony [2004].

unresolved issues relating to a theoretical description of ceramic target ablation, but from a practical point of view, UV lasers are preferred for cleaner processing of commercial-grade AlN ceramics [Lumpp and Allen, 1997], thus particulate production in films is also less likely in PLD when using shorter wavelengths. Finally, a comment on recent progress in the area of femtosecond ablation of nitrides that has given some clear insight into the effect of pulse duration on both the irradiated target region and plume diagnostics. Target decomposition can be practically avoided when using subpicosecond laser pulses [Hirayama et al., 2001; Liu et al., 2002; Ristoscu et al., 2003], presumably because the thermally heated zone is very much limited compared with nanosecond ablation. Furthermore, analysis of the plume has revealed AlN^+ molecules are dominant in AlN target ablation using femtosecond pulses, whereas for nanosecond ablation Al atoms and ions dominate [Ristoscu et al., 2003]. Despite indications of congruent ablation in this study, significant quantities of Al were subsequently identified in the plume, particularly when the number of shots on the target increases to several hundred. Furthermore, Kim et al. [2001] reported a Ga residue surrounding the ablation crater of a GaN target ablated in air with femtosecond pulses indicating that the plume contains free Ga. Thus it remains to be seen whether there is a distinct advantage in using femtosecond lasers for PLD of Group III nitrides.

13.3.2.2 Metal Target Ablation in Vacuum

The ablation characteristics of commonly used metals such as Al have received considerable attention for several decades now (see, e.g., Dreyfus [1991] and references therein); here we limit the discussion to some relevant aspects pertaining to Group III nitride PLD using Group III metals. For Al, a fluence of ~3 J cm^{-2} using nanosecond UV laser pulses yields sufficient ablation rates for PLD (~10 nm per pulse) [Timm et al., 1996; Thestrup et al., 2002], although the threshold and yield seems to be quite strongly wavelength dependent [Kelly et al., 1998; Torrisi et al., 2000]. Corresponding ablation data for In and Ga is limited; nevertheless, it was shown that the mass loss for nanosecond ablation of In and Al targets at 355 nm scaled according to their melting temperatures [Thestrup et al., 2002] and presumably such behavior may also hold for Ga. This work also reports that for Al target ablation at a fluence of 2 J cm^{-2}, the ionization fraction in the plume was 0.6, so the ionic component of the plume is likely to play a major role in subsequent processes in the gas phase or at the substrate.

In and particularly Ga have low melting temperatures; therefore, it is worth considering some interesting behavior observed in fast-imaging studies of laser-ablated molten metal target surfaces.

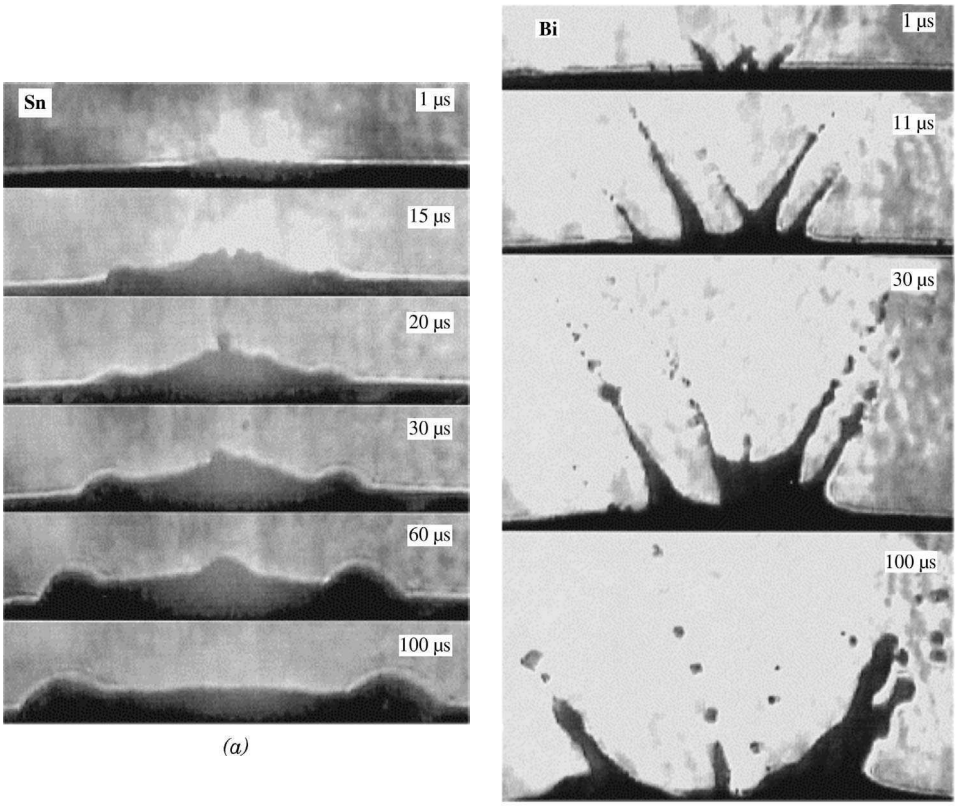

Figure 13.4 Surface dynamics for liquid–metal targets ablated with a 10-ns 248-nm laser pulse [Toth et al., 1999]: (a) wavelike formation on the surface of a molten Sn target and (b) droplet expulsion from a liquid Bi target. In both cases, the fluence was 5.5 J cm^{-2} and the background gas pressure was 10^{-6} mbar. The frame width is approximately 0.8 mm. Reprinted with permission from Elsevier and the authors (© 1999).

Toth et al. [1999] have studied the surface dynamics of liquid targets ablated at medium fluence (5.5 J cm^{-2}, $\lambda = 193$ nm) and observed that a rippled structure developed on the surface, as illustrated in Figure 13.4a. They also noted that the relaxation time for these ripples could be of the order of seconds, and a dramatic expulsion of liquid droplets occurred when ablating Bi targets with a fluence of 5.5 J cm^{-2} (Fig. 13.4b). However, splashing ceased once the fluence was reduced to $\sim$2 J cm^{-2}. Similarly, in laser ablation of liquid AlGa alloy targets [Rupp et al., 2002], droplet production was avoided by limiting the fluence to below 5 J cm^{-2}. From the point of view of avoiding particulate accumulation in PLD using liquid targets, it would be useful to establish some criteria to identify thresholds for the onset of splashing. In this regard, the discussion by Von Allmen [1976] on liquid expulsion in laser ablation may be worth considering.

13.3.3 Plume–Background Gas Interaction

For PLD in a background gas, there is a complicated interaction between the ablation plume and the gas, which at low background pressures (typically 0.001–0.01 mbar) involves scattering and broadening of the angular distribution of the plume [Saenger, 1994] and subsequently a reduction of the number of ablated particles reaching a substrate placed directly in front of the target. When the gas pressure is increased such that the corresponding mean free path of the plume particles in the background gas is

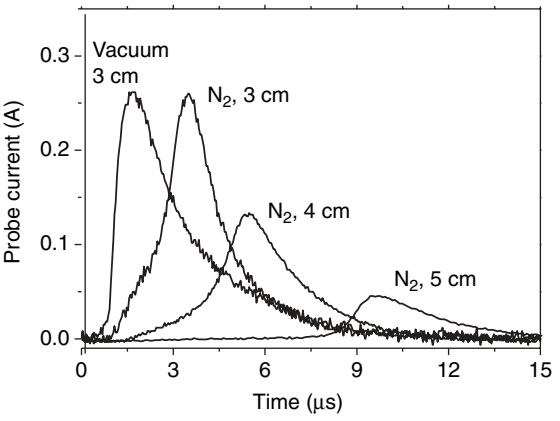

Figure 13.5 Ion TOF signals for excimer (248 nm, 27 ns) laser ablation at 2.5 J cm^{-2} of GaN in high vacuum (at 3 cm) and 0.13 mbar N_2 (at 3, 4, and 5 cm) measured using a Langmuir ion probe. Adapted from O'Mahony et al. [2003b].

reduced to less than ~1 cm, the plume particles undergo a significant number of collisions with the background gas, which in turn leads to compression of the gas and the launch of a shock wave [Zel'dovich and Raizer, 1965]. Much of the ablated material is contained in the volume inside the shock front, and as the front slows, the kinetic energy of the initial ablation plume is thermalized. At sufficiently high pressures and/or longer distances, the material is transported toward the substrate via diffusion. The role and importance of the background gas pressure can vary considerably in PLD, from subtle crystallographic effects to dramatic changes in composition, and this discussion is not intended to be an exhaustive overview of the many areas of influence involving gases. Instead, the focus will be on the influence on film composition, particularly in the case of growth using N_2, since this is perhaps most relevant to PLD and has been the major stumbling block for other Group III nitride growth techniques in the past.

Evidence pointing to a strong interaction between the background gas and ablation plume can be found in dynamical and compositional features of the plume and in the dependence of the film properties on gas pressure. Studies of the plume dynamics using various time-of-flight (TOF) techniques (e.g., Fig. 13.5) [Giardini Guidoni et al., 1997; McKiernan and Mosnier, 2002; O'Mahony et al., 2003b] reveal an obvious deceleration of the plume species at pressures of the order of ~0.1 mbar at a distance of a few centimeters from the target (it should be noted that the important quantity is the pressure–distance product rather than pressure or distance separately; see, for example, Koopman [1971]). As the pressure is increased, the interaction time of the plume material with the substrate is also extended, which may benefit the growth of some materials. Both ions and neutrals undergo significant scattering, though scattering cross-section estimates for both indicate that neutrals may be more strongly scattered under typical PLD conditions [Koopman, 1972; Willmott et al., 1997]. Whether decoupling of the plume's kinetic energy component leads to significant internal modification of the plume species (e.g., excitation, ionization, or reactions between ablated species) is not clear for Group III ablation but has been predicted for oxide ablation in O_2 [Gordillo-Vazquez and Gonzalo, 2003]. Furthermore, the ionization fraction for Ti ablated in N_2 increased two orders of magnitude by optimizing the timing of the interaction using a pulsed N_2 source [Willmott et al., 1997]. It is clear that significant activation of the background gas can be achieved. Dissociation and ionization of a comparatively inert gas such as molecular nitrogen (dissociation/ionization energy = 9.8 eV/15 eV) has been predicted for Al and Ti ablation in N_2 [Hermann and Dutouquet, 2002] and confirmed experimentally for Ga [Rupp et al., 2002] and Ti [Willmott et al., 1997] ablation in N_2. Other than neutral and ionized atomic nitrogen, excited molecular species may also be present in significant

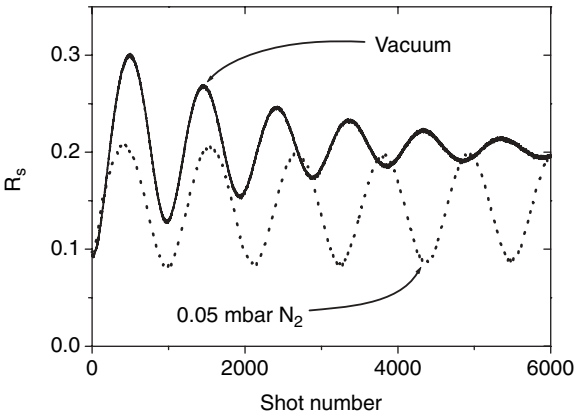

Figure 13.6 Reflectivity vs. laser shot number at 635 nm and 25° incidence for deposition on sapphire at room temperature using a GaN target ablated at 2.5 J cm^{-2}. The solid line shows the variation of the *s*-polarized reflectivity (R_s) with increasing film thickness in high vacuum (10^{-5} mbar) while the dotted line shows the reflectivity for deposition in 0.05 mbar N_2. Adapted from O'Mahony [2004].

quantities since it has a lower activation energy ($\sim$6 eV) compared with ionization or dissociation [Newman, 1997] (refer to Section 13.4.3.2).

There is ongoing speculation as to whether the dominant nitridation reaction takes place during the plume expansion, that is, before it reaches the substrate [Zhou and Andrews, 2000] or at the substrate [Willmott et al., 1997; Hermann and Dutouquet, 2002] or indeed both. Evidence proposing the existence of MN (M = Al, Ga or In) in the gas phase before reaching the substrate is not convincing [Giardini Guidoni et al., 1997], but several authors [Andrews et al., 2000; Li and Brenner, 2004] have proposed that this does not preclude the existence of other nitrides of the form M_xN_y $(x, y > 1)$. Indeed, it has been suggested that the diatomic nitride (MN) is the most unstable of several possible gas-phase nitride compounds (e.g., M_3N) and is insignificant with regard to the likely makeup of either the gas-phase species or important film growth precursors in Group III nitride film growth [Li and Brenner, 2004]. TOF mass spectroscopy for Al ablation in ammonia has revealed that the plume contained clusters of the form $Al(NH_3)_n$ where $n = 3, 4, 5$ [Giardini Guidoni et al., 1997], and clusters of $In(NH_3)_n$ were identified when ablating indium in NH_3 [Di Palma et al., 1997], thus suggesting similar behavior for other nitrogen sources. Whatever the nitriding mechanism involved, the beneficial effects of using an adequate background gas pressure for film growth is clearly illustrated by the change in film properties following the introduction of the gas. For example, films grown in high vacuum on unheated (room temperature) substrates by PLD using a GaN target show optical absorption features typical of a semimetal (metal-rich GaN_{1-x}), whereas this absorption characteristic is absent in films deposited at (0.05) mbar N_2 (Fig. 13.6). While the films grown in high vacuum were metallic-like (mirror) in appearance, those grown in 0.05 mbar N_2 were transparent with a slightly yellow coloring [O'Mahony et al., 2003a]. Even at higher substrate temperatures (900°C), Al metal has been detected by X-ray diffraction (XRD) in films deposited using an AlN target in vacuum but a background gas pressure of 5×10^{-2} Pa N_2 was sufficient to overcome the nitrogen deficiency.

13.4 GUIDELINES FOR FILM GROWTH

13.4.1 Setting the Growth Parameters

At first glance, a survey of the reported "optimum" deposition conditions might suggest that the guidelines for Group III nitride growth by PLD might not be so clearly defined as deposition has

been carried out under quite a wide range of conditions. Target materials, laser fluence, background gas types and pressures, as well as substrate types and temperatures used have all varied considerably. However, some general trends have emerged, and these can be understood in terms of the material properties and features of the plume–gas interaction discussed in the previous sections. In particular, the type of target greatly influences the range of background gas pressure and laser fluence that should be used. The following sections consider some basic guidelines for growth using either a metal or ceramic target in various environments.

13.4.2 Film Growth in N_2

In nitride film deposition, the growth rate is limited by competing deposition and decomposition (i.e., thermal evaporation) processes at the substrate. For nanosecond ablation of ceramic nitride targets at a fluence of a few J cm^{-2} and a background gas pressure of $\sim$0.1 mbar, the deposition rate may be reduced slightly due to scattering of plume species by the gas, but at the same time compensated by the nitriding effects associated with the plume gas interaction. In any case, an N_2 background gas pressure of this magnitude at a fluence of 2–5 J cm^{-2} has proved suitable for achieving sufficient growth rates ($\sim$5 nm/min at 10 Hz shot repetition rate) and obtaining stoichiometric material [Norton et al., 1991; Feiler et al., 1997; O'Mahony et al., 2003a].

Stoichiometric nitride film growth has been achieved with metal targets using N_2, but comparatively high fluence, in the range 5–25 J cm^{-2}, is required to achieve useful deposition rates [Dinescu et al., 1998; Willmott and Antoni, 1998; Mah et al., 2002]. For these high fluences, sputtering is to be expected [van de Riet et al., 1993; Dorneles et al., 2005] unless a sufficiently high background gas pressure is used to moderate the directed energy of the ablated material. Indeed the background gas pressures used are often an order of magnitude higher than those used in conjunction with ceramic targets [Deiss et al., 2001; Mah et al., 2002], but growth rates are still significantly lower compared with growth in N_2 or indeed when using metal targets in ammonia [Willmott et al., 2000]. Recall also that the use of high fluence also leads to droplet expulsion due to the ablation of a modulated surface and splashing (Section 13.3.2.2). Selective deposition using an off-axis deposition configuration [Mizuno et al., 2002] (and see Chapter 6), to avoid droplet accumulation may also be necessary if high-grade material is to be obtained using N_2 in conjunction with a Ga target.

13.4.3 Film Growth in Other Atmospheres

13.4.3.1 Growth in Ammonia

Despite the fact that the reaction of ammonia with the Group III metals to form a nitride is characterized by a lower heat of formation compared with that of N_2 (e.g., see Newman [1998]), it seems that there is still a requirement for relatively high fluence (>5 J cm^{-2}) when using it as a background gas in PLD with metal targets [Xiao et al., 1996; Giardini Guidoni et al., 1997]. For GaN film growth from a ceramic target, deposition in ammonia has yielded higher growth rates than in N_2 and some high-quality material [Cole and Lunney, 1997; Willmott et al., 2000]. However, Willmott et al. [2000] have shown that while GaN grown in NH_3 by PLD contained less than 0.2 at % hydrogen impurities, the optical quality of these films was considerably lower than that of films grown in N_2. They concluded that for growth in NH_3, the surface mobility of Ga was hindered by prompt reaction with the nitriding species. Postgrowth treatments are required to obtain *p*-type conduction nitride films grown by other techniques using ammonia as the nitrogen source [Amano et al., 1989] and nitride films deposited in ammonia by PLD have invariably been *n*-type (Section 13.5.2). Therefore, the use of NH_3 for the effective growth of high-grade material is debatable.

13.4.3.2 Growth with Nitrogen Plasma Sources

Plasma sources provide considerable control of the flux and type (e.g., molecular, atomic, ionic, or neutral, etc.) of excited nitrogen species delivered to the nitride growth environment. The ideal

source should provide active species with low kinetic energies to limit film sputtering [van de Riet et al., 1993]. Anders and co-workers have shown that in the small-anode direct current (DC) discharge developed by Miljevic [1984], the ion energies are less than 20 eV, making it suitable for MBE growth of GaN [Anders et al., 1996]. Since a low-pressure deposition environment (<0.1 mbar) is required to operate this source, it should also be suitable for discharge-assisted PLD of nitrides. To date, a range of discharge sources has been used in PLD with metal targets and yielded good control of the III : V ratio in films [Fernandez et al., 2000; Deiss et al., 2001; Merel et al., 2001; Basillais et al., 2005]. For discharge-assisted PLD, the laser fluence is usually somewhat lower, and the gas pressure much lower, than the typical values for deposition in N_2 or NH_3. Further work is required to clarify which nitrogen species, that is, atoms, excited molecules, or ions, are most suited to PLD growth of Group III nitrides. The high GaN growth rates achieved with a source delivering $(A^3\Sigma_u^+)$ excited molecular N_2 to an MBE growth environment suggest that it is highly suited to nitride growth due to its low reaction exothermicity with the Group III metal [Jordan et al., 2000]. In addition, Newman [1997] has suggested that moderate ion energies (5–10 eV) may produce a substantial enhancement in surface diffusion in GaN film growth, while the kinetic energies of the reacting species should not exceed 27 eV if sputtering of the film is to be avoided. Observations relating to GaN films grown by PLD [Mizuno et al., 2002] and magnetron sputtering [Meng and Perry, 1994] indicate that the threshold energy for significant sputtering is indeed of this magnitude.

13.4.4 Substrates and Growth Temperature

The most widely used substrate in Group III nitride film growth is sapphire because it has a hexagonal structure, is stable at typical film growth temperatures ($\sim$1000 K) and in aggressive environments, and is of relatively low cost compared with better lattice-matched substrates such as SiC [Strite and Morkoc, 1992]. Typically in thin-film growth, the substrate temperature is chosen to be 50–75% of the melting temperature of the film [Newman, 1997], whereas practical heating equipment limitations and decomposition rules out using such high temperatures in Group III nitride growth. Maximum substrate temperatures of $\sim$950, 850, and 450°C have been reported for PLD-grown AlN, GaN, and InN, respectively, on sapphire. For deposition of Group III nitrides on sapphire, epitaxial growth is observed only at temperatures above 500°C for GaN [Mah et al., 2002] and AlN [Vispute et al., 1999]. Group III nitrides have also been grown on Si [Willmott and Antoni, 1998; Fernandez et al., 2000] since it seems to allow crystalline growth at considerably lower growth temperatures (200–300°C). Crystalline AlN films have even been deposited on room temperature substrates [Seki et al., 1992; Ren et al., 2000; Ohta et al., 2002]. Recently, large-area (50 mm diameter) freestanding GaN wafers, with excellent lattice and thermal matching properties have become commercially available, obtained by separating or slicing thick (up to 1 mm) GaN layers from sapphire substrates, have become commercially available [Xu et al., 2003].

13.5 SELECTIVE REVIEW OF THE PROPERTIES OF AlN, GaN, AND InN FILMS GROWN BY PLD

13.5.1 Structural Properties

Group III nitride thin films tend to have a high density of defects ($\geq 10^6$ cm^{-2}) at the film–substrate interface in comparison with other layered structures used in the fabrication of electronic and optoelectronic devices. This is primarily due to the significant lattice mismatch between nitride films and commonly used substrates, particularly in the case of sapphire. Somewhat surprisingly, the effects of these defects on electrical and optical performance are not as detrimental as might be expected, that is, as in GaAs or Si, but it remains one of the main challenges facing Group III nitride film growers. For MOCVD-grown layers, lattice mismatch was greatly reduced by incorporating a low-temperature ($\sim$400°C) amorphous buffer layer in the film growth stage [Nakamura et al., 1993].

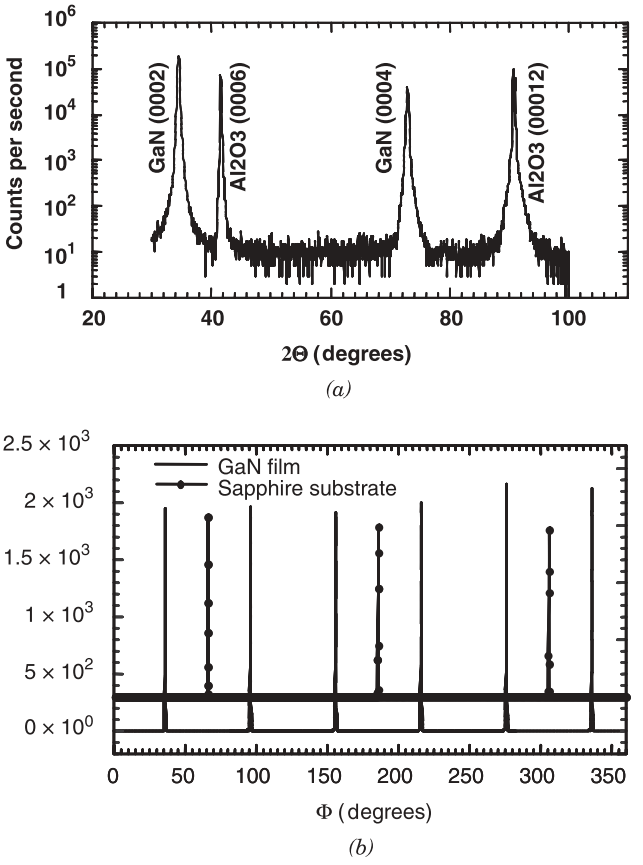

Figure 13.7 X-ray diffraction spectra for a 0.5-μm GaN film grown by PLD from a GaN target on (0001) sapphire (no intentional buffer layer growth) (Vispute et al., 1999). (a) θ-2θ pattern indicating strong c-axis growth. (b) ϕ-scans showing the {1011} GaN film and {1014} sapphire substrate reflections indicating a 30° in-plane rotation of the film with respect to the substrate. Reprinted with permission from the Minerals, Metals and Materials Society and the authors (© 1999).

Buffer layer growth can be achieved in a number of ways; for example, a nitride layer may be deposited at a lower temperature than the main growth value [Henn et al., 2002] or it may be formed by exposing the heated substrate, typically at temperatures >1000°C, to a reactive atmosphere such as NH_3 or nitrogen plasma [Deiss et al., 2001; Merel et al., 2001]. It also seems that an unintentionally grown buffer layer may form during the early stages of film growth on bare sapphire [Vispute et al., 1999]. Alternatively, a non-nitride layer, for example, ZnO, with lattice parameters intermediate between the nitride and the substrate, can be used [Xiao et al., 1996].

Figure 13.7a shows the θ-2θ XRD scan for a GaN film grown in NH_3 at 750°C on (0001) sapphire [Vispute et al., 1999], where the authors noted the existence of an unintentionally grown buffer layer. Clearly the film is highly oriented, with the c-axis normal to the substrate. The in-plane orientation of these films was determined using XRD ϕ-scan (Fig. 13.7b), which revealed a 30° in-plane rotation of the film with respect to the substrate such that GaN$[1\bar{1}00]$ || $Al_2O_3[11\bar{2}0]$. These authors reported the same epitaxial relationship for AlN on sapphire. Feiler et al. [1997] also observed this alignment for AlN and GaN films grown on (0001) sapphire. However, for InN growth, they reported a 60° in-plane rotation of the film with respect to the substrate, such that InN$[1\bar{1}00]$ || Al_2O_3 $[10\bar{1}0]$. High structural quality GaN has also been grown using a cooled Ga target with the aid of an atomic

nitrogen source [Merel et al., 2001], thus it seems that single-crystal epitaxial growth of Group III nitrides can be achieved with PLD. While sapphire is the most commonly used substrate for Group III nitride PLD, there is considerable interest in exploring the potential of using Si as a substrate since this would facilitate the integration of nitride devices with conventional Si microcircuitry. Willmott and Antoni [1998] have used pulsed reactive crossed-beam laser ablation (PRCLA) with a Ga target in N_2 to grow films of GaN on Si (001). They found that crystalline growth can be achieved at lower temperatures on Si than on sapphire, but the cubic structure of Si may not facilitate single-crystal epitaxy. Rather, the authors have identified a locked-twinned growth mode for GaN on Si (001) where the sides of GaN hexagonal crystallites tend to align along both of the equivalent Si$\langle 110 \rangle$ azimuths. As a result, the regions between the crystallites are likely to contain a high density of defects and possibly amorphous material.

Whereas most of the interest to date has been directed toward crystalline growth of nitrides, there are possible applications for amorphous material. For example, amorphous GaN prepared by reactive sputtering was shown to have a larger bandgap (3.9 eV) than hexagonal wurtzite GaN [Nonomura et al., 1996]. Considering the difficulties associated with thermal decomposition, this may be an area of interest in the future, and recently room temperature luminescence was observed at $\sim$2.8 eV in amorphous GaN grown by off-axis PLD on unheated quartz substrates [Shim et al., 2005].

13.5.2 Electronic Properties

Group III nitride films grown by techniques other than PLD are, in general, intrinsically *n*-doped and require postgrowth treatments, such as annealing [Nakamura et al., 1993] or electron-beam irradiation [Amano et al., 1989], to enhance film quality. For PLD, GaN films grown in NH_3 [Xiao et al., 1998] and ultra-high vacuum (UHV) [Feiler et al., 1997] were *n*-type, whereas growth in N_2 has yielded *p*-type films. Feiler et al. [1997] measured a room temperature Hall mobility of 300 cm^2 V^{-1} s^{-1} for *n*-type GaN films grown under UHV conditions, whereas *p*-type films deposited in 0.013 mbar N_2 had a mobility of 150 cm^2 V^{-1} s^{-1}. These values compare well with GaN films deposited by other techniques [Chin et al., 1994]. For InN, *p*-type films grown in N_2 showed considerably higher mobility (240 cm^2 V^{-1} s^{-1}) compared to those grown under UHV conditions (30 cm^2 V^{-1} s^{-1}). In both cases, the target used was a pressed InN powder pellet. Rupp et al. [2002] observed *n*-type conduction for InN films grown from an In metal target in 0.13 mbar N_2 and measured an electron mobility of 350 cm^2 V^{-1} s^{-1}. Similarly, their GaN films grown from a liquid gallium target in a nitrogen background were *n*-type. The *p*-type doping of GaN has been attempted using MgGa alloy targets, containing up to 10% Mg [Rupp et al., 2002]. At low doping fraction ($\sim$0.01), a hole concentration of $\sim 10^{19}$ cm^{-3} was measured, but the films became highly resistive when the Mg composition in the target was increased above 8%.

13.5.3 Optical Properties

Several groups have measured the bandgap of PLD-grown nitride films using photoluminescence (PL) and optical transmission techniques [Cole and Lunney, 1997; Huang et al., 1999; Vispute et al., 1999]. Cazzanelli et al. [1998] have measured the temperature dependence of the PL decay time for a PLD-grown GaN film and observed room temperature radiative lifetimes of the order of tens of nanoseconds. While strong band-edge emission has been reported at room temperature [Huang et al., 1999], yellow-green luminescence (indicating defects) is also usually observed for both AlN and GaN [Vispute et al., 1999]. GaN films deposited in high vacuum (10^{-6} mbar) showed considerably stronger yellow-green emission than those grown in 0.1 mbar N_2 [Cole and Lunney, 1997]. A comparison of the luminescence properties of GaN films grown in N_2 and NH_3 atmospheres revealed considerably stronger yellow-green luminescence for those grown in NH_3 [Willmott et al., 2000]. This was attributed to antisite defects, that is, Ga atoms in N sites and vice versa, resulting from limited Ga surface mobility associated with growth in NH_3. The benefits of

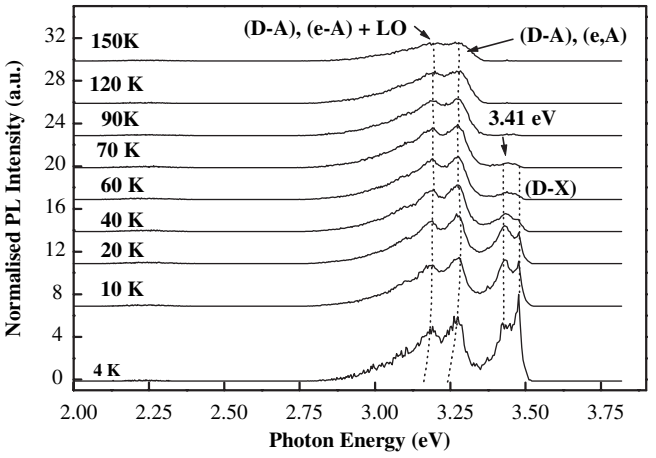

Figure 13.8 Temperature variation in the photoluminescence spectra for a GaN film grown on (0001) sapphire [Mah et al., 2001]. The film was grown at 700°C in 0.3 mbar N_2 from a ceramic GaN target. Reprinted with permission from Elsevier (© 2001).

incorporating a buffer layer were noted by Vispute et al. [1999] who observed that GaN films grown with an AlN buffer had considerably fewer structural defects and significantly intensified band-edge emission than those grown on bare sapphire substrates. Figure 13.8 shows the temperature dependence of the photoluminescence (PL) for a GaN film deposited on sapphire in 0.3 mbar N_2 with the yellow-green PL virtually absent for temperatures up to 150 K [Mah et al., 2001]. Indicated in the figure are some of the luminescence peaks that are generally observed at low temperature in GaN thin films. The donor-bound exciton (D-X) was observed at 3.471 eV, with a full-width at half-maximum (FWHM) of 15 meV, which is comparable to GaN grown by MOCVD and MBE. The neutral donor-to-acceptor (D-A) transition is observed at 3.278 eV, with a transition corresponding to a longitudinal optical (LO) phonon replica at 3.186 eV. The origin of the 3.41-eV peak is still unclear, though it may be due to oxygen impurities [Huang et al., 1999] or cubic inclusions in the predominantly wurtzite structure [O'Donnell et al., 1997].

13.6 NOVEL AREAS OF RESEARCH

13.6.1 Composites for Electronic and Optoelectronic Applications

Although the commercial potential of electronic devices from PLD-grown nitride films has yet to be fully explored, PLD has been used to fabricate devices for microelectronic applications ranging from insulating layers in Josephson device heterostructures [Orgiani et al., 2005] and piezoelectric actuation in MEMS resonator devices [Wickenden et al., 2003]. PLD-grown AlN/BN has also been identified as a suitable capping layer combination for ion-implanted SiC [Ruppalt et al., 2003]. Vispute et al. [2000] have fabricated metal–insulator–semiconductor (MIS) capacitors composed of TiN-AlN-SiC. The current–voltage characteristics showed comparatively low leakage currents ($\sim 10^{-3}$ A/cm^2) even at 450°C in a field of 2 MV/cm^2. Similar structures, incorporating 100-nm Pt layers and 200-nm AlN on SiC substrates, have been developed as sensors for combustible gas detection [Samman et al., 2000]. Attaching low-resistance electrode contacts with adequate adhesion is especially challenging in the fabrication of nitride-based LEDs [Strite and Morkoc, 1992], and in this regard PLD may prove an effective alternative for depositing suitable conductors, such as TiGaN [Ren et al., 1998].

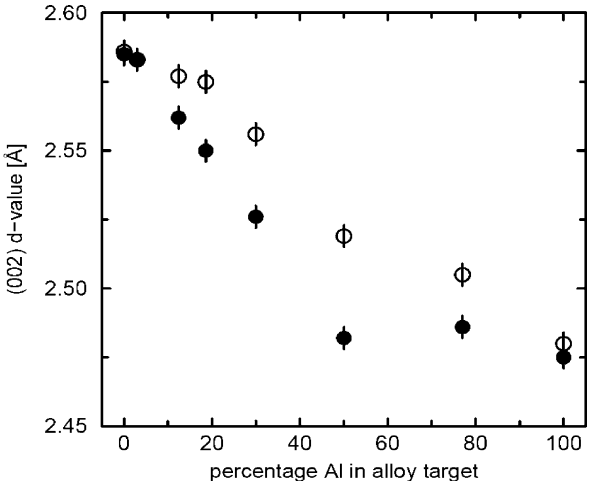

Figure 13.9 Variation of (0002) lattice plane spacing for $Al_xGa_{1-x}N$ films grown in N_2 (solid circles) and in NH_3 (open circles) as a function of the Al percentage in the liquid alloy target [Willmott et al., 2000]. Reprinted with permission from the American Institute of Physics and the authors (© 2000).

Ternary compounds of the form $A_xB_{1-x}N$ (where A and B are Group III elements) could facilitate tuning of the bandgap over the full spectral range of the nitrides, from the near UV to red wavelengths (200–650 nm). Furthermore, it has been shown that In-doped GaN quantum layers greatly enhance the internal quantum efficiency of LEDs and LDs, so from a device engineering point of view, it is important to have capabilities in this area of compositional control [Bhuiyan et al., 2003].

Fernandez et al. [2000] have grown $In_xGa_{1-x}N$ films by laser ablation of a liquid In–Ga mixture comprised of 29% Ga in a radio frequency (RF) nitrogen discharge. Films grown at higher temperatures had a smaller lattice constant and larger bandgap, indicating a lower indium fraction, presumably due to the preferential evaporation of In from the film surface. This behavior may provide a simple method for tuning the In : Ga ratio and subsequently the bandgap. $Al_xGa_{1-x}N$ thin films have also been grown from liquid metal Al : Ga targets [Willmott et al., 2000]**.** The films were grown in both N_2 and NH_3 background gases, and the Al concentration was varied from 0 to 100%. Figure 13.9 shows how the *c*-lattice parameter of these films varies with Al concentration in the target. While growth in NH_3 generally resulted in films with Al concentrations that were very close to the target preparations, films grown in N_2 had consistently higher Al concentrations than in the target, due to a higher Ga evaporation rate in N_2 where the nitriding reaction is slower than in NH_3. A similar substrate temperature dependence was observed in the Group III metal ratio for $Al_xGa_{1-x}N$ films grown from metal alloy targets [Rupp et al., 2002].

Alternatively, ceramic targets, prepared by mixing nitride powders, have been used for PLD of single-phase $Al_xGa_{1-x}N$ with up to 0.6 mol fraction Al [Huang and Harris, 1998]. However, the films were heavily *n*-doped, most probably due to the limited purity of the target powders. Otherwise, ternary nitrides can also be prepared by alternating the ablation between two targets; the composition can be varied by changing the relative number of shots on each target [Vispute et al., 2000].

13.6.2 Magnetic Doping: Diluted Magnetic Semiconductors for Spin Electronics

Diluted magnetic semiconductor (DMS) growth has recently become an area of intense research with the aim of developing room temperature semiconductor-based spin-transport electronic devices for regulating the flow of spin-polarized current [Ball, 2000; Liu et al., 2005]. The growth of DMS

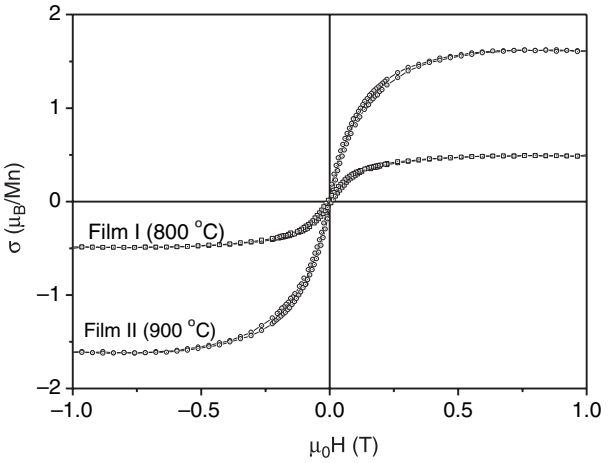

Figure 13.10 Room temperature magnetization for (Ga,Mn)N films grown at 800°C (film I: 26% Mn) and 900°C (film II: 21% Mn) on (0001) sapphire measured in a SQUID magnetometer [O'Mahony et al., 2004]. The films were grown in a N_2 background (0.1 mbar) using a $Ga_{1-x}Mn_xN$ target with Mn concentration, $x = 0.1$. The diamagnetic contribution of the sapphire substrate has been subtracted from the data. Reprinted with permission from Elsevier (© 2004).

materials involves doping a semiconductor such as GaAs or GaN with small concentrations of a transition metal (e.g., Mn or Fe). However, the thermal equilibrium solubility of Mn in III–V semiconductors is limited to about 2% [Szyszko et al., 2001], whereas higher concentrations (∼5%) are predicted to be necessary to obtain above-room temperature ferromagnetic transition (Curie) temperatures in GaMnN and AlMnN [Dietl et al., 2000; Litvinov and Dugaev, 2001]. Reed et al. [2001] succeeded in obtaining room temperature ferromagnetic GaMnN films; they used PLD to deposit a Mn layer on MOCVD-grown GaN and annealed the sample at 250–800°C to obtain ∼1% Mn films that showed hysteresis at 300 K. Much interest has been generated by reports of high-temperature ferromagnetism in various doped wide bandgap oxides grown by PLD, in particular, the observation of a giant Co moment in Co-doped tin oxide [Ogale et al., 2003; Venkatesan et al., 2004]. Recently (Ga,Mn)N films, exhibiting room temperature ferromagnetic behavior, have been grown on (0001) sapphire by PLD using a Mn-doped GaN target [O'Mahony et al., 2004; Dorneles et al., 2005]. The films, which seem to require higher growth temperatures than undoped GaN to maintain epitaxy, exhibit hysteresis at room temperature and the estimated moment per Mn dopant was as high as 1.6 μ_B (Fig. 13.10). These results are promising, but further characterization is necessary to establish the dopant solubility, the nature of the ferromagnetic coupling, and the spin coherence length.

13.7 SUMMARY AND OUTLOOK

Since PLD was first used to grow Group III nitride films in the early 1990s, interest in both the ablation and deposition processes has increased steadily, often opening up new areas of broadly applicable research. For example, before the growth of GaN and InN from their respective Group III metals, liquid target ablation was seldom used for compound material film growth in PLD. Laser ablation of single-crystal and ceramic nitride materials have revealed that for nanosecond pulses there is significant decomposition at the surface after ablation. Though it is not clear if laser decomposition is a problem for nitride PLD, it is a topic that requires further study in order to optimize the potential of UV laser etching and laser lift-off processes in device fabrication. The

existing literature on the thermodynamics of nitride reactions has provided some understanding of laser decomposition and the necessary conditions for nitride growth. In particular, these considerations have drawn attention to the possible benefits of using plasma discharge sources of excited nitrogen for assisted PLD of nitrides. However, while the general features of PLD of Group III nitrides are quite well understood, the details of the rather complex chemistry in the plume and at the plume–film interface have yet to be clarified.

Keeping in mind the recent success of MOCVD and MBE techniques for the fabrication of GaN-based multilayer structures for optoelectronic applications, PLD does not appear to be a commercially competitive film growth process in this technology area. Nevertheless, it is likely that PLD will continue to have a role for the deposition of novel nitride materials for research (e.g., DMS and nanostructures [Goodwin et al., 1997]), where exploration of a wide range of target compositions and doping combinations is often required. Discharge sources of excited nitrogen have accommodated the use of the high-purity metal targets, and it seems likely that this combination will be the preferred choice for the PLD of electronic-grade material, if sufficient growth rates and film stoichiometry can be obtained at low laser fluence to avoid droplet contamination. Indeed, it is the stoichiometry control of complex film structures and the extended solubility limits for bandgap tuning or magnetic doping that, perhaps, offer the best opportunity for establishing PLD as a niche area in nitride film growth.

Acknowledgments

Enterprise Ireland, under project SC/1998/751, and the Program for Research in Third-Level Institutions (PRTLI) funded by the Higher Education Authority (HEA) of Ireland supported this work. The authors acknowledge helpful discussions with Dr P. Willmott, Paul Scherrer Institute, Switzerland.

REFERENCES

Akane, T., K. Sugioka, S. Nomura, K. Hammura, N. Aoki, K. Toyoda, Y. Aoyagi, and K. Midorikawa (2000), *Appl. Surf. Sci.* **168**, 335–339.

Amano, H., M. Kito, K. Hiramatsu, and I. Akasaki (1989), *Jpn. J. Appl. Phys. Pt. 2* **28**, 2112–2114.

Anders, A., N. Newman, M. Rubin, M. Dickinson, E. Jones, P. Phatak, and A. Gassmann (1996), *Rev. Sci. Instrum.* **67**, 905.

Andrews, L., M. F. Zhou, G. V. Chertihin, W. D. Bare, and Y. Hannachi (2000), *J. Phys. Chem. A* **104**, 1656–1661.

Anisimov, S. I., B. S. Luk'yanchuk, and A. Luches (1996), *Appl. Surf. Sci.* **96–98**, 24–32.

Averyanova, M. V., I. N. Przhevalskii, S. Y. Karpov, Y. N. Makarov, M. S. Ramm, and R. A. Talalaev (1997), *Mater. Sci. Eng.* **B43**, 167–171.

Ball, P. (2000), *Nature* **404**, 918–920.

Basillais, A., R. Benzerga, H. Sanchez, E. Le Menn, C. Boulmer-Leborgne, and J. Perriere (2005), *Appl. Surf. Sci*. **80**, 851–859.

Bhattacharya, P., T. K. Sharma, S. Singh, A. Ingale, and L. M. Kukreja (2002), *J. Crystal Growth* **236**, 5–9.

Bhuiyan, A. G., A. Hashimoto, and A. Yamamoto (2003), *J. Appl. Phys.* **94**, 2779–2808.

Bogdanov, M. V., S. E. Demina, S. Y. Karpov, A. V. Kulik, M. S. Ramm, and Y. N. Makarov (2003), *Crystal Res. Technol.* **38**, 237–249.

Bor, J., and C. Bartholomew (1967), *Proc. of the Physical Society of London*, **90**, 1153.

Borisov, B. F., E. V. Charnaya, T. Loeser, D. Michel, C. Tien, C. S. Wur, and Y. A. Kumzerov (1999), *J. Phys. Condens. Matt.* **11**, 10259.

Cappelli, E., L. Esposito, F. Pinzari, G. Mattei, and S. Orlando (2002), *Diam. Relat. Matter* **11**, 1731–1746.

Cazzanelli, M., D. Cole, J. F. Donegan, J. G. Lunney, P. G. Middleton, K. P. O'Donnell, C. Vinegoni, and L. Pavesi (1998), *Appl. Phys. Lett.* **73**, 3390–3392.

Chin, V. W. L., T. L. Tansley, and T. Osotchan (1994), *J. Appl. Phys.* **75**, 7365–7372.

Chu, C. F., C. K. Lee, C. C. Yu, Y. K. Wang, J. Y. Tasi, C. R. Yang, and S. C. Wang (2001), *Mater. Sci. Eng. B—Solid State Mater. Adv. Technol.* **82**, 42–44.

Cole, D., and J. G. Lunney (1997), *Mater. Sci. Eng. B.* **50**, 20–24.

Deiss, J. L., C. Hirlimann, J. L. Loison, M. Robino, and G. Versini (2001), *Mater. Sci. Eng. B.* **B82**, 68–70.

Dickinson, J. T., S. C. Langford, J. J. Shin, and D. L. Doering (1994), *Phys. Rev. Lett.* **73**, 2630–2633.

Dietl, T., H. Ohno, F. Matsukura, J. Cibert, and D. Ferrand (2000), *Science* **287**, 1019–1022.

Dinescu, M., P. Verardi, C. Boulmer-Leborgne, C. Gerardi, L. Mirenghi, and V. Sandu (1998), *Appl. Surf. Sci.* **127–129**, 559–563.

Di Palma, T. M., A. Latini, A. Giardini Guidoni, A. Mele, S. Piccirillo, V. Marotta, and A. Santagata (1997), *Nucl. Instrum. Methods Phys. Res. B* **122**, 415–419.

Do, T., and N. S. McIntyre (1999), *Surf. Sci.* **440**, 438–450.

Dorneles, L. S., D. O'Mahony, C. B. Fitzgerald, F. McGee, M. Venkatesan, I. Stanca, J. G. Lunney, and J. M. D. Coey (2005), *Appl. Surf. Sci.* **248**, 406–410.

Dreyfus, R. W. (1991), *J. Appl. Phys.* **69**, 1721–1729.

Edgar, J. H. (Ed.) (1994), *Properties of Group III Nitrides*, INSPEC, London.

Feiler, D., R. S. Williams, A. A. Talin, H. Yoon, and M. S. Goorsky (1997), *J. Crystal Growth* **171**, 12–20.

Fernandez, F. E., E. Rodrigez, M. Pumarol, T. Guzman, W. Jia, and A. Martinez (2000), *Thin Solid Films* **377/378**, 781–787.

Fujii, T., Y. Gao, R. Sharma, E. L. Hu, S. P. DenBaars, and S. Nakamura (2004), *Appl. Phys. Lett.* **84**, 855–857.

German, R. M. (1996), in *Sintering Theory and Practice,* Wiley, New York, p. 1.

Giardini Guidoni, A., A. Mele, T. M. Di Palma, C. Flamini, S. Orlando, and R. Teghil (1997), *Thin Solid Films* **295**, 77–82.

Gilgenbach, R. M., C. H. Ching, J. S. Lash, and R. A. Lindley (1994), *Phys. Plasmas* **1**, 1619–1625.

Goodwin, T. J., V. J. Leppert, S. H. Risbud, I. M. Kennedy, and H. W. H. Lee (1997), *Appl. Phys. Lett.* **70**, 3122–3124.

Gordillo-Vazquez, F. J., and J. Gonzalo (2003), *J. Appl. Phys.* **94**, 7427–7432.

Gunster, J., R. Gorke, J. G. Heinrich, and R. Souda (2001), *Appl. Surf. Sci.* **173**, 76–83.

Hampshire, S. (1986), *Sintering of Nitrogen Ceramics,* Parthenon, Carnforth, United Kingdom, pp. 47–52.

Hansen, T. N., J. Schou, and J. G. Lunney (1999), *Appl. Phys. A* **A69**, 601–604.

Harrison, W. A. (1989), in *Electronic Structure, and the Properties of Solids*, 2nd ed., Dover, New York, p. 176.

Henn, G., T. Rupp, and H. Schroder (2002), *Mater Sci. Eng. B* **93**, 49–54.

Hermann, J., and C. Dutouquet (2002), *J. Appl. Phys.* **91**, 10188–10193.

Hirayama, Y., H. Yabe, and M. Obara (2001), *J. Appl. Phys.* **89**, 2943–2949.

Huang, T. F., and J. S. Harris, Jr. (1998), *Appl. Phys. Lett.* **72**, 1158–1160.

Huang, T. F., A. Marshall, S. Spruytte, and J. S. Harris, Jr. (1999), *J. Crystal Growth* **200**, 362–367.

Ichige, K., Y. Matsumoto, and A. Namiki (1988), *Nucl. Instrum. Methods Phys. Res. B.* **B33**, 820–823.

Jayaganthan, R., and Hajra, J. P. (1996), *Mat. Sci. Eng. B*. **38**, 96–102.

Jiemin, Z., and M. Lamvik (1998), *High Temp. High Press.* **30**, 307–314.

Jordan, D. C., I. S. T. Tsong, D. J. Smith, B. J. Wilkens, and R. B. Doak (2000), *Appl. Phys. Lett.* **77**, 3030–3032.

Karpinski, J., J. Jun, and S. Porowski (1984), *J. Crystal Growth* **66**, 1–10.

Kelly, M. K., A. O. Ambacher, B. Dahlheimer, G. Groos, R. Dimitrov, H. Angerer, and M. Stutzmann (1996), *Appl. Phys. Lett.* **69**, 1749–1751.

Kelly, R., A. Miotello, A. Mele, A. G. Guidoni, J. W. Hastie, P. K. Schenck, and H. Okabe (1998), *Appl. Surf. Sci.* **133**, 251–269.

Kim, T., H. S. Kim, M. Hetterich, D. Jones, J. M. Girkin, E. Bente, and M. D. Dawson (2001), *Mater. Sci. Eng. B* **82**, 262–264.

Kitanin, E. L., M. S. Ramm, V. V. Ris, and A. A. Schmidt (1998), *Mater. Sci. Eng. B* **55**, 174–183.

Kofman, R., P. Cheyssac, and J. Richard (1977), *Phys. Rev. B.* **16**, 5216–5224.

Kofman, R., P. Cheyssac, and R. Garrigos (1979), *J. Phys. F.* **9**, 2345.

Kolevzon, V. (1999), *J. Phys. (Condens. Matter)* **11**, 8785

Koopman, D. W. (1971), *Phys. Fluids* **14**, 1707–1716.

Koopman, D. W. (1972), *Phys. Fluids* **15**, 1959–1969.

Krishnan, S., and P. C. Nordine (1993), *Phys. Rev. B* **48**, 4130–4131.

Krukowski, S., A. Witek, J. Adamczyk, J. Jun, M. Bockowski, I. Grzegory, B. Lucznik, G. Nowak, M. Wroblewski, A. Presz, S. Gierlotka, S. Stelmach, B. Palosz, S. Porowski, and P. Zinn (1998), *J. Phys. Chem. Solids* **59**, 289–295.

Li, Y. X., and D. W. Brenner (2004), *Phys. Rev. Lett.* **92**, 075503-1–075503-4.

Lide, D. R. (Ed.) (1998) *Handbook of Chemistry and Physics*, CRC Press, Florida.

Litvinov, V. I., and N. K. Dugaev (2001), *Phys. Rev. Lett.* **86**, 5593–5596.

Liu, W.-M., R.-Y. Zhu, S.-X. Qian, S. Yuan, and G.-Y. Zhang (2002), *Chin. Phys. Lett.* **19**, 1711–1713.

Liu, C., F. Yun, and H. Morkoc (2005), *J. Mater. Sci. Mater. Electron.* **16**, 555–597.

Lowndes, D. H. (1998), in *Laser Ablation, and Desorption*, J. C. Miller and R. F. Haglund (Eds.), Academic, London, pp. 475–557.

Lumpp, J. K., and S. D. Allen (1997), *IEEE Trans. Compon. Packag. Manuf. Technol. Part B—Adv. Packag.* **20**, 241–246.

Mah, K. W., E. McGlynn, J. Castro, J. G. Lunney, J.-P. Mosnier, D. O'Mahony, and M. O. Henry (2001), *J. Crystal Growth* **222**, 497–502.

Mah, K. W., J.-P. Mosnier, E. McGlynn, M. O. Henry, D. O'Mahony, and J. G. Lunney (2002), *Appl. Phys. Lett.* **80**, 3301–3303.

McKiernan, A. P., and J.-P. Mosnier (2002), *Appl. Surf. Sci.* **197/198**, 325–330.

Meng, W. J., and T. A. Perry (1994), *J. Appl. Phys.* **76**, 7824–7828.

Merel, P., M. Chaker, M. Tabbal, and H. Pepin (2001), *Appl. Surf. Sci.* **177**, 165–171.

Miljevic, V. (1984), *Rev. Sci. Instrum.* **55**, 931–933.

Mizuno, K., Y. Masuyama, M. Kiso, J. Suzuki, and T. Kobayashi (2002), *Appl. Surf. Sci.* **197**, 490–493.

Morita, N., T. Watanabe, and Y. Yoshida (1989), *Appl. Phys. Lett.* **54**, 1974–1975.

Munir, Z., and A. Searcy (1965), *J. Chem. Phys.* **42**, 4223–4228.

Muth, J. F., A. J. H. Lee, I. K. Shmagin, R. M. Kolbas, H. C. Casey, Jr., B. P. Keller, U. K. Mishra, and S. P. DenBaars (1997), *Appl. Phys. Lett.* **71**, 2572–2574.

Nakamura, S., M. Senoh, and T. Mukai (1993), *Appl. Phys. Lett.* **62**, 2390–2392.

Namiki, A., K. Katoh, Y. Yamashita, Y. Matsumoto, H. Amano, and I. Akasaki (1991), *J. Appl. Phys.* **70**, 3268–3274.

Newman, N. (1997), *J. Crystal Growth* **178**, 102–112.

Newman, N. (1998), in *Gallium Nitride (GaN),* J. I. Pankove and T. D. Moustakas (Eds.), Academic, San Diego, pp. 55–98.

Nonomura, S., S. Kobayashi, T. Gotoh, S. Hirata, T. Ohmori, T. Itoh, S. Nitta, and K. Morigaki (1996), *J. Non-Crystal Solids* **198–200**, 174–177.

Norton, M. G., P. G. Kotula, and C. B. Carter (1991), *J. Appl. Phys.* **70**, 2871–2873.

O'Donnell, K. P., M. Umlauff, M. Kraushaar, H. Kalt, and O. Briot (1997), *Mater. Sci. Eng. B* **50**, 264–267.

Ogale, S. B., R. J. Choudhary, J. P. Buban, S. E. Lofland, S. R. Shinde, S. N. Kale, V. N. Kulkarni, J. Higgins, C. Lanci, J. R. Simpson, N. D. Browning, S. Das Sarma, H. D. Drew, R. L. Greene, and T. Venkatesan (2003), *Phys. Rev. Lett.* **91**, 077205–077201.

Ohta, J., H. Fujioka, S. Ito, and M. Oshima (2002), *Appl. Phys. Lett.* **81**, 2373–2375.

Okumura, H., K. Ohta, G. Feuillet, K. Balakrishnan, S. Chichibu, H. Hamaguchi, P. Hacke, and S. Yoshida (1997), *J. Crystal Growth* **178**, 113–133.

O'Mahony, D. (2004), "A Study of the Film Growth Environment in Pulsed Laser Deposition of GaN," Ph.D. Thesis, Trinity College, Dublin.

O'Mahony, D., E. de Posada, J. G. Lunney, E. McGlynn, and J. P. Mosnier (2003a), *Proc. SPIE* **4876**, 508–516.

O'Mahony, D., J. G. Lunney, G. Tobin, and E. McGlynn (2003b), *Solid State Electron.* **47**, 533–537.

O'Mahony, D., F. McGee, M. Venkatesan, J. G. Lunney, and J. M. D. Coey (2004), *Superlattices Microstruct.* **36**, 403–408.

Onderka, B., J. Unland, and R. Schmid-Fetzer (2002), *J. Mater. Res.* **17**, 3065–3083.

Orgiani, P., Y. Cui, A. V. Pogrebnyakov, J. A. Redwing, V. Vaithyanathan, D. G. Schlom, and X. X. Xi (2005), *IEEE Trans. Appl. Supercond.* **15**, 228–231.

Pankove, J. I., and T. D. Moustakas (Eds.) (1998), *Gallium Nitride (GaN) I*, Academic, San Diego.

Porowski, S., and I. Grzegory (1997), *J. Crystal Growth* **178**, 174–188.

Ranade, M. R., F. Tessier, A. Navrotsky, V. J. Leppert, S. H. Risbud, F. J. DiSalvo, and C. M. Balkas (2000), *J. Phys. Chem. B* **104**, 4060–4063.

Reed, M. L., N. A. El-Masry, H. H. Stadelmaier, M. K. Ritums, M. J. Reed, C. A. Parker, J. C. Roberts, and S. M. Bedair (2001), *Appl. Phys. Lett.* **79**, 3473–3475.

Regan, M. J., H. Tostmann, P. S. Pershan, O. M. Magnussen, E. DiMasi, B. M. Ocko, and M. Deutsch (1997), *Phys. Rev. B* **55**, 10786–10790.

Ren, J. Z., G. A. Rose, R. S. Williams, C. H. Booth, and D. K. Shuh (1998), *J. Appl. Phys.* **83**, 7613–7617.

Ren, Z. M., Y. F. Lu, H. Q. Ni, T. Y. F. Liew, B. A. Cheong, S. K. Chow, M. L. Ng, and J. P. Wang (2000), *J. Appl. Phys.* **88**, 7346–7350.

Ristoscu, C., I. N. Mihailescu, M. Velegrakis, M. Massaouti, A. Klini, and C. Fotakis (2003), *J. Appl. Phys.* **93**, 2244–2250.

Rupp, T., G. Henn, and H. Schroder (2002), *Appl. Surf. Sci.* **186**, 429–434.

Ruppalt, L. B., S. Stafford, D. Yuan, K. A. Jones, M. H. Ervin, K. W. Kirchner, T. S. Zheleva, M. C. Wood, B. R. Geil, E. Forsythe, R. D. Vispute, and T. Venkatesan (2003), *Solid-State Electron.* **47**, 253–257.

Saenger, K. L. (1994), in *Pulsed Laser Deposition of Thin Films,* D. B. Chrisey and G. K. Hubler (Eds.), Wiley, New York, pp. 199–225.

Safadi, M. R., J. S. Thakur, and G. W. Auner (2005), *J. Appl. Phys.* **97**, 084901–084906.

Samman, A., S. Gebremariam, L. Rimai, X. Zhang, J. Hangas, and G. W. Auner (2000), *J. Appl. Phys.* **87**, 3101–3107.

Schoonmaker, R. C., A. Buhl, and J. Lemley (1965), *J. Phys. Chem.* **69**, 3455–3460.

Seki, K., X. Q. Xu, H. Okabe, J. M. Frye, and J. B. Halpern (1992), *Appl. Phys. Lett.* **60**, 2234–2236.

Shiles, E., T. Sasaki, M. Inokuti, and D. Y. Smith (1980), *Phys. Rev. B* **22**, 1612–1628.

Shim, S. H., K. B. Shim, J. W. Yoon, Y. Shimizu, T. Sasaki, and N. Koshizaki (2005), *Thin Solid Films* **472**, 11–15.

Slack, G. A. (1973), *J. Phys. Chem. Solids* **34**, 321–335.

Slack, G. A., and T. F. McNelly (1976), *J. Crystal Growth* **34**, 263–279.

Spells, K. E (1936), *Proc. Phys. Soc.* **48**, 299.

Strite, S., and H. Morkoc (1992), *J. Vac. Sci. Technol. B.* **10**, 1237–1266.

Szyszko, T., G. Kamler, B. Strojek, G. Weisbrod, S. Podsiadlo, L. Adamowicz, W. Gebicki, J. Szczytko, A. Twardowski, and K. Sikorski (2001), *J. Crystal Growth* **233**, 631–638.

Tavernier, P. R., and D. R. Clarke (2001), *J. Appl. Phys.* **89**, 1527–1536.

Thestrup, B., B. Toftmann, J. Schou, B. Doggett, and J. G. Lunney (2002), *Appl. Surf. Sci.* **197**, 175–180.

Timm, R., P. R. Willmott, and J. R. Huber (1996), *J. Appl. Phys.* **80**, 1794–1802.

Torrisi, L., G. Ciavola, S. Gammino, L. Ando, A. Barna, L. Laska, and J. Krasa (2000), *Rev. Sci. Instrum.* **71**, 4330–4334.

Toth, Z., B. Hopp, T. Smausz, Z. Kantor, F. Ignacz, T. Szorenyi, and Z. Bor (1999), *Appl. Surf. Sci.* **138/139**, 130–134.

Unland, J., B. Onderka, A. Davydov, and R. Schmid-Fetzer (2003), *J. Crystal Growth* **256**, 33–51.

van de Riet, E., J. C. S. Kools, and J. Dieleman (1993), *J. Appl. Phys.* **73**, 8290.

Venkatesan, M., C. B. Fitzgerald, J. G. Lunney, and J. M. D. Coey (2004), *Phys. Rev. Lett.* **93**, 177206-1–177206-4.

Vispute, R. D., S. Choopun, R. Enck, A. Patel, V. Talyansky, R. P. Sharma, T. Venkatesan, W. L. Sarney, L. Salamanca-Riba, S. N. Andronescu, A. A. Iliadis, and K. A. Jones (1999), *J. Electron. Mater.* **28**, 275–286.

Vispute, R. D., R. Enck, A. Patel, B. Ming, R. P. Sharma, T. Venkatesan, C. J. Scozzie, A. Lelis, F. B. McLean, T. Zheleva, and K. A. Jones (2000), *Mater. Sci. Forum* **338–342**, 1503–1506.

Von Allmen, M. (1976), *J. Appl. Phys.* **47**, 5460–5463.

Watanabe, H., H. Sugiyama, T. Ichikawa, and M. Hasegawa (1996), *Surf. Sci.* **357/358**, 115–118.

Wickenden, A. E., L. J. Currano, T. Takacs, J. Pulskamp, M. Dubey, S. Hullavarad, and R. D. Vispute (2003), *Integr. Ferroelectr.* **54**, 565–574.

Willmott, P. R., and F. Antoni (1998), *Appl. Phys. Lett.* **73**, 1394–1396.

Willmott, P. R., R. Timm, and J. R. Huber (1997), *J. Appl. Phys.* **82**, 2082–2092.

Willmott, P. R., F. Antoni, and M. Dobeli (2000), *J. Appl. Phys.* **88**, 188–195.

Wittenberg, L. J., and R. DeWitt (1972), *J. Chem. Phys.* **56**, 4526–4533.

Wong, W. S., T. Sands, and N. W. Cheung (1998), *Appl. Phys. Lett.* **72**, 599–601.

Xiao, R. F., H. B. Liao, N. Cue, X. W. Sun, and H. S. Kwok (1996), *J. Appl. Phys.* **80**, 4226–4228.

Xiao, R. F., X. W. Sun, and H. S. Kwok (1998), *Appl. Surf. Sci.* **127–129**, 425–430.

Xu, X. P., R. P. Vaudo, and G. R. Brandes (2003), *Opt. Mater.* **23**, 1–5.

Zel'dovich, Y. B., and Y. P. Raizer (1965), in *Physics of Shock Waves, and High Temperature Hydrodynamic Phenomena*, W. D. Hayes and R. F. Probstein (Eds.), Academic, London, p. 94.

Zhang, J., K. Sugioka, S. Wada, H. Tashiro, K. Toyoda, and K. Midorikawa (1998), *Appl. Surf. Sci.* **129**, 793–799.

Zhou, M. F., and L. Andrews (2000), *J. Phys. Chem. A* **104**, 1648–1655.

CHAPTER 14

Pulsed Laser Deposition of High-Temperature Superconducting Thin Films and Their Applications

BERND SCHEY

AxynTeC Thin Film Technology GmbH, Augsburg, Germany

14.1 INTRODUCTION

In a challenging decade, after the discovery of the first high-temperature superconductor (HTS) $La_{1.85}Ba_{0.15}CuO_4$ with a transition temperature (T_c) of 35 K in 1986 [Bednorz and Müller, 1986] many new superconducting oxide materials were found, increasing the maximum T_c up to 135 K ($HgBa_2Ca_2Cu_3O_{8+y}$) [Putilin et al., 1993]. The hallmarks in history of superconductors and HTS are schematically summarized in Figure 14.1. The newly found HTS materials caused great interest among many groups of scientists, inducing three main directions of worldwide researching activities that are still developing: the first was the fundamental physical understanding of the mechanism of superconductivity in these new ceramic materials, the second the search for novel HTS materials with higher T_c's, and the third is the design and the realization of HTS devices utilizing the promising advantages of high-temperature superconductivity. The initial euphoria concerning a fast evolution and production of HTS devices for industrial application was damped by the occurrence of various complications during the development of such devices. These complications were due to the incomplete understanding of the physical correlations and interactions inside the new superconducting materials and with other integrated materials, respectively. Based on the fundamental research on HTS materials, most of these initial difficulties are nearly overcome, and the first HTS devices are now entering the market. According to the excellent physical properties of the HTS materials, a great number of applications of HTS thin films exists.

The ceramic nature of HTS materials rules out the fabrication of bulk wires; therefore, most of the applications are based on thin films that are deposited on various substrates. An ideal deposition technique for producing such ceramic HTS thin films is pulsed laser deposition (PLD). There are two major benefits of the PLD technique in contrast to other thin-film technologies (thermal and e-beam evaporation, sputtering, chemical vapor deposition, etc). First of all, the simple and exact transfer of the complex target stoichiometry to the substrate. The second benefit of PLD is the small number of parameters that have to be controlled during deposition. Both of these make PLD one of the most powerful tools for HTS thin-film development and production as well as for basic research. The following section concentrates on HTS thin films developed by PLD for electronic and medical

Pulsed Laser Deposition of Thin Films: Applications-Led Growth of Functional Materials
Edited by Robert Eason

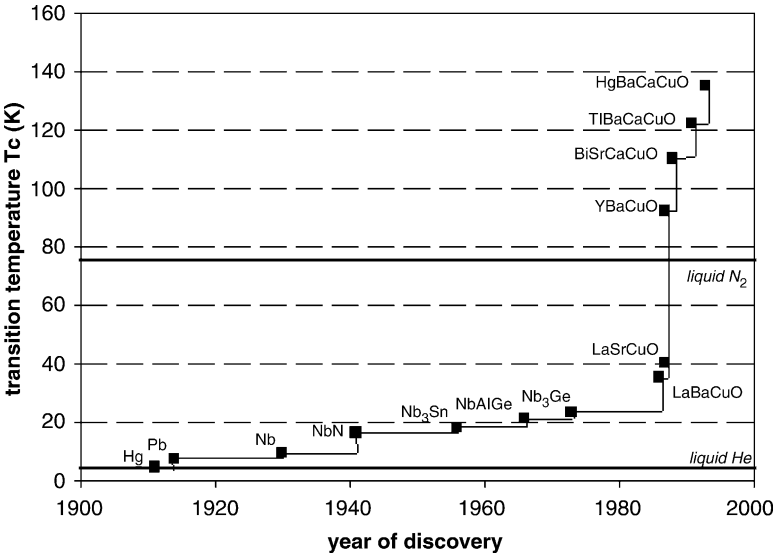

Figure 14.1 Hallmarks in the history of low-temperature superconductors since 1911 and the CuO-based HTS since 1986.

applications as well as for promising electric power applications. The last section gives an assessment of the potential of PLD in the commercialization of HTS in large-scale applications.

14.2 HIGH-TEMPERATURE SUPERCONDUCTOR DEVICES FOR ELECTRONIC AND MEDICAL APPLICATIONS

One of the most important and actually realized applications of HTS thin films is in the field of communication technology where HTS films are used either as active or passive devices. Other applications based on thin-film Josephson Junctions (JJ) are junction arrays for digital electronics or systems based on superconducting quantum interference devices (SQUIDs) to measure very small magnetic fields. This is, for example, very interesting for quality control of metals or semiconductors in industry. This extraordinary magnetic sensitivity also enables the SQUID to be used in medical diagnostic systems in magnetocardiography (MCG), the magnetic equivalent to electrocardiography (ECG). It has also been tried to use superconducting coherence for building so-called qubits, which may be the central point in developing future superconducting computer architectures.

14.2.1 High-Temperature Superconductor Communication

In comparison to conventional microwave materials (Cu, Au), high-temperature superconductors exhibit very small surface resistance $R_s(f, H)$ resulting in high-unloaded quality factors Q (10^3–10^5) leading to low insertion loss in transmission devices and sharp skirt characteristics in resonant devices. These excellent properties of HTS are utilized to apply HTS thin films to the manufacturing of various microwave devices for mobile and satellite communications [Mansour et al., 2001] with an additional reduction in size and weight.

14.2.1.1 Microwave Devices

Typical units made of planar HTS films are filters with special resonator designs (Fig. 14.2) and multiplexers consisting of several filter systems (Fig. 14.3). The use of HTS transmission or

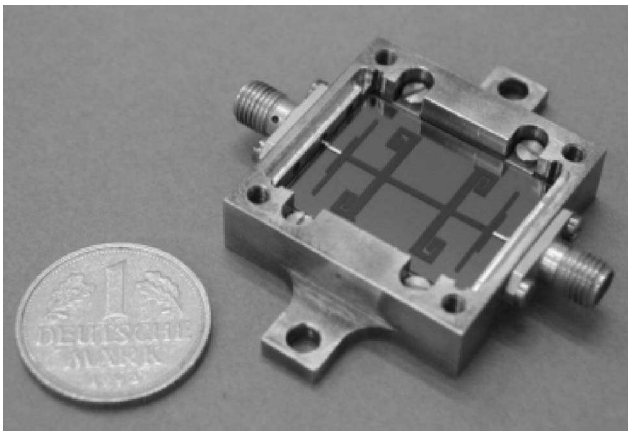

Figure 14.2 Five-pole elliptic HTS filter (www.conectus.org).

delay lines allow the realization of compact microwave filter devices with low dispersion due to their frequency-independent penetration depth and low insertion loss. Using the appropriate design (Fig. 14.4), the HTS microwave devices can be adapted to the desired frequency band (Table 14.1).

High-temperature superconductor thin films have to meet certain requirements to be used as filters that are the basic components integrated in passive devices for wireless communication. First of all these films must provide a minimal surface resistance R_s with a high-quality factor Q especially at high microwave power. Second, homogeneous and large-area HTS layers are necessary to realize special filter designs. Typical substrates used for microwave applications are MgO,

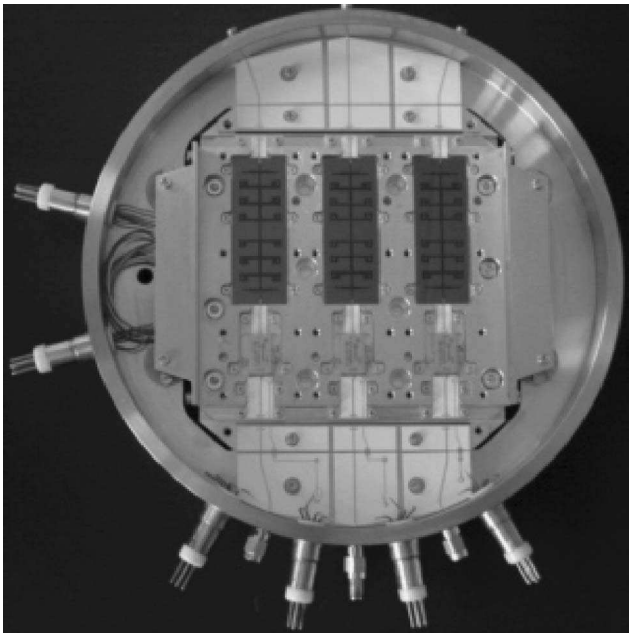

Figure 14.3 Installed HTS filter system (www.conectus.org).

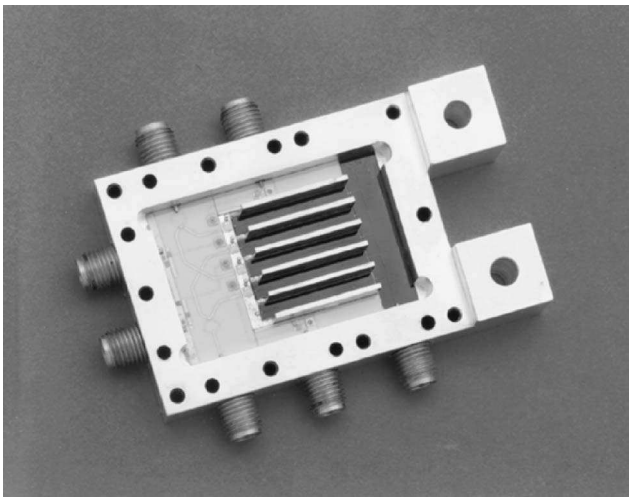

Figure 14.4 HTS channelized X-band receiver with four 100-MHz contiguous channels.

$LaAlO_3$, sapphire (Al_2O_3), and $(La_{0.3}Sr_{0.7})(Al_{0.65}Ta_{0.35})O_3$ (LSAT) because of their low dielectric losses.

Surface Resistance R_s Bollmeier et al. [1997] have prepared homogeneous $YBa_2Cu_3O_{7-x}$ (YBCO) thin films by PLD on 2-inch $LaAlO_3$ substrates with R_s of about 150 μΩ at 19 GHz and $T = 4.2$ K. Lorenz et al. [2001] achieved the HTS deposition via PLD on 3-inch sapphire substrates providing R_s (77 K) values of 500–600 μΩ at 10 GHz and 40–60 mΩ at 145 GHz. The microwave performance of these films was comparable to that of high-quality films deposited by other techniques such as sputtering [Aidam et al., 2001] and thermal coevaporation [Kinder et al., 1997]. Due to the importance of providing low surface resistance R_s, much effort has been put into the understanding of the mechanism leading to microwave loss in HTS films and finding solutions to reduce it. The total microwave loss is divided into two parts: the extrinsic loss that was mostly induced by grain boundaries [Halbritter, 1990] and the intrinsic loss depending on the quasi-particle number density, scattering time, impurities, and so forth [Hardy et al., 1994]. One way to influence the intrinsic loss is by doping the HTS films with other metal elements. Zhang et al. [1993] observed a reduction of R_s in YBCO films by adding small amounts of Zn impurities, which in dilute quantities strongly alter the inelastic scattering. Lorenz et al. [1999] found that Ag doping of YBCO lowers and improves the homogeneity of R_s. The doping also affects the temperature dependence of R_s, which is crucial for designing HTS devices. For example, doping $LuBa_2Cu_3O_{7-x}$ with Pr leads to

TABLE 14.1 Microwave Frequency Bands

Band	Frequency (GHz)	Wavelength (cm)
P-band	0.225–0.39	133–77
L-band	0.39–1.55	77–19
S-band	1.55–3.90	19–7.7
C-band	3.90–6.20	7.7–4.8
X-band	5.75–10.9	5.2–2.8
Ku-band	10.9–18.0	2.8–1.7
Ka-band	18.0–36.0	1.7–0.8

anomalous peaks in R_s vs. T curves, whereas these peaks are absent in the undoped film [Srinivasu et al., 1997]. Compared with the best YBCO films, thallium-based HTS [$Tl_2Ba_2CaCu_2O_8$ (Tl-2212), $Tl_2Ba_2Ca_2Cu_3O_{10}$ (Tl-2223), $TlBa_2Ca_2Cu_3O_9$ (Tl-1223)] exhibit the highest transition temperature, the lowest microwave surface resistance R_s, and are robust in humid atmosphere [Li, 2000]. However, the high vapor pressure and the toxicity of thallium may be a limiting factor in the application of these HTS materials in microwave devices.

Filter Designs The resonators in the design of HTS filters mostly consist of lumped or distributed elements. Microstrip half-wavelength [Vargas et al., 2001] or quarter-wavelength resonators are the elements of planar HTS filters using hairpin-shaped [Kim et al., 2001], ''H''-type [Chung and Han, 2001], ''T''-type [Vlasov et al., 2001], and meander or comb line designs [Marcilhac et al., 2001]. To reduce the filter size lumped elements are favored, however, the Q factor in lumped elements is lower than in distributed elements. The Q of lumped elements based on HTS materials is much higher than in normal metals. This high unloaded quality factor Q of the HTS filters, which is determined by

$$Q = \frac{f_0}{\Delta f(1 - |S_{21}(f_0)|)}$$

where f_0 is the center frequency, Δf is the bandwidth of the resonance curve, and S_{21} is the insertion loss, provides very sharp skirt characteristics and therefore an efficient frequency utilization in mobile communication systems. Besides these, sharply defined filtering properties generate greater demands on fabrication tolerances and design procedure. The resonance frequency of the HTS filter is very sensitive to film properties and substrate dimensions. As a result there is a great effort to realize tunable HTS filters adjusting the device characteristics after assembly or to compensate temperature fluctuation or degradation over time due to aging effects.

Tunable Filters Besides mechanical tuning [Xu et al., 2001] the most common method to tune the resonance frequency is to integrate ferroelectric and ferromagnetic materials into the filter design and to change their nonlinear dielectric constant by electric and magnetic methods, respectively. To grow epitaxial ferroelectric/ferromagnetic and superconducting layers on one substrate these two materials must have closely matched lattice constants and must not show any interdiffusion or chemical reactions at the interfaces. An ideal ferroelectric material that meets these requirements is $SrTiO_3$ (STO). Woodall et al. [2001] reported a 580-MHz agility range of a comb-type resonator [YBCO (400 nm)/STO (400 nm)/LAO(001)] at 5.8 GHz induced by a bias of 500 V. In this case the unloaded Q is higher than 600 over 75% of the agility range. The problems of a ferroelectric STO layer are the dielectric constant and dielectric loss tan δ, which are usually an order of magnitude lower and higher, respectively, than in single crystals. To reduce the dielectric loss, Moeckly and Zhang [2001] tried doping of STO with different elements, including Ce, Ca, Cr, Mo, Mn, W, Co, Y, Ga, and Ir, but in each case they found an increase in tan δ. In optimized undoped STO layers, they realized a minimum loss tangent of 0.0025 at 60 K.

Using HTS/ferri- or ferromagnetic heterostructures for tunable microwave devices, there are additional demands for the magnetic material: narrow ferri- or ferromagnetic resonance linewidth and a large saturation magnetization that is necessary for a high operation frequency. Ferrimagnetic materials used in combination with HTS layers are based on rare-earth iron garnet ($RE_3Fe_5O_{12}$, REIG). However, the lattice mismatch between YBCO and REIG is high and chemical reactions are observed at the interface [Hontsu et al., 2001]. Typical ferromagnetic materials are the perovskite-type manganite $RE_{1-x}Ca_xMnO_3$ (RE = La, Pr). Terakago et al. [2001] reported the deposition of epitaxial YBCO (100 nm)/$Pr_{1-x}Ca_xMnO_3$ ($x = 0.15$ and 0.25) (100 nm)/LSAT with a superconducting transition temperature of 87 K and a loss tangent of 0.008 for $x = 0.25$ and 0.006 for $x = 0.15$ measured at $T = 30$ K. Applying direct current (DC) magnetic fields of 70 and 320 Oe on a filter based on this heterostructure, the filtered frequency can be adjusted between 2.2 and 3.1 GHz.

14.2.1.2 Commercialization of HTS Microwave Devices

The application of superconductivity in wireless and satellite communication was expected to be the first area to enter the global market and this proved to be the case. HTS filter subsystems with much better performance than conventional wireless systems are manufactured in especially large scale. Up until 2002, nearly 2000 of these HTS subsystems have been working worldwide with many millions of hours of cumulative operations. According to the Cellular Telecommunications & Internet Association (CTIA) in December 2002 nearly 1 million base stations worldwide (about 150,000 being in the United States alone) were connecting more than 1 billion wireless customers. The number of customers in the United States has grown up to nearly 140 million by December 2002 (an average growth rate per year of 14%), and the monthly minutes of use per person increases about 26% each year and has exceeded 400 min in 2002 resulting in an exponential increase of total wireless traffic. This vast increase in traffic additionally leads to increased interference effects negatively influencing the communication by dropped or blocked calls, for example. Even these negative effects can be avoided using HTS-based microwave subsystems with much better performance than conventional microwave components. Therefore, the evolution of the wireless (3G, UMTS) as well as the satellite communication market and the upcoming demands on microwave devices (interference protection, high sensitivity, weight reduction, size reduction) promote the deployment of microwave HTS components worldwide.

14.2.2 Digital Electronics

In the last few years semiconductor digital electronics have progressed very fast and have already reached clock frequencies over 3 GHz in microprocessing units (MPUs). These MPUs are based on very small transistor structures. The physical limit of miniaturization will be reached in the near future where scaling limits and atomic level fluctuations become a real problem. Superconducting devices characterized by their low energy dissipation that is about two or three orders of magnitude lower than in semiconductors and by their high switching speed are becoming promising candidates in high-performance digital electronics. Tahara et al. [2001] reported some possible applications of superconducting electronic devices for which they are vastly superior over semiconductors: these include digital samplers, analog/digital (A/D) or digital/analog (D/A) converters, high-speed switches, and digital signal processors (DSP).

14.2.2.1 Josephson Junction (JJ)

One of the basic components of superconducting electronic devices is the Josephson Junction (JJ), where two superconductors are separated by a thin insulating layer. In developing thin-film JJs there are two geometrical constraints that have to be considered: first, the junction must be large enough to avoid thermal fluctuations, and, second, the junction should be smaller than the Josephson penetration depth [Kadin et al., 2001]. In order to deposit thin films for production of JJs the deposition method should produce epitaxial thin films with a flatness of nanometer dimension and only a small number of particles whose sizes are smaller than the precision of the junction structures [Kusumori and Muto, 1999]. Additionally the thin-film JJ must provide critical currents (I_c) of 100–500 μA with a weak temperature dependence, normal resistance (R_n) in the range of several Ω, inductance of a few pH, uniformity of these parameters with a σ spread less than 10%, stability under multilayer process conditions, and flexibility of junction placement on the chip [Sung and Kim, 2001]. The most common kind of electronic circuits are based on rapid single-flux quantum (RSFQ) logic, developed by Likharev and Semenov [1991]. In the RSFQ the information is carried by the absence or presence of single-flux quantum (SFQ) voltage pulses generated by damped JJ. Up to now most logic circuits have been developed using low-temperature superconductors (LTS) as thin-film materials. These complex digital circuits consisting of thousands of homogeneous JJ are based on Nb with an operational temperature of liquid helium. The LTS-JJ with the simplest fabrication technology is the Nb-trilayer ($Nb/AlO_x/Nb$, superconductor/insulator/superconductor, SIS-type JJ) invented by Gurvitch et al. [1983]. Five years later Kupriyanov and

Lukichev [1988] proposed a SINIS (N: normal conductor) type JJ to realize damped JJ elements where no external shunt is needed in contrast to SNS-type JJ. Using SINIS-type JJ, the circuit can be scaled down to the size of the junction, thus increasing the junction density on the chip [Balashov et al., 2001], decreasing the probability of unwanted flux trapping, and avoiding parasitic shunt inductances [Khabipov et al., 2001]. These SINIS-based RSFQ circuits were first tested by Khabipov et al. up to 200 GHz in T-flip-flops (TFF). SNS-based RSFQ circuits using 68-submicron junctions based on a Nb trilayer created by Chen et al. [1999] exhibit the fastest digital circuits with speeds up to 770 GHz.

14.2.2.2 High-Temperature Superconductor Josephson Junctions

In the case of LTS-JJ, the resistive shunt layer reduces the I_cR_n product that acts as a limiting factor for the maximal usable operation frequency of the digital circuit. On the other hand HTS devices provide higher I_cR_n products and energy gaps leading to much better switching behavior than LTS junctions. Furthermore the HTS-JJ can be operated by a more compact cryocooler because of the higher operating temperature. This is a big advantage especially for applications where small units are crucial. There are quite a few kinds of implementation of HTS-JJ devices using step-edge structures, bicrystals, planar multilayer systems, *c*-axis microbridge (CAM), or ramp-edge junctions. The most common type of HTS-JJ fabricated so far was realized by ramp-edge-type junctions due to their high I_cR_n product, their great flexibility in designing electronic devices, and the controllability of junction parameters, which are determined by the thickness and conductivity of the barrier material [Park et al., 2001a]. The main problem in developing these junctions is the required reproducibility of the JJ properties, for example, the I_c spread. The main reason for the high scatter in the JJ properties is the film roughness typically induced by the steplike growth of the oxide barriers [Verhoeven et al., 1996]. In 1997 Moeckly and Char [1997] succeeded in developing highly reproducible HTS-JJ using ramp-edge junctions without any artificial barrier layer, by modifying the superconducting bottom layer. The systematic modification of the HTS bottom layer surface to that of an insulator can be achieved by plasma treatment [Moeckly and Char, 1997], ion beam treatment [Heinsohn et al., 1999], chemical treatment [Hunt et al., 1999], or doping [Schneider et al., 1999]. Such modified junctions are called interface-engineered junctions (IEJ, Fig. 14.5).

Satoh et al. [1998, 1999] fabricated ramp-edge HT-JJs with modified interfaces (IEJ) by PLD and obtained a tiny spread in the junction parameters of σ less than 8% for 100 JJ and 10% for 1000 JJ at 4.2 K. Park et al. [2001b] investigated the effect of ion beam damage and heat treatment on PLD-IEJ. They deposited a YBCO (200 nm)/STO (150 nm) bilayer on a single-crystal STO substrate that was covered with a YBCO top layer after the formation of the ramp edge by Ar milling, ion beam damage of the YBCO ground layer, and heat treatment of the bilayer. They found that the best junction properties with RSJ-like behavior and $I_c > 100\,\mu A$ and $R_n > 1\,\Omega$ at 77 K can be achieved for an Ar ion beam energy of 700 eV and followed by annealing at 450°C under a 75-mTorr oxygen flow. Soutome et al. [2001] reported that the IEJ technology increases the I_cR_n products up to 3 mV at 4.2 K with a σ spread of 10% for 200 JJ of ramp-edge junctions deposited by PLD. Controlling the annealing temperature T_A between 710 and 770°C after ion milling, the critical current density (j_c) of the YBCO/CeO_2/YBCO/LSAT device can be varied from 2×10^3 A/cm^2 to 7×10^5 A/cm^2, and the I_cR_n product can be adjusted from 0.6 to 3 mV, respectively. To increase the I_cR_n product for higher operation frequencies Schneider et al. [1999] and Sonnenberg et al. [2001] tried to locally increase

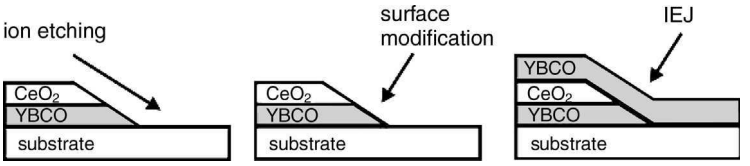

Figure 14.5 Schematic illustration of an interface-engineered junction (IEJ) based on YBCO and CeO_2.

the critical current I_c in the ramp-edge junction by doping the interface or the superconducting electrode. Additionally an increased I_c allows thicker barrier layers that reduces the spread of the JJ properties. Sonnenberg et al. [2001] observed more than doubling of the I_c at 4.2 K for different barrier thickness by doping the $DyBa_2Cu_3O_{7-x}$ (DBCO) ground plane with 20% Ca.

Another important point that should be considered in the fabrication of ''low spread'' IEJ is the reduction of roughness of the modified layer. $NdBa_2Cu_3O_{7-x}$ (NBCO) known as the 123-HTS material with the highest T_c (96 K) and j_c, provides much smoother surfaces than the best quality YBCO thin films grown by PLD and shows a higher decomposition temperature with lower chemical reactivity than YBCO. Li and Tanabe [1998] found that high-quality NBCO films can be grown with a smooth surface (<1 nm) using a slightly Ba-rich target under optimized deposition parameters. The droplet density could be reduced from 10^6 to 10^2 droplets/cm^2 and the critical current densities increased up to 6.7×10^6 A/cm^2 (77 K) by ablating from a single-crystal NBCO—target [Li et al., 1998]. Based on a NBCO/YBCO system, Makita et al. [2001] realized ramp-edge junctions with a roughness of 0.5 nm and an I_cR_n product of 1.6 mV at 4.2 K.

14.2.2.3 High-Temperature Superconductor Digital Devices

Analog/digital converters that allow direct digital conversion of analog signals will become the key elements of the next generation of digital receivers. For example, Sonnenberg et al. [2001] reported the successful test of an HTS-based A/D converter by using a 3.4-kHz input signal that is sampled at different clock frequencies from 20 GHz up to 174 GHz at 10 K. Tahara et al. [2001] fabricated a HTS SFQ sampler that consists of 5 ramp-edge JJs for observation of ultrafast signals with high time resolution. They measured signals with $dI/dt = 12\,\mu$A/ps and a 2.5-μA sensitivity at 25 K. Toggle flip-flop (TFF) devices are able to transfer a high data rate to a lower one allowing further processing by conventional technology. A TFF circuit based on 9 HTS ramp edge JJ shows a correct voltage-divider operation up to 155 GHz at 15 K and 19 GHz at 27 K [Saitoh et al., 2001]. In the near future, computer systems based on HTS will be hybrid computers that consist of superconductor and semiconductor logic devices. To combine these two materials, the difference of their device operation voltage has to be adjusted by amplifying the SFQ signal ($\sim$1 μV) up to several millivolts. One possibility to amplify the SFQ signal is the use of quasi-particle injection devices that have already been investigated in the late 1980s [Kobayashi et al., 1989]. Shiga and Okabe [2001] realized a three-terminal quasi-particle injection device without an insulating layer between the injection electrode and the YBCO bridge, whereas the contact resistance between the Au top layer and the YBCO bridge still has to be reduced to get the needed amplification factor of 1000.

14.2.3 SQUID Systems

The measurement of very small magnetic fields is a challenging factor in many disciplines such as material science, physics, medical science, and geophysics. A powerful device to detect magnetic fields down to about 10^{-14} Tesla is the superconducting quantum interference device (SQUID). SQUIDs also enable the measurement of small electrical currents produced by electrochemical corrosion [Bellingham et al., 1987], during solid combustion processes or liquid–solid reactions [Nersesyan et al., 1999].

There are two main types of SQUIDs, named according to the applied bias, that is, DC and alternating current (AC) [or radio frequency (RF)]. A DC SQUID consists of a superconducting loop interrupted by two JJs. The principle of the DC SQUID is based on a constant current flowing across the JJ. The resulting voltage drop across the junction will be modulated by the magnetic flux through the superconducting loop. An RF SQUID needs only one Josephson Junction, which makes this type of device more popular for production reasons. The stimulation of the RF SQUID and the extraction of the signal is realized by a resonant circuit working in the MHz regime. The evolution of RF SQUID designs has been reported by Zhang [2001]. Most of the planar SQUIDs are fabricated using bicrystals or step-edge junctions (SEJ). For many years the properties of LTS SQUIDs were superior to HTS-based SQUIDs concerning field resolution, but with optimization of the deposition

processes, planar SQUID designs and read-out electronics now produce field resolutions of several fT/$\sqrt{}$Hz at 1 kHz and 77 K, which are comparable to LTS devices at 4.2 K ($\sim$1fT/$\sqrt{}$Hz). Drung et al. [1996] reported a field resolution of a PLD multilayer SQUID of 9.7 fT/$\sqrt{}$Hz at 1 kHz.

14.2.3.1 Low-Frequency Noise

A further increase of the field resolution that is necessary for applications in unshielded environments can only be realized by improving the low-frequency noise that limits the field resolution. The low-frequency noise itself is influenced by several factors. Random weak links or defects and imperfections in the superconducting thin films induced by the deposition process negatively affect the noise properties of the HTS-JJ as well as the effect of thermally activated flux motion and the degradation of the I_c. One way to provide a high field resolution in unshielded environments is to incorporate the SQUID into a gradiometer. The first HTS SQUID gradiometer was based on a SEJ deposited by laser ablation [Eidelloth et al.,1991]. Three of the most common kinds of gradiometer are flip-chip gradiometers [Dantsker et al., 1997], where the HTS SQUID is localized on a small chip and the flux transformer on a bigger chip, direct-coupled one-chip gradiometers [Tian et al., 1999], which consist of a SQUID and at least one larger pick-up coil that is directly connected to the SQUID, and electronic gradiometers based on two or more magnetometers [Vrba, 1996]. There are two different approaches to build an electronic gradiometer [Matlashov et al., 2001]: first, the signals from the primary and the background sensors are subtracted by a differential amplifier, or second, the signal from the background sensor is inverted and converted to a magnetic field at the primary SQUID sensor. The best gradient field resolution of a directly coupled single-layer SQUID gradiometer, which was fabricated on a 24° $SrTiO_3$ bicrystal substrate by PLD, was 50 fT/(cm$\sqrt{}$Hz) and 260 fT/(cm$\sqrt{}$Hz) in a shielded and unshielded environment, respectively. Eulenburg et al. [1999] measured these values at 77 K and 1 kHz. Another phenomenon that causes an increase of low-frequency noise is the thermal motion of trapped flux. This flux motion can be avoided using structures with slots and dams. In 1995 Koch et al. [1995] introduced the dam design on laser-ablated YBCO SEJ to prevent the flux lines entering the magnetometer in an external magnetic field up to 50 μT. Beneath these optimization processes based on the design of gradiometers, the low-frequency noise can additionally be reduced by applying special software tools calculating the real signal without noise from the measured one [Adachi et al., 2001; Bick et al., 2001].

14.2.3.2 SQUID Applications

The fundamental application of SQUIDs is the measurement of magnetic fields with an unrivaled sensitivity. The challenge in developing SQUID magnetometers is keeping the high field resolution in unshielded environments that is very important in geophysics, for nondestructive evaluation (NDE) in material science, or in medical diagnostics. Schultze et al. [2001], who use YBCO SQUIDs deposited by PLD on bicrystal $SrTiO_3$ substrates, favor directly coupled magnetometers with pick-up coils consisting of several narrow parallel loops (dam design) for operation in unshielded environments (Fig. 14.6). In geophysics there are various electromagnetic methods used to explore ore, petroleum, or geological structures: transient electromagnetic (TEM), magneto-tellurics (MT), and controlled source audio magnetotellurics (CSAMT). In these geophysical methods the exploration via a HTS SQUID magnetometer has significant advantages over the common large induction coil systems. Bick et al. [1999], for example, presented a highly sensitive RF SQUID vector (x,y,z) magnetometer system that is able to operate stably in long-term operation without any magnetic shielding. This system, which meets the requirement for TEM, was based on YBCO SEJ deposited by PLD providing a white noise level of 40 fT/$\sqrt{}$Hz above 100–300 Hz in the earth's magnetic field.

Another application of SQUIDs is the quality control of materials and devices based on nondestructive evaluation (NDE). The NDE technique can be divided into two types: (a) measurement of weak permanent magnetic fields (e.g., induced by magnetic impurities) and (b) measurement of AC-magnetic fields (e.g., induced by currents). The second type combined with an

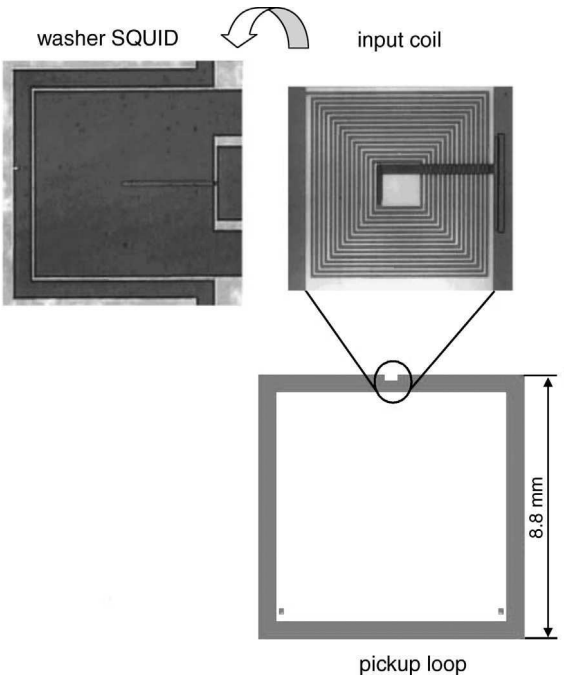

Figure 14.6 SQUID magnetometer consisting of a large pickup coil loop with an integrated multiturn input coil, thus forming a flux transformer, and a washer SQUID. The input coil is placed against a washer-type SQUID in a flip-chip configuration (IPHT Jena, Department of Quantum Electronics).

eddy current (EC) excitation can be used for testing conducting samples (e.g., aircraft parts, wires) to find very small or deep defects like cracks or flaws. Hohmann et al. [2001] developed a testing system for aircraft wheels that consists of a HTS SQUID sensor (made by Jülicher SQUID GmbH based on a PLD-YBCO film) with a differential EC excitation. This system proved to be reliable due to the stability of operation in unshielded environments. The SQUID NDE system of von Kreutzbruck et al. [2001] applied on riveted aircraft multilayer samples was able to detect defects with a size that is one order of magnitude smaller than can be detected by conventional eddy current technique. To investigate the local magnetic field near a sample surface HTS SQUID scanning microscopes (SSM) have been developed [Black et al., 1993; Vu et al., 1993] to provide magnetic images with very high magnetic sensitivity and spatial resolution. The main application of SSM is the imaging of defects in conducting films and wires, superconducting and magnetic films, or semiconducting circuits integrated on wafers.

In medical diagnostics, magnetocardiography (MCG), the magnetic equivalent to electrocardiography (ECG), is one of the most promising applications of SQUID systems [Koch, 2001] especially in fetal cardiology where the ECG cannot be applied. The electrically active cells of the heart muscle induce detectable biosignals. Another diagnostic method is the measurement of neural activity inside brains [magnetoencephalography (MEG)]. Because SQUIDs can operate at acquisition rates much higher than the highest frequency of interest in the signals emitted by the brain (kilohertz), MEG achieves excellent temporal resolution. These biomagnetic diagnostic methods require simultaneous detection of biosignals over large areas and therefore a multichannel SQUID magnetometer system was introduced. Barthelmess et al. [2001] developed an 8-channel DC-SQUID array system based on YBCO thin films deposited by PLD on $SrTiO_3$ bicrystals that achieved a noise level $< 50\,\mathrm{fT}/\sqrt{\mathrm{Hz}}$ at 10 Hz and 77 K. This system shows the same quality of the detected signal compared with a LTS multichannel system and identified magnetic signals of the heart with an amplitude of about 25 pT.

Also MEG measurements of electrically invoked magnetic signals in the brain have been demonstrated. In the fetal MCG a magnetic resolution of about 2 pT and a noise below 20 fT/$\sqrt{}$Hz in a bandwidth of 100 Hz is required [Faley et al., 2001]. This is already achieved by PLD-SQUIDs [Drung et al., 1996]. Another medical application of SQUID systems is the detection of biological antigen–antibody reactions (biological immunoassays) where the antibody is labeled with a magnetic marker, for example, magnetic nanoparticles [Enpuku et al., 2001]. The experiment of Enpuku et al. [2001] show that the sensitivity of the SQUID system is 10 times better than that of conventional methods that use optical markers.

14.3 ELECTRIC POWER AND ENERGY

Based on the dramatic development of electrical power demand worldwide, which has grown relentlessly from 1×10^{12} kWh in 1950 to 13×10^{12} kWh in 2000 and is predicted to reach 60×10^{12} kWh in 2050 [Rosner, 2001], there is a great effort to replace conventional conductor (Cu, Al) technology with HTS. In contrast to LTS the fabrication of HTS wires is really a technological challenge because of their ceramic nature. The first generation of HTS cables were made by the OPIT (oxide-powder-in-tube) technique where generally BiSrCaCuO (BSCCO) is used as the oxide powder that is filled in silver tubes and subsequently rolled and annealed creating a multifilament flexible wire. Such cables are already produced commercially in lengths more than 100 m, providing electrical currents over 100 A at 77 K in zero magnetic field. However, these superconducting tapes have poor properties in higher magnetic fields resulting in a strongly reduced I_c. The second generation of HTS tapes overcomes this problem and shows critical currents in magnetic fields two orders of magnitude higher than the OPIT tapes. This second generation is based on thin-film deposition of $REBa_2Cu_3O_7$ (RE = rare-earth element) compounds on flexible substrates: the coated conductors (CC). Moreover the CC show an AC loss that is a factor 75 smaller than that of an OPIT tape at power frequencies and in AC fields perpendicular to the tape plane. But the most important incentive for developing high-quality CC lies in achieving significantly lower production costs than for OPIT tapes [Malozemoff et al., 2003] and see also Chapter 9.

14.3.1 Applications of Coated Conductors

These coated conductors enable the important field of high current and power applications. The most common applications where coated conductors are the key technology are transmission lines (TL), magnets, motors and generators, transformers, fault current limiters (FCL), and superconducting magnetic energy storage (SMES).

Using superconducting transmission lines generates higher efficiency due to the reduced resistive losses resulting in a much higher power density. The TL can easily be integrated in the existing tunnel networks or pipelines by simply replacing the ''old'' and conventional underground cables that will soon reach their capacity limit in congested areas around the world. So the expense of digging new underground tunnels becomes unnecessary.

In HTS magnets, motors, generators, as well as transformers, the coils are made of CC to create the magnetic fields. Besides their low losses, the high critical current increases the efficiency of these components up to 99.5%, whereas conventional generators operate at 97–98%, motors at 90–96%, and the Cu-based transformers exhibit losses of about 3–6%. Additionally their sizes and weights will be reduced by even more than 50%. On the other hand HTS transformers exhibit much lower risk of fire or environmental hazards because the oil required for insulation is no longer needed [Donnier-Valentin et al., 2001].

The purpose of FCL is to protect the utility grid against current spikes within a very short time. The advantage of HTS-based FCL are: first, the strong reduction of the fault current by phase transition within milliseconds down to a few percent of the original value, and second, the automatic recovery of the FCL in contrast to conventional circuit breakers.

Superconducting magnetic energy storage systems allow the direct storage of electricity only by circulating electrical current without loss in a superconducting coil made by CC providing an energy efficiency of more than 90%. Using such systems occasional excessive requirements of electric energy can be covered without the ineffective step of starting additional generators for short terms only.

The above-mentioned applications of HTS, which actually cannot be realized with this efficiency by conventional conductors, motivate great efforts and activities in material science in the last decade to fabricate coated conductors based on $REBa_2Cu_3O_7$ (RBCO) providing high j_c over long lengths (kilometers) even in high magnetic fields. This means that if high-quality CC can be fabricated over long lengths the described power applications will become reality and revolutionize the electricity market.

14.3.2 Coated Conductors: State of Development

14.3.2.1 Substrates and Buffer Layers

The requirement for high j_c HTS thin films are *c*-axis-oriented layers with small grain boundary angles [Dimos et al., 1990; Hilgenkamp and Mannhart, 2002], that is, good biaxial texture. Using single crystalline substrates with small lattice mismatch, the fabrication process of high-quality HTS films with j_c of a few MA/cm^2 at 77 K is well known. The deposition of HTS thin films on technical, noncrystalline and nonexpensive substrates is still a challenge, however. The most important point is to create a substrate surface with a highly biaxially texture with good lattice match where the HTS film can be deposited. Today there are three approaches to provide these textured surfaces:

1. Ion-beam-assisted deposition (IBAD)
2. Inclined substrate deposition (ISD)
3. Rolled assisted biaxially textured substrates (RABiTS)

The IBAD process uses an ion beam (mainly noble gas ions) that is focused on the substrate under a defined angle during the film deposition. This ion beam induces a preferential sputtering so creating textured growth of the buffer layer on a nontextured substrate. The deposition methods used in combination with the IBAD process are e-beam or thermal evaporation [Wang et al., 1997], sputtering [Iijima et al., 1992], or PLD [Reade et al., 1991; Schey, 1998]. The typical buffer material deposited by IBAD is Y_2O_3-stabilized ZrO_2 (YSZ) [Iijima et al., 1992], where the in-plane orientation of the YSZ layer is improved with increasing layer thickness. However, deposition rate of IBAD-YSZ (0.08 nm/s) [García-Moreno et al., 1999] is too low for commercial production of CC. Therefore, there is considerable effort to find buffer materials that evolve high in-plane orientation at much smaller film thickness. Iijima et al. [2001] found a Zr-based oxide buffer material that generally has a 5° sharper in-plane orientation than YSZ so reducing deposition time by a factor of about 2. At the European Conference on Applied Superconductivity (EUCAS) 2003 Iijima et al. [2003] and Yamada et al. [2003] presented the deposition of a ''self-epitaxial'' CeO_2–buffer layer on IBAD–$Gd_2Zr_2O_7$ (GZO), which improves the texture and decreases the deposition time once more so that tape deposition speeds of 5 m/h can be achieved. Wang et al. [1997] reported the IBAD of MgO on amorphous Si_3N_4 providing an in-plane alignment of 7° at 10 nm in contrast to 13° alignment of YSZ at 500 nm. Using the MgO system for YBCO-CC an additional diffusion barrier layer has to be deposited to prevent contamination of the YBCO layer. Based on the IBAD-MgO, Kreiskott et al. [2003] optimized the buffer multilayer system: STO or $LaMnO_3$/epitaxial MgO/IBAD–MgO/Y–seed layer/Hastelloy, which yields an inplane orientation of 3° in the top PLD-YBCO layer.

The ISD process produces the in-plane orientation of the buffer layer by inclining the substrate with respect to the incoming deposition material. This means the incoming material acts as the coating material as well as the ion beam of the IBAD process. Sato et al. [2001] uses PLD to create biaxially textured YSZ buffer layers on a metallic tape obtaining in-plane alignments of 25°–30°

over a length of 6 m. The subsequent deposition of YBCO by PLD results in a 6-m-long CC with a critical current of 62.4 A at 77 K. The disadvantage of the ISD–buffer layer is their columnar growth that cannot prevent the diffusion processes during the deposition of YBCO at higher temperatures.

The third approach, the RABiTS method has proved to be very successful and cost effective. The advantage of this technique is the possibility to fabricate long metal tapes that possess a biaxially textured surface [Goyal et al., 1996]. This texture develops by heavy rolling of the face-centered cubic (fcc) metals and a subsequent recrystallization process at high temperatures (up to 1000°C). Ni or Ni-based alloys are favored for RABiTS because of their improved recrystallization and the good lattice match ($a_{Ni} = 3.52$ Å) with YBCO. Additionally the tape material must be nonmagnetic at the superconductor's operation temperature and must provide high mechanical stability to realize very thin tapes ($< 50\,\mu m$) for high engineering current density (note: the engineering current denstiy is the current density due to the complete substrate cross section) [Goldacker et al., 1997]. To meet these requirements Ni is alloyed with other metal components such as Cr, Fe, Cu, Al, V, Mn, Mo, or W [Nekkanti et al., 2001; Thieme et al., 2001; de Boer et al., 2001; Petrisor et al., 1999]. Thieme et al. [2001], for example, reported a grain alignment angle of 7°–8° and 8°–9° in Ni-13 wt % Cr and Cu-48 wt % Ni-1.5 wt % Al, respectively, which is sufficient for the growth of high-quality YBCO.

The problem of Ni-based substrates is the diffusion of Ni at high temperatures during the growth of YBCO and subsequent deterioration of superconductivity. To prevent this Ni diffusion into YBCO, a buffer layer has to be deposited. The demands on the buffer material are chemical stability due to the Ni alloy and YBCO, good lattice and thermal expansion match with YBCO, as well as perfect barrier properties to suppress Ni diffusion and epitaxial growth on the RABiT substrates. These requirements emphasize the important role of the buffer system in fabrication of coated conductors. Therefore the majority of research is concentrated on buffer layer development generally using PLD as the deposition method. The most common buffer systems are based on YSZ and rare-earth oxides, for example, CeO_2, Y_2O_3, Gd_2O_3 [Rupich et al., 2001], or perovskites like $LaAlO_3$ and $SrTiO_3$ [Carlson et al., 1998] deposited by PLD leading to critical currents of the YBCO layers on small substrates up to 1–2 MA/cm^2 at 77 K. These buffer materials are deposited at high temperatures (600–900°C) in an oxygen atmosphere leading to an undesired oxidation of the Ni resulting in a NiO (111) surface that negatively influences the epitaxial quality of the buffer system. To avoid this oxidation the buffer layer deposition was carried out in a reducing atmosphere for the initial growth and then changed to oxygen working gas. Another solution is a selective oxidation of the Ni surface at temperatures of 1000–1200°C producing a NiO (100) texture with a better lattice match than pure Ni ($a_{NiO} = 4.17$ Å). This process is called surface oxidation epitaxy (SOE) [Matsumoto et al., 1998]. Additionally, this NiO layer between the Ni tape and the buffer layer acts as a diffusion barrier. Matsumoto et al. [2001] reported an average in-plane alignment of the SOE NiO of about 16° over a length of 50 m. On this textured NiO layer the other oxide buffers can easily be deposited without using a two-step process with a reducing atmosphere. However, Matsumoto et al. [1999] found that due to the high oxidation temperatures the grain boundaries were separated by grooves with a depth of 30–150 nm, whereas these grooves can be flattened by deposition of the buffer layer (CeO_2, MgO, YSZ). Using this technique critical currents of 0.3 MA/cm^2 at 77 K were found in short YBCO/MgO/NiO/Ni tape [Matsumoto et al., 2001].

14.3.2.2 Coated Conductors

The deposition of YBCO on buffered Ni or Ni-alloy tapes is achieved by various coating methods, namely thermal coevaporation (TE) [Knauf et al., 2001: 1.2 MA/cm^2 at 77 K along a 10 cm tape], e-beam [Peng et al., 2001: 5 KA/cm^2 at 77 K], liquid-phase epitaxy (LPE) [Izumi et al., 2001: 0.1 MA/cm^2 at 77 K], metal organic deposition (MOD) [Araki et al., 2001: 0.8 MA/cm^2 at 77 K; Goyal et al., 2001: 0.1 MA/cm^2 at 77 K along a 1-m tape], and sol–gel [Dawley et al., 2001: 2 MA/cm^2 at 77 K on a single crystalline substrate]. On small single crystalline substrates nearly every deposition method results in superconducting films with critical current densities on the order of MA/cm^2 at 77 K. But on technical (non-single-crystalline) substrates only a few techniques (TE and PLD) are able to realize high j_c values on longer tapes. However, the longest CC combined with the

highest critical currents per tape width at 77 K up to now were realized by PLD and IBAD buffered substrates. At the EUCAS 2003 Usoskin et al. [2003] presented a 10-m-long PLD-YBCO/IBAD-YSZ/stainless steel tape with a critical current density of 480 A/cm × width, Iijima et al. [2003] introduced a PLD-YBCO/PLD-MgO/IBAD-GZO/Hastelloy-CC, which shows a critical current of 38 A over a length of 100 m corresponding to $j_c = 0.8\,\mathrm{MA/cm^2}$, and Kreiskott et al. [2003] measured an I_c of over 150 A along a 1-m-long tape based on PLD-YBCO/PLD-$LaMnO_3$/MgO/IBAD-MgO/Y-seed layer/Hastelloy system, which can be fabricated at a rate of 36 m/h.

Due to the progress in the laser technology, excimer lasers are available providing repetition rates up to 300 Hz at a laser energy of 1 J/pulse. Using this type of laser Usoskin et al. [2003] realized an integral deposition rate of $> 35\,\mathrm{nm\,m^2/h}$, which is higher than the highest rates reported for TE ($30\,\mathrm{nm\,m^2/h}$) making PLD very attractive for the production of CC.

14.3.3 Future Trends

To realize even higher critical currents there are two main directions in fabricating CC: first, the deposition of thick HTS films while keeping the j_c constant, or second, the improvement of j_c itself. In the first approach the limiting factor is the crack formation for thicker films due to the different thermal expansion coefficients of the HTS film and buffer–substrate system. The second approach is still a challenge where the problem of the exponential j_c reduction by large-angle grain boundaries that originates from the noncrystalline substrates used has to be overcome. If there is a possibility to enhance the intergrain critical currents without improving the texture of the buffer layer the result will be shorter deposition times and lower production costs. Schmehl et al. [1999] found a way to increase the intergrain critical current by homogeneous Ca doping of YBCO. The Ca-doped PLD-YBCO films provide j_c, which exceed the values of undoped materials by a factor of seven and a misorientation angle of 24° but only at 4.2 K. Hammerl et al. [2000] found a way to increase j_c also at 77 K by growing multilayers of undoped and doped layers utilizing grain boundary diffusion of Ca along the grain boundary. The grain boundaries are optimized therefore while the bulk properties are left untouched, also resulting in an enhancement of j_c by a factor of 7 over the whole temperature range. Based on these results, Weber et al. [2003] deposited via PLD a 20-nm $Y_{0.7}Ca_{0.3}Ba_2Cu_3O_{7-x}$ top layer on a PLD-YBCO/IBAD-YSZ/poly-YSZ and measured an improvement of j_c (77 K) by a factor of 1.4–2.2 compared to the undoped film. Calculating the current percolation through a disordered network of grain boundaries with different inplane textures, Hammerl et al. [2002] found that the critical current can additionally be improved up to the intragrain j_c values by elongating the grains to get large grain boundary areas. To reduce the production costs there are many efforts to use cheaper nonvacuum techniques for fabrication of CC, but up to now there are no results that are able to compete with superconducting properties of PLD-CC, espescially CC where all layers are deposited by nonvacuum methods.

14.4 POTENTIAL OF PLD IN THE COMMERCIALIZATION OF HTS

Superconducting Technologies Inc., which is the largest of the HTS wireless companies, uses PLD as the deposition method for the production of Tl-2212 thin-film filters. The success of commercialization of PLD microwave HTS devices is reflected by the number of different HTS systems offered by Superconducting Technologies Inc. and by the number of about 2000 HTS subsystems sold up to January 2003. For the development of HTS digital electronic circuit devices and SQUIDs, laser ablation is the most common thin-film deposition process as judges by the high number of scientific publications. However, the potential of PLD in the commercialization of HTS digital electronics depends on the success and the performance of the electronic devices that still must be further developed. The HTS-SQUID-based characterization methods for material investigations such as nondestructive evaluation (NDE) [Hohmann et al., 2001] or the scanning SQUID microscope (SSM, www.neocera.com) have already proved their reliability and stability and

have now come to market. This is reflected by several companies (Jülicher SQUID GmbH, Neocera Inc.) that use PLD for SQUID production.

The success of HTS-SQUID systems in medical diagnostics depends on the improvement of sensitivity and low-frequency noise reduction to be able to operate in unshielded environments that drastically reduce the investment costs. To be competitive with conventional techniques (e.g., ECG) the diagnostic system for MCG or MEG should provide multichannel measurement to achieve large-area detection, whereas the data acquisition, analysis, and visualization take place in real time [Koch, 2001]. Based on the developments up to now, these requirements will be met in the near future, so that the MCG and MEG techniques will become standard diagnostic methods in medical science.

The HTS cables of the second generation (CC) whose production costs will be decreased down to 10 US$/kAm, even with the PLD technique [Usoskin et al., 2003], in the next 10 years [Freyhardt, 2003, Tsukamoto, 2003], which is much cheaper than the OPIT cables (first generation, today: 150 US$/kAm [Kellers and Masur, 2003]), have a good chance to break into the big market of electric power applications. Additionally, the environmental needs, which include the ever-increasing level of global electrification resulting from increased population growth, the environmental protection, the climate-change conditions, and the limited fossil fuel resources [Rosner, 2001], all indicate an increasing acceptance of HTS CC. Especially in the United States where the electrical power grid has to be renewed in the near future [Chu, 2003] and based on a study conducted by the EPRI (Electric Power Research Institute), which predicts savings of over 18 billion US$ annually in the United States alone using HTS CC, there is a great chance to achieve this radical level of modernization using the baseline technology of CC.

Even if nonvacuum methods improve for fabrication of CC, the potential of PLD in the production of CC will maintain its position due to the decreasing operating costs of the modern excimer lasers and the ideal deposition geometry for the inline production of buffer and YBCO layers on tapes. This potential is also utilized in Japan where a new project has started in 2003 to produce 500-m-long CC based on the system: PLD-YBCO/PLD-CeO_2/IBAD-GZO/Hastelloy. The aim is to realize critical currents of 300 A/cm $\times$ width with a fabrication speed of 5 m/h until 2007 [Tsukamoto, 2003].

Although there have been many doubts in past years if there is a realistic chance for HTS materials and devices to enter the market, the commercialization of HTS thin films is becoming more and more a reality. Especially for such a complex material the large number of publications in fabrication of HTS thin films up to now shows the enormous potential of PLD as a technique for thin-film development of highly sophisticated materials. Additionally many large-area PLD systems have been developed and successfully tested in the last years [Greer et al., 1992; and see Chapter 9; Lorenz et al., 1999; Schey et al., 1999; Usoskin et al., 2003] and already proven for production (Supercondcuting Technologies Inc.). Based on these achievements PLD will play a decisive role among the vacuum techniques concerning the commercial production of HTS thin films on wafers and tapes.

REFERENCES

Adachi, Y., M. Shimogawara, M. Higuchi, Y. Haruta, and M. Ochiai (2001), *IEEE Trans. Appl. Supercond.* **11**(1), 669.

Aidam, R., J. Geerk, G. Linker, F. Ratzel, J. Reiner, R. Schneider, R. Smithey, A. G. Zaitsev, E. Gaganidze, and R. Schwab (2001), *IEEE Trans. Appl. Supercond.* **11**(1), 357.

Araki, T., Y. Takahashi, K. Yamagiwa, T. Yuasa, Y. Iijima, K. Takeda, S. B. Kim, Y. Yamada, and I. Hirabayashi (2001), *IEEE Trans. Appl. Supercond.* **11**(1), 2869.

Balashov, D., M. Khabipov, F.-I. Buchholz, and J. Niemeyer (2001), *IEEE Trans. Appl. Supercond.* **11**(1), 1070.

Barthelmess, H.-J., M. Halverscheid, B. Schiefenhövel, E. Heim, M. Schilling, and R. Zimmermann (2001), *IEEE Trans. Appl. Supercond.* **11**(1), 657.

Bednorz, J. G., and K. A. Müller (1986), *Z. Phys. B* **64**, 189.

Bellingham, J. G., M. L. A. MacVicar, and M. Nisefoff (1987), *IEEE Trans. Magn.* **23**, 477.

Bick, M., G. Panaitov, N. Wolters, Y. Zhang, H. Bousack, A. I. Braginski, U. Kalberkamp, H. Burkhardt, and U. Matzander (1999), *IEEE Trans. Appl. Supercond.* **9**(2), 3780.

Bick, M., K. Sternickel, G. Panaitov, A. Effern, Y. Zhang, and H.-J. Krause (2001), *IEEE Trans. Appl. Supercond.* **11**(1), 673.

Black, R. C., A. Mathai, F. C. Wellstood, E. Danstker, A. H. Milklich, D. T. Nemeth, J. J. Kingston, and J. Clarke (1993), *Appl. Phys. Lett.* **62**, 2128.

Bollmeier, T., W. Biegel, B. Schey, B. Stritzker, W. Diete, T. Kaiser, and G. Müller (1997), *J. Alloys Comp.* **251** (1/2), 176.

Carlson, C. M., J. C. Price, P. A. Parilla, D. S. Ginley, D. Niles, R. D. Blaughter, A. Goyal, M. Paranthaman, D. M. Kroeger, and D. K. Christen (1998), *Phys. C* **304**, 82.

Chen, W., A. V. Rylyakov, V. Patel, J. E. Lukens, and K. K. Likharev (1999), *IEEE Trans. Appl. Supercond.* **9**, 3212.

Chu, P. C. W (2003), paper presented at EUCAS 2003, Sorrento, Italy.

Chung, D.-C., and B.-S. Han (2001), *IEEE Trans. Appl. Supercond.* **11**(1), 388.

Dantsker, E., O. M. Froehlich, S. Tanaka, K. Kouznetsov, J. Clarke, Z. Lu, V. Matijasevic, and K. Char (1997), *Appl. Phys. Lett.* **71**, 1712.

Dawley, J. T., P. G. Clem, M. P. Siegal, D. L. Overmyer, and M. A. Rodriguez (2001), *IEEE Trans. Appl. Supercond.* **11**(1), 2873.

de Boer, B., N. Reger, L. Fernandez, J. Eickemeyer, B. Holzapfel, L. Schultz, P. Berberich, and W. Prusseit (2001), *IEEE Trans. Appl. Supercond.* **11**(1), 3477.

Dimos, D., P. Chaudhari, and J. Mannhart (1990), *Phys. Rev. B* **41**, 4038.

Donnier-Valentin, G., P. Tixador, and E. Vinot (2001), *IEEE Trans. Appl. Supercond.* **11**(1), 1498.

Drung, D., F. Ludwig, W. Müller, U. Steinhoff, L. Trahms, H. Koch, Y. Q. Shen, M. B. Jensen, P. Vase, T. Holst, T. Freltoft, and G. Curio (1996), *Appl. Phys. Lett.* **68**, 1421.

Eidelloth, W., B. Oh, R. P. Robertazzi, W. J. Gallagher, and R. H. Koch (1991), *Appl. Phys. Lett.* **59**, 3473.

Enpuku, K., T. Minotani, M. Hotta, and A. Nakahodo (2001), *IEEE Trans. Appl. Supercond.* **11**(1), 661.

Eulenburg, A., E. J. Romans, C. Carr, A. J. Millar, G. B. Donaldson, and C. M. Pegrum (1999), *Appl. Phys. Lett.* **75**, 2301.

Faley, M. I., U. Poppe, K. Urban, D. N. Paulson, T. N. Starr, and R. L. Fagaly (2001), *IEEE Trans. Appl. Supercond.* **11**(1), 1383.

Freyhardt, H. C. (2003), paper presented at EUCAS 2003, Sorrento, Italy.

García-Moreno, F., A. Usoskin, H. C. Freyhardt, A. Issaev, J. Wiesmann, J. Hoffmann, K. Heinemann, S. Sievers, and J. Dzick (1999), *IEEE Trans. Appl. Supercond.* **9**(2), 2260.

Goldacker, W., B. Ullmann, E. Brecht, and G. Linker (1997), *Inst. Phys. Conf. Ser.* **158**, 1279.

Goyal, A., D. P. Norton, J. D. Budai, M. Paranthaman, E. D. Specht, D. M. Droeger, D. K. Christen, Q. He, B. Saffian, F. A. List, D. F. Lee, P. M. Martin, C. E. Klabunde, E. Hatfield, and V. K. Sikka (1996), *Appl. Phys. Lett.* **69**, 1795.

Goyal, A., D. F. Lee, F. A. List, E. D. Specht, R. Feenstra, M. Paranthaman, X. Cui, S. W. Lu, P. M. Martin, D. M. Kroeger, D. K. Christen, B. W. Kang, D. P. Norton, C. Park, D. T. Verebelyi, J. R. Thompson, R. K. Williams, T. Aytug, and C. Cantoni (2001), *Phys. C* **357–360**, 903.

Greer, J. A. (1992), *J. Vac. Sci. Technol.* **A10**(4), 1821.

Gurvitch, M., M. A. Washington, and H. A. Huggins (1983), *Appl. Phys. Lett.* **42**, 472.

Halbritter, J. (1990), *J. Appl. Phys.* **68**, 6315.

Hammerl, G., A. Schmehl, R. R. Schulz, B. Goetz, H. Bielefeldt, C. W. Schneider, H. Hilgenkamp, and J. Mannhart (2000), *Nature* **407**, 162.

Hammerl, G., A. Herrnberger, A. Schmehl, A. Weber, K. Wiedenmann, C. W. Schneider, and J. Mannhart (2002), *Appl. Phys. Lett.* **81**, 3209.

Hardy, W. N., S. Kamal, D. A. Bonn, K. Zhang, R. Liang, E. Klein, D. C. Morgan, and D. J. Baar (1994), *Phys. B* **147**, 609.

Heinsohn, J.-K., R. H. Hadfield, and R. Dittmann (1999), *Phys. C* **326/327**, 157.

Hilgenkamp, H., and J. Mannhart (2002), *Rev. Mod. Phys.* **74**, 485.

Hohmann, R., D. Lomparski, H.-J. Krause, M. von Kreutzbruck, and W. Becker (2001), *IEEE Trans. Appl. Supercond.* **11**(1), 1279.

Hontsu, S., T. Sakatani, H. Nishikawa, M. Nakamori, A. Fujimaki, and T. Kawai (2001), *Jpn. J. Appl. Phys.* **40**, 1100.

Hunt, B. D., M. G. Forrester, J. Talvacchio, and R. M. Young (1999), *IEEE Trans. Appl. Supercond.* **9**, 3362.

Iijima, Y., N. Tanabe, O. Kohno, and Y. Ikeno (1992), *Appl. Phys. Lett.* **60**, 769.

Iijima, Y., K. Kakimoto, and K. Takeda (2001), *IEEE Trans. Appl. Supercond.* **11**(1), 3457.

Iijima, Y., K. Kakimoto, Y. Sutoh, and T. Saitoh (2003), paper presented at EUCAS 2003, Sorrento, Italy.

Izumi, T., N. Hobara, K. Kakimoto, T. Izumi, K. Hasegawa, M. Kai, T. Honjo, X. Yao, H. Fuji, Y. Nakamura, and Y. Shiohara (2001), *IEEE Trans. Appl. Supercond.* **11**(1), 2917.

Kadin, A. M., C. A. Mancini, M. J. Feldmann, and D. K. Brock (2001), *IEEE Trans. Appl. Supercond.* **11**(1), 1050.

Kellers, J. K., and L. J. Masur (2003), paper presented at EUCAS 2003, Sorrento, Italy.

Khabipov, M., D. Balashov, F.-I. Buchholz, and J. Niemeyer (2001), *IEEE Trans. Appl. Supercond.* **11**(1), 1074.

Kim, C.-S., S. C. Song, and S. Y. Lee (2001), *IEEE Trans. Appl. Supercond.* **11**(1), 407.

Kinder, H., P. Berberich, W. Prusseit, S. Rieder-Zecha, R. Semerad, and B. Utz (1997), *Phys. C* **282**, 107.

Knauf, J., R. Semerad, W. Prusseit, B. deBoer, and J. Eickemeyer (2001), *IEEE Trans. Appl. Supercond.* **11**(1), 2885.

Kobayashi, T., K. Hashimoto, U. Kabasawa, and M. Tonouchi (1989), *IEEE Trans. Magn.* **25**, 927.

Koch, H. (2001), *IEEE Trans. Appl. Supercond.* **11**(1), 49.

Koch, R. H., J. Z. Sun, V. Foglietta, and W. J. Gallagher (1995), *Appl. Phys. Lett.* **67**, 709.

Kreiskott, S., B. J. Gibbons, A. T. Findikoglu, Y. C. Coulter, and V. Matias (2003), paper presented at EUCAS 2003, Sorrento, Italy.

Kupriyanov, M. Y., and V. F. Lukichev (1988), *Sov. Phys. JETP.* **67**, 1163.

Kusumori, T., and H. Muto (1999), *Phys. C* **321,** 247.

Li, L. (2000), *Mater. Sci. Eng.* **29**, 153.

Li, Y., and K. Tanabe (1998), *J. Appl. Phys.* **83**, 7744.

Li, Y., X. Yao, and K. Tanabe (1998), *J. Appl. Phys.* **84**, 4797.

Likharev, K. K., and V. K. Semenov (1991), *IEEE Trans. Appl. Supercond.* **1**(1), 3.

Lorenz, M., H. Hochmuth, D. Natusch, G. Lippold, V. L. Svetchnikov, T. Kaiser, M. A. Hein, R. Schwab, and R. Heidinger (1999), *IEEE Trans. Appl. Supercond.* **9**(2), 1936.

Lorenz, M., H. Hochmuth, D. Natusch, M. Kusunoki, V. L. Svetchnikov, V. Riede, I. Stanca, G. Kästner, and D. Hesse (2001), *IEEE Trans. Appl. Supercond.* **11**(1), 3209.

Makita, T., K. Toma, K. Ishikawa, H. Zama, T. Utagawa, U. Kawabe, and K. Tanabe (2001), *IEEE Trans. Appl. Supercond.* **11**(1), 155.

Malozemoff, A. P., D. T. Verebelyi, S. Fleshler, D. Aized, and D. Yu (2003), *Phys. C* **368**, 424.

Mansour, R. R., T. Romano, S. Ye, S. Peik, T. Nast, D. Enlow, C. Wolker, and J. Warner (2001), *IEEE Trans. Appl. Supercond.* **11**(1), 806.

Marcilhac, B., D. G. Crété, Y. Lemaître, D. Mansart, J. C. Mage, K. Bouzehouane, C. Dolin, E. Jacquet, P. Woodall, and J. P. Contour (2001), *IEEE Trans. Appl. Supercond.* **11**(1), 438.

Matlashov, A., M. Espy, R. H. Kraus, Jr., K. R. Ganther, Jr., and L. D. Snapp (2001), *IEEE Trans. Appl. Supercond.* **11**(1), 876.

Matsumoto, K., Y. Niiori, I. Hirabayashi, N. Koshizuka, T. Watanabe, Y. Tanaka, and M. Ikeda (1998), *Adv. Superconduct.* **X**, 611.

Matsumoto, K., S. B. Kim, J. G. Wen, I. Hirabayashi, T. Watanabe, N. Uno, and M. Ikeda (1999), *IEEE Trans. Appl. Supercond.* **9**(2), 1539.

Matsumoto, K., T. Watanabe, T. Tanigawa, T. Maeda, S. B. Kim, and I. Hirabayashi (2001), *IEEE Trans. Appl. Supercond.* **11**(1), 3138.

Moeckly, B. H., and K. Char, (1997), *Appl. Phys. Lett.* **71**, 2526.

Moeckly, B. H., and Y. Zhang, (2001), *IEEE Trans. Appl. Supercond.* **11**(1), 450.

Nekkanti, R. M., V. Seetharaman, L. Brunke, I. Maartense, D. Dempsey, G. Kozlowski, D. Tomich, R. Biggers, T. Peterson, P. Barnes, and C. E. Oberly (2001), *IEEE Trans. Appl. Supercond.* **11**(1), 3321.

Nersesyan, M. D., J. R. Claycomb, Q. Ming, J. H. Miller, Jr., J. T. Richardson, and D. Luss (1999), *Appl. Phys. Lett.* **75**, 1170.

Park, J. H., J. H. Kim, G. Y. Sung, K. R. Jung, J. H. Kang, and T. S. Hahn, (2001a), *IEEE Trans. Appl. Supercond.* **11**(1), 932.

Park, W. K., H. J. Lee, J. I. Kye, J. H. Yun, S.-M. Lee, S. H. Moon, and B. Oh (2001b), *IEEE Trans. Appl. Supercond.* **11**(1), 147.

Peng, L. S.-J., W. Wang, W. Jo, T. Ohnishi, A. F. Marshall, R. H. Hammond, M. R. Beasley, E. J. Peterson, and R. E. Ericson (2001), *IEEE Trans. Appl. Supercond.* **11**(1), 3375.

Petrisor, T., V. Boffa, G. Celentano, L. Ciontea, F. Fabbri, U. Gambardella, S. Ceresara, and P. Scardi (1999), *IEEE Trans. Appl. Supercond.* **9**(2), 2256.

Putilin, S. N., E. V. Antipov, O. Chmaissen, and M. Marezio (1993), *Nature* **362,** 226.

Reade, R. P., X. L. Mao, and R. E. Russo (1991), *Appl. Phys. Lett.* **59**, 739.

Rosner, C. H. (2001), *IEEE Trans. Appl. Supercond.* **11**(1), 39.

Rupich, M. W., Q. Li, S. Annavarapu, C. Thieme, W. Zhang, V. Prunier, M. Paranthamann, A. Goyal, D. F. Lee, E. D. Specht, and F. A. List (2001), *IEEE Trans. Appl. Supercond.* **11**(1), 2927.

Saitoh, K., Y. Soutome, T. Fukazawa, Y. Tarutani, and K. Tagaki (2001), *IEEE Trans. Appl. Supercond.* **11**(1), 791.

Sato, Y., K. Matsuo, Y. Takahashi, K. Muranaka, K. Fujino, S. Hahakura, K. Ohmatsu, and H. Takei (2001), *IEEE Trans. Appl. Supercond.* **11**(1), 3365.

Satoh, T., M. Hidaka, and S. Tahara (1998), *IEICE Trans. Electron.* **E81-C**, 1532.

Satoh, T., M. Hidaka, and S. Tahara (1999), *IEEE Trans. Appl. Supercond.* **9**(2), 3141.

Schey, B. (1998), Ph.D thesis, ''Laserdeposition großflächiger YBa2Cu307-x—Schichten auf einkristallinen und technischen Substraten mit Textur-Untersuchungen zur ionenunterstützten Laserablation von Ceroxid,'' Shaker Verlag, Aachen.

Schey, B., W. Biegel, M. Kuhn, and B. Stritzker (1999), *Appl. Phys. A* **69**, 419.

Schmehl, A., B. Goetz, R. R. Schultz, C. W. Schneider, H. Bielefeldt, H. Hilgenkamp, and J. Mannhart (1999), *Europhys. Lett.* **47**, 110.

Schneider, C. W., R. R. Schulz, B. Goetz, A. Schmehl, H. Bielefeldt, H. Hilgenkamp, and J. Mannhart (1999), *Appl. Phys. Lett*. **75**, 850.

Schultze, V., N. Oukhanski, V. Zakosarenko, R. Ijsselsteijn, J. Ramos, A. Chwala, and H.-G. Meyer (2001), *IEEE Trans. Appl. Supercond.* **11**(1), 1319.

Shiga, H., and Y. Okabe (2001), *IEEE Trans. Appl. Supercond.* **11**(1), 940.

Sonnenberg, A. H., I. Oomen, H. Hilgenkamp, G. J. Gerritsma, and H. Rogalla (2001), *IEEE Trans. Appl. Supercond.* **11**(1), 200.

Soutome, Y., R. Hanson, T. Fukazawa, K. Saitoh, A. Tsukamoto, Y. Tarutani, and K. Tagaki (2001), *IEEE Trans. Appl. Supercond.* **11**(1), 163.

Srinivasu, V. V., P. Raychaudhuri, C. P. ĎSouza, R. Pinto, and R. Vijayaraghavan (1997), *Solid State Commun.* **102**(5), 409.

Sung, G. Y., and J. Kim (2001), *IEEE Trans. Appl. Supercond.* **11**(1), 151.

Tahara, S., S. Yorozu, Y. Kameda, Y. Hashimoto, H. Numata, T. Satoh, W. Hattori, and M. Hidaka (2001), *IEEE Trans. Appl. Supercond.* **11**(1), 463.

Terakago, M., S. Mine, T. Sakatani, S. Hontsu, H. Nishikawa, M. Nakamori, H. Tabata, and T. Kawai (2001), *Supercond. Sci. Technol.* **14**, 1140.

Thieme, C. L. H., S. Annavarapu, W. Zhang, V. Prunier, L. Fritzemeier, Q. Li, U. Schoop, M. W. Rupich, M. Gopal, S. R. Foltyn, and T. G. Holesinger (2001), *IEEE Trans. Appl. Supercond.* **11**(1), 3329.

Tian, Y. J., S. Linzen, F. Schmidl, L. Dörrer, R. Weidl, and P. Seidel (1999), *Appl. Phys. Lett.* **74**, 1302.

Tsukamoto, O. (2003), paper presented at EUCAS 2003, Sorrento, Italy.

Usoskin, A., A. Issaev, J. Knoke, and H. C. Freyhardt (2003), paper presented at EUCAS 2003, Sorrento, Italy.

Vargas, J. M., P. Brown, T. Khan, Y. Hijazi, Y. A. Vlasov, and G. L. Larkins, Jr., (2001), *IEEE Trans. Appl. Supercond.* **11**(1), 392.

Verhoeven, M. A. J., R. Moermann, M. E. Bijlsma, A. J. H. Rijnders, D. H. A. Blank, G. J. Gerritsma, and H. Rogalla (1996), *Appl. Phys. Lett.* **68**, 1276.

Vlasov, Y. A., J. M. Vargas, P. Brown, and G. L. Larkins, Jr. (2001), *IEEE Trans. Appl. Supercond.* **11**(1), 385.

von Kreutzbruck, M., K. Allweins, T. Rühl, M. Mück, C. Heiden, H.-J. Krause, and R. Hohmann (2001), *IEEE Trans. Appl. Supercond.* **11**(1), 1032.

Vrba, J. (1996) in *SQUID Sensors: Fundamentals, Fabrication and Applications,* H. Weinstock (Ed.), Kluwer Academic Publishers, Dordrecht, p. 117.

Vu, L. N., M. S, Wistrom, and D. J. van Harlingen (1993), *Appl. Phys. Lett.* **63**, 1693.

Wang, C. P., K. B. Do, M. R. Beasley, T. H. Geballe, and R. H. Hammond (1997), *Appl. Phys. Lett.* **71**, 2955.

Weber, A., G. Hammerl, A. Schmehl, C. W. Schneider, J. Mannhart, B. Schey, M. Kuhn, R. Nies, B. Utz, and H.-W. Neumüller (2003), *Appl. Phys. Lett.* **82**, 772.

Woodall, P., K. Bouzehouane, B. Marcilhac, D. G. Crété, E. Jacquet, J. C. Mage, and J. P. Contour (2001), *IEEE Trans. Appl. Supercond.* **11**(1), 1150.

Xu, H., E. Gao, and Q. Y. Ma (2001), *IEEE Trans. Appl. Supercond.* **11**(1), 353.

Yamada, Y., T. Muroga, H. Iwai, S. Miyata, T. Watanabe, T. Izumi, Y. Shiohara, Y. Iijima, T. Saitoh, T. Kato, Y. Sugawara, and T. Hirayama (2003), paper presented at EUCAS 2003, Sorrento, Italy.

Zhang, K., D. A. Bonn, R. Liang, D. J. Baar, and W. N. Hardy (1993), *Appl. Phys. Lett.* **62**, 3020.

Zhang, Y. (2001), *IEEE Trans. Appl. Supercond.* **11**(1), 1038.

CHAPTER 15

Diamond-Like Carbon: Medical and Mechanical Applications

ROGER J. NARAYAN

Joint Department of Biomedical Engineering, University of North Carolina at Chapel Hill, Chapel Hill, North Carolina

15.1 INTRODUCTION

Synthesis of diamond-like carbon (DLC) thin films by pulsed laser deposition is a leading area in advanced materials research, and this chapter will describe pulsed laser deposition of DLC thin films. A brief review of the history of DLC processing will be presented, followed by a review of methods to improve the adhesion of DLC thin films, a discussion of DLC thin-film applications in medical and mechanical devices. Finally, directions in DLC thin-film research will be discussed.

15.2 PHYSICAL AND CHEMICAL PROPERTIES OF CARBON

Carbon is a unique element. It is able to form tetrahedral (sp^3), trigonal (sp^2), and linear (sp^1) bond coordinations. Diamond, graphite, fullerenes, nanotubes, and DLC are among the large variety of natural and synthetic forms of carbon [Kroto et al., 1985]. Diamond and graphite are the two major crystalline allotropes of carbon. At low pressures or temperatures, diamond is thermodynamically unstable with respect to graphite; however, extremely slow kinetics allows diamond and graphite to coexist at room temperature and atmospheric pressure.

In diamond, each carbon atom is covalently bonded to its four carbon neighbors, in what is referred to as sp^3 hybridization. These σ bonds are directional and quite strong. As a result, diamond possesses a modified face-centered cubic (fcc) structure of tetrahedrally coordinated atoms. This diamond cubic lattice consists of two interpenetrating fcc lattices displaced by one-quarter of the cube diagonal. The diamond cubic lattice can also be considered as a three-dimensional array of six-membered carbon rings in the ''chair'' conformation. These ring layers are stacked in an ABC/ABC/ABC sequence along $<111>$ directions. This cubic lattice is sometimes referred to as the ''ultimately cross-linked crystalline carbon polymer'' because it possesses the highest atomic number density of any material.

The properties of diamond derive from this unique structure. Diamond is the hardest known material (80–104 GPa) and has the largest bulk modulus of any solid. It is an electrical insulator, with an indirect gap of 5.5 eV and a direct gap of 6 eV. Diamond possesses the largest room temperature

Pulsed Laser Deposition of Thin Films: Applications-Led Growth of Functional Materials
Edited by Robert Eason

thermal conductivity (900–2100 $W\,m^{-1}\,K^{-1}$, which is approximately five times that of copper). In addition, it exhibits a large optical bandgap, transparency from the ultraviolet to the infrared, and a high refractive index (2.42). Diamond is chemically inert and is essentially nonreactive up to 800°C. Finally, diamond possesses excellent friction and wear properties. In fact, dangling carbon bonds on the surface of diamond can react to form hydrocarbon or graphite lubrication films.

Diamond has many industrial applications, including use in heat sinks, grinding wheels, and optics. Needless to say, large crystals of natural diamond are very expensive. Polycrystalline diamond thin films are a low-cost alternative to bulk diamond. These coatings can be prepared using a variety of plasma, microwave, hot filament, ion beam, and electron beam chemical vapor deposition (CVD) processes. Polycrystalline diamond coatings are created from strongly activated hydrocarbon gases in a hydrogen atmosphere. There are several limitations to polycrystalline diamond coatings.

First, these CVD processes require toxic and hazardous precursor materials. Second, these processes produce films with large grains. In addition, adhesion of diamond thin films is generally poor because there is a large thermal expansion mismatch between diamond and most substrate materials. Also, diamond thin-film processing requires high substrate temperatures of at least 800°C. Films grown at lower temperature contain hydrogen and graphite impurities that reduce film properties. This requirement restricts deposition on polymers and many metals. For example, high-temperature processes may lead to dimensional changes, phase transformations, or overtempering. Finally, diamond thin films are polycrystalline and contain open corrosion paths to the substrate. As a result, these coatings cannot be considered for use in corrosive environments. CVD diamond film technology has yet to overcome these major shortcomings.

Carbon can also exist in an amorphous state that does not possess long-range order. Micro- or nanocrystalline graphite domains may be observed in the amorphous matrix. This metastable material contains a mixture of sp^3- and sp^2-hybridized carbon atoms. These materials demonstrate properties intermediate between those of graphite and those of diamond.

The first hard amorphous carbon coatings were deposited by Aisenberg and Chabot at the former NASA Electronics Research Center in 1971 [Aisenberg and Chabot, 1971]. They created amorphous, transparent, hard, insulating carbon films using a beam of carbon ions produced in an argon plasma on room temperature substrates.

They initially coined the term ''diamond-like'' to signify that the properties of this material are similar to those of diamond. Since that time, the term ''diamond-like'' has been indiscriminately used to refer to several types of noncrystalline, hard carbonaceous films. Although no universally accepted nomenclature has been agreed upon, DLC often refers to amorphous carbon with some sp^3 component. These carbon-based solids exhibit atomic number densities greater than 3.19 g atom/cm^3. DLC films have been observed with densities closer to that of diamond (3.51 g/cm^3) than that of graphite (2.26 g/cm^3) [Moravec et al., 1980]. Many researchers refer to a predominantly sp^3-hybridized carbon film ($sp^3 > 70\%$) with a tetrahedral local carbon configuration as tetrahedral amorphous carbon, or ta-C. This term may more accurately reflect the fact that the reduced density function and the electron scattering data for highly sp^3-hybridized amorphous carbon films appear very similar to those for amorphous germanium or amorphous silicon. The terms amorphous diamond (AD) and amorphic diamond have also been used to describe this material [Santavirta et al., 1999].

When sp^3 fraction in the DLC film exceeds 70%, the sp^3-hybridized atoms form a continuous matrix that is linked together by conjugated chains. This structure has been modeled by the reverse Monte Carlo technique [Siegal et al., 2000a]. Tetrahedrally coordinated carbon atoms are located in distorted ring structures that range in size from 3 to 9 units, with 5- and 6-membered rings dominating. A smaller number of 3- and 4-membered rings may also be observed [Marks et al., 1996]. In this matrix, sp^2-hybridized atoms may be clustered in pairs, chains, or rings. These clusters of trigonally coordinated carbon atoms contain an even number of atoms [Ferrari and Robertson, 2000]. This clustering phenomenon has been observed using high-resolution transmission electron microscopy and Raman spectroscopy [Ravi et al., 1996].

15.3 PULSED LASER DEPOSITION OF DLC

The DLC thin films have been prepared by a variety of deposition techniques. Deposition of DLC requires (1) a carbon source and (2) an energy source to create excited carbon species. The energy source for the carbon species can involve one of these four processes: (1) momentum transfer during collision with energetic species (sputtering), (2) bombardment with energetic species (ion-assisted deposition), (3) electrostatic acceleration of carbon ions, or (4) energy transfer during laser ablation or arc discharge. These processes produce carbon species with kinetic energies on the order of 100–1000 kT (2.5–25 eV), whereas thermal processes (e.g., evaporation) generate species with energies on the order of kT (0.025 eV at ambient temperature) [Rohlfing, 1988]. Such high energies are necessary to promote the $2s$ electron to the $2p$ orbital and create the sp^3-hybridized carbon bond. Cathodic arc deposition, pulsed laser deposition, direct ion beam deposition, plasma-enhanced chemical vapor deposition, ion beam sputtering, and direct current/radio frequency (DC/RF) sputtering are common DLC deposition processes. Of these, only ultraviolet (UV) pulsed laser deposition, filtered vacuum cathodic arc deposition, and mass-selected ion beam deposition are able to produce hydrogen-free DLC thin films with a high fraction of sp^3-hybridized carbon atoms [Chhowalla et al., 1997]. Upon optimization, pulsed laser deposition produces DLC films superior to those produced using filtered cathodic vacuum arc (FCVA) deposition and mass-selected ion beam (MSIB) deposition techniques.

Pulsed laser deposition of DLC is a straightforward process, that involves ablation of a carbon-containing target, which results in the formation of a film with some fraction of sp^3-hybridized carbon atoms. The most commonly used target is high purity graphite; other target materials have included pressed diamond powder, glassy carbon, and polycarbonate [Guseva et al., 1994; Kikuchi et al., 1993; Voevodin et al., 1995a]. Nonhydrogenated carbon sources lead to hydrogen-free DLC films, whereas hydrocarbon sources lead to DLC films with significant hydrogen and/or hydrocarbon incorporation. The reported growth rates of DLC films deposited using a 248-nm excimer laser is on the order of 0.01 nm/pulse [Voevodin et al., 1996]. The laser processing of DLC thin films involves several interdependent factors, including: (1) the kinetic energy of the carbon species, (2) background environment, (3) substrate temperature, (4) the use of hybrid deposition techniques (e.g., substrate biasing), and (5) the presence or absence of a significant amount of hydrogen within the film. These parameters have tremendous bearing on the film properties, including the sp^3/sp^2 ratio, the presence of sp^2 clustering, and the adhesion of the film to the substrate [Voevodin et al., 1995b].

15.3.1 Effect of Wavelength and Fluence

Laser fluence and wavelength critically influence the film microstructure. The first attempt to synthesize hydrogen-free DLC films by laser ablation was reported by Fujimoro et al. in 1982. They used a continuous-wave CO_2 laser ($\lambda = 10.6\,\mu m$) to ablate powdered graphite and powdered diamond source materials. Films prepared from powdered diamond exhibited high electrical resistivity ($\sim 10^3\,\Omega\,cm$) and high optical transmittance. On the other hand, films synthesized from powdered graphite demonstrated a predominantly graphitic structure.

The majority of early investigations used Nd : YAG lasers ($\lambda = 1064$ nm). In 1985, Davanloo et al. reported deposition of DLC films by ablating a rotating solid carbon rod with the primary line of a Q-switched Nd : YAG laser. They suggested a ''shock synthesis model'' based on ''preferential sputtering of the more weakly bonded carbon atoms'' as a mechanism of hard carbon formation. Using this model, they determined that a threshold fluence of 5×10^{11} W/cm^2 must be exceeded to produce DLC with $\sim 75\%$ sp^3, which corresponds to the soft (4 on the Moh-scale scratch hardness tests) to hard (>7 on the Moh-scale scratch hardness tests) transition threshold. Collins and co-workers subsequently termed this threshold energy density for obtaining good quality DLC films the ''Nagel criterion'' [Collins et al., 1991]. Although the Nagel criterion appears valid for the 1064-nm laser wavelength, it does not hold for other laser wavelengths.

In 1987, Sato and co-workers demonstrated ultraviolet pulsed laser deposition of DLC films by ablating a graphite target with a XeCl excimer laser ($\lambda = 308$ nm). They demonstrated the formation of DLC at fluences $\sim 3 \times 10^8$ W cm^{-2}. These films were amorphous, with refractive index ~ 2.1; bandgap ~ 1.4 eV; and electrical resistivity $\sim 10^8\ \Omega$ cm [Sato et al., 1987, 1988].

In 1989, Narayan and co-workers produced hydrogen-free high-quality DLC films using a KrF pulsed excimer laser ($\lambda = 248$ nm, fluence $\sim 5 \times 10^8$ W cm^{-2}) to ablate a graphite target (Narayan et al., 1995). Narayan's group pioneered UV laser ablation of carbon to produce hydrogen-free DLC films. The films obtained were extremely smooth, hard, adherent, hydrogen free, and infrared transparent. They proposed a detailed model to account for the physical phenomena involved in the interaction of high-powered nanosecond excimer laser pulses with graphite, including evaporation, plasma formation, and deposition processes.

Karpman and co-workers and Xiong and co-workers reported the pulsed laser deposition of DLC films with an ArF laser ($\lambda = 193$ nm) at fluences of 5×10^8 W cm^{-2}. From electron energy loss spectroscopy studies, they determined that the fraction of sp^3 hybridized carbon atoms was between 84 and 95% [Karpman et al., 1994; Xiong et al., 1993].

Perhaps the best comparison study detailing the influence of wavelength on graphite ablation was performed by Peeler and Murray [1994]. Nd : YAG and excimer lasers were used at wavelengths of 1064, and 532 nm and 248 and 193 nm, respectively. These lasers were tuned to produce pulses of the same duration (15 ns) and fluence range ($\sim 2 \times 10^8$ W cm^{-2}), and the resulting plumes were analyzed with a time-of-flight (TOF) mass spectrometer. Films grown with the 1064-nm laser appear graphitic, while amorphous films with significant sp^3 bonding were produced at shorter wavelengths. Interestingly, the difference in sp^3 content between DLC films produced using KrF (248 nm) and ArF (193 nm) beams was small, 68% for KrF versus 72% for ArF. Ultraviolet wavelengths are critical to reach the minimum kinetic energy needed for DLC film growth. The trend toward using shorter wavelengths for pulsed laser deposition of DLC can be seen in current publications in which 193- and 248-nm wavelengths are most commonly used.

Visible plume luminescence reveals a great deal of information on the kinetic energy of the carbon species [Germain et al., 1995]. At low laser intensities, only a slowly propagating component of luminescence is seen. This component of luminescence contains low kinetic energy carbon dimers (C_2), trimers (C_3), and higher carbon clusters (C_n). A broader ball of luminescence explodes from the slow-moving clusters at intermediate laser intensities. This ball contains atomic carbon neutrals. A very fast ball of luminescence containing C^+ ions forms at high laser intensities. These C^+ species are considered to be critical in forming sp^3-hybridized bonds. Time evolution of the three components demonstrates 193- and 248-nm UV photons are more efficient than other photons in breaking up clusters and ionizing atoms. Strong absorption of short-wavelength photons converts the slow cluster component of the plume into the fast ion component.

As noted above, shorter wavelength lasers require smaller fluences to reach the threshold for DLC formation. For infrared (IR) lasers with 1064-nm wavelength, the threshold level is about 10^{11} W/cm^2, while for UV lasers with 193-, 248-, or 308-nm wavelength, this threshold level is about 10^8 W/cm^2 [Jelinek et al., 1994].

An increase in laser intensity results in increased luminescence of the energetic C^+ component relative to the atomic cluster component. There is a general tendency that higher fluences provide higher ionization rates and higher energy depositing species. However, there is an upper limit to carbon ion energy. Detailed plasma plume diagnostic studies indicate that a kinetic energy of about 90 eV produces a maximum fraction of sp^3-bonded carbon [Yamagata et al., 1999]. Above this limit, surface heating and displacement damage processes lead to graphitic phase formation.

15.3.2 Effect of Substrate Temperature and Vacuum

Another important parameter is substrate temperature. Researchers have performed pulsed laser deposition at substrate temperatures between -196 and 400°C. The typical deposition temperature is between 20 and 75°C. More specifically, room temperature is most commonly used.

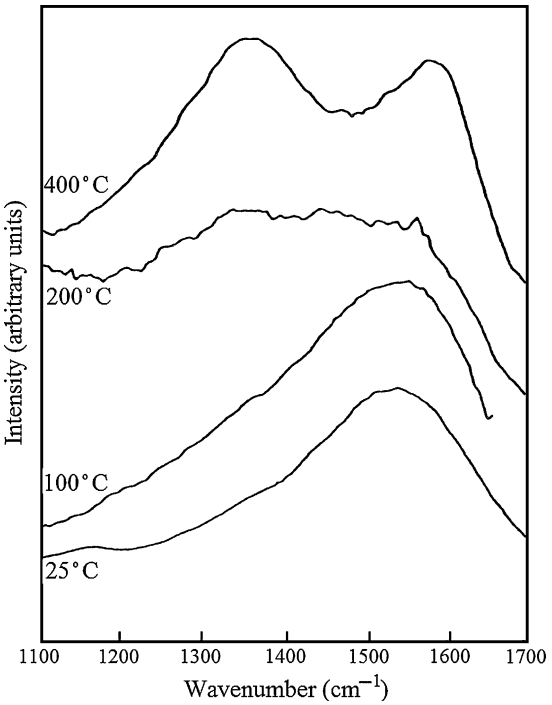

Figure 15.1 Visible Raman spectra of hydrogen-free DLC thin films on silicon (100) substrates deposited as a function of temperature. The presence of a *D* peak in the films deposited at 200 and 400°C is readily observed.

Diamond-like carbon is only formed if the deposition is carried out below a critical temperature of around 150–200°C, which is known as T_1. The value of T_1 is variable and decreases with increasing energy fluence. Oriented nanocrystalline graphite films are produced at deposition temperatures above T_1 [Lifshitz et al., 1995]. In these films, the basal plane is perpendicular to the film surface.

The microstructure of DLC can be evaluated using Raman spectroscopy. Disordered graphite has a peak at around 1350 cm^{-1} of A_{1g} symmetry labeled *D* for disorder. This peak can be correlated with the amount of aromatic clusters in the DLC film. DLC thin films deposited at room temperature have no *D* peak in their Raman spectra. The *D* peak appears at deposition temperatures immediately below T_1. As the deposition temperature is raised, the *D* peak increases in size (Fig. 15.1).

Cuomo and co-workers have deposited films using low-energy deposition ($\sim$10–20 eV) on substrates held at 77 K (-196°C) [Cuomo et al., 1991]. These films possessed $>70\%$ sp^3 fraction, which was significantly higher than that observed in films deposited at 300 K. They concluded two conditions are necessary for the formation of DLC thin films. These include (1) high energies are necessary to initiate strong sp^3 interatomic bonds and (2) low substrate temperatures are necessary to maintain low adatom mobility.

Vacuum conditions are another requirement for growing hard (60–70 GPa) DLC coatings. At a pressure of about 10^{-6} Pa vacuum, the plume leading edge contains ions and excited atoms with energies up to 1.5 keV. This leading edge is followed by a tail of lower energy atoms and multiatom clusters. When background pressures of about 10^{-4} Pa are used, the plume energy is reduced by collisional losses, which causes a reduction in coating hardness to 40–50 GPa. At pressures higher then 10 Pa, only graphite-like coatings are deposited.

15.4 MODIFICATIONS TO THE PULSED LASER DEPOSITION TECHNIQUE

A number of independently controllable modifications, including sample biasing, ion beams, and electrodes, have sought to increase the energy of deposited carbon species. More energetic ionic species thus produced have been found to be useful for achieving high growth rates and better quality films. Formation of ''nanophase diamond'' is the significant development achieved through these hybrid techniques.

Early researchers applied negative bias to the substrate using a hybrid ''L-PVD'' technique, in which an electric field of 150–500 V was applied between the grounded graphite target and the substrate during the laser ablation process [Wagal et al., 1988]. This Faraday cage was able to create a large ratio of ions to neutrals as compared to the conventional setup. High growth rates on the order of 20 $\mu m\,h^{-1}$ were observed. Film uniformity and coverage were found to be significantly enhanced due to the spreading of the plasma.

Krishnaswamy and co-workers also employed a capacitive discharge laser ablation deposition hybrid [Krishnaswamy et al., 1990]. In their ''plasma hybrid'' technique, a ring electrode between the graphite target and the substrate was capacitively coupled with the target. An XeCl excimer laser (308 nm) at a power density of 1.25×10^5 W/cm^2 was used to ablate a graphite target. These films demonstrated better optical properties, hardness, and uniformity than films produced by conventional pulsed laser deposition.

Davanloo et al. [1990] published results of their experiments with a rod electrode placed between the substrate and target. This electrode provided a positive or negative DC bias of 2000 V across the plasma in order to ionize the laser plume. In this experiment, the laser source was a Nd : YAG laser, operating at $\lambda = 1064$ nm with fluence $\sim 5 \times 10^{11}\,W\,cm^{-2}$. The high current discharge considerably increased the energy of depositing species. These films were distinguished by a characteristic nodular ''nanophase diamond'' structure, which consists of 10–100 nm cubic and hexagonal diamond nodules as well as sp^2/sp^3-hybridized carbon voids [Gruen, 1999]. Nanophase diamond can also be prepared by laser ablation of pure carbon at high-energy densities ($10^{11}\,W\,cm^{-2}$). Nanophase diamond is much smoother than polycrystalline diamond and is adherent to aluminum, silver, gold, copper, titanium, stainless steel, quartz, glass, and polyimide substrates. In addition, this material exhibits relatively low compressive stress values (0.8 GPa in micron-thick films). Friction coefficients as low as 0.1 have been observed in nanophase diamond.

It should be noted that these plasma-enhancing processes may also increase target erosion. Karpman et al. [1994] developed a discharge-enhanced 193-nm laser pulsed laser deposition (PLD) process. They observed extensive film contamination by ejected graphite fragments. These micrometer-sized graphite inclusions affected overall film properties.

Another modification to the PLD process is the laser-induced vacuum arc (laser arc) technique, which was advanced by Schultrich et al. [1998]. This technique combines the advantages of laser processing with the energy efficiency of an arc source. In the laser arc technique, plasma is generated by pulsed vacuum arc erosion of the cathode (target) material. The laser pulse is focused on the cathode surface. A small plasma cloud is produced, which ignites the vacuum arc. The laser-induced vacuum arc deposition process provides better control over cathode erosion than the continuous arc technique. As a result, microparticle emission is significantly reduced.

Plasma diagnostics reveal that the laser arc process creates a nearly fully ionized plasma. Optical emission spectroscopy has demonstrated a very high degree of ionization (100% C^+ ions) in the laser arc plasma at a peak arc current of 1 kA. These films possess Young's moduli up to 400 GPa and gap energies up to 2.0 eV. Average deposition rates greater than 10 $\mu m\,h^{-1}$ have been achieved using the laser-induced vacuum arc deposition technique. This growth rate is significantly higher than can be achieved using filtered vacuum cathodic arc deposition, mass-selected ion beam deposition, or conventional PLD techniques.

Several modifications to the pulsed laser deposition technique have been attempted to reduce particulate generation. Sato et al. [1988] first described the presence of particulates in carbon plumes. Target fragmentation and fragment ejection lead to $\sim$0.1- to $\sim$10-μm graphitic

microparticles (inclusions) that are embedded within the DLC film. These particulates, which result from local heating and melting of the target, degrade the mechanical, optical, and electronic properties of the film and prevent lithographic patterning. This process is worse in target materials with low melting points and low thermal conductivities and for long laser wavelengths, and high laser intensities [Gyorgy et al., 2004].

Both passive and active techniques are able to minimize the size and number of particulate generated during the ablation process. The passive techniques for minimizing particulate generation include using short-wavelength (e.g., ultraviolet) lasers and conditioning the target prior to deposition. Short-wavelength lasers reduce particulates by enhancing ablation through photon sputtering. This process reduces the target surface area exposed to overheating. Conditioning the target involves maintaining a smooth surface by laser beam scanning over the target surface. Active methods for reducing particulate generation include plume filtration and novel target ablation techniques. The plume can be mechanically filtered using a rotating vane. This process intercepts many large particulates and transmits the high-velocity component of the plume. Off-axis ablation, two laser depositions, laser beam scanning, and target rotation all serve to prevent target overheating.

15.5 GROWTH OF DLC FILMS

The pulsed laser deposition process itself is responsible for several features observed in DLC thin films. The region of the film closest to the substrate may demonstrate chemical interaction with the substrate; for example, DLC films on titanium alloys often possess a carbide layer at the film–substrate interface. The outermost surface layer of the DLC film can be best described as defective, graphitic, and porous. This film morphology may result from ''subplantation'' of carbon species during film growth, and we discuss this process in detail below. The surface layer of the growing DLC film is damaged by the incoming flux of energetic carbon species [Lifshitz et al., 1997]. Cross-section electron energy loss spectroscopy and angular resolved surface analysis have demonstrated that the defective layer thickness is proportional to the carbon ion energy [Uhlmann et al., 1998]. Steffen et al. [1991] examined this phenomenon using Auger electron spectroscopy.

Internal compressive stress is observed regardless of the processing technique used. There are several schools of thought on the origin of stress within DLC thin films. One of the earliest theories on stress development in DLC thin films was proposed by Bewilogua et al. [1982]. He suggested that an ion cascade leads to a shock wave, which in turn promotes the formation of sp^3-hybridized carbon atoms. This theory has some similarities to later models but inadequately describes processes that occur at higher ion energies.

McKenzie et al. [1994] have proposed that ion bombardment leads to compressive stress, which in turn forms and stabilizes the sp^3-hybridized phase [McCulloch et al., 2000]. They also suggest that a phase transition from an sp^2-rich to an sp^3-rich phase occurs at a critical value of compressive stress (~ 4 GPa), which is related to the graphite–diamond transition in the pressure–temperature phase diagram of carbon. Specifically, it is thought that the stability of sp^2 and sp^3 bonding in amorphous carbon follows the phase diagram of crystalline carbon. It is believed that some component of sp^3-hybridized carbon formation can be described by thermodynamics, even though the pulsed laser deposition process clearly produces nonequilibrium carbon species.

Cuomo and co-workers [1991] have described a ''quenching'' model for DLC film deposition. Essentially, this theory states that atoms cannot completely change from sp^3 hybridization to sp^2 hybridization after deposition on cold substrates. Cuomo et al. [1991] observed increased densities and sp^3 fraction in films prepared at lower substrate temperatures. Incidentally, his group also successfully demonstrated DLC deposition down to 77 K (described above) [Cuomo et al., 1991; Pappas et al., 1992]. This theory is supported by the observation that films with a high fraction of sp^3-hybridized atoms are not obtained at relatively high substrate temperatures (e.g., $>300°C$). Relaxation processes occur at these higher substrate temperatures, which lead to formation of a graphitic structure. Huai et al. [1994] have subsequently described this process in greater detail.

Kelires [2000] has proposed a similar process in which internal compressive stress in DLC films originates from stressed nonequilibrium local structures that are frozen during the growth process. He suggests that the local structures do not have sufficient energy to overcome the potential barrier to form a stress-free structure.

Lifshitz has described a low-energy subsurface implantation process that is known as subplantation [Kasi et al., 1988; Lifshitz, 1996]. They suggested the shallow implantation of energetic carbon ions with energies between 10 and 1000 eV to depths of 1–10 nm during film growth. The surface layer is quenched when deposition takes place at room temperature. Carbon species are trapped in subsurface sites due to restricted carbon species mobility, and this process induces the creation of internal compressive stress. Energetic carbon species penetrate to subsurface positions, where they are trapped and incorporated into the densifying film. As a result, the density of the carbon species increases during film growth. They demonstrated subsurface growth of DLC thin films using Auger electron spectroscopy. Molecular dynamics simulation has confirmed that DLC film growth is indeed an internal growth process for energies greater than 40 eV [Uhlmann et al., 1998].

They also suggested that sp^3-hybridized carbon sites accumulate from the preferential displacement of sp^2-hybridized carbon sites. A pure carbon layer evolves and grows upon successive bombardment. On the other hand, thermal migration and radiation damage may reduce local carbon species density and relax the structure. Lifshitz et al. [1995] have also proposed a diffusion-activated process for $sp^3 \rightarrow sp^2$ phase transformation in films deposited at substrate temperatures above 150°C.

Robertson has proposed a similar theory in which the subplantation process creates a metastable increase in density. This process in turn allows local carbon species to form sp^3-hybridized bonds [Robertson, 2002]. Roberston's model suggests film relaxation may occur through formation of clusters or microcrystallinity, which may potentially lead to zero stress films.

15.6 REDUCING INTERNAL COMPRESSIVE STRESS IN DLC THIN FILMS

Adhesion of DLC thin films is dependent on several factors, including film stress, film–substrate chemical bonding, and substrate topology [Koski et al., 1996; Morshed et al., 2003]. One major limitation preventing the practical application of DLC films is large internal compressive stress, which has been observed as high as 10 GPa [Schwan et al., 1997]. Unfortunately, these very high stress values limit the maximum film thickness to 0.1–0.2 μm. Delamination of the DLC film can occur when the internal stress exceeds a critical value, which sets the upper limit on film thickness. Delamination of DLC often occurs in a characteristic sinusoidal buckling pattern that can be correlated with compressive stress release. This pattern can be modeled using the thin-shell theory. The Stoney formula can be used to calculate internal stress in the DLC thin-film system. This equation can be written as

$$\sigma(f) = (6R)^{-1}\left[\frac{E(s)d(s)^2}{1 - v(s)}\right]d(f) \tag{15.1}$$

where R is the radius of curvature of the system due to stress, $E(s)$ is the Young's modulus of the substrate, modulus, d is the substrate thickness, $v(s)$ is Poisson's ratio of the substrate, and $d(f)$ is the thickness of the film. Values of $\sigma(f)$ are established through determination of R using interference fringe or beam deflection techniques [Dekempeneer et al., 1992]. An alternative technique for measuring the internal stress involves measuring the shift in the Raman G peak that occurs in DLC thin films under compressive stress. This value is compared against a stress-free reference material. Raman spectroscopy evaluates the atomic vibration frequency, which is a stress-dependent property. When a material is stressed, the equilibrium separation between atoms and the atomic vibrational

frequency are distorted. The magnitude of the Raman shift can be related to the residual stress σ using the following relation:

$$\sigma = 2G\left(\frac{1+v}{1-v}\right)\left[\frac{\Delta\omega}{\omega(0)}\right] \tag{15.2}$$

where $\Delta\omega$ is the shift in the Raman wavenumber, $\omega(0)$ is the Raman wavenumber of a reference state, G is the shear modulus of the material, and v is Poisson's ratio of the material. Wei and co-workers have demonstrated the relationship between intrinsic compressive stress and the Raman spectra of pulsed laser deposited DLC films. They demonstrated that compressive stress shifts the G peak higher by as much as $45\,\mathrm{cm}^{-1}$ [Wei et al., 1998, 1999].

Traditional approaches for creating DLC films with low internal compressive stress levels involve increasing the deposition temperature or decreasing the energies of carbon species arriving at the substrate surface. These approaches inevitably produce DLC thin films with low amounts of sp^3-hybridized carbon atoms. As a result, thin-film researchers have continually attempted novel approaches for reducing internal compressive stress in DLC films, and several of these techniques are described below.

McCulloch et al. [1997] demonstrated internal compressive stress reduction using room temperature irradiation with a 200-keV Xe^+ ion beam. This process transformed DLC into conducting amorphous carbon with a sp^3 fraction of 40%. At higher temperatures, the same irradiation process created a highly graphitic material with a sp^3 fraction of 20%. Anttila et al. [1997] achieved considerably improved adhesion of DLC on silicon by treating the silicon substrate with 140-eV argon ions prior to DLC film deposition. In addition, higher energies were imparted to the carbon species during the first stage of deposition to ensure a mixed interface. They also attempted to improve adhesion by coating the silicon substrate with a thick soft metal. These metals were chosen based on their ability to promote relaxation (copper, aluminum) or adhesion (titanium). Thick films with Vickers hardness values under 3 GPa were produced, but, unfortunately, compressive stress introduced during the preparation process caused the silicon substrate layer to delaminate.

Another method for improving the adhesion of DLC thin films is by increasing the energy imparted to the depositing carbon species. At higher energies, these energetic carbon species are implanted deeper within the substrate. As a result, a thicker interfacial carbide transition layer between the DLC film and the substrate may be formed. For example, Collins et al. [1992a] introduced additional energy to the ablated plumes and demonstrated the formation of a 10- to 20-nm-thick titanium carbide interfacial layer between a titanium substrate and a DLC film. This titanium carbide interfacial layer provided chemical bonding of the DLC film to the substrate and improved resistance against abrasive erosion.

Siegal and co-workers have developed layered high-density/low-density DLC films. They obtained a periodic layer sequence by periodically changing the bias (carbon energy), and these films demonstrate reduced stress [Siegal et al., 1998].

Ugolini et al. [1990] and others have discussed the deposition of interlayers prior to the growth of DLC thin films. They specifically mentioned the advantages of promoting adhesion using a carbide-forming interlayer, such as iron, silicon, chromium, tantalum, or tungsten. This intermediate layer should also yield locally into the substrate in order to absorb the compressive stress. Bentzon et al. [1994] found that copper–chromium interlayers provided the best improvement in adhesion for DLC thin films on steel. Although copper does not form a chemical bond with carbon, it does serve as a compliant layer that provides stress relief.

Silicon has been used as an interlayer material by Anders et al. [1997b] for hydrogen-free DLC films and by Meneve et al. [1996] for hydrogenated DLC films. In addition, a 2- to 4-nm-thick amorphous silicon interlayer is especially useful for glass and silicide-forming substrates [Grill et al., 1988].

Voevodin et al. [1995c] have successfully used multitarget ablation schemes to deposit multiple supporting interlayers. They have demonstrated combined magnetron sputtering of

titanium and laser ablation of graphite to create functionally gradient crystalline titanium, titanium carbide, and DLC composite coatings [Voevodin et al., 1995a]. Gradual transitions of chemistry and structure between metal, metal carbide, and amorphous carbon were achieved using this technique. These functionally graded DLC coatings contain an adhesive thin-metal layer, a load-supporting carbide layer, a metal-doped DLC layer, and/or multiple pairs of metal–DLC or carbide–DLC layers. As such, no sharp interfaces that could serve as crack initiation sites are formed. These films demonstrated total thickness values of 2–3 μm and hardness values around $\sim$65 GPa. In addition, scratch adhesion studies of these films demonstrated neither adhesion failure nor peripheral cracking. Quite high loads (nearly 50 N) were required for substrate penetration and film delamination. Functionally gradient Ti–TiC–DLC coatings remained intact for over 10^5 cycles, and multilayer Ti–TiC–DLC–[Ti–DLC] coatings maintained a friction coefficient of 0.1 for over 10^6 cycles. On the other hand, single-layer DLC coatings failed by delamination after the first few cycles and composite DLC/H:DLC coatings were worn after several thousand cycles.

Other researchers have demonstrated the incorporation of modifying elements within diamond-like carbon films using a conventional PLD system. For example, modifying element targets and graphite targets can be co-ablated during the PLD process. Several modifying elements, including gold, chromium, copper, silicon, oxygen, tungsten, titanium, iron, platinum, niobium, nickel, silicon, tin, and tantalum, have been incorporated within DLC thin films [Amaratunga et al., 1995; Amir et al., 1991; Donnet et al., 1997; Grill and Patel, 1996; Grill et al., 1998; Grischke et al., 1998; Wei et al., 1998, 1999].

Narayan et al. [1995] have developed a variant of the conventional PLD process to incorporate modifying elements into growing DLC films [Wei et al., 1998, 1999]. Briefly, a single multi-component target is loaded into the pulsed laser deposition chamber; this target contains pure graphite covered by a piece of the desired modifying element target. The focused laser beam sequentially ablates the graphite target component and the modifying element target component to form composite layers. They observed that the presence of metal causes the visible Raman spectrum *G* peak to shift to smaller wavenumbers. As mentioned above, these results suggest that internal compressive stress is decreased. Furthermore, the modifying element can be incorporated in a controlled manner during the PLD process. For example, functionally gradient films have been created by gradually decreasing the modifying element concentration from the coating–substrate interface to the surface. Adherent, 1-μm thick DLC–titanium and DLC–silver films have been demonstrated using this technique.

These DLC–metal composite films demonstrate two different microstructures. Carbide-forming elements (e.g., titanium) demonstrate segregation of the carbide layers within the DLC matrix at high metal concentrations. On the other hand, non-carbide-forming modifying elements form uniformly distributed nanoparticles within the DLC matrix. A cross-sectional transmission electron micrograph of a DLC–silver nanocomposite film is shown in Figure 15.2. The size of these nanoparticles depends on the ratio of modifying element/graphite ablated, the type of modifying element, and the deposition parameters.

The electrical and mechanical properties of these DLC composites are dependent on the size and density of the modifying element component. Chemical reactivity, elasticity, electrical conductivity, hardness, internal stress, oxidation behavior, thermal expansion coefficient, and other material properties can be effectively tuned by controlling the concentration of the modifying element within the DLC composite film. For example, increasing the fraction of metal within a DLC composite film may increase electrical conductivity by 12 orders of magnitude. DLC–metal composite films generally have a reduced sp^3 content; however, hardness and Young's modulus may remain essentially intact. Hardness values, ranging from 5 to 20 GPa, and Young's moduli, ranging from 50 to 200 GPa, have been reported for different DLC–metal composite thin films [Benndorf et al., 1991a, 1991b; Bewilogua and Dimigen, 1993; Dimigen and Klages, 1991; Wang et al., 1992]. Many of these DLC–metal composites are opaque. DLC–silicon composites, on the other hand, are transparent and can be used in optical applications.

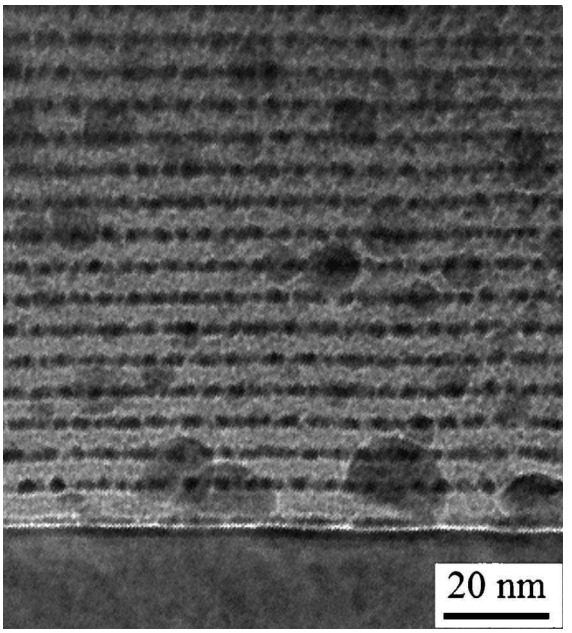

Figure 15.2 Bright-field transmission electron micrograph of DLC-silver nanocomposite film.

There are several new applications for DLC–metal composite films [Chen et al., 2001a, 2001b, 2001c; Fiaccabrino et al., 1996; Wachter et al., 1998]. For example, DLC–metal composites can be used as emitters in advanced field emission devices. In fact, DLC–metal composite films may have better field emission performance than DLC films [Tay and Zhang, 2002]. DLC–silicon composite thin films exhibit lower oxygen plasma etching rates than DLC thin films, and can serve as an etch stop. Modified DLC films may possess improved friction and tribological properties. For example, DLC–silicon films may possess lower friction coefficients than DLC films. Similarly, fluorinated DLC films possess lower surface energies and lower friction coefficients than DLC films.

Dorfman has described the properties of diamond-like nanocomposites (DLN), which consist of atomic-scale carbon and silicon composite random networks [Dorfman, 1992]. The carbon within this network is stabilized by the presence of hydrogen and the silicon within this network is stabilized by the presence of oxygen. This network structure prevents growth of a graphitic phase, enhances adhesion, and reduces internal stress. Metals can also be introduced into these diamond-like nanocomposite films, and the metal component may either form a disordered network or remain as separate atoms within the diamond-like nanocomposite matrix. The amorphous carbon, amorphous silicon, and amorphous metal networks are interwoven together. They have shown that diamond-like bonding and properties are preserved within this composite material.

Postdeposition annealing is yet another technique for reducing internal compressive stress in DLC thin films. Highly tetrahedral DLC thin films can be annealed at temperatures up to 1000–1100°C in vacuum. It should be noted, however, that films with a lower sp^3 content or films containing nitrogen are less stable [Anders et al., 1997b].

This high-temperature postdeposition annealing process has been described extensively in the literature. Friedman et al. [1996] described a process that involves depositing a 100- to 200-nm DLC film at room temperature. This film is then annealed at 600°C for 2 min, since annealing at lower temperatures (up to 300°C) causes roughening. Additional DLC deposition can be performed once

the film is cooled to room temperature. These annealed films demonstrate large sp^3 fractions, exceptional hardness values, large elastic moduli, good adhesion to the underlying substrates, and either reduced residual compressive stress (less than 0.2 GPa) or tensile stress. DLC films with thicknesses of 1.2 μm have been demonstrated using this technique.

The thermal annealing process has been modeled, and stress reduction has been correlated with the diffusion of sp^2-hybridized carbon sites into larger clusters [Chhowalla et al., 2000; Ferrari et al., 1999; Ferrari and Robertson, 2000; Friedmann et al., 1997; Kalish et al., 1999; Sullivan et al., 1997]. The sp^3 fraction remains essentially constant during this process. The sp^2-hybridized carbon sites diffuse within the sp^3-hybridized carbon matrix at lower energies/temperatures than are required for the conversion of sp^3-hybridized carbon sites to sp^2-hybridized carbon sites. The activation energy for the diffusion of sp^2 sites is estimated to be in the range of 2.5 eV. On the other hand, the activation energy for the conversion of sp^3-hybridized carbon to sp^2-hybridized carbon is estimated to be in the range of $\sim$3.5 eV. Annealing allows the lower energy sp^2 site diffusion process to occur. This clustering process is also noted during high-temperature deposition of DLC thin films.

Sullivan et al. [1997] have suggested that the π planes within these graphitic clusters align in the plane of compression to remove compressive stress. The graphite c axis orients perpendicular to the film surface, and the graphite basal plane orients parallel to the film surface. Nearly 2% of sp^3 sites need to convert to sp^2 sites for this strain relaxation process to occur.

Annealed DLC films have been characterized using a variety of techniques [Siegal et al., 2000b; Martinez-Miranda et al., 2001]. Electron energy loss spectroscopy studies suggest the total number of sp^3 sites remains essentially unchanged. On the other hand, the clustering of sp^2-hybridized carbon atoms does alter the visible Raman spectrum. The D peak appears, and the G peak becomes increasingly skewed. The appearance of a D peak suggests that the sp^2-hybridized carbon atoms rearrange within the sp^3-hybridized carbon matrix, segregating into large aromatic clusters. Siegal et al. [2000b] have demonstrated the presence of these nanophase clusters in annealed films using cross-section transmission electron microscopy. More dense amorphous carbon clusters are observed within a less dense amorphous carbon matrix. The clusters are estimated to be between 3–5 nm in size, and possess 5–10% greater density than the surrounding matrix. It appears that these inclusions grow on existing nuclei that are already present in as-deposited films. The sp^2 clusters in as-deposited films may arise from a stress reduction mechanism during film growth. The annealed films were studied using nanoindentation and exhibit 15% greater hardness than as-deposited films. Hardness and modulus values determined from an Oliver–Pharr analysis were 80.2 and 552 GPa, respectively [Friedmann et al., 1997]. Annealing also causes resistivity to decrease and optical gap to drop to zero [Ferrari et al., 1999; Siegal et al., 2000b].

The advantage of the thermal annealing process for stress reduction in DLC thin films is that pure films can be prepared. Unfortunately, one of the disadvantages of the thermal annealing process is that film throughput may be decreased. In addition, the thermal budget for a microelectronic device undergoing this annealing process may be sharply reduced [Nir, 1987; Wagner et al., 1989]. Polymer substrates are precluded from thermal annealing, and some metal substrates may undergo overtempering during thermal cycling. There is no current mechanism for significantly reducing or eliminating internal compressive stress in DLC thin films that can be applied to any substrate material and allows for continuous growth of pure, thick films. Thin-film researchers are continuing to develop novel methods for overcoming this major obstacle.

15.7 HYDROGENATED AND HYDROGEN-FREE DLC

"Hydrogen-free" DLC films are produced by ablating a high-purity graphite target in 10^{-5} Pa vacuum, and these films contain very low amounts of hydrogen (between 0.01 and 0.1 atom %). Structurally, these films are best described as amorphous networks containing large amounts of

sp^3-hybridized carbon atoms and they exhibit densities at or exceeding 3.0 g/cm^3. In addition, these films possess a high level of residual compressive stress.

Hydrogenated DLC can be described as an exceptionally dense polymer. These films contain up to 30 atom % hydrogen and up to 10 atom % oxygen within an amorphous carbon matrix. The hydrogen and oxygen are contained within CH_3 and O–CH_3 inclusions; the density of hydrogenated DLC is approximately 2.2 g/cm^3. Hydrogenated DLC (HDLC) may also be referred to as amorphous carbon hydrogenated (a-C:H) or diamond-like hydrocarbon (DLHC).

These films may be produced by pulsed laser deposition of polymer targets [Voevodin et al., 1995a] and often contain polymer fragments due to target splashing. In addition, HDLC films can be prepared by ablation of a graphite target in a hydrogen atmosphere. For example, Malshe et al. [1990] created a HDLC thin film by ablating a graphite target with a 694-nm ruby laser in a 60-Pa hydrogen atmosphere at a substrate temperature of 50°C. The laser wavelength is a critical parameter for pulsed laser deposition of hydrogenated DLC, as the absorption coefficient for the hydrogen (H_2) molecule exhibits a pronounced wavelength dependence. As a result, the amount of chemically active hydrogen atoms within the hydrogenated DLC film can vary widely based on laser wavelength.

Under certain conditions, pulsed laser deposition growth of hydrogenated DLC films is similar to chemical vapor deposition growth of diamond films. Rengen et al. [1992] were able to deposit micron-sized diamond crystals with dominant diamond octahedral faceting using a modified pulsed laser deposition process in which a graphite target was ablated using a KrF laser. The laser plume was extended and heated using a ring electrode. During these depositions, a hydrogen background pressure of 13 Pa was maintained. Depositions at substrate temperatures between 100 and 860°C provided microcrystalline diamond films. Polo et al. [1995] demonstrated conventional pulsed laser deposition of microcrystalline diamond thin films on diamond powder-treated substrates. For example, they deposited 20-μm diamond crystals on silicon substrates by ArF laser ablation of a graphite target at a substrate temperature of 450°C. These depositions were performed in hydrogen atmosphere of 100 Pa. Tetrahedral bonding in these films was demonstrated using Raman spectroscopy.

Early thin-film researchers believed that the incorporation of hydrogen into DLC films promoted sp^3 stabilization and increased the sp^3 fraction. As a result, the development of hydrogenated DLC films exceeded that of hydrogen-free DLC films during the early and mid-1980s. Hydrogenated DLC–metal films demonstrated adequate adhesion, mechanical, optical, and tribological properties in many environments, and, as a result, these coatings made their way into many industrial applications. By the late 1980s, several factors led to a general preference of hydrogen-free DLC films over hydrogenated DLC films. By that time, hydrogen-free DLC films were created at similar or higher deposition rates than hydrogenated DLC films. In addition, hydrogen-free DLC films possess better adhesion, mechanical, optical, and tribological properties than hydrogenated DLC films. For example, hydrogen-free DLC films demonstrate higher densities, elastic moduli, and hardness values than unhydrogenated diamond-like films. Hydrogen-free diamond-like films may possess hardness values over 50 GPa, whereas unhydrogenated diamond-like films typically possess hardness values around 10 GPa. In addition, hydrogenated DLC films are often rougher than their hydrogen-free counterparts. As a result, hydrogenated DLC films were found to possess higher wear rates than hydrogen-free DLC films. Hydrogen-free films were also found to exhibit better adhesion than hydrogenated films. In addition, the friction coefficients of hydrogenated DLC films were found to be much higher than those of hydrogen-free diamond carbon films, especially in humid environments. In fact, the coefficient of friction for hydrogenated DLC can approach ~ 0.3 in humid test environments [Voevodin et al., 1995b]. It should be noted that several researchers have recently demonstrated that the friction coefficient of hydrogenated DLC can be made impervious to humidity through the incorporation of 4 atom % hydrogen [Gilmore and Hauert, 2000, 2001; Oguri and Arai, 1990; Wu et al., 1998] or silicon [Gangopadhyay et al., 1997]. Finally, hydrogen-free DLC demonstrates much better thermal stability than hydrogenated DLC. Hydrogen-free DLC converts to nanocrystalline graphite at

800°C in vacuum, and at 550°C in an oxygen atmosphere. On the other hand, hydrogenated DLC converts to graphite at 300°C in vacuum, and 250°C in an oxygen atmosphere [Friedmann et al., 1996]. As a result, high-temperature annealing cannot be used to remove compressive stress in hydrogenated films. Finally, carbon–hydrogen bonds create interference in infrared transmission. As a result, hydrogen-free DLC is considered a more satisfactory material than hydrogenated DLC for a wide variety of devices, including hard disk coatings, tape coatings, antireflective infrared coatings, medical coatings, and tribological coatings.

15.8 PROPERTIES OF DLC

Cohen [1985] has used a semiempirical approach to determine the mechanical properties for tetrahedrally bonded materials. The hardness of materials in the absence of major defects is found to scale with bulk modulus (B), as given by $B = -Vdp/dv = Vd^2u/dV^2$, where V is the volume, P is the pressure and U is the energy. The bulk modulus can be approximated by $N_c/4 \times (1972–220\,I)/d^{3.5}$ (GPa), where N_c is the coordination number, d is the bond length, and I is the ionicity parameter. The ionicity parameter accounts for charge transfer; this value is 0 for Group IV elements, 1 for Group IV and V elements, and 2 for Group II and VI elements. For tetrahedrally bonded materials, $N_c = 4$, and in this case, the relation for B can be simplified as $(3263–3641)N^{1.167}$. Based on this equation, the hardest materials contain either boron (covalent radius = 0.88 Å), carbon (covalent radius = 0.77 Å), or nitrogen (covalent radius = 0.70 Å), which exhibit covalent bonding with minimum charge transfer. Using the above formulas, crystalline diamond ($d = 1.54$ Å, $I = 0$, and $N_c = 4$) should possess a Young's modulus of 435 GPa. This value is in agreement with the experimental value of 443 GPa. Based on the above equation, DLC should possess a very high Young's modulus. The sp^3/sp^2 ratio in DLC films determines the mechanical properties of the film. In fact, the elastic modulus (<900 GPa), mechanical hardness (<80 GPa), and density (>3.0 g/cm^3) of DLC films demonstrate a range of values [Donnet and Grill, 1997; Enke et al., 1980; Ronkainen et al., 2001], which are correlated with the sp^3/sp^2 ratio. Coefficient of friction values under 0.05 have been obtained by several groups, depending on the counterface material, the testing apparatus, and the testing environment [Bull, 1995].

On the other hand, the electrical and optical properties of DLC thin films depend primarily on the presence of the sp^2-bonded carbon clusters. Local bandgaps are dependent on the local configuration and size of these clusters; in general, smaller clusters lead to larger bandgaps [Robertson et al., 1987; Robertson et al., 1995]. The amount of distortion of π bonding in the sp^2 clusters by the sp^3 matrix also determines bandgap. Dangling bonds or single sp^2 atoms do not occur in substantial numbers; instead, these atoms pair up to form π-bonding states outside the bandgap. Undoped DLC is a p-type semiconductor in which the Fermi level is located 0–22 eV higher than the effective valence band edge [Veerasamy et al., 1994]. Although it demonstrates a poor doping response, it can be doped with boron, nitrogen, phosphorus, or other impurities to exhibit n- or p-type semiconducting behavior [McKenzie et al., 1994]. DLC exhibits a relatively wide bandgap and a high hole mobility. Unfortunately, low carrier mobility, wide-band tails, and a large density of midgap states have slowed large-scale application of DLC thin films in electronic applications [Milne, 1996]. DLC is transparent in the infrared region and visible region. The optical gap increases with sp^3 fraction; a Tauc gap up to 2.0 eV is observed in samples with a high (~90%) sp^3 fraction [McKenzie et al., 1994]. Hydrogen-free DLC exhibits relatively high thermal conductivities on the order of 10 W/m K (nearly five times greater than that of copper). On the other hand, hydrogenated DLC demonstrates thermal conductivities on the order of ~1 W/m K [Bullen et al., 2000; Morath et al., 1994]. Finally, DLC is essentially chemically inert below 800°C. These unique characteristics have led many researchers to propose a wide variety of applications for DLC thin films. Some of these potential applications are listed in Table 15.1. The following sections will detail potential and current applications for DLC thin films in medical and mechanical devices.

TABLE 15.1 Possible Applications for DLC Thin Films

Property	Applications
High thermal conductivity	Electronic device heat sink
Biological inertness	Medical prosthesis, biosensor, medical instrument coating
Chemical inertness	Chemical reactor vessel, fuel cell anode coating, nuclear reactor wall coating
Low electron affinity	Cold cathode for flat-panel display, Schottky diode
Optical transparency	Lens, optical fiber coating, laser bar code scanner coating, infrared window antireflective coating
Electrical conductivity (n or p type)	Radiation- and temperature-resistant devices
Hardness, wear resistance, and low friction	Cutting tool coating, abrasive, microelectromechanical system coating, ball bearing coating, wear protection of sliding part, magnetic recording coating, engine injection pump coating, gear coating
High sound propagation velocity	Speaker tweeter, speaker diaphragm

15.9 DLC APPLICATIONS

15.9.1 Medical Applications

The majority of adverse host responses to implantation of a medical implant are related to poor surface properties. Corrosion, fatigue, friction, and wear are only some of the factors that must be eliminated or minimized to promote healing and long-term function of a prosthesis, biosensor, or drug delivery device.

Most biomaterials were originally adopted from unrelated technical areas. Stainless steel, cobalt–chromium–molybdenum alloy (ASTM F75), titanium–aluminum–vanadium alloy (ASTM F316), polyurethane, polycarbonate, and ultra-high-molecular-weight polyethylene were originally developed for aerospace, chemical, or other industries, and were slowly absorbed into the medical armamentarium. The time delay between material innovation and medical acceptance is slowly narrowing, but many hurdles remain.

There are several requirements for implantable biomaterial surfaces and coatings. First of all, they must not be toxic when in contact with the host environment. Second, the surface must be corrosion resistant in the 1% NaCl environment of the human body, in order to prevent release of allergenic, carcinogenic, or toxic metal ions, monomers, or plasticizers from the bulk metal, ceramic, composite, or polymer [Grill, 2003]. Cobalt, chromium, nickel, aluminum, and vanadium ions have been cited for carcinogenic or toxic interactions with human tissues [Swierenga et al., 1987]. Third, the surface must have sufficient fatigue properties to resist an environment that includes considerable stresses and an extremely large number of cycles per year (up to 10^6–10^9). Many medical biomaterials perform a ''structural'' function; structural integrity is essentially for long-term performance. Fourth, the material surface must be wear resistant. Fifth, the coating must have good adhesion to the bulk biomaterial surface, and sixth, a well-controlled surface finish is necessary, especially in low friction or tissue-bonding environments.

Carbon biomaterials have been used for over 30 years, and the first of these were low-temperature isotropic (LTI) pyrolytic carbons. These dense, isotropic materials are deposited from a hydrocarbon gas (e.g., methane) in a fluidized-bed reactor at temperatures below 1500°C. In 1969 De Bakey introduced a pyrolytic carbon-coated aortic valve prosthesis that incorporated carbon-coated metal struts and a carbon-coated hollow ball [DeWall et al., 2000]. These valves demonstrated biocompatibility, inertness, and immunity to fatigue. Pyrolytic carbon remains a common valve prosthesis biomaterial, but more recently, DLC has been considered for use in medical prostheses and surgical instruments.

Diamond-like carbon thin films have also been shown to possess excellent biocompatibility. For example, in vitro studies of DLC involving mouse peritoneal macrophages, mouse fibroblasts, human myeloblastic ML-1 cells, osteoblast-like cells, and human embryo kidney 293 cells have demonstrated the absence of an inflammatory response [Allen et al., 1994; Linder et al., 2002; Lu et al., 1993; Thomson et al., 1991]. Morphological examination and biochemical data suggest that DLC-exposed cells undergo no cellular damage. For example, osteoblast-like cell lines exposed to DLC coatings did not demonstrate any change in creation of proteins, including alkaline phosphatase, type I collagen, and osteocalcin [Allen et al., 2001]. In addition, neuronal growth readily occurs on DLC surfaces [Ignatius et al., 1998].

Diamond-like carbon has been considered for use in a variety of vascular medical devices [Dion et al., 1993; Thomson et al., 1991; Tran et al., 1999], including coronary artery stents [De Scheerder et al., 2000; Gutensohn et al., 2000], synthetic heart valves [Jones et al., 2000; Yin et al., 1999; Yu et al., 2000], left ventricular assist devices [Alanazi et al., 2000], and artificial hearts [Yamazaki et al., 1998]. A common problem with artificial heart valves and cardiac stents is thrombus formation and blood vessel closure [Allen et al., 2001; Jones et al., 1999, 2000; Parker et al., 1994; Schroeder et al., 2000; Tiainen, 2001]. Thrombus formation is a multi-step process that occurs on the biomaterial surface and involves plasma protein adsorption, platelet adhesion and activation, and clotting factor activation [Courtney et al., 1994; Lyman et al., 1972]. The clotting process is dependent on fluid flow and device surface properties and is initiated by platelet activation. These blood clots can break loose and cause damage in the brain, kidneys, or lungs.

Diamond-like carbon thin films demonstrate outstanding hemocompatibility. These films exhibit decreased platelet activation and reduced thrombus formation [Monties et al., 1997]. Furthermore, DLC possesses an extremely low coefficient of friction. This feature may increase the rate of blood flow and improve other hemodynamic properties.

Several studies have shown that DLC can greatly improve the hemocompatibility of a medical device. Measurements of in vitro platelet adhesion involving I-125-labeled platelets demonstrate a larger number of platelets adhere to titanium than to DLC-coated titanium [Krishnan et al., 2002]. Also, in vitro studies demonstrate platelet activation and platelet adhesion occur less often on DLC-coated surfaces than on titanium, titanium carbide, titanium nitride, and stainless steel surfaces [Chu et al., 2001; Jones et al., 1999, 2000; Yu et al., 2000]. The albumin adhesion–fibrinogen adhesion ratio is an important hemocompatiblity factor; this value is inversely correlated with the amount of platelet adhesion. Cui and Li [2000] found that the albumin adhesion–fibrinogen adhesion ratios for DLC-coated surfaces were higher than those for poly(methyl methacrylate) (PMMA). In addition, Gutensohn et al. [2000] demonstrated that a DLC coating on 316L stainless steel reduces the generation of platelet activation antigens and the proliferation of smooth muscle cells. Uncoated stainless steel and nickel–titanium alloy stents release a significant amount of nickel and/or chromium metal ions when exposed to human plasma, while on the other hand, DLC-coated stents release negligible amounts of these ions. These factors suggest thrombus formation should be reduced on DLC-coated surfaces, and, in fact, one in vitro study suggests DLC coatings may resist platelet adhesion and thrombus formation better than pyrolytic carbon coatings [Tran et al., 1999]. It is interesting to note that Chen et al. [2002] found a correlation between the fraction of sp^3-bonded carbon, and the number of adherent platelets [De Scheerder et al., 2000]. Cell adhesion to DLC films has also been correlated with surface energy [Jones et al., 2000] and surface texture [McLaughlin et al., 1996].

Medical devices coated with DLC have been demonstrated in a number of in vivo (animal) studies. For example, De Scheerder et al. [2000] found coronary artery stents coated with Si:O containing DLC were biocompatible. These coated stents demonstrated reduced inflammation and decreased thrombus formation [Neerinck et al., 1998]. The number of inflammatory cells was lower on the Si:O DLC stent surface than on the DLC stent surface. A DLC-coated ventricular assist device, intended to assist blood pumping, demonstrated minimal thrombosis during implantation studies involving calves [Yamazaki et al., 1998].

Another medical application for DLC thin films is use on the surface of hip or knee joint prostheses. It is believed that approximately 25 million people have a partial or total joint replacement prosthesis [Goldring et al., 1993], and these are now being implanted in more active, younger patients, who are placing additional requirements on these devices. A cobalt–chromium–molybdenum alloy, cobalt–nickel–chromium–molybdenum alloy, or a titanium–aluminum–vanadium alloy surface articulates against an ultra-high-molecular-weight polyethylene surface in a total joint prosthesis. These components are fixed in place using PMMA bone cement. Current devices have exceedingly short lifetimes, however, and it is believed that 10–20% of the implants have to be replaced after 10 years, with some needing replacement in as little as 5 years [Malchau et al., 1993]. Loosening, wear, corrosion, uneven stress distributions, and tissue inflammation contribute to these short lifetimes [Witt et al., 1991].

Stress shielding, another phenomenon that affects joint prostheses, refers to an uneven load distribution at the bone–prosthesis interface that can lead to prosthesis loosening [Head et al., 1995], and this problem affects every current metal prosthesis component. For example, cobalt–chromium–molybdenum alloy exhibits a modulus of elasticity of 220 GPa. This value is 10 times higher than that of the surrounding bone (17 GPa), and as a result stress shielding is quite significant. An alternative metal component material is titanium–aluminum–vanadium alloy. This biocompatible, highly corrosion-resistant alloy exhibits a modulus of elasticity of 110 GPa [Williams, 1977]. Unfortunately, titanium–aluminum–vanadium alloy demonstrates poor wear resistance and exhibits crevice corrosion when fixed using PMMA bone cement [Peters et al., 1992; Scales, 1991].

Wear of orthopedic implant materials is another serious issue. A cobalt–chromium–molybdenum alloy/polyethylene implant generates a large number of polyethylene wear particles [Santavirta et al., 1998]. Polyethylene wear is estimated at 0.10–0.20 mm/year; in fact, some investigators have suggested 100,000 polyethylene particles are released with each step [Doorn et al., 1996; Goodman et al., 1990]. Wear of the metal component of the joint prosthesis also occurs. For example, cobalt–chromium–molybdenum alloy degrades at an average rate of 0.02–0.06 mm in 10 years. Titanium–aluminum–vanadium alloy is more prone to mechanical wear, especially at the titanium–aluminum–vanadium alloy/polyethylene interface. On the other hand, cobalt–chromium–molybdenum alloy particles cause greater tissue toxicity than polyethylene particles or titanium–aluminum–vanadium alloy particles.

In addition, the PMMA bone cement presents many problems. Bone cement assists in distributing stresses between bone and metal and can be loaded with antibiotics. Unfortunately, micromotion at the implant–bone interface may lead to the release of a large amount of bone cement particles [Jones and Hungerford, 1987; Santavirta et al., 1991, 1998]. Also, stress concentrations at the implant–PMMA interface may lead to microfracture of PMMA. Metal, polymer, and bone cement debris can generate third-body wear of the metal and polymer prosthesis components [Santavirta et al., 1999]. Finally, these wear particles induce inflammation in the surrounding tissues, bone breakdown (osteolysis), and implant loosening [Rae, 1981].

Several ceramic–ceramic total joint prostheses have been available since 1969; however, the success of these devices has been mixed because ceramic microstructure and prosthesis geometry have not been well controlled [Boutin et al., 1988]. As a result, many orthopedic biomaterials researchers have sought to combine a bulk material possessing a modulus of elasticity close to that of bone with a wear-resistant, low-friction, hard, biocompatible coating. Titanium nitride coating, nitrogen ion implantation, nitrogen diffusion hardening, and oxygen diffusion hardening are current techniques for surface modification of total joint replacement materials [Williams et al., 1989]. Unfortunately, abrasion and oxidative wear may allow removal of these layers.

Diamond-like carbon is an ideal surface coating for prosthetic joints because it is atomically smooth, low friction, wear resistant, inert, and immune to scratching by third-body wear particles [Santavirta et al., 1999]. Furthermore, it prevents the release of metal ions into the surrounding tissues. Hydrogen-free DLC is greatly preferred over hydrogenated DLC thin films for joint prosthesis applications in which a low-friction surface under humid conditions is required.

Investigators have also compared the wear and corrosion behavior of DLC-coated materials to uncoated materials [Tiainen, 2001]. The friction and wear properties of DLC-coated metal hip prostheses against DLC-coated cups have been determined by multiple investigators using pin-on-disk and hip joint simulators. For example, Tiainen [2001] demonstrated extremely low coefficients of friction for hydrogen-free DLC coatings created using a pulsed arc discharge method. The coefficients of friction for DLC-coated, metal–polyethylene and metal–metal pairs were 0.05, 0.05, and 0.14, respectively. In addition, they demonstrated that the wear in the DLC-coated metal/DLC-coated metal wear couple is 10^5–10^6 times lower than in conventional metal–polyethylene and metal–metal wear couples. Furthermore, DLC can reduce the wear of polyethylene in a DLC-coated metal/ultra-high-molecular-weight polyethylene wear couple by 10–600. Santavirta et al. [1999] also demonstrated the wear resistance of pulsed plasma-arc-deposited DLC using a commercial hip simulator. Similarly, Davidson and Mishra [1995] found DLC-coated titanium–aluminum–vanadium alloy samples exhibited no discernible wear at the one million cycle mark. On the other hand, nitrogen ion implanted samples demonstrated significant wear. Onate et al. [2001] and Dong et al. [1999] demonstrated significant reductions in wear of polyethylene against DLC coatings using a pin-on-disk instrument and a knee wear simulator, respectively.

On the other hand, some investigators have found little difference between DLC-coated materials and conventional materials. For example, Sheeja et al. [2001] performed wear testing of the cobalt–chromium–molybdenum/ultra-high-molecular-weight polyethylene and multilayer DLC/ultra-high-molecular-weight polyethylene wear couples, and found little difference in wear between the DLC and cobalt–chromium–molybdenum couples. These contradicting results suggest other factors, including choice of lubricant, may play a significant role in determining overall wear rates. For example, investigators who found decreased wear of the ultra-high-molecular-weight polyethylene component of a DLC/ultra-high-molecular-weight polyethylene wear couple generally used distilled water or saline solution as a testing lubricant [Ahlroos et al., 1997; Saikko et al., 1997]. Conversely, investigators using a simulated body fluid (e.g., bovine serum) as a lubricant generally found no difference in wear between DLC/ultra-high-molecular-weight polyethylene and metal/ultra-high-molecular-weight polyethylene wear couples [Affatato et al., 2000; Scholes et al., 2000; Sheeja et al., 2001;]. It is believed that some physiological lubricants do not allow graphitic surface layers to form on the wear couple components [Hauert et al., 2003]. In addition, DLC coatings containing particulates and pits may demonstrate much higher wear rates [Dong et al., 1999]. Finally, surface defects (e.g., scratches) may significantly affect the wear rate of DLC-coated prostheses; for example, the wear rate of ultra-high-molecular-weight polyethylene against DLC containing 2-mm-deep scratches was found to be seven times larger than that against intact DLC [Firkins et al., 1998].

Fortunately, the data regarding the corrosion properties of DLC-coated metals is far more uniform in its conclusions. For example, hydrogen-free DLC-coated cobalt–chromium–molybdenum alloy and cobalt–chromium–molybdenum alloy were placed in saline solution equivalent to placement in body fluid for 2 years at a temperature of 37°C. The DLC-coated cobalt–chromium–molybdenum alloy had a 10^5 lower corrosion rate than cobalt–chromium–molybdenum alloy [Tiainen et al., 2001]. Similarly, the corrosion rate of DLC-coated titanium–aluminum–vanadium alloy in saline solution was extremely low [Franks et al., 1989].

Furthermore, no histopathological changes have been seen during in vivo studies in which DLC-coated metals have been implanted in animals [Dowling et al., 1997]. Allen et al. [2001] implanted DLC-coated cobalt–chromium alloy into the femur of sheep for up to 90 days and demonstrated good biocompatibility. Mohanty et al. [2002] implanted DLC-coated titanium alloy into the skeletal muscle of rabbits for up to 1 year and confirmed the biocompatibility of DLC. Dowling et al. [1997] implanted hydrogenated DLC-coated stainless steel cylinders into sheep cortical bone and muscular tissue for between 4 and 12 weeks. They also found that the DLC coatings did not induce inflammation or toxicity in adjacent bone or muscle tissue. Santavirta et al. [1998] implanted DLC-coated titanium alloy into the femur of rats and observed a thin fibrous layer around the implants.

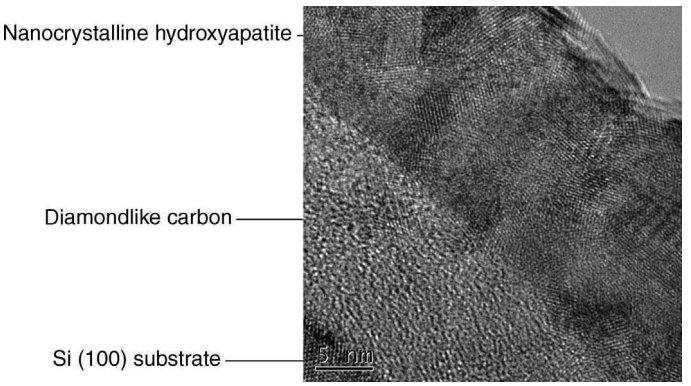

Figure 15.3 Cross-section transmission electron micrograph of hydroxyapatite–DLC nanocomposite. These interlayers may serve to prevent degradation of the bulk biomaterial and improve adhesion of the bioactive ceramic thin film. Both nanocrystalline hydroxyapatite and DLC layers were deposited at room temperature using pulsed laser deposition.

The absence of a thick implant capsule suggests cement-free implant fixation (direct bonding of tissue to implant) may be possible [Santavirta et al., 1998]. Guglielmotti et al. [1999] implanted zirconium, titanium, aluminum, and DLC-coated zirconium in Wistar rats for a 30-day period. They found DLC-coated zirconium and zirconium implants exhibited better tissue responses than titanium or aluminum implants. Finally, DLC-coated steel fracture fixation rods implanted in a human body for 7 months were found to prevent rod corrosion and metal ion release [Zolynski et al., 1996]. This case study suggests more rapid wound healing times and improved wound healing properties may be possible using DLC-coated orthopedic implants.

Diamond-like carbon can also serve as an interlayer material between a bioactive ceramic surface coating and a bulk biomaterial. The DLC interlayer can serve to prevent degradation of the bulk biomaterial and improve adhesion of bioactive surface layer. The surface layer could include hydroxyapatite, Bioglass, fluoroapatite, or other bioactive ceramics. An example of this bioactive ceramic/DLC structure is shown in Figure 15.3. No in vitro or in vivo studies have been performed on these hybrid coatings, but this design may prove useful in next-generation orthopedic prostheses.

Biomedical polymers have been coated with DLC to provide chemical inertness and increase device rigidity. It has been claimed that DLC can increase polymer stability in biological fluid by 10- to 15-fold [Elinson et al., 1999]. DLC coatings also prevent diffusion of oxygen, wear, and degradation. Furthermore, the surface properties of the diamond-like coating can be modified to provide a variety of contact wetting angles and/or antibacterial activity. Specifically, carbon films containing a positive charge may be deposited. These coatings are surrounded by cationic media, which create barriers to microbial biofilm growth. DLC coatings have also been suggested for use on poly(vinyl chloride) and PMMA-based devices, such as hard contact lenses, implantable catheters, and drainage tubes. In addition, DLC coatings on contact lenses provide optical transparency and UV protection. Due to their high index of refraction ($n = 2.4$–2.5), DLC coatings may allow device thickness to be reduced.

Some investigators have found that DLC coatings on polyethylene and polyurethane demonstrate a ''woven'' structure. It is believed that this woven structure results from plastic deformation of the substrate [Evans et al., 1991]. These DLC films on the polymers remain adherent, with bonding strengths in the range of $\sim 150\,\mathrm{kg\,cm^2}$. As a result, these DLC films can bend with the substrate (within certain limits).

Microporous polycarbonate membranes coated with DLC have been studied for use as implantable sensor coatings. There are several factors that account for the enhanced enzyme electrode performance of DLC-coated polymer membranes. As mentioned earlier, pulsed laser

deposition is often performed at room temperature. As a result, it is an ideal technique for temperature-sensitive and charge-sensitive polymers. Coating thickness and permeability can be more easily controlled using pulsed laser deposition processes than using solution deposition processes [Mullen et al., 1986]. Finally, DLC exhibits blood, protein, and tissue interaction properties that minimize biofouling (protein and cell adhesion) to the sensor surface. For example, DLC-coated microporous polycarbonate membranes for hydrogen-peroxide-based glucose enzyme electrodes demonstrated increased enzyme electrode stability during in vivo studies involving exposure to whole blood [Higson et al., 1993]. It was also found that glucose and oxygen transport across DLC-coated membranes can be easily tuned to enhance detection of low-molecular-weight solutes. Scanning electron micrographs of these membranes demonstrated reduced protein and red blood cell adhesion. In addition, membranes with lower glucose/oxygen permeability coefficient ratios were found to possess extended linearities.

The DLC films can be doped with a variety of elements to promote specific cellular responses. For example, the addition of SiO_x to DLC reduces the generation of inflammatory processes. In addition, silver, copper, and platinum can be employed separately or in combination to create an antimicrobial surface. DLC can be doped with fluorine to create a hydrophobic surface. DLC–vanadium coatings have been created to introduce cytotoxic vanadium ions to tissues surrounding an implant [Francz et al., 1999]. These coatings have been designed to prevent cell attachment and cell proliferation. Such cytotoxic coatings may be beneficial for temporary implants (e.g., implantable sensors and implantable drug delivery devices) in which cell attachment to the implant is not desired. DLC films have been doped with calcium oxide compounds to promote the formation and growth of bone [Dorner-Reisel et al., 2002]. Proliferation and morphology studies involving L929 mouse fibroblasts reveal improved biocompatibility. Increased cell proliferation and healthy cell morphology were observed for the DLC–calcium oxide films. In addition, wetting angle was decreased. It is believed that calcium carbonate, a bioactive molecule, is somehow incorporated within these films. Unfortunately, the addition of calcium oxide also decreased the fraction of sp^3/sp^2-bonded carbon and the film hardness. Schroeder et al. [2000] studied DLC films containing 7–13% titanium. They demonstrated DLC–titanium films had a positive effect on cell proliferation. The titanium content in a DLC–titanium film determines the extent and type of protein adsorption. These processes influence cell attachment and cell proliferation. Bone fixation by osteointegration increases through increased osteoblast differentiation and reduced (osteoclast bone-destroying cell) activity [Francz et al., 1999; Hauert et al., 1997, 1999].

15.9.2 Mechanical and Tribological Applications

The DLC tribological coatings are also used for a variety of applications, including magnetic disks, engine components, satellite direction mechanisms, chemical plants, and cutting tools. As mentioned above, the mechanical properties of DLC films (e.g., elastic modulus, hardness, internal stress, wear resistance, coefficient of friction) depend on the sp^3 fraction. As a result, films deposited at shorter wavelengths and/or higher fluences exhibit higher hardness values [Holmberg et al., 1994]. DLC thin films with the highest hardness values have been obtained using the hybrid PLD techniques mentioned above. Nanophase diamond films created using hybrid techniques have demonstrated nanohardness values of 80–100 GPa and elastic moduli of 300–400 GPa [Collins et al., 1991b]. On the other hand, amorphous DLC thin films obtained through conventional pulsed laser deposition exhibit hardness values of 50–60 GPa and elastic moduli of 500 GPa [Pharr et al., 1996]. Hirvonen et al. [1997] studied the hardness of hydrogen-free DLC films obtained using mass selected ion beam deposition (MSIBD), and demonstrated hardness values as high as 120 ± 20 GPa at a load of 200 g. Several experimentally derived relations between sp^3 fraction and mechanical properties have been developed. For example, Collins et al. [1993] have developed a linear relation between sp^3 fraction and Vickers hardness values. For hydrogen-free DLC films, 10% sp^3 fraction corresponds to 2000–3000 Hv, 50% sp^3 fraction corresponds to 7000–8000 Hv, and 100% sp^3 fraction corresponds to 10,000 Hv. More recently, Schneider et al. have developed a relation between

sp^3 fraction and elastic modulus. For hydrogen-free DLC films, sp^3 fractions between 0 and 90% correspond to elastic moduli between 300 and 800 GPa. In contrast, typical hardness and elastic moduli values for hydrogenated DLC films are 17 GPa and 50–200 GPa, respectively [Dean et al., 2000; Schneider et al., 1997]. Chemical composition (e.g., the type and concentration of noncarbon atoms) also plays a significant role [Wei et al., 1998, 1999]. In general, hardness and noncarbon element concentration are inversely related.

Diamond-like carbon also provides a low friction sliding surface. The friction coefficient value depends on ambient atmosphere (e.g., humidity), topology, and the sliding partner [Tsai et al., 1997]. Perhaps the most important parameter determining the coefficient of friction for hydrogenated DLC is relative humidity. Friction values for hydrogenated DLC can be as low as 0.01–0.3 in vacuum but greatly increase with humidity [Dean et al., 2000]. Hydrogenated DLC forms a graphitic transfer layer on a non-DLC partner surface. This contact asperity graphitization process is driven by a combination of local contact stresses and local temperatures that can reach >1000°C [Erdemir et al., 1995; Liu et al., 1996]. Under low-humidity conditions, these hydrophobic hydrogenated DLC layers contact one another and form weak van der Waals interactions. As a result, a low friction coefficient is generally observed. Hydrogen may be desorbed by annealing, increasing sliding velocity, and increasing applied load; this process may increase lubricity [Liu et al., 1996]. Under high-humidity conditions, this transfer layer may be inadequately formed. In addition, the transfer surface may be hydrated or oxidized by ambient gaseous species (e.g., oxygen or water). As a result, the friction coefficient is much higher. This variation can be correlated with hydrogen/carbon ratio in the precursor material. As the hydrogen content in the precursor material increases, the friction coefficient demonstrates a greater positive correlation with ambient humidity. As such, hydrogenated DLC films produced from hydrogen-diluted methane demonstrate lower friction coefficients than other hydrogenated DLC films in ambient humidity. Erdemir et al. ascribes this relation to the fact that hydrogenated DLC produced from hydrogen-diluted methane contains fewer dangling carbon bonds than other hydrogenated DLC films.

On the other hand, hydrogenated DLC–silicon coatings maintain low friction coefficients regardless of humidity [Oguri et al., 1992; Voevodin et al., 1996]. Voevodin et al. found hydrogen-free DLC possesses a slightly higher friction coefficient than hydrogenated DLC in vacuum (0.1–0.15). The friction coefficient of hydrogen-free DLC slightly decreases with increasing humidity. Hydrogen-free DLC is transformed into graphite at the contact area, which serves as a solid lubricant during sliding. Micro Raman studies have shown that several thousand cycles are required to cause $sp^3 \rightarrow sp^2$ transformation and form these graphite-like transfer films. Moreover, this graphitic material can form a transfer layer on the partner surface. As a result, friction and wear at the contact site are reduced. Under high-humidity conditions, water enters these graphitic layers and lowers the friction coefficient. The kinetics of this graphitization process is determined by the load applied and the sliding rate [Ronkainen et al., 2001]. Deposition parameters may be modified to further improve friction properties; for example, Lempert et al. [1993] found increased graphitization and increased surface roughness led to improved friction properties for hydrogen-free DLC films. In all of these cases, the unusual friction properties of DLC are dependent on the development of a transfer film that allows shear at the interface.

This combination of hardness and friction properties allows DLC to provide ideal wear protection to a sliding material [Homberg et al., 1994]. Hirvonen et al. [1990] found that the wear resistance of DLC is better than that of SiC, WC–Co, silicon nitride, or alumina by factors of 40, 60, 230, and 290, respectively. Hydrogen-free DLC has a wear rate of $10^{-9}\,\mathrm{mm^3\,N^{-1}\,m^{-1}}$, which is 100 times lower than that of hydrogenated DLC ($10^{-7}\,\mathrm{mm^3\,N^{-1}\,m^{-1}}$) [Voevodin et al., 1995b]. As mentioned earlier, DLC films typically suffer from poor adhesion due to compressive stresses. As a result, high local contact pressures initiate DLC cracking and delamination. In addition, many DLC substrate materials are significantly softer than DLC. High contact pressures can lead to substrate deformation and coating failure. Substrate hardening by surface nitriding leads to reduced subsurface deformation and longer DLC film lifetimes [Voevodin et al., 1996].

Diamond-like carbon is a hydrophobic material. Low surface energies (40–44 $mN\,m^{-1}$) and large contact angles (75°–80°with water) are typically observed [Grischke et al., 1998; Han et al., 1999]. Many practical applications for DLC require a hydrophobic surface that is less likely to demonstrate stiction (stickiness and friction). Grischke et al. [1996] have modified the surface energy of DLC by incorporating fluorine, nitrogen, oxygen, or silicon. They found fluorine, silicon, and silicon–oxygen decrease surface energy by reducing dangling bonds, sp^2-hybridized surface carbon atoms, and other polarized species. Incorporation of iron or aluminum may also reduce the surface energy [Chen et al., 2001, 2001c].

Microelectromechanical Systems (MEMS) require inert, wear-resistant, low stiction, rigid thin films that can be integrated with current electronic device processing technology, and DLC meets all of these requirements. Most importantly, DLC exhibits wear resistance up to 10,000 times greater than polysilicon, the most common current MEMS material [Sullivan et al., 2001]. Moreover, hydrogen-free DLC is deposited at room temperature, which allows for deposition on temperature-sensitive substrates. MEMS require extremely low friction surfaces because the friction force term in movement equations decreases as the second power of the scale, but the inertia term decreases as the third power of the scale. DLC exhibits one of the lowest friction coefficients of any material. The major disadvantage of hydrogen-free DLC films is their intrinsic stress; an ideal MEMS material should have residual stress values under 10 MPa. Sullivan et al. [2001] have overcome this problem and demonstrated several hydrogen-free DLC-based MEMS using pulsed laser deposition. They developed an electrostatic comb-drive motor from stress-free DLC films using pulsed laser deposition. In particular, they relieved internal stresses by postdeposition thermal annealing for several minutes at a temperature of 600°C in a process described earlier.

Magnetic disks have been used for over a decade in the magnetic recording industry, and DLC coatings have been applied to evaporated metal tapes, magnetic coatings on disks, and disk heads. The continuous demand for increased hard-disk storage capacity has required a gradual decrease in the distance between the magnetic recording head and the disk [also known as the head–disk interface (HDI)]. As a result, the protective coating on the head and disk surface must be continuously decreased. Current HDI materials must meet a number of requirements, including thickness under 25 nm, low coefficient of friction, wear resistance, corrosion resistance, and low surface roughness [Lappalainen et al., 1998].

The disk is a multilayer structure: a plated or sputtered magnetic thin layer stores the data, a DLC protective layer prevents corrosion and wear, and a thin (10 Å) liquid perfluoropolyether (PFPE) layer serves as a lubricant. The PFPE lubricant must not only adhere to the DLC film, but also move on the continuously spinning DLC film to prevent local lubricant depletion. This confinement of the PFPE layer on the hydrogenated DLC layer occurs through van der Waals interactions.

Originally, magnetron sputtered sp^2-hybridized carbon coatings were employed to simply prevent corrosion [Marchon et al., 1990]. Currently, hydrogenated DLC films on the disk and head surfaces eliminate magnetic disk–head adhesion during stop–start cycles [Robertson et al., 2001]. Although these DLC layers are currently deposited by an ion beam technique, pulsed laser deposition and cathodic arc may be considered for the deposition of even thinner films.

Hydrogenated DLC coatings containing fluorine, nitrogen, oxygen, or silicon have been developed to reduce stiction (interfacial adhesion between head and disk surfaces) [Endo et al., 1999; Donnet et al., 1997; Grill et al., 1996; Labelle et al., 1997; Miyake et al., 1993]. In particular, surface fluorination has been reported to reduce the friction and microwear of these films [Trojan et al., 1994], but the effect of fluorination on hydrogenated DLC films is controversial. Grill et al. [1996] have demonstrated that fluorinated hydrogenated DLC films deposited using plasma-activated chemical vapor deposition from pure difluorobenzene (DFB) exhibited similar wear resistance to nonfluorinated hydrogenated DLC films. Other investigators have obtained only scratchable, soft films [Seth et al., 1993]. In addition, hydrogen released from HDLC thin films can interact with fluorine emitted from degrading PFPE lubricant or fluorinated DLC films to create hydrogen fluoride. These hydrogen fluoride molecules can catalyze a variety of decomposition reactions, including breakdown of the PFPE lubricant. As a result, amorphous carbon nitride

(α-CN_x) and hydrogen-free DLC have been considered as replacement hard-disk coating materials [Bhatia et al., 1999; Cutiongco et al., 1996]. Finally, it is unclear if these coatings have any long-term effect on device performance. Patton et al. [1998] demonstrated that DLC coatings on hard-disk components prevented head–disk contact and abrasive wear but did not significantly improve overall tape durability.

Diamond-like carbon is also a suitable coating for engine parts, including gears, piston rings, cylinders, and fuel injectors. Enke et al. [1999] have described DLC coatings on SiC to reduce the friction observed in chemical pumps. DLC coatings have also been considered for use in satellite pointing mechanisms that must undergo tens of millions of oscillation cycles with little or no wear. Although it is degraded by oxidation at high temperatures, DLC is acceptable for low-temperature cutting environments. For example, Djouadi et al. [1999] have demonstrated DLC-coated knife blades for pulp and paper applications.

15.10 CLOSING REMARKS

Pulsed laser deposition of DLC thin films remains an area of active research. The history of work in this area can be divided into three distinct eras. The 1980s saw the development of several hydrogen-free and hydrogenated DLC thin films. Hydrogen-free DLC films with properties close to those of diamond were demonstrated. In the 1990s, work concentrated on overcoming many of the problems seen in as-grown DLC thin films. Development of over 1-μm-thick DLC thin films was clearly the crowning achievement of this era. Furthermore, the unique hardness, wear resistance, low friction, and biological properties of DLC were more fully understood. This decade will see the widespread commercialization of DLC thin films in medical, mechanical, and other applications.

Pulsed laser deposition offers great advantages for processing DLC thin films, allowing precise control of DLC growth parameters at low deposition temperatures. There are several technological hurdles that must be overcome, however. First, compressive stress remains the major stumbling block preventing widespread application of these films, and newer technologies to control compressive stress in DLC films must be found. In addition, new techniques for creating films with greater uniformity from deposition to deposition must be developed. Splashing of particulates onto growing films during PLD remains a serious problem. In addition, new pulsed laser deposition techniques need to be developed that allow complex geometries (e.g., holes, curved surfaces) to be coated, and it remains a challenge to scale the current laboratory-based pulsed laser deposition process up to an industrial scale (see Chapter 9). Finally, pulsed laser deposition of DLC needs to be cost competitive with direct ion beam deposition, plasma-enhanced chemical vapor deposition, ion beam sputtering, and other techniques. If these obstacles can be overcome, pulsed laser deposition of DLC may become a significant industrial process in the coming decades.

REFERENCES

Affatato, S., Frigo, M., and Toni, A. (2000), *J. Biomed. Mater. Res.* **53**, 221–226.

Ahlroos, T., and Saikko, V. (1997), *Wear* **211**, 113–119.

Aisenberg, S., and Chabot, R. (1971), *J. Appl. Phys.* **42**, 2953.

Alanazi, A., Nojiri, C., Kido, T., Noguchi, T., Ohgoe, Y., Matsuda, T., Hirakuri, K., Funakubo, A., Sakai, K., and Fukui, Y. (2000), *Artif. Org.* **24**, 624–627.

Allen, M., Law, F., and Rushton, N. (1994), *Clin. Mater.* **17**, 1.

Allen, M., Myer, B., and Rushton, N. (2001), *J. Biomed. Mater. Res.* **58**, 319–328.

Amaratunga, G. A. J., Robertson, J., Veerasamy, V. S., Milne, W. I., and Mckenzie D. R. (1995), *Diamond Related Mater.* **4**, 637–640.

Amir, O., and Kalish, R. (1991), *J. Appl. Phys.* **70**, 4958–4962.

Anders, S., Callahan, D. L., Pharr, G. M., Tsui, T. Y., and Bhatia, C. S. (1997a), *Surf. Coat. Technol.* **94**, 189–194.

Anders, S., Diaz, J., Ager, J. W., Lo, R. Y., and Bogy, D. B. (1997b), *Appl. Phys. Lett*. **71**, 3367–3369.

Anttila, A., Lappalainen, R., Tiainen, V. M., and Hakovirta, M. (1997), *Adv. Mater.* **9**, 1161.

Benndorf, C., Fryda, M., Klages, C. P., Taube, K., and Haubold, H.G. (1991a), *Mater. Sci. Eng. A* **140**, 795–801.

Benndorf, C., Boettger, E., Fryda, M., Haubold, H. G., Klages, C. P., and Koberle, H. (1991b), *Synthetic Metals* **43**, 4055–4058.

Bentzon, M. D., Mogensen, K., Hansen, J. B., Barholm-Hansen, C., Taholt, C., Holiday, P., and Eskildsen, S. S. (1994), *Surf. Coat. Technol*. **68/69**, 651–655.

Bewilogua, K., and Dimigen, H. (1993), *Surf. Coat. Technol*. **61**, 144–150.

Bewilogua, K., Dietrich, D., Holzhuter, G., and Weissmantel, C. (1982), *Phys. Status Solidi A* **71**, 57–59.

Bhatia, C. S., Fong, W., Chen, C. Y., Wei, J. J., Bogy, D. B., Anders, S., Stammler, T., and Stohr, J. (1999), *IEEE Trans. Mag*. **35**, 910–915.

Boutin, P., Christel, P., Dorlot, J. M., Meunier, A., Deroquancourt, A., Blanquaert, D., Herman, S., Sedel, L., and Witvoet, J. (1988), *J. Biomed. Mater. Res*. **22**, 1203–1232.

Bull, S. J. (1995), *Diamond Related Mater.* **4**, 827–836.

Bullen, A. J., O'Hara, K. E, Cahill, D. G., Monteiro, O., and von Keudell, A. (2000), *J. Appl. Phys*. **88**, 6317–6320.

Chen, G. Y., Chen, J. S., Sun, Z., Li, Y. J., Lau, S. P., Tay, B. K., and Chai, J. W. (2001a), *Appl. Surf. Sci*. **180**, 185–190.

Chen, J. S., Lau, S. P., Tay, B. K., Chen, G. Y., Sun, Z., Tan, Y. Y., Tan, G., and Chai, J. W. (2001b), *J. Appl. Phys*. **89**, 7814–7819.

Chen, J. S., Lau, S. P., Sun, Z., Chen, G. Y., Li, Y. J., Tay, B. K., and Chai, J. W. (2001c), *Thin Solid Films* **398**, 110–115.

Chen, J. Y., Wang, L. P., Fu, K.-Y., Huang, N., Leng, Y., Leng, Y. X., Yang, P., Wang, J., Wan, G. J., Sun, H., Tian, X. B., and Chu, P. K. (2002), *Surf. Coat. Technol.*, **156**, 289–294.

Chhowalla, M., Yin, Y., Amaratunga, G. A. J., Mckenzie, D. R., and Frauenheim T. (1997), *Diamond Related Mater.* **6**, 207–211.

Chhowalla, M., Ferrari, A. C., Robertson, J., and Amaratunga, G. A. J. (2000), *Appl. Phys. Lett*. **76**, 1419–1421.

Chu, P. K., Tang, B. Y., Wang, L. P., Wang, X. F., Wang, S. Y., and Huang, N. (2001a), *Rev. Sci. Instrum.* **72**, 1660–1665.

Cohen, M L. (1985), *Phys. Rev. B* **32**, 7988–7991.

Collins, C. B., Davanloo, F., Jander, D. R., Lee, T. J., Park, H., and You, J. H. (1991), *J. Appl. Phys*. **69**, 7862–7870.

Collins, C. B., Davanloo, F., Lee, T. J., Jander, D. R., You, J. H., Park H., and Pivin, J. C. (1992a), *J. Appl. Phys*. **71**, 3260–3265.

Collins, C. B., Davanloo, F., Lee, T. J., You, J. H. H., and Park, H. T. (1992b), *Am. Ceram. Soc. Bull*. **71**, 1535–1542.

Collins, C. B., Davanloo, F., Lee, T. J., Park, H., and You, J. H. (1993), *J. Vac. Sci. Technol. B* **11**, 1936–1941.

Courtney, J. M., Lamba, N. M. K., Sundaram, S., and Forbes, C. D. (1994), *Biomaterials* **15**, 737–744.

Cui, F. Z., and Li, D. J. (2000), *Surf. Coat. Technol*. **131**, 481–487.

Cuomo, J. J., Pappas, D. L., Bruley, J., Doyle, J. P., and Saenger, K. L. (1991), *J. Appl. Phys*. **70**, 1706–1711.

Cutiongco, E. C., Li, D., Chung, Y. W., and Bhatia, C. S. (1996), *J. Tribol*. **118**, 543–548.

Davanloo, F., Juengerman, E. M., Jander, D. R., Lee, T. J., and Collins, C. B. (1990), *J. Appl. Phys*. **67**, 2081–2087.

Davidson, J. A., and Mishra, A. K. (1995) "Surface Modification Issues for Orthopaedic Implant Bearing Surfaces," in *Surface Modification Technologies*, Vol. 5, T. S. Sudarshan and J. F. Braza (Eds.), Institute of Materials London, pp. 1–14.

Dean, K. A., and Chalamala, B. R. (2000), *Appl. Phys. Lett*. **76**, 375–377.

Dekempeneer, E. H. A., Jacobs, R., Smeets, J., Meneve, J., Eersels, L., Blanpain, B., Roos, J., and Oostra, D. J. (1992), *Thin Solid Films* **217**, 56–61.

De Scheerder, I., Szilard, M., Huang, Y. M., Ping, X. B., Verbeken, E., Neerinck, D., Demeyere, E., Coppens, W., and van de Werf, F. (2000), *J. Invasive Cardiol.* **12**, 389–394.

DeWall, R. A., Qasim, N., and Carr, L. (2000), *Ann. Thorac. Surg*. **69**, 1612–1621.

Dimigen, H., and Klages, C. P. (1991), *Surf. Coat. Technol*. **49**, 543–547.

Dion, I., Roques, X., Baquey, C., Baudet, E., Basse, B., and More, N. (1993), *Bio-Med. Mater. Eng*. **3**, 51–55.

Djouadi, M. A., Beer, P., Marchal, R., Sokolowska, A., Lambertin, M., Precht, W., and Nouveau, C. (1999), *Surf. Coat. Technol*. **119**, 508–516.

Dong, H., Shi, W., and Bell, T. (1999), *Wear* **229**, 146–153.

Donnet, C., and Grill, A. (1997), *Surf. Coat. Technol*. **94**, 456–462.

Donnet, C., Fontaine, J., Grill, A., Patel, V., Jahnes, C., and Belin, M. (1997), *Surf. Coat. Technol*. **94/95**, 531–536.

Doorn, P. F., Campbell, P. A., and Amstutz, H. C. (1996), *Clin. Orthopaed*. **329**, 206–216.

Dorfman, V. F. (1992), *Thin Solid Films* **212**, 267–273.

Dorner-Reisel, A., Schurer, C., Irmer, G., Simon, F., Nischan, C., and Muller, E. (2002), *Anal. Bioanal. Chem*. **374**, 753–755.

Dowling, D. P., Kola, P. V., Donnelly, K., Kelly, T. C., Brumitt, K., Lloyd, L., Eloy, R., Therin, M., and Weill, N. (1997), *Diamond Related Mater.* **6**, 390–393.

Elinson, V. M., Sleptsov, V. V., Laymin, A. N., Potraysay, V. V., Kostuychenko, L. N., and Moussina, A. D. (1999), *Diamond Related Mater.* **8**, 2103–2109.

Endo, K., Shinoda, K., and Tatsumi, T. (1999), *J. Appl. Phys*. **86**, 2739–2745.

Enke, K. (1999), *Surf. Coat. Technol*. **116**, 488–491.

Enke, K., Dimigen, H., and Hubsch, H. (1980), *Appl. Phys. Lett*. **36**, 291–292.

Erdemir, A., Bindal, C., Pagan, J., and Wilbur, P. (1995), *Surf. Coat. Technol*. **77**, 559–563.

Evans, A. C., Franks, J., and Revell, P. J. (1991), *Surf. Coat. Technol*. **47**, 662–667.

Ferrari, A. C., and Robertson, J. (2000), *Phys. Rev. B* **61**, 14095–14107.

Ferrari, A. C., Kleinsorge, B., Morrison, N. A., Hart, A., Stolojan, V., and Robertson, J. (1999), *J. Appl. Phys*. **85**, 7191–7197.

Fiaccabrino, G. C., Tang, X. M., Skinner, N., Derooij, N. F., and Koudelkahep, M. (1996), *Sensors Actuators B* **35**, 247–254.

Firkins, P., Hailey, J. L., Fisher, J., Lettington, A. H., and Butter, R. (1998), *J. Mater. Sci. Mater. Med*. **9**, 597–601.

Francz, G., Schroeder, A., and Hauert, R. (1999), *Surf. Interface Anal*. **28**, 3–7.

Franks, J. (1989), *J. Vac. Sci. Technol. A*. **7**, 2307–2310.

Friedmann, T. A., McCarty, K. F., Barbour, J. C., Siegal, M. P., and Dibble, D. C. (1996), *Appl. Phys. Lett*. **68**, 1643–1645.

Friedmann, T. A., Sullivan, J. P., Knapp, J. A., Tallant, D. R., Follstaedt, D. M., Medlin, D. L., and Mirkarimi, P. B. (1997), *Appl. Phys. Lett*. **71**, 3820–3822.

Fujimori, S., Kasai, T., and Inamura, T. (1982), *Thin Solid Films*, **92**, 71.

Gangopadhyay, A. K., Willermet, P. A., Tamor, M. A., and Vassell, W. C. (1997), *Tribol. Int.* **30**, 9–18.

Germain, C., Girault, C., Aubreton, J., Catherinot, A., Bec, S., and Tonck, A. (1995), *Diamond Related Mater.* **4**, 309–313.

Gilmore, R., and Hauert, R. (2000), *Surf. Coat. Technol*. **133**, 437–442.

Gilmore, R., and Hauert, R. (2001), *Thin Solid Films* **398**, 199–204.

Goldring, S. R., Clark, C. R., and Wright, T. M. (1993), *J. Bone Joint Surg*. **75**, 799–801.

Goodman, S. B., Fornasier, V. L., Lee, J., and Kei, J. (1990), *J. Biomed. Mater. Res*. **24**, 517–524.

Grill, A. (2003), *Diamond Related Mater.* **12**, 166–170.

Grill, A., Meyerson, B., and Patel, V. (1988), *J. Mater. Res*. **3**, 214–218.

Grill, A., and Patel, V. V. (1996), *Diamond Films Technol*. **6**, 13–21.

Grill, A., Patel, V., and Jahnes, C. (1998), *J. Electrochem. Soc*. **145**, 1649–1653.

Grischke, M., Bewilogua, K., Trojan K., and Dimigen, H. (1996), *Surf. Coat. Technol*. **74/75**, 739.

Grischke, M., Hieke, A., Morgenweck, F., and Dimigen, H. (1998), *Diamond Related Mater.* **7**, 454–458.

Gruen, D. M. (1999), *Ann. Review Mater. Sci*. **29**, 211–259.

Guglielmotti, M. B., Renou, S., and Cabrini, R. L. (1999), *Int. J. Oral Maxillofacial Implants* **14**, 565–570.

Guseva, M. B., Babaev, V. G., Khvostov, V. V., Valioullova, Z. K., Bregadze, A. Y., Obraztsov, A. N., and Alexenko, A. E. (1994), *Diamond Related Mater.* **3**, 328–331.

Gutensohn, K., Beythien, C., Bau, J., Fenner, T., Grewe, P., Koester, R., Padmanaban, K., and Kuehnl, P. (2000), *Thrombosis Res.* **99**, 577–585.

Gyorgy, E., Mihailescu, I. N., Kompitsas, M., and Giannoudakos, A. (2004), *J. Optoelectron. Adv. Mater.* **6**, 39–46.

Han, H., Ryan, F., and McClure, M. (1999), *Surf. Coat. Technol*. **121**, 579–584.

Hauert, R., and Muller, U. (2003), *Diamond Related Mater.* **12**, 171–177.

Hauert, R., Muller, U., Francz, G., Birchler, F., Schroeder, A., Mayer, J., and Wintermantel, E. (1997), *Thin Solid Films* **308**, 191–194.

Hauert, R., Knoblauch-Meyer, L., Francz, G., Schroeder, A., and Wintermantel, E. (1999), *Surf. Coat. Technol*. **121**, 291–296.

Head, W. C., Bauk, D. J., and Emerson, R. H. (1995), *Clin. Orthopaed*. **311**, 85–90.

Higson, S. P. J., and Vadgama, P. M. (1993), *Anal. Chim. Acta* **271**, 125–133.

Hirvonen, J. P., Koskinen, J., Lappalainen, R., and Anttila, A. (1990), *Mater. Sci. Forum* **52**, 197.

Holmberg, K., and Mathews, A. (1994), *Thin Solid Films* **253**, 173–178.

Huai, Y., Chaker, M., Broughton, J. N., Gat, E., Pepin, H., Gu, T., Bian, X., and Sutton, M. (1994), *Appl. Phys. Lett.* **65**, 830–832.

Ignatius, M. J., Sawhney, N., Gupta, A., Thibadeau, B. M., Monteiro, O. R., and Brown, I. G. (1998), *J. Biomed. Mater. Res.* **40**, 264–274.

Jelinek, M., Olsan, V., Soukup, L., Charalabidis, D., Hontzopoulos, E., and Georgiou, E. (1994), *Diamond Related Mater.* **3**, 1128–1131.

Jones, L. C., and Hungerford, D. S. (1987), *Clin. Orthopaed*. **225**, 192–206.

Jones, M. I., McColl, I. R., Grant, D. M., Parker, K. G., and Parker, T. L. (1999), *Diamond Related Mater.* **8**, 457–462.

Jones, M. I., McColl, I. R., Grant, D. M., Parker, K. G., and Parker, T. L. (2000), *J. Biomed. Mater. Res.* **52**, 413–421.

Kalish, R., Lifshitz, Y., Nugent, K., and Prawer, S. (1999), *Appl. Phys. Lett*. **74**, 2936–2938.

Karpman, J., Riabkina-Fishman, M., Zahavi, J., and Dhamelincourt, D. (1994), *Diamond Related Mater.* **4**, 10–14.

Kasi, S. R., Lifshitz, Y., Rabalais, J. W., and Lempert, G. (1988), *Ang. Chem.*, **27**, 1203–1209.

Kelires, P. C. (2000), *Phys. Rev. B* **62**, 15686–15694.

Kikuchi, N., Ohsawa, Y., and Suzuki, I. (1993), *Diamond Related Mater.* **2**, 190–196.

Koski, K., Holsa, J., Ernoult, J., and Rouzaud, A. (1996), *Surf. Coat. Technol*. **80**, 195–199.

Krishnan, L. K., Varghese, N., Muraleedharan, C. V., Bhuvaneshwar, G. S., Derangere, F., Sampeur, Y., and Suryanarayanan, R. (2002), *Biomol. Eng*. **19**, 251–253.

Krishnaswamy, J., Rengan, A., Srivatsa, A. R., Matera, G., and Narayan, J. (1990), *SPIE Proc*. **1190**, 109–117.

Kroto, H. W., Heath, J. R., O' Brien, S. C., Curl, R.F, and Smalley, R. E. (1985) *Nature* **318**, 162–163.

Labelle, C. B., Limb, S. J., and Gleason, K. K. (1997), *J. Appl. Phys.* **82**, 1784–1787.

Lappalainen, R., Heinonen, H., Anttila, A., and Santavirta, S. (1998), *Diamond Related Mater.* **7**, 482–485.

Lempert, G. D., Lifshitz, Y., Rotter, S., Armini, A. J., and Bunker, S. (1993), *Nucl. Instrum. Methods Phys. Res.* **80**, 1502–1506.

Leppavuori, S., Levoska, J., Vaara, J., and Kusmartseva, O. (1993), *Mater. Res. Soc. Symp. Proc*. **285**, 557.

Lifshitz, Y. (1996), *Diamond Related Mater.* **5**, 388–400.

Lifshitz, Y., Lempert, G. D., Grossman, E., Avigal, I., Uzansaguy, C., Kalish, R., Kulik, J., Marton, D., and Rabalais, J. W. (1995), *Diamond Related Mater.* **4**, 318–323.

Lifshitz, Y., Lempert, G. D., Grossman, E., Scheibe, H. J., Voellmar, S., Schultrich, B., Breskin, A., Chechik, R., Shefer, E., Bacon, D., Kalish, R., and Hoffman, A. (1997), *Diamond Related Mater.* **6**, 687–693.

Linder, S., Pinkowski, W., and Aepfelbacher, M. (2002), *Biomaterials* **23**, 767–773.

Liu, E., Blanpain, B., Celis, J. P., Roos, J. R., Alvarezverven, G., and Priem, T. (1996a) *Surf. Coat. Technol*. **80**, 264–270.

Liu, Y., Erdemir, A., and Meletis, E. (1996b), *Surf. Coat. Technol*. **86**, 564–568.

Lu, L., Jones, M. W., and Wu, R. L. C. (1993), *Bio-Med. Mater. Eng.* **3**, 223.

Lyman, D. J., Hill, D. W., Stirk, R. K., Adamson, C., and Mooney, B. R. (1972), *Trans. Am. Soc. Artificial Internal Org*. **18**, 19–24.

Malchau, H., Herberts, P., and Ahnfelt, L. (1993), *Acta Orthopaed. Scand*. **64**, 497–506.

Malshe, A. P., Kanetkar, S. M., Ogale, S. B., and Kshirsagar, S. T. (1990), *J. Appl. Phys*. **68**, 5648–5652.

Marchon, B., Heiman, N., and Khan, M. R. (1990), *IEEE Trans. Magn*. **26**, 168–170.

Marks, N. A., McKenzie, D. R., Pailthorpe, B. A., Bernasconi, M., and Parrinello, M. (1996) *Phys. Rev. B* **54**, 9703–9714.

Martinez-Miranda, L. J., Siegal, M. P., and Provencio, P. P. (2001), *Appl. Phys. Lett*. **79**, 542–544.

McCulloch, D. G., Mckenzie, D. R., Prawer, S., Merchant, A. R., Gerstner, E. G., and Kalish, R. (1997), *Diamond Related Mater.* **6**, 1622–1628.

McCulloch, D. G., McKenzie, D. R., and Goringe, C. M. (2000), *Phys. Rev. B* **61**, 2349–2355.

McKenzie, D. R., Yin, Y., Marks, N. A., Davis, C. A., Pailthorpe, B. A., Amaratunga, G. A. J., and Veerasamy, V. S. (1994), *Diamond Related Mater.* **3**, 353–360.

McLaughlin, J. A., Meenan, B., Maguire, P., and Jamieson, N. (1996), *Diamond Related Mater.* **5**, 486–491.

Meneve, J., Dekempeneer, E., Wegener, W., and Smeets, J. (1996), *Surf. Coat. Technol*. **86**, 617–621.

Milne, W. I. J. (1996), *Non-Crystalline Solids* **200**, 605–610.

Miyake, S., Miyamoto, T., and Kaneko, R. (1993), *Wear* **168**, 155–159.

Mohanty, M., Anilkumar, T. V., Mohanan, P. V., Muraleedharan, C. V., Bhuvaneshwar, G. S., Derangere, F., Sampeur, Y., and Suryanarayanan, R. (2002), *Biomol. Eng*. **19**, 125–128.

Monties, J. R., Dion, I., Havlik, P., Rouais, F., Trinkl, J., and Baquey, C. (1997), *Artificial Org*. **21**, 730–734.

Morath, C. J., Maris, H. J., Cuomo, J. J., Pappas, D. L., Grill, A., Patel, V. V., Doyle, J. P., and Saenger, K. L. (1994), *J. Appl. Phys*. **76**, 2636–2640.

Moravec, T. J., Schmidt, P., and Spencer, E. G. (1980) *Am. Ceram. Soc. Bull*. **59**, 329.

Morshed, M. M., McNamara, B. P., Cameron D. C., and Hashmi M. S. J. (2003), *Surf. Coat. Technol*. **163**, 541–545.

Mullen, W. H., Keedy, F. H., Churchouse, S. J., and Vadgama, P. M. (1986), *Anal. Chim. Acta* **183**, 59–66.

Narayan, J., Vispute, R. D., and Jagannadham, K. (1995), *J. Adhesion Sci. Technol*. **9**, 753–767.

Neerinck, D., Persoone, P., Sercu, M., Goel, A., Venkatraman, C., Kester, D., Halter, C., Swab, P., and Bray, D. (1998), *Thin Solid Films* **317**, 402–404.

Nir, D. (1987), *Thin Solid Films* **146**, 27–43.

Oguri, K., and Arai, T. (1990), *J. Mater. Res*. **5**, 2567–2571.

Oguri, K., and Arai, T. (1992), *J. Mater. Res*. **7**, 1313–1316.

Onate, J. I., Comin, M., Braceras, I., Garcia, A., Viviente, J. L., Brizuela, M., Garagorri, N., Peris, J. L., and Alava, J. I. (2001), *Surf. Coat. Technol*. **142**, 1056–1062.

Pappas, D. L., Saenger, K. L., Bruley, J., Krakow, W., Cuomo, J. J., Gu, T., and Collins, R. W. (1992), *J. Appl. Phys*. **71**, 5675–5684.

Parker, T. L., Parker, K. L., McColl, I. R., Grant, D. M., and Wood, J. V. (1994), *Diamond Related Mater.* **3**, 1120–1123.

Patton, S. T., and Bhushan, B. (1998), *IEEE Trans. Mag*. **34**, 575–587.

Peeler, D. T., and Murray, P. T. (1994), *Diamond Related Mater.* **3**, 1124–1127.

Peters, P. C., Engh, G. A., Dwyer, K. A., and Vinh, T. N. (1992), *J. Bone Joint Surg*. **74**, 864–876.

Pharr, G. M., Callahan, D. L., McAdams, S. D., Tsui, T. Y., Anders, S., Anders, A., Ager, J. W., Brown, I. G., Bhatia, C. S., Silva, S. R. P., and Robertson, J. (1996), *Appl. Phys. Lett*. **68**, 779–781.

Polo, M. C., Cifre, J., Sanchez, G., Aguiar, R., Varela, M., and Esteve, J. (1995), *Diamond Related Mater.* **4**, 780–783.

Rae, T. (1981), *J. Bone Joint Surg*. **63**, 435–440.

Ravi, S., Silva, P., Xu, S., Tay, B. X., Tan, H. S., and Milne, W. I. (1996) *Appl. Phys. Lett*. **69**, 491–493.

Rengan, A., Narayan, J., Jahnke, C., Bedge, S., Park, J. I., and Li, M. (1992), *Mater. Sci. Eng. B* **15**, 15–24.

Robertson, J. (1995), *Diamond Related Mater.* **4**, 297–301.

Robertson, J. (2001), *Thin Solid Films* **383**, 81–88.

Robertson, J. (2002), *Mater. Sci. Eng. R*. **37**, 129–281.

Robertson, J., and O'Reilly, E. P. (1987), *Phys. Rev. B* **35**, 2946–2957.

Rohlfing, E. A. (1988), *J. Chem. Phys*. **89**, 6103–6112.

Ronkainen, H., Varjus, S., Koskinen, J., and Holmberg, K. (2001), *Wear* **249**, 260–266.

Saikko, V., and Ahlroos, T. (1997), *Wear* **207**, 86–91.

Santavirta, S., Konttinen, Y. T., Bergroth, V., and Gronblad, M. (1991), *Acta Orthopaed. Scand*. **62**, 29–32.

Santavirta, S., Konttinen, Y. T., Lappalainen, R., Anttila, A., Goodman, S. B., Lind, M., Smith, L., Takagi, M., Gomez-Barrena, E., Nordsletten, L., and Xu, J. W. (1998), *Curr. Orthopaed*. **12**, 51–57.

Santavirta, S. S., Lappalainen, R., Pekko, P., Anttila, A., and Konttinen, Y. T. (1999), *Clin. Orthopaed*. **369**, 92–102.

Sato, T., Furuno, S., Iguchi, S., and Hanabusa, M. (1987), *Jpn. J. Appl. Phys. P. 2* **26**, 1487–1488.

Sato, T., Furuno, S., Iguchi, S., and Hanabusa, M. (1988), *Appl. Phys. A* **45**, 355–360.

Scales, J. T. (1991), *J. Bone Joint Surg*. **73**, 534–536.

Schneider, D., Schwarz, T., Scheibe, H. J., and Panzner, M. (1997), *Thin Solid Films*, **295**, 107–116.

Scholes, S. C., Unsworth, A., and Goldsmith, A. A. J. (2000), *Phys. Med. Biol*. **45**, 3721–3735.

Schroeder, A., Francz, G., Bruinink, A., Hauert, R., Mayer, J., and Wintermantel, E. (2000), *Biomaterials* **21**, 449–456.

Schultrich, B., Scheibe, H. J., Drescher, D., and Ziegele, H. (1998), *Surf. Coat. Technol*. **98**, 1097–1101.

Schwan, J., Ulrich, S., Theel, T., Roth, H., Ehrhardt, H., Becker, P., and Silva, S. R. P. (1997), *J. Appl. Phys*. **82**, 6024–6030.

Seth, J., and Babu, S. V. (1993), *Thin Solid Films* **230**, 90–94.

Sheeja, D., Tay, B. K., Shi, X., Lau, S. P., Daniel, C., Krishnan, S. M., and Nung, L. N. (2001a), *Diamond Related Mater.* **10**, 1043–1048.

Sheeja, D., Tay, B. K., Lau, S. P., and Nung, L. N. (2001b), *Surf. Coat. Technol*. **146**, 410–416.

Siegal, M. P., Barbour, J. C., Provencio, P. N., Tallant, D. R., and Friedmann, T. A. (1998), *Appl. Phys. Lett*. **73**, 759–761.

Siegal, M. P., Tallant, D. R., Martinez-Miranda, L. J., Barbour, J. C., Simpson, R. L., and Overmyer, D. L. (2000a), *Phys. Rev. B* **61**, 10451–10462.

Siegal, M. P., Tallant, D. R., Provencio, P. N., Overmyer, D. L., Simpson, R. L., and Martinez-Miranda, L. J. (2000b), *Appl. Phys. Lett*. **76**, 3052–3054.

Steffen, H. J., Roux, C. D., Marton, D., and Rabalais, J. W. (1991), *Phys. Rev. B* **44**, 3981–3990.

Sullivan, J. P., Friedmann, T. A., and Baca, A. G. (1997), *J. Electron. Mater.* **26**, 1021–1029.

Sullivan, J. P., Friedmann, T. A., and Hjort, K. (2001), *MRS Bull*. **26**, 309–311.

Swierenga, S. H. H., Gilman, J. P. W., and Mclean, J. R. (1987), *Cancer Metastasis Rev.* **6**, 113–154.

Tiainen, V. M. (2001), *Diamond Related Mater.* **10**, 153–160.

Tay, B. K., and Zhang, P. (2002), *Thin Solid Films* **420**, 177–184.

Thomson, L. A., Law, F. C., Rushton, N., and Franks, J. (1991), *Biomaterials* **12**, 37–40.

Tran, H. S., Puc, M. M., Hewitt, C. W., Soll, D. B., Marra, S. W., Simonetti, V. A., Cilley, J. H., and Delrossi, A. J. (1999), *J. Invest. Surg*. **12**, 133–140.

Trojan, K., Grischke, M., and Dimigen, H. (1994), *Phys. Status Solidi* **145**, 575.

Tsai, H. C., and Bogy, D. B. (1987), *J. Vac. Sci. Technol*. **5**, 3287–3312.

Ugolini, D., Eitle, J., and Oelhafen, P. (1990), *Vacuum* **41**, 1374–1377.

Uhlmann, S., Frauenheim, T., and Lifshitz, Y. (1998), *Phys. Rev. Lett*. **81**, 641–644.

Veerasamy, V. S., Amaratunga, G. A. J., Davis, C. A., Milne, W. I., and Hewitt, P. (1994), *Solid-State Electron*. **37**, 319–326.

Voevodin, A. A., Laube, S. J. P., Walck, S. D., Solomon, J. S., Donley, M. S., and Zabinski, J. S. (1995a), *J. Appl. Phys*. **78**, 4123–4130.

Voevodin, A. A., Donley, M. S., Zabinski, J. S., and Bultman, J. E. (1995b), *Surf. Coat. Technol*. **77**, 534–539.

Voevodin, A. A., Rebholz, C., and Matthews, A. (1995c), *Tribol. Trans*. **38**, 829–836.

Voevodin, A. A., and Donley, M. S. (1996), *Surf. Coat. Technol*. **82**, 199–213.

Voevodin, A. A., Phelps, A. W., Zabinski, J. S., and Donley, M. S. (1996), *Diamond Related Mater*. **5**, 1264–1269.

Wachter, R., Cordery, A., Proffitt, S., and Foord, J. S. (1998), *Diamond Related Mater.* **7**, 687–691.

Wagal, S. S., Juengerman, E. M., and Collins, C. B. (1988), *Appl. Phys. Lett*. **53**, 187–188.

Wagner, J., Ramsteiner, M., Wild, C., and Koidl, P. (1989), *Phys. Rev. B* **40**, 1817–1824.

Wang, M., Schmidt, K., Reichelt, K., Dimigen, H., and Hubsch, H. (1992), *J. Mater. Res*. **7**, 667–676.

Wei, Q., Narayan, R. J., Narayan, J., Sankar, J., and Sharma, A. K. (1998), *Mater. Sci. Eng. B* **53**, 262–266.

Wei, Q., Narayan, R. J., Sharma, A. K., Sankar, J., and Narayan, J. (1999), *J. Vac. Sci. Technol. A* **17**, 3406–3414.

Williams, D. F. (1977), *J. Med. Eng. Technol*. **1**, 195.

Williams, J. M., Buchanan, R. A., and Lee, I. S. (1989), *Nucl. Instrum. Methods Phys. Res*. **37**, 676–681.

Witt, J. D., and Swann, M. (1991), *J. Bone Joint Surg*. **73**, 559–563.

Wu, W. J., Pai, T. M., and Hon, M. H. (1998), *Diamond Related Mater.* **7**, 1478–1484.

Xiong, F. L., Wang, Y.Y, Leppert, V., and Chang, R. P. H. (1993), *J. Mater. Res*. **8**, 2265–2272.

Yamagata, Y., Sharma, A., Narayan, J., Mayo, R. M., Newman, J. W., and Ebihara, K. (1999), *J. Appl. Phys*. **86**, 4154–4159.

Yamazaki, K., Litwak, P., Tagusari, O., Mori, T., Kono, K., Kameneva, M., Watach, M., Gordon, L., Miyagishima, M., Tomioka, J., Umezu, M., Outa, E., Antaki, J. F., Kormos, R. L., Koyanagi, H., and Griffith, B. P. (1998), *Artificial Org*. **22**, 466–474.

Yin, G. F., Luo, J. M., and Zheng, C. Q., Tong, H. H., Huo, Y. F., and Mu, L. L. (1999), *Thin Solid Films* **345**, 67–70.

Yu, L. J., Wang, X., Wang, X. H., and Liu, X. H. (2000), *Surf. Coat. Technol*. **128**, 484–488.

Zolynski, K., Witkowski, P., Kaluzny, A., Has, Z., Niedzielski, P., and Mitura, S. (1996), *J. Chem. Vapor Depos*. **4**, 232.

CHAPTER 16

Pulsed Laser Deposition of Metals

HANS-ULRICH KREBS

Institut für Materialphysik, University of Göttingen, Göttingen, Germany

16.1 INTRODUCTION

Since Buckel and Hilsch [1954] it has been known that the condensation of metallic alloys from the vapor phase often leads to the formation of solids far from thermal equilibrium. Metallic supersaturated solid solutions and metastable crystalline or amorphous phases have been mainly prepared by techniques such as thermal evaporation or sputtering. In the case of metallic multilayers, the interphase roughness and mixing strongly depends on the growth mode, the kinetic energy of the deposited particles and the heat of mixing between the different constituents.

In 1969, elemental metals were deposited for the first time by pulsed laser deposition (PLD) [Schwartz and Tourtellotte, 1969]. By 1978, PLD had been tried out for more than half the metals in the periodic table [Boyakov et al., 1978]. Nevertheless, it was not until some years later that PLD was systematically applied to the deposition of metallic alloys and multilayers [Gavigan et al., 1991; Singh et al., 1992; Krebs and Bremert, 1993]. By now, a further 10 years of intense work in this field have been accomplished since the introduction of PLD of metals by Kools in the book of Chrisey and Hubler [1994]. Many interesting experiments show that PLD is a versatile technique for the growth of metallic alloys and multilayers in ultrahigh vacuum (UHV) with features different from conventional deposition techniques such as evaporation or sputtering. Deposition in an inert gas environment is also of special interest because it provides an additional parameter to systematically vary the properties of metal films.

The aim of this chapter is to briefly give an overview on the growth and properties of metallic systems prepared by PLD, on the specific mechanisms leading to the particular properties, and on their potential for applications.

16.2 DEPOSITION TECHNIQUE

16.2.1 Typical Setup

A typical setup for the deposition of metallic alloys and multilayers consists of a UHV chamber with a base pressure of at least $\sim 10^{-8}$ mbar in which elemental foils or alloy targets are ablated at an angle of 45° by a pulsed and focused laser (in many cases an excimer laser with KrF radiation, wavelength 248 nm, pulse duration 30 ns is used). The atoms and ions ablated from the target(s)

Pulsed Laser Deposition of Thin Films: Applications-Led Growth of Functional Materials
Edited by Robert Eason

are deposited on substrates (e.g., Si or Al_2O_3) clamped on a heater with the surface parallel to the target surface with a target-to-substrate distance of typically 2–10 cm. To obtain a steady ablation rate (see Section 16.4.1) from the target, the laser is scanned (e.g., by an eccentric rotation of the focusing lens and by additionally sweeping the target under the laser pulses) over a sufficiently large target area.

Although the target preparation of alloys is relatively simple because the small quantities needed (about $1\,cm^2$) of most alloys can be homogeneously prepared by arc melting, it is often more convenient to use elementary targets. Then, during preparation of alloys, the average composition of the film obtained can be varied by the number of pulses on each target. However, to get homogeneous alloys, one has to take care that the thicknesses obtained are always less than one monolayer for each element. In the case of multilayers, the single-layer thicknesses and the period can also be controlled by the number of pulses on each target.

16.2.2 Droplet Reduction

Additional to the deposition of atoms and ions, some spherical droplets (typically less than 1% of the deposited material) with two characteristic sizes of <0.5 and about 1–3 μm, respectively [Krebs and Bremert, 1993], are found on the metal film surface (see Fig. 16.1). The number of droplets depends on the laser fluence, target material, and surface roughness and strongly increases with the number of pulses on the same target location [van de Riet et al., 1993b; Weaver and Lewis, 1996; Spindler et al., 1996; Fähler et al., 1997].

For some applications, the occurrence of these droplets on the film surface is a limitation of the PLD method, as their formation is in principle unavoidable during deposition in UHV from solid targets (hydrodynamic sputtering). Because conelike structures pointing in the direction of the laser beam gradually develop on the target surface when illuminated under a constant angle, scanning the laser beam over variable angles of incidence is an advantage. With increasing laser fluence, the average droplet diameter increases, but the actual number of particulates is reduced [Leuchtner et al., 1998]. To reduce the droplet number, the laser fluence used and position of the substrate can be optimized, and the target surface has to be as smooth (and dense) as possible. Completely droplet-free films can be obtained by using mechanical velocity filters between target and substrate [Barr, 1969; Dubowski, 1986; Cherief et al., 1993], which allow the fast atoms and ions to reach the substrate but remove the slower droplets with velocities of $<200\,m/s$ [Dupendant et al., 1989; Spindler et al., 1996; Fähler et al., 1997] during their transit to the substrate. Another interesting technique to avoid droplets is to use a dual-beam ablation geometry, where the line-of-sight direction to the substrate is obscured by shutters [Pechen et al., 1992; Gorbunov et al., 1996], and also see Chapter 6.

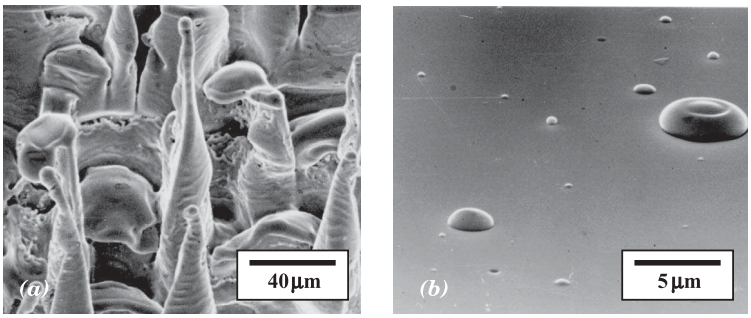

Figure 16.1 Scanning electron micrographs of (a) a Fe–Nb target surface after 1000 shots at $7\,J/cm^2$ and (b) of the film surface with droplets viewed at an angle of 20°, see also Krebs and Bremert [1993].

16.3 ENERGETIC PARTICLES

Most metallic systems studied so far have been deposited under UHV conditions, although the film properties can be tuned by using an inert background gas, as will be discussed in Section 16.5. In UHV, more or less energetic particles are formed depending on the laser fluence, which influences the film growth and the properties obtained.

16.3.1 Formation of Energetic Particles

The typical brightness of metals originates from the high reflectivity, typically more than 90%, of a (visible) electromagnetic wave at a metal surface. But above the Langmuir frequency ω_p (plasmon frequency), this high reflectivity of metals is lost. For ultraviolet (UV) radiation (and at 248 nm in particular) the reflectivity R of most metals is in the range of only between 10 and 50% (Al is a special case with a reflectivity of 90% even at 248 nm) [von Allmen, 1987]. The energy of an incident UV wave is therefore partially coupled into the electronic system, distributed to many electrons or plasmons and then shared with the lattice on a time scale of typically a few picoseconds. Therefore, the surface of metallic targets is heated up by a nanosecond duration laser pulse almost immediately (with respect to the relevant nanosecond time scale). The absorption depth of a metallic target is in the range of about 10–20 nm. During a 30-ns laser pulse, the temperature of the surface layer is affected to a depth of more than 1 μm due to the large heat conductance of metals. Although the target heating takes place in a few nanoseconds with a heating rate of the order of 10^{12} K/s, the ablation process is usually (see, e.g., Kelly and Rothenberg [1985]) thermodynamically described by an equilibrium evaporation rate $J(T)$ by the so-called Hertz–Knudsen equation (which originally described thermal evaporation from a Knudsen cell):

$$J(T) = \frac{p_e(T)}{\sqrt{2\pi m_A kT}} \tag{16.1}$$

with a temperature-dependent equilibrium pressure $p_e(T)$, given by the Clausius–Clapeyron equation, the Boltzmann constant k, and the mass of the target atoms m_A. For such a thermal process, the number of ions n_i compared to the number of neutrals n_n per cubic centimeter depends on the temperature T and the ionization energy E_i according to the Eggert–Saha equation [von Allmen, 1987]:

$$\frac{n_i^2}{n_n} = \left(\frac{2\pi m_e kT}{h^2}\right)^{3/2} \times \exp\left(\frac{-E_i}{kT}\right) \tag{16.2}$$

with the mass of the electron m_e and the Planck constant h. Due to the absorption of the incoming laser energy (e.g., by inverse bremsstrahlung) by the ablated particles forming a dense so-called Knudsen layer in front of the target, a highly ionized plasma is formed close to the target surface. The absorption coefficient α_p of the inverse bremsstrahlung process is given by Phipps et al. [1988] as

$$\alpha_p = \frac{\frac{4}{3}\sqrt{2\pi/3kT_e} \cdot Zn_e^2 e^6 g_{ff}[1 - \exp(-h\nu/kT_e)]}{hcm_e^{3/2}\nu^3} \tag{16.3}$$

with the frequency of the laser radiation ν, the degree of ionization Z, the electron density n_e, and temperature T_e, and quantum mechanical correction term g_{ff} (with a value close to 1). Lunney and Jordan [1998] argued that the plasma absorption is even stronger than indicated by inverse bremsstrahlung, probably due to bound–bound and photoionization processes. Due to the absorption of the laser energy, the plasma is further heated up (up to temperatures of the order of 10,000 K and more), while the metal target itself is partially screened by the plasma and is already cooling down during the pulse. This screening effect is seen in calculations of Fähler and Krebs [1996] at higher

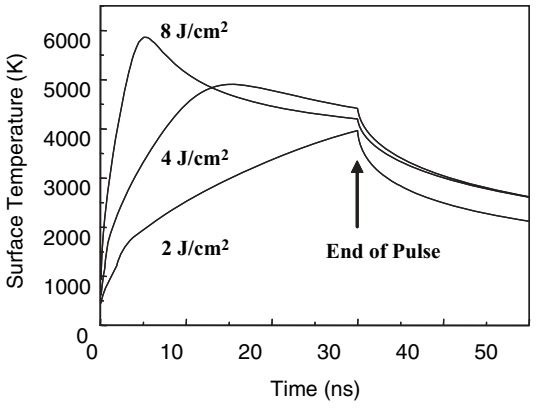

Figure 16.2 Time dependence of the calculated surface temperatures at different laser fluences. At high fluences the absorption in the evaporated material causes target shielding and a decrease of surface temperature after about 5 ns. Details of the calculations are described in Fähler and Krebs [1996].

laser fluence (Fig. 16.2). The expansion of the plasma (with velocities v_z perpendicular to the target surface) is normally described under the assumption that thermodynamics and hydrodynamics can be applied [Kelly and Dreyfus, 1988; Kools et al., 1992] and the number of collisions within the Knudsen layer is sufficiently high to produce a shifted Maxwell–Boltzmann center-of-mass velocity distribution $f(v_z)$ with a center-of-mass velocity u_{cm} of the form

$$f(v_z) \propto v_z^3 \cdot \exp\left[\frac{-m_A(v_z - u_{\mathrm{cm}})^2}{2kT_{\mathrm{eff}}}\right] \tag{16.4}$$

with an effective temperature T_{eff}. An adiabatic collisionless expansion then occurs. In Figure 16.3, time-of-flight (TOF) measurements at different laser fluences are shown for the ablation of Fe [see also Fähler and Krebs, 1996]. Indeed, the velocity distributions of the ablated ions are well represented by the above equation. Ion fractions within the evaporated material of 50% and more,

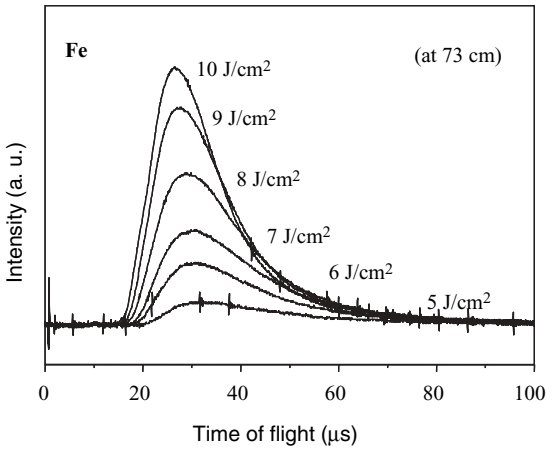

Figure 16.3 Time-of-flight spectra of Fe taken at 73 cm distance from the target at different laser fluences, see also Fähler and Krebs [1996].

and ion velocities of up to a few 10^6 cm/s are obtained for different metals [Lunney, 1995; Duffey et al., 1995]. These velocities correspond to average kinetic energies of the ablated ions of about 100 eV [Geohegan, 1992; Kools and Dieleman, 1993]. Nevertheless, at the deposition threshold fluence (about 1 J/cm^2) the average ion energy only lies in the range of 10–20 eV comparable to the particle energy during sputtering, but it increases linearly with increasing laser fluence up to 150 eV at 12 J/cm^2 [Fähler and Krebs, 1996]. The high kinetic energy of the ablated ions results from an acceleration of the ions in the strongly increasing space-charge field produced by the more mobile electrons, collectively moving away from the ions [Demtröder and Jantz, 1970]. Measurements of the angular-resolved energy distribution of laser-ablated Ag ions even showed ion energies exceeding 500 eV for angles close to the normal, while the energy distributions are shifted strongly toward lower energies with increasing angle [Hansen et al., 1998].

In most cases, the *average* kinetic energy of the neutral component was measured to be lower, on the order of 5–10 eV [Dyer, 1989; von Gutfeld and Dreyfus, 1989; Dieleman et al., 1992]. The angular distribution of the electron density and temperature in the laser ablation plume was experimentally determined by Toftmann et al. [2000] using TOF spectroscopy with ion probes. For Ag, values of kT_e of between 0.1 and 0.5 eV were measured at 0.8 J/cm^2.

16.3.2 Influence on Film Growth

Molecular dynamics (MD) simulations indicate that kinetic energies of less than about 10 eV (as exist for atoms during deposition) lead to an enhanced adatom mobility without formation of defects. From this, films with a strong fiber texture or epitaxy are expected. At higher particle energies, MD simulations predict defect formation in the films during deposition. At about 15 eV, defects occur only in the surface layer, as shown in MD simulations for the case of a deposition of Cr atoms on body-centered cubic (bcc) CrTi [Krebs et al., 1997]. The displacement threshold of bulk atoms is on the order of 15–25 eV for most metals [Ullmaier, 1997]. Thus, at higher particle energies, surface atoms are resputtered and energetic ions are implanted a few layers deep (and more, if channeling processes occur) below the film surface leading to ballistic displacements of atoms within the film and to the formation of bulk defects. Additionally, atomic mixing in alloys and interface mixing in multilayers are expected. From sputtering it is known that the deposition of energetic ions induces shot-peening effects [Windischmann, 1987; Thornton and Hoffman, 1989] combined with a densification of the deposited material, stress formation, and relaxation into dislocations. In Figure 16.4, all these expected effects are schematically summarized. They are

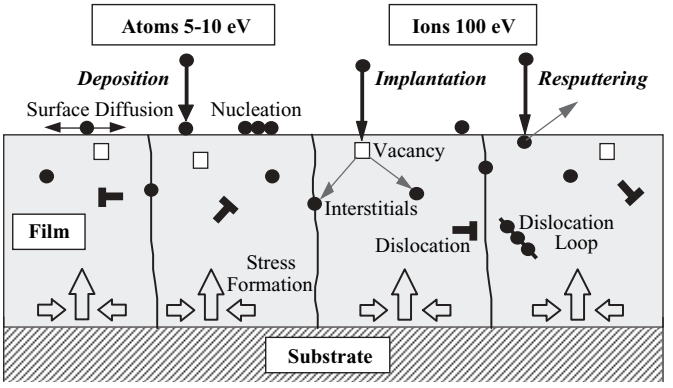

Figure 16.4 Atomic processes occurring during laser deposition of ablated particles in ultrahigh vacuum. While the atoms are deposited on the film surface, the energetic ions lead to implantation below the film surface, resputtering and compressive stress due to shot-peening. Vacancies, interstitials, agglomeration of point defects, and large numbers of dislocations are formed.

indeed observed in laser-deposited metallic systems grown in UHV, as will be discussed in the following section.

16.4 DEPOSITION IN ULTRAHIGH VACUUM

In this section, at first, those characteristic properties of metallic alloys are described, which occur in UHV and are more or less independent of the metallic material investigated (and are even mainly observed—at different laser fluences—for oxides, carbides, nitrides, or other materials during PLD, too). Although the phases formed by PLD are usually similar to those of conventional deposition techniques, some characteristic features occur, which are summarized below.

16.4.1 Deposition Rate and Angular Distribution

Significant growth rates of the order of 0.01–0.05 nm per pulse are observed for metals above a fluence threshold of about 0.5–5 J/cm^2, depending on the material used [Krebs and Bremert, 1993; Svendsen et al., 1996]. Therefore, with a repetition rate of 10 Hz an average deposition rate of a few angstroms per second similar to a typical evaporation or sputtering rate is obtained. But, before a steady deposition rate is obtained, a reduction of the ablated flux by a factor of about 2 is observed due to roughening of the target surface.

Pulsed laser deposition of metals with a focused laser beam leads to a strong angular dependence of the deposition rate. The angular distribution can be described by $\cos^n \varphi$ functions with exponents of between 8 and 40, with φ being the angle toward the normal of the target surface [Fähler et al., 1999a]. For comparison, in the case of thermal evaporation from a Knudsen cell, a $\cos^4 \varphi$ function is expected for the film thickness on a substrate parallel to the target surface.

The dynamics and lateral shape of the plume produced by PLD and the so-called flip-over effect produced by an elliptical or rectangular laser spot was investigated in detail by Toftmann et al. [2003]; see also Figure 16.5. For this, an ensemble of quartz crystal microbalances were used to

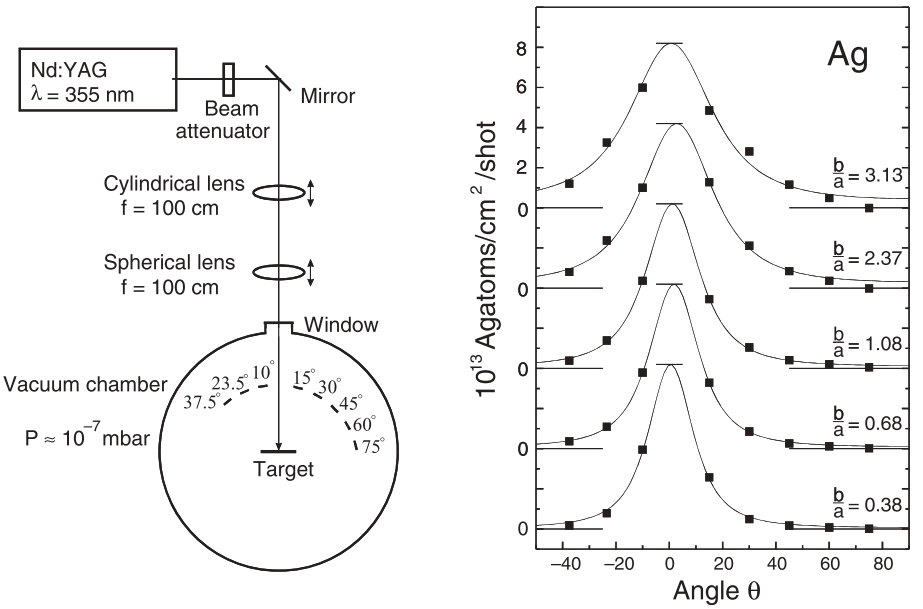

Figure 16.5 Experimental setup and absolute deposition rate as a function of angle for different values of the aspect ratio b/a of an elliptical laser spot (2 J/cm^2 at 355 nm). Fits based on the Anisimov's model [Anisimov et al., 1993] are shown. For more details see Toftmann et al. [2003].

quantitatively study how the shape of the plume varies as the aspect ratio (a/b) of an elliptical laser spot is varied by about a factor of 10. The results were fitted by using the adiabatic expansion model of Asinimov et al. [1993].

In practice, films with uniform thickness can be obtained, for instance, by scanning the laser beam spot over a large target area, by increasing the target-to-substrate distance, by moving or rotating the substrate during deposition, and by an asymmetric deposition on a rotating substrate.

16.4.2 Stoichiometry Transfer

In most cases, the stoichiometry of deposited alloy films is close to that of the metallic targets used, as studied for a series of $Fe_{0.5}M_{0.5}$ (M = metal) alloys by Krebs and Bremert [1993]. Deviations from the film stoichiometry [van de Riet et al., 1993a] can be explained by unusually high vapor pressures of one component, different angular distributions of the elements, and especially by preferential resputtering induced by energetic ions (see Section 16.4.11).

16.4.3 Homogeneity of Alloy Films

Laser-deposited films are often much more homogeneous than sputtered or evaporated films. For instance, in the case of PLD, a decomposition of Fe–Nb is not present at all, as observed by Störmer and Krebs [1995]. In contrast to sputtered films, laser-deposited samples are either completely amorphous or supersaturated solid solutions (see Fig. 16.6). For other systems like Co–Cr, the homogeneity of the deposited alloys was confirmed on an atomic scale by field-ion microscopy combined with an atomic probe (FIM/AP) by Krebs et al. [1997a], while sputtered films decompose during deposition [Pundt et al., 1994]. Nevertheless, in demixing systems like Co–Cu, Fe–Ag, Ni–Ag, or Fe–In, the decomposition could not be prevented at medium concentrations as confirmed by FIM/AP by Färber [1995], transmission electron microscopy (TEM), and X-ray diffraction [Störmer and Krebs, 1995; Krebs and Störmer, 1995; see also Fig. 16.7]. Atomic mixing processes induced by deposition and implantation of energetic particles seem to be responsible for the better film homogeneity.

16.4.4 Improved Film Growth

Due to an enhanced surface mobility, improved *crystallographic textures* have been observed in PLD films in comparison to sputtered samples by Störmer and Krebs [1995]. For instance, in

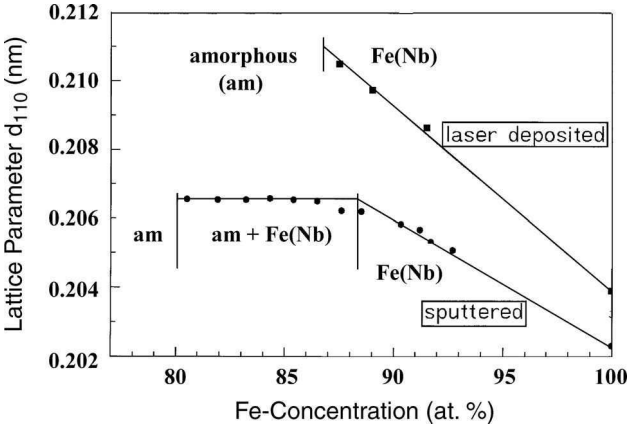

Figure 16.6 Concentration dependence of the lattice spacings d_{110} of the Fe(Nb) solid solution and region of the amorphous phase of Fe–Nb films, ■ laser deposited at 9 J/cm^2 and ● sputtered at room temperature, respectively. More results are described in Störmer and Krebs [1995].

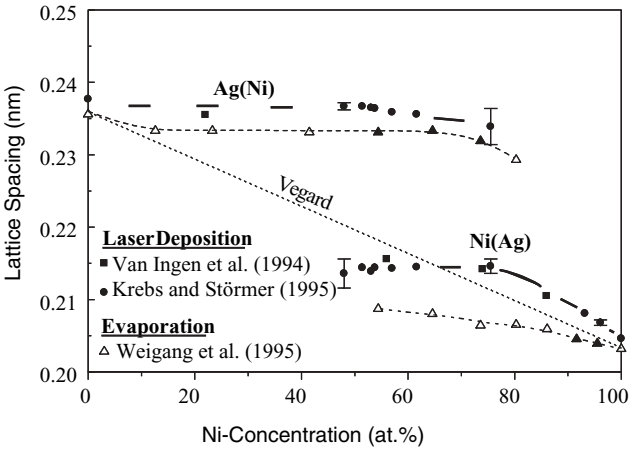

Figure 16.7 Concentration dependence of the lattice spacings d_{111} of the Ni(Ag) and Ag(Ni) solid solution of laser deposited Ni–Ag films (■: van Ingen et al. [1994]; ●: Krebs and Störmer [1995]) in comparison to thermally evaporated samples (Δ: Weigang et al. [1995]). The Vegard's line of a substitutional solution is included.

laser-deposited Ag films a (111) texture was observed on different substrates, while sputtered films were untextured. In alloys, rocking curves of films often show a much sharper texture in the case of PLD. *Epitaxial growth* at room temperature has been observed for Pt films on MgO by Cillessen et al. [1993] or Mo on Al_2O_3 by Malikov and Mikhailov [1997]. Epitaxial growth at room temperature was also observed for Cu or Fe on Ag (and vice versa) by in situ reflection/transmission high energy electron diffraction (RHEED/THEED) by Fähler et al. [2000]. In comparison to thermal deposition, improved *layer-by-layer growth* (see Fig. 16.8) has been observed for Fe and Fe–Cu on Cu(111) using scanning tunneling microscopy and RHEED [Jenniches et al., 1996; Sundar Manoharan et al., 1998; Shen et al. 1998]. Also Zheng et al. [1999] reported that Co films can be grown on Cu (111) with good layer-by-layer morphology and significantly fewer stacking faults by PLD in contrast to thermal deposition.

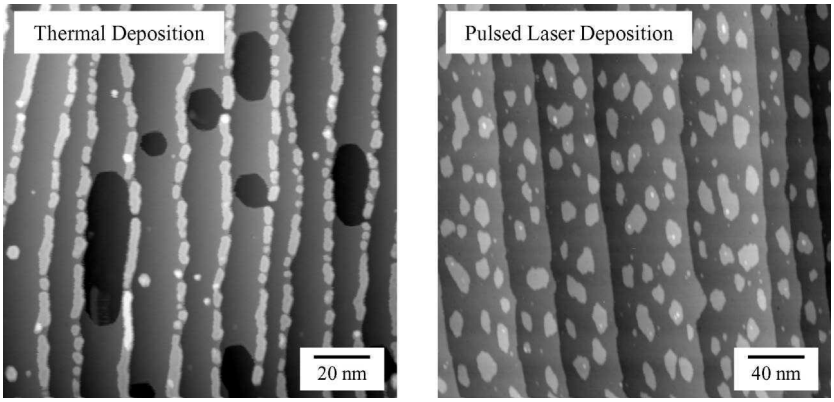

Figure 16.8 Fe on Cu(111) deposited by thermal deposition (0.37 monolayer) and PLD (0.22 monolayer) at 300 K. The different characteristic features are: decoration of the Cu terrace edges and 2- or 3-monolayer-high islands during thermal deposition, and layer-by-layer growth during PLD, see also Jenniches et al. [1996].

16.4.5 Small Grain Size

Most metallic alloys grown by PLD are either amorphous or *nanocrystalline* with a typical grain size of only about 5 nm over wide concentration ranges [e.g., Ni–Ag: 50–80 at % Ni, Fe–Ag: 40–90 at % Fe). This is deduced from the broadness of the X-ray reflections by using the Scherrer formula [Cullity, 1978] and was confirmed by TEM. The cause of this seems to be the 10^5–10^6 times higher momentary deposition rate of the *pulsed* laser deposition process, leading to smaller grains. During PLD, the conditions for film growth are similar to when reduced substrate temperatures are used, as discussed by Krebs et al. [1995a].

16.4.6 Internal Stress

In all laser-deposited metallic elements and alloys investigated so far (e.g., Ni–Ag, Fe–Ag, Fe–In, Fe–Zr, Fe–Nb, Cu–Co, and more), a larger lattice expansion in the growth direction (of up to about 1%) is observed compared to films grown by other deposition techniques (see Fig. 16.6 and 16.7). It increases with rising laser fluence during deposition (see Fig. 16.6) and is much larger than expected for a substitutional solid solution from King's table [King, 1966]. The expansion of the in-plane lattice parameters is much smaller, as confirmed by grazing incidence diffraction experiments using synchrotron radiation and four-circle diffractometry by Störmer et al. [1999]. These measurements are an indication of high compressive stress of the order of 1–2 GPa in PLD metallic films.

Detailed in situ stress measurements were performed on polycrystalline Permalloy and Ag thin films. For small film thicknesses, interface stress, capillarity-induced stress, and island zipping stress dominates the measurements, while for thicker films (>5 nm) stress due to shot-peening and implantation is dominant [Sturm et al., 2000; Scharf et al., 2003]. The compressive stress caused by shot-peening effects is produced by the deposition and implantation of energetic particles, influencing a region of about 3 nm below the surface of the already grown film. As described in Section 16.3.2, such shot-peening effects leading to intrinsic compressive stress are known from sputtered films.

16.4.7 Defect Formation

High-resolution transmission electron microscopy (HRTEM) and FIM measurements [Störmer et al., 1999; Borchers et al., 2000] show that a large number of bulk defects exist in metallic films laser deposited in UHV (see Fig. 16.9). HRTEM investigations in cross section give clear evidence

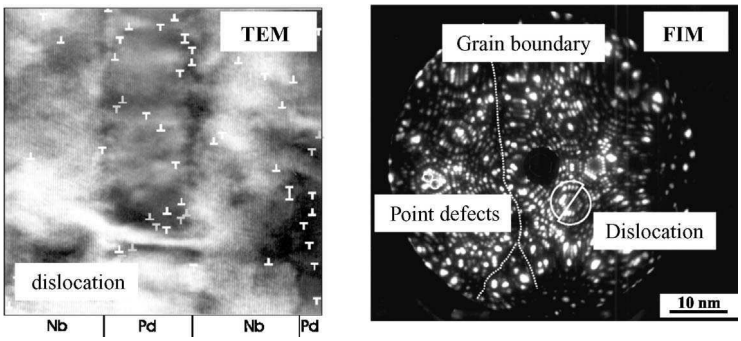

Figure 16.9 High-resolution transmission electron microscopy (HRTEM) and field ion microscope (FIM) images of a Pd/Nb multilayer, deposited by PLD on a Si substrate and on a W tip, respectively. Point defects, dislocations, and grain boundaries can be seen. These structures are marked to guide the eye. The defect structure of laser deposited films is described in more detail by Borchers et al. [2000] and Störmer et al. [1999].

for different types of structural defects. Many dislocations on (110) planes were observed in Fe films on Si, probably formed during a partial release of high compressive stress. In Fe, Fe–Ag and Pd–Nb films dislocation densities of up to $10^{12}/cm^2$ were measured. Columnar growth with a typical column diameter of about 20 nm was observed in supersaturated Fe–Ag samples. In FIM images, grain boundaries, screw dislocations, and point defects (probably vacancies) have been directly observed with atomic resolution.

16.4.8 Interface Mixing

In metallic systems, many experiments show interface mixing. For instance, in Co/Pd multilayers, a depth of mixing at the interfaces was determined to be 0.6 nm by simulation of X-ray diffraction patterns [Enrech et al., 1994]. In situ resistance measurements [Fähler et al., 2000] give indications that in Fe/Zr, Cu/Ag, and Fe/Ag multilayers the thickness of intermixing is in the range of about 1–2 nm. This was also confirmed by X-ray diffraction (XRD), Rutherford backscattering (RBS), Auger electron spectroscopy (AES), and conversion electron Mößbauer spectroscopy (CEMS) [Luo and Krebs, 1995; Gupta et al., 2003]. Due to interface mixing, at bilayer periodicities of less than about 4 nm, laser-deposited Fe/Nb multilayers are completely amorphous, while in sputtered multilayers only a small fraction of an amorphous phase occurs. In Fe/Ag and Cu/Ag, a continuous concentration change is measured at the interface over a few nanometer thickness. For Co/Cr multilayers grown on W, an interface mixing was directly observed by Krebs et al. [1997] on a nanometer scale by FIM in combination with an atom probe. In Fe/Al multilayers, the intermixing of adjacent layers was described by Noetzel et al. [1999] in terms of ballistic mixing followed by chemical mixing. By using negative bias voltages of up to 10 kV, a 7.6-nm depth of damage below the Si surface was observed by Qi et al. [2001] during implantation of laser-ablated Fe ions into Si.

16.4.9 Interface Roughness

As proved by different experimental techniques, multilayers with sharp interfaces can be grown by PLD at least in systems with a positive heat of mixing. Simultaneously, in most cases, the morphology of the films is improved remarkably in comparison to thermal evaporation or sputtering. In the case of Co/Pd, Fe/Ag, and Pd/Nb, satellite reflections occur in wide-angle X-ray diffraction patterns indicating sharp interfaces [Enrech et al., 1994; Luo and Krebs, 1995; Krebs et al., 1995b; Yang et al., 1996]. HRTEM investigations were performed on Ni/C multilayers to determine the interface roughness [Dietsch et al., 1998]. Also X-ray reflectivity measurements in the Permalloy/Ag, Cu/Ag, Fe/Ag, Fe/MgO, Ti/MgO, and Permalloy/MgO systems were analyzed in detail by structural simulations including surface and interface roughnesses [Faupel et al., 2002; Fuhse et al., 2004]. All these experiments indicate a typical interface roughness of only about one or two monolayers, depending only slightly on the number of deposited bilayers.

16.4.10 Metastable Phase Formation at Interfaces

As discussed above, the formation of amorphous interlayers is observed in laser-deposited multilayers of systems with negative heat of mixing. But also the formation of crystalline metastable phases at interfaces of multilayers is typical for the PLD process. For instance, in Fe/Ag, Cr/Ag, and Co/Cr multilayers, the formation of metastable phases over 2–4 nm was studied in situ by transmission high-energy electron diffraction (THEED) experiments [Fähler et al., 1999a; Störmer et al., 1999]. At larger layer thicknesses, face-centered cubic (fcc)–bcc phase transformations occur, which can be described via Bain transformations. It is assumed that the metastable phase formation is induced by the implantation of energetic particles a few monolayers deep below the substrate surface. This causes the formation of an alloy within the topmost few monolayers with a continuous concentration change up to a final concentration, where a transformation into the equilibrium phase takes place.

Layer-by-layer growth was observed by Shen et al. [1998] during growth of ultrathin nonequilibrium fcc Fe on Cu (111) at room temperature. These films exhibit a high magnetic moment of more than $2\,\mu_B$, which is much larger than that obtained during thermal evaporation. Sundar Manoharan et al. [1998] prepared artificial metastable fcc Fe–Cu alloys by stacking one monolayer of Fe and one monolayer of Cu alternately onto a Cu(001) substrate using PLD. In this case, a nearly layer-by-layer growth was observed and alloys up to 22 bilayers obey fcc structure, which for larger thicknesses changes to bcc structure.

16.4.11 Resputtering Effects

Resputtering effects caused by energetic particles exist during PLD in UHV. The first indications were, for instance, differences in the numbers of ablated and deposited particles as measured during deposition of Cu [Jordan et al., 1995], a reduced Pb concentration during PLD of Pb–Zr–Ti–O in low oxygen pressure [Hau et al., 1995], a reduced Ga content in Fe–Si–Ga–Ru thin films [van de Riet et al., 1993a], and stoichiometry changes during PLD of Cu–Ni and Ag–Ni [van Ingen et al., 1994].

To *quantify* resputtering, measurements of deposition rates on tilted substrates and at interfaces of multilayers were performed. At $4.5\,\mathrm{J/cm^2}$ sputter yields $Y_{\mathrm{Fe}\to\mathrm{Fe}} = 0.17$, $Y_{\mathrm{Ag}\to\mathrm{Ag}} = 0.55$, $Y_{\mathrm{Fe}\to\mathrm{Ag}} = 0.67$, and $Y_{\mathrm{Ag}\to\mathrm{Fe}} = 0.02$, respectively, were determined by Fähler et al. [1999b] and Sturm and Krebs [2001]. This means that especially in the case of the deposition on Ag resputtering effects are significant. In an $A - B$ system, the experimental results are described by a model, which includes atom deposition on the film surface, implantation of energetic ions below the surface, and resputtering of atoms from the top monolayer. The assumption is then plausible that the mass increase rate $R[c_A(p)]$ mainly depends on the actual concentration $c_A(p)$ of A atoms in the surface monolayer, which continuously changes with increasing number of pulses p, and on the individual sputter yields. The rate is given by

$$R[c_A(p)] = n_A m_A - n_A\{Y_{A\to A}c_A(p)m_A + Y_{A\to B}[1 - c_A(p)]m_B\} \tag{16.5}$$

It was further shown that preferential resputtering and composition deviations of alloy films can be reduced at laser fluences close to the ablation threshold, where the kinetic energy of the deposited particles is lower.

16.5 DEPOSITION IN INERT GAS ATMOSPHERE

Depositing in inert gas atmospheres is easy to achieve to reduce the kinetic energy of the deposited particles because the expanding plasma plume interacts with the surrounding gas by scattering of ablated ions and atoms by gas atoms. As expected, the reduction of kinetic energy is combined with strong changes of the film properties.

16.5.1 Reduction of Implantation and Resputtering

With increasing Ar gas pressure, the reduction of particle energy is accompanied by a *decrease of implantation and resputtering*. This is combined with a decrease of interface mixing and decreasing sputtering yields. As studied by in situ rate measurements [Sturm et al., 2000; Scharf and Krebs, 2002], in the case of Ag, the sputter yield $Y_{\mathrm{Ag}\to\mathrm{Ag}}$, which is 0.55 in UHV, continuously changes with increasing gas pressure and is reduced to 0.10 at 0.04 mbar Ar.

16.5.2 Changes in the Deposition Rate

In all metallic systems, at high pressures, scattering of ablated material out of the deposition path between target and substrate leads to a decrease of the deposition rate. But in systems with a high

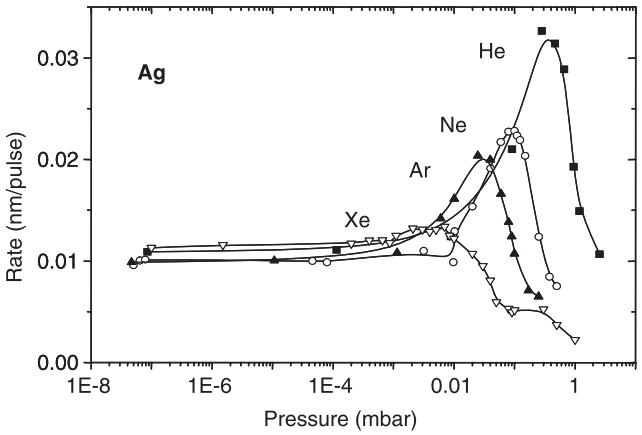

Figure 16.10 Rates of Ag deposited in different inert gas atmospheres, see also Scharf and Krebs [2002].

sputtering yield like Ag, the reduction of resputtering first leads to an *increase and a maximum of the deposition rate* with increasing gas pressure [Sturm et al., 2000; Scharf and Krebs, 2002] (see Fig. 16.10). For the background gases Xe and Ar these processes strongly overlap but are separated in He because of the lower atomic mass and hence lower capability to scatter heavier ions. At an Ar pressure of 0.04 mbar or a He pressure of about 0.4 mbar, the kinetic energy of the deposited particles is so far reduced (to about 10–20 eV) that the maximum deposition rate is reached and implantation of particles is avoided.

16.5.3 Changes of Film Properties

Under these conditions (0.04 mbar in Ar, 0.4 mbar in He) *stoichiometric* metallic alloy films and multilayers with *sharp interfaces* are obtained. With increasing gas pressure, the *intrinsic stress changes* from compressive to tensile (see Fig. 16.11 and Scharf et al., 2003). This is accompanied

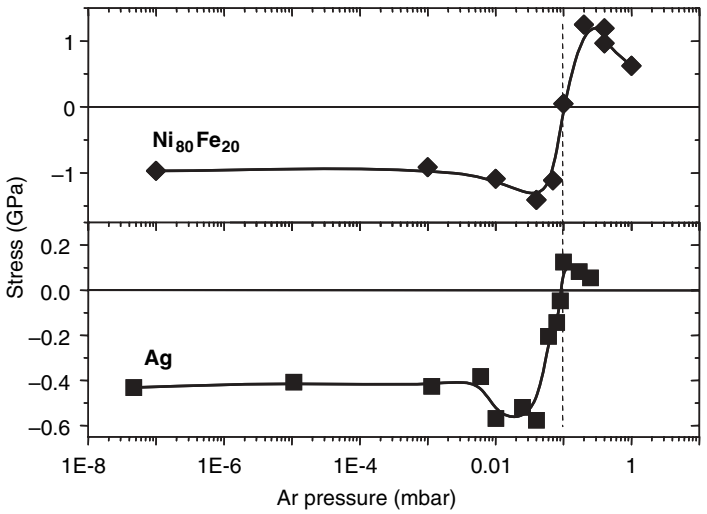

Figure 16.11 Intrinsic stress of Permalloy and Ag deposited in different inert gas atmospheres, for details see Scharf et al. [2003].

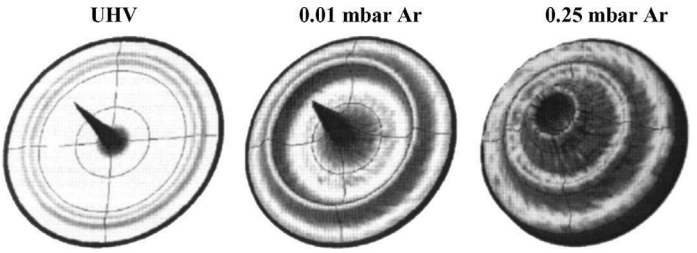

Figure 16.12 Change of the Permalloy thin-film texture, depending on the Ar gas pressure during PLD at room temperature: strong (111)-texture in UHV, increasing (200)-texture, and (321)-texture in 0.01 mbar Ar and 0.25 mbar Ar, respectively. Additional results are given in Scharf et al. [2003].

with a *change of film texture* (as shown for Permalloy in Fig. 16.12) *and microstructure*. While the compressive stress at low Ar pressure is combined with a high density of the film caused by shot-peening effects, the tensile stress obtained at high pressures is a sign for an open structure as often observed in evaporated films or during sputtering in high background gas pressures [Vink and van Zon, 1991].

For low pressures, the experimental results are explained by a model of scattering of a dense cloud of ablated material in a dilute surrounding gas [Kools, 1993; Itina et al., 1997; Sturm and Krebs, 2001]. As soon as the particle energy and associated resputtering effects decrease, the deposition rate increases. At high gas pressures, the interaction cannot be explained by single scattering events, as the number of gas atoms in the deposition channel is much higher than the number of ablated particles. In this case, the plasma expansion leads to a shock front between the plasma plume and the surrounding gas [Chrisey and Hubler, 1994; Gusarov et al., 2000; Scharf and Krebs, 2002].

16.6 POTENTIAL FOR APPLICATIONS

Despite the potentially large expense of laser-based facilities, PLD has good potential for special applications because it allows the preparation of films with specialist properties difficult to achieve with more conventional deposition techniques. Laser-deposited alloys and multilayers possess potential for applications, especially due to energetic particles supporting the deposition process and the difficulty of preparing complex systems with accurate stoichiometry by other thin-film techniques. Potential for applications lies mainly in the formation of nonequilibrium alloys, systems with pronounced giant magnetoresistance, soft and hard magnetic thin films, and multilayers useful as X-ray mirrors.

16.6.1 Nonequilibrium Phases

In most metallic alloys investigated so far (Fe–Nb, Fe–Cu, Co–Cr, Cu–Co, Fe–Ag, Ni–Ag, Fe–In), a higher supersaturation of the solid solutions (see Fig. 16.6 and 16.7) is observed than from conventional deposition techniques. This has already been discussed by Krebs [1997]. In the Fe–Nb system with negative heat of mixing, a single-phase bcc Fe(Ag) solid solution up to 13 at % Ag is obtained, while during sputtering a lower solid solubility (up to 11 at % Ag) is reached and a two-phase region between the Fe(Nb) phase and the amorphous Fe–Nb phase exists. Also in systems with a large positive heat of mixing such as Ni–Ag and Fe–Ag, where almost no solubility exists in thermodynamic equilibrium, the solid solutions can be supersaturated up to 20 at % Ag and 14 at % Ag, respectively, but are decomposed at higher concentrations during deposition at room temperature. At lower substrate temperatures (150 K), nanocrystalline and homogeneous bcc Fe(Ag)

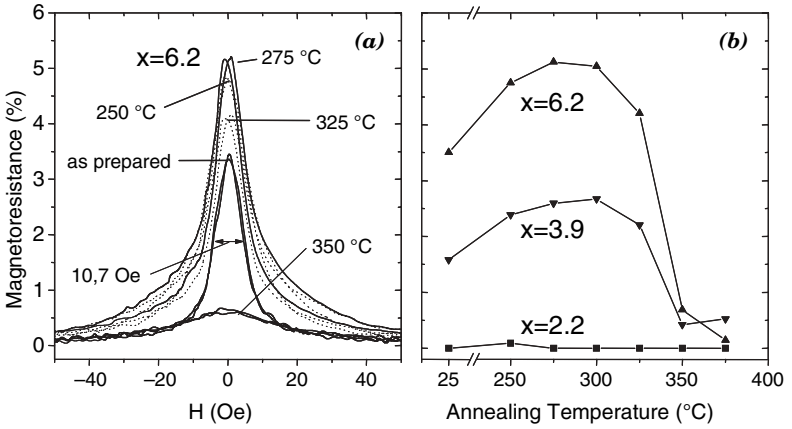

Figure 16.13 GMR vs. magnetic field H curves (a) and maximum GMR values (b) for $[Ag(x\ nm)/Py(1.4\ nm)]_{20}$ samples (Py = Permalloy) with different Ag-spacer thicknesses x as a function of annealing temperatures. More details are described by Faupel et al. [2002].

films with much higher Ag content (of 40 at %) are achieved [Kahl and Krebs, 2001]. Amorphous Fe–Zr, Cu–Zr, Pd–Si, and Fe–Nb alloys were grown at room temperature over wide concentration regions [Krebs et al., 1996; Störmer et al., 1999]. Al–Pd–Mn quasi-crystal thin films have been obtained by lowering the substrate temperature to that of liquid nitrogen [Ichikawa et al., 1994].

16.6.2 Giant Magnetoresistance

Giant magnetoresistance (GMR) of up to 9.5% in 1.5 Tesla was observed at 14 K in *granular* $Co_{19}Cu_{81}$ thin films prepared by PLD [Jackson et al., 1996]. The as-grown films show a small GMR effect of only 2.5% at room temperature as well as at low temperatures, but this can be enhanced by a factor of 4 by appropriate annealing. Phase segregation and GMR behavior (27% at 4.2 K under a magnetic field of 4.7 Tesla) was also observed in as-deposited Co–Ag granular films grown by PLD, unlike with films deposited by sputtering, where a postannealing step is required to achieve the phase segregation [Zhang et al., 1997].

In as-prepared laser-deposited $Ni_{80}Fe_{20}$/Ag (Permalloy/Ag) *multilayers* a GMR value of 3.5% in low fields of about 0.001 Tesla was observed at room temperature by Faupel et al. [2002], as depicted in Figure 16.13. Strong columnar growth in combination with preferential sputtering of Ag from the film surface during deposition of the $Ni_{80}Fe_{20}$ layer helps to directly create a discontinuous multilayer structure necessary for high GMR values without postannealing. In contrast, such multilayers prepared at room temperature by sputtering [Hylton et al., 1994] or molecular beam epitaxy (MBE) [Farrow et al., 1994] show negligible GMR in the as-prepared state. In all cases, during annealing the GMR effect increases to about 5%. Here, only PLD appears to be a suitable technique for the preparation of Permalloy/Ag films with considerable GMR in a one-step process.

16.6.3 Soft and Hard Magnetic Materials

Soft magnetic materials require the combination of high remanence and low coercivity to conduct alternating magnetic flux with low losses. Besides the selection of a material with appropriate intrinsic magnetic properties (high saturation magnetization, low magnetic anisotropy, and magnetostriction), it is necessary to tailor an appropriate microstructure (a small grain size down to the amorphous state, low stress, and an induced anisotropy along the application direction). Soft

magnetic films are used in writing heads for magnetic data storage, audio and video applications, and have prospective applications in magnetic sensors, switches, and concentrators. Complex CoCr(Ta,Pt) alloys [Ishikawa et al., 1994] prepared by PLD combine coercivities ($\mu_0 H_c$) of 0.013–0.025 Tesla with a film smoothness improved over that of sputtered samples. Amorphous magnetic FeCoNiSiB films have been produced by laser ablation from amorphous magnetic ribbons [Nikitin et al., 1997]. They possess well-defined uniaxial anisotropy and demonstrate coercivity and anisotropy field values comparable to those of the initial ribbon. In soft magnetic FeBSiC metallic glasses the orientation of the magnetic moment can be changed from in-plane to out-of-plane by increasing the laser fluence during deposition [Sorescu et al., 1999].

Pulsed laser deposition can also be applied to the deposition of hard magnetic films. Permanent magnets are intended as a storage medium for magnetic fields and as such they combine a high remanence with a high coercivity. The optimal microstructure exhibits a uniaxial texture of the easy axis parallel to the application direction and a multiphase microstructure, which contains small but crystalline grains of the highly anisotropic magnetic phase. The key application areas for hard magnetic films are media for magnetic data storage and microelectromechanical systems (MEMS). SmCo-based films with a small grain size prepared on moderately heated substrates (100°C) exhibit high coercivities of 1.1 Tesla and smooth hysteresis loops [Cadieu et al., 1998]. At higher temperatures crystalline SmCo films can be prepared, which achieve a coercivity up to 2.25 Tesla when deposited with a shadow technique [Cadieu et al. 1999]. The effect of rare-earth content on the microstructure and magnetic properties has been studied by Neu et al. [2002]. The alternate ablation from elemental Sm and Co targets allows a simple variation of composition and the study of different hard magnetic phases existing in this system. While in Sm–Co films the easy axis predominantly lies within the film plane, it can be perpendicular to the substrate in NdFeB films, and such NdFeB thin films with the desired phase were grown by Geurtsen et al. [1996], Yang et al. [1998], Neu et al. [2002], and Hannemann et al. [2002]. These films typically have a perpendicular magnetic anisotropy and coercivities up to 1 Tesla. PLD was the first method successfully applied to the deposition of epitaxial $Nd_2Fe_{14}B$ films [Hannemann et al., 2003]. The epitaxial growth results in a perfect alignment of the easy axis perpendicular to the substrate and the formation of a regular rectangular grain shape (Fig. 16.14). Due to the deposition of surplus Nd, the grains are magnetically isolated resulting in a high coercivity up to 2 Tesla. Recent experiments by Weisheit et al. [2004] show that PLD can be used to prepare granular epitaxial FePt films on MgO (100). These films exhibit out-of-plane coercivities up to 5.6 Tesla, values that have not been reached with other deposition methods.

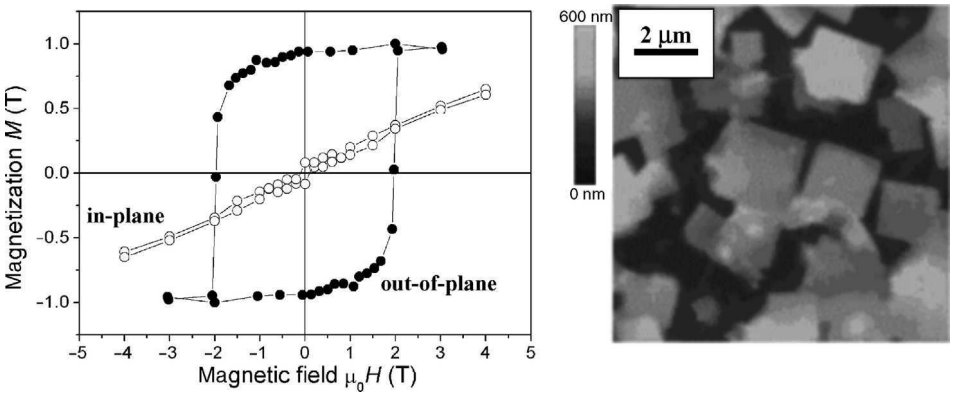

Figure 16.14 Hysteresis of an epitaxial NdFeB film deposited by PLD on Al_2O_3(0001) using a Ta(110) buffer, and granular microstructure consisting of isolated rectangular $Nd_2Fe_{14}B$ grains. More details on the microstructure and magnetic properties of NdFeB are given by Hannemann et al. [2003].

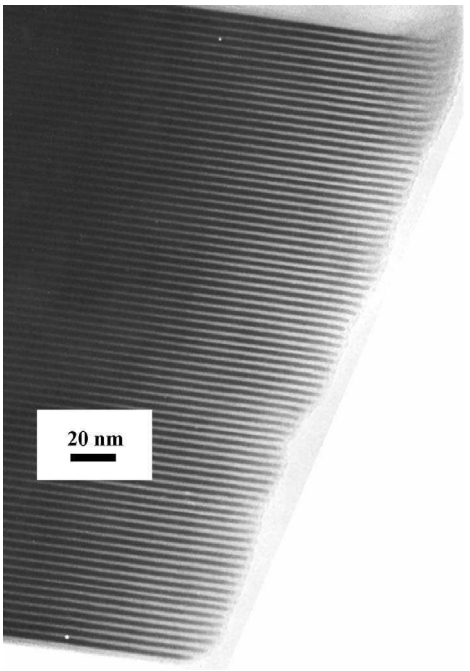

Figure 16.15 Morphology of total layer stack of 75-period Ni/C graded multilayer (HRTEM image) with mean period thickness of 3.65 nm, for details see Dietsch et al. [1998].

16.6.4 X-ray Mirrors

The PLD growth of Ni/C multilayers leads to a very low level of interface roughness as shown by Mai and Pompe [1992]. High precision, large-area PLD of X-ray optical Ni/C multilayers was realized by double-beam PLD on cylindrical targets by Dietsch et al. [1998]. The result of optimized deposition parameters for Ni/C multilayer synthesis is demonstrated by the high-resolution electron microscopy (HRTEM) micrograph of Figure 16.15. Multilayer interface roughnesses of the order of 0.1 nm are deduced from these measurements at fluences close to the deposition threshold. With higher laser fluences the interface roughness increases.

Amorphous $Ni_{50}Nb_{50}$/C multilayers for soft X-ray mirrors with sharp interfaces and lateral correlation length on the order of 180 nm were laser-deposited by Vitta et al. [1995]. Amorphous alloy/ceramic oxide multilayers of metal/MgO (metal = Fe, Ti, $Ni_{80}Nb_{20}$) with periods of less than 4 nm have been made by PLD and characterized by means of grazing-incidence X-ray reflectivity [Vitta et al., 2001, 2003; Fuhse et al., 2004]. The interface roughness was found to be < 0.4 nm at the two interfaces leading to a peak reflectivity of $\sim 38\%$ (for hard X-rays). These multilayers are promising candidates as soft X-ray mirrors in the water-window region, as was proved by reflectivity measurements using a laser-plasma-based soft X-ray reflectometer (at $\lambda = 3.374$ nm). Their thermal stability is suitable for applications up to 300°C.

16.6.5 Compound Materials

Because PLD is a versatile technique, which in most cases ensures stoichiometric transfer, it allows the formation of complex compound materials, as discussed by Krebs et al. [2003]. As described above, complex metal/ceramic multilayers with sharp interfaces for X-ray mirrors can be grown. But, due to the pulsed nature of PLD, other complex systems such as polymer–metal films can also be produced. For instance, Sn clusters embedded in polyamide (PA) matrix were

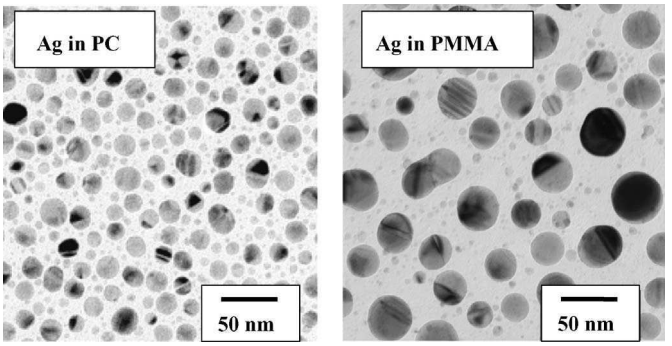

Figure 16.16 TEM images of Ag grains embedded in polycarbonate (left side, see also Faupel and Krebs [2004]) and poly(methyl methacrylate) (right side, for details see Röder and Krebs [2006]).

prepared by Gitay et al. [1991]. Ag grains were embedded in polycarbonate (PC) by Faupel et al. [2004] and in poly(methyl methacrylate) (PMMA) by Röder and Krebs [2006]; see Figure 16.16. In the case of PC and Ag, completely different laser fluences are necessary for the deposition of the polymer and metal, respectively. PC has to be prepared at low laser fluences of about 60 mJ/cm^2 to optimize the chemical structure, while the Ag clusters are deposited at a fluence of 2 J/cm^2, which is $\sim$30 times higher. By this technique, even PC/Ag multilayers were grown for the first time with low interface roughness [Faupel et al., 2004].

Metal nanocomposite thin films formed by Cu and Ag nanocrystals embedded in an amorphous Al_2O_3 host have been synthesized in UHV and in a buffer gas (Ar) by PLD [Afonso et al, 1999; Ballesteros et al., 1999; Serna et al., 2001; de Sande, 2002]. These composites show interesting linear and nonlinear optical properties, which are partially caused by quantum confinement effects in which the major contribution is associated with electronic interband transitions. Furthermore, Yang et al. [2002] have demonstrated that films consisting of Ag nanoclusters embedded in $BaTiO_3$ show large optical nonlinearities.

16.7 CONCLUSIONS

Pulsed laser deposition is a versatile technique for the preparation of metallic systems for many reasons. Because the energy source is outside the deposition chamber, the use of UHV and inert gas pressure is possible. In UHV, the kinetic energy of the ions of about 100 eV lies well above the displacement threshold of bulk atoms. Therefore, implantation and intermixing effects lead to the formation of metastable phases, for instance, nanocrystalline highly supersaturated solid solutions and amorphous alloys. On the other hand, preparation in inert gas atmospheres makes it possible to tune the film properties such as stress, texture, magnetic properties, and the like by varying the kinetic energy of the deposited particles.

For metallic systems, two different interesting growth regimes exist during PLD. The first is just above the deposition threshold (2–5 J/cm^2) or in an appropriate inert gas pressure (0.04 mbar in Ar or 0.4 mbar in He), where the kinetic energy is so far reduced that the particle energies lie in the range of 10–20 eV, similar to sputtering. In this case, surface processes are activated promoting the formation of textures and epitaxial growth, but the damage of the films is minimized. For the case of multilayers, this leads to films with sharp interfaces, but scarcely any intermixing or resputtering effects. On the other hand, laser fluences above 8 J/cm^2 favor the production of metastable phases and strongly supersaturated solid solutions because at such high fluences the probability of ballistic mixing by energetic ions increases and decomposition processes can be prevented. The film growth can then be described by a subsurface growth

mode, characterized by implantation and mixing processes in which the material does not grow on top, but rather within the topmost few monolayers of the already deposited film.

In summary, the combination of stoichiometry transfer with the possibility of easily varying the particle energy in the range of 10–100 eV makes PLD very interesting for the deposition of metallic systems.

Acknowledgments

The author would like to thank C. N. Afonso, W. Blum, W. Bolse, C. Borchers, O. Bremert, P. E. Dyer, S. Fähler, J. Faupel, C. Fuhse, R. Gupta, M. Hamp, D. Hesse, S. Kahl, R. Kelly, R. Kirchheim, K. H. Lieb, J. G. Lunney, Y. Luo, A. Meschede, T. H. Metzger, G. von Minnigerode, A. Pundt, J. Röder, K. Samwer, P. Schaaf, T. Scharf, J. Schou, M. Seibt, M. Störmer, K. Sturm, E. Süske, H. Teichler, S. Vitta, M. Weisheit, and J. Winkler for helpful discussions concerning the characteristics of PLD of metals.

REFERENCES

Afonso, C. N., J. Gonzalo, R. Serna, J. C. G. de Sande, C. Ricolleau, C. Grigis, M. Gandais, D. E. Hole, and P. D. Towsend (1999), *Appl. Phys. A* **69**, S201.

Anisimov, S. I., D. Bäuerle, and B. S. Luk'yanchuk (1993), *Phys. Rev. B* **48**, 12076.

Ballesteros, J. M., J. Solis, R. Serna, and C. N. Afonso (1999), *Appl. Phys. Lett*. **74**, 2791.

Barr, W. P. (1969), *J. Phys. E: J. Sci. Instrum*. **2**, 1112.

Borchers, C., U. Laudahn, A. Pundt, S. Fähler, H. U. Krebs, and R. Kirchheim (2000), *Philos. Mag. A* **80**, 543.

Boyakov, V. M., V. M. Epikhin, B. A. Kalin, M. K. Makhatov, I. N. Nikolaev, and G. N. Shiskin (1978), *Sov. J. Quant. Electron*. **8**, 902.

Buckel, W., and R. Hilsch (1954), *Z. Phys*. **138**, 109.

Cadieu, F. J., R. Rani, X. R. Qian, and L. Chen (1998), *J. Appl. Phys*. **83**, 6247.

Cadieu, F. J., R. Rani, T. Theodoropoulos, and L. Chen (1999), *J. Appl. Phys*. **85**, 5895.

Cherief, N., D. Givord, A. Lienard, K. Mackay, O. F. K. McGrath, J. P. Rebouillat, F. Robout, and Y. Souche (1993), *J. Magn. Magn. Mater.* **121**, 94.

Cillessen, J. F. M., R. M. Wolf, and D. M. de Leeuw (1993), *Thin Solid Films* **226**, 53.

Chrisey, D. B., and G. K. Hubler (Eds.) (1994), *Pulsed Laser Deposition of Thin Films*, Wiley, New York.

Cullity, B. D. (1978), *Elements of X-Ray Diffraction*, Addison-Wesley, Reading, MA.

Demtröder, W., and W. Jantz (1970), *Plasma Phys*. **12**, 691.

De Sande, J. C. G., R. Serna, J. Gonzalo, C. N. Afonso, D. E. Hole, and A. Naudon (2002), *J. Appl. Phys*. **91**, 1536.

Dieleman, D., E. van de Riet, and J. C. S. Kools (1992), *Jpn. J. Appl. Phys*. **31**, 1964.

Dietsch, R., T. Holz, H. Mai, C. F. Meyer, R. Scholz, and B. Wehner (1998), *Appl. Surf. Sci*. **127–129**, 451.

Duffey, T. P., T. G. McNeela, T. Yamamoto, and J. Mazumder (1995), *Phys. Rev. B* **51**, 14652.

Dubowski, J. J. (1986), *Proc. Soc. Photo-Opt. Instrum. Eng*. **668**, 97.

Dupendant, H., J. P. Gavigan, D. Givord, A. Lienard, J. P. Rebouillat, and Y. Souche (1989), *Appl. Surf. Sci*. **43**, 369.

Dyer, P. E. (1989), *Appl. Phys. Lett*. **55**, 1630.

Enrech, M., J. G. Lunney, R. Skomski, and J. M. D. Coey (1994), *Mater. Sci. Eng. B* **23**, 25.

Fähler, S., and H. U. Krebs (1996), *Appl. Surf. Sci*. **96–98**, 61.

Fähler, S., M. Störmer, and H. U. Krebs (1997), *Appl. Surf. Sci*. **109/110**, 433.

Fähler, S., M. Weisheit, S. Kahl, K. Sturm, and H. U. Krebs (1999a), *Appl. Phys. A* **69**, S459.

Fähler, S., K. Sturm, and H. U. Krebs (1999b), *Appl. Phys. Lett*. **75**, 3766.

Fähler, S., S. Kahl, M. Weisheit, K. Sturm, and H. U. Krebs (2000), *Appl. Surf. Sci*. **154/155**, 419.

Färber, B. (1995), Diplom Thesis, "Mikrocharakterisierung stark übersättigter und rasch abgeschreckter Cu-Co-Legierungen," Universität Göttingen.

Farrow, R. F. C., R. F. Marks, T. A. Rabedeau, M. F. Toney, D. Dobbertin, R. Beyers, and S. S. P. Parkin (1994), *J. Appl. Phys*. **76**, 3688.

Faupel, J., H. U. Krebs, A. Käufler, Y. Luo, K. Samwer, and S. Vitta (2002), *J. Appl. Phys*. **92**, 1171.

Faupel, J., C. Fuhse, A. Meschede, C. Herweg, H. U. Krebs, and S. Vitta (2004), *Appl. Phys. A* **79**, 1233.

Fuhse, C., H. U. Krebs, S. Vitta, and G. Johansson (2004), *Appl. Opt*. **43**, 6265.

Gavigan, J. P., D. Givord, A. Lienard, J. P. Rebouillat, and Y. Souche (1991), *J. Appl. Phys*. **69**, 279.

Geohegan, D. B. (1992), *Thin Solid Films* **220**, 138.

Geurtsen, A. J. M., J. C. S. Kools, L. de Wit, and J. C. Lodder (1996), *Appl. Surf. Sci*. **96–98**, 887.

Gitay, M., B. Joglekar, and S. B. Ogale (1991), *Appl. Phys. Lett*. **58**, 197.

Gorbunov, A. A., W. Pompe, A. Sewing, S. V. Gaponov, A. D. Akhsakhalyan, I. G. Zabrodin, I. A. Kas'kov, E. B. Klyenkov, A. P. Morozov, N. N. Salaschenko, R. Dietsch, H. Mai, and S. Völlmar (1996), *Appl. Surf. Sci*. **96–98**, 649.

Gupta, R., M. Weisheit, H. U. Krebs, and P. Schaaf (2003), *Phys. Rev. B* **67**, 075402.

Gusarov, A. V., A. G. Gnedovts, and I. Smurov (2000), *Appl. Surf. Sci*. **154/155**, 66.

Hannemann, U., S. Fähler, S. Oswald, B. Holzapfel, and L. Schultz (2002), *J. Magn. Magn. Mater*. **242–245**, 1294

Hannemann, U., S. Fähler, V. Neu, B. Holzapfel, and L. Schultz (2003), *Appl. Phys. Lett*. **82**, 3710.

Hansen, T. N., J. Schou, and J. G. Lunney (1998), *Appl. Phys. Lett*. **72**, 1829.

Hau, S. K., K. H. Wong, P. W. Chan, and C. L. Choy (1995), *Appl. Phys. Lett*. **66**, 245.

Hylton, T. L., K. R. Cofey, M. A. Parker, and J. K. Howard (1994), *J. Appl. Phys*. **75**, 7058.

Ichikawa, N., O. Matsumoto, T. Hara, T. Kitahara, T. Yamauchi, T. Matsuda, T. Takeuchi, and U. Mizutani (1994), *Jpn. J. Appl. Phys*. **33**, L736.

Ishikawa, A., K. Tanahashi, Y. Yahisa, Y. Hosoe, and Y. Shiroshi (1994), *J. Appl. Phys*. **75**, 5978.

Itina, T. E., W. Marine, and M. Autric (1997), *J. Appl. Phys*. **82**, 3536.

Jackson, T. J., S. B. Palmer, H. J. Blythe, and A. S. Halim (1996), *J. Magn. Magn. Mater.* **159**, 269.

Jenniches, H., M. Klaua, H. Höche, and J. Kirschner (1996), *Appl. Phys. Lett*. **69**, 3339.

Jordan, R., D. Cole, J. G. Lunney, K. Mackay, and D. Givord (1995), *Appl. Surf. Sci*. **86**, 24.

Kahl, S., and H. U. Krebs (2001), *Phys. Rev. B* **63**, 172103.

Kelly, R., and R. W. Dreyfus (1988), *Nucl. Instrum. Methods Phys. Res. B* **54**, 341.

Kelly, R., and J. E. Rothenberg (1985), *Nucl. Instrum. Methods Phys. Res. B* **7/8**, 755.

King, H. W. (1966), *J. Mater. Sci*. **1**, 79.

Kools, J. C. S. (1993), *J. Appl. Phys*. **74**, 6401.

Kools, J. C. S., and J. Dieleman (1993), *J. Appl. Phys*. **74**, 4163.

Kools, J. C. S., T. S. Baller, S. T. De Zwart, and J. Dieleman (1992), *J. Appl. Phys*. **71**, 4547.

Krebs, H. U. (1997), *Int. J. Non-equilib. Process*. **10**, 3.

Krebs, H. U., and O. Bremert (1993), *Appl. Phys. Lett*. **62**, 2341.

Krebs, H. U., and M. Störmer, *Phys. Rev. Lett*. **75** (1995) 3966.

Krebs, H. U., O. Bremert, M. Störmer, and Y. Luo (1995a), *Appl. Surf. Sci*. **86**, 90.

Krebs, H. U., Y. Luo, M. Störmer, A. Crespo, P. Schaaf, and W. Bolse (1995b), *Appl. Phys. A* **61**, 591.

Krebs, H. U., O. Bremert, Y. Luo, S. Fähler, and M. Störmer (1996), *Thin Solid Films* **275**, 18.

Krebs, H. U., M. Störmer, S. Fähler, O. Bremert, M. Hamp, A. Pundt, H. Teichler, W. Blum, and T. H. Metzger (1997), *Appl. Surf. Sci*. **109/110**, 433.

Krebs, H. U., M. Störmer, J. Faupel, E. Süske, T. Scharf, C. Fuhse, M. Seibt, H. Kijewski, D. Nelke, E. Pachenko, and M. Buback (2003), *Adv. Solid State Phys*. **43**, 505.

Leuchtner, R. E., J. S. Horwitz, and D. B. Chrisey (1998), *J. Appl. Phys*. **83**, 5477.

Lunney, J. G. (1995), *Appl. Surf. Sci*. **86**, 79.

Lunney, J. G., and R. Jordan (1998), *Appl. Surf. Sci*. **127–129**, 941.

Luo, Y., and H. U. Krebs (1995), *J. Appl. Phys*. **76**, 1482.

Mai, H., and W. Pompe (1992), *Appl. Surf. Sci*. **54**, 215.

Malikov, I. V., and G. M. Mikhailov (1997), *J. Appl. Phys*. **82**, 5555.

Neu, V., U. Hannemann, S. Fähler, B. Holzapfel, and L. Schultz (2002), *J. Appl. Phys*. **91**, 8180.

Nikitin, P. I., A. A. Beloglazov, A. Y. Toporov, M. V. Valeiko, V. I. Konov, A. Perrone, A. Luches, L. Mirenghi, and L. Tapfer (1997), *J. Appl. Phys.* **82**, 1408.

Noetzel, J., K. Brand, H. Geisel, A. Gorbunov, A. Tselev, E. Wieser, and W. Möller (1999), *Appl. Phys. A* **68**, 497.

Pechen, E. V., S. I. Krasnosvobodtsev, G. Kessler, A. Richter, M. Panzner, O. Grossman, and A. Teresiak (1992), *Phys. Status Solidi A* **131**, 179.

Phipps, C. R., T. P. Turner, R. F. Harrison, G. W. York, W. Z. Osborne, G. K. Anderson, X. F. Corlis, L. C. Haynes, H. S. Steele, K. C. Spicochi, and T. R. King (1988), *J. Appl. Phys.* **64**, 1083.

Pundt, A., R. Busch, and C. Michaelsen (1994), *Mater. Res. Soc. Symp. Proc.* **343**, 309.

Qi, B., R. M. Gilgenbach, Y. Y. Lau, M. D. Johnston, J. Lian, and L. M. Wang (2001), *Appl. Phys. Lett.* **78**, 3785.

Röder, J., and H. U. Krebs (2006), in preparation.

Scharf, T., and H. U. Krebs (2002), *Appl. Phys. A* **75**, 551.

Scharf, T., J. Faupel, K. Sturm, and H. U. Krebs (2003), *J. Appl. Phys.* **94**, 4273.

Schwartz, H., and H. A. Tourtellotte (1969), *J. Vac. Sci. Technol.* **6**, 373.

Serna, R., J. Gonzalo, C. N. Afonso, and J. C. G. de Sande (2001), *Appl. Phys. B* **73**, 339.

Shen, J., P. Ohresser, C. H. Mohan, M. Klaua, J. Barthel, and J. Kirschner (1998), *Phys. Rev. Lett.* **80**, 1980.

Singh, R. K., D. Bhattacharya, S. Sharan, P. Tiwari, and J. Narayan (1992), *J. Mater. Res.* **7**, 2639.

Sorescu, M., L. Tsakalakos, and T. Sands (1999), *J. Appl. Phys.* **85**, 6652.

Spindler, H. L., R. Gilgenbach, and J. S. Lash (1996), *Appl. Phys. Lett.* **68**, 3245.

Störmer, M., and H. U. Krebs (1995), *J. Appl. Phys.* **76**, 7080.

Störmer, M., K. Sturm, S. Fähler, M. Weisheit, J. Winkler, S. Kahl, P. Kesten, A. Pundt, M. Seibt, S. Senz, and H. U. Krebs (1999), *Appl. Phys. A* **69**, 455.

Sturm, K., and H. U. Krebs (2001), *J. Appl. Phys.* **90**, 1061.

Sturm, K., S. Fähler, and H. U. Krebs (2000), *Appl. Surf. Sci.* **154/155**, 462.

Sundar Manoharan, S., M. Klaua, J. Shen, J. Barthel, H. Jenniches, and J. Kirschner (1998), *Phys. Rev. B* **58**, 8549.

Svendsen, W., O. Ellegaard, and J. Schou (1996), *Appl. Phys. A* **63**, 247.

Thornton, J. A., and D. W. Hoffman (1989), *Thin Solid Films* **177**, 5.

Toftmann, B., J. Schou, T. N. Hansen, and J. G. Lunney (2000), *Phys. Rev. Lett.* **84**, 3998.

Toftmann, B., J. Schou, and J. G. Lunney (2003), *Phys. Rev. B* **67**, 104101.

Ullmaier, H. (1997), *Mater. Res. Soc. Bull.* **22**, 14.

Van de Riet, E., J. C. S. Kools, and J. Dieleman (1993a), *J. Appl. Phys.* **73**, 8290.

Van de Riet, E., C. H. C. M. Nillesen, and J. Dieleman (1993b), *J. Appl. Phys.* **74**, 2008.

Van Ingen, R. P., R. H. J. Fastenau, and E. J. Mittemeijer (1994), *Phys. Rev. Lett.* **72**, 1871.

Vink, T. J., and J. B. A. D. van Zon (1991), *J. Vac. Sci. Technol.* **A9**, 124.

Vitta, S., T. H. Metzger, H. Mai, and J. Peisl (1995), *Appl. Phys. Lett.* **67**, 1547.

Vitta, S., M. Weisheit, T. Scharf, and H. U. Krebs (2001), *Opt. Lett.* **26**, 1448.

Vitta, S., M. Weisheit, and H. U. Krebs (2003), *Appl. Opt.* **42**, 3297.

Von Allmen, M. (1987), *Laser Beam Interactions*, Springer, Berlin, Chapter 5.

Von Gutfeld, R. J., and R. W. Dreyfus (1989), *Appl. Phys. Lett.* **54**, 1212.

Weaver, I., and C. L. S. Lewis (1996), *Appl. Surf. Sci.* **96–98**, 663.

Weigang, G., H. Hecht, and G. Von Minnigerode (1995), *Z. Phys. B* **96**, 349.

Weisheit, M., L. Schultz, and S. Fähler (2004), *J. Appl. Phys.* **95**, 7489.

Windischmann, H. J. (1987), *Appl. Phys.* **62**, 1800.

Yang, C. J., A. W. Kim, and J. S. Kang (1998), *J. Appl. Phys.* **83**, 6620.

Yang, G., W. Wang, Y. Zhou, H. Lu, G. Yang, and Z. Chen (2002), *Appl. Phys. Lett.* **81**, 3969.

Yang, Q. M., G. Schmitz, S. Fähler, H. U. Krebs, and R. Kirchheim (1996), *Phys. Rev. B* **54**, 9131.

Zhang, W., I. W. Boyd, N. S. Cohen, Q. T. Bui., Q. A. Pankhurst, M. Elliott, and W. Herrenden-Harkerand (1997), *J. Appl. Phys.* **81**, 5211.

Zheng, M., J. Shen, C. V. Mohan, P. Ohresser, J. Barthel, and J. Kirschner (1999), *Appl. Phys. Lett.* **74**, 425.

SECTION 4

CHAPTER 17

Optical Waveguide Growth and Applications

ROBERT W. EASON, STEPHEN J. BARRINGTON, CHRISTOS GRIVAS, TIMOTHY C. MAY-SMITH, and DAVID P. SHEPHERD

Optoelectronics Research Centre, University of Southampton, Southampton, United Kingdom

17.1 INTRODUCTION

Optical waveguide fabrication is the essential technology that powers today's worldwide communications network. From the active waveguides within the laser diodes that generate the light, to the lithium niobate integrated waveguide modulators that encode the light, to the passive optical fibers that carry and distribute the light, waveguide fabrication is the uniquely important enabling process technology. An immediate and impressive comparison can be made here, however, between the optical properties of fibers and of devices such as modulators. Whereas modulators may have lengths of a few centimeters with typical transmission losses of perhaps 10%, optical fiber has a loss of $\sim 4\%$ (0.2 dB) *per kilometer*. It is very easy to appreciate, therefore, that optical waveguides and their associated fabrication technology are a prerequisite not only to the field of optical communications but to the far wider context of optical and material science, laser devices, amplifiers, fluorescent sources, and much more.

Waveguides have many intrinsic advantages over their bulk media counterparts. Confinement of light in a guided-wave geometry produces an intensity–length product that can be many orders of magnitude higher than for bulk materials that are in general restricted to the use of focused laser light only. While the intensity in the focal region of a laser beam can be high, the more tightly a beam is focused, the faster it will subsequently diverge. As many nonlinear optical effects have an intensity dependence that can be quadratic (or even higher order), maintaining a high intensity over distances that can vary from the approximately millimeter dimensions for laser diodes to tens of meters for doped fiber lasers is an enormous advantage. Lasing power thresholds can be considerably lower in waveguide geometries, enabling specific lasing transitions that would require impractically high pump powers in nonwaveguide format [Mackenzie et al., 2003]. Nonlinear effects such as harmonic generation, parametric frequency conversion, or four-wave mixing all similarly benefit from the enhanced efficiency or faster response time afforded by waveguide geometries.

The key factors that relate to waveguide implementation, however, are the costs of production, the sizes achievable, the optical quality and propagation losses, and the ease of growth of doped, graded, or integrated structures that lead to highly functional compact and efficient optical devices.

Pulsed Laser Deposition of Thin Films: Applications-Led Growth of Functional Materials
Edited by Robert Eason

We need, therefore, to briefly review established, and hence rival, methods of optical waveguide growth before addressing the benefits and uses of pulsed laser deposition (PLD) grown waveguides.

17.2 THIN-FILM WAVEGUIDE FABRICATION METHODS

Each waveguide fabrication technique may not be universally applicable to every class of material (glasses, crystals, polymers, semiconductors, etc.). Some techniques, for example, in-diffusion, have reached a stage of routine implementation that produces waveguides with extremely high quality and very low propagation loss ($<0.1\,\mathrm{dB\,cm^{-1}}$) but are in general restricted to specific well-tested diffusion couples. Other techniques, such as proton exchange, produce guiding for one polarization state only. Ion beam implantation requires extremely expensive capital equipment and can require postprocessing of the guides to reduce propagation loss. For all these techniques, the important parameters are fabrication cost, the degree of complexity or number of separate processing steps required, the flexibility to produce variable waveguide dimensions or formats such as planar or channel guides, and, finally, of relevance to this chapter, the ability to include dopants to achieve lasing or amplification.

Fabrication techniques can be classified into two broad categories: those that grow a waveguide *onto* a substrate producing, in general, a step change in the refractive index and those that define a waveguiding region *inside* an existing material, and usually produce a graded-index guided structure. Many texts exist that describe these processes in considerable detail [Ohring, 1992], so a brief and of necessity selective summary only is given below.

17.2.1 Waveguide Growth on an Existing Substrate

Physical vapor transport techniques are the simplest methods of producing layers or coatings on a substrate. Well-established methods exist such as evaporation, which involves the heating and vaporization of a material, or sputtering, which requires the impact from high-energy ions inside a vacuum chamber. The main drawback of both techniques is that the incongruent evaporation or lack of stoichiometric transfer for materials other than simple elements leads in general to amorphous or polycrystalline film growth that does not reproduce that of the original starting material. More involved techniques such as ''grain-by-grain'' evaporation can grow polycrystalline films [Muller et al., 1963], and sputtering can lead to active film growth [Wada and Miyazaki, 1994]. Under careful optimization, epitaxial films of ternary oxides have also been grown with acceptably low propagation losses of $1\,\mathrm{dB\,cm^{-1}}$ [Schwyn-Thony et al., 1992].

More sophisticated techniques such as chemical vapor deposition (CVD) and its many variants such as low-pressure, plasma-, and laser-enhanced CVD, involve the decomposition at high temperatures of chemical vapors or gases, termed precursors, which contain the elements required for incorporation into the final film. Deposition rates can be low ($<1\,\mu\mathrm{m}$ per hour) when attempting to grow crystalline films [Studebaker et al., 1997], and the elements that can be deposited are restricted by the often toxic or undesirable precursor gases required. Molecular beam epitaxy (MBE) is perhaps the most precise technique used to grow ultra-high-purity epitaxial single-crystal, primarily semiconductor layers, and is the deposition technique of choice when control of layer thickness is required at the single-atom level. This level of precision comes at a price, however, and MBE machines are neither cheap ($\sim\$1$ million) nor capable of growth rates that exceed $\sim 1\,\mu\mathrm{m}$ per hour. The ultra-high-vacuum ultraclean requirements restrict the flexibility of MBE growth, and machines are routinely dedicated to growth of a single material such as GaAs. Complex ternary oxides such as $LiNbO_3$ [Betts and Pitt, 1985] and $BaTiO_3$ [McKee et al., 1991] have been grown, as have rare-earth doped materials [McFarlane et al., 1995], but propagation losses, an unequivocal method of assessing growth quality, are not always reported. Liquid phase epitaxy (LPE) involves dipping a substrate into a supersaturated melt of oxides and can produce epitaxial crystalline waveguides of high quality and low propagation loss ($<0.05\,\mathrm{dB\,cm^{-1}}$)

[Chartier et al., 1992], but thickness control can be difficult and surface quality can also be a problem.

17.2.2 Waveguide Definition in an Existing Host

An alternative approach for waveguide fabrication involves the modification of the refractive index profile inside a host material using a range of techniques such as in- or out-diffusion, ion exchange, or implantation or direct writing using beams of photons, electrons, or ions. All of these techniques require an existing host, and each technique has its own advantages and shortfalls. In-diffusion is perhaps the most widely adopted technique and is used extensively to fabricate waveguides in a range of optical and nonlinear crystalline materials. High temperatures ($\sim$1000°C) and accurate temperature control must be achieved over extended processing times of tens of hours. Photolithography is required to define the waveguide location and width, and the diffusant (usually an element such as Ti, Zn, or Mg) creates a localized region of increased refractive index. Proton exchange [Jackel et al., 1982] or ion exchange [Ramaswamy and Najafi, 1986] are alternative techniques that require immersion in heated baths of acids or molten salts, respectively, but such techniques do not necessarily permit waveguide performance that is polarization independent, and the intrinsic material properties, such as electrooptic coefficients, may be severely reduced by this treatment.

Two final techniques that should be mentioned are ion beam implantation [Townsend, 1976; Field et al., 1991] and direct writing [Mailis et al., 2003]. The former involves the incidence on the waveguide host of a stream of energetic light ions (approximately a few MeV volts) that penetrate some few microns before coming to rest. Material modification occurs at the end of the ion range leading ideally to a damage layer of lower refractive index. Multiple implants may be required, and the waveguide can show fairly high (a few dB per cm) residual losses. Direct writing is a somewhat newer technique, utilizing a scanned laser beam of an appropriate wavelength to permanently modify the local refractive index and shows great promise for fast waveguide writing. This last method requires no photolithographic patterning or clean-room facilities, which should make the unit cost of waveguide devices appreciably lower. More sophisticated implementations involving multiphoton absorption or femtosecond laser pulses have also been demonstrated, and this area is set to expand considerably.

17.2.3 Pulsed Laser Deposition Waveguide Growth

Pulsed laser deposition is a relatively new technique for the growth of optical waveguides but has many advantages compared to those techniques discussed earlier. The only real constraint is that the material being deposited has a higher refractive index than the substrate to allow waveguiding to occur. Deposition rates can be high, of order 25 μm per hour for growth of materials such as Al_2O_3, permitting fast growth and rapid systematic investigation of optimum waveguide fabrication parameters. Multilayer, capped, or clad waveguides (see Section 17.6) are easy to fabricate, and doping can be included via step or graded structures. The targets used can be single crystal if the material already exists in this form or prepared as sintered pellets with a stoichiometry that can compensate for loss of volatile elements such as lithium, sodium, or potassium in the deposition process [Zaldo et al., 1994]. Lastly, crystal structures can be grown that are difficult or impossible to source commercially as bulk samples, and one-off growth runs can yield results in a matter of days, compared to months or even longer for conventional bulk crystal growth techniques.

One problem that must be addressed in waveguide growth via PLD is that of the particulates that are an inherent and seemingly unavoidable part of the PLD process. As we shall describe in Section 17.5, the presence of particulates need not be an overwhelming problem, however, and waveguides have recently been grown that exhibit losses of only two to three times that of the bulk crystal material, yielding values of $\sim 0.1\,\mathrm{dB\,cm^{-1}}$ for the final waveguide device [May-Smith et al., 2004; Grivas et al., 2004].

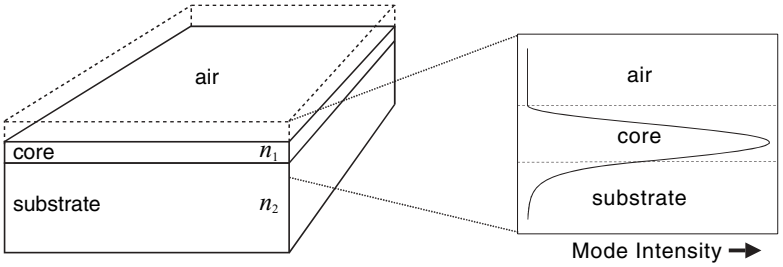

Figure 17.1 Basic planar waveguide structure with asymmetric refractive index profile and associated optical mode intensity profile within each region.

17.3 WAVEGUIDE STRUCTURES

Pulsed laser deposition of materials with a higher refractive index than the substrate forms a planar waveguide with an asymmetric refractive index profile as shown in Figure 17.1. Light is confined in the deposited film (the waveguide core) due to total internal reflection at the upper boundary with the surrounding air and at the lower boundary with the substrate.

As the index difference between the core and the air is normally much greater than that between the core and the substrate, the mode intensity falls to zero very quickly at the upper boundary, whereas it can penetrate a significant distance into the substrate region. Thus the asymmetry in the refractive index profile leads to an asymmetry in the intensity profile of the guided modes. The large refractive index difference at the upper boundary can also lead to high scattering losses from imperfections in the surface. It can therefore be advantageous to deposit a cladding layer on top of the core region that has a refractive index more closely matched to, but still lower than, the core. If the cladding layer has the same refractive index as the substrate, as shown in Figure 17.2, then a symmetric index profile is obtained, leading to symmetric mode profiles, which can be advantageous for certain applications such as coupling light into optical fibers.

One of the attractive features of PLD for making optical waveguides is that it allows a great freedom of choice over the fundamental waveguide design parameters of core thickness, d, and numerical aperture, $\mathrm{NA} = (n_1^2 - n_2^2)^{1/2}$, which together govern the size and number of propagation modes, p, at a given wavelength, λ. For a symmetric waveguide this is given by

$$p = \frac{2d\,\mathrm{NA}}{\lambda} + 1 \tag{17.1}$$

For example, waveguides with NA values as high as 0.73 have been achieved by epitaxial growth of GGG ($Gd_3Ga_5O_{12}$), on YAG ($Y_3Al_5O_{12}$), and the same combination has been used to demonstrate

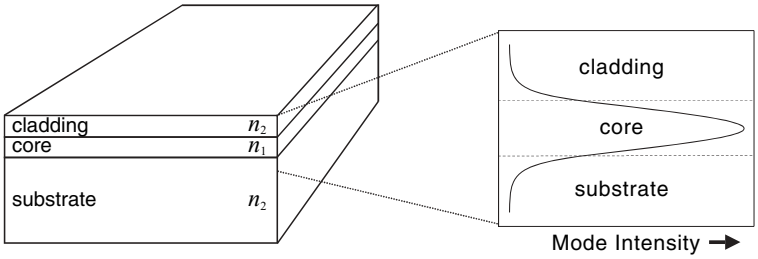

Figure 17.2 Symmetric planar waveguide structure where the core region is surrounded by cladding and substrate materials of the same refractive index. Note the symmetric optical mode intensity profile in this case.

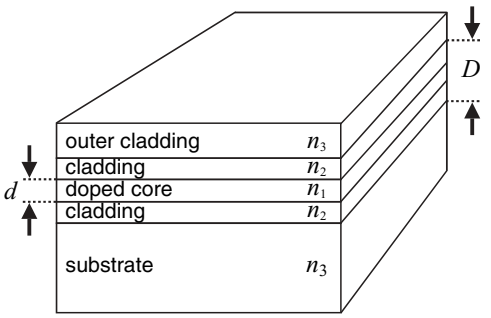

Figure 17.3 Five-layer symmetric waveguide structure that can be used as a large-mode-area or double-clad waveguide.

core depths as large as 135 μm [May-Smith et al., 2004]. For such a high NA, even a 1 μm thick guide is multimode at a wavelength $\lambda = 1\mu$m. If, however, a guide were fabricated by growing Nd-doped GGG on undoped GGG, leading to an NA of 0.04, single-mode propagation would occur for waveguide depths up to 13 μm.

One of the main areas of interest for planar waveguides of the type described so far is for high-power diode-pumped lasers [Shepherd et al., 2001; Lee et al., 2002], as the planar film can be seen as an ultrathin slab with all of the associated good thermal management properties. Another attractive feature is that the asymmetry of the output of high-power diode pump sources can be matched to that of the planar waveguide, especially in side-pumped configurations, leading to simple and efficient coupling designs. High values of NA, such as those described above, can even allow simple direct proximity coupling of diode bars without the requirement for any in-coupling optics. PLD also allows the possibility of fabricating multilayered structures, which can be thought of as the analog of large-mode-area and double-clad designs used in high-power fiber lasers. Figure 17.3 shows a typical design that can act as a large-mode-area or double-clad waveguide depending on the parameters used.

In both cases the inner cladding waveguide parameters [depth D, NA $= (n_2^2 - n_3^2)^{1/2}$] are chosen to produce a highly multimode guide that can easily be coupled to one or more high-power diode pump lasers, with consequent absorption of the pump light in the doped core region. In the cladding-pumping case the parameters of the doped core are chosen such that it forms an independent single-mode waveguide that delivers diffraction-limited output laser power. The pump absorption length, however, will be increased by the ratio D/d, which may be too large for practical planar devices. For the large-mode-area design the size and index difference of the core is kept at a level where it does not act as an independent waveguide but rather simply acts to select fundamental mode laser operation from the multimode cladding guide, due to the better spatial overlap of the gain with this mode. It has been shown [Bhutta et al., 2002] that such a design can robustly select fundamental mode operation even under conditions of high gain saturation and with D/d ratios of just 1.7.

For many applications a channel structure giving guidance in two dimensions is preferred. Such waveguides can be fabricated by a variety of techniques, depending upon the materials used, once the initial layers have been grown by PLD. Figure 17.4 shows various options for the channel structures where $n_1 > n_2, n_3$. In all cases lateral confinement occurs because the average index under the raised regions is higher than the surroundings (assuming the structures are surrounded by air). The strip-loaded guide (a) can be formed by etching of a cladding layer deposited over a core layer, while the ridge (b) and rib (c) are fabricated by directly etching the core layer. Techniques such as ion exchange, ion diffusion, or optical writing may also be used to create channel structures if the deposited layers are compatible with such techniques.

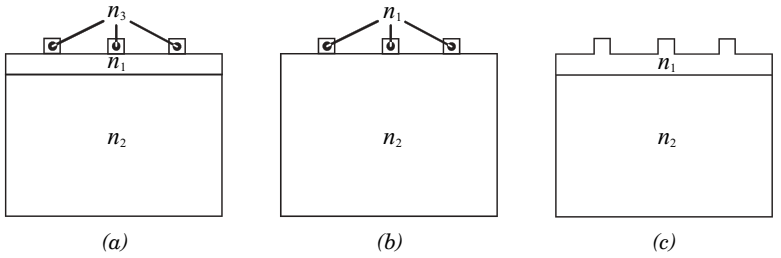

Figure 17.4 Three examples of routes to channel structures from planar guides: (a) strip-loaded guide, (b) ridge guide, and (c) rib guide.

17.4 OPTICAL QUALITY AND WAVEGUIDE LOSS

One of the most important aspects of waveguide fabrication is that the technique used should not introduce any additional propagation losses over those present in the bulk material or alter properties such as nonlinearity, electrooptic coefficients, or the valence state of dopants required for subsequent laser action, for example. As described in Section 17.1, this goal is not met for all techniques, however, and any such increase in propagation loss or modification of material parameters may result in unwanted effects such as reduction of gain or efficiency, increased values of threshold or time response, and many other deleterious effects that reduce the intrinsic benefit to be obtained from such waveguide geometries. It is very important, therefore, when growing films by PLD, to be able to accurately quantify propagation losses and to undertake detailed spectroscopic studies of the films produced to determine parameters such as the concentration, valence state, lifetime, and spatial distribution of any dopant that is intended for inclusion within the waveguide region. As will be discussed in Section 17.5, spectroscopy can readily reveal the correlation of these properties with the quality of the host material itself.

Clearly, if the waveguide host is of poor crystal quality, then dopant inclusion that is intended to be substitutional can no longer be so readily achieved, leading to spectral broadening of absorption and emission processes, which in turn leads to increased pump laser thresholds and reduced gain. In this sense, optimization of host quality and dopant inclusion must be addressed together, a difficult task in some cases, as growth parameters such as background chamber pressure, laser fluence, or target stoichiometry can be quite different for each process. The solution we have adopted is to grow waveguides from materials such as garnets, which grow relatively easily and are readily available as single-crystal targets that can be sourced commercially with a range of initial dopant concentrations. For waveguide growth of materials such as $Ti:Al_2O_3$, the situation is more complicated still, as single-crystal sapphire (α-alumina) does not grow below a substrate temperature of $\sim$950°C [Yu and Nastasi, 1994; Lucuta et al., 1992], while the concentration of the Ti dopant, present in the desired Ti^{3+} valence state, progressively decreases above $\sim$1000°C [Anderson et al., 1997a]. We have chosen, therefore, to focus on a limited range of host–dopant combinations and have concentrated on optimized growth of low-loss, high crystalline quality active waveguide devices, reporting values of waveguide loss as a matter of routine.

The final aspect of PLD growth of waveguides concerns the issue of particulates within the film. It is an unfortunate coincidence that the average size of such particulates (0.1–1.0 μm) is an almost perfect match to the size of particle that contributes most to the increase of optical propagation loss, being roughly equal to the value of the wavelength of light used in the waveguide. Our solution to this, detailed in Section 17.4.3, has been twofold: first, to attempt to remove the particulate inclusion in the film by use of a synchronized pulsed gas-jet and, second, to bury those particulates that are present within the film by a second capping layer, thus producing a more symmetric waveguide structure.

17.4.1 Waveguide Loss

It is unfortunate that accurate and routine measurement of propagation loss for millimeter–centimeter length samples is extremely difficult, unlike the case for an optical fiber, for example, where loss measurement is comparatively straightforward when many kilometers of fiber are available and the simple cut-back technique is used. Propagation losses are perhaps the most important factor in judging the quality of PLD waveguides, and publications that do not quote this value are of little use in assessing the utility of guides where waveguide action is stated or implied as the prime motivation for growth.

Loss is conventionally measured in decibels per centimeter (dB cm^{-1}), where the decibel is defined as:

$$\mathrm{dB} = -10 \log\left(\frac{P_{\mathrm{out}}}{P_{\mathrm{in}}}\right) \tag{17.2}$$

and P_{in} and P_{out} are defined as the optical power that is in-coupled and out-coupled at the waveguide entrance and exit faces, respectively. The minus sign is often omitted in Eq. (17.2) when it is clear that the decibel value relates to optical *loss*. Care must be taken when using Eq. (17.2), however, as factors such as the Fresnel intensity reflection coefficients from the waveguide end faces and reflection losses that occur from all coupling optics must be taken into account when quoting *absolute* values of waveguide loss. Even relatively high losses of order 10 dB cm^{-1}, equivalent to an intensity transmission of 10%, may be acceptable, if, for example, the device length used is only 1 mm. As stated earlier, it is imperative to faithfully report all values of waveguide loss when these have been measured.

There are three main processes that contribute to loss in a normal straight optical waveguide. In order of importance for PLD waveguides, these are:

1. *Scattering* Scattering loss is normally the dominant form of loss in dielectric waveguides. Imperfections or defects in the guide structure or the presence of surface particulates can cause out-of-plane scattering, which can lead to large (10's of dB cm^{-1}) values of propagation loss. Poor crystallinity, mixed growth phases, or incorrect stoichiometry can all contribute to scattering loss, and tools such as X-ray diffraction (XRD) analysis are poor at providing an insight into what is, or is not, a low-loss PLD waveguide. In our experience, films that are highly nonuniform or uneven and, therefore, unsuitable for waveguide applications can still show reasonable XRD spectra, for example. The only way to evaluate PLD waveguides is to measure their loss using methods described below. Growth of complex uniaxial or biaxial films can be particularly prone to scattering loss, as any polycrystalline or mosaic growth will introduce refractive index inhomogeneity, which renders the film effectively useless for waveguide device applications. For this reason we have optimized the growth of garnet hosts, such as YAG, YGG ($Y_3Ga_5O_{12}$), and GGG, which are cubic materials and hence suffer much less from this form of refractive index nonuniformity.

2. *Mode Conversion* This is also a form of scattering, but the light is retained within the guide, rather than being scattered to the outside medium. Mode conversion can occur from guided modes to radiation modes that are no longer confined to the waveguide core region, from a mode of one order to a higher order, or between modes of the same order but different polarization states, that is, from transverse electric (TE) to transverse magnetic (TM), for example.

3. *Optical Absorption* As in bulk materials, this occurs from the presence of either intentionally incorporated dopant atoms or unintentionally incorporated impurities. For lasing waveguides, dopant inclusion is a prerequisite, but there is the additional consideration of the correct valence state required for these atoms. In studies of the growth of Ti : Al_2O_3, ourselves and other groups [Anderson et al., 1997a; Dyer et al., 1997] have sought to maintain the correct Ti^{3+} valence state, while minimizing the highly absorbing Ti^{4+} alternative. Control of these valence states in PLD-grown films is possible through the normal deposition parameters such as laser

fluence and background gas pressures used, but such precision is not always achievable for all host–dopant combinations. The incorporation of unintentional impurities can also be minimized through optimized substrate heating techniques. We routinely use a raster-scanned CO_2 laser for substrate heating [Barrington and Eason, 2000], rather than more conventional hot filament heaters, as the latter invariably heats the entire deposition chamber to excessive temperatures, where outgassing of previously deposited materials can introduce unwanted impurities, and hence loss into the growing film.

17.4.2 Loss Measurement Techniques

Accurate determination of propagation loss is always complicated when nondestructive methods are required, and the waveguide is intended for some future application. If the reverse is true, and the sole purpose is to evaluate the loss, then the method of *cut-back* can be used as applied routinely for optical fibers. Several methods exist for estimation, or ideally, precise measurement of waveguide loss, and while it is comparatively easy to tell if the guide is either extremely good (low loss) or extremely poor (high loss), obtaining accurate measurements for guides where the loss falls in the $\sim 0.1-1.0\,\mathrm{dB\,cm^{-1}}$ region is often frustratingly difficult. We have resorted to loss evaluation, for our best guides, via the Findlay–Clay method [Findlay and Clay, 1966], which requires laser action within the guide using a range of different reflectivity output coupling mirrors. Using this technique, losses of order $0.1\,\mathrm{dB\,cm^{-1}}$ are relatively easily determined.

17.4.2.1 Cut-back Technique

As the name suggests, the cut-back technique relies on repeated measurement of the out-coupled power from a waveguide whose length is progressively reduced following each measurement of output power. The in-coupled power is assumed or arranged to be constant for each measurement, so the only unknown, the waveguide transmission, is readily determined from the gradient of a plot of out-coupled power versus guide length. If the guide is, for example, 1 cm in length, then this technique may be implemented using an angled-polished sample, as illustrated in Figure 17.5.

Light is launched into, and out-coupled from, the guide using two microscope objective lenses, whose transmissions have been measured to be T_1 and T_2, respectively. Taking account of the Fresnel intensity reflection coefficients R_1 and R_2, for the waveguide's input and output faces, the in-coupling and out-coupling efficiencies C_1 and C_2, and the values of input power P_1, and output power P_2, measured before and after the two microscope objectives respectively, the powers present in the guide at the input and output faces, P_{in} and P_{out}, are therefore given by:

$$P_{\mathrm{in}} = P_1 T_1 (1 - R_1) C_1 \tag{17.3}$$

$$P_{\mathrm{out}} = \frac{P_2}{T_2 (1 - R_2) C_2} \tag{17.4}$$

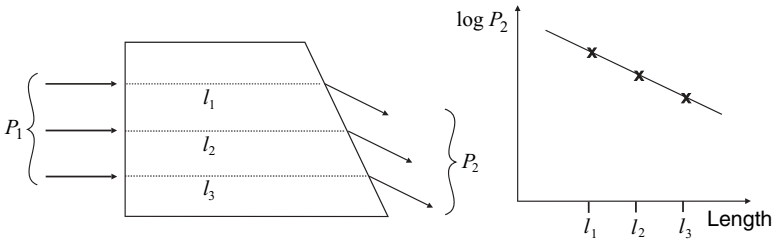

Figure 17.5 Implementation of cut-back technique to evaluate optical waveguide loss in a single planar waveguide sample.

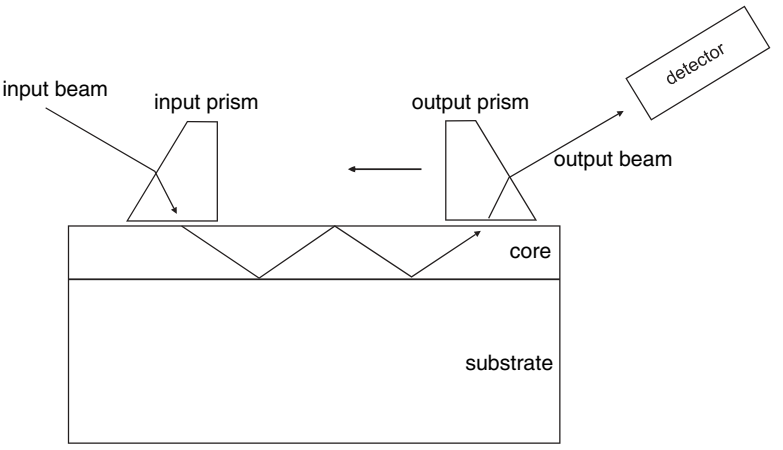

Figure 17.6 Sliding prism technique for loss measurement in a planar waveguide.

Although the values of T_1, T_2, R_1, and R_2 are known or calculable, values of C_1 and C_2 always remain uncertain. Using Eqs. 17.3 and 17.4, measurements of P_1 and P_2 for several different lengths of guide allows the values of C_1 and C_2 to be eliminated, and the loss can be determined from the gradient of the graph of log P_2 versus guide length. With reference to Figure 17.5, sequential measurements of P_2 across the guide width yield a good estimate of propagation loss. The one assumption here, which may not always be rigorously true, is that C_1 and C_2 do not vary between each measurement.

17.4.2.2 Sliding Prism Technique

This method is a nominally nondestructive technique that uses prisms instead of microscope objectives to couple light into and out of the top face of the waveguide instead of the ends [Weber et al., 1973]. As shown in Figure 17.6, two prisms are clamped onto the surface of the waveguide and, as with the cut-back method, incident and exit powers, P_1 and P_2, are measured. The unknown coupling efficiencies can again be eliminated by measuring P_2 as a function of the separation between the two prisms, and a plot of log P_2 versus separation yields a value of propagation loss.

This technique has several drawbacks, however. First, the out-coupling prism must have the same out-coupling efficiency for each measurement, a requirement that can be hard to fulfill if the waveguide surface is uneven or has defects or large numbers of particulates. Second, the prisms are usually made from rutile, TiO_2, a material that is extremely hard and can easily damage the waveguide during the measurements. The best procedure is to move the out-coupling prism *toward* the input prism, thereby eliminating spurious measurements from any previously damaged sections of waveguide.

17.4.2.3 Streak Imaging

This is a more recent method that uses a charge-coupled device (CCD) camera to image, capture, and analyze the streak of light that is visible from a waveguide whose loss is high enough to show some measurable scattering [Okamura et al., 1983]. Although it is easy to perform, calibration of the CCD camera is all-important, and the technique is somewhat self-defeating. If the loss is high enough to produce a visible and measurable streak of light, it is probably much higher than the value you would like. If, however, the loss is low, the precision of the technique is also low, and hence an accurate loss evaluation is hard to obtain. Other variants that can be usefully implemented use an optical fiber to collect the light instead of a CCD camera [Nourshargh et al., 1985].

17.4.2.4 Findlay–Clay Method

Propagation losses calculated using the Findlay–Clay method give a ''worst-case scenario'' estimation for loss and are the preferred method for lasing waveguide samples. For a four-level laser transition, significant depopulation of the ground state does not occur, and the absorbed pump power threshold for lasing is then only dependent upon the propagation loss and the value of output coupling, as given in Eq. (17.5):

$$P_{\text{th}} = C[(2\alpha_{\text{PL}} l) - \ln(R_1 R_2)] \tag{17.5}$$

where P_{th} is the incident power threshold for lasing, C is a constant containing material and waveguide parameters and the launch and absorption efficiencies, α_{PL} is the propagation loss coefficient, l is the laser cavity length, R_1 is the intensity reflectivity of the input coupling mirror, and R_2 is the intensity reflectivity of the output coupling mirror.

The threshold power for lasing must be measured using output coupling mirrors with various different values of reflectivity. A plot of absorbed power threshold for lasing versus $-\ln(R_1R_2)/2l$ should then give a straight-line trend. The intercept corresponding to the value $P_{\text{th}} = 0$ yields a value of the propagation loss coefficient α_{PL}, from which the loss in dB per cm is obtained via Eq. (17.6):

$$\text{Propagation loss } (\text{dB cm}^{-1}) = 10 \log_{10}(e^{-\alpha_{\text{PL}}}) \tag{17.6}$$

To date, as will be discussed in Section 17.5, our lowest value of waveguide loss has been measured as $<0.1\,\text{dB cm}^{-1}$ for Nd:GGG, a value that is close to the bulk value for this material.

17.4.3 Particulates on the Waveguide Surface

Particulates are extremely undesirable for waveguide applications of PLD films, and much effort has been expended to both reduce the particulate density and the effect of their presence on lasing performance. After consideration of the full range of particulate removal schemes, which include cross plumes, spinning targets, mechanical shutters, and velocity selectors, we have investigated the use of a synchronized pulsed gas-jet, achieving a reduction in the number of particles by at least one order of magnitude. Given the fact that *total* removal is almost impossible, we have also grown lasing waveguides over a range of thicknesses and investigated the effect of overgrowing capping layers on existing lasing guides. We observe a significant improvement in lasing performance by these means and have investigated the reduction in absolute particle number as a function of gas-jet operating parameters. Although the gas-jet is useful for particle reduction, it must be stated that the technique is still not entirely systematic, and further work is required to optimize this method. We show here the best, rather than the typical, results we have obtained.

The trials with the pulsed oxygen gas-jet followed the earlier work of Murakami [1992]. The gas valve used was a piezoelectric device (highly modified Maxtek, MV-112, USA) with an opening time of $\sim$200 μs, positioned with the nozzle 2 mm below the ablated target area. Typical time delays between gas valve and laser pulse triggering were 1 ms. The backing pressure of the oxygen was 2 bar, and the valve was kept open for a duration of 3 ms, to achieve an oxygen chamber pressure of $\sim 5 \times 10^{-2}$ mbar. Figure 17.7 shows optical microscope pictures of two films of GGG grown on (100) YAG substrates, without (a) and with (b) the gas-jet directed into the plume.

It is clear that the film grown with gas-jet assist has a substantially lower particulate density. A study was performed of total particulate count for various gas-jet parameters, and films were grown with densities of between 10^4 and 10^7 particulates cm^{-2}. It is difficult to state that this reduction is entirely due to the gas-jet, as some variability in particulate density is an intrinsic part of all PLD growth and depends on target degradation and other factors. A comparison was made, however, between particulate size distributions with and without gas-jet assist, and this is shown in Figure 17.8 [Barrington et al., 2000].

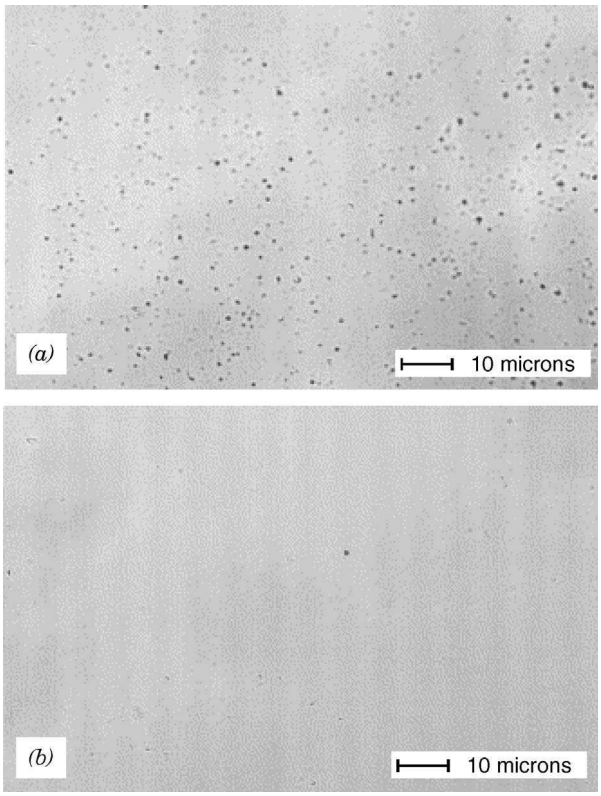

Figure 17.7 Optical microscope pictures of two films of GGG grown on (100) YAG substrates, without (a) and with (b) the gas-jet directed into the plume.

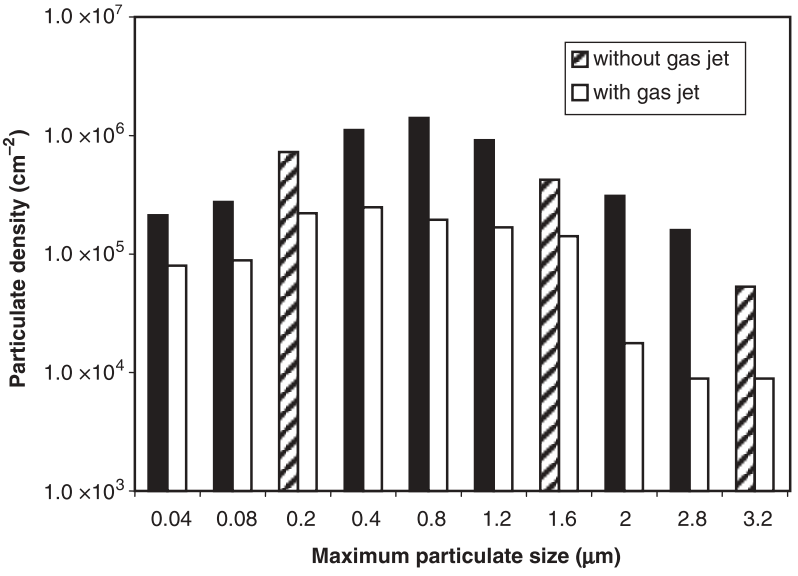

Figure 17.8 Particulate size distributions with and without gas-jet assist.

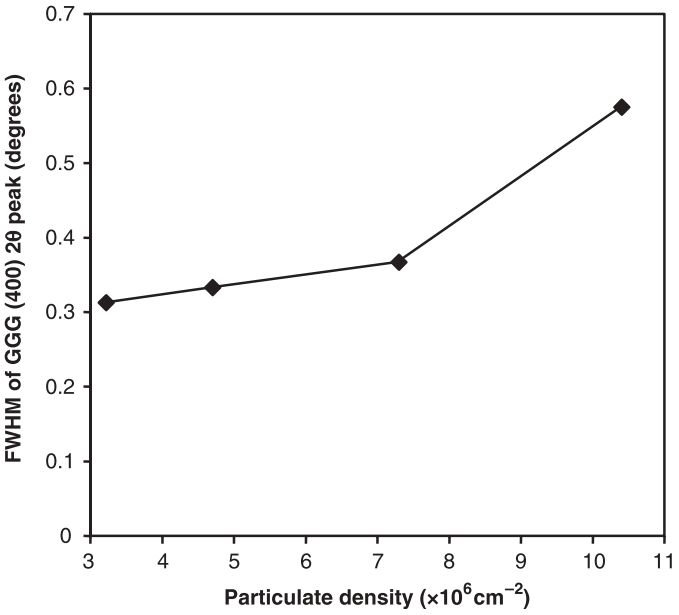

Figure 17.9 FWHM for the (400) GGG XRD peak as a function of the measured particulate density.

It is seen therefore that there is an approximate order of magnitude reduction in particulate density at particle sizes of order 1 μm, and this translates into correspondingly lower waveguide loss, and hence laser threshold. A final comparison was made between the XRD spectra for films grown with a fairly high particulate density between 3×10^6 and $1.1 \times 10^7\,\mathrm{cm}^{-2}$, and the results are shown in Figure 17.9. The XRD peak was the (400) reflection from a 4-μm-thick GGG film, and the full-width at half-maximum (FWHM) value is seen to increase in proportion to the particulate density indicating the progressive degradation of crystalline quality.

17.5 WAVEGUIDES GROWN BY PLD

A wide range of optically waveguiding materials have been grown by PLD. Only a selection of these materials has been chosen, however, for further discussion within this chapter. The rationale behind this decision concerns the difference between publications that refer to waveguide end goals on the one hand (we have found more than 500 references to date) and those that report quantitative performance in terms of optical loss, gain, lasing, amplification, or other functional performance.

17.5.1 Garnets

Garnet crystals (possessing the generic formula $A_3B_2C_3O_{12}$ or often $A_3B_5O_{12}$) have been used as bulk laser host materials for almost 30 years [Singh et al., 1974] and are still perhaps the most useful and adaptable solid-state laser hosts available. Doped garnets have the unique combination required for laser materials: good spectral and stimulated emission properties, a high degree of mechanical strength and hardness, broad-band transparency, considerable thermal conductivity, and can be grown to large sizes for comparatively modest costs. In thin-film form, all these desirable properties are combined with the waveguide advantages discussed previously, and therefore PLD growth of these lasing films is a logical and technologically useful research goal.

The range of alternative fabrication techniques suitable for thin-film growth of such ternary compounds is rather limited, however, and hence PLD presents itself as perhaps the ideal process. To date most of PLD growth of garnets has focused on YAG and GGG, due to both their relative ease of growth, and their closely matched lattice constants (YAG: 12.006 Å, GGG: 12.383 Å), which results in a 3.1% overall lattice mismatch. All these crystals are cubic, and hence optically isotropic, leading to potentially very low values of waveguide loss for epitaxial thin-film growth.

The growth of undoped GGG was first reported in 1995 [Gill et al., 1995a], and since then, the successful growth of Nd-doped GGG on YAG substrates has been reported several times, with losses that have fallen from initial values of $\sim 5.7\,\mathrm{dB\,cm^{-1}}$ [Gill et al., 1996] to $\sim 0.5\,\mathrm{dB\,cm^{-1}}$ [Bonner et al., 1997, Anderson et al., 1997b]. Other dopants such as Cr [Fukaya et al., 2001a], and co-doping with Nd and Cr [Fukaya et al., 2001b] have also been incorporated into GGG. More recently, a 40-μm-thick film of Nd : GGG has been grown and successfully operated as a laser [May-Smith et al., 2004; Grivas et al., 2004], allowing a Findlay–Clay loss measurement of $0.1\,\mathrm{dB\,cm^{-1}}$ to be deduced; this extremely low level of loss is very encouraging for further integrated optical PLD laser designs. The laser performance of such Nd:doped GGG waveguide lasers is discussed in Section 17.6.

In general, the structure of the GGG on YAG films show properties that are similar but not exactly equivalent to their bulk counterparts. Rutherford backscattering (RBS) analysis of all GGG on YAG films grown to date reveals a slight Ga deficiency, and this translates into a fluorescence spectrum that is broadened and reduced in peak height when normalized to the spectrum obtained from the target GGG crystal used. This broadening in fluorescence spectrum is mirrored by a broadening of the absorption spectrum from the Nd dopant; in fact this turns out to be a useful consequence in terms of a higher absorption efficiency when pumping the waveguide laser with diode laser sources, whose spectral bandwidth can be broader than the intrinsic absorption bandwidth for perfect GGG crystal samples. Attempts to correct the Ga deficiency have not so far been made through the use of a secondary Ga source or nonstoichiometric GGG targets.

Rare-earth and transition-metal-ion-doped YAG films have also been grown by PLD, but to date YAG-based films have not successfully been operated as laser media. Growth of Nd : YAG on various substrates [Ezaki et al., 1995, 1996; Kumagai et al., 1997; Vainos et al., 1998] has been reported by many groups, while other dopants such as Cr [Fukaya et al., 2001a], Tb [Hirata et al., 1996], Yb [Shimoda et al., 2001], and Er [Jelinek et al., 2002a] have received less attention. YAG film thicknesses up to 5 μm only have been grown by PLD, and, as before, the fluorescence properties are a close match to existing bulk YAG samples. The drawback of growing YAG thin films, however, is that there is no convenient garnet substrate that would enable subsequent waveguide action to occur, as YAG has the lowest refractive index of the commonly available garnet family, as shown in Table 17.1. Other substrate materials with common mechanical and thermal properties and a refractive index of ~ 1.8 or less would therefore be required.

Aside from lasing thin-film materials, YIG ($Y_3Fe_5O_{12}$), a magneto-optic host material has also been successfully grown via PLD for applications in magnetic field sensing. The first report of YIG growth was in 1991 [Kidoh et al., 1991], and since then buried single-mode waveguides with losses of $\sim 1\,\mathrm{dB\,cm^{-1}}$ have also been grown [Katoh et al., 1992, 1993]. More recently, YIG planar waveguide magneto-optic devices have been developed for applications in areas such as optical current transformers [Hayashi et al., 2002a] and electric current sensors [Hayashi et al., 2002b].

Other ternary garnets such as $Y_3Ga_5O_{12}$ (YGG) and $Gd_3Al_5O_{12}$ (GAG), as well as quaternary garnets such as $Y_3Sc_2Ga_3O_{12}$ (YSGG), $Y_3Sc_2Al_3O_{12}$ (YSAG), $Gd_3Sc_2Ga_3O_{12}$ (GSGG), and $Gd_3Sc_2Al_3O_{12}$ (GSAG) present themselves as an attractive way for PLD to achieve epitaxial multilayer structures suitable for cladding pumped laser designs because of the good lattice match and most importantly slightly different refractive indices of these alternative garnets. So far, however, there has been only one report of the growth of such a material by PLD, namely Nd,Cr : GSGG [Willmott et al., 2000]. We have recently conducted feasibility experiments for several of

TABLE 17.1 Material Properties of a Range of Garnet Hosts[a]

Material	Refractive Index (at $\lambda = 1.06\,\mu m$)	Thermal Expansion Coefficient ($\times 10^{-6}\ K^{-1}$)	Lattice Constant (Å)	Lattice Mismatch to YAG (%)
YAG	1.82	6.9	12.006	—
YGG	1.91	—	12.273	2.2
YSAG	1.86	—	12.271	2.2
YSGG	1.93	8.1	12.446	3.7
GAG	—	—	12.113	0.89
GGG	1.95	8.3	12.383	3.1
GSAG	1.89	7.7	12.389	3.2
GSGG	1.94	8.0	12.544	4.5

[a]All values from an extended literature and web search.

these alternative garnets, including YGG, YSAG, GSAG, and GSGG, and have found that they all grow very successfully with similar optimal conditions as were used for GGG films previously. The possibility of growing alternative garnets such as these appears to only be limited by the availability of suitable targets. Table 17.1 summarizes the available data on materials within the garnet family showing their respective refractive indices and lattice constants.

17.5.2 Oxide Materials

Binary compounds such as sapphire (Al_2O_3) and yttria (Y_2O_3) are frequently used laser hosts, owing to their excellent transparency range (~ 0.2 to $> 6.0\,\mu m$), low thermal expansion, high mechanical strength, and good thermal conductivity. Their relatively simple stoichiometry (A_2O_3) make them ideal materials for PLD growth, and when grown as a doped homoepitaxial layer, for example, Ti-doped Al_2O_3 on Al_2O_3, excellent film quality can result [Anderson et al., 1997a].

Sapphire, (α-Al_2O_3), is only one of a range of at least seven structural phases that have been identified for the Al_2O_3 crystalline family, and the structure can be classified as either rhombohedral or hexagonal. This anisotropy, which is not present, for example, in the garnet family of laser hosts, makes the growth of high-quality single-crystal material a very important factor when waveguide applications are the intended goal. Below a temperature of $\sim 950°C$, PLD growth leads to the presence of other Al_2O_3 phases, and this will inevitably lead to unacceptably high levels of scattering and hence waveguide loss.

Thin sapphire films have been grown with the inclusion of various dopants, although the most widely reported element has been titanium. Commercial Ti : sapphire is available with moderate dopant levels of $\sim 0.1\%$ only, as the titanium ion has limited solubility within the sapphire lattice. Lasing thin films of Ti : sapphire have been grown with thicknesses exceeding $10\,\mu m$ [Anderson et al., 1997c; Vainos et al., 1998] and losses as low as $1.5\,dB\,cm^{-1}$. Er has also been used as a dopant in sapphire thin films [Serna and Afonso, 1996], but to date no lasing action has been observed. Such planar waveguides can be further processed to fabricate ridge or rib waveguides that can be optimized for single-mode propagation, using the techniques of lithography followed by reactive ion beam etching or Ar^+ beam milling. Such ribs have been successfully etched on Ti : sapphire PLD films [Crunteanu et al., 2002; Grivas et al., 2003], and the resulting measured values of loss of $1.7\,dB\,cm^{-1}$ indicate that such postprocessing does not contribute any significant extra loss. The excellent optical confinement properties within these rib guides and measured beam propagation factors M_x^2 and M_y^2 of 1.12 and 1.16 for the in-plane and out-of plane axes, respectively, show that the formation of channel waveguides in existing PLD planar thin films is an extremely useful secondary processing step. Laser operation of such Ti : sapphire ribs has recently been performed and will be discussed in detail later in this chapter.

Yttria thin films have been grown by PLD [Craciun et al., 1999], and good results have also been achieved for Er-doped yttria using (0001)-oriented sapphire substrates [Korzenski et al., 2001;

Lecoeur et al., 2002] where single-crystal growth of (222)-oriented yttria has been observed. Sapphire is a good choice of substrate material for yttria films because it has the required lower refractive index (yttria: $n = 1.78$; sapphire: $n = 1.75$ at $\lambda = 1.06\,\mu m$), making optical waveguiding possible for this combination. For Er-doped films, optical losses have been reported as $\sim 1\,dB\,cm^{-1}$ [Korzenski et al., 2001; Pons-Y-Moll et al., 2002]. Nd-doped YAP films (yttrium aluminum perovskite) have also been grown with similar $\sim 1\,dB\,cm^{-1}$ reported loss values, with thicknesses up to $11.2\,\mu m$, and good fluorescence properties in agreement with their bulk material counterparts [Lancok et al., 1999].

17.5.3 Ferroelectrics

There is a continuing interest in ferroelectric thin-film materials because of their unique combination of material properties and applications. Their nonlinear, electrooptic, piezoelectric, acoustooptic, photoelastic, photorefractive, and pyroelectric properties make them ideal for use in optical devices for a range of applications such as switches, sensors, microelectromechanical systems (MEMS), and integrated optoelectronic components. Planar and subsequent channel or waveguide devices can be fabricated from PLD-grown films with suitable further processing. Problems can be experienced with ferroelectric films due to both their physical fragility, and also due to their susceptibility to optical damage (via the photorefractive effect). Ferroelectric materials are optically anisotropic, so thin films must be single crystal to be of any significant use for optical or nonlinear optical applications. Furthermore, these single-crystal films must also be oriented as single *domain* materials for any application that is dependent on those tensorial coefficients that determine nonlinear, piezoelectric, pyroelectric, or other properties. Initially multidomain samples can be converted into single domain films by repoling after growth, but this process relies on electric field postprocessing and hence electrodes are required above and below the PLD-grown film.

Lithium niobate is perhaps the archetypal ferroelectric material that is currently in widespread use in integrated waveguide modulators. Although its range of coefficients is not as large as some ferroelectric hosts, it is a well-understood material, and, in bulk crystal form, is readily available with consistent material properties. Thin films have been grown on sapphire by many groups [Noh et al., 1998; Kim et al., 1998; Tomov et al., 2000], with reported losses as low as $3\,dB\,cm^{-1}$ [Kim et al., 1998], and also on silicon with a SiO_2 buffer layer [Guo et al., 1996], for which films of $2\,\mu m$ thickness have been grown. The most important point, however, is to grow and demonstrate *active* ferroelectric films, and this has been done with both undoped lithium niobate where second-harmonic generation was observed [Chaos et al., 2000], and doped films, where fluorescence properties of Nd-doped films [Alfonso et al., 1997], and enhanced second-harmonic generation in Er-doped films has been reported [Gonzalo et al., 2002].

Other ferroelectric thin films grown by PLD include potassium niobate on MgO substrates [Zaldo et al., 1994; Beckers et al., 1998a], with thicknesses up to $1\,\mu m$, intended for nonlinear and electrooptic applications, and strontium barium niobate (SBN) films on MgO and fused silica substrates [Schwyn-Thony et al., 1994; Fernandez et al., 2002] with thicknesses up to $6\,\mu m$. For these amorphous substrate materials partially crystalline films only were obtained, which would severely limit any subsequent optical application. Lithium tantalate thin films have been grown on sapphire substrates [Agostinelli et al., 1993; Shibata et al., 1993] with reported losses of order $\sim 1.0\,dB\,cm^{-1}$, and have been successfully used as surface acoustic wave (SAW) filters.

Thin-film ferroelectric materials are perhaps one of the most important examples of PLD waveguide devices due to their potential for real end applications, as has been indicated above. With this in mind, it is very important that authors report on the *optical* quality of films produced where waveguide action is required and devices such as modulators or frequency conversion are intended. Barium titanate ($BaTiO_3$), a material with the largest known value of electrooptic coefficient ($1600\,pm\,V^{-1}$) among inorganic crystals, is just such a material. The first report of PLD growth of $BaTiO_3$ [Davis and Gower, 1989] did not, of necessity, address issues such as optical

losses, domain orientation, or applications. The most recent reports [Beckers et al., 1998b; Petraru et al., 2002; Wang et al., 2002] show that factors such as losses, buffer layers, domain orientation, and device performance are the criteria by which successful growth is to be judged. Twin target techniques have also been used for growth of cobalt-doped $BaTiO_3$ films in an attempt to simultaneously improve the photorefractive gain coefficient and decrease the response time [Ito et al., 1997].

Thin waveguide ferroelectrics have also been grown for applications such as second-harmonic generation. Beta barium borate (BBO) is a highly suitable material for this application due to its wide transparency range, large second-harmonic generation (SHG) coefficients, and high damage threshold, and thin-film BBO has been grown on Si, SiO_2, and Al_2O_3 substrates [Liao et al., 1997]. Potassium titanyl phosphate (KTP) displays similar properties to BBO, and both undoped [Xiong et al., 1994] and Er-doped film growth [Wang et al., 1998; Wang et al., 2001] have been reported. A third material is barium sodium niobate (BNN), which in its bulk form is difficult to grow. Optical quality films of BNN grown on KTP substrates have been reported with losses at the $\sim 1.0\,\mathrm{dB\,cm^{-1}}$ level [Liu et al., 1996; Zhang et al., 1999].

17.5.4 Glasses

Thin-film glass deposition might be considered as a natural and straightforward application area for PLD. Glass is an optically isotropic material, with a wide and controllable transparency range, and deposition should not require any considerations of epitaxy and hence single-crystal substrate materials. In fact, the losses associated with PLD glass films appear to be considerable, and are up to a factor of ~ 10 times higher than the typical best values for crystalline material growth. Er–Yb co-doped glass films have been reported with losses at the $\sim 11\,\mathrm{dB\,cm^{-1}}$ level [Serna et al., 1998], while chalcogenide (nonoxide) glasses have been deposited to thicknesses of a few microns with measured losses of $\sim 6\,\mathrm{dB\,cm^{-1}}$ [Youden et al., 1993; Gill et al., 1995b]. PLD-grown chalcogenide films have been used for studies of photobleaching, photodarkening, photodoping, and the writing of gratings using both laser and electron beam irradiation [Gill et al., 1995b]. The lowest losses reported for glass films, to the best of our knowledge, is $2.1\,\mathrm{dB\,cm^{-1}}$ for lead germinate glasses [Mailis et al., 1998, 1999], which were grown to explore their photosensitivity and applications in waveguide grating devices.

Further work is clearly needed to develop glass deposition to the point where losses of order $< 1\,\mathrm{dB\,cm^{-1}}$ can be achieved. Atomic force microscopy (AFM) examination of films grown to date [Mailis et al., 1999] reveals a surface that is formed from 50- to 100-nm-diameter particles, rather than a continuous smooth and glassy surface. We do not believe this is an intrinsic characteristic of PLD glass deposition, however, and further work is in progress in this area. Interestingly enough, there was a distinct difference between film deposition using the excimer laser wavelengths of 248 and 193 nm. At 248 nm, the films displayed particulate growth but were highly photosensitive, displaying induced refractive index changes of $\sim 1\%$, while the 193 nm grown films were considerably smoother but appeared to be nonphotosensitive.

17.5.5 Semiconductors

This topic is covered in several other chapters and hence we will not explore the area in any detail here. In passing, we note that CdS and CdSe films have been grown and examined for their photoluminescence and lasing properties [Perna et al., 2001; Bagnall et al., 2000]. The resultant in-plane hexagonal periodic structures can form microcavities, and lasing has been observed in particular from CdS films. ZnO, which is the subject of Chapter 12, has also been observed to lase in this fashion, producing ultraviolet laser emission via such self-assembled microcrystallite structures [Tang et al., 1998].

A summary of a representative range of PLD grown waveguide materials as discussed in section 17.5 is presented in Table 17.2.

TABLE 17.2 Representative Range of PLD Waveguide Materials and Their Thickness, Optical Loss, and End Use

Material	Max Film Thickness (μm)	Lowest Loss ($dB\,cm^{-1}$)	Most Significant Results
Garnet Crystals			
GGG	135 [May-Smith et al., 2004]	0.1 [May-Smith et al., 2004; Grivas et al., 2004]	Lasing
YAG	5 [Fukaya et al., 2001a; Shimoda et al., 2001]	—	Fluorescence
YIG	4.5 [Higuchi et al., 2001]	1 [Katoh et al., 1993]	Waveguiding and MO effect
GSGG	—	—	Fluorescence
Oxides			
Al_2O_3	12.3 [Vainos et al., 1998; Anderson et al., 1997c]	1.5 [Vainos et al., 1998]	Lasing of planar and rib waveguides
Y_2O_3	1.5 [Lancok et al., 2004]	1 [Korzenski et al., 2001; Lecoeur et al., 2002; Pons-Y-Moll et al., 2002; Lancok et al., 2004]	Fluorescence
YAP	11.2 [Lancok et al., 1999]	<1 [Lancok et al., 1999]	Fluorescence
Ferroelectrics			
$LiNbO_3$	2 [Guo et al., 1996]	3 [Kim et al., 1998]	Waveguiding, SHG, EO effect, and fluorescence
$KNbO_3$	1 [Zaldo et al., 1994]	—	—
SBN	6 [Fernández et al., 2002]	—	Fluorescence
$LiTaO_3$	0.8 [Agostinelli et al., 1993]	0.6 [Agostinelli et al., 1993]	Waveguiding
$BaTiO_3$	9 [Ito et al., 1997]	3 [Beckers et al., 1998b; Buchal et al., 1998; Petraru et al., 2002]	Waveguiding and EO effect
$LaTiO_3$	—	—	Waveguiding
BBO	—	—	SHG
KTP	1 [Xiong et al., 1994]	—	Waveguiding, SHG, and fluorescence
BNN	—	1 [Liu et al., 1994]	Waveguiding
Glasses			
Doped glass	1.5 [Serna et al., 1998]	11 [Afonso et al., 1996]	Waveguiding
GaLaS	1.5 [Youden et al., 1993]	7 [Gill et al., 1995b]	Waveguiding
Lead germanate	2.7 [Mailis et al., 1999]	2.1 [Mailis et al., 1999]	Waveguiding and photosensitivity
Semiconductors			
CdS	2 [Bagnall et al., 2000]	—	Lasing
ZnO	1 [Hu et al., 1996; Ryu et al., 2000; Bae et al., 2000]	2.8 [Hu et al., 1997]	Lasing
Others			
Nd : KGW	—	5 [Jelinek et al., 2002b]	Waveguiding and fluorescence

17.6 WAVEGUIDE LASING DEVICES

17.6.1 Introduction to PLD Waveguide Lasers and Active Optical Devices

Although there have been a considerable number of reports on PLD growth of high-quality active waveguide films of laser materials in the past few years, lasing action itself has so far been

demonstrated in a relatively few PLD-grown films such as Ti : sapphire [Anderson et al., 1997c] and Nd : GGG, both as thin films [Gill et al., 1996; Bonner et al., 1997] and thick film planar devices [Grivas et al., 2004]. The majority of these studies concerned growth from single-crystal laser hosts and materials that have attracted perhaps the most attention were garnets, for reasons that are detailed in Section 17.4.1. In this final section, therefore, we discuss only those materials where lasing has been reported and discuss material parameters that lead to both low-loss and high-optical-quality waveguide performance.

17.6.2 Pulsed Laser Deposition Grown Waveguide Lasers

The discussion is limited to the development of waveguide lasers based on Ti : sapphire and Nd : GGG PLD-grown layers, which represent the two basic classes of oxide and garnet laser hosts.

17.6.2.1 Ti : Sapphire Waveguide Lasers

Ti : sapphire is a particularly interesting laser material because it offers the most widely tunable output of all current lasers (650–1100 nm), and is characterized by a wide absorption band (400–650 nm). Unfortunately though, an adverse side effect of this wide tunability is a low peak emission cross section and a short fluorescence lifetime that in turn imposes the requirement for use of high pump power densities to achieve efficient continuous wave (CW) lasing. This prerequisite for high pump power densities is the reason for adopting a waveguide geometry.

The first reports on the PLD fabrication of Ti : sapphire films appeared relatively recently [Dyer et al., 1996, 1997]. The main problem encountered by all the research groups working with PLD-grown Ti : sapphire was the poor optical quality of the guides produced due to the presence of particulates on the film surface, which induce high propagation losses [Jelinek et al., 1998; Uetsuhara et al., 1999], restricting the suitability of the films for development of planar waveguide devices. An approach adopted to minimize this deleterious effect involved growth from molten Al–Ti alloy targets [Willmott et al., 1999; Manoravi et al., 1999], a technique that has previously proven suitable for tailoring the concentration and type of dopant in PLD films. Dopant control is of particular importance for the growth of Ti : sapphire layers in order to avoid parasitic absorption and subsequent limitation in the laser performance due to the presence of tetravalent titanium (Ti^{4+}). Neither report, however, discussed the effect of this innovative method on the level of the waveguide propagation losses. Another approach toward fabrication of films with smooth features involves the use of a high-speed rotating target [Uetsuhara et al., 1999], which can lead in principle to a significant decrease in the concentration of the surface particulates that had initially contributed to a propagation loss as high as $\sim 8.7\,\mathrm{dB\,cm^{-1}}$.

To date, however, there are only two reports, both from our research group, on the realization of PLD-grown Ti : sapphire waveguide lasers in planar [Anderson et al., 1997c] and rib [Grivas et al., 2005] geometries. As detailed in an earlier work from the same group [Anderson et al., 1997a], growth was performed on undoped sapphire substrates at a temperature of $\sim 975^{\circ}\mathrm{C}$, in an argon atmosphere, from single-crystal Ti : sapphire targets with a doping level of 0.12 wt % Ti_2O_3. The films had a degree of crystal perfection and dopant levels comparable with commercial bulk targets, and the titanium was incorporated substitutionally for the Al^{3+} in the correct lattice position. This latter point was confirmed by the presence of the (0003) and (0009) XRD peaks that are forbidden reflections for the sapphire space group. The difference in scattering factors, however, for Al and Ti results in nonzero structure factors for all (000l) $l = 3n$ reflections, where n is an integer.

Figure 17.10 shows a comparison of the fluorescence spectra obtained from a Ti : sapphire waveguide and the bulk crystal target, revealing similar traces for both polarization states. CW

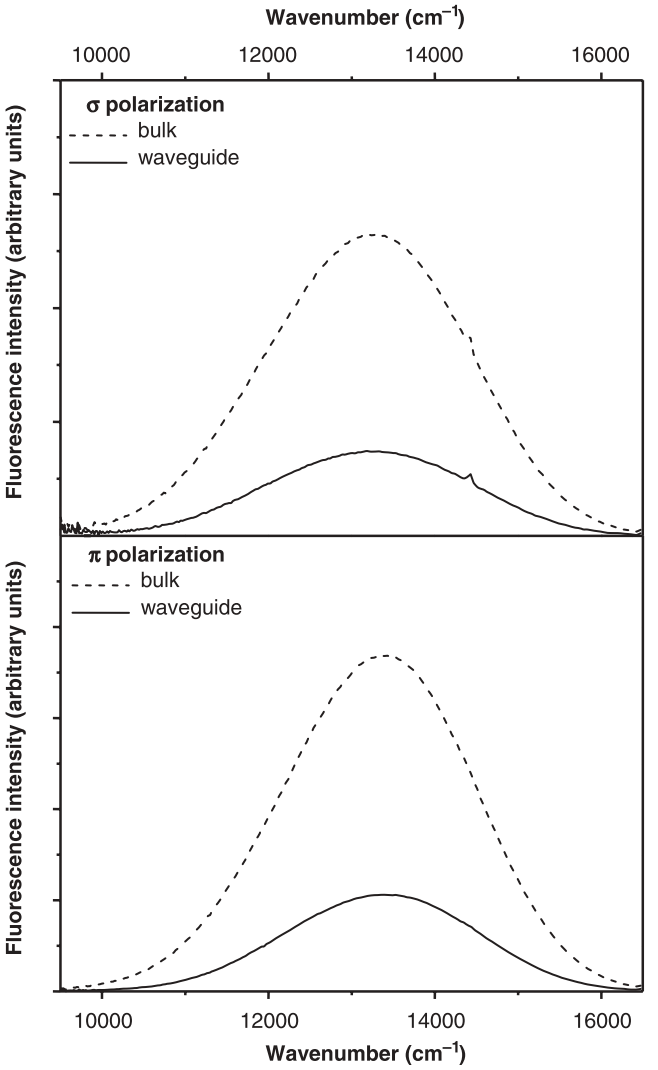

Figure 17.10 Fluorescence spectra for a PLD Ti : sapphire planar waveguide (full lines) and the bulk target (dotted lines) for (a) σ and (b) π polarizations.

laser operation was demonstrated at room temperature at an absorbed pump power threshold of 0.72 W, and the spectra obtained were centered at 808 nm, as shown in Figure 17.11. The comblike spectral output is due to the presence of an etalon effect within the output coupling mirror and some instability (mode-hopping) was observed in the spectral output obtained. The waveguide loss was deduced to be 1.8 dB cm^{-1} and was determined via a Findlay–Clay plot as described in Section 17.4.2.4; this loss was assumed to be due to surface scattering originating from particulates that were present on the film. The maximum recorded output was 357 mW for 3.44 W of absorbed power using an output coupler with a transmission of 35% at the lasing wavelength, corresponding to a slope efficiency of 26%. The output characteristics as a function of absorbed pump power are summarized in Figure 17.12, for two different values of output coupler transmission.

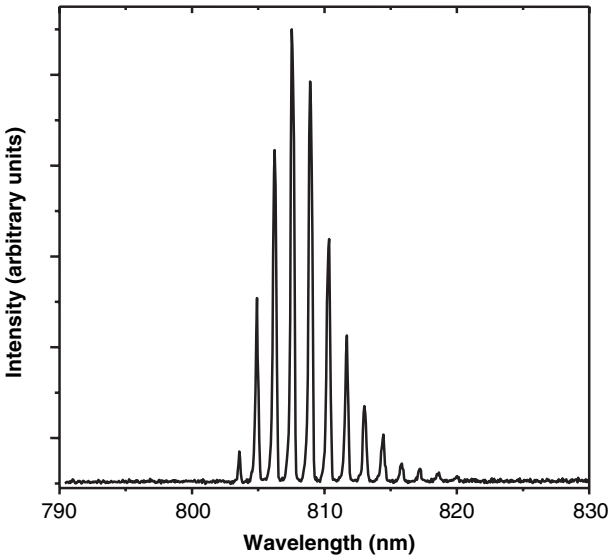

Figure 17.11 Lasing spectrum from a Ti : sapphire planar waveguide laser, showing modulation due to etalon effects associated with the output coupling mirror.

Single-mode channel waveguide laser geometries show a number of advantages over their unstructured planar film counterparts such as lower thresholds, due to the enhanced lateral confinement of both the pump and laser modes in the formerly unguided plane, as well as improved efficiency provided that the fabrication process does not itself introduce any additional loss. Furthermore, they are capable of providing a fully diffraction-limited, near circular, single-transverse-mode output beam. Recently, rib waveguides based on PLD-grown Ti : sapphire thin

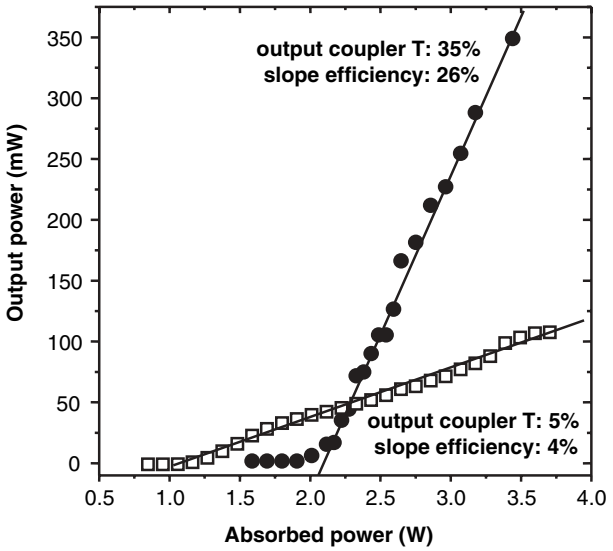

Figure 17.12 Output power characteristics from a Ti : sapphire planar waveguide laser for two output couplers with transmission T of 5% and 35% at the lasing wavelength.

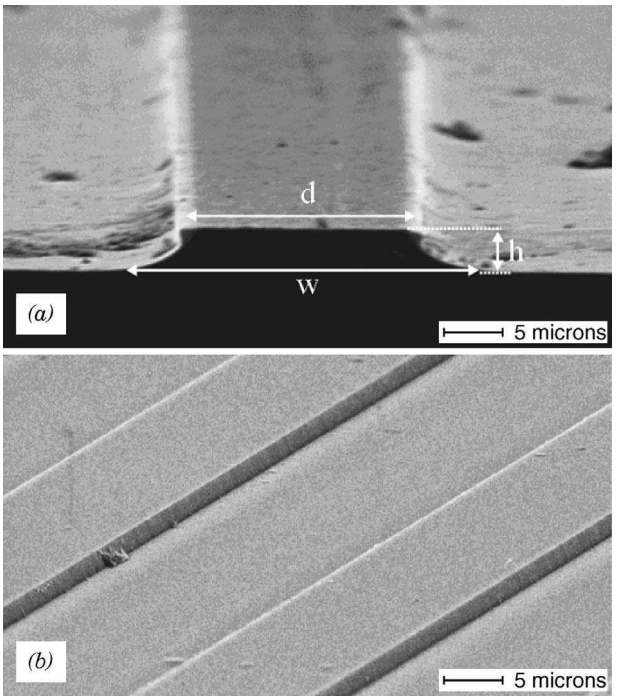

Figure 17.13 SEM micrographs of a Ti : sapphire rib waveguide: (a) detail of waveguide end face and (b) angled view to show overall uniformity of the structure.

films have been developed using photolithographic patterning and subsequent Ar^+ beam milling [Grivas et al., 2003] or reactive ion beam etching (RIE) [Crunteanu et al., 2002]. Figure 17.13 shows scanning electron micrographs (SEM) of these rib structures, produced by PLD and Ar^+ beam milling, from which it can be seen that the ridge structuring is a well-controlled process that does not contribute any significant surface roughness. This postprocessing approach has proven quite efficient, since nondestructive loss measurements using the self-pumped phase conjugation technique (SPPC) [Brülisauer et al., 1995] have shown that the rib fabrication steps do not increase the value of propagation loss by more than $\sim 0.2\,\mathrm{dB\,cm^{-1}}$ compared to the background loss level of other PLD-grown Ti : sapphire thin films. Fluorescence intensity profiles from ribs of three different transverse dimensions are shown in Figure 17.14, and it is clear that high optical confinement has been achieved by this method. The measured values for the beam propagation factors M_x^2 and M_y^2 were 1.12 and 1.16, respectively, indicating single transverse mode emission.

Laser action for structures of this type has recently been demonstrated at the Optoelectronics Research Centre, University of Southampton, United Kingdom [Grivas et al., 2005]. The device contained multiple arrays of rib waveguides with depth 3.5 μm, widths varying from 10 to 24 μm, and rib-to-rib separations ranging from 20 to 60 μm. The sample was covered with a 5-μm-thick sapphire cladding layer to reduce scattering losses. For a 10-μm rib, the absorbed pump power threshold for laser operation was 265 mW, which was more than a factor of 2 lower in comparison to their planar counterparts [Anderson et al., 1997c]. The lasing spectrum, as recorded by a spectrum analyzer at an absorbed pump power of 350 mW is shown in Figure 17.15. Measured beam propagation factors M_x^2 and M_y^2 of 1.3 and 1.2, respectively, indicated single-transverse-mode laser emission at the wavelength of 792.5 nm. The inset in Figure 17.15 shows the laser mode profile obtained using an output coupler with 4.6% transmission at the lasing wavelength.

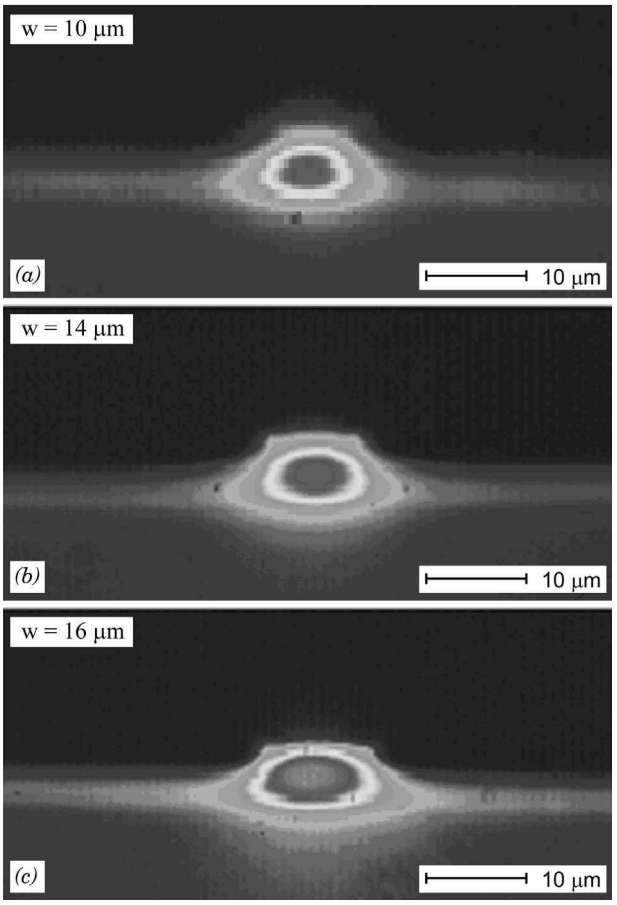

Figure 17.14 Fluorescence emission profiles measured at the exit face of a Ti : sapphire rib waveguide with a depth of 5 μm and width w of (a) 10, (b) 14, and (c) 16 μm.

For 1 W of absorbed pump power, the rib waveguide laser emitted 27 mW and, as shown in Figure 17.16, a slope efficiency of 5.3% was achieved. This value is higher than the one obtained from the planar version of this waveguide (4%).

Compact fluorescence, amplified spontaneous emission, and laser devices based on Ti : sapphire in channel geometries are particularly interesting for applications in optical coherence tomography (OCT) due to their high brightness and their emission in the near infrared, which ensures adequate penetration of the light in the tissue, as well as their potential to provide fully diffraction-limited, near circular, single-mode beams that would allow integration with OCT fiber interferometric arrangements. Recent preliminary results using the arrays of Ti : sapphire rib waveguides reported in Grivas et al. [2005] showed that it is possible to develop parallel emitting fluorescence sources from the same miniature sample, and there is a clear potential for the integration of such devices in parallel OCT configurations [Bourquin et al., 2005]. Such a system with 16 parallel Ti : sapphire ribs separated by a distance of 60 μm, generated a bandwidth of 174 nm, and provided a depth resolution of 1.9 μm, which corresponds to 1.5 μm in the tissue.

A future direction of the research in this area would be to combine the Ti : sapphire channel waveguides with semiconductor saturable absorber mirrors (SESAM) and saturable Bragg reflector

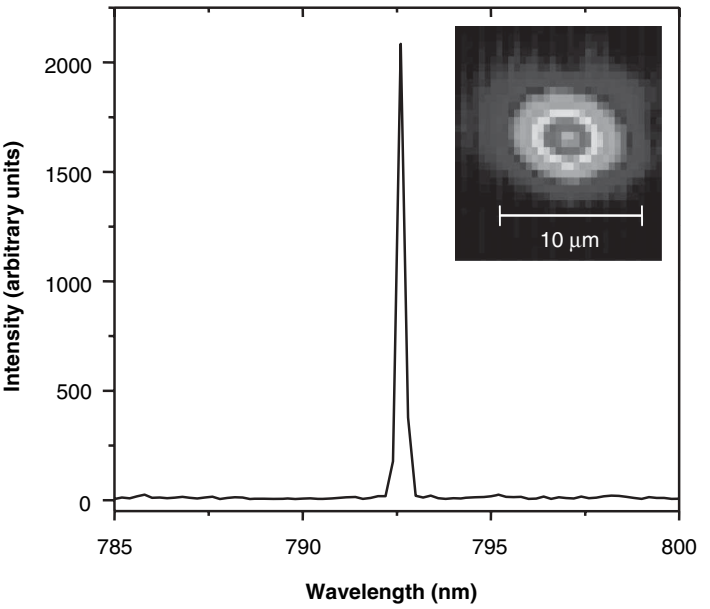

Figure 17.15 Lasing spectrum originating from a Ti : sapphire rib waveguide 3.5 and 10 μm in height and width, respectively, for an absorbed power of 350 mW. The corresponding laser mode profile, which was obtained using an output coupler with 4.6% transmission at the lasing wavelength, is shown in the inset.

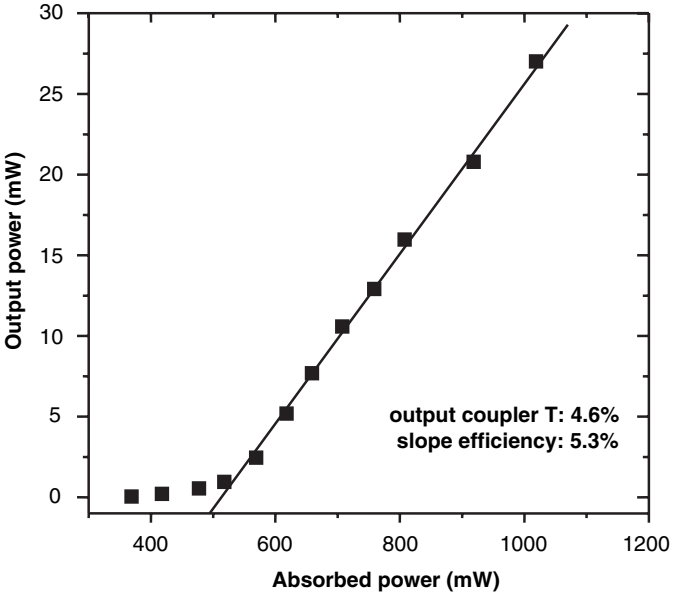

Figure 17.16 Output power from a rib waveguide laser with height and width of 3.5 and 10 μm, respectively, as a function of the absorbed pump power for an output coupler with 4.6% transmission at the lasing wavelength.

(SBR) technologies, and therefore open up the possibility of developing a compact and portable broadly tunable laser with the potential to produce high-repetition-rate mode-locked pulses. Such a source would be ideal for use in a range of applications such as photobiology, photomedicine, communications, and particularly in OCT because the attributes of high-intensity pulses combined with the low average power and large bandwidth allow the study of live cells/tissues with high longitudinal resolution.

17.6.2.2 Nd : GGG Waveguide Lasers

The first successful operation of a waveguide laser fabricated by PLD was reported for Nd : GGG layers deposited on YAG (111) substrates [Gill et al., 1996]. Single-crystal film growth was observed and films had a thickness between 2.5 and 3 μm. Lasing action was demonstrated at an absorbed pump power threshold of 91 mW at 1059 and 1062 nm simultaneously, or at 1060 and 1063 nm, which corresponds to the ${}^4F_{3/2} \rightarrow {}^4I_{11/2}$ transition of Nd^{3+}. Growth was performed by pulsed laser deposition from a 1 at % Nd-doped GGG ceramic target as, at the time, Nd-doped single-crystal targets could not be obtained. Consequently, the deposited films were characterized by a high propagation loss, typically on the order of 6 dB cm^{-1}, which in turn resulted in particularly low output power levels.

Subsequent experiments were directed at improvements in the fabrication techniques primarily involving the use of a scanned CO_2 laser beam for substrate heating, and of single-crystal Nd : GGG target material, which lead to films with a thickness of around 10 μm [Anderson et al., 1997b]. The scanned laser method enabled highly localized heating of the substrate and minimized contamination through desorption from the walls of the chamber. The substitution of a single-crystal target for the previous ceramic one led to a significant decrease in the number of particulates on the film surface by a factor of ~20. Additional minor changes adopted in the deposition procedure, which also reduced the particulate density, were the use of longer substrate–target distances as well as lower energy densities and repetition rates for the excimer laser [Bonner et al., 1997]. The second set of waveguides possessed essentially identical crystalline and spectroscopic properties, however.

The fluorescence spectra of the Nd : GGG waveguides in the spectral regions around 1060 and 940 nm, which correspond to the ${}^4F_{3/2} \rightarrow {}^4I_{11/2}$ and ${}^4F_{3/2} \rightarrow {}^4I_{9/2}$ transitions, respectively, are shown in Figure 17.17. It is clear that the main features are similar for bulk and waveguide samples, although there is a broadening and a slight shift of a few nanometers of some of the spectral lines. The shape of the fluorescence spectra for the ~1060-nm region was identical for a range of films produced, implying a very systematic growth process. One of the main features of the waveguides obtained at this stage was their capability to demonstrate lasing not only at the normal 1060-nm four-level laser transition for Nd^{3+}, but also, as seen for the first time in Nd : GGG, laser action on the quasi-three-level ${}^4F_{3/2} \rightarrow {}^4I_{9/2}$ transition at 937 nm. Figures 17.18a and 17.18b show typical lasing spectra for these two spectral regions. A plot of output power versus absorbed pump power is shown in Figure 17.19, from which it can be seen that the threshold pump power for the 1060-nm transition is of order 2 mW. The slope efficiency for both transitions was measured to be the same, at 20%.

It is clear that these new guides had a much reduced value of waveguide loss. A Findlay–Clay measurement shown in Figure 17.20 yielded a value of loss of order 0.3–0.5 dB cm^{-1}, a reduction by an order of magnitude over the previous guides grown from a ceramic target.

Considerable effort has gone into routes to reduce the particle density on the surface of these lasing waveguides. The first approach via a synchronized pulsed gas-jet has been described in Section 17.4.3. The second approach involved the growth of capping layers on top of the existing waveguide layer, effectively burying the particles within an outer cladding layer. The waveguide layer was Nd-doped GGG grown on YAG, and the outer capping layer was also YAG [Barrington et al., 2000]. For an uncapped waveguide of 2 μm thickness, an increase in particulate density from 3.5×10^4 to 10^6 cm^{-2} led to an increase in the absorbed pump power threshold

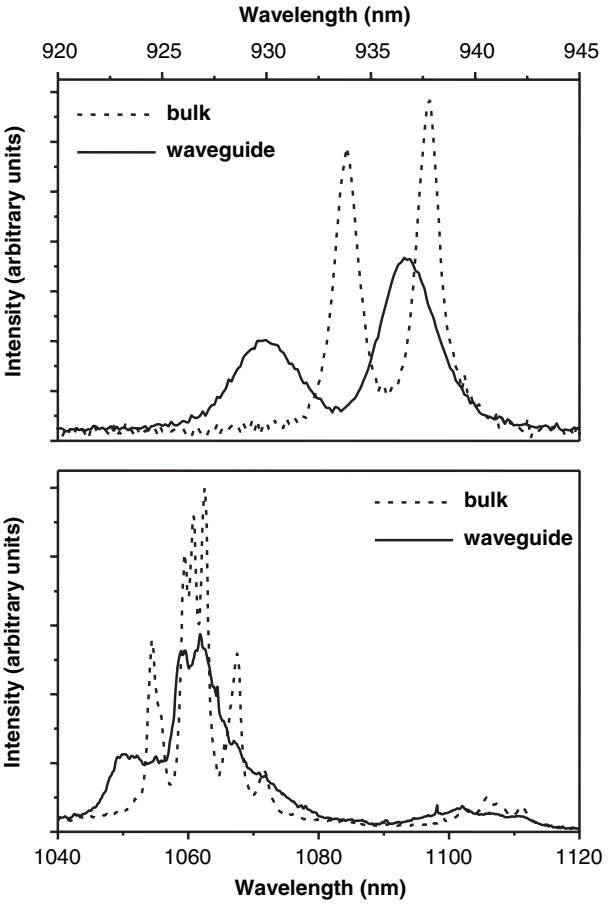

Figure 17.17 Fluorescence spectra from a Nd : GGG planar waveguide (full line) and the bulk crystal target (dotted line) for the ${}^4F_{3/2} \rightarrow {}^4I_{9/2}$ transition at 937 nm and the ${}^4F_{3/2} \rightarrow {}^4I_{11/2}$ transition at 1060 nm.

from 2.5 to 167 mW. This effect was much less marked for a 4-μm-thick guide, however, as a guide with a particulate density of $3.6 \times 10^6\,\mathrm{cm}^{-2}$ lased easily at a threshold of 19 mW, while at this particulate density, a 2-μm guide would have been unable to reach threshold. Finally, an 8-μm-thick guide showed good lasing performance almost irrespective of surface particulate density, lasing at a threshold value of 12.2 mW for a very high particulate count of $6.6 \times 10^6\,\mathrm{cm}^{-2}$.

These guides were then selectively capped with YAG overlayers to evaluate the reduction in lasing threshold for guides with particularly high initial particulate densities. A 4-μm-thick guide was chosen with a particulate density of $1.5 \times 10^7\,\mathrm{cm}^{-2}$, a value that precluded any lasing action prior to cladding. After the YAG overcladding layer was deposited, a lasing threshold of 15 mW was obtained, comparable to the value measured for an unclad guide with a particulate density four orders of magnitude lower. This somewhat surprising, but technologically useful, result points the way to further experiments in multilayer growth of such guides. The overcladding has shown itself as a dramatic and easy method to radically improve the optical quality of all such PLD-grown waveguides.

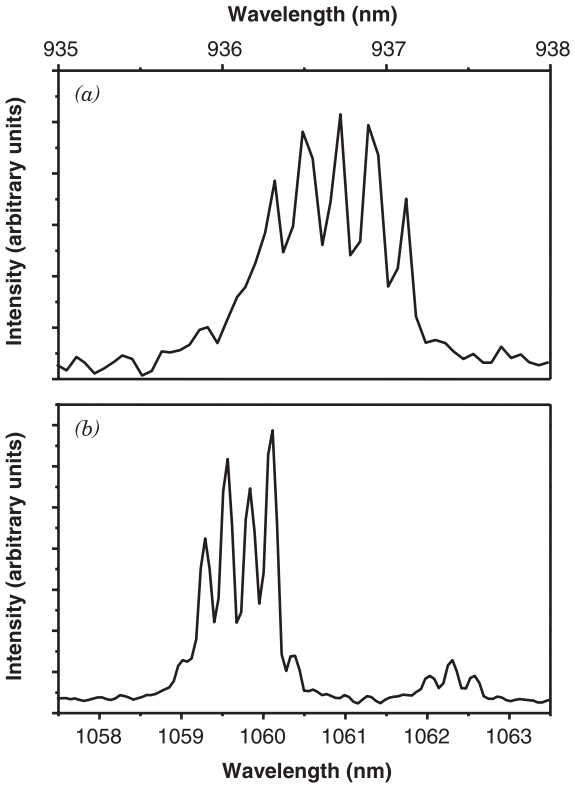

Figure 17.18 Typical lasing spectra from the Nd : GGG waveguide for the (a) ${}^4F_{3/2} \rightarrow {}^4I_{9/2}$ and (b) ${}^4F_{3/2} \rightarrow {}^4I_{11/2}$ transition showing operation on several longitudinal modes.

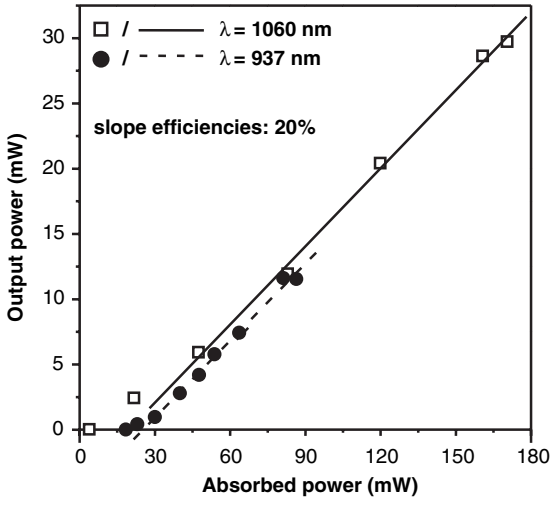

Figure 17.19 Output power versus absorbed pump power for the (●) 937 nm and (□) 1060 nm spectral regions for a thin (8 μm) Nd : GGG waveguide laser.

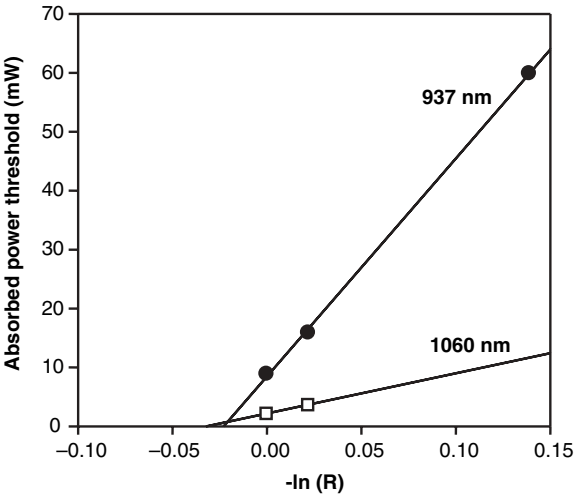

Figure 17.20 Absorbed pump power threshold for lasing versus logarithm of the output coupler reflectivity for 1060 and 937 nm laser operation of a thin (8 μm) Nd : GGG waveguide laser.

17.6.2.3 Thick (>25 μm) Nd : GGG Waveguide Lasers

The final part of this section concerns the growth and application of what must be considered *thick* PLD-grown optical films. We are not aware of the current record concerning the maximum thickness grown for any PLD material, but layers of thickness >25 μm are rarely, if ever, reported. Thick layer growth has been performed here for Nd : GGG on YAG with the goal of developing waveguides with optimized multilayer structures that incorporate a double cladding layer, an ideal geometry for high-power diode pumping. The high values of NA obtainable for PLD multilayers open up the possibility for the development of large-mode-area (LMA) and cladding-pumped LMA waveguide designs, for which it is essential to have layers with a thickness of several tens of microns. Such schemes combine the potential for high-power diode pumping with the possibility to control the spatial output of the waveguide and should be capable of delivering tens of watts (or even more) of output power of near-diffraction-limited beam quality.

In recent experiments we have grown epitaxial single-crystal thick Nd : GGG films with thicknesses of up to 40 and 135 μm, when grown in single and multiple deposition runs, respectively. Laser action has been demonstrated in a 40-μm-thick guide grown in a single deposition run, and in a 50-μm-thick guide that was grown using multiple deposition runs. The performance of the two guides was investigated in terms of threshold pump power requirement, output slope efficiencies, and propagation losses; the results from the 40-μm-thick film have been reported previously [Grivas et al., 2004].

Figure 17.21 shows the dependence of the laser output from the 40-μm-thick waveguide on the absorbed pump power for two output couplers with transmissions of 2.2 and 4.5% at the lasing wavelength, from which slope efficiency values of 12.5 and 17.5% have been deduced. These values are slightly lower than those obtained for thinner Nd : GGG films [Bonner et al., 1997], due to the inherent multimode output from such a thick guide, which has led to a poor overlap between the pump and lasing modes. Evaluation of the propagation losses has been performed for the 40-μm-thick waveguide using the Findlay–Clay method, and as shown in Figure 17.22, the very low-loss value of 0.1 dB cm^{-1} has been deduced for this thick guide. We believe this is the lowest loss ever reported for any PLD-grown film and represents perhaps a benchmark in the optical quality of PLD lasing waveguide films.

As a prelude toward the ultimate goal of diode-pumped multilayer waveguide structures, a 50-μm-thick single-layer waveguide was fabricated by PLD to perform initial tests with launching

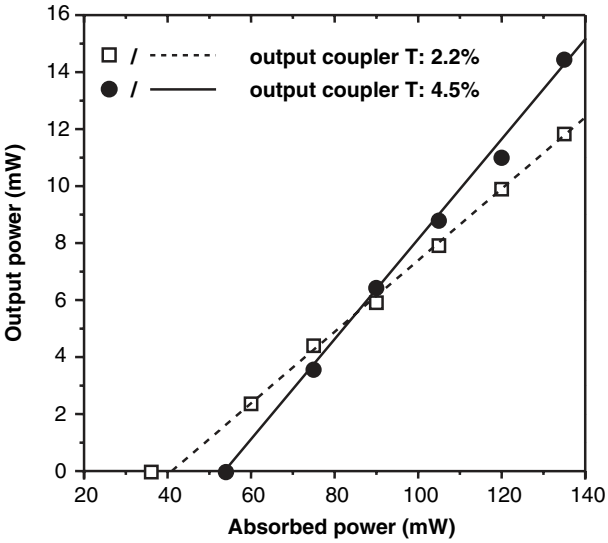

Figure 17.21 Dependence of the output power from a 40-μm-thick Nd : GGG waveguide laser as a function of the absorbed power for two output couplers with transmissions of (□) 2.2% and (●) 4.5%. Slope efficiencies of 12.3 and 17% have been obtained using these two output couplers, respectively.

of diode light. The waveguide was grown using several deposition runs and the target position was reset between runs; this was found to prevent the frequency of particulates increasing as the target surface degrades throughout a long deposition run (>2 h). Side pumping with diodes could not be performed, however, because of problems with cracking at the polishing stage of waveguide preparation. However, end pumping with a diode stack was successful and the 50-μm-thick

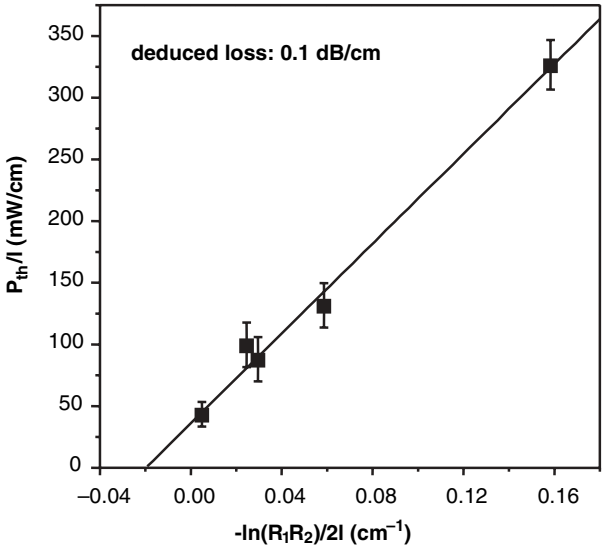

Figure 17.22 A plot of P_{th}/l as a function of $-\ln(R_1R_2)/2l$ for a 40-μm thick Nd : GGG waveguide laser. The position of the intercept on the x-axis yields the propagation attenuation coefficient ($\alpha_L \sim 2\,\text{m}^{-1}$) from which a propagation loss of 0.1 dB cm^{-1} has been calculated.

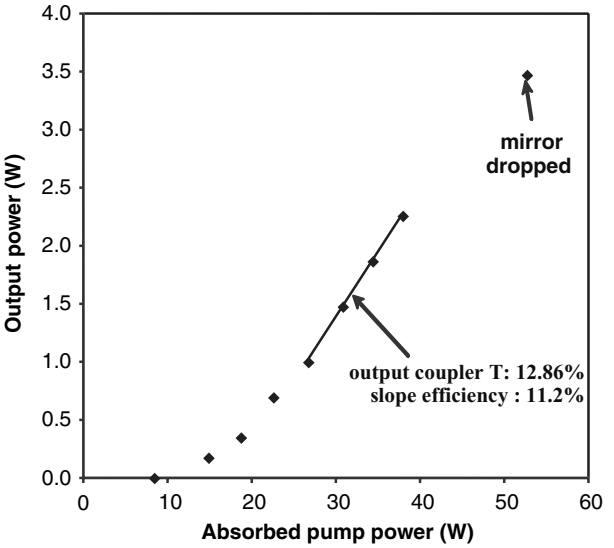

Figure 17.23 Dependence of the output power from a 50-μm-thick Nd : GGG waveguide laser end-pumped by a diode stack as a function of the absorbed power using an output coupler with a transmission of 12.86%. A slope efficiency of 11.2% was obtained for this device.

waveguide lased with a minimum absorbed power threshold of 7.44 W. End pumping through the cavity mirrors was not ideal, and a lower threshold may have been obtained if side pumping would have been possible. Figure 17.23 shows a plot of the output power from the 50-μm-thick guide against the absorbed diode pump power. An output coupler of 12.86% transmittance yielded a slope efficiency of 11.2%. This is lower than the slope efficiencies obtained using Ti : sapphire pumping, but this is expected because of the poorer overlap of the pump and laser beams. The downside of end pumping with such high power levels is also shown in Figure 17.23. Note the highest point in the graph is not in line as would be expected. This is because the fluid used to attach the cavity mirrors was prone to boiling when the power incident on the input face was >100 W.

17.6.3 Future Directions

It is now well established that PLD growth of optical waveguide materials can produce high-optical-quality guides with losses that compare very favorably with any other technique currently available. Low loss is the key to success, and we now have the knowledge to achieve this in a systematic manner. High-power devices are imminent with diode pumping at the 100s of watts level. We believe the two types of devices most likely to break the laser output records for PLD films are multilayer cladding-pumped structures that can be pumped by high-power diode arrays and highly doped films that may be suitable for operation as thin-disk lasers. The next two subsections detail our latest advances toward these two types of devices. Arguably, the most significant challenge that needs to be addressed in the future to allow such devices to survive the polishing process more easily is the relaxation of stresses that build up to self-destructive levels in films greater than 50 μm in thickness. The third subsection here provides a discussion on the possible causes of the problem and how one might go about trying to reduce its effect.

17.6.3.1 Multilayer Structures and Alternative Garnets

We have yet to achieve a lasing example of the vertical multilayered (five-layer) growth that we require for high-power diode-pumped structures, but an example of such a structure using

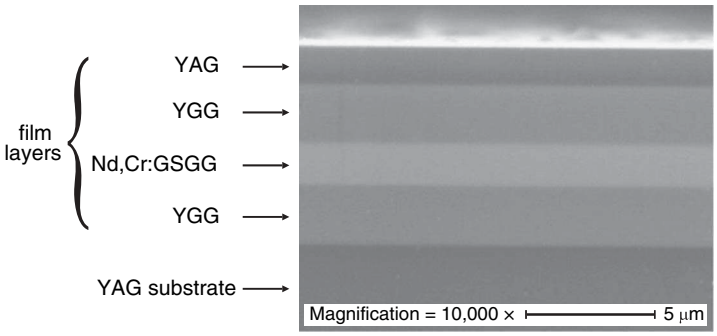

Figure 17.24 SEM micrograph of a multilayer garnet crystal sample cross section.

thin layers (1–2 μm) has been grown as a proof of principle that layers will accept overgrowth of further layers without a significant deterioration in quality occurring. The multilayer sample consisted of a Nd,Cr : GSGG core layer surrounded by two YGG cladding layers on a YAG substrate with a YAG capping layer deposited on top. Figure 17.24 shows an SEM micrograph of the sample cross section and the separate layers can be seen clearly. Figure 17.25 shows an XRD spectrum of the multilayer sample. The peaks corresponding to the different layers and crystal orientations are labeled. The YAG capping layer and substrate peaks do not overlap because the PLD-grown crystal does not have a perfectly stoichiometric composition. The peaks have small full-width half-maxima and there are no other peaks present other than those for the expected (100)-oriented crystal layers. This proves that the film layers are high-quality textured crystal. The growth of this trial multilayer film has shown how compatible the range of garnets are for these sort of experiments with PLD. We are now closer than ever to a designer multilayer structure of garnet crystal layers by PLD.

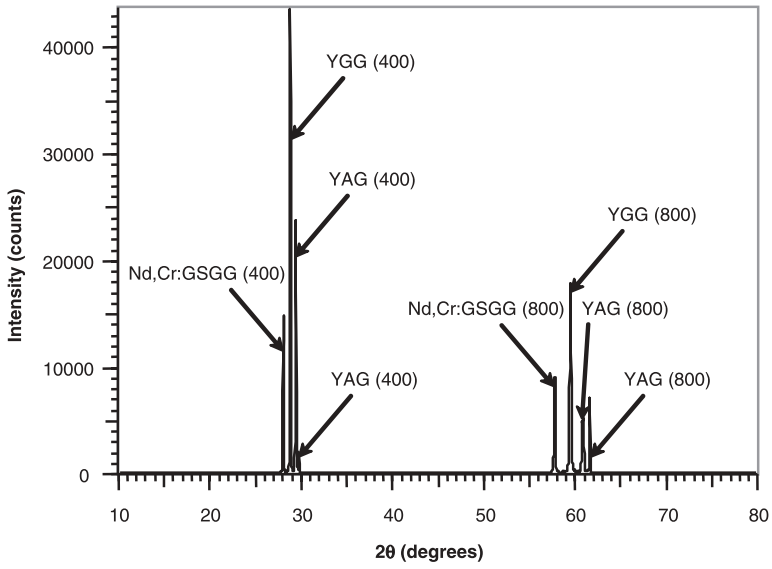

Figure 17.25 XRD spectrum of the multilayer garnet crystal sample.

17.6.3.2 Films Used as Thin-Disk Lasers

The thin-disk laser has been a focus of attention in recent years due to the advantages of such a system over bulk lasers. Efficient cooling is possible because of the large surface-area-to-volume ratio, and the effect of thermal lensing is small because the temperature gradient is in line with the laser axis. By using multiple passes of the pump beam and increasing the pumped area, the output power of the thin-disk laser is highly scalable and can reach kilowatt levels [Stewen et al., 2000]. To achieve efficient operation of a thin-disk laser, it is desirable to have a very high dopant concentration. YAG can be doped with very high concentrations of ytterbium (up to 100%) because the ionic radii of Yb^{3+} and Y^{3+} are so similar. The optical efficiency is ultimately optimal for a ytterbium concentration of 100%, but the optimal thickness for such a high dopant concentration is $<100\,\mu m$ [Stewen et al., 2000], and a disk this thin would be very fragile. Films of Yb : YAG solve the problem of fragility that arises as the disk thickness decreases below 100 μm, and the substrate can be used to dissipate heat from the film. PLD is an ideal technique for the fabrication of Yb : YAG films that will fulfill the necessary requirement of a thin-disk laser material, which is to have a very low loss, and the possibility of depositing layers additional to the laser film allow specialist devices to be made. For example, a *Q*-switched Yb : YAG thin-disk laser film may be fabricated by the addition of a layer doped with the saturable absorber ion Cr^{4+} [Buryy et al., 2004].

We have grown a 100%-doped Yb : YAG film of 18 μm in thickness for use as a thin-disk laser device. The substrate was polished parallel flat prior to the film deposition, and the film surface was also polished parallel flat to the substrate faces. The film appeared to be of a similar quality to previously grown thick Nd : GGG films, in terms of propagation loss and crystallinity; however, no success has been experienced so far with laser operation of the device. The relative peak heights of the absorption spectrum for the Yb : YAG film did not match a bulk piece of crystal, and we therefore believe that all of the Yb may not be in the desired Yb^{3+} valence state, and as a result of this the device did not lase. This serves as a reminder of a critical condition for PLD films to be successfully operated as laser devices; the growth conditions must be controlled so that the dopant is in the correct valence state. Nd-doped films have been very successful, due to the Yb^{3+} valence state assumed in garnet hosts. When using dopants such as Yb, Cr, and Ti, either the growth conditions must be suitable for the desired valence state or postannealing may be necessary to correct the film afterwards.

17.6.3.3 Pushing the Thickness Limit of Films

Since particluates no longer pose a significant problem for thick and capped films, perhaps the most critical current problem to be solved is the occurrence of high levels of stress in the PLD grown films that arises due to thermal expansion mismatch and deficiencies in the crystal structure. It is no longer enough to fabricate a crystal film with narrow XRD peaks. Even if the crystal is of high quality and mostly free of deficiencies with a lattice-matched substrate, when going above a thickness of about 40 μm, we have found that stresses in the film can make the sample impossible to polish without the vibrations involved in the process causing it to crack. Thicker substrates can be used, and we have found that this stops the whole sample from breaking up, but the film faces are still prone to cracking off, making it impossible to achieve a usable polished face. We know from previous RBS and EDX (energy dispersive X-ray) compositional analysis of our films that they are not fully stoichiometric, and XRD peaks are slightly shifted. Also, the stress that we see in our samples is opposite to what we would expect from thermal expansion mismatch. It therefore seems that thick films are less tolerant of poor compositional quality, and the only way to prevent future films from cracking due to built-up stresses is to try and grow them with a composition closer to bulk crystal.

17.7 CONCLUSIONS AND CLOSING REMARKS: TIPS FOR SUCCESSFUL WAVEGUIDE GROWTH

We can now set out some general advice and guidelines concerning the optimum procedures to ensure high-quality waveguide growth by PLD. Many of these points may seem obvious, but

it is important to bear in mind the fact that the number of publications in the PLD area that report optical waveguide growth far exceeds the number that report on actual or useful devices. The area has moved on from growing material X on substrate Y: Unless the waveguide exhibits high optical quality, and hence low loss, it is of little value as a practical optical device.

1. Adopt a film–substrate combination that is well matched in terms of lattice constant and thermal expansion coefficients, consistent of course with the constraint imposed for waveguide propagation that the guiding layer must have a higher refractive index than the substrate. Any mismatch that leads to cracking or film defects will also lead to increased optical waveguide loss, which is to be avoided.
2. Homoepitaxial growth can lead to high-quality structures such as Ti : sapphire on sapphire or doped YAG on YAG, which grow relatively easily and can possess essentially perfect crystalline properties.
3. Cubic materials (e.g., garnets) are more tolerant than uniaxial or biaxial materials in terms of optical loss. Polycrystalline cubic host materials will not contribute to optical scattering loss to anything like the degree of polycrystalline uniaxial or biaxial hosts, which are anisotropic and hence extremely inhomogeneous in their local refractive index.
4. To ensure high-quality polished end faces for lasing waveguides, the waveguide and substrate material should have closely matched values of hardness. If the waveguide is softer than the substrate, polishing will selectively remove and damage the end face of the waveguide, rendering the structure useless for device construction.
5. Particulates need not pose too much of a problem if capping layers are used. Particularly in cubic materials, burying the particulates effectively removes them from participating in any interaction with the propagating optical mode.
6. The production of particulates is directly linked to the condition of the target surface. If long depositions are to be performed where the target surface is significantly degraded, break the deposition up into multiple runs and reposition or recondition the target before continuing. Taking this measure will significantly reduce the occurrence of particulates.
7. We have found that the constancy of growth conditions can have an effect on the quality of films grown. Take care to ensure that conditions such as temperature and gas pressure do not drift throughout depositions and if using multiple runs it is critical that the conditions are the same for every run.

Acknowledgments

The authors are grateful to the UK Engineering and Physical Science Research Council for research funding, and to colleagues and collaborators at the Foundation of Research and Technology Hellas, (FO.R.T.H.) in Crete, Greece, for use of their laser facilities. Thanks also go to former students, Katharine Youden, Devinder Gill, Andrew Anderson, Catherine Bonner, Jing Wang, and Tajamal Bhutta who have worked in this area at the University of Southampton.

REFERENCES

Afonso, C. N., Ballesteros, J. M., Gonzalo, J., Righini, G. C., and Pelli, S. (1996), *Applied Surface Science* **96–98**, 760–763.

Agostinelli, J. A., Braunstein, G. H., and Blanton, T. N. (1993), *Appl. Phys. Lett.* **63**, 123–125.

Alfonso, J. E., Martin, M. J., and Zaldo, C. (1997), *Appl. Phys. Lett.* **71**, 2904–2906.

Anderson, A. A., Eason, R. W., Jelinek, M., Grivas, C., Hickey, L. M. B., Rogers, K., and Lane, D. (1997a), *Thin Solid Films* **300**, 68–71.

Anderson, A. A., Bonner, C. L., Shepherd, D. P., Eason, R. W., Grivas, C., Gill, D. S., and Vainos, N. (1997b), *Opt. Commun.* **144**, 183–186.

Anderson, A. A., Eason, R. W., Hickey, L. M. B., Jelinek, M., Grivas, C., Gill, D. S., and Vainos, N. A. (1997c), *Opt. Lett.* **22**, 1556–1558.

Bae, S. H., Lee, S. Y., Jin, B. J., and Im, S. (2000), *Applied Surface Scienc*, **154**, 458–461.

Bagnall, D. M., Ullrich, B., Sakai, H., and Segawa, Y. (2000), *J. Crystal Growth* **214**, 1015–1018.

Barrington, S. J., and Eason, R. W. (2000), *Rev. Sci. Instrum.* **71**, 4223–4225.

Barrington, S. J., Bhutta, J., Shepherd, D. P., and Eason, R. W. (2000), *Opt. Commun.* **185**, 145–152.

Beckers, L., Buchal, C., Fluck, D., Pliska, T., and Gunter, P. (1998a), *Mater. Sci. Eng. A.* **253**, 292–295.

Beckers, L., Schubert, J., Zander, W., Ziesmann, J., Eckau, A., Leinenbach, P., and Buchal, C. (1998b), *J. Appl. Phys.* **83**, 3305–3310.

Betts, R. A., and Pitt, C. W. (1985), *Electron. Lett.* **21**, 960–962.

Bhutta, T., Mackenzie, J. I., and Shepherd, D. P. (2002), *J. Opt. Soc. Am. B* **19**, 1539–1543.

Bonner, C. L., Anderson, A. A., Eason, R. W., Shepherd, D. P., Gill, D. S., Grivas, C., and Vainos, N. (1997), *Opt. Lett.* **22**, 988–990.

Bourquin, S., Laversenne, L., Rivier, S., Lasser, T., Salathé, R. P., Pollnau, M., Grivas, C., Shepherd, D. P., and Eason R. W. (2005), *Proc. SPIE* **5690**, 209–213.

Brülisauer, S., Fluck, D., Solcia, C., Pliska, T., and Günter, P. (1995), *Opt. Lett.* **20**, 1773–1775.

Buchal, C., Beckers, L., Eckau, A., Schubert, J., and Zander, W. (1998), *Materials Science and Engineering B-Solid State Materials for Advanced Technolog*, **56**, 234–238.

Buryy, O. A., Ubiszkii, S. B., Melnyk, S. S., and Matkovskii, A. O. (2004), *Appl. Phys. B.* **78**, 291–297.

Chaos, J. A., Pruneri, V., Gonzalo, J., and Afonso, C. N. (2000), *J. Appl. Phys.* **88**, 3768–3770.

Chartier, I., Ferrand, B., Pelenc, D., Field, S. J., Hanna, D. C., Large, A. C., Shepherd, D. P., and Tropper, A. C. (1992), *Opt. Lett.* **17**, 810–812.

Craciun, V., Howard, J., Lambers, E. S., Singh, R. K., Craciun, D., and Perriere, J. (1999), *Appl. Phys. A—Mater. Sci. Process.* **69**, S535–S538.

Crunteanu, A., Pollnau, M., Janchen, G., Hibert, C., Hoffmann, P., Salathe, R. P., Eason, R. W., Grivas, C., and Shepherd, D. P. (2002), *Appl. Phys. B—Lasers Opt.* **75**, 15–17.

Davis, G. M., and Gower, M. C. (1989), *Appl. Phys. Lett.* **55**, 112–114.

Dyer, P. E.,Jackson, S. R., Key, P. H., Metheringham, W. J., and Schmidt, M. J. J. (1996), *Appl. Surf. Sci.* **96/98**, 849–854.

Dyer, P. E., Gonzalo, J., Key, P. H., Sands, D., and Schmidt, M. J. J. (1997), *Appl. Surf. Sci.* **110**, 345–349.

Ezaki, M., Kumagai, H., Kobayashi, K., Toyoda, K., and Obara, M. (1995), *Jpn. J. Appl. Phys. Pt. 1—Regul. Pap. Short Notes Rev. Pap.* **34**, 6838–6841.

Ezaki, M., Obara, M., Kumagai, H., and Toyoda, K. (1996), *Appl. Phys. Lett.* **69**, 2977–2979.

Fernandez, F. E., Gonzalez, Y., Liu, H. M., Martinez, A., Rodriguez, V., and Jia, W. Y. (2002), *Integr. Ferroelectr.* **42**, 219–233.

Field, S. J., Hanna, D. C., Large, A. C., Shepherd, D. P., Tropper, A. C., Chandler, P. J., Townsend, P. J., and Zhang, L. (1991), *Opt. Commun.* **86**, 161–166.

Findlay, D., and Clay, R. A. (1966), *Phys. Lett.* **20**, 277–278.

Fukaya, S., Adachi, K., Obara, M., and Kumagai, H. (2001a), *Opt. Commun.* **187**, 373–377.

Fukaya, S., Hasegawa, T., Ishida, Y., Shimoda, T., and Obara, M. (2001b), *Appl. Surf. Sci.* **177**, 147–151.

Gill, D. S., Eason, R. W., Mendiola, J., and Chandler, P. J. (1995a), *Mater. Lett.* **25**, 1–4.

Gill, D. S., Eason, R. W., Rutt, H. N., Zaldo, C., and Vainos, N. A. (1995b), *J. Non-Crystal Sol.* **191**, 321–326.

Gill, D. S., Anderson, A. A., Eason, R. W., Warburton, T. J., and Shepherd, D. P. (1996), *Appl. Phys. Lett.* **69**, 10–12.

Gonzalo, J., Chaos, J. A., Suarez-Garcia, A., Afonso, C. N., and Pruneri, V. (2002), *Appl. Phys. Lett.* **81**, 2532–2534.

Grivas, C., Shepherd, D. P., May-Smith, T. C., Eason, R. W., Pollnau, M., Crunteanu, A., and Jelinek, M. (2003), *IEEE J. Quant. Elec.* **39**, 501–507.

Grivas, C., May-Smith, T. C., Shepherd, D. P., and Eason, R. W. (2004), *Opt. Commun.* **229**, 355–361.

Grivas, C., Shepherd, D. P., May-Smith, T. C., Eason, R. W., and Pollnau, M. (2005), *Opt. Express* **30**, 210–215.

Guo, X. L., Liu, Z. G., Zhu, S. N., Yu, T., Xiong, S. B., and Hu, W. S. (1996), *J. Crystal Growth* **165**, 187–190.

Hayashi, H., Iwasa, S., Vas, N. J., Yoshitake, T., Ueda, K., Yokoyama, S., Higuchi, S., Takeshita, H., and Nakahara, M. (2002a), *Appl. Surf. Sci.* **197**, 463–466.

Hayashi, H., Iwasa, S., Vasa, N. J., Yoshitake, T., Ueda, K., Yokoyama, S., and Higuchi, S. (2002b), *Jpn. J. Appl. Phys. Pt. 1—Regul. Pap. Short Notes Rev. Pap.* **41**, 410–411.

Higuchi, S., Ueda, K., Yahiro, F., Nakata, Y., Uetsuhara, H., Okada, T., and Maeda, M. (2201), *IEEE Transactions on Magnetic* **37**, 2451–2453.

Hirata, G. A., Lopez, O. A., Shea, L. E., Yi, J. Y., Cheeks, T., McKittrick, J., Siqueiros, J., Avalos-Borja, M., Esparza, A., and Falcony, C. (1996), *J. Vac. Sci. Technol. A—Vac. Surf. Films* **14**, 1694–1696.

Hu, W. S., Liu, Z. G., Sun, J., Guo, X. L., Yang, Z. J., Shi, L. J., and Feng, D. (1996), *Materials Science and Engineering B-Solid State Materials for Advanced Technology* **40**, 165–169.

Hu, W. S., Liu, Z. G., Sun, J., Zhu, S. N., Xu, Q. Q., Feng, D., and Ji, Z. M. (1997), *Journal of Physics and Chemistry of Solids* **58**, 853–857.

Ito, A., Machida, A., and Obara, M. (1997), *Appl. Phys. Lett.* **70**, 3338–3340.

Jackel, J. L., Rice, C. E., and Veselka, J. J. (1982), *Appl. Phys. Lett.* **41**, 607–608.

Jelinek, M., Eason, R. W., Lancok, J., Anderson, A. A., Grivas, C., Fotakis, C., Jastrabik, L., Flory, F., and Rigneault, H. (1998), *Thin Solid Films* **322**, 259–262.

Jelinek, M., Klini, A., Grivas, C., Lancok, J., Studnicka, V., Chval, C., Mackova, A., and Fotakis, C. (2002a), *Appl. Surf. Sci.* **197/198**, 416–420.

Jelinek, M., Lancok, J., Pavelka, M., Atanasov, P. A., Mackova, A., Flory, F., and Garapon, C. (2002b). *Applied Physics A-Materials Science & Processing* **74**, 481–485.

Katoh, Y., Sugimoto, N., Tate, A., and Shibukawa, A. (1992), *Jpn. J. Appl. Phys. Pt. 2—Lett.* **31**, L652–L654.

Katoh, Y., Sugimoto, N., Tate, A., and Shibukawa, A. (1993), *Jpn. J. Appl. Phys. Pt. 2—Lett.* **32**, L508–L510.

Kidoh, H., Morimoto, A., and Shimizu, T. (1991), *Appl. Phys. Lett.* **59**, 237–239.

Kim, D. W., Oh, S. M., Lee, S. H., and Noh, T. W. (1998), *Jpn. J. Appl. Phys. Pt. 1—Regul. Pap. Short Notes Rev. Pap.* **37**, 2016–2020.

Korzenski, M. B., Lecoeur, P., Mercey, B., Camy, P., and Doualan, J. L. (2001), *Appl. Phys. Lett.* **78**, 1210–1212.

Kumagai, H., Adachi, K., Ezaki, M., Toyoda, K., and Obara, M. (1997), *Appl. Surf. Sci.* **109/110**, 528–532.

Lancok, J., Jelinek, M., Grivas, C., Flory, F., Lebrasseur, E., and Garapon, C. (1999), *Thin Solid Films* **346**, 284–289.

Lancok, J., Garapon, C., Martinet, C., Mugnier, J., and Brenier, R. (2004), *Appl. Phys. A* **79**, 1263–1265.

Lecoeur, P., Korzenski, M. B., Ambrosini, A., Mercey, B., Camy, P., and Doualan, J. L. (2002), *Appl. Surf. Sci.* **186**, 403–407.

Lee, J. R., Baker, H. J., Friel, G. J., Hilton, G. J., and Hall, D. R. (2002), *Opt. Lett.* **27**, 524–526.

Liao, H. B., Xiao, R. F., Yu, P., and Wong, G. K. L. (1997), *J. Crystal Growth* **174**, 434–439.

Liu, J. M., Zhang, F., Liu, Z. G., Zhu, S. N., Shi, L. J., Wu, Z. C., and Ming, N. B. (1994), *Applied Physics Letters* **65**, 1995–1997.

Liu, J. M., Liu, Z. G., Zhu, S. N., Zhu, Y. Y., and Ming, N. B. (1996), *Appl. Surf. Sci.* **96/98**, 819–822.

Lucuta, P. G., Halliday, J. D., and Christian, B. (1992), *J. Mater. Sci.* **27**, 6053–6061.

Mackenzie, J. I., Li, C., and Shepherd, D. P. (2003), *IEEE J. Quant. Electron.* **39**, 493–500.

Mailis, S., Anderson, A. A., Barrington, S. J., Brocklesby, W. S., Greef, R., Rutt, H. N., and Eason, R. W. (1998), *Opt. Lett.* **23**, 1751–1753.

Mailis, S., Riziotis, C., Wang, J., Taylor, E., Anderson, A. A., Barrington, S. J., Rutt, H. N., Eason, R. W., Vainos, N. A., and Grivas, C. (1999), *Opt. Mater.* **12**, 27–33.

Mailis, S., Riziotis, C., Wellington, I. T., Smith, P. G. R., Gawith, C. B. E., and Eason, R. W. (2003), *Opt. Lett.* **28**, 1433–1435.

Manoravi, P., Willmott, P. R., Huber, J. R., and Greber, T. (1999), *Appl. Phys. A* **69**, S865–S867.

May-Smith, T. C., Grivas, C., Shepherd, D. P., Eason, R. W., and Healy, M. J. F. (2004), *Appl. Surf. Sci.* **223**, 361–371.

McKee, R. A., Walker, F. J., Conner, J. R., Specht, E. D., and Zelmon, D. E. (1991), *Appl. Phys. Lett.* **59**, 782–784.

McFarlane, R. A., Lui, M., and Yap, D. (1995), *IEEE J. Selected Top. Quant. Electron.* **1**, 82–91.

Muller, E. K., Nicholson, B. J., and Francombe, M. H. (1963), *Electrochem. Technol.* **1**, 158.

Murakami, K. (1992), in *Laser Ablation of Electronic Materials*, E. Fogarassy and S. Lazare (Eds.), Elsevier, The Netherlands.

Noh, T. W., Lee, S. H., Kim, D. W., Oh, S. M., Lim, M. J., Lee, S. D., Han, S. H., and Wu, J. W. (1998), *J. Korean Phys. Soc.* **32**, S1307–S1310.

Nourshargh, N., Starr, E. M., Fox, N. I., and Jones, S. G. (1985), *Electron. Lett.*, **21**, 818–820.

Ohring, M. (1992), *The Materials Science of Thin Films*, Academic, San Diego.

Okamura, Y., Yoshinaka, S., and Yamamoto, S. (1983), *Appl. Opt.* **22**, 3892–3894.

Perna, G., Capozzi, V., Pagliara, S., Ambrico, M., and Lojacono, D. (2001), *Thin Solid Films* **387**, 208–211.

Petraru, A., Schubert, J., Schmid, M., and Buchal, C. (2002), *Appl. Phys. Lett.* **81**, 1375–1377.

Pons-Y-Moll, O., Perriere, J., Millon, E., Defourneau, R. M., Defourneau, D., Vincent, B., Essahlaoui, A., Boudrioua, A., and Seiler, W. (2002), *Journal of Applied Physics* **92**, 4885–4890.

Ramaswamy, R. V., and Najafi, S. I. (1986), *IEEE J. Quant. Electron.* **22**, 883–891.

Ryu, Y. R., Zhu, S., Budai, J. D., Chandrasekhar, H. R., Miceli, P. F., and White, H. W. (2000), *Journal of Applied Physics*, **88**, 201–204.

Schwyn-Thony, S., Lehmann, H. W., and Gunter, P. (1992), Physical and optical characterisation of epitaxial waveguiding $KNbO_3$ thin films grown by sputter deposition, Conference on Lasers and Electro-optics (CLEO), paper CPD6, Anaheim, CA.

Schwyn-Thony, S., Youden, K. E., Harris, J. J. S., and Hesselink, L. (1994), *Appl. Phys. Lett.* **65**, 2018–2020.

Serna, R., and Afonso, C. N. (1996), *Appl. Phys. Lett.* **69**, 1541–1543.

Serna, R., Ballesteros, J. M., de Castro, M. J., Solis, J., and Afonso, C. N. (1998), *J. Appl. Phys.* **84**, 2352–2354.

Shepherd, D. P., Hettrick, S. J., Li, C., Mackenzie, J. I., Beach, R. J., Mitchell, S. C., and Meissner, H. E. (2001), *J. Phys. D. Appl. Phys.* **34**, 2420–2432.

Shibata, Y., Kaya, K., Akashi, K., Kanai, M., Kawai, T., and Kawai, S. (1993), *Appl. Phys. Lett.* **62**, 3046–3048.

Shimoda, T., Ishida, Y., Adachi, K., and Obara, M. (2001), *Opt. Commun.* **194**, 175–179.

Singh, S., Smith, R. G., and Van Uitert, L. G. (1974), *Phys. Rev. B* **10**, 2566–2572.

Stewen, C., Contag, K., Larionov, M., Giesen, A., and Hugel, H. (2000), *IEEE J. Sel. Top. Quant. Electron.* **6**, 650–656.

Studebaker, D. B., Stauf, G. T., Baum, T. H., Marks, T. J., Zhou, H., and Wong, G. K. (1997), *Appl. Phys. Lett.* **70**, 565–567.

Tang, Z. K., Wong, G. K. L., Yu, P., Kawasaki, M., Ohtomo, A., Koinuma, H., and Segawa, Y. (1998), *Appl. Phys. Lett.* **72**, 3270–3272.

Tomov, R. I., Kabadjova, T. K., Atanasov, P. A., Tonchev, S., Kaneva, M., Zherikhin, A., and Eason, R. W. (2000), *Vacuum* **58**, 396–403.

Townsend, P. D. (1976), *Inst. Phys. Conf. Ser.* **28**, 104–111.

Uetsuhara, H., Goto, S., Nakata, Y., Vasa, N., Okada, T., and Maeda, M. (1999), *Appl. Phys. A* **69**, S719–S722.

Vainos, N. A., Grivas, C., Fotakis, C., Eason, R. W., Anderson, A. A., Gill, D. S., Shepherd, D. P., Jelinek, M., Lancok, J., and Sonsky, J. (1998), *Appl. Surf. Sci.* **129**, 514–519.

Wada, M., and Miyazaki, Y. (1994), *IEICE Trans. Electron.* **E77C**, 1138–1145.

Wang, K., Shi, B., Cue, N., Zhu, Y., Xiao, R., Lu, F., Li, W., and Liu, Y. (1998), *Appl. Phys. Lett.* **73**, 1020–1022.

Wang, K. M., Shi, B. R., Cue, N., Zhu, Y. Y., Xiao, R. F., Lu, F., Hu, H., and Liu, Y. G. (2001), *J. Vac. Sci. Technol. A—Vac. Surf. Films* **19**, 394–397.

Wang, F. X., Li, W., Lu, F., Hu, H., Wang, J. M., Liu, Z. G., and Yong, Z. (2002), *Nucl. Instrum. Methods Phys. Res. Sect. B—Beam Interact. Mater. Atoms* **191**, 778–782.

Weber, H. P., Dunn, F. A., and Leibolt, W. N. (1973), *Appl. Opt.* **12**, 755.

Willmott, P. R., Manoravi, P., Huber, J. R., Greber, T., Murray, T. A., and Holliday, K. (1999), *Opt. Lett.* **24**, 1581–1583.

Willmott, P. R., Manoravi, P., and Holliday, K. (2000), *Appl. Phys. A—Mater. Sci. Process.* **70**, 425–429.

Xiong, F., Chang, R. P. H., Hagerman, M. E., Kozhevnikov, V. L., Poeppelmeier, K. R., Zhou, H., Wong, G. K., Ketterson, J. B., and White, C. W. (1994), *Appl. Phys. Lett.* **64**, 161–163.

Youden, K. E., Grevatt, T., Eason, R. W., Rutt, H. N., Deol, R. S., and Wylangowski, G. (1993), *Appl. Phys. Lett.* **63**, 1601–1603.

Yu, N., and Nastasi, M. (1994), *Appl. Phys. Lett.* **65**, 180–182.

Zaldo, C., Gill, D. S., Eason, R. W., Mendiola, J., and Chandler, P. J. (1994), *Appl. Phys. Lett.* **65**, 502–504.

Zhang, M. S., Zhang, P., Yin, Z., and Liu, J. (1999), *Appl. Phys. A—Mater. Sci. Process.* **69**, 389–395.

CHAPTER 18

Biomaterials: New Issues and Breakthroughs for Biomedical Applications

VALENTIN NELEA and ION N. MIHAILESCU

National Institute for Lasers, Plasma and Radiation Physics, Bucharest, Romania

MIROSLAV JELÍNEK

Institute of Physics ASCR, Prague, Czech Republic

18.1 INTRODUCTION

This chapter explains why biomedical thin layers, which are already widely used in implants in animal and human bodies, have even brighter future prospects. We critically discuss the potential of biocompatible, bioactive thin layers for specific applications in bone and dental surgery and implantology, focusing on new materials specifically developed for these purposes over the last decade. Practical work in this area moves forward alongside and in constructive interaction with academic research on live tissues and new materials for deposition as thin films and structures. The chapter contains direct references not only to materials but also to methods and current applications, including a comparative analysis of their advantages and shortcomings.

In all cases we mention future expected and/or mandatory developments to completely adapt new implants and other surgical devices to long-term, absolutely safe use inside the human body. The deposition of bioactive, biocompatible thin films is not a new task, and several techniques have been tested for the past half-century. Commercial devices, especially for plasma spraying, are available. Short- and medium-term experience of using these devices, as well as in vivo and in vitro tests, has revealed, however, some limitations to their large-scale implementation.

Pulsed laser deposition (PLD) emerged in the early 1990s as a rather easy to implement method and a compelling alternative for depositing bioactive, biocompatible, highly adherent, uniform thin films from a broad variety of materials used in implantology and surgery as a whole. The method was, and still is, universal, efficient, free of pollution due to the use of light sources for deposition, and readily adaptable to different geometries and complex structures.

The main goal of this chapter is to review all recent work in the field, including academic studies on, and direct applications of, novel materials and PLD techniques. We describe successful applications of depositions, discuss adhesion lifetime, and review the testing methods currently in

Pulsed Laser Deposition of Thin Films: Applications-Led Growth of Functional Materials
Edited by Robert Eason

use. We also outline the existing limits and adverse effects, indicating wherever possible, how they could be overcome.

18.2 BIOMATERIALS

18.2.1 Biocompatible Materials Overview

Defined as man-made materials designed to induce a specific biological activity [Williams, 1988], biomaterials are currently used for the repair and reconstruction of diseased or damaged parts of the musculo-skeletal system of vertebrates. Decades ago, materials were called *biocompatible* if they evoked a *minimal biological response*, that is, biocompatibility was defined by what it did not do, namely, trigger adverse effects. As a result, materials used to be divided into categories such as *compatible*, or *nontoxic*, and *noncompatible*, or *toxic.* At present, biocompatibility is described as the ability of a material to behave satisfactorily in a considered application [van Loon and Mars, 1997].

Biocompatible materials must meet several general requirements. They must:

1. Resist corrosion and chemical attacks by physiological fluids.
2. Withstand any mechanical stresses that may be applied to them or happen during their operating life.
3. Mold easily into a given shape.
4. Cause no allergic or toxic reactions.
5. Stop short of perturbing, or interfering with the immunological system.
6. Generate no damage to the blood (e.g., clotting) or plasma proteins [Hulbert, 1969].

Polymers, metals, ceramics, carbons, glasses, and composites have so far emerged as biocompatible materials [Ratner and Hench, 1999], and they can be in the form of powder, single crystals, polycrystalline, vitreous and/or glassy-ceramics.

No material implanted in a living tissue is inert; all materials elicit a response from the host tissue. According to the required types of implants/tissues, biomaterials fall into four categories [Ratner and Hench, 1999]:

1. *Biologically Inactive, Nearly Inert* The tissue responds by wrapping them up in a non-adherent fibrous capsule (*encapsulation*, *mechanical interlock-morphological fixation*). This is the case for metals and metal alloys (stainless steel, CoCrNi, CoCrMo, Ti, Ti alloy), alumina (Al_2O_3), zirconia (ZrO_2), carbon, carbon fiber-reinforced carbon, carbon fiber-reinforced triazine, latex, polyethylene, polymethylmethacrylate (PMMA), and so on.

2. *Porous* They facilitate tissue ingrowth into the pores (*biological fixation*): examples are microporous hydroxylapatite (HA) and HA-coated metals.

3. *Bioactive* They firmly bind to tissues (*bioactive fixation* through a chemical bond at the bone–implant interface). Bioactive materials elicit a specific biological response at the interface of the material leading to the formation of a natural bond (first shown in 1969) and development of de novo mineralized bone tissue. Materials in this class include dense calcium phosphate ceramics, bioactive glasses (45S5 Bioglass), bioactive glass–ceramics (Cerevital, Wollastonite A/W glass–ceramics, machinable glass–ceramics), bioactive composites (Palavital, stainless-steel fiber-reinforced Bioglass, polyethylene–HA mixtures, and so forth) [Hench, 1991].

4. *Resorbable* They are gradually replaced with tissue over time: Tricalcium phosphate (TCP), calcium aluminates, polylactic acid (PLA), poly-L-acetate fall into this category [Yamamuro and Hench, 1990].

As an effect of biomechanical limitations, bioglasses, glass–ceramics, and calcium phosphate ceramics are mainly used in *low* or *non-load-bearing* applications [Cao and Hench, 1996]. For

TABLE 18.1 Some Physical Properties of HA and Ti

Parameter	HA	Ti
Density[a] ($g\,cm^{-3}$)	3.15	4.51
Young's modulus[a] (GPa)	85–90	115
Knoop hardness[a] (MPa)	3450	4000
Tensile strength[a] ($MPa\,m^{-2}$)	120	340
Poisson coefficient	0.3	0.32
Thermal expansion[a] ($\times 10^{-6}\,K^{-1}$)	11	10
Melting point[a] (°C)	1660	1668
Specific heat[a] ($cal\,g^{-1}\,K^{-1}$)	0.15	0.13
Thermal conductivity[a] ($W\,cm^{-1}\,K^{-1}$)	0.01	0.2

[a]Handbook data from Torrisi and Setola [1993], reprinted with permission from Elsevier.

obvious reasons, metals are mechanically suitable for *load-bearing* orthopedic and dental implants. Nevertheless, various problems related to corrosion, wear, and poor tissue interactions have been reported [Hench and Ethridge, 1982]. Coating the metallic implants with thin layers of bioactive material combines mechanical advantages with excellent biocompatibility. For chemically binding coatings (orthopedic, dental, and maxillofacial prosthetics), HA, bioactive glasses, and bioactive glass–ceramic layers are applied. The mechanical properties and other parameters of HA and Ti are summarized for comparison in Table 18.1. For tissue ingrowth (cardiovascular, orthopedic, dental, and maxillofacial prosthetics), Al_2O_3 layers have been tested. For thromboresistant coating, pyrolitic, diamond-like, and glassy carbon are largely used. Carbon surfaces are thromboresistant, compatible with the cellular elements of blood, and therefore suitable for prosthetic heart valves [Hench, 1991].

18.2.2 Hydroxylapatite and Other Calcium Phosphates

Calcium phosphates (CaP) belong to the class of orthophosphates. Material is built around a network of PO_4 groups that confer a good stability to the structure. There are various CaP compounds that differ from one another in key parameters such as molar Ca/P ratio and solubility [Elliott, 1994]. In the case of pure compounds, the Ca/P atomic ratio ranges from 0.5 to 2. Materials are more acidic and water soluble as their Ca/P ratio decreases. Table 18.2 lists the most important CaP compounds with biocompatibility and bioactivity relevance.

Hydroxylapatite (HA), $Ca_{10}(PO_4)_6(OH)_2$, is a crystalline hydrated calcium phosphate the chemical composition and crystallographic structure of which are similar to the mineral part of bone and teeth [Elliot, 1994; Suchanek and Yoshimura, 1998]. HA is the most stable, least soluble in aqueous media of all calcium phosphates [Elliot, 1994]. The natural mineral component of bone ($\sim$50% weight and $\sim$70% volume) basically consists of HA.

Stoichiometric HA belongs to the *monoclinic* space group $P2_1/b$ and has the following lattice parameters: $a = 9.4214(8)$ Å, $b = 2a$, $c = 6.8814(7)$ Å, and $\gamma = 120°$. It has twice as many formula units per unit cell as the hexagonal unit and is the best organized, most thermodynamically stable HA form. A monoclinic to *hexagonal* phase transition [space group $P6_3/m$, (no. 176)] takes place above 250°C. Impurities like partial substitutions of hydroxide by fluoride or chloride ions stabilize the hexagonal structure of HA at ambient temperatures.

Ordinary HA (containing impurities and substitution ions) is hexagonal with the lattice parameters $a = b = 9.418$ (± 0.003) Å, $c = 6.884$ (± 0.003) Å, and $Z = 2$. Figure 18.1 displays a projection in the (001) basal plane of the hexagonal unit cell of HA.

Fluorapatite (FA), $Ca_{10}(PO_4)_6F_2$, is present in the dental enamel. It is a very stable compound, similar to HA in structure.

TABLE 18.2 Calcium Phosphate Compounds with Biocompatibility and Bioactivity Relevance

Acronym	Chemical Formula	Compound Name	Ca/P Ratio
HA	$Ca_{10}(PO_4)_6(OH)_2$	Hydroxylapatite	1.67
FA	$Ca_{10}(PO_4)_6F_2$	Fluorapatite	1.67
CDHA	$Ca_{10-x}(HPO_4)_x(PO_4)_{6-x}(OH)_{2-x}$ $(0 < x < 2)$	Calcium-deficient hydroxylapatite	1.33–1.67
BA	$Ca_{8.3}(PO_4)_{4.3}(CO_3 : HPO_4)_{1.7}(OH)_{0.3}$ BA = carbonated CDHA$(x = 1.7)$	Biological apatite	1.38–1.93
OHA	$Ca_{10}(PO_4)_6(OH)_{2-2x}O_x\square_x^a$ $(0 < x < 1)$	Oxyhydroxylapatite	1.67
OA	$Ca_{10}O(PO_4)_6$	Oxyapatite	1.67
MCPM	$Ca(H_2PO_4)_2 \cdot H_2O$	Monocalcium phosphate monohydrate	0.5
MCPA	$Ca(H_2PO_4)_2$	Monocalcium phosphate anhydrate	0.5
DCPD	$CaHPO_4 \cdot 2H_2O$	Dicalcium phosphate dihydrate (*Brushite*)	1
DCPA	$CaHPO_4$	Dicalcium phosphate anhydrate (*Monetite*)	1
OCP	$Ca_8(HPO_4)_2(PO_4)_4 \cdot 5H_2O$	Octacalcium phosphate	1.33
α-TCP	$Ca_3(PO_4)_2$ (*monoclinic*)	Tricalcium phosphate (phase α)	1.5
β-TCP	$Ca_3(PO_4)_2$ (*rhombohedral*)	Tricalcium phosphate (phase β, *Whitlockite*)	1.5
TTCP	$Ca_4O(PO_4)_2$	Tetracalcium phosphate	2
α-DCP	$Ca_2P_2O_7$ (*orthorhombic*)	Dicalcium phosphate (phase α)	1
β-DCP	$Ca_2P_2O_7$ (*tetragonal*)	Dicalcium phosphate (phase β) (Calcium pyrophosphate)	1
ACP	$Ca_x(PO_4)_y \cdot nH_2O$	Amorphous calcium phosphate	1.2–2.2

[a] □ indicates a vacancy in the crystallographic lattice.

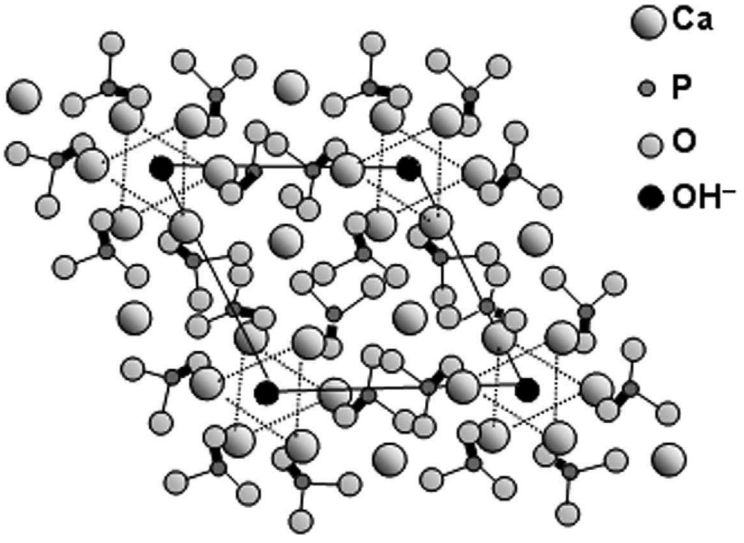

Figure 18.1 Projection in the (001) basal plane of the hexagonal unit cell of hydroxylapatite.

Biological hydroxylapatite (BA, *dahllite phase*, present in natural mineralized bony tissues) contains carbonate $(CO_3)^{2-}$ [Dorozhkin and Epple, 2002]. Half of the $(CO_3)^{2-}$ is adsorbed on the crystal surface, while the other half resides in the bulk in the $(PO_4)^{3-}$ and OH^- positions. Carbonate accounts for as little as 3–6% of human body hard tissue. BA also includes small amounts of hydrogen phosphate ions $(HPO_4)^{2-}$ and alkali metals, namely Na^+. In terms of structure, BA is a poorly crystallized, nonstoichiometric HA. The Ca/P ratio ranges from close to 2 for carbonate-rich apatites to 1.33 for $(HPO_4)^{2-}$-rich apatites. During aging, $(CO_3)^{2-}$, which is low in young tissues, replaces $(HPO_4)^{2-}$ ions. The composition therefore keeps constant in time, in agreement with the initial BA, that is, $Ca_{8.3}(PO_4)_{4.3}(CO_3{:}HPO_4)_{1.7}(OH)_{0.3}$ [Brès and Hardouin, 1988].

Carbonated apatite (CA) occurs in two forms: *type A*, where hydroxyl partly substitutes for carbonate ions, and *type B*, where carbonate replaces phosphate ions in the apatite lattice [Cao and Hench, 1996]. BA is mainly *type*-B carbonated with a small amount of *type*-A.

CaP phase stability strongly depends on temperature and water presence during processing in ambient atmospheres. At human body temperature, two forms of CaP only are stable: DCPD for pH lower than 4.2 and HA for pH higher than 4.2. Other phases, such as anhydrous β-TCP or TTCP, are stable at higher temperatures and form HA by interaction with water or body fluids at ca. 37°C.

There are two main ways to synthesize HA powders: *wet methods* and *solid-state reactions* [Suchanek and Yoshimura, 1998]. Wet methods include precipitation, hydrothermal processing, and hydrolysis of aqueous CaP solutions. Solid-state reactions usually give rise to well-crystallized, stoichiometric products. Other methods to produce HA powders are sol–gel, electrocrystallization, spray pyrolysis, freeze–drying, microwave irradiation, mechano-chemical synthesis, mechanical alloying, emulsion processing, and biomimetics.

18.2.3 Hydroxylapatite-Based Composites

Reinforcement materials (*ceramics*, *metals*, or *polymers*) have been tested to improve the reliability of HA ceramics [Hench, 1991; Suchanek and Yoshimura, 1998]. They were applied as particles, platelets, whiskers, long fibers, dispersoids, and nanoparticles (nanocomposites). Table 18.3 summarizes the most important HA composites.

18.2.4 Diamond-like Carbon and Carbon-Based Materials

Carbon exists as amorphous, glassy, and crystalline. Carbon has become well established as a material with excellent biocompatibility, perhaps due to its unique position as a basic element for all organic systems. Its ability to form bonds in sp^1, sp^2, and sp^3 configurations forms the basis for the diversity of carbon materials [Butter and Lettington, 1995]. There are two forms of carbon most frequently used as coating in biomedical applications: pyrolitic carbon and diamond-like carbon (DLC). Pyrolitic carbon layers are fabricated by thermal decomposition of hydrocarbons at temperatures 1000–2400°C [Bokros, 1969]. Such layers are frequently used for coating of heart valves. During the past decade DLC also became an excellent candidate coating material for use in medical applications. DLC layers are amorphous or contain microcrystalline or nanocrystalline diamond and graphite as well as a disordered structure of a mixture of configurations. DLC can be hydrogen free (*a*-C) or contain hydrogen [hydrogenated amorphous carbon (*a*-C:H)]. DLC films demonstrate excellent physical and chemical properties and a high level of biocompatibility [Dumkum et al., 1997]. The films are dense, mechanically hard, smooth, impervious, abrasion resistant, infrared (IR) transparent, chemically inert, resistant to attack by either acids or bases, have a low coefficient of friction, low wear rate, and are biocompatible and thromboresistant [Robertson, 1992]. DLC coatings are adherent on a range of biomaterials and no toxicity toward certain living cells and no inflammatory response or loss of cell integrity has been reported [Cui and Li, 2000]. The properties of DLC coating depend strongly on the hydrogen content and sp^3/sp^2 ratio, which in turn are determined by the deposition process and its parameters. The spread of properties of DLC

TABLE 18.3 Hydroxylapatite Composites

Mixing Material	Form	Extent	Function	Remarks	References
Ti, Ti6Al4V	Particles	—	Reinforcing	—	Khor et al., 2000
Ti6Al4V	Coatings	—	Bond strength	By plasma spraying	Khor et al., 2000
Ti	Coatings	5–75 vol %	increasing	By RF magnetron sputtering	Ding et al., 1999
Fe–Cr alloy	Fibers	20–30 vol %	Reinforcing	Corrosion in body fluids, bad reaction with tissues	Suchanek and Yoshimura, 1998
Ni_3Al	Fibers	—	Reinforcing	Corrosion in body fluids, bad reaction with tissues	Suchanek and Yoshimura, 1998
316L SS	Fibers	20 vol %	Reinforcing	Microcracks in HA matrix	Miao, 2003
ZrO_2	Fibers	10 vol %	Reinforcing	Wear resistance	Suchanek and Yoshimura, 1998
	Coatings	10 wt %	Bond strength increasing	By plasma spraying	Chou and Chang, 2002
ZrO_2 (PSZ)[a]	Particles	10–50 vol %	Reinforcing	Degradation in wet media	Cao and Hench, 1996; Suchanek and Yoshimura, 1998
CaF_2–ZrO_2	Particles	<5 vol % CaF_2 <40 vol % ZrO_2	Reinforcing	Suppression of HA to β-TCP decomposition	Kim et al, 2002
Al_2O_3	Fibers	10 vol %	Reinforcing	Wear resistance,	Cao and Hench, 1996; Suchanek and Yoshimura, 1998
	Particles	5–30 vol %		Low corrosion	
	Powders	30–85 vol %			Li et al., 1995
TiO_2	Particles	—	Reinforcing	Wear resistance	Cao and Hench, 1996
	Coatings	50 vol %	Bond strength increasing	By sol–gel	Milella et al., 2001
C	Fibers	10 vol %	Reinforcing	—	Suchanek and Yoshimura, 1998
	Nanoparticles	5 wt %		Wear resistance	
SiC	Platelets	5–15 vol %	Reinforcing	Low corrosion	Suchanek and Yoshimura, 1998
	Whiskers	5–60 vol %		Toxicity doubts	
Si_3N_4	Whiskers	5–60 vol %	Reinforcing	Toxicity doubts	Suchanek and Yoshimura, 1998
Diopside[b]	Whiskers	5–60 vol %	Reinforcing	—	Suchanek and Yoshimura, 1998

TABLE 18.3 (*Continued*)

Mixing Material	Form	Extent	Function	Remarks	References
HA	Whiskers	20 vol %	Reinforcing + bioactivity	—	Suchanek and Yoshimura, 1998
TCP	Powder	—	Biodegradability	—	Suchanek and Yoshimura, 1998
$CaSO_4$[c]	Powder	—	Biodegradability	—	Suchanek and Yoshimura, 1998
Bioglass/ Glass–ceramic	Powder	—	Reinforcing + bioactivity	—	Suchanek and Yoshimura, 1998
	Coatings	4 wt %		By plasma spraying	Silva et al., 1998.
Polyethylene	—	50–60 vol %	Stiffness decreasing	Brittle-ductile transition for 40–45 vol % HA	Bonfield, 1988
Polyhydroxy-butyrate	—	60 vol %	Stiffness decreasing	—	Bonfield, 1988
Polyhexa-methylene-adipamide	Solution	>35 vol %	Artificial bone	—	Wang et al., 2002
Polyamide 66	Solution	35 wt %	Artificial bone	Porous scaffold for tissue eng.	Jie and Yubao, 2004
Polyether etherketone	Injection moulded	>59 vol % >37 wt %	Stiffness decreasing	—	Abu Bakar et al. 2003
Polyvinyl-acetate	Coating	4 wt %	Bond strength increasing	By electro-chemistry	Hu et al., 2002
Poly(L-lactide)	—	—	Biocompatibility	Toxicity doubts	Suchanek and Yoshimura, 1998
Poly (D,L-lactide/ ε-caprolactone)	Solution	40–80 vol %	Biodegradability	HA reduces degradation rate	Ural et al., 2000
Chitosan	Solution	—	Artificial bone	—	Chen et al., 2002
Collagen	Fibers,	—	Osteoconduction	—	Suchanek and Yoshimura, 1998
	Membrane				Silva et al., 2001
Gelatin	Films	40–95 wt %	Mechanical anisotropy	—	Bigi et al., 1998
Elastin peptides	Colloids	—	ECM[d] generation	—	Rovira et al., 1993

[a]PSZ = partially stabilized zirconia (3 mol % Y_2O_3-ZrO_2).
[b]Diopside = calcium magnesium silicate ($CaMgSi_2O_6$).
[c]$CaSO_4$ = also called *plaster of Paris*.
[d]ECM = extracellular matrix.

produced by different methods and under different process parameters is considerable. The biological behavior of an implant is strongly influenced by the chemical situation on the surface, and consequently, bioreactions can be tuned by changing the surface chemistry. DLC, as a biocompatible base material, can be easily alloyed with other biocompatible materials such as titanium or silicon, or with toxic materials such as silver, copper, and vanadium. By changing the alloy element concentration, it should be possible to tailor the bioreaction to any desired point between the bioproperties of DLC and those of the added element. This allows for preparing surfaces with tunable antibacterial effects. Analogous to the tailoring of the mechanical properties of DLC by deposition conditions or alloying, the biological properties of DLC can also be altered [Hauert and Muller, 2003]. DLC shows an excellent hemocompatibility, a decreased tendency of thrombus formation and coated heart valves and stents are already commercially available [Hauert and Muller, 2003]. Excellent mechanical properties justify usage of DLC in different tribological applications. DLC is a hard solid lubricant, implying that it cannot be pushed out of the contact area between the friction pair in contrast to oil or grease. For more details on DLC and tribological coatings, please refer to Chapters 15 and 23, respetively.

18.3 PROCESSING METHODS

18.3.1 Current Deposition Methods: Advantages and Limitations

Calcium phosphate bioceramics have been used in medicine and dentistry for more than 20 years [Hench, 1991]. The main applications are coatings of orthopedic prosthesis and dental implants, alveolar ridge augmentation, maxillofacial surgery, otolaryngology, spinal surgery, and bone growth scaffolds. They are also used as powders in total hip and knee surgery, as small, unloaded implants, low-loaded porous implants, and as bioactive phases in a polymer–bioactive ceramic composite [Hench, 1991; Suchanek and Yoshimura, 1998].

Bioglass and glass–ceramics have been used in bone prosthesis and dental porcelain manufacturing. Carbon in pyrolytic form and DLC is largely used to coat artificial heart valves, but coating of dental and orthopedic implants, joint replacement, and more recently coronary stents have also been studied. Research was also conducted on fluorinated carbonaceous thin films with polymer-like structure that have proven to have excellent hemocompatibility and antithrombogenicity [Clarotti et al., 1992].

Table 18.4 presents a synopsis of the methods most widely used for HA and CaP deposition. Some of these methods are frequently applied, while others are still in their testing phase. There is plenty of literature available on physical deposition methods (*dry processes*) such as vacuum or atmospheric plasma spraying, detonation-gun spraying, high-velocity oxyfuel process (generally known as *thermal processing*), radio frequency (RF) or direct current (DC) magnetron sputtering, electron beam evaporation, pulsed laser deposition, ion beam sputtering, ion-beam-assisted deposition, and simultaneous vapor deposition. Chemical methods (*wet processes*) like sol–gel, immersion coating, hot-isostatic pressing, electrophoretic deposition, electrochemical deposition, (micro)-emulsion routes, dip coating sintering, frit enameling, spark anodization followed by hydrothermal treatment, or biomimetic routes have also been applied. Other techniques, including laser cladding and screen-printing of mechanically alloyed HA nanocrystals, have recently been tested.

Carbon and DLC coatings can be prepared by a variety of chemical vapor deposition (CVD) and physical vapor deposition (PVD) methods, including plasma decomposition of hydrocarbons, hot filament, microwave plasma, RF or DC plasma-enhanced CVD, RF and DC reactive magnetron sputtering, ion beam plating, ion beam sputtering, ion beam deposition, ion-beam-assisted deposition, laser-CVD, and pulsed laser deposition [Robertson, 1992]. In CVD, layers are usually obtained by chemical reactions between methane and hydrogen, and the resulting films contain residual hydrogen. In PVD processes, however, the films usually do not include hydrogen. In PLD, high-quality DLC films have been grown from graphite targets in vacuum ambient, at low substrate temperatures and very high laser intensities (10^{10}–10^{14} W cm^{-2}).

TABLE 18.4 Most Common Methods to Deposit HA Thin Films and Coatings

Methods	Working Gas	Typical Thickness (μm)	Surface Morphology	Advantages	Disadvantages	References
Plasma spraying	Ar, N_2, H_2	50–200	Very rough, irregular and porous	Macroporosity may enhance bone in-growth Large deposition area High deposition rate *High-temperature processing*	Poor cohesive and bond strength Very irregular morphology Large amount of amorphous material Undesired secondary phases	Gross and Berndt, 1994
Magnetron sputtering	Ar, Ar/O_2	<2	Smooth, uniform	High density, high adherence Uniformity over large areas even on awkward shape objects	Amorphousness, TTCP and CaO Low deposition rate (~ 1 μm/h) Ca/P atomic ratio >1.67	van Dijk et al., 1995
Ion beam (assisted) deposition Ion beam sputtering	Vacuum	<1	Smooth	High adherence	High vacuum mandatory Amorphousness	Solnick-Legg and Legg, 1989
Pulsed laser deposition	Inert gas, O_2, H_2O or mixtures of them, N_2O	<1	Smooth/rough depending on deposition parameters and target properties	High density, high crystallinity Proper stoichiometry Well-controlled Ca/P ratio Excellent adherence, clean process *Moderate temperature processing*	Limitation in deposition on large area and in thickness uniformity	Cottel, 1994; Cottel et al.,1993
Laser cladding	Inert gas	300–400	Smooth	Controlled clad shape Localized processing heating Strong fusion bonding between coating and Ti	CaP phases other than HA: α-TCP, CaP glass (amorphous) with same Ca/P ratio as HA	Lusquiños et al., 2001
Sol–gel	—	~ 1	Rough, sometimes porous	Various substrate shapes *Moderate temperature processing*	Poor integrity and microstructure	Lopatin et al., 1998

TABLE 18.4 (*Continued*)

Methods	Working Gas	Typical Thickness (μm)	Surface Morphology	Advantages	Disadvantages	References
Electrophoretic deposition	—	<20	Rough	Efficient covering of complex-shaped substrates and cavities of porous substrates	Poor bond strength Shrinkage and cracking	Ducheney et al., 1990
Biomimetic deposition	—	Tens of μm	Rough, porous	Variability of stoichiometry and Ca/P formed material	Low adhesion to the substrate Necessity to treat/ functionalize the substrate surface	Kawai et al., 2004
Screen printing	—	20–400	Granular, rough	No melting of HA powders, because printing paste material is obtained by mechanical alloying Acceptable stoichiometry	Nonuniformity and –continuity of the surface	Silva et al., 2005

18.3.2 Pulsed Laser Deposition of Hydroxylapatite and Other Calcium Phosphate Thin Films

18.3.2.1 Introductive Insight

The prime advantages of PLD applied to HA-based bioceramics are its ability to grow pure, crystalline, stoichiometric HA films in conjunction with its flexibility to control the morphology, phase, crystallinity, and chemical composition of other CaP compounds. As these characteristics have a preferential influence on biological properties, such as bioresorbability (or dissolution involved in the osseointegration of coatings), PLD may be used to make in situ ''biodevices,'' mainly consisting of different nanostructured biomaterials and bioinspired materials. Moreover, nanocrystalline HA-based ceramics (with small grains) may exhibit enhanced strength and toughness, and thermal expansion coefficients that practically match those of the substrates (Si or Ti-alloy), due to the large volume fraction of atoms located at the grain boundaries [Narayan, 2005]. A cross section through a bone implant is outlined in Figure 18.2.

Sintered artificial CaP and HA materials, natural (mineral) bulk samples of different apatites, and human and animal teeth and bones were used as deposition targets.

18.3.2.2 Laser Systems Used for Deposition

Laser wavelength, fluence, and pulse duration are critical parameters governing target ablation and subsequent CaP film deposition. They determine the morphology, phase, crystallinity, and stoichiometry of deposited coatings. Most studies were performed with excimer laser sources generating pulses of 20–35 ns at 248 nm KrF* and 193 nm ArF* [Cotell el al., 1992; Mayor et al., 1998]. A XeCl excimer laser (308 nm) was also applied in one study [Nelea, 2002]. A TEA CO_2 laser (10.6 μm) with pulses of 100 ns or $\geq$1 μs was also used [Antonov et al., 1995]. Some studies reported the use of continuous-wave (cw) CO_2 lasers for the homogenous heating of real cylindrical Ti dental implants as the intended substrates for deposition [Jelínek et al., 1996]. Pioneering PLD work with a *Q*-switched ruby laser source (694 nm, 25 ns) was done by Torrisi and Setola [1993]. HA depositions were also performed using the pulsed second (532 nm), third (355 nm), and fourth (266 nm) harmonics of an Nd : YAG laser [Nistor et al., 2004; Fernández-Pradas et al., 2002a; Zeng and Lacefield, 2000]. The cw 1064-nm emission of Nd : YAG was also used for the soft laser treatment of PLD pseudowollastonite (α-$CaSiO_3$) thin films [D'Allesio et al., 2001]

18.3.2.3 Deposition Conditions

The first successful PLD of HA nanocrystalline layers was reported by Cotell et al. [1992]. The most important contributions and issues concerning PLD of HA since Cotell's works to date are summarized in Table 18.5. Some relevant experimental results are presented in Figures 18.3.–18.5.

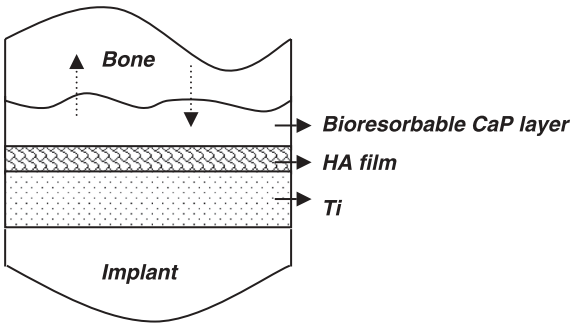

Figure 18.2 Scheme of a biofunctional bone implant.

TABLE 18.5 Main Research Work of PLD of HA

Laser/ Wavelength/ Pulse Duration	Substrate	Laser Fluence ($J\,cm^{-2}$)	Substrate Temperature, T (°C)	Deposition Environment	Environ, Pressure p (Pa)	Post-deposition Annealing Temp. (°C)/ Environment	Phase	Film Characteristics At. Ca/P Ratio	Surface/Growth Morphology	References
KrF* 248 nm 25 ns	Si	2–3	500–600	O_2, Ar, N_2, H_2O Ar/H_2O	6.6–67	—	TCP in Ar HA + TCP in O_2 HA in Ar/H_2O	1.65–1.8	Smooth with few particulates	Singh et al., 1994
KrF* 248 nm 20; 30 ns TEA CO_2 10.6 μm 1 μs; 100 ns	Ti, Ti6Al4V Polyethylene PTFE (Teflon) Poly-L-lactide Poly-ε-caprolactone	0.7–20	RT, 400	Vacuum, residual air	10^{-3}–100	400–575 Ar, Ar/H_2, Res. air, Res. air/H_2 1 h	ACP (as-deposited) HA (after annealing)	1.62–2.3	Dense, smooth with macroparticles More rougher with TEA CO_2	Antonov et al., 1995 Bagratashvili et al., 1995 Antonov et al., 2003
KrF* 248 nm 20; 30 ns	Ti, Ti6Al4V fused silica Dental implant: Ti-sand blasted	3–13	200–780	Vacuum, H_2O, Ar/H_2O	10^{-3}–100	—	ACP ($T < 400$°C) HA (in Ar/H_2O and $T > 400$°C) Traces of TTCP, TCP, and CaO TiO_2 (anatase, rutile) at high T	1.6–3.33	Smooth with particulates	Jelínek et al., 1995 Jelínek et al., 1996
ArF* 193 nm 21 ns	Ti (grade 2) (sand blasted)	*Not specified*	500–600	Ar/H_2O	6.7	—	HA	1.99	Rough with particulates columnar growth	Wang et al., 1997
ArF* 193 nm 20 ns	Ti, α-Al_2O_3 SiO_2//Si (100) Polyimide Silicone rubber PTFE, PET	1	RT 100	O_2	5×10^{-3}	550 O_2/H_2O 240–360 O_2/H_2O	HA	2.03–2.08	Smooth, following the substrate shape	Hontsu et al., 1996

ArF* 193 nm 23 ns		3.5	575		15–150		HA	—	Highly dense, smooth particulates free	
KrF* 248 nm 23; 34 ns	Ti6Al4V	1–5.2	RT–600	H_2O	0.02–45	—	ACP at RT HA Traces of TTCP and TCP	1.5–2	Compact grains with particulates, rough than with ArF*	Fernández-Pradas et al., 1998
Nd:YAG 355 nm 10 ns		2.2–7.8	RT–600		10; 45		ACP ($T < 400°C$) HA + α-TCP	1.2–2	Glassy structure with more particulates, rough, granular growth	Fernández-Pradas et al., 2002a
ArF* 193 nm 20 ns	Ti, Ti6Al4V, Si (100), Si (111)	0.8–1.6	295–525	H_2O	15–80	—	Carbonated HA	1.48–2.32	Quite smooth, compact	Arias et al., 2000 Arias et al., 2002
KrF* 248 nm 20 ns	Si(100)	4	650	N_2O	10^{-3}–10	450, O_2, UV (172 nm),	HA + TCP trace Pure HA after annealing	1.67–1.72	—	Craciun et al., 1999
Nd:YAG 355 nm 266 nm 5 ns	Ti (grade 2) Si	2–6.5	RT-600	Ar/H_2O	40–106	—	ACP ($T < 400°C$) HA + TCP trace ($T > 400°C$)	1.77–2	Highly porous, rough (at 355 nm rougher than at 266 nm)	Zeng and Lacefield, 2000
KrF* 248 nm 20 ns	Ti5Al2.5Fe coated or not with TiN, Al_2O_3, ZrO_2		RT 525 675 800	Vacuum	10^{-3}	550, air, 1h — — —	HA ACP + HA + TCP + TTCP TTCP TTCP + CaO	1.73–2	Somewhat porous rather rough, particulates	Nelea et al., 2000 Nelea, 2002

(*Continued*)

TABLE 18.5 (*Continued*)

Laser/ Wavelength/ Pulse Duration	Substrate	Laser Fluence ($J\,cm^{-2}$)	Substrate Temperature, T (°C)	Deposition Environment	Environ, Pressure p (Pa)	Post-deposition Annealing Temp. (°C)/ Environment	Phase	Film Characteristics At. Ca/P Ratio	Surface/Growth Morphology	References
XeCl* 308 nm 30 ns	316L stainless steel	1–2	RT	Vacuum	10^{-3}	550, air, 1h	HA + traces of TCP and TTCP	2.2	Rather rough with particulates	Nelea et al., 2000; Nelea, 2002
KrF* 248 nm 23 ns	Ti, Glass KBr	0.75–4.5	250	Vacuum	2.7×10^{-3}	550, air, 2h	Carbonated HA *(target from teeth powders)*	—	Rough, features with $<3\,\mu m$ in diameter	Smausz et al., 2004
ArF* 193 nm 20 ns		0.75–12								
ArF* 193 nm 25 ns	Biomorphic SiC	4.2	290–490	H_2O	15–80	—	Carbonated HA best crystalline film at 45 Pa	1.53–1.82	—	Borrajo et al., 2005
KrF* 248 nm 25 ns	DLC-coated Si and -Ti6Al4V	3	RT	*Not specified*	—	—	Polycrystalline HA nanocrystals: 5–15 nm	—	Smooth with sporadic micron-size particulates	Narayan, 2005
KrF* 248 nm	Ti	5	RT	H_2O	133	—	ACP Polycrystallized domains for a 900°C-sintered target	1.7–2	Micrometric particulates, some ablating debris	Katto et al., 2002 Katto et al., 2005
KrF* 248 nm	SiO_2//Si	2	600	H_2O	1.33–133	—	HA at $p > 17$ Pa high-density HA at 33 Pa TTCP + CaO at 2.7 Pa	1.8–2.5 decrease with $p(H_2O)$	Smooth, granular particulates at low $p(H_2O)$ Porous at grain boundaries when $p(H_2O)$ increases	Lee et al., 2005

Nd:YAG 532 nm Nd:YAG 335 nm	Ti- and TiN-coated Si	1.4–4.4 5.7	300	Vacuum	$1–3 \times 10^{-2}$	—	Polycrystalline HA nanocrystals $<$ 50 nm	—	Continuous, rough Polyhedral and spherical particulates	Nistor et al., 2004
KrF* 248 nm	Ti Ti6Al4V	4–7	625–850	Ar/H_2O	40–80	—	HA + α-TCP Biphasic HA/TTCP		smoother at 355 nm, —	Kim et al., 2005
Nd:YAG 532 nm 10 ns	Ti	12.3	RT	Vacuum	1.5×10^{-4}	—	No HA amorphousness	1.88–1.98 wt.	Spherical grains, ablation fragments, glassy-like	Ferro et al., 2005
KrF* 248 nm 25 ns	Si(100) Ti6Al4V	4–5	RT	Vacuum	3×10^{-6}	$T \leq 800$	ACP HA (annealed at $T \geq 340°C$) *340°C:* amorphous → crystalline transition temperature	—	Micrometric particulates, grain-like particles	Johnson et al., 2005

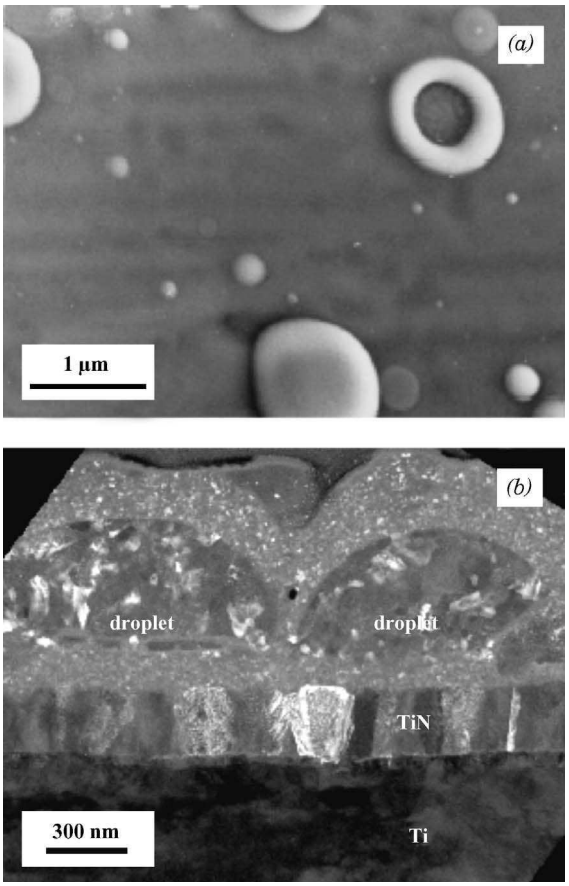

Figure 18.3 (a) SEM image of an HA film deposited with a KrF* laser at 5.8 J cm^{-2} fluence in 2 Pa residual air at RT. Tablet-shaped particulates with a depression at the center were observed on the film surface [Bagratashvili et al., 1995], with permission from the American Institute of Physics. (b) XTEM image of a HA/TiN/Ti multilayer specimen showing particulates trapped into HA film depth. The HA film was grown with a KrF* laser at 1–2 J cm^{-2} fluence in vacuum at RT and annealed in air at 550°C for 1 h. HA crystallites were 20–30 nm in size. Particulates were semispheres of submicrometer radius constituted of crystals (100–150 nm size) that grew perpendicularly to the interface [Iliescu et al., 2004a], with permission from Elsevier.

Most studies were performed with pure HA targets. Ferro et al. [2005] performed depositions from 10% FA-HA targets with a Nd : YAG laser (532 nm) at high fluence. The FA content in the target had no influence on film morphology that mainly consists of spherical grains and ablation fragments. No apatite phase was detected in the film; only a calcium-depleted CaP phase, that is, $Ca(PO_3)_2$, possibly textured, was present. Narayan [2005] has reported the deposition of HA-DLC bilayered nanocomposites. The authors suggest that the DLC layer serves to improve the adhesion of the HA coating and to prevent corrosion or third-body wear in bulk implant material. Moreover, a continuous nanocrystalline HA layer adjacent to the substrate surface may have greater cohesive strength due to an increased number of intra- and interlamellar bonding. Biocompatible carbonated HA thin films doped with divalent Mn^{2+} ions deposited on an etched Ti substrate by PLD were reported [Gyorgy et al., 2004]. Stoichiometric and crystalline coatings were obtained by deposition in 10 Pa O_2 atmosphere, 400°C, with a KrF* excimer laser. Films were subjected to postdeposition

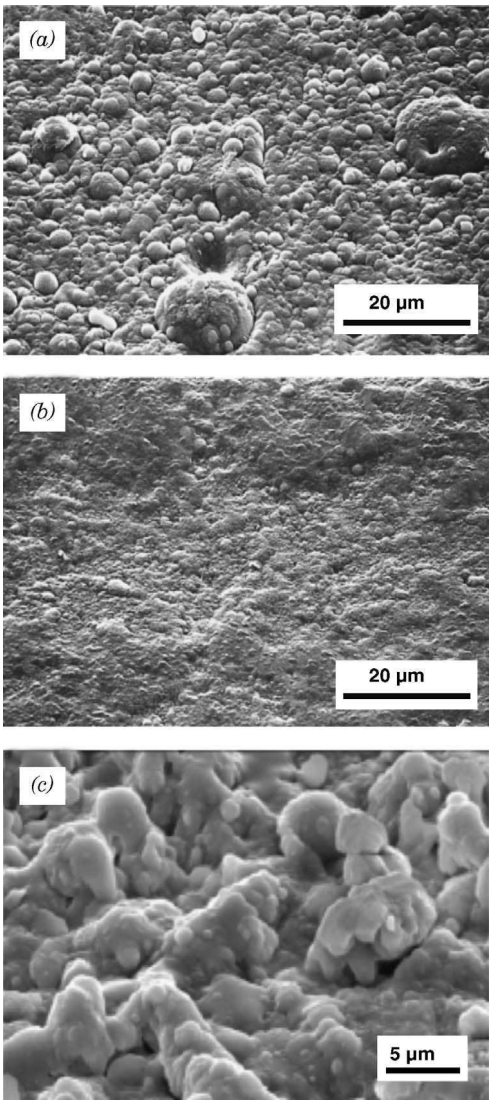

Figure 18.4 SEM images of HA coatings deposited with (a) KrF* (248 nm), (b) ArF* (193 nm), and (c) Nd:YAG (355 nm) lasers. Coatings were grown in 15–150 Pa (a,b) and 45 Pa (c) water vapors at 3.5 (a,b) and 2.2 J cm^{-2} (c) laser fluence on Ti6Al4V substrates heated at 575°C. Films grown with Nd:YAG were granular and rough. Films grown with excimer lasers were dense and contained embedded droplets (KrF*), or were particulate-free (ArF*) [Fernández-Pradas et al., 1998, 2002a], with permission from Elsevier.

heat treatments in hot-water-vapor-enriched environments at 400°C. The manganese divalent ions, supposed to activate integrins and accelerate cell adhesion, were correctly transferred in the films.

A new generation of bioactive CaP, namely $Ca_8(HPO_4)_2(PO_4)_4 \cdot 5H_2O$ (OCP) was the subject of recent PLD experiments [Iliescu et al., 2004a; Socol et al., 2004]. OCP occurs as a transient compound in the precipitation of HA and natural BA. Because of this, OCP is believed to play an essential role in the in vivo mineralization and ossification processes of

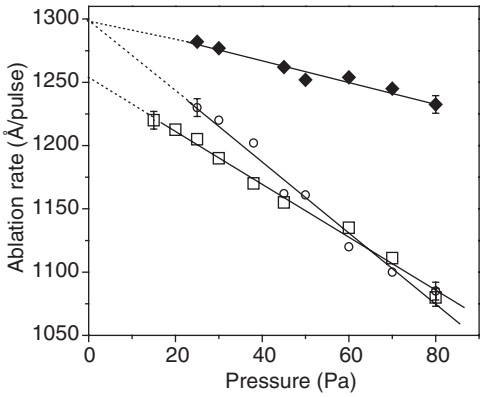

Figure 18.5 Ablation rate vs. pressure of (□) H_2O, (○) Ar, and (◆) O_2 for HA target irradiated with an ArF laser at $0.9\,J\,cm^{-2}$ fluence. The ablation rate decreases when the pressure increases [Arias et al., 2003a].

mammalian bones and teeth. Deposited OCP films were essentially amorphous, but did contain embedded crystalline grains [Iliescu et al., 2004a]. Coatings have rather porous surface morphology with cauliflower-like aggregates. A view across such an aggregate shows a dense brushlike layer on the top. OCP nanoparticles nucleate, coalesce, and accrete perpendicularly to the substrate in a porous treelike structure, comparable to a coral reef (Fig. 18.6.)

18.3.2.4 Postdeposition Annealing and Other Treatments

Craciun et al. [1999] have deposited HA films in low-pressure N_2O on Si substrates heated to 650°C. N_2O is a very strong oxidizing agent, more reactive than oxygen. After deposition, films were annealed under vacuum ultraviolet (VUV) irradiation (172 nm) of a Xe excimer lamp. Optical annealing proved highly efficient for growing high-quality HA layers at low substrate temperatures. Pure, crystalline, and stoichiometric HA thin-films deposition without the use of water vapors have been presented by Nelea et al. [Nelea et al.,2000; Nelea, 2002]. Coatings are obtained at room temperature (RT) on pure Ti and Ti-alloy with a KrF* laser followed by postdeposition annealing at 550°C in standard pressure ambient air. Buffer layers of TiN, Al_2O_3, or ZrO_2 were inserted at the HA coating–Ti substrate interface [Nelea et al., 2000]. For surface modification and greater densification of these films, a high-energy (MeV range) ion beam implantation with Ar^+ or N^+ ions was applied [Nelea et al., 2002a; Pelletier et al., 2004]. Ion implantation proves to be an efficient tool for HA film densification at low temperature with increased nanohardness and elastic modulus and no altering of the HA crystalline phase of the film.

18.3.2.5 Hybrid Processing Approaches

Nelea et al. [2003] reported deposition of high-quality CaP thin films by in situ UV-assisted PLD. UV radiation (184.9 nm) generated by a low-pressure Hg lamp induces photodissociation of molecular oxygen and formation of highly reactive oxidizing species, such as ozone and atomic oxygen. Processing on substrates that cannot withstand heating at high temperatures, like polymers and thermoplastic, become feasible. Films, consisting of mixtures of anhydrous CaP phases, were crystalline and had Ca/P $\approx$ 2. Katto et al. [2002] and Nakayama et al. [2004] monitored depositions of HA thin films by a method they called *laser-assisted laser ablation* (LALA). They used two UV excimer laser beams, the first applied for ablation (KrF*) and the second (ArF*) to ''assist'' the film growth and substrate annealing. Non-laser-assisted film regions contained significant amount of

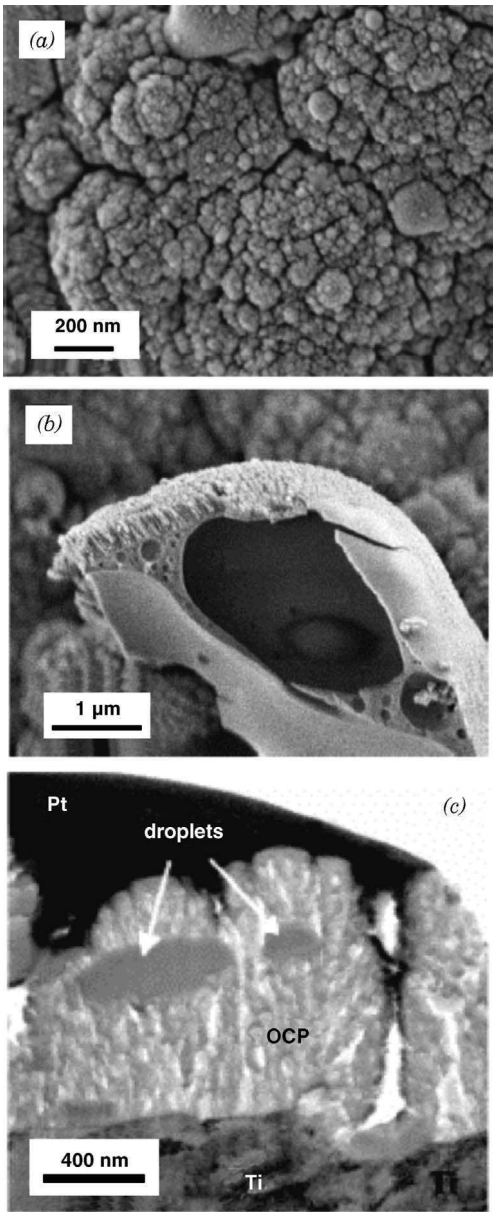

Figure 18.6 SEM micrographs of KrF* PLD OCP coating processed at 150°C: (a) Cauliflower-like aggregates, (b) cross section of an aggregate showing a dense brush-layer on its top, and (c) XTEM micrograph showing the OCP film coral-reef-like nanostructure [Iliescu et al., 2004a], with permission from Elsevier.

ACP (amorphous calcium phosphate) that rapidly dissolves in simulated body fluids (SBF). Oppositely laser-assisted coatings contain crystallizated HA material and withstand in SBF solution. A delay of 5–30 µs of the ArF* pulse was used with respect to the KrF* pulse. Shorter delays are found to be more beneficial to obtain crystalline layers. Jiménez et al. [2004] applied an autonomous

electric discharge during PLD, with depositions being carried out in water atmospheres. The authors reported that the electric discharge help the promotion of crystallinity and processing at low temperature. They used an ArF* laser at low fluence and a 45-Pa water vapor atmosphere. Ionization currents of the discharge were varied from 0 to 80 mA. Crystalline coatings with majority HA phase were obtained at 300–350°C, with crystallinity increasing with the ionization current. The optimum Ca/P value of 1.67 (HA) was obtained at the highest current used (80 mA). Solla et al. [2005] reported PLD of HA assisted by an RF plasma gas discharge, ignited at 275 kHz and 0–300 V alternating voltage. No significant differences of film composition and structure were observed by applying the RF discharge, and it did not affect the Ca/P ratio whose values were around 1.9. However, a significant increase of the growth rate accompanied by a slight improvement of crystallinity of the films was apparent.

18.3.2.6 Relative Merits of Laser-Deposited Films for Biomedical Applications

Several papers reported PLD of HA films in comparison to other methods. García-Sanz et al. [1997] made a comparative study between HA coatings produced by plasma spraying and PLD, and they observed differences in film morphology and structure due to different deposition mechanisms. Lo et al. [2000] presented a comparative study of HA films grown by PLD versus capacitive-coupled RF plasma sputtering. Sputtered coatings are smooth and continuous and followed the contours of the substrate surface. PLD coatings (grown with a KrF* laser in 2-Pa residual air at RT) contained numerous spherical particulates. Both sputtered and PLD coatings were annealed after deposition at 400°C in Ar. Post-annealing led to the increase of film crystallinity up to 87–98 vol %. These films are more stable in SBF and both the stability and cell activity increase. Sputtered coatings showed greater chemical stability than the unannealed PLD coatings and contained $\sim 15\%$ crystalline phase, increasing to $\sim 65\%$ after annealing. Nelea et al. [2002b] reported a comparative study of CaP and HA films grown by PLD and UV-assisted PLD. UV-assisted PLD films are smoother, harder, and better withstand mechanical wear. They consist of a mixture of anhydrous CaP, while PLD films are stoichiometric and nanocrystalline HA. Nelea et al. [2004] also performed a comparative study of HA thin films grown by PLD and RF magnetron sputtering (RF-MS). Both PLD and sputtered films mostly contained the HA phase and exhibited good mechanical characteristics. CaO was noticed as a secondary phase within the sputtered films. They were smoother than PLD coatings, and RF-MS films were harder, more mechanically resistant, and have a higher Young's modulus.

18.3.3 Pulsed Laser Deposition of Bioglass and Other Bioceramics

D'Alessio et al. [2001] performed thin-film deposition of bioactive glass (Bioglass 45S5). Films were grown with a Nd : YAG laser (532-nm wavelength, 7-ns pulse duration) in a gas pressure of 10^{-4} Pa on Ti6Al4V alloy in an *off-axis* geometry. Films preserve the target stoichiometry and bioactivity over a large range of experimental conditions. Serra et al. [2001] obtained Bioglass coatings by PLD in N_2O at different pressures using a Bioglass target and an ArF* laser, and the target composition was successfully transferred to the substrate. Film properties can be modified using different N_2O atmospheres, and Fourier transform infrared (FTIR) measurements showed that the formation of nonbridging oxygen bonds in the coatings can be controlled. These bond units determine the nucleation and growth of apatite nanocrystals at the surface of bioactive glass coatings after being soaked in SBF, as an essential characteristic of biocompatibility. Gonzales et al. [2003] deposited bioactive glass in the system SiO_2–Na_2O–K_2O–MgO–CaO–P_2O_5 on biomorphic SiC ceramic substrates. Experiments were carried out with an ArF* laser in vacuum at 200°C substrate temperature. Borrajo et al. [2005a, 2005b, 2005c] deposited silica-based glass coatings with an ArF laser at 200°C substrate temperature in low pressure Ar or mixtures of Ar with Si_2H_6 and NH_3.

Pseudowollastonite (α-$CaSiO_3$) films have been obtained by PLD [Fernández-Pradas et al., 2002b]. Coatings were deposited in 10 Pa oxygen on Ti heated to 550°C using a Nd : YAG laser (355-nm wavelength, 10-ns pulse duration). Films consist of the *pseudowollastonite* phase and of amorphous material, and they have a porous granular structure and poor cohesion. After treatment, coating crystallinity and cohesion were improved. Nave et al. [2004] reported PLD experiments of materials of marine origin. Using the second harmonic (532 nm) of a pulsed Nd : YAG laser ($\sim$ 5-ns pulse duration; 10-Hz repetition rate), the authors performed depositions on glass substrates or carbon-coated copper grids from targets of biofabricated coralline skeletal material, *Porites lutea*. This material consists of one of the most abundant existing biominerals, that is, calcium carbonate ($CaCO_3$). Depositions were performed in low vacuum (2–4 mTorr) at RT at fluences of 7 and 10 $J\,cm^{-2}$ in both *on-axis* and *off-axis* configurations. The as-deposited coatings partially retained the $CaCO_3$ of the target, while mostly consisting of CaO. The crystalline $CaCO_3$ phase was changed from solely *aragonite* in the target to a mixture of *aragonite* and *calcite* microparticles, and CaO nanocrystals. Coatings grown in the *off-axis* configuration show a smaller density of micron-size particles in the film surface, as a result of the reduced deposition rate.

18.4 CHARACTERIZATION OF NANOSTRUCTURED MATERIALS

The deposited nanostructures must be carefully characterized to obtain information about their physical properties and subsequently about their biomedical properties. In this case it is possible to tune the deposition parameters to achieve film properties that exhibit proper reaction with soft or hard tissue of the human body. To facilitate characterization, a range of substrates are chosen for deposition, depending on their respective properties and suitability for subsequent film analysis. The substrate characteristics are given in Table 18.5. Ti and Ti alloy (Ti6Al4V and Ti5Al2.5Fe) metals with good biocompatibility and very good mechanical characteristics, polished to different surface finishes, and etched or sand blasted have been used. Silicon crystals, fused silica, glass, or freshly cleaved KCl or KBr crystals were also used, mainly for electron microscopy or infrared spectrometry investigations. Due to the large variety of biomaterials, depositions were extended to other type of substrates, to include ceramics (alumina, SiC) and polymers (see Table 18.5), and substrates of different shapes were also used, for example, disk, plate, sheet, or foil. Jelínek et al. [1996] reported HA deposition on real dental implants, using cylindrical Ti rods of 2–3.5 mm diameter and 10–12 mm long, previously sand blasted to improve adhesion.

18.4.1 Chemical Composition and Stoichiometry

HA film composition and stoichiometry were usually assessed by determining the Ca/P atomic ratio (being 1.67 for stoichiometric HA), which strongly depends on deposition conditions, and hence is interdependent on film crystallinity, phase, and structure. Ca/P values ranging from 1.2 to 4.5 have been reported, as determined by energy dispersive X-ray analysis (EDX). Jelínek et al. [1995] determined Ca/P atomic ratios of HA films by both Rutherford backscattering spectrometry (RBS) (using 1.3 MeV ^4He ions) and particle-induced X-ray emission (PIXE) (using 2.5-MeV protons). For low substrate temperature and high laser fluence, Ca/P ratios in the films were found to be close to that of stoichiometric HA. RBS and Auger emission spectroscopy (AES) were applied to determine the film composition and thickness [Torrisi and Setola, 1993]. Semiquantitative analyses of Ca/P atomic ratios by X-ray photoelectron spectroscopy (XPS) was also performed [Zeng and Lacefield, 2000]. Because detection is surface sensitive, results do not always match with the bulk stoichiometry determined by EDX. Systematic studies of HA films by FTIR spectroscopy were performed [Mayor et al., 1998; Arias et al., 2000], and orthophosphate $(PO_4)^{3-}$ ions and OH^- functional group were observed, and carbonate $(CO_3)^{2-}$ ions are present as contaminants. For crystalline HA films, FTIR absorption peaks characteristic of the $(PO_4)^{3-}$ ions

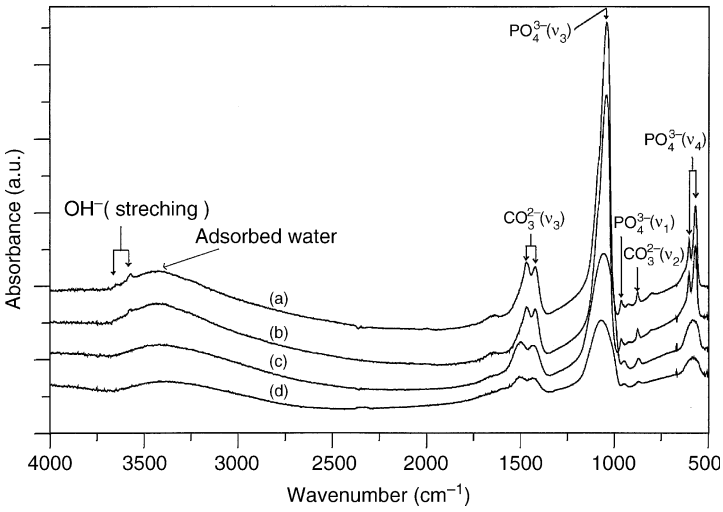

Figure 18.7 FTIR spectra of HA films deposited with an ArF* laser at 45 Pa water vapor pressure and (a) 525°C, (b) 485°C, (c) 430°C, and (d) 295°C Si substrate temperatures. Vibrations of $(PO_4)^{3-}$ and OH^- groups characteristic to HA, carbonate substitution, and adsorbed water in HA molecule are observed [Mayor et al., 1997], with permission from Elsevier.

are narrower and better resolved. According to Mayor et al. [1998], whenever Ca/P ratios increase the concentration of PO_4^{3-} forming apatite is lower, being substituted by $(CO_3)^{2-}$ to maintain the crystalline structure.

Figure 18.7. shows FTIR spectra of HA films deposited with an ArF* laser at different Si substrate temperatures from 295 to 525°C. Vibrational band positions and assignments detected by FTIR for PLD HA films are given in Table 18.6. Micro-Raman spectroscopy was used to determine

TABLE 18.6 Infrared Absorption Bands and Assignments of Typical PLD HA Films

Band (cm^{-1})	Assignment[a]	References
3700–3300	Stretching of water absorbed in the coating	
~3645	Stretching vibration of –OH group in $Ca(OH)_2$ phase	
~3571	Stretching vibration of –OH	
1600–1641	Deformation mode of water absorbed in the coating	
1410–1465	Asymmetric stretching v_3 of $(CO_3)^{2-}$ substituting $(PO_4)^{3-}$	
1450–1576	Asymmetric stretching v_3 of $(CO_3)^{2-}$ substituting –OH	Mayor et al., 1998
1030–1090	Asymmetric stretching v_3 of P–O bond of $(PO_4)^{3-}$	
~960	Symmetric stretching v_1 of P–O bond of $(PO_4)^{3-}$	
~880	Asymmetric bending v_2 of $(CO_3)^{2-}$ substituting –OH	Arias et al., 2000
~872	Asymmetric bending v_2 of $(CO_3)^{2-}$ in the surface or substituting $(PO_4)^{3-}$	
~865	Incorporation of $(HPO_4)^{2-}$ substituting $(PO_4)^{3-}$	
~930 ; ~715	Incorporation of $(P_2O_7)^{4-}$ occurred by $(HPO_4)^{2-}$ dehydration	
~630	Librational mode of –OH	
575–610	Bending v_4 of O–P–O bonds of $(PO_4)^{3-}$	
430–475	Bending v_2 of O–P–O bonds $(PO_4)^{3-}$	

[a] CO_3^{2-} = carbonate ion
HPO_4^{2-} = hydrogen phosphate ion
$P_2O_7^{4-}$ = pyrophosphate ion

the type of CaP phases and their distribution [Fernández-Pradas et al., 2002a]. Vibrations of $(PO_4)^{3-}$ are FTIR and Raman active because the hydroxyl group of HA is located slightly above or below the mirror plane. Craciun et al. [1999] showed by optical transmission spectroscopy (OTS) that the improvement of crystallinity of VUV-annealed HA films. Nistor et al. [2004] applied electron paramagnetic resonance (EPR) to evaluate the stoichiometry of oxygen in HA films and did not observe any transitions that could be associated with paramagnetic points [oxygen-based centers and singly charged oxygen vacancies (O_2^-, O_2^{3-}, O_3^-, or O_3^{3-})] in the film structure.

18.4.2 Surface Morphology and Roughness Parameters

Surface morphology depends on deposition conditions as well as on the nature and mode of preparation of the target. Films can have smooth or rough surfaces, be granular or with fine features, and particulates are found deposited together the nanometric coating. Roughness parameters of HA films have been determined by confocal white-light optical microscopy (COM) [Nelea et al., 2000], and mean roughness value (R_a) was most frequently calculated. A typical example for HA films grown on polished Ti5Al2.5Fe alloy in vacuum at RT and annealed in air at 550°C is $R_a = 210$ nm, measured over a surface area of $170 \times 170\,\mu m^2$. Smoother films ($R_a = 5$–100 nm) were typically measured by atomic force microscopy (AFM) [Antonov et al., 1997]. Film thickness was usually checked by standard profilometry or ellipsometry [Masetti et al., 1996].

18.4.3 Structure and Crystallinity

The crystallinity status and crystallographic structure of HA-based films were routinely analyzed by X-ray diffraction (XRD), and Figure 18.8. displays XRD patterns for HA. Figure 18.9. shows typical transmission electron microscopy (TEM) images and their associated selected area electron diffraction (SAED) patterns for HA [Nelea et al., 2003]. Figure 18.10. shows several examples of cross-sectional TEM (XTEM) and cross-sectional SEM (XSEM) applied to the in-depth study of film microstructure.

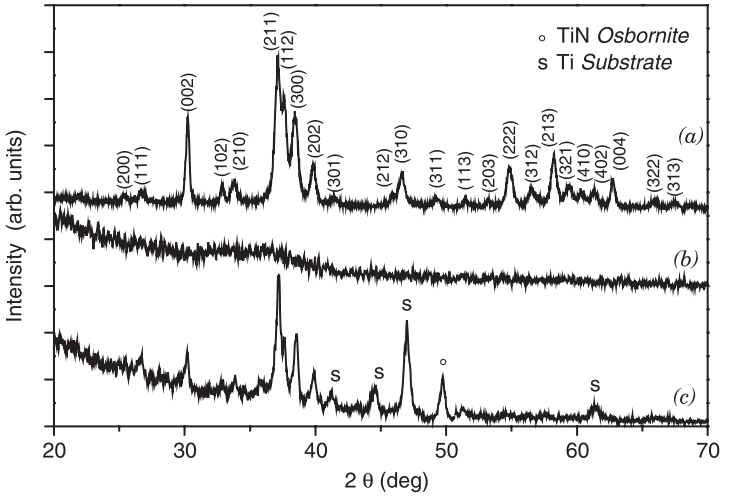

Figure 18.8 Typical XRD pattern for (a) HA target and GIXRD patterns (0.5° attack angle of surface) for (b) amorphous HA/Si, and (c) crystalline HA/TiN/Ti films. X-ray source: CoKα, 0.179 nm wavelength. Film (c) has a HA polycrystalline structure [Nelea, 2002].

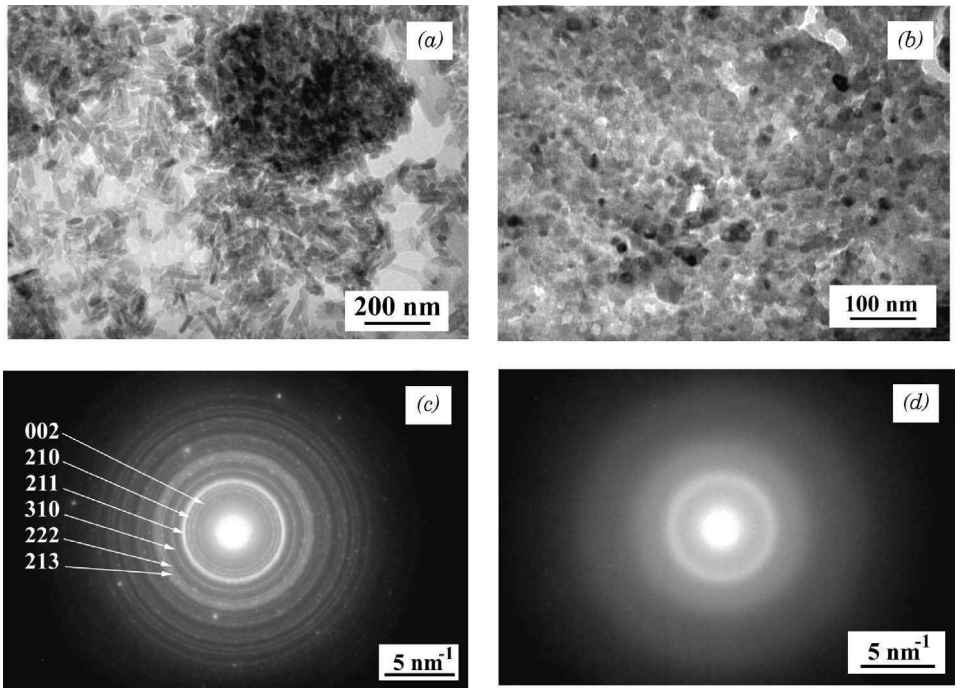

Figure 18.9 TEM patterns of (a) HA powder and (b) a crystalline film grown by PLD with a KrF* laser ($\lambda = 248$, $\tau \simeq 7$ ns) in vacuum (10^{-4} Pa) at RT and annealed in air at 550°C for 1 h. The powder consists of crystallites of 20 nm width and 60 nm length. The film shows prevalent 25 nm equiaxed grains. (c) SAED pattern of film (b) and (d) typical SAED pattern of an amorphous HA film [Nelea et al., 2002a], reprinted with permission from Kluwer-Springer.

18.4.4 Mechanical Properties and Performances

The adherence of HA layers to the substrate was routinely assessed by scratch and pull-off tests. Adhesion and mode of film failure are strongly influenced by the material nature, morphology, microstructure, and residual stress developing during deposition. Pioneering adhesion scratch tests of HA film on Ti6Al4V were performed by Cotell et al. [Cotell et al., 1992; Cotell, 1994], and no evidence for film decohesion was observed. At high load (96 N) the film deforms by bending, without delamination. Nelea et al. [2000] determined nanohardness (H) and Young's modulus (E) of HA thin films using an ultra-low-load indentation system, equipped with a triangular diamond Berkovich tip. HA films grown on TiN interlayers demonstrate improved mechanical properties, with nanohardness of 2.5–3 GPa and Young's modulus of 90–120 GPa [Nelea et al., 2002; Nelea, 2002b]. Films grown directly on Ti-alloy are less hard ($H = 0.5$–1 GPa). The nanohardness of HA films grown on TiN layers was increased to 4–5 GPa after an Ar^+ ion implantation treatment [Nelea et al., 2002a]. Large values of H (6–7 GPa) and E (150–170 GPa), uncommonly high for CaP bulk ceramics, were obtained for films deposited by in situ UV-assisted PLD [Nelea et al., 2003]. Nanoscratch tests of HA films have been reported in Nelea et al. [2000].

Jelínek et al. [1995] showed that Knoop microhardness of HA films increases with the deposition substrate temperature, and they also checked the HA film adherence by scratching. Films deposited at high temperature (780°C) in low-pressure H_2O vapors have poor adhesion. Arias et al. [2003b] explored micro- and nanotesting of amorphous and crystalline HA films grown with an ArF* laser. Friction force and acoustic signals emitted under loading were recorded. Crystalline coatings deform plastically, and both amorphous and crystalline HA coatings have lower values of Young's modulus

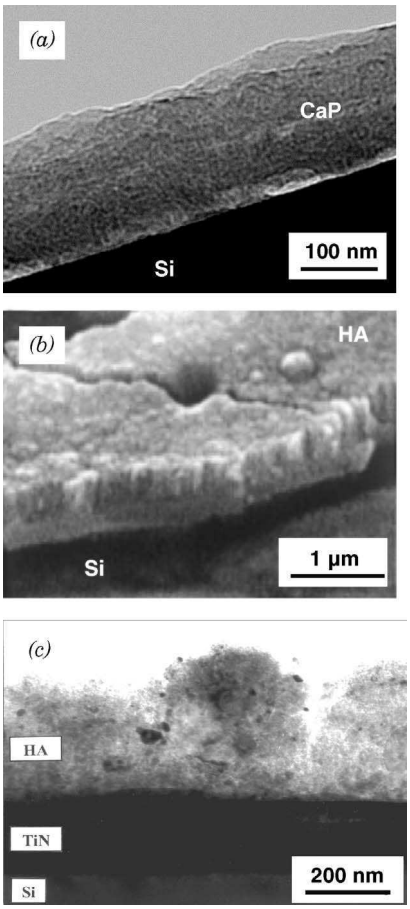

Figure 18.10 (a) Typical XTEM of a dense CaP film grown at 500–600°C by UV-assisted KrF* PLD in 10^{-2}–10^{-1} Pa oxygen. The film has granular morphology with $\sim$20 nm grain size [Nelea et al., 2003], with permission from Elsevier, (b) XSEM through a dense HA film grown by KrF* PLD at 575°C in 45 Pa water vapors [Fernández-Pradas et al., 2001], with permission from Elsevier; (c) XTEM of a HA/TiN/Si multilayer. HA film was grown by KrF* PLD in vacuum (10^{-4} Pa residual pressure) at RT and annealed in air at 550°C for 1 h. Film has a spongy morphology with isolated crystal grains, $\sim$20 nm large, scattered over the porous matrix [Nelea et al., 2000], with permission from Elsevier.

than titanium ($E_{Ti} = 115$ GPa). Fernández-Pradas et al. [2001] discuss failure mechanisms of HA films deposited by a KrF* laser, and it is seen that the critical load decreases with the film thickness. Thin layers (less than 200 nm thick) plastically deform and show cohesive failure. Amorphous films have poor adhesion, due to the brittleness of the glassy structure. Antonov et al. [1995] show that after chemical cleaning (with hydrofluoric acid) or laser KrF* cleaning of the deposition substrates, adhesion of HA films is always higher than by conventional rinsing with solvents such as acetone. Garcia-Sanz et al. [1997] reported a pull-off test of HA films based on a modified ASTM C633 procedure. The tensile strength of films grown at 480°C was 58 MPa. When the temperature is increased (up to 550°C), the tensile strength drops suddenly to 3 MPa. Failure occurs at the coating–substrate interface, most probably due to substrate oxidation. HA films show low bond strength to polymers [Hontsu et al., 1996], due to weak van der Waals bonding forces. Tables 18.7 and 18.8 summarize the mechanical properties of PLD HA films.

TABLE 18.7 Mechanical Response to Indentation and Scratch Tests of Pulsed Laser Deposited HA Thin Films

	Tests						
	Scratch				Micro- and Nanoindentation		
Film Characteristics	Tip Geometry/Type	Load Range (N)	Critical Load (N)	Remarks	Nanohardness (GPa)	Young Modulus (GPa)	References
HA/Ti6Al4V	Al_2O_3 spherical stylus Diameter: 0.125 inch	0–200	96 Mean deformation pressure: 1.7×10^{10} Pa	No decohesion from substrate; film is deformed on bending	—	—	Cottel et al., 1992 Cottel, 1994
HA/Ti5Al2.5Fe	Berkovich diamond Radius: < 40 nm	0.005–0.025	—	No delamination for any film	0.5–1 [a]HV = 350	90–120	Nelea, 2002
• with TiN buffer				• rough loading profile (particulates)	2.5–3 HV = 480	50–70	Nelea et al., 2000
• with TiN + Ar^+ implant				• smooth loading profile	4–5	130–150	Nelea et al., 2002a
• UV-assisted				• smoothest loading profile	6–7	150–170	Nelea et al., 2003
HA/Ti6Al4V Substrate temperature:	Rockwell C diamond Radius: 200 μm	—		Poor adhesion at high substrate temperature	>[b]$HK(Ti)_{25g} \approx 180$	—	Jelínek et al., 1995
• 200–400°C			59				
• 600–780°C			30–40				
Environment:							
• vacuum					$HK_{25g} = 400–500$		
• Ar / H_2O					$HK_{25g} = 850–900$		
Amorphous/Ti	Rockwell C diamond Radius: 200 μm	0–30	9.6	Low internal cohesion strength Coating partly removed and squashed into the scratch groove; pile-up at borders Coating does not effectively detach and is more ductile than Ti	0.55–1.06 (0.4 on Si)	74–107 (68.5 on Si)	Arias et al., 2003b

Crystalline/Ti	Rockwell C diamond Radius: 200 μm	0–30	9.8	Coating plastically deformed Coating does not detach and is more ductile than Ti	1.6 (2.3 on Si)	93 (127 on Si)	Arias et al., 2003b
Amorphous/Ti6Al4V Thickness: 1.7 μm	Spherical diamond stylus Radius: 50 μm	0.5–18	0.16	Low adhesion (brittle glassy material) Coating detached from substrate	—	—	Fernández-Pradas et al., 2001
Crystalline/Ti6Al4V				Plastic deformation			
Thickness: 1.5 μm			0.3	Cohesive failure			
350 nm			2.9				
170 nm			5.7				
Amorphous porous/Ti Amorphous denser/Ti	Al_2O_3 corundum needle Diameter: 20 μm	—	Mean deformation pressure: $\sim 10^{10}$ Pa	Low adhesion Good adhesion Better adhesion for chemically etched, laser (KrF) cleaned substrates	—	—	Antonov et al., 1995

[a] HV = Vickers microhardness (kgf/mm^2)
[b] HK = Knoop microhardness (kgf/mm^2)

TABLE 18.8 Bond Strength as Measured by Pull-off Tests of HA Thin Films Deposited by PLD and Other Methods

Deposition Conditions	Thickness (μm)	Substrate	Bond Strength (MPa)	Remarks	References
ArF, 45 Pa H_2O	~1	Flat Ti, passivated with nitric acid		Good adhesion at moderate	García-Sanz et al., 1997
• 480°C			58	temperature;	
• >550°C			3	Failure occurs at interface due to TiO_2 Formation;	
ArF, 57 Pa Ar/H_2O 500–600°C	~10	Sand-blasted Ti	30–40	—	Wang et al., 1997
Nd:YAG (266, 355 nm) 40–106 Pa Ar/H_2O; 500–520°C	1–4	Ground Ti Polished Ti	~30 ~20	Additional mechanical interlocking of rougher surfaces;	Zeng et al., 2000
ArF, 5×10^{-3} Pa O_2 100°C + annealing up to 400°C for a few hours	~1	Polyimide PTFE	~10 0.4	Poor bond strength due to lower van der Waals forces bonding HA and polymer	Hontsu et al., 1996
Plasma-sprayed coating	50–200	Sand-blasted Ti	10–15	Weak adhesion; Uncontrolled HA stoichiometry Other CaP phases and ACP	Khor et al., 2000
Ion beam deposited film	~1	Polished Ti	20–65	Large adhesion range; acceptable adhesion in some conditions	Choi et al., 2000
				Uncontrolled HA purity	Ding et al., 1999
RF magnetron sputtered film	~1	Polished Ti	60–70	Presence of TTCP, CaO and other secondary phases	

18.5 BIOCOMPATIBILITY STUDIES AND RESPONSE TO LIVING MEDIA

18.5.1 Overview of Biomedical Tests

Several factors influence biocompatibility. The chemical composition and structure of materials affects the type and amounts of released chemical species, and the characteristics of the site of use and mechanical factors are also important. Any material implanted in the body presents a source of potentially harmful agents, and these can occur in the form of wear particles, leachable chemicals, or degradation products. Chemical factors, such as bacterial metabolic products, water, enzymes, and polar and nonpolar solvents, can accelerate the release of components. Any particle formed may be hazardous to macrophages or to synovial fibroblasts in close proximity to particles. Investigations of material biocompatibility need to assess both cellular toxicity and the induction of other adverse reactions such as inflammation, granuloma formation, and neoplastic changes. For this reasons, the biocompatibility of a material is usually empirically determined.

Biocompatibility of medical and dental materials can be evaluated by in vitro tests (also called *initials*), in vivo tests (called *secondary tests*), and *usage tests*, but sometimes, there is a lack of

correlation between in vitro and in vivo tests [Hench, 1991]. The combination of in vivo and in vitro studies leads to a better understanding of surface reactions of bioactive ceramics in the body, their effect on bone growth and cell function [Ducheyne and Qiu, 1999], and provides a sensitive method of revealing adverse reactions.

In vitro evaluation of biocompatibility is well established as a valid initial step in the testing of biomaterials. Biocompatibility is studied using cells, culture methods, and assays. The cells are cultured on various materials and their behavior such as viability, activity, adhesion, migration, or spreading is monitored [Ball et al., 2001; Dubois et al., 1999].

Eminently suitable cells for in vitro testing are the macrophages, which play a major role in inflammation and the response to foreign bodies [Thomson et al., 1991]. However, although important for primary screening of materials, tissue culture techniques can only provide guidance to reactions at the cellular level. For *initials* tests, mutagenesis, complement activation assay, hemolysis assay, oral and intraperitoneal L050 assays are used. However, usually attention is paid mainly to the tests of cytotoxicity and immune function.

In vivo experiments are carried out using laboratory animals, such as pigs, sheep, goats, dogs, rabbits, rats, and mice. This is the only way to assess systemic effects and the response of the whole organism [Thomson et al., 1991], and tests performed on experimental animals simulate their human counterparts [Hench, 1991]. Wound-healing events around implants have been mainly studied by histological and histometrical methods. Nevertheless, the complexity of the interactions between implant material, various cells, extracellular matrix components, and growth factors during wound healing has sometimes made it difficult to draw conclusions about the cause-and-effect relationship in the process. In vivo conditions and the cell types surrounding an implant during wound healing vary with the type of tissue. Usually, as *secondary tests,* the mucous membrane irritation test and skin sensitization tests are applied. Very often also *implantation tests* are utilized. These tests are required for samples that will contact tissue or bone and evaluate a material potential to cause chronic inflammation or tumor growth. Short-term tests last from 1 to 11 weeks. Long-term tests are performed similarly but extend from 1 to 2 years.

For dental implants, the usage tests are pulp irritation tests, mucous membrane and *gingiva* (gum) tests, and placing of dental implants into bone. There are three basic evaluations for the success of implants: the penetration of a periodontal probe along the side of an implant, mobility of the implant, and bone–implant integration. A successful implant should have no mobility, no periimplant radiolucency, minimal vertical bone loss, minimal fibrous encapsulation (preferably none), and no soft tissue complications. Ideally, the bone will contact the implant with strong, healthy tissue without any fibrous encapsulation.

Most standards concerning biocompatibility have been published by the International Organization for Standardization in EN ISO 10993 series from 1992–1997 and upgraded in 2002.

18.5.2 Biomedical Applications of Laser-Fabricated Hydroxylapatite and Bioglass Layers

The biocompatibility of laser-fabricated HA and glass layers has been tested very infrequently and nonsystematically. Attention has usually been focused on in vitro study of film dissolution, erosion, and stability, and there are only a few studies of in vivo behavior and response of coatings.

18.5.2.1 Tests in vitro and Cell Culture

Tucker et al. [1996] measured the kinetics of dissolution of HA layers using the dual constant composition method, and dissolution rates decreased as film crystallinity increased. Antonov et al. [1998] determined toxicity and cell growth. The chemical stability in simulated body fluids and the Ca/P ratios of the coated samples were correlated with their ability to support the attachment and growth of a murine fibroblast substrate-dependant cell line (3T3-L1). It was found that the size, distribution, and topography of the surface microparticles strongly influence cell morphology and compatibility. Lo et al. [2000] studied the human osteoblast-like cell responses to PLD HA, and coatings were assayed for proliferation and phenotypic expression. The XRD, FTIR, and cell culture

results showed that at low deposition temperatures the coatings do not posses long-term stability and do not therefore encourage osteoblast interaction. FTIR was also used for determination of the stability to erosion of HA coatings [Antonov et al., 1996], which were exposed to a phosphate-buffered saline solution. At higher laser fluences, the film adhesion and erosion resistance were increased. Ball et al. [2001] studied the activity and morphology of osteoblasts grown on HA surfaces. Primary human osteoblasts were seeded onto the material surfaces and cytoskeletal actin organization was examined by microscopy. The annealed surfaces supported greater cell attachment and more defined cytoskeletal actin organization. Cell activity, measured using the alamar Blue assay, was also found to be significantly higher on the annealed samples. Zeng and Lacefield [2000] tested HA coatings with respect to their dissolution/reprecipitation in a semidynamic simulated physiological solution. The dissolution of the non-HA phases played a major role in the reprecipitation of HA-like material. Significant reprecipitation was observed, resulting in a clear, distinct morphology.

Cléries et al. [1999] determined dissolution kinetics during immersion of calcium phosphate coatings in Ca^{2+}-free Hanks solution. They grew crystalline HA, α-;β-TCP and ACP coatings on Ti6Al4V that were then incubated in a potentially osteogenic cell culture of rat bone marrow [Cléries et al., 2000]. The amount and formation routes of mineralized bone matrix were evaluated after 2 weeks. The resistance to cellular resorption by osteoclasts was also studied. The bone matrix delaminated from ACP, while it remained on HA and α-;β-TCP even after fracturing. A cementlike line was seen as the immediate contiguous interface with the nondegrading dense HA surface and with the surface of the remaining porous β-TCP coating. Highly dense and crystalline HA coatings do not dissolve and are capable of establishing a strong bond with the bone matrix grown on top. Cellular resorption was not observed on HA, but it was observed on α-;β-TCP layers. Resorption took place as a dissolution mechanism due to the acidic microenvironment. Antonov et al. [2003] performed in vitro evaluation of CaP coatings on bioresorbable polymers (poly-ε-caprolactone and poly-L-lactide). Human osteoblasts derived from femoral head trabecular bone were used for cultures. Both polymers support osteoblast growth, with increased cell activity, alkaline phosphatase activity, and total protein content. Katto et al. [2002] confirmed biocompatibility of HA layers by SBF immersion. Amorphous phases were dissolved, but the crystallized coating remained and grew in the solution. Lusquiños et al. [2003] studied the biological properties of the HA coatings obtained by Nd : YAG laser cladding. Tests were assessed in vitro with human osteoblast-like MG-63 cells. Overall biological results conclude that laser cladding could be a promising method to use in the biomedical field. Kim et al. [2005b] reported in vitro dissolution of biphasic HA/TTCP coatings under tissue culture conditions in an Earle's balanced salt solution (EBSS) for 1 week. Dissolution experiments on HA/TTCP coatings yield distinct dissolution behavior when compared to pure HA films. XRD scans for pure HA after soaking show that the coating remains essentially unaltered at the test endpoint (1 week). In turn, all of the TTCP phase in the HA/TTCP coating dissolves within 12 h. While scanning electron microscopy (SEM) images of pure HA coatings taken prior to and after a 1-week dissolution experiment are virtually indistinguishable, signs of reprecipitation from the solution and coating fracture can be seen on images taken from a biphasic coating with highly oriented TTCP phase. The formation of precipitates on synthetic apatite materials is an important response parameter in in-vitro investigations.

In vitro cell growth demonstrates a high adherence and biocompatibility of osteoblasts and fibroblasts on both OCP and Mn-doped carbonated HA (Mn-CHA) coatings [Mihailescu et al., 2005; Bigi et al., 2005]. Human osteoblasts display normal proliferation and viability, and good differentiation behavior of alkaline phosphatase (ALP), collagen type I (CICP), transforming growth factor β1 (TGFβ1), almost similar to OCP and Mn-CHA. After 7 days TGFβ1 values of the control polystyrene culture dish and Ti samples reach a maximum level, then decrease. The TGFβ1 in the CaP (including HA) coated materials increases from 7 to 21 days, the content indicating bone growth after 3 weeks of implantation. TGFβ1 protein, synthesized by osteoblasts, modulates cell proliferation and differentiation and enhances the deposition of extracellular matrix (ECM) during developmental processes. In vitro tests show that human osteoblast cultures proliferate, reach a normal morphology, display good differentiation, and remain viable on both OCP and Mn-CHA coatings. These promising results render the OCP and Mn-CHA coatings as good potential solutions for biomimetic medical implants.

D'Alessio et al. [2001] used XRD monitoring for study of Bioglass 45S5 film bioactivity after exposure of the coating to a simulated body fluid. Borrajo et al. [2005a] studied the role of thickness and substrate nature on the in vitro bioactivity of silica-based glass coatings (42% SiO_2, 20% Na_2O, 10% K_2O, 5% MgO, 20% CaO, and 3% P_2O_5) grown by PLD with an ArF* laser. Bioglass coatings on Si and Ti substrates with thickness of 8, 20, and 30 μm were studied after 72 h immersion in SBF at 36.5°C. The same in vitro tests were performed for 30-μm-thick glass coatings on *Eucalyptus*-based biomorphic SiC for different immersion times up to 1 week. Besides the critical coating thickness and substrate nature, the ratio of surface area to the SBF volume is found to be decisive in the context of viable bioactive coatings. For the case of 8-μm-thick glass coatings a thin CaP film grows substituting the initial glass layer deposited on Si, while a thin SiO_2 layer replaces the glass film on the Ti substrate. As revealed by SEM and EDX, for 20-μm-thick coatings, in both cases of Si and Ti substrates a rich SiO_2 layer is formed with some grains of CaP on top, but the glass layer disappeared. The 30-μm-thick coatings transform into a superposition of thin glass, silica-rich, and CaP layers when Si substrates are used and totally change into silica-rich and CaP layers for Ti substrates. The authors find 30 μm to be the critical thickness to generate and complete the bioactive reactions and propose that the Si substrates better sustain CaP formation, probably due to different chemical reactions between the ablated species and those of the substrate.

The second part of their studies describes these processes developed in SBF for the case of 30-μm-thick glass coatings on biomorphic SiC. The density of CaP nuclei over the silica-rich layer formed over the glass coatings increases in time, but without generating a continuous CaP layer during the maximum experimental time of 1 week. As this CaP layer appeared on the Si and Ti substrates, even for shorter times, the authors advance the idea of an optimum ratio surface area/SBF volume, which was not reached in the case of the SiC substrate, because of porous, hence extended, morphology.

PLD *Pseudowollastonite* (α-$CaSiO_3$) coatings on Ti alloy substrates were immersed in SBF for different periods in order to investigate nucleation and growth of HA-like formation on their surface [Fernández-Pradas et al., 2002b]. The structure of the coatings before soaking was analyzed by XRD and SEM. Interfacial reaction products were examined by thin-film XRD, SEM, TEM, and EDX microanalyses. Additional changes in ionic concentration, using inductively coupled plasma atomic emission spectroscopy were determined, as well as pH exactly at the coatings–SBF interface using an ion-sensitive field-effect transistor. The solution composition changes, increasing the Ca^{2+} and Si^{4+} concentration and pH as a function of the soaking time, while HPO_4^{2-} decreases. The coating surfaces were covered by an HA-like layer, which indicated that the *pseudowollastonite* coating possesses good bioactivity and also suggests that the mechanism of HA-like layer formation in SBF was similar to that showed in in vitro tests by other silica-based materials.

18.5.2.2 Tests in vivo

In vivo biocompatibility of KrF* and CO_2 laser-fabricated thin films was studied by Antonov et al. [1998], who inserted coated and uncoated implants into adult rat femurs. Suppression of the fibrous tissue formation was found around the uncoated metal implants. Laser-deposited coatings encouraged early and long-lasting anchoring of implants in the bony cavity. Coatings deposited by the CO_2 laser exhibited a markedly higher osseointegration rate than those obtained by a KrF* laser. After careful studies of in vitro fibroblast proliferation, morphological evaluation of macrophages and activity of lymphocytes of HA-coated substrates, Jelínek et al. [1996] and Dostálová et al. [2001] performed in vivo tests of osseointegration of HA layers deposited on actual shapes of tooth prostheses. The implant was rotated during deposition and simultaneously heated by CO_2 laser radiation (Fig. 18.11). Coated and noncoated (reference) prostheses were implanted onto the lower jaws of minipigs. Freshly formed bone and the percentage of bone–implant contact were determined by standardized radiography, micrography, and by transmission and fluorescent microscopy. The study was performed for the case of unloaded (Fig. 18.12a) and loaded (Fig. 18.12b) regimes.

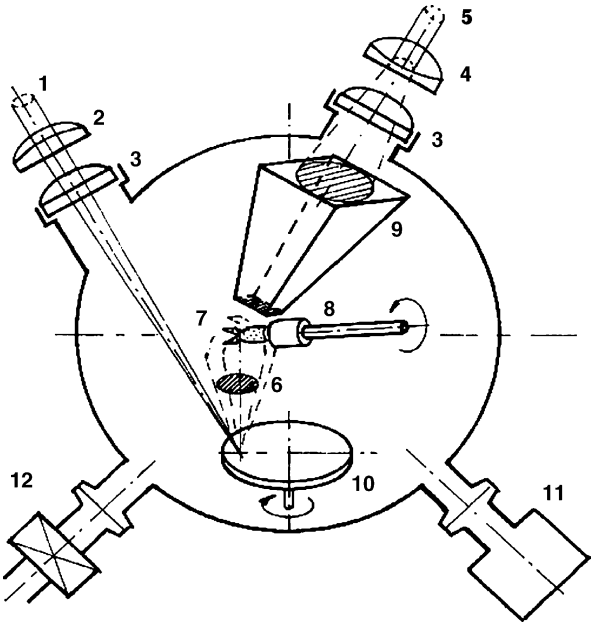

Figure 18.11 Scheme of laser deposition of HA layers onto real dental prostheses (1, KrF* excimer laser beam; 2, focusing lens; 3, windows; 4, ZnSe lens; 5, CO_2 laser beam; 6, plasma plume; 7, dental implant; 8, ceramic holder; 9, homogenizer; 10, target; 11, gauge; 12, Ar/water vapor input [Jelínek et al., 1996], with permission from SPIE.

The area of bone–implant contact evolves from 62.5% for Ti implants to 77.5% for implants coated with HA layer.

Manzanares et al. [2005] evaluated tissue interactions established between cortical bone and Ti implants covered with PLD CaP layers. Five different CaP layers, ranging from ACP to crystalline HA, were obtained on Ti implants by tuning the PLD parameters. The surgical protocol applied consisted of simultaneous implantation of the five types of implants in both the tibial dyaphisis of three Beagle dogs, sacrificed, respectively, one, two, and three months after the last surgical procedures. After sacrifice, samples were submitted to a scheduled procedure of embedding in plastic polymers without prior decalcification to perform ultrastructural studies using SEM with secondary and backscattered electrons (BS-SEM). Observations show that both in terms of the calcified tissues appearing as a response to the presence of the different coatings and of time of recovery, the implants coated with crystalline CaP layers present better results than the ACP-coated implants. Moreover, the constant presence of chondroid tissue—related to the mechanical induction by forces applied on the recovering area—suggested that mechanisms implied in osseointegration are related to endomembranous, rather than endochondral ossification processes.

Kim et al. [2005b] performed in vivo tests of biphasic HA/TTCP thin films produced by PLD from crystalline HA targets. Experiments involve the insertion of coated metallic implants in the proximal tibia and distal femur of New Zealand white rabbits. Eight weeks following implantation the analysis of 20-μm thin sections of femur-implanted samples yield an average of $48.4 \pm 5.9\%$ mineralized bone at the bone-coating interface for pure HA coatings and $62.7 \pm 3.8\%$ mineralized bone for HA/TTCP biphasic coatings. Tibia-implanted samples give $51.3 \pm 5.8\%$ mineralized bone for pure HA coatings and $56.4 \pm 5.1\%$ for HA/TTCP biphasic coatings. All samples exhibited good integration with no significant foreign body response. These histomorphometric studies on implant samples after surgical extraction show that HA/TTCP coatings may lead to enhanced osseointegration compared to pure HA coatings.

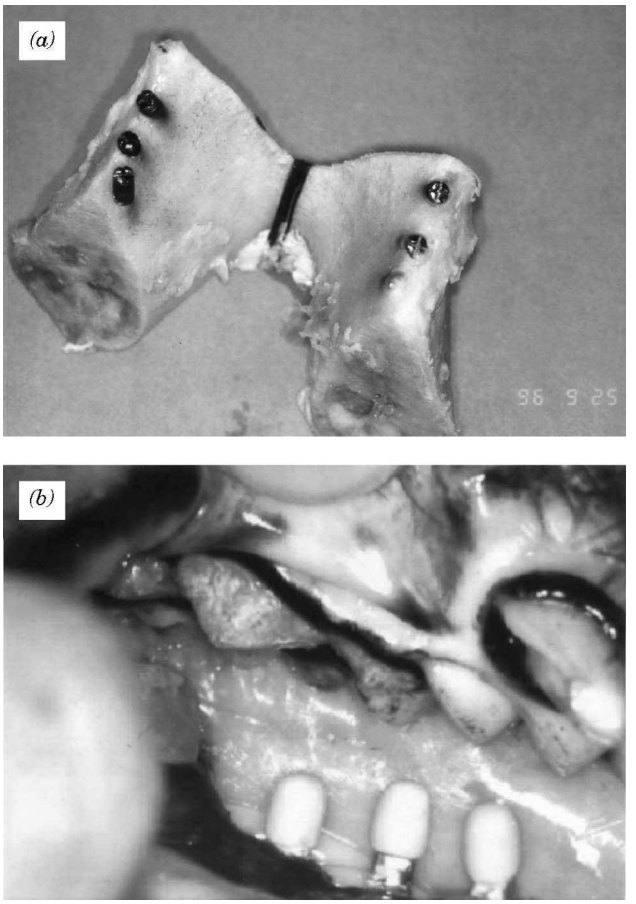

Figure 18.12 (a) Lower jaw of minipig with implants (unloaded regime); (b) lower jaw of minipig with mounted metal–ceramic crowns (loaded regime) [after Dostálová et al., 2001], with permission from Taylor and Francis.

18.5.3 Biomedical Application of Laser-Produced Carbon and DLC Thin Films

Low-temperature isotropic (LTI) pyrolytic carbon was used in humans as coatings of artificial heart valve as early as 1969. Almost all commonly used prosthetic heart valves today have LTI carbon coatings for the orifice and/or occluder due to their excellent thromboresistance (impeding blood clot formation) and long lifetime to failure [Hench, 1991]. For biological applications of DLC coatings two main developing fields are found in the literature. These are DLC in blood containing applications to prevent thrombus formation such as heart valves, blood pumps, and coronary stents or in load-bearing applications to reduce wear. There is considerable interest in coating the femoral head of artificial hip joints, knee prostheses, needles for ophthalmic use, barriers for a glucose enzyme electrode, maxillofacial surgery prostheses, and the like [Butter and Lettington, 1995]. Interest in DLC (and carbon nitride) films has led to the publication of a number of in vitro and in vivo studies [Ducheney et al., 1990]. The biocompatibility of CVD-grown films was tested on animals such as sheep, rabbits, pigs, and guinea pigs. Laser-fabricated DLC films have also been tested on rats

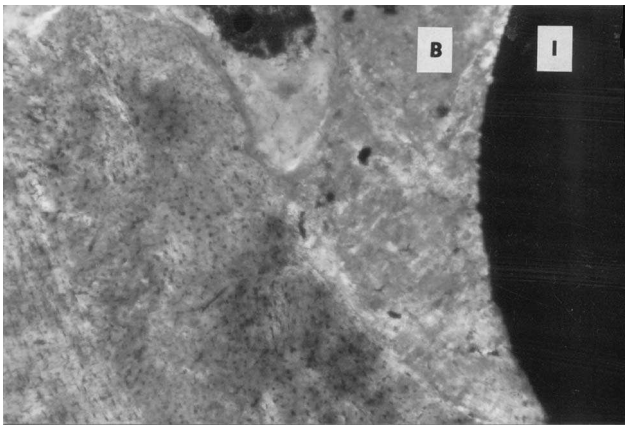

Figure 18.13 Osseointegration of DLC-coated Ti6Al4V prostheses implanted into the femur of a rat. Fully integrated implant (B, bone; I, implant; 100 × magnification) [Jelínek et al., 1996], reprinted with permission from SPIE.

[Jelínek et al., 1996]. Figure 18.13. shows the osseointegration of a DLC-coated Ti6Al4V prostheses implanted into a femur of a rat.

18.6 DEVELOPMENT TRENDS

As many diseases/malfunctions of tissues and organs and other medical conditions cannot be healed or even treated successfully by conventional medical procedures, the field of biomaterials will obviously continue to witness tremendous development over the coming years. Health-care consumers nowadays need increasingly more advanced devices for diagnosis and treatment. New materials and innovative procedures and protocols to speed up osseointegration and subsequent bone repair and healing will particularly need to be developed. PLD has been proven a feasible, efficient mechanism for the production of biocoatings and biomaterials with controlled (tailored) specific properties at both the microscopic and nanoscopic scales. Outstanding advances have recently been made in the development and synthesis of new functional structures capable of interacting with living materials, and PLD will certainly become a great tool for this purpose. Among the biomaterials with great potential to be tested in future, there are:

1. New metallic alloys (namely those based on Ti) with improved mechanical properties and more compliant to the micromechanics of the bone
2. Further, more bioactive, nanocrystalline CaP ceramics, including Ca-substituted HA and HA doped with mineral cations (Zn, Mg, etc.)
3. Newly formulated bioglasses and glass/ceramics
4. Gels and hydrogels as well as polymers with natural relevance (collagen, chitosan, silk, etc.) and composites of these materials

Of course, the properties and functions of every one of these will have to be systematically tested and validated both in vitro and in vivo, in animal models, and by clinical trials if necessary. So far, although numerous studies (around 100 counted so far since 1990) have reported the PLD of HA-based coatings, only a few have addressed their in vivo behavior. We believe that the present lack of information and inconsistency of data will be corrected during the next decade.

An anticipated trend is the search for ways to deposit nano-sized bonelike apatite crystals on fine fibers of nondegradable polymer in a three-dimensional knitted framework. Bioactive composites having both bonelike structure and improved mechanical properties will be developed. The use of HA precursors, such as OCP in conjunction with collagen-like polymeric material, has been envisaged to create a hybrid mineral-organic nanomaterial with an intimate structure resembling that of bone. Pioneering attempts to synthesize such materials have been made using biomimetic processes in chemical liquid solutions. PLD could turn up as the ideal tool to deposit such material into coatings or thin films with both inorganic and organic phases and variable crystalline status as in the actual human bone (e.g., nano- and microcrystalline domains embedded in amorphous phase of the mineral part). In spite of many promising efforts, the characteristics of the above bonelike materials have remained different from those of natural bone, mainly because of the absence of the naturally intricate ''intelligent'' self-organizing interaction between the mineral part and protein component. Therefore, new functional nano-sized biomaterials for bone replacement and regeneration should include polymeric–ceramic composites, such as collagen-HA, chitosan-HA, and the like, incorporating cell-adhesion biomolecules, growth factors, and/or living cells. More generally, smart bioinspired nanosurfaces for scaffolds that are used in cells, tissues, and artificial organs continue to be in high demand.

The use of HA-based surfaces as a platform for the growth and differentiation of stem cells (namely bone marrow stem cells that are responsible for generating osteoprogenitor cells) is expected to become extremely important. Applying micropatterning techniques, surfaces with micro-/nanofeatures of hydroxylapatite may be very useful for controlling the differentiation of stem cells in the phenotype of osteoblastic- or cartilage-like cells. As PLD is a processing technique that possesses an excellent spatial control at submicrometric scale, it may be easily extended to generate such small-sized patterns. We anticipate a significant increase in research studies on the regulation and signalization of human pluripotent mesenchymal stem cells controlled by nanoprocessed/modified surfaces. The critical shortage of human organs for transplants has strongly revived interest in artificial organs and organ parts. To avoid immediate rejection, all these have to be protected by functional, bioactive, extremely adhesive layers before insertion in the human body.

New PLD techniques are soon expected to transfer human cells by matrix-assisted pulsed laser evaporation (MAPLE), which may make it possible to reconstruct different parts of bone tissue, teeth, or even whole organs, cell by cell, by very accurate PLD from specially prepared targets. As a parent technique of MAPLE, PLD is envisaged to become a unique tool in nanotechnology for the deposition of drugs, enzymes, cytokines, and pharmaceutical substances with specific activity on biomedical devices for the targeted stimulation and/or healing of injured living microsites. Drug delivery systems, stents, catheters, heart valves, and implantable biosensors and biochips are only a few of the smart minidevices the research and development of which is vigorously expanding nowadays.

As has been demonstrated, the DLC properties of thin films obtained by PLD can be controlled over a broad range. By this route, the biological behavior of an implant, strongly influenced by surface chemistry, can be tuned by its thin-film properties. The tailoring of bioreactions will thus become possible to any desired point between the bioproperties of DLC and those of any added element. The preparation of surfaces with tunable antibacterial effects can be foreseen. New versatile, reliable laser sources of tunable wavelength and tailored pulse duration, operating at high repetition rate at any fluence, which are simple to computerize, miniaturize, and automate, are being developed. They should make it possible to deposit implants with specific particularly multistructured compositions, exceptional adhesion, and controlled roughness, covering only areas of biomedical interest. All of the PLD biomedical methods described in this chapter will thus become cheaper, more easily applied, and more attractive for new commercial firms entering the market.

We conclude that laser approaches will be among the main, most powerful tools for the processing of biomedical minidevices and tissue-engineered materials. In particular, tailoring and customizing the properties of materials through PLD will be the key to many extremely promising applications.

REFERENCES

Abu Bakar, M. S., P. Cheang, and K. A Khor (2003), *Composite Sci. Technol.* **63**, 421.

Antonov, E. N., V. N. Bagratashvili, V. K. Popov, E. N. Sobol, T. Parker, K. Parker, and S. M. Howdle (1995), *J. Adv. Mater.* **2**(3), 228.

Antonov, E. N., V. N. Bagratashvili, V. K. Popov, E. N. Sobol, and S. M. Howdle (1996), *Spectrochim. Acta A* **52**,123.

Antonov, E. N., V. N. Bagratashvili, V. K. Popov, E. N. Sobol, M. C. Davies, S. J. B. Tendler, C. J. Roberts, and S. M. Howdle (1997), *Biomaterials* **18**(15), 1043.

Antonov, E. N., V. N. Bagratashvili, V. K. Popov, E. N. Sobol, S. M. Howdle, C. Joiner, K. G. Parker, T. L. Parker, A. A. Doktorov, V. B. Likhanov, A. I. Volozhin, S. S. Alimpiev, and S. M. Nikiforov (1998), *J. Biomed. Opt.* **3**(4), 423.

Antonov, E. N., V. N. Bagratashvili, V. K. Popov, M. D. Ball, D. M. Grant, S. M. Howdle, and C. A. Scotchford (2003), *J. Mater. Sci. Mater. Med.* **14**, 151.

Arias, J. L., M. B. Mayor, J. Pou, B. León, and M. Pérez-Amor (2000), *Appl. Surf. Sci.* **154/155**, 434.

Arias, J. L., M. B. Mayor, J. Pou, B. León, and M. Pérez-Amor (2002), *Vacuum* **67**, 653.

Arias, J. L., M. B. Mayor, J. Pou, B. León, and M. Pérez-Amor (2003a), *Appl. Surf. Sci*. **208/209**, 57.

Arias, J. L., M. B. Mayor, J. Pou, Y. Leng, B. León, and M. Pérez-Amor (2003b), *Biomaterials* **24**, 3403.

Bagratashvili, V. N., E. N. Antonov, E. Sobol, V. K. Popov, and S. M. Howdlee (1995), *Appl. Phys. Lett.* **66**(19), 2451.

Ball, M. D., S. Downes, C. A. Scotchford, E. N. Antonov, V. N. Bagratashvili, V. K. Popov, W. J. Lo, D. M. Grant, and S. M. Howdle (2001), *Biomaterials* **22**, 337.

Bigi, A., S. Panzavolta, and N. Roveri (1998), *Biomaterials* **19**, 739.

Bigi, A., B. Bracci, F. Cuisinier, R. Elkaim, M. Fini, I. Mayer, I. N. Mihailescu, G. Socol, L. Sturba, and P. Torricelli (2005), *Biomaterials* **26**(15), 2381.

Bokros, J. C. (1969), in *Chemistry and Physics of Carbon*, Vol. 5, P. L. Walker, Jr. (Ed.), Marcel Dekker, New York.

Bonfield, W. (1988), *Ann. NY Acad. Sci.* **523**,173.

Borrajo, J. P., P. González, S. Liste, J. Serra, S. Chiussi, B. León, and M. Pérez-Amor (2005a), *Mater. Sci. Eng. C* **25**(2), 187.

Borrajo, J. P., J. Serra, S. Liste, P. González, S. Chiussi, B. León, and M. Pérez-Amor (2005b), *Appl. Surf. Sci*. **248**, 355.

Borrajo, J. P., P. González, S. Liste, J. Serra, S. Chiussi, B. León, and M. Pérez-Amor (2005c), *Appl. Surf. Sci.* **248**, 369.

Brès, E., and P. Hardouin (1988), *Calcium Phosphate Materials. Fundamentals*, Sauramps Medical, Montpellier, France.

Butter, R. S., and A. H. Lettington (1995), *J. Chem. Vapor Dep.* **3**, 182.

Cao, W., and L. L. Hench (1996), *Ceram. Int.* **22**, 493.

Chen, F., Z. C. Wang, and C. J. Lin (2002), *Mater. Lett.* **57**, 858.

Choi, J. M., H. E. Kim, and S. Lee (2000), *Biomaterials* **21**, 469.

Chou, B.Y., and E. Chang (2002), *Surf. Coat. Technol.* **153**, 84.

Clarotti, G., F. Schue, J. Sledz, A. Ait Ben Aoumar, K. E. Geckeler, A. Orsetti, and G. Paleirac (1992), *Biomaterials* **13**(12), 832.

Cléries, L., J. M. Fernández-Pradas, G. Sardin, and J. L. Morenza (1999), *Biomaterials* **20**, 1401.

Cléries, L., J. M. Fernández-Pradas, and J. L. Morenza (2000), *J. Biomed. Mater. Res.* **49**, 43.

Cotell, C. M. (1994), in *Pulsed Laser Deposition of Thin Films*, D. B. Chrisey and G. K. Hubler (Eds.), Wiley, New York.

Cotell, C. M., D. B. Chrisey, and K. S. Grabowski (1992), *Mater. Res. Soc. Symp. Proc.* **252**, 2.

Craciun, V., I. W. Boyd, D. Craciun, P. Andreazza, and J. Perriere (1999), *J. Appl. Phys.* **85**(12), 8410.

Cui, F. Z., and D. J. Li (2000), *Surf. Coat. Technol.* **131,** 481.

D'Allesio, L., D. Ferro, V. Marotta, A. Santagata, R. Teghil, and M. Zaccagnino (2001), *Appl. Surf. Sci.* **183**, 10.

De Aza, P. N., J. M. Fernández-Pradas, and P. Serra (2004), *Biomaterials* **25**(11), 1983.

Ding, S. J., C. P. Ju, and J. H. Chern Lin (1999), *J. Biomed. Mater. Res*. **44**, 266.

Dorozhkin, S., and M. Epple (2002), *Angew. Chem. Int. Ed.* **41**, 3130.

Dostálová, T., L. Himmlová, M. Jelínek, and C. Grivas (2001), *J. Biomed. Opt.* **6**(2), 239.

Driessens, J., C. Merry, I. Gibson, S. Best, and W. Bonfield (2001), *J. Appl. Phys.* **90**(8), 4231.

Ducheyne, P., and Q. Qiu (1999), *Biomaterials* **20**, 2287.

Ducheney, P., S. Radin, M. Heughebaert, and J. C. Heughebauert (1990), *Biomaterials* **11**, 244.

Dubois, J. C., C. Souchier, M. L. Couble, P. Exbrayat, and M. Lissac (1999), *Biomaterials* **20**, 1481.

Dumkum, C., D. M. Grant, and I. R. McColl (1997), *Diamond Relat. Mater.* **6**, 802.

Elliott, J. C. (1994), *Structure and Chemistry of the Apatites and Other Calcium Orthophosphates*, Elsevier, Amsterdam.

Fernández-Pradas, J. M., G. Sardin, L. Clèries, P. Serra, C. Ferrater, and J. L. Morenza (1998), *Thin Solid Films* **317**, 393.

Fernández-Pradas, J. M., L. Clèries, E. Martínez, G. Sardin, J. Esteve, and J. L. Morenza (2001), *Biomaterials* **22**, 2171.

Fernández-Pradas, J. M., L. Clèries, G. Sardin, and J. L. Morenza (2002a), *Biomaterials* **23**, 1989.

Fernández-Pradas, J. M., P. Serra, J. L. Morenza, and P. N. De Aza (2002b), *Biomaterials* **23**, 2057.

Ferro, D., S. M. Barinov, J. V. Rau, R. Teghil, and A. Latini (2005), *Biomaterials* **26**(7), 805.

García-Sanz, F. J., M. B. Mayor, J. L. Arias, J. Pou, B. León, and M. Pérez-Amor (1997), *J. Mater. Sci. Mater. Med.* **8**, 861.

Gonzales, P., J. Serra, S. Liste, S. Chiussi, B. Leon, M. Perez-Amor, J. Martinez-Fernandez, A. R. de Arellano-Lopez, and F. M. Varela-Feria (2003), *Biomaterials* **24**, 4827.

Gyorgy, E., P. Toricelli, G. Socol, M. Iliescu, I. Mayer, I. N. Mihailescu, A. Bigi, and J. Werckmann (2004), *J. Biomed. Mater. Res. A* **71A**(2), 353.

Gross, K. A., and C. C. Berndt (1994), *J. Mater. Sci. Mater. Med.* **5**, 219.

Hauert, R., and U. Muller (2003), *Diamond Relat. Mater.* **12**, 171.

Hench, L. L. (1991), *J. Amer. Ceram. Soc.* **74**(7), 1487.

Hench, L. L., and E. C. Ethridge (1982), *Biomaterials. An Interfacial Approach*, Academic, New York.

Hench, L. L., R. J. Splinter, W. C. Allen, and T. K. Greenlee, Jr. (1972), *J. Biomed. Mater. Res*. **2**(1), 117.

Hontsu, S., M. Nakamori, H. Tabata, J. Ishii, and T. Kawai (1996), *Jpn. J. Appl. Phys*. **35**, 1208.

Hu, H. B., C. J. Lin, R. Hu, and Y. Leng (2002), *Mater. Sci. Eng. C* **20**, 209.

Hulbert, S. F. (1969), in *Use of Ceramics in Surgical Implants*, S. F. Hulbert and F. A. Young (Eds.), Gordon and Breach Science Publishers, New York.

Iliescu, M., V. Nelea, J. Werckmann, I. N. Mihailescu, G. Socol, A. Bigi, and B. Bracci (2004a), *Thin Solid Films,* **453/454**, 157.

Iliescu, M., V. Nelea, J. Werckmann, and I. N. Mihailescu (2004b), *Surf. Coat. Technol.* **187**(1), 131.

Jelínek, M., V. Olšan, L. Jastrabík, V. Studnička, V. Hnatowicz, J. Kvítek, V. Havránek, T. Dostálová, I. Zergioti, A. Petrakis, E. Hontzopoulos, and C. Fotakis (1995), *Thin Solid Films* **257**, 125.

Jelínek, M., T. Dostálová, L. Himmlová, and C. Grivas (1996), *SPIE Proc.* **2887**, 120.

Jelínek, M., T. Dostálová, L. Himmlová, C. Grivas and C. Fotakis (2002), *Mol. Cryst. Liq. Cryst.,* **374**, 599.

Jie, W., and L. Yubao (2004), *Eur. Polym. J*. **40**(3), 509.

Jiménez, E., J. L. Arias, B. León, and M. Pérez-Amor (2004), *Thin Solid Films* **453/454**, 422.

Johnson, S., M. Haluska, R. J. Narayan, and R. L. Snyder (2005), *Mater. Sci. Eng. C.*, in press.

Katto, M., M. Nakamura, T. Tanaka, and T. Nakayama (2002), *Appl. Surf. Sci*. **197/198**, 768.

Katto, M., K. Kurosawa, A. Yokotani, S. Kubodera, A. Kameyama, T. Higashiguchi, T. Nakayama, and M. Tsukamoto (2005), *Appl. Surf. Sci.* **248**, 365.

Kawai, T., C. Ohtsuki, M. Kamitakahara, T. Miyazaki, M. Tanihara, Y. Sakaguchi, and S. Konagaya (2004), *Biomaterials* **25**(19), 4529.

Khor, K. A., Z. I. Dong, C. H. Quek, and P. Cheang (2000), *Mater. Sci. Eng. A* **281**, 221.

Kim, H. W., Y. J. Noh, Y. H. Koh, H. E. Kim, and H. M. Kim (2002), *Biomaterials* **23**, 4113.

Kim, H., R. P. Camata, Y. K. Vohra, and W. R. Lacefield (2005a), *J. Mater. Sci. Mater. Med.* **16**, 961.

Kim, H., R. P. Camata, Y. K. Vohra, and W. R. Lacefield (2005b), *Key Mater. Eng.* **284–286**, 207.

Lee, W. J., S. W. Lee, H. Kim, and D. J. Kim (2005), *J. Korean Phys. Soc.* **47**(1), 1.

Li, J., B. Fartash, and L. Hermansson (1995), *Biomaterials* **16**, 417.

Lo, W. J., D. M. Grant, M. D. Ball, B. S. Welsh, S. M. Howdle, E. N. Antonov, V. N. Bagratashvili, and V. K. Popov (2000), *J. Biomed. Mater. Res*. **50**, 536.

Lopatin, C. M., V. Pizziconi, T. L. Alford, and T. Laursen (1998), *Thin Solid Films* **326**, 227.

Lusquiños, F., J. Pou, J. L. Arias, M. Boutinguiza, B. León, M. Pérez-Amor, F. C. M. Driessens, J. C. Merry, I. Gibson, S. Best, and W. Bonfield (2001), *J. Appl. Phys.* **90**(8), 4231.

Lusquiños, F., A. De Carlos, J. Pou, J. L. Arias, M. Boutinquiza, B. Leon, M. Perez-Amor, F. C. Driessens, K. Hing, I. Gibson, S. Best, and W. Bonfield (2003), *J. Biomed. Mater. Res. A* **64**(4), 630.

Manzanares, M. C., et al. (2001), *Bull. Group. Int. Rech. Sci. Stomatol. Odontol.* **43**(3), 100.

Masetti, E., M. Jelínek, and C. Grivas (1996), *SPIE Proc.* **2965**, 128.

Mayor, B., J. Arias, S. Chiussi, F. Garcia, J. Pou, B. León Fong, and M. Pérez-Amor (1998), *Thin Solid Films* **317**, 363.

Miao, X. (2003), *Mater. Lett.* **57**, 1848.

Mihailescu, I. N., P. Torricelli, A. Bigi, I. Mayer, M. Iliescu, J. Werckmann, G. Socol, F. Miroiu, F. Cuisinier, R. Elkaim, and G. Hildebrand (2005), *Appl. Surf. Sci.* **248**, 344.

Milella, E., F. Cosentino, A Licciulli, and C. Massaro (2001), *Biomaterials* **22**, 1425.

Murray, D. W., and N. Rushton (1990), *J. Bone Joint Surg.* **72B**, 989.

Narayan, R. J. (2005), *Mater. Sci. Eng. C* **25**(3), 398.

Nakayama, T., T. Tanaka, Y. Tsumoto, H. Katayama, and M. Katto (2004), *Appl. Phys. A* **79** 833.

Nave, D., S. Rosenwaks, R. Vago, and I. Bar (2004), *J. Appl. Phys.* **95**(12), 8309.

Nelea, V. (2002), "Growth and Characterization of Hydroxyapatite Thin Films Obtained by Pulsed Laser Deposition," Ph.D. Thesis, University of Strasbourg.

Nelea, V., C. Ristoscu, C. Chiritescu, C. Ghica, I. N. Mihailescu, H. Pelletier, P. Mille, and A. Cornet (2000), *Appl. Surf. Sci,* **168**(1–4), 127.

Nelea, V., H. Pelletier, D. Muller, N. Broll, P. Mille, C. Ristoscu, and I. N. Mihailescu (2002a), *Appl. Surf. Sci.* **186**(1–4), 483.

Nelea, V., M. Iliescu, C. Ghica, H. Pelletier, C. Ristoscu, I. N. Mihailescu, V. Craciun, and J. Werckmann (2002b), *J. Mater. Sci. Mater. Med.* **13**, 1167.

Nelea, V., V. Craciun, M. Iliescu, I. N. Mihailescu, H. Pelletier, P. Mille, and J. Werckmann (2003), *Appl. Surf. Sci,* **208/209**, 638.

Nelea, V., C. Morosanu, M. Iliescu, and I. N. Mihailescu (2004), *Appl. Surf. Sci.* **228**, 346.

Nistor, L. C., C. Ghica, V. S. Teodorescu, S. V. Nistor, M. Dinescu, D. Matei, N. Frangis, N. Vouroutzis, and C. Liutas (2004), *Mater. Res. Bull.* **39**, 2089.

Pelletier, H., V. Nelea, P. Mille, and D. Muller (2004), *Nucl. Instrum. Meth. Phys. Res. B* **216**, 269.

Ratner, B. D., and L. Hench (1999), *Curr. Opin. Solid State Mater. Sci.* **4**, 379.

Robertson, J. (1992), *Surf. Coat. Technol.* **50**, 185.

Rovira, A., R. Bareille, I. Lopez, F. Rouais, L. Bordenave, C. Rey, and M. Rabaud (1993), *J. Mater. Sci. Mater. Med.* **4**, 372.

Serra, J., P. González, S. Chiussi, B. León, and M. Pérez-Amor (2001), *Key Eng. Mater.* **192–195**, 635.

Silva, P. L., J. D. Santos, F. J. Monteiro, and J. C. Knowles (1998), *Surf. Coat. Technol.* **102**, 191.

Silva C., D. Thomazini, A. G. Pinheiro, N. Aranha, S. D. Figueiro, J. C. Goes, and A. S. B. Sombra (2001), *Mater. Sci Eng. B* **86**, 210.

Silva, C. C., H. H. B. Rocha, F. N. A. Freire, M. R. P. Santos, K. D. A. Saboia, J. C. Goes, and A. S. B. Sombra (2005), *Mater. Chem. Phys.* **92**, 260.

Singh, R. K., F. Qian, V. Nagabushnam, R. Damodaran, and B. M. Moudgil (1994), *Biomaterials* **15**(7), 522.

Smausz, T., B. Hopp, H. Huszar, Z. Toth, and G. Kecskemeti (2004), *Appl. Phys. A* **79**, 1101.

Socol, G., P. Torricelli, B. Bracci, M. Iliescu, F. Miroiu, A. Bigi, J. Werckmann, and I. N. Mihailescu (2004), *Biomaterials* **25**(13), 2539.

Solla, E. L., J. P. Borrajo, P. González, J. Serra, S. Liste, S. Chiussi, B. León, and M. Pérez-Amor (2005), *Appl. Surf. Sci.* **248**, 360.

Solnick-Legg, H., and K. Legg (1989), *MRS Bull.*, **14**, 27.

Suchanek, W., and M. Yoshimura (1998), *J. Mater. Res*. **13**(1), 94.

Thomson, L. A., F. C. Law, K. H. James, and N. Rushton (1991), *Biomaterials* **12**, 781.

Torrisi, L., and R. Setola (1993), *Thin Solid Films* **227**, 32.

Tucker, B. E., C. M. Cottel, R. C. Y. Auyeung, M. Spector, and G. H. Nancollas (1996), *Biomaterials* **17**, 631.

Ural, E., K. Kesenci, L. Fambri, C. Migliaresi, and E. Piskin (2000), *Biomaterials* **21**, 2147.

van Dijk, K., H. G. Schaeken, J. C. G. Wolke, C. H. M. Maree, F. H. P. M. Habraken, J. Verhoeven, and J. A. Jansen (1995), *J. Biomed. Mater. Res*. **29**, 269.

van Loon, J., and P. Mars (1997), Biocompatibility: The Latest Developments, *Medical Device Technology.* Chester, UK.

Wang, C. K., J. H. Chern Lin, C. P. Ju, H. C. Ong, and R. P. H. Chang (1997), *Biomaterials* **18**, 1331.

Wang, X., Y. Li, J. Wei, and K. de Groot (2002), *Biomaterials* **23**, 4787.

Williams, D. F. (1988), in *Advances in Biomaterials*, Vol. 8, C. de Putter, G. L. de Lange, K. de Groot, and A. J. C. Lee (Eds.), Elsevier Science Publishers, Amsterdam.

Yamamuro, T., and L. L. Hench (1990), in *CRC Handbook of Bioactive Ceramics*, J. Wilson (Ed.), CRC Press, Boca Raton, FL.

Zeng, H., and W. R. Lacefield (2000), *J. Biomed. Mater. Res.* **50**, 239.

Zeng, H., W. R. Lacefield, and S. Mirov (2000), *J. Biomed. Mater. Res.* **50**, 248.

CHAPTER 19

Thermoelectric Materials

ANNE DAUSCHER and BERTRAND LENOIR

Laboratoire de Physique des Matériaux, Ecole Nationale Supérieure des Mines de Nancy, Nancy, France

19.1 INTRODUCTION

Thermoelectric effects provide a means by which thermal energy can be converted into electricity and by which electricity can be used for heat pumping or refrigeration. The Seebeck and the Peltier effects were discovered early in the nineteenth century, but it was only in the second half of the twentieth century that thermoelectric generation became reasonably efficient and that thermoelectric refrigeration became even practicable.

Thermoelectric devices offer many advantages over conventional thermodynamic systems: no moving parts, high reliability, independence of efficiency as a function of size, absence of harmful gases, compactness, quietness, and the like. Despite all these obvious advantages, so far thermoelectrics can only be found in niche markets in which their desirable features outweigh their relatively high cost and low performance. For example, thermoelectric refrigeration has enjoyed some success in domestic food refrigerators, air conditioning, and cooling of CCDs (charge-coupled devices) infrared detectors. Thermoelectric generators have been successfully built for powering NASAs deep-space probes over extended periods of time (over 22 years) and are more recently of interest for the generation of electrical power using low-level waste heat sources.

The identification of materials with high thermoelectric performance has proven to be a challenging task [Dauscher et al., 2002c]. After 30 years of slow progress, thermoelectric materials research experienced a resurgence at the beginning of the 1990s, stimulated by the development of new concepts and theories in both bulk materials and nanostructures [Nolas et al., 2001a; Dauscher et al., 2002c]. New classes of materials such as semiconductors and semimetals with complex open crystal structures show great promise with thermoelectric performance exceeding those of state-of-the-art thermoelectric materials. Reduced dimensionality, occurring in films, quantum wells, or quantum wires, has also been considered as a promising approach for increasing the thermoelectric performance.

The current applications of thermoelectric devices are based on bulk materials, but due to the increasing trend of miniaturization and the growing demand in either small power sources or spot cooling refrigeration of electronic components, the technology of thermoelectric thin films becomes a relevant topical subject. Thin films of thermoelectric materials have been deposited by different methods such as vacuum evaporation, sputtering, molecular beam epitaxy, or metal organic chemical vapor deposition. Pulsed laser deposition (PLD) is yet another interesting approach to thermoelectric

Pulsed Laser Deposition of Thin Films: Applications-Led Growth of Functional Materials
Edited by Robert Eason

thin-film deposition. PLD is a versatile method well-suited for the deposition of complex materials including high Tc-superconductors, oxides, polymers, and the like [Chrisey and Hubler, 1994]. This technique has also been used successfully to synthesize thermoelectric materials with the desired stoichiometry including conventional and novel materials.

After briefly introducing the fundamentals of thermoelectricity, this chapter will review current research on thermoelectric materials grown by PLD, including state-of-the-art and novel thermoelectric materials. Attention has been focused on the growth conditions often related to the thermoelectric transport properties of the films. Given the large number of parameters for experiments associated with PLD, we have tried to state for each material the parameters used for growth. The last section of this chapter presents a brief description of thermoelectric microdevices and their applications.

19.2 CURRENT STATE OF THERMOELECTRICITY

Solid-state energy conversion based on thermoelectric effects utilizes the heat generated (as a consequence of the Peltier effect) when an electric current is passed through a thermoelectric material to yield a temperature difference with heat being absorbed on the cold side and rejected at the sink, thus providing a refrigeration or heat pump capability. Similarly, an imposed temperature difference applied on the material will result in a voltage (as a consequence of the Seebeck effect) or current, that is, power generation. The Peltier coefficient, π, and the Seebeck coefficient, or thermopower, α, are related through the Kelvin relation:

$$\pi = \alpha T \tag{19.1}$$

where T is the absolute temperature.

A cross section of a typical thermoelectric refrigerator is shown in Figure 19.1a. *p*-Type and *n*-type semiconductor branches are interconnected at the cold and the hot sides, such that a current flows through all the branches in series, while the energy they carry (by electrons and holes) leaves the cold side in parallel. Thermoelectric generators work in reverse to thermoelectric

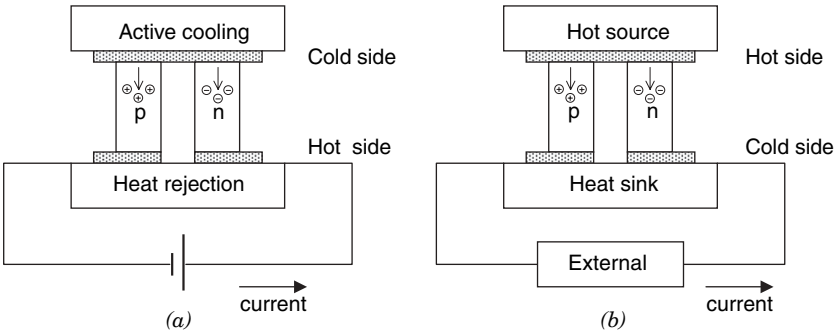

Figure 19.1 Schematic diagram of a single thermocouple configured for (a) refrigeration or (b) power generation. The thermoelectric couple consists of a *p*-type and a *n*-type semiconducting branch. Actual thermoelectric devices are typically composed of a plurality of such thermoelectric couples connected electrically in series and thermally in parallel to form a module. When an electric current is passed through the module, heat is absorbed at one side (cold side) of the module and rejected at the other side (hot side) and the device operates as a cooler. Conversely, if an external temperature difference is applied to the module, electrical power will be delivered to an external load and the device operates as a power generator.

coolers, as shown in Figure 19.1b. Because the hot side has a higher temperature, electrons and holes are driven to the cold side through diffusion and flow through an external load to do useful work.

In addition to the temperature at the hot and cold sides, which are important parameters in all thermodynamic engines, the coefficient of performance (COP) of thermoelectric refrigerators or the efficiency of generators depends also on the parameter $Z_{np}T_m$ [Nolas et al., 2001a], where T_m is the average temperature of the thermocouple over which the device operates and Z_{np} is the figure of merit of the thermocouple defined by:

$$Z_{np} = \frac{(\alpha_p - \alpha_n)^2}{[(\rho_p \lambda_p)^{1/2} + (\rho_n \lambda_n)^{1/2}]^2} \tag{19.2}$$

where ρ is the electrical resistivity, λ the thermal conductivity, and the subscripts p and n refer to the positive and negative branches, respectively.

To have a high efficiency, it can be shown that the factor $Z_{np}T_m$ must be maximized [Nolas et al., 2001a], that is, a high value of Z_{np} must be obtained over as wide a temperature range as possible. Similarly, this condition is also necessary to reach a high COP.

It is important to note that Eq. (19.2) refers to a couple, while in the materials development problem it is more convenient to have a criterion describing the quality of a single material. For this reason, the figure of merit of a single material, Z, is defined as:

$$Z = \frac{\alpha^2}{\rho\lambda} \tag{19.3}$$

The ratio α^2/ρ is called the power factor; it involves only electronic properties, whereas the thermal conductivity λ contains a lattice contribution, λ_L, in addition to its electronic part, λ_E:

$$\lambda = \lambda_L + \lambda_E \tag{19.4}$$

The central issue in thermoelectric materials research is to increase ZT. The power factor is typically optimized as a function of carrier concentration (typically around 10^{19} carriers/cm^3 at room temperature), through doping, to give the largest ZT. High-mobility carriers are most desirable in order to have the lowest electrical resistivity. ZT can also be raised by decreasing the lattice contribution λ_L. However, ρ is related to λ_E, through the Wiedemann–Franz law, and the ratio is essentially constant at a given temperature. Heavily doped semiconductor compounds and/or alloys based on heavy elements of the periodic table satisfy the necessary criteria better than any other material, and for that reason they have been primarily the materials of choice for thermoelectric applications.

The $(Bi_{1-x}Se_x)_2(Te_{1-y}Se_y)_3$ and $Bi_{1-x}Sb_x$ alloys are considered as state-of-the-art materials for thermoelectric refrigeration for room temperature and low-temperature applications, respectively (Fig. 19.2). Higher temperature materials that are used for power generation include PbTe and $Si_{1-x}Ge_x$ alloys. Figure 19.2 shows that for all state-of-the-art materials, the maximum dimensionless figure of merit ZT is nearly equal to unity in their temperature range of operation, which gives a thermoelectric performance at least twice lower than that of vapor compression refrigeration systems. Although $ZT \sim 1$ has been a practical upper limit for more than 30 years, there is no theoretical or thermodynamic reason why it cannot be larger [Mahan, 1998]. Several plausible extrapolations based on optimum values for known materials have estimated that ZT values of 2–4 are possible [Slack, 1995]. It is clear that, if materials with $ZT \sim 2$–3 could be developed, many more applications for thermoelectric devices would become more practical.

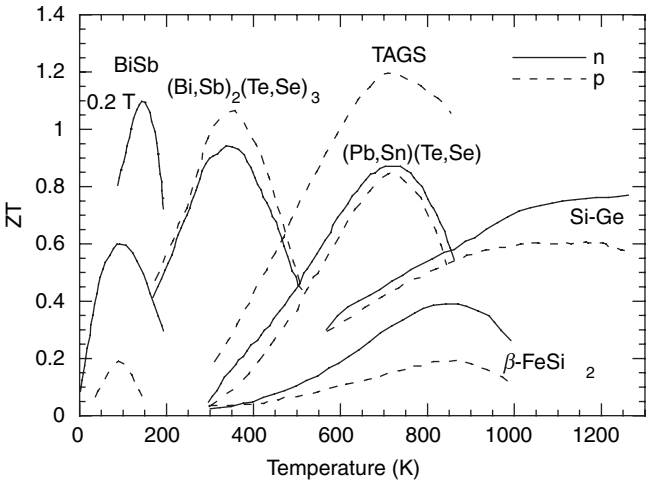

Figure 19.2 Schematic representation of the typical temperature dependences of the dimensionless figure-of-merit *ZT* as a function of temperature for several *n*- and *p*-type established materials.

Over the past few years, there has been substantial renewed research interest in the investigation of new and/or significantly more efficient thermoelectric materials for applications in solid-state refrigeration or power generation. The enhanced interest in new materials has been driven by the need for higher performances and extended temperature regimes for thermoelectric devices in many civilian, spatial, and military applications.

Much of the recent research in new materials has revolved around the concept of the ''phonon glass electron crystal'' model (PGEC) developed by Slack [1995]. This model suggests that a good thermoelectric material should conduct electricity like a crystal but conduct heat like a glass. To find such a material, Slack advocates crystal structures containing weakly bound atoms or molecules that ''rattle'' within an atomic cage allowing for very low lattice thermal conductivity. In this connection, several classes of materials have been investigated such as skutterudites [Uher, 2001], clathrates [Nolas et al., 2001b], and Chevrel phases [Caillat et al., 1999]. So far, encouraging results have been obtained at elevated temperature in both *n*- and *p*-type skutterudite compounds with *ZT* values around 1.2–1.6, making them excellent candidates for power generation. Other materials such as half-Heusler intermetallic compounds [Poon, 2001], β-Zn_4Sb_3 [Caillat et al., 1997], Chevrel phases [Roche et al., 1999], and quasi-crystals [Tritt et al., 1998] have also attracted considerable interest as potential new thermoelectric materials.

Reduced dimensionality as occurs in thin films, quantum wells, quantum wires, or quantum dots has also been considered as a promising direction for increasing *ZT* [Dresselhaus et al., 2001; Venkatasubramanian, 2001; Chen, 2001; Mahan, 2001], and different physical approaches have been proposed. Quantum size effects have been suggested to increase the power factor and boundary scattering to reduce the lattice thermal conductivity in the in-plane direction of the films (or the wire direction). In the cross-plane direction, one approach is to utilize the increased phonon scattering in superlattice interfaces to decrease the lattice thermal conductivity without degrading the electronic properties. The systems under investigation are often constituted of good bulk conventional thermoelectric materials. For example, superlattices based on PbTe [Harman et al., 1999, 2002] or Bi_2Te_3 [Venkatasubramanian et al., 2001; Beyer et al., 2002] showed great promise. Figure 19.3 shows the evolution of the reported *ZT* values over the last 50 years. One can see a breakthrough has been achieved within these last few years in low-dimensional materials with *ZT* values at least twice as high as current state-of-the-art materials.

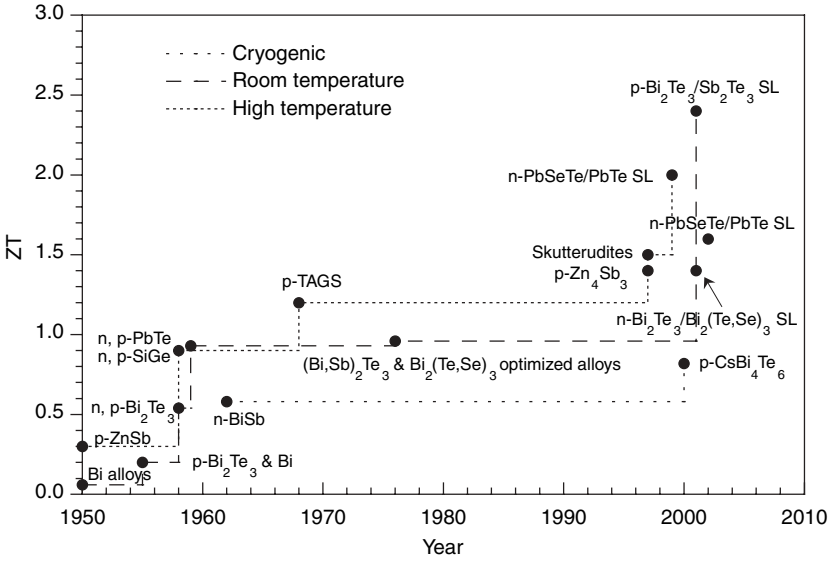

Figure 19.3 History of the dimensionless figure-of-merit *ZT* of materials for cryogenic, room temperature, and high-temperature applications (SL is the abbreviation for superlattice).

19.3 THERMOELECTRIC THIN FILMS

19.3.1 Pulsed Laser Deposition of Conventional Thermoelectric Materials

The preparation of conventional materials in thin-film form is of particular interest for studying fundamental aspects of thermoelectricity as well as for applications in thermoelectric microdevices, and there are a few studies dealing with their preparation by PLD. In this section we will present the investigations performed on several state-of-the-art thermoelectric materials such as bismuth-telluride-based compounds, bismuth, lead-telluride-based compounds, and iron disilicide. All these studies remained essentially parametric. The most relevant features related to PLD will be highlighted.

19.3.1.1 Bi_2Te_3 and Related Compounds

Because of their high *ZT* values, bulk Bi_2Te_3 and its solid solutions with Sb_2Te_3 and Bi_2Se_3 have become the industrial standard for near room temperature thermoelectric applications [Rowe and Bandari, 1983; Scherrer and Scherrer, 1995]. Recently, films of such materials have attracted much attention because of their potential application in the microfabrication of integrated thermoelectric devices [Shafai and Brett, 1997; Stark and Stordeur, 1999; Kim, 2000; Müller et al., 2000]. The development of high-quality Bi_2Te_3-based films for miniaturized thermoelectric applications is a technological challenge. It is very important to obtain materials of high chemical homogeneity and of controlled crystallographic orientation. Actually, these materials are highly anisotropic and very low deviations from stoichiometry may induce huge changes in the thermoelectric properties and thus hamper any development. The values of the transport coefficients are very sensitive indicators of film quality and stoichiometry and thus a measure of the value of the approach to processing thin films.

Numerous deposition techniques including radio frequency (RF) sputtering, flash evaporation, co-evaporation, electrodeposition, metal organic chemical vapor deposition (MOCVD), hot-wall epitaxy (HWE), and molecular beam epitaxy (MBE) have been attempted to grow Bi_2Te_3-based films on various substrates. In general, all these studies showed the difficulties in obtaining a stoichiometric composition, especially at low temperature. PLD has been reported since 1974 as a way to achieve mosaic single-crystalline Bi_2Te_3 films supported on mica or NaCl

substrates from a *Q*-switched laser [Bykovskii et al., 1974], and it is only quite recently that renewed interest in PLD synthesis for these materials has appeared [Dauscher et al., 1996; Yamasaki et al., 1998; Müller et al., 2000; Makala et al., 2002, 2003]. Polycrystalline films having the target stoichiometry have been achieved by PLD on amorphous substrates at room temperature from a Nd : YAG laser ($\lambda = 266$ or 532 nm, 10 Hz, 5 J/cm^2) provided the substrate is in a particular position with regard to the target [Dauscher et al., 1996]. Generally, the optimum deposition temperature for obtaining good-quality stoichiometric films is much higher, in the range $230 \leq T_s \leq 320$°C for films deposited by evaporation [Zou et al., 2002], MBE [Cho et al., 1999; Nurnus et al., 1999], or HWE [Tedenac et al., 1999], and reaches 400–500°C for MOCVD-prepared films [Venkatasubramanian et al., 1997; Boulouz et al., 1998]. Only sputtering, which similarly to PLD involves high kinetic energy species, allows the growth of crystallized films at low temperature, the films exhibiting an excess of Te of 5.5 at % [Shing et al., 1983]. In the PLD process, congruent transfer of stoichiometry from target to film was only reached on a specific area of the substrate, when depositing on large-scale (55×55 mm^2) substrates [Dauscher et al., 1996]. This area is located outside the plume center propagation axis opposite to the impinging side of the laser beam on the target. Noncongruent transfer has been evidenced outside this area with compositions ranging from 68 to 37 at % Bi, covering all the domains of existence of the Bi–Te system (Bi_7Te_2 to Bi_2Te_3). Generally, a large excess of Bi was encountered. Secondary ion mass spectroscopy analyses suggested an erratic deposition in the noncongruent transfer zones, as shown by the random variation of the Bi/Te ratio along the depth profile, whereas this ratio was quasi-constant in the stoichiometric areas. The deviation from stoichiometry is, however, too high ($\pm$ 1 at % Te) to achieve reproducible thermoelectric performance with this material even in the zone of congruent transfer.

This aspect of noncongruent transfer of stoichiometry was not discussed by either Yamasaki et al. [1998] or Makala et al. [2002]. Both groups worked with a similar laser to Dauscher et al. [1996] ($\lambda = 266$ nm), but the deposits were performed at higher temperature on single-crystalline substrates, Si(111), and mica, respectively. The first group showed that the Bi_xTe_y composition largely depends on deposition temperature and ambient pressure. The Te/Bi ratio decreased from 1.64 to 1.18 while increasing the temperature from 250 to 400°C under an Ar pressure of 1×10^{-3} Torr. The presence of an ambient gas helps the non-reevaporation of Te as it has a very high vapor pressure. Stoichiometry was achieved at 300°C. Reduction of droplet number and size was found to be effective by enhancing the laser fluence from 80 mJ/cm^2 to 4 J/cm^2. Sb_2Te_3 films as well as Bi_2Te_3/Sb_2Te_3 multilayers of similar thickness have also been synthesized by the same group [Yamasaki et al., 1998]. Bi_2Te_3/Sb_2Te_3 superlattices are of primary importance since high *ZT* values have been reported in these systems grown by MOCVD by Venkatasubramanian et al. [2001]. Yamasaki et al. [1998] observed similarly to Venkatasubramanian et al. [2001] substantial reduction of the cross-plane thermal conductivity in Bi_2Te_3/Sb_2Te_3 multilayers when decreasing the layer thickness. Values (~ 0.11 Wm^{-1} K^{-1} for a layer thickness of 6 nm) far lower than those in the Bi_2Te_3 (~ 1.1 Wm^{-1} K^{-1}) and Sb_2Te_3 (~ 1.9 Wm^{-1}K^{-1}) single films were achieved. Unfortunately, attempts to evaluate the other transport properties proved to be unsuccessful.

Ternary compounds have also been investigated by PLD. Makala et al. [2002] obtained highly oriented, single-crystalline films of *p*-type $Bi_{0.5}Sb_{1.5}Te_3$ and *n*-type $Bi_2Te_{2.7}Se_{0.3}$ at 300–350°C, under a base vacuum of 5×10^{-7} Torr. Preliminary transport property measurements on these films indicated that the Seebeck coefficient and the mobility of the charge carriers were much lower than in bulk materials (of similar carrier concentration). They suggest improvement could be expected by a better control of the stoichiometry and reduction of defects in the films (pores, particulates, atomic level point defects).

Pulsed laser deposition has been recently used to fabricate the *p*-type legs, made of $Bi_{0.5}Sb_{1.5}Te_3$, of the thermocouples involved in thermoelectric infrared sensor arrays [Müller et al., 2000]. The preparation conditions, other than the deposition temperature of 300°C, were not specified, however. The reported power factor was found to be close to that of the bulk value and better than the power factor of sputtered films prepared by the same authors. Problems with droplets were also underlined.

19.3.1.2 Bismuth

Bismuth is a semimetal that crystallizes with a rhombohedral structure. It is a very attractive material for low-dimensional thermoelectrics because of its unique properties: low carrier density (5 orders of magnitude lower than ordinary metals), and very small electron effective masses along certain axes. Bulk bismuth has a dimensionless figure of merit at 300 K equal to 0.4 [Gallo et al., 1963]. This relatively low value is due to a low Seebeck coefficient resulting from the fact that it is a two-band material; thus the contribution for the holes essentially cancels that for the electrons. However, the behavior of a bismuth quantum well, properly orientated, may be quite different from bulk bismuth. As the quantum well width decreases, the lowest conduction subband rises relative to the highest valence subband that falls, so that a semimetal–semiconductor transition is expected as the well width decreases [Sandomirskii, 1967; Lutskii, 1970]. At 300 K, the theory predicts high ZT values for optimally doped Bi quantum wells less than 30 nm in thickness when quantum confinement is in the trigonal direction [Hicks and Dresselhaus, 1993].

Because of the peculiar electronic properties of Bi in thin-film form, a considerable effort has been expended in the production of Bi films and Bi-based multilayers or superlattices [Dauscher et al., 1997, and references therein]. Numerous deposition techniques have been employed, including PLD. However, fabricating high-quality films to test theoretical predictions has proved to be very challenging because of the absence of a good barrier material for the synthesis of reliable quantum wells with good interfaces. Despite the encouraging results provided by theoretical models, the progress in developing Bi quantum structures for thermoelectric applications has been disappointing thus far. The most relevant features concerning the preparation of bismuth films by PLD are summarized in the next paragraph.

One of the greatest challenges was to reduce the huge amount of droplets generally encountered with this material when prepared by PLD. From a Nd : YAG laser ($\lambda = 532$ nm) and a crystalline Bi target, it has been found that reducing both the repetition rate from 10 to 5 Hz and the target to substrate distance from 6 to 4.5 cm decreases the droplet density [Boffoué, 1999] of Bi films deposited on glass substrates. An important decrease of droplet density was reached by an appropriate method of scanning the laser beam onto the rotating target surface [Jacquot et al., 1999, 2000], to promote a homogeneous distribution of the laser spots onto the whole target and thus a homogeneous erosion. It was, however, evidenced that the enhancement of droplet density was more linked to macroscopic rather than to microscopic degradation of the surface target. Another approach to reduce the droplet density on Bi films was tested by Szörényi et al. [1999] by using molten Bi as the target. In the same work, the authors revealed that this method is quite effective for materials having low melting points, as shown in the case of In and Sn. They worked with a KrF excimer laser ($\lambda = 248$ nm, repetition rate < 1 Hz, 3.2 J/cm^2, vacuum). The results were, however, not conclusive with Bi. From pictures taken by ultrafast photography during the ablation process at a fluence of 5.5 J/cm^2, it was shown that the molten Bi surface emits a remarkable amount of material in the form of droplets originating from liquid jets [Toth et al., 1999]. Droplet emission could be reduced by decreasing the laser fluence. Micro-Rutherford backscattering spectrometry was applied to Bi films grown by PLD to determine surface topography. This method is efficient in the case of rough surfaces and/or in the presence of particulates [Simon et al., 2001; Kantor et al., 2003]. However, Bi films deposited from an ArF laser ($\lambda = 193$ nm, 5 Hz, 2 J/cm^2, in vacuum) on Si(100) substrates at room temperature displayed fewer droplets [De Sande et al., 1996]. These films exhibited reliable optical constants that are independent of film thickness and with an improved stability to oxidation.

Surprising features in thickness profiles were observed by Jacquot et al. [2000], with a maximum shifted toward the opposite side of the arrival of the laser beam on the target. Kantor et al. [1999] and del Coso et al. [1999] also observed particular bismuth thickness profiles that could not be fitted with a classical $\cos^n$ law.

The surface roughness and density of the Bi films were found to depend highly on the ambient atmosphere and deposition temperature. Deposition under a base dynamic vacuum of 10^{-8} mbar led to the highest film quality [Boffoué et al., 1998]. Working under He pressure as

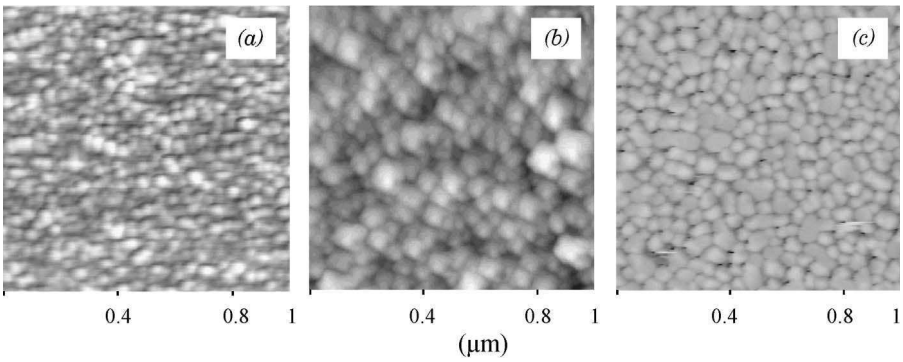

Figure 19.4 Atomic force microscopy topographies of bismuth films deposited on glass substrates at: (a) 20°C (RMSR = 1.8 nm), (b) 80°C (RMSR = 2.0 nm), (c) 120°C (RMSR = 6.5 nm) ($\lambda = 532$ nm, 5 J/cm^2, 3000 shots) [Boffoué et al., 1997]. RMSR: root-mean-square roughness.

low as 5×10^{-7} mbar increased the roughness by a factor of 10 with regard to deposition under high vacuum. The density of the films was even improved under static atmosphere (vacuum or gaseous) but the droplet density was also increased. The optimum deposition temperature was found to be about 80°C [Boffoué et al., 1997], giving rise to films exhibiting a root-mean-square (rms) roughness of about 2 nm and grain sizes of about 100 nm. The changes in morphology with temperature are illustrated in Figure 19.4. Higher deposition temperature gave rise to enhanced surface roughness (mean surface roughness up to 17.6 nm at 180°C) and to film discontinuities. Even with other deposition methods, a temperature of about 80°C was often reported as being the best suited for achieving high-quality bismuth films.

The microstructure of Bi films deposited on glass substrates from an Nd : YAG laser ($\lambda = 532$ nm, 5 Hz, 3 J/cm^2) strongly depends on film thickness. As revealed by transmission electron microscopy, films of 25 nm consist of channels that are electrically continuous, whereas thicker films consist of polyhedral-shaped grains [Dauscher et al., 1998]. Island formation at the beginning of growth followed by columnar growth are typical growth mechanisms for Bi films whatever the deposition method and the nature of the substrate, when they are directly deposited onto the substrate. The grain size increased from 4 to 650 nm for thicknesses ranging from 20 to 120 nm, accompanied by an enhancement of the rms surface film roughness from 3 to 11 nm [Boffoué, 1999]. De Sande et al. [1996] also obtained exceptionally large laminar Bi grains (> 1 μm) when using the PLD technique (KrF, $\lambda = 193$ nm, 5 Hz, 2 J/cm^2, in vacuum) as compared to the direct current (DC) sputtering method. Generally, a grain size of 100–200 nm seems to be the limit reached for Bi films synthesized by any deposition technique other than PLD. The crystalline quality is all the better when the film thickness is larger [Boffoué et al., 2000]. The films grow with the trigonal axis of the hexagonal cell of Bi perpendicular to the substrate plane. This preferential growth direction has generally been encountered with Bi films, irrespective of the substrate nature and the deposition method used, for substrate temperatures lower than 100°C.

Transport property measurements performed on such textured samples prepared by PLD by Boffoué et al. [2000] revealed pronounced size effects as shown by the electrical resistivity increase with the thickness decrease (Fig. 19.5a). Moreover, the resistivity decreases as the temperature increases. This semiconductor-like behavior is different from that of single-crystalline bulk bismuth. The particular features observed in these polycrystalline thin films were explained qualitatively by considering both the temperature-dependent increase of the carrier density and decrease of the carrier mobility. In the bulk form, the carrier density (n) varies with a $T^{3/2}$ law for $T > 50$ K and the components of the mobility (μ) tensor follow a $T^{-5/2}$ variation (the dominant scattering is phonon scattering), so that the electrical resistivity ($\rho = ne\mu$, where e is the elementary electrical charge)

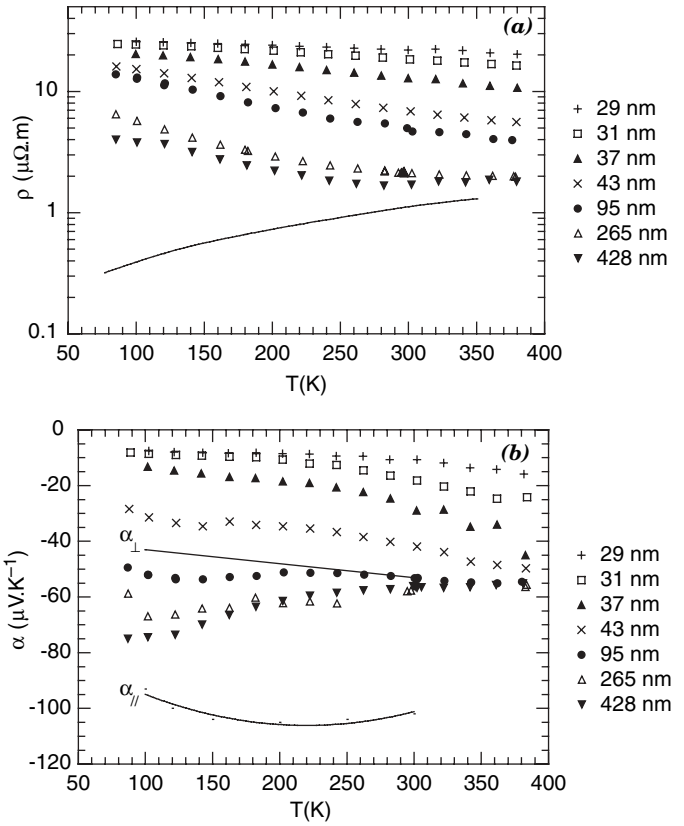

Figure 19.5 The temperature dependence of the transport properties of Bi thin films of different thickness deposited on glass substrates at room temperature ($\lambda = 532$ nm, 5 Hz, 3 J/cm^2) is plotted: (a) electrical resistivity and (b) Seebeck coefficient [Boffoué et al., 2000]. The behavior of the different coefficients for bulk bismuth is shown as a solid line. [Gallo et al., 1963; Michenaud and Issi, 1972].

increases with increasing temperature. In polycrystalline thin films, the carriers will be subjected to additional scattering at film surfaces, crystallite boundaries, and so forth, resulting in a strong decrease of the carrier mobility and also in a smoother temperature dependence. It is then expected that the temperature dependence of the carrier density will be more pronounced than that of the mobility, explaining the decrease of resistivity with increasing temperatures.

The thermopower of these layers was negative over the entire temperature range investigated and for any thickness (Fig. 19.5b). These results suggested that, as in the bulk form, it is likely that the contribution of electrons to the transport is higher than that of holes, resulting in *n*-type behavior [Boffoué et al., 2000]. The size effect, which is also clearly obvious for thermopower, was not discussed in detail because several factors can contribute simultaneously as, for instance, the anisotropy, the grain size, and the thickness.

Attempts have been made to grow single-crystalline films by depositing bismuth on single-crystalline $BaF_2(111)$ substrates [Dauscher et al., 2002a]. The deposition temperature (75–260°C), the location of the substrate with regard to ablation plume center, and an annealing treatment were shown to have a great influence on the morphology and structure of the films. Epitaxy has, however, not yet been proven, but the films are nevertheless highly textured and different orientations can be achieved according to the deposition conditions used. The influence of deposition temperature on the crystallographic structure of the films is illustrated in Figure 19.6.

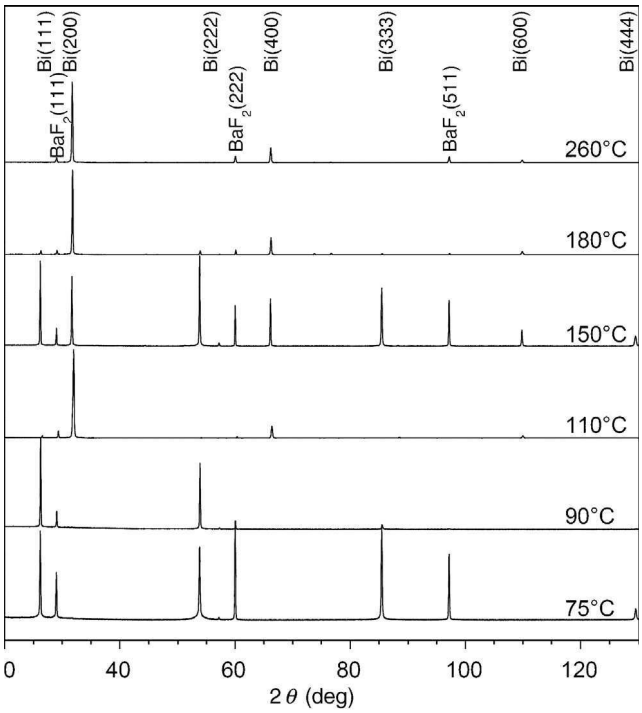

Figure 19.6 Influence of the deposition temperature on the crystallographic structure of $Bi/BaF_2(111)$ films ($\lambda = 532$ nm, 5 Hz, 2 J/cm^2). Note the change of texture [Dauscher et al., 2002a].

19.3.1.3 PbTe and Related Compounds

Lead telluride (PbTe) is a narrow bandgap semiconductor that has proven to be an attractive material in the bulk form for thermoelectric power generation in the temperature range 500–900 K. Its preparation in thin-film form has been stimulated not only for its extensive use in infrared (IR) optoelectronics for manufacturing IR lasers and detectors but also more recently to prove the basic ideas of enhanced thermoelectric properties in quantum confined systems [Harman et al., 1996, 1997, 1999, 2002]. MBE or HWE have been widely used to prepare high-quality PbTe-based thin films, multilayers, and superlattices. The group of Baleva (Sofia University, Bulgaria) and our group have performed parametric investigations on the preparation of PbTe thin films by PLD. The influence of several parameters, especially deposition temperature, substrate nature and fluence, on the growth process, crystalline and morphological qualities, and stoichiometric transfer has been studied. Baleva's group has demonstrated the spontaneous growth of high-pressure interfacial metastable PbTe phases up to 700 nm in thickness, followed by the growth of the stable NaCl phase. The growth of the metastable phases is governed by the high rate of supercooling induced in the nonequilibrium PLD technique (pulsed Nd : glass laser; pulse duration: 0.8 ms; target-to-substrate distance: 3–6 cm; energy per pulse: 2–3 J). The films were initially deposited on glass, KCl(100), KBr(100), and $BaF_2(111)$ substrates [Baleva and Bakoeva, 1986; Baleva et al., 1985, 1993; Baleva and Mateeva, 1996], and more recently on Si(100) substrates [Baleva and Surtchev, 2003]. In this last study, they concluded that when working in the range of thermodynamical possibilities for metastable growth, the formation of the interfacial metastable phases can be avoided if the substrate has no surface periodic relief and if its linear thermal expansion coefficient strongly differs from that of the deposited material. Deposition temperature mainly influences the possibility of growing a particular phase type: metastable CsCl-type phase near room temperature, metastable GeS-type

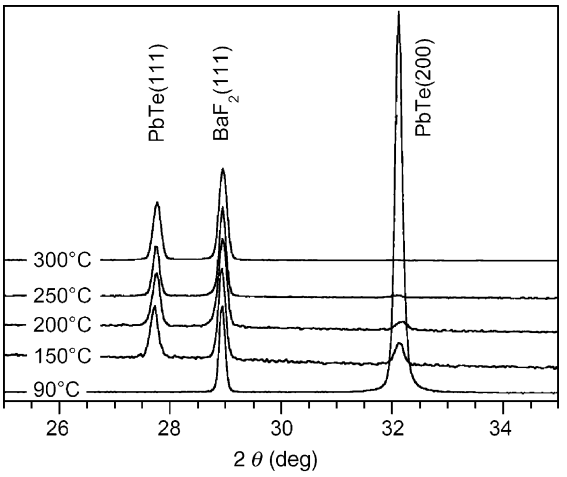

Figure 19.7 Influence of the deposition temperature on the crystallographic structure of PbTe films deposited on BaF_2 (111). The intensity is normalized on the BaF_2(111) peak ($\lambda = 532$ nm, 5 Hz, 3 J/cm^2, vacuum) [Dauscher et al., 2000].

phase around 180°C, and stable face-centered cubic (fcc) phase around 330°C [Baleva and Mateeva, 1996]. Particular electronic and optical properties have been observed in metastable films compared to bulk materials [Baleva et al., 1992]. Moreover, the films were found to exhibit heterophase junctions between a sublayer with metastable phases and a sublayer with the stable phase [Baleva and Mateeva, 1993].

Our group, working with a *Q*-switched Nd : YAG laser ($\lambda = 532$ nm, 5 Hz, pulse duration: 10 ns), has never observed metastable phases for any deposition temperature (Fig. 19.7), fluence, or nature of the substrate. A clear change of growth direction is observed according to the deposition temperature; when the films are deposited on BaF_2(111) [Dauscher et al., 2000], highly textured films are obtained at 90 and 300°C, in the (100) and (111) directions, respectively. The change of growth direction is very sharp, occurring between 90 and 150°C.

From pole figure analyses, it was shown that the films deposited at 90°C exhibit a perfect fiber structure in the [100] direction, showing that all the crystallites have their *c* axis perpendicular to the substrate but that they are twinned along their *a* axis. At 300°C, the expected threefold symmetry of an epitaxial layer, twinned 180° with respect to the substrate, as is always encountered [Holloway, 1980], has been achieved [Dauscher et al., 2001]. Epitaxial films in the [111] direction can thus be grown at 300°C, at a temperature about 50–80°C lower than those generally used for MBE deposits [Springholz and Bauer, 1995; Beyer et al., 1999]. Particularly remarkable is the achievement of highly textured PbTe films on glass substrates with the (h00) planes lying parallel to the substrate plane, whatever the deposition temperature used [Jacquot et al., 1999]. The presence of Pb was identified for depositions carried out at low fluence (2–3 J/cm^2) but not at higher fluence (13 J/cm^2). Less textured samples have been obtained on Si(100) or Si(111) substrates, especially at higher deposition temperature. Similar crystallographic orientations have been obtained with PbSe films grown by PLD on the same substrates from a XeCl excimer laser ($\lambda = 308$ nm, 10 Hz, pulse duration: 20 ns, 5 J/cm^2, 273°C) [Rumianowski et al., 2003].

Chemical compositions of the films were found to be homogeneous over the whole substrate as well as through the entire film thickness. However, strong dependence was observed with deposition temperature (Fig. 19.8) [Dauscher et al., 2001]. The films display Pb excess, except in the narrow deposition temperature range of 150–200°C, for a fluence of 2 J/cm^2. Metev and Sendova [1988] and Metev [1994] suggested the existence of a critical temperature T_c below which the film composition

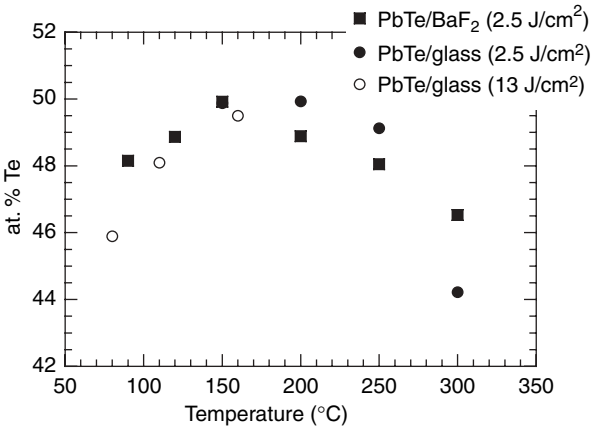

Figure 19.8 Influence of deposition temperature on the mean chemical composition of PbTe films deposited by PLD on glass and $BaF_2(111)$ substrates ($\lambda = 532$ nm, 5 Hz, vacuum) [Dauscher et al., 2001].

deviates significantly from stoichiometry (Nd : glass laser, free-running regime, pulse duration: 400 ns, power density higher than 10^6 Wcm^{-2}). T_c was found to be 500, 350, and 300 K for PbS, PbSe, and PbTe, respectively, for a target-to-substrate distance of 3 cm. T_c becomes higher as the target-to-substrate distance decreases. Baleva and Bakoeva [1986] reproduced the target stoichiometry whatever the deposition temperature was, with Pb contents that differ from the stoichiometry within ± 5 wt % for the different samples prepared. At the given temperature of 150°C, it was also shown that the stoichiometry can be slightly modulated according to the fluence (Fig. 19.9) [Dauscher et al., 2001]. Stoichiometric PbTe films or films containing a small excess of Te or Pb can thus be easily synthesized, without any additional material source, which is important because an excess of Te or Pb act as a dopant. The transport properties of the films can thus be easily tailored by a simple change of laser fluence.

Morphological changes induced by deposition temperature in PbTe films deposited on BaF_2 substrates are illustrated in Figure 19.10 [Dauscher et al., 2002b]. The round-shaped hillocks

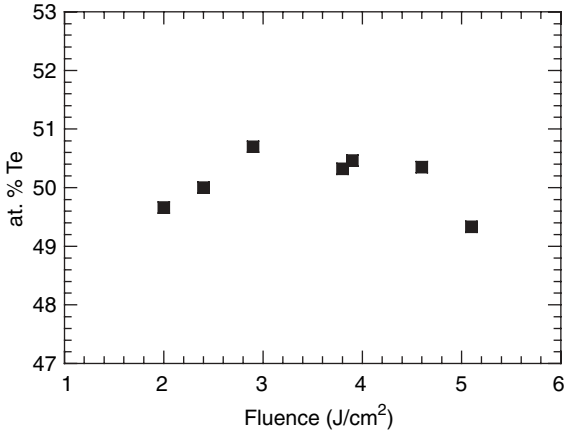

Figure 19.9 Influence of laser fluence on the mean chemical composition of PbTe films deposited by PLD on $BaF_2(111)$ substrates ($\lambda = 532$ nm, 5 Hz, 150°C, vacuum) [Dauscher et al., 2001].

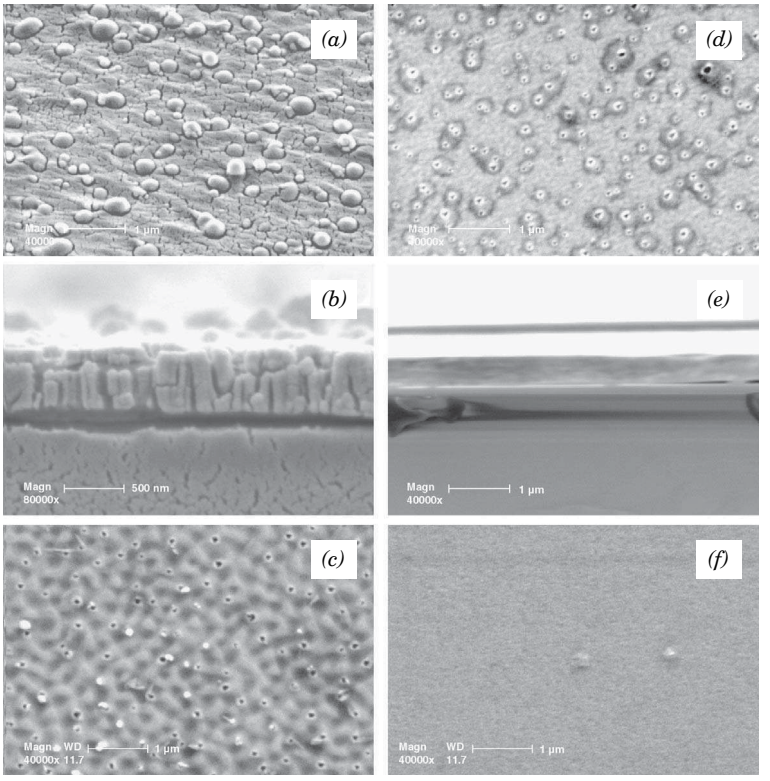

Figure 19.10 Influence of some parameters on the morphology of PbTe films deposited by PLD on $BaF_2(111)$ substrates. (a) 150°C, as-grown, top view (the cracked aspect is due to the morphology change of the gold coverage under the electron beam, but it reveals grain size of the underlaying PbTe film), (b) 150°C, as grown, cross section, (c) 300°C, as grown, top view, (d) 150°C, annealed in situ under vacuum for 1 h just after preparation, top view, (e) 150°C, annealed in situ under vacuum for 1 h just after preparation, cross section, (f) 150°C, $30(Bi_{120}/PbTe_{1200})$ (the subscript represents the number of laser pulses), as grown, top view ($\lambda = 532$ nm, 5 Hz, 2–3 J/cm^2, high vacuum) [Dauscher et al., 2002b].

(400 nm in height) emerging from the surface when the PbTe films are deposited at 150°C (Fig 19.10a and 19.10b) seem to disappear in the films deposited at 300°C (Fig. 19.10c).

Improvements of film morphology could be achieved for PbTe films deposited at 150°C, either by applying a short (1 h) annealing treatment at 300°C (Figs. 19.10d and 19.10e) [Dauscher et al., 2002b] or by introducing nanoinclusions of Bi in the PbTe matrix (Fig. 19.10f). This was realized by depositing Bi/PbTe multilayers. The overall Bi content is about 5 wt %, with regard to the relative deposition rates of Bi and PbTe. Enhancing the number of bilayers leads to increasingly smooth surfaces. These two approaches also produced highly textured films exhibiting only the desired [111] growth direction. This is in agreement with the absence of the columnar structure generally observed in the PbTe films grown at 150°C, as evidenced, for example, for an annealed film in Figure 19.10e.

Electrical characterization has been performed on several PbTe films prepared in our group. While they generally exhibit *n*-type conductivity, some *p*-type samples could be achieved when prepared with adequate fluence, and only when deposited on $BaF_2(111)$ substrates. As illustrated in

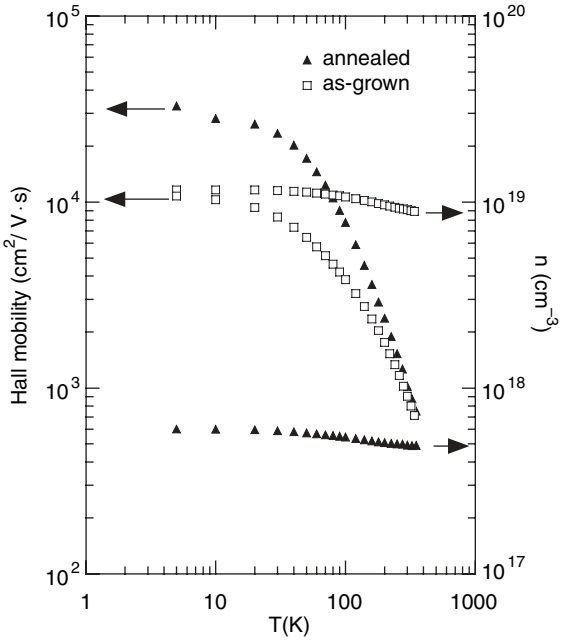

Figure 19.11 Hall mobility and carrier concentration (n) as a function of temperature for PbTe/BaF_2(111) samples prepared at 150°C. One is as grown and the other has been annealed in situ under vacuum for 1 h at 300°C just after preparation ($\lambda = 532$ nm, 5 Hz, 2–3 J/cm^2, vacuum) [Dauscher et al., 2002b].

Figure 19.11, the structural quality of the films is attested by the high value of the Hall mobility at low temperatures (3–5 $\times$ 10^4 cm^2/V s), despite the carrier concentrations being different (5 $\times$ 10^{17}–10^{19} cm^{-3}) [Dauscher et al., 2002b]. With PbSe films prepared by PLD, Sendova [1987] reported Hall mobilities of 18,000 cm^2/V s at 77 K for a carrier concentration as low as 8 $\times$ 10^{17} cm^{-3}, whereas Rumianowski et al. [2003] obtained Hall mobilities at room temperature between 100 and 700 cm^2/V s for carrier concentrations of 3–6 $\times$ 10^{18} cm^{-3}.

19.3.1.4 $FeSi_2$

Pulsed laser deposition has also been successfully applied to the preparation of semiconducting β-$FeSi_2$ thin films that may be interesting for thermoelectric applications near 800 K (Fig. 19.2) but also for optoelectronic and solar cell devices [Powalla and Herz, 1993; Leong et al., 1997]. The challenge lies in obtaining the single β phase that is semiconducting, the other phases being metallic, and a mixture of different phases would alter the physical properties expected from the semiconducting phase alone. The first attempts to grow β-$FeSi_2$ by PLD on Si(111) substrates were performed by Olk et al. [1994] from a pulsed KrF excimer laser ($\lambda = 248$ nm, 2–10 Hz, 300–800 mJ, in ultrahigh vacuum). Single-phase, stoichiometric films grew with the epitaxial relationship β-$FeSi_2$//Si(111) on substrates held between 570 and 630°C. Optical gaps were found to depend on the defect density [Olk et al., 1995]. The growth of stoichiometrically well-controlled β-$FeSi_2$ on Si(100) was also reported by Kakemoto et al. [1997]. Films were prepared from an ArF excimer laser ($\lambda = 193$ nm, 5 Hz, 1 J/cm^2, in ultrahigh vacuum) at temperatures of 550–650°C. From reflected high energy electron diffraction (RHEED) and X-ray diffraction (XRD) analyses, the samples showed polycrystalline features and the surface was mostly β(220) oriented. By optical absorption measurements, they found the bandgap energy to be 0.81 and 0.96 eV for direct and indirect optical transitions, respectively. Other attempts to grow this material were performed by Liu et al. [1999, 2001]. Yoshitake et al. [2001] made an in-depth investigation of the influence of

deposition temperature (between 20 and 800°C) on the film growth. Using an ArF excimer laser ($\lambda = 193$ nm, 10 Hz, pulse duration: 24 ns, 1.5–5 J/cm^2, in high vacuum), they succeeded in the deposition of stoichiometric polycrystalline β-$FeSi_2$ single phase on Si(100) at room temperature. For deposition temperatures higher than 700°C, the epitaxial relation was found to be β-$FeSi_2$ (041) or (014)//Si(220) at the beginning of deposition, but it became disordered with increased film thickness. In a further study, they adapted a vane velocity filter to decrease the droplet density [Yoshitake et al., 2002]. The droplets could be completely eliminated at a suitable cutoff velocity of the filter. The maximum velocity of droplets was at most 65 m/s.

The main advantage of PLD over other techniques underlined by all authors is the obtaining of the β-$FeSi_2$ phase without the need of any further annealing. It is unfortunate that no measurement of the transport properties has been performed on these intermetallic materials as they are stable with respect to oxidation, sublimation, evaporation, and diffusion.

19.3.2 Pulsed Laser Deposition of New Thermoelectric Materials

Among new materials, PLD of skutterudite materials has received the greatest attention to date [Christen et al., 1997; Caylor et al., 1999a, 1999b, 2001a, 2001b; Song et al., 2000; Suzuki et al., 2000; Durand et al., 2000; Suzuki, 2001]. These publications were mainly motivated by the promising *ZT* values of this class of materials obtained when prepared in bulk form [Uher, 2001]. Other new thermoelectric materials like half-Heusler phases or Chevrel phases were also prepared by PLD, but the experimental results are rather limited. Although PLD seems to be an appropriate method for the growth of all these new materials, it is difficult to comment about the performances of the thin films produced because the transport measurements are either incomplete or still at an early stage of development.

19.3.2.1 Skutterudites

Binary skutterudites have the general formula MX_3 where M = Co, Ir, Rh and X = P, As, Sb. They crystallize with a body-centered-cubic (bcc) structure, space group *Im3* and the unit cell, illustrated in Figure 19.12, contains 32 atoms. The transition-metal atoms, M, are arranged in a simple cubic lattice and the pnicogen atoms, X, are distributed in six rectangular four-membered rings. There are

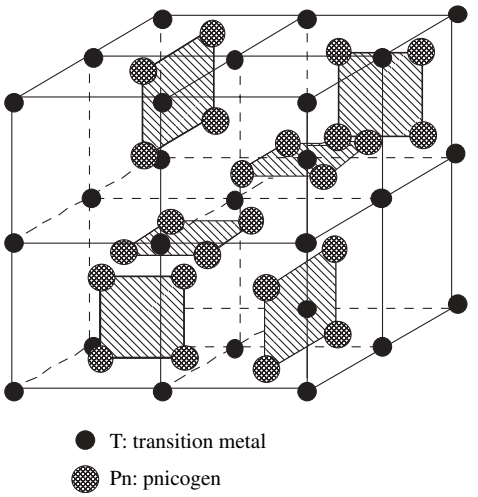

Figure 19.12 Skutterudite unit cell is shown. The transition-metal atoms (Co, Rh, Ir) form a cubic sublattice, and the pnicogen atoms (P, As, Sb) are arranged in planar rectangular four-membered rings. Two of the eight small cubes are empty, giving rise to two voids (cages) per unit cell.

eight small cubes and two are empty in the unfilled version. By filling the two empty voids of the structure, one can obtain new skutterudite compounds often referred to as filled skutterudites. Their general formula can be described as RT_4X_{12}, where R is the filler than can be a lanthanide, actinide, or alkaline-earth ion and T stands for Fe, Ru, or Os. Filled skutterudites have much lower thermal conductivities than their binary counterparts because the guest atoms ''rattle'' inside these oversized cages, disrupting phonon transport. The skutterudites that have attracted by far the greatest attention are compounds based on $CoSb_3$ as they show the best thermoelectric characteristics [Uher, 2001].

A systematic investigation of unfilled-skutterudite $CoSb_3$ thin films made by PLD under vacuum was performed by Suzuki et al. [2000] on silicon substrates over a wide range of laser fluences (0.6–3.5 J/cm^2) and deposition temperatures (70–350°C). Using an ArF excimer laser ($\lambda = 193$ nm) with a repetition rate of 40 Hz and a stoichiometric target, a $CoSb_3$ single-phase skutterudite film was obtained for a laser fluence of 2 J/cm^2 and for a substrate temperature of 70°C, suggesting that the high kinetic energies of species in the plume may contribute to the crystal growth. With other combinations of laser fluence–substrate temperature, it was found that slightly Co-rich or Sb-rich films were formed. It was also noted that films showed a high density of surface particles.

Another detailed investigation concerning the film growth parameters of binary skutterudite compounds ($CoSb_3$ and $IrSb_3$) was reported by Caylor et al. [2001a]. The experiments were conducted with a KrF excimer laser ($\lambda = 248$ nm) on Si substrates. In addition to the substrate temperature, the target composition, the target-to-substrate distance, and the growth atmosphere were taken into account to produce high crystalline and low stress films of the desired stoichiometry. As previously noted by Christen et al. [1997] and Suzuki et al. [2000], the growth temperature is important due to the difference in volatility between the transition metal and antimony. It was found that above 250°C, the stoichiometric flux 1 : 3 was insufficient to stabilize the skutterudite phase and the antimony deficient $CoSb_2$ or $IrSb_2$ phases appeared. However, increasing the flux of antimony by adding excess antimony to the target increased the temperature range over which the skutterudite phase is stable. By increasing the deposition temperature and using targets with excess antimony, film crystallinity was increased and film stoichiometry was found to be 1 : 3. In addition to the issue of substrate temperature and antimony volatility, this system provided an interesting case to study the effect of target-to-substrate distance on film morphology. It was reported that the energy and stoichiometry of the incoming particles vary with the target-to-substrate distance due to plume tilting. At greater distances, there was more uniform film coverage across the growth surface and less film stress. However, if the distance was too large, the films were no longer a pure single phase. The addition of an inert background gas (Ar) was found to dramatically lower the flux of ions, thus lowering the internal stress of the films and limiting blistering. Finally, the synthesis of high-quality, uniform, blister-free thin films of $CoSb_3$ and $IrSb_3$ was possible from targets with excess antimony at a temperature of 270°C with a target-to-substrate distance of 7 cm and a background argon gas pressure of 10 mTorr. Preliminary results on the electrical properties at room temperature revealed that these optimized films are degenerate *p*-type semiconductors with hole concentrations in the range of previously measured bulk values. Hole mobilities were found to be lower than those measured in large grains or single-crystalline bulk samples due likely to very small grain sizes (about 250 nm) of the polycrystalline films.

Pulsed laser deposition was also successfully used by the same group for the growth of $IrSb_3$/$CoSb_3$ multilayers [Caylor et al., 1999b] as an attempt to explore the effect of interfaces and grain boundaries on the thermal conductivity in these low-dimensional systems [Song et al., 2000]. Experimental results on the temperature-dependent cross-plane thermal conductivity were reported on several polycrystalline films grown by PLD, including $IrSb_3$, $CoSb_3$, $Ir_{0.5}Co_{0.5}Sb_3$ single layers, and $IrSb_3$/$CoSb_3$ multilayers of various periods [Song et al., 2000]. The cross-plane thermal conductivity of these systems was measured with the 3ω method [Lee and Cahill, 1997; Jacquot et al., 2002a] from 80 to 300 K. Significant reduction in thermal conductivity was observed for both the single-layer skutterudite films and the multilayers compared to their respective values in bulk samples. These reductions were attributed to the combined effect of grain boundary scattering, mass difference scattering, and interface scattering.

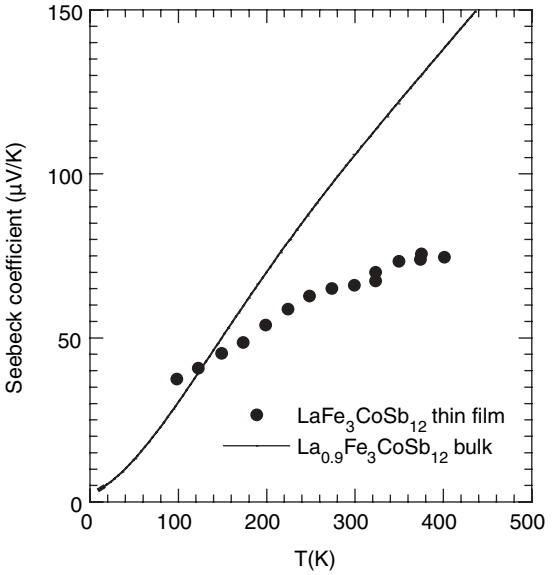

Figure 19.13 Temperature dependence of the Seebeck coefficient of a La-filled skutterudite prepared in the bulk form [Sales et al., 1997] and in the thin-film form by PLD ($\lambda = 193$ nm, 40 Hz, 1.5 J/cm^2) [Suzuki, 2001].

Pulsed laser deposition proved also to be a well-suited technique for the synthesis of La-filled skutterudite thin films. $LaFe_3CoSb_{12}$ layers were grown in a high-vacuum chamber using an ArF excimer laser (40 Hz) on glass substrates by Suzuki [2001]. Single-phase filled skutterudites were achieved for different combinations of laser fluence and temperature. Typical values were about 1.5–3 J/cm^2 and 100–160°C. Transmission electron microscopy (TEM) analyses revealed that films were composed of small grains (20–100 nm in size). Electrical measurements at room temperature confirmed that the films are *p*-type as expected but with carrier concentrations one order of magnitude higher that those expected for completely filled materials [Sales et al., 1997]. The temperature dependence of the Seebeck coefficient of the films proved to be similar to that of the bulk (Fig. 19.13) but with lower values especially at high temperature. It was suggested that the deviations of the transport properties of the thin films relative to bulk samples could be due to the effect of small grains on the electronic properties.

A second possible way of transport property improvement, other than the use of filled skutterudites, could arise from growing the skutterudites epitaxially, as epitaxial growth could alleviate the problem of the small grains dominating transport properties. First attempts for epitaxial $CoSb_3$ film growth by PLD were conducted on different substrates such as CaF_2, sapphire, $SrTiO_3$, and TiO_2 by Christen et al. [1997]. Unfortunately, it was clearly seen by X-ray diffraction that no epitaxy was achieved with these particular substrates. The reason why no epitaxy was found, even in the case of the lattice-matched TiO_2, was attributed to different type of chemical bonding within the substrate (more ionic bonding) and within the film (more covalent bonding). More recently, Caylor et al. [2001b] demonstrated that heteroepitaxial growth of $CoSb_3$ on (001) InSb substrates is possible by PLD using a substrate temperature of 270°C and a bulk $CoSb_3$ target with 0.75 at % excess Sb. The InSb ($a = 6.478$ Å) substrate was chosen for its lattice matching with the antimonide skutterudite ($a = 9.034$ Å) on the basis of a presumed 45° rotated relationship with the InSb zincblende structure. X-ray diffraction and transmission electron microscopy (Fig. 19.14) confirmed both the structure of the films and their epitaxial relationship: $(001)_{CoSb3}//(001)_{InSb}$; $[100]_{CoSb3}//[110]_{InSb}$.

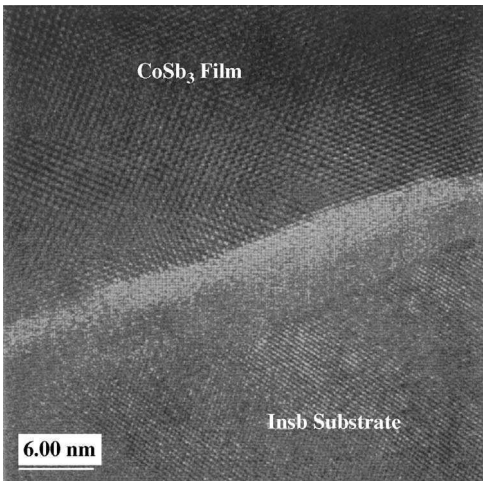

Figure 19.14 Cross-sectional transmission electron micrograph showing the interfacial area of $CoSb_3$ film and InSb substrate as well as the {110} lattice planes in the film and the {111} planes in the substrate [after Caylor et al., 2001b].

19.3.2.2 Other Materials

The decrease of thermal conductivity due to rattling motion of a host atom in an open structure can also be expected in Chevrel phases, of general formula $M_xMo_6X_8$ (M: rare-earth or transition-metal cation, X: S, Se, or Te) in which the cations can be easily inserted [Yvon, 1979; Chevrel and Sergent, 1982]. This class of materials has been primarily studied for their superconducting properties [Fischer, 1978] and then for intercalation–deintercalation processes [Potel et al., 1984; Tarascon et al., 1988]. Their potential as thermoelectrics was revealed by Caillat and Fleurial [1997] and Caillat et al. [1999] with selenide phases. Studies on bulk materials were further pursued by several groups including Tsubota et al. [1999], Nunes et al. [1999], Roche et al. [1999], and Ohta et al. [2001]. Even if studies on thin films are so far not concerned with thermoelectricity, one has to note the successful application of PLD ($\lambda = 308$ nm, 2 Hz, $T_s = 810$–890°C, 5 J/cm^2) to the synthesis of $Cu_xMo_6S_8$ layers on various substrates. Moreover, epitaxially grown Chevrel phase thin films were achieved for the first time [Lemée et al., 1997, 1999], whereas only textured films were obtained by other deposition methods [Neal, 1988]. The crystalline quality was largely dependent on deposition temperature and pressure. The high kinetic energy of the evaporated species in the PLD process was assumed to be responsible for the epitaxial growth of these compounds, in a similar manner to other materials [Guilloux-Viry and Perrin, 2000].

Among other potential thermoelectric materials, the class of ternary compounds related to half-Heusler phases attracted a great deal of attention. Two groups of compounds have been particularly studied: the rare-earth nickel antimonide compounds, RNiSb [Karla et al., 1998; Sportouch et al., 1998], and the intermetallic stannide compounds, MNiSn, M = Ti, Hf, Zr [Hohl et al., 1997; Uher et al., 1999; Shen et al., 2001]. Interest arises from the fact that these compounds have been predicted by band structure calculations to be narrow-bandgap semiconductors [Aliev et al., 1990; Ogut and Rabe, 1995; Larson et al., 1999]. The challenge for these materials lies in the fact that they have high thermal conductivity. Having them in the thin-film form could lead to a decrease of the thermal conductivity resulting in an improved figure of merit if the electrical properties are maintained. To the best of our knowledge, it has never been done with these classes of ternary compounds. Thin films of NiMnSb half-Heusler phases have, however, been studied for potential magneto-transport and spin-polarized transport applications. They have been prepared by several techniques, and quite recently by PLD [Giapintzakis, 2002a, 2002b; Grigorescu et al., 2003]. They tested several

deposition conditions and concluded that the best films based on morphology were produced using a KrF excimer laser ($\lambda = 248$ nm, 600 mJ/pulse maximum), from a crystalline target that maintained better initial stoichiometry compared to a sintered target. The most striking result was to get stoichiometric films, of high-crystalline quality at a much lower temperature (200°C) than those used with other deposition methods ($\geq$250°C) [Caballero et al., 1997; Hordequin et al., 1998]. It is of particular importance because high-temperature deposition is incompatible with multilayer structures suitable for devices due to interdiffusion and granular character. The crystalline quality in the pulsed-laser-deposited films is, however, not as good as in epitaxial films grown at 400°C by DC facing-targets sputtering [Ristoiu et al., 2000], as evidenced by the higher residual resistivity value ($\sim 48\,\mu\Omega\,$cm compared to $\sim 5.3\,\mu\Omega\,$cm). An annealing treatment of 1 h at 500°C restores the value to that of the bulk material ($\sim 18\,\mu\Omega\,$cm) [Giapintzakis, 2002b].

Finally, some attempts were also made to grow quasi-crystals by PLD [Brien et al., 2003a, 2003b; Ichikawa et al., 1994; Mele et al., 2002; Teghil et al., 2000, 2003]. Interest in this class of material is motivated by the unique transport properties displayed in these nonperiodic crystallographic structures. For more details about the results obtained by PLD, the reader is also referred to Chapter 25.

19.4 THERMOELECTRIC MICRODEVICES AND APPLICATIONS

Due to their distinct advantages over other technologies (no moving parts, high reliability, localized cooling, absence of harmful gases, etc.) and due to the increasing trend of miniaturization in all fields of microelectronic and microtechnology, thermoelectric microdevices based on thin or thick films should complete and extend the current applications of commercial modules based on bulk materials. Actually, their geometry cannot be reduced indefinitely by keeping the same fabrication technology and the same cost. At present, large efforts are made in many groups to expand the technology of thermoelectric devices into the field of microsystem technologies. The next paragraphs summarize potential applications of thermoelectric microdevices and recent developments. For a more detailed review, the reader is invited to refer to Böttner [2002].

Thermoelectric microdevices should find applications in many areas, such as instruments, industrial, telecommunication, military, aerospace, industrial, or commercial products. Microcoolers can play an important role in the thermal management and temperature stabilization of certain electronic and optoelectronic components [Chu and Simons, 1999]. For example, they could be used to dissipate the heat generated by most computing modules made by complementary metal oxide semiconductor (CMOS) transistors on a small scale.

For the operation of small electronic devices and systems, a power supply of some few microwatts is sufficient in most cases. Provided a temperature difference exists between the location of the device and the ambient surroundings, thermoelectric microgenerators could be used to generate the required electrical power. For example, we usually find a temperature difference of some degrees between the surface of the human body and its environment. Exploiting this temperature gradient, wristwatches can be powered thermoelectrically [Kishi et al., 1999]. Waste heat as an energy source could be also used advantageously to generate power at a low level. At present, thin-film thermoelectric generators are commercially available [Stordeur and Stark, 1997; Stark and Stordeur, 1999].

Integrated circuit (IC) and microelectromechanical systems (MEMS) technologies offer a promising approach to fabricate thermoelectric microdevices. Two types of device configurations, cross-plane and in-plane are possible. In cross-plane devices, current and heat flow are perpendicular to the film plane. This configuration is similar to devices made of bulk materials (Fig. 19.1). In in-plane devices, heat and current flow parallel to the film plane. Each device has its own advantages and disadvantages. The cross-plane devices face the challenge of establishing a large temperature difference across thin films of a few micrometers thick; the in-plane devices face the issue of heat leakage through the supporting substrate. Using standard IC technology

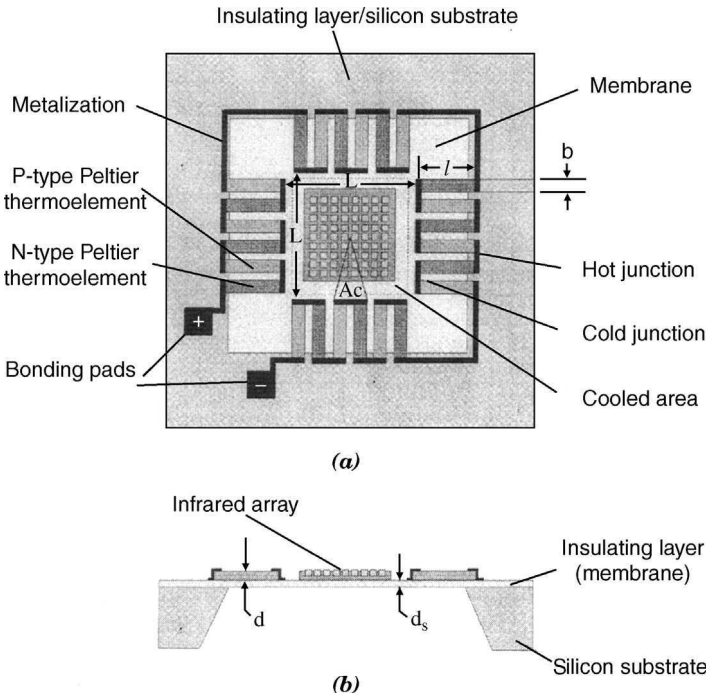

Figure 19.15 Schematic diagrams showing an integrated thermoelectric micro-cooler with infrared components integrated onto central region. (a) plan view and, (b) cross-sectional view [Min and Rowe, 1999].

and micromachining it is also possible to fabricate thermoelectric microsensors. Examples of working prototypes include microthermopiles for IR radiation detection, thermoelectric vacuum microsensors, gas flow microsensors, and thermoelectric microtips for atomic force microscopy [Völklein, 2000].

The Jet Propulsion Laboratory [Fleurial et al., 1997, 1999] and Infineon Technologies associated with Fraunhofer IPM [Böttner et al., 2001; Böttner, 2002; Diliberto et al., 2002; Jaegle et al., 2002] have developed cross-plane microdevices based on Bi_2Te_3 and its related compounds. The deposition of these thermoelectric materials was made either by electrodeposition or by sputtering. In each case the layers were a few tens of micrometers thick. The device fabrication was based on wafer technologies. Promising experimental results have been obtained in the two working modes, cooler or generator. Large efforts were also made to develop in-plane thermoelectric microdevices [Stordeur and Stark 1997; Stark and Stordeur, 1999; Min and Rowe, 1999; Völklein et al., 1999; Jacquot et al., 2002b]. The approach based on the use as the substrate of a very thin membrane of extremely low thermal conductance is particularly interesting to minimize the substrate thermal bypass. Figure 19.15 represents schematics of a proposed thin-film thermoelectric cooler with infrared component integrated onto the cooled central region [Min and Rowe, 1999]. A membrane of low thermal conductivity can be fabricated from SiC or SiN_x with a SiO_2 thin-film deposition on the top of a silicon substrate. Subsequent micromachining removes a portion of the substrate at the desired location. *n*-Type and *p*-type thermoelectric legs are then deposited on the membrane to form thermocouples. The thermocouples are configured so that the central region, which is to be cooled, is surrounded by the cold junctions of the thermocouples, while the hot junctions are located on the outer peripheral area, which rests on the silicon frame. Heat is pumped laterally from the central region to the silicon frame and then dissipated vertically through it to an external heat sink.

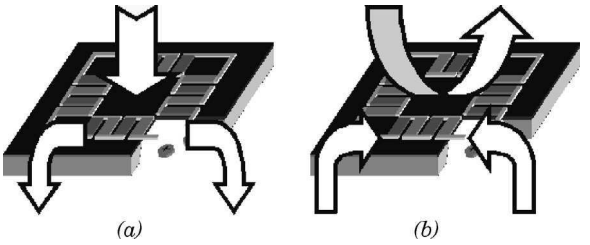

Figure 19.16 Working modes of a thermoelectric microgenerator: (a) heat source on the membrane and (b) heat source at the silicon frame [Jacquot et al., 2002b].

Modeling and first calculations show promising cooling parameters [Min and Rowe, 1999; Völklein et al., 1999].

This arrangement can also be used advantageously as a thermoelectric microgenerator. As shown in Figure 19.16, two working modes can be anticipated [Jacquot et al., 2002b]. The first mode of working is when the heat source is on the center of the membrane (e.g., heat dissipated from electronic devices). The silicon frame that sustains the membrane is the cold side. A large temperature difference along the thermoelectric legs is expected even with small heat sources because the thermal conductance is low. The second mode of working takes advantage of the large surface-to-volume ratio of the membrane to use it as a heat sink, the hot side being the silicon frame. The heat source may be, for example, the heat generated by a human body while the coolant could simply be air. The fabrication of such in-plane thermoelectric microgenerators has been demonstrated with polycrystalline silicon as the thermoelectric material and the proof-of-principle was proved experimentally [Jacquot et al., 2002b]. Modeling helped to identify the crucial parameters necessary to a successful design and fabrication sequence of a realistic microgenerator [Jacquot, 2003].

19.5 CONCLUSION

The studies on the preparation of thermoelectric narrow-bandgap semiconductors by pulsed laser deposition are rather limited in number. For each material studied, specific problems have been identified and have had to be solved. Because of the wide range of elements constituting these materials, no general recipe using the various PLD parameters could be applied to achieve high-quality stoichiometric thin films. PLD offered the opportunity to easily tailor the film properties by acting on their microstructure and stoichiometry. Only preliminary results have been obtained concerning the transport property coefficients. Actually, accurate measurements of the transport properties in thin films are particularly critical, especially concerning their thermal conductivity. PLD is certainly the most promising method for the synthesis of the new interesting identified classes of thermoelectric materials, which are often ternary or quaternary materials. Future developments for thermoelectric applications lie in the improvement in thickness homogeneity over large-scale substrates to provide reliable transport properties.

Acknowledgments

The authors would like to apologize for any inadvertent omissions or incorrect statements of fact or opinion attributed to others. They also wish to thank all the members of the laboratory, especially O. Boffoué and A. Jacquot, who have contributed to this work and would like to acknowledge the collaboration with M. Dinescu at the National Institute of Plasma and Laser Physics of Bucaresti (Romania).

REFERENCES

Aliev, F. G., V. V. Kozyrkov, V. V. Moshchalkov, R. V. Skolozdra, and K. Durczwski (1990), *Z. Phys. B* **80**, 353.

Baleva, M., and D. Bakoeva (1986), *J. Mater. Sci. Lett*. **5**, 37.

Baleva, M., and E. Mateeva (1993), *Phys. Rev. B* **48**, 2659.

Baleva, M., and E. Mateeva (1996), *J. Mater. Sci*. **31**, 1213.

Baleva, M., and M. Surtchev (2003), *Vacuum* **69**, 419.

Baleva, M., M. Christova, A. Iordanov, S. Metev, and S. Peneva (1985), *J. Mater. Sci. Lett*. **4**, 353.

Baleva, M., E. Mateeva, and M. Momtchilova (1992), *J. Phys. Condens. Matter* **4**, 8997.

Baleva, M., L. Bozukov, and E. Tzukeva (1993), *Semicond. Sci. Technol*. **8**, 1208.

Beyer, H., A. Lambrecht, J. Nurnus, H. Böttner, H. Griessmann, A. Heinrich, L. Schmitt, M. Blumers, and F. Völklein (1999), in *Proceedings of the XVIII International Conference on Thermoelectrics*, *Baltimore*, IEEE, Piscataway, NJ, p. 687.

Beyer, H., J. Nurnus, H. Böttner, A. Lambrecht, T. Roch, and G. Bauer (2002), *Appl. Phys. Lett*. **80**, 1216.

Boffoué, M. O. (1999), Ph.D. Thesis, Elaboration par ablation laser de couches minces de Bi et de PbTe. Caractérisation microstructurale et propriétés de transport. INPL, Nancy, France.

Boffoué, M. O., B. Lenoir, L. Hennet, N. Maloufi, H. Scherrer, and A. Dauscher (1997), *Proc. SPIE* **3404**, 61.

Boffoué, M. O., B. Lenoir, H. Scherrer, and A. Dauscher (1998), *Thin Solid Films* **322**, 132.

Boffoué, M. O., B. Lenoir, A. Jacquot, H. Scherrer, A. Dauscher, and M. Stölzer (2000), *J. Phys. Chem. Solids* **61**, 1979.

Böttner, H. (2002), in *Proceedings XXI International Conference on Thermoelectrics*, *Long Beach*, IEEE, Piscataway, NJ, p. 511.

Böttner, H., A. Schubert, K. H. Schlereth, D. Eberhard, A. Gavrikov, M. Jägle, G. Kühner, C. Künzel, J. Nurnus, and G. Plescher (2001), in *Proceedings VI European Workshop on Thermoelectrics*, *Freiburg*.

Boulouz, A., A. Giani, F. Pascal-Delannoy, M. Boulouz, A. Foucaran, and A. Boyer (1998), *J. Crystal Growth* **194**, 336.

Brien, V., A. Dauscher, P. Weisbecker, and F. Machizaud (2003a), *Appl. Phys. A* **76**, 187.

Brien, V., A. Dauscher, P. Weisbecker, J. Ghanbaja, and F. Machizaud (2003b), *J. Crystal Growth* **256**, 407.

Bykovskii, Yu. A., A. G. Dudoladov, V. P. Kozlenkov, and A. A. Leont'ev (1974), *JETP Lett*. **20**, 135.

Caballero, J. A., F. Petroff, Y. D. Park, A. Cabbibo, R. Morel, and J. R.Childress (1997), *J. Appl. Phys*. **81**, 2740.

Caillat, T., and J.-P. Fleurial (1997), in *Proceedings of the XVI International Conference on Thermoelectrics*, *Dresden*, A. Heinrich and J. Schumann (Eds.), IEEE, Piscataway, NJ, p. 446.

Caillat, T., J.-P. Fleurial, and A. Borshchevsky (1997), *J. Phys. Chem. Solids* **58**, 1119.

Caillat, T., J.-P Fleurial, and G. J. Snyder (1999), *Solid State Sci*. **1**, 535.

Caylor, J. C., A. M. Stacey, T. Sands, and R. Gronsky (1999a), *Mater. Res. Soc. Symp. Proc*. **546**, 327.

Caylor, J. C., A. M. Stacy, B. Bloom, R. Gronsky, T. Sands, W. W. Fuller-Mora, A. Ehrlich, D. Song, and G. Chen (1999b), in *Proceedings of the XVIII International Conference on Thermoelectrics*, *Baltimore*, IEEE, Piscataway, NJ, p. 656.

Caylor, J. C., A. M Stacy, R. Gronsky, and T. Sands (2001a), *J. Appl. Phys*. **89**, 3508.

Caylor, J. C., M. S. Sander, A. M. Stacy, J. S. Harper, R. Gronsky, and T. Sands (2001b), *J. Mater. Res*. **16**, 2467.

Chen, G. (2001), *Semiconductors and Semimetals* **71**, 203.

Chevrel, R., and M. Sergent (1982), in *Topics in Current Physics: Superconductivity in Ternary Compounds I*, Vol. 32, O. Fischer and M. B. Maple (Eds), Springer Verlag, Berlin, p. 25.

Cho, S., Y. Kim, A. DiVenere, G. K. L. Wong, J. R. Meyer, and J. B. Ketterson (1999), *Mater. Res. Soc. Symp. Proc*. **545**, 183.

Chrisey, D. B., and G. K. Hubler (Eds.) (1994), *Pulsed Laser Deposition of Thin Films*, Wiley, New York.

Christen, H. M., D. G. Mandrus, D. P. Norton, L. A. Boatner, and B. C. Sales (1997), *Mater. Res. Soc. Symp. Proc*. **478**, 217.

Chu, R. C., and R. E. Simons (1999), in *Proceedings of the XVIII International Conference on Thermoelectrics*, *Baltimore*, IEEE, Piscataway, NJ, p. 270.

Dauscher, A., A. Thomy, and H. Scherrer (1996), *Thin Solid Films* **280**, 61.

Dauscher, A., B. Lenoir, M. O. Boffoué, X. Devaux, R. Martin-Lopez, and H. Scherrer (1997), in *Proceedings of the XVI International Conference on Thermoelectrics*, *Dresden*, A. Heinrich and J. Schumann (Eds.), IEEE, Piscataway, NJ, p. 429.

Dauscher, A., M. O Boffoué, B. Lenoir, R. Martin-Lopez, and H. Scherrer (1998), *Appl. Surf. Sci*. **138/139**, 188.

Dauscher, A., A. Jacquot, B. Lenoir, H. Scherrer, M. Dinescu, and M. Stölzer (2000), in *Proceedings of the XIX International Conference on Thermoelectrics*, *Cardiff*, D. M. Rowe (Ed.), Babrow Press, Wales, UK, p. 420.

Dauscher, A., B. Lenoir, O. Boffoué, and A. Jacquot (2001), *Proc. SPIE* **4762**, 52.

Dauscher, A., A. Jacquot, and B. Lenoir (2002a), *Appl. Surf. Sci*. **186**, 513.

Dauscher, A., B. Lenoir, A. Jacquot, C. Bellouard, and M. Dinescu (2002b), *Mater. Res. Soc. Symp. Proc*., **691**, G.8.3.1.

Dauscher, A., B. Lenoir, H. Scherrer, and T. Caillat (2002c), *Recent Res. Devel. Mater. Sci*. **3**, 181.

del Coso, R., A. Perea, R. Serna, J. A. Chaos, J. Gonzalo, and J. Solis (1999), *Appl. Phys. A* **69**, S553.

de Sande, J. C. G., T. Missana, and C. N. Afonso (1996), *J. Appl. Phys*. **80**, 7023.

Diliberto, S., S. Michel, C. Boulanger, J. M. Lecuire, M. Jägle, S. Drost, and H. Böttner (2002), in *Proceedings of the VII European Workshop on Thermoelectrics*, *Pamplona*.

Dresselhaus, M. S., Y.-M. Lin, T. Koga, S. B. Cronin, O. Rabin, M. R. Black, and G. Dresselhaus (2001), *Semiconductors and Semimetals* **71**, 1.

Durand, H. A., K. Nishimoto, K. Ito, and I. Kataoka (2000), *Appl. Surf. Sci*. **154/155**, 387.

Fischer O. (1978), *Appl. Phys*. **16**, 1.

Fleurial, J.-P., A. Borshchevsky, M. A. Ryan, W. Phillips, E. Kolawa, T. Kacisch, and R. Ewell (1997), in *Proceedings of the XVI International Conference on Thermoelectrics*, *Dresden*, A. Heinrich and J. Schumann (Eds.), IEEE, Piscataway, NJ, p. 641.

Fleurial, J.-P., G. J. Snyder, J. A. Herman, P. H. Giauque, W. M. Phillips, M. A. Ryan, P. Shakkottai, E. A. Kolawa, and M. A. Nicolet (1999), in *Proceedings of the XVIII International Conference on Thermoelectrics*, *Baltimore*, IEEE, Piscataway, NJ, p. 294.

Gallo, C. F., S. F. Chandrasekhar, and P. H. Sutter (1963), *J. Appl. Phys*. **34**, 144.

Giapintzakis, J., R. Grigorescu, A. Klini, A. Manousaki, V. Zorba, J. Androulakis, Z. Viskadourakis, and C. Fotakis (2002a), *Appl. Surf. Sci*. **197/198**, 421.

Giapintzakis, J., R. Grigorescu, A. Klini, A. Manousaki, V. Zorba, J. Androulakis, Z. Viskadourakis, and C. Fotakis (2002b), *Appl. Phys. Lett*. **80**, 2716.

Grigorescu, C. E., S. A. Manea, M. Mitrea, O. Monnereau, R. Notonier, L. Tortet, R. Keschawarz, J. Giapintzakis, A. Klini, V. Zorba, J. Androulakis, and C. Fotakis (2003), *Appl. Surf. Sci*. **212/213**, 78.

Guilloux-Viry, M., and A. Perrin (2000), *Recent Res. Devel. Crystal Growth* **2**, 1.

Harman, T. C., D. L. Spears, and M. J. Manfra (1996), *J. Electron. Mater*. **25**, 1121.

Harman, T. C., D. L. Spears, D. R. Calawa, S. H. Groves, and M. P. Walsh (1997) in *Proceedings of the XVI International Conference on Thermoelectrics*, *Dresden*, A. Heinrich and J. Schumann (Eds.), IEEE, Piscataway, NJ, p. 4416.

Harman, T. C., D. L. Spears, and M. P. Walsh (1999), *J. Electron. Mater*. **28**, L1.

Harman, T. C., P. J. Taylor, M. P. Walsh, and B. E. Laforge (2002), *Science* **297**, 2229.

Hicks, L. D., and M. S. Dresselhaus (1993), *Phys. Rev. B* **47**, 12727.

Hohl, H., A. P. Ramirez, W. Käfer, K. Fess, Ch. Thurner, Ch. Kloc, and E. Bucher (1997), *Mater. Res. Soc. Symp. Proc*. **478**, 109.

Holloway, H. (1980), *Phys. Thin Films* **11**, 105.

Hordequin, C., J. P. Noziéres, and J. Pierre (1998), *J. Magn. Magn. Mater*. **183**, 225.

Ichikawa, N., O. Matsumoto, T. Hara, T. Kitahara, T. Yamauchi, T. Matsuda, T. Takeuchi, and U. Mizutani (1994), *Jpn. J. Appl. Phys*. **33**, 736.

Jacquot, A. (2003), Ph.D. Thesis, Ingénierie des matériaux et des minogénérateurs thermoélectriques planaires, INPL, Nancy, France.

Jacquot, A., B. Lenoir, M. O. Boffoué, and A. Dauscher (1999), *Appl. Phys. A* **S69**, 613.

Jacquot, A., M. O. Boffoué, B. Lenoir, and A. Dauscher (2000), *Appl. Surf. Sci*. **156**, 169.

Jacquot, A., B. Lenoir, A. Dauscher, J. Meusel, and M. Stölzer (2002a), *J. Appl. Phys*. **91**, 4733.

Jacquot, A., W. L. Liu, G. Chen, J.-P. Fleurial, A. Dauscher, and B. Lenoir (2002b), in *Proceedings of the XXI International Conference on Thermoelectrics*, *Long Beach*, IEEE, Piscataway, NJ, p. 561.

Jaegle, M., S. Drost, H. Böttner, S. Michel, N. Stein, S. Diliberto, and C. Boulanger (2002), in *Proceedings of the VII European Workshop on Thermoelectrics*, *Pamplona*.

Kakemoto, H., Y.Makita, A. Obara, Y. Tsai, S. Sakuragi, S. Ando, and T. Tsukamoto (1997), *Mater. Res. Soc. Symp. Proc*. **478**, 273.

Kantor, Z., T. Szörényi, Z. Toth, A. Simon, and L. Gombos (1999), *Appl. Surf. Sci*. **138/139**, 599.

Kantor, Z., A. Simon, and M. Kovacs (2003), *Appl. Surf. Sci*. **208/209**, 540.

Karla, I., J. Pierre, and R.V. Skolozdra (1998), *J. Alloys Comp*. **265**, 421.

Kim, I. H. (2000), *Mater. Lett*. **43**, 221.

Kishi, M., H. Nemoto, M. Yamamoto, S. Sudou, M. Mandai, and S. Yamamoto (1999), in *Proceedings of the XVIII International Conference on Thermoelectrics*, *Baltimore*, IEEE, Piscataway, NJ, p. 301.

Larson, P., S. D. Mahanti, S. Sportouch, and M. G. Kanatzidis (1999), *Phys. Rev. B* **59**, 15660.

Lee, S.-M., and D. G. Cahill (1997), *J. Appl. Phys*. **81**, 2590.

Lemée, N., M. Guilloux-Viry, J. Padiou, A. Perrin, M. Sergent, J. Lesueur, and F. Lalu (1997), *Solid State Commun*. **101**, 909.

Lemée, N., M. Guilloux-Viry, A. Perrin, M. Kugler, O. Fischer, Z. Z. Li, and H. Raffy (1999), *Thin Solid Films* **353**, 62.

Leong, D., M. Harry, K. J. Reeson, and K. P. Homewood (1997), *Nature* **387**, 686.

Liu, Z., M. Okoshi, and M. Hanabusa (1999), *J. Vac. Sci. Technol. A* **17**, 619.

Liu, Z., M. Watanabe, and M. Hanabusa (2001), *Thin Solid Films* **381**, 262.

Lutskii, V. N. (1970), *Phys. Status Solidi A* **1**, 199.

Mahan, G. D. (1998), *Solid State Phys*. **51**, 81.

Mahan, G. D. (2001), *Semiconductors and Semimetals* **71**, 157.

Makala, R. S., J. Jagannadham, B. C. Sales, and H. Wang (2002), *Mater. Res. Soc. Symp. Proc*. **691**, G8.4.1.

Makala, R. S., J. Jagannadham, and B. C. Sales (2003), *J. Appl. Phys*. **94**, 3907.

Mele, A., H. Liu, R. E. Russo, X. Mao, A. Giardini, and M. Satta (2002), *Appl. Surf. Sci*. **186**, 322.

Metev, S. (1994), in *Pulsed Laser Deposition of Thin Films*, D. B. Chrisey and G. K. Kubler (Eds.), Wiley-Interscience, New York, p. 255.

Metev, S., and M. S. Sendova (1988), *Proc. SPIE* **1033**, 260.

Michenaud, J.-P., and J.-P. Issi (1972), *J. Phys. C: Solid State Phys*. **5**, 3061.

Min, G., and D. M. Rowe (1999), *Solid-State Electron*. **43**, 923.

Müller J., V. Baier, U. Dillner, R. Güttich, and E. Kessler (2000), in *Proceedings of the MICRO.tec 2000*, Vol. 1, Hanover, VDE Verlag (Berlin), p. 465.

Neal, M. J., T. P. Orlando and J. M. Tarascon (1988), *Adv. Cryo. Eng.* **34**, 689.

Nolas, G. S., J. W. Sharp, and H. J. Goldsmid (2001a), *Thermoelectrics: Basic Principles and New Materials Developments*, Springer, Berlin.

Nolas, G. S., G. A. Slack, and S. B. Schujman (2001b), *Semiconductors and Semimetals* **69**, 255.

Nunes, R. W., I. I. Mazin, and D. J. Singh (1999), *Phys. Rev. B* **59**, 7969.

Nurnus J., H. Böttner, H. Beyer, and A. Lambrecht (1999), in *Proceedings of the XVIII International Conference on Thermoelectrics*, *Baltimore*, IEEE, Piscataway, NJ, p. 696.

Ogut, S., and K. M. Rabe (1995), *Phys. Rev. B* **51**, 10443.

Ohta, Y., H. Uchida, C. Roche, H. Tanahashi, A. Kasama, H. Scherrer, and S. Scherrer (2001), in *Proceedings of the XX International Conference on Thermoelectrics, ICT 2001*, *Beijing*, IEEE, Piscataway, NJ, p. 258.

Olk, C. H., O. P. Karpenko, S. M. Yalisove, and G. L. Doll (1994), *J. Mater. Res*. **76**, 2202.

Olk, C. H., S. M. Yalisove, and G. L. Doll (1995), *Phys. Rev. B*. **52**, 1692.

Poon, S. J. (2001), *Semiconductors and Semimetals* **70**, 37.

Potel, M., P. Gougeon, R. Chevrel, and M. Sergent (1984), *Rev. Chimie Min*. **21**, 509.

Powalla, M., and K. Herz (1993), *Appl. Surf. Sci*. **65/66**, 482.

Ristoiu, D., J. P. Noziéres, and L. Ranno (2000), *J. Magn. Magn. Mater.* **219**, 97.

Roche, C., R. Chevrel, A. Jenny, P. Pecheur, H. Scherrer, and S. Scherrer (1999), *Phys. Rev. B* **60**, 16442.

Rowe, D. M., and C. M. Bandhari (1983), *Modern Thermoelectrics*, Reston Publishing, Reston, VA.

Rumianowski, R. T., R. S. Dyagdala, W Jung, and W. Bala (2003), *J. Crystal Growth* **252** 230.

Sales, B. C., D. Mandrus, B. C. Chakoumakos, V. Keppens, and J. R. Thompson (1997), *Phys. Rev. B* **56**, 15081.

Sandomirskii V. B. (1967), *Sov. Phys. JEPT* **25**, 101.

Scherrer, H., and S. Scherrer (1995) in *CRC Handbook of Thermoelectrics*, D. M. Rowe (Ed.), Chemical Rubber, Boca Raton, FL, p. 211.

Sendova, M. S. (1987), *J. Mater. Sci. Lett*. **6**, 285.

Shafai, C., and M. J. Brett (1997), *J. Vac. Sci. Technol. A* **15**, 2798.

Shen, Q., L. Chen, T. Goto, T. Hirai, J. Yang, G. P. Meisner, and C. Uher (2001), *Appl. Phys. Lett*. **79**, 4165.

Shing, Y. H., Y. Chang, A. Mirshafii, L. Hayashi, S. S. Roberts, J. Y. Josefowicz, and N. Tran (1983), *J. Vac. Sci. Technol. A* **1**, 503.

Simon, A., Z. Kantor, I. Rajta, T. Szorenyi, and A. Z. Kiss (2001), *Nucl. Instrum. Meth. Phys. Res. B* **181**, 360.

Slack, G. A. (1995), in *CRC Handbook of Thermoelectrics*, D. M. Rowe (Ed.), Chemical Rubber, Boca Raton, FL, p. 407.

Song, D. W., W. L. Liu, T. Zeng, T. Borca-Tasciuc, and G. Chen (2000), *Appl. Phys. Lett*. **77**, 3854.

Sportouch, S., P. Larson, M. Bastea, P. Brazis, J. Ireland, C. R. Kannewurf, S. D. Mahanti, C. Uher, and M. G. Kanatzidis (1998), *Mater. Res. Soc. Symp. Proc*. **545**, 421.

Sprinholz, G., and G. Bauer (1995), *J. Appl. Phys*. **77**, 540.

Stark, I., and M. Stordeur (1999), in *Proceedings of the XVIII International Conference on Thermoelectrics*, *Baltimore*, IEEE, Piscataway, NJ, p. 465.

Stordeur, M., and I. Stark (1997), in *Proceedings of the XVI International Conference on Thermoelectrics*, *Dresden*, A. Heinrich and J. Schumann (Eds.), IEEE, Piscataway, NJ, p. 575.

Suzuki, A. (2001), in *Proceedings of the XX International Conference on Thermoelectrics*, *Beijing*, IEEE, Piscataway, NJ, p. 318.

Suzuki, A., H. A. Durand, and I. Kataoka (2000), in *Proceedings of the XIX International Conference on Thermoelectrics*, *Cardiff*, D. M. Rowe (Ed.), Babrow Press, Wales, UK, p. 263.

Szörényi, T., Z. Kantor, Z. Toth, and P. Heszler (1999), *Appl. Surf. Sci*. **138/139**, 275.

Tarascon, J. M., T. P. Orlando, and M. J. Neal (1988), *J. Electrochem. Soc*. **135**, 308.

Tedenac, J. C., S. Dal Coso, A. Haidoux, S. Charar, and B. Liautard (1999), *Mater. Res. Soc. Symp. Proc*. **545**, 93.

Teghil, R., L. d'Alessio, M. A. Simone, M. Zaccagnino, D. Ferro, and D. J. Sordelet (2000), *Appl. Surf. Sci*. **168**, 267.

Teghil, R., L. d'Alessio, A. Santagata, M. Zaccagnino, D. Ferro, and D. J. Sordelet (2003), *Appl. Surf. Sci*. **210**, 307.

Toth,, Z., B. Hopp, T. Smausz, Z. Kantor, F. Ignacz, T. Szorenyi, and Z. Bor (1999), *Appl. Surf. Sci*. **138/139**, 130.

Tritt, T. M., A. L. Pope, M. Chernikov, S. Feuerbacher, R. Legault, R. Gagnon, and J. Strom-Olsen (1998), *Mater. Res. Soc. Symp. Proc*. **553**, 489.

Tsubota, T., M. Ohtaki, and K. Eguchi (1999), *J. Ceram. Soc. Jpn*. **107**, 697.

Uher, C. (2001), *Semiconductors and Semimetals* **69**, 139.

Uher, C., J. Yang, S. Hu, D. T. Morelli, and G. P. Meisner (1999), *Phys. Rev. B* **59**, 8615.

Venkatasubramanian, R. (2001), *Semiconductors and Semimetals* **71**, 175.

Venkatasubramanian, R., T. Colpitts, E. Watko, M. Lamvik, and N. El-Masry (1997), *J. Crystal Growth* **170**, 817.

Venkatasubramanian, R., E. Sivola, T. Colpitts, and B. O'Quinn (2001), *Nature* **413**, 597.

Völklein, F., (2000), in *Proceedings of the XIX International Conference on Thermoelectrics*, *Cardiff*, D. M. Rowe (Ed.), Babrow Press, Wales, UK, p. 37.

Völklein, F., G. Min, and D. M. Rowe (1999), *Sensors and Actuators* **75**, 95.

Yamasaki, Y., R. Yamanaka, M. Mikami, H. Sonobe, Y. Mori, and T. Sasaki (1998), in *Proceedings of the XVII International Conference on Thermoelectrics*, *Nagoya*, IEEE, Piscataway, NJ, p. 210.

Yoshitake, T., T. Nagamoto, and K. Nagayama (2001), *Thin Solid Films* **381**, 236.

Yoshitake, T., G. Shiraishi, and K. Nagayama (2002), *Appl. Surf. Sci*. **197/198**, 379.

Yvon, K. (1979), in *Current Topics in Materials Science*, Vol. 3, E. Kaldis (Ed.), North Holland Publishing, Amsterdam, p. 53.

Zou, H., D. M. Rowe, and S. G. K. Williams (2002), *Thin Solid Films* **408**, 270.

CHAPTER 20

Piezoelectrics

FLORIANA CRACIUN

Instituto dei Sistemi Complessi, Consiglio Nazionale delle Richerche, Rome, Italy

MARIA DINESCU

National Institute for Lasers, Plasma and Radiation Physics, Bucharest, Romania

20.1 INTRODUCTION

Piezoelectrics are materials in which polarization can be produced by a mechanical stress. Alternatively, if an electric field is applied to a piezoelectric material, the material will change its shape. Piezoelectric materials are divided into polar (which possess a net dipole moment) and nonpolar crystals (whose dipolar moments summed over the different directions give a null total moment). Among the 20 non centrosymmetric piezoelectric classes, 10 have a spontaneous polarization [Nye, 1979; Setter, 2002]. Polar materials can be further classified into ferroelectrics and nonferroelectrics. The primary feature distinguishing ferroelectrics from other polar materials is that the spontaneous polarization can be reversed with an applied electric field. When the polarization is measured as a function of an applied electric field, a hysteresis loop is obtained [Lines and Glass, 1977; Xu, 1991; Wadhawan, 2000; Strukov and Levanyuk, 1998]. Ferroelectric thin films show strong piezoelectric properties and are consequently most used in applications like microelectromechanical systems (MEMS), acoustic wave transducers, sensors, resonators, and the like [Damjanovic, 1998]. Among nonferroelectric piezoelectric thin films, the most studied are ZnO and AlN.

In piezoelectric materials the thermal, elastic, and electrical parameters are coupled through different relationships that can be deduced from thermodynamics [Nye, 1979; Setter, 2002; Lines and Glass, 1977]. This is based on the series development of thermodynamic potential, for example, in the stress tensor X and electric field E up to the quadratic term. From this expression the strain $\boldsymbol{x}$ and dielectric induction D can be obtained as the derivatives of the thermodynamic potential:

$$D_l = d_{l\mu}X_\mu + \varepsilon^X_{lm}E_m \tag{20.1}$$

$$x_\lambda = s^E_{\lambda\mu}X_\mu + d_{m\lambda}E_m \tag{20.2}$$

where d is the piezoelectric tensor that describes the direct piezoelectric effect [in Eq. (20.1)] and the converse effect [in Eq. (20.2)] (summation over the subscript μ and λ extends from 1 to 6, and over the subscript m and l from 1 to 3); s^E is the elastic compliance tensor at constant electric field and ε^X

Pulsed Laser Deposition of Thin Films: Applications-Led Growth of Functional Materials
Edited by Robert Eason

the dielectric permittivity tensor at constant stress. The efficiency of energy conversion between electric and elastic forms is characterized by the electromechanical coupling factor $k_{m\lambda}$, which is given by the relationship

$$k_{m\lambda}^2 = \frac{d_{m\lambda}^2}{\varepsilon_{mm}^T s_{\lambda\lambda}^E} \tag{20.3}$$

The present review also includes relaxor thin films, although they do not show a piezoelectric effect. However, in the presence of an external bias, an effective piezoelectric response is obtained. For example, for a [001]-orientation, $d_{33}^{\text{eff}} = 2Q_{333}\varepsilon_{33}P_3$, where P_3 is the induced polarization parallel to the [001]-axis, and Q_{333} is a component of the electrostrictive tensor defined through the relationship $x_\lambda = Q_{\lambda kl}P_kP_l$ [Xu, 1991].

The physical properties of piezoelectric thin films depend on many parameters, including composition, crystalline structure, orientation, film thickness and microstructure, internal stress, presence of secondary phases, dopants, interface layers, misfit strain, and so forth [Craciun et al., 2002]. In addition, the piezoelectric response in ferroelectric thin films is affected by the displacement of domain walls [Damjanovic, 1998].

Recent progress in the growth and understanding of piezoelectric thin films has improved dramatically due to the development of new tools for compositional, structural, morphological, and electrical characterization. These include techniques such as scanning force microscopy (SFM) and piezoresponse force microscopy (PFM) in investigating nanoscale piezoelectric and ferroelectric behavior [Gruverman et al., 2001; Christman et al., 2000; Roelofs et al., 2003; Colla and Stolichnikov, 2003].

Deposition of piezoelectric thin films has been achieved by many different methods (for a recent review article see Craciun et al. [2002]). Pulsed laser deposition (PLD) is a versatile technique for the growth of complex multicomponent materials in thin-film form with oriented or epitaxial structure. In the following section the most important aspects of the PLD deposition of piezoelectric thin films will be discussed. The structural, dielectric, and piezoelectric properties of the most important piezoelectric materials in thin-film form will be reviewed. Finally their applications will be presented, with some examples.

20.2 OPTIMIZATION OF THE DEPOSITION CONDITIONS

The growth of piezoelectric thin films by PLD involves the identification of the optimum set of growth parameters for obtaining the right stoichiometry, good crystalline structure, and electrical properties on an appropriate surface for further applications. Many piezoelectric and ferroelectric materials contain a volatile component (e.g., Pb, Li, Bi, or K), and small deviations from the correct stoichiometry can lead to films with undesirable phases. For this reason, an accurate control over the process is required to avoid loss of such volatile components and formation of metastable phases (e.g., pyrochlore), which are detrimental for the dielectric and piezoelectric properties. Synergy of gas pressure, substrate temperature, and laser fluence results in a broad range of conditions that allows the growth of high-quality piezoelectric thin films. Several of the most important and often studied materials grown by PLD will be discussed from the point of view of composition, crystallinity, morphology, and electrical properties.

20.2.1 Piezoelectric Thin Films with Ferroelectric Properties

Ferroelectric thin films have been intensively studied due to their large piezoelectric response [Damjanovic, 1998; Yoon and Song, 2002]. Ferroelectrics undergo a structural phase transition from a high-temperature paraelectric phase into a low-temperature ferroelectric phase at the Curie temperature T_C [Lines and Glass, 1977; Strukov and Levanyuk, 1998]. Most materials with good

ferroelectric and piezoelectric properties have complex compositions based on solid solutions that allow tailoring of optimum properties by varying the composition. On the other hand the properties of these materials are often controlled by contributions from domain-wall movement, which enhance their piezoelectric properties and are responsible for their frequency and field dependence [Strukov and Levanyuk, 1998; Damjanovic, 1998]. The correct understanding of these phenomena and their theoretical treatment is of considerable complexity. Moreover finite-size effects associated with nanometer-size grains and/or thickness interact with ferroelectric and piezoelectric properties.

Polycrystalline randomly oriented ferroelectric thin films need to be poled in order to be piezoelectric. In ferroelectric thin films, domain-wall contributions are very important because they respond to the applied field and contribute to the polarization and to the piezoelectric response. Only non-180° wall movements can change sample dimensions and thus contribute to piezoelectric response. Displacement of domain walls contributes to the dielectric and mechanical loss especially near a phase transition. The movement of domain walls can be inhibited by pinning defects [Strukov and Levanyuk, 1998; Damjanovic, 1998]. The mobility of these defects influences the time variation of dielectric and piezoelectric properties, a phenomenon called aging.

Other factors that influence the piezoelectric response of ferroelectric thin films include mechanical clamping to the substrate, the orientation of the film, the level of polarization, the presence of interfacial layers, depolarization fields, internal stresses, and so forth. Domain-wall contributions can be also different in thin films due to variations in the configuration and number of pinning centers.

An extensive review of results obtained in PLD deposition of ferroelectric thin films including applications up to 1994 can be found in the first edition of this book [Chrisey and Hubler, 1994]. Table 20.1 summarizes the dielectric, ferroelectric, and piezoelectric properties of PLD-deposited piezoelectric thin films reported in the literature over the past 10 years.

20.2.1.1 Lead Titanate Zirconate

Among ferroelectric thin films the most studied is lead zirconate titanate $Pb(Zr_xTi_{1-x})O_3$ (PZT), due to its large piezoelectric coefficients. PZT has a perovskite cubic structure in its paraelectric phase that deforms to a rhombohedral or tetragonal structure, below the Curie temperature. The ferroelectric and piezoelectric properties of PZT ceramics are sensitive to both crystallographic structure and compositional ratio Zr/Ti. These properties are at a maximum near a value of the Zr/Ti ratio of about 53/47, which roughly separates the rhombohedral (Zr-rich) and tetragonal (Ti-rich) symmetry in the PZT phase diagram. It has been found that the appearance of a monoclinic phase in a very narrow range of composition around this value is responsible for the increase of piezoelectric and dielectric properties [Noheda et al., 1999, 2000].

PZT thin films have been mostly studied for nonvolatile ferroelectric memory applications (NVRAM) [Scott, 1998] due to their large remanent polarization and low coercive field. The large piezoelectric constants and electromechanical coupling factors make these materials very useful for applications in the field of MEMS and other piezoelectric microdevices [Muralt et al., 2002].

Many physical and chemical methods have been used to grow PZT thin films (for a recent review and comparison between different methods see Craciun et al. [2002]). PLD has been demonstrated as a technique that can be used to obtain high-quality crystalline, oriented, and epitaxial thin films. The main difficulty in obtaining stoichiometric films results from the low Pb vapor pressure, which makes it difficult to control its incorporation in the film.

For thin-film samples, it is not obvious that this ideal Zr/Ti ratio of 53/47 must also occur. An exhaustive study of this problem can be found in Tanaka et al. [1996] in which the authors discuss the film formation diagram for $Pb(Zr_xTi_{1-x})O_3$ films for different Zr content and deposition conditions. It has been found that PZT 70/30 films have the largest value of dielectric constant.

In PLD of multicomponent oxides, excimer lasers (KrF at 248 nm, ArF at 193 nm, XeCl at 308 nm) are typically used but also the Nd : YAG fundamental at 1064 nm and its harmonics (532, 355, and 266 nm). Typical fluence ranges vary over values of 2–10 J/cm^2, repetition rates

TABLE 20.1 Dielectric, Piezoelectric, and Ferroelectric Properties of PLD-Deposited Piezoelectric Thin Films

Composition	Substrate	Dielectric Constant (at 1 kHz, RT)	tan δ (at 1 kHz, RT)	P_r ($\mu C/cm^2$)	E_c (kV/cm)	d_{33} (pm/V)	Other Constants	References
PZT 20/80	LSCO/LAO			40	90			Nagarajan et al., 1999a
PZT 20/80	LSCO/STO/Si					$\sim 50^a \sim 80^b$		Nagarajan et al., 2002
PZT 20/80	LSCO/Si					50^a 400^b		Ma et al., 2005
PZT 50/50	LSCO/STO/Si					$\sim 200^a \sim 300^b$		Nagarajan et al., 2002
PZT 52/48	YBCO/STO/MgO/ TiN/Si		0.08–0.1	24	47			Sharma et al., 2000
PZT 52/48	LSMO/YBCO/YSZ/Si	1678	0.04–0.05	53	60			Goh et al., 2005
PZT 52/48	PLT/Pt/Ti/SiO_2/Si			33.4				Lee et al., 2005
PZT 52/48	BLT/SRO/STO(011)			28.1	33.7			Bao et al., 2005
PZT 53/47	Au/Pt/Si	500	0.02	15	100	40		Craciun et al., 2000
PZT 53/47	PT/diamond	500–650 (at 100 kHz)				50–350	Acoustic damping rate 0.006 ns^{-1} ($f_{SAW} < 500$ MHz)	Du et al., 1999
PZT 65/35	YBCO/MgO	210–630	0.02–0.06	7–15	35–50	20–50		Sternberg et al., 1997
PZT 65/35	LSCO/MgO	210–380	0.03	9–17	45	24		Sternberg et al., 1997
(PZT 52/48-PMWSN) 96/4	Pt/Ti/SiO_2/Si			34			$K_p = 0.56$ $Q_m = 2344$	Kim et al., 2003
$Pb_{0.99}Nb_{0.02}$ ($Zr_{0.57}$ $Sn_{0.38}$ $Ti_{0.05})_{0.98}O_3$	Pt/Si	540 (at 100 kHz)	0.001 (100 kHz)					Bharadwaja et al., 2000
PLZT 5/70/30	Pt/Si	1346 (at 10 kHz)	0.07					Yeh et al., 1995a
PLZT 5/70/30	SRO/STO/Si	490 (100 kHz)						Yeh et al., 1995b
PLZT 4.5/65/35	LSCO/MgO	325–450	0.025–0.035	5.5	35	24		Sternberg et al., 1997 Tyunina et al., 1998b
PLZT 6/65/35	YBCO/MgO	210	0.09	7	50			Sternberg et al., 1997 Tyunina et al., 1998b
PLZT 6/65/35	LSCO/MgO	250–350	0.025–0.035	3.5	50	40–60		Sternberg et al., 1997 Tyunina et al., 1998b

PLZT 8/65/35	LSCO/MgO	230–350	0.03	1.5	30	40–48		Sternberg et al., 1997 Tyunina et al., 1998b
PLZT 9/65/35	Pt/Si	200–400	0.02–0.05					Craciun et al., 2004 Scarisoreanu et al., 2004
PLZT 9.75/65/35	YBCO/MgO	350–500	0.02–0.05	5–7	30–50	10–18		Sternberg et al., 1997 Tyunina et al., 1998b
PLZT 9.75/65/35	LSCO/MgO	350–700	0.035	3	60	20		Sternberg et al., 1997 Tyunina et al., 1998b
PT	Pt/MgO					80		Kim et al., 2004b
PLT 28 mol % La	Pt/Ti/SiO_2/Si	1395						Han et al., 2003
PLT 14 mol % La	Pt/Ti/SiO_2/Si			10	35			Dong et al., 2003
$PbZrO_3$	Si			23	100			Chattopadhyay et al., 1998
PMN	YBCO/MgO	1000					Strain 0.2% at 600 kV/cm	Catalan et al., 1999
PMN	PZT/Pt/Si	300	0.02			60–80		Verardi et al., 2000
PMN	Au/Pt/NiCr/sapphire	880				40–60		Scarisoreanu et al., 2004
PMN (100 nm)	LSCO/CeO_2/YSZ	800	0.1					Wakiya et al., 2001
PMN	LSCO/MgO	1300	0.02			40	$Q_{33}(10^{-2}\,C^{-2}\,cm^4)$ 2.9 ± 0.2 strain 0.1%	Donnelly et al., 2003
PMN	LSCO/MgO	~ 2400	~ 0.05			~ 35		Shvartsman et al., 2005
PMN-PT 93/7	LSCO/MgO	1500	0.025			90	$Q_{33}(10^{-2}\,C^{-2}\,cm^4)$ 6.6 ± 0.3 strain 0.12%	Donnelly et al., 2003
PMN-PT 90/10	LSCO/MgO	2200	0.04	10	20		Q_{33} $(10^{-2}\,C^{-2}\,cm^4)$ 2.2 ± 0.1 strain 0.3%	Donnelly et al., 2003
PMN-PT 90/10	BST	1200						Nakamura et al., 1996
PMN-PT 90/10 (100–400 nm)	LSCO/LAO	300–1800				10–85		Nagarajan et al., 1999b

(*Continued*)

TABLE 20.1 (*Continued*)

Composition	Substrate	Dielectric Constant (at 1 kHz, RT)	tan δ (at 1 kHz, RT)	P_r ($\mu C/cm^2$)	E_c (kV/cm)	d_{33} (pm/V)	Other Constants	References
PMN-PT 90/10 (100 nm)	LSCO/LSAT	1500				40		Nagarajan et al., 2000
PMN-PT 90/10 (100 nm)	LSCO/STO	1600				50		Nagarajan et al., 2000
PMN-PT 90/10 (100 nm)	LSCO/MgO	2000				60		Nagarajan et al., 2000
PMN-PT 80/20	LSCO/MgO	1500	0.03			90	Q_{33} (10^{-2} C^{-2} cm^4) 9.0 ± 0.1 strain 0.2%	Donnelly et al., 2003
PMN-PT 70/30	LSCO/MgO	650	0.1	20	40	160	Q_{33} (10^{-2} C^{-2} cm^4) 1.4 ± 0.1 strain 0.2%	Donnelly et al., 2003
PMN-PT 70/30	SRO/LAO	1500		13–20				Maria et al., 1998
PMN-PT 68/32	LSCO/MgO	1300	0.05	20	28–32	25		Tyunina et al., 1999
PMN-PT 65/35	LSCO/MgO	2000	0.05					Tantigate et al., 1995
PMN-PT 65/35	MgO	1160	0.05					Wang et al., 2004
(1-*x*) PMN-*x*PT[c]	LSCO/Pt/Si	$\sim$4700	$\sim$0.03					Ranjith et al., 2005
PSN-PT 58/42	LSCO/MgO	1600	0.05	20	28–32			Tyunina et al., 1999
PybN-PT	SRO/LAO SRO/STO	1300		70				Bornard and Trolier-McKinstry, 2000
NKN $Na_{0.5}K_{0.5}NbO_3$	PtIr	550	0.02	12				Cho and Grishin, 2000
BLT $(Bi_{3.25}La_{0.75})$ Ti_3O_{12}	$IrO_2/TiO_2/SiO_{2/Si}$			21[d]		12.8		Adachi et al., 2005
BLT	LAO	358 along (100)						Lee et al., 2004a

BLT	$Pt/Ti/SiO_2/Si$			19.6[d]	188[e]			Zhang et al., 2004
BTZ ($Bi_4Ti_{2.8}Zr_{0.2}O_{12}$)	$Pt/Ti/SiO_2/Si$			25.3[d]	139.8[e]			Zhang et al., 2004
BLTZ ($Bi_{3.25}La_{0.75}Ti_{2.8}Zr_{0.2}O_{12}$)	$Pt/Ti/SiO_2/Si$			24.1[d]	109.1[e]			Zhang et al., 2004
BNT ($Bi_{3.25}Nd_{0.75}$) Ti_3O_{12}				22[d]		16.9		Adachi et al., 2005
BST ($Bi_{3.25}Sm_{0.75}$) Ti_3O_{12}				28[d]		16.6		Adachi et al., 2005
(1-x)NBT-xBT, $x = 0.09$	LAO	327						Cheng et al., 2004
(1-x)NBT-xBT, $x = 0.06$	LAO	187						Cheng et al., 2004
(1-x)NBT-xBT, $x = 0.06$	MgO	1330						Dinescu et al., 2005
$BaTiO_3$	$Pt/TiO_2/Si$	160–210	0.03	9[d]	80[e]			Canulescu et al., 2004
$BaTiO_3$	$Pt/Ta/SiO_2/Si$	570				14.3		Kim et al., 2005
$BaTiO_3$	$LSCO/Pt/Ta/SiO_2/Si$	1000				54		Kim et al., 2005
$Ba(Zr_{0.15}Ti_{0.85})O_3$	$Pt/Ti/SiO_2/Si$			3.3	93.5			James and Prakash, 2004
$SrBi_2Nb_2O_9$	Pt/sapphire	132	<0.02	6	140			Duclère et al., 2003
ZnO	Si, sapphire					8		Dinescu and Verardi, 1996 Verardi and Dinescu, 1995
AlN	α-Al_2O_3, Si and 6H-SiC						$\rho = 6$ $10^{13}\ \Omega$ cm, BF 5×10^6 V/cm	Vispute et al., 1997
AlN	Sapphire						SAW velocity 5980 m/s	Meinschien et al., 1999

[a]Measured on continuous films.
[b]Measured on patterned submicron islands.
[c]Multilayers with compositional variation on each layer $x = 0.3, 0.2, 0.1, 0$.
[d]$2P_r$
[e]$2E_c$

between 3 to 10 Hz, and pulse duration between 5 and 30 ns. In most cases oxygen was used as the reactive gas, at pressures below 0.9 mbar. More reactive oxidizers such as N_2O [Auciello et al., 1993] and mixtures containing O_2 and ozone, are sometimes used [Tanaka et al., 1996]. The controlled cooling (5–10°C/min) is performed in oxygen, at a pressure close to 1000 mbar. In some experiments a postdeposition annealing was used to improve the film crystallinity and orientation [Auciello et al., 1993].

The piezoelectric properties of the films are strongly influenced by the structure and reactivity of the electrode. Interfacial layers can sometimes dominate the electrical properties of a piezoelectric capacitor. Different substrate–bottom electrode–buffer layer configurations have been used for improving the interface properties (decreasing of the oxygen vacancies, of elemental interdiffusion, intermediate undesirable compound formation, etc.). Silicon, diamond, $LaAlO_3$ (LAO), MgO, $SrTiO_3$ (STO), GaAs, and glass have all been used as substrates. The most frequently used bottom electrode was Pt (with Ti as an intermediate layer) but also Au or Ni-based alloy [Craciun et al., 2002]. It was found that perovskite conductive oxides act as diffusion barrier layers and allow the absorption of oxygen vacancies thus diminishing the fatigue that appears after long bipolar switching when a Pt electrode is used [Aggarwal et al., 1999; Yan et al., 2003]. Thus the most often used oxide electrodes are $La_{0.5}Sr_{0.5}CoO_3$ (LSCO) (5% lattice mismatch with PZT) and $SrRuO_3$ (SRO) (2.7% mismatch) [Cho and Park, 1999; Bao et al., 2005; So et al., 2005]. $LaAlO_3$ has also been used as a substrate to deposit LSCO/PZT(53/47)/$LaCoO_3$, PZT(53/47)/SRO [Cho and Park, 1999], PZT(20/80)/LSCO [Nagarajan et al. 1999a], and $La_{0.7}Sr_{0.3}MnO_3$ (LSMO)/PZT/LSMO epitaxial heterostructures [Wu et al., 2000].

The selection of suitable buffer and electrode layers is a crucial factor to obtain epitaxial growth on Si. An epitaxial PZT/YBCO/STO/MgO/TiN/Si(100) heterostructure has been obtained by optimizing the growth conditions for each layer [Sharma et al., 2000]. Although the lattice constants are very different, the growth of TiN on Si(100) occurred via domain-matching epitaxy where the four lattice constants of TiN match with three of Si.

A pseudoepitaxial growth of PZT on Si has been achieved by using the heterostructure LSMO/YBCO/YSZ [Goh et al., 2005]. A KrF excimer laser was used to deposit $Pb(Zr_{0.52}Ti_{0.48})O_3$ at a substrate temperature of 350°C. The sample was then annealed at 700°C for 60 min in 1 atm oxygen atmosphere. Only preferentially oriented (001) PZT was observed. The in-plane and out-of-plane orientations of PZT film are similar to an epitaxial film with a cube-on-cube crystal growth orientation with respect to Si substrate. However, the XRD Φ scan peaks of the PZT were broad, indicating that the epitaxial quality was not perfect.

All-epitaxial $(Bi,La)_4Ti_3O_{12}$(BLT)/$Pb(Zr_{0.4}Ti_{0.6})O_3$/BLT trilayered thin films have been successfully grown on SRO-covered STO(011) substrates by PLD using a KrF excimer laser [Bao et al., 2005]. The temperature and oxygen pressure for the growth of BLT layers were kept at 750°C and 0.4 mbar, respectively, whereas the PZT layer was deposited in 0.2 mbar oxygen pressure at a substrate temperature of 600°C. The BLT layer is essential for obtaining fatigue-free ferroelectric heterostructures, and these have been obtained also with $(Ba,Sr)TiO_3$ (BST) layers between PZT and Pt electrode [Yan et al., 2003]. Epitaxial PZT films (with Zr/Ti ratio = 40/60) have been obtained also on MgO (001) substrates [Lee et al., 2002a].

Another substrate successfully used is diamond due to the high piezoelectric coefficients of PZT combined with the very high propagation velocity of acoustic waves in diamond, which makes the combination very attractive for surface acoustic wave (SAW) device applications [Du et al., 1999]. The growth of pure perovskite PZT on diamond is promoted via the use of a $PbTiO_3$ (PT) buffer layer, at a substrate temperature in the range of 550–650°C, oxygen pressure of 100–200 mTorr and laser fluence of 1–2 J/cm^2. A cross-sectional scanning electron microscopy (SEM) image showing a remarkably dense columnar structure is shown in Figure 20.1.

Growth of PZT can be controlled also by the substrate morphology, and control of domain structure of epitaxial $PbZr_{0.2}Ti_{0.8}O_3$ thin films could be achieved by using vicinally cut (100) STO substrates, as reported in Nagarajan et al. [2001]. An STO substrate with 3°-vicinal cut toward (010) has been chemically etched to achieve a configuration of terraces of width 200 nm and step height

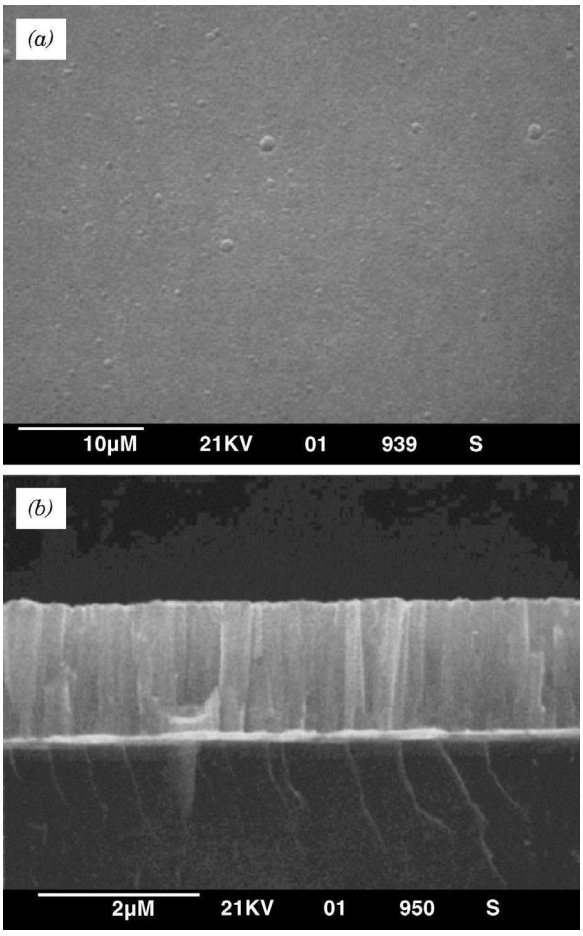

Figure 20.1 SEM images of the surface (top image) and the cross section of a PZT film with a PT buffer layer, deposited on diamond. Reprinted with permission from Du et al. [1999], © 1999, American Institute of Physics.

7–10 nm. It has been observed that there is a preferential location of the nucleation of the *a* domains along the step edges of the underlying substrate. By piezoresponse microscopy, it has been shown that all *a* domains have their polarization aligned along the same direction.

The substrate temperature strongly influences the film composition and crystalline orientation: Its influence should be discussed together with oxygen deposition pressure effects and the laser fluence. Both the lead content and the Zr/Ti ratio in the film depend on these parameters. For example, it was demonstrated that films deposited at a substrate temperature higher than 400°C and an oxygen pressure lower that 0.1 mbar are lead deficient [Horwitz et al., 1991]. For a substrate temperature during deposition of 550°C, the increase of oxygen pressure to 0.2–0.3 mbar results in an increasing of the Pb content in the film to a value of 0.42 (from the optimum value of 0.5). If argon is used instead of oxygen, a low-Pb content is obtained in the film. Low fluence prolonged ablation also produces films with low-Pb content because of the evaporation of lead [Tanaka et al., 1996; Catalan et al., 1999]. PZT thin films have also been grown on Si substrates at a remarkably low substrate temperature (375–400°C) by PLD [Craciun et al., 1998, 1999, 2000; Verardi et al., 1998, 1999]. These films have been deposited on different types of electrodes (Pt, Au/Pt, TiN, etc.) at an oxygen pressure of 0.2 mbar and high laser fluence (about 25 J/cm^2).

Films deposited at room temperature were found to be predominantly amorphous [Watts et al., 1991]. After postdeposition annealing at 450°C films become polycrystalline with both tetragonal and rhombohedral phases; only the tetragonal phase (together with other phases of some unidentified compounds) is observed after annealing at temperatures up to 650°C. The disappearance of the rhombohedral phase is attributed to the Zr depletion by reaction with the glass substrate.

(00l)-Epitaxial PZT films were grown on $SrTiO_3$ and MgO single crystals by PLD [Horwitz et al., 1991; Tyrrell et al., 1996] at the same temperature and oxygen pressure ($T = 550–560$°C and $p(O_2) = 0.25$ mbar) but with different laser wavelengths and fluences. Films with polycrystalline structure, which contain 70–90 % of the perovskite phase, were grown at 600°C on Pt-coated GaAs and Si substrates [Horwitz et al., 1991]. In Tyunina et al. [1998a] it was found that Pb/Ti, Zr/Ti and Zr/Pb ratios are independent of the laser fluence, while the lead content increases with the deposition pressure.

A change in the Pb distribution has been observed for PZT films deposited at room temperature in vacuum, and a dip in the lead distribution, at the target surface normal position, has been observed [Ma et al., 1996]. This dip can be explained by the sputtering effects caused by the high laser fluence, which generates gas phase species with high kinetic energy. When the deposition pressure is increased, the kinetic energy of particles decreases due to collisions within the plume.

A complex PLD method has been reported in Auciello et al. [1993] in which a multitarget system containing the three basic oxides ZrO_2, TiO_2, and PbO is used. Two excimer lasers were used, one for ablation and the other with the beam parallel with the substrate surface, for producing atomic oxygen by dissociation of the background gas (N_2O or O_2). After an annealing process (at 600°C, in an oxygen atmosphere, for 60 min) a (110)-oriented PZT layer is obtained.

Compositionally graded PZT films have been deposited by laser ablation of two PZT half targets with 75/25 and 55/45 stoichiometry, which were placed adjacent to one another with the interface at a 45° angle to the vertical [Brazier et al., 1998, 1999]. The laser beam was horizontally scanned across the target while its vertical position was increased after each scan. In this way, starting from the part with 75/25 stoichiometry, the thickness of the 55/45 layer increases, while the 75/25 layer decreases. The films were highly (111) oriented, with a large polarization offset of 425 $\mu C/cm^2$; this is due to a very smooth composition gradient and is a function of the spontaneous polarization of the material.

There are many reports in the literature on in situ investigations of the plasma plume during the PLD process [Iembo et al., 1993]. Techniques such as fluorescence spectroscopy of the atomic species and their oxides and mass spectroscopy of ionic species show an increase of the quantity of oxide species (TiO, PbO, and ZrO) contained in the plume in the deposition zone. For a set of deposition conditions [XeCl (308 nm), 3.3 J/cm^2, 3 Hz, O_2 pressure of 0.2 mbar] it was found that at 10 mm from the target the relative concentration of the ionic oxides increases while clusters represent 75% of the total ionized species near the target and decrease at intermediate distances. In this way it was established that the right distance where the substrate should be placed corresponds to the place where the oxides and cluster concentration increase.

20.2.1.2 Lead Titanate and La-Doped Lead Titanate

Lead titanate, $PbTiO_3$, (PT), is ferroelectric up to a high transition temperature (about 500°C) where its structure changes from tetragonal to the paraelectric cubic phase. The dielectric and piezoelectric properties are lower than those of PZT materials, but they are stable up to much higher temperatures.

Epitaxial PT thin films have been deposited on MgO(001) [Lee and Baik, 2000] and on Pt(001)/MgO(001) by PLD by using a KrF excimer laser at a laser fluence of 1.2 J/cm^2, substrate temperature of 650°C and an oxygen pressure of 50 mTorr [Kim et al., 2004a]. It has been found that the compressive misfit strain at the growth temperature critically influenced the domain structure of the films obtained.

La-doped lead titanate $Pb_{1-3x/2}La_xTiO_3$ (PLT) shows interesting ferroelectric, piezoelectric, and electrooptic properties. Its properties can be tailored for different applications by changing the La

content: for $x > 0.27$ it is a paraelectric relaxor while for $x < 0.27$ it is ferroelectric with a tetragonal structure.

The ferroelectric behavior of PLT thin films for different La content has been investigated by Dong et al. [2003]. Doping of La in PT drastically changes the microstructure of films from round particles with diameters ranging from 30 to 100 nm to a coral-like structure that may correspond to the preferred (100) orientation observed by X-ray diffraction (XRD). To compensate the Pb loss during the deposition process, 10% PbO was added to the initial target composition. An optimum amount of La (14 mol %) was found to suppress oxygen vacancy generation and diffusion and result in good ferroelectric properties, with a lower coercive field than pure PT films.

Properties of PLT are strongly dependent on grain size in the deposited film. Significant changes in the electrical properties of thin films deposited on Pt(111)/Ti/SiO_2/Si(100) substrates have been found in a set of films with different grain sizes ranging from 110 to 350 nm, as reported in Han et al. [2003].

The integration of PLT on semiconductor substrates requires the use of buffer layers. PLT deposition on $SrTiO_3$/InP and several other buffer layers was reported by Vasco et al. [1999, 2003]. The successful integration of PLT on InP could be used to obtain acoustic and optoelectronic interaction in the same microdevice. (001) and (100) textured $Pb_{0.775}La_{0.15}TiO_3$ films with a uniform composition close to that of the target and a roughness of 2% were obtained.

20.2.1.3 Lithium Niobate

Lithium niobate, $LiNbO_3$, (LNO) has been extensively investigated due to its high piezoelectric and electrooptical constants. LNO is used in many devices such as low-loss wide-band pass filters and high-efficiency acoustooptic integrated devices. LNO is uniaxial at all temperatures, with a structural phase transition from paraelectric to ferroelectric at 1200°C. Its low symmetry structure consists of a sequence of distorted oxygen octahedra joined by their faces along a trigonal polar axis. Many studies have been dedicated to LNO thin-film deposition and the integration on Si, for applications as integrated SAW devices, integrated electrooptical devices, and the like. For these applications LNO films must be epitaxial, single phase, with very smooth surfaces and free of domains and twinning. The main parameters to be controlled for deposition of single-phase, stoichiometric $LiNbO_3$ layers are the Li/Nb ratio in the target, substrate temperature during the film deposition, and type and gas pressure inside the deposition chamber.

The preparation of textured LNO thin films by off-axis laser deposition was reported by Kaemmer et al. [1996]. The films have been deposited on (0102) sapphire, (0001) sapphire, and (100) $LaAlO_3$ single-crystalline substrates. The presence of a secondary $LiNb_3O_8$ phase was also sometimes observed but could be eliminated by changing the deposition parameters.

The epitaxial growth of $LiNbO_3$ thin films on sapphire substrates and the evaluation of the surface acoustic wave properties of these films have been described in Shibata et al. [1995, 1996]. LNO thin films have also been grown on fused silica substrates [Wu et al., 1998], where it was observed that the application of an electric field during the deposition helped to achieve a complete (001) orientation.

The structural evolution of epitaxial LNO thin films deposited on sapphire substrates during growth has been studied by Veignant et al. [1999] by investigating the structure of the deposited films at different stages of growth by transmission electron microscopy (TEM). The large lattice mismatch (8.6% at the temperature of deposition and 7.7% at room temperature) between Al_2O_3 ($a = 4.79$ Å) and LNO ($a = 5.22$ Å) induces considerable stress in the LNO films and misfit dislocations to accommodate it. The elastic deformation is fully relaxed in 220-nm-thick films where cracks and twinning appear.

The background gas composition and pressure influence film stoichiometry. An argon–oxygen ratio of 400 mTorr Ar/100 mTorr O_2 was identified to be the optimum to obtain the correct stoichiometry, while for a smaller Ar concentration traces of $LiNb_3O_8$ are present in the film. By increasing the Ar beyond 450 mTorr a mixture of different phases appears [Ogale et al., 1992]. The deposition process is very sensitive to the deposition pressure, which influences both the Li content

in the film and the valence state of the Nb ions. An increase of oxygen pressure from 10^{-3} Torr to 5×10^{-2} Torr produces a decrease in the Li content in the film due to collisions between the Li atoms and the oxygen species, which results in the decrease in the number of Li atoms arriving at the substrate surface [Shibata et al., 1992]. For a decrease in the pressure below 10^{-3} mTorr a dramatic change in film color is noticed, which is due to the presence of oxygen vacancies and mixed valence states of the Nb ions. The effects can be adjusted by a postdeposition annealing at 700°C or by deposition in a more oxidizing atmosphere containing 8% O_3 [Shibata et al., 1992, 1995]. The Li content can be also controlled by tuning the Li/Nb ratio in the target, between 1 and 3. Stoichiometric, single-phase $LiNbO_3$ films have been deposited for a Li/Nb ratio of 2, at 500°C and 10^{-2} Torr O_2 pressure [Shibata et al., 1992, 1995] and at 825°C [Fork and Anderson, 1993] and at 20°C and 6×10^{-2} mbar O_2 pressure [Afonso et al., 1995]. In Fork and Anderson, [1993] the substrate was GaAs or MgO-coated GaAs, a structure appropriate for monolithic electrooptic applications.

Epitaxial films were grown at low temperatures on (0001) sapphire substrates by ablation of a single-crystal $LiNbO_3$ target [Lee et al., 1995]. The laser fluence was varied within the range of 1.4–10 J/cm^2. The critical parameter was found to be substrate temperature and not gas pressure. At 350°C the films were not crystallized, and at 500 and 550°C the Li-deficient phase $LiNb_3O_8$ was observed in XRD spectra. Films deposited at 400 and 450°C are strongly oriented irrespective of O_2 pressure and epitaxial at 50 mTorr oxygen. All films were annealed in 10–400 Torr O_2 at 400°C for 30 min. Strongly textured (012) and (024) $LiNbO_3$ films have been deposited at high oxygen pressure (1 Torr) on high-temperature (720°C) sapphire substrates. The refractive index value was found to be less sensitive to gas pressure and a temperature window for which a standard value of $n = 2.238$ was identified [Marsh et al., 1993].

Deposition of high-quality textured LNO thin films on Si substrates by PLD was reported by Ghica et al. [1999]. This result is important for the use of LNO thin films on devices integrated with Si. By adjusting the deposition parameters, the presence of undesired Li-deficient phases was avoided. The measurement of the refractive indices demonstrates good agreement with the corresponding single-crystal bulk values over the entire visible spectral range.

The investigation of the ablation process established a cause of low Li content in films deposited by PLD [Chaos et al., 2000]. Studies by vapor-phase optical absorption measurements on a plasma produced from a LNO target at a low laser fluence (0.06 J/cm^2) in vacuum showed the delayed release of Li atoms, 2–20 μs after the excimer laser pulse. Consequently, these atoms do not suffer gas-phase collisions within the plume and are not directed in the same forward sense as other species.

The orientation of LNO films was found to be strongly influenced by an applied electric field during the deposition process [Hu et al., 1996; Wu et al., 1998]. Using a Kr laser with a fluence of 2–2.5 J/cm^2 to ablate a single-crystal $LiNbO_3$ target and adding a low bias voltage of 110 V, a complete *c*-axis-oriented film has been deposited.

20.2.1.4 Relaxors

Relaxor ferroelectrics are characterized by a broad dielectric peak in the dielectric permittivity versus temperature curve, which shifts toward lower temperatures when the driving signal frequency is decreased. Examples are $Pb(Mg_{1/3}Nb_{2/3})O_3$ (PMN), $Pb(Zn_{1/3}Nb_{2/3})O_3$ (PZN), their solid solutions with PT: PMN-PT, PZN-PT, and so forth. It has been generally accepted that their behavior can be explained through the existence of nanoscale polar domain clusters. Their properties are intermediate between those of glassy systems and ferroelectrics; for a recent review see Samara [2003].

The interest in relaxor ferroelectrics has been specially stimulated by their very large induced piezoelectric response and unique dielectric properties, which make them attractive for actuators, multilayer capacitor structures, MEMS, and the like. In bulk materials, relaxor systems and their solid solutions with ferroelectrics have been most widely studied in terms of electromechanical properties and electrostrictive coefficients showing large unipolar strains of about 1.7% along the (001) direction and a longitudinal piezoelectric coefficient d_{33} of 2500 pm/V [observed, e.g., in

Pb(ZN-PT) single crystal]. Attempts to transpose these materials to thin-film form have therefore dramatically increased in the last few years.

PMN and PMN-PT The pure relaxor PMN forms a crystalline solid solution with a normal ferroelectric PT: $(1-x)$PMN-xPT (PMN-PT). For $x<0.35$ the solution exhibits relaxor ferroelectric behavior and transforms into a normal ferroelectric at $x > 0.35$. For compositions with x within a narrow domain around 0.35, a new monoclinic phase has been identified by Ye et al. [2001] and Noheda et al. [2002]. Single-crystal PMN-PT with these compositions shows a very high dielectric permittivity and an exceptionally high coefficient of electromechanical coupling [Park and Shrout, 1997; Zhang et al., 2003a]. Many papers report the growth of PMN-PT thin films with different compositions, but in contrast to expectations neither the dielectric nor the electromechanical response of single-crystal or ceramic PMN-PT has been obtained in films. Thus the maximum dielectric constant was found to be smaller by two orders of magnitude than in bulk material. Moreover additional broadening of the dielectric peak and increase of dispersion above T_m was observed ([Tyunina and Levoska, 2001] and references therein). Among the different possible causes considered, we can identify at least two: the influence of the film–electrode interface and the growth strain in films.

The dielectric response of PMN is characterized by a broad peak at about $-5°C$, where the dielectric constant reaches a maximum of about 20,000, and a strong frequency dispersion around and below this temperature. The frequency dispersion obeys a Vogel–Fulcher relationship implying that polar nanoregions are freezing and generate a glassy state below about 220 K. Huge electromechanical strain of about 0.6% can be obtained in single crystals of PMN-PT, and therefore the possibility of growth by PLD of textured films with defined orientation, already demonstrated for different structures, is very attractive for obtaining films with enhanced properties compared to polycrystalline ceramics. Furthermore, this technique allows variation of many growth parameters.

A compromise between a lower deposition temperature (around 600°C), oxygen pressure in the range of 0.3–0.4 mTorr, and laser fluence [working with nanosecond ultraviolet (UV) excimer lasers] of $1-3\,J/cm^2$ was adopted as the optimum window for production of crystalline films with smooth surfaces.

PMN-PT thin films were grown on different buffer layers and/or bottom electrode substrate configurations. Lead titanate (PT), barium titanate (BT), and barium strontium titanate (BST) were used in Nakamura et al. [1996]. The obtained films were formed from perovskite (over 95% for the film grown on BST) and pyrochlore. No interdiffusion between the bottom electrode, the buffer layer, and the PMN-PT layers was observed. The dielectric constant obtained was about 1200.

The growth of PMN-PT films with $x = 0.3$ (PMN-PT 70/30) on SRO/LAO substrates was reported in Maria et al. [1998]. A KrF laser was used to deposit both the SRO and PMN-PT layers at fluences in the range of $1.5–2.2\,J/cm^2$, temperatures of 620–710°C and a reactive 90%O_2–10% O_3 gas mixture at pressures of 100–700 mTorr. PMN-PT ceramic targets with 15–40% PbO excess were used. It was demonstrated that a very narrow window of experimental parameters results in pyroclore-free films; however, an excess of PbO_x in the films results in structures with better electrical properties (large resistivities and low-loss tangent values). Epitaxial films of PMN-PT 70/30 with this orientation are very promising for MEMS applications since huge piezoelectric coefficients and electromechanical strains have been obtained for single crystals of rhombohedral relaxors along the (001) direction [Park and Shrout, 1997]. Figures 20.2 and 20.3 show the temperature dependence of the dielectric constant and loss and room temperature polarization hysteresis of the obtained films.

PMN-PT 68/32 thin films have been grown predominantly by excimer laser ablation [Tyunina and Levoska, 2001; Tyunina et al., 1999, 1998b; Levoska et al., 2000; Sternberg et al., 1997]. A XeCl laser working at $3\,J/cm^2$ laser fluence, 0.2–0.8 mbar oxygen pressure, and 600–650°C substrate temperature was used. An LSCO buffer layer was deposited on an MgO substrate prior to PMN-PT deposition. The films were highly oriented with two orientation relationships: either (001) or (110) type planes parallel to the substrate, the main orientation being (001). They contained grains with

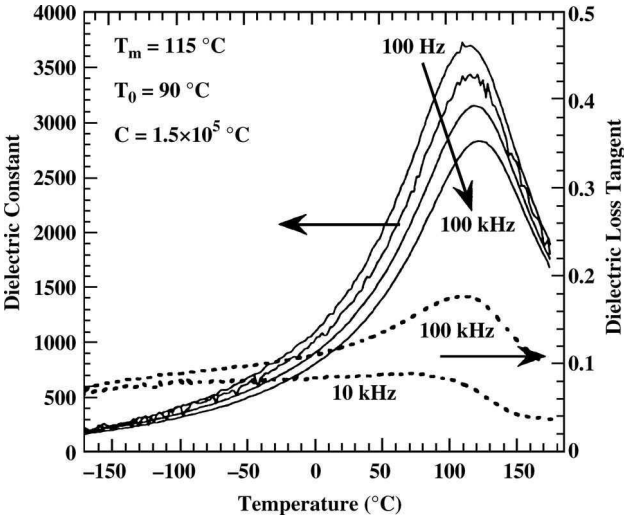

Figure 20.2 Temperature dependence of dielectric constant and loss of a PMN-PT 70/30 film. Reprinted with permission from Maria et al. 1998, © 1998, American Institute of Physics.

maximum lateral dimensions up to 100–150 nm. The properties of the films were found to be influenced by the small grain size, a high density of the grain boundaries being related to a high concentration of defects.

Wakiya et al. [2001] demonstrated the heteroepitaxial growth of PMN thin films on Si(001) using an LSCoO/CeO_2/YSZ triple-buffer layer. By using this particular combination of triple buffer, they succeeded in obtaining single-phase materials and to completely suppress pyrochlore formation.

The growth of PMN and PMN-PT thin films at low substrate temperature has been reported in the literature [Verardi et al., 2000; Craciun et al., 2003; Scarisoreanu et al., 2004]. The use of a PZT layer

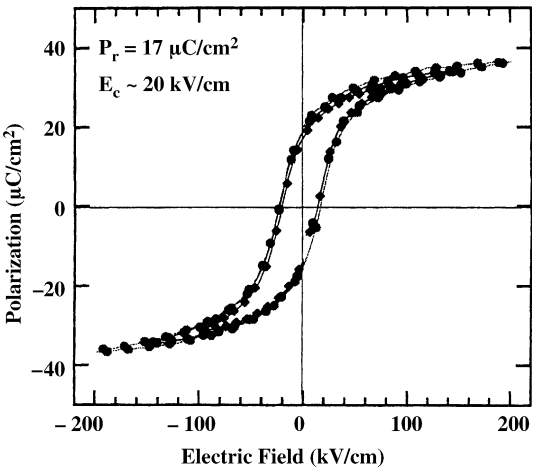

Figure 20.3 Polarization hysteresis loop of a PMN-PT 70/30 film at room temperature. Reprinted with permission from Maria et al. [1998], © 1998, American Institute of Physics.

as template enabled the growth of an oriented crystalline PMN film with a minor pyrochlore content at a relatively low temperature (500°C), working in an oxygen atmosphere of 0.4 mbar. The values obtained for the dielectric constant have been found to be smaller than that of bulk PMN, due to the presence of a very thin passive layer with low dielectric constant at the electrode–film interface (which was observed by secondary-ion mass spectrometry (SIMS) analysis) and to the minor pyrochlore content.

In Donnelly et al. [2003], the growth of $(1-x)$PMN-xPT thin films with different compositions ($x = 0$, 0.07, 0.1, 0.2, and 0.3) on LSCO/MgO substrates has been investigated. A KrF excimer laser operating at a laser fluence of 1.7 J/cm^2 and a repetition rate of 10 Hz was used. Film depositions were carried out at temperatures between 600 and 675°C in an oxygen atmosphere of 0.15 mbar. The obtained films were highly oriented and with uniform dense columnar structure.

Epitaxial PMN-PT 65/35 thin films have been deposited on (001) MgO substrates using a KrF excimer laser operating at a laser beam fluence of 2 J/cm^2 and repetition rate of 6 Hz. The growth has been performed in an oxygen atmosphere at a pressure of 200 mTorr and substrate temperature of 660°C. After deposition the film was annealed in situ at 660°C for 10 min and then cooled down in oxygen. The film was grown with a ''cube-on-cube'' epitaxy and with an in-plane-strain (calculated from the measured lattice parameter) of -0.38%, an order of magnitude less than the lattice misfit (-4.8%). The average grain size was about 40 nm. The in-plane dielectric properties, obtained by using coplanar interdigital transducers, were lower than in bulk materials [Wang et al., 2004].

Epitaxial PMN thin film have been obtained also on (001)LSCO/(001)MgO substrates [Shvartsman et al., 2005]. PMN films were pure perovskite, oriented with (001) planes parallel to the substrate surface.

The epitaxial growth of PMN-PT films on Si substrates is difficult due to the large lattice mismatch. To overcome this problem, Tsang et al. used MgO and TiN buffer layers [Tsang et al., 2003]. TiN is usually grown epitaxially on Si via domain-matching epitaxy. To avoid the detrimental effect of oxidation during the growth of PMN-PT 65/35 films in oxygen atmosphere, an MgO buffer layer is deposited on top to protect the TiN layer. The films are cube-on-cube grown on a Si(100) substrate with the epitaxial relationship: PMN-PT(100)||MgO(100)||TiN(100)||Si(100).

Recently $(1-x)$PMN-xPT multilayered structures with enhanced dielectric properties were deposited on LSCO/Pt/Si substrates using multitarget PLD with a KrF excimer laser [Ranjith et al., 2005]. The composition of the layers varied from the bottom electrode to the surface as follows: $x = 0.3$, 0.2, 0.1, 0. Each layer of different composition was deposited at 650°C at an oxygen ambient pressure of 100 mTorr. The compositional heterogeneity along with the lattice strain may offer additional advantages in tuning the physical properties of the system. The phase transition was found to be broad and the dielectric constant was almost constant (about 4700) for a wide range of temperatures (25–100°C). These multilayer films also showed a slim hysteresis loop, characteristic of relaxors.

PLZT La-doped PZT (PLZT) compositions show high dielectric, ferroelectric, electromechanical, and electrooptic properties and are therefore used in a wide range of applications such as memories, MEMS, light valves, optical storage display devices, optical spectral filters, linear and quadratic electrooptic modulators, optical switches and the like. [Lines and Glass, 1977; Xu, 1991]. These materials can be found in different low-symmetry phases such as ferroelectric rhombohedral, ferroelectric tetragonal, or relaxor cubic, according to the Zr/Ti ratio and La content [Lines and Glass, 1977; Xu, 1991]. Generally the effect of La is to increase disorder and induce a gradual phase transformation from the ferroelectric to the relaxor cubic phase with properties similar to glassy systems. The phase boundary between ferroelectric PLZT and relaxor PLZT is gradually shifted toward minor La content for PZT compositions with increasing rhombohedral distortion. For example, the tetragonal PZT 20/80 becomes a cubic relaxor when 22% of A-site positions are occupied by La, while the rhombohedral PZT 65/35 needs only 9% La to transform in a relaxor.

For the growth of films with different compositions $Pb_{1-x}La_x(Zr_{1-y}Ti_y)_{1-x/4}O_3$ (or PLZT $x/1-y/y$), different deposition parameters have been selected. For the synthesis of PLZT 5/70/30

on Pt/Si and STO/Si substrates [Yeh et al., 1995a, 1995 b], a XeCl excimer laser, working at 3 J/cm^2 was used. It was found that for high oxygen pressure (1 mbar) the deposition temperature should be higher than 650°C for pure perovskite phase growth: below this value there is a competition between pyroclore and zirconium containing oxides. A two-step process, deposition at room temperature and annealing in O_2 at 450 or 550°C, contributes to the complete elimination of Pb-deficit phases. The use of a preferentialy oriented (110) STO buffer layer induces the growth of highly textured (110) PLZT films. The growth process is supposed to take place in two steps: (i) the adherence of species coming from the laser-induced plasma plume onto the substrate forming clusters and (ii) the subsequent crystallization of the structure. It was shown that the use of an STO buffer layer supresses the Pb loss, and the main source of Pb deficiency is the reevaporation of Pb species from the adherent clusters. The correlated effects of the deposition rate and annealling time have been analyzed in Yeh et al. [1995a]. It was shown that increasing the deposition rate by increasing the laser frequency to 15 Hz results in the formation of the rutile phase of TiO_2. This is because the adhered species have no time to transform to the perovskite phase during the deposition process, Thus clusters accumulate in an amorphous form and the Pb^{2+} ions are lost by reevaporation, since in the amorphous phase this process is much more probable. The prolonged annealing time also induces the loss of PbO. Films deposited on Pt/Si at room temperature in 0.01 mbar O_2 pressure and annealed for 10 min at 450°C in 1 atm O_2 exhibit pure perovskite content and show the highest dielectric constant (1346 at 10 kHz).

Tyunina et al. [1998b, 1998c] report the growth of epitaxial (001) PLZT thin films with different La content (0–9.75 at %) on (001)LSCO/MgO(100) by using an XeCl excimer laser at 3 J/cm^2, a substrate temperature of 600°C, and an oxygen pressure of 0.2–1 mbar. A broad peak of the dielectric permittivity was observed, as typical for relaxors. Consistent with bulk behavior, PLZT thin films with higher La content demonstrated broader peaks in the dielectric permittivity and a lower temperature T_m of the maxima: T_m decreased from 350 to 105°C with an increase in La content from 0–8 at %. Heterostructures of yttria-stabilized zirconia (YSZ)/LSCO/$Pb_{0.9}La_{0.1}Zr_{0.2}Ti_{0.8}O_3$/LSCO have been deposited by PLD on Si substrates [Ramesh et al., 1994]. Ru or Ru/TiN/SiO_2 have been used as buffer–electrode layers for deposition of (Pb-4% La)$(Zr_{0.3}Ti_{0.7})O_3$ on Si [Bandaru et al., 1998]. A KrF laser working at 4–7 J/cm^2 and 3 Hz was used. The substrate temperature varied between 200 and 600°C and the oxygen pressure from 25 to 300 mTorr. Rapid thermal annealling (RTA) for 15–40 s at temperatures in the range of 450–700°C of films deposited at 400°C in oxygen at 50 mTorr pressure was found to produce films with good electrical properties, superior to films deposited at 620°C, where reaction at the interface leads to the formation of $PbRuO_{7-x}$.

The deposition of $Pb_{1-x}La_x(Zr_{0.65}Ti_{0.35})_{1-x/4}O_3$ thin films with different content of La has been reported in Verardi et al. [2003, 2004, 2005] and Craciun [2004]. PLZT x/65/35 shows ferroelectric properties for $x < 0.09$ and relaxor properties for $x > 0.09$. These films have been grown by PLD assisted by radio frequency (RF) discharge in oxygen, which allows an increase in the plasma reactivity and a reduction of the oxygen vacancies in films and at the film–bottom electrode interface [Dinescu et al., 2004]. Dielectric permittivity versus temperature variation for samples with $x = 0.09$ was typical of relaxor ferroelectrics, with a broad peak that shifted toward lower temperature for lower driving signal frequency. The temperature of the dielectric maximum was close to that obtained in bulk (about 70°C), but the permittivity value was much lower. This was attributed to two causes: (i) the presence of small quantities of pyrochlore phase and (ii) a low-permittivity interface layer.

The deposition of good relaxor ferroelectric PLZT 22/20/80 has been obtained by employing PLD and RF-PLD [Craciun et al., 2005a, 2005b]. Films grown by RF-PLD on Pt(111)/Si are (100) oriented and are free of pyrochlore or amorphous phases. The crystalline structure is perovskite cubic with a lattice parameter of 3.981 Å. PLZT 22/20/80 films showed slim-tilted hysteresis loops typical of relaxors with a coercive field of about 20 kV/cm and a remanent polarization of about 0.3 μC/cm^2. The dielectric constant, measured under variable direct current (DC) bias field, showed a nonlinear decrease, almost without hysteresis, with field amplitude.

Other Relaxors Among the different relaxor ferroelectric-PT solutions, Pb $(Yb_{1/2}Nb_{1/2})O_3$-$PbTiO_3$ (PYbN-PT) has the highest transition temperature ($\sim 360°C$) at 50% PT content. As has been shown [Tyunina et al., 1999] the largest piezoelectric coefficients, electrically induced strains, and coupling constants are observed in the [001] direction in rhombohedral crystals. Bornard and Trolier-McKinstry reported the first successful PLD growth of heteroepitaxial (001) PYbN-PT [Bornard and Trolier-McKinstry, 2000; Bornard et al., 2000]. The films were deposited on (001) SRO/(100) LAO and (111) SRO/(111)STO substrates. The heteroepitaxial arrangement was found to follow a pseudocube-on-pseudocube relationship between the film and the bottom electrode. Both (100) and (111) structures show dense, homogeneous, columnar microstructures, but their morphology was different: (111)-oriented structures exhibit microstructures with smaller grain sizes.

Relaxor $PbSc_{0.5}Nb_{0.5}O_3$ thin films have been deposited by PLD on LSCO/MgO substrates, and their dielectric behavior is reported in Tyunina and Levoska [2004].

20.2.1.5 Lead-Free Ferroelectrics

Lead-free piezoelectrics are thought to be future replacements for lead-based ferroelectrics, to avoid lead oxide toxicity. For a review on these materials the reader is referred to the chapter in Demartin Maeder and Damjanovic [2002] and references therein. Besides this environmental issue, there is also interest in developing piezoelectric materials that are biocompatible. Moreover, there is also a need to develop new piezoelectric materials that work at high temperatures. It must be pointed out that up to now lead-free materials are far from achieving the overall performance of lead-based ferroelectrics but may be considered as alternatives for special applications. In this category belong the well-known classical polar and nonpolar piezoelectrics such as $KNbO_3$ (KNO), LNO, $LiTaO_3$ (LTO), $BaTiO_3$ (BT), AlN, ZnO, and the like.

In recent years attention has been directed toward materials such as KNO and its solid solutions, $(Na,K)NbO_3$ (NKN), $(Na_{0.5}Bi_{0.5})TiO_3$ (NBT) and its solid solutions, layer-structured bismuth-based ferroelectrics like bismuth titanate $Bi_4Ti_3O_{12}$(BIT), and the like.

KNO crystals in certain cuts exhibit very high coupling coefficients of interest for high-frequency medical transducers. KNO in solid solution with $NaNbO_3$ exhibits increased values of piezoelectric coefficients close to that of PZT. This material appears also to be compatible with human tissue. Several compositions belonging to the bismuth titanate family such as, for example, $SrBi_4Ti_4O_{15}$ exhibit the absence of piezoelectric hysteresis, nonlinearity, and frequency-independent piezoelectric response at room temperature, showing an apparent absence of domain-wall contributions to the piezoelectric response.

NBT-based solutions are considered among the best candidates for replacing lead-based materials in devices, due to their high dielectric and piezoelectric properties. NBT is a relaxor ferroelectric perovskite whose solid solutions with BT, $(1-x)$NBT-xBT, show a morphotropic phase boundary with enhanced properties at $x = 0.06 - 0.07$. Excellent piezoelectric properties ($d_{33} = 450\,pC/N$) and strain up to 0.85% have been reported in Chiang et al. [1998] for $x = 0.06$.

NBT-BT thin films with different BT contents in the range 0.02–0.44 have been deposited by a modern PLD-based combinatorial technique on (001)LAO substrates, by using a KrF excimer laser [Cheng et al., 2004]. Deposition has been performed sequentially from ceramic NBT and BT targets using three quaternary masks, at room temperature, and the ratio of NBT and BT was estimated by the growth time. To mix the different layers homogeneously and obtain crystallized films, a post-deposition three-step annealing process was adopted. The films obtained are (101) oriented. It was found that the dielectric constants reach a peak of about 327 at $x = 0.09$, much higher than that at $x = 0.06$ (about 187). This indicates that the MPB in NBT-BT thin films is located at a slightly higher BT content than in bulk materials. The authors obtained similar results for the MPB composition by growing films from a NBT-BT ($x = 0.09$) ceramic target at a substrate temperature of 750°C, without postannealing treatment. Another combinatorial PLD technique based on temperature-gradient growth and continuous compositional-spread was employed to grow $Sr_xBa_xNb_2O_6$ (SBN) thin films [Ohkubo et al., 2004]. These combinatorial techniques allow one

to obtain multisample film growth in different simultaneous conditions and are powerful tools for the quick optimization of composition and growth parameters of new materials.

The deposition of NBT-BT ($x = 0.06$) thin films with high dielectric constant was reported in Dinescu et al. [2005]. Films have been grown on MgO(100) single-crystal substrates at a temperature of 600–650°C using a Nd:YAG laser (wavelength 355 nm, pulse length 10 ns, repetition rate 10 Hz) operating at a fluence of 1.9 J/cm^2. Films were pure crystalline perovskite with (100) and (110) orientations. The dielectric constant, measured on metallic interdigital transducers deposited on top of the films, ranged between 1230 and 1330, for films deposited at different temperatures and with different cooling protocols. The best results have been obtained for films grown at 650°C in 0.5 mbar oxygen ambient and cooled at 10°C/min in 10 mbar oxygen ambient.

The successful deposition of lanthanide-substituted BIT thin films with good ferroelectric and piezoelectric properties have been reported in Adachi et al. [2005]. $(Bi_{3.25}Ln_{0.75})Ti_3O_{12}$ (Ln = La, Nd, Sm) were grown on Pt(111)/TiO_2/SiO_2/Si and IrO_2(110)/TiO_2/SiO_2/Si substrates by PLD at a temperature of 700°C in 1 Torr oxygen. The laser fluence was approximately 2.5 J/cm^2 at a repetition rate of 5 Hz. Films grown on Pt(111) electrodes were *c*-axis oriented, while films grown on IrO_2(110) showed predominant (111) and (110) orientations. The last showed larger piezoelectric coefficient and remanent polarization. Strong anisotropic dielectric properties have been found also in epitaxial (001)-oriented $Bi_{3.25}La_{0.75}Ti_3O_{12}$ (BLT) thin films deposited on LAO(001) substrates [Lee et al., 2004a]. The dielectric constants measured along the (100), (1$\underline{1}$0), and (001) crystal directions were 358, 160, and 80, respectively. The largest dielectric constant was obtained along the *a*-axis, which is the direction of the major spontaneous polarization in these layered perovskite materials.

An improvement of ferroelectric properties of BIT films by using compositions with different A-site (La) and B-site (Zr) substitutions have been reported in Zhang et al. [2004].

Results on PLD epitaxial growth of Nd-doped BIT films have been reported in Garg et al. [2003] and Zhang et al. [2003b]. Although these studies are primarily directed to investigate ferroelectric properties for use in ferroelectric memory applications, these materials are also interesting lead-free piezoelectrics, as shown in Adachi et al. [2005] and Maiwa et al. [2003].

$BaTiO_3$ (BT) is another lead-free ferroelectric with good piezoelectric properties, athough its low Curie temper]ature (120°C) is a disadvantage for certain applications. BT thin films with good ferroelectric and piezoelectric properties have been deposited by PLD with a KrF excimer laser on different electrodes [Kim et al., 2005a]. The best properties have been obtained for films deposited on LSCO/Pt electrodes. Ultrathin epitaxial BTO thin films (down to 3 nm) have been grown by PLD (KrF excimer laser) on SRO/STO substrates [Kim et al., 2005b]. A critical thickness of 5 nm above which the existence of ferroelectricity is demonstrated has been experimentally established. The growth of polycrystalline BT thin films on Pt/Si at relatively low temperatures of 600–650°C and without postdeposition annealing has been obtained by using RF-PLD [Dinescu et al., 2004; Canulescu et al., 2004].

Among lead-free materials, sodium–potassium niobate $Na_xK_{1-x}NbO_3$ ceramics show a wide range of ferroelectric and piezoelectric properties depending on their composition. For example, for $x = 0.5$, $Na_{0.5}K_{0.5}NbO_3$ (NKN) (which is rhombohedral from -130 to 200°C) shows a radial electromechanical coupling coefficient of 0.39 and a large piezoelectric coefficient $d_{33} = 160$ pm/V. These values are small compared to lead-based ferroelectric piezoelectrics or relaxor single crystals, but are high among the lead-free ferroelectrics. Recently the perovskite sodium–potassium niobate thin films have attracted attention due to their interest for microelectromechanical devices and biocompatible applications. Growth of NKN films by PLD has been demonstrated by Cho and Grishin [Cho and Grishin, 1999, 2000; Cho et al., 2002]. The growth of NKN films is very difficult due to the high mobility of both Na and K. The structure and properties of the films obtained change radically from ferroelectric to relaxor if they are grown in high or low oxygen pressures. NKN films grown at high ($\sim$400 mTorr) oxygen pressure (HP-NKN) (a key factor for the thermalization of all neutrals and for achieving stoichiometry of complex oxide films with volatile components [Cho and Grishin, 2000]) have been found to be single phase, highly *c*-axis oriented, with a strong effect of self-assembling both on slightly textured and even amorphous substrates.

Films grown at low oxygen pressure (~ 10 mTorr) (LP-NKN) are inhomogeneous ferroelectrics containing mixed phases of ferroelectric NKN and paraelectric potassium niobate, due to a Na deficiency caused by insufficient thermalization of species with different atomic masses.

20.2.2 Nonferroelectric Piezoelectrics

20.2.2.1 ZnO

Zinc oxide is one of the most common nonferroelectric piezoelectrics. Due to its high piezoelectricity and electromechanical coupling factor, ZnO has been used in many practical applications such as ultrasonic transducers, SAW devices and sensors, resonators, filters, and the like [Ieki and Kadota, 1999; Osbond et al., 1999; Lakin, 1999]. The crystal structure of zinc oxide is hexagonal (wurtzite type). Each Zn atom is tetrahedrally coordinated with four O atoms and the Zn *d* electrons hybridize with the oxygen *p* electrons. Although stoichiometric ZnO has a very high resistivity, it usually contains excess zinc atoms, which influence the electrical conductivity, piezoelectricity, and defect structure. The wurtzite structure is polar and a mechanical compression in the *c* direction will produce either a positive or negative voltage in this same direction, depending on the polarity of the *c*-axis. Along the polar axis Zn atom layers define the positive face (0001 direction) and the O atom layers the negative face ($000\bar{1}$ direction). These two crystal faces behave differently regarding their surface energies, growth rates, and etch and abrasive characteristics. The oxygen face has a lower surface energy, slower growth rate, and abrades and etches more rapidly than the Zn face. In film growth, ZnO shows a strong tendency to grow with its *c*-axis perpendicular to the substrate surface even if the substrate is amorphous. However, the degree of orientation is influenced by growth conditions such as temperature, background gas composition and pressure, particle energy, substrate type, and surface condition.

For details on ZnO thin-film growth and properties the reader is referred to Chapter 12.

20.2.2.2 AlN

Aluminum nitride, AlN, belongs to the hexagonal class (wurtzite structure). It has a low piezoelectric constant (5.4 pm/V) when compared with ferroelectric piezoelectrics but shows remarquably low losses together with a high electrical resistivity ($10^{14}\,\Omega$ cm). Thin films of AlN have been developed especially for high-frequency transducers since this material has a very high acoustic wave velocity (10,400 m/s) that allows coverage with film thicknesses of 2.5–0.5 μm of the range from 2 to 10 GHz in the fundamental resonance mode. Compared with ZnO, AlN has a lower coupling constant, but it has the advantage of a much higher electrical resistance. It also shows a high breakdown voltage and low dielectric loss. Moreover, the low thermal expansion coefficients should lead to small thermal drifts of the characteristics. Based on its electromechanical coupling coefficient and its superior optical qualities, AlN layers have been considered to be one of the most promising materials for optical waveguides, acoustooptic interaction media, surface acoustic wave, and bulk acoustic wave transducers.

Usually AlN films exhibit columnar growth in a (002) direction perpendicular to the substrate. The degree of the preferential orientation is reduced by the spreading of column direction that is also detrimental for the piezoelectric properties. Moreover, if different regions in AlN film have different orientations of the polar axis (with Al atom or N atom toward the upper surface), the overall piezoelectric effect will be decreased in proportion to these inversion domains [Ruffner et al., 1999].

High-quality optoelectronic-grade epitaxial AlN films grown on α-Al_2O_3, Si, and 6H-SiC by PLD have been obtained by Vispute and al. [1997]. The measured bandgap was found to be 6.1 eV, the electrical resistivity $5-6 \times 10^{13}\Omega$ cm, and the breakdown field 5×10^6 V/cm. The same group previously reported the PLD growth, for the first time, of AlN epitaxial thin films on Si(111) substrates ablating high–density sintered AlN targets with an excimer laser (KrF, 10–30 Hz, 2–10 J/cm^2) [Vispute et al., 1995]. A sharp AlN/Si interface was obtained, without any indication of interfacial reaction, and films showed smooth surface morphology. Films were

oriented with the *c*-axis normal to the surface. Since the lattice parameters of AlN and Si are significantly different, a domain-matching epitaxy was proposed as a possible mechanism for the epitaxial growth.

Oxygen impurities in nitride thin films degrade their qualities because they lead to highly *n*-type conduction that influences the electrical, optical, piezoelectric, and elastic properties of the film [Jagannadham et al., 1998]. A key factor for obtaining high-quality oxygen-free AlN films was found to be the elimination of the oxidation of the AlN target surface [He et al., 1998]. Even if the deposition chamber was previously evacuated down to 2×10^{-7} Torr, releasing of oxygen impurities from the sintered polycrystalline AlN target was possible, as confirmed by SIMS analysis on the films obtained [Jagannadham et al., 1998].

AlN thin films have also been deposited by laser ablation of an Al target in a reactive nitrogen atmosphere [Verardi et al., 1997a, 1997b].

The properties of PLD-deposited AlN films, reported over the last few years, are listed in Table 20.1.

20.3 DIELECTRIC AND PIEZOELECTRIC PROPERTIES

20.3.1 Effects of Internal Stress and Other Factors on Ferroelectric Piezoelectric Thin Films

In ferroelectrics the domain walls are a major contributor to the dielectric and piezoelectric properties. For example, in piezoelectric ceramics at room temperature this contribution is about 70% to the dielectric and 66% to the piezoelectric response of the total response for PZT 52/48 [Zhang et al., 1994]. In PZT there exist two groups of domain walls: 180° walls and non-180° walls. Their role is different since the first are not ferroelastically active and, therefore, contribute only to the dielectric properties, while the second contribute to both responses. It is therefore important to establish which domain-wall configuration is present and which is active under weak driving fields or switching fields. This problem is even more complicated in thin films where the influence of crystallographic orientation, substrate clamping, misfit strain, pinning of domain walls by defects (grain boundaries, dislocations), oxygen vacancies, and the like are important. It has been shown, for example, that in PZT thin films with thicknesses smaller than 1 μm the piezoelectric response due to non-180° domain wall motion is limited [Trolier-McKinstry et al., 1997].

Systematic studies have only been seldom done, especially for PLD thin films, since the separation of different factors is very difficult to achieve.

20.3.1.1 Internal Stress and Mechanical Constraint; Domain Structure in Thin Films

The influence of mechanical constraint on the dielectric and piezoelectric behavior has been observed, for example, in epitaxial PMN-PT 90/10 thin films grown on (001) LAO substrates, with LSCO layers as top and bottom electrodes, all deposited by PLD [Nagarajan et al., 1999b]. It was found that the full-width at half-maxima (FWHM) of the ω scan around the (200) PMN-PT peak gradually decreased from 0.69° to 0.49° when the film thickness increased from 100 to 400 nm, indicating a decrease of local strain and an improvement in the crystallinity. Dramatic differences in the dielectric and piezoelectric behavior of the films are shown in Figures 20.4 and 20.5, respectively.

The value of the maximum relative dielectric constant ε_m increased from about 250 for 100-nm to about 1800 for 400-nm-thick films, while the temperature T_m of the dielectric maximum decreased from about 200°C for a 100-nm-thick film to about 60°C (bulk value) for 400-nm-thick films. The increase of dielectric constant was accompanied by an increase of the d_{33} coefficient from about 10 pm/V for the 100-nm film to about 85 pm/V for the 400-nm film. The shift of the temperature T_m with respect to its bulk value was attributed to the presence of large internal compressive stress in

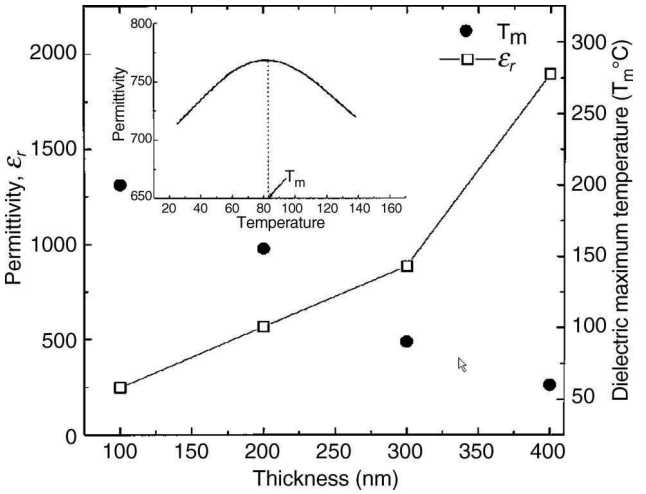

Figure 20.4 Dielectric permittivity and the temperature of the dielectric maximum T_m as a function of film thickness for an epitaxial PMN-PT 90/10 on LSCO/LAO. The inset shows the dependence of permittivity on temperature for a 300-nm-thick film. Reprinted with permission from Nagarajan et al. [1999b], © 1999, American Institute of Physics.

very thin films due to unrelaxed heteroepitaxial stress and thermal stress. After the transition to the relaxor state the average stress is transformed into a nonuniform stress distribution of alternating sign whose amplitude is related to the stress state before the transformation, and therefore is larger in thin films, as shown by the broader ω scans of the thinner films. Consequently, thin films are much stiffer, and, therefore, the dielectric constant as well as piezoelectric coefficient is smaller. Nevertheless, clamping by the substrate changes the measured value of the piezoelectric coefficient in films d_{33}^f according to the equation: $d_{33}^f = d_{33} - 2d_{31} \times s_{13}^E/(s_{11}^E + s_{12}^E)$ [Lefki and Dormans, 1994]. More general relations for the piezoelectric coefficients of substrate-clamped PZT films with different orientations have been given in Ouyang et al. [2004, 2005].

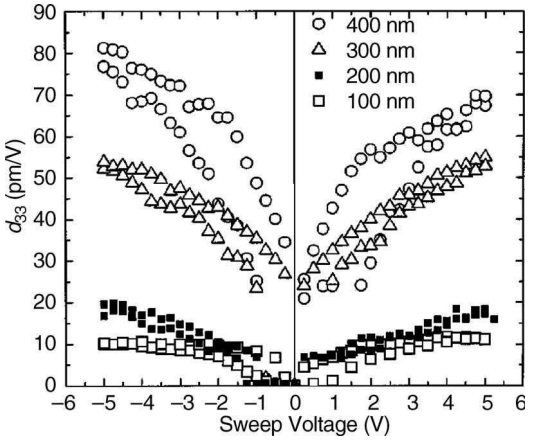

Figure 20.5 Longitudinal piezoelectric coefficient d_{33} vs. sweep voltage for different film thicknesses for an epitaxial PMN-PT 90/10 on LSCO/LAO. Reprinted with permission from Nagarajan et al. [1999b], © 1999, American Institute of Physics.

A finite-element modeling (FEM) of piezoresponse in patterned ferroelectric thin films was used to calculate the influence of substrate clamping [Li et al., 2004]. The analyses revealed that, besides the intrinsic piezostrain, d_{33} measured through the surface displacement includes contributions from the strain induced by substrate constraint, the substrate local deformation, and top electrode deformation. The local deformation of the substrate significantly reduces the measured d_{33}, while the contribution of the top electrode is negligible when the film is free from constraint (lateral dimensions of the patterned islands are comparable with thickness) or the film is fully clamped by the substrate. Experimental measurements made by piezoresponse force microscopy on two hetrostructures $PbZr_{0.2}Ti_{0.8}O_3$/STO and $PbZr_{0.5}Ti_{0.5}O_3$/STO/Si confirmed the FEM predictions [Li et al., 2004].

Nagarajan et al. [2002] measured the intrinsic piezoresponse of PZT films in epitaxial patterned PZT/LSCO/STO/Si heterostructures, by reducing the lateral dimensions of the patterned islands below 1 μm to eliminate the substrate clamping effect. Moreover, the PZT films were only 100 nm thick to avoid complications from the formation of ferroelastic 90° domains. In these conditions, the differences between measurements on continuous films and on patterned submicron capacitors could be attributed only to substrate clamping effects. The d_{33} piezoelectric constant measured at different electric fields on (a) a PZT 50/50 film and (b) a PZT 20/80 film is presented in Figure 20.6. The

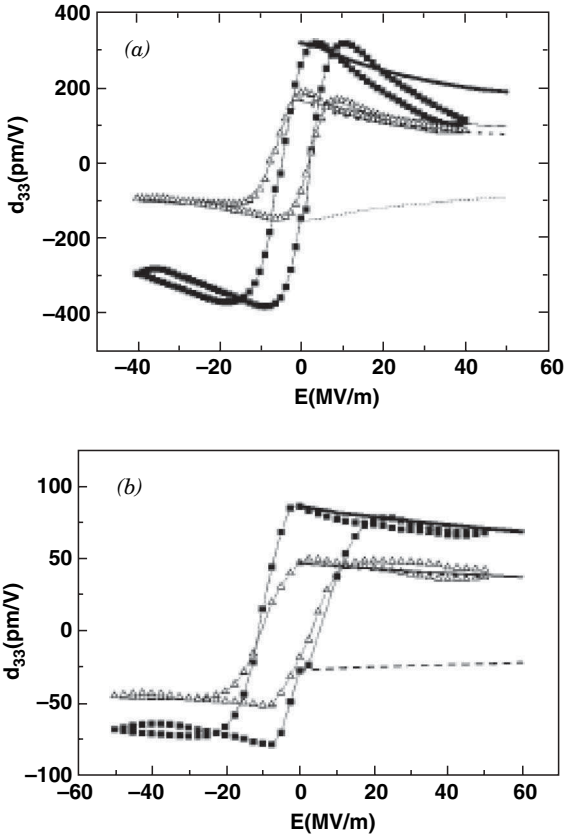

Figure 20.6 Piezoelectric response for (a) a PZT 50/50 film and (b) a PZT 20/80 film. The measurements have been performed by AFM on a clamped 50-μm-diameter capacitor (open triangle symbols) and 0.5 × 0.5 μm capacitor (full square symbols). Reprinted with permission from Nagarajan et al. [2002], © 2002, American Institute of Physics.

measurements have been performed by atomic force microscopy (AFM) on a clamped 50-μm-diameter capacitor (open triangle symbols) and $0.5 \times 0.5\,\mu m$ capacitor (solid square symbols). A large difference is observed between d_{33} values measured on the clamped and laterally free PZT film, for both compositions.

The substrate clamping effect has been observed also by studying the variation of domain structure in epitaxial $PbTiO_3$ thin films grown on MgO(001) and Pt(001)/MgO(001) following patterning into discrete islands [Lee et al., 2004b]. The island sizes, patterned lithographically on the same film of thickness of about 500 nm, varied between $100 \times 100\,\mu m^2$ and $2 \times 2\,\mu m^2$. As the island size decreased, the substrate clamping effect significantly reduced. The evolution of 90° domain structure was investigated by reciprocal space mapping using syncrotron X-ray radiation. As the island size reduced, some of the *a* domains turned into *c* domains due to the relaxed tensile strain, for the film grown on MgO(001), while in the patterns grown on Pt/MgO the formation of 90° domains was enhanced by the reduction in compressive misfit strain.

Thermodynamic calculations and phase-field simulations [Li et al., 2003] showed that the phase diagram for a PZT film constrained by a substrate is drastically different from the corresponding bulk stress-free phase diagram with different transition temperatures, stable ferroelectric phases, and the position of the morphotropic phase boundary (MPB) between rhombohedral (R) and tetragonal (T) phases.

Lee and Baik [2005] investigated experimentally the influence of substrate clamping on MPB in PZT thin films. The coexistence of T and R phases in discrete epitaxial patterns was characterized as a function of lateral dimensions of the islands as in Lee et al. [2004b]. The 600-nm-thick epitaxial $Pb(Zr_{0.55}Ti_{0.45})O_3$ and $Pb(Zr_{0.60}Ti_{0.40}O_3$ grown on Pt(001)/MgO(001) were highly rich in T phase, although these compositions are rhombohedral in bulk, due to the two-dimensional film stress. As the films were patterned progressively in smaller sizes, the misfit strain was relaxed and the phase content was restored to the original R composition.

In ferroelectric thin films, especially in epitaxially grown films, the elastic strain induced by lattice-matching constraints between the film and the substrate has a strong influence on crystalline properties, domain structure, dielectric, ferroelectric, and piezoelectric properties. The knowledge of different strain factors such as misfit strain, thermal strain, and transformation strain occurring near the Curie temperature is crucial for tailoring the domain structure of ferroelectric thin films and, ultimately, their physical properties. Over the last few years, several results on the influence of misfit strain on ferroelectric thin films deposited by PLD have been reported (see the review in Alpay [2002]).

Nagarajan et al. [1999a] have studied the effect of misfit strain on the microstructure and electrical properties of PZT thin films and have changed the misfit strain by varying the film thickness and studied the thickness effect on the domain formation of epitaxial $PbZr_{0.2}Ti_{0.8}O_3$ grown on LSCO/(001) (LAO) substrates. The nominal thickness of PZT films was varied from 60 to 400 nm. Two mechanisms for strain relaxation have been identified: misfit dislocation generation at the deposition temperature and polydomain formation below the paraelectric-to-ferroelectric transformation temperature. Polydomain formation in epitaxial films undergoing a phase transformation is a mechanism that relaxes the total strain energy by formation of an *a/c/a/c* polydomain structure, where the fraction of *c* domains depends on film thickness [Alpay and Roytburd, 1998]. Analyses of the deposited heterostructures show that the first layers of PZT are deposited on a highly strained LSCO layer therefore the PZT *c*-axis lattice parameter is higher in a 60-nm film than in a 400-nm film. This indicates that the epitaxial strain in the film relaxes as the film thickness is increased. The *c*-domain abundance decreases continuously to a value of 67% for the 400-nm film, while the *c*-axis lattice parameter decreases from 0.416 nm for the 60-nm film to 0.413 nm for the 400-nm film, thus the 60-nm film is under very high in-plane compressive stresses. The 300- and 400-nm films show a lattice parameter of 0.413 nm indicating almost full relaxation. This was confirmed also from the tetragonal *c/a* ratio calculated from electron diffraction, which was found to decrease from 1.08 in a 60-nm film to 1.051 in a 400-nm film. The cross-sectional images also show that the relative volume fraction of the 90° domains increases with film thickness,

confirming XRD results. The contraction of the *c*-lattice parameter is commensurate with the relaxation behavior of the film. It begins to decrease when the film relaxes via polydomain formation. The decrease in the *c*-lattice parameter causes a decrease in the tetragonal *c/a* ratio of the ferroelectric layer, which influences the static and dynamic ferroelectric behavior.

The formation of a polydomain *a/c/a/c* pattern as a mechanism of strain energy relaxation in epitaxial PZT films undergoing a cubic-tetragonal phase transformation and the role of 90° domain walls on the nucleation of reversed domains have been discussed in Ganpule et al. [2000a]. The investigated film was a 400-nm-thick epitaxial $PbZr_{0.2}Ti_{0.8}O_3$ film grown on LSCO/(001) STO. Piezoresponse microscopy, based on the detection of the piezoelectric response of the ferroelectric thin fims when probed using an ac field, showed 90° domains (with *c*-axis in the plane of the film) of width 20–40 nm and spacing 100 nm. Since the piezoresponse for the *c*-oriented domains is much larger than for the *a* domains, it is possible to observe the *a* domains as regions of low piezosignal. It has been confirmed that 90° domains do not switch under the experimental conditions, that is, a maximum applied DC field of 10 V, due to substrate clamping. However, Lee et al. reported the in situ observation of ferroelectric 90° domain switching in epitaxial $PbZr_{0.32}Ti_{0.68}O_3$ thin films by synchrotron X-ray radiation [Lee et al., 2001]. It has been found that, within the experimental region of electric field up to 24 kV/cm, a maximum 27.8% of 90° domains were reoriented.

It has been recently shown [Ma et al., 2005] that 90° domain movement gives a large extrinsic contribution to the piezoresponse in patterned ($1 \times 1 \times 1$ μm) PZT/LSCO/STO/Si heterostructures. Due to decreased substrate clamping the movement of 90° domain walls in these islands increases the effective d_{33} up to 400 pm/V, while in the continuous film the measured value is only 50 pm/V.

Bai et al. [2004] have shown that epitaxial constraint in (001)-oriented $BaTiO_3$ thin films induces a dramatic increase in the temperature of the tetragonal structural phase transition. For 200-nm-thick films grown by PLD on STO substrates a tetragonal-cubic phase transition was found on heating at about 680°C, whereas for films of the same thickness grown on a buffer layer, which relaxes the epitaxial constraint, the transition occurs almost at the same temperature as in bulk crystals (130°C).

The influence of the strain type (expansion or compression) was investigated by Nagarajan et al. [2000] in 100-nm-thick PMN-PT 90/10 epitaxial films grown on (001) (LAO), $(La,Sr)(Al,Ta)O_3$ (LSAT), STO, and MgO substrates with top and bottom LSCO electrodes. XRD results indicated that films on LAO, LSAT, and STO were biaxially stressed in compression in the film–substrate interface while the films on MgO are stressed in tension. An increase of the dielectric constant and the piezoelectric coefficient d_{33} and a decrease in the temperature of the dielectric maximum T_m was observed with decreasing in-plane epitaxial compressive stresses. Films with in-plane tension (grown on MgO) showed the highest dielectric constant and piezoelectric coefficient. A variation of in-plane strain from -0.46% (LAO) to $+0.32\%$ (MgO) induces a variation in dielectric constant (at room temperature) from about 400 to 2000 and a variation of d_{33} from about 10 pm/V to about 60 pm/V.

Lee and Baik [2000] found strong effects of misfit strain on domain formation of epitaxial $PbTiO_3$ thin films grown on MgO(001) substrates by PLD. They have investigated the effects of relaxation of elastic misfit strains induced by heteroepitaxy on domain formation. The thickness-dependent evolution of twin domain structures was characterized by two-dimensional reciprocal space mapping using a synchrotron X-ray source. Figure 20.7 shows two-dimensional reciprocal space mapping results on the HK plane of $PbTiO_3$ (100) reflections, which gives information about the evolution of *a* domains.

It can be observed that directional tilting of *a* domains starts to develop for films 650 Å thick and shows a complete splitting at 2000 Å. The dependence of domain population on film thickness was closely related to an effective misfit strain at the growth temperature. High tensile misfit strain acts against *c*-domain formation in very thin films.

Recently, Kim et al. [2004a] investigated the effect of a compressive misfit strain on the ferroelectric domain structure in PT films with different thicknesses grown epitaxially on Pt(001)/Mg(001) substrates. Unlike the films grown directly on MgO(001) substrates [Lee and Baik, 2000], PT films grown on an epitaxial Pt interlayer experienced compressed misfit strain at the growth

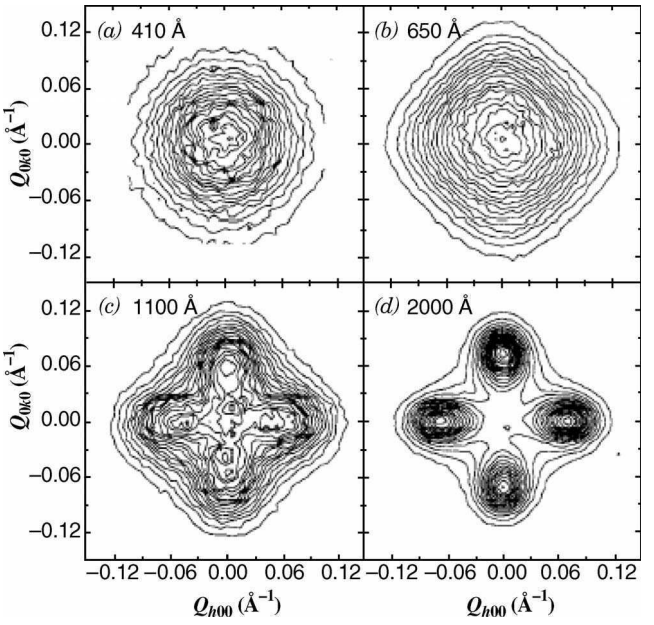

Figure 20.7 XRD contour maps for HK-reciprocal space of $PbTiO_3$ (100) reflections showing the evolution of *a* domains as a function of film thickness. Reprinted with permission from Lee and Baik [2000], © 2000, American Institute of Physics.

temperature (650°C) because Pt has a smaller lattice constant than PT. At the Curie temperature PT film transformed to almost a fully *c*-axis-oriented structure due to the large compressive strain. As the film thickness increased, relaxation of the compressive misfit strain was enhanced, reducing the initial *c*-domain abundance. The domain structure and switching behavior were investigated by using scanning force microscopy, and direct evidence of *a*-domain switching was observed under an external electric field [Kim et al., 2004b]. However, its contribution to the total piezoelectric response was found to be negligible. Thinner epitaxial PT films with higher *c*-domain population and larger tetragonality presented higher d_{33} piezoelectric coefficients, indicating that the key factor controlling the piezoelectric response in these films is not the *a*-to-*c* domain switching but apparently the population of *c* domains and their tetragonality [Kim et al., 2004b].

Goh et al. [2005] showed that avoiding the tensile stress in the growth of ferroelectric PZT thin films leads to films with improved ferroelectric properties. A granular pseudoepitaxial thin film was deposited on an LSMO/YBCO/YSZ heterostructure template. Despite the imperfect epitaxial quality, the PZT thin film exhibited a larger remanent polarization than an epitaxial PZT thin film. This improvement is attributed to the partial relief of the tensile stress due to the granular pseudoepitaxial structure with nanometer-sized pores.

20.3.1.2 Dielectric Passive Layers

Many works report lower values for the dielectric, ferroelectric, and electromechanical properties in thin films than in bulk. This has been attributed to different factors such as depolarization fields, the junction between the film and the electrode, the presence of nonswitching passive layers, and the presence of intrinsic dead layers [Tagantsev et al., 1995a; Miller et al., 1990; Watanabe, 1998].

Analysis of the behavior of relaxor ferroelectric thin films assimilating the heterostructure with a stacked capacitor formed from a relaxor ferroelectric layer and a nonswitching, passive, low-permittivity dielectric layer permitted the true dielectric properties to be obtained, as reported in Tyunina and Levoska [2001]. The investigated heterostructures (obtained by in situ PLD

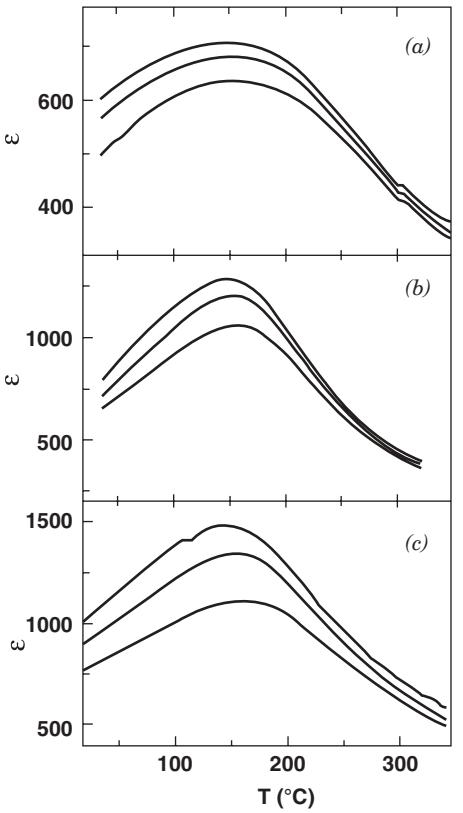

Figure 20.8 Dielectric permittivity for three sets of PMN-PT68/32/LSCO/MgO heterostructures. Reprinted with permission from Tyunina and Levoska [2001], © 2001, American Physical Society.

deposition) were formed of (001) PMN-PT films over (100) $La_{0.5}Sr_{0.5}CoO_3$/(100)MgO. Figure 20.8 shows dielectric permittivity ε vs. T for three sets of heterostructures with small microstructural differences. A broad maximum in ε around 150°C and a high-frequency dispersion of ε can be observed.

The maximum of the dielectric constant ε_m shifted to higher temperatures with increasing frequency, as in bulk samples, but its absolute value was considerably smaller. After applying the stacked capacitor model (detailed analysis can be found in Tyunina and Levoska [2001]), the reconstructed dielectric response was obtained (Fig. 20.9) and shows high values for the PMN-PT film, similar to bulk values.

20.3.1.3 Depletion Layers

In thin films depletion layers (layers poor in charge carriers) are formed at the film–electrode interfaces due to different work functions [Tagantsev et al., 1995b]. They are responsible for the variation of film properties with thickness, as, for example, in the results reported by Wakiya et al. [2001] (Fig. 20.10) for heteroepitaxial (001)PMN/(001)LSCO/CeO_2/YSZ/Si(001).

It can be observed that the dielectric constant dramatically decreases from 800 to very low values when the film thickness decreases from 130 nm to a few nanometers. This effect was attributed to the depletion width (the depletion width reported for ferroelectric perovskite oxides is about 6 nm [Scott, 1999]). The drastic increase of current density and dielectric loss was attributed to Fowler–Nordheim tunneling.

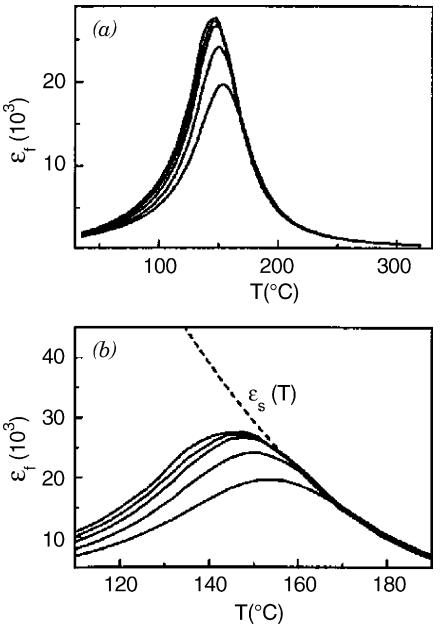

Figure 20.9 Reconstructed dielectric permittivity of the relaxor PMN-PT 68/32 film, without the dielectric passive layer. Reprinted with permission from Tyunina and Levoska [2001], © 2001, American Physical Society.

20.3.1.4 Oxygen Vacancies

The number of oxygen vacancies plays an important role in the dielectric properties of the film. They can be created either by modifying the basical target composition with suitable dopants (e.g., K or Fe in PZT) or by growing films in a low-pressure oxygen ambient. Oxygen vacancies can move within the oxygen octahedral network; therefore, the defect dipoles will align parallel with the polarization vector in the domains and stabilize the domain structure. Further reorientation of domains by external fields will require reorientation of aligned defect dipoles, and the field and time response of the ferroelectrics will thus be modified.

The influence of oxygen content on dielectric and electromechanical properties of (001) PMN films deposited epitaxially on (001)LSCO/(100)MgO was reported in Catalan et al. [1999], where varying the oxygen pressure during deposition changed the oxygen content of the films. The observed increased frequency dispersion above the temperature of the dielectric permittivity peak T_m was attributed to the space-charge field produced at the dielectric–electrode interface, whose intensity is directly correlated to the density of oxygen vacancies [Fukuda et al., 1996]. Films with high oxygen content (reduced number of oxygen vacancies) show reduced dielectric relaxation above T_m, low DC voltage-driven leakage current, and high electromechanical strain.

Recent studies [Wu et al., 2004, 2005a] showed the influence of oxygen vacancies on polydomain formation in epitaxial $Pb(Zr_{0.52}Ti_{0.48})O_3$ films grown on LSMO/LSAT(001) substrates. After annealing at reduced oxygen pressures, it was found that oxygen vacancies created at the PZT bottom interface drive the polydomain formation in PZT films well below the Curie temperature, by introducing a strain gradient at the interface.

Oxygen vacancies are also responsible for the gradual reduction of switchable polarization after repeated alternating voltage pulses or switching cycles (fatigue). Fatigue is induced by dense oxygen vacancies or point defects accumulating near the PZT–Pt interface after some switching cycles, due to an internal electric field in the Schottky barrier [Yan et al., 2003, and references therein]. However, adding a $(Ba_{0.5}Sr_{0.5})TiO_3$ buffer layer between the Pt electrode and the PZT film (or using an oxide

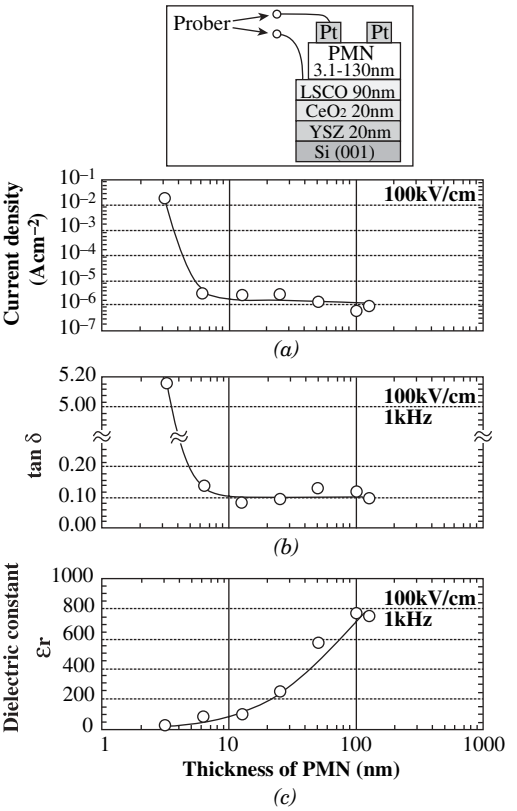

Figure 20.10 Variation of dielectric constant and loss of a heteroepitaxial PMN/LSCO/CeO_2/YSZ/Si(001) structure with PMN thickness. Reprinted from Wakiya et al. [2001], © 2001, with permission from Elsevier.

electrode) allows absorption of the oxygen vacancies from the PZT film and hence heterostructures with good fatigue properties. As has been shown in Gerber et al. [2005], the study of ferroelectric fatigue is of interest not only for ferroelectric heterostructures but also for piezoelectric microdevices.

The role of oxygen vacancies on the high frequency dielectric properties of epitaxial $(Ba_{0.5}Sr_{0.5})TiO_3$ thin films has been investigated by Kim et al. [2000]. Films with a high content of oxygen vacancies show a higher dielectric constant ($\varepsilon \sim 500$) and low dielectric loss ($\tan\delta \sim 0.02$). At high frequencies an increased number of oxygen vacancies enhances the total polarizability by increasing the number of defect dipoles [Park and Chadi, 1997].

The influence of the motion of oxygen vacancies on the dielectric response in PLD (Ba, Sr)TiO_3 was reported by Saha and Krupanidhi [2000]. The value of the activation energy (about 1 eV) for the oxygen vacancies within the film was found from Arrhenius plots of both alternating and direct current (AC and DC) conductivities in reciprocal Torrs.

20.3.1.5 Orientation Dependence

Dielectric, ferroelectric, and piezoelectric properties of thin films depend on the film orientation. A recent review of experimental results showing this dependence can be found in Craciun et al. [2002].

Optimal ferroelectric properties of $Bi_{3.25}La_{0.75}Ti_{0.3}O_{12}$ of uniform *a*-axis orientation on Si substrates have been reported by Lee et al. (remanent polarization of about 32 $\mu C/cm^2$) [Lee et al.,

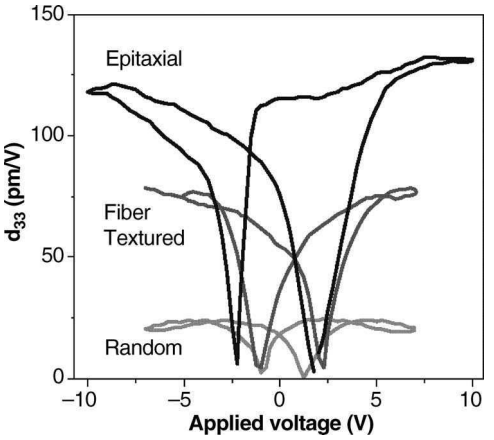

Figure 20.11 The influence of film orientation on the piezoelectric properties of PZT thin films. Reprinted from Ramesh and Schlom [2002], with permission.

2002b; Lee and Hesse, 2002]. The *c*-axis-oriented films, which are much easier to grow, have a negligible polarization component along the film normal, since the vector of the major spontaneous polarization is along the *a*-axis. The orientation dependence of ferroelectric properties and fatigue behavior in $Pb(Yb_{1/2}Nb_{1/2})O_3$–$PbTiO_3$ with 40%PT and 50%PT have also been reported by Bornand and Trolier-McKinstry [Bornard and Trolier-McKinstry, 2000; Bornard et al., 2000].

Figure 20.11 shows the importance of film orientation on the piezoelectric properties of PZT. Epitaxial films show a d_{33} piezoelectric coefficient of about twice that of fiber textured, and six times higher than in randomly oriented films [Ramesh and Schlom, 2002]. Recent papers [Ouyang et al., 2004, 2005] showed the importance of orientation for clamped ferroelectric films. The intrinsic effective piezoelectric coefficient e_{31} has been numerically evaluated for PZT films with different compositions and orientations. Thus it has been found that for a rhombohedral PZT film e_{31} is maximized for the orientation (001) rotated 54.7° away from the polar direction [111], while for a tetragonal film this happens along the polar direction (001) [Ouyang et al., 2005].

A study of orientation effect on nanoscale polarization and dielectric and piezoelectric properties was reported in [Kim et al., 2005]. $BaTiO_3$ (BT) thin films have been deposited by PLD on Pt and LSCO/Pt electrodes. BT films grown on Pt exhibited highly (101) preferred orientation with higher in-plane polarization components, whereas films grown on LSCO/Pt showed (001) and (101) orientations with higher out-of-plane polarizations. The measured dielectric constant and piezoelectric d_{33} constant were 570 and 14.3 pm/V for the former and 1000 and 54 pm/V, for the latter, respectively.

In relaxor ferroelectric thin films the orientation is crucial for obtaining electromechanical and piezoelectric properties similar to those of single crystals, where the best properties are obtained along the (001) direction for rhombohedral compositions. Electrical properties approaching those of bulk single crystals have been reported in Maria et al. [1998] for epitaxial (001) PMN-PT 70/30 grown on SRO/LAO substrates by PLD.

20.3.2 Finite Size Effects

Variations in critical temperature, polarization, and related properties with respect to the corresponding bulk values have been found in ferroelectric piezoelectrics, especially when the grain size is decreased to a few tens of nanometers. The understanding of finite size effects is essential since they ultimately limit the miniaturization of devices based on these materials. The critical size below which the ferroelectric state becomes unstable has been determined by increasingly precise methods. Surface or

interface effects should strongly affect polarization stability in nanosized ferroelectrics since the translational invariance of the system is broken on the surface and the local symmetry and behavior of soft modes is changed. In Li et al. [1997] mean-field theory was used to examine ferroelectric phase instability in perovskite ferroelectrics. A critical thickness of 4 nm for $PbTiO_3$ and 8 nm for $Pb(Zr_{0.5}Ti_{0.5})O_3$ was predicted. Experimental results have confirmed the existence of grain size effects in ferroelectric materials (see references in Craciun et al. [2002]).

Over the past years many studies on size effects in piezoelectric films have also been performed [Keijser et al., 1991; Glinchuk et al., 2003; Nagarajan et al., 1999b; Tybell et al., 1999; Roytburd et al., 2000; Tuttle et al., 1995; Waser, 1997; Wu et al., 2005b]. They include not only crystallite size but also film thickness effects. The most frequent finite size effects are variation of lattice parameters, changes in ferroelectric domain configuration, phase transition type, and critical temperature. It has been shown by Chattopadhyay et al. [1998] that *c*-axis-oriented films of the antiferroelectric $PbZrO_3$ deposited on Si by PLD have antiferroelectric behavior for films with thicknesses greater than 300 nm, and an apparent ferroelectric behavior when thinner than 300 nm. The ferroelectric parameters of, for example, 260-nm-thick films were spontaneous polarization $P_s = 31\,\mu C/cm^2$, coercive field $E_c = 100\,kV/cm$, and remanent polarization $P_r = 23\,\mu C/cm^2$. Moreover, often the quality of grain boundaries, porosity, or presence of segregated phases will also influence physical (especially electrical) properties.

Recently,Wu et al. [2005b] found essential differences between ferroelectric properties of ultrathin films and bulk crystal. By using a first-principle-based approach, the strain–temperature phase diagram of $Pb(Zr_{0.5}Ti_{0.5})O_3$ with a thickness of four unit cells was investigated. A rich variety of ferroelectric phases was found, including monoclinic phases and a vortex stripe domain forbidden in the bulk crystal.

A systematic investigation of thickness size effects in epitaxial *c*-axis-oriented $PbZr_{0.2}Ti_{0.8}O_3$ grown on SRO/STO substrates with thicknesses varying from 80 to 4 nm has been reported in Nagarajan et al. [2004]. It has been found that down to 15 nm there is no observable drop in the switchable polarization, while below 15 nm it progressively decreases to approximately $11\,\mu C/cm^2$ for the 4-nm film.

A search for critical thickness of $BaTiO_3$ films is presented in Kim et al. [2005b]. Ultrathin films with thicknesses ranging betweem 30 and 3 nm have been epitaxially grown by KrF-PLD as fully strained SRO/BT/SRO heterostructures on STO substrates. Ferroelectricity has been proved for films thicker than 5 nm by measuring polarization versus electric field hysteresis loops. Phase diagrams of epitaxial $BaTiO_3$ ultrathin films obtained from first-principles calculations are presented in Lai et al. [2005].

Grain size effects have been found to influence the piezoelectric coefficient of PMN-PT 90/10 thin films deposited by PLD on LSCO/Pt/Ti/SiO_2/Si(100) substrates [Shvartsman et al., 2002]. The piezoelectric d_{33} coefficient was locally measured by SFM, from piezoelectric hysteresis loops acquired in the interior of grains of different sizes. Small grains (about 100 nm) exhibit low d_{33} values, whereas relatively strong piezoelectric activity was found in larger grains.

20.3.3 Domain-Wall Pinning and Relaxation

The field dependence of the permittivity and piezoelectric properties in ferroelectric thin films at low fields has been analyzed with the Rayleigh model of domain-wall dynamics [Damjanovic, 1998; Damjanovic and Robert, 2002]. It has been found that the dielectric permittivity of PZT thin films [Taylor and Damjanovic, 1997] shows a linear dependence on the AC field amplitude, which was attributed to the pinning of domain walls on randomly distributed defects.

Figure 20.12 shows the frequency dependence of the dielectric constant for (001 + 110)-oriented PMN-PT (68/32) and 0.58 ($PbSc_{1/2}Nb_{1/2}O_3$)–0.42 PT (PSN-PT 58/42) grown by PLD on LSCO/MgO(100) [Tyunina et al., 1999], to a film thickness of 250 nm. For PMN-PT the dielectric constant shows an almost linear decrease with the logarithm of frequency between 100 Hz and 100 kHz, followed by a sudden decrease.

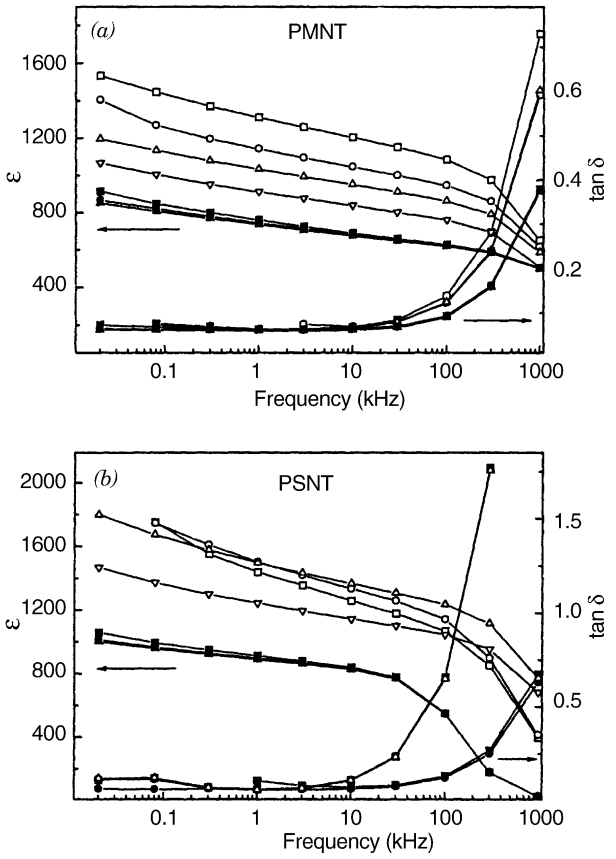

Figure 20.12 Dependence of dielectric constant and loss on frequency for a PMN-PT 68/32 (upper graph) and a PSN-PT 58/42 thin film. Reprinted with permission from Tyunina et al. [1999], © 1999, American Institute of Physics.

A similar dependence was reported also in Craciun et al. [2005] for relaxor PLZT 22/20/80 thin films grown by RF-PLD on Pt/Si. While in ferroelectrics the linear decrease of the permittivity with the logarithm of field frequency was attributed to domain-wall pinning processes [Taylor and Damjanovic, 1997], in relaxors it has been shown that a logarithmic decay with frequency of the dielectric constant is obtained with a uniform distribution of the relaxation times [Kamba et al., 2000]. Indeed a wide distribution of relaxation times is the typical feature of relaxor dynamics.

Ferroelectric aging has been also observed in ferroelectric thin films [Grossmann et al., 2002, and references therein]. It is suggested that the mechanism responsible for the logarithmic time decrease of permittivity in ferroelectric thin films is different from that found in bulk ferroelectrics, where oriented defect dipoles clamp the domain walls in their current position and, hence, lead to a reduction of the domain-wall mobility contribution to the dielectric constant. In $PbZr_{0.3}Ti_{0.7}O_3$ thin films doped with different concentrations of Fe-acceptor or Nb-donor dopant additions, the time decrease of permittivity is related to the interfacial capacitance decreasing in time, due to a temperature-activated increase of the thickness of the surface layer.

Polarization relaxation in ferroelectric thin films has been investigated by Ganpule et al. [2000b] in epitaxial 400-nm-thick $PbZr_{0.2}Ti_{0.8}O_3$ films grown on a LSCO/(001)STO substrate. Piezo-response images of the surface of the PZT film evidenced the presence of long, needlelike orthogonal structures that have been identified to be 90° twin domains that formed to relax the misfit

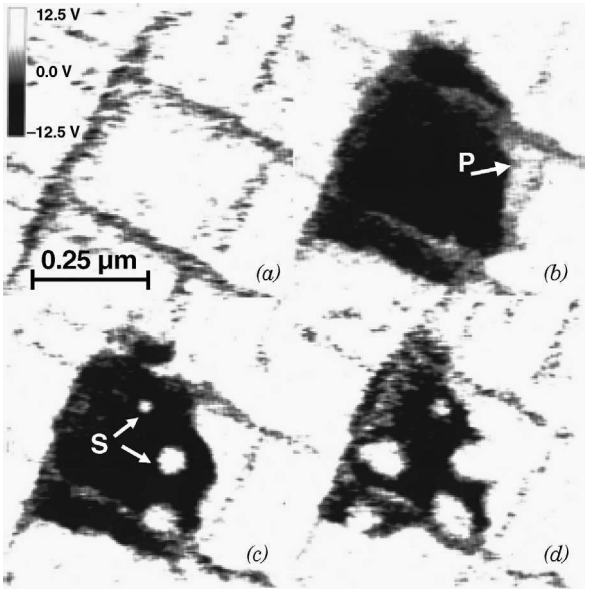

Figure 20.13 Piezoresponse scan of a 200 × 200 nm area in $PbZr_{0.2}Ti_{0.8}O_3$ thin film that was switched into the opposite polarization. Figures (b)–(d) illustrate the spontaneous reversal of polarization within this region after wait times of (b) 2.8×10^3, (c) 5.7×10^3, and (d) 1.8×10^4 s. Reprinted with permission from Ganpule et al. [2000b], © 2000, American Institute of Physics.

and thermal strains. The relaxation kinetics have been investigated by switching a 3-μm × 3-μm area of the sample from its original state to the reversed state and by recording piezoresponse images as a function of time, from a few minutes to several days. The observations made on a 200-nm × 200-nm cell (Fig. 20.13) showed an initial time period t_0 (about 1 h) for the nucleation of the first reversed domain. During this time, there was no measurable evidence of reversal in the investigated area. As the relaxation proceeded, other secondary nuclei were formed (Fig. 20.13c) and ultimately coalesced with the primary nuclei (Fig. 20.13d). Figure 20.14 plots the fraction of the

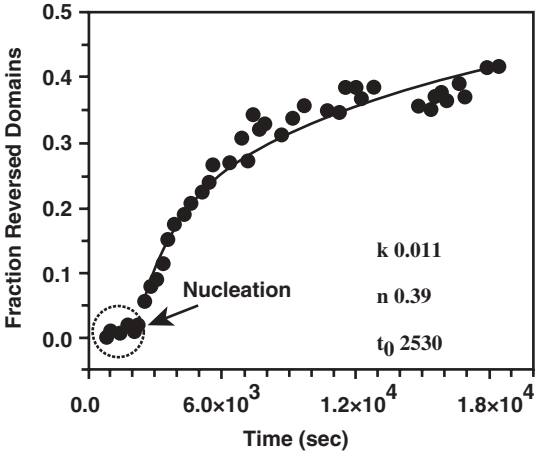

Figure 20.14 Fraction of reversed domains vs. time for the same area shown in Figure 20.13. Reprinted with permission from Ganpule et al. [2000b], © 2000, American Institute of Physics.

reversed region f as a function of time t. The best data fit was obtained with a stretched exponential law $f = 1 - e^{-k(t-t_0)^n}$, with parameters $t_0 = 2530$ s, $k = 0.011$, and $n = 0.39$. Stretched exponential relaxation phenomena are observed in many materials including magnetic spin glasses and ferroelectric relaxors. A possible explanation in the case of ferroelectric PZT thin films is related to the transport of point defects to and away from domain surfaces [Ganpule et al., 2000b].

Local piezoresponse force microscopy (PFM) has been employed to study the relaxation of the induced d_{33} piezoelectric coefficient in 250-nm-thick epitaxial relaxor PMN thin films grown on (001)LSCO/(001)MgO [Shvartsman et al., 2005]. Without a DC bias, no piezoelectric activity was measured, while applying DC voltage pulses of sufficiently large magnitude produced ferroelectric-like order and hysteresis. By applying short voltage pulses of 1.5–2 V, a reorientation of the polar clusters and their subsequent corsening was obtained. After removing the field, the piezoresponse slowly relaxed, probably due to the thermally activated breakup of grown domains. The relaxation of the induced piezoresponse was found to be a two-stage process with the kinetics governed by the Kohlrausch–Williams–Watt type of dependence [Shvartsman et al., 2005, and references therein].

20.4 APPLICATIONS

Piezoelectric thin films have a wide range of applications that are continually extended to new devices. Mature fields are high-frequency (HF) devices (resonators, filters, etc.) for telecommunication systems, where low-loss nonferroelectric piezoelectric thin films like ZnO and AlN are mostly employed, and MEMS, generally based on highly efficient ferroelectric piezoelectric films.

Applications that exclusively involve the ferroelectric properties, such as ferroelectric memories, are not discussed here (for a review article see Scott [1998]). Furthermore, tunable ferroelectric microwave devices, based on the field dependence of permittivity, are also not included (see Chapter 21 for more on these topic areas). Many of the listed applications have been based on piezoelectric thin films grown by other methods. Nevertheless they have been presented since they can equally well be fabricated via PLD.

20.4.1 Microelectronic Devices

These devices are employed in a wide range of telecommunication applications. The requirement for higher transmission data rates imposes the need for systems with wider transmission bandwidths and higher frequencies and reflects a strong developmental requirement for high-frequency devices based on thin piezoelectric films. One of the most developed field is wireless networks in the spectrum from 0.5 to 6 GHz (mobile phones, satellite communication, navigation), where there is an increasing need for high-performance frequency control devices such as front-end filters that protect receivers from adjacent channel interference [Lakin, 1999]. The required bandwidth amounts typically to 2–4% of the carrier frequency. Review articles on these applications can be found in the literature [Lakin, 1999; Muralt and Lanz, 2002].

20.4.1.1 Surface Acoustic Wave (SAW) Devices

Most devices (filters, resonators, delay lines, etc.) are based on surface acoustic waves that are excited by means of interdigital electrodes (IDT). The wave propagates to a second IDT, where it is partially reconverted into an electrical signal. The periodicity of the IDT must correspond to the wavelength. A wide range of SAW devices are produced commercially [Krishnaswami et al., 1993]: intermediate frequency (IF) filters for TV receivers, delay line tunable oscillators for mobile radio, bandpass filters, programmable tapped delay lines for radar applications, correlators, acoustooptic devices, and the like. Applications of SAW devices are limited below 5 GHz since at high

frequencies the strip widths required in transducers are very narrow (below 1 μm), which causes fabrication problems.

Various SAW filters have been constructed for different applications and some of the references include Ieki and Kadota [1999] and Tomabechi et al. [1999]. For example, filters reported in Ieki and Kadota [1999] are based on the Sezawa wave on a ZnO/sapphire substrate combination, due to the low loss. Epitaxial ZnO films with thickness of about 1 μm were grown by RF planar magnetron sputtering. The SAW filters produced had low insertion loss and are compatible with mass production. These devices, produced by Murata (Japan), are used in the following applications: front-end filters of receiving circuits in Japanese digital cellular PDC1500 handsets, filters for GPS receivers, filters for mobile satellite communications, and so forth.

Recently, high-quality ferroelectric thin films such as PZT have been grown epitaxially on different substrates, thus allowing their use in high-frequency devices. A nonconventional SAW device based on piezoelectric transducers consisting of a series of ferroelectric domains with alternating polarization states was realized using high-quality epitaxial $Pb(Zr_{0.2}Ti_{0.8})O_3$ grown by off-axis magnetron sputtering on metallic (001) Nb-doped STO substrates [Kumar et al., 2004]. The artificial modification of the ferroelectric domain structure was performed by using an atomic force microscope tip as a source of electric field, allowing local switching of the polarization. SAW devices with central frequencies in the range 1.50–3.50 GHz have been obtained with a modulation wavelength of polarization of 1.2 and 0.8 μm.

20.4.1.2 Bulk Acoustic Wave (BAW) Devices

In the past years a considerable effort has been directed toward BAW resonators [Krishnaswami et al., 1993]. In these devices the resonant frequency is related to the longitudinal wave velocity and to the thickness of the piezoelectric film and frequencies as high as 10 GHz have been obtained. As thin films are grown on substrates, an ultrasonic wave excited in the piezoelectric thin film is not totally reflected at the film–substrate interface, but partially propagates in the substrate and only a certain fraction of mechanical energy is reconverted into the electrical signal. This can be prevented by etching the substrate locally below the film, thus obtaining quasi-free-standing resonators called thin-film bulk acoustic resonators (TFBAR). A second method consists of applying an acoustic reflector to send the acoustic power back into the piezoelectric thin film. This device is called a solidly mounted resonator (SMR). The reflector consists of a set of quarter-wave layers of alternating high and low acoustic impedance materials. Such BAW resonators are produced by several companies. The most suitable materials used in SAW and BAW devices are AlN and ZnO. A summary of their relevant properties for these applications is given in Table 20.2 [Lakin, 1999]

Different types of BAW resonators (SMR and TFBAR) based on RF-sputtered AlN thin films have been reported by Dubois and Muralt [Dubois and Muralt, 1999; Dubois et al., 1999]. The acoustic isolation from the substrate was achieved by micromachining an air gap on the backside of

TABLE 20.2 Summary of AlN and ZnO Thin Films Properties Relevant to Filter Bandwith Applications

Property	AlN	ZnO
Velocity (m/s)	11300	6080
K^2, piezoelectric coupling coefficient (bulk value) (%)	6.5	8.5
K^2_{eff}, effective coupling coefficient (film value) (%)	6	7.5
Temperature coefficient, frequency (ppm/°C)	−25	−60
Temperature coefficient, SMR	−20	−48
Required filter bandwith (MHz)	64.3	70.3
Required filter bandwith (%)	3.42	3.74

Reprinted with permission from Lakin [1999], © 1999 IEEE.

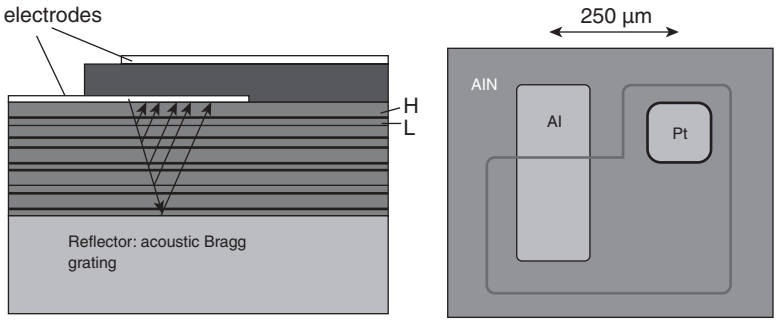

Figure 20.15 A schematic drawing of the cross section of a SMR device (left) and a top view. Reprinted with permission from IEEE. From Muralt and Lanz [2002], Setter [2002], and Dubois et al. [1999].

the resonating structure or alternatively by a set of $\lambda/4$ thick layers between resonator film and the substrate to serve as an acoustic reflector. The reflector stack of the SMR consisted of five pairs of AlN and SiO_2 layers. A schematic drawing and a top view of the SMR device is shown in Figure 20.15. Its fundamental frequency was 2.4 GHz.

The structure of a TFBAR device is shown in Figure 20.16. The fundamental frequency of the resonator was 3.6 GHz, and the temperature coefficient of frequency was very small. This type of resonator is suitable for production of acoustic filters for wireless communication devices.

The construction of TFBARs based on ZnO thin films has been reported in Osbond et al. [1999], with a resonant frequency of about 2 GHz. The design of a passband ladder filter, based on TFBAR elements connected in series and parallel, was also presented.

Bulk acoustic wave transducers based on PLD-deposited ZnO films have been reported in Verardi and Dinescu [1995], with resonant frequencies of 1.9 and 2.9 GHz. Small conversion losses and high coupling coefficient have been obtained. Other BAW devices based on PLT thin films have been proposed by Yamada et al. [1999], and devices operating at 1.4 and 2 GHz with effective coupling coefficients of 11 and 9.4 %, respectively, have been reported.

The possibility of the use of PZT thin films in the ultra-high-frequency (UHF) range has also been demonstrated [Hanajima et al., 1997]. BAW membrane transducers were constructed by employing PZT thin films obtained by the sol–gel technique on Pt–Si substrates with subsequent micromachining. Transducers with a resonant frequency of 1.7 GHz and a high electromechanical coupling coefficient have been reported.

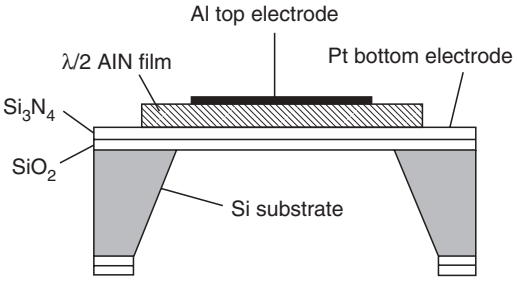

Figure 20.16 Schematic drawing of a TFBAR device. Reprinted with permission from Dubois and Muralt [1999], © 1999, American Institute of Physics.

20.4.2 Microelectromechanical Systems (MEMS)

One of the most important fields of applications of piezoelectric thin films is MEMS. These systems integrate electromechanical microdevices with microelectronics. An article that reviews the current state of integration and device fabrication of piezoelectric thin films, and especially of PZT, in MEMS can be found in Muralt et al. [2002]. Examples of MEMS based on piezoelectric materials are ultrasonic micromotors, linear microactuators, micropumps, transducers for ultrasound imaging, microaccelerometers, and the like. In MEMS working at frequencies up to a few megahertz, most materials used are ferroelectric, especially PZT thin films. Usually flexural structures are employed in order to amplify deflection and strain response. High-frequency applications in RF-MEMS employ piezoelectric thin films with very low losses in the 2- to 10-GHz range such as AlN and ZnO, even if they are less efficient in transduction, and they are based on standing bulk acoustic waves across the film thickness.

There are some problems related to the integration of piezoelectric/ferroelectric materials in MEMS. PLD offers the advantage of in situ growth of crystalline films at relatively low temperatures, with stoichiometric composition without postannealing treatments. Nevertheless PLD cannot be considered as a large-scale production technique for functional layers in MEMS, unless critical problems related to low-cost technology of piezoelectric thin films with reproducible and stable properties have been solved.

20.4.2.1 Ultrasonic Micromotors

Ultrasonic microactuators present various advantages, due to their small volume, flatness, and high torques at low speeds [Muralt et al., 2002; Muralt, 1999]. They are based on the conversion of a standing flexural wave excited in a thin silicon membrane (stator) by a piezoelectric thin film, into a rotation by a rotor that has tilted elastic legs or fins. A schematic design of a device described in Muralt et al. [1995] is shown in Figure 20.17. The rotor moves inside the etched cavity to release the compression produced by the stator deflection on the elastic fins and transmitted through friction (see the enlarged part in the inset in Fig. 20.17). When the membrane moves toward the fins, these are bent but do not slip because of frictional forces, so the rotor turns in order to release the compression; when the membrane moves away from the fins, these are decompressed and free to glide, following the rotor. The membrane of the stator was obtained by silicon bulk micromachining. The active layer is a PZT thin film of thickness 1 μm obtained by sol–gel chemical solution deposition. The silicon membrane was about 50 μm. In comparison with electrostatic micromotors, ultrasonic motors need about 30 times less voltage for the same torque, support normal loads, and

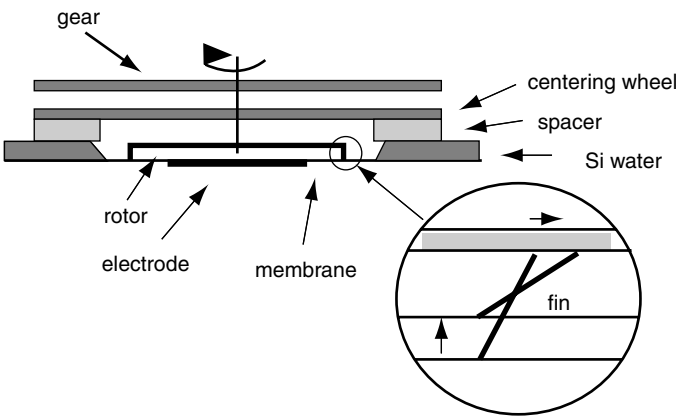

Figure 20.17 Construction of an ultrasonic micromotor. Reprinted from Muralt et al. [1995], © 1995, with permission from Elsevier.

have a flat profile. Therefore ultrasonic micromotors show attractive features for different applications as, for example, in wristwatches.

20.4.2.2 Bimorph Microactuators

The construction of a low-voltage cantilever bimorph actuator has been reported by Lappalainen et al. [1995]. The bimorph actuator structure consists of a bending Si cantilever (50 μm thick) on which Pt electrodes and Nd-doped PZT layers have been deposited by PLD. This device can be employed in many actuator applications where accurate positioning is needed. Moreover, it can be used as a motion sensor or accelerometer in hydrophones and the like. A similar device has been realized by Gaucher et al. [1998].

20.4.2.3 Microvalve Matrix Using Piezoelectric Actuators

A microvalve matrix for gas flow control, based on a PZT thin film, was proposed by Watanabe and Kuwano [1997]. This device is based on a large number of microvalves integrated on the same small area. Each microvalve can be open or closed via the piezoelectric effect by a controller and can handle a very small gas flow. While generally microsystems have relatively large error, the proposed microvalve matrix can control gas flow very precisely in very small steps over the range from zero flow to fully open flow by digitally opening and closing the appropriate number of valves.

20.4.2.4 Imaging Microtransducer Arrays

Different MEMS applications of piezoelectric films with ferroelectric properties have been demonstrated in Xu et al. [2000]. Megahertz-range two-dimensional transducer arrays for miniaturized, high-resolution acoustic imaging have been developed. Potential applications of these devices include hand-held diver's sonar, medical ultrasound imaging, and nondestructive testing. The two-dimensional arrays with a resonant frequency at 0.8 MHz were fabricated using PZT thin films deposited by the sol–gel technique on Pt-buffered Si wafers. By silicon micromachining technology an array of 8×8 transducers can be made in an area of about $14.5 \times 14.5\,\text{mm}^2$, with nine such arrays in one wafer, being thus cost effective for mass production. An acoustic lens using such a design has been produced by Cosmo Optics Inc. (U.S.A.).

20.4.2.5 Microelectromechanical Systems for Blood Testers

A microelectromechanical blood tester based on SAW was described by Uchino [2002]. PZT thin films are deposited on a silicon wafer that is then micromachined to leave a membrane for fabricating MEMS. Figure 20.18 illustrates a blood tester developed by Uchino in collaboration with Omron Corporation (Japan). Applying a voltage to two surface interdigital electrodes, the PZT film

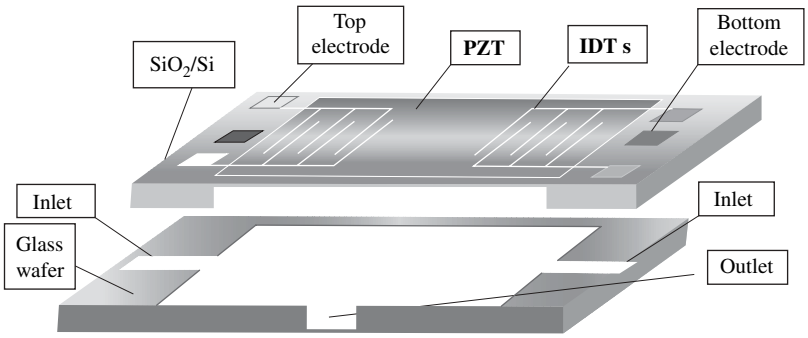

Figure 20.18 Structure of a PZT/silicon MEMS blood tester device. Reprinted with permission from Uchino [2002].

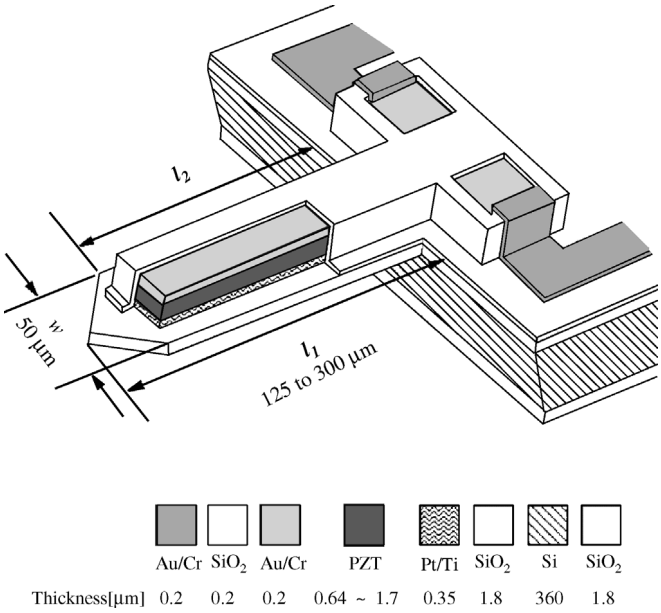

Figure 20.19 Schematic drawing of a piezoelectric force sensor based on a PZT thin layer. Reprinted with permission from Lee et al. [1997], © 1997, American Institute of Physics.

generates surface membrane waves that soak up blood and the test chemicals from the two inlets, then mix them in the center part, and send the mixture to the monitor part through the outlet.

20.4.2.6 Scanning Force Microscopy Microcantilever

A piezoelectric force-sensing microcantilever for use in dynamic scanning force microscopy (SFM), based on a PZT thin film, was reported in Lee et al. [1997]. This device overcomes the inconvenience of the external optical sensing of cantilever deflection and thus allows the development of miniaturized stand-alone SFMs. Among other force sensors (piezoresistive and capacitive), the piezoelectric cantilever is the most appropriate for dynamic SFM since it can be excited by an applied AC voltage without disturbing the sensing. Moreover, it can perform both the actuation of z-axis tip-sample separation as well as the self-force sensing, while the other two sensors must be combined with the z-axis displacement actuator.

A schematic drawing of the piezoelectric force sensor based on PZT thin films, obtained by the micromachining technique, is shown in Figure 20.19. The resonant frequency of the cantilever was about 180 kHz for a cantilever length of about 125 μm. The PZT film was obtained by sol–gel deposition with a thickness of about 1 μm. The sensitivity was about 1 fC/m, a value 4.5 times larger than the sensitivity of ZnO force sensors.

Applications of PZT thin films in a self-oscillating piezoelectric cantilever used in high-vacuum SFM has been reported in Chu et al. [1997].

20.4.2.7 Pulse Wave Sensor

Flexible pulse wave sensors based on AlN piezoelectric thin films were proposed by Akiyama et al. [2003]. These are more suitable than traditional pulse wave sensors for use in preventive medicine (e.g., hypertension and cardiac failure risk) because they do not need direct contact on an arm and thus can be used for long-term continuous monitoring. Figure 20.20 shows a sketch of the sensor made of AlN layers of thickness 1 μm deposited by RF sputtering on aluminum foils of 16 μm.

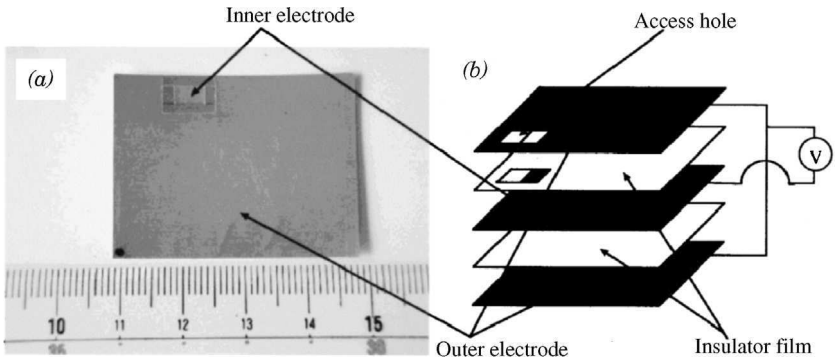

Figure 20.20 Photograph of the pulse wave sensor based on AlN thin film (left) and a schematic diagram of sensor structure. Reprinted with permission from Akiyama et al. [2003], © 2003, American Institute of Physics.

The AlN layer is columnar and oriented with the c-axis perpendicular to the substrate. Due to the double AlN layer the sensor generates twice the electric charge in comparison to a single layer. The testing revealed a linear response with pressure over the frequency range 0.1 to 100 Hz. The sensor sensitively responded to the pulse wave form and detected four kinds of waves which are important for pulse diagnosis. Moreover the sensor allows automatic measurement of pulsed waves and long term monitoring is made simpler by the use of this device.

20.4.2.8 Integrated Acoustic Emission Sensors

Piezoelectric microsensors for integrated diagnostics of acoustic emission sensing of crack propagation are based on piezoelectric thin films integrated on silicon with amplification, signal processing, and telemetry circuits.

The majority of the devices detecting acoustic emission (AE) are based on bulk AE sensors. Acoustic emission from crack propagation in material leads to sound waves that are sensed by the piezoelectric sensor. Despite their high potential use (including aircraft testing for microcrack growth due to stress of materials), there are only a few works reporting integrated AE microsensors based on thin films [Polla and Francis, 1996; Cho et al., 1999]. Good results have been reported for AE microsensors based on PZT films, which showed a faster rise time and shorter ring-down than commercial sensors [Cho et al., 1999].

20.4.2.9 Surface Acoustic Wave Sensors

Surface acoustic wave sensors are based on the sensitivity of the SAW velocity to changes in substrate density, stiffness, temperature, electrical conductivity, and the like. A variation of velocity induces a variation in the delay time between delay line transducers or a shift in the resonance frequency of a SAW resonator. SAW resonator sensors have been employed in SAW vapor sensors used to detect a wide variety of vapors: water, ethanol, SO_2, H_2, NO_2, NH_3, H_2S, HCl, hydrocarbon compounds, organophosphorous compounds, and the like at very low concentrations [Krishnaswami et al., 1993]. The SAW resonator sensors trap acoustic energy between reflecting grids. A chemically sensitive film in the trapped-wave area can be made to be selective to a certain type of gas or vapor and, consequently, changes the resonant frequency of the device.

A SAW device for gas-sensing applications, entirely fabricated by PLD, has been reported in Verardi et al. [2002]. The device consists of a delay line formed by two interdigital SAW transducers realized on ZnO films, deposited by PLD on Si or ST–quartz substrates. Pt/Ni and Pd/Ni metallic membranes with 1–3% at. Ni content have been deposited by alternative laser ablation of high purity Pt, Pd, and Ni target on the space between the two IDT transducers. The deposited membranes have been used as sensitive elements in gas sensor devices and a compact test device was constructed. Other specific applications have been discussed in a review article [Krishnaswami et al., 1993].

20.4.2.10 Dynamical Deformation Sensor

Modern sensors of mechanical quantities (deformation, stress, velocity, acceleration, etc.) use piezoelectric thin films as active elements. In Surowiak et al. [1995] the use of a PZT thin film was demonstrated in two types of sensors: isotropic sensors characterized by a signal proportional to the sum of the main components of the deformation sensor and anisotropic sensors of dynamical deformation. The PZT film was obtained by RF sputtering on stainless steel. The isotropic sensors were essentially small capacitors, while the anisotropic sensors were based on IDT transducers deposited on the ferroelectric film. The stability of the sensors under different conditions of deformation and temperature was tested up to about 70°C.

20.5 CONCLUSIONS AND FUTURE PERSPECTIVES

Pulsed laser deposition has been found to be an attractive technique for growth of thin films with piezoelectric properties. Its efficiency was demonstrated mainly for compounds with complicated stoichiometry, where the transfer of the composition from target to the films can be easily achieved even at low substrate temperatures. Using multitarget systems, it is possible to deposit complex heterostructures without successive heating processes that can induce cracks and interface damage because of different thermal expansion coefficients of the materials used. The association of PLD with other techniques expands further its capabilities. The incorporation of oxygen in many cases (or nitrogen) can be improved by a radio frequency discharge addition, which increases the reactivity by creating excited and ionized species. A similar effect can be obtained by UV lamp in situ irradiation. New lead-free piezoelectric materials have been deposited in thin-film format using PLD. ''Multisample'' approaches based on the principles of combinatorial materials technology have been introduced to more quickly determine ideal growth conditions for new materials. In the last few years many groups have reported the successful PLD growth of all-epitaxial heterostructures including piezoelectric thin films and different combinations of electrodes, buffer layers, and substrates. This opens a large area of applications of PLD in the fabrication of modern microdevices based on piezoelectric thin films.

REFERENCES

Adachi, Y., Su, D., Muralt, P., and Setter, N. (2005), *Appl. Phys. Lett*. **86**, 172904-1-3.

Afonso, C. N., Gonzalo, J., Vega, F., Dieguez, E., Wong, J. C. C., Ortega, C., Siejka, J., and Amsel G. (1995), *Appl. Phys. Lett*. **66**, 1452–1455.

Aggarwal, S., Perusse, S. R., Nagaraj, B., and Ramesh, R. (1999), *Appl. Phys. Lett*. **74**, 3023–3026.

Akiyama, M., Ueno, N., Nonaka, K., and Tateyama, H. (2003), *Appl. Phys. Lett*. **82**, 1977–1979.

Alpay, S. P. (2002), ''Twinning in Ferroelectric Thin Films: Theory and Structural Analysis,'' in *Handbook of Thin Film Materials*, Vol. 3: *Ferroelectric and Dielectric Thin Films*, H. S. Nalwa (Ed.), Academic, San Diego, pp. 517–543.

Alpay, S. P., and Roytburd, A. L. (1998), *J. Appl. Phys*. **83**, 4714–4719.

Auciello, O., Manteze, L., Duarte, J., Chen, X., Rou, S. H., Kingon, A. I., Schreiner, A. F., and Kraus, A. R. (1993), *J. Appl. Phys*. **73**, 5197–5204.

Bai, F., Zheng, H., Cao, H., Cross, L. E., Ramesh. R., Li, J., and Viehland, D. (2004), *Appl. Phys. Lett*. **85**, 4109–4111.

Bandaru, J., Sands, T., and Tsakalakos, L. (1998), *J. Appl. Phys*. **84**, 1121–1128.

Bao, D., Lee, S. K., Zhu, X., Alexe, M., and Hesse D. (2005), *Appl. Phys. Lett*. **86**, 082906.

Bharadwaja, S. S. N., and Krupanidhi, S. B. (2000), *Appl. Phys. Lett*. **77**, 4208–4210.

Bornard, V., and Trolier-McKinstry, S. (2000), *J. Appl. Phys*. **87**, 3958–3964.

Bornard, V., Trolier-McKinstry, S., Takemura, K., and Randall, C. A. (2000), *J. Appl. Phys*. **87**, 3965–3972.

Brazier, M., McElfresh, M., and Mansour, S. (1998), *Appl. Phys. Lett*., **72**, 1121–1124.

Brazier, M., McElfresh, M., and Mansour, S. (1999), *Appl. Phys. Lett*., **74**, 299–301.

Canulescu, S., Dinescu, G., Epurescu, G., Matei, D. G., Grigoriu, C., Craciun, F., Verardi, P., and Dinescu, M. (2004), *Mater. Sci. Eng. B* **109**, 160–166.

Catalan, G., Corbett, M. H., Bowman, R. M., and Gregg, J. M. (1999), *Appl. Phys. Lett*. **74**, 3035–3037.

Chaos, J. A., Dreyfus, R. W., Perea, A., Serna, R., Gonzalo, J., and Afonso, C. N. (2000), *Appl. Phys. Lett*. **76**, 649–652.

Chattopadhyay, S., Ayyub, P., Palkar, V. R., Multani, M. S., Pai, S. P., Purandare, S. C., and Pinto, R. (1998), *J. Appl. Phys*. **83**, 7808–7812.

Cheng, H. W., Zhang, X. J., Zhang, S. T., Feng, Y., Chen, Y. F., Liu, Z. G., and Cheng, G. X. (2004), *Appl. Phys. Lett*. **85**, 2319–2321.

Chiang, Y. M., Farrey, G. W., and Soukhojak, A. N. (1998), *Appl. Phys. Lett*. **73**, 3683–3685.

Cho, C. R., and Grishin, A. (1999), *Appl. Phys. Lett*. **75**, 268–270.

Cho, C. R., and Grishin, A. (2000), *J. Appl. Phys*. **87**, 4439–4448.

Cho, J. H., and Park, K. C. (1999), *Appl. Phys. Lett*. **75**, 549–552.

Cho, C. R., Francis, L. F., and Jang, M. S. (1999), *Jpn. J. Appl. Phys*. **38** (P. 2), L751–L754.

Cho, C. R., Katardjev, I., Grishin, M., and Grishin, A. (2002), *Appl. Phys. Lett*. **80**, 3171–3173.

Chrisey, D. B., and Hubler, G. K. (Eds.) (1994), *Pulsed Laser Deposition of Thin Films*, Wiley, New York.

Christman, J. A., Kim, S. H., Maiwa, H., Maria, J. P., Rodriguez, B. J., Kingon, A. I., and Nemanich, R. J. (2000), *J. Appl. Phys*. **87**, 8031–8034.

Chu, J., Itoh, T., Lee, C., and Suga, T. (1997), *J. Vac. Sci. Tecnol. B* **15**, 1647–1651.

Colla, E. L., and Stolichnikov, I. (2003), in *Proceedings of POLECER Symposium on Polar Oxides. Properties, Characterization and Immaging*, Ed. R. Waser, U. Böttger, S. Tiedke, M. Garcia, and M. Heins, (Eds.), RWTH, Aachen, pp. 313–335.

Craciun, F., Verardi, P., Dinescu, M., Dinelli, F., and Kolosov, O. (1998), *Thin Solid Films* **336**, 281–285.

Craciun, F., Verardi, P., Dinescu, M., and Guidarelli, G. (1999), *Thin Solid Films* **343/344**, 90–93.

Craciun, F., Verardi, P., Dinescu, M., Mirenghi, L., and Dinelli, F. (2000), in *Piezoelectric Materials: Advances in Science, Technology and Applications*, C. Galassi, M. Dinescu, K. Uchino, and M. Sayer (Eds.), Kluwer Academic Publishers, Dordrecht, pp. 273–284.

Craciun, F., Verardi, P., and Dinescu, M. (2002), ''Piezoelectric Thin Films: Processing and Properties,'' in *Handbook of Thin Film Materials*, Vol. 3: *Ferroelectric and Dielectric Thin Films*, H.S. Nalwa (Ed.), Academic, San Diego, pp. 231–308.

Craciun, F., Verardi, P., Brodoceanu, D., Morar, M., Galassi, C., Grigoriu, C., and Dinescu, M. (2003), *Mater. Sci. Semiconductor Process.* **5**, 227–232.

Craciun, F., Dinescu, M., Verardi, P., Scarisoreanu, N., Galassi, C., and Piazza, D. (2004), *Ferroelectrics* **302**, 313–318.

Craciun, F., Dinescu, M., Verardi, P., Scarisoreanu, N., Moldovan, A., Purice, A., and Galassi, C. (2005a), *J. Eur. Ceram. Soc*. **25**, 2299–2303.

Craciun, F., Dinescu, M., Verardi, P., Scarisoreanu, N., Moldovan, A., Purice, A., and Galassi, C. (2005b), *Appl. Surf. Sci.* **248**, 329–333.

Damjanovic, D. (1998), *Rep. Prog. Phys*. **61**, 1267–1324.

Damjanovic, D., and Robert, G. (2002), in *Piezoelectric Materials in Devices*, N. Setter (Ed.), N. Setter, EPFL Swiss Federal Institute of Technology, Lausanne, pp. 353–388.

Demartin Maeder, M., and Damjanovic, D. (2002), in *Piezoelectric Materials in Devices*, N. Setter (Ed.), N. Setter, EPFL Swiss Federal Institute of Technology, Lausanne, pp. 389–412.

Dinescu, M., and Verardi, P. (1996), *Appl. Surf. Sci.* **106**, 149–153

Dinescu, G., Matei, D., Brodoceanu, D., Scarisoreanu, N., Morar, M., Verardi, P., Craciun, F., Toma, O., Pedarnig, J. D., and Dinescu, M. (2004), *Proc. SPIE* **5448**, 136–144.

Dinescu, M., Craciun, F., Scarisoreanu, N., Verardi, P., Moldovan, A., Purice, A., and Galassi, C. (2005), *Appl. Phys. A*, in press.

Dong, Z., Shen, M., and Cao, W. (2003), *Appl. Phys. Lett*. **82**, 1449–1451.

Donnelly, N. J., Catalan, G., Morres, C., Bowman, R. M., and Gregg, J. M. (2003), *J. Appl. Phys*. **93**, 9924–9929.

Du, H., Johnson, D. W., Jr., Zhu, W., Graebner, J. E., Kammlott, G. W., Jin, S., Rogers, J., Willett, R., and Fleming, R. M. (1999), *J. Appl. Phys*. **86**, 2220–2225.

Dubois, M. A., and Muralt, P. (1999), *Appl. Phys. Lett*. **74**, 3032–3034.

Dubois, M. A., Muralt, P., and Plessky V. (1999), *1999 IEEE Ultrason. Symp. Proc.*, 907–910.

Duclère, J.-R., Guilloux-Viry, Bouquet, V., Perrin, A., Cattan, E., Soyer, C., and Rèmiens, D. (2003), *Appl. Phys. Lett*. **83**, 5500–5502.

Fork, D. K., and Anderson, G. B. (1993), *Appl. Phys. Lett*. **63**, 1029–1032.

Fukuda, Y., Numata, K., Aoki, K., and Nishimura, A. (1996), *Jpn. J. Appl. Phys*. **35**, (P. 1), 5178–5183.

Ganpule, C. S., Nagarajan, V., Li, H., Ogale, A. S., Steinhauer, D. E., Aggarwal, S., Williams, E., Ramesh, R., and De Wolf, P. (2000a), *Appl. Phys. Lett*. **77**, 292–294.

Ganpule, C. S., Nagarajan, V., Ogale, S. B., Li, H., Roytburd, A. L., Williams, E. D., and Ramesh, R. (2000b), Appl. Phys. Lett. **77**, 3275–3277.

Garg, A., Barber, Z. H., Dawber, M., Scott, J. F., Snedden, A., and Lightfoot, P. (2003), *Appl. Phys. Lett*. **83**, 2414–2416.

Gaucher, P., Eichner, D., Hector, J., and Von Munch, W. (1998), *J. Phys. IV France* **8**, Pr9–235–Pr9–238.

Gerber, P., Kügeler, C., Ellerkmann, U., Schorn, P., Böttger, U., and Waser, R. (2005), *Appl. Phys. Lett*. **86**, 112908-1–112908-3.

Ghica, D., Ghica, C., Gartner, M., Nelea, V., Martin, C., Cavaleru, A., and Mihailescu, I. N. (1999), *Appl. Surf. Sci.* **138/139**, 617–621.

Glinchuk, M. D., Eliseev, E. A., Stepanovich, V. A., and Farhi, R. (2003), *J. Appl. Phys*. **93**, 1150–1159.

Goh, W. C., Yao, K., and Ong, C. K. (2005), *Appl. Phys. Lett*. **87**, 072906-1–072906-3.

Grossmann, M., Lohse, O., Bolten, D., Boettger, U., Schneller, T., and Waser, R. (2002), *Appl. Phys. Lett*. **80**, 1427–1429.

Gruverman, A., Kholkin, A., Kingon, A., and Tokumoto, H. (2001), *Appl. Phys. Lett*. **78**, 2751–2754.

Han, K. B., Jeon, C. H., Jhon, H. S., and Lee, S. Y. (2003), *Mater. Sci. Semiconductor Process.* **5**, 249–252.

Hanajima, N., Tsutsumi, S., Yonezawa, T., Hashimoto, K., Nanjo, R., and Yamaguchi, M. (1997), *Jpn. J. Appl. Phys*. **36** (P. 1), 6069–6072.

He, M., Cheng, N., Zhou, P., Okabe, H., and Halpern, J. B. (1998), *J. Vac. Sci. Technol*. **16**, 2372–2375.

Horwitz, J. S., Grabovski, K. S., Chrisey, D. B., and Leuchtner, R. E. (1991), *Appl. Phys. Lett*. **59**, 1565–1568.

Hu, W. S., Liu, Z. G., and Feng, D. (1996), *Appl. Phys. Lett*. **80**, 7089–7092.

Ieki, H., and Kadota, M. (1999), *Proc. 1999 IEEE Ultrasonics Symp.*, 281–289.

Iembo, A., Fuso, F., Allegrini, M., Arimondo, E., Beradi, V., Spinelli, N., Leccabue, F., Watts, B. E., Franco, G., and Chiorboli, G. (1993), *Appl. Phys. Lett*. **63**, 1194–1197.

Jagannadham, K., Sharma, A. K., Wei, Q., Kalyanraman, R., and Narayan, J. (1998), *J. Vac. Sci. Technol*. **A16**, 2804–2815.

James, A. R., and Prakash, C. (2004), *Appl. Phys. Lett*. **84**, 1165–1167.

Kaemmer, K., Franke, K., Holzapfel, B., Stephan, D., and Weihnacht, M. (1996), *Proc. 1996 IEEE Ultrasonics Symp*., 243–246.

Kamba, S., Bovtun, V., Petzelt, J., Rychetsky, I., Mizaras, R., Brilingas, A., Banys, J., Grigas, J., and Kosec, M. (2000), *J. Phys. Condens. Matter* **12**, 497–519.

Keijser, M. de, Dormans, G. J. M., van Veldhoven, P. J., and de Leeuw, D. M. (1991), *Appl. Phys. Lett*. **59**, 3556–3559.

Kim, W. J., Chang, W., Qadri, S. B., Pond, J. M., Kirchoefer, S. W., Chrisey, D. B., and Horwitz, J. S. (2000), *Appl. Phys. Lett.* **76**, 1185–1187.

Kim, C. S., Kim, S. K., and Lee, S. Y. (2003), *Mater. Sci. Semiconductor Process*. **5**, 93–96.

Kim, Y. K., Lee, K., and Baik, S. (2004a), *J. Appl. Phys*. **95**, 236–240.

Kim, Y. K., Kim, S. S., Shin, H., and Baik, S. (2004b), *Appl. Phys. Lett*. **84**, 5085–5087.

Kim, I. D., Avrahami, Y., Tuller, H. L., Park, Y. B., Dicken, M. J., and Atwater, H. A. (2005a), *Appl. Phys. Lett*. **86**, 192907-1–192907-3.

Kim, Y. S., Kim, D. H., Kim, J. D., Chang, Y. J., Noh, T. W., Kong, J. H., Char, K., Park, Y. D., Bu, S. D., Yoon, J. G., and Chung, J. S. (2005b), *Appl. Phys. Lett*. **86**, 102907-1–192907-3.

Krishnaswami, S. V., McAvoy, B. R., and Francombe, M. H. (1993), "Thin Films in Microwave Acoustics," in *Physics of Thin Films*, vol. 17, M. H. Francombe and J. L. Vossen (Eds.), Academic, Boston, pp. 145–223.

Lakin, K. M. (1999), *Proc. 1999 IEEE Ultrasonics Symp*., 895–906.

Lai, B. K., Kornev, I. A., Bellaiche, L., and Salamo, G. J. (2005), *Appl. Phys. Lett*. **86**, 132904-1–132904-3.

Lappalainen, J., Franti, J., Moilanen, H., and Leppavuori, S. (1995), *Sensors Actuators A* **46-47**, 104–109.

Lee, K. S., and Baik, S. (2000), *J. Appl. Phys*. **87**, 8035–8038.

Lee, K., and Baik., S. (2005), *Appl. Phys. Lett*. **86**, 202901-1–202901-3.

Lee, H. N., and Hesse, D. (2002), *Appl. Phys. Lett*. **80**, 1040–1043.

Lee, S. H., Song, T. K., Noh, T. W., and Lee, J. H. (1995), *Appl. Phys. Lett*. **67**, 43–46.

Lee, C., Itoh, T., Maeda, R., and Suga, T. (1997), *Rev. Sci. Instrum*. **68**, 2091–2100.

Lee, K. S., Kim, Y. K., Baik, S., Kim, J., and Jung II, S. (2001), *Appl. Phys. Lett*. **79**, 2444–2446.

Lee, S. H., Jang, H. M., Sung, H. H., and Yi, H. (2002a), *Appl. Phys. Lett*. **81**, 2439–2441.

Lee, H. N., Hesse, D., Zakharov, N., and Gösele, U. (2002b), *Science* **296**, 2006–2009.

Lee, J. S., Kang., B. S., Lin, Y., Li, Y., and Jia, Q. X. (2004a), *Appl. Phys. Lett*. **85**, 2586–2588.

Lee, K., Kim, K., Kwon, S. J., and Baik, S. (2004b), *Appl. Phys. Lett*. **85**, 4711–4713.

Lee, E. S., Chung, H. W., Lim, S. H., and Lee, S. Y. (2005), *Appl. Phys. Lett*. **86**, 032903-1–032903-3.

Lefki, K., and Dormans, G. J. M. (1994), *J. Appl. Phys*. **76**, 1764–1767.

Levoska, J., Tyunina, M., Sternberg, A., and Leppavuori, S. (2000), *Appl. Phys. A Mater. Sci. Process*. **70**, 269–274.

Li, S., Eastman, J. A., Vetrone, J. M., Foster, C. M., Newnham, R. E., and Cross, L. E. (1997), *Jpn. J. Appl. Phys*. **36**, 5169–5174.

Li, Y. L., Choudry, S., Liu, Z. K., and Chen, L. Q. (2003), *Appl. Phys. Lett*. **83**, 1608–1610.

Li, J. H., Chen, L., Nagarajan, V., Ramesh, R., and Roytburd, A. L. (2004), *Appl. Phys. Lett*. **84**, 2626–2628.

Lines, M. E., and Glass, A. M. (1977), *Principles and Applications of Ferroelectrics and Related Materials*, Clarendon, Oxford.

Ma, C. S., Hau, S. K., Wong, K. H., Chan, P. W., and Choy, C. L. (1996), *Appl. Phys. Lett*. **69**, 2030–2033.

Ma, Z., Zavaliche, F., Chen, L., Ouyang, J., Melngailis, J., Roytburd, A. L., Vaithyanathan, V., Schlom, D. G., Zhao, T., and Ramesh, R. (2005), *Appl. Phys. Lett*. **87**, 072907-1–072907-3.

Maiwa, H., Iizawa, N., Togawa, D., Hayashi, T., Sakamoto, W., Yamada, M., and Hirano, S. I. (2003), *Appl. Phys. Lett*. **82**, 1760–1762.

Maria, J. P., Hackenberger, W., and Trolier-McKinstry, S. (1998), *J. Appl. Phys*. **84**, 5147–5154.

Marsh, A. M., Harkness, S. D., Qian, F., and Singh, R. K. (1993), *Appl. Phys. Lett*. **62**, 952–955.

Meinschien, S., Behme, G., Falk, F., and Stafast, H. (1999), *Appl. Phy. A* **69** (Suppl.), S683–S686.

Miller, S. L., Nasby, R. D., Schwank, J. R., Rodgers, M. S., and Dressendorfer, P. V. (1990), *J. Appl. Phys*. **68**, 6463–6471.

Muralt, P. (1999), *J. Electroceram.* **3**(2), 143–150.

Muralt, P., and Lanz, R. (2002), in *Piezoelectric Materials in Devices*, N. Setter (Ed.), N. Setter, EPFL Swiss Federal Institute of Technology, Lausanne, pp. 303–314.

Muralt, P., Kohli, M., Maeder, T., Kholkin, A., Brooks, K. G., Setter, N., and Luthier, R. (1995), *Sensors Actuators A* **48**, 157–162.

Muralt, P., Baborowski, J., and Ledermann, N. (2002), in *Piezoelectric Materials in Devices*, N. Setter (Ed.), N. Setter, EPFL Swiss Federal Institute of Technology, Lausanne, pp. 231–260.

Nagarajan, V., Jenkins, I. G., Alpay, S. P., Li, H., Aggarwal, S., Salamanca-Riba, L., Roytburd, A. L., and Ramesh, R. (1999a), *J. Appl. Phys*. **86**, 595–602.

Nagarajan, V., Ganpule, C. S., Nagaraj, B., Aggarwal, S., Alpay, S. P., Roytburd, A. L., Williams, E. D., and Ramesh, R. (1999b), *Appl. Phys. Lett*. **75**, 4183–4185.

Nagarajan, V., Alpay, S. P., Ganpule, C. S., Nagaraj, B. K., Aggarwal, S., Williams, E. D., Roytburd, A. L., and Ramesh, R. (2000), *Appl. Phys. Lett*. **77**, 438–440.

Nagarajan, V., Ganpule, C. S., Li, H., Salamanca-Riba, L., Roytburd, A. L., Williams, E. D., and Ramesh, R. (2001), *Appl. Phys. Lett*. **79**, 2805–2807.

Nagarajan, V., Stanishevsky, A., Chen, L., Zhao, T., Liu, B. T., Melngailis, J., Roytburd, A. L., Ramesh, R., Finder, J., Yu, Z., Droopard, R., and Eisenbeiser, K. (2002), *Appl. Phys. Lett*. **81**, 4215–4217.

Nagarajan, V., Prasertchoung, S., Zhao, T., Zheng, H., Ouyang, J., Ramesh, R., Tian, W., Pan, X. Q., Kim, D. M., Eom, C. B., Kohlstedt, H., and Waser, R. (2004), *Appl. Phys. Lett*. **84**, 5225–5227.

Nakamura, T., Masuda, A., Morimoto, A., and Shimizu, T. (1996), *Jpn. J. Appl. Phys*. **35** (P. 1), 4750–4754.

Noheda, B., Cox, D. E., Shirane, G., Gonzalo, J. A., Cross, L. E., and Park, S. E. (1999), *Appl. Phys. Lett*. **74**, 2059–2062.

Noheda, B., Gonzalo, J. A., Cross, L. E., Guo, R., Park, S. E., Cox, D. E., and Shirane, G. (2000), *Phys. Rev. B* **61**, 8687–8692.

Noheda, B., Cox, D. E., Shirane, G., Gao, J., and Ye, Z. G. (2002), *Phys. Rev. B* **66**, 054104-1–054104–5.

Nye, J. F. (1979), *Physical Properties of Crystals*, Oxford University Press, Oxford.

Ogale, S. B., Nawathey-Dikshit, R., Dikshit, S. J., and Kanektar, S. M. (1992), *J. Appl. Phys*. **71**, 5718–5725.

Ohkubo, I., Christen, H. M., Kalinin, S. V., Jellison, G. E., Jr., Rouleau, C. M., and Lowndes, D. H. (2004), *Appl. Phys. Lett*. **84**, 1350–1352.

Osbond, P., Beck, C. M., Brierley, C. J., Cox, M. R., Marsh, S. P., and Shorrocks, N. M. (1999), *Proc. 1999 IEEE Ultrasonics Symp*., 911–914.

Ouyang, J., Yang, S. Y., Chen, L., Ramesh, R., and Roytburd, A. L. (2004), *Appl. Phys. Lett*. **85**, 278–280.

Ouyang, J., Ramesh, R., and Roytburd, A. L. (2005), *Appl. Phys. Lett*. **86**, 152901-1–152901-3.

Park, C. H., and Chadi, D. J. (1997), *Phys. Rev. B* **57**, R13861–R13864.

Park, S. E., and Shrout, T. R. (1997), *J. Appl. Phys*. **82**, 1804–1809.

Polla, D. L., and Francis, L. F. (1996), *MRS Bull.* **21**, 59–65.

Ramesh, R., and Schlom, D. G. (2002), *Science* **296**, 1975–1976.

Ramesh, R., Dutta, B., Ravi, T. S., Lee, J., Sands, T., and Keramidas, V. G. (1994), *Appl. Phys. Lett*. **64**, 1588–1591.

Ranjith, R., Laha, A., and Krupanidhi, S. B. (2005), *Appl. Phys. Lett*. **86**, 092902-1–092902-3.

Roelofs, A., Shneller, T., Böttger, U., Szot, K., and Waser, R. (2003), in *Proceedings of POLECER Symposium on Polar Oxides. Properties, Characterization and Immaging*, R. Waser, U. Böttger, S. Tiedke, M. Garcia, and M. Heins (Eds.), RWTH Aachen, pp. 301–311.

Roytburd, A. L., Alpay, S. P., Nagarajan, V., Ganpule, C. S., Aggarwal, S., Williams, E. D., and Ramesh, R. (2000), *Phys. Rev. Lett.* **85**, 190–193.

Ruffner, J. A., Clem, P. G., Tuttle, B. A., Dimos, D., and Gonzales, D. M. (1999), *Thin Solid Films* **354**, 256–261.

Saha, S., and Krupanidhi, S. B. (2000), *J. Appl. Phys*. **87**, 849–854.

Samara, G. A. (2003), *J. Phys. Condens. Matter* **15**, R367–R411.

Sarin Kumar, A. K., Paruch, P., Triscone, J. M., Daniau, W., Ballandras, S., Pellegrino, L., Marré, D., and Tybell, T. (2004), *Appl. Phys. Lett*. **85**, 1757–1759.

Scarisoreanu, N., Craciun, F., Dinescu, G., Verardi, P., and Dinescu, M. (2004), *Thin Solid Films* **453/454**, 399–405.

Scott, J. F. (1998), *Ferroelec. Rev.* **1**, 1–129.

Scott, J. F. (1999), *Ferroelectrics* **232**, 25–30.

Setter, N. (2002), in *Piezoelectric Materials in Devices*, N. Setter (Ed.), N. Setter, EPFL Swiss Federal Institute of Technology, Lausanne, pp. 1–28.

Sharma, A. K., Narayan, J., Jin, C., Kvit, A., Chattopadhyay, and Lee, C. (2000), *Appl. Phys. Lett*. **76**, 1458–1460.

Shibata, Y., Kaya, K., Akashi, K., Kanai, M., Kawai, T., and Kawai, S. (1992), *Appl. Phys. Lett*. **61**, 1000–1003.

Shibata, Y., Kaya, K., Akashi, K., Kanai, M., Kawai, T., and Kawai, S. (1995), *J. Appl. Phys*. **77**, 1498–1503.

Shibata, Y., Kuze, N., Kaya, K., Matsui, M., Kanai, M., Kawai, T., and Kawai, S. (1996), *Proc. 1996 IEEE Ultrasonics Symp*., 247–254.

Shvartsman, V. V., Emelyanov, A.Yu., Kholkin, A. L., and Safari, A. (2002), *Appl. Phys. Lett*. **81**, 117–119.

Shvartsman, V. V., Kholkin, A. L., Tyunina, M., and Levoska, J. (2005), *Appl. Phys. Lett*. **86**, 222907-1–222907-3.

So, Y. W., Kim, D. J., Noh, T. W., Yoon, J. G., and Song, T. K. (2005), *Appl. Phys. Lett*. **86**, 092905-1–092905-3.

Sternberg, A., Tyunina, M., Kundzinsh, M., Zauls, V., Ozolinsh, M., Kundzinsh, K., Shorubalko, I., Kosec, M., Pardo, L., Calzada, M. L., Alguero, M., Kullmer, R., Bäuerle, D., Levoska, J., Leppavuori, S., and Martoniemi, T. (1997), in *Ferroelectric Thin Films*, *Proceedings of the COST 514 European Concerted Action Workshop*, ETS, Pisa, pp. 95–102.

Strukov, B. A., and Levanyuk, A. P. (1998), *Ferroelectric Phenomena in Crystals*, Springer, Berlin.

Surowiak, Z., Czekaj, D., Bakirov, A. A., and Dudkevich, V. P. (1995), *Thin Solid Films* **256**, 226–233.

Tagantsev, A. K., Landivar, M., Colla, E., and Setter, N. (1995a), *J. Appl. Phys*. **78**, 2623–2630.

Tagantsev, A. K., Landivar, M., Cola, E., and Setter, N. (1995b), in *Science and Technology of Electroceramic Thin Films*, O. Auciello and R. Waser (Eds.), Kluwer Academic, Dordrecht, pp. 301–314.

Tanaka, H., Tabata, H., Kawai, T., Yamazaki, Y., Oki, S., and Gohda, S. (1996), *Thin Solid Films* **289**, 29–33.

Tantigate, C., Lee, J., and Safari, A. (1995), *Appl. Phys. Lett*. **66**, 1611–1613.

Taylor, D. V., and Damjanovic, D. (1997), *J. Appl. Phys*. **82**, 1973–1975.

Tomabechi, S., Wada, K., Saigusa, S., Matsuhashi, H., Nakase, H., Masu, K., and Tsubouchi, K. (1999), *1999 IEEE Ultrasonics Symp. Proc*., 263–267.

Trolier-McKinstry, S., Shepard, J. F., Jr., Su, T., Lacey, J. L., Zavala, G., and Fendler, J. (1997), *Ferroelectrics* **206/207**, 381–386.

Tsang, W. S., Chan, K. Y., Mak, C. L., and Wong, K. H. (2003), *Appl. Phys. Lett*. **83**, 1599–1601.

Tuttle, B. A., Garino, T. J., Voigt, J. A., Headley, T. J., Dimos, D., and Eatough, M. O. (1995), in *Science and Technology of Electroceramic Thin Films*, O. Auciello and R. Waser (Eds.), Kluwer Academic, Dordrecht, pp. 117–130.

Tybell, T., Ahn, C. H., and Triscone, J. M. (1999), *Appl. Phys. Lett*. **75**, 856–859.

Tyrrell, G. C., York, T. H., Coccia, L. G., and Boyd, I. W. (1996), *Appl. Surf. Sci.* **96/98**, 769–774.

Tyunina, M., and Levoska, J. (2001), *Phys. Rev. B* **63**, 224102-1–224102–8.

Tyunina, M., and Levoska, J. (2002), *Phys. Rev. B* **65**, 132101-1–132101–4.

Tyunina, M., and Levoska, J. (2004), *Appl. Phys. Lett*. **85**, 4720–4722.

Tyunina, M., Levoska, J., and Lepavuori, S. (1998a), *J. Appl. Phys*. **83**, 5489–5494.

Tyunina, M., Levoska, J., Sternberg, A., Zauls, V., Kundzinsh, M., Shorubalko, I., and Leppavuori, S. (1998b), *J. Phys. IV France* **8**, Pr9-261–Pr9-264.

Tyunina, M., Levoska, J., Sternberg, A., and Leppavuori, S. (1998c), *J. Appl. Phys*. **84**, 6800–6806.

Tyunina, M., Levoska, J., Sternberg, A., and Leppavuori, S. (1999), *J. Appl. Phys*. **86**, 5179–5184.

Uchino, K. (2002), in *Piezoelectric Materials in Devices*, N. Setter (Ed.), N. Setter, EPFL Swiss Federal Institute of Technology, Lausanne, pp. 83–102.

Vasco, E., Vazquez, L., and Zaldo, C. (1999), *Appl. Phys*. **A69**(Suppl.), S827–S831.

Vasco, E., Polop, C., Coya, C., Kling, A., and Zaldo, C. (2003), *Appl. Surf. Sci.* **208/209,** 512–517.

Veignant, F., Gandais, M., Aubert, P., and Garry, G. (1999), *J. Crystal Growth* **196**, 141–150.

Verardi, P., and Dinescu, M. (1995), *Proc. IEEE Ultrasonics Symp*., 1015–1018

Verardi, P., Dinescu, M., Gerardi, C., Mirenghi, L., and Sandu, V. (1997a), *Appl. Surf. Sci.* **109/110**, 371–375.

Verardi, P., Dinescu, M., Stanciu, C., Gerardi, C., Mirenghi, L., and Sandu, V. (1997b), *Mater. Sci. Eng. B* **50**, 223–227.

Verardi, P., Dinescu, M., Craciun, F., and Perrone, A. (1998), *Appl. Surf. Sci.* **127–129**, 457–461.

Verardi, P., Dinescu, M., Craciun, F., Dinu, R., Sandu, V., Tapfer, L., and Capello, A. (1999), *Sensors Actuators* **74**, 41–44.

Verardi, P., Dinescu, M., Craciun, F., Dinu, R., and Vrejoiu, I. (2000), *Appl. Surf. Sci.* **168**, 340–344.

Verardi, P., Craciun, F., Grigoriu, C., Matei, D. G., Scarisoreanu, N. D., Yatsui, K., Suematsu, H., Suzuki, T., Andrei, A., and Dinescu, M. (2002), paper presented at the E-MRS Symposium, Strasbourg, 2002.

Verardi, P., Craciun, F., Scarisoreanu, N., Dinescu, M., Grigoriu, C., Galassi, C., and Costa, A. L. (2003), *Ferroelectrics* **293**, 189–199.

Verardi, P., Craciun, F., Scarisoreanu, N., Epurescu, G., Dinescu, M., Vrejoiu, I., and Dauscher, A. (2004), *Appl. Phys. A* **79**, 1283–1285.

Verardi, P., Craciun, F., Dinescu, M., Scarisoreanu, N., Moldovan, A., Purice, A., and Galassi, C. (2005), *Mater. Sci. Eng. B* **118**, 39–43.

Vispute, R. D., Narayan, J., Wu, H., and Jagannadham, K. (1995), *J. Appl. Phys*. **77**, 4724–4728.

Vispute, R. D., Narayan, J., and Budai, J. D. (1997), *Thin Solid Films* **299**, 94–103.

Wadhawan, W. K. (2000), *Introduction to Ferroic Materials*, Gordon and Breach, Amsterdam.

Wakiya, N., Shinozaki, K., and Mizutani, N. (2001), *Thin Solid Films* **384**, 189–194.

Wang, Y., Cheng, Y. L., Cheng, K. C., Chan, H. L. W., Choy, C. L., and Liu, Z. R. (2004), *Appl. Phys. Lett*. **85**, 1580–1582.

Waser, R. (1997) *Integr. Ferroelec*. **15**, 39–46.

Watanabe, Y. (1998), *Phys. Rev. B* 57, R5567–R5570.

Watanabe, T., and Kuwano, H. (1997), *Microsystem Technol*., 107–111.

Watts, B. E., Leccabue, F., Bocelli, G., Calestani, G., Calderon, F., de Melo, O., Gonzales, P. P., Vidal, L., and Carillo, D. (1991), *Mater. Lett.* **11**, 183–186.

Wu, Z. C., Hu, W. S., Liu, J. M., Wang, M., and Liu, Z. G. (1998), *Mater. Lett.* **34**, 332–335.

Wu, W., Wong, K. H., Choy, C. L., and Zhang, Y. H. (2000), *Appl. Phys. Lett*. **77**, 3441–3443.

Wu, W., Wang, Y., Pang, G. K. H, Wong, K. H., and Choy, C. L. (2004), *Appl. Phys. Lett*. **85**, 1583–1585.

Wu, W., Wong, K. H., Pang, G. K. H., and Choy, C. L. (2005a), *Appl. Phys. Lett*. **86**, 072904-1–072904-3.

Wu, Z., Huang, N., Wu, J., Duan, W., and Gu, B. L. (2005b), *Appl. Phys. Lett*. **86**, 202903-1–202903-3.

Xu, Y. (1991), *Ferroelectric Materials and Their Applications*, North-Holland, Amsterdam.

Xu, B., Cross, L. E., and Bernstein, J. J. (2000), *Thin Solid Films* **377/378**, 712–718.

Yamada, A., Maeda, C., Uchikawa, F., Misu, K., and Honma, T. (1999), *Jpn. J. Appl. Phys*. **38**, (P. 1), 5520–5523.

Yan, F., Wang, Y., Chan, H. L. W., and Choy, C. L. (2003), *Appl. Phys. Lett*. **82**, 4325–4327.

Ye, Z. G., Noheda, B., Dong, M., Cox, D., and Shirane. G. (2001), *Phys. Rev. B* **64**, 184114-1–184114–7.

Yeh, M. H., Liu, K. S., and Lin, I. N. (1995a), *Thin Solid Films* **270**, 82–85.

Yeh, M. H., Liu, K. S., Ling, Y. C., Wang, J. P., and Lin, I. N. (1995b), *J. Appl. Phys*. **77**, 5335–5340

Yoon, J. G., and Song, T. K. (2002), ''Fabrication and Characterization of Ferroelectric Oxide Thin Films,'' in *Handbook of Thin Film Materials*, Vol. 3: *Ferroelectric and Dielectric Thin Films*, H. S. Nalwa (Ed.), Academic, San Diego, pp. 309–367.

Zhang, Q. M., Wang, H., Kim, N., and Cross, L. E. (1994), *J. Appl. Phys*. **75**, 455–461.

Zhang, R., Jiang, B., and Cao, W. (2003a), *Appl. Phys. Lett*. **82**, 787–790.

Zhang, S. T., Zhang, X. J., Cheng, H. W., Chen, Y. F., Liu, Z. G., Ming, N. B., Hu, X. B., and Wang, J. Y. (2003b), *Appl. Phys. Lett*. **83**, 4378–4380.

Zhang, S. T., Chen, Y. F., Wang, J., Cheng, G. X., Liu, Z. G., and Ming, N. B. (2004), *Appl. Phys. Lett*. **84**, 3660–3662.

CHAPTER 21

Ferroelectric Thin Films for Microwave Device Applications

CHONGLIN CHEN

Department of Physics and Astronomy, University of Texas at San Antonio, San Antonio, Texas, and TcSUH and Department of Physics, University of Houston, Houston, Texas

JIM S. HORWITZ

Materials Sciences and Engineering Division, Office of Basic Energy Sciences, U.S. Department of Energy, Washington, D.C.

21.1 INTRODUCTION

Transition-metal oxides belong to a fascinating class of natural materials that exhibit a very wide range of properties and phenomena that range from insulating to semiconducting to conducting to superconducting, from diamagnetic to paramagnetic to ferromagnetic to antiferromagnetic, from dielectric to ferroelectric to piezoelectric to antiferroelectric, from nonlinear optical to electrooptical, and many others [Rao and Reveau, 1995]. Numerous new phenomena and important properties have been found within this family, which have yielded advanced device developments and fabrications. For instance, highly ionic conductive oxides have been considered the best candidates for electrode and electrolyte materials for solid-state fuel cells and chemical sensors. High-temperature superconductors are under development for large current high electric power carriers and superconductor quantum interference devices (SQUID). Ferroelectric materials have been used for smart sensors, optoelectronic devices, microelectromechanical systems, tunable microwave elements, and many others. This class of materials has motivated scientists and engineers to systematically investigate their synthesis, microstructure, and physical properties. It should be noted that many of these novel materials are related to the perovskite ABO_3 family, as seen in Figure 21.1, where the $[BO_3]$ is a host lattice with corner-sharing BO_6 octahedra.

Perovskites belong to one of the largest oxide groups. Vastly interesting physical properties and important applications have been found in this system [Landolt-Bornstein, 1981; Hellwege and Hellwege, 1981; Lines and Glass, 1977] Among the perovskite family, the most important, but not the only one, is the ferroelectric oxide class, which displays extremely high values of dielectric constant and low dielectric loss, as well as good dielectric tunability. The dielectric constant can be tuned by different physical parameters, such as electrical field, mechanical stress, optical, temperature, and others. For example, electrically tuned ferroelectric microstrips have been widely used in wireless tunable microwave elements for space communication applications.

Pulsed Laser Deposition of Thin Films: Applications-Led Growth of Functional Materials
Edited by Robert Eason

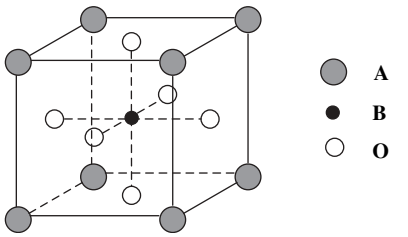

Figure 21.1 Schematic showing the typical ABO_3 perovskite structure.

Most device fabrication requires sophisticated techniques for synthesizing high-quality oxide thin films to understand their unique physical properties and device performance. Many advanced techniques have been developed to synthesize high-quality single-crystalline oxide thin films varying from physical deposition, chemical deposition, and hybrid synthesis, such as sputtering, metalorganic chemical vapor deposition (MOCVD), particle (electron, ion, laser) beam evaporation, oxide molecular beam epitaxy (MBE), and others.

Compared with other deposition techniques, pulsed laser deposition (PLD) offers many advantages such as good stoichiometry, a high deposition rate, good epitaxial quality, and relatively low cost, and it has become the most powerful technique for oxide thin-film fabrication. Details regarding its principles can be found from a number of sources in the literature [Chrisey and Hubler, 1994]. The main goal of this chapter is to contribute to ferroelectric thin-film fabrication by pulsed laser deposition and describe their applications in the fabrication of tunable microwave elements. It should be noted that the concept for utilizing the voltage-dependent dielectric constant of ferroelectric materials and thin films for tunable microwave elements is not new [Gikow, 1971]; previous designs for tunable microwave devices in bulk ferroelectric materials have resulted in low capacitances and very high applied voltages. Thin-film ferroelectrics promise an advantage over the bulk materials for practical device applications.

21.1.1 Microwave Oscillators

A microwave dielectric oscillator [Chang, 1989] is a circuit that serves as a frequency-locked local high-Q resonance cavity to clean up the broadband phase noise in a communication channel conveying digital data with phase modulation on a carrier signal. It is a frequency determining element [Panov and Stankov, 1986; Walls et al., 1990] or stabilizing discriminator [Dick and Santiago, 1992; Santiago and Dick, 1993]. The resonance cavity usually consists of a high dielectric constant ceramic, either in bulk or thin film, for confining the electromagnetic fields to the dielectric region, and its immediate vicinity by reflections at the dielectric–air interface. This requires the dielectric materials to have a highly unloaded quality factor (Q), a high relative dielectric constant, and a low-temperature coefficient of the dielectric constant.

Although many microwave oscillators have been developed in the traditional crystalline structures, these are not suitable in practical applications in microwave communications because they have excessive phase noise and are electrically untuned and electronically unlocked in frequency. The recent development of a discriminator-stabilized superconductive/ferroelectric oscillator from the National Aeronautics and Space Administration (NASA) Glenn Research Center [Romanofsky et al., 1998] offers the great opportunity for significantly improving the operational performance of a microwave oscillator with electrical tuning and electronic frequency locking and a concomitant reduction in phase noise. The oscillator is a pseudomorphic high-electron-mobility transistor connected to a microstrip ring resonator with integral coupled lines. The coupled lines are formed from a thin film of a high-temperature superconductor over a thin film of a ferroelectric material such as $Ba_xSr_{1-x}TiO_3 (0 < x < 1)$. The combination of the high-temperature

superconductor (HTS) and the ferroelectric material is chosen to obtain the high resonance quality factor, Q, needed for low phase noise; the phase noise is proportional to Q^{-2}.

21.1.2 Microwave Phase Shifters

A phase shifter is a device that provides a phase change, a variable insertion phase, in a microwave signal path without changing the physical path length. There are two types of microwave phase shifters [Chang, 1989; Koul and Bhat, 1991]: mechanical shifters and electronic shifters and both require low insertion loss. Different types of microwave phase shifters, from the earliest mechanical version [Fax, 1947] to the most current electrical-field tunable system [Van Keuls et al., 1997] have been developed for application in microwave communication circuits and systems. In contrast to other types of microwave phase shifters, electronically variable phase shifters based on the dielectric properties of ferroelectric materials, especially ferroelectric thin films, offer great potential for the development of small, light, tunable microwave phase shifters for wireless communication applications. Ferroelectric phase shifters have been fabricated with an excellent phase shift behavior of near 400° in an eight-element $YBa_2Cu_3O_{7-\delta}$(YBXO)/$SrTiO_3$(STO)/$LaAlO_3$(LAO) coupled microstrip line phase shifter operated at 16 GHz and 40 K. More recently, room temperature microwave phase shifters have been developed for practical applications, and results have been achieved from several groups in various ferroelectric thin films, such as a 280° phase shift with a figure of merit of 43°/dB and a 250° phase shift with a figure of merit of 53°/dB from ferroelectric (Ba,Sr)TiO_3 (BSTO) thin films. More work on improving the electrical field tuned microwave phase shift systems is in progress by various techniques including annealing, doping, and searching for other low dielectric loss materials with large dielectric tunability.

21.1.3 Filters

A passive microwave filter is a circuit that transmits the desired signal frequency with the minimum possible attenuation. More specifically, the main function of microwave filters is to channel only the desired signal frequencies while the undesired frequencies are attenuated. The circuit element usually consists of only lumped (inductor, capacitor, and resistor) or distributed (waveguide or microstrip or other medium) elements or the combination of both. Various types of microwave filters have been developed including the traditional low-pass filter systems. Current microwave filters used in most space communication satellites are typical satellite multiplexers with dual-mode cavity or dielectric resonator filters that are large and heavy. To reduce the size, weight, and cost of these multiplexers, a new class of dual-mode microstrip filters was recently developed in the NASA Glenn Research Center by adopting high-temperature superconductor/ferroelectric multilayers. This dual-mode microstrip filter with a high-temperature superconductor thin-film printed circuit is dramatically smaller and lighter than either the traditional dual-mode cavity or dielectric resonator filters.

21.2 EPITAXIAL GROWTH OF FERROELECTRIC THIN FILMS BY PULSED LASER ABLATION

21.2.1 Optimal Growth Conditions and Effects on the Epitaxy

Epitaxial growth of single crystalline complex oxide thin films, such as perovskite ferroelectric thin films, requires crucial growth knowledge and processing conditions. It is well known that the structure formed on oxide surfaces can be very complicated. The nucleation and the initial monolayer formation might result in the formation of different oxide or phase structures. Strain accumulation and relief from the lattice misfit would completely alter the surface roughness and interface structures. Growth procedures such as temperature, pressure, pre-, and post-treatment can

significantly affect the microstructure, defect density, epitaxial quality, and physical properties of the as-grown films. Therefore, knowledge of the oxide thin-film growth mechanisms, atomic-scale growth kinetics and dynamics, and the processing effects will enable the control of the microstructures, physical properties, epitaxial quality, and interface structures. To optimize the highly epitaxial film with good single-crystal quality and desired physical property, it is mandatory to pay great attention to the following aspects: the effects from temperature and pressure, the selection of substrate material and surface quality, and the controlling of growth dynamics during processing.

The effects of temperature on the film growth have been well studied, and there are a large number of references in the literature that can be applied in various areas [Park et al., 2000; Messier et al., 1984]. Briefly, to achieve a highly epitaxial thin film, the deposition temperature should be controlled in the granular and extensive epitaxial temperature zone that is usually above half the melting point, T_m, of the growth material. Most perovskite ferroelectric thin films can be epitaxially grown at a processing temperature higher than 750°C. For instance, highly epitaxial ferroelectric BSTO thin films can be achieved at a deposition temperature of 750–850°C with excellent resultant physical properties and epitaxial behavior [Kim et al., 2000; Chen et al., 1999]. Theoretically, any higher processing temperatures will benefit the epitaxial growth of such oxide thin films. However, the high temperature will cause the interdiffusion reaction at the interface between the film and substrate or substrate surface reconstruction that strongly alters the physical properties of the as-grown films. Even within the optimal grown temperature range, different deposition temperatures can result in the different lattice parameters yielding different physical properties of the films. One of the best examples is that of BSTO (60 : 40) films grown on (001) MgO substrates, for which the BSTO films grown at 875°C had a larger out-of-plane lattice parameter ($a = 0.3989$ nm) than its bulk ceramic counterpart ($a = 0.3965$ nm) [Gim et al., 2000] while the film grown at 800°C had nearly the same lattice parameter ($a = 0.3964$ nm) as the bulk. The crystallinity of the as-grown films is highly dependent upon the processing temperature, and the film grown at 800°C had a far better crystallinity than other films. The temperature dependence on the epitaxial film quality by pretreatment and postannealing will be discussed later in this chapter.

We focus here on how the deposition pressure affects the microstructure and epitaxial quality as well as the surface morphology of the as-grown ferroelectric thin films. Different deposition pressures yield BSTO thin films that are cubic ($a = c$), in tension ($a > c$), or compression ($a < c$) [Treece et al., 1997; Carlson, 2000a]. BSTO thin films deposited on (001) STO, (001) LAO, and (001) MgO substrates indicate that the c-axis parameter increases with the increase of oxygen deposition pressure between 65 and 250 mTorr, and the a-axis parameter increases rapidly with an increase of oxygen deposition pressure between 65 and 150 mTorr while slightly decreasing for oxygen pressures larger than 150 mTorr. Furthermore, films deposited at an oxygen pressure of less than 85 mTorr reveal that the c-axis parameter is larger than that of the a-axis and the films deposited at 85 mTorr are cubic.

Recently, Chen and his co-workers [Yuan et al., in press] have systematically investigated the oxygen partial pressure effect in PLD growth of BSTO systems and found that the oxygen partial pressure can significantly alter the epitaxial quality and surface morphology of as-grown ferroelectric BSTO thin films on (001) STO. As seen from Figure 21.2, scanning force microscopic images show the surface morphology of ferroelectric $BaTiO_3$ (BTO) thin films deposited at 840°C and an oxygen partial pressures of 150, 230, and 300 mTorr with surface roughness figures of 47, 5.4, and 35 (nm/cm^2), respectively. When the film was deposited under low oxygen partial pressures, the film had a very high density of surface particles and a very large value of surface roughness. Also, a number of pinholes appear on the image. If the oxygen partial pressure was increased to 230 mTorr, which is very close to the optimal value, the film becomes much smoother than under a lower pressure and shows far fewer surface particles. However, under a higher oxygen deposition pressure, the film again becomes rough with a high density of surface particles, although no pinholes can be found on the surface. The growth features of BSTO on (001) STO and (001) LAO show very similar phenomena. Although the mechanisms that cause the change of these surface features are still

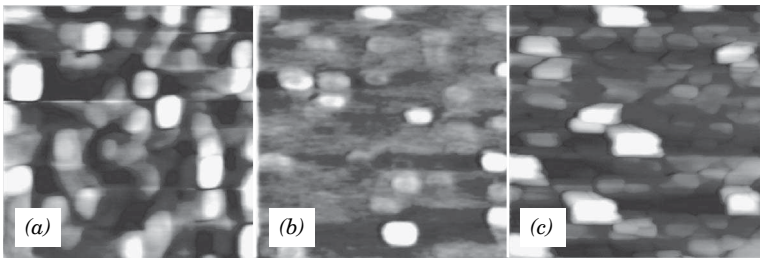

Figure 21.2 Atomic force microscope images showing the surface morphology of epitaxial $BaTiO_3$ thin films on (001) $SrTiO_3$ surfaces at various oxygen partial pressures: (a) 150 mTorr, (b) 230 mTorr, and (c) 300 mTorr.

unclear, the evidence related to the oxygen partial pressure effects might be addressed in the near future to guarantee that epitaxial growth can occur to produce atomically smooth ferroelectric thin films.

Another very important aspect that should be carefully considered for oxide thin-film epitaxy is the substrate selection and surface pretreatment. The theoretical concept of textbook ''epitaxy'' is defined to be the formation of a single-crystal film in a layer-by-layer fashion on a single-crystal substrate surface. Ideally, the lattice constant of the film should coincide with that of the substrate. Therefore, the crystallographic properties of the substrate surface are obviously one of the main factors in determining the atomic recrystallization processes from the gaseous foreign atoms condensing on the substrate surface. Thus, crystal symmetry, surface lattice parameter, and surface energy will significantly influence the epitaxial growth behavior. The first few atomic layers of the substrate surface will act as a strong driving force in the nucleation process and subsequent epitaxial quality for the film growth on the substrate surface [McKee et al., 1994]. A good lattice match between the film and substrate (both lattice parameter and crystal symmetry) can minimize the interface energy, especially the electrostatic repulsion potential. The substrate orientation can determine the surface structure and surface lattice parameters. Traditionally, the lattice mismatch f is defined as

$$f = \frac{\Delta a}{a_{\text{sub}}} = \frac{a_{\text{film}} - a_{\text{sub}}}{a_{\text{sub}}}$$

where a is the lattice parameter. Lattice parameters in heteroepitaxial growth are essentially unmatched. A small lattice mismatch value of less than 5% is universally desired for achieving a high-quality epitaxial film. Furthermore, this small lattice mismatch value will ensure a correspondingly small strain in the film. If $\Delta a < 0$, the film is compressed or strained, and if $\Delta a > 0$, the film is tensioned or relaxed heteroepitaxially. As an example, a BSTO (60 : 40) thin film grown on a (001) LAO substrate has a lattice mismatch value of $+3.8\%$ indicating that the epitaxial film has a relaxed heteroepitaxial growth. By contrast, this film grown on a (001) MgO substrate has a lattice mismatch of -5.8% indicating a strained heteroepitaxial growth. It should be noted that the strain energy would rapidly accumulate with increasing film thickness because ionic bonding in most oxide materials plays a key role resulting in the inherent stiffness. When the film thickness is larger than its critical thickness, the strain energy will be released through the formation of misfit edge dislocations and twinning, local phase transitions, surface morphology transformations, or a two- or three- dimensional growth transition. Formation of specific structures is usually governed by the competition between surface microstructures, interface strain energy, and the film growth dynamics. Further details will be given later in the chapter.

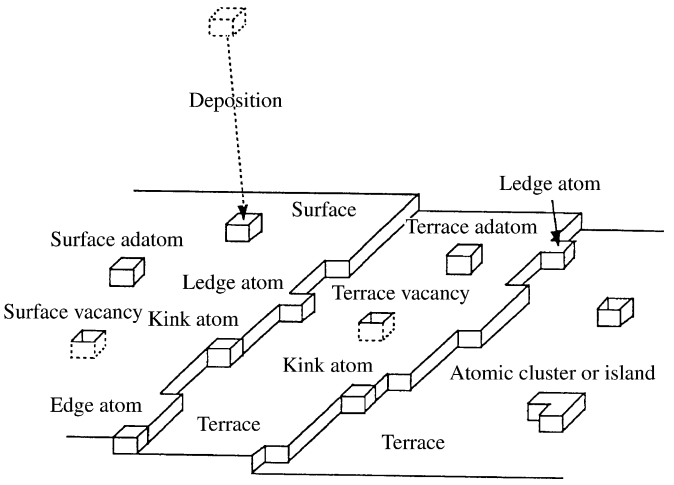

Figure 21.3 Schematic diagram showing various surface defects on a real crystal surface.

It is well known that any real surface consists of many surface defects such as adatoms, atomic clusters and islands, terraces and edges, and vacancies and various atomic sites, as seen in Figure 21.3. An oxide surface is a good example of a complex crystallography with a very complicated combination of physical and chemical properties and high surface defect concentrations, resulting in problems of achieving a reproducible surface composition and physical properties. Note that the establishment of an ordered surface structure does not mean that a stoichiometric surface has been achieved. Surface physical properties, for example, are highly dependent upon various surface treatments [Henrich and Cox, 1994]. Therefore, appropriate substrate surface preparation before film deposition is definitely important and becomes essential to surface science and thin-film technology. Rigorous substrate treatment not only enables the removal of surface contamination but also allows the control of the surface defect density and microstructure.

Figure 21.4a is a typical scanning tunneling microscope (STM) image of a (001) STO surface showing detailed information of a practical STO surface morphology. Ideally, on the (001) STO surface, there are two types of termination planes that are atomically flat when cleaved, that is, SrO and TiO_2 terminations. The real cleaved surface should consist of equal areas of surface terraces but have different surface energies, which results in different ratios between the two types of surfaces after various treatments. Recent experimental studies have indicated that the top layer of the surface

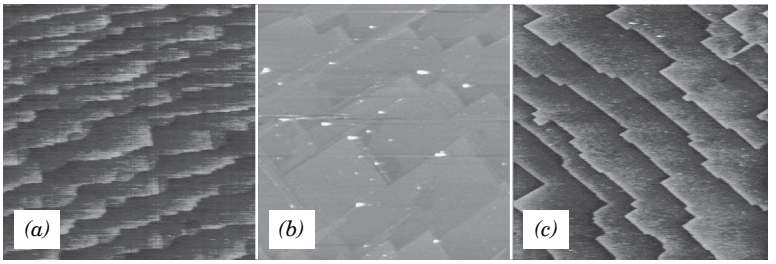

Figure 21.4 Scanning tunneling microscopy images showing the surface morphology of (a) a (001) $SrTiO_3$ single-crystal substrate with single unit-cell step height terraces, (b) an annealed (001) $SrTiO_3$ surface with multi-unit-cell height surface step terraces, and (c) a $SrRuO_3$ thin film on an (001) $SrTiO_3$ substrate with single unit-cell height surface terraces.

is TiO_2 termination with oxygen vacancies after surface treatments [Matsumoto et al., 1992]. On the other hand, the surface terrace after high-temperature annealing at 850°C forms very sharp rectangular surface structures, as seen in Figure 21.4b, that consists of many surface facets. These surface facets were determined by the well-known Wulff plot to form the lowest energy structure for the surface. The terrace edges were found to be along the $<100>$ directions. With rigorous surface treatment, near prefect highly epitaxial $SrRuO_3$ single crystalline thin films were grown with identical atomically flat surface morphology, as seen in Figure 21.4c [Chen et al., 1997]. Most oxide substrate surfaces after high-temperature treatment will form the lowest surface energy facets and termination layers. It should be pointed out here that the same substrate surface via different treatments might have completely different surface terminations. A good example is that of an (001) LAO substrate that will be terminated by a LaO top layer after annealing at 850°C [Gao et al., 1999] but with an AlO top layer for annealing at a temperature higher than 900°C. These phenomena have recently been confirmed by SIMS studies also [Jacobson, personal communication]. To achieve the desired substrate surface structures, different substrates and orientations should involve different treatment procedures. Further details may be found in the literature [Henrich and Cox, 1994].

21.2.2 Epitaxial Growth of Ferroelectric (Ba,Sr)TiO_3 Thin Films

Ferroelectric barium strontium titanates (BSTO) belong to the perovskite family and are solid solutions of BTO and STO with different ratio x. The ferroelectric properties of BSTO are known to depend dramatically on the composition ratio x between STO and BTO components and belong to a class of nonlinear dielectrics that exhibit an electric-field-dependent dielectric constant, as seen in Table 21.1. The Curie temperatures and the room temperature dielectric constants of bulk BSTO varies from 135 to -240°C and a few thousand to 300, respectively, for x values between 0.0 and 1.0. These dielectric tunability properties of BSTO systems offer a unique opportunity for the development of various microwave devices such as microstrip lines, phase shifters, tunable filters, and high-Q resonators. Thin films of ferroelectric BSTO offer considerable advantages over bulk ferroelectrics for tunable microwave device applications because of the large electric field that can be applied in thin films (0.5 μm) with low bias voltages (0–10 V) [Horwitz et al., 1995]. As with bulk ferroelectrics, thin-film ferroelectrics can also exhibit high dielectric constant values (ε), and low dielectric loss (δ) as well as large dielectric tunability by applying an electric field. These advantages enable the developments of small, light-weight, tunable microwave components for wireless communication and radar applications. Much effort has been extended in the technological development of microwave devices in the last decade [Jia et al., 2000, 2002; Tidrow et al., 2002; Galt et al., 1993; Knauss et al., 1996; Carroll et al., 1993].

To date, the best results achieved in terms of the largest tunability, the maximum dielectric constant, and the lowest dielectric loss are from the highly epitaxial STO thin films on (001) LAO with superconductor yttrium barium copper oxide (YBCO) microstrips operated at 40 K [Van Keuls et al., 1997]. A relative insertion phase shift of near 400° was obtained with an eight-element

TABLE 21.1 Electronic Properties of BSTO Bulk Ceramics Measured at 1 kHz and 25°C

Barium Content	Dielectric Constant	Dielectric Loss	Tunability (%)	Curie Temperature
0.00	349.04	0.00022	0.000	33°C
0.30	760.04	0.00025	2.200	168
0.40	1199.12	0.00030	7.900	208
0.45	1280.83	0.01184	15.20	−45
0.50	1907.99	0.05538	25.55	−25
0.55	2771.73	0.03904	33.40	−15
0.60	5160.64	0.00961	56.30	10
0.70	4322.86	0.03355	48.60	40
1.00	2082.38	0.03675	18.00	135

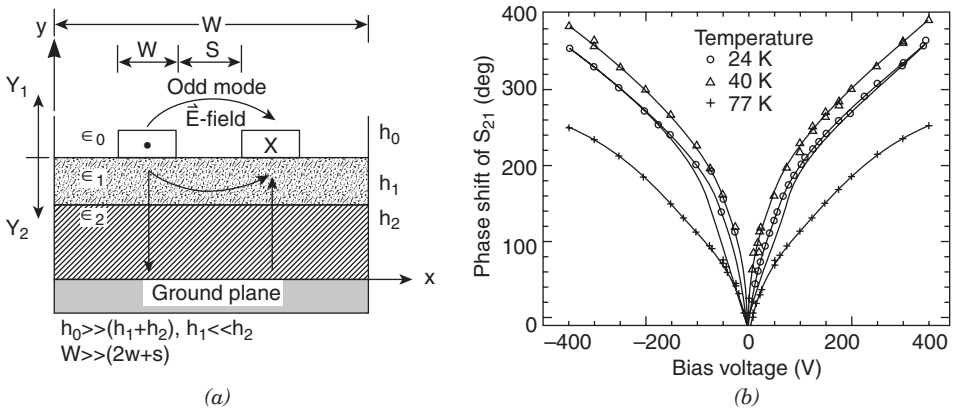

Figure 21.5 (a) Schematic diagram showing the design of the CMPS structures, and (b) the as-achieved phase shift from the $SrTiO_3$ thin film on (001) $LaAlO_3$ using this design [Van Keuls et al. 1997].

YBCO/STO/LAO coupled microstrip line phase shifter (CMPS) operating at 16 GHz. Figure 21.5a shows the design of the CMPS structures where both ferroelectric and superconductive thin films were deposited in situ on a (001) LAO single-crystal substrate. Figure 21.5b is the as-achieved phase shift from this design. This great achievement has opened a gateway to the practical applications of ferroelectric thin films in tunable microwave elements.

However, as seen in Table 21.1, no dielectric tunability was achieved from STO at room temperature. The development of room temperature tunable microwave elements requires ferroelectrics with large dielectric tunability at room temperature with low dielectric loss. The excellent room temperature dielectric tunability of BSTO with the ratio x from 0.5 to 0.7 indicates that room temperature tunable microwave elements can be achieved with these compounds. Thus, the fabrication of highly epitaxial single crystalline BSTO films with high ε and low-loss tangent ($\tan\delta$) values have become a very important technological issue for utilizing these materials in practical applications.

Recently, many excellent results [Chen et al., 1999, 2002a; Horwitz et al., 1995; Carlson, 2000a] have been achieved on various single crystalline substrates, that is, LAO, STO, MgO, and others. These substrates exhibit very low dielectric loss (10^{-5}), low dielectric constant (~ 10), and a good lattice match with the BSTO lattice. Depositions normally take place at temperatures higher than 700°C and oxygen pressures of 100–300 mTorr. Under optimal conditions, the as-grown BSTO thin films on all of these substrates (LAO, STO, and MgO) are c-axis oriented with good single crystallinity to form the cube-on-cube epitaxy. The interface relationship between the BSTO films and substrates have been determined to be $<100>_{BSTO}//<100>_{sub}$. The lattice misfit therefore can be estimated from this epitaxial relationship in each epitaxial system. For instance, a (50 : 50) BSTO thin film grown on a (001) LAO substrate has a lattice misfit of about 3.8% and a (60 : 40) BSTO thin film on (001) MgO gives a misfit of 6.3%. Details about the interface structures and epitaxial behavior will be discussed later. Measurements of dielectric properties indicate that high dielectric constant, low dielectric loss, and large dielectric tunability can only be achieved with highly epitaxial BSTO thin films. Figure 21.6 shows the dielectric properties of a BSTO film on a (001) LAO substrate as a function of temperature for different values of direct current (DC) bias, which yield a room temperature dielectric constant (ε) of 1600 and dielectric loss (δ) of 0.004 with a 33% tunability in an applied field of 2.33 V/μm. The BSTO films grown on the (001) MgO substrates reveal excellent dielectric properties with a dielectric constant of $\sim$2000, dielectric loss of 0.008, and a tunability of as much as 47% at 3.0 V/μm. This clearly suggests that ferroelectric BSTO thin films can be developed for high-frequency room temperature tunable microwave elements. Figure 21.7 shows a

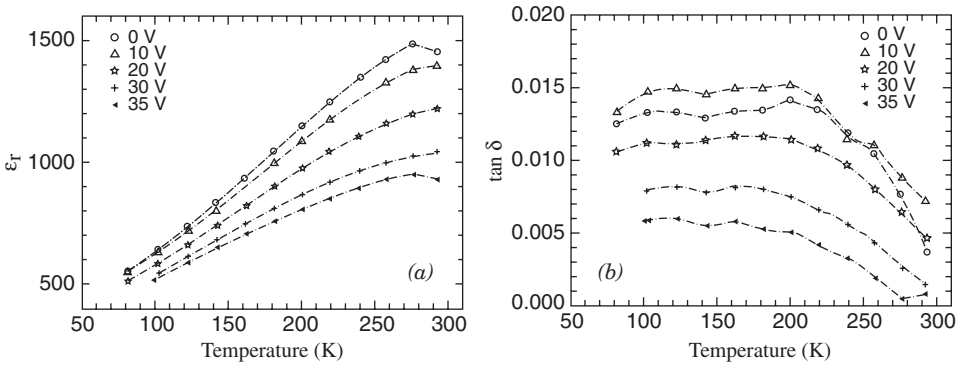

Figure 21.6 Dielectric properties of a BSTO (50 : 50) thin film on (001) LAO measured as a function of temperature from 80 to 300 K at a DC bias between 0 and 35 V: (a) dielectric constant and (b) dielectric loss [Chen et al., 1999].

room temperature microwave phase shifter that has been developed from BSTO thin films grown on (001) MgO substrates. The performance of this device developed from the as-grown BSTO thin films on MgO is closer to that needed for practical applications in wireless communications.

21.2.3 Epitaxial Growth of Ferroelectric (Pb,Sr)TiO_3 Thin Films

Another key material system meeting the requirements of high dielectric constant, low dielectric loss, and large dielectric tunability for high-frequency communication device applications is (Pb,Sr)TiO_3, (PSTO), which is also a solid solution of $PbTiO_3$ (PTO) and STO. This family of ferroelectric materials has very similar dielectric properties to those in the BSTO system. The dielectric constants and Curie temperatures can be adjusted via the composition ratio of Pb to Sr, as seen in Figure 21.8. However, the ferroelectric properties of PSTO thin films have not yet been widely studied for tunable microwave devices. Recently, polycrystalline ferroelectric PSTO thin films have been fabricated by using sol–gel technology [Kim and Kim, 2002; Jain et al., 2003b] or pulsed laser ablation [Kuo et al., 2002], showing that PSTO with compositions from (20 : 80) to (40 : 60) has a very good dielectric tunability and low dielectric loss, with a tunability value of near 40% reported for a PSTO (40 : 60) thin film. These preliminary results indicate that high-quality

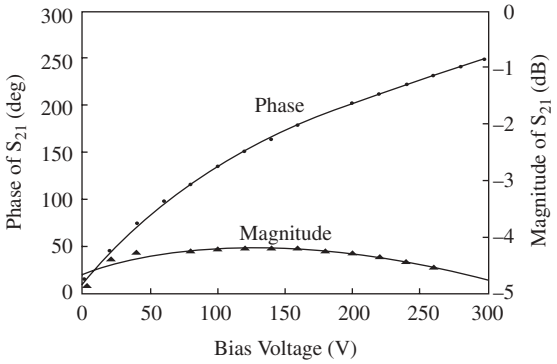

Figure 21.7 Phase shift and insert ion loss measured at 23.7 GHz and 300 K from an eight-element coupled microstrip phase shifter on BSTO films on (001) MgO [Chen et al., 2002].

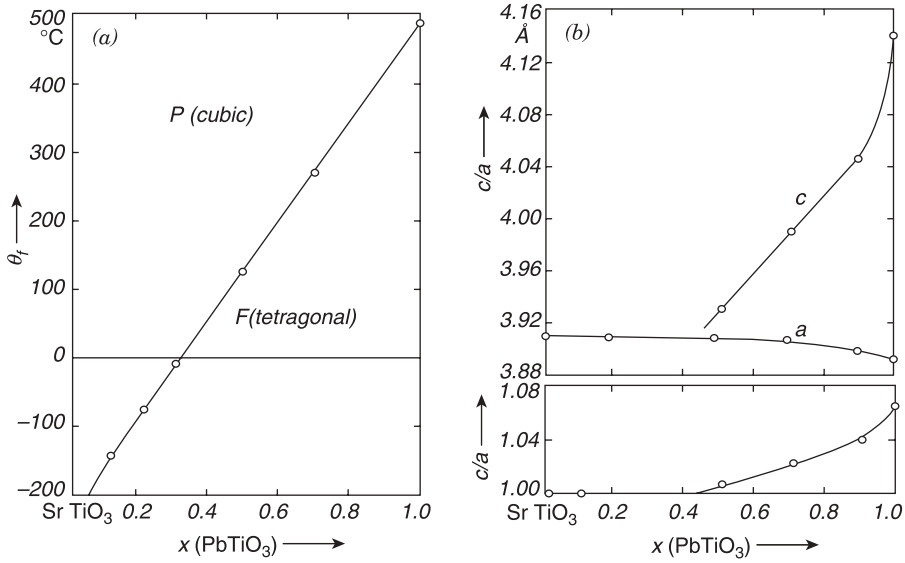

Figure 21.8 Physical properties and lattice structures of $(Pb,Sr)TiO_3$ [Landolt-Bornstein, 1981].

tunable microwave elements should be able to be developed from these highly epitaxial PSTO thin films. Unfortunately, data on single crystalline PSTO films has been infrequently reported probably due to the lead oxide volatility resulting in the difficulty of controlling the stoichiometric structures and compositions in these PSTO thin films. Only very recently has the epitaxial growth of single crystalline PSTO (35 : 65) thin films been achieved on (001) LAO [Liu et al., 2004] and (110) $NdGaO_3$ (NGO) [Lin et al., 2004] substrates in the University of Houston by carefully controlling the deposition parameters in a Pb-enriched target.

The PSTO films were deposited at a temperature of 820°C and 250 mTorr of oxygen. Figure 21.9 is a θ-2θ X-ray diffraction pattern of the as-grown PSTO films on a (001) LAO substrate indicating that

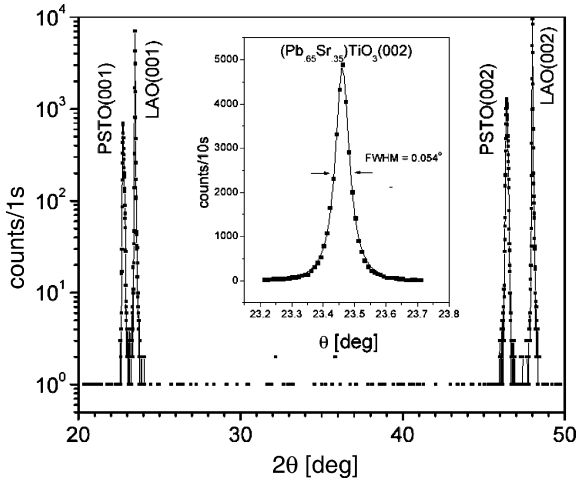

Figure 21.9 X-ray diffraction pattern of a $\theta - 2\theta$ scan shows the PSTO films on (001) LAO. The inset is the rocking curve measurements from the $(002)_{PSTO}$ reflection [Liu et al., 2004].

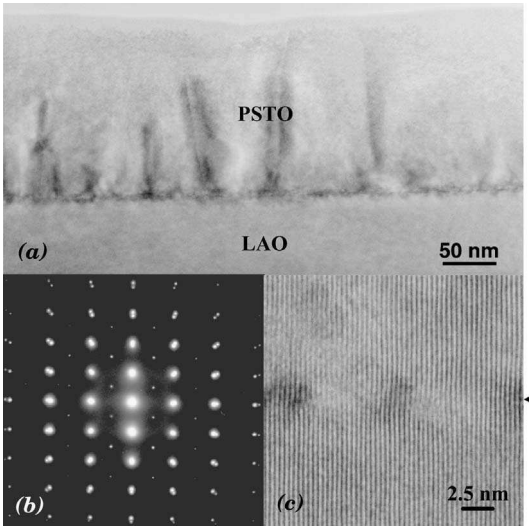

Figure 21.10 TEM studies show the epitaxial behavior of a PSTO film (35 : 65) on (001) LAO. (a) Low-magnification, bright-field image, (b) SAED (selected area electron diffraction) covering at the interface between the PSTO and LAO, (c) HREM (high-resolution electron mapping) image taken at the interface [Liu et al., 2004].

only (00*l*) reflections appear in the pattern, indicating that the films are *c*-axis oriented. As seen in the inset of Figure 21.9, the crystallinity of the PSTO films was studied by rocking curve measurement from the (002) reflection, revealing that the full-width at half-maximum (FWHM) is only 0.05°, which is similar to the FWHM value from the single-crystal substrate of 0.03°, implying that the as-grown films have excellent single-crystal quality. This has also been verified from the χ scan X-ray diffraction on the (110) reflection in which only the sharp {110} reflections appear on the pattern. The interface relationship was determined to be $<100>_{PSTO}//<100>_{LAO}$ and $(001)_{PSTO}//(001)_{LAO}$, which is consistent with the result from cross-sectional electron microscopy, as seen in Figure 21.10. The low-magnification, bright-field image (Fig. 21.10a) shows that the film has a sharp interface, smooth surface, and good epitaxial behavior. The sharp spots in the selected area electron diffraction (SAED) pattern (Fig. 10b), which is a simple superposition of the PSTO film and LAO substrate, with no satellites or broadening demonstrates that the as-grown PSTO films have excellent single crystallinity and epitaxial quality. This can be further verified from the high-resolution electron microscopy (HREM) image at the interface between the PSTO film and LAO substrate, as seen in Figure 21.10c. A similar epitaxial behavior has also been achieved on a (110) NGO substrate as shown in Figure 21.11 [Lin et al., 2005].

21.2.4 Other Ferroelectric Thin Films

Ferroelectric $Pb(Zr,Ti)O_3$ (PZT) is a solid solution with a wide compositional variation and broad range of dielectric properties. The modification of PZT with La^{3+} substituting for Pb^{2+} has resulted in a dielectric constant up to 7000 [Land et al., 1974]. Ferroelectric PZT thin films have been the most widely studied of any of the ferroelectric materials [Tuttle and Schwartz, 1995]. However, it is well known that precise control of film stoichiometry is difficult because of the lead oxide volatility, which leads to the difficulty of reproducible PZT samples. It should be noted that highly epitaxial PZT thin films have a high dielectric constant and low dielectric loss in the frequency range up to 1.0 GHz. This suggests that PZT thin films can be used for low-frequency applications that require high capacitance such as decoupling capacitors in digital circuits.

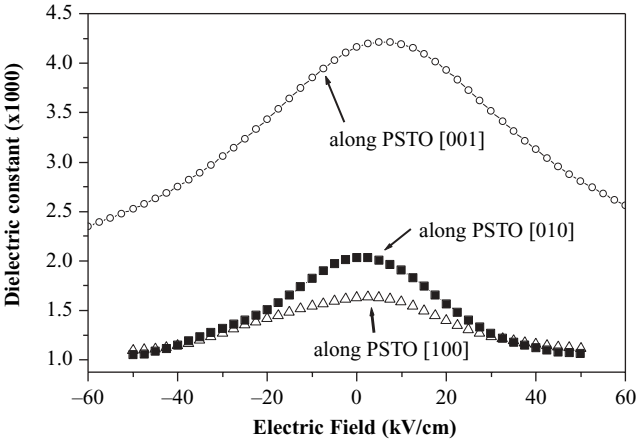

Figure 21.11 Dielectric properties measured from the PSTO (35 : 65) films grown on (110) NGO and (001) LAO, respectively. The dielectric constant is dependent upon the processing conditions and the substrate materials, probably due to the different strain in the films [Liu et al., 2004; Lin et al. 2004, 2005].

Other ferroelectric materials that are appropriate for tunable dielectric application are $Pb(Mg,Nb)O_3$ (PMN) [Tyunina and Levoska, 2001], and $Na_{0.5}K_{0.5}NbO_3$ (NKN) [Abadei et al., 2002]. However, the fabrication of PMN or NKN thin films encounters the same or similar problems as the PZT or PSTO thin films, namely the Na and K volatility. These preliminary results indicate that the dielectric constant and tunability of NKN decrease with an increase in frequency, implying that the ferroelectrically active modes in NKN become frozen as the frequency increases. This high-frequency frozen active mode in NKN and the increase in dielectric loss in PZT and PNM prohibit the use of these ferroelectric materials in high-frequency tunable microwave device applications.

21.3 CHARACTERIZATIONS OF FERROELECTRIC THIN FILMS

To understand the quality of the as-grown ferroelectric thin films, it is necessary to characterize them in terms of their microstructures and chemical and physical properties. The microstructures include two types of categories, that is, crystallinity and epitaxial behavior. The crystallinity usually refers to the crystal states—that is, single crystalline, polycrystalline, or amorphous—and the crystal structures—that is, cubic, tetragonal, orthorhombic, and so forth—of the films grown on substrate surfaces. The epitaxial behavior describes the interface structures and interface relationships, the film orientations, strain and interface defects, domain structures, and surface morphology. The term ''chemical'' above usually refers to the stoichiometry, composition, doping and impurities, period and composition of multilayers, and any interface reaction or precipitation in thin films. The physical properties of the ferroelectric thin films mainly refer to the dielectric constant (polarization), dielectric loss, dielectric dissipation, and dielectric tunability, as well as any effects due to defects or strains.

The microstructure and chemistry of thin films can usually be characterized by a variety of techniques such as X-ray diffraction (XRD), electron microscopy, Rutherford backscattering spectrometry (RBS), electron energy dispersion/loss spectrum (EDS/EELS), scanning probe microscopy (SPM), and many others. Among them, XRD is the most widely used technique for understanding the crystallinity and epitaxial behavior of the as-grown films. Glancing angle XRD can also provide detailed information about the interface structures and surface morphology. Transmission electron microscopy (TEM) is also a great technique for providing much of this same information but with a higher resolution than that obtainable from XRD. It is the best technique to

directly identify the atomic structure, defect, interface, and surface structure. The combination of TEM with EELS can give precise information about atomic structure and stoichiometric chemistry. RBS provides details not only on the compositions inside the films, but also the epitaxial behavior from channeling studies. SPM yields surface morphology information of both the substrate and the film with atomic resolution. The physical properties of the as-grown films can be characterized by measuring the capacitance, impedance, and I–V curves at different temperatures. Some typical examples of these processes are described below.

21.3.1 Microstructure, Composition, Surface Morphology, and Epitaxial Behavior

X-ray diffraction is the most powerful and nondestructive technique for crystallinity studies of thin films. Interpretation of the diffraction spectrum provides very detailed information of the orientation, crystallinity, and interfacial relationship for both film and substrate. Details of XRD processing can be found in the literature [Cowley, 1981; Cullity, 1978]. Briefly, a θ–2θ XRD scan provides information of the orientation of both film and substrate, whereas an XRD rocking curve measurement gives information about the crystallinity of both film and substrate. According to the Bragg law, or $2d_{hkl} \sin \theta = n\lambda$, Bragg reflection peaks from both film and substrate should appear in the diffraction pattern. Figure 21.12a is a typical θ–2θ XRD pattern of a BSTO thin film on (001) LAO substrate. Only (00l) reflections from both the film and the LAO substrate appear in the spectrum, indicating that the film is *c*-axis oriented.

From the shape and position of the Bragg reflection, information on crystallinity and strain, both uniform and nonuniform, can be obtained: A uniform strain only results in a shift of the Bragg reflection peak, whereas a nonuniform strain produces peak broadening. The width of a rocking curve is a direct measurement of the range of orientation in the area under study because each crystal grain of a typical mosaic crystal successively undergoes Bragg diffraction as the film is rotated. As seen from the inset of Figure 21.12a, the FWHM from the (001) reflection is less than 0.11°, suggesting that the film has good single crystallinity. To better understand the crystallinity of the as-grown thin films, an XRD pole figure study can show precisely the film orientation in a graphic description that is a stereographic projection with a specified orientation relative to the film. If the film is polycrystalline, the poles plotted on the projection will be uniformly distributed. If the film has preferred orientation, the poles will tend to cluster together in certain areas of the projection. If the film has good single-crystal quality, each cluster should form a high intensity spot, as seen in Figure 21.12b showing

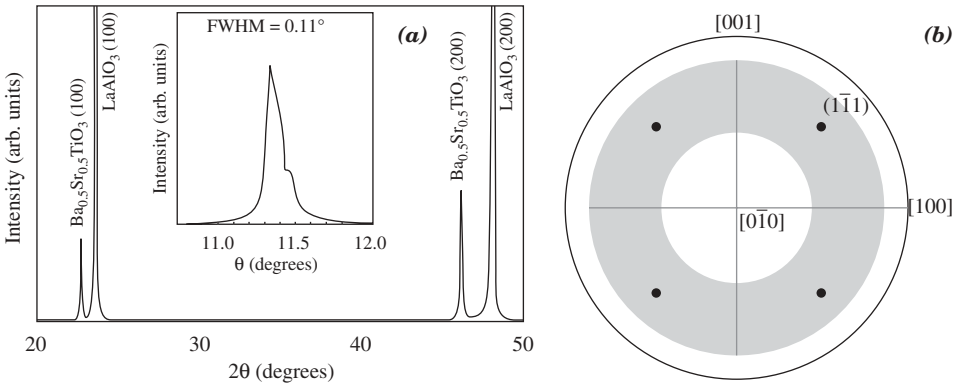

Figure 21.12 (a) X-ray diffraction of the $\theta - 2\theta$ scans from a BSTO (50 : 50) film on a (001) LAO. The inset is an X-ray rocking curve measurement showing that the FWHM from the (001) reflection of the BSTO film is about 0.11°. (b) The pole figure plot of an as-epitaxial BSTO film on (001) LAO [Chen et al., 1999].

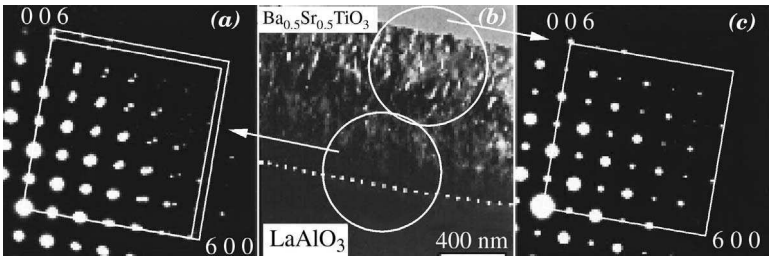

Figure 21.13 Cross-section TEM studies showing a highly epitaxial single-crystalline BSTO thin film on (001) LAO (center) and SAED patterns (right and left). Both SAED patterns from the interface between the film and substrate and the top area of the film have the same single-crystal structure [Chen et al., 2002b].

that the BSTO film on (001) LAO is indeed of excellent single-crystal quality. This data can be simply collected by using the X-ray diffractometer digital recorder and is referred to as a χ scan.

Transmission electron microscopy (TEM), with its unique atomic resolution, is considered to be another powerful technique for fully understanding the microstructures and defect nature of thin films. It provides a means for direct observation of microstructure, crystallinity, and interface structures over scale lengths from atomic resolution to micron dimensions. When equipped with the various analytic spectra, such as parallel electron energy loss spectrum (PEELS) and energy dispersive X-ray spectrometers (EDX), this allows researchers to pinpoint the nature of defects and localized (interface) structures. Details for the operational principles and procedures can be found in the literature [Jiang and Chen, 2001; Cowley, 1981] Traditionally, TEM studies involve two distinct stages, that is, cross-sectional and plan-view studies.

Cross-sectional TEM is used to image the crystal structure of thin films perpendicular to the film surface, whereas plan-view study is for imaging along the normal of the film. Figure 21.13 shows a bright-field image of a BSTO (50 : 50) thin film on a (001) LAO substrate with good single crystallinity and two typical selected area electron diffraction (SAED) patterns taken from the interface area and the top area of the film. The sharp SAED patterns with no satellite or broadening confirm that the entire film is of single-crystal quality. However, careful examination of the diffraction patterns show that the lattice is slightly distorted with ($a = b$) larger than c by 1.4%. This example illustrates that TEM is a powerful technique for studying the epitaxial behavior of thin films.

High-resolution TEM (HRTEM) is often used to study the atomic structures at the interface between the film and substrate. Figure 21.14a shows a typical HRTEM image of the periodic misfit dislocations formed at the interface between a BSTO (50 : 50) film and a (001) LAO substrate. These misfit dislocations are often present in heteroepitaxial film systems as a result of the interface strain

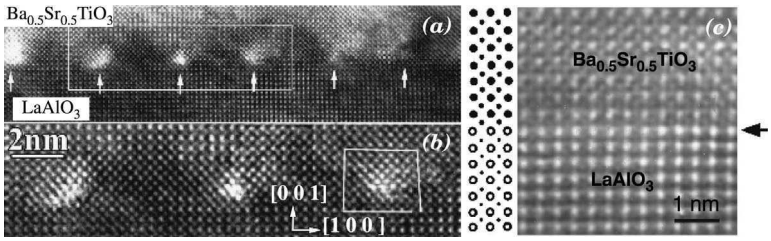

Figure 21.14 (a) HRTEM image showing the nearly periodically arranged misfit dislocations at the interface (top) and the enlarged image of the selected area in the top image [Chen et al., 2002b]. (b) Z-contrast STEM dark-field image at the interface showing the epitaxial sequence in the BSTO film on LAO [Gao et al., 1999].

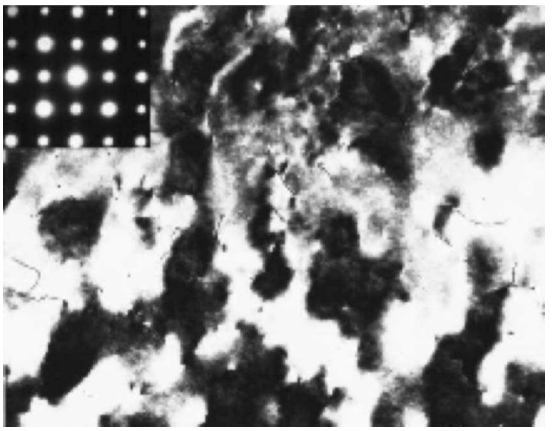

Figure 21.15 Plan-view, dark-field TEM image shows the microstructures of a BSTO (60 : 40) epitaxial film on a (001) MgO substrate. The inset is a SAED pattern from this film along the [001] zone [Jiang et al., 2002].

energy resulting from the lattice mismatching. It is interesting to note that these are only pure edge dislocations with the Burgers vector $b = [100]\mathbf{a}$, although some of the misfit dislocations tend to decompose into partials. From this HRTEM image, the average period of the misfit dislocations was determined to be about 17.5 unit cells of the LAO lattice, which reflects a 5.7% lattice mismatch. This value is much larger than the 4.13% expected from the lattice parameters of bulk materials [Gao et al., 1999]. Furthermore, cross-sectional *Z*-contrast HRTEM [Pennycook, 1997; MaGibbon et al., 1995] can be used for studying the detailed nature and atomic structures of the interface. Figure 21.14b shows a *Z*-contrast HRTEM image taken along the $[010]_{LAO}$ zone axis, which shows the atomically sharp and flat interface between the film and the substrate with the detailed stacking sequence across the interface. The last plane of the substrate is seen to be the La plane, while growth of the BSTO is seen to initiate with the Ti plane. No precipitates or other phases are present in the film or at the interface.

Plan-view TEM studies have frequently been used to investigate the microstructure and crystallinity of the as-grown thin films. Figure 21.15 is a dark-field image formed using a (020) reflection of a BSTO (60 : 40) thin film on a (001) MgO substrate [Jiang et al., 2002]. This image shows that the BSTO film has good single-crystal structure. The inset in Figure 21.15 is a SAED pattern taken from the plan-view sample along the [100] MgO zone axis. The sharp diffraction spots with no diffusion satellites demonstrate, as for the plan-view image, that the film is of good single crystallinity. Overall, TEM is a most powerful technique to study thin-film epitaxy and atomic structures. It can provide a great deal of detailed information, such as dislocations, interface structures, and epitaxial nature.

Rutherford backscattering spectrometry (RBS) is also a very popular thin-film characterization technique; details of its principle and operation can be found in the literature [Bird and Williams, 1989]. Briefly, RBS uses a very high energy and low-mass ion beam, such as He^+, with MeV energy, that penetrates up to a depth of a few microns into the films and film–substrate, with a subsequent collection of the elastically scattering ions from the Coulomb repulsion that occurs between the ion and nucleus, and is known as Rutherford backscattering. By analyzing the energy spectrum from the scattered ions, one can determine the stoichiometry of thin-film compositions with accuracies of $\pm 1.0\%$. If the incident high-energy ion beam is aligned along a particular crystal channel structure, the channeling spectroscopy can yield many details about the crystallinity, interface phenomena, and epitaxial quality. Usually, a yield, defined as the ratio between the detected reflected ions from the channeling and random spectra, of less than 25% in the RBS channeling studies can be considered as epitaxial or textured films. However, a good epitaxial film normally has

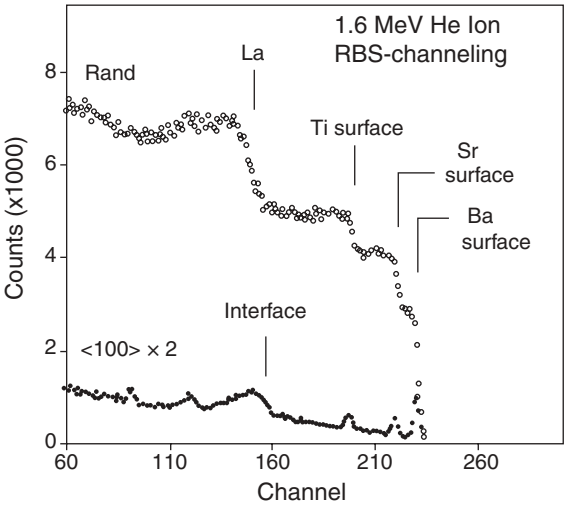

Figure 21.16 RBS ion-channeling spectra showing the epitaxial behavior of a BSTO (50 : 50) thin film on a (001) LAO substrate. The film has an excellent single-crystal quality and epitaxial behavior as revealed from the small yield of 2.6% at the surface and 8.9% (overlap with the La signal) at the interface [Chen et al., 1999].

a yield value of a only a few percent. Figure 21.16 shows the RBS ion channeling spectrum for the as-grown BSTO film on a (001) LAO substrate and indicates an excellent single-crystal and epitaxial quality because the yield from the spectrum can be estimated to be 2.6% at the surface and 8.9% (overlap with the La signal) at the interface. The small yields suggest that the BSTO film has good single-crystal structure and excellent epitaxial quality, which is consistent with the XRD and TEM studies.

Scanning probe microscopy (SPM) is a versatile and popular tool to investigate the surface morphology for both film and substrate, as seen in Figure 21.4. As an example, Figure 21.17 is an

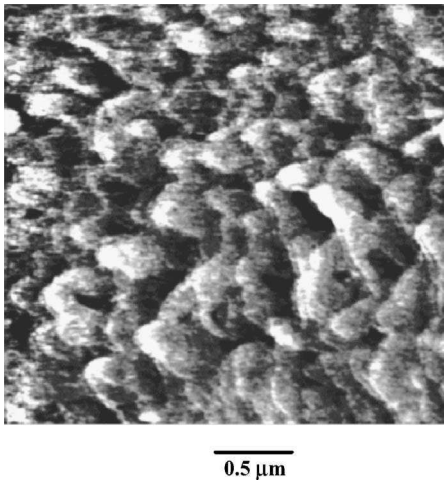

Figure 21.17 Atomic force microscopy image showing the surface morphology of a BSTO film on a (001) LAO substrate over an area of 2.54 μm × 2.54 μm with surface roughness of only about 1.2 nm/μm^2.

atomic force microscope (AFM) image showing that the BSTO film on a (001) LAO substrate has an atomically smooth surface with a roughness of only 1.2 nm/μm^2. The surface step terraces can be clearly resolved in the image. Most steps are single unit-cell height, although a few of them are of double unit-cell height. No half unit-cell height structure was observed from the as-grown film surface, indicating that only one type of surface termination exists on the surface. This is probably due to the high-temperature growth of the films that is similar to the high-temperature treatment of a STO substrate that results in the TiO_2 termination on the surface. It should be pointed out here that a scanning microwave microscope has been used to investigate the local dielectric properties and also to polarize the domain structures in thin-film ferroelectrics [Steinhauer et al., 1999; Wang et al., 2001].

21.3.2 Dielectric Properties of Ferroelectric Thin Films

The most common property of ferroelectric thin films is that they exhibit a much broader temperature coefficient of capacitance than their bulk counterparts. This key difference is indicative of the diffuse Curie temperatures and the significant reduction of dielectric permittivity peaks at the Curie temperature in ferroelectric thin films. Although the mechanisms causing this phenomenon are not yet well understood, research [Tilley, 1996] suggests that the effects from the thin-film dimensions, defects, and strain are the predominate factors that contribute here. The broadened temperature coefficient of dielectric constants provides a much less variable dielectric constant around the Curie temperature than that of either bulk or single-crystal materials. This wide temperature range for relatively stable dielectric constant values promises the development of ferroelectric thin films in room temperature tunable microwave devices, which requires fabrication of high-quality single-crystal ferroelectric thin films with good microwave dielectric properties.

Precise characterization of the physical properties of ferroelectric thin films become a key issue in the development of tunable microwave devices. Parallel-plate measurements show that highly epitaxial STO thin films display great tunability with no discernable dispersion in dielectric constant and dielectric loss as well as tuning [Findikoglu et al., 1993]. The voltage-dependent dielectric constant near the Curie temperature becomes the most prominent characteristic in highly epitaxial BSTO thin films with a high dielectric constant and the highest dielectric tunability [Carter et al., 1997]. However, most tunable microwave ferroelectric thin-film elements, such as microstrips, resonators, and phase shifters, should use interdigital structures in which coplanar electrode configurations are fabricated on the ferroelectric thin films. This characterization structure offers many advantages over the parallel-plate method because the capacitance value can be readily designed to have a good impedance matching to the rest of the circuit and can control the microwave propagation in the ferroelectric films. Normally, this interdigital structure has gaps of a few microns between the electrodes in coplanar geometry. By using the conformal mapping based models of Gevorgian et al. [1996], both the dielectric constant and dielectric loss can be extracted from the capacitance measured using the interdigital setup. These conformal mapping models have been applied to the characterizations of dielectric constant, dielectric loss, and dielectric tunability of ferroelectric thin films at various microwave frequencies and different biases [Kirchoefer et al., 1998].

Another important physical factor to determine the quality of dielectric thin films is the figure of merit, M, defined as the tunability/tan δ in zero field, that is,

$$M = \frac{\varepsilon_0 - \varepsilon_V}{\varepsilon_0 \tan \delta}$$

where δ is the dielectric loss. For tunable ferroelectric thin-film applications, M should be as large as possible, which requires the highest dielectric constant together with the lowest value of dielectric loss.

21.4 DEFECTS IN FERROELECTRIC THIN FILMS AT HIGH FREQUENCIES

21.4.1 Point Defects

Point defects in ferroelectric thin films have been found to play an important role in determining the dielectric constant, dielectric loss, and dielectric tunability. Vacancies, substitutional impurities, and interstitial defects result in electronic charge storage within the ferroelectric thin films. Interstitial defects and ions in the wrong lattice sites, referred to as electrically neutral Schottky disorder, do not significantly affect the physical properties of the films [Waser, 1988]. However, oxygen vacancies in a stoichiometric compound result in the formation of negatively charged acceptor centers, which have been recognized to significantly alter the electrical properties of ferroelectric thin films [Chan and Smyth, 1976]. Details about such defect chemistry can be found in the literature [Waser and Smyth, 1996].

Recently, Kim et al. [2000] have systematically investigated the oxygen vacancy effects on the ferroelectric properties and found that a strong correlation exists between the structure and the microwave dielectric properties of epitaxial BSTO (50 : 50) thin films on (001) MgO substrates deposited at 750°C as the oxygen pressure varied from 3 to 1000 mTorr. The ratio of in-plane (Fig. 21.18a) and surface normal (Fig. 21.18c) lattice parameters, $D = a/c$, of these films varies from 0.996 at 3 mTorr to 1.003 at 800 mTorr, as seen in Figure 21.18 a. The influence of oxygen pressure on the microstructure and lattice parameters of the BSTO film in fact resulted from oxygen vacancies in the BSTO film. This can be represented by

$$O_{BSTO} \Leftrightarrow V_O + \tfrac{1}{2}O_2 + 2e \tag{21.1}$$

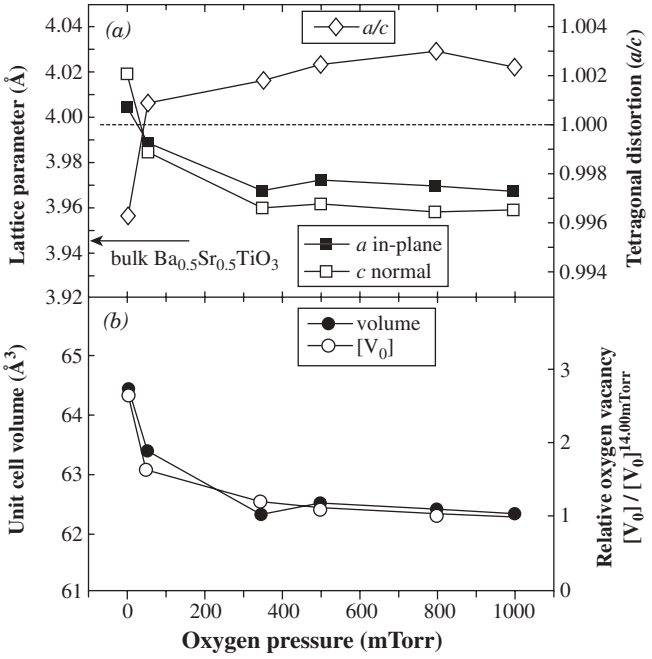

Figure 21.18 Lattice parameters of in-plane, *a,* and the normal plane, *c*, and the ratio between *a* and *c* from the BSTO (50:50) thin films on a (001) MgO substrate plotted as a function of the oxygen deposition pressure [Kim et al., 2000].

where O_{BSTO} and V_O represent oxygen and oxygen vacancy in BSTO, respectively. From a simple mass-action equation, the oxygen concentration can be expressed by

$$[V_O][e]^2 \propto \exp\left(-\frac{\Delta H}{kT}\right) P_{O_2}^{-1/2} \tag{21.2}$$

where $[V_O]$ is the concentration of oxygen vacancies, ΔH is the enthalpy for generating oxygen vacancies, and P_{O_2} is the pressure of oxygen in the chamber. $[O_{BSTO}]$ is constant because of the relatively small number of oxygen vacancies in the BSTO matrix. Based on the assumption that $[V_O]$ is $1/2[e]$, the concentration of the oxygen vacancies at constant T is

$$[V_O] \propto P_{O_2}^{-1/6} \tag{21.3}$$

Oxygen vacancies affect the nearest-neighbor distance by reducing the Coulomb attractive force between cation and anion atoms, resulting in an increased lattice parameter and unit-cell volume. The volume of the unit cell (v) and the relative oxygen vacancy concentration ($[V_O]/[V_O]^{1000\,mTorr}$) shows a strong relationship with oxygen deposition pressure (Fig. 21.18b). Films deposited at low oxygen pressures have more oxygen vacancies than those deposited at higher oxygen pressures. In fact, the lattice parameter and the tetragonal distortion changes of the films result from both the lattice mismatch and the thermal expansion difference between the film and the substrate, and the number of oxygen vacancies.

The dielectric property studies indicate that BSTO films with low distortion have higher dielectric constants (~ 500) and lower dielectric loss (tan ~ 0.02) than films with higher distortions at microwave frequencies (1–20 GHz). BSTO films grown at an oxygen deposition pressure of 50 mTorr exhibit a large dielectric constant change and a low dielectric loss at the same time, which corresponds to a film under low stress ($\Delta = 1.0004$). These results are consistent with published works for BSTO (60 : 40) by Carlson et al. [2000b]. Figure 21.19 shows the dielectric

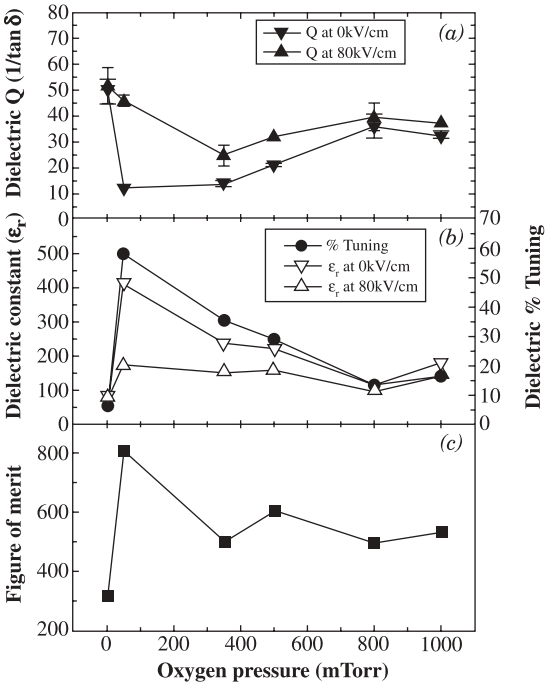

Figure 21.19 Dielectric properties of the BSTO films measured at 10 GHz [Kim et al., 2000].

loss (which is defined as $1/Q$, Q being the dielectric quality factor), dielectric constant, and the figure of merit, measured at 10 GHz, of these BSTO films grown at different oxygen pressures. The films grown at 3 and 50 mTorr oxygen pressure have a high dielectric quality factor Q (~ 50), which increases monotonically with the increase of oxygen partial pressures from 350 to 1000 mTorr. The dielectric constant and its percent tunability are maximized at 50 mTorr, which coincides with the minimum in the film stress ($\Delta = 1.0004$). The dielectric constant and tunability increase monotonically with the decrease of oxygen pressure from 1000 to 50 mTorr. Furthermore, the figure of merit of the film with the minimum stress (at 50 mTorr) shows a maximum value ~ 800. This strongly suggests that films with low stress are highly desirable for tunable microwave device applications.

21.4.2 Strain Effects on Dielectric Properties

The fact that oxygen vacancies affect the ferroelectric properties considered above is only one of many contributing factors. Oxygen vacancies formed in thin films in fact also alter the lattice parameters and the thermal expansion. During film growth, the expanded BSTO lattice will distort and expand along the in-plane direction due to the larger MgO lattice parameter ($a = 4.2113$ Å), resulting in a tetragonally distorted BSTO lattice. During cooling to room temperature, the BSTO film will experience a compressive stress due to the different thermal expansion coefficients between the BSTO film and the MgO substrate. The observed tetragonal distortion change from $a/c > 1$ over 350 mTorr to $a/c < 1$ below 3 mTorr and the monotonic increase in the unit-cell volume with decreasing oxygen pressure could be the overall result from the lattice mismatch, thermal expansion coefficient difference, oxygen vacancies, and attractive force among atoms in the film.

Strain effects on the dielectric properties of ferroelectric thin films have been widely studied both in theory and via experiment over the past several years. Their effect on the shift of the Curie temperature and the reduction and broadening on the dielectric constant have been treated by using nonlinear thermodynamic and phenomenological models on the misfit strain field [Rossetti et al., 1991; Ban and Alpay, 2003; Emelyanov et al., 2002]. Recent experimental studies [Rossetti et al., 1991; James and Xi, 2002; Chang et al., 2002; Huang and Berger, 2003; Li et al., 2001; Canedy et al., 2000] have shown that internal stresses strongly affect the dielectric properties of BSTO thin films on various substrates, and the dielectric constant change can be as much as an order of magnitude in epitaxial BSTO thin films. The internal stress is generated either from different substrate materials or different film thicknesses. Experimental results also reveal that the dielectric tunability of BSTO films is highly dependent upon the lattice misfit (the misfit strain). It is very interesting and important to note that the annealing treatments for reducing residual stresses in BSTO thin films have significantly improved the tunability from 36 to 52% at a 57-kV/cm field on a ''compressive'' LAO substrate but reduced the tunability from 47 to 38% on ''tensile'' MgO substrates [Carlson et al., 2000b], as seen in Figure 21.20. Hyun and Char [2001] have studied the strain effect and the dielectric properties of STO ($a = 0.3905$ nm) thin films grown on (001) STO and (001) LAO with $SrRuO_3$ ($a = 0.393$ nm) and $CaRuO_3$ ($a = 0.385$ nm) bottom electrodes, which produce opposite lattice mismatches between the BSTO films and bottom electrodes. They used both a ''compressive'' bottom electrode of $CaRuO_3$ and a ''tensile'' bottom electrode of $SrRuO_3$ and found that the dielectric constant and tunability are strongly dependent on the bottom electrode material, as seen in Figure 21.21. The in-plane lattice parameters are smaller than those normal to the plane for films on $CaRuO_3$ electrodes and larger for films on $SrRuO_3$ bottom electrodes. The films with compressive strain (on $CaRuO_3$) have much larger tunability than those on the relaxed ones. These phenomena of the effects on the dielectric properties from the misfit strain in epitaxial ferroelectric films are consistent with the theoretical predictions, and this implies that the dielectric properties, both dielectric constant and tunability, can be significantly improved by selecting ''compressive'' substrates for future development of high-quality tunable microwave devices.

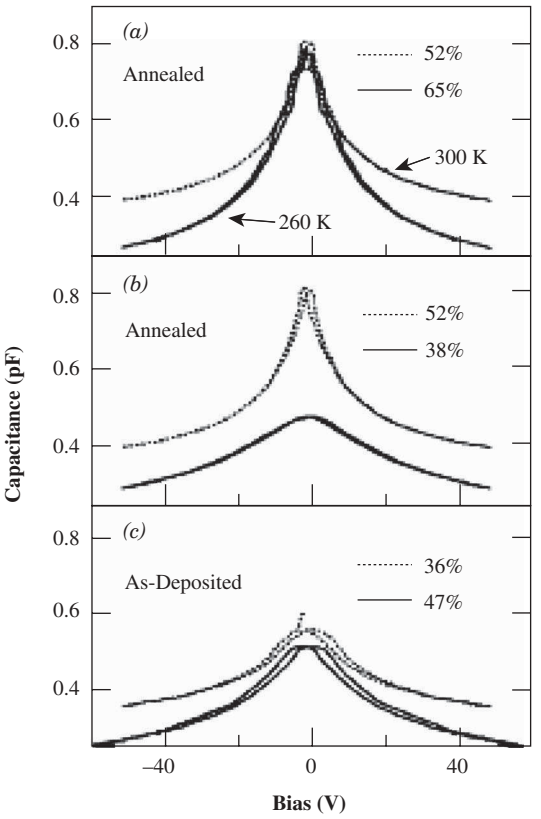

Figure 21.20 High-frequency tunability of BSTO films on (a) LAO and (b) MgO and their comparison (c) showing the effects of sample treatments with and without postannealing [Carlson et al., 2000a].

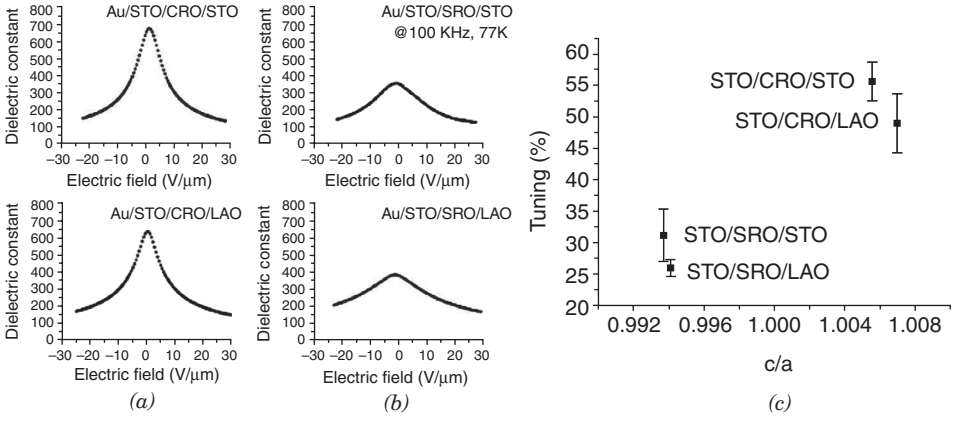

Figure 21.21 (a)–(d) Dielectric constant vs. electric field of STO thin films on different electrodes and substrates in parallel plate capacitors. (e) Tunability measured at 10 V/mm vs. lattice ratio of STO films [Hyun and Char, 2001].

21.4.3 Formation of Antidomain Structures in Ferroelectric Thin Films

The domain structures, epitaxial quality, and dielectric properties can also be influenced by the substrate surface structures, that is, surface terraces, steps, and many surface defects. Even films grown under optimal conditions, as discussed previously, cannot achieve optimum ferroelectric properties, as the lattice matching and surface-step-terrace structure can alter the film microstructure. Generally, the interface strain energy from this lattice mismatch can be released by the formation of edge dislocations at the interface if the film thickness is larger than the critical thickness. Figure 21.22a is a dark-field image using the common (020) reflection of both BSTO (60 : 40) and MgO. As seen in Figure 21.22b, the HRTEM image shows the equally spaced misfit dislocations formed at the interface. The average distance between two adjacent dislocations is about 3.2 nm. Equally spaced dislocations (marked by arrows) were again observed at the interface for every 16 (020) lattice planes of BSTO, or 15 (020) lattice planes of MgO along the [010] MgO direction. This lattice mismatch value is very close to the theoretical value, suggesting that the strain arising from the lattice mismatch is fully relaxed at the interface by forming misfit dislocations.

It should be noted that the surface terminations of MgO have the same atomic structures but are displaced a half unit cell along the [100] MgO direction with respect to each other. Each termination has a half unit-cell step height difference on the (001) MgO surface. Recent research indicates that the growth of the initial layer of BSTO film on the (001) MgO surface is a TiO_2 monolayer [Jiang et al., 2002]. Thus, the BSTO thin films on a (001) MgO substrate form two types of epitaxial domain that have a half unit-cell shift along the *c*-axis direction. The steps with different heights will result in the formation of different domains (antidomains) in the films. Figure 21.22c is a TEM image showing an antidomain boundary of a BSTO thin film formed on a (001) MgO, and Figure 21.22d is an HRTEM image detailing the antidomain boundary directly formed from the surface step terrace. This can be well explained by the schematic in Figure 21.23a showing the detailed surface structures of a MgO surface. When BSTO thin films grow on a (001) MgO substrate that normally consists of steps with a height of half a unit cell [$\frac{1}{2}a_{MgO}$ (step 2 in Fig. 21.22d)] or unit-cell height [a_{MgO} (step 1

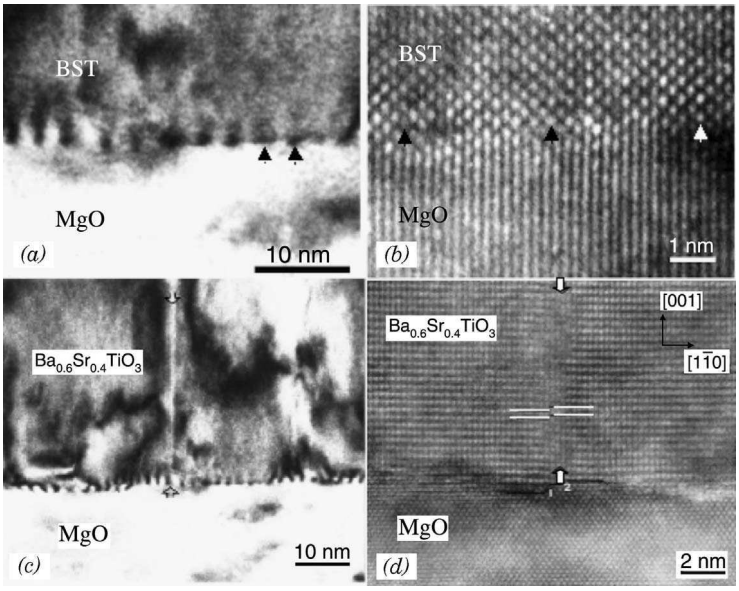

Figure 21.22 Cross-section TEM images show the edge dislocations and antidomain boundary formed at the interface of the BSTO thin film and MgO substrate. The arrows in (a) and (b) indicate the locations of the edge dislocations. The broad arrows in (c) and (d) point to the antidomain boundaries [Jiang et al., 2002].

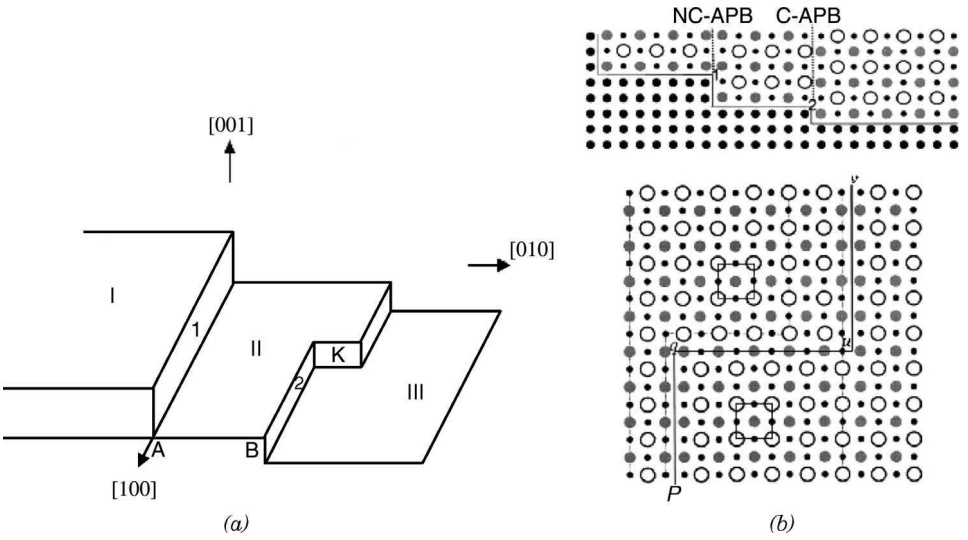

Figure 21.23 Schematic of a perovskite film on a rock salt substrate: (a) the substrate surface structures, (b) cross-sectional view along the [100] substrate direction, and (c) the [001] direction view of the antidomain boundaries [Jiang et al., 2002].

in Fig. 21.22d)], the BSTO crystal grown on terrace II will be displaced by ½a_{BSTO} along the [001] MgO growth direction with respect to the structure on terrace III. Thus, a conservative antiphase boundary (with the displacement vector parallel to the boundary plane) that is parallel to the growth direction, is formed between these two steps. A half unit-cell height shift between these two domains can be clearly revealed in the image. Similarly, the terrace structures of the substrate will also affect the microstructure of the thin films. As stated above, the first monolayer of the BSTO thin films on the MgO substrate was identified as the TiO_2 monolayer. It is reasonable to assume that the BSTO film growth follows this atomic sequence during the film growth on MgO surface. This suggests that the first atomic layer, which is the adjacent layer to the substrate step terrace, is theTiO_2 or Ti—O chain. If the substrate surface terrace width is equal to n unit cells of the BSTO films and the first adjacent atom is Ti, the atom at the end of the terrace should be O. Hereafter, the next adjacent atom from the second layer of the lower (half a unit-cell different) step terrace will be an O atom again, which will result in an O—O atomic chain at the domain boundary; and so on. Similarly, when a terrace width is equal to $(n + \frac{1}{2})$ BSTO unit cells and is of a single MgO step height, the initial row and the last row will be Ti—O atomic chains. Accordingly, in the as-grown BSTO structure, the first and the last crystal planes that are parallel to both growth direction and step, would be the TiO_2 planes. The TiO_2 planes of two adjacent terraces will adhere at the last or topmost TiO_2 plane. In other words, the BSTO grown on the terrace with a width of an odd number of a_{MgO} will be displaced by a_{BSTO} with respect to that on the adjacent terraces along the direction that is perpendicular to the steps. A step one-half unit-cell high in the MgO substrate forces the cubic structure of BSTO to slightly adjust itself to compensate for the half unit-cell displacement. A nonconservative antiphase boundary (with the displacement vector perpendicular to the boundary plane) that is parallel to the growth direction and the step, subsequently forms between the structures grown on the adjacent terraces (NC-APB in Fig. 21.23b). Within a thin film grown on a terrace with a width of an even number of a_{MgO}, a nonconservative antiphase boundary will not be formed in the BSTO structures grown on the adjacent terraces. These results indicate that the substrate surface can strongly affect the microstructures of as-grown films. These growth models can be extended to all other perovskite thin films on MgO surfaces and other materials. Also, the strong effects from surface step terraces have recently been observed from miss-cut substrates, as described below.

TABLE 21.2 Dielectric Properties of BSTO Films on Miss-cut (001) MgO at 2.0 GHz

Sample Types	Film Thickness (μm)	C_{0V} (pF)	ε_r(0V)	C_{40V} (pF)	ε_r (40V)	Gap Tuning (%)	ε_r Tuning (%)
(001)-0.0° off	0.3	0.930	1996	0.493	915	47	54
(001)-1.0° off	0.3	0.774	1664	0.442	800	43	52
(001)-3.0° off	0.3	0.473	1059	0.345	663	27	37
(001)-5.0° off	0.3	0.924	1655	0.440	635	52	62

21.4.4 Effects from Vicinal Surfaces

Recently, Chen and Horwitz [submitted] have systematically investigated the epitaxial behavior and physical properties of ferroelectric BSTO (60 : 40) thin films on vicinal (001) MgO substrates with different off-cut angles of 0.0°, 1.0°, 3.0°, and 5.0°. They have discovered that the BSTO thin films grown on 1.0° and 5.0° off-cut (001) MgO substrates have similar dielectric properties to those on (001) MgO substrates, as seen in Table 21.2. However, the BSTO thin films grown on the 3.0° off-cut MgO substrates display much worse dielectric properties, that is, lower dielectric constant and lower dielectric tunability as well as higher dielectric loss. Similar results have been observed in the Naval Research Laboratory [Wu, personal communication] as well as on Mn-doped BSTO thin films [Yuan et al., 2005]. Microstructure studies from cross-sectional TEM reveal that the BSTO thin films grown on 1.0° and 5.0° off-cut (001) MgO substrates have excellent single-crystal quality and epitaxial behavior with very smooth film surfaces, as seen in Figure 21.24a and 21.24e. Periodical misfit dislocations are formed at the interfaces between the BSTO films and MgO substrates (Fig. 21.24b and 21.24f). However, the films grown on 1.0° off-cut (001) MgO substrates are largely polycrystalline toward the upper film areas, although a good single-crystal layer with a thickness of only 150 nm is grown on the substrate surface. The BSTO film surfaces become very rough. Particlelike structures are formed on the top surface areas, as seen in Fig. 21.23c. Furthermore, misfit

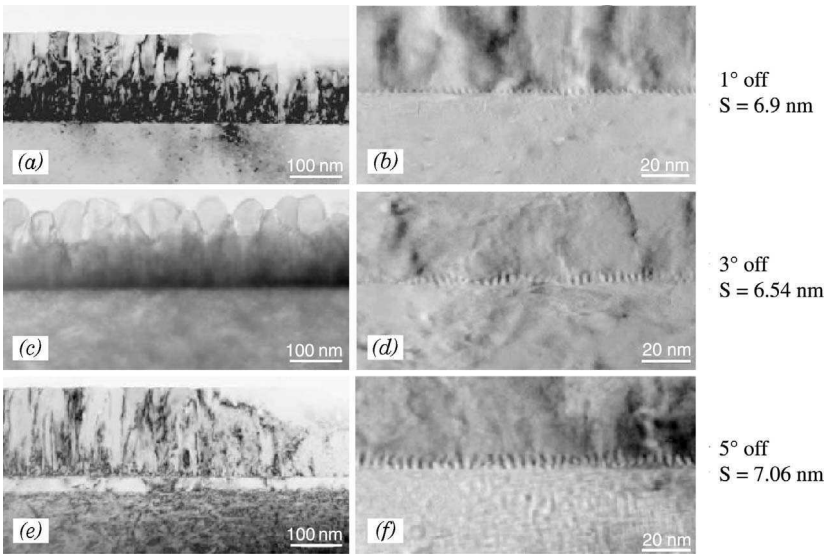

Figure 21.24 Cross-sectional TEM images showing the interface structures and edge dislocation distributions of BSTO thin films on (001) vicinal MgO substrates: (a) 1.0° off, (b) 3.0° off, and (c) 5.0° off [Chen and Horwitz, submitted].

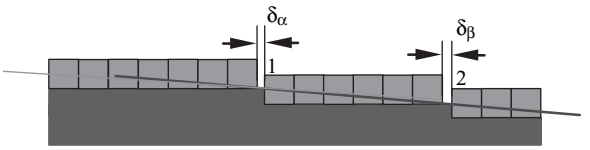

Figure 21.25 Schematic showing lattice gaps formed at the substrate terraces by lining up different numbers of unit cells of films [Chen and Horwitz, submitted].

dislocations form quasi-periodic structures at the interface between the films and substrate surfaces. Therefore the strain energy at the interface is not uniformly distributed, which can be directly observed in the images (Fig. 21.23d).

To understand the mechanisms that cause these interesting and unusual dielectric properties, Chen and Horwitz [submitted] have systematically examined the relationship of epitaxial behavior and substrate surface structures. They note that the different off-cut angles give different step widths on the vicinal MgO surface terraces. Early studies [Jiang et al., 2002] indicate that the antiphase domain boundaries, both conservative and nonconservative, formed on the MgO surface were highly dependent upon the surface step width. If the BSTO films grown on the MgO surface terrace is the same sequence as what grows on pure (001) MgO surface, then the line up of BSTO unit cells on the MgO terraces might result in various gaps δ_α at the surface terrace edges (Fig. 21.25), in which δ_α depends on the step width of the off-cut substrate. Theoretical estimations show that both 1.0° and 5.0° off-cut substrates will have 17.38 and 3.47 BSTO unit cells on the vicinal MgO surface terraces. Both numbers suggest that antidomain boundaries form at the MgO surface step terrace edges with tensile stresses of 0.75 and 0.85%. However, the BSTO films on 3.0° off-cut surfaces result in either a compressive stress of 3.7% or a tensile stress of 5.1%. The large extra strain energies together with the lattice misfit strain energy will cause many dislocations to form in the films and result in the polycrystalline structures on the top of film surface to relieve the strain energy.

21.5 TECHNIQUES TO IMPROVE DIELECTRIC PROPERTIES OF FERROELECTRIC THIN FILMS

It is well known that the physical properties and microstructure of ferroelectric thin films, that is, BSTO, PSTO, PZT, and others, are highly dependent upon the processing conditions and treatments. Controlling the processing temperatures and oxygen pressures as well as and posttreatments can significantly influence the crystallinity and physical properties of the as-grown thin films. To improve the dielectric properties, that is, increase tunability and decrease the dielectric loss, many attempts have focused on the improvement of epitaxial single crystalline quality, the control of films stress, and the modification of the compositions of the films. The techniques for improving the as-grown film quality include controlling the interface structures to reduce interface strain energy and grow highly epitaxial films, optimize processing conditions for achieving cubic phase dielectric structures with oxygen vacancies, and alter the chemistry by introducing small amounts of variable valence elements to neutralize the donor action of the oxygen vacancies. Recently, Bubb et al., [submitted] has achieved a high dielectric constant (500) with extremely low dielectric loss (1/600) for BSTO thin films on (001) MgO substrates in the 1–20 GHz frequency range by using a low oxygen partial pressure (50 mTorr) during deposition and a high temperature (1000°C) and high oxygen pressure (1 atm) postannealing procedure. This impressive result further verifies the previous conclusions of the oxygen pressure and vacancy effects on the physical properties of the BSTO thin films, as seen in Section 21.4.

Another important technique to improve the microwave dielectric properties, both low loss and large tunability, at microwave frequencies is to modify the chemicals in the ferroelectric thin films by introducing small concentrations of acceptor dopants into the films, which has been found to

dramatically alter the properties of ferroelectric materials. The most common acceptor dopants for reducing the dielectric loss in ferroelectric BSTO and related perovskite thin films are those variable valence elements such as Fe, Co, Mn, Ni, W, and Mg, which can occupy the B sites of the $A^{2+}B^{4+}O_3$ perovskite structure. It should be noted that doping with donors, such as Nb, to substitute for the Ti ions in BSTO films leads to highly electrical conductive films. Recently, Mg- and Mn-doped BSTO thin films have become the most attractive systems because they can significantly reduce the dielectric loss, enhance the resistivity of the films, and increase dielectric tunability [Cole et al., 2000; Joshi and Cole, 2000]. The mechanisms responsible for improving the dielectric and insulating properties of ferroelectric thin films concerns those elements that can neutralize the donor action of the oxygen vacancies because the acceptor-type dopants can prevent the reduction of Ti^{4+} to Ti.$^{3+}$ The key factor in the dielectric loss mechanism is that the electrons (the space charge) generated from the oxygen vacancies can hop between different titanium ions whereas the acceptor dopants such as Mg^{2+} and Mn^{2+} can compensate for the charges for oxygen vacancies with the correct amount to lower the dielectric loss. On the other hand, the doping can reduce and broaden the dielectric phase transition resulting in a smaller temperature coefficient of capacitance in the dielectric thin films as compared with undoped materials.

Recently, many excellent results have been achieved in BSTO thin films by using Mg- or Mn-doping [Joshi and Cole, 2000; Ahn et al., 2002; Jain et al., 2003b; Chang and Sengupta, 2002; Cole et al., 2003]. For instance, Cole (2003) obtained a dielectric constant of 348 with a dielectric loss value of 0.007 in 1 mol % Mg doped BSTO thin films. Yuan et al. [2005] have achieved an excellent result of a particularly high dielectric constant of 1200 with an extremely low dielectric loss of 0.005 at 12 GHz in the 0.5% Mn-doped BSTO thin films. An exceptionally large dielectric tunability of 67% has been attained for an applied electric field of 4.0 V/μm.

Other techniques for improving the microwave dielectric thin-film properties include the doping of BSTO thin films by using TiO_2 and increasing the film thickness. Jia et al. [2002] and Im et al. [2002] have independently found that TiO_2-doped BSTO thin films can significantly reduce the dielectric loss in the BSTO thin films. Although the mechanisms are not well understood yet, the extra Ti in the BSTO films may compensate the charge distribution generated by the presence of oxygen vacancies.

21.6 SUMMARY

Pulsed laser deposition is one of the most powerful techniques in oxide thin-film synthesis, especially for the epitaxial growth of complex ferroelectric thin-film materials. With this unique technique, many highly epitaxial ferroelectric thin films with excellent physical properties and good stoichiometry have been achieved in the past two decades, which enable scientists and engineers to perform both fundamental and applied thin-film materials research for the development of material strategies in microelectronic thin-film devices.

In the area of high-frequency room temperature tunable microwave device fabrication, pulsed laser deposition has played a key role for ferroelectric thin-film epitaxy. The highest performances in tunable microwave elements, such as microstrip phase shifters, have only recently been achieved. Highly epitaxial growth of ferroelectric thin-films, such as BSTO, PSTO, and others, allows further investigations of the epitaxial behavior and physical properties relationships. In conclusion, pulsed laser ablation of thin films will continually remain one of the most important techniques in ferroelectric thin-film synthesis and tunable microwave device fabrication.

Acknowledgments

The authors gratefully acknowledge the support of the National Science Foundation (NSF0528873) and the State of Texas through the Texas Center for Superconductivity at the University of Houston. We would like to thank Dr. S. W. Liu, Miss J. Weaver, and Miss Z. Yuan for their assistance during the preparation of this chapter.

REFERENCES

Abadei, S., Gevorgian, S., Cho, C. R., and Grishin, A. (2002), *Appl. Phys. Lett*. **91**, 2267.

Ahn, K. H., Baik, S., and Kim, S. S. (2002), *J. Appl. Phys*. **92**, 2651.

Ban, Z. G., and Alpay, S. P. (2003), *J. Appl. Phys*. **93**, 504.

Bird, J. R., and Williams, J. S. (eds.) (1989), *Ion Beams for Materials Analysis*, Academic, Sydney.

Bubb, D. M., Horwitz, J. S., Qadri, S. B., Kirchoefer, S. W., Hubert, C., and Levy, J. (submitted), *Appl. Phys. Lett.*

Canedy, C. L., Li, H., Alpay, S. P., Salamanca-Riba, L., Roytburd, A. L., and Ramesh, R. (2000), *Appl. Phys. Lett*. **77**, 1695.

Carlson, C. M., Parilla, P. A., Rivkin, T. V., Perkins, J. D., and Ginley, D. S. (2000a), *Appl. Phys. Lett.* **77**, 3278.

Carlson, C. M., Rivikin, T. V., Parilla, P. A., Perkins, J. D., Ginley, D. S., Kozyrev, A. B., Oshadchy, V. N., and Pavlov, A. S. (2000b), *Appl. Phys. Lett*. **76**, 1920.

Carroll, K. R., Pond, J. M., Chrisey, D. B., Horwitz, J. S., Leuchtner, R. E., and Grabowski, K. S. (1993), *Appl. Phys. Lett*. **62**, 1845.

Carter, A. C., Horwitz, J. S., Chrisey, D. B., Pond, J. M., Kirchoefer, S. W., and Chang, W. (1997), *Integr. Ferroelectr.* **17**, 273.

Chan, N. H., and Smyth, D. M. (1976), *J. Electrochem. Soc*. **123**, 1584.

Chang, K. (1989), *Handbook of Microwave and Optical Components*, Vol. 1: *Microwave Passive and Antenna Components*, Wiley, New York.

Chang, W., and Sengupta, L. (2002), *J. Appl. Phys*. **92**, 3941.

Chang, W., Kirchoefer, S. W., Pond, J. M., Horwitz, J. S., and Sengupta, L. (2002), *J. Appl. Phys*. **92**, 1528.

Chen, C. L., Cao, Y., Huang, Z. J., Jiang, Q. D., Zhang, Z., Sun, Y. Y., Kang, W. N., Dezaneti, L. M., Chu, W. K., and Chu, C. W. (1997), *Appl. Phys. Lett*. **71**, 1047.

Chen, C. L., Feng, H. H., Zhang, Z., Brazdeikis, A., Miranda, F. A., Van Kewls, F. W., Romanofsky, R. R., Huang, Z. J., Liou, Y., Chu, W. K., and Chu, C. W. (1999), *Appl. Phys. Lett.* **75**, 412.

Chen, C. L., Shen, J., Chen, S. Y., Luo, G. P., Chu, C. W., Miranda, F. A., Van Keuls, F. W., Jiang, J. C., Meletis, E. I., and Chang, H. Y. (2002a), *Appl. Phys. Lett*. **78**, 652.

Chen, J. H., Jia, C. L., Urban, K., and Chen, C. L. (2002b), *Appl. Phys. Lett*. **81**, 1291.

Chen, C. L., Horwitz, J. S., et al. (Submitted), *Nature*.

Chrisey, D. B., and Hubler, G. K. (1994), *Pulsed Laser Deposition of Thin Films*, Wiley, New York.

Cole, M. W., Joshi, P. C., Ervin, M. H., Wood, M. C., and Pfeffer, R. L. (2000), *Thin Solid Films* **374**, 34.

Cole, M. W., Nothwang, W. D., Hubbard, C., Ngo, E., and Ervin, M. H. (2003), *J. Appl. Phys*. **93**, 9218.

Cowley, J. M. (1981), *Diffraction Physics*, 2nd ed., North-Holland, Amsterdam.

Cullity, B. D. (1978), *Elements of X-Ray Diffraction*, 2nd ed., Addison-Wesley, Reading, MA.

Dick, G. J., and Santiago, D. (1992), *IEEE Freq. Control Symp. Proc.* **46**, 176–182.

Emelyanov, A. Y., Pertsev, N. A., and Kholkin, A. L. (2002), *Phys. Rev. B* **66**, 214108.

Fax, A. G. (1947), *Proc. IRE* **35**, 1489.

Findikoglu, A. T., Doughty, C., Anlage, S. M., Li, Q., Xi, X. X., and Venkatesan, T. (1993), *Appl. Phys. Lett*. **63**, 3215.

Galt, D., Price, J. C., Beall, J. A., and Ono, R. H. (1993), *Appl. Phys. Lett*. **63**, 3078.

Gao, H. J., Chen, C. L., Rafferty, B., Pennycook, S. J., Luo, G. P., and Chu, C. W. (1999), *Appl. Phys. Lett*. **75**, 2542.

Gevorgian, S., Carlsson, E., Rudner, S., Wernlund, L. D., Wang, X., and Helwersson, U. (1996), *IEEE Proc. Microm. Antennas Propag*. **143**, 397.

Gikow, E. (1971), U. S. Patent No. 3,569,795.

Gim, Y., Hundson, T., Fan, Y., Kwon, C., Findikoglu, A. T., Gibbons, B. J., Park, B. K., and Jia, Q. X. (2000), *Appl. Phys. Lett*. **77**, 1200.

Hellwege, K. H., and Hellwege, A. M. (1981), "Ferroelectrics and Related Substances," subvolume a: Oxides, in *Landolt-Bornstern Numerical Data and Functional Relationships in Science and Technology*, Vol. 16. K. -H. Hellwege (Ed.), Springer, Berlin.

Henrich, V. E., and Cox, P. A. (1994), *The Surface Science of Metal Oxides,* Cambridge University Press, Cambridge, MA.

Horwitz, J. S., Chrisey, D. B., Pond, J. M., Auyeung, R. C. Y., Cotell, C. M., Grabowski, K. S., Dorsey, P. C., and Kluskens, M. S. (1995), *Integ. Ferroelectr.* **8**, 53.

Huang, G. F., and Berger, S. (2003), *J. Appl. Phys*., **93**, 2855.

Hyun, S., and Char, K. (2001), *Appl. Phys. Lett*. **79**, 254.

Im, J., Auciello, O., and Streiffer, S. K. (2002), *Thin Solid Films* **413**, 243.

Jacobson, A. J., personal communication.

Jain, M., Majumder, S. B., Katiyar, R. S., Bhalla, A. S., Agrawal, D. C., Van Keuls, F. W., Miranda, F. A., Romanofsky, R. R., and Mueller, C. H. (2003a), *Proc. Mater. Res. Soc*. **748**, U3.17.1.

Jain, M., Majumder, S. B., Katiyar, R. S., Miranda, F. A., and Van Keuls, F. W. (2003b), *Appl. Phys. Lett*. **82**, 1911.

James, A. R., and Xi, X. X. (2002), *J. Appl. Phys*. **92**, 6149.

Jia, Q. X., Miranda, F. A., Oates, D. E., and Xi, X. X. (2000), "Materials Issues for Tunable RF and Microwave Devices," *MRS Proc.* **603**.

Jia, Q. X., Park, B. H., Gibbons, B. J., Huang, J. Y., and Lu, P. (2002), *Appl. Phys. Lett*. **81**, 114.

Jiang, J. C., and Chen, C. L. (2001), "Applications of Electron Microscopy in Superconductors and Related Materials," in *Industrial Applications of Electron Microscopy*, R. Li (Ed.), Marcel Dekker, New York, pp. 421–458.

Jiang, J. C., Lin, Y., Chen, C. L., Chu, C. W., and Meletis, E. I. (2002), *J. Appl. Phys.* **91**, 3188.

Joshi, P. C., and Cole, M. W. (2000), *Appl. Phys. Lett*. **77**, 289.

Kim, K. T., and Kim, C. I. (2002), *Thin Solid Films* **420/421**, 544.

Kim, W. J., Chang, W., Qadri, S. B., Pond, J. M., Kirchoefer, S. W., Chrisey, D. B., and Horwitz, J. S. (2000), *Appl. Phys. Lett*. **76**, 1185.

Kirchoefer, S. W., Pond, J. M., Carter, A. C., Chang, W., Agarwal, K. K., Horwitz, J. S., and Chrisey, D. B. (1998), *Microwave Opt. Technol. Lett.*, **18**, 168.

Knauss, L. A., Pond, J. M., Horwitz, J. S., Chrisey, D. B., Mueller, C. H., and Treece, R. (1996), *Appl. Phys. Lett*. **69**, 25.

Koul, S. K., and Bhat, B. (1991), *Microwave and Millimeter Wave Phase Shifters*, Vol. 1: *Dielectric and Ferrite Phase Shifters*, Artech House, Norwood, 1991.

Kuo, S. Y., Li, C. T., and Hsieh, W. F. (2002), *Appl. Phys. Lett.* **81**, 3019.

Land, C. E., Thacher, P. D., and Haertlin, G. H. (1974), *Electroopt. Ceram.* **4**, 137.

Landolt-Börnstein (1981), in *Numerical Data and Functional Relationships in Science and Technology*, Vol. 16, K.-H. Hellwege and A. M. Hellwege (Eds.), Springer, Berlin.

Li, H., Roytburd, A. L., Alpay, S. P., Tran, T. D., Salamanca-Riba, L., and Ramesh, R. (2001), *Appl. Phys. Lett*. **78**, 2354.

Lin, Y., Chen, X., Liu, S. W., Chen, C. L., Lee, J.-S., Li, Y., Jia, Q. X., and Bhalla, A. (2004), *Appl. Phys. Lett*. **84**, 577.

Lin, Y., Chen, X., Liu, S. W., Chen, C. L., Lee, J. -S., Li, Y., Jia, Q. X., and Bhalla, A. (2005), *Appl. Phys. Lett*. **86**, 142902.

Lines, M. E, and Glass, A. M. (1977), "Macroscopic and Phenomenology," in *Principles and Applications of Ferroelectrics and Related Materials*, Clarendon, Oxford, pp. 59–86.

Liu, S. W., Weaver, J., Lin, Y., Donner, W., Chen, X., Chen, C. L., Jiang, J. C., Meletis, E. I., and Bhalla, A. S. (2004), *Appl. Phys. Lett*. **85**, 3202.

MaGibbon, A. J., Pennycook, S. J., and Angelo, J. E. (1995), *Science* **269**, 519.

Matsumoto, T., Tanaka, H., Kawai, T., and Kawai, S. (1992), *Surf. Sci*. **278**, L153.

McKee, R. A., Walker, F. J., Specht, E. D., Jellison, J. G. E., and Boatner, L. A. (1994), *Phys. Rev. Lett.* **72**, 2741.

Messier, R., Giri, A. P., and Roy, R. (1984), *J. Vac. Sci. Technol*. **A2**, 500.

Panov, V. I., and Stankov, P. R. (1986), *Radiotech. Electron.* **31**, 213–223.

Park, B. H., Gim, Y., Fan, Y., Jia, Q. X., and Lu, P. (2000), *Appl. Phys. Lett*. **77**, 2587.

Pennycook, S. J. (1997), "STEM: Z-contrast," in *Handbook of Microscopy*, S. Amelinckx, D. Van Dyck, J. Van Landuyt, and G. Van Tendeloo, (Eds.), VCH, Weinheim, p. 595.

Rao, C. N. R., and Reveau, B. (1995), *Transition Metal Oxides*, VCH Publishers, New York.

Romanofsky, R. R., Van Keuls, F. W., and Miranda, F. A. (1998), *J. Phys.* **8**, 171.

Rossetti, G. A., Cross, L. E., and Kushida, K. (1991), *Appl. Phys. Lett*. **59**, 2524.

Santiago, D., and Dick, G. J. (1993), *IEEE Freq. Control Symp. Proc.* **47**, 774–778.

Steinhauer, D. E., Vlahacos, C. P., Wellstood, F. C., Anlage, S. M., Canedy, C., Ramesh, R., Stanishevsky, A., and Melngailis, J. (1999), *Appl. Phys. Lett*. **75**, 3180.

Tidrow, S. C., Horwitz, J. S., Xi, X. X., and Levy, J. (2002), ''Materials Issues for Tunable RF and Microwave Devices III,'' *MRS Proc.* **720**.

Tilley, D. R. (1996), ''Finite Size Effects on Phase Transistion in Ferroelectric,'' in *Ferroelectric Thin Films: Sythesis and Basic Properties*, C. P. de Araujo, J. F. Scott, and G. W. Taylor (Eds.), Gordon and Breach.

Treece, R. E., Thompson, J. B., Mueller, C. H., Rivkin, T., and Cromar, M. W. (1997), *IEEE Trans. Appl. Supercond*. **7**, 2363.

Tuttle B. A., and Schwartz, R. W. (1995), *MRS Proc.* 361.

Tyunina, M., and Levoska, J. (2001), *Phys. Rev. B* **63**, 224102.

Van Keuls, F. W., Romanofsky, R. R., Bohman, D. Y., Winters, M. D., Miranda, F. A., Mueller, C. H., Treece, R. E., Rivkin, T. V., and Galt, D. (1997), *Appl. Phys. Lett*. **71**, 3075.

Walls, F. L., Felton, C. M., and Martin, T. D. (1990), *IEEE Freq. Control Symp. Proc.* **44**, 542–547.

Wang, Y. G., Reeves, M. E., Kim, W. J., Horwitz, J. S., and Rachford, F. J. (2001), *Appl. Phys. Lett.* **78**, 3872.

Waser, R. (1988), *J. Am. Ceram. Soc*. **71**, 58.

Waser, R., and Smyth, D. M. (1996), ''Defect Chemistry, Conduction, and Breakdown Mechanism of Perovskite-Structure Titanates,'' in *Ferroelectric Thin Films: Sythesis and Basic Properties*, C. P. de Araujo, J. F. Scott, and G. W. Taylor (Eds.), Gordon and Breach.

Wu, J., and Horwitz, J. S., personal communication.

Yuan, Z., Chen, C. L., Lin, Y., Jiang, J. C., Meletis, E. I., and Subramanyam, G. (2005), *Appl. Phys. Lett.* **87**, 152901.

Yuan, Z., Xu, X. M., Liu, J., and Chen, C. L. (in press), *Surf. Sci.*

CHAPTER 22

Films for Electrochemical Applications

MACARENA J. MONTENEGRO and THOMAS LIPPERT
Paul Scherrer Institut, General Energy Research Department, Villigen, Switzerland

22.1 INTRODUCTION

The potential of thin films prepared by pulsed laser deposition (PLD) for electrochemical applications has only been recognized recently, but the number of studies is increasing steadily. There are also still new directions in electrochemistry to be explored, where PLD films have not yet been applied, but with a large future potential. Some examples are discussed in the context of possible future directions and in the conclusions of this chapter. The reason for the late recognition of PLD films for electrochemical studies is probably related to the fact that many electrochemical studies are associated with wet chemistry, that is, liquid electrolytes. This environment is probably still quite exotic for many groups that work in the typical vacuum environment of PLD. Another reason is the fact that electrochemistry is a fairly applied research field, where many of the materials are mass products and therefore not really a target for PLD films.

The recent importance of renewable energy sources has sparked research in electrochemistry on very fundamental and applied levels. The most prominent applications are rechargeable batteries and fuel cells, and many car manufacturers have already built a fuel cell car because fuel cell cars are considered to be one of the most promising options for future sustainable mobility [Junker et al., 2001; Folkesson et al., 2003; Linssen et al., 2003; Shukla et al., 2003]. Both types of electrochemical power storage/generation have been, in principle, known for a long time (a short history is given below), but fuel cell technology is not yet cost-competitive. One of the most important drawbacks are the materials, which are either very expensive noble metals (e.g., Pt as catalysts in polymer electrolyte membrane fuel cells) or are lacking in performance and/or stability. It is therefore one of the main future tasks to identify and develop new materials that will fulfill the necessary requirements. PLD has the potential to be a very useful tool for this research and can play an important role in two different ways: that is, for material development and as a method to produce model systems for parametric studies.

The first approach utilizes one of the major strengths of PLD, that is, the synthesis of materials that cannot be obtained by other methods (metastable phases [Gupta et al., 1994; Lowndes et al., 1996; Krebs 1997; Gorbunov et al., 2002; Levin et al., 2003]), or in combination with the recent development of combinatorial approaches [Koida et al., 2002; Lippmaa et al., 2002; Takahashi et al., 2002; Aronova et al., 2003; Ohkubo et al., 2003] to PLD as a fast screening method for a systematic variation of material compositions. Both approaches can easily be utilized to test and develop new more efficient catalysts, for example, the systematic variation of an $A_xA'_{1-x}BO_3$ perovskite where x

Pulsed Laser Deposition of Thin Films: Applications-Led Growth of Functional Materials
Edited by Robert Eason

is varied in discrete steps. The other important role of PLD is the possibility of preparing model systems, which is, of course, closely related to the above described material developments.

Most electrochemical systems have one major feature in common: They are applied as electrodes, electrolytes, and electrocatalyst in electrodes. Electrodes, for example, are normally complex systems that often contain an electrocatalyst, a catalyst support material, and many other components. One of the most common materials in electrodes is carbon, which has the necessary conductivity, but is also active for many catalytic reactions, for example, oxygen reduction and evolution (see Figs. 22.12 and 22.13). The other important parameter for electrochemical systems is the stability of its components, for example, the catalyst in an environment that is chemically very reactive, that is in alkaline or acidic solution with an applied potential. The two important parameters for the electrocatalyst, that is, the stability and reactivity are therefore nearly impossible to study with real electrodes that contain many elements.

The activity of the electrode, for example, cannot be directly assigned to the catalyst but is very often a superposition of all components, including the active carbon, and parameters such as the active area of the catalyst, which is nearly impossible to determine with a porous multicomponent electrode, where the catalyst is on a support material. The stability of the catalyst can also not really be tested in these electrodes because the failure of any given component or of the mechanical stability of the electrode determines this process. PLD films are, therefore, the ideal candidates to test the activity and stability of various electrocatalysts, electrodes, and electrolytes because it is possible to prepare dense films with well-known surface areas, without any support material on an electrochemically inactive substrate, such as MgO. The well-defined surface area of PLD films allows the direct comparison of the catalytic activity for different materials, or even for different crystallographic properties, such as amorphous versus single-crystalline materials.

All of these special features of PLD films and the PLD technique with all of its variations are, therefore, a perfect match for electrochemical studies. In the following paragraphs a short overview of the history and function of the most important electrochemical systems is given to provide the necessary background to understand the aim and application of PLD films in electrochemistry. The figures in the description part show also the structure of the different electrochemical devices and can be used to identify the functionality of the materials that are prepared by PLD.

22.1.1 Description and History of the Most Important Electrochemical Systems

22.1.1.1 Batteries

History During the last decade batteries have become one of the most important objects in our everyday lives because they deliver power to a plethora of often portable devices, such as clocks, detectors, remote controls, and computers. Batteries have come a long way since the first ''battery,'' which was dated around 250 B.C. (Baghdad, Iraq), but there are still many possibilities for further improvements. The first batteries were used in simple operations to electroplate objects with a thin layer of metal while the next generation of batteries was invented as a matter of curiosity, in the anatomical studies of frogs. Luigi Galvani observed that the muscles in a frog's leg would contract when jolted with a static electrical spark delivered from a Leyden jar. He additionally noticed that the frog's leg also reacted to two different metals being applied to the muscle, deducing that the muscle was producing electricity. Based on the results of Galvani, Alessandro Volta developed in 1798 a device made of alternating pieces of electrolyte (sodium chloride salt) soaked disks, zinc, and copper disks stacked in a column with a wire connected to a copper plate on the top, and a wire connected to a zinc plate on the bottom. This more or less started modern electrochemistry and the unit of electrical potential was named ''volt,'' to honor one of the first inventors. In the nineteenth century various incremental improvements and discoveries for batteries were implemented. The next important invention came from Gaston Plantè, who developed the lead–acid cell in 1859. This was the first successful storage cell, or rechargeable battery. The following major development was the wet cell invented by Leclanché in

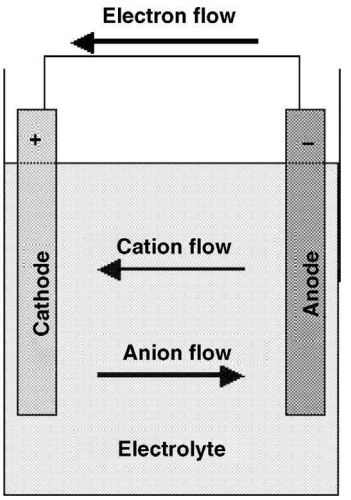

Figure 22.1 Schematic of a battery, indicating the charge flow and charge carriers inside and outside of the battery. Electrons start to flow from the anode to the cathode when the external circuit is closed. This current flow is compensated in the battery by a flow of ions between the electrodes.

1866. Further improvements of battery technology were limited by the liquid electrolyte, however. The dry cell, which is very similar to today's carbon–zinc batteries, was developed in 1888 by Carl Gassner and first sold in 1896. The twentieth century was characterized by the development and optimization of new materials, which resulted in 1959 in the first commercially available alkaline battery. In the 1960s the first silver oxide system and the first nickel cadmium rechargeable batteries became available, followed by rechargeable Li ion batteries in 1962 and Ni metal hydride batteries in the late 1960s [McNicol and Rand, 1984].

Description A battery, which is actually an electric cell, is a device that produces electricity from a chemical reaction. Strictly speaking, a battery consists of two or more cells connected in series or parallel, but the term can also be generally used for a single cell. A cell consists of a negative electrode, an electrolyte, which conducts ions, a separator, which is also an ion conductor, and a positive electrode. The electrolyte may be aqueous or nonaqueous, as a liquid, paste, or also in solid form. The negative electrode supplies a current of electrons that flow through the load and are accepted by the positive electrode (Fig. 22.1) when the cell is connected to an external load or device to be powered. The reaction stops when the external load is removed. Two types of batteries exist, depending on how the stored energy in the cell is produced. A primary battery can convert its chemicals into electricity only once and is then discarded (one way battery). A secondary battery has electrodes that can be reconstituted by passing electricity back through them. This type of battery is called a storage or rechargeable battery and can be reused many times.

The voltage of a battery is a characteristic of the cell design and the chemical reactions taking place inside. Nevertheless, the voltage changes with temperature, age of the cell, and load. A single cell can produce anything from a small fraction of a volt to more than 3 V, depending on the type of battery. In this context we would like to remind the reader about some fundamental definitions about batteries, which will be used later in this chapter. The capacity of a battery is the amount of electricity or electric charge that can be delivered during discharge at constant current until the final discharge voltage is reached. The standard unit to measure the capacity is the coulomb (C). The battery capacity is generally expressed by ampere-hours (Ah) or milliampere-hours (mAh). The total energy of a battery is expressed by watt-hours (Wh) (capacity $\times$ voltage), while the storage density of a battery is the ratio of capacity to its weight [McNicol and Rand, 1984].

Selected Battery Types

ZN–AIR BATTERIES The first Zn–air cell employing an alkaline electrolyte was patented in 1894 and consisted of a central Zn electrode, a porous separator, an inner fine particulate carbon layer, an outer particulate carbon layer, and a perforated Ni current collector. Cells of this type have capacities in the range from 300 to 3000 Ah, with a specific power of less than 1 W/kg. Recently, the interest in this type of battery was renewed, as many technical problems could be solved and batteries of this type became commercially available. The Zn–air battery is the battery that offers the highest storage density, which is due to the fact that one of the components in the reaction comes from outside of the battery, that is, atmospheric oxygen from the air as cathode reactant. A Zn–air battery is also characterized by a long stable life when sealed, for example, a loss of only ≈2% of its capacity is experienced after one year of storage (for a cell voltage of 1.65 V).

The recent design of a Zn–air battery consists of two electrodes, that is, Zn paste and a bifunctional oxygen electrode with an integrated electrocatalyst for reduction and evolution of oxygen. The reactions during discharge and charge, involving a bifunctional catalyst, can be described as follows:

Discharge	Charge
Zn Electrode	
$Zn + 4\ OH^- \Leftrightarrow Zn(OH)_4^{-2} + 2e^-$	$Zn(OH)_4^{-2} \Leftrightarrow ZnO + H_2O + 2OH^-$
Bifunctional Air Electrode	
$\frac{1}{2}O_2 + H_2O + 2e^- \Leftrightarrow 2OH^-$	$2OH^- \Leftrightarrow \frac{1}{2}O_2 + H_2O + 2e^-$

The reversible oxygen electrode potential is 0.401 V in an alkaline solution. One characteristic of this electrode is the large overpotential in the range of 0.2–0.4 V for both O_2 reactions [McNicol and Rand, 1984].

LI ION BATTERIES Lithium is an excellent material for a storage device, as electrons are very easily delivered and the element is of intrinsically low weight. One of the major problems of Li-based systems is the reactivity toward moisture, resulting in the requirement of a moisture-free environment for the production of Li ion batteries. Li ion batteries can be divided into nonrechargeable and rechargeable systems. The most common material in a nonrechargeable battery is the lithium–manganese spinel ($LiMn_2O_4$), where Li is used as the anode, the spinel as the cathode, with a carbonate electrolyte. The cell voltage of this type of battery is about 3 V. The latest generation of nonrechargeable batteries uses a polymer electrolyte and are intended for lightweight portable equipment. Rechargeable lithium ion batteries are important for space and portable power applications. The development of rechargeable batteries using lithium started in 1912, but only became commercially available in 1991 (by Sony). The rechargeable Li ion batteries were an instant success due to their light weight and long shelf life. Current systems use a carbon anode that inserts lithium ions from the cathode through the electrolyte (Fig. 22.2). The latest step in lithium ion battery development (1996) was the replacement of the liquid electrolyte with a polymer gel electrolyte, resulting in a high product safety [McNicol and Rand, 1984].

22.1.1.2 Fuel Cells

History The first fuel cell was developed by Sir William Robert Grove in 1839, who mixed hydrogen and oxygen in the presence of an electrolyte and produced electricity and water. The invention, which later became known as a fuel cell, did not produce enough electricity to be useful,

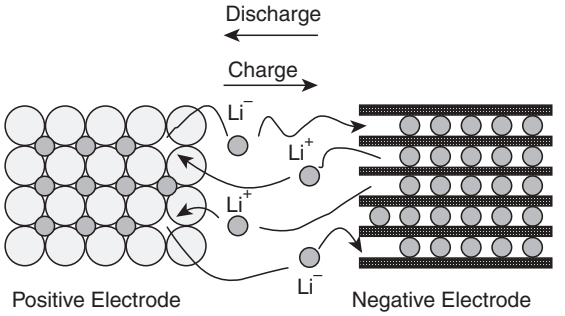

Figure 22.2 Schematic of a lithium ion battery, with the positive and negative electrode, which are separated by an electrolyte. If the electric circuit is closed, Li^+ ions are intercalated from the negative electrode through the electrolyte into the positive anode. This process can be inverted by applying a reverse outer current.

however. In 1889, the term "fuel cell" was probably first coined by Mond and Langer, who attempted to build a working fuel cell using air and industrial coal gas, while other sources attribute the term to W. Jaques. Jaques was also the first researcher to use phosphoric acid in the electrolyte bath. Fuel cell research in Germany paved the way in the 1920s to the development of today's carbonate cycle and solid oxide fuel cells. Important developments in 1959 by F. Bacon resulted in a design that was applied for a 5-kw fuel cell that could power a welding machine. In October 1959, Harry Karl Ihrig, demonstrated a 20-hp tractor that was the first vehicle ever powered by a fuel cell. The first bus powered by a fuel cell was completed in 1993, and several fuel cell cars are now being built in Europe, Japan, and in the United States. Daimler Benz and Toyota launched prototype fuel-cell-powered cars in 1997, while Daimler Chrysler unveiled the liquid hydrogen vehicle NECAR 4, in April 1999, with a top speed of 90 mph and a 280-mile tank capacity. Another fuel cell car has been developed by the Volkswagen group and a group of researchers based in Switzerland (PSI, ETH, Montena SA, FEV Motorentechnik GmbH, EMPA) and was tested in January 2002.

Description Fuel cells are based on reverse electrolysis and resemble batteries because their direct current (DC) electrical output is due to an electrochemical process: unlike batteries, they will continue to deliver energy as long as fuel is supplied. Fuel cells consist of two electrodes, which are separated by an electrolyte. An oxidant is fed to the cathode to supply oxygen, while hydrogen is supplied at the anode side (Fig. 22.3). An individual fuel cell generates from 0.6 to 0.8 V DC, with a conversion efficiency of up to 50%. High power outputs can be generated by designing large numbers of cells that are connected in series. There are various types of fuel cells that operate at different temperatures (i.e., from below 100°C to above 1000°C). In general, two classes of fuel cells are known, termed alkaline and acidic. There is just one type of alkaline fuel cell, which is also the longest known technology, which is still used in aerospace applications. There are four types of acidic fuel cells: the phosphoric acid fuel cell (PAFC), the proton exchange (or polymer) membrane (PEM)

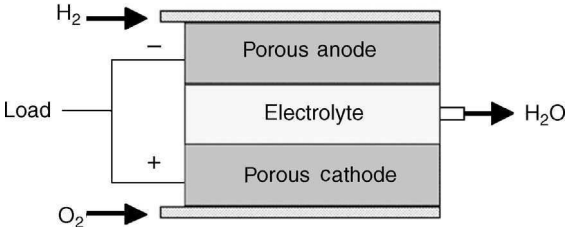

Figure 22.3 Schematic of a fuel cell, consisting of two electrodes separated by the electrolyte. An oxidant is fed to the cathode, while hydrogen is supplied to the anode.

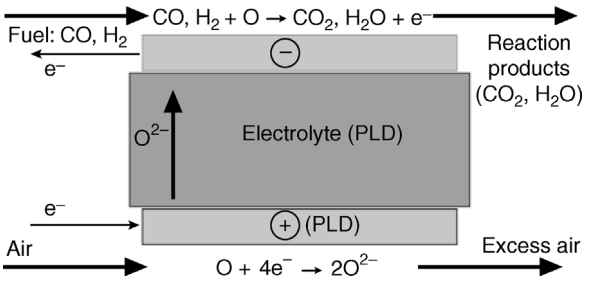

Figure 22.4 A SOFC consists of two electrodes separated by a solid electrolyte. Fuel that is delivered to the anode reacts with oxygen ions from the electrolyte and releases electrons into the external circuit. The cathode accepts electrons from the external circuit to supply the electrolyte with O^{2-} ions to maintain the overall electric charge balance.

fuel cell, the molten carbonate fuel cell (MCFC), and the solid oxide fuel cell (SOFC). The PAFC is the only acidic fuel cell that is in commercial use for stationary power generation. The PEM fuel cell was originally developed by General Electric in the late 1950s but is not yet commercially applied, except in the prototype fuel cell cars. However, there has been considerable work on the application of the PEM fuel cell in automobiles due to their low weight and low operating temperature.

Selected Types

SOLID OXIDE FUEL CELLS Solid oxide fuel cells (SOFC) are high-temperature devices and were studied by Baur and Preis in the late 1930s using zirconium, yttrium, cerium, lanthanum, and tungsten as solid oxide electrolytes. In the 1940s, O.K. Davtyan added monazite sand to a mix of sodium carbonate, tungsten trioxide, and soda glass to increase the conductivity and mechanical strength, but various undesired chemical reactions occurred. The SOFC still reveals problems due to the high internal resistance, melting, and semiconductivity, which can result in a short circuit. Westinghouse experimented with a cell using zirconium oxide and calcium oxide (1962), but only recently have advances in materials technology revived the interest in these SOFCs.

In SOFCs hard ceramics are applied as electrolytes instead of a liquid and the operating temperatures can reach 1000°C. The electrolyte is often a mixture of zirconium and calcium oxide that forms a crystal lattice, but other oxide combinations have also been tested. The solid electrolyte is coated on both sides with special porous electrode materials. At the higher applied temperatures, the oxygen ions (negatively charged) migrate through the crystal lattice of the electrolyte and oxidize the fuel at the anode side (Fig. 22.4). The efficiency can be as high as 60%, but the temperature requirement mainly results in stationary applications [McNicol and Rand, 1984]. Nevertheless, the solid electrolyte is still one of the key materials for future improvements.

22.2 SELECTED ELECTROCHEMICAL MATERIALS PREPARED BY PLD

22.2.1 Spinels

The spinel structure has the form of AB_2O_4, where A is a metal ion with a + 2 valence and B is a metal ion with a + 3 valence. This structure is viewed as a combination of the rock salt and zinc-blend structures. The oxygen ions are in a face-centered-cubic (fcc) close packing, where the A and B ions occupy tetrahedral and octahedral interstitial sites. The spinel structure can be divided into two types: normal and inverse spinels. In normal spinels, A^{2+} ions are on tetrahedral sites and the B^{3+} ions are on octahedral sites. In inverse spinels $B(AB)O_4$, the A^{2+} ions and half of the B^{3+} ions are on octahedral sites; the other half of the B^{3+} ions are on tetrahedral sites [Giacovazzo et al., 1999].

22.2.2 Perovskites

Perovskites are metal oxides with an empirical formula ABO_3, which crystallize into a cubic, tetragonal, orthorhombic, or rhombohedral structure. The cubic form of this material is referred to as ideal perovskite and has a unit-cell edge length of approximately 4 Å. In reality, only a few perovskite-type materials have this ideal cubic structure at room temperature, but many reach it at higher temperatures [Galasso, 1969]. In the fcc structure the *A cations* are located at the corners while the O atoms are on the faces. The *B cation* is in the center of the unit cell. A tolerance factor t was defined by Goldschmit [Chandler et al., 1993] to describe the stability limits of the perovskite structure [Eq. (22.1)]:

$$t = (R_A + R_O)/2^{1/2}\,(R_B + R_O) \tag{22.1}$$

where R_A, R_B, and R_O are the ionic radii. The perovskites are stable within the range of $0.75 < t < 1.0$ with t normally between 0.8 and 0.9. The stable structures below this limit are ilmenite and corundum [Wells, 1986]. The perovskite structure possesses a high degree of compositional flexibility, which allows the accommodation of a wide variety of A and B cations. Consequently, perovskites exhibit many interesting conducting and chemical properties, including catalytic activity and oxygen transport capability.

22.3 APPLICATIONS OF PLD FILMS

22.3.1 Spinels in Li Ion Batteries

Various materials have been studied over the last few years as solid electrolytes and positive/negative electrodes for lithium ion batteries. In commercial batteries the electrodes consist of a composite material (i.e., active material, binders, and conductive additives). Nevertheless, the application of thin films as model systems is becoming more and more popular due to the possibility of studying the stability and reactivity of new materials in well-defined systems. The first application of PLD as a deposition technique for Li ion battery related materials, studying mainly materials used as cathodes, was published at the end of the 1990s [Jiang et al., 1999]. Only in the last 4 years have materials for anodes and the solid electrolyte also been studied.

22.3.1.1 Cathode Materials

The most studied compound is $LiMn_2O_4$, which is used as the cathode material. One general problem for the deposition of Li-containing thin films is the fact that the films are Li deficient, but this problem can be overcome by using targets that are enriched in lithium. Inaba et al. [1999] studied the properties of a thin film of $LiMn_2O_4$ by cyclic voltammetry and scanning tunneling microscopy (STM) and observed that the surface morphology changed during potential cycling. Small spherical particles appeared on the surface after cycling. The number of particles increased while the particle size decreased with the number of cycles (shown in Fig. 22.5). The discharge

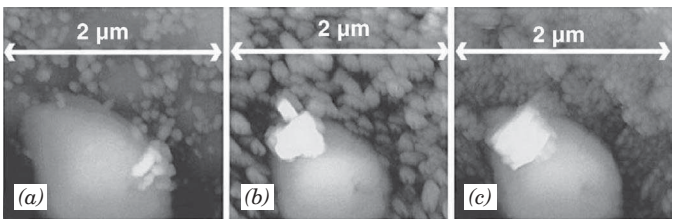

Figure 22.5 STM images ($2 \times 2\,\mu m$) of a $LiMn_2O_4$ thin film obtained after (a) 1, (b) 20, and (c) 75 cycles between 3.50 and 4.25 V in 1 *M* $LiClO_4$/propylene carbonate electrolyte solution. The sample and tip potentials were 3.5 and 3.0 V, respectively. The figure has been adapted from Inaba et al. [1999].

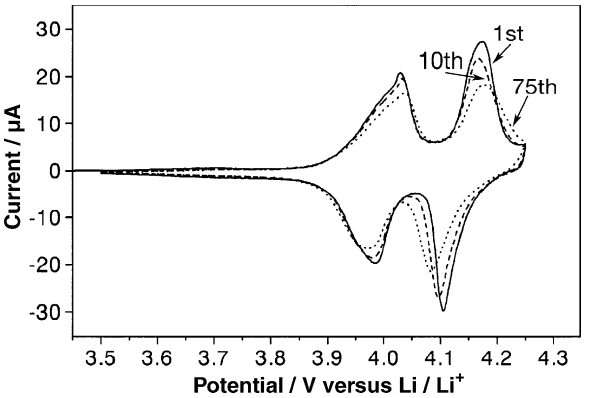

Figure 22.6 Cyclic voltammograms of a $LiMn_2O_4$ thin film deposited on Au at 873 K for 1 h. The electrolyte solution was 1 *M* $LiClO_4$/propylene carbonate electrolyte solution. The scan rate was 1 mV s^{-1}. The figure has been adapted from Inaba et al. [1999].

capacity decreased by 6% from the initial capacity in the 75th charge/discharge cycle in the range of 3.5 to 4.25 V (as derived from the cyclic voltammograms shown in Fig. 22.6).

The influence of the PLD parameters on the resulting thin films has been studied by Julien et al. [2000], who used mixtures of $LiMn_2O_4$ and Li_2O powders as targets to avoid the lithium deficiency in the resulting films. The main factor that determines the film morphology is the substrate temperature, with higher temperatures resulting in less porous films. The resulting films crystallized in a polycrystalline spinel structure and were applied in microbatteries, which presented a good specific capacity of 120 mC/cm^2 (shown in Fig. 22.7) that was attributed to the high degree of crystallinity.

One application of $LiMn_2O_4$ films has been suggested in 2001 by Singh et al. [2001] who applied the thin films in microelectromechanical systems, that is, in small-scale sensors (chip with a sensor). The deposited and applied films were highly crystalline and revealed a good kinetic behavior, cyclability, and capability for Li extraction/intercalation. Films that were deposited at higher temperatures revealed a lithium deficiency, probably due to the high vapor pressure of Li. An

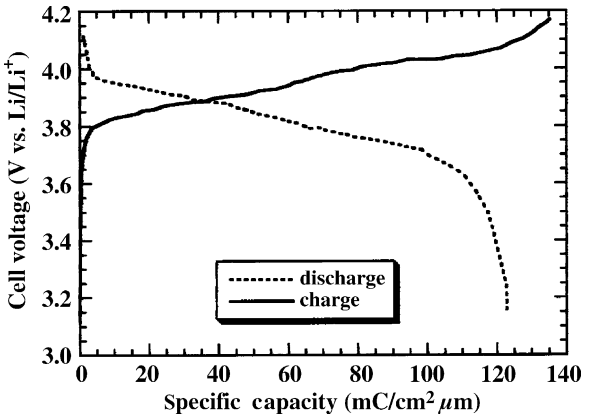

Figure 22.7 First discharge curve of a Li//$LiMn_2O_4$ microbattery using a $LiMn_2O_4$ film grown by PLD in 100 mTorr oxygen pressure onto a substrate heated to 300°C. The figure has been adapted from Julien et al. [2000].

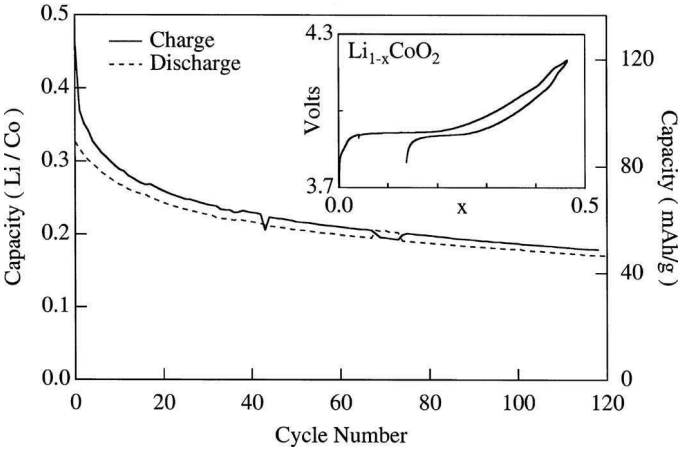

Figure 22.8 Capacity, in units of Li exchanged per Co, vs. cycle number for a 390-nm-thick $LiCoO_2$ film grown at 600°C in 200 mTorr of oxygen. The film was cycled between 3.8 and 4.2 V vs. Li at a constant current of 5 μA in a 1 *M* $LiClO_4$/propylene carbonate electrolyte solution. The inset shows the voltage vs. Li content for the first charge and discharge cycles. The figure has been adapted from Perkins et al. [1999].

ultraviolet (UV)-assisted PLD system (248 laser + UV lamp) was developed in 2002 [Singh et al., 2002] to produce films with higher crystallinity than films grown by standard PLD under the same conditions. The films with the higher crystallinity also revealed superior properties, such as a capacity loss of only 5% over a period of 1300 charge/discharge cycles.

Since 1999 [Perkins et al., 1999] other cathode materials have been studied in their pure ($LiCoO_2$) and doped ($LiCo_{1-x}Al_xO_2$) form. Perkins et al. [1999] have deposited both materials and obtained films where the Li and Co layers were oriented parallel to the substrate. The $LiCo_{1-x}Al_xO_2$ had to be deposited on a substrate with temperatures that were ≈100°C higher than in the case of $LiCoO_2$ to obtain similar grain sizes and crystallinity. For $LiCo_{1-x}Al_xO_2$ the charge/discharge curves indicates an asymmetry between Li extraction and intercalation (Fig. 22.8), which results in a capacity for the doped electrode that is three times lower than for the $LiCoO_2$ film electrode.

The influence of the film crystallinity on the Li ion diffusion has been studied by the potentiostatic intermittent titration technique (PITT) [McGraw et al., 1999]. The results indicate that the chemical diffusion coefficients are quite similar for amorphous and crystalline films, indicating that the better performance of the electrodes with higher crystallinity is not due to the Li ion diffusion. Another electrode material that has been studied is $Li_xV_2O_5$, where a completely reversible Li ion intercalation was observed. The chemical diffusion coefficient for Li ions into $LiCo_{0.5}Al_{0.5}O_2$ is at least 1–2 orders of magnitude smaller than for $LiCoO_2$. One possibility to overcome this problem is to control the amount of extracted Li, which may improve the discharge capability.

The Li ion positions in the film were analyzed as a function of the texture of the PLD films. The Li layers are oriented parallel to the substrate and perpendicular to the diffusion direction for the (003) texture in $LiCoO_2$ films, while the Li layers are separated by one cobalt and two oxygen layers along the (001) direction, which impedes the Li diffusion compared to the (003) texture [Iriyama et al., 2001]. Additional studies in the last few years [Julien et al., 2001; Julien and Gastro-Garcia, 2001] address the structure, morphology, and crystallography of Li-containing films without detailed electrochemical characterization of the films. These studies confirmed the data from older studies that indicate that it is necessary to use targets that are enriched in Li to obtain the correct stoichiometry in the resultant films. Kim et al. [2002, 2003] studied the influence of a 10-nm-thick Al_2O_3 coating on thin films of $LiCoO_2$. The coating resulted in a faster Li ion diffusion and

migration after 80 charge/discharge cycles than in films without a coating. The cycle life performance could be improved when the films were cycled only between 2.75 and 4.4 V. The reason for this improvement is the inhibition of Co dissolution during cycling. $LiCoO_2$ films loose 75% of their original capacity, while the Al_2O_3-coated films loose only 25%.

Another possible material for the cathode is V_2O_5. The first studies on thin films were performed by Julien et al. [1999] who analyzed different deposition conditions such as oxygen pressure and substrate temperature to achieve the correct film stoichiometry. Films deposited at 300°C with an oxygen background pressure of 100 mTorr present an orthorhombic polycrystalline phase where the *c*-axis is oriented perpendicular to the substrate plane. Fang et al. [2001] studied a mixture of vanadium and tungsten oxides and also the pure oxides. One innovation in this study is the application of a double layer of $WO_3(V_2O_5$ doped)/$V_2O_5(TiO_2$ doped) and not the usual mixture of the materials in the target to produce films with mixed elements. The WO_3 films degraded upon cycling, while for the V_2O_5 films the peak current density increased by up to 3% for the first three cycles followed by a constant current density over the next 1000 cycles. This long-term stability could only be obtained when the voltage sweep was limited to a *safe* range between 1.5 and 2.0 V. This limited range for the applicable voltage is due to the structure of the films where the Li ion mobility is higher between layers than across the layers. The peaks in the cyclic voltammograms for the $WO_3(V)/V_2O_5(Ti)$-layered films are due to the insertion and extraction of lithium in both layers of the double structure film (Fig. 22.9). The top layer $V_2O_5(Ti)$ is nanocrystalline and oriented in the *c* direction, which results in an improved transport of the Li ions and an increase of the cycle stability and reversibility of the $WO_3(V)$ layer.

Other dopants for V_2O_5 have been studied in the last few years to improve the electrochemical properties of this material. Huang et al. [2003] applied a composite material, such as $Li_2Ag_{0.5}V_2O_5$. The reason for choosing this material was the idea that the electrochemical properties will improve due to an expansion in the interlayer distance and an increase in the specific area of the material, which will provide better defined diffusion pathways for the Li ions. A preliminary result indicated that the PLD film could not improve the Li ion mobility during the electrochemical cycling but may still be useful as a cathode material for all-solids-state thin-film batteries. The electrochemical

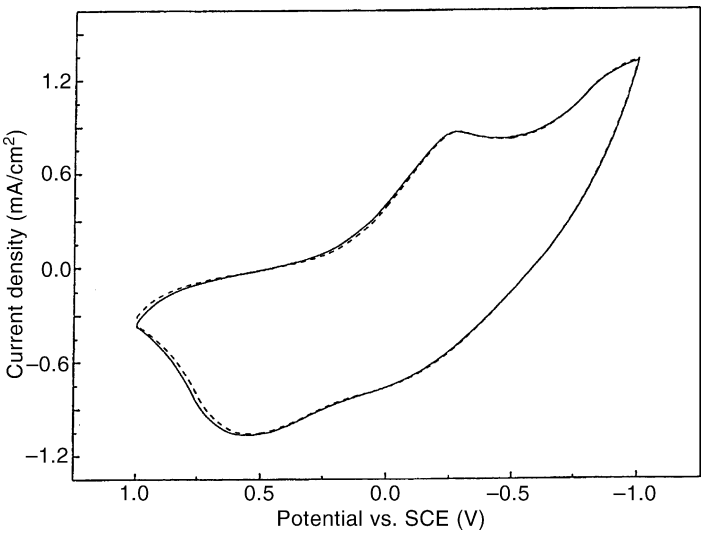

Figure 22.9 Cyclic voltammograms of WO_3 (V)/V_2O_5 (Ti) double-layer thin films deposited at 200°C on ITO with a sweep rate of 50 mV s^{-1}. The solid line represents the 4th cycle, while the dashed line represents the 1000th cycle. A saturated calomel electrode (SCE) has been used as reference electrode. The figure has been adapted from Fang et al. [2001].

properties of these films are better than for pure V_2O_5 and $Ag_{0.5}V_2O_5$ films. A capacity of 60 μAh/μm cm^2 at a current density of 7 μA/cm^2 could be reached when these films were used as cathodes. Another doped material that has been studied is NiO–V_2O_5 [Liu et al., 2003] where $(NiO)_{0.5}V_2O_5$ could be identified as the best material. The orthorhombic crystalline structure of V_2O_5 changes to an amorphous phase when the NiO content is increased. A mechanistic study concerning the extraction/insertion of Li, based on the X-ray diffraction (XRD) and X-ray photoelectron spectroscopy (XPS) results, suggests that one part of the Li ions insert and release from the vacant position within the V_2O_5 layers. The other Li ions react with the NiO, leading to the formation of metallic Ni and Li_2O. Both processes contribute to the specific capacity of the composite film, which is in the range of 340 mAh/g.

Another class of materials that has been studied are Ta_2O_5-ZnO composite films and films from the single compounds Ta_2O_5 and ZnO [NuLi et al., 2003]. Composite films with a Ta/Zn molar ratio of 2.5 exhibit the best performance in both the reversible capacity and capacity retention (up to 90% of its original capacity for up to 50 cycles). The analysis of these films revealed the formation of a crystalline orthorhombic $ZnTa_2O_6$ phase proving that the films are not just a physical mixture of ZnO and Ta_2O_5. The improvement of the Li capacity is attributed to the crystalline orthorhombic $ZnTa_2O_6$ phase.

Studies of the insertion and transport of Li in Ta_2O_5 have been made by Fu and Qin [2000a] using electrochemical methods and the isothermal transient ionic current method. The electrochemical and electrical properties of the film are strongly dependent on the film annealing parameters. Several values for diffusion constants of Li in Ta_2O_5 could be obtained in these studies, with values ranging from 2.6 to 5.2×10^{-15} cm^2/s. The anatase phase of TiO_2 was used as an alternative material [Fu and Qin, 2000b] and diffusion coefficients of Li ions in the range of $1.95–16 \times 10^{-13}$ cm^2/s were obtained. The high quality of the anatase films prepared by PLD was confirmed by XRD.

22.3.1.2 Anode Materials

Only recently have the first studies been performed on anode materials, which may be an alternative to the currently used carbon materials. The first study was performed by Ding et al. [1999], utilizing SnO_2 as an electrode material. The main results indicate that there are many differences in the electrochemical properties between bulk SnO_2 and thin-film materials. The bulk material is amorphous, where the Sn(II)-O sites act as active centers for Li ion intercalation. The thin films consist mainly of nanoscale SnO crystals in an amorphous oxide matrix, where the crystalline SnO contributes to the intercalation of the Li ions. The thin films loose 56% of their capacity during the first discharge cycle compared to only 37% for the bulk material. Additionally, indications for an irreversible reaction have been detected where SnO_2 is reduced to metallic Sn during the insertion of lithium. This reaction is probably the main reason for the fast loss of capacity.

Various other materials, mainly oxides, have been studied recently as anode materials, including CeO_2 [Jiang et al., 1999], Co_3O_4 [Wang et al., 2003c], Ta_2O_5 [Fu et al., 2003], and Mg_2Si [Song et al., 2003]. The CeO_2 thin films are oxygen deficient, with a polycrystalline monoclinic structure of Ce_6O_{11}. The thin films revealed a good cycling stability with a reversible capacity of 45 mC/cm^2 (for cycling in the range of 0.1–1.5 V).

The Co_3O_4 films consist mainly of nanocrystalline particles with an average size of 50 nm. Discharge/charge cycles and cyclic voltammetry measurements reveal an irreversible reduction process during the first cycle, but also a high cycle performance following the first cycle.

The Ta_2O_5 films were amorphous and were used in rechargeable lithium ion batteries, which revealed a high reversible capacity of 400 mAh/g. This high value for the reversible capacity corresponds to more than 6 Li entering one Ta_2O_5 unit to form $Li_xTa_2O_5$. The volumetric capacity of these films is approximately four times larger than for typical graphite electrodes (5 μA/cm^2). This high capacity is due to the reaction of Ta_2O_5 with 8Li to form $2Ta_2O$ and $4Li_2O$.

The 30-nm-thick Mg_2Si films delivered a capacity that is larger than 2000 mAh/g for more than 100 cycles, suggesting the good stability of this electrode material during cycling. Thicker films (i.e., 296 and 380 nm) showed a fading rate of the capacity of about 0.5–0.6% per cycle for up to 140 cycles.

Another type of material that has been studied is $LiTi_2(PO_4)_3$, which presents a NASICON-type structure [Wang et al., 2003a]. This compound crystallizes in a rhombohedral structure with a maximum amount of 5.2 mol of Li ions that can be electrochemically intercalated per mole of $LiTi_2(PO_4)_3$. Impedance measurements indicate a quite high Li diffusion coefficient (in the range of $10^{-7}-10^{-5}\,cm^2/s$).

22.3.1.3 Solid Electrolytes

The solid electrolyte is another very important component for the development of Li ion batteries, especially for the miniaturization of Li ion batteries as all-solid-state devices. High ion conductivity and a negligible electronic conductivity are necessary for this type of battery. Lithium phosphorus oxynitride (LiPON) as a solid electrolyte was first deposited by radio frequency (RF) magnetron sputtering, and several studies have been performed by Bates et al. [1993, 1995] who headed the development of this material and devices. Recently Zhao et al. [2002] presented the first results of amorphous LiPON films produced by PLD. An increase in the ionic conductivity could be observed when a higher concentration of nitrogen was incorporated in the films. This can be achieved by increasing the N_2 background pressure during deposition and/or by increasing the laser fluence. However, a saturation of the ionic conductivity was observed for fluences $\geq 15\,J/cm^2$. Unfortunately, no measurements with the PLD LiPON films were performed in batteries. These measurements will be absolutely necessary to test whether the material can be used in thin-film rechargeable lithium batteries. Another material that was also studied by Zhao and Qin [2003] is Li–V–Si–O. These thin PLD films were produced from a target that was a mixture of Li_2CO_3, V_2O_5, and SiO_2. The electrochemical window for testing this material is narrower than for LiPON and therefore less promising.

An alternative method for the fabrication of all-solid microbatteries is the so-called matrix-assisted pulsed laser evaporation (MAPLE)-DW process (see Chapter 3), where thin layers are transferred from a layered material by laser onto a substrate [Pique et al., 2001]. This method allows the fabrication of a multilayer structure, such as a battery, but without the control over crystallinity of the materials that can be achieved by PLD.

22.3.2 Perovskites in Solid Oxide Fuel Cells

Thin-film materials have significant advantages in SOFC because they allow a decrease of the operational temperature, which results in fewer problems with degradation. SOFCs consist typically of an $La_{1-x}Sr_xCoO_3$ (LSCO) layer as the cathode, an yttria-stabilized zirconia (YSZ) or $La_{1-x}Sr_xGa_{1-y}Mg_yO_3$ (LSGM) layer as electrolyte, and a metallic layer as the anode (usually nickel) (see also Fig. 22.4). The thin films must have two properties, namely high electronic and high oxygen ion conductivity. The perovskite LSCO fulfills these requirements and is therefore the most studied material. The first application of PLD as the deposition technique for cathodes and electrolytes in SOFCs was published in 1996 [Coccia et al., 1996]. The application of PLD films in electrochemical studies is not really developed and all the publications about PLD thin films in SOFCs so far only claim the importance of the material but do not present detailed results about the electrochemical properties, which are of course the most important factors to determine the possible future application of these films and materials.

22.3.2.1 Cathode Materials

The most studied compound to date is $La_{0.5}Sr_{0.5}CoO_3$. Chen et al. [1999a] have deposited this material on $LaAlO_3$ (LAO), on YSZ, and on LSGM, which itself had been deposited on $LaAlO_3$. The results indicate that on LAO and on LSGM/LAO epitaxial films were grown, while on YSZ substrates the orientation of the deposited film depends on the deposition temperature and on the oxygen background pressure. An increase of the LSCO film porosity can increase the gas transport to the reaction sites in the electrolyte (YSZ) [Chen et al., 1999b]. Epitaxial films with low resistivity ($10^{-3}\,\Omega cm$) were obtained at substrate temperatures of 550°C, while at room

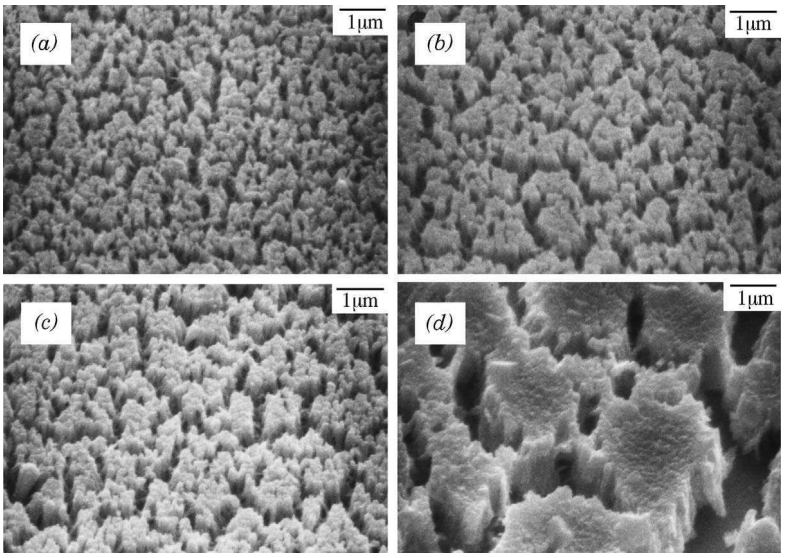

Figure 22.10 SEM images of LSCO/YSZ films annealed at different temperatures: (a) 450, (b) 550, (c) 650, and (d) 750°C. The figure has been adapted from Chen et al. [1999b].

temperature porous films were produced that reveal a high resistivity ($> 10^3\,\Omega$cm). An annealing step in air was added to reduce the resistance of the porous films, resulting in an improved resistivity of $10^{-2} - 1\,\Omega$cm. The final resistivity after annealing is a function of the annealing temperature. The size of the pores increases with increasing annealing temperature as shown in the scanning electron microscopy (SEM) image in Figure 22.10. An additional change in the structure of the film from amorphous to polycrystalline was also observed. The oxygen transport properties are another important parameter for the application of LSCO thin films in SOFCs. The effect of oxygen pressure and temperature during deposition on the crystallographic and conduction properties of the film has been analyzed [Chen et al., 1999c] in detail. (100) orientation is mainly observed for films deposited at 650°C and an oxygen background pressure of 150 mTorr, while for depositions at higher temperatures or lower oxygen pressures a preferential (110) orientation is obtained. Chen et al. [2002] studied the oxygen surface exchange coefficient of LSCO films deposited on LAO, using an electrical conductivity relaxation technique. The measured curves were fitted with a surface exchange-limited model, and the values for the epitaxial films are much smaller than those of polycrystalline films. However, a high-temperature treatment increases the surface exchange for the epitaxial films due to an increase in roughness and an increase in the number of active sites.

The composition and morphology of an LSCO target after ablation was also studied by Span et al. [1999]. Complete dissociation of the surface is achieved for fluences $> 0.7\,\text{J/cm}^2$. In this fluence range a steady-state target surface composition is obtained within 30 pulses. CoO nuclei are observed for fluences below $0.7\,\text{J/cm}^2$, which have a pronounced influence on the target composition and morphology and therefore also on the quality of the growing films.

Other materials that have been studied can be classified as variations of LSCO with a stoichiometric index of 0.5 for Ca and Sr. Coccia et al. [1996] studied $La_{0.7}Sr_{0.3}CoO_3$ and $La_{0.7}Sr_{0.3}Co_{0.2}Fe_{0.8}O_3$ as possible cathode materials, and $Ce_{0.9}Gd_{0.1}O_{1.95}$ (CGO) as possible materials for the electrolyte. The crystallographic quality of the films used as cathodes can be controlled by varying the deposition parameters, while congruent ablation of the CGO electrolyte could not be achieved. These films were enriched in Gd, by a factor of 2, compared to the target composition.

The deposition of $La_{0.8}Sr_{0.2}MnO_3$ on LAO and sapphire substrates was studied by Gnanasekar et al. [2002]. The films on LAO were highly *c*-axis oriented while the films on sapphire were highly *a*-axis oriented, but no studies on the electrochemical properties were performed or reported.

Another interesting application of $La_{1-x}Sr_xCoO_3$ is the possibility to use the films as a thermocouple, which is not directly related to SOFCs, but the thermal stability is, of course, an important property in their use in high-temperature SOFCs [Bhatt et al., 1999]. The LSCO films decompose at high temperatures, losing Co, which results in a material that consists of La_2O_3 or La_2O_3•2SrO. The highest phase stability was obtained for $La_{0.7}Sr_{0.3}CoO_3$, which again is important information for SOFCs application.

The stability of $SrFe_yCo_{1-y}O_x$ [Tunney et al., 2003] was also studied and the Fe-rich films (i.e., $y = 0.5$, 0.75, and 1.0) revealed for a thermochemical reduction treatment (2% H_2/argon gas mixture) a reversible structural change from perovskite (ABO_3) to brownmillerite ($ABO_{2.5}$).

22.3.2.2 Electrolyte Materials

The material that is mostly applied as the electrolyte in SOFCs is yttria-stabilized zirconia, but only a few studies of PLD films of this material have been performed. Hanus and Laude [1998] described the deposition of polycrystalline zirconia by PLD, where different targets were prepared that are based on zirconia and a stabilizer (i.e., Y_2O_3, MgO or CaO). The structure of the film was either tetragonal or cubic, depending on the stabilizing oxide (i.e., tetragonal for Y_2O_3 and cubic for CaO). The results also indicated that the phase structure of the deposited films was identical to that of the initial target material, independent of either the target or substrate temperature. The deposition of YSZ on NiO/YSZ was also studied [Hobein et al., 2002], and the films revealed a cubic phase with traces of the tetragonal phase for low oxygen pressures. Film deposition was also performed under various background pressures, but no improvements in gas leakage compared to the uncoated YSZ substrates was observed. One of the demands on a electrolyte is the property to prevent gas exchange between the two electrodes (O_2, H_2) but to allow the diffusion of oxygen ions. This property was evaluated by measuring the He leakage rate, which was around 2×10^{-3} mbar l/cm^2 s, compared to the requirements for fuel cells of a He leakage rate $< 1 \times 10^{-4}$ mbar l/cm^2 s. As YSZ cannot yet fulfill all requirements, other materials have also been analyzed.

Another class of material that has been used as a solid electrolyte is $La_{1-x}Sr_xGa_{1-y}Mg_yO_3$ (LSGMO). A first study of electrical conductivity was performed by Joseph et al. [2002]. Congruent film deposition of LSGMO was obtained in vacuum or by annealing of the films in air. The electrical conductivity measurements indicated that polycrystalline films are more conductive by a factor of 10 than single-crystalline films. The high quality of the LSGMO films deposited on LSCO substrates suggests a potential application of this material in SOFCs. In another study [Kanazawa et al., 2003] results were presented on the deposition of LSGMO on NiO. The as-deposited films were amorphous but crystallization was achieved by postannealing of these films. Films with a thickness of 45 μm revealed no gas leakage, which is important for SOFC applications. One theoretical study about the conduction path and disorder of the $La_{0.8}Sr_{0.2}Ga_{0.8}Mg_{0.15}Co_{0.05}O_{2.8}$ oxides at high temperatures was presented by Yashima et al. [2003]. The results suggest that the conduction path of the oxide ions is not linear between the ideal positions but reveals an arc shape starting from the sites of the $Ga_{0.8}Mg_{0.15}Co_{0.05}$ cations.

22.3.3 Perovskites in Rechargeable Zn–Air Batteries

Thin-film materials have significant advantages for Zn–air batteries because it is possible to study different catalysts without the interference of carbon, which is always used in electrodes. Most studies until now utilize the catalyst as a powder and different perovskites are used as catalysts in the electrode material [Muller et al., 1994; Hyodo et al., 1996] that also contains carbon. The main problem of identifying the best bifunctional catalyst is always the fact that in most cases a compromise between activity and stability has to be found. Until now the best performance was obtained for $La_{0.6}Ca_{0.4}CoO_3$ [Muller et al., 1994], but a recent study by Wang et al. [2003b]

presented new promising results for a combination of mixed catalysts. These catalysts are based on a mixture of $La_{0.6}Ca_{0.4}CoO_3$ with various amounts of MnO_2, CaO, or $Ni(OH)_2$. The results indicate that the catalyst composition of 15 wt % of $La_{0.6}Ca_{0.4}CoO_3$, 5 wt % of MnO_2, and 15 wt % of $Ni(OH)_2$ presents the highest discharge capacity of 1819 mAh, compared to the 1205 mAh for the normal $La_{0.6}Ca_{0.4}CoO_3$ electrode. Other new materials that have been developed for Zn–air batteries are a new type of electrolyte [Yang and Lin, 2002], that is, a composite of PEO (polyethylene oxide), PVA (polyvinyl alcohol), and a glass-fiber material. The results obtained for this material indicate that the electrolyte has an excellent mechanical strength and an electrochemical stability in the range of up to 2.4 V. An all-solid-state Zn–air battery was also assembled that revealed an electrochemical performance that was much better than those of conventional cells with polyethylene/polypropylene or cellulose separators. These recent developments are just a few examples of the ongoing developments in this field, but they suggest also new research directions that can be followed by PLD.

The first results of PLD films of a bifunctional catalyst for a Zn–air battery were shown by Striebel et al. [1995]. The rates of the oxygen reduction and evolution reactions of PLD films of $La_{0.6}Ca_{0.4}CoO_3$, $La_{0.6}Ca_{0.4}MnO_3$, and $La_{0.5}Sr_{0.5}FeO_3$ were measured with the rotating ring disk electrode technique. The order of activity was $La_{0.6}Ca_{0.4}MnO_3 > La_{0.5}Sr_{0.5}FeO_3 > La_{0.6}Ca_{0.4}CoO_3$. The $La_{0.6}Ca_{0.4}MnO_3$ film showed a slow increase in porosity with measurement time, while the $La_{0.5}Sr_{0.5}FeO_3$ was unstable. The $La_{0.6}Ca_{0.4}CoO_3$ was stable and also active for H_2O_2 reduction, and partially carbon-coated films showed higher currents for oxygen reduction than the bare films, due to oxygen reduction on the carbon. It has been determined that the oxygen reduction proceeds through a four-electron process, and that the crystallinity of the catalyst has an influence on the catalytic activity.

Thin films of $La_{0.6}Ca_{0.4}CoO_3$ have also been studied in detail by Montenegro et al. [2002]. The films revealed an epitaxial growth on (001) MgO in the (200) orientation (*c* direction of the MgO substrate) with a cubic symmetry. The epitaxial growth was also confirmed by high-resolution transmission electron microscopy (TEM) images (shown in Fig. 22.11). The activity of the PLD films for both oxygen reactions (O_2 evolution and O_2 reduction) was determined by using a three-electrode arrangement. The polarization curves in Figure 22.12 show a comparison of the activity of a PLD film, of a real electrode, and of pure carbon. The curves reveal clearly that carbon is an active material for the oxygen reactions, confirming the concept of PLD films as model systems. The

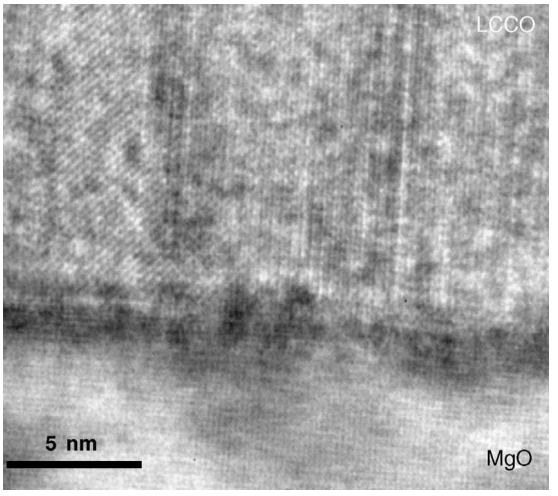

Figure 22.11 TEM image of a $La_{0.6}Ca_{0.4}CoO_3$ (LCCO) film deposited on MgO (001). The interface between the MgO and LCC is clearly visible as a darker region in the lower half of the image.

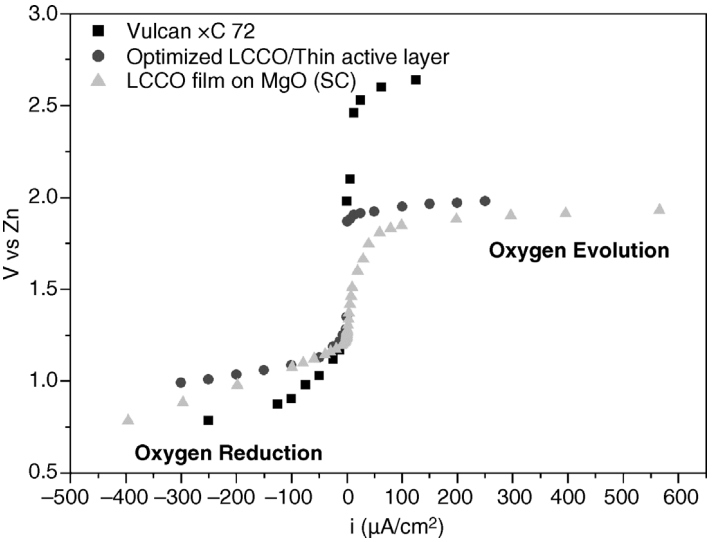

Figure 22.12 Polarization curves for carbon (Vulcan XC 72), a PLD film (LCCO film on MgO [SC (single crystalline)] and a "real" gas diffusion electrode (Optimized LCCO/thin active layer). Zn was used as a reference electrode.

polarization curves also show that PLD films present a slightly smaller overpotential than the optimized gas diffusion electrode, but also a slightly lower activity for the oxygen reduction reaction. A comparison of the activity of single-crystal and polycrystalline films (Fig. 22.13) shows a higher current density at the same voltage for a single-crystalline film on MgO than for a polycrystalline film on stainless steel. This result shows for the first time for this type of electrocatalyst that the crystallinity has a pronounced influence on the catalytic activity, that is,

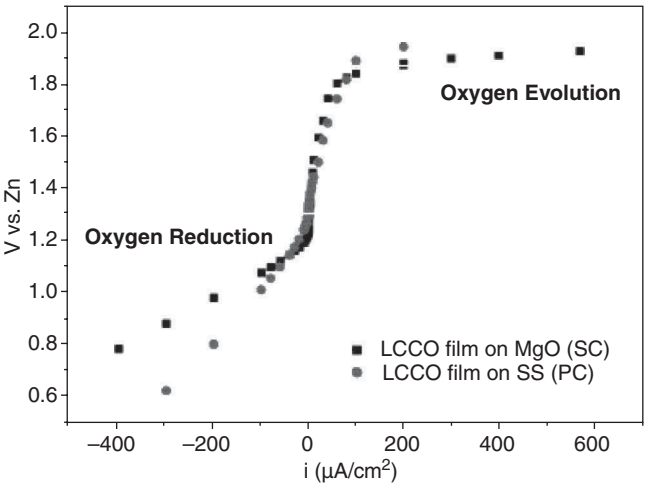

Figure 22.13 Polarization curves for a single-crystalline $La_{0.6}Ca_{0.4}CoO_3$ electrode on MgO (100) [SC (single crystalline)] and a polycrystalline LCCO electrode [PC (polycrystalline)] on stainless steel (SS). Zn was used as a reference electrode.

higher activity of the epitaxial film. This is even more remarkable when we consider that the reactions are performed in a liquid alkaline solution with an applied potential, where changes of the surface are expected.

22.4 OTHER ELECTROCHEMICALLY ACTIVE MATERIALS DEPOSITED BY PLD

22.4.1 NASICON

The growing interest in solid-state sensors has resulted in various new developments, such as gas sensors, based on advanced ionic conductors [Saito and Maruyama, 1988; Miura et al., 1994], such as NASICON (*Na S*uper*I*onic *CON*ductors). NASICON is a ceramic with a complex stoichiometry ($Na_{1+x}Zr_2Si_xP_{3-x}O_{12}$ with x ranging between 0 and 3) where the specific metal can also be varied, for example, Zr or Ti. The reason for testing PLD films lies in the fact that devices usually require bulk ceramics or thick membranes, and these materials have relatively low ion conductivity and require, therefore, a high operating temperature. Thin ionic conducting films are therefore necessary for sensors to be used at room temperature as well as for microscale integration. Such films can, of course, be prepared by other methods, such as sol–gel [Schmutz et al., 1993] or sputtering [Ivanov et al., 1994], but these methods normally result in porous films with a possible deficiency of P and Na. PLD is a potential candidate for the preparation of thin NASICON films because one of its inherent capabilities is to achieve congruent film deposition of materials with complex stoichiometries.

The first NASICON PLD film was deposited on SiO_2/Si substrates. X-ray photoelectron measurements were performed to prove that congruent transfer from the target had been achieved. The films revealed lower roughness when deposited at lower fluences; at higher fluences rough surfaces with columnar structures were obtained. Electrical measurements revealed good ionic conductivity with an activation energy for ion transport of 0.5 eV, which is in good agreement with the value of 0.46 eV obtained for NASICON pellets [Izquierdo et al., 1996]. Thin NASICON films on Si with varying compositions, such as $NaM_2(PO_4)_3$ with M = Zr or Ti, have been studied with various techniques [Morcrette et al., 1997). Titanium-based compositions yield smooth films that can only be crystallized by postdeposition techniques, while zirconium-based films crystallize during the deposition process but exhibit a rough morphology. Mixtures of Ti and Zr in the target lead to smooth partly crystallized films. The composition of the films was analyzed by Rutherford backscattering spectrometry (RBS), and a systematic deviation of the Zr-based film composition from the target (Zr enrichment with P depletion) was found. In the case of Ti-based NASICON films a loss of phosphorus was also detected, but this loss could be minimized by increasing the oxygen background pressure during deposition, and nearly congruent transfer was achieved for a pressure of 0.5 mbar. No tests of the ion conductivity were performed for these films.

Another application of NASICON films is in electrolysis and bipolar membrane electrodialysis cells for splitting salts into their acid and base components. Thick NASICON films ($> 25\,\mu m$) [Joshi et al., 1994] and composite membranes [Yelon et al., 1999] have been used as sodium selective membranes for sodium sulfate splitting, which is used for the regeneration of chemicals. The composite membrane combines the advantages of polymeric membranes (thin and flexible but with low selectivity and lifetime) and ceramic membranes (high selectivity, long lifetime, but rather thick). One way to produce these composite membranes is the deposition of the ceramic NASICON onto a polymeric membrane (e.g., Raipore). PLD has been used to deposit NASICON films on Raipore and resistivities between $3 \times 10^3\,\Omega$cm and $5 \times 10^4\,\Omega$cm have been obtained (depending on deposition conditions), which are slightly larger than the best values for crystalline and amorphous bulk NASICON. Almost no Na depletion on the membranes was detected by elastic recoil detection analysis (ERDA), if the polymeric membrane was soaked prior to deposition in Na_2SO_4. The performance of the membranes was evaluated by measuring the current efficiency for the production of NaOH from Na_2SO_4 using electrolysis. The composite membrane with the

PLD-deposited NASICON film showed a 23% improvement compared to the polymeric Raipore membrane [Izquierdo et al., 1997; Meunier et al., 1998]. Further tests of the composite membranes with the NASICON film grown by PLD revealed a remarkable resistance of the membrane to fouling by iron compared to the polymer membrane. The ceramic layer did not affect the water transport properties of the base polymeric membrane or its selectivity to potassium and sodium. The lower electrical resistance of the thin composite membrane compared to thick freestanding ceramic membranes resulted in lower energy requirements for the production of NaOH and H_2SO_4 from Na_2SO_4 [Girard et al., 1999]. A comparison between composite membranes where the ceramic NASICON film was deposited by PLD or magnetron sputtering revealed that there was nearly no difference between the composite membranes fabricated by the two deposition techniques, although the PLD-deposited films appeared to degrade less (physically and chemically) during electrolysis [Cormier et al., 2002].

22.4.2 Noble Metals in Polymer Electrolyte Membrane Fuel Cells

It has been known for years that the cost of polymer electrolyte membrane fuel cells (PEMFCs) must be lowered to realize a commercially viable product. The amount of the platinum catalyst must be reduced to the lowest possible levels, and a first step has been taken by applying supported platinum on carbon black. This has already reduced the amount of Pt loading from several mg/cm^2 to about 0.4 mg/cm^2, but further reductions are still necessary. One possibility to lower the Pt loading is to use a deposition technique that allows very precise control of the amount of deposited Pt. One very promising techniques is PLD where deposition rates of approximately 6.75×10^{-7} mg Pt/cm^2/pulse [Cunningham et al., 2003] can be achieved. The Pt was deposited onto commercially available (E-TEK) uncatalyzed gas diffusion electrodes and compared to standard electrodes with a Pt loading of 0.4 mg/cm^2. The PLD-loaded electrodes that contained as little as 0.017 mg Pt/cm^2 performed as well as the standard electrodes that contain about 25 times more Pt (shown in Fig. 22.14). XRD and SEM analysis of the PLD-deposited Pt suggests that the deposits are made of 13-nm-diameter crystalline Pt that is evenly dispersed on the electrode. This study clearly proves that the Pt loading in PEMFCs can be further reduced, which is one important step in the direction of commercially available PEMFCs.

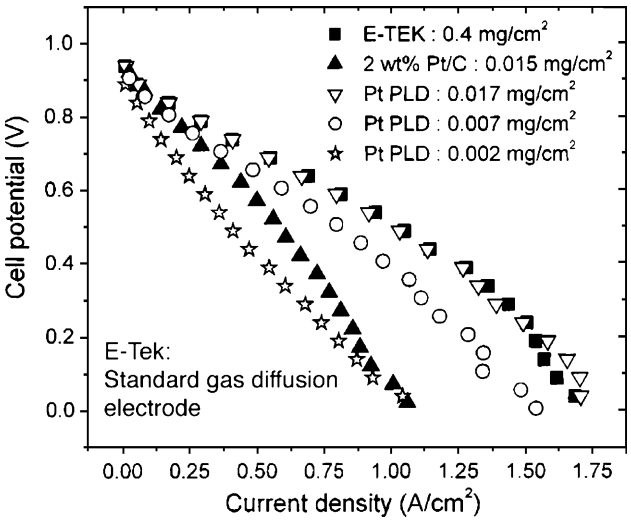

Figure 22.14 Fuel cell tests using Pt PLD electrodes on the anode side. Polarization curves for the standard E-TEK (0.4 mg Pt/cm^2) and for 2 wt % Pt/C are shown for comparison. The cathode is always a standard E-TEK (0.4 mg Pt/cm^2). The figure has been adapted from Cunningham et al. [2003].

22.5 FUTURE DIRECTIONS: DIAMOND-LIKE CARBON

One class of materials that has been prepared by PLD but has not been tested in an electrochemical context is diamond-like carbon (DLC). The properties of amorphous carbon films, both hydrogenated (a-C:H) and pure (a-C), resemble those of polycrystalline diamond films: they are very hard, electrically insulating, chemically inert, very good heat conductors, light weight, with large bandgaps, and a high index of refraction. Therefore, a-C and a-C:H are commonly referred to as diamond-like carbon, with its unique mixture of sp^2 and sp^3 carbon bonding. The combination of ceramic-like (high-hardness) and polymeric-like (high ratio of hardness to elastic modulus and low surface energy) properties suggests tribological applications that have recently been reviewed for PLD films by Voevodin et al. [1997], and see Chapter 23. Applications of DLC in electrochemical applications can be as corrosion protection of materials such as superconductors, ferroelectrics [Aoqui et al., 1998], and magnetic materials [Tomcik et al., 2000]. An additional field of application is possible for conductive doped DLC (doped with transition metals, nitrogen, boron, etc.). The resistivities of the doped DLC can be lower by 18 orders of magnitude (10^{-4} Ωcm) than for undoped films (10^{14}–10^{15} Ωcm) [Bozhko et al., 1995]. The low resistivity of these films allows an application as electrodes for electrochemical analysis [Kautek et al., 1996; Zeng et al., 2003]. Special features of a conductive-DLC electrode are a low double-layer capacitance, a large electrochemical potential window, and a relatively high electrochemical activity toward reduction of various species, such as ferricyanide. In addition, these electrodes may exhibit catalytic activity as well as durability to high anodic potential, and a high signal for the trace analysis of, for example, Pb^{2+}. These characteristics demonstrate a great potential of DLC films as a novel electrode material for electrochemical analysis [Pleskov et al., 2002; Ting and Lee 2002; Zeng et al., 2002]. Both types of application (protective coating and as an electrode) have not yet been tested for DLC films prepared by PLD. For a full discussion of PLD-deposited DLC, see Chapter 15.

22.6 CONCLUSION

The application of PLD films for electrochemical applications is still a young and growing field. Most advanced electrochemical studies to date are directed at Li ion batteries, where all components, that is, cathode, anode, and solid electrolyte, have been prepared by PLD, which were used to assemble complete all-solid-state Li ion batteries that have, of course, a great potential in the future field of miniaturization. PLD has clearly shown its potential to explore new materials, for example, the $ZnTa_2O_6$ phase, or the layered structures that cannot be prepared easily by other methods. An improved understanding of the functionality of different materials and of the processes, such as the Li intercalation (Li diffusion coefficients), is an important aspect of Li ion battery research. Further improvements of Li ion battery technology are closely related to the development of improved material research, and PLD is a very promising technique for these studies. Another already quite advanced research field of NASICON films as electromembranes has already resulted in a patent about the application of PLD for membrane synthesis.

The utilization of PLD films in other electrochemical fields still requires detailed electrochemical characterization of the thin films, and this is especially true for films related to SOFCs, where many studies stop with the physical/structural characterization of the films. A better correlation between film growth and electrochemical application is imminent in this new exciting field. The design and characterization of the electrocatalysts in Zn–air batteries and polymer electrolyte fuel cells have already proven that PLD has an important future in electrochemistry. The application of PLD films for a fundamental understanding of the catalytic processes in Zn–air batteries has already provided detailed insight and yielded new results. It could be determined that the oxygen reduction proceeds through a four-electron process, and that the crystallinity of the catalyst has an influence on the catalytic activity. Future studies will also help to identify better catalysts. Another strength of PLD, namely the precise control over the deposited material, could be used to determine the minimum

amount of Pt necessary as a catalyst in PEM fuel cells, which is of great importance for cost reduction. The high cost of PEM fuel cells is one of the major drawbacks, and the Pt concentration is one important contribution.

Other future directions of PLD lie in the preparation of miniaturized all-solid-state devices, such as Li ion batteries, Zn–air batteries, SOFCs, and even supercapacitors (where RuO_2 films could be used as electrodes).

Acknowledgments

Financial support of the Paul Scherrer Institut is gratefully acknowledged.

REFERENCES

Aoqui, S., Ebihara, K., and Yamagata, Y. (1998), *Carbon*, **36**, 591–594.

Aronova, M. A., Chang, K. S., Takeuchi, I., Jabs, H., Westerheim, D., Gonzalez-Martin, A., Kim, J., and Lewis, B. (2003), *Appl. Phys. Lett.* **83**, 1255–1257.

Bates, J. B., Dudney, N. J., Gruzalski, G. R., Zuhr, R. A., Choudhury, A., Luck, C. F., and Robertson, J. D. (1993), *J. Power Sources* **43**, 103–110.

Bates, J. B., Dudney, N. J., Lubben, D. C., Gruzalski, G. R., Kwak, B. S., Yu, X. H., and Zuhr, R. A., (1995), *J. Power Sources* **54**, 58–62.

Bhatt, H. D., Vedula, R., Desu, S. B., and Fralick, G. C. (1999), *Thin Solid Films* **350**, 249–257.

Bozhko, A., Ivanov, A., Berrettoni, M., Chudinov, S., Stizza, S., Dorfman, V., and Pypkin, B. (1995), *Diamond Relat. Mater.* **4**, 488–491.

Chandler, C. D., Roger, C., and Hampdensmith, M. J. (1993), *Chem. Rev.* **93**, 1205–1241.

Chen, X., Wu, N. J., and Ignatiev, A. (1999a), *J. Eur. Ceram. Soc.* **19**, 819–822.

Chen, X., Wu, N. J., Ritums, D. L., and Ignatiev, A. (1999b), *Thin Solid Films* **342**, 61–66.

Chen, X., Wu, N. J., Ignatiev, A., Zhang, Z. H., and Chu, W. K. (1999c), *Thin Solid Films* **350**, 130–137.

Chen, X., Wang, S., Yang, Y. L., Smith, L., Wu, N. J., Kim, B. I., Perry, S. S., Jacobson, A. J., and Ignatiev, A. (2002), *Solid State Ionics* **146**, 405–413.

Coccia, L. G., Tyrrell, G. C., Kilner, J. A., Waller, D., Chater, R. J., and Boyd, I. W. (1996), *Appl. Surf. Sci.* **96-8**, 795–801.

Cormier, L. M., Ma, F., Bah, S. T., Guetre, S., Meunier, M., Paleologou, M., and Yelon, A. (2002), *J. Electrochem. Soc.* **149**, D21–D26.

Cunningham, N., Irissou, E., Lefevre, M., Denis, M. C., Guay, D., and Dodelet, J. P. (2003), *Electrochem. Solid-State Lett.* **6**, A125–A128.

Ding, F., Fu, Z. W., Zhou, M. F., and Qin, Q. Z. (1999), *J. Electrochem. Soc.* **146**, 3554–3559.

Fang, G. J., Yao, K. L., and Liu, Z. L. (2001), *Thin Solid Films* **394**, 64–71.

Folkesson, A., Andersson, C., Alvfors, P., Alakula, M., and Overgaard, L. (2003), *J. Power Sources* **118**, 349–357.

Fu, Z. W., and Qin, Q. Z. (2000a), *J. Electrochem. Soc.* **147**, 4610–4614.

Fu, Z. W., and Qin, Q. Z. (2000b), *J. Phys. Chem. B* **104**, 5505–5510.

Fu, Z. W., Huang, F., Chu, Y. Q., Zhang, Y., and Qin, Q. Z. (2003), *J. Electrochem. Soc.* **150**, A776–A782.

Galasso, F. S. (1969), *Structure: Properties and Preparation of Perovskite-type Compounds*, Pergamon, London.

Giacovazzo, H., Monaco, H. L., Artiolio, G., Viterbo, D., Ferraris, G., Gilli, G., Zanotti, G., and Gatti, M. (1999), *Fundamentals of Crystallography*, Oxford, University Press, Oxford.

Girard, F., Izquierdo, R., Quenneville, E., Bah, S. T., Paleologou, M., Meunier, M., Ivanov, D., and Yelon, A. (1999), *J. Electrochem. Soc.* **146**, 2919–2924.

Gnanasekar, K. I., Jiang, X., Jiang, J. C., Aghasyan, M., Tiltsworth, R., Hormes, J., and Rambabu, B. (2002), *Solid State Ionics* **148**, 575–581.

Gorbunov, A., Levin, A. A., Mensch, A., Meyer, D. C., Tselev, A., Paufler, P., Pompe, W., and Eckert, D. (2002), *Appl. Surf. Sci.* **197**, 475–480.

Gupta, A., Mercey, B., Hervieu, H., and Raveau, B. (1994), *Chem. Mater.* **6**, 1011–1016.

Hanus, F., and Laude, L. D. (1998), *Appl. Surf. Sci.* **129**, 544–548.

Hobein, B., Tietz, F., Stover, D., and Kreutz, E. W. (2002), *J. Power Sources* **105**, 239–242.

Huang, F., Fu, Z. W., and Qin, Q. Z. (2003), *Electrochem. Commun.* **5**, 262–266.

Hyodo, T., Hayashi, M., Miura, N., and Yamazoe, N. (1996), *J. Electrochem. Soc.* **143**, L266–L267.

Inaba, M., Doi, T., Iriyama, Y., Abe, T., and Ogumi, Z. (1999), *J. Power Sources* **81**, 554–557.

Iriyama, Y., Inaba, M., Abe, T., and Ogumi, Z. (2001), *J. Power Sources* **94**, 175–182.

Ivanov, D., Currie, J., Bouchard, H., Lecours, A., Andrian, J., Yelon, A., and Poulin, S. (1994), *Solid State Ionics* **67**, 295–299.

Izquierdo, R., Hanus, F., Lang, T., Ivanov, D., Meunier, M., Laude, L., Currie, J. F., and Yelon, A. (1996), *Appl. Surf. Sci.* **96-8**, 855–858.

Izquierdo, R., Quenneville, E., Trigylidas, D., Girard, F., Meunier, M., Ivanov, D., Paleologou, M., and Yelon, A. (1997), *J. Electrochem. Soc.* **144**, L323–L325.

Jiang, L. Z., Zhou, M. F., Liu, X. N., and Qin, Q. Z. (1999), *Acta Phys.-Chim. Sin.* **15**, 752–756.

Joseph, M., Manoravi, P., Tabata, H., and Kawai, T. (2002), *J. Appl. Phys.* **92**, 997–1001.

Joshi, A. V., Liu, M., Bjorseth, A., and Renberg, L. (1994), U.S. Patent No. 5,290,405.

Julien, C., and Gastro-Garcia, S. (2001), *J. Power Sources* **97-8**, 290–293.

Julien, C., Haro-Poniatowski, E., Camacho-Lopez, M. A., Escobar-Alarcon, L., and Jimenez-Jarquin, J. (1999), *Mater. Sci. Eng. B.* **65**, 170–176.

Julien, C., Haro-Poniatowski, E., Camacho-Lopez, M. A., Escobar-Alarcon, L., and Jimenez-Jarquin, J. (2000), *Mater. Sci. Eng. B.* **72**, 36–46.

Julien, C., Camacho-Lopez, M. A., Escobar-Alarcon, L., and Haro-Poniatowski, E. (2001), *Mater. Chem. Phys.* **68**, 210–216.

Junker, M., Bocquet, L., Bendif, M., and Karboviac, D. (2001), *Ann. Chim.-Sci. Mater.* **26**, 117–130.

Kanazawa, S., Ito, T., Yamada, K., Ohkubo, T., Nomoto, Y., Ishihara, T., and Takita, Y. (2003), *Surf. Coat. Technol.* **169**, 508–511.

Kautek, W., Pentzien, S., Conradi, A., Kruger, J., and Brzezinka, K. W. (1996), *Appl. Surf. Sci.* **106**, 158–165.

Kim, Y. J., Kim, T. J., Shin, J. W., Park, B., and Cho, J. P. (2002), *J. Electrochem. Soc.* **149**, A1337–A1341.

Kim, Y. J., Kim, H., Kim, B., Ahn, D., Lee, J. G., Kim, T. J., Son, D., Cho, J., Kim, Y. W., and Park, B. (2003), *Chem. Mater.* **15**, 1505–1511.

Koida, T., Lippmaa, M., Fukumura, T., Itaka, K., Matsumoto, Y., Kawasaki, M., and Koinuma, H. (2002), *Phys. Rev. B* **66**, art. no.-144418.

Krebs, H. U. (1997), *Int. J. Non-Equilib. Pr.* **10**, 3–24.

Levin, A. A., Meyer, D. C., Gorbunov, A., Mensch, A., Pompe, W., and Paufler, P. (2003), *J. Alloys Compd.* **360**, 107–117.

Linssen, J., Grube, T., Hoehlein, B., and Walbeck, M. (2003), *Int. J. Hydrogen. Energy* **28**, 735–741.

Lippmaa, M., Koida, T., Minami, H., Jin, Z. W., Kawasaki, M., and Koinuma, H. (2002), *Appl. Surf. Sci.* **189**, 205–209.

Liu, H. R., Chu, Y. Q., Fu, Z. W., and Qin, Q. Z. (2003), *J. Power Sources* **124**, 163–169.

Lowndes, D. H., Geohegan, D. B., Puretzky, A. A., Norton, D. P., and Rouleau, C. M. (1996), *Science* **273**, 898–903.

McGraw, J. M., Bahn, C. S., Parilla, P. A., Perkins, J. D., Readey, D. W., and Ginley, D. S. (1999), *Electrochim. Acta* **45**, 187–196.

McNicol, B. D., and Rand, A. A. J. (Eds.) (1984), *Power Sources for Electric Vehicles*, Elsevier, Amsterdam.

Meunier, M., Izquierdo, R., Hasnaoui, L., Quenneville, E., Ivanov, D., Girard, F., Morin, F., Yelon, A., and Paleologou, M. (1998), *Appl. Surf. Sci.* **129**, 466–470.

Miura, N., Yao, S., Shimizu, Y., and Yamazoe, N. (1994), *Solid State Ionics* **70**, 572–577.

Montenegro, M. J., Dobeli, M., Lippert, T., Muller, S., Schnyder, B., Weidenkaff, A., Willmott, P. R., and Wokaun, A. (2002), *Phys. Chem. Chem. Phys.* **4**, 2799–2805.

Morcrette, M., Barboux, P., Laurent, A., and Perriere, J. (1997), *Solid State Ionics* **93**, 283–290.

Muller, S., Striebel, K., and Haas, O. (1994), *Electrochim. Acta* **39**, 1661–1668.

NuLi, Y. N., Fu, Z. W., Chu, Y. Q., and Qin, Q. Z. (2003), *Solid State Ionics* **160**, 197–207.

Ohkubo, I., Matsumoto, Y., Ueno, K., Chikyow, T., Kawasaki, M., and Koinuma, H. (2003), *J. Crystal Growth* **247**, 105–109.

Perkins, J. D., Bahn, C. S., Parilla, P. A., McGraw, J. M., Fu, M. L., Duncan, M., Yu, H., and Ginley, D. S. (1999), *J. Power Sources* **82**, 675–679.

Pique, A., Swider-Lyons, K. E., Weir, D. W., Love, C. T., and Modi, R. (2001), *Proc. SPIE* **4274**, 316.

Pleskov, Y. V., Krotova, M. D., Polyakov, V. I., Khomich, A. V., Rukovishnikov, A. I., Druz, B. L., and Zaritskiy, I. (2002), *J. Electroanal. Chem.* **519**, 60–64.

Saito, Y., and Maruyama, T. (1988), *Solid State Ionics* **28**, 1644–1647.

Schmutz, C., Basset, E., Barboux, P., and Maquet, J. (1993), *J. Mater. Chem.* **3**, 393–397.

Shukla, A. K., Jackson, C. L., and Scott, K. (2003), *Bull. Mater. Sci.* **26**, 207–214.

Singh, D., Houriet, R., Giovannini, R., Hofmann, H., Craciun, V., and Singh, R. K. (2001), *J. Power Sources* **97-8**, 826–831.

Singh, D., Kim, W. S., Craciun, V., Hofmann, H., and Singh, R. K. (2002), *Appl. Surf. Sci.* **197**, 516–521.

Song, S. W., Striebel, K. A., Reade, R. P., Roberts, G. A., and Cairns, E. J. (2003), *J. Electrochem. Soc.* **150**, A121–A127.

Span, E. A. F., Roesthuis, F. J. G., Blank, D. H. A., and Rogalla, H. (1999), *Appl. Surf. Sci.* **150**, 171–177.

Striebel, K. A., Deng, C. Z., and Cairns, E. J. (1995), *Proc. Electrochem. Soc.* **26**, 112.

Takahashi, R., Matsumoto, Y., Koinuma, H., Lippmaa, M., and Kawasaki, M. (2002), *Appl. Surf. Sci.* **197**, 532–535.

Ting, J. M., and Lee, H. (2002), *Diamond Relat. Mater.* **11**, 1119–1123.

Tomcik, B., Osipowicz, T., and Lee, J. Y. (2000), *Thin Solid Films* **360**, 173–180.

Tunney, J. J., Whitfield, P., Du, X. M., and Post, M. L. (2003), *Thin Solid Films* **426**, 221–231.

Voevodin, A. A., Donley, M. S., and Zabinski, J. S. (1997), *Surf. Coat. Technol.* **92**, 42–49.

Wang, G. X., Bradhurst, D. H., Dou, S. X., and Liu, H. K. (2003a), *J. Power Sources* **124**, 231–236.

Wang, X. Y., Sebastian, P. J., Smit, M. A., Yang, H. P., and Gamboa, S. A. (2003b), *J. Power Sources* **124**, 278–284.

Wang, Y., Fu, Z. W., and Qin, Q. Z. (2003c), *Thin Solid Films* **441**, 19–24.

Wells, A. F. (1986), *Structural Inorganic Chemistry, Clarendon*, Oxford.

Yang, C. C., and Lin, S. J. (2002), *J. Power Sources* **112**, 497–503.

Yashima, M., Nomura, K., Kageyama, H., Miyazaki, Y., Chitose, N., and Adachi, K. (2003), *Chem Phys. Lett.* **380**, 391–396.

Yelon, A., Paleologou, M., Ivanov, A., Izquierdo, R., and Meunier, M. (1999), U.S. Patent No. 5,968,326.

Zeng, A., Liu, E., Tan, S. N., Zhang, S., and Gao, J. (2002), *Electroanalysis* **14**, 1110–1115.

Zeng, A., Liu, E., Zhang, S., Tan, S. N., Hing, P., Annergren, I. F., and Gao, J. (2003), *Thin Solid Films* **426**, 258–264.

Zhao, S. L., and Qin, Q. Z. (2003), *J. Power Sources* **122**, 174–180.

Zhao, S. L., Fu, Z. W., and Qin, Q. Z. (2002), *Thin Solid Films*, **415**, 108–113.

CHAPTER 23

Pulsed Laser Deposition of Tribological Coatings

ANDREY A. VOEVODIN, JEFFREY S. ZABINSKI, and JOHN G. JONES

Air Force Research Laboratory, Materials and Manufacturing Directorate,
Wright-Patterson Air Force Base, Ohio

23.1 INTRODUCTION

The application of pulsed layer deposition (PLD) for growing wear-resistant and friction-reducing coatings dates back to the early experiments on laser ablation of carbon to obtain hard diamond-like carbon (DLC) coatings [Fujimori et al., 1982; Marquardt et al., 1985]. These were followed by extensive research with several reviews of DLC growth by PLD [Ogale et al., 1993; Voevodin and Donley, 1996; Wei and Narayan, 2000]. Chapter 15 of this book summarizes the most recent developments. Although DLC remains a good example of a successful application of PLD, much progress has been made with respect to deposition of new materials and advancement of PLD processes. In the first book on PLD deposition published 10 years ago, a special chapter was devoted to tribological applications with examples provided on hard coatings made of carbides and nitrides and solid lubricant coatings made of chalcogenides and oxides [Donley and Zabinski, 1994]. Since that book was published, PLD has flourished and has been key in the nanostructured materials revolution. This chapter provides a brief summary of the most recent developments in PLD for tribological applications and encompasses process configuration, interrelation of deposition parameters with plasma chemistry and coating properties, process control, use of PLD in hybrid deposition methods, new tribological coating materials, and new coating architectures.

Much of the material in this chapter is based on the authors' own experience in the development of PLD for advanced tribological coatings in the Air Force Research Laboratory (AFRL). This activity has been ongoing for the past few decades and has produced a number of new process configurations, hybrid deposition arrangements, and new tribological materials. In fact, several unique functional gradient and nanocomposite tribological materials were first successfully synthesised in AFRL and the PLD process is being scaled up to evaluate commercialization of those coatings. Some of the nanostructured materials have shown such high potential that alternate, commercially available, deposition technologies are being sought to reproduce them as the PLD technique continues to mature. The success in rapidly discovering new nanostructures confirms that PLD remains a leading tool in the exploration and synthesis of new materials. At the same time, laser power is increasing and laser cost is decreasing so that PLD is advancing toward commonly

Pulsed Laser Deposition of Thin Films: Applications-Led Growth of Functional Materials
Edited by Robert Eason

accepted methods of tribological coating growth, such as magnetron sputtering and vacuum arc technologies. PLD is becoming more competitive with such processes on a cost basis in addition to its capability of producing unique and often superior coatings. There is growing interest within both the research and industrial communities in using PLD for ''engineering'' applications, such as wear and friction-reducing coatings. This chapter is intended to provide a solid foundation for those who decide to look into the PLD process for tribological coating applications.

23.2 PULSED LASER DEPOSITION CONFIGURATION FOR TRIBOLOGICAL COATING GROWTH

A general introduction and overview of PLD process equipment has already been provided earlier, with specific reference given in Chapter 9 to commercial PLD systems. In this section, attention is focused on specific PLD configurations for producing wear-resistant and friction-reducing coatings. Tribological applications require coating deposition on engineering components that are subjected to severe contact conditions and that operate in severe environments. This dictates a certain deviation of the process configuration from what is used for microelectronic or optical applications.

The coated parts can have very complex geometries compared to flat Si wafers and, thus, more sophisticated substrate positioning is needed to achieve uniform coating growth. Most typically, a planetary motion mechanism is used to rotate parts through the plumes generated by PLD. These mechanisms require large deposition chambers and loading is simplest using batch processing (Fig. 23.1). Deposition chambers are designed with heating elements for quick bake-out of the residual water vapor after each batch of parts is processed.

Deposition temperatures typically do not exceed 400°C due to the danger of annealing or shape distortion of engineering substrates, which are most commonly made of steels and metal alloys. At such relatively low growth temperatures, coating adhesion is not enhanced by interface diffusion between coating and substrate. However, strong adhesion is a paramount requirement due to the extreme stresses caused by mechanical loading during operation. To compensate for the lack of

Figure 23.1 Large deposition chamber for pulsed laser ablation and magnetron sputter depositing hybrid. Laser ablation target is in the upper center of the chamber and two magnetron sputter guns are at the chamber upper left and right.

strong diffusion bonding, an effort is made to provide good chemical and mechanical matching between the substrate and the coating. Plasma etching is frequently used to clean metal surfaces and remove oxide layers to produce good interfacial bonding. Typically, etching is accomplished using an inert gas (e.g., Ar) plasma created with a negative high voltage supplied to the substrates (e.g., 800–1000 V). Furthermore, specially designed coating architectures are used to match chemical and mechanical properties at the coating–substrate interface and then coating properties are gradually transitioned to those required by the application (i.e., wear and friction resistance). This may require the use of different PLD targets or combinations of PLD with other deposition methods. Hybrids of PLD with magnetron sputtering and ion beam bombardment are described in the following section. A separate section in this chapter is devoted to gradient coatings, one function of which is to improve adhesion.

Coating structure control is critical for most tribological coatings, whether this is a monolithic hard coating, a low friction solid lubricant, or a multilayer or composite coating. The most effective method of controlling structure is to adjust the energy and density of the generated plasma plumes, which in turn controls the chemistry, crystallinity, and/or texture. A typical procedure is to vary laser beam fluence, which, however, changes both flux density and energy of the plumes. An alternative method is to maximize ion concentration in the plasma and use the substrate bias to accelerate them to a selected energy (see following sections).

Coating growth rate should be reasonably high to ensure a practical thickness (few micrometer coating) may be produced in a couple of hours. This dictates the use of high fluences (on the order of 10 J/cm^2) and high repetition rates (20–40 Hz) of the pulsed laser. The ongoing increase in commercial laser output power and repetition rates may soon bring PLD to the same production rate as those from modern magnetron sputtering and vacuum arc techniques, which are now at about 3–5 μm/h.

Finally, some droplet emission from laser–target interaction can be tolerated for most tribological coating applications. However, high laser fluences on metallic targets lead to considerable droplet contamination and low deposition rates, which suggests that a combination of laser ablation for ceramic targets with other plasma sources for metals is the best overall strategy.

23.3 CORRELATIONS BETWEEN PROCESS PARAMETERS, PLASMA CHARACTERISTICS, AND TRIBOLOGICAL COATING PROPERTIES

The most typical PLD process parameters are laser wavelength, energy density or flux, repetition rate, background gas pressure, and substrate temperature. Other important parameters are substrate bias potential and target-to-substrate distance. Each of them can be critical for obtaining the required coating chemistry and structure. Most of them control plasma chemistry, composition, and energy, which, in turn, control coating growth and, hence, coating properties. Therefore, the most efficient growth control is achieved when correlations between PLD parameters, plasma characteristics, and coating properties are available and understood. Several examples of such correlations for tribological coating development are provided here.

23.3.1 Laser Wavelength and Fluence

It follows from the physics of laser–solid interactions, that shorter wavelengths, which correspond to higher photon energies, lead to higher levels of energy absorbed per unit of subsurface target volume. This results in the intensification of all processes at the ablated target, including generation of highly energetic ionic and neutral species. One tribological material, whose synthesis is critically influenced by the selected wavelength, is DLC. Successful DLC deposition typically has two distinctive features. First, the process involves high-energy carbon ions, atoms, or clusters (i.e., several orders of magnitude above thermal energy). Second, films are grown at a relatively low temperature (25–100°C). These two conditions, when the energy of arriving atoms is sufficient to

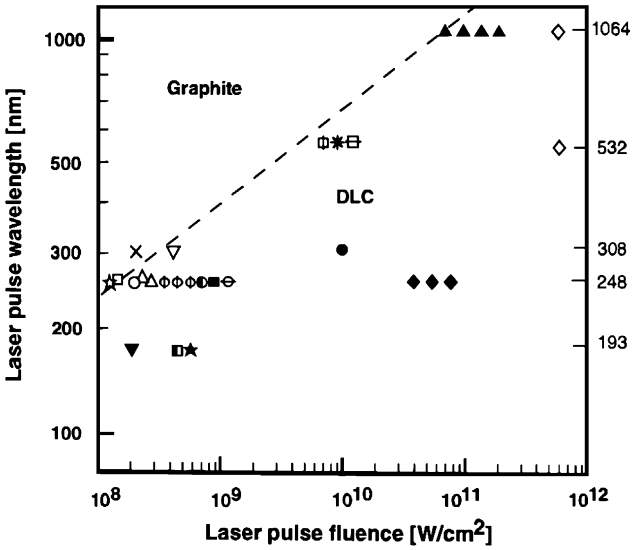

Figure 23.2 Schematic representation of fluence-wavelength regions for the growth of diamond-like and graphite-like films in pulsed laser ablation from graphite targets. The wavelengths (in nanometers) of the five most commonly used lasers are indicated on the right side of the graph.

initiate strong sp^3 interatomic bonds (typically within 50–150 eV) and when adatom mobility is reduced due to a low substrate temperature (reduces relaxation to sp^2 bonding), are required for the DLC growth [Voevodin and Donley, 1996].

A detailed study of the influence of laser wavelength has been performed for graphite ablation [Murray and Peeler, 1993, 1994]. Nd : YAG and excimer lasers were used at wavelengths of 1064 and 532 nm and 248 and 193 nm, respectively. The lasers were tuned to produce pulses of the same duration of 15 ns and a fluence range of 1.8×10^8–2×10^8 W/cm^2 (2.7–3 J/cm^2). Their results clearly showed that the shorter wavelengths produce smaller carbon species with higher kinetic energy. For example, C^+ ions with kinetic energy of 600 eV were obtained with a 193-nm laser, even though the laser fluence was relatively small. A higher fluence produces species with increased kinetic energy and helps to better dissociate molecular species in the plume, providing an increase in atomic and ionic components. Using data published on the synthesis of a high-quality (high sp^3/sp^2 ratio) DLC films by various researchers, a wavelength/fluence process parameter field was established for production of high-quality DLC [Voevodin and Donley, 1996], which is schematically depicted in Figure 23.2. The schematic shows that shorter wavelengths permit the use of smaller fluences to reach the region of high-quality DLC. More information on DLC synthesis by PLD can be found in Chapter 15.

23.3.2 Background Gas Effects and Target to Substrate Distance

The presence of a background gas critically influences film growth in PLD through several phenomena. First, the background environment acts as a retarding media for energetic plasma plumes, and higher pressures result in higher plume scattering and thermalization. Second, the background environment can change plume chemical composition and energy. Both of these effects were found critical in the synthesis of fullerene-like CN_x tribological materials, which are made of fragmented and strongly curved graphitic planes with a high degree of cross-linking caused by the incorporated nitrogen atoms [Hultman et al., 2001, 2003].

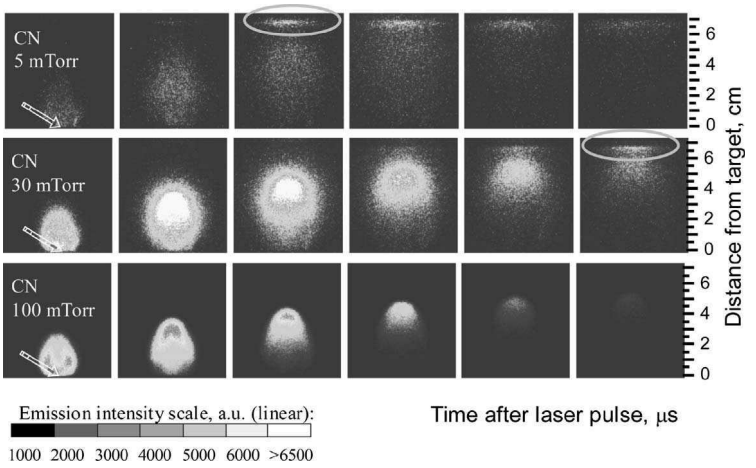

Figure 23.3 ICCD images tracing the spatial locations of molecular CN radicals at different times after the laser pulse for graphite ablation in 5, 30, and 100 mTorr N_2 background. The characteristic emission was extracted by a 391-nm narrow-bandpass filter. The images were recorded with 1-μs exposures. Near substrate additional plasma excitation is marked by ovals.

The coatings were produced by 248-nm laser ablation of graphite in a nitrogen environment. A series of experiments was performed to map the carbon and carbon–nitride species location and energy as a function of background pressure and time after the pulse, using the characteristic wavelengths of CN, C_2, and atomic C [Voevodin et al., 2002b, 2002c]. At a relatively low pressure of 5 mTorr N_2, there was little influence of the background on the trajectory of different species. There was also a very interesting phenomenon of emission intensification near the substrate (Fig. 23.3), which corresponds to plume excitation by collision with either the substrate surface or with species rebounding from the substrate surface. This near-substrate excitation was long lasting, with detectable emission up to 30 μs after the pulse. The reason for the persistence is that large and slowly moving species (e.g., atom clusters) ablated from the target arrive at the substrate significantly behind the more energetic leading edge [Geohegan, 1994].

At pressures above 15 mTorr, a plasma ''bubble'' was formed that separated from the target and moved toward the substrate, causing significant near-substrate excitation upon arrival. The plasma ''bubble'' development and near-substrate surface excitation was especially clear in photographs of emission from CN radicals at 30 mTorr (Fig. 23.3). Formation of the confined plasma was caused by collisions of the ablated plumes with N_2 molecules, resulting in both additional excitation and plume deceleration. For pressures above 75 mTorr, collisional deceleration caused plume termination without reaching the substrate (Fig. 23.3).

Plume collisions with background gas reduce the average kinetic energy of the ablated species but may also provide an increase in the vibrational energy of molecular species. For example, in the synthesis of CN_x discussed above, kinetic energies were found within 10–20 eV for monoatomic carbon, 30–55 eV for CN, and 20–40 eV for C_2. Excited CN and C_2 molecules were generated by collisions of the plume with the background gas and substrate surface. Their vibrational energies were strongly influenced by nitrogen pressure and time after the laser pulse. For pressures between 10 and 30 mTorr, vibrational energy was as high as 4.0 eV at 2–4 μs for CN and 2.5 eV at 8–10 μs for C_2. The high vibrational temperature was suggested to be beneficial for the growth of fullerene-like CN_x films based on correlations between plasma parameters and film composition and bonding. Synthesis of the fullerene-like structures required both high molecular temperatures and concentrations of CN radicals at the condensation surface [Voevodin et al., 2002b, 2002c].

23.3.3 Substrate Bias Influence

The laser-ablated plumes always have some ionic component, and its energy can be controlled by substrate biasing with respect to the plasma potential. Optimization of the background gas can promote both plume ionization and separation of the leading edge ion component from the rest of the plume. This is illustrated here in application to the growth of yttria-stabilized zirconia (YSZ) hard coatings. The coatings were produced by 248-nm laser ablation of YSZ targets in the presence of argon and oxygen gases.

A detailed analysis of ablated YSZ plasma [Voevodin et al., 2000; Jones et al., 2001] indicated an increased fraction of Zr^+ ions for depositions in 0.2-Pa Ar and larger quantities of excited YO and ZrO molecules for depositions in 0.2-Pa O_2. Zr^+ ions had higher velocities than the rest of the plume. Figure 23.4 demonstrates this with an example of the YSZ ablation in oxygen. From fitting curves in this figure, the Zr^+ velocity distributions did not follow a shifted center-of-mass Maxwell–Boltzmann model of a supersonic molecular beam, which is typically applied to laser-ablated plasmas [Geohegan, 1994]. This suggests that zirconium ions escape velocity attenuation processes within the Knudsen layer at the target surface and fly toward the substrate before the rest of the plume. The average kinetic energy of Zr^+ was 95–105 eV, while for other species it was about 50–60 eV. For the substrate-target distance used here, the lead arrival time of Zr^+ ions was about 3 μs during YSZ film growth [Voevodin et al., 2001c].

Energetic Zr^+ ions, arriving before the bulk of the ablated material, bombard the condensation surface and may rearrange atoms deposited during a previous laser pulse. However, the 95–105 eV kinetic energy was not enough to induce detectable structural modification. Films were found to be nanoscopically smooth with amorphous character. This was drastically changed when a negative potential of 200 V was applied to the substrate for additional acceleration to Zr^+. Crystallite features were detected with sizes of 50–100 nm for depositions in argon and 100–150 nm for depositions in oxygen. The larger crystal growth in oxygen was correlated with a larger availability of chemically active ZrO and YO molecules, accelerating bond formation and growth of YSZ crystals [Voevodin et al., 2001c, 2001d].

One intriguing result was that YSZ films were grown with (002) texture inependently of substrate material, when an ion accelerating bias was supplied to the substrate. Thus, it was not necessary to use (200) textured Ni or Hastelloy substrates to ensure [001] film orientation, as is done for high-temperature depositions [Yang et al., 1998]. Similar quality YSZ coatings were

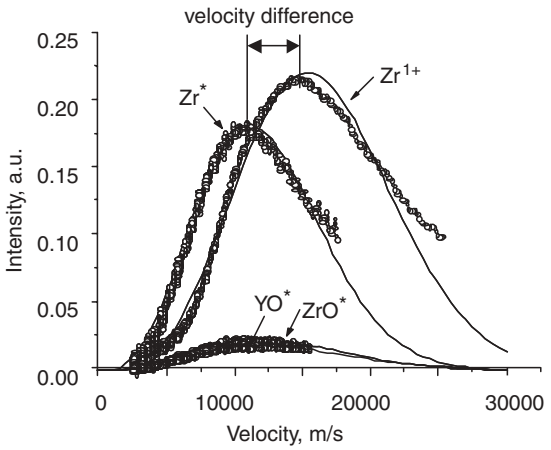

Figure 23.4 Velocity distributions of ionized Zr^+ and excited Zr^* atoms, ZrO^*, and YO^* molecules in YSZ plasma plumes produced by laser ablation in 1.5-mTorr argon. Thin solid lines represent experimental data fits in according with a supersonic molecular beam model given by $f(v) \sim v^3 \exp[-m(v - v_0)^2/2kT]$.

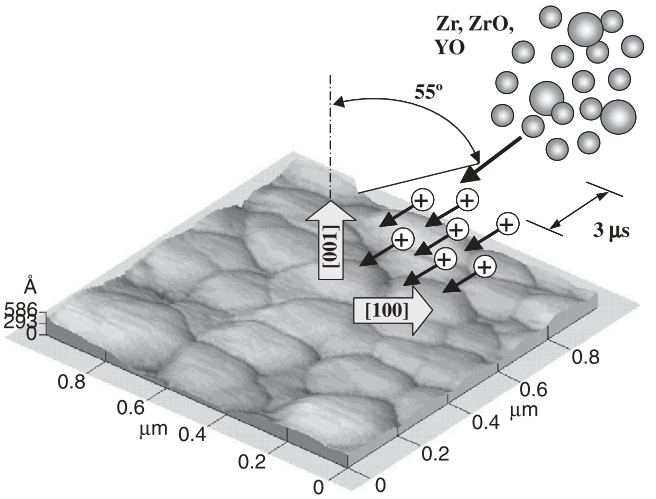

Figure 23.5 Atomic force microscope image of YSZ film grown under inclined Zr^+ bombardment with a schematic of the deposition process and preferred growth direction orientations.

produced on different substrate materials: single-crystal Si wafers with [001] orientation, (200) textured Ni, (200) textured Hastelloy, polycrystalline Cu, and polycrystalline 440C steel [Voevodin et al., 2001d].

The insensitivity of film nucleation and growth processes to substrate chemistry and structure was explained by key properties of the PLD process. First, it provided ablated plasma pulses of only 8-μs duration, which were followed by much longer pauses of 25 ms between laser shots. This limited substrate heating and prevented thermal migration of deposited atoms to energy well sites on the condensation surface. Second, the high density of the laser ablated plasma forced arriving atoms to form a substrate-independent structure rather than to follow a substrate surface template. Finally, pulsed and very short (3-μs) duration Zr^+ bombardment provided a short-range adatom mobility. This mobility was enough to rearrange deposited atoms into YSZ crystals but was not long enough for surface reconstruction in accordance to the substrate crystal template. The realized YSZ growth under Zr^+ bombardment is schematically shown in Figure 23.5.

Substrate bias rearranges and densifies coating structure and builds compressive stress in the coatings. It can be used to effectively control film mechanical properties [Voevodin et al., 2001d]. Figure 23.6 shows hardness variation with applied bias, where hardness monotonically increases over the entire voltage range, reaching maximum values of about 30 GPa for 300-V bias. The elastic modulus of the films increased in a similar fashion from 240 to 320 GPa. This value is above the modulus of 233 GPa for single-crystal cubic YSZ due to the high compression stress in the film plane.

23.3.4 Substrate Temperature

The role of substrate temperature on material synthesis by PLD is the same as in other thin-film growth techniques—it increases atom mobility on the surface and within the bulk at sufficiently high temperature. As the temperature increases, the adatom mobility at the condensation surface increases causing film structure to progress from amorphous to polycrystalline and further to single-crystal epitaxial growth. For the majority of tribological coating applications, the use of high deposition temperatures is limited because they cause microstructural and chemical changes that defeat the annealing and tempering treatments that provide steels with good mechanical properties.

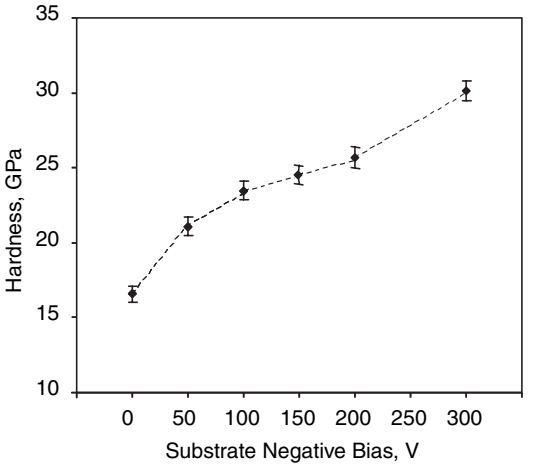

Figure 23.6 Hardness variation of crystalline YSZ films grown in 1.5-mTorr Ar at 100°C with different bias voltage.

Thus, tribological coatings are typically produced with amorphous or polycrystalline structures. The energetic character of the plasma plumes produced by PLD is used to compensate for the low substrate temperature in synthesis of crystalline materials. For example, crystalline coatings of TiC, TiCN, WC, and YSZ were produced at temperatures around 100°C [Capano et al., 1997; Voevodin et al., 1997a, 1997c, 1999a, 2001d]. This provides an exceptional advantage of PLD over other deposition techniques, where high temperatures are routinely required for the production of similar coatings.

23.4 PLASMA CHARACTERIZATION, SENSORS, AND PROCESS CONTROL

The PLD process can be viewed as three subprocesses: (1) laser–target interaction, (2) material transport through vacuum or gas, and (3) film growth at the substrate. Using this template, the PLD process can be analyzed in detail and unwanted process variability can be removed through process control. In the case of the first subprocess, although the laser wavelength is generally fixed, the manner in which the beam is moved across the target will determine thermal effects of the target, uniformity of the film, and target wear. Typically target materials are rotated to prevent coning, promote uniform wear of the target, and mitigate thermal effects. The second subprocess, material transport, can be monitored experimentally using real-time plume sensors to determine physical and chemical parameters. The third subprocess, film growth, is relatively more difficult to be measured in situ. Tribological coatings are typically applied to substrates of various geometries and compositions, and this restricts applicability of in situ ellipsometry or other techniques that require flat substrates. Thus, plume characterization becomes a critical step in linking the plume composition to film properties such as composition, structure, morphology, and thickness. Here, a short description of in situ sensors and process control algorithms from the practice of tribological coating growth is provided.

23.4.1 Plasma Characterization

While the plume appears to be continuous using a simple video monitor or the eye, it is really a highly energetic process in which species are ejected from the target surface at speeds in excess of

10 km/s. The wavelengths of light that are emitted as these species travel and collide with other particles and background gas species are dependent upon the composition of the target material and the background gas composition and pressure. The light emitted by the target and background gas species can be characterized using a spectrometer. In addition, plasma temperature, potential, and ion/electron density may be measured using a Langmuir probe. By collecting spectroscopic and Langmuir probe data as a function of time and in localized regions of space a temporal and spatial map of plasma chemistry and physics can be generated.

An optical multichannel analyzer (OMA) uses an intensified charge-coupled device (ICCD) array in which a voltage pulse is used to gate the array. In this manner, images can be taken with nanosecond precision for microsecond durations with resolutions of several hundred pixels in both the horizontal and vertical directions. To display the evolution of the plume, many laser pulses need to be imaged sequentially, and then the images at defined time intervals can be added together and displayed. By attaching a spectrometer grating in which regions of spectra are mapped across the ICCD array, spectra can be collected at very high resolution and the data appended as necessary to show very broad spectral ranges. For molecular species in the plume, vibrational temperatures can be determined from emission line intensity measurements of different vibrational levels and fitting the data to a Boltzmann plot of energy state population density. Once spectral analysis of a plume generated by a particular target has been accomplished, and hopefully unique wavelength ranges have been identified, optical bandpass filters can be obtained having 10-nm bandwidths. These filters can be used in conjunction with ICCD cameras to image the location of selected species in time and/or with photomultiplier tubes to track species concentrations and kinetic energies in time and space.

23.4.2 Real-Time Sensors

An effective way to monitor the plume generated by PLD is by using a photomultiplier tube (PMT) in conjunction with a monochromator and oscilloscope. A monochromator provides for the selection of a particular wavelength of light to monitor, which will then be converted to a voltage signal by the PMT and captured with high fidelity by an oscilloscope. Digital oscilloscopes can average plume emission signals from several laser pulses, thereby removing high-frequency noise and variability that arises such as from steering of the laser beam across a target area, while maintaining much longer time constant effects such as changes in process conditions like pressure or laser fluence.

An inexpensive substitute for a spectrometer can be constructed using a collimating tube containing an aperture at each end and a fixed wavelength bandpass filter, typically having a 10-nm bandwidth. Furthermore, use of a filter wheel in which several filters may be sequentially selected is an inexpensive but much more functional solution to plume emission monitoring than using a fixed wavelength monochromator.

A Langmuir probe provides the ability to measure current–voltage characteristics of the ablated plasma. Through use of a probe with sequentially different potentials, measurements of the resulting current allow the evaluation of the plasma potential, electron temperature, and ion density in the ablated plasma.

A quartz-crystal microbalance measures the change in frequency of a circuit to determine changes in thickness. This change in frequency results due to the thin-film coating being deposited onto the oscillating crystal. This method requires that the crystal sensor be near the substrate, and for large areas or substrates requiring high temperatures this method may not be practical.

23.4.3 Process Control

The challenge for PLD to become commercially viable involves being able to grow coatings using known recipes, on demand, for long periods of time. By applying feedback, or closed-loop

control, PLD parameters that are known to be of importance can be maintained. Regulation of the PLD process first requires the ability to monitor the desired parameter, using techniques mentioned above to capture waveforms from an oscilloscope that are representative of the plume plasma emissions. The desired parameter to be maintained could be the peak plume intensity or the time of flight (TOF) that is detected at the start of a deposition. An algorithm can continuously monitor the desired process parameter, and when there is deviation of a prescribed significance, a control variable, for example, laser pulse energy, is adjusted. Modern techniques employing fuzzy logic may be used to overcome the limitations of direct predetermined algorithms for process control.

Use of fuzzy logic can make implementation of process control for PLD straightforward and deterministic. Fuzzy logic requires an expert to define linguistic terms for a few processing parameters, and outputs. For example, one parameter could be a deviation or error in set point of peak intensity and actual measured peak intensity. This error could be defined by fuzzy membership functions of zero, small, and large. A rate of change of the error, or error rate, is defined by fuzzy membership functions as zero, positive, or negative. With these definitions, an expert must define how the process should behave for each combination of fuzzy membership functions of error and error rate. Thus, the expert defines how the process will behave at key states: for a large error and positive error rate, there should be a large decrease; whereas for a large error and negative error rate there should be a small decrease. The expert defines these membership functions once, and then subsequently this rule's matrix or fuzzy associative memory (FAM) is repeatedly used to compute an output from the two vectors of error and error rate. The change in process output is then calculated as the center of gravity of an output matrix through a process known as defuzzification (Fig. 23.7). This provides a more flexible and fast reacting ''expert'' algorithm to keep the controlled parameters at the desired values.

Implementation of a fuzzy controller as detailed above provides the ability to regulate the plume by using changes in laser energy density, chamber pressure, magnetron power, and the like as control variables. The choice of which variable is controlled depends on the particular application, but multiple variables could also be controlled simultaneously if desired, such as the laser energy and chamber pressure.

The importance of using process control can be demonstrated by using a hybrid technique of magnetron sputtering and pulsed laser deposition (MSPLD) to deposit YSZ and Au simultaneously. Any variability in the plume fluence over time would result in undesirable variability of the film composition. For this YSZ/Au material system, monitoring of the Zr^* species was accomplished using a 470-nm bandpass filter and corresponding collimating tube with a PMT, while the Au^* species was monitored using a fiber-optic monochromator set to 310 nm. For the first of two films that were grown, the laser was set to a fixed energy setting and the resulting peak intensity monitored over 90 min. For the second YSZ/Au film, the fuzzy logic process control algorithm described above was used to maintain an initial peak intensity of Zr^* for 90 min by adjusting the laser energy setpoint.

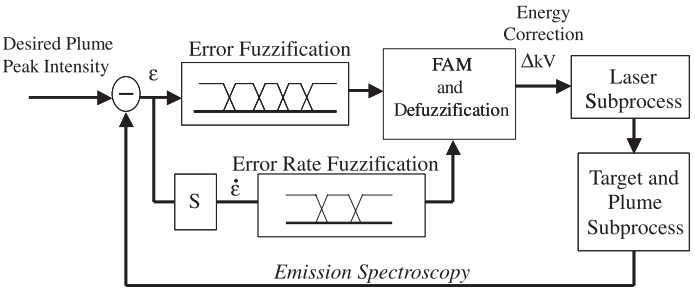

Figure 23.7 Process control schematic using an emission spectroscopy sensor and a fuzzy logic algorithm to correct laser pulse energy to achieve a desired plume peak intensity for laser ablation depositions.

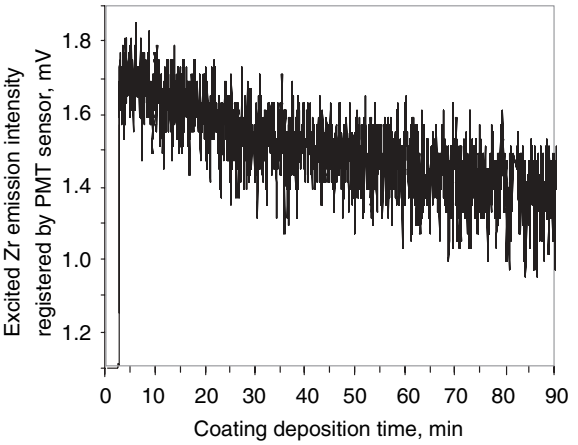

Figure 23.8 Variation of peak emission intensity of Zr excited atoms in plumes produced by laser ablation of an YSZ target with Au co-sputtering. Signal degradation with time is caused by the laser window coating, leading to a decrease of laser fluence on the YSZ target.

During the growth of the first film, the peak intensity of Zr^* decreased monotonically (Fig. 23.8). X-ray photoelectron spectroscopy (XPS) of the first film showed a monotonic increase in Au composition with the lowest composition of about 9.6% increasing to 12.5% at the coating surface (Fig. 23.9). For the second film, the Zr^* peak intensity was maintained by the process control algorithm through continuous updates to the laser energy over the course of the deposition. XPS of the second film shows that the composition was essentially constant throughout the depth of the sample, with 11.6% Au (Fig. 23.10).

For a simple case in which desired plume fluence on the target is to be maintained over a long period of time, a problem can be seen in that the chamber windows were being coated, thereby reducing the plume fluence. Even when special windows are used to control the rate of deposition on the window, some changes in optical transmission are inevitable. By using process control, the laser energy was increased overcoming this effect.

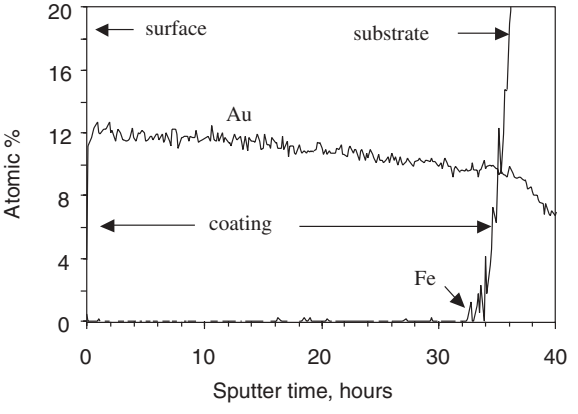

Figure 23.9 Profile distribution of Au in a YSZ/Au nanocomposite coating produced by MSPLD without process control. X-ray photoelectron spectroscopy with a 1-keV Ar sputtering was used for the depth profiling of Au concentration. A high concentration of Au at the coating surface is due to a decrease in supply of YSZ component in a result of a laser fluence variation.

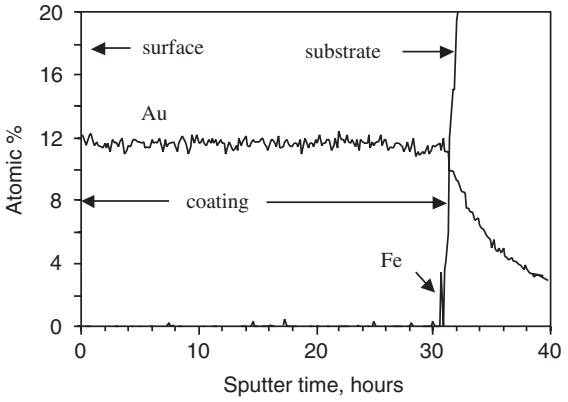

Figure 23.10 Profile distribution of Au in a YSZ/Au nanocomposite coating produced by MSPLD with a fuzzy logic process control. X-ray photoelectron spectroscopy with a 1-keV Ar sputtering was used for the depth profiling of Au concentration. Constant concentration of Au across coating depth is a result of a laser fluence control based on an emission signal.

23.5 HYBRIDS OF PLD WITH OTHER DEPOSITION TECHNIQUES

The major drawback of PLD in comparison to other deposition techniques, for example, magnetron sputtering or vacuum arc, is a relatively low deposition rate. This is aggravated by the high initial investment expense for laser equipment, which results in high coating cost. Evaluation of process economics under those circumstances limits PLD to mainly microelectronic applications, where precision in composition control and film purity may override higher cost. However, the cost of laser energy has drastically decreased in recent years, and the low deposition rate has become the predominant factor restricting broader commercial use of PLD. This is especially true for film growth using laser ablation of carbides, nitrides, some oxides, and graphite. A possible solution to the problem is combining PLD with other deposition methods to increase deposition rate. The additional plasma sources may be selected to overcome specific limitations of laser deposition. For example, deposition of many oxides and DLC is quite effective using PLD compared to magnetron deposition, whereas metal deposition is usually more effective via magnetron. Hybridization of PLD with other techniques can also facilitate a high degree of structural control at low substrate temperatures, permitting growth of materials that are not possible to produce by other methods. Development of two such hybrid technologies is discussed in this section: One is a combination of PLD and magnetron sputtering deposition, and the other is a combination of PLD and ion beam deposition.

23.5.1 Hybrid of Magnetron Sputtering and Pulsed Laser Deposition

A hybrid of magnetron sputtering and pulsed laser deposition (MSPLD) was initially developed for preparation of functionally gradient transition-metal carbides and multilayer structures in the TiC and DLC material systems [Voevodin et al., 1996a, 1997a]. MSPLD was then expanded toward WC/DLC, WC/DLC/WS_2, YSZ/Au, and YSZ/Au/MoS_2/DLC nanocomposites for wear protection of engineering components [Voevodin et al., 1999a, 1999d, 2001b, 2002a]. The technique was adapted by other researchers for the synthesis of TiC/Ag nanocomposite coatings with advanced mechanical characteristics [Endrino et al., 2002; Phani et al., 2002].

A schematic of MSPLD is shown in Figure 23.11. A pulsed laser beam is used to generate a carbon flux, while a magnetron generates a flux of titanium, tungsten, or tungsten + sulfur atoms.

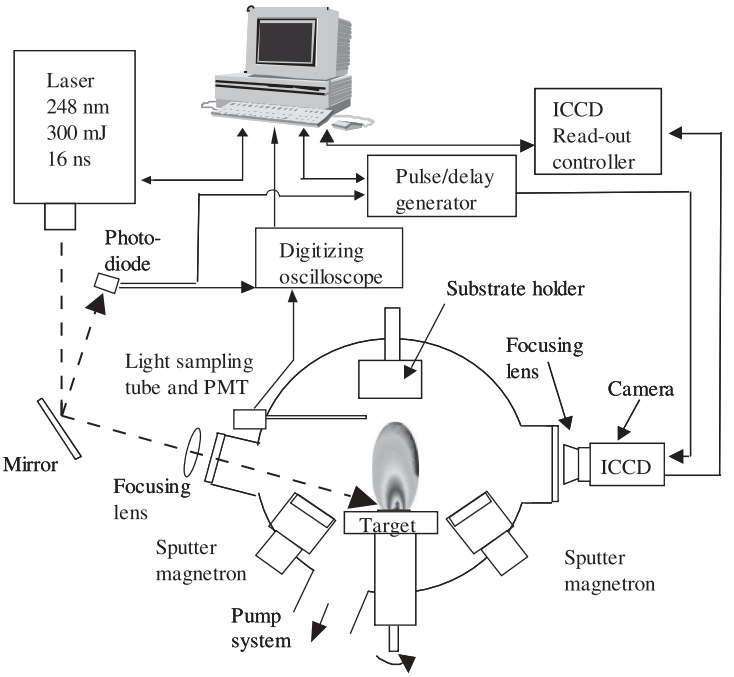

Figure 23.11 Schematic of MSPLD arrangement. Magnetron sputter sources provide W, Ti, and/or WS_2 fluxes, while laser ablation provides the carbon plume.

The target orientations define the point of intersection of the fluxes from the different sources. Magnetrons are placed into an unbalanced configuration to sputter metal (Ti, W, Au, Ag, etc.) and/or dichalcogenide (WS_2, MoS_2) materials with kinetic energies of several electron volts in the direction of the substrate. For sputtering, an argon pressure of 0.2 Pa is typically maintained in the deposition chamber, which is low enough to prevent thermalization of the ablated plumes. The main task of magnetron sputtering is to deliver a high flux of metal and/or sulfur atoms to the condensation surface and thus provide a high growth rate. Carbon plumes from the laser ablation of graphite or Y–Zr–O plumes from YSZ targets are also directed to the condensation surface, intersecting with the metal atom flux from magnetron sputtering, as shown in Figure 23.12.

In the case of carbide growth, the independent operation of metal and C sources provided a means to control composition and was based on the relationship between film stoichiometry and the deposition rates of each element. In particular, a direct dependence of the Ti_xC_y and W_xC_y film stoichiometry on the laser repetition rate (R) and a linear relationship between R and the ablation rate of carbon was found, which made composition control easy. When a y/x ratio of stoichiometric coefficients is used, the film composition can be predicted with the following equation:

$$y/x = \alpha\beta R$$

where α is the ratio of the product of mass and density for the two elements $\alpha = (M_{Ti}\rho_C)/(M_C\rho_{Ti})$, and β is the ratio of the sputtering rate of Ti or W to the ablation rate of C. The energetic carbon atoms arriving at the condensation surface provide sufficient energy for the growth of nanocrystalline carbide phases at low substrate temperatures.

With MSPLD, crystalline TiC, WC, and ZrO_2 coatings with grain sizes regulated between 10 and 100 nm were grown at near room temperature, and the deposition rates were similar to that in magnetron sputtering. MSPLD has a significant advantage over regular magnetron sputtering, where

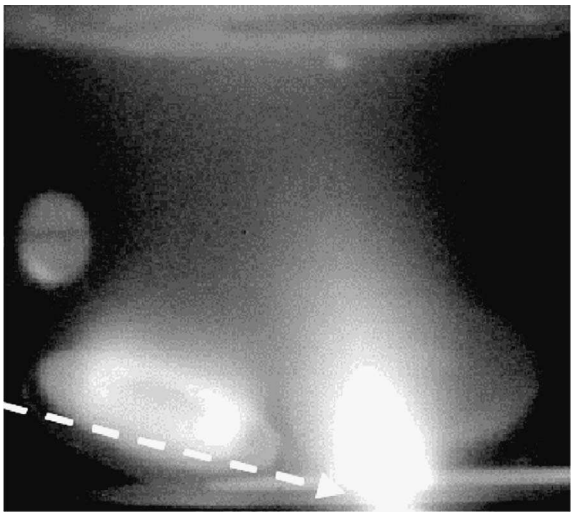

Figure 23.12 Photograph of the MSPLD process, showing intersection of plasma fluxes from magnetron (left) and laser ablation (bottom) on a substrate holder above.

substrate temperatures of at least 350–400°C are required for carbides and 500–600°C for ZrO_2. Furthermore, MSPLD opens the possibility for growing ''next-generation'' coatings of unique composite materials made of amorphous DLC, MoS_2, WS_2, and crystalline carbide or oxide phases. The task is not trivial, which is evident from the fact that DLC is typically grown at temperatures below 200°C to escape graphitization during growth, while carbides require 350–500°C temperatures to form crystalline phases. Similarly, both MoS_2 and WS_2 dissociate at the typical growth temperatures of crystalline ZrO_2. MSPLD solved these problems by compensating for a low substrate temperature with a high kinetic energy of laser-ablated carbon or zirconium atoms, providing crystalline carbide and oxide formation without raising substrate temperature. Growth rates of about 1 μm/h were maintained, which were close to that of magnetron sputtering. While local growth rates on a par with magnetron sputtering have been achieved, additional work is required to coat numerous parts at once—in other words, scaleup is the next issue (see Chapter 9 for a full discussion of industrial-scale PLD systems). Tribological properties of some composite coatings produced by MSPLD are briefly reviewed in later sections of this chapter.

23.5.2 Hybrid of Ion Beam and Pulsed Laser Deposition

The combination of ion beam bombardment and PLD is sometimes referred as ion-beam-assisted pulsed laser deposition (IAPLD). IAPLD was found to be very successful in structure control of Y_2O_3–ZrO_2 and CeO_2 buffer layers for subsequent epitaxial growth of superconductive oxides [Reade et al., 1995]. Another application of IAPLD was the production of β-C_3N_4 [Niu et al., 1993] and cubic-BN [Friedmann et al., 1994] hard films for surface wear protection. In both cases, high kinetic energy and activation of gas species in the ion beam plasma were key factors for film synthesis.

A generally accepted model of IAPLD growth considers separately the processes of film deposition during short (5–10 μs) pulses of ablated plasma and structure/chemistry adjustment by ion bombardment during relatively long (10–100 ms) pauses between laser pulses. Until recently, little attention was paid to a synergistic interaction between the plasma generated by the ion beam and laser. However, such interaction could lead to new chemical reactions in the plasma as well as the generation of additional excitation states important for control of film growth.

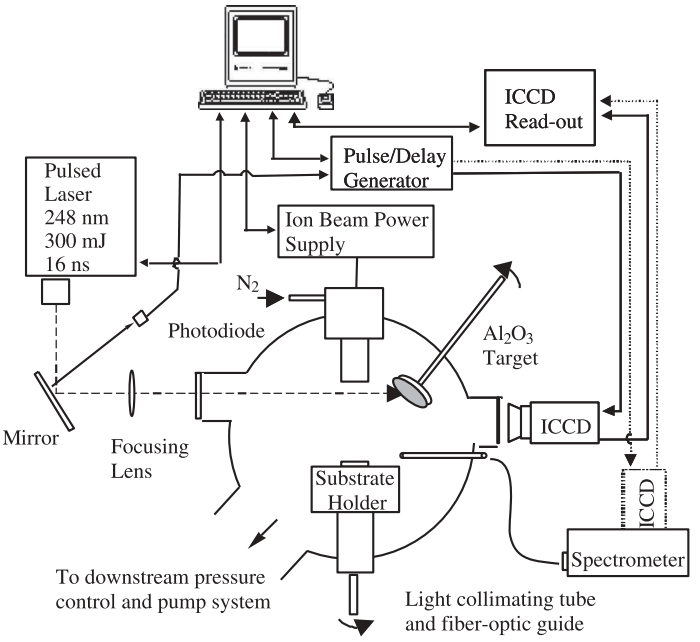

Figure 23.13 Schematic of IAPLD arrangement for AlON film growth. An ion beam source above the substrate provides the N^+ beam, while laser ablation is used to generate plasma plumes from an alumina target.

Some of these interactions were explored while growing Al–O–N films [Voevodin and Zabinski, 2001], which have enhanced thermal, tribological, and dielectric properties. Plasma plumes from laser ablation of Al_2O_3 and a nitrogen ion beam were intersected in the vicinity of the substrate (Fig. 23.13). A KrF excimer laser (Lambda Physik, COMPex 205) produced pulses of 248 nm wavelength and 300 mJ energy with 20 Hz frequency. The laser beam was directed onto a rotating polycrystalline Al_2O_3 (alumina) target under a 45° angle and focused to an instantaneous energy density of about 1.5 GW/cm^2. A 3-cm-diameter Kaufman ion beam source (Commonwealth Scientific Corp.) was operated using high-purity nitrogen gas at a beam voltage of 300 V. Temporal and spatial plasma distributions of the plasma generated by laser ablation and the ion beam were investigated with a gated image-intensified charge-coupled detector (ICCD) camera at nitrogen background pressures from 0.1 to 3.9 Pa.

An interaction effect was discovered, revealing plasma channels connecting the ion beam plasma and laser-ablated plume (Fig. 23.14). These plasma channels existed only during the short period of the ablated plume development, and their spatial location was dependent on the nitrogen background pressure in the chamber. Increasing the pressure resulted in interaction channel locations closer to the plasma sources and away from the substrate. The plasma connection between the ion beam and laser ablation sources resulted in an instantaneous 40–60% increase of the current extracted from the ion beam source during laser plume development. Furthermore, plasma spectroscopic analyses indicated the presence of excited NO molecules during this short 5- to 10-μs interaction event. These molecules were identified from rotation/vibration $A^2\Sigma^+ \rightarrow X^2\Pi$ and $B^2\Pi \rightarrow X^2\Pi$ excitation transitions. There were also additional excitation and ionization states for atomic nitrogen and oxygen occurring within plasma interaction channels. The ionization level of atomic aluminum was not dependent on the ion beam source operation, and the emission bands of AlO or AlN molecules were not detected.

This interesting result demonstrated the influence of short-duration plasma interactions in the IAPLD process on plasma chemistry and allowed identification of film growth mechanisms.

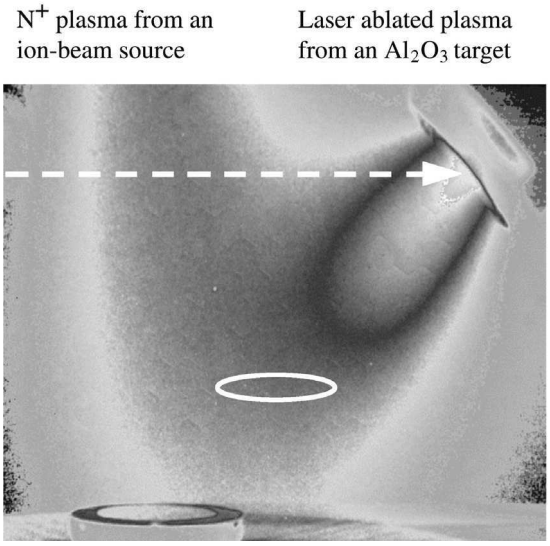

Figure 23.14 Photograph of the IAPLD process obtained at 10-ms ICCD exposure, showing a plasma interaction channel between the ion beam and laser ablation sources. The white circle indicates the substrate position, where AlON films with a high nitrogen content were produced.

The maximum development of NO radical lines coincided with the arrival of the plasma plume at the substrate at about 4–6 μs, followed by quick deterioration of line intensities (Fig. 23.15). From the main chemically active elements in the plasma, Al, N, O, and NO radicals, it was reasonable to suggest that nitrogen and oxygen predominately react with each other in the gas phase to form

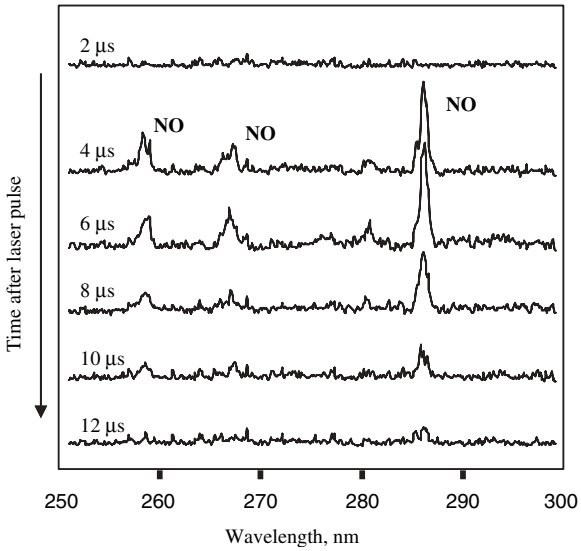

Figure 23.15 Development of NO molecular emission bands in the plasma interaction channels between ion beam and laser-ablated plumes in IAPLD on a real-time scale after the laser pulse. Spectra were obtained using 500-ns exposures of ICCD detector with 2–12 μs exposure delays after a laser pulse.

molecular NO. The reaction may occur only during short intervals of the interaction between the ion beam, supplying nitrogen, and laser-ablated plumes, supplying oxygen. The growth of Al–O–N films then occurs through a heterogeneous reaction on the sample surface between arriving atomic Al and molecular NO species.

The synergistic effect of plasma enhancement in IAPLD growth was used to produce highly nitrogenated (20–30 at % N) AlON films by moving substrates into the brightest part of the interaction channel (Fig. 23.14), where the strongest emission signal from excited NO radicals was detected. This sample location was off-axis from the nitrogen ion beam source and thus would not be considered as an optimum location to maximize nitrogen content, when considering ion beam source operation separately from laser ablation. However, this location provided a factor of 2 increase in film nitrogen content as compared to the film grown on a substrate located at the centerline of the ion beam source. Furthermore, the increase in plasma excitation of both atomic and molecular species helped to produce nanocrystalline AlON films at about 300°C substrate temperature. Such moderate temperature was very favorable in comparison to 600–800°C temperatures required by other deposition techniques to achieve film crystallinity. This success of IAPLD technology confirmed once more that hybrids of PLD with other deposition techniques have great potential for the discovery and production of unique materials.

23.6 TRIBOLOGICAL COATINGS PRODUCED BY PLD AND HYBRID TECHNIQUES

There are a number of good reviews on hard tribological coatings that have been published lately. Monolithic coatings of transition-metal carbides/nitrides and oxides dominate the literature [Holmberg and Matthews, 1994; Bushan and Gupta, 1991], however, attention has recently been focused on moving away from monolithic coatings to duplex, functionally gradient, multilayer, and nanocomposite coating architectures to improve overall friction and wear response. The same trend is observed with respect to coatings produced by PLD technology. The coating examples discussed in this section are divided into monolithic or single-phase coatings, gradient and/or layered coatings, nanocomposite coatings, and advanced multifunctional tribological coatings.

23.6.1 Monolithic Coatings

Over a number of years, PLD has been successfully used to produce a number of single-phase monolithic tribological coatings, which are briefly reviewed in this section. They include both hard wear-resistant coatings and solid lubricants.

Hard ceramic coatings have been the most widely explored for PLD synthesis. They include coatings made of TiC, SiC, Cr_3C_2, WC, c-BN, and TiN [Donley and Zabinski, 1994]. Most of the hard coating research demonstrates that PLD provides excellent structure control, but they also report slow growth rates, reducing their commercial impact.

Solid lubricant coating growth with PLD has been one of the prime focuses of our recent efforts. PLD is an excellent tool to permit the growth of near stoichiometric coatings, with respect to target composition, with a minimum loss of low-melting-point elements. Therefore, it provides a simple and technologically robust process for depositing MoS_2, WS_2, NbS_2, $NbSe_2$, $NbTe_2$, and similar coatings [Donley and Zabinski, 1994]. These coatings provide very low friction coefficients and can be tailored to both vacuum and atmospheric applications.

Lubricious oxide materials are another class of monolithic tribological coatings produced by PLD. These oxide coatings, for example, PbO and ZnO, are beneficial for friction and wear reduction at elevated temperatures [Zabinski et al., 1992, 1993]. They can also be incorporated into composites, by preparing laser ablation targets by mixing powders of different materials. One interesting combination is the PbO–MoS_2 composite, which was shown to exhibit adaptive lubrication by chemical transition from MoS_2/PbO to $PbMoO_4$ as the temperature is increased from

room temperature to 1000°C [Zabinski et al., 1996]. Cs_2MoOS_3 coatings have been prepared by PLD to provide low friction at temperatures up to 700°C [Strong and Zabinski, 2002].

Hydrogen-free superhard DLC coatings are produced only by either PLD or filtered vacuum arc techniques. In the PLD process, ultraviolet lasers are used for graphite ablation with instant power densities of 10^8–10^9 W/cm^2 per laser pulse, which is sufficient to form hard DLC coatings on steel substrates at temperatures below 150°C [Voevodin et al., 1996b]. Coatings have mainly sp^3 C–C interatomic bonding, hydrogen contamination below 0.1 at %, and a density of about 3.0 g/cm^3. Their nanoindentation hardness is about 70 GPa and elastic modulus is about 600 GPa. These superhard DLC coatings have a friction coefficient as low as 0.05–0.10 in sliding against steel and sapphire counterparts in dry, humid, and vacuum environments [Voevodin et al., 1995a]. However, they possess large compressive stresses and can be easily fractured and delaminate from steel substrates if a transition layer interface is not provided. The problem is mitigated by DLC doping with metal atoms, as, for example, in a PLD growth from sectioned graphite/metal targets or sequential ablation of graphite and metal targets [Wei et al., 1998, 1999a]. Incorporation of carbide forming metals, for example, Si and Ti, was found beneficial for the stress reduction and adhesion improvement of DLC coatings produced by PLD.

Hydrogenated DLC is less hard and more flexible, due to the termination of strong σ-type C–C bonds. H:DLC coatings can be produced in high-vacuum conditions by ultraviolet (UV) ablation of polymer targets, such as polycarbonate [$C_{13}O_3H_{14}$]. Carbon, hydrogen, and oxygen are then incorporated into an amorphous DLC network, as well as some amount of polymer fragments. These coatings contain approximately 25 at % H and have sp^3-type CH_3 and polymer O–CH_3 interatomic bonds. Their density is about 2.2 g/cm^3, hardness values are about 15 GPa, and elastic moduli are about 180 GPa [Voevodin et al., 1995b].

Composite H:DLC/DLC coatings were prepared by PLD, where laser ablation targets were constructed from graphite and polycarbonate sectors (Fig. 23.16). The resulting coatings consisted of a mixture of DLC and H:DLC layers, with incorporation of polymer particulates, which can be seen in Figure 23.16. Even with nonuniform morphology, the coatings were dense and had considerable fractions of sp^3-bonded carbon, which yielded hardnesses of about 20 GPa and elastic moduli of about 270 GPa [Voevodin et al., 1997b].

Fullerene-like CN_x is another carbon-based tribological material recently produced by PLD. These coatings were originally synthesized by magnetron sputtering and have a unique resilient behavior, providing hard and yet flexible material [Hultman et al., 2003]. The fullerene-like CN_x coatings were reported to contain about 20 at % N, have predominantly sp^2 configuration of interatomic bonding, a high degree of graphite plane bending and cross-linking, hardness around 10–20 GPa, elastic modulus of 40–120 GPa, and friction coefficients of about 0.3 at ambient conditions [Hultman et al., 2003; Neidhardt et al., 2003; Broitman et al., 2001]. Using the PLD process, fullerene-like CN_x coatings can be obtained by graphite ablation in a nitrogen gas background. The process needs to be tuned for production of hexagonal graphitic-like clusters, where nitrogen is used to improve coating stiffness as described above. In comparison to magnetron sputtering, PLD provides less order in the graphitic plane arrangements, a considerably higher hardness of 30 GPa, and elastic modulus of about 200 GPa [Voevodin et al., 2002b, 2002c].

23.6.2 Functionally Gradient and Nanolayered Coatings

One approach for improving the toughness and adhesion of DLC is to use a multilayer architecture, where the superhard DLC layers are separated with metal layers and are incorporated in a functionally gradient coating to accommodate stresses and reduce microcracking. This coating design includes a gradual transition of chemistry, structure, and properties from substrate material to DLC producing no sharp interfaces, which are potential locations for crack initialization [Voevodin et al., 1997a]. A typical architecture includes formation of an adhesive thin-metal layer, a transition to a load-supporting carbide layer, then addition of a metal-doped DLC layer, and subsequent deposition of multiple pairs of metal–DLC or carbide–DLC layers [Voevodin et al., 1997d].

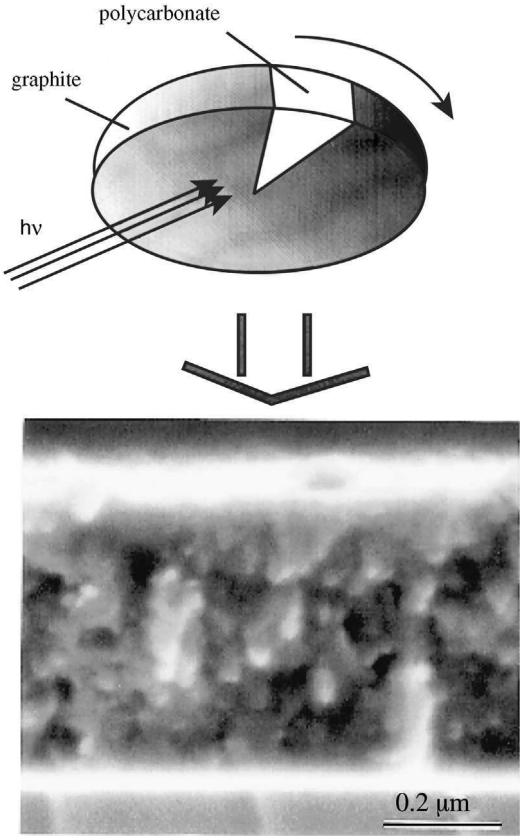

Figure 23.16 A PLD schematic with a composed graphite/polycarbonate target and a scanning microscope image of a cross-section fracture of a DLC/H:DLC composite coating.

For example, a coating with a Ti–TiC–DLC–20[TiC–DLC] architecture was designed and produced by MSPLD, where 20 pairs of 60-nm-thick DLC and 10-nm-thick TiC layers were deposited on top of a Ti–TiC–DLC layer. The composition of this coating was gradually varied from pure Ti on the substrate surface to $Ti_{1-x}C_x$, a columnar carbide layer, to Ti-doped DLC, and then to pure carbon in the first DLC layer, after which the TiC–DLC multilayer stack was deposited (Fig. 23.17). The result was a gradient coating with an upper nanolayered structure consisting of amorphous DLC and crystalline TiC layers. From composite mechanics, such a structure arrests and deflects cross-sectional cracks, improving the toughness. This can be seen in a cross-sectional fracture micrograph of this coating (Fig. 23.18).

In contact toughness tests, the upper critical load (65 N) exceeded the toughness of wear-resistant single-layer ceramics. A maximum contact pressure of about 10 GPa was estimated to correspond to the critical load from the contact geometry measurements. It is important to note that this coating maintained a 0.1 friction coefficient for over 1,000,000 cycles in sliding against a sapphire ball in an ambient environment at initial contact pressures of about 1.4 GPa. The concept of functionally gradient and nanolayered DLC-based composites was also tested on coatings with stacks of Ti–DLC and CN_x–DLC layers. Both these coatings passed one million cycle tests in similar sliding conditions. For the CN_x–DLC multilayer coating, the friction coefficient was about 0.07, while the Ti–DLC multilayer coating had a friction coefficient of about 0.12.

Pulsed laser deposition processes with a sequential ablation from different targets or from rotating targets made of different segments can provide a simple and well-controlled way of building

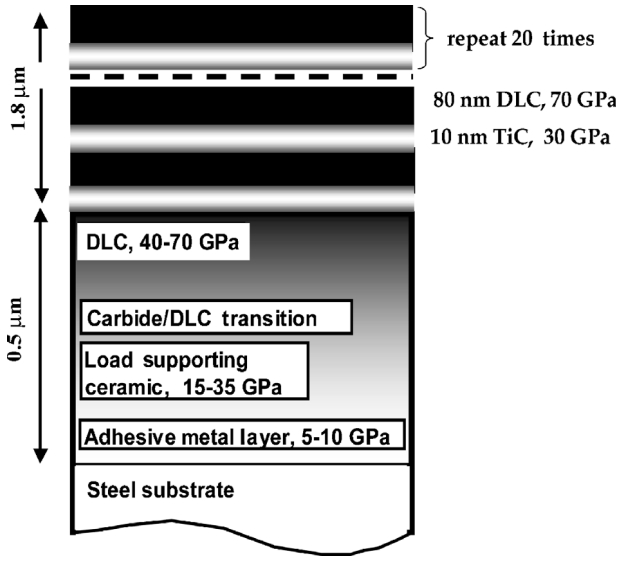

Figure 23.17 Schematic of a DLC/TiC multilayer with a functionally gradient Ti–TiC–DLC interface and a top layer stack of DLC/TiC pairs. Gradation of composition and hardness across the coating thickness is indicated.

nanolayered and gradient structures from nitrides, carbides, and metals. Such PLD processes were used to build microlaminates of B_4C/TiC with a high hardness [Radder et al., 2002] and functionally gradient DLC coatings, where Cu, Ag, and Ti were incorporated to enhance tribological coating adhesion [Wei et al., 1999b]. Considerable enhancements in mechanical and tribological properties of these materials open the way to use PLD as an alternative tool in producing multilayer and functionally gradient tribological coatings.

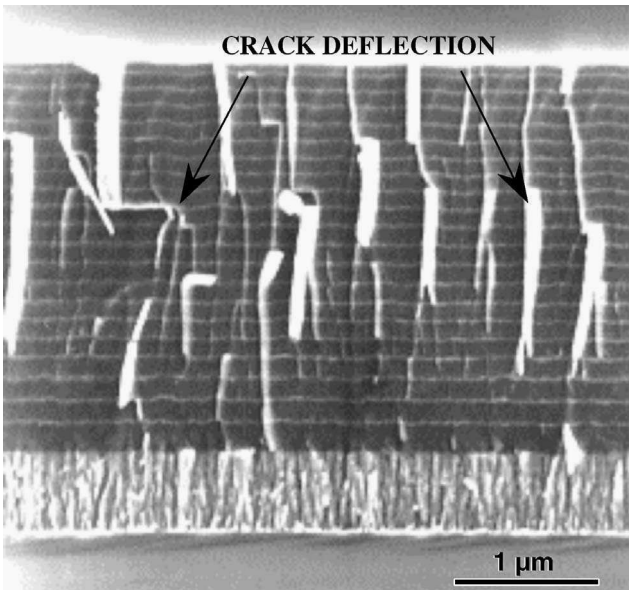

Figure 23.18 Scanning microscope image of a cross-section fracture of a Ti + TiC + DLC + 20[TiC/DLC] multilayer coating.

23.6.3 Nanocrystalline/Amorphous Composites

Incorporation of nanocrystalline grains in an amorphous matrix generates unique improvement in hardness [Veprek, 1999], due to suppressing formation and motion of cross-grain dislocations in favor of deformations by grain boundary mechanisms. These nanostructure designs can be also applied to improve toughness [Mitterer et al., 1999] by activating grain boundary deformation mechanisms, and they can improve wear resistance and friction reduction by appropriate selection of crystalline and amorphous matrix material [Voevodin et al., 1999d].

The first wear resistant nanocrystalline/amorphous materials synthesized by PLD were TiC/DLC and WC/DLC nanocomposite coatings, produced by MSPLD in a configuration similar to the one shown in Figure 23.11. In the case of TiC/DLC nanocomposites, deposition parameters were tuned to produce coatings with a $Ti_{0.3}C_{0.7}$ stoichiometry as determined by XPS. In such overstoichiometric films, the carbon was bonded in both TiC and DLC phases, producing two characteristic peaks in XPS in the C_{1s} region at 281.8 and 284.6 eV. Formation of nanocrystalline TiC was confirmed in transmission electron microscopy (Fig. 23.19). Sizes of TiC crystallites were about 5–10 nm and they were completely encapsulated in the DLC matrix.

Nanoindentation hardness of the TiC/DLC composite was about 32 GPa. This was higher than the 27-GPa hardness of nanocrystalline stoichiometric TiC, but not so high as 60-GPa hardness of hydrogen-free DLC. However, the TiC/DLC composite showed 40% plasticity during indentation deformation, which was four times more than that observed for superhard, but brittle, DLC. An extremely high contact toughness was found for these coatings. TiC/DLC coatings (0.5-μm thick on steel substrates) withstood 70-N load without brittle failure. At this load, considerable substrate deformation is inevitable, which can lead to brittle failure of hard coatings, such as DLC or ceramics. In comparison tests, the contact toughness of TiC/DLC composites exceeded the toughness of nanocrystalline TiC and single-layer DLC by 400 and 600%, respectively, permitting the designation of these composites as supertough.

Very similar dramatic enhancement in coating toughness was observed for WC/DLC composites prepared by MSPLD [Voevodin et al., 1999a]. Friction tests of both TiC/DLC and WC/DLC composites showed friction coefficients of about 0.15 in unlubricated sliding against a steel ball

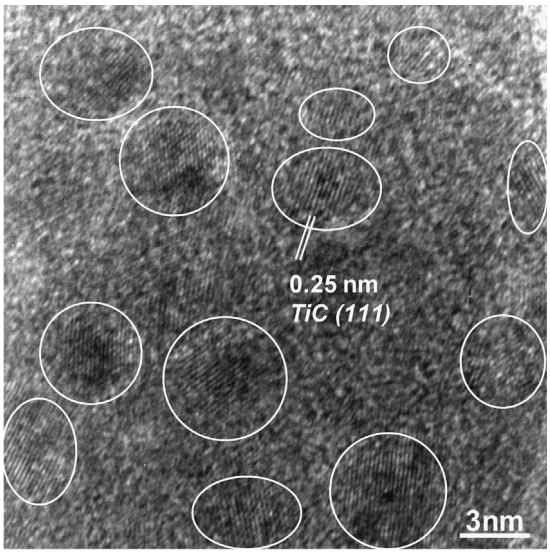

Figure 23.19 Transmission electron microscope image of a TiC/DLC nanocomposite coatings. Randomly oriented nanocrystalline inclusions of TiC (circled) are embedded in amorphous DLC matrix.

in air with 50% relative humidity. This was considerably lower than the friction coefficients of TiN, CrN (0.5–0.6), and TiC (0.3–0.4) films in similar sliding conditions.

The universal applicability of the nanocrystalline/amorphous design concept was proved in the synthesis of such structures using entirely different material systems. Nanocrystalline YSZ was used as a hard nanograin component together with an amorphous Au/YSZ matrix to provide a crystalline/amorphous tribological coating with improved high-temperature lubrication [Voevodin et al., 2001a, 2001b]. The MSPLD process was able to provide (i) size and orientation control of nanocrystalline YSZ grown at near room temperature; (ii) toughness enhancement by embedding 5- to 10-nm crystals of YSZ separated by about 5 nm into an amorphous YSZ/Au matrix, which required about 10 at % Au in the film composition; and (iii) high-temperature lubrication with gold through nucleation of approximately 100-nm-sized gold grains on the coating surface during 500°C sliding tests.

23.6.4 Multifunctional and Adaptive Coatings

Nanocomposite coatings offer a unique opportunity to design and produce adaptive or smart tribological coatings, which have been termed ''chameleon'' for their ability to resist friction and wear by changing surface chemistry and microstructure in response to environment and loading changes [Voevodin and Zabinski, 2000; Voevodin et al., 2002a], much like a chameleon changing its skin color to avoid predators.

Although quite challenging, practical realization of smart coatings is extremely rewarding for tribological pairs subjected to multiple environmental changes, as, for example, in aerospace applications. The first realization of such coating growth with PLD was made using a mixture of oxides and dichalcogenides (PbO/MoS_2, CF_x/WS_2, ZnO/WS_2), which could operate over a broad range of temperatures [Zabinski et al., 1992, 1993, 1996]. Advanced multilayer structures were then designed to combine these composites with buried diffusion barrier layers and achieve surface self-adaptation during repeated temperature cycling. Recently, novel wear-resistant materials were developed that combine nanocrystalline carbides (TiC, WC), oxide-based ceramics (YSZ and AlON), dichalcogenides (MoS_2, WS_2), and amorphous diamond-like carbon (DLC) into nanocomposite structures [Voevodin and Zabinski, 2000; Voevodin et al., 2001a, 2002a].

For example, chameleon coatings made of amorphous DLC matrix with incorporation of nanocrystalline TiC [Voevodin et al., 1997c; Voevodin and Zabinski, 1998], WC [Voevodin et al., 1999a, 1999c], WS_2 [Voevodin et al., 1999b; Voevodin and Zabinski, 2000], and laser-processed MoS_2 reservoirs [Voevodin et al., 1998] have demonstrated an order of magnitude improvement in toughness above that of single-phase carbides while maintaining the same level of hardness, a low friction coefficient in cycling from dry to humid environments, and an extremely long life in both ambient and space environments. The surface chemistry, structure, and mechanical behavior of these nanocomposite materials were shown to *reversibly* change in tribological contact, depending on applied loads and operational environment to maintain low friction and prevent wear.

To achieve reversible adaptation, the following design concepts should be fulfilled and combined with the concepts of tough nanocomposites described above:

1. Solid lubricant reservoirs are introduced as amorphous or poorly crystalline inclusions to minimize reduction in composite hardness and elastic modulus, since crystalline solid lubricants are typically very soft [Voevodin et al., 1999d; Voevodin and Zabinski, 2000].
2. Friction forces and surface reactions with the environment are used to generate a lubricious transfer film or ''skin'' at the tribological contact, which can self-adjust with each environmental change [Voevodin et al., 1999d; Voevodin and Zabinski, 2000]; that is, coating components serve as reservoirs to supply material for the ''tribo-skin,'' where formation of a lubricating film with the required chemistry and structure reduces friction.

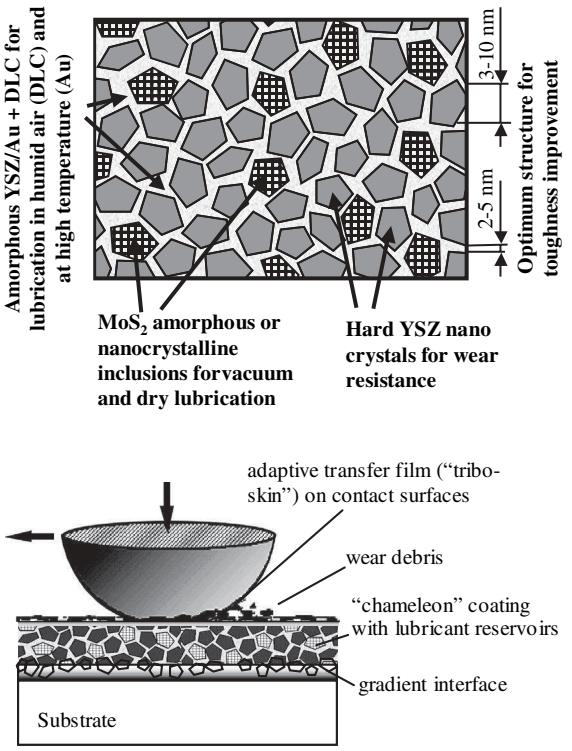

Figure 23.20 Schematic of a YSZ/Au/MoS_2/DLC tribological coating with chameleon-like surface adaptive behavior: (a) composite layer structure and (b) cross section of a coating at the friction contact.

Because they are made of nanosized lubricant inclusions, the reservoirs are always just underneath the rubbing surface. Therefore, the active tribo-skin can adapt immediately to changes in the environment.

Figure 23.20 presents a schematic of the YSZ/Au/MoS_2/DLC coating design structure. Individual phases of the coating are marked together with their tribological function in Figure 23.20a, and coating cross-sectional layout is shown in Figure 23.20b together with the expected formation of an environmentally adaptive transfer film on the friction surfaces. Similar to the previous chameleon coating examples discussed above, an amorphous matrix and a hard nanocrystalline phase (YSZ) were used to optimize mechanical performance and load support. Nanocrystalline and amorphous Au, MoS_2, and DLC were added to achieve chemical and structural adjustment of transfer films formed in friction contacts during dry/humid environment and low/high temperature variations. The coating design in Figure 23.20 was primarily tailored to aerospace applications, but similar design concepts can be applied for chameleon coating development for other applications.

23.7 FUTURE DIRECTIONS

Pulsed laser deposition is an effective tool for producing coatings for many different applications, and the tribological coating category is rapidly growing with the emergence of hybrid deposition techniques and the new nanostructured coatings that they enable. Recently, coating hardness was significantly increased by evolving away from monolithic designs toward those with multiple

components and layers. Now it is realized that the properties of nanostructures can be harnessed to not only provide high hardness but also to improve toughness and control friction. Therefore, present and future R&D will progressively concentrate on nanostructured and multiphase tribological coatings, such as heterostructures and nanocomposites. Following this trend, PLD may soon develop into a mature technology for engineering applications. There are several foreseeable directions of this progress. First, the process configuration will change from that of ''standard'' PLD to fit more closely engineering applications. This includes larger deposition chambers, complex rotation substrate tables, substrate biasing and heating arrangements, reliable process control based on in situ plasma diagnostic technologies, and powerful cost-effective lasers with short wavelengths. Second, PLD will likely be integrated with other deposition techniques to permit growth of unique materials and to allow for better process flexibility, both technologically and economically.

The unique advantage of PLD is that it can be used to synthesize tribological materials, which are not possible or very difficult to produce by other methods. Superhard DLC was the first of such materials, which was followed by a variety of hard coatings, solid lubricants, high-temperature lubricants, fullerene-like structures, functional gradient materials, and multifunctional smart nanocomposites. The list is rapidly expanding and PLD will continue to lead new material discoveries in the field of tribological coatings and interfaces.

REFERENCES

Broitman, E., Hellgren, N., Wanstrand, O., Johansson, M. P., Berlind, T., Sjostrom, H., Sundgren, J.-E., Larsson, M., and Hultman, L. (2001), *Wear* **248**, 55–64.

Bushan, B., and Gupta, B. K. (1991), *Handbook of Tribology: Materials, Coatings, and Surface Treatments*, McGraw-Hill, New York.

Capano, M. A., Voevodin, A. A., Bultman, J. E., and Zabinski, J. S. (1997), *Scripta Mater.* **36**, 1101–1106.

Donley, M. S., and Zabinski, J. S. (1994), in *Pulsed Laser Deposition of Thin Films*, D. B. Chrisey and G. K. Hubler (Eds.), Wiley, New York, pp. 431–454.

Endrino, J. L., Nainaparampil, J. J., and Krzanowski, J. E. (2002), *Surf. Coat. Technol*. **157**, 95–101.

Friedmann, T., Mirkarimi, P. B., Medlin, D. L., McCarty, K. F., Klaus, E. J., Boehme, D. R., Johnsen, H. A., Mills, M. J., Ottesen, D. K., and Barbour, J. C. (1994), *J. Appl. Phys*. **76**, 3088–3101.

Fujimori, S., Kasai, T., and Inamura, T. (1982), *Thin Solid Films* **92**, 71–80.

Geohegan, D. B. (1994), in *Pulsed Laser Deposition of Thin Films*, D. B. Chrisey and G. K. Hubler (Eds.), Wiley, New York, pp. 115–165.

Holmberg, K., and Matthews, A. (1994), *Coatings Tribology: Properties, Techniques, and Applications in Surface Engineering*, Elsevier, Amsterdam.

Hultman, L., Stafstrom, S., Czigany, Z., Neidhardt, J., Hellgren, N., Brunell, I. F., Suenaga, K., and Colliex, C. (2001), *Phys. Rev. Lett*. **87**, 225503-1–225503-4.

Hultman, L., Neidhardt, J., Hellgren, N., Sjostrom, H., and Sundgren, J.-E. (2003), *MRS Bull*. **28**, 194–202.

Jones, J. G., Voevodin, A. A., and Zabinski, J. S. (2001), *Surf. Coat. Technol*. **146/147**, 258–262.

Marquardt, C. L., Williams, R. T., and Nagel, D. J. (1985), *Mater. Res. Soc. Symp. Proc*. **38**, 325–335.

Mitterer, C., Mayrhofer, P. H., Beschliesser, M., Losbichler, P., Warbichler, P., Hofer, F., Gibson, P. N., Gissler, W., Hruby, H., Musil, J., and Vlcek, J. (1999), *Surf. Coat. Technol*. **120/121**, 405–411.

Murray, P. T., and Peeler, D. T. (1993) in *Laser Ablation: Mechanisms and Applications II*, J. C. Miller and D. B. Geohegan (Eds.), AIP Press, New York, pp. 359–364.

Murray, P. T., and Peeler, D. T. (1994), *J. Electr. Mater*. **23**, 855–859.

Neidhardt, J., Czigany, Z., Brunell, I. F., and Hultman, L. (2003), *J. Appl. Phys*. **93**, 3002–3014.

Niu, C., Lu, Y. Z., and Lieber, C. M. (1993), *Science* **261**, 334–337.

Ogale, S. B., Malshe, A. P., and Kanetkar, S. M. (1993), *Mater. Manuf. Process*. **8**, 15–58.

Phani, A. R., Nainaparampil, J. J., and Krzanowski, J. E. (2002), *Mater. Res. Soc. Symp. Proc*. **697**, 409–424.

Radder, M., Sikder, A. K., and Kumar, A. (2002), *Mater. Res. Soc. Symp. Proc*. **697**, 297–303.

Reade, R. P., Church, S. R., and Russo, R. E. (1995), *Rev. Sci. Instrum.* **66**, 3610–3614.

Strong, K. L., and Zabinski, J. S. (2002), *Thin Solid Films* **406**, 174.

Veprek, S. (1999), *J. Vac. Sci. Technol. A* **17**, 2401–2420.

Voevodin, A. A., and Donley, M. S. (1996), *Surf. Coat. Technol.* **82**, 199–213.

Voevodin, A. A., and Zabinski, J. S. (1998), *J. Mater. Sci.* **33**, 319–327.

Voevodin, A. A., and Zabinski, J. S. (2000), *Thin Solid Films* **370**, 223–231.

Voevodin, A. A., and Zabinski, J. S. (2001), *SPIE Proc.* **4157**, 269–274.

Voevodin, A. A., Donley, M. S., Zabinski, J. S., and Bultman, J. E. (1995a), *Surf. Coat. Technol.* **76/77**, 534–539.

Voevodin, A. A., Laube, S. J. P., Walck, S. D., Solomon, J. S., Donley, M. S., and Zabinski, J. S. (1995b), *J. Appl. Phys.* **78**, 4123–4130.

Voevodin, A. A., Capano, M. A., Safriet, A. J., Donley, M. S., and Zabinski, J. S. (1996a), *Appl. Phys. Lett.* **69**, 188–190.

Voevodin, A. A., Walck, S. D., Solomon, J. S., John, P. J., Ingram, D. C., Zabinski, J. S., and Donley, M. S. (1996b), *J. Vac. Sci. Technol. A* **14**, 1927–1932.

Voevodin, A. A., Capano, M. A., Laube, S. J. P., Donley, M. S., and Zabinski, J. S. (1997a), *Thin Solid Films* **298**, 107–115.

Voevodin, A. A., Donley, M. S., and Zabinski, J. S. (1997b), *Surf. Coat. Technol.* **92**, 42–49.

Voevodin, A. A., Prasad, S. V., and Zabinski, J. S. (1997c), *J. Appl. Phys.* **82**, 855–858.

Voevodin, A. A., Walck, S. D., and Zabinski, J. S. (1997d), *Wear* **203/204**, 516–527.

Voevodin, A. A., Bultman, J. E., and Zabinski, J. S. (1998), *Surf. Coat. Technol.* **107**, 12–19.

Voevodin, A. A., O'Neill, J. P., Prasad, S. V., and Zabinski, J. S. (1999a), *J. Vac. Sci. Technol. A* **17**, 986–992.

Voevodin, A. A., O'Neill, J. P., and Zabinski, J. S. (1999b), *Surf. Coat. Technol.* **116–119**, 36–45.

Voevodin, A. A., O'Neill, J. P., and Zabinski, J. S. (1999c), *Thin Solid Films* **342**, 194–200.

Voevodin, A. A., O'Neill, J. P., and Zabinski, J. S. (1999d), *Tribol. Lett.* **6**, 75–78.

Voevodin, A. A., Jones, J. G., and Zabinski, J. S. (2000), *J. Appl. Phys.* **88**, 1088–1096.

Voevodin, A. A., Hu, J. J., Fitz, T. A., and Zabinski, J. S. (2001a), *Surf. Coat. Technol.* **146/147**, 351–356.

Voevodin, A. A., Jones, J. G., Hu, J. J., Fitz, T. A., and Zabinski, J. S. (2001b), *Thin Solid Films* **401**, 187–195.

Voevodin, A. A., Jones, J. G., and Zabinski, J. S. (2001c), *Appl. Phys. Lett.* **78**, 730–732.

Voevodin, A. A., Jones, J. G., and Zabinski, J. S. (2001d), *J. Vac. Sci. Technol. A* **19**, 1320–1324.

Voevodin, A. A., Hu, J. J., Fitz, T. A., and Zabinski, J. S. (2002a), *J. Vac. Sci. Technol. A* **20**, 1434–1444.

Voevodin, A. A., Jones, J. G., Zabinski, J. S., Czigany, Zs., and Hultman, L. (2002b), *J. Appl. Phys.* **92**, 4980–4988.

Voevodin, A. A., Jones, J. G., Zabinski, J. S., and Hultman, L. (2002c), *J. Appl. Phys.* **92**, 724–735.

Wei, Q., and Narayan, J. (2000), *Int. Mater. Rev.* **45**, 133–164.

Wei, Q., Narayan, R. J., Narayan, J., Sankar, J., and Sharma, A. K. (1998), *Mater. Sci. Eng. B* **53**, 262–266.

Wei, Q., Sharma, A. K., Sankar, J., and Narayan, J. (1999a), *Composites* **30B**, 675–684.

Wei, Q., Sharma, A. K., Yamolenko, S., Sankar, J., and Narayan, J. (1999b), *Mater. Res. Soc. Symp. Proc.* **593**, 323–328.

Yang, C.-Y., Babcock, S. E., Goyal, A., Paranthaman, M., List, F. A., Norton, D. P., Kroeger, D. M., and Ichinose, A. (1998), *Physica C* **307**, 87–98.

Zabinski, J. S., Donley, M. S., Dyhouse, V. J., and McDevit, N. T. (1992), *Thin Solid Films* **214**, 156–163.

Zabinski, J. S., Donley, M. S., and McDevit, N. T. (1993), *Wear* **165**, 103–108.

Zabinski, J. S., Prasad, S. V., and McDevit, N. T. (1996), Agard Conference Proceedings, Issue 589, 3-1–3-8.

SECTION 5

CHAPTER 24

Laser Ablation Synthesis of Single-Wall Carbon Nanotubes: The SLS Model

ANDRÉ GORBUNOFF
University of Applied Sciences–Dresden, Dresden, Germany

OLIVER JOST
University of Technology–Dresden, Dresden, Germany

24.1 INTRODUCTION

In sufficiently dense gas atmospheres, the gaseous products of laser ablation can condense before they reach any solid substrate. Among such nanoclustered materials are new forms of carbon discovered in the soot produced by laser ablation under a background gas pressure. This chapter describes the laser ablation synthesis of the most intriguing form of carbon—single-wall carbon nanotubes.

The chemical element carbon has a unique ability to hybridize its outer electron orbitals in three different ways and thus to exist in a number of allotropies with completely different properties. The graphitic forms of carbon consist of subunits of covalently sp^2-bonded atoms organized in a trigonally coordinated network. These graphitic subunits (graphene sheets) are held together by weak van der Waals forces. The natural stress- and defect-free spatial organization of these subunits is a parallel stack with an interplanar separation of 0.335 nm (Fig. 24.1a). This spatial organization of the crystal is responsible for the known softness and lubricating nature of the most common graphitic representative graphite.

It appears, however, that the flat stack is not the only possible form of spatial organization of graphene sheets. In carbon onions and nanotubes, the graphene layers are arranged in unusual concentric and coaxial shells with the intershell separation about that of planar graphite (Fig. 24.1b). The study of Radushkevich and Lukyanovich [1952] is perhaps the earliest published observation of such a tubularly organized carbon phase. They have observed hollow carbon ''particles'' less than 100 nm in diameter and many micrometers long in the soot of iron-catalyzed, thermally decomposed CO. However, the clarification of the structural details of these particles was only possible with more recent advances in the electron microscopy. It is well established now [Dresselhaus et al., 1988] that they consist of coaxially rolled graphene sheets with a maximum length up to millimeters and a diameter in the nanometer range. Although this is typical in biological macromolecules, this tubular structure is rather uncommon for inorganic materials. They can be also synthesized from other

Pulsed Laser Deposition of Thin Films: Applications-Led Growth of Functional Materials
Edited by Robert Eason

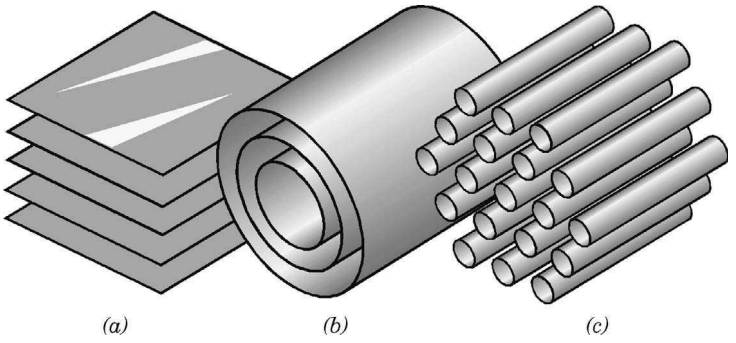

Figure 24.1 Spatial organization of graphene sheets in different graphitic forms of carbon: (a) a graphite crystal, (b) a multiwall nanofiber, and (c) a bundle of single-wall nanotubes.

layered materials such as h-BN, mixed BN/C, BC_3, WS_2, and MoS_2 (see, e.g., Feldmann et al. [1995], Suenaga et al. [1999], and Tremel [1999]).

A detailed description of physical properties and expected applications of carbon nanotubes can be found in a number of reviews and books currently available [Dresselhaus et al., 1996; Yakobson and Smalley, 1997; Ebbesen, 1997; Subramoney, 1998; Saito et al., 1998a; Tanaka et al., 1999; Ajayan, 1999; Tomanek and Enbody, 2002]. The potential applications of nanotubes are mostly related to their small dimensions and outstanding electronic and mechanical properties. One expects they can find use as interconnects, arrays of resistors, quantum electronic devices, ''suspended'' circuitry, artificial muscles in MEMS, low-k dielectric insulators or intercalation for battery applications, field emitters in flat displays, high-Q nanoresonators, reinforced composite ultralight materials, functionalized/customized nanoprobes for scanning probe microscopes, or as a new zeolite-type hydrogen-storage material for fuel-cell electric vehicles and many others. At the same time a broad spread of physical properties of individual nanotubes associated with a statistically distributed number of concentric layers creates complications in their practical implementation.

When the diameter of a single nanotube becomes comparable to the graphite interplanar separation, they cannot be surrounded by the second carbon shell due to purely geometric reasons, and as a result, they cannot form coaxial structures. Instead they stick together into thick honeycomb-packed bundles (Fig. 24.1c). Such single-wall nanotubes (SWNTs, Fig. 24.2) do not have these layer number-related structural variations and their properties are much more predictable. Some selected properties of bundled SWNTs are summarized in Table 24.1.

Since the covalent carbon σ bonds in graphene sheets are among the strongest in nature, the SWNTs have a high inherent structural strength and a correspondingly high phonon thermal conductivity. At the same time, the material is extremely light, making its strength–density ratio 1–2 orders of magnitude higher than that of steel.

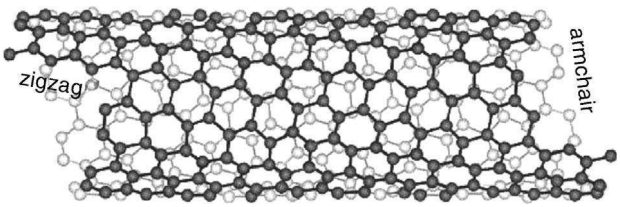

Figure 24.2 Fragment of helical single-wall carbon nanotube with a diameter of 1.05 nm. The wrapping angle determines the helicity of the nanotube.

TABLE 24.1 Selected Properties of Diamond, Graphite, and Bundles of Single-Wall Nanotubes

Physical Property	Diamond	Graphite	SWNT
Lattice structure	Cubic	Hexagonal	Hex. packaged bundles
Bond length, Å	1.54	1.42	1.42
Interlayer spacing, Å	—	3.35	3.38 (10,10 armchair)
Density, g/cm^3	3.52	2.26	1.33 (10,10 armchair)
Thermal conductivity, W/cm K	25	1.29	20
Electrical conductivity	$\sim 10^{-20}$ $(\Omega\ \text{cm})^{-1}$	800 $(\Omega\ \text{cm})^{-1}$ (polycryst.)	$n(12.9\ \text{k}\Omega)^{-1}$ (quantized)
Bandgap, eV	5.5	-0.04 (band overlap)	0 (metallic) $\sim$0.5 (semiconducting)
Elastic modulus, GPa	107	>10 (polycryst.)	1000
Maximum tensile strength, GPa	0.7	2–20 (fiber)	$30 \geq 200$

The untwisted armchair SWNTs (the tubes having an armchair atomic arrangement as viewed in cross section, see Fig. 24.2) always have a metallic-type conductance. They can transmit current densities in excess of 10^9 A/cm^2, which is orders of magnitudes higher than noble metals [Radosavljevic et al., 2001]. The large critical current density can be attributed to the strong covalent bonding of the atoms in the tube with no defect scattering. The majority of helical SWNTs (as sketched in Fig. 24.2) are semiconducting.

The thinnest SWNTs can be fabricated in the zeolite crystal channels and have a diameter, d_{SWNT}, as small as 0.4 nm [Wang et al., 2000]. The thicker the SWNTs, the less mechanically stable they become. According to calculations of Gao et al. [1998], SWNTs with $d_{\text{SWNT}} > 3$ nm should tend to collapse. This is in accordance with observations of Cheung et al. [2002] who have managed to synthesize mechanically very unstable SWNTs with $d_{\text{SWNT}} > 8$ nm.

Single-wall nanotubes were first synthesized by Iijima and Ichihashi [1993] and Bethune et al. [1993] in an arc discharge. To date a number of techniques including arc discharge, laser evaporation, solar furnace, chemical vapor deposition, and high-pressure CO disproportionation have been demonstrated for synthesizing macroscopic quantities of SWNTs [Ebbesen, 1997; Journet and Bernier, 1998; Laplaze et al., 1998; Terrones et al., 1999; Nikolaev et al., 1999] and one can purchase these commercially. A distinguishing feature of the SWNT synthesis in all these techniques is the necessity of the addition of 1–50 at % of an iron-group metal catalyst (usually Fe, Co, Ni, or their mixtures) into the initial carbon material source. Binary catalysts have been proven to function better than elementary ones [Guo et al., 1995; Takizawa et al., 2000; Jost et al., 2004]. SWNTs appear to grow radially from these catalyst particles closed with hemispherical domes [Subramoney et al., 1993; Zhou et al., 1994; Saito, 1995; Saito et al., 1995].

Despite the enormous progress in synthesis, understanding of the catalytic growth of SWNTs currently lags behind. To a certain extent this is a consequence of the fact that the abundance and properties of SWNTs are sensitive to practically all the process variables, including the composition of the source material, synthesis parameters, and methods of SWNT collection and purification.

It is widely accepted that the SWNT synthesis is a multistep process that comprises atomization of the starting material, nucleation, and growth stages. In continuous techniques like arc discharge, solar furnace, continuous-wave, or long-pulse laser evaporation, as well as CO disproportionation, the SWNT growth conditions are closely connected with the carbon source material atomization and cannot easily be controlled independently. A better management of the growth conditions is achieved using a laser-furnace method first implemented by Guo et al. [1995]. In this technique, a graphite target containing a metal catalyst is ablated by nanosecond duration laser pulses, thereby temporally separating the target atomization and the SWNT formation stages.

The influence of the main operator-controlled variables (such as the environmental conditions, the target composition, the laser power, the process temperature, and geometry), perhaps up to a

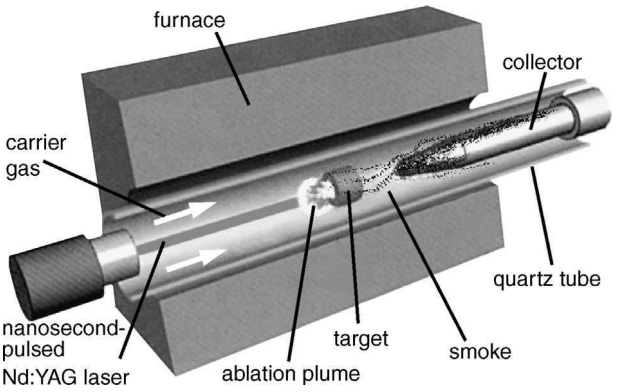

Figure 24.3 Typical laser-furnace setup for the laser ablation synthesis of SWNTs. The sketch is adapted from Yakobson and Smalley [1997].

dozen parameters in total, on the product output even in the laser-furnace technique, still remains contradictory. In this chapter we review the known experimental findings about the laser synthesis of SWNTs, describing them on the basis of a unique solid–liquid–solid growth mechanism and summarize them in a temporal scenario of the first one second of the SWNT life.

24.2 LASER-FURNACE TECHNIQUE

24.2.1 Typical Experimental Setup

Figure 24.3 presents a typical setup for the laser ablation synthesis of SWNTs. A solid target pressed from intimately mixed powders of pure charcoal and metal catalyst is positioned in a high-temperature tube furnace. The target is ablated by pulsed Q-switched laser radiation, in a streaming chemically inactive carrier gas (typically Ar or N_2) at a pressure somewhat below 1 atm. The ablation products in the form of smoke are transported by the carrier gas and deposited onto a water-cooled collector positioned downstream from the target. The soot can then be washed off the collector using water. Typical experimental conditions are summarized in Table 24.2.

TABLE 24.2 Typical Synthesis Conditions of SWNTs in Laser-Furnace Technique

Furnace tube diameter	25–50 mm
Pressure P_0	66 kPa
Carrier gas flow velocity V_0	1 cm/s
Furnace temperature T_0	1200°C
Laser wavelength	532 nm, 1064 nm
Laser pulse frequency	10–30 Hz
Laser pulse length τ	10 ns
Laser fluence Φ	1.5 J/cm^2
Target metal content	1 at % Co + 1 at % Ni
Mean bundle diameter	20 nm
Estimated nanotube yield	50%

[Guo et al., 1995; Bower et al., 1998; Bandow et al., 1998; Rinzler et al., 1998; Yudasaka et al., 1999c, 2002; Gorbunov et al., 1999; Puretzky et al., 2000, 2002; Jost et al., 2002, 2004].

24.2.2 Characterization of SWNTs-Containing Soot

24.2.2.1 Microscopic Characterization

Scanning electron microscopy (SEM) and high-resolution transmission electron microscopy (HRTEM) are the most important microscopic methods used in the majority of experimental studies. A typical appearance of the SWNTs containing soot is presented in Figure 24.4. It consists of SWNTs hexagonally packed into bundles of up to 20 nm thickness and many micrometers long, apparently extruding from round particles of metal catalyst 2–15 nm in diameter. These particles are partly encapsulated by a graphitic cage. Gorbunov et al. [2002b] have postulated that this graphitic cage builds up through massive precipitation of dissolved carbon upon solidification of metal–carbon melt when quenching the smoke on the collector. When this is the case, the initial carbon concentration in the molten particle should be as high as 50 at %. Besides the SWNT bundles, the soot contains a pronounced amount of amorphous carbon. Some amount of fullerenes can also be traced in the reaction products. As will be shown in Section 24.3, both species play an important role

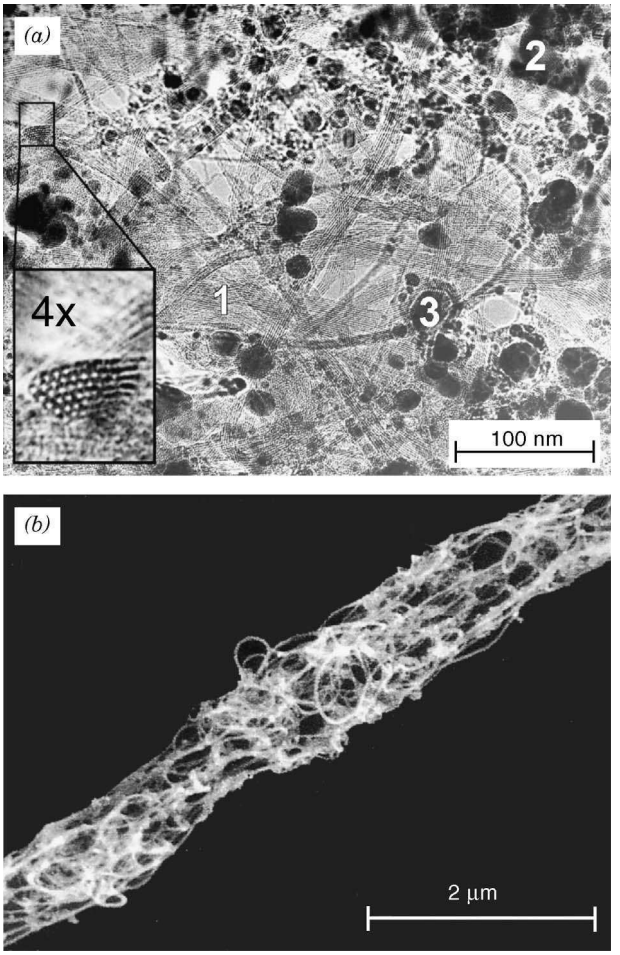

Figure 24.4 (a) High-resolution TEM image of the soot synthesized under typical synthesis conditions: (1) bundles of SWNTs, (2) amorphous carbon, and (3) round metallic particles. The 4× enlarged insert demonstrates a hexagonal packing of nanotubes in a bundle. (b), SEM image of a rope of bundled SWNTs.

in the SWNT synthesis as a metastable carbon source material and presumably nucleation agents. No other forms of carbon are usually found, and this is typical for most physical SWNT synthesis techniques.

Despite the direct imaging, all the microscopic methods suffer from the lack of overall averaging. As a matter of fact, the soot is very inhomogeneous even within the same sample and one cannot extend any locally measured property to all of the material synthesized. Despite this principal difficulty, HRTEM pictures are widely used for a subjective estimation of the *absolute* SWNT abundance in the unrefined soot. By our own conservative estimate, the absolute abundance of SWNTs in the soot derived from the HRTEM images never exceeds 50%, although some groups report it to be above 70% [Thess et al., 1996; Bower et al., 1998; Rinzler et al., 1998].

24.2.2.2 SWNT Abundance and Diameters

Due to their resonant nature, Raman spectroscopy and optical absorption spectroscopy hold a central position among spectroscopic methods for SWNT characterization. These methods provide sample-averaged quantitative information on the structural and electronic properties of SWNTs including the *relative* abundance Y and diameter distribution of SWNTs in the soot.

Along with G- and D-bands, which are characteristic for all polycrystalline graphitic materials, the Raman spectrum of SWNTs contains a strong low-frequency band of radial breathing mode vibrations, which is specific to the tubular geometry and provides a good indication of the nanotube abundance in the soot [Rao et al., 1997]. The position of this band is controlled by the circumference of the nanotubes and to a good approximation is inversely proportional to $d_{\mathrm{SWNT}} : \omega[\mathrm{cm}^{-1}] = 224/d_{\mathrm{SWNT}}[\mathrm{nm}]$ [Saito et al., 1998b].

The characterization of SWNTs by optical absorption spectroscopy provides comparable data on d_{SWNT} [Jost et al., 1999a, 2002; Liu et al., 2002] and is based on the existence of one-dimensional van Hove singularities in their electronic density of states (DOS) as first proposed by Kataura et al. [1999]. Within the simple tight-binding model, the gap between these sharp DOS spikes is inversely proportional to d_{SWNT}:

$$E_g = \frac{2\gamma a_{\mathrm{C-C}}}{d_{\mathrm{SWNT}}}$$

where γ is the overlap integral between the next pπ-orbitals, and $a_{\mathrm{C-C}} \approx 1.42$ Å is the carbon bond length. For graphite $\gamma = 3.16$ eV. In SWNTs γ is usually smaller and is controlled by both d_{SWNT} and specific tube–tube interactions in SWNT bundles.

Early investigations of Y and d_{SWNT} in the laser-furnace technique have been reviewed by Journet and Bernier [1998]. More recent studies of the impact of most operator-controlled process parameters on these two basic properties of SWNTs are summarized in Table 24.3. The degree of influence of these parameters is roughly evaluated on a three-score system. Parameters having no observable influence on the SWNT formation are indicated by ($-$). An observable but not decisive impact is labeled with a ($\pm$) symbol. The process parameters, which have a pronounced effect on Y and d_{SWNT}, are assigned a ($+$) symbol, and when not properly chosen, the latter can completely inhibit SWNT formation.

As seen in Table 24.3, almost all synthesis parameters influence to a variable degree the SWNT abundance Y in the soot. By comparison, only the furnace temperature T_0, carrier gas type, pressure P_0, and the catalyst relative composition (not the absolute percentage!) can influence their mean diameter.

The furnace temperature T_0 belongs to the most critical process parameters. No SWNT formation was observed at T_0 below some minimal temperature (about 800°C for a graphite target) and above the equilibrium eutectic temperature of the metal–carbon mixture. The maximum Y lies near the upper limit of this interval (Fig. 24.5). Within the allowed temperature window and a given catalyst, a monotonic d_{SWNT} increase with T_0 is observed [Bandow et al., 1998; Kataura et al., 2000]. Under the typical synthesis conditions listed in Table 24.2 $d_{\mathrm{SWNT}} \approx 1.2$ nm. Thin SWNTs with $d_{\mathrm{SWNT}} = 0.83$ nm were synthesized by Kataura et al. [2000] by using a low-melting-point RhPd

TABLE 24.3 Influence of Various Process Parameters on SWNT Abundance and Diameter[a]

Process Parameter	Abundance			Diameter		
	Dependence			Dependence		
	Degree	Type	References	Degree	Type	References
Target carbon source	±		Zhang and Iijima, 1999; Zhang et al., 2001	?		
Target morphology	±		Yudasaka et al., 2000	?		
Catalyst quantity	+	Peaked	Jost et al., 1999b	−		Jost et al., 1999b
Catalyst type	+	Complex	Guo et al., 1995	+	Complex	Kataura et al., 1998, 2000; Jost et al., 2004
Catalyst mixtures	+	Peaked	Guo et al., 1995; Yudasaka et al., 1999b	+	Logarithmic	Jost et al., 2004
Furnace temperature	+	Peaked	Jost et al., 1999a, 2002; Kataura et al., 2000	+	Linear	Bandow et al., 1998; Kataura, 2000; Jost et al., 2004
Type of gas	+	Complex	Jost et al., 2002; Nishide et al., 2003	+	Complex	Jost et al., 2004
Gas pressure	+	Peaked	Munoz et al., 2000; Jost et al., 2002	+	Logarithmic	Saito et al., 2000; Jost et al., 2004
Gas flow velocity	+	Peaked	Gorbunov et al., 1999; Jost et al., 2001a	−*		Sen et al., 2000
Number of laser pulses	±		Yudasaka et al., 1999c	?		
Plume confinement	±		Rinzler et al., 1998	±*		Rinzler et al., 1998
Laser pulse rate	±		Yudasaka et al., 1999a	−*		Jost et al., 2001b
Combined laser beams	±		Thess et al., 1996	−*		Bower et al., 1998
Laser pulse duration	±		Eklund et al., 2002	−*		Eklund et al., 2002
Laser beam wavelength	±		Braidy et al., 2002b	−*		Braidy et al., 2002b
Laser fluence	+	Peaked	Gorbunov et al., 1999; Braidy et al., 2002a	±*		Dillon et al., 2000; Braidy et al., 2002a

[a]The degree of the influence is marked according to the scheme: (+) pronounced, (±) observable, (−) negligible or none, (?) unknown, (*) although reported, cannot be unambiguously attributed.

catalyst. With a more refractory RhPt catalyst, they observed an effective SWNT formation up to 1450°C and d_{SWNT} up to 1.35 nm.

Other parameters that pronouncedly influence the SWNT synthesis are the carrier gas pressure P_0 and velocity V_0 and the laser fluence Φ (Fig. 24.5). SWNT formation is only observable at $P_0 \geq 8$ kPa, although the amount of ablated target material is practically independent of P_0. With an increase in P_0, Y rises and reaches a broad maximum at a P_0 value that depends on the carrier gas type. Jost et al. [2002] have established that the synthesis conditions, which provide the maximum Y, correspond to an optimal gas kinetic coefficient

$$D = \frac{\bar{c}\lambda}{3} \propto \frac{T_0^{3/2}}{P_0 \sigma \sqrt{m}}$$

of 1.5–3 $cm^2\ s^{-1}$, where $\bar{c}$, λ, σ, and m are the root-mean-square thermal velocity, mean-free path, gas-dynamic cross section, and mass of the carrier gas molecules. This optimal gas kinetic coefficient appears to be the same for all gases studied (He, Ar, N_2).

The optimum laser fluence Φ lies rather close to the laser ablation threshold of graphite, which is $\sim$1 J/cm^2. However, the overall amount of collected soot decreases drastically at low laser fluences.

The carrier gas flow velocity V_0 determines the drift time t_{drift} of the ablation products suspended in the carrier gas through the hot zone of the furnace before they are quenched at the cold collector. Surprisingly, it also has a profound impact on Y (Fig. 24.5). This dependence has brought Gorbunov et al. [1999] to the conclusion that SWNTs nucleate at an early stage of the synthesis process and grow the whole way between the ablation and quenching sites of the reactor.

24.3 SOLID–LIQUID–SOLID SWNT FORMATION MODEL

The observed experimental dependencies reflect a complex interaction of a number of competing processes, which makes theoretical consideration of the background mechanisms of SWNT formation especially complicated and restricts many potential applications of SWNTs. A number of

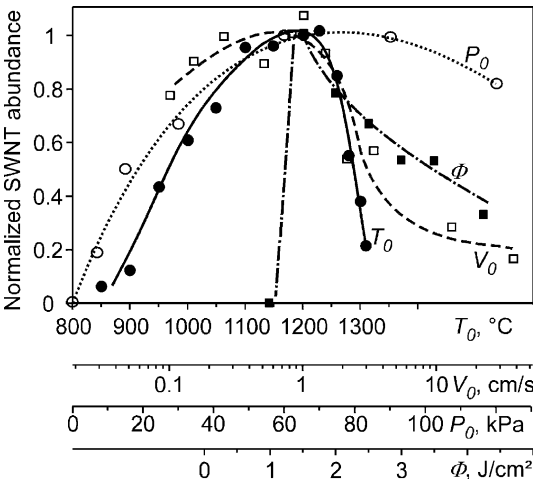

Figure 24.5 Influence of the furnace temperature T_0 (solid circles, solid line), the carrier gas flow velocity V_0 (open squares, broken line) and pressure P_0 (open circles, dotted line), and the laser fluence Φ (solid squares, dash-dot line) on the relative SWNT abundance in the laser evaporated soot (after Gorbunov et al. [1999]). Each curve represents the effect of variation of one parameter with all other specified in Table 24.2 being constant.

proposals have been put forward to explain why the precipitating graphitically coordinated carbon atoms prefer to form tiny tubes instead of flat stacked sheets as in conventional graphite. In the following section we concentrate on the solid–liquid–solid model first proposed by Gorbunov et al. [2001, 2002a, 2002b], which traces the SWNT formation from starting materials to the finished product, provides a self-consistent interpretation of the majority of the experimental dependencies, giving answers to the following key questions:

- What carbon phase is *immediately* converted in SWNTs?
- How does the catalyst metal catalyze the SWNT synthesis?
- What forces SWNTs to nucleate?
- What is the driving force for the elongation of SWNTs?

24.3.1 Condensed-State Process

Immediately after the discovery of SWNTs the belief was that their growth occurs solely in a *vapor phase* by adding new carbon atoms directly onto the *open edge* of the growing tube. This point of view has been criticized by Gorbunov et al. [1999], who argued that SWNTs growth starts initially some relatively long time *after the condensation* of the parent carbon vapor cloud. They have established a relationship that connects the whole nanotube growth time t_{SWNT} with other characteristic time scales of the ablation process in the background gas:

$$\tau \ll t_P < t_{\mathrm{cond}} < t_T \ll t_{\mathrm{drift}} \approx t_{\mathrm{SWNT}} \tag{24.1}$$

Here $\tau \approx 10\,\mathrm{ns}$ is the duration of the laser pulse.

$t_P \approx 1\,\mu\mathrm{s}$ is the characteristic time of the ''fireball'' formation. Gorbunoff [2002] has estimated this time by adapting the problem of a point explosion in the atmosphere [Sedov 1967] to the conditions of the laser-furnace SWNT synthesis.

$t_{\mathrm{cond}} < 2\,\mathrm{ms}$ is the time scale of condensation of the ablation products, which has been established in a number of time-resolved studies of the condensation of carbon from laser-ablated targets in gas atmospheres [Kokai et al., 1999, 2000; Kawashima et al., 1999; Arepalli et al., 2000; Scott et al., 2001]. Puretzky et al. [2000] have found that the disappearance of C_2 and C_3 bands in the ablation plume (which corresponds to the aggregation of C) takes place at $t_{\mathrm{cond}} \sim 200\,\mu\mathrm{s}$, whereas the clustering time of the catalyst metal is an order of magnitude longer. On the contrary, according to Kokai et al. [2000], the single Co atom radiation disappears at a time scale between 1 and $10\,\mu\mathrm{s}$, whereas the decay of C_2 lasts $100\,\mu\mathrm{s}$.

t_T is the characteristic time for the thermal equalization of the fireball with the background ambient. The temporal behavior of the thermal emission of carbon species in the decaying pulsed laser ablation products has been studied experimentally by Arepalli et al. [2000] and Ishigaki et al. [2000]. They provide t_T in the range between $20\,\mu\mathrm{s}$ and several milliseconds. Gorbunoff [2002] has provided an upper limit of $t_T < 20\,\mathrm{ms}$ by considering the time needed for a thermal wave to penetrate the hot carbon vapor fireball.

t_{drift} is the drift time of the reaction products through the hot zone of the furnace. At $V_0 = 1\,\mathrm{cm/s}$ it is of the order of few seconds [Gorbunov et al., 1999; Kokai et al., 1999; Sen et al., 2000; Puretzky et al., 2000, 2002].

It follows from the relationship (24.1) that the SWNT synthesis is a completely *condensed-state* transformation of one *solid* form of carbon into another. It is now widely accepted that SWNTs lengthen with a closed end, while carbon atoms are supplied through the precipitation of carbon species to the ''root'' of the nanotube where it is anchored to the metal catalyst particle. This *root*

growth mechanism has been known since the pioneering works of Baker et al. [1972], Oberlin et al. [1976], and Tibbetts [1984] on chemical vapor deposition (CVD) grown tubular carbon fibers. In these early works the precipitating carbon atoms originated as a result of catalytic decomposition of hydrocarbons on the surface of the catalyst particles. In contrast, in the laser-furnace method, the effect of the gaseous carbon phase during the SWNT growth can be neglected. This inference has been supported by direct observations of elongation of SWNT ''seeds'' after postannealing of the soot by Geohegan et al. [2001] and Gorbunov et al. [2001, 2002a, 2002b]. We now need to find out which carbon phase is converted in SWNTs in this case.

As mentioned in Section 24.1, thin SWNTs cannot be surrounded by a second carbon shell due to their small diameter. This restriction does not alter, however, the graphitic nature of individual nanotubes. Consequently, SWNT bundles can be considered as crystals with a unique spatial organization of the *tubular graphitic carbon phase* (Fig. 24.1c). Gorbunov et al. [1999, 2001, 2002a, 2002b] have proposed and justified a hypothesis that the SWNT synthesis is a kind of catalytic graphitization of a nongraphitic phase, a reaction that is in many respects similar to the high-pressure catalytic synthesis of diamond. The fact that counts in favor of the hypothesis is that the same transition metal catalysts are most effective in both SWNT and diamond synthesis, as well as in catalytic carbonization of hydrocarbons.

The driving force behind the catalytic graphitization is a higher chemical potential of the initial carbon phase and consequently its higher solubility in molten metal catalysts as compared to the ordered graphite. The catalyst metal thus plays a role of the ''atomizing'' agent, which dissolves the nongraphitic carbon phase and transports carbon atoms from the dissolution to the precipitation sites by bulk diffusion. Since there are no other carbon species available in sufficient quantities (especially no gaseous carbon species), only the amorphous carbon condensed during the time t_{cond} has an increased chemical potential with respect to the more stable graphitic phase and can serve as an immediate source material for the growing SWNTs.

24.3.2 Nucleation of SWNTs

In the root growth mode, the diameter of the tubes is determined by the size of the initial nucleus and remains constant along the whole tube. Dai et al. [1996] and Kataura et al. [2000] have proposed that the partly dissolved fullerene caps can serve as master precursors for the growing nanotubes. Indeed, there exists a body of evidence of a close relationship between fullerene and SWNT formation in the laser-furnace technique. Both processes have similar pressure dependence [Yudasaka et al, 1998], temperature limits [Ishigaki et al., 2000], and activation energies [Kasuya et al., 1999; Jost et al., 2002]. A considerable reduction of the lower temperature limit to 400°C observed by Zhang and Iijima [1999], who have used fullerene materials instead of the usual graphite in the target material, counts also in favor of the fullerene nucleation hypothesis. The decomposition of fullerenes on an Ni surface has been observed by Pedio et al. [1999] at a temperature as low as 420°C.

Alternatively, Kanzow and Ding [1999] have suggested that the SWNT nucleation takes place through some molecular oscillations of the precipitated graphitic monolayer on the surface of molten supersaturated metal–carbon droplets. In order to explain the existence of the molten catalyst particles at a low synthesis temperature, they have assumed that the particles' temperature rises above the equilibrium eutectic value due to a release of heat during the catalytic decomposition of carbon-containing gas molecules. Krivoruchko et al. [1993] have demonstrated, however, that this heating effect is negligibly small in the gross energy balance and cannot explain the low-temperature catalyst particle melting.

An alternative mechanism to root growth nucleation has been proposed by Louchev and Hester [2003]. In their ''nanosheet-nanoring'' mechanism, the SWNT nucleus is formed through folding of a graphene nanosheet around the catalytic nanoparticle. In this case only SWNTs with a diameter equal to or larger than the catalytic particles can form. Such SWNTs with a rather large diameter of

3–8 nm have been synthesized by Zhang et al. [2002] and Cheung et al. [2002] by CVD from specially prepared monosize catalyst nanoparticles. However, such large-diameter SWNTs have never been observed in the unprocessed soot in the laser-furnace technique.

An original zipping mechanism of Rotkin and Gogotsi [2002] is based on the experimentally observed reconstruction of the graphite crystal edge through the ''lip-lip'' bond formation between the next graphene sheets. According to their simulations, the pop-up of a wider sleeve and its collapse into two thinner SWNTs with an optimum diameter of 1.4–2 nm may be a way of releasing the additional strain energy associated with these special types of graphite crystal edge reconstruction.

It must be mentioned, however, that mechanisms involving any graphitic structures as precursors for SWNT formation imply a considerable amount of crystalline graphite that should be observable in the SWNT soot. Since this is not the case in the majority of the SWNT experiments (Fig. 24.4a), these mechanisms seem to be less likely.

Irrespective of the exact formation mechanism, once formed, a SWNT nucleus has to be viable. Following the approach of Kuznetsov et al. [2001], Gorbunoff [2002] has estimated the work of the formation of a hollow hemispherical nucleus of N_{nucl} carbon atoms with a diameter d_{nucl} on the surface of an elementary nickel catalyst (Fig. 24.6). This work can be presented as a sum by

$$U_{\text{nucl}} = -\Delta G + U_{\text{edge}} + U_{\text{surf}} + U_{\text{sp}} \tag{24.2}$$

where $\Delta G \approx N_{\text{nucl}} k_B T_0 \ln(C_{aC}/C_G)$ is the free-energy difference of N_{nucl} carbon atoms in the amorphous and graphitic phases, k_B is the Boltzmann constant, C_{aC} and C_G are the atomic solubilities of amorphous carbon and crystalline graphite in the catalytic metal under the synthesis conditions. $U_{\text{edge}} = \pi d_{\text{nucl}} \varepsilon$ is the energy of the edge metal–carbon bonds. According to Kuznetsov et al. [2001], the linear energy density of these bonds $\varepsilon \approx 12\text{eV/nm}$. $U_{\text{surf}} = \pi d_{\text{nucl}}^2 \sigma_{\text{nucl}}$ is the work of formation of inside and outside surfaces of a hemispherical nucleus, where the surface energy $\sigma_{\text{nucl}} \approx \sigma$ (graphite) $\approx 0.08\,\text{J/m}^2$. This term is negligibly small as compared to ΔG and U_{edge}. $U_{\text{sp}} \approx 6E_5$ is the term arising due to the incorporation of six pentagons with an excess energy E_5 in the graphene sheet to form a hemisphere. This term is independent of d_{nucl}. The diameter of the critical nucleus d_{nucl}^* can be obtained by setting $dU_{\text{nucl}}/dd_{\text{nucl}}^* = 0$:

$$d_{\text{nucl}}^* = \frac{2\varepsilon}{ak_B T \ln(C_{aC}/C_G) - 4\sigma_{\text{nucl}}} \tag{24.3}$$

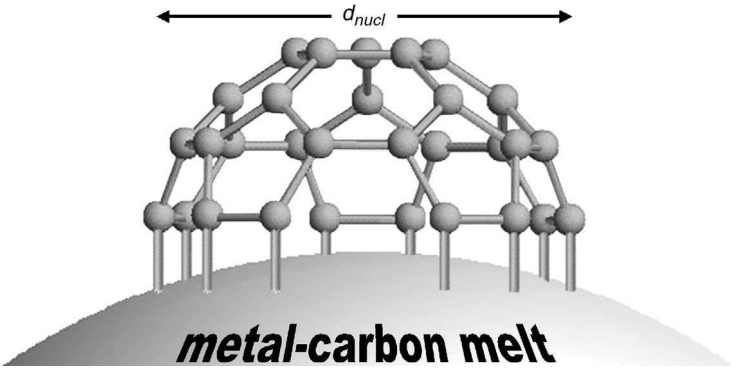

Figure 24.6 A SWNT nucleus with a diameter d_{nucl} on the surface of a larger catalytic particle.

The equilibrium solubility of carbon in liquid nickel from a graphitic source at the equilibrium eutectic point $C_G = 8-10$ at % and its alteration with the particle size (the Gibbs–Thompson effect; see Section 24.3.3) cannot be considerable. On the contrary, following Gorbunov et al. [2001, 2002a, 2002b], C_{aC} can be as high as 50 at % at $T_0 = 800°C$. It means that the supersaturation of carbon in the nanoparticles C_{aC}/C_G under this temperature can be as high as 6, which yields a reasonable $d^*_{\text{nucl}} = 1\,\text{nm} \approx d_{\text{SWNT}}$.

An increase in the synthesis temperature should be accompanied by a weakening of the driving force of the amorphous carbon–graphite transformation due to the diminution of the free-energy difference of amorphous and graphitic carbon phases. As a result, the supersaturation C_{aC}/C_G will decrease and d^*_{nucl} grows in accordance with the experimental observations [Bandow et al., 1998; Kataura et. al., 2000]. Fedorov et al. [1978] have calculated $C_{aC}/C_G \approx 1.2$ at T_{eut}, which corresponds to a critical nucleus with $d^*_{\text{nucl}} > 10\,\text{nm}$, which is unrealistically large. The critical nucleus enlargement is, therefore, the main reason why the abundance of SWNTs in the soot decreases as the synthesis temperature approaches T_{eut}.

24.3.3 Nonequilibrium Melting of Catalyst Particles

The equilibrium binary alloy phase diagrams of carbon and metals, which are catalytically active in the SWNT synthesis, consist of simple eutectics and a very limited solubility of these metals in the graphitic carbon phase. The synthesis of SWNTs is typically carried out at a synthesis temperature T below the eutectic point T_{eut}. Moreover, the abundance of the SWNTs in the soot diminishes as T reaches T_{eut} (Fig. 24.5). At first glance one would infer that the melting of the catalyst particles is incompatible with the SWNT formation. It turns out, however, that exactly the opposite is the case.

First, Puretzky et al. [2002] have experimentally established the growth rates of SWNTs as between 0.6 and 5.1 μm/s depending on the furnace temperature. The SWNT growth rate in the arc discharge method is also ≈ 1 μm/s [Saito et al., 1995]. This growth rate of SWNTs exceeds the growth rate of carbon nanofibers catalyzed by solid metals by at least one order of magnitude [Baker et al., 1972, 1973].

Second, according to Rodriguez [1993], Zhou et al. [1994], and Khassin et al. [1998], the solid catalyst metal should completely lose any catalytic activity due to the formation of a thick carbonaceous overlayer at a synthesis temperature $T_0 \geq 800°C$.

Gorbunov et al. [2001, 2002b] have presented experimental evidence that the melting of the catalyst particles *always* accompanies the SWNT formation, even at $T_0 < T_{\text{eut}}$. The typical increase of 1–2 orders of magnitude in the diffusion coefficient upon melting provides an immediate explanation of the enhanced SWNT growth rate as compared to that of the multiwall NTs and other carbon nanofilament structures catalyzed by solid catalysts.

The finding of Gorbunov et al. [2001, 2002b] can be interpreted within the framework of the dependence of the liquefaction temperature T_l on the radius r of the catalytic particle (the Gibbs–Thompson effect) in contact with graphitic and amorphous carbon phases. For a binary alloy of constant composition, this temperature equals the equilibrium eutectic temperature T_{eut} corrected for the effects of surface energy and capillary pressure. To a first approximation,

$$T_l(r) = T_{\text{eut}}\left(1 + 3\frac{\Delta\sigma\, v_s}{\Omega r} + 2\frac{\sigma_s\, \Delta v}{\Omega r}\right) \tag{24.4}$$

where $\Delta\sigma = \sigma_l - \sigma_s$ and $\Delta v = v_l - v_s$ are the differences in the interface energy and specific volume of liquid and solid phases of the particle material in contact with a specific carbon phase, Ω is the heat of fusion, and T_{eut} is the eutectic temperature of an infinitely large piece of the material, which is slightly dependent on the nature of the carbon phase in contact with the metal.

Since the thermophysical characteristics of the metal–carbon solutions are not accurately known, Gorbunoff [2002] has proposed modeling of the system by using the thermophysical properties of nickel with the surface tension of the melt as a parameter. As the solubility of carbon in solid metals under consideration is small, its influence on the thermophysical properties of the metal–carbon alloy can be neglected to a first approximation, and $\sigma_s \approx \sigma_s(\text{Ni}) = 2.1\,\text{J/m}^2$. On the other hand, the solubility of carbon in a metallic melt at the eutectic point is higher and can vary from 8 at % in the case of an equilibrium metal–graphite interface to as high as 50 at % under the SWNT synthesis conditions (see Section 24.2.2.1). Following Gorbunoff [2002], the influence of this dissolved carbon can be accounted for by assuming that σ_l lies somewhere between $\sigma_l(\text{Ni}) = 1.8\,\text{J/m}^2$ and $\sigma(\text{graphite}) = 0.08\,\text{J/m}^2$. The former σ_l value with $T_{\text{eut}} = T_{\text{eut}}$ (Ni–graphite) $= 1327°\text{C}$ models the Ni–graphitic phase carbon precipitation site, whereas the latter σ_l value with $T_{\text{eut}} = T_{\text{eut}}$ (Ni–amorphous carbon) $= 1294°\text{C}$ [Fedorov et al., 1978] models the Ni–amorphous carbon dissolution site of the catalyst particle.

The $T_l(r)$ dependencies were calculated with Eq. (24.4) by using the specified values and are presented in Figure 24.7. As expected, the $T_l(r)$ dependence for the Ni–graphitic phase carbon (the Ni–gC curve) precipitation site is only slightly dependent on the catalytic particle radius. On the other hand, the reduction of the liquefaction temperature for the Ni–amorphous carbon interface (the Ni–aC curve) becomes very pronounced at $r < 10\,\text{nm}$, which is a typical catalyst particle size in the SWNT-containing soot. This means, therefore, there is a high probability of liquefaction of a nanosize metal particle once it comes in contact with the amorphous carbon phase which has condensed at early stages of the ablation cloud evolution. At the same time both the $T_l(r)$ curves in Figure 24.7 represent the absolute limits for the existence of the solid (below the Ni–gC curve) and liquid (above the Ni–aC curve) metastable metal–carbon alloys.

In the region between these limiting curves in Figure 24.7, the catalytic nanoparticle in contact with amorphous carbon is molten and supersaturated with respect to a more thermodynamically favorable graphitic phase. It is the region of a high driving force of the catalytic graphitization. Which one of the possible graphitic phases sketched in Figure 24.1 will form in the course of the catalytic graphitization will depend on d_{nucl} and on the degree of wetting of the precipitating graphitic phase by the catalyst material.

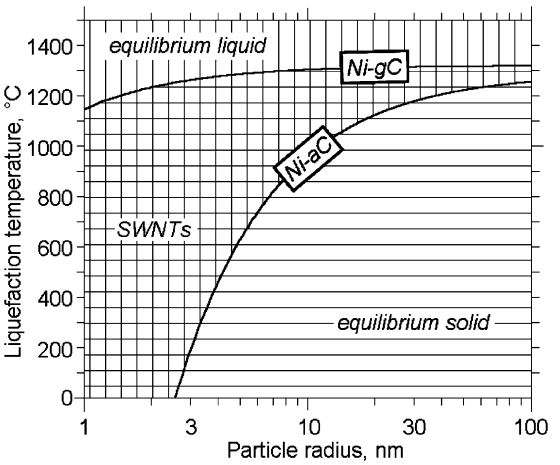

Figure 24.7 Liquefaction temperature T_l of nickel–carbon alloy as a function of the catalyst particle radius calculated from Eq. (24.4). The Ni–gC curve: $\sigma_l = \sigma_l$ (Ni) and $T_{\text{eut}} = T_{\text{eut}}$(Ni−graphite). The Ni–aC curve: $\sigma_l \approx \sigma$ (graphite) and $T_{\text{eut}} = T_{\text{eut}}$(Ni–amorphous carbon). Crosshatched is the region of supersaturated liquid solutions with a high driving force for the SWNT precipitation.

24.3.4 Wetting Factor

Within the framework of the solid–liquid–solid (SLS) model of Gorbunov et al. [2001, 2002a, 2002b], the main reason for the radial SWNT growth (as opposed to the concentric graphitic cage) is the alteration of the character of the wetting interaction between a precipitating graphitic phase and the surface of the catalytic nanoparticle upon its liquefaction.

Indeed, the degree of wetting of graphite by the catalyst material is known to play a determining role in the crystalline perfection of carbon tubular nanostructures [Rodriguez, 1993]. *Solid* catalytic metals of the iron group undergo a strong wetting (even spreading) interaction with graphite surfaces at elevated temperatures. As a result, the precipitating graphene layers tend to cover any suitable face of the solid metal catalyst particle and to form highly ordered graphitelike overlayers. Consequently, onionlike graphite particles and graphitic nanofibers with different morphologies—tubular, herringbone, or even stacklike—can be synthesized depending on the crystallography of the solid catalyst particle [Oberlin et al., 1976; Tibbetts, 1984; Baker et al., 1997].

The interaction of *liquid* metals with graphite is more complicated. The experiments of Naidich [1981] on the wettability of solid graphite by melts of iron group metals have revealed a pronounced dependence of the contact angle on the carbon content in the melt. Pure metal melts exhibit an intensive reactive spreading along the graphite surface, simultaneously dissolving it. However, the higher the carbon content in the melt, the poorer it wets the graphite surface. At the solubility limit (i.e., the saturated metal–carbon solution corresponding to the given experimental temperature), the metal–carbon melt does not wet graphite at all and the contact angle between both materials approaches 90°.

As applied to the SWNT synthesis, this experimental finding leads to the inference that graphene layers precipitating from the supersaturated metal–carbon melt will tend to reduce the contact between its basal surface and the melt as much as possible. A way to do so is to form graphitic structures oriented perpendicular to the ground catalytic surface. By taking into account the extra energy associated with the dangling bonds at graphene sheet edges, one can easily conclude that the tubular graphitic precipitates on the uncovered nonwettable catalytic surface is the most energetically favorable form of the graphitic precipitation. Even without any other nucleation stimuli, any local defect of the graphene sheet (e.g., associated with a high curvature of the catalyst nanoparticle or transverse thermal vibrations [Kanzow et al., 2001]) can thus result in its delamination or buckling followed by the nucleation of an SWNT. Recent calculations of total excess energies of different carbon atom arrangements on the surface of metal liquid of Fan et al. [2003] supports this inference.

24.3.5 The SLS Model

With the arguments above, one can reasonably interpret the existence of the temperature window for the SWNT formation. Irrespective of the neighboring carbon phase, the catalyst particle below the Ni–aC curve in Figure 24.7 is solid. Although the driving force for the graphitization can be strong, a high wetting interaction forces the graphitic phase to precipitate ''parallel'' to the surface of the solid catalyst particle.

Above the Ni–gC curve in Figure 24.7, the saturated metal–carbon particle is molten and the graphitic phase does not wet its surface. However, the difference ΔG between the amorphous and graphitic phases at these high temperatures is minimal and, according to Eq. (24.3), the SWNT formation requires a large critical nucleus. Only between the two limiting curves in Figure 24.7 are both conditions—a high driving force for graphitization and a low wettability of contacting materials—simultaneously fulfilled. This region on the *T-r* diagram in Figure 24.7 is favorable for the SWNT formation.

A schematic of the SLS model of the SWNT nucleation and growth is sketched in Figure 24.8. When a small enough molten metallic nanoparticle comes in contact with an amorphous carbon aggregate, it starts consuming carbon atoms. Due to its small volume and a rather high diffusion

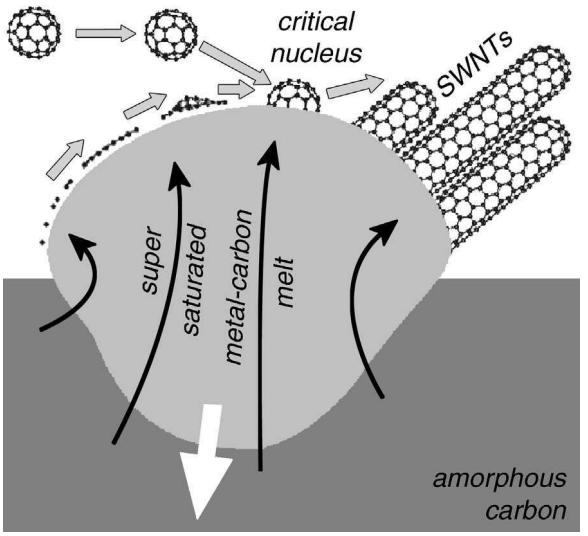

Figure 24.8 SLS mechanism of the SWNT formation. The critical nuclei are shown to form either through an instability at a single graphene sheet on the nonwetting supersaturated metal–carbon melt or through a partial dissolution of fullerenes of an overcritical size.

coefficient of carbon in the metal melt, it quickly becomes saturated with respect to the amorphous carbon but supersaturated with respect to a graphitic phase. The latter will tend to precipitate at the open side of the particle. If a critical nucleus forms at that moment through one of the mechanisms discussed in Section 24.3.2, the precipitating carbon atoms will be continuously incorporated to the root of the growing nanotube. It will elongate and the process of the amorphous carbon dissolution–melt diffusion–SWNT precipitation assumes a steady-state character provided the amorphous carbon is continuously supplied.

If the critical nuclei do not form, the precipitating carbon atoms arrange themselves in ''parallel'' graphitic cages around the catalytic particle cutting off the supply of the amorphous carbon and making the particle catalytically inactive.

24.3.6 First Second of the SWNT Life

Summarizing the results of Gorbunov et al. [1999, 2002a], Puretzky et al. [2000, 2002], Sen et al. [2000], and Yudasaka et al. [2002], one can propose the following scenario of the SWNT synthesis in the laser-furnace method.

- $t = 0 - 10$ ns. The laser pulse ablates the metal–carbon composite target. The ablation products consist of ionic/atomic/molecular species with a temperature T above the sublimation point of graphite (4000°C) and a pressure of the order of some kilobars.
- $t = t_P \approx 1$ μs. The pressure of the ablation products relaxes to P_0. The ''fireball'' forms.
- $t \approx 100$ μs. The fireball detaches from the target surface and moves quickly off the target. The ablation products cool down below 4000°C. The condensation of carbon atoms in fullerenes and amorphous carbon sets in. The releasing heat of condensation keeps $T \approx$ constant at 2500°C.
- $t \approx 1$ ms. The temperature of the ablation products decreases below 2500°C. The condensation of metal atoms into molten nanoparticles sets in. If both carbon and metal condensates come in contact, the metal nanoparticles start to consume the amorphous carbon.

$t \approx 2$ ms. Practically all the ablation products have condensed into fullerenes, large amorphous carbon aggregates, and molten saturated metal–carbon nanoparticles. The cloud of the ablation products takes the typical vortex ring form. At this instant T reaches T_{eut}. Further cooling down of the catalyst nanoparticles makes them supersaturated with carbon with respect to graphitic phases. It corresponds to the appearance of the driving force for the catalytic graphitization.

$t = t_T \approx 5$ ms. The condensed ablation products are thermalized to T_0. Catalytic particles in contact with amorphous carbon remain molten and highly supersaturated. The precipitation of a graphitic phase sets in. Provided a critical nucleus is formed, the precipitating carbon atoms are added preferentially to its circumference, which corresponds to the onset of the SWNT growth. If no critical nucleus forms, the precipitation of carbon atoms results in an encasement of particle with a graphitic cage and its catalytical deactivation.

$t > 5$ ms. Steady-state SWNT growth with a rate controlled by the rate of carbon dissolution and diffusion to the SWNT roots. Nucleation of new SWNTs at this stage is improbable.

$t \approx 1$ s. The cloud of the reacting metal–carbon species attains its highest altitude above the target's surface of a few centimeters and is slowly blown away with the carrier gas toward the water-cooled collector.

$t = t_{\text{drift}}$. In the neighborhood of the cold collector, the cloud experiences a thermophoretic force toward the cold collector's surface where it settles down. The reacting species are quenched to room temperature, the catalytic particles crystallize, the dissolved carbon massively precipitates, and the SWNT growth is interrupted. The reagents assume the typical form of SWNT-containing soot as seen in Figure 24.4. One can induce further growth of the SWNTs by subsequent heating of the soot to a temperature between 800°C and T_{eut}.

24.3.7 Optimization of SWNT Synthesis

A key for the SWNT synthesis improvement is to secure a timely monosize SWNT nucleation on the one hand and to maintain an unperturbed SWNT growth under optimal conditions for as long as possible on the other hand. On the basis of the SLS model one can suggest the following guidelines for an optimal SWNT synthesis in the laser-furnace technique:

1. The enrichment of the evaporation products with fullerenes seems to intensify the SWNT nucleation. They can be either immediately added to the target material or supplied with the carrier gas from an external source in a closed-loop reactor as proposed by Bolshakov et al. [2002].
2. The optimal synthesis temperature lies 100-200 K below the equilibrium eutectic temperature of the metal catalyst-carbon alloy [Gorbunov et al., 1999; Kataura et al., 2000]. It has to be maintained as long as possible during the growth of nucleated SWNTs. This temperature provides a sufficient driving force for the SWNT nucleation and growth through the amorphous carbon graphitization by molten supersaturated catalyst nanoparticles.
3. An optimal catalyst particle size, which seems to be of the order of 10 nm, has to be provided. On one hand, the probability of deactivation through the graphitic encapsulation should be inversely proportional to the surface area of the particles and should grow with the reduction of r. On the other hand, much larger particles solidify at $T_0 < T_{\text{eut}}$. The particles' size can be controlled by the metal catalyst content in the target material, its evaporation rate, and the carrier gas pressure. Presumably, the enhanced SWNT yield in the double-laser pulse evaporation technique of Thess et al. [1996] results from the improvement of the particles' size distribution.

4. It is important to extend the existence time of the molten catalytically active nanoparticles in order that they could transform the most amorphous carbon into SWNTs. One can prolong their residence time in the hot zone of the reactor either by reducing the carrier gas flow speed or by mechanically constraining the outflow of the reactants as is done, for example, by Rinzler et al. [1998] and Arepalli et al. [2000]. On the other hand, the number density of the catalyst particles in the carrier gas should be kept low to avoid their coarsening and solidification [Jost et al., 2001a].

Generally, the SLS model of the SWNT formation does not seem to be unique to the laser-furnace technique. Critical inspection of the literature data shows that it should also play a role in other physical vapor deposition techniques of the SWNT synthesis like continuous-wave (cw) laser, solar furnace, and arc discharge.

24.4 CONCLUSIONS

Single-wall carbon nanotubes (SWNTs) represent a new form of graphitic carbon with promising physical and chemical properties. Separation of the target atomization and SWNT growth in the laser-furnace technique permits a deeper insight into the underlying synthesis mechanisms and a better control of the SWNT growth conditions as compared to the other physical synthesis techniques. The existing amount of experimental and theoretical data on the SWNT formation allows drawing the following conclusions.

1. The SWNT synthesis in the laser-furnace technique is a condensed-state process. Under optimum synthesis conditions, it proceeds through a quick relaxation, condensation, and thermalization stage, during which the SWNT precursors are formed, a stage of the SWNT nucleation on the surface of the catalyst nanoparticles, and a longer stage of the steady-state SWNT growth with a rate of the order of micrometer length per second before the ablation products are quenched on the cold collector.
2. In the framework of the solid–liquid–solid model, the underlying mechanism of the SWNT formation is a special radial kind of catalytic graphitization of amorphous carbon by molten supersaturated catalyst particles, which can be realized under the conditions of a high driving force for graphitization and a low wettability of contacting graphitic carbon and molten catalyst materials.
3. The nonequilibrium melting of supersaturated metal–carbon catalyst particles in contact with amorphous carbon is a necessary condition for the SWNT synthesis. The melting of the catalytic nanoparticles leads to a pronounced increment of the carbon solubility, which alters the character of the wetting interaction of the precipitating graphitic form of carbon with the catalyst particle and promotes the SWNT nucleation on its surface. It is only possible in a temperature window that lies below the equilibrium eutectic temperature of the metal catalyst–carbon alloy and is determined by the size of the catalytic particles.

Acknowledgments

The authors wish to thank L. Dunsch, J. Fink, R. Friedlein, M.S. Golden, A. Graff, J. Möller, W. Pompe, and M. Reibold for their valuable contributions in performing experiments and discussing results at different stages of the work. Different parts of the work were supported by the German Federal Ministry for Education and Research (BMBF), German Research Foundation (DFG), and Saxonian Ministry for Science and Arts (SMWK).

REFERENCES

Ajayan, P. M. (1999), *Chem. Rev.* **99**, 1787–1799.

Arepalli, S., P. Nikolaev, W. Holmes, and C. D. Scott (2000), *Appl. Phys. A* **70**, 125–133.

Baker, R. T. K., M. A. Barber, P. S. Harris, F. S. Feates, and R. J. Waite (1972), *J. Catal.* **26**, 51–62.

Baker, R. T. K., P. S. Harris, R. B. Thomas, and R. J. Waite (1973), *J. Catal.* **30**, 86–95.

Baker, R. T. K., M. S. Kim, A. Chambers, C. Park, and N. M. Rodriguez (1997), in C. H. Bartholomew and G. A. Fuentes (Eds.), *Catalyst Deactivation,* Elsevier, Amsterdam, pp. 99–109.

Bandow, S., S. Asaka, Y. Saito, A. M. Rao, L. Grigorian, E. Richter, and P. C. Eklund (1998), *Phys. Rev. Lett.* **80**, 3779–3782.

Bethune, D. S., C. H. Klang, M. S. de Vries, G. Gorman, R. Savoy, J. Vazquez, and R. Beyers, (1993), *Nature* **363**, 605–607.

Bolshakov, A. P., S. A. Uglov, A. V. Saveliev, V. I. Konov, A. A. Gorbunov, W. Pompe, and A. Graff (2002), *Diam. Relat. Mater.* **11**, 927–930.

Bower, C., S. Suzuki, K. Tanigaki, and O. Zhou (1998), *Appl. Phys. A* **67**, 47–52.

Braidy, N., M. A. El Khakani, and G. A. Botton (2002a), *Carbon* **40**, 2835–2842.

Braidy, N., M. A. El Khakani, and G. A. Botton (2002b), *J. Mater. Res.* **17**, 2189–2192.

Cheung, C. L., A. A. Kurtz, H. Park, and C. M. Lieber (2002), *J. Phys. Chem. B* **106**, 2429–2433.

Dai, H., A. Rinzler, P. Nikolaev, A. Thess, D. T. Colbert, and R. E. Smalley (1996), *Chem. Phys. Lett.* **260**, 471–475.

Dillon, A. C., P. A. Parilla, J. L. Alleman, J. D. Perkins, and M. J. Heben (2000), *Chem. Phys. Lett.* **316**, 13–18.

Dresselhaus, M. S., G. Dresselhaus, K. Sugihara, I. L.Spain, and H. A. Goldberg (1988), *Graphite Fibers and Filaments*, Springer Series in Materials Science, Vol. 5, Springer-Verlag, New York.

Dresselhaus, M. S., P. C. Eklund, and G. Dresselhaus (Eds.) (1996), *Science of Fullerenes and Carbon Nanotubes*, Academic, New York.

Ebbesen, T. W. (Ed.) (1997), *Carbon Nanotubes. Preparation and Properties*, CRC Press, Boca Raton, FL.

Eklund, P. C., B. K. Pradhan, U. J. Kim, Q. Xiong, J. E. Fischer, A. D. Friedman, B. C. Holloway, K. Jordan, and M. W. Smith (2002), *Nano Lett.* **2**, 561–566.

Fan, X., R. Buczko, A. A. Puretzky, D. B. Geohegan, J. Y. Howe, S. T. Pantelides, and S. J. Pennycook (2003), *Phys. Rev. Lett.* **90**, 145501–145504.

Fedorov, V. B., M. H. Shorshov, and D. K. Khakimova (1978), *Carbon and Its Interaction with Metals*, Metallurgija-Publishers, Moscow (in Russian).

Feldmann, Y., E. Wasserman, D. Srolovitz, and R. Tenne (1995), *Science* **267**, 222–225.

Gao, G., T. Cagin, and W. A. Goddard III (1998), *Nanotechnology* **9**, 184–191.

Geohegan, D. B., H. Schittenhelm, X. Fan, S. J. Pennycook, A. A. Puretzky, M. A. Guillorn, D. A. Blom, and D. C. Joy (2001), *Appl. Surf. Sci.* **78**, 3307–3309.

Gorbunoff, A. (2002), *Laser-Assisted Fabrication of Thin Film Nanostructures*, Fortschritt-Berichte VDI, Düsseldorf.

Gorbunov, A. A., R. Friedlein, O. Jost, M. S. Golden, J. Fink, and W. Pompe (1999), *Appl. Phys. A* **69**(Suppl.), S593–S596.

Gorbunov, A., A. Graff, O. Jost, and W. Pompe (2001), *Proc. SPIE* **4423**, 212–217.

Gorbunov, A., O. Jost, W. Pompe, and A. Graff (2002a), *Carbon* **40**, 113–118.

Gorbunov, A., O. Jost, W. Pompe, and A. Graff (2002b), *Appl. Surf. Sci.* **197/198**, 563–567.

Guo, T., P. Nikolaev, A. Thess, D. T. Colbert, and R. E. Smalley (1995), *Chem. Phys. Lett.* **243**, 49–54.

Iijima, S., and T. Ichihashi (1993), *Nature* **363**, 603–605.

Ishigaki, T., S. Suzuki, H. Kataura, W. Krätschmer, and Y. Achiba (2000), *Appl. Phys. A* **70**, 121–124.

Jost, O., A. Gorbunov, W. Pompe, T. Pichler, R. Friedlein, M. Knupfer, M. Reibold, H.-D. Bauer, M. S. Golden, L. Dunsch, and J. Fink (1999a), *Appl. Phys. Lett.* **75**, 2217–2219.

Jost, O., R. Friedlein, A. Gorbunov, T. Pichler, M. Reibold, H.-D. Bauer, M. Knupfer, M.S. Golden, L. Dunsch, J. Fink, and W. Pompe (1999b), *AIP Conf. Proc.* **486**, 288–291.

Jost, O., A. Gorbunov, J. Möller, W. Pompe, A. Graff, R. Friedlein, X. Liu, M. S. Golden, and J. Fink (2001a), *Chem. Phys. Lett.* **339**, 297–304.

Jost, O., A. Gorbunov, L. C. Ciacchi, W. Pompe, X. Liu, T. Pichler, L. Dunsch, M. S. Golden, and J. Fink (2001b), *AIP Conf. Proc.* **591**, 341–344.

Jost, O., A. Gorbunov, J. Möller, W. Pompe, X. Liu, P. Georgi, L. Dunsch, M.S. Golden, and J. Fink (2002), *J. Phys. Chem. B* **106**, 2875–2883.

Jost, O., A. Gorbunov, X. Liu, W. Pompe, and J. Fink (2004), *J. Nanosci. Nanotechnol.,* **4**, 433–440.

Journet, C., and P. Bernier (1998), *Appl. Phys. A* **67**, 1–9.

Kanzow, H., and A. Ding (1999), *Phys. Rev. B* **60**, 11180–11186.

Kanzow, H., C. Lenski, and A. Ding (2001), *Phys. Rev. B* **63**, 125402.

Kasuya, D, T. Ishigaki, T. Suganuma, Y. Ohtsuka, S. Suzuki, H. Shiromaru, Y. Achiba, and T. Wakabayashi (1999), *Eur. Phys. J. D* **9**, 355–358.

Kataura, H., A. Kimura, Y. Ohtsuka, S. Suzuki, Y. Maniwa, T. Hanyu, and Y. Achiba (1998), *Jpn. J. Appl. Phys.* **37**, L616–L618.

Kataura, H., Y. Kumazawa, Y. Maniwa, I. Umezu, S. Suzuki, Y. Ohtsuka, and Y. Achiba (1999), *Synth. Metals* **103**, 2555–2558.

Kataura, H., Y. Kumazawa, Y. Maniwa, Y. Ohtsuka, R. Sen, S. Suzuki, and Y. Achiba (2000), *Carbon* **38**, 1691–1697.

Kawashima, T., K. Sasaki, T. Wakasaki, and K. Kadota (1999), *Appl. Phys. A* **69**(Suppl.), S767–S770.

Khassin, A. A., T. M. Yurieva, V. I. Zaikovskii, and V. N. Parmon (1998), *React. Kinet. Catal.* **64**, 63–71.

Kokai, F., K. Takahashi, K. Shimizu, M. Yudasaka, and S. Iijima (1999), *Appl. Phys. A* **69**(Suppl.), S223–S227.

Kokai, F., K. Takahashi, M. Yudasaka, and S. Iijima (2000), *J. Phys. Chem. B* **104**, 6777–6784.

Krivoruchko, O. P., V. I. Zaikovskii, and K. I. Zamaraev (1993), *Dokl. Akad. Nauk* **329**, 744–748 (in Russian).

Kuznetsov, V. L., A. N. Usoltseva, A. L. Chuvilin, E. D. Obraztsova, and J.-M. Bonard (2001), *Phys. Rev. B* **64**, 235401.

Laplaze, D., P. Bernier, W. K. Maser, A. Loiseau, G. Flamant, and T. Guillard (1998), *Carbon* **36**, 685–688.

Liu, X, T. Pichler, M. Knupfer, M. S. Golden, J. Fink, H. Kataura, and Y. Achiba (2002), *Phys. Rev. B* **66**, 045411.

Louchev, O. A. and J. R. Hester (2003), *J. Appl. Phys.* **94**, 2002–2010.

Munoz, E., W. K. Maser, A. M. Benito, M. T. Martinez, G. F. de la Fuente, Y. Maniette, A. Righi, E. Anglaret, and J. L. Sauvajol (2000), *Carbon* **38**, 1445–1451.

Naidich, J. V. (1981), *Prog. Surf. Membr. Sci.* **14**, 353–483.

Nikolaev, P., M. J. Bronikowski, R. K. Bradley, F. Rohmund, D. T. Colbert, K. A. Smith, and R. E. Smalley (1999), *Chem. Phys. Lett*. **313**, 91–97.

Nishide, D., H. Kataura, S. Suzuki, K. Tsukagoshi, Y. Aoyagi, and Y. Achiba (2003), *Chem. Phys. Lett.* **372**, 45–50.

Oberlin, A., M. Endo, and T. Koyama (1976), *J. Crystal Growth* **32**, 335–347.

Pedio, M., K. Hevesi, N. Zema, M. Capozi, P. Perfetti, R. Gouttebaron, J.-J. Pireaux, R. Caudano, and P. Rudolf (1999), *Surf. Sci.* **437**, 249–260.

Puretzky, A. A., D. B. Geohegan, X. Fan, and S. J. Pennycook (2000), *Appl. Phys. A* **70**, 153–160.

Puretzky A. A., H. Schittenhelm, X. D. Fan, M. J. Lance, L. F. Allard, and D. B. Geohegan (2002), *Phys. Rev. B* **65**, 245425.

Radosavljevic, M., J. Lefebvre, and A. T. Johnson (2001), *Phys. Rev. B* **64**, 241307.

Radushkevich, L. V., and V. M. Lukyanovich (1952), *Zh. Fiz. Khim.* **26**, 88–95 (in Russian).

Rao, A. M., E. Richter, S. Bandow, B. Chase, P. C. Eklund, K. A. Williams, S. Fang, K. R. Subbaswamy, M. Menon, A. Thess, R. E. Smalley, G. Dresselhaus, and M. S. Dresselhaus (1997), *Science* **275**, 187–191.

Rinzler, A. G., J. Liu, H. Dai, P. Nikolaev, C. B. Huffman, F. J. Rodriguez-Macias, P. J. Boul, A. H. Lu, D. Heymann, D. T. Colbert, R. S. Lee, J. E. Fischer, A. M. Rao, P. C. Eklund, and R. E. Smalley (1998), *Appl. Phys. A* **67**, 29–37.

Rodriguez, N. M. (1993), *J. Mater. Res.* **8**, 3233–3250.

Rotkin, S. V., and Y. Gogotsi (2002), *Mater. Res. Innovat.* **5**, 191–200.

Saito, Y., (1995), *Carbon* **33**, 979–988.

Saito, Y., M. Okuda, M. Tomita, and T. Hayashi (1995), *Chem. Phys. Lett.* **236**, 419–426.

Saito, R., G. Dresselhaus, and M. S. Dresselhaus (1998a), *Physical Properties of Carbon Nanotubes,* World Scientific, London.

Saito, R., T. Takeya, T. Kimura, G. Dresselhaus, and M. S. Dresselhaus (1998b), *Phys. Rev. B* **57**, pp.4145–4153.

Saito, Y., Y. Tani, and A. Kasuya (2000), *J. Phys. Chem. B* **104**, 2495–2499.

Scott, C. D., S. Arepalli, P. Nikolaev, and R. E. Smalley (2001), *Appl. Phys. A* **72**, 573–580.

Sedov, L. I. (1967), *Similarity and Dimensional Methods in Mechanics*, Academic, New York.

Sen, R., Y. Ohtsuka, T. Ishigaki, D. Kasuya, S. Suzuki, H. Kataura, and Y. Achiba (2000), *Chem. Phys. Lett.* **332**, 467–473.

Subramoney, S. (1998), *Adv. Mater.* **10**, 1157–1171.

Subramoney, S., R. S.Ruoff, D. C. Lorents, and R. Malhotra (1993), *Nature* **366**, 637.

Suenaga, K., F. Willaime, A. Loiseau, and C. Colliex (1999), *Appl. Phys. A* **68**, 301–309.

Takizawa, M., S. Bandow, M. Yudasaka, Y. Ando, H. Shimoyama, and S. Iijima (2000), *Chem. Phys. Lett.* **326**, 351–357.

Tanaka, K., T. Yamabe, and K. Fukui (1999), *The Science and Technology of Carbon Nanotubes*, Elsevier, Oxford.

Terrones, M., W. K. Hsu, H. W. Kroto, and D. R. M. Walton (1999), *Top. Curr. Chem.* **199**, 189–234.

Thess, A., R. Lee, P. Nikolaev, H. Dai, P. Petit, J. Robert, C. Xu, Y. H. Lee, S. G. Kim, A. G. Rinzler, D. T. Colbert, G. E. Scuseria, D. Tomanek, J. E. Fischer, and R. E. Smalley (1996), *Science* **273**, 483–487.

Tibbetts, G. G. (1984), *J. Crystal Growth* **66**, 632–638.

Tomanek, D. and Enbody R. J. (Eds.) (2002), *Science and Application of Nanotubes*, Kluwer, New York.

Tremel, W. (1999), *Angew. Chem. Int. Edit.* **38**, 2175–2179.

Wang, N., Z. K. Tang, G. D. Li, and J. S. Chen (2000), *Nature* **408**, 50–51.

Yakobson, B. I., and R. E. Smalley (1997), *Am. Sci.* **85**, 324–337.

Yudasaka, M., T. Komatsu, T. Ichihashi, Y. Achiba, and S. Iijima (1998), *J. Phys. Chem. B* **102**, 4892–4896.

Yudasaka, M., F. Kokai, K. Takahashi, R. Yamada, N. Sensui, T. Ichihashi, and S. Iijima (1999a), *J. Phys. Chem. B* **103**, 3576–3581.

Yudasaka, M., N. Sensui, M. Takizawa, S. Bandow, T. Ichihashi, and S. Iijima (1999b), *Chem. Phys. Lett.* **312**, 155–160.

Yudasaka, M., T. Ichihashi, T. Komatsu, and S. Iijima (1999c), *Chem. Phys. Lett.* **299**, 91–96.

Yudasaka, M., M. Zhang, and S. Iijima (2000), *Chem. Phys. Lett.* **323**, 549–553.

Yudasaka, M., Y. Kasuya, F. Kokai, K. Takahashi, M. Takizawa, S. Bandow, and S. Iijima (2002), *Appl. Phys. A* **74**, 377–385.

Zhang, Y., and S. Iijima (1999), *Appl. Phys. Lett.* **75**, 3087–3089.

Zhang, Y., M. Yudasaka, and S. Iijima (2001), *Chem. Phys. Lett.* **336**, 196–200.

Zhang, Y., Y. Li, W. Kim, D. Wang, and H. Dai (2002), *Appl. Phys A* **74**, 325–328.

Zhou, D., S. Seraphin, and S. Wang (1994), *Appl. Phys. Lett.* **65**, 1593–1595.

CHAPTER 25

Quasicrystalline Thin Films

PHILIP R. WILLMOTT

Swiss Light Source, Paul Scherrer Institute
CH-5232 Villigen, Switzerland

25.1 INTRODUCTION

Since the first report of quasicrystals (QCs) in 1984 [Shechtman et al., 1984], quasi-periodic order exhibiting 5- or 10-fold rotational symmetry has been found in over 50 intermetallic alloys, based mainly on either aluminum or titanium. The most common class of QCs has icosahedral symmetry. The second class can be described as a periodic stacking of aperiodically ordered planes and is therefore quasicrystalline in two dimensions and classically crystalline in the third dimension. Such two-dimensional QCs have the symmetry of a decagonal prism (see Fig. 25.1). The icosahedral and decagonal quasicrystalline phases are identified by prefacing the QC alloy with *i*- and *d*-, respectively.

Quasicrystals have several physical and chemical properties of technological importance: Their conductivities decrease in a similar manner to those for semiconductors due to a pseudogap at the Fermi energy, most are very resistant to corrosion, show high hardness, and have a low coefficient of friction. These last three properties make QCs especially interesting as protective and tribological coatings, particularly because bulk QCs are highly brittle [Feuerbacher et al., 2001]. In addition, the Ti-based QCs can reversibly store large quantities of hydrogen, making them potential candidates for solid-state batteries [Viano et al., 1998] (see also Chapter 22). These work most efficiently with a large surface area/volume ratio, such as offered by thin films. A list is given in Table 25.1 of some of the most interesting properties of QCs in comparison with those of industry standards.

As well as having many potential technological applications, QCs are of fundamental interest to the condensed-matter physicist. There is still a great deal to be learned about the influence of an aperiodic structure with long-range order on both surface and bulk properties [McGrath et al., 2002]. Despite the fact that different combinations of metals can exhibit a quasicrystalline phase, they share many physical qualities, suggesting that it is the aperiodic structure itself, rather than the specific elements that combine to make it, that largely determines the physical properties. The aperiodic structure of QCs, including the atomic decorations of the canonical-cell tiling geometry [Hennig et al., 2000, 2003], requires novel methods for detailed structural analysis. Fabricating QCs as high-quality thin films may help answer fundamental questions regarding their surface properties (friction, conductivity, corrosion, etc.) by providing well-defined and controllable surface conditions [Jenks and Thiel, 1998; McGrath et al., 2002]. Ultimately, one would like to be able to achieve a degree of registry between a crystalline substrate with translation symmetry and a QC film with rotational symmetry.

Pulsed Laser Deposition of Thin Films: Applications-Led Growth of Functional Materials
Edited by Robert Eason

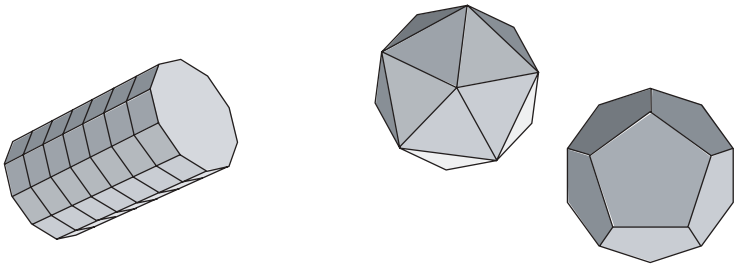

Figure 25.1 Symmetries of quasicrystals. Decagonal QCs are made from a periodic stacking of aperiodic arrays of atoms exhibiting 10-fold symmetry. The more common QC types show icosahedral (or, equivalently, dodecahedral) symmetry.

Lastly, the stability of a quasicrystalline phase may depend on the physical extent of the system. For example, does the quasicrystalline phase spontaneously nucleate from the beginning, or is there a phase change to the quasicrystalline phase after the alloy reaches some characteristic size? Such problems may be resolved by monitoring film growth in situ.

25.2 PRESENT STATUS OF THIN-FILM GROWTH OF QUASICRYSTALS

When one considers the technological importance of producing QCs as thin films or coatings, it is surprising how little basic research has been performed to this end. By August 2005, a simple search on the ISI Web of Knowledge publication database, using the algorithm ''quasicrystal*'' AND (''thin film*'' OR ''coating*'') yields 115 papers on QC thin-film growth and/or analysis since 1988, after some manual filtering to remove spurious hits. Many of these relate to thermal spray coating. Excluding the ''coating*'' keyword reduces the number of publications to a mere 71. By contrast, there have been well over 1600 papers on studies of colossal magnetoresistive thin films since 1994. What is the cause for such a discrepancy? The primary reason is that QC thin films are difficult to produce.

The successful growth of metallic alloy thin films and especially QCs, is dogged by both technological and fundamental problems, which are briefly covered here. As a result, it will be seen that physical vapor deposition methods are more favorable, of which pulsed laser deposition (PLD) is among the most promising.

TABLE 25.1 Comparison of Some of the Most Important Properties of Quasicrystals with Industry Standards

Property	Standard	QC
Surface energy	PTFE (teflon)	*i*-Al–Pd–Mn
[Jm^{-2}]	1.8×10^{-2}	2.4×10^{-2}
Coefficient of dry friction	Steel	*i*-Al–Cu–Fe
	0.4	0.08
Vickers hardness	Al_2O_3	*i*-Al–Cu–Fe
[kg m^{-2}]	2×10^9	1×10^9
Electrical conductivity at 300 K	Silicon	*i*-Al–Cu–Fe
[Ω^{-1} m^{-1}]	10^4–10^5	1.4×10^4
Thermal conductivity	Aluminum	*i*-Al–Cu–Fe
[W $kg^{-1}K^{-1}$]	170	2
Hydrogen storage	TiFe	*i*-Ti–Ni–Zr
[H-atom per host atom]	1	2

25.2.1 General Problems

The first QCs to be discovered were binary alloys of Al and were thermodynamically metastable. They could only be produced by rapid quenching from the melt. It was later discovered that the addition of a small amount of a third element could thermodynamically stabilize the system, and large single ''crystals'' could be grown using classical methods such as the Czochralski melt technique. In general, however, the quasicrystalline phase only forms over a narrow range of chemical compositions within a few percent of the optimal value. In addition, many QCs are closely structurally related to true crystalline approximants. These can be thought of as having unit cells that are fragments of a quasicrystalline structure, and hence their chemical compositions are very close to that of the quasicrystalline phase. It is therefore essential in QC film growth to have optimal control over the relative deposition rates of the constituent elements.

Growth of QC thin films using thermal deposition techniques such as chemical vapor deposition or thermal evaporation [Barna et al., 1988] has two technological obstacles. First, the degree of control of the film composition is insufficient, unless highly sophisticated growth monitors are employed, and deposition of the elements is sequential. Second, many of the elements found in QCs must be heated to well over 1500°C before they have sufficient vapor pressures for reasonable deposition rates, while metallorganic precursors are normally unusable due to the immediate incorporation of fragments of the organic ligand in the film after the cracking process.

Indeed, oxygen incorporation during the synthesis of quasicrystalline alloys is a particular concern. With some exceptions [Kelton, 1993], the presence of oxygen of around 1 at % can destroy the quasicrystalline structure [Chang et al., 1995; Bonasso et al., 2002]. In the case of the icosahedral Ti–Ni–Zr (*i*-TNZ) QC system, even levels as low as a few hundred parts-per-million can stabilize the Ti_2Ni phase and eliminate both the quasicrystalline and Laves phases [Stroud et al., 1997]. As typical growth rates of thin films of QCs are about 0.1 monolayer (ML) per second, partial background pressures of oxygen-containing gas species must be held well below 10^{-8} Pa [i.e., ultrahigh vacuum (UHV) conditions] to avoid detrimental oxygen incorporation when growing *i*-TNZ.

25.2.2 Growth Techniques

The most successful techniques to grow QC thin films have in general been nonthermal physical vaporization methods, such as sputtering [Eisenhammer and Trampert, 1997], ion beam mixing [Plenet et al., 1993], electron beam evaporation [Yoshioka et al., 1995], and PLD [Ichikawa et al., 1994; Teghil et al., 2000, 2003; Copola et al., 2002; Brien et al., 2003a, 2003b; Willmott et al. 2004, 2005]. Deposition of the constituent elements may be either simultaneous (from either a single source or a set of individual sources) or sequential [Bonasso and Pigeat, 2003; Willmott et al., 2004]. Recently, elemental multilayers were grown using e-beam evaporation, followed by postannealing, whereby the desired QC was produced by interdiffusion of the layers [Grenet et al., 2002]. Almost all reports to date on QC thin-film growth have involved postannealing of the film.

Although there are many thermodynamically stable QCs, suppression of related crystalline phases is generally best achieved by high nucleation rates, which is often synonymous with rapid cooling (such as in liquid strip metal quenching [Inoue et al. 1992]). Rapid cooling, however, limits the diffusion rate, and crystallite sizes are generally small. This apparent ''conflict of interests'' will be discussed in more detail in the context of PLD below.

25.3 PULSED LASER DEPOSITION OF QUASICRYSTALS

25.3.1 Why PLD?

Pulsed laser deposition has two properties that set it apart from other deposition techniques and make it particularly attractive for the growth of QC thin films.

25.3.1.1 Congruent Material Transfer

There is a wealth of literature that has shown that PLD can reproduce the chemical composition of chemically complex bulk materials in thin films with greater fidelity than other film growth techniques [Hubler, 1994]. The narrow range of chemical compositions that leads to QC growth perhaps sets the most stringent test on this much-vaunted property of PLD, and we discuss this in more detail here.

For those materials for which one elemental component has a very high vapor pressure, such as oxygen in the growth of $YBa_2Cu_3O_{7-x}$, the degree of its incorporation in the film can normally be assured using chemical techniques (more precisely, by applying Le Chatalier's principle and forcing a reaction equilibrium to one extreme by introducing an excess of the volatile component). When the target material contains no such volatile component, the degree of congruent material transfer depends on the one hand mainly on three laser parameters, that is, the laser wavelength λ, the pulse duration τ, and the energy flux F, and on the other, the physical properties of the target, in particular the optical absorption depth and reflectivity at the laser wavelength being used, the thermal diffusion length, and the heat of vaporization.

Congruent transfer in PLD is in general satisfied if most of the deposited laser energy results in nonthermal vaporization (i.e., ''rue'' ablation). This occurs if the thermal diffusion length, given by $l_T = \sqrt{2D\tau}$, where D is the thermal diffusivity, is short compared to the optical absorption depth, given by $l_A = \lambda/4\pi k$, where k is the imaginary part of the refractive index (i.e., the optical absorption coefficient) at the laser wavelength λ.

This condition is in general not met for metallic alloys, for which the optical absorption depth is around 10 nm at ultraviolet wavelengths, while the thermal diffusion length is measured in microns for nanosecond (ns) laser pulses. However, if the vaporization temperature is high and the vapor pressure at the melting temperature is low, ablation can still be fairly congruent. Early work by van Ingen et al. [1994] and Krebs et al. [1995b] showed that thin films grown by the ablation of binary transition metal alloy targets had stoichiometries that typically lay within ± 5 percentile of the targets' 50 : 50 atomic mixtures (a notable exception was the ablation of Fe : Sn targets, due to the large difference in their elemental vapor pressures). While this degree of control compares favorably with most other film growth techniques, it is questionable as to whether it meets the stringent requirements of QCs.

Arnold and Aziz noted that the steady-state stoichiometry of Si–Ge films grown by ns-PLD differed substantially from that of the target, which they attributed to differential scattering in the plume [Arnold and Aziz, 1999]. In their discussion of possible sources for this difference, they made the reasonable assumption that surface segregation could be excluded as the cause of this difference, as the melt depth l_M, ablation depth l_A, and segregation depth l_S, are all of similar magnitude. This is not true for metals, where $l_m \sim 1\mu m$ [Timm et al., 1996] and the segregation depth $l_S = D_{AB}/v_M \sim 10^{-9} m^2\,s^{-1}/1\ m\,s^{-1} = 1nm$, where D_{AB} is the diffusion coefficient of element A in B and v_M is the velocity of the retreating melt front to the surface, as described in detail by Aziz [1996]. Consider Figure 25.2. Irradiation of a fresh sample results in the segregation front traveling to the surface, which may have a stoichiometry very different from that of the bulk down to l_S (Fig. 25.2a). Because l_A is typically an order of magnitude larger than l_S, the next ablation event will entirely remove the surface segregated layer, and the depleted layer beginning at l_M will become larger (Fig. 25.2b). Assuming that the melt front remains flat and homogeneous, this will continue until the depletion front approaches the surface (Fig. 25.2c), after which the stoichiometry will begin to approach the bulk value as the average composition of the ablated material equals that of the bulk (Fig. 25.2d).

This steady-state mass flux is only reached after a depth of the order of magnitude of l_M has been ablated, that is, $\sim 1000\,nm/10\,nm = 100$ shots. Because the ablation target is normally being rotated and/or translated during an experiment, in order to avoid target roughening and macroscopic particulate production, the number of shots to achieve steady-state mass flux is equal to $100\times$ the ratio of the ablated target area to the ablation spot area, and is typically of the order of 100,000. Until then, film growth will therefore be incongruent and the film stoichiometry will change only very slowly with the aggregate number of laser shots.

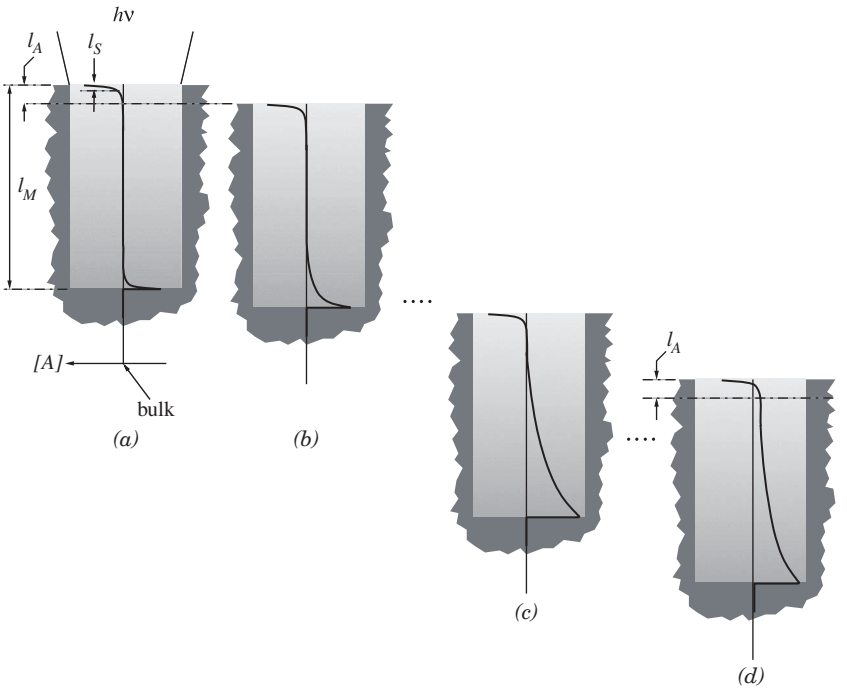

Figure 25.2 Change in the concentration [*A*] of element A in an alloy ablation target due to segregation effects. The target is melted down to a depth l_M and ablated to a depth l_A by the laser pulse. A fraction of element A is transported to the surface region of depth l_S due to segregation effects as the material solidifies and the melt front retreats. Eventually, steady state is achieved as the average concentration of A in the ablated volume equals that of the bulk.

This problem has been tackled by readjusting the composition of the target to compensate for any effects leading to incongruent transfer. For example, Brien et al. [2003a] found that using a target composition of $Ti_{45}Ni_{17}Zr_{38}$, they could grow films with the optimal composition of $Ti_{41.5}Ni_{17}Zr_{41.5}$. The cause of this incongruent transfer was not uniquely established, though as they used the fundamental infrared Nd : YAG wavelength of 1064 nm, ablation was certainly thermal in nature. Depth profiling of the subsequent film using secondary neutral mass spectroscopy (SNMS) showed that there was a transition regime of some 15,000–18,000 laser shots, during which the ratio of Ti to Zr in the film changed from 38 : 50 to 41 : 41. After this, the composition changed only very slowly, typically from 41 : 41 to 40 : 44 over 50,000 shots [Brien et al., 2003a] (see Fig. 25.3).

Unfortunately, adapting the target composition to correct for incongruent transfer is complicated by its dependence on laser fluence and angular position relative to the target normal. There are normally drifts in the laser fluence during an experiment, especially due to the buildup of ablated material on the inside of the vacuum laser entrance window, which can cause significant reflection and/or absorption, especially when one is depositing metals—even ignoring reflection losses, a 4-nm deposition at the laser entrance port for a metal with an absorption depth of 15 nm will result in an $\sim$25% reduction in laser power. The reader is also referred to Chapter 16 on PLD of metals, in which other important issues of preferential resputtering of the deposited film by the high-energy tail of the ablation plasma, and how this can be controlled by ablation in a background gas, are outlined.

In summary, PLD offers perhaps the simplest control of the stoichiometry of QC films grown using alloy targets. Incongruent transfer due to differential scattering in the plume, surface segregation, preferential ablation, and resputtering by the impinging ablation plume species at the

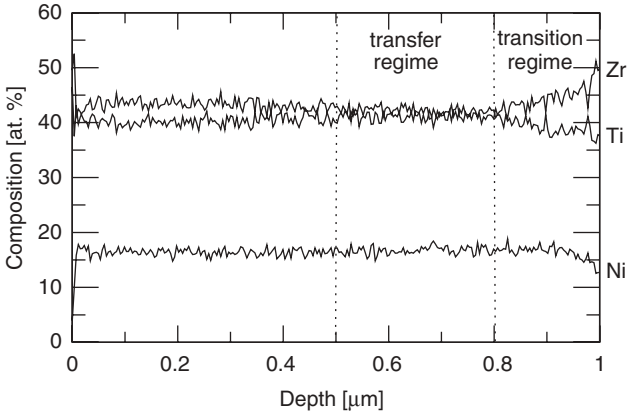

Figure 25.3 The SNMS stoichiometric depth profile of an *i*–Ti–Ni–Zr film grown by PLD using infrared nanoscond pulses and a crystalline alloy target. Adapted from Brien et al. [2003a].

film surface can be corrected by adjustment of the target composition. Hence, under carefully calibrated and constant experimental conditions, the degree of stoichiometric control is sufficient to reliably achieve the desired composition for the quasicrystalline phase. However, other intermetallic phases will be favored by even small excursions from the ideal growth conditions.

25.3.1.2 Instantaneous Deposition Flux

The single feature unique to PLD is its pulsed nature. Its instantaneous deposition rate is orders of magnitude higher than that of other growth techniques: Typically, a single ablation plume will deposit 0.01 of a monolayer (ML) in 5 μs, yielding an instantaneous deposition rate of 2000 ML s^{-1}. This has important consequences on the film growth kinetics by placing growth far from thermal equilibrium. It is therefore unsurprising that the growth modes in PLD are different from those of other techniques.

Stable nucleation of seed islands in thin-film growth requires that the gain in volume free energy exceeds the loss due to increased surface energy. The density of stable nucleation sites N^* therefore depends on the critical free-energy change ΔG^* needed to obtain stable nuclei such that [Ohring, 2002]

$$N^* = n_s \exp(-\Delta G^*/kT) \tag{25.1}$$

where n_s is the maximum possible nucleation site density. In general (i.e., for both homoepitaxy and heteroepitaxy), ΔG^* is inversely proportional to the square of the change in chemical free energy per unit volume due to condensation, ΔG_V, that is,

$$\Delta G^* = \frac{16\pi\gamma_{fv}^3}{3\Delta G_V^2}\left\{\frac{2 - 3\cos\theta + \cos^3\theta}{4}\right\} \tag{25.2}$$

where γ_{fv}, γ_{sv}, and γ_{fs} are the film-vapor, surface-vapor, and film-surface interfacial energies, respectively, and θ is the contact angle between the nucleus and substrate (see Fig. 25.4). Hence, large absolute values of ΔG_V will result in a high density of stable nucleation sites. In its turn, the dependence of ΔG_V on the supersaturation $S = (P_V - P_S)/P_S \approx P_V/P_S$ is logarithmic, that is,

$$\Delta G_V = \frac{kT}{\Omega}\ln\frac{P_V}{P_S} \tag{25.3}$$

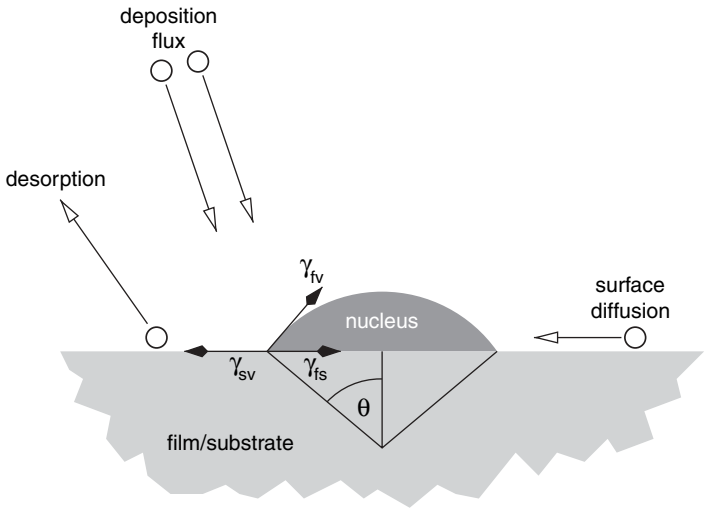

Figure 25.4 Competing processes during nucleation of a film on a substrate.

where Ω is the atomic volume, P_V is the vapor pressure of the supersaturated impinging flux, and P_S is the equilibrium vapor pressure above the solid. Equating pressure with flux is only strictly true for thermal systems for which there is no net velocity of the supersaturated vapor above the surface. While this is approximately valid for methods such as chemical vapor deposition (CVD) and molecular beam epitaxy (MBE), it most certainly is not for PLD. The *effective* pressure is in fact higher still than that calculated by the number density in the ablation plume. This ambiguity can be avoided by replacing the pressures P_V and P_S with the more general deposition and desorption rates R_V and R_S. Because of the logarithmic dependence of ΔG_V on S, a significant increase in N^* can only be realized with a technique for which the vapor pressure of the impinging flux is orders of magnitude higher than for standard techniques. This is exactly the case for PLD.

The nucleation rate $\dot{N}$ is proportional to N^* and to the rate of impingement, hence high values of $\dot{N}$ are normally associated with the growth of films composed of many small crystallites. This would happen for rapid thermal deposition at low temperatures, and PLD has been likened to this regime [Krebs et al, 1995a].

A high density of nucleation sites can therefore normally be associated with kinetically hindered systems. Although film nucleation in PLD yields similar nucleation densities to those for low-temperature thermal growth, it is because there is such a large instantaneous flux (R_V), and not because the desorption and surface diffusion rates $(R_S \text{ and } R_{SD})$ are *absolutely* low. Hence, in between deposition pulses, processes that would be frozen out in low-temperature growth, such as Ostwald ripening, can occur and large crystallites can be formed.

What consequences do the high supersaturation and nucleation rates in PLD have on the growth of quasicrystalline systems? In general, liquids transform to ordered phases as they are cooled below their equilibrium melting temperature T_m, due to a lowering of the free energy. It has long been known, however, that very pure metallic liquids can be supercooled far below T_m without freezing [Turnbull and Cech, 1950]. Such large undercooling is normally associated with high activation barriers to the ordered phase, which seemed surprising for metallic systems, whose liquid and solid phases have similar densities and physical properties. As long ago as 1952, Frank proposed that the supercooled liquid metal contained local structures with icosahedral order that, due to their incompatibility with periodic crystallinity, act as a barrier to freezing [Frank, 1952]. Very recently, Kelton and co-workers have been able to directly link enhanced nucleation of icosahedral short-range ordered structures in supercooled liquid alloys with growing icosahedral order in *i*-TNZ

[Kelton et al. 2003]. This explains why QCs are more often than not most easily formed by rapid quenching.

The nucleation model outlined above for PLD describes condensation of particles out of the gas phase and nucleation on a growing surface. The exact phase of the condensed nuclei was not specified. For growth temperatures well below T_m, the impinging particles will physisorb on the surface and transfer their kinetic energy to the local volume on the time scale of several picoseconds. This results in local melting to a depth of a few atomic radii and also surface diffusion over a few tens of picoseconds, for typical energies of a few tens of electron volts [Gilmore and Sprague, 1991; Hubler and Sprague, 1996; Park, 1997; Jacobsen et al., 1998]. This is one to two orders of magnitude longer than typical vibrational frequencies; hence, we can expect the adatom to hop a distance of $\sim\sqrt{100} = 10$ atomic spacings before it is thermalized. Seitz and Koehler [1956] were among the first to develop a model describing the distance that an atom can migrate on a surface due to a transient high-temperature spike. By equating the kinetic energy of the impinging species with a temperature, their model predicted that depositing species with energies of several tens of electron volts increased the mobility radius to some 10 atomic radii, in good agreement with our simple argument above. More recent molecular dynamics calculations, in which local surface melting caused by an energetic collision cascade promotes diffusion over several picoseconds, yield similar values for the enhanced diffusion radius [Diaz de la Rubia et al., 1987; Park, 1997].

The smallest cluster showing icosahedral short-range order contains approximately 40–50 atoms. For example, the so-called Bergman cluster consists of three layered shells containing 1, 12, and 32 atoms. Formation of these seed clusters therefore requires near-free diffusion over 1 nm or more [Hennig et al., 2000], which is well satisfied in the transient ''melt'' directly after impingement of hyperthermal species in PLD. Hence, the high nucleation rate, thermal spike, and subsequent rapid quenching of PLD should promote the quasicrystalline phase by freezing the icosahedral seeds before the crystalline phase can be formed.

25.3.1.3 Summary of QC Films Grown to Date by PLD

There has been so little research into PLD of QC thin films, that it is possible to give a more or less comprehensive summary, which is presented here in chronological order.

Pulsed laser deposition of QCs was first reported by Ichikawa et al. [1994]. They grew films of *i*-Al-Pd-Mn (*i*-APM) by ablation of crystalline alloy disk targets with the same chemical composition as that desired in the film. Despite the fact that the composition of the films agreed with that of the targets within a few percent, the quasicrystalline phase could only be obtained if the substrate was held at liquid-nitrogen temperatures during growth (see Fig. 25.5). Under these conditions, however, only the quasicrystalline phase was found in X-ray diffraction (XRD) patterns of the films. No postannealing was required.

This precise technique was repeated for both *i*-APM and *i*-Al-Cu-Fe (*i*-ACF) in 1997, using the same laser wavelength (248 nm) and similar deposition rates. Despite this, no quasicrystalline phase could be identified by XRD analysis [Šonský et al., 1997]. The authors maintained that the quasicrystalline phase was produced, however, by citing the abnormally high electrical resistivity of the films compared to that expected for a crystalline alloy, although it was also several orders of magnitude higher than that reported in the literature for the bulk QCs. They explained this by claiming that the crystallite size was too small to be identified by XRD, which also led to electron localization. No information was given, however, about the vacuum quality during deposition, and it remains an open question as to whether strong oxidization could not have also led to this result.

Teghil et al. [2000] also investigated the growth of *i*-ACF thin films using frequency-doubled Nd : YAG (532 nm) ns-laser pulses. They found that the nature of the ablation target played a critical role in obtaining the quasicrystalline phase. Ablation of a crystalline alloy target resulted in films that were rich in Al and showed no quasicrystalline phase. If, however, the target was itself a QC, essentially perfect stoichiometric transfer was achieved above a critical laser fluence of approximately $6\,\mathrm{J\,cm^{-2}}$. This could be explained by the fact that the thermal conductivity of the quasicrystalline phase is several orders of magnitude lower than for the crystalline alloy. The thermal

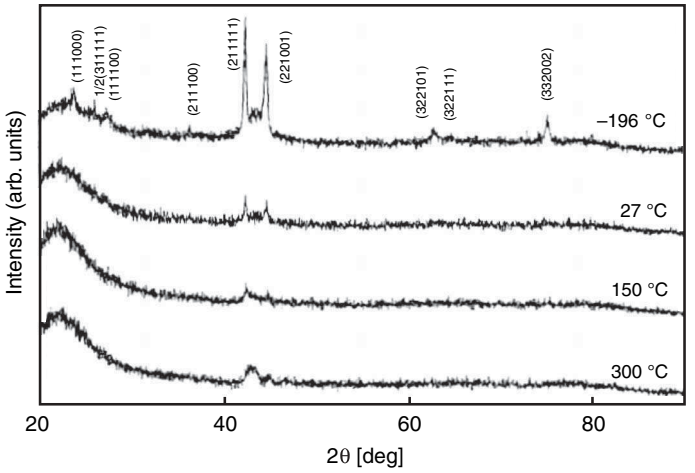

Figure 25.5 XRD patterns of *i*-Al–Pd–Mn films grown on quartz substrates at different temperatures. From Ichikawa et al. [1994].

diffusion length is therefore smaller than the optical absorption depth and ablation is nonthermal. A natural question to ask is whether the surface region of a QC target remains quasicrystalline after irradiation with high-power ns-laser pulses. Mao has recently demonstrated that the QC phase survives laser fluences typical for nanosecond ablation [Mao, 2003]. An Al–Cu–Fe target was irradiated with 266-nm, 3-ns pulses with a fluence of $0.1\,\mathrm{J\,cm^{-2}}$. The target crystallinity was then measured using micro-X-ray diffraction. The results are shown in Figure 25.6—there is no significant difference in either the lattice constants or intensities between the regions outside and inside the ablated area. This can be heuristically explained by the rapid cooling rates of laser-melted surfaces, which will promote the quasicrystalline phase, as described above.

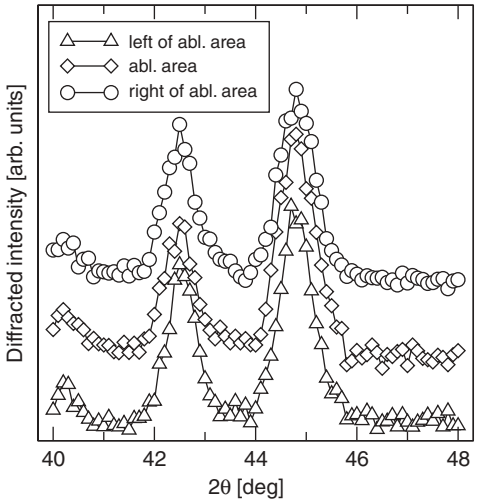

Figure 25.6 Micro-XRD patterns of an Al–Cu–Fe quasicrystalline target irradiated with 266-nm, 3-ns pulses at a fluence of $0.1\,\mathrm{J\,cm^{-2}}$ and a laser focus of 100 μm. The ablated area shows essentially the same diffraction pattern as those for the two regions 1 mm to its left and right. From Mao [2003].

Using a QC target, Teghil et al. [2003] could grow films containing a mixture of the icosahedral and crystalline Laves phase at room temperature. The high laser fluence required to achieve stoichiometric transfer, however, resulted in rapid target roughening and macroscopic particulate ejection, which compromised the film quality. This is a particular problem of nanosecond ablation of Al-based alloys, due to their low melting temperatures.

With this in mind, Teghil and co-workers [2003] later investigated the effect of using picosecond (ps) and femtosecond (fs) laser pulses. Here, the laser pulse duration is shorter than the time required to couple energy from the electrons to the lattice. Heat diffusion should be negligible, there is no collateral damage to the target, and material ejection is entirely nonthermal, resulting in perfectly congruent material transfer [Willmott and Huber, 2000]. This was indeed found to be the case, but the films contained both crystalline and quasicrystalline phases and were also found to be exceedingly rough, consisting of coalesced particles with typical dimensions of the order of microns. The film morphology was found to be independent of the substrate temperature, indicating that it did not arise from classical strain relief and wetting phenomena, but that macroscopic particles released from the target during the ablation process were again accumulating on the film surface. Explosive melting by volumetric heating [Tokarev and Kaplan, 1999] was invoked as the most likely mechanism responsible for macroscopic particle ejection.

Copola et al. [2002] attempted to grow *i*-ACF and *i*-Al–Cu–Fe–Cr (*i*-ACFC) thin films from crystalline and QC targets, respectively. Films were grown on different substrate types in order to determine the influence of the substrate crystallinity on the growth mode. Growth on glass and Si(001) substrates at room temperature resulted in amorphous films, though annealing those films grown on Si at around 650°C for 1 h resulted in a mixture of the icosahedral and approximant phases. Growth on metallic substrates (Al or stainless steel) promoted the nucleation of crystalline phases.

In 2003, Brien et al. [2003a] were the first to report the successful growth of Ti-based QC films. They grew *i*-TNZ thin films on $Al_2O_3(0001)$ substrates at an optimal temperature of 275°C using 1064-nm nanosecond laser radiation and a very high laser fluence of $72\,J\,cm^{-2}$. The films were textured and consisted of nanosized grains with the fivefold axes at an angle of approximately 6° from the film normal.

In a subsequent publication, Brien et al. [2003b] reported on a systematic study of the effect of substrate temperature on the microstructure and morphology of *i*-TNZ grown on glass substrates, using both X-ray diffraction and transmission electron microscopy/diffraction. They found that above approximately 100°C, the films transformed from consisting of nanometer-sized grains in an amorphous matrix to being comprised of densely packed quasicrystalline columnar structures with lateral dimensions of the order of 50 nm that seeded from a very thin amorphous initial layer of a few nanometers (see Fig. 25.7).

Willmott et al. [2004] have also grown *i*-TNZ thin films on $Al_2O_3(0001)$ using the fourth harmonic of an Nd : YAG laser (266 nm, 5 ns, $4\,J\,cm^{-2}$, 10 Hz). Deposition experiments were performed in a UHV chamber, with a base pressure of 7×10^{-9} Pa. They adopted a novel approach to the problem of stoichiometric transfer by using a target geometry that allowed any desired alloy stoichiometry of $Ti_xNi_yZr_{1-x-y}$ to be synthesized over a large range of x and y. The ablation target rod consisted of Ti and Zr sections, separated by a short Ni section (see Fig. 25.8). During ablation, the rod was both translated up and down between two turning points at a velocity large enough to ensure that less than 1 ML material was deposited per stroke of the target, resulting in the growth of alloy material.

This approach circumvents some problems associated with using a fixed-composition alloy target. First, the film stoichiometry can be varied over a large range by adjusting the turning points of the translational movement. Second, because each elemental component is ablated sequentially, the problem of incongruent transfer by segregation, preferential ablation, or differential scattering in the plume is circumvented. Lastly, high-purity elemental target material with low oxygen content is easy and cheap to obtain, while similar purity bulk *i*-TNZ targets are both difficult to produce and also tend to form ingots containing open needlelike structures, which promotes the production of macroscopic particles and droplets. In contrast, Ti, Ni, and Zr all behave very well under nanosecond

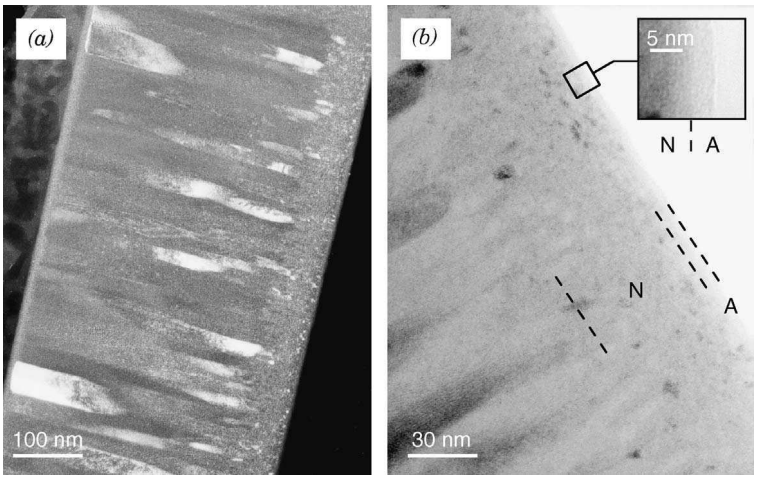

Figure 25.7 Transmission electron microscopy data of an *i*-Ti–Ni–Zr film deposited at 275°C. The columnar quasi-crystal structures seen in the (a) dark-field image extend over the full thickness of the film and have typical widths of 50 nm. In (b), the bright-field image at higher resolution shows that the columnar structures are seeded in a nanocrystalline layer (N) just above a thin amorphous layer (A) in contact with the glass substrate. From Brien et al. [2003b].

ablation [Timm et al., 1996; Willmott and Spillmann, 2002] and no laser droplets on the film were found. The relative deposition rates of the three elemental components, and thereby the required amount of each section of the rod to ablate, were established by Rutherford backscattering spectrometry of the final films.

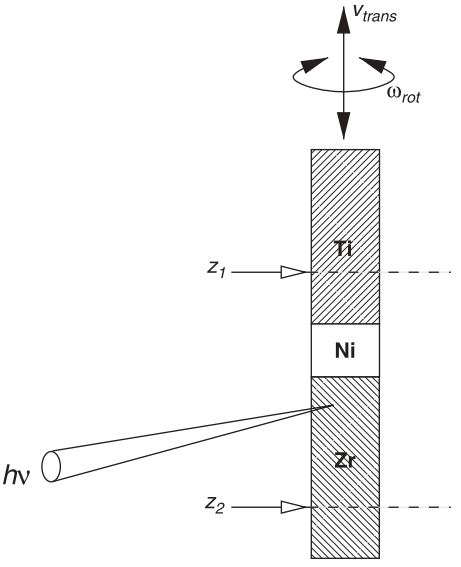

Figure 25.8 Schematic diagram of a compound target rod geometry used for QC thin-film synthesis. During ablation, the rod is translated up and down along its axis with a velocity v_{trans} between the two limits z_1 and z_2 and rotated with an angular velocity ω_{rot}. v_{trans} is sufficiently large that less than 1 atomic layer is deposited for every full stroke of the target rod. Adapted from Willmott et al. [2003a].

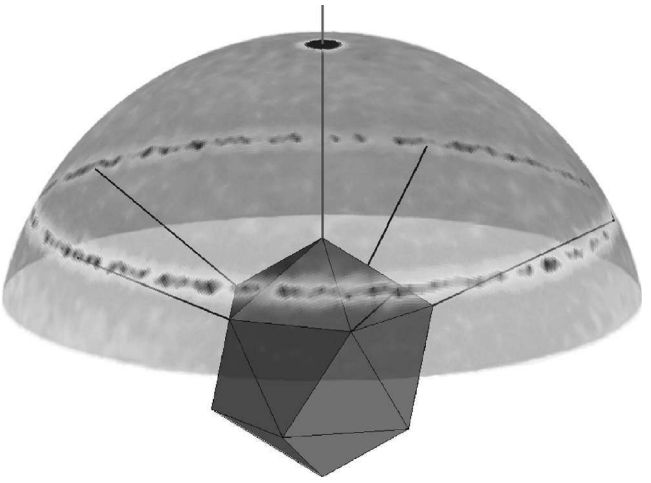

Figure 25.9 Pole figure of the (100000) fivefold reflection of a 100-nm-thick *i*-Ti–Ni–Zr film mapped on to the surface of a hemisphere. An icosahedron has been placed at the center for purposes of understanding. The pole figure shows the out-of-plane texture as the intense spot at the pole, plus a ring that lies exactly at the dodecahedral dihedral angle of 63.43° and demonstrates the random distribution of crystallites around the fivefold axis in the plane of the film. Adapted from Willmott et al. [2005].

The crystallographic properties of the films were similar to those found by Brien et al., although the fivefold axis was shown to point exactly along the surface normal [Willmott et al., 2005]. This was confirmed by pole figures for both the fivefold and twofold reflections (see Fig. 25.9).

In further growth studies performed in situ in a UHV PLD chamber mounted on a 5-circle surface diffractometer at the Materials Science beamline of the Swiss Light Source synchrotron facility at the Paul Scherrer Institute ($\lambda = 1$ Å), the evolution of the QC phase as a function of film thickness was investigated [Willmott et al., 2005]. The results are summarized in Figure 25.10 for in-plane diffraction studies, in which only the upper 30 Å of the film were probed at any one time. They confirmed the general findings suggested by Brien et al. in their scanning electron microscopy (SEM) studies [Brien et al., 2003b] and additionally showed that the initial amorphous layer had an anomalously low density, and that the preferred out-of-plane orientation of the crystallites (along the fivefold axis) only began to dominate after 15 to 20 nm, and was driven by energy minimization of the surface to adopt the most densely packed plane perpendicular to the fivefold axis.

For the same reason, all films showed clear Kiessig fringes in the X-ray reflectivity curves even up to thicknesses well over 100 nm, indicating film roughnesses of the order of 1 nm. This is consistent with modern opinion on the development of surface morphologies of QCs. It is now thought that the role of energetically and mechanically stable clusters [Jeong and Steinhardt, 1994; Mikulla et al., 1998] plays a secondary role to the energy minimization of the closest packed surface, normal to the fivefold axis [Chattopadhyay et al., 1997; Barbier et al., 2002]. Crystallites with other orientations perpendicular to the growth direction hence grow more slowly and are kinetically hindered.

25.4 SUMMARY AND OUTLOOK

Despite both the obvious advantages in fundamental studies and the enormous technological promise of producing QCs as thin films, there has been very little effort to use PLD to this end. This seems surprising, in the light of its otherwise ubiquitous application in synthesizing thin films

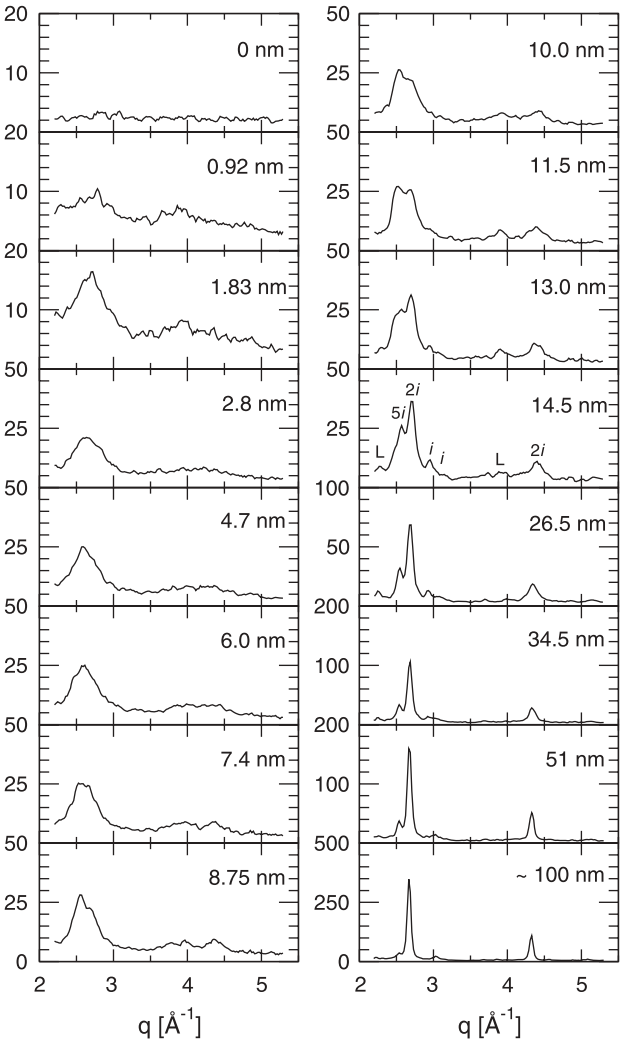

Figure 25.10 In-plane grazing-incidence X-ray diffraction patterns of *i*-Ti–Ni–Zr thin films as a function of the momentum transfer $q = 4\pi \sin \theta/\lambda$ and film thickness. Intensities between different film thicknesses can be directly compared. The XRD pattern for the 14.5-nm film is labeled, as it contains the important features, including the in-plane equivalent (100000) fivefold axis reflection (5*i*), the $(01\bar{1}000)$ and $(0100\bar{1}0)$ twofold reflections (2*i*), two further weak reflections *(i)* associated with the icosahedral phase, and the two Laves phases, (L). Note that, because the twofold icosahedral axes are perpendicular to the fivefold axes, the in-plane patterns are dominated by the two inequivalent twofold reflections as the film become thicker, in agreement with data shown in Figure 25.9. From Willmott et al. [2005].

of other inorganic materials. The reasons are twofold—first, the control required in chemical composition makes QCs perhaps the most challenging class of materials to date, and second, the best vacuum conditions must be maintained in order to avoid the deleterious effects of oxidation and other impurities. A further reason is, perhaps, more based on conventions than science—PLD has traditionally been used for chemically complex materials and materials for which true nonthermal ablation occurs, while metals and alloys have been more the province of sputtering techniques, for which there is a great deal more literature on QC thin-film growth. A comparison of issues relating to

TABLE 25.2 Comparison of Issues Concerned with PLD of QCs, Crystalline Metals/Alloys, and Complex Metal Oxides[a,b]

		Influence of ...					
Material	Laser Desorption Mechanism	Impurities	Deposition Conditions	Changes in Stoichiometry	Deposition Flux	Substrate Orientation, Mismatch	Processing Temperature
QCs	Xstal target: thermal QC target: nonthermal	**Very sensitive to O**	**Very sensitive**	**Critical**	**High instantaneous flux QC phase**	**Low/none**	**No post-annealing needed**
Metals/ Alloys	Thermal	Moderate/ high	Low/ moderate	None/ low	**High K.E. process temp. ⇓, surf, mobility ⇑**	Strong	**Lowered by K.E. of flux**
Oxides	**Nonthermal ("true")**	Low	Low	Moderate (e.g., Pb-containing compounds)	**High K.E. process temp. ⇓, surf, mobility ⇑**	Strong	**Lowered by K.E. of flux**

[a]Comments in bold indicate important issues.
[b]K.E. refers to kinetic energy.

PLD of QCs, crystalline metals and metallic alloys, and complex metal oxides, highlighting the problems faced with QC growth, is given in Table 25.2.

With few exceptions, films grown by sputtering and other techniques only become quasicrystalline after a postannealing process. As was pointed out by Grenet et al., [2002], PLD is notable in that QC thin films can be grown at modest temperatures without the need for further heat treatment. The reasons for this should be further investigated.

All QC films grown by PLD to date have been icosahedral. No decagonal thin films have been grown, although this has been successfully achieved using sputtering [Li et al., 1997; Widjaja and Marks, 2003]. Because decagonal QCs are periodic in one direction, they would be ideally suited for growing ''heteroepitaxially'' and with atomic flatness on conventional crystalline substrates. Such systems could therefore be used for detailed and systematic studies of the microscopic properties of QCs.

Many QCs contain aluminum, and ablation of aluminum-containing alloys is fraught with technological difficulties, due mainly to droplet production, and aluminum's relatively high vapor pressure. Such problems may be ameliorated by using sub-nanosecond laser pulses, though Teghil et al. [2003] found that using pulses of around 1 ps or less also resulted in macroscopic particulate production. An ideal pulse length may lie in the 100–500 ps range.

Finally, the incorporation of thin-film constructions based on QCs in, for example, solar cell or fuel cell applications, presents a formidable challenge. PLD may play an important role in producing such devices, in which widely different material types must be combined in a single device.

Acknowledgments

The author wishes to thank Professor Walter Steurer, Mr. Kai Hassdenteufel, and Professor Patricia Thiel for valuable discussions regarding quasi-crystal growth and critical reading of the manuscript, and Professors Michael Aziz, Craig Arnold, and Hans-Ulrich Krebs for their insights into PLD of metallic alloys.

REFERENCES

Arnold, C. B., and M. J. Aziz (1999), *Appl Phys. A* **69**, S23.

Aziz, M. J. (1996), *Metall. Mater. Trans. A* **27A**, 671.

Barbier, L., D. Le Floc'h, Y. Calvayrac, and D. Gratias (2002), *Phys. Rev. Lett.* **88**, 085506.

Barna, P. B., G. Rodnoczi, A. Csanady, and K. Urban (1988), *Scripta Metall. Mater.* **22**, 373.

Bonasso, N., and P. Pigeat (2003), *Mater. Sci. Eng. A* **349**, 224.

Bonasso, N., P. Pigeat, D. Rouxel, and B. Weber (2002), *Thin Solid Films* **409**, 165.

Brien, V., A. Dauscher, P. Weisbecker, and F. Machizaud (2003a), *Appl. Phys. A* **76**, 187.

Brien, V., A. Dauscher, P. Weisbecker, J. Ghanbaja, and F. Machizaud (2003b), *J. Crystal Growth* **256,** 407.

Chang, S. L., W. B. Chin, C. M. Zhang, C. J. Jenks, and P. A. Thiel (1995), *Surf. Sci.* **337**, 195.

Chattopadhyay, K., N. Ravishankar, and R. Goswami (1997), *Prog. Crystal Growth Charact.* **34**, 237.

Copola, J., F. Audebert, and S. Duhalde (2002), *Mater. Sci. Forum* **403**, 27.

Diaz de la Rubia, T., R. S. Averback, R. Benedek, and W. E. King (1987), *Phys. Rev. Lett.* **59**, 1930.

Eisenhammer, T., and A. Trampert (1997), *Phys. Rev. Lett.* **78**, 262.

Feuerbacher, D., P. Schall, Y. Estrin, and Y. Brechet (2001), *Philos. Mag. Lett.* **81**, 473.

Frank, F. C. (1952), *Proc. R. Soc. London* **215**, 43.

Gilmore, C. B., and J. A. Sprague (1991), *Phys. Rev. B* **44**, 8950.

Grenet, T., F. Giroud, K. Loubet, A. Bergman, G. Safran, J. Labar, P. Barna, J. L. Jouland, and M. Capitan (2002), *J. Alloys Comp.* **342**, 2.

Hennig, R. G., E. H. Majzoub, A. E. Carlsson, K. F. Kelton, C. L. Henley, W. B. Yelon, and S. Misture (2000), *Mater. Sci. Eng.* **294–296**, 361.

Hennig, R. G., K. F. Kelton, A. E. Carlsson, and C. L. Henley (2003), *Phys. Rev. B* **67**, 134202.

Hubler, G. K. (1994), in *Pulsed Laser Deposition of Thin Films,* D. B. Chrisey and G. K. Hubler (Eds.), Wiley, New York.

Hubler, G. K., and J. A. Sprague (1996), *Surf. Coat. Technol.* **81**, 29.

Ichikawa, N., O. Matsumoto, T. Hara, T. Kitahara, T. Yamauchi, T. Matsuda, T. Takeuchi, and U. Mizutani (1994), *Jpn. J. Appl. Phys.* **33**, L736.

Inoue, A., M. Watanabe, H. M. Kimura, F. Takahashi, A. Nagata, and T. Masumoto (1992), *Mater. Trans. JIM* **33**, 723.

Jacobsen, J., B. H. Cooper, and J. P. Sethna (1998), *Phys. Rev. B* **58**, 15847.

Jeong, H.-C., and P. J. Steinhardt (1994), *Phys. Rev. Lett.* **73**, 1943.

Jenks, C. J., and P. A. Thiel (1998), *Langmuir* **14**, 1392.

Kelton, K. (1993), *Int. Mater. Rev.* **38**, 105.

Kelton, K. F., G. W. Lee, A. K. Gangopadhyay, R. W. Hyers, T. J. Rathz, J. R. Rogers, M. B. Robinson, and D. S. Robinson (2003), *Phys. Rev. Lett.* **90**, 195504.

Krebs, H.-U., O. Bremert, M. Störmer, and Y Luo (1995a), *Appl. Surf. Sci.* **86**, 90.

Krebs, H.-U., S. Fähler, and O. Bremert, (1995b), *Appl. Surf. Sci.* **86**, 86.

Li, G., D. Zhang, H. Jiang, W. Lai, W. Liu, and Y. Wang (1997), *Appl. Phys. Lett.* **71**, 897.

McGrath, R., J. Ledieu, E. J. Cox, and R. D. Diehl (2002), *J. Phys. Condens. Matter* **14**, R119.

Mao, S. S., private communication.

Mikulla, R., J. Stadler, F. Krul, H.-R. Trebin, and P. Gumbsch (1998), *Phys. Rev. Lett.* **81**, 3163.

Ohring, M., *Materials Science of Thin Films,* 2nd ed., Academic, San Diego, 2002.

Park, B. (1997), *J. Appl. Phys.* **82**, 4219.

Plenet, J. C., A. Perez, J. Rivory, and O. Laborde (1993), *Phys. Rev. B* **47**, 3021.

Seitz, F., and J. S. Koehler (1956), *Solid State Phys.* **2**, 305.

Shechtman, D., I. Blech, D. Gratias, and J. W. Cahn (1984), *Phys. Rev. Lett.* **53**, 1951.

Šonský, J., M. Jelínek, L. Jastrabík, V. Studnička, and D. Chvostová (1997), *Czech. J. Phys.* **47**, 1019.

Stroud, R. M., K. F. Kelton, and S. T. Misture (1997), *J. Mater. Res.* **12**, 434.

Teghil, R., L. D'Alessio, M. A. Simone, M. Zaccagnino, D. Ferro, and D. J. Sordelet (2000), *Appl. Surf. Sci.* **168**, 267.

Teghil, R., L. D'Alessio, A. Santagata, M. Zaccagnino, D. Ferro, and D. J. Sordelet (2003), *Appl. Surf. Sci.* **210**, 307.

Timm, R., P. R. Willmott, and J. R. Huber (1996), *J. Appl. Phys.* **80**, 1794.

Tokarev, V. N., and A. F. H. Kaplan (1999), *J. Phys. D* **32**, 1526.

Turnbull, D., and R. E. Cech (1950), *J. Appl. Phys.* **21**, 804.

van Ingen, R. P., R. H. J. Fastenau, and E. J. Mittemeijer (1994), *J. Appl. Phys.* **76**, 1871.

Viano, A. M., E. H. Majzoub, R. M. Stroud, M. J. Kramer, S. T. Misture, P. C. Gibbons, and K. F. Kelton (1998), *Philos Mag. A* **78**, 131.

Widjaja, E. J., and L. D. Marks (2003), *Philos. Mag. Lett.* **83**, 47.

Willmott, P. R., and J. R. Huber (2000), *Rev. Mod. Phys.* **72**, 315.

Willmott, P. R., and H. Spillmann (2002), *Appl. Surf. Sci.* **197/198**, 432.

Willmott, P. R., R. Herger, and C. M. Schlepütz (2004), *Thin Solid Films* **453/454**, 436.

Willmott, P. R., C. M. Schlepütz, R. Herger, B. D. Patterson, K. Hassdenteufel, and W. Steurer (2005), *Phys. Rev. B* **71**, 094203.

Yoshioka, A., K. Edagawa, K. Kimura, and S. Takeuchi (1995), *Jpn. J. Appl. Phys.* **34**, 1606.

INDEX

Pulsed Laser Deposition of Thin Films: Applications-Led Growth of Functional Materials
Edited by Robert Eason